HAKONE XII

12th International Symposium on High Pressure Low Temperature Plasma Chemistry

Book of Contributed Papers

Trenčianske Teplice, Slovakia
September, 12-17, 2009

Edited by J. Országh, P. Papp, Š. Matejčík

Book of Contributed Papers of 12th International Symposium on High Pressure Low Temperature Plasma Chemistry
Symposium organised by Department of Experimental Physics, Faculty of Mathematics, Physics and Informatics, Comenius University in Bratislava (Slovakia); Society for plasma research and applications in Trenčianske Teplice, 12th-17th September 2010

Editors:	J. Országh, P. Papp, Š. Matejčík
Publisher:	Department of Experimental Physics, Faculty of Mathematics, Physics and Informatics, Comenius University in Bratislava (Slovakia); Society for plasma research and applications in cooperation with Library and Publishing Centre CU, Bratislava, Slovakia
Issued:	September 2010, Bratislava, fist issue
Number of pages:	576
Print:	125 pieces
URL:	http://neon.dpp.fmph.uniba.sk/hakoneXII
ISBN:	978-80-89186-72-3

International Scientific & Organizing Committee

Miroslav CERNAK	(Czech Republic)
Nicolas GHERARDI	(France)
Tony HERBERT	(Ireland)
Haruo ITOH	(Japan)
Ulrich KOGELSCHATZ	(Switzerland)
Masuhiro KOGOMA	(Japan)
Kirill Vadimovich KOZLOV	(Russia)
Matti LAAN	(Estonia)
Jerzy MIZERACZYK	(Poland)
Massimo REA	(Italy)
Henryka-Danuta STRYCZEWSKA	(Poland)
Hans-Erich WAGNER	(Germany)
Chobei YAMABE	(Japan)

Local Organizing Committee

Stefan MATEJCIK	(Slovakia)
Peter PAPP	(Slovakia)
Juraj ORSZAGH	(Slovakia)
Jan MATUSKA	(Slovakia)
Gabriel HORVATH	(Slovakia)

Reading Committee

Stefan MATEJCIK	(Slovakia)
Peter PAPP	(Slovakia)
Juraj ORSZAGH	(Slovakia)
Gabriel HORVATH	(Slovakia)
Anna ZAHORANOVA	(Slovakia)
Miroslav CERNAK	(Slovakia)

Organizers

Department of Experimental Physics, Faculty of Mathematics, Physics and Informatics, Comenius University, Bratislava, Slovakia

Society for Plasma Research and Applications, Bratislava, Slovakia



Professor Ján Dušan Skalný
1944 – 2008

PREFACE

Slovakia hosts the HAKONE conference for the second time already. The first conference took place in Bratislava in 1995 and Prof. Ján Dušan Skalný was the chair of the LOC. Ján Dušan Skalný passed away suddenly on October 17, 2008 and the local organising committee would like to dedicate the HAKONE XII conference to him. He was a member of the International Scientific Committee of the HAKONE conference for many years and it was his effort to host HAKONE XII in Slovakia. He planned that this conference will be his farewell with this community.

Ján Dušan Skalný will always be associated with the Comenius University in Bratislava, where he spent his whole professional career as a scientist and teacher. His original research was focused on the development of high pressure discharges, especially corona discharge and it was a field in which he established an international reputation. He was member of several international scientific committees (e.g. HAKONE, SAPP, ESCAMPIG) and a referee of many journals, always providing authors a thoughtful insight and often a list of relevant references they had not quoted! Ján Dušan Skalný also willingly organised many conferences (e.g. HAKONE, ESCAMPIG, and many SAPP meetings), always taking great care not only to ensure a strong scientific programme but that the conference has plenty of time for networking and building those personal links that lead to so much of our science.

The HAKONE XII conference is taking place in Trenčianske Teplice in Slovakia. At the conference 125 scientists are participating, arriving from 20 different countries. The participants submitted 125 regular papers in 9 different topics.

The local organising committee wishes that you enjoy the conference, that the conference is productive for you and that it will contribute to further development in the field of high pressure discharges and the high pressure plasma chemistry.

Bratislava, September 2010

Štefan Matejčík
Chair of HAKONE XII LOC

SPONSORS


EPJ AP
Applied Physics


Heinzinger®
power supplies
supplies your world


PFEIFFER VACUUM


MESTO
TRENČIANSKE TEPLICE

OmniStar™



The new Gas Analysis Systems!

Modular Design. Intelligent Software.
Wide Range of Applications.

- Qualitative and quantitative gas analysis
- Low detection limit
- Compact, easy-to-operate analysis unit
- Heated capillary inlet, up to 350 °C
- Utmost sensitivity thanks to enclosed ion source and field axis technology
- Monitoring of up to 128 masses
- Mass ranges up to 300 amu



PFEIFFER VACUUM

Pfeiffer-Vacuum Austria · Pobočka Praha
Novodvorská 1010/14 B · 142 01 Praha 4
office@pfeiffer-vacuum.cz · Tel. 00420 257 923 888

www.pfeiffer-vacuum.net

TRENČIANSKE TEPLICE

Town Trenčianske Teplice lies in the valley of the river Teplička at the foothill of Strážov mountains, 272 metres above sea level.

In Trenčianske Teplice there are used 5 natural healing springs. Water is sulphated, of calcium and magnesium and sulphuric. Its composition is favourable for curing inflammatory and degenerative diseases of the locomotive apparatus. Baths are also suitable for treatment of neurological diseases while water drinking positively influences digestive track.

Trenčianske Teplice offers ideal conditions for congress tourism, bat sports - tenis, touristic are very popular, too. We can not omitt agritourism, mainly horse-riding in the nearby region in Omšenie or Motešice. In 50km distance are located some very well equipped ski centres.

Annually there are held a lot of significant events in Trenčianske Teplice.

- Karel Čapek prize
- Film festival Art Film and awarding of the prize Actor´s Mission. On this occassion an award - brass tablet – is placed on the Bridge of Fame. There are awards for such filmstars as Gina Lolobrigida, Sophia Loren, Jean-Paul Belmondo, Franco Nero and many others.
- Musical Summer, the oldest music festival in Slovakia, which succeeded the Central European festival of chamber music that was first introduced in 1937
- Festival of folk handicrafts
- Equestrian competition with the first prize – Award of the town mayor



CONTENTS

	B. Bernecker, T. Callegari, J.-P. BOEUF	
T1IL	PATTERN FORMATION IN DIELECTRIC BARRIER DISCHARGES	19
	M. ALLAN, O. May, D. Kubala	
T2IL	MEASURING ABSOLUTE ELECTRON-ATOM AND ELECTRON-MOLECULE CROSS SECTIONS RELEVANT TO PLASMAS	31
	Y. AKISHEV, G. Aponin, A. Balakirev, M. Grushin, V. Karalnik, A. Petryakov, N. Trushkin	
T4IL	INTERPLAY OF VOLUME AND SURFACE PROCESSES IN THE SUSTAINING OF MICRODISCHARGES IN STEADY-STATE DBD	38
	H.-H. KIM, A. Ogata	
T6IL	NONTHERMAL PLASMA ACTIVATES CATALYST: FROM CURRENT UNDERSTANDING AND FUTURE PROSPECTS	43
	K.-D. WELTMANN, T. v. Woedtke	
T8IL	BASIC REQUIREMENTS FOR PLASMA SOURCES IN MEDICINE	56
	M. JANDA, A. Niková, V. Martišovitš, Z. Machala	
T1O1	TRANSIENT SPARK - DC DRIVEN NANOSECOND PULSED DISCHARGE IN ATMOSPHERIC AIR	69
	J. PODLIŃSKI, A. Berendt, J. Mizeraczyk	
T1O2	ELONGATED DBD WITH FLOATING ELECTRODES FOR ACTUATORS	74
	M. SABO, Š. Matejčík	
T1O3	USING IMS EQUIPED WITH CORONA DISCHARGE TO DETECT TRACE AMOUNTS OF IMPURITIES IN HIGH PURITY NITROGEN	79
	M. V. SOKOLOVA, K. V. Kozlov, S. A. Krivov, L. A. Maslova, A. N. Mitin, P. A. Tatarenko, V. G. Samoilovich	
T1O4	THE INFLUENCE OF DIELECTRIC FILMS ON THE MACRO- AND MICROSCOPIC PROPERTIES OF THE BARRIER SURFACE DISCHARGES	84
	H. Luo, X. WANG, Z. Liang, Z. Guan, L. Wang	
T1O5	STUDY OF DIELECTRIC BARRIER DISCHARGE IN NITROGEN AT ATMOSPHERIC PRESSURE	89
	Y. YOSHIOKA, N. Osawa	
T1O6	CONDITIONS OF GENERATING THE ATMOSPHERIC PRESSURE TOWNSEND DISCHARGE IN AIR BY THE BARRIER DISCHARGE DEVICE USING ALUMINA AS A BARRIER MATERIAL	94
	M. ČERNÁK, A. Zahoranová, J. Halanda, J. Kúdelčík	
T1P2	PRACTICAL IMPLICATIONS OF THE STREAMER THEORY FOR NEGATIVE CORONA TRICHEL PULSES	99
	M. DANKO, J. Országh, A. Ribar, J. Kočíšek, Š. Matejčík	
T1P3	ELECTRON IMPACT EXCITATION OF THE SECOND POSITIVE SYSTEM OF N_2	103
	Y. KANO, Y . Ehara	
T1P4	DISCHARGE PROPERTY OF POROUS CERAMIC ELECTRODE	108
	M. KLAS, Š. Matejčík	
T1P5	DC BREAKDOWN IN AIR, OXYGEN AND NITROGEN AT MICROMETER SEPARATIONS	112
	M. KUČERA, M. Stano, Š. Matejčík	
T1P6	MEASUREMENT OF ELECTRON ATTACHMENT RATE TO O_2 AT AMBIENT PRESSURE USING IMS	117

	J. MATÚŠKA, M. Krajči, J. Urban, Š. Matejčík	
T1P7	THEORETICAL DETERMINATION OF THE MOBILITY OF NO_3^- ION IN NITROGEN DRIFT GAS	122
	Y. OKUYAMA, S. Suzuki, H. Itoh	
T1P8	NEGATIVE ION MOBILITY IN O_2/O_3 MIXTURES MEASURED BY VARYING O_3 CONCENTRATION AT ATMOSPHERIC PRESSURE	126
	A. Berendt, J. PODLIŃSKI, J. Mizeraczyk	
T1P9	SAW-LIKE ELECTRODES FOR DBD PLASMA ACTUATORS	131
	M. SABO, Š. Matejčík	
T1P10	IMS/MS AND APCDIMS STUDY OF NEGATIVE CORONA DISCHARGE IN HIGH PURITY O_2	136
	L. STOLLENWERK, U. Stroth	
T1P11	SPATIO-TEMPORAL AND GLOBAL SURFACE CHARGE MEASUREMENT IN A PATTERNED DBD	141
	S. SUZUKI, H. Itoh	
T1P12	COLLISIONAL QUENCHING OF $N_2(A^3\Sigma_u^+)$ BY XYLENE AND THIN FILM DEPOSITION ON ELECTRODE	146
	T. Sekizawa, Y. Kashiwagi, S. SUZUKI, H. Itoh	
T1P13	DETERMINATION OF SECONDARY IONIZATION COEFFICIENT OF MgO	151
	M. Bogaczyk, G. Fedoseev, R. Wild, H.-E. WAGNER	
T1P14	INVESTIGATION OF BARRIER DISCHARGE IN He/N_2 MIXTURES BY CROSS-CORRELATION SPECTROSCOPY AND SURFACE CHARGE MEASUREMENTS	156
	N. Bonifaci, Z. Li, A. Denat, V. ATRAZHEV, V. Shakhatov	
T2O1	SPECTROSCOPIC INVESTIGATIONS OF CORONA DISCHARGE IN HIGH PRESSURE HELIUM AT 300K	163
	R. BRANDENBURG, H. Grosch, T. Hoder, K.-D. Weltmann	
T2O2	PHASE RESOLVED CROSS-CORRELATION SPECTROSCOPY ON SURFACE BARRIER DISCHARGES IN AIR AT ATMOSPHERIC PRESSURE	168
	J. JÁNSKÝ, F. Tholin, Z. Bonaventura, A. Bourdon	
T2O3	SIMULATION OF THE DISCHARGE PROPAGATION IN A CAPPILARY GLASS TUBE IN AIR AT ATMOSPHERIC PRESSURE	173
	K. KOZLOV, V. Korolenko, A. Zagoskin, T. Nikitina, V. Samoilovich	
T2O4	SPATIALLY RESOLVED KINETIC SPECTROSCOPY OF THE ATMOSPHERIC PRESSURE BARRIER DISCHARGE PLASMA TORCH	178
	B. M. OBRADOVIĆ, S. Ivković, N. Cvetanović, M. M. Kuraica, J. Purić	
T2O5	TIME-SPACE RESOLVED MEASUREMENT OF ELECTRIC FIELD IN DIELECTRIC BARRIER DISCHARGE IN HELIUM	183
	M. ŠIMEK	
T2O6	ICCD MICROSCOPY AND SPECTROSCOPY OF A SINGLE SURFACE COPLANAR DBD MICRO-DISCHARGE DRIVEN IN N_2, O_2 AND IN SYNTHETIC AIR AT ATMOSPHERIC PRESSURE	188
	C. Klett, S. Touchard, A. Vega, M. Redolfi, X. DUTEN, K. Hassouni	
T2O7	AN EXPERIMENTAL AND MODELLING STUDY OF ACETALDEHYDE OXIDATION BY AN ATMOSPHERIC NON-THERMAL PLASMA DISCHARGE	193
	S. Gaychet, H. Grosch, T. Hoder, D. Bessières, A. Bourdon, F. Lemont, R. BRANDENBURG, N. Soulem, J.-H. Paillol	
T2P1	INVESTIGATION OF THE TRICHEL DISCHARGE IN AIR AT ATMOSPHERIC PRESSURE BY INTENSIFIED CCD CAMERA AND CROSS-CORRELATION SPECTROSCOPY	198

	A. ANNUŠOVÁ, P. Čermák, J. Rakovský, V. Martišovitš, P. Veis	
T2P2	TIME RESOLVED BROADBAND SPECTROSCOPY OF DBD OPERATING FROM HOMOGENOUS TO FILAMENTARY REGIME IN PURE N_2 WITH O_2 TRACES	202
	T. HODER, M. Černák, H.-E. Wagner	
T2P4	SURFACE DISCHARGE DEVELOPMENT IN COPLANAR BARRIER DISCHARGE AT OVERVOLTAGE AND REDUCED PRESSURE IN AIR	207
	F. Tholin, Z. Bonaventura, S. Celestin, J. JANSKY, A. Bourdon	
T2P5	INFLUENCE OF AMBIENT GAS TEMPERATURE ON THE GLOW REGIME OF NANOSECOND REPETITIVELY PULSED DISCHARGES BETWEEN TWO POINT ELECTRODES IN AIR AT ATMOSPHERIC PRESSURE	212
	M. KOCIK, M. Tański, J. Mizeraczyk, R. Ichiki, S. Kanazawa, J. Dembski	
T2P6	RECONSTRUCTION OF 3D STRUCTURE OF POSITIVE CORONA STREAMER BY LOCAL METHODS	217
	P. MACH, M. Krajči, J. Matúška, J. Urban	
T2P7	THEORETICAL STUDY OF INTERACTIONS OF NO_3^- WITH NEUTRAL MOLECULES	221
	L. Leštinská, V. Martišovitš, Z. MACHALA	
T2P8	CORONA AS A TEMPERATURE PROBE FOR ATMOSPHERIC AIR MICROWAVE PLASMA	223
	O. A. NEDYBALIUK, S. V. Olszewski, V. Ya. Chernyak	
T2P10	PLASMA-LIQUID SYSTEM WITH REVERSE VORTEX FLOW OF “TORNADO” TYPE	228
	D. Skacelova, P. SLAVICEK	
T2P11	ELECTRON DENSITY OF PLASMA PENCIL DISCHARGE ESTIMATED BY BROADENING OF THE SPECTRAL ATOMIC LINES	233
	X. TU, H. J. Gallon, J. C. Whitehead	
T2P12	ELECTRICAL AND SPECTROSCOPIC DIAGNOSTICS OF ATMOSPHERIC NITROGEN DIELECTRIC BARRIER DISCHARGE: EFFECT OF PACKING CATALYSTS	238
	M. VISSER, A. Schenk, K.-H. Gericke	
T2P14	TIME AND SPACE RESOLVED NH AND NH_2 DENSITIES IN AN RF MICROPLASMA	243
	R. WILD, M. Bogaczyk, H.-E. Wagner	
T2P15	THE INFLUENCE OF DIFFERENT ELECTRODE CONFIGURATIONS ON BARRIER DISCHARGES IN ARGON AND HELIUM AT ATMOSPHERIC PRESSURE	248
	H. J. GALLON, X. Tu, M. V. Twigg, J. C. Whitehead	
T3O1	PLASMA REDUCTION OF A NiO/Al_2O_3 CATALYST FOR DRY REFORMING OF CH_4	255
	G. HORVATH, F. Krcma, L. Polachova, K. Klohnova, N. J. Mason, M. Zahoran, S. Matejcik	
T3P2	AN OPTICAL EMISSION SPECTROSCOPY OF ATMOSPHERIC GLOW DISCHARGE BETWEEN SHAPED ELECTRODES IN CH_4-N_2 GAS MIXTURE	260
	J. ORSZÁGH, M. Duffy, Z. Lichvanová, C. Sima, Š. Matejčík, N. J. Mason, P. Papp, R. Vladoiu	
T3P4	GENERATION OF CARBON MONOXIDE IN POSITIVE CORONA DISCHARGE FED BY MIXTURE OF CARBON DIOXIDE WITH ARGON AND HELIUM	265
	L. POLACHOVA, G. Horvath, F. Krcma, K. Klohnova, N. J. Mason, M. Zahoran, S. Matejcik	
T3P5	TITAN’S ATMOSPHERE CHEMISTRY SIMULATION IN ATMOSPHERIC GLOW DISCHARGE	270

	J. VYHNALÍKOVÁ, F. Krčma, R. Balaštíkova	
T3P6	DECOMPOSITION OF VOC IN SURFACE AND VOLUME DIELECTRIC BARRIER DISCHARGES COMBINED WITH IN SITU PHOTOCATALYZIS	275
	N. OSAWA, H. Kaga, Y. Fukuda, S. Harada, Y. Yoshioka, R. Hanaoka	
T4O1	COMPARISON OF THE OZONE GENERATION EFFICIENCY BY TWO DIFFERENT DISCHARGE MODES OF DIELECTRIC BARRIER DISCHARGE	282
	S. PEKÁREK	
T4O2	NON TRADITIONAL APPROACHES LEADING TO ENHANCED OZONE GENERATION	287
	M. TAGUCHI, Y. Ochiai, R. Kawagoe, Y. Kato, K. Teranishi, S. Suzuki, H. Itoh	
T4O3	INVESTIGATION OF OZONE ZERO PHENOMENON USING NEW ELECTRODE AND SURFACE ANALYSIS TECHNIQUE	291
	C. YAMABE, S. Gnapowski, K. Kayashima, S. Ihara	
T4O4	OZONE-ZERO PHENOMENA AND A NITROGEN ADDITION EFFECT ON AN OZONE GENERATION	296
	S. JODZIS	
T4P1	OZONE SYNTHESIS UNDER MIXED CORONA-SURFACE DISCHARGES CONDITION	301
	F. KRČMA, Z. Kozáková, E. Krejsková, I. Halamová V. Sázavská	
T4P2	INFLUENCE OF SOLID SURFACE MATERIAL ON OZONE DECOMPOSITION	306
	M. Salvermoser, U. KOGELSCHATZ	
T4P3	INFLUENCE OF HUMIDITY ON THE YIELD OF OZONE GENERATORS	311
	M. TAGUCHI, Y. Kato, H. Itoh	
T4P4	PROPERTIES OF OZONE GENERATION USING HIGH PURITY OXYGEN GAS	316
	K. TERANISHI, Y. Takano, T. Anabuki, N. Shimomura, S. Suzuki, H. Itoh	
T4P5	A COMPACT OZONE GENERATION SYSTEM USING PIEZOELECTRIC TRANSFORMER	321
	K. TERANISHI, Y. Shimada, N. Shimomura, H. Itoh	
T4P6	MEASUREMENT OF OZONE CONCENTRATION BASED ON VISIBLE PHOTO-ABSORPTION METHOD	325
	M. M. GUIVAN, A. A. Malinina, H. M. Guyvan	
T5P1	MULTI-WAVELENGTH MODE OF DIELECTRIC BARRIER DISCHARGE OPERATED WITH THE MERCURY BROMIDE/RARE GASES MIXTURES	332
	I. JÕGI, V. Bichevin, V. Sabre, A. Haljaste, M. Laan, H. Käämbre	
T6O1	NO OXIDATION BY DIELECTRIC BARRIER DISCHARGE AND CATALYST: EFFECT OF TEMPEREATURE AND WATER VAPOR	338
	S. Pstrągowska, M. Młotek, J. Sentek, B. Ulejczyk, K. KRAWCZYK, K. Schmidt-Szałowski	
T6O2	METHANE CONVERSION WITH CARBON DIOXIDE IN PLASMA-CATALYTIC SYSTEM	343
	P. LUKES, M. Clupek, V. Babicky, P. Sunka, E. Spetlikova, J. Rihova Ambrozova, V. Janda, D. Vinklarkova, E. Marsalkova, B. Marsalek	
T6O3	BIOLOGICAL DECONTAMINATION OF WATER BY HIGH POWER DC DIAPHRAGM UNDERWATER DISCHARGE	348
	E. Marotta, M. Schiorlin, E. Ceriani, V. Shapoval, C. Ceretta, M. Rea, C. PARADISI	
T6O4	CHARACTERIZATION OF PLASMA INDUCED PHENOL ADVANCED OXIDATION PROCESS IN DBD REACTOR	353
	K. SATOH, K. Nagao, H. Itoh	
T6O5	DECOMPOSITION CHARACTERISTICS OF BENZENE, TOLUENE AND XYLENE IN AN ATMOSPHERIC DC CORONA DISCHARGE	358

	A. VEGA-GONZÁLEZ, C. Klett, K. Hassouni, S. Touchard, X. Duten	
T6O6	ACETALDEHYDE OXIDATION USING TWO DIFFERENT ATMOSPHERIC PRESSURE NON THERMAL PLASMA / CATALYST CONFIGURATIONS	363
	Y. ITO, Y. Ehara, T. Yamamoto, Y. Oya, M. Iwata	
T6P1	EFFECT ON VOC DECOMPOSITION USING HONEYCOMB TYPE REACTOR	368
	V. KOVAČEVIĆ, B. M. Obradović, M. M. Kuraica, J. Purić	
T6P2	INVESTIGATION OF ELECTRICAL AND SPECTRAL CHARACTERISTICS OF WATER FALLING FILM DBD IN DIFFERENT GASES	371
	A. Górska, K. KRAWCZYK, K. Schmidt-Szałowski	
T6P3	NON-OXIDATIVE METHANE COUPLING IN HYBRID PLASMA-CATALYTIC SYSTEM	376
	M. KUBOSHIMA, Y. Kawamoto, Y. Ehara, T. Yamamoto, A. Zukeran, H. Kawakami	
T6P4	STUDY OF DIESEL EXHAUST PARTICLE COLLECTION USING ELECTROSTATIC PRECIPITATOR	381
	B. P. Dojčinović, B. M. Obradović, D. Manojlović, G. M. Roglić, M. Kostić, M. M. KURAICA	
T6P5	DECOLORIZATION OF FOUR AZO DYES USING WATER FALLING FILM DBD REACTOR	385
	T. MIMURA, Y. Ehara, T. Yamamoto	
T6P7	COMPARISON BETWEEN EHD ESP AND CONVENTIONAL ESP FOR COLLECTION OF DIESEL PARTICLES	389
	M. MŁOTEK, K. Krawczyk, B. Ulejczyk, K. Schmidt-Szałowski	
T6P8	PLASMA ASSISTED CONVERSION OF METHANE AND CARBON DIOXIDE	394
	L. NEMCOVA, F. Krcma, A. Nikiforov, C. Leys	
T6P9	INFLUENCE OF CURRENT AND KIND OF GAS ON THE HYDROGEN PEROXIDE GENERATION IN THE WATER SOLUTIONS	398
	O. Koeta, N. Blin-Simiand, S. PASQUIERS, A. Bary, F. Jorand, C. Postel	
T6P10	REMOVAL OF ACETALDEHYDE BY A DIELECTRIC BARRIER DISCHARGE: EFFECT OF TEMPERATURE AND OXYGEN PERCENTAGE	402
	J. PAWŁAT, H. D. Stryczewska, K. Ebihara, F. Mitsugi	
T6P11	PLASMA STERILIZATION FOR BACTERICIDAL SOIL CONDITIONING	407
	N. PINHÃO, A. Janeco, J. Branco	
T6P12	OXIDATION OF METHANE IN $He/CH_4/CO_2$ MIXTURES: EXPERIMENTAL RESULTS AND ELECTRON KINETICS	412
	D. PIROI, M. Magureanu, N. B. Mandache, V. Parvulescu	
T6P13	REMOVAL OF ORGANIC POLLUTANTS FROM WATER USING NON-THERMAL PLASMA	417
	G. B. SRETENOVIĆ, B. M. Obradović, V. V. Kovačević, M. M. Kuraica	
T6P15	PULSED CORONA DRIVEN BY A COMPACT REPETITIVE MARX GENERATOR	422
	I. TOTHOVA, P. Lukes, M. Clupek, V. Babicky, V. Janda	
T6P16	CHEMICAL ACTIVITY OF THE PULSED CORONA DISCHARGE IN WATER IN DEPENDENCE ON SOLUTION CONDUCTIVITY – YIELDS OF H_2O_2 AND H_2	427
	B. ULEJCZYK, S. Jodzis, K. Krawczyk, K. Schmidt-Szałowski	
T6P17	CONVERSION OF TETRACHLOROMETHANE BY PULSED CORONA DISCHARGE	432
	V. YUKHYMENKO, V. Chernyak, S. Olszewski, S. Sidoruk, D. Levko, A. Shchedrin, V. Naumov, V. Demchina	
T6P18	INFLUENCE OF THE GAS FLOW ON PLASMA REFORMING OF FUELS IN PLASMA-LIQUID SYSTEM	437

	G. ZVEREVA	
T6P19	INVESTIGATIONS OF WATER VAPOR PHOTOLYSIS BY MEANS OF VUV EXCIMER LAMPS	442
	P. A. F. HERBERT, J. Jaroszyńska-Wolińska	
T7O2	A DIRECT COMPARISON BETWEEN GAS STATE AND ATOMISED LIQUID STATE PRECURSOR IN THE DEPOSITION OF FUNCTIONAL COATINGS BY PIN CORONA PLASMA	448
	D. KOVÁČIK, Z. Tučeková, J. Kubincová, A. Zahoranová, M. Zahoran, M. Černák	
T7O3	STUDY OF EFFECTS RELATED TO THE CONTINUOUS OPERATING REGIME OF DCSBD	453
	M. KOGOMA, K. Tsuji, K. Tanaka	
T7O4	POLYMERIZATION OF ALLYL ALCOHOL USING ATMOSPHERIC PRESSURE GLOW DISCHARGE	458
	I. KULYK, M. Scapinello, M. Stefan	
T7O5	MICRO RAMAN SPECTROSCOPY STUDY OF THE PENETRATION OF THE DBD TREATMENT EFFECT INTO THE WOOL FIBRE	462
	J. Pulpytel, S. Bhatt, F. KRČMA, V. Mazánková, F. Arefi-Khonsari	
T7O7	ATMOSPHERIC PRESSURE PLASMA JET FOR THE DEPOSITION OF OXIDES THIN FILMS AT HIGH RATES	467
	M. KALCZEWSKA, T. Opalińska, M. Więch	
T7P2	EFFECT OF ELECTRODES CONFIGURATION ON POLYIMIDE SURFACE ETCHING PROCESS IN BARRIER DISCHARGE	472
	Y. K. KIM, G. T. Kim	
T7P4	THE EFFECTS OF OXYGEN ON PLASMA-POLYMERIZATION OF HMCTSO USING AN ATMOSPHERIC PRESSURE DIELECTRIC BARRIER DISCHARGE	477
	J. KUBINCOVÁ, D. Kováčik, O. Bogár, A. Zahoranová, M. Černák	
T7P5	PERMANENT HYDROPHILIC SURFACE MODIFICATION OF NONWOVEN FABRICS BY PLASMA INDUCED GRAFTING IN GAS PHASE	481
	V. PRYSIAZHNYI, M. Cernak, P. Vasina	
T7P8	ATMOSPHERIC PRESSURE DCSBD PLASMA TREATMENT OF Al SURFACE: STUDY OF SURFACE MORPHOLOGY AND CHEMICAL COMPOSITION	486
	R.-B. ZENOBIA, Z. Agnieszka, L. Wojciech, K. Aneta, K. Krzysztof	
T7P9	EFFECT OF THE PARAMETERS OF COATING DEPOSITION, FROM DECAMETHYLTETRASILOXANE AS PRECURSOR, ON THEIR TRIBOLOGIC PROPERTIES	491
	D. SKÁCELOVÁ, P. Sťahel, M. Haničinec, M. Černák	
T7P11	INVESTIGATION OF SILICON SURFACE WETTABILITY AFTER PLASMA TREATMENT	496
	Z. SZALAY, Z. Machala, K. Hensel, J. Ráheľ	
T7P12	SELF-CLEANING EFFECT OF Al_2O_3 COPLANAR BARRIER DISCHARGE ELECTRODE WITH TiO_2 FUNCTIONAL COATING	501
	K. TANAKA, K. Takahashi, M. Kogoma	
T7P13	FLUORINE REMOVAL TREATMENT OF POLYTETRAFLUOROETHYLENE SURFACE BY ATMOSPHERIC PRESSURE GLOW PLASMA WITH BORON COMPOUNDS	506
	D. TRUNEC, P. Sťahel, V. Buršíková, L. Zajíčková, F. Studnička, V. Peřina	
T7P14	DEPOSITION OF THIN FILMS IN ATMOSPHERIC PRESSURE HOMOGENEOUS DISCHARGE	511

	A. ZAHORANOVÁ, R. Krumpolec, A. Buček, D. Kováčik, M. Černák	
T7P15	APPLICATION OF LOW-TEMPERATURE PLASMA GENERATED AT ATMOSPHERIC PRESSURE FOR MODIFICATION OF GLASS SURFACES	516
	A. ZAHORANOVÁ, V. Medvecká, D. Kováčik, T. Plecenik, J. Greguš, M. Černák	
T7P16	ACTIVATION OF THE SILICON SUBSTRATES SURFACE IN LOW TEMPERATURE PLASMA GENERATED AT ATMOSPHERIC PRESSURE	521
	T. Izdebski, M. DORS, J. Mizeraczyk	
T8O1	INACTIVATION OF MICROORGANISMS IN RIVER WATER USING ELECTRICAL DISCHARGES	528
	K. LACHMANN, A. Dohse, M. Thomas, S. Pohl, W. Meyring, K. E. J. Dittmar, W. Lindenmeier, C.-P. Klages	
T8O2	SURFACE MODIFICATION OF CLOSED PLASTIC BAGS FOR ADHERENT CELL CULTIVATION	533
	Z. MACHALA, L. Chládeková, M. Pelach, B. Tarabová	
T8O3	BIOCIDAL AGENTS IN BIO-DECONTAMINATION BY DC DISCHARGES IN ATMOSPHERIC AIR	538
T8P1	***K. Landsberg, K. Wende, E. Kindel, R. BRANDENBURG, U. Lindequist, K.-D. Weltmann, T. v. Woedtke***	
	SELECTIVE INACTIVATION OF STAPHYLOCOCCUS EPIDERMIDIS ON HUMAN KERATINOCYTES BY NON-THERMAL ATMOSPHERIC PRESSURE PLASMA JET (APPJ)	544
T8P2	***K. Oehmigen, R. BRANDENBURG, J. Winter, M. Hähnel, K.-D. Weltmann, T. v. Woedtke***	
	PLASMA-WATER-INTERACTIONS IN AMBIENT AIR: CHEMICAL AND ANTIMICROBIAL IMPACTS	549
	A. ULRICH, T. Heindl, T. Dandl, R. Krücken, J. Wieser	
T9O2	LOW ENERGY ELECTRON BEAM DRIVEN RADIOLYSIS	556
	S. PEKÁREK	
T9P1	EFFECT OF THE MAGNETIC FIELD ON ELECTRICAL CHARACTERISTICS OF THE DC CORONA DISCHARGE	561
	S. M. SIDORUK, V. Y. Chernyak, S. V. Olszewski	
T9P3	PULSED PLASMA ASSISTED PYROLYSIS OF ETHANOL	565
	H. D. STRYCZEWSKA, J. Diatczyk, G. Komarzyniec, T. Janowski	
T9P4	INFLUENCE OF ARGON CONCENTRATION ON THE PROCESSING GAS ON GLIDING ARC DISCHARGE'S POWER CONSUMPTION	570

Invited lectures

PATTERN FORMATION IN DIELECTRIC BARRIER DISCHARGES

Benoît Bernecker, Thierry Callegari, Jean-Pierre Boeuf

Université de Toulouse; UPS, INPT; LAPLACE (Laboratoire Plasma et Conversion d'Energie); 118 route de Narbonne, F-31062 Toulouse cedex 9, France.
CNRS; LAPLACE; F-31062 Toulouse, France.
E-mail: jpb@laplace.univ-tlse.fr

The plasma of dielectric barrier discharges (DBDs) operating in a transient glow discharge regime at high pressure exhibits under most conditions a filamentary structure. This filamentary structure is often chaotic in appearance, but under specific conditions the filaments form self-organized patterns that are typical of reaction-diffusion systems. The purpose of this paper is to analyse the mechanisms of pattern formation in DBDs on the basis of numerical simulations and experiments.

1. Streamer, glow discharge, and Townsend regimes of DBDs

The aim of this section is to define clearly the discharge regime that is discussed in this paper. Dielectric Barrier Discharges can operate in streamer, glow discharge, or Townsend regimes. These regimes can be classically defined as follows.

In the streamer regime, the electron multiplication in the gap reaches very large values (on the order of 10^8), so that a single electron avalanche can lead to the formation of a plasma channel. The streamer current is limited by the charging of the dielectric capacitance. In this regime the plasma is filamentary in nature and it is impossible to form a homogeneous plasma for a very long time (a large pre-ionization can help maintaining a uniform plasma for some time, as in gas discharge laser applications).

In the glow discharge regime transient glow discharges form in the gap and are quenched by the charging of the dielectric surface. The properties of these transient discharges are those of classical glow discharges, and they are sustained by electron impact ionisation in the discharge volume and secondary electron emission by ion impact on the surface (in the dc case, the electron multiplication M in the gap is related to the secondary emission coefficient γ by the Townsend criterion $M = 1 + 1/\gamma$). Although all the details of electron emission from a dielectric surface are not completely understood it is clear and well recognized that secondary electron emission by ion impact plays an important role in DBDs (the operation of plasma display panels, which provide a good example of DBD operating in a glow discharge regime, can be very well reproduced by models assuming a given secondary electron emission by ion impact on the dielectric surface[1]). Secondary emission due to the impact of metastables or photons on the dielectric surface can of course contribute to the overall secondary electron emission. These mechanisms are generally second order with respect to secondary emission due to ion impact in the glow discharge regime. For pressure larger than several 10s of torr and electrode length on the order of a few cm, the transient glow discharges that form in a DBD are generally filamentary although homogeneous plasma regimes are in principle possible and have been experimentally observed under very specific conditions[2].

In the Townsend regime, the discharge operates at low current and a quasi-neutral plasma is not present in the gap (the ion density is much larger than the electron density and the electric field is not or only slightly distorted by the space charge). In these conditions it is much easier to obtain a homogeneous discharge than in the glow discharge and streamer regimes.

It is useful to define the limits between the streamer regime and the glow discharge regime and to understand how this limit depends on the gas and pd (pressure x gap length) product. A simple way to do it is to look at the Paschen curves of different gases. More precisely, we have plotted in Fig. 1 the calculated voltage as a function of pd product, corresponding to a constant multiplication in the gap in neon and nitrogen. These curves help understand why, for a pd product of 100 torr.cm (e.g. 1.3 mm at 760 torr) it is possible to obtain a glow discharge regime in neon but not in nitrogen (streamer regime). We assume that the secondary emission coefficient by ion impact on the cathode surface is 0.3 in neon,

and 0.05 in nitrogen. Therefore a discharge could be sustained by a multiplication-secondary emission mechanism if the multiplication is equal to 4.33 $(1+1/\gamma)$ in neon, and 21 in nitrogen.

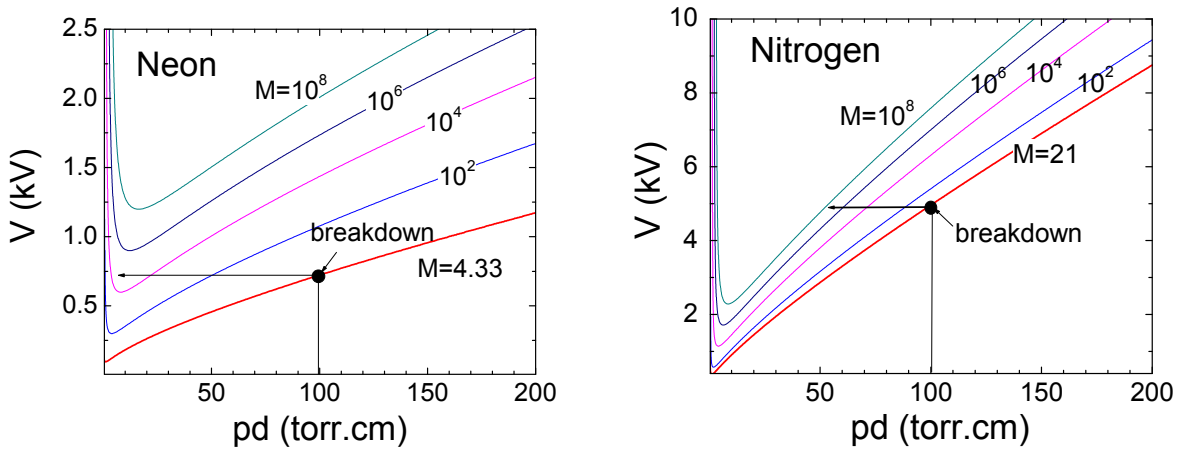


Fig. 1. Voltage vs pd curves corresponding to a constant electron multiplication in neon and nitrogen. The point indicated "breakdown" corresponds to the Townsend breakdown for a pd product of 100 torr.cm in neon and nitrogen, assuming secondary electron emission coefficient equal to 0.3 and 0.05 respectively (i.e. electron multiplication of 4.33 and 21 respectively).

Figure 1 shows that this is possible with an applied voltage of about 720 V in neon, and 5000 V in nitrogen. Let us suppose that voltages slightly above these breakdown voltages are applied to the gap for the neon and nitrogen cases. We assume for simplicity that there is no external circuit (and no dielectric layers). Since the voltage is slightly larger than breakdown, a glow discharge plasma first forms. This process is relatively slow since ions generated by ionisation in the gap must go back to the cathode, generate secondary electrons etc… As the plasma expands, the voltage drop (the applied voltage) takes place over a shorter length between the cathode and the plasma. The multiplication in this region (the transient sheath) therefore increases as approximately shown by the horizontal arrows starting at the breakdown point in Fig. 1 (this is approximate since the field in the sheath between cathode and plasma is not uniform, but the average field is the same as the field used in the calculations corresponding to Fig. 1). We see that in nitrogen, the multiplication can reach values as large as 10^8 as soon as the plasma occupies half of the gap length, while the multiplication stays much lower in neon. This shows that even though Townsend breakdown takes place in both cases, the discharges in nitrogen will generally evolve toward a streamer regime while the discharge in neon will stay in a glow regime. In the case of a DBD, the only way to avoid the streamer regime in nitrogen under similar conditions would be to operate with a very slowly increasing voltage or a very small dielectric layer capacitance. In that case the discharge would operate in a Townsend regime, i.e. the continuous charging of the dielectric would maintain a constant voltage across the gap, equal to the Townsend breakdown voltage, during the rise of the electrode voltage. The Townsend regime of DBDs has been described by Massines et al. in Ref. [3] in the case of nitrogen. Note also that the Townsend regime of DBDs has been used for a long time in Plasma Display Panels[4,1] to generate seed electrons (priming) in all the panel discharge cells before the cells are addressed (in order to prevent addressing failure due to the lack of seed electrons in the cells) and to minimise the light emitted during that phase[1] (in order to keep a good contrast, since the light emitted in the Townsend regime is much less intense than in the glow regime).

One consequence of this discussion is that in the considered range of pd products a homogeneous glow discharge regime is theoretically possible in neon (although difficult to obtain because the glow discharge regime tends to be filamentary in these conditions, as we will see below) but practically impossible to obtain in nitrogen (the streamer regime is by nature filamentary, and a glow regime, even filamentary, seems very difficult to obtain in these conditions in nitrogen).

Basically, a glow discharge regime is possible for a DBD around 100 torr.cm in rare gases like neon or helium where the slope of the breakdown curves of Fig. 1 is relatively small but not in nitrogen. These

differences are due to differences in the variations of the first ionisation coefficient with the reduced electric field. Note that, looking at Fig.1, a glow regime seems possible in nitrogen for smaller pd products, i.e. for example 10 torr.cm (e.g. 130 μm gap at atmospheric pressure).
The results discussed in this paper have been obtained mainly in neon (a few results are shown for helium and nitrogen) and for pd products below 50 torr.cm (typically 2 mm gap and pressure between 50 and 200 torr), i.e. under conditions where, according to Fig. 1, the discharge clearly operates in a glow regime in the case of neon.

2. Experimental set-up and modelling

Experiments have been performed for two different electrode configurations (see Fig. 2). In the first one (Fig. 2a) the electrodes are two disks made out of ITO deposited on a glass layer or of a fine metallic (transparent) grid stuck to a glass layer. In that case the discharges and two-dimensional pattern formations can be observed through the electrodes with a simple camera or a CCD camera. In the second configuration (Fig. 2b) the electrodes are two metallic stripes that are deposited or stuck on the dielectric layers. The width of the electrodes is small and, in the considered conditions, only one filament could form within the electrode width while several filaments could be distributed along the electrode length. The observed structure or pattern was therefore one-dimensional in that case. A similar 1D electrode configuration was used in the paper by Guikema et al[5]. The advantages of the 1D configuration of Fig. 2b are that 1) the filaments can be observed with a CCD camera both along the discharge axis and perpendicular to it, and, 2) the experimental results can be directly compared to results from 2D models of the DBD. However it is clear that the variety of patterns that can be observed in this configuration is not as large as in the configuration of Fig. 2a.

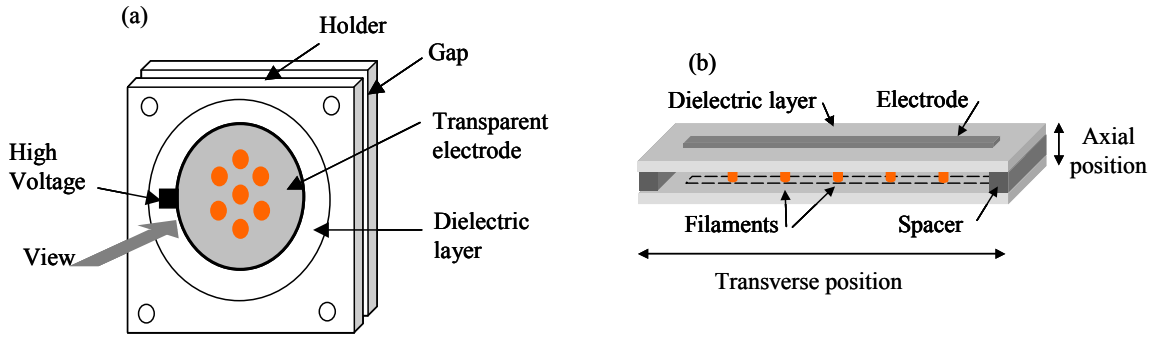


Fig. 2. Configurations of DBDs used in the experiments. In the (a) configuration 2D structures or patterns can be observed through the transparent electrodes. In the (b) configuration the electrodes are linear and 1D structures can be observed. The discharge development between the dielectric surfaces can be easily studied in the (b) configuration but not in the (a) configuration.

The space and time evolution of the filamentary discharges was analysed with an ICCD camera in both configurations of Fig. 2.
In this paper the experimental results in the linear configuration of Fig. 2b are compared with results from a 2D fluid model of the discharge. The model is based on coupled solutions of two-moment electron and ion transport equations and Poisson's equation. The two-moment transport equations consist in continuity and momentum equations in the drift-diffusion form. The set of moment equations is closed by the local equilibrium assumption (ionisation coefficient depends on the local electric field) and by assuming a constant characteristic energy (diffusion coefficient over mobility) for both electrons and ions. These assumptions are standard for collisional plasmas and are used in a number of published papers on DBD or streamer modelling.
The conditions considered in the model results presented in this paper are: DBD in neon, with dielectric thickness and gas gap of 2 mm, electrode length of 2 cm (see Fig. 3), gas pressure from 50 to 200 torrs, voltage frequency on the order of 20 kHz, secondary electron emission coefficient of neon ions on the surface equal to 0.3. Under these conditions the DBDs operate in a transient glow discharge regime.

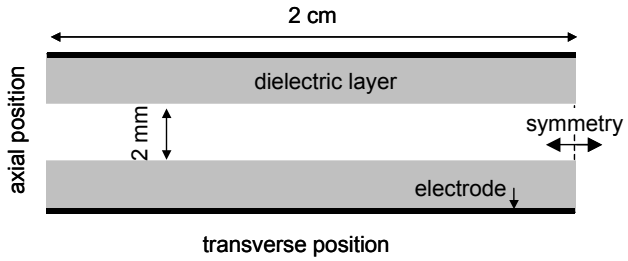


Fig. 3. Electrode and dielectric geometry in the 2D simulations. The thickness of each dielectric layer and the gas gap are 2 mm. The relative permittivity of the dielectric is 5. Symmetry boundary conditions are used on the edge of the simulation domain. This 2D geometry allows to study 1D arrangements of the discharge filaments in the transverse direction, and to observe the discharge formation in the gas gap, as in the experimental linear electrode configuration of Fig. 2b.

The aim of the simulation was not to perform detailed comparisons between model and experiments, but to show how a basic glow discharge model assuming only direct electron impact ionisation and secondary electron emission by ion impact can reproduce many features that can be observed experimentally, and can help us understand the mechanisms of pattern formation in DBDs.

3. Observation and simulation of pattern formation in DBDs

Figure 4 shows three typical pictures of DBDs viewed through the transparent electrode for the 2D electrode geometry of Fig. 2a. The discharge in Fig. 4a appears to be homogenous, Fig. 4b shows a striped pattern and Fig. 4c displays an hexagonal pattern of filaments. These pictures have been obtained in neon and helium (see the figure caption). The structure can change abruptly when one of the control parameters (voltage, frequency, pressure) is slightly changed and bifurcations between different patterns can be observed.

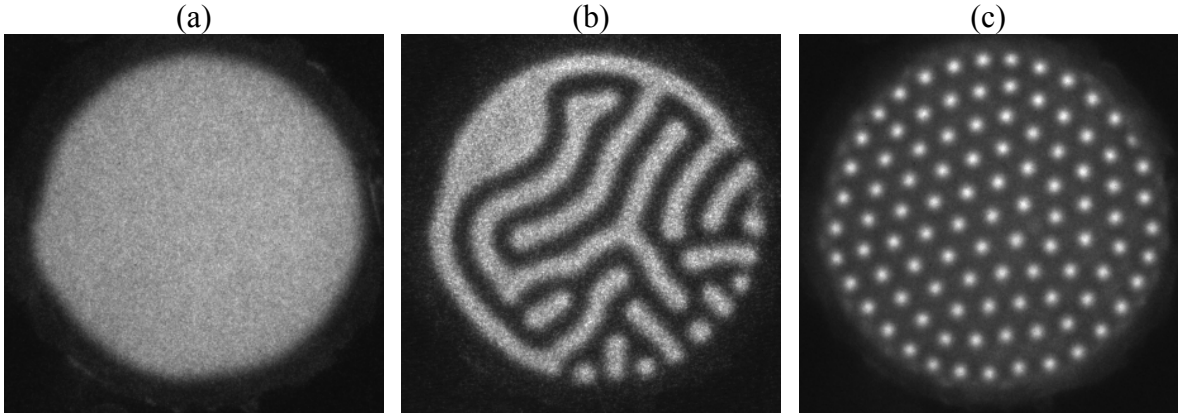


Fig. 4. Typical structures of the plasma in DBDs in the 2D electrode configuration of Fig. 2a, viewed through the transparent electrode. The gas gap and dielectric thickness (each layer) are 1 mm; (a) homogeneous discharge in neon, 400 torr, voltage amplitude U=600 V, frequency f = 20 kHz, exposure time 25 μs (accumulated over 10 ms, i.e. 200 cycles); (b) stripe structure in helium, 100 torr, U= 432 V, f = 50 kHz, exposure time 15 ns over 100 ms; (c) hexagonal filamentary structure in helium with less than 1% argon, 100 torr, U= 464 V, f = 50 kHz, exposure time 10 μs over 10 ms. Reproduction from the PhD thesis of B. Bernecker[6].

Similar and more complex (concentric rings, spirals, target) DBD patterns have been reported in a number of papers and are reported in a recent review by Kogelschatz[7].

Figure 5 illustrates the experimental results obtained with the 1D electrode configuration of Fig. 2b. The discharge in the conditions of Fig. 5 forms a regular 1D array of filaments distributed in space, with a spacing on the order of 8 mm. In these conditions, light is emitted by the discharge along the discharge axis but also close to the dielectric surface. The light emitted along the surface is associated with the spreading of the ion sheath along the dielectric layer on the temporary cathode side, and of the electrons along the layer on the anode side.

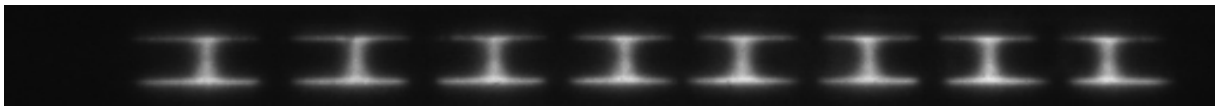


Fig. 5. Example of filamentary structure observed in the 1D electrode arrangement of Fig. 2b (electrode length 7 cm, gas gap 3 mm, dielectric thickness 1 mm) ; nitrogen, 50 torr, 2 kV, 20 kHz. The exposure time is 30 µs and the image is integrated over 10 ms. Reproduction from the PhD thesis of B. Bernecker[6].

It is interesting to look at model predictions under 1D electrode configurations similar to that of Fig. 5. As indicated in the caption to Fig. 3, symmetry boundary conditions are used on the two edges of the simulation domain in the direction perpendicular to the discharge axis. The simulations are performed by assuming a given initial distribution of electrons and ions in the gas gap at t=0, and by calculating the time evolution of the charged particle densities and electric field when a sinusoidal voltage waveform of given amplitude and frequency is applied between the electrodes. The initial density of electrons and ions are chosen equal and generally small (i.e. the gas is weakly ionised and is not plasma at t=0). If the voltage amplitude is above breakdown, a plasma forms over a time duration or number of cycles that depends on the initial density and on the overvoltage. The space distribution of the initial density has an influence on the transient evolution of the discharge toward a "steady state" DBD regime. Because of the symmetry boundary condition on the edges of the simulation domain, one could expect that, if the initial density of electrons and ions is chosen to be uniform in space, the plasma stays homogeneous in the transverse direction during the successive cycles (and current pulses) of the applied voltage. This corresponds to solutions of the model equations where all the transverse gradients are equal to zero (i.e. the solution is 1D along the discharge axis). Although such solution is mathematically possible, it turns out that in most cases, the plasma does not stay homogeneous along the successive cycles, but progressively becomes filamentary. This filamentary state can be stable and periodic, i.e. the same pattern is reproduced cycle after cycle, but can also be apparently chaotic, depending on the conditions. More precisely, an homogeneous solution, identical to the solution that could be obtained with a 1D model can actually be obtained in the 2D simulations, if the length of the electrodes is small enough (e.g. below 1 mm at 50 torr), but the solution becomes filamentary for sufficiently long electrodes (i.e. longer than the spacing between filaments that is obtained at steady state).
The calculated current density for a homogeneous (1D model) DBD in neon at 100 torr, 600 V and 25 kHz voltage amplitude and frequency is shown in Fig. 6. We see that one current pulse appears at each half cycle. This current pulse is associated with the formation of a transient glow discharge in the gap, as shown in Fig. 7.

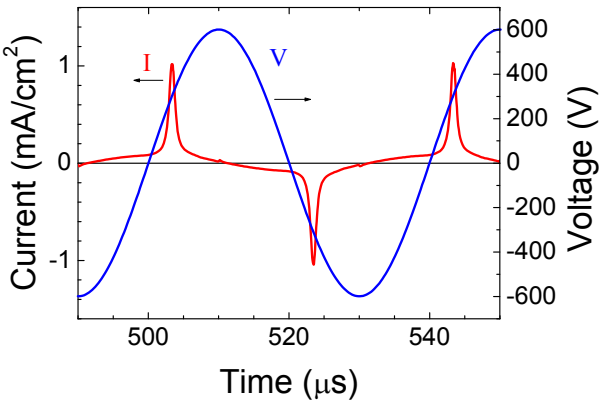


Fig. 6. Applied voltage and calculated current density with a 1D discharge model (or with a 2D model and short electrode length) in neon, 100 torr, gas gap and dielectric layer thickness 2 mm, voltage amplitude 600 V, frequency 25 kHz, secondary electron emission coefficient 0.3.

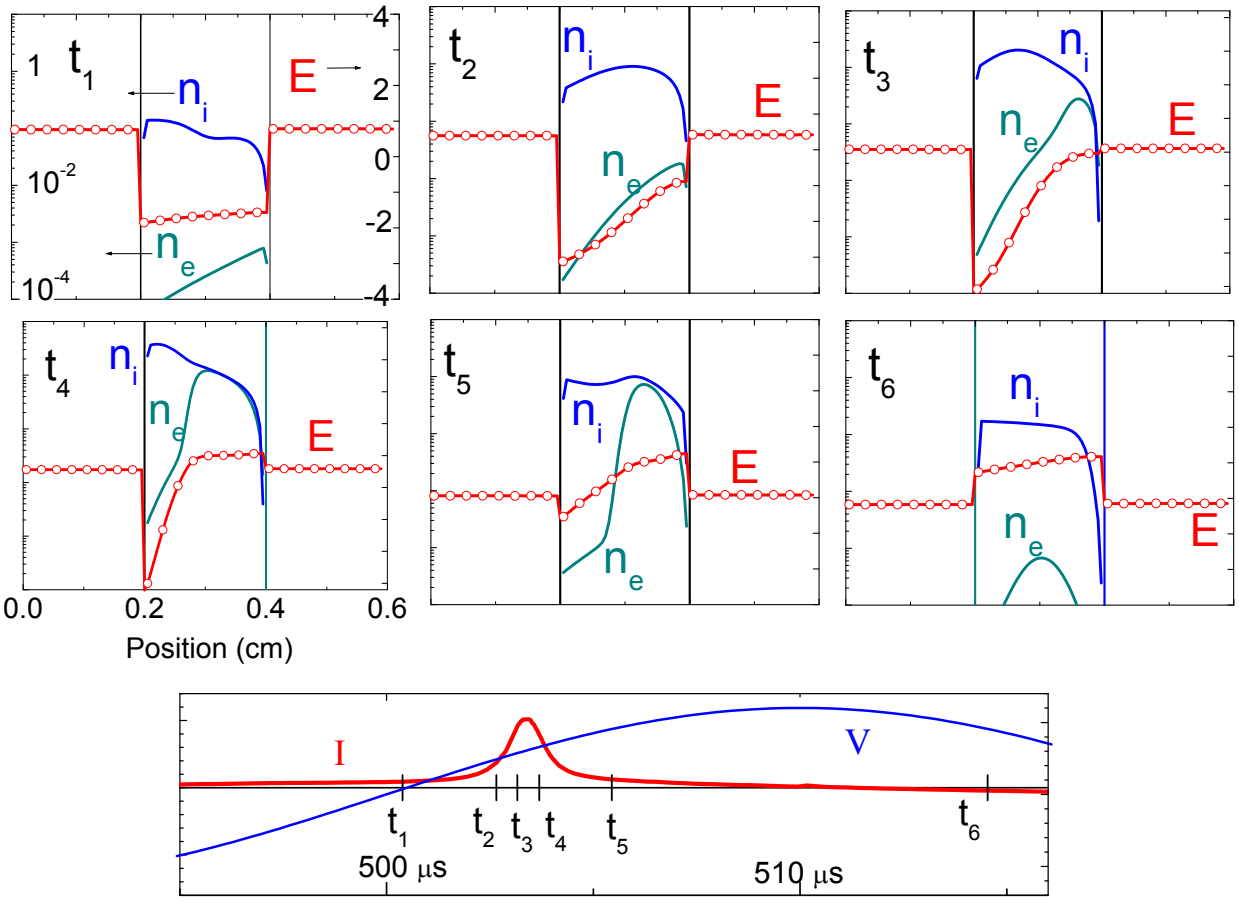


Fig. 7. Axial distributions of the electron, ion densities, and electric field (symbols) at 6 different times (indicated on the current and voltage plots in the bottom of the figure) during the current pulse in the conditions of Fig. 5. The unit of the density is 10^{10}cm^{-3} and the densities are plotted in a log scale between 10^{-4} and 10 x 10^{10} cm^{-3}. The electric field is plotted on a linear scale between –4 and + 4 kV/cm. The position of the dielectric layer surfaces are indicated by the two vertical lines.

The space and time variations of the charged particle densities and electric field displayed in Fig. 7 are typical of a transient glow discharge. We see the pre-breakdown, Townsend phase (t_1) where the ion density is much larger than the electron density but too small to significantly perturb the geometric field. The ion density continues to grow during the breakdown phase and the field become strongly distorted by the ion space charge (t_2) until the plasma forms (t_3) in the anode region and the current starts growing. The sheath and plasma regions are clearly seen during the current pulse (t_3, t_4). The field drops in the gap due to the charging of the dielectric surface (t_5), ambipolar diffusion takes place (t_5) and the plasma decays (t_5, t_6) till the voltage across the gap increases again above the breakdown voltage and a new current pulse forms.

When the length of the electrode is larger than a few mm, the 2D simulation in the conditions of Figs. 6 and 7 no longer gives an homogeneous plasma, and filaments form. Under these conditions, the filaments are self-organized and the spacing between them is on the order of 5 mm, i.e. 4 filaments form when an electrode length of 2 cm is used in the simulations, as in Fig. 8.

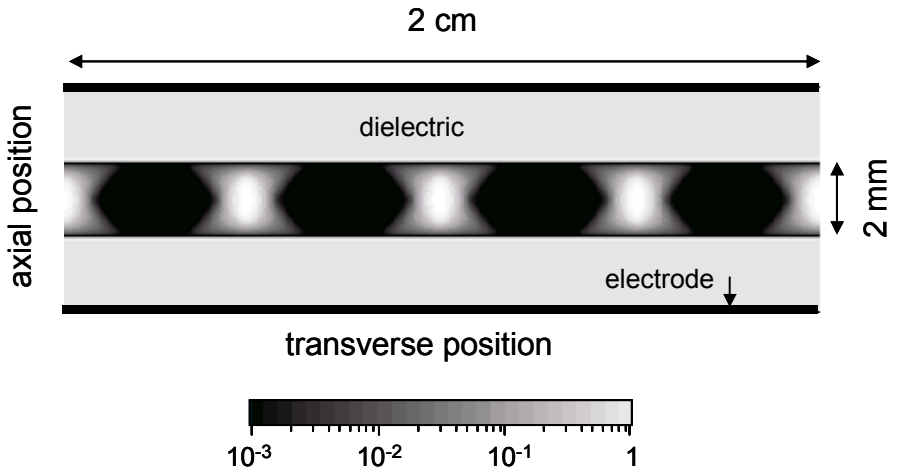


Fig. 8. Electron density averaged over one cycle for a DBD in neon, 100 torr, 600 V and 25 kHz voltage amplitude and frequency (same conditions as Figs. 6 and 7 except that the length of the electrode is now 2 cm and a filamentary pattern has formed). The density is represented in a log scale over 3 decades (dark grey corresponds to low values). The maximum (time averaged over one cycle) density is 7.5 10^9 cm^{-3}.

It is interesting that the periodic structure of Fig. 8 (4 filaments, or 3 filaments and 2 half filaments on the edges of the domain) is obtained whatever the space distribution of the initial density, as shown in Fig. 9 which displays the evolution with the cycle number, of the electron density integrated in the axis direction and time averaged over each cycle for three different initial density distributions.

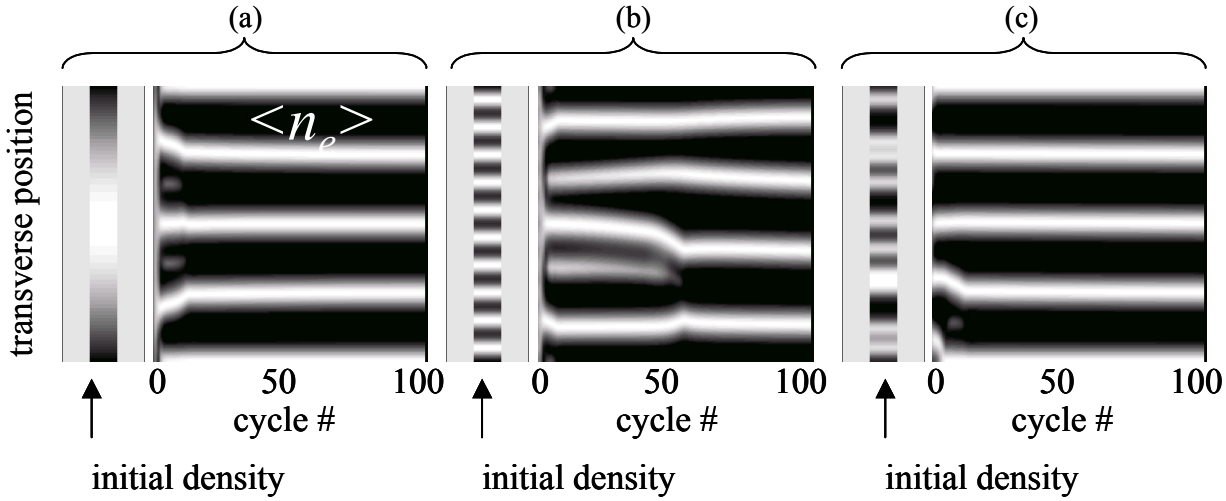


Fig. 9. Time evolution of the transverse electron density integrated along the axis direction and time averaged over each cycle, as a function of the cycle number over 100 cycles, for three different initial density distributions (constant along the discharge axis and non uniform in the transverse direction), in the conditions of Fig. 8. The initial electron and ion density distributions are equal and plotted on the left of each figure (linear grey scale, maximum 10^8 cm^{-3}). The transverse distribution of the electron density is plotted on a 3 decades log scale as in Fig. 8. The initial density of (a) corresponds to an initial Gaussian distribution with a standard deviation of 1 cm, (b) is the sum of 10 Gaussian distributions of standard deviation 0.5 mm each, uniformly distributed along the electrode, and (c) corresponds to the sum of 10 Gaussian distributions of standard deviation 0.5 mm each, randomly distributed along the electrode.

For the initial distribution of Fig. 9b, we see that five filaments first form until a re-organization takes place, two filaments merge, and finally a steady state sets up, with four filaments uniformly distributed along the electrode. When a perfectly uniform initial distribution is assumed (not shown) the system

also evolves toward a four filaments structure similar to those of Fig. 9. In that case, the round-off errors of the simulations play the role of perturbations[8] and the unstable homogeneous solution evolves after a few cycles toward the filamentary structure of Fig. 8.

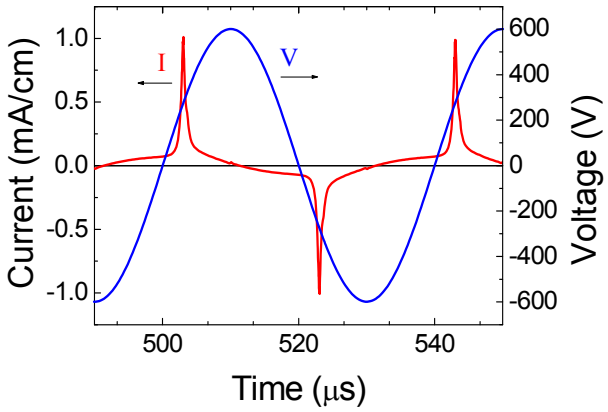


Fig. 10. Applied voltage and calculated current with a 2D discharge model in the conditions of Fig. 8 (electrode length 2 cm). The current density is integrated along the electrode so that the plotted current is given in mA/cm, i.e. per unit length of the electrode in the direction perpendicular to the simulation domain (the discharge is supposed to be homogeneous in this direction in a 2D model).

The calculated current for the filamentary structure of Fig. 8 and displayed in Fig. 10 is very similar to the current density in the homogeneous conditions (Fig. 6), i.e. one current pulse is present at each half cycle. The current in Fig. 10 is integrated along the 2 cm electrode and is given in mA/cm, i.e. per unit length of the electrode in the direction perpendicular to the simulation domain. The peak electron current is around 1 mA/cm, which corresponds to an averaged (along the electrode length) peak current density of 0.5 mA/cm^2 , i.e. smaller than the current density in the homogeneous case. The fact that there is only one current pulse per half cycle for the filamentary structure of Fig. 8 is due to the perfect temporal synchronization of the four filaments in these conditions. The time evolutions of the charged particle densities along the axis of each filament are identical and qualitatively not very different from those obtained in the homogenous regime and plotted in Fig. 7. The values of the maximum densities are however significantly larger in the filamentary structure, compared with the homogeneous case.
The filamentary structure observed in the simulations in the conditions of Fig. 8 is very “standard”, and corresponds to the expected behaviour of stable patterns in DBDs, i.e. each filament is stable and reproduces itself at the same location at each half cycle of the applied voltage. An unexpected structure was observed in the electrode arrangement of Fig. 2a both in the experiments and in the simulations. We call this structure the *quincunx* structure in the following.

(a)

(b)

(c)

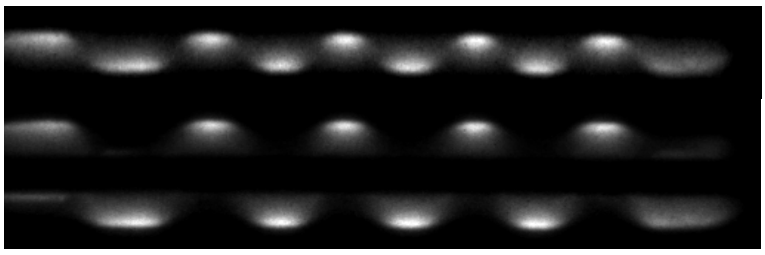


Fig. 11. Experimental observation of a filamentary « quincunx » structure in the linear electrode arrangement of Fig. 2a, in neon, 50 torr, gap length 3 mm, dielectric thickness 1 mm, electrode length 7 cm, voltage amplitude and frequency 524 V and 30 kHz respectively ; the picture of (a) is integrated over one cycle of the applied voltage (and accumulated over several cycles), while the pictures of (b) and (c) are taken over two successive half cycles (the sum of (b) and (c) gives (a)).

Figure 11 shows an example of quincunx structure observed in the experiments. In this filamentary structure, the discharges of two successive half-cycles do not take place at the same locations but the

filaments of a given half-cycle form in between the filaments of the previous half cycle. This result is not at all intuitive and is actually rather surprising but this kind of structure appeared to form in a relatively large range of conditions. We see clearly on Fig. 11 the maximum of light emission on the cathode side, at the plasma-sheath boundary.

We also found that the models could reproduce the intriguing filamentary structures of Fig. 11 (actually these structures were first observed in the simulations, and later in the experiments!). Figure 12 show simulations results under a set of conditions where stable quincunx filamentary structures formed.

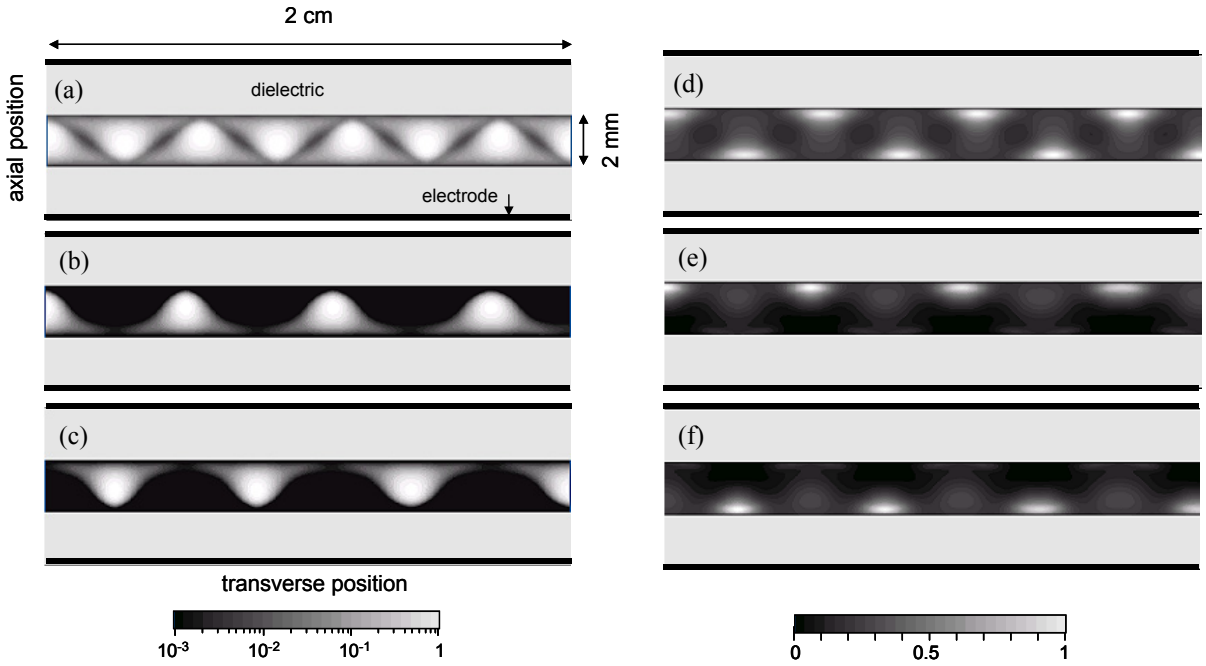


Fig. 12. Space distribution of the electron density (a), (b), (c), and ionisation rate (d), (e), (f) from the 2D model in a quincunx filamentary regime in the geometry of Fig. 3, neon, 50 torr, 700 V and 20 kHz voltage amplitude and frequency ; (a), (d) the density and ionisation rate are averaged over one cycle, (b), (e) over a half-cycle, (c), (g) over the following half-cycle. The densities are plotted on a 3 decades log scale, with a maximum of $2\ 10^{9}$ cm^{-3} for (a) and $4\ 10^{9}$ cm^{-3} for (b), (c). The ionisation rates are on a linear scale with maximum $0.5\ 10^{16}$ $cm^{-3}s^{-1}$ for (d), and 10^{16} $cm^{-3}s^{-1}$ for (e) and (f).

A careful analysis of the numerical results of Fig. 12 helps understanding the quincunx structures. In a "standard" filamentary regime, the charged particle densities between filaments are not necessary zero. Under some conditions, we showed in Ref. [9] that a Townsend discharge can actually forms in between filaments (possibly with some delay in time). The existence of a negative slope part in the current-voltage characteristics of dc discharges can lead to bi-stable regimes or to the coexistence of a Townsend regime and a filamentary glow-discharge regime. The analysis of the simulation results in the quincunx regime shows that during a given half-cycle, a Townsend discharge develops between filaments, around the end of the current pulses associated with the filaments. This discharge is such that at the end of the half-cycle the ion density between filaments is much larger than the density at the locations of the filaments. One expects that, at the next half-cycle, a discharge will develop at the location of the filaments of the previous half-cycle because of the memory charges deposited on the dielectric surface at these locations. In the quincunx regime, there is actually a competition between the effect of the memory charges on the dielectric surfaces at the location of the previous filaments and on the remaining positive charge in the gap between the filaments, and it turns out that the new discharges develop faster where the remaining ion density is larger and the new discharges form in between the previous filaments. In other word, in this competition between the effect of memory charges on the dielectric surface, and of memory charges in the discharge volume, the volume memory charges take over in the quincunx regime.

The quincunx regime has been so far observed in a 1D electrode configuration and it is not clear what would be the equivalent of the quincunx regime in a 2D electrode configuration. We however suspect that the concept of competition between surface charges and volume charges on the development of new discharges at the next half cycle can also be applied to 2D configuration and may be responsible for some of the complex structures or dynamical filament behaviours that are observed in 2D systems.

4. Dynamical aspects of DBD patterns

Under specific conditions, the filaments of DBDs are not static but appear to be moving along the dielectric surface and interact with each other (merging or division of filaments). The filaments motion can be chaotic in appearance but is sometimes organized.
An example of apparent motion of filaments is shown in Fig. 13.

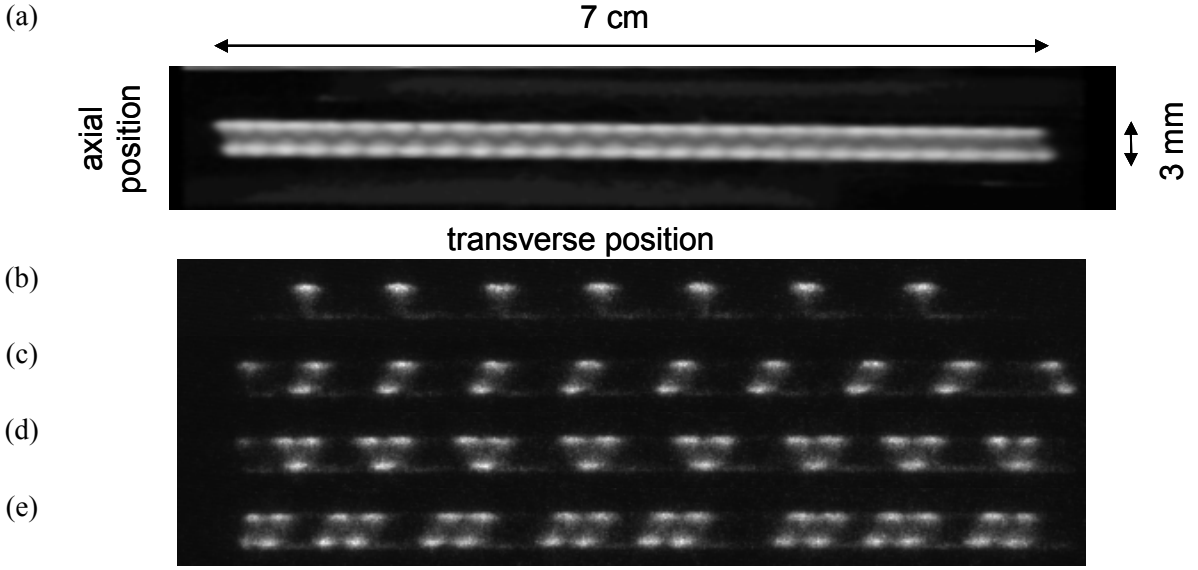


Fig. 13. Multiperiodic filamentary discharge in a 1D DBD experiment in neon, 300 torr, 880 V, 50 kHz, 3 mm gap, 2 mm dielectric layers: (a) time integrated picture of the discharge (standard camera); (b), (c), (d), (e), pictures of the discharge taken with an ICCD camera and integrated over gates of 10, 20, 30, and 40 μs, i.e. 1, 2, 3, 4 half-cycles respectively.

Figure 13a shows the time integrated picture (taken with a standard camera) of an experimental linear DBD in neon, 300 torr, 880 V and 50 kHz voltage amplitude and frequency, 3 mm gap. On this figure, the discharge seems to correspond to a static quincunx filamentary regime similar to the one described above (Fig. 11). Figures 13b, c, d, e actually show that the discharge is more complex and present some dynamical features that are periodic with a period equal to three times the period of the applied voltage. The picture of Fig. 13b has been taken with a gate of 10 μs (i.e. one half-cycle) and show that only 1/3 of the filaments expected in a half-cycle quincunx pattern are actually present. Integrating in time over two successive half-cycles gives the picture of Fig. 13c. The filaments of the second half-cycle are shifted by half a spatial period of the quincunx structure of Fig. 13a (the cathode sheath is on the opposite side with respect to the previous filaments). Figures 13d and 13e show that at each half cycle, the new filaments are shifted by a half a spatial period. The structure of Fig. 13 is therefore not static and presents an apparent organized motion of several filaments from right to left. The period of this motion is equal to 3 periods of the applied voltage (integrating over 6 half-cycles would give a picture close to that of Fig. 13a).
The experimental results of Fig. 13 are very interesting since they show that the motion of filaments can be due to mechanisms similar to those responsible for the existence of the quincunx regime (i.e. remaining charges in the discharge volume close to a filament trigger the next discharge on the side of this filament). The fact that the motion appears to be from right to left in Fig. 13 is not clear (broken symmetry) and may be associated with the discharge history and memory charge effects.
In the 1D electrode configuration of Fig. 13, we were able to capture many other dynamical features (not reported here) of the filaments, such as filament merging and division. Some of these features could be reproduced with the models.

5. DBDs as a reaction-diffusion system

The 2D structures of filamentary patterns in DBDs are very similar to the patterns observed in a variety of biological, chemical, and physical systems (hexagons, stripes, spirals, targets) and that corresponds, for two-component systems (u,v) to solutions of reaction-diffusion equations of the form:

$$\partial_t u - D_u \Delta u = F(u,v)$$

$$\partial_t v - D_v \Delta v = G(u,v)$$

One well known class of reaction-diffusion systems leading to these kinds of pattern are the activator-inhibitor systems (see, e.g., Ref. [10]) which are two-component systems where one component stimulates the production of both components while the other one inhibits their growth (this is also possible with multi-component systems). An important factor leading to the formation of patterns is that the inhibitor must diffuse faster than the activator. Attemps at representing discharges in series with a resistive ("ohmic barrier") layer as activator-inhibitor system have been made by Purwins and coworkers[11]. In order to characterize a DBD as an activator-inhibitor system one must choose the components that play the roles of activator and inhibitor. A possible choice is to define the ion density in the sheath as the activator and the charge on the dielectric surface as the inhibitor: during the transient glow discharge, an increase of ion density in the sheath leads to an increase of the sheath field and therefore of the ionization rate, which in turn leads to an increase of the ion density; the charging of the dielectric layers increases with increasing ion density in the sheath but inhibits the growth of the ion density because it reduces the gap voltage. The spreading of the ion sheath along the dielectric layer leads to a transverse diffusion (or advection) of the inhibitor faster than the diffusion of the activator.

It has been recently shown by Raizer and Mokrov[12] that in ohmic barriers DC discharges in the conditions of those studied by the Purwins group, pattern formation seems to be induced by thermal effects and not by the presence of a negative slope region in the discharge I-V characteristics. This is apparently not the case in DBDs (i.e. discharges with capacitive barriers) since patterns with properties very close to the experimental ones can be reproduced with simple 2D (Refs. [6], [8], and this paper) or 3D[13] models without invoking temperature effects. Developing reaction-diffusion models of DBD discharges less phenomenological than the previous models and able to reproduce the complexity of the observed structures is still a challenge and would be extremely useful to help understand the parameters controlling the different regimes.

6. Conclusion

Dielectric Barrier Discharges exhibit patterns that are typical of reaction-diffusion and activator-inhibitor systems. Simple discharge models based on fundamental, first order mechanisms, i.e. drift-diffusion transport coupled with Poisson's equation, secondary emission by ion impact and volume ionization can reproduce (at least qualitatively) a number of experimental observations.

For 1D electrode configurations, the model can reproduce the formation of periodic 1D structures of filaments that are independent on the initial conditions. The model also predicts the existence of a regime that has not been reported before, and where the filaments of two successive half-cycles are not aligned but are shifted by half a spatial period (i.e. the filaments of a given half-cycle form between the filaments of the previous one). This "quincunx" regime is also observed in the experiments, and bifurcations from the standard filamentary regime to the quincunx regime are observed when one of the discharge parameters is changed. The model results show the importance of the remaining ion density in the gap between filaments at the end of a half-cycle in the emergence of the quincunx structure and in some of the dynamical properties of the filaments.

The transient filamentary discharges of DBDs also present very interesting dynamical aspects. Filament motion along the dielectric surface, merging and division of filaments can be observed when the applied voltage amplitude is decreased or increased, or, in some cases, for constant operating conditions. Some aspects of this non-linear dynamical behaviour also seems to be contained in the basic discharge models.

Finally, note that although the simple discharge models seem to be able to reproduce a number of experimental observations and complex features of the DBD patterns, phenomena that are not included in the basic discharge model used in this paper (Penning ionization, ionization of metastables, secondary emission by metastable impact on the surfaces etc…) can also play a role in the formation and dynamics of patterns, or in the existence or not of a homogeneous regime.

7. References

[1] J.P. Boeuf, "Plasma display panels- physics, recent developments and key issues", J. Phys. D: Appl. Phys. 36, 6 (2003)

[2] F. Massines, A Rabehi, P Decomps, R. B. Gadri, P Ségur, and Ch Mayoux "Experimental and theoretical study of a glow discharge at atmospheric pressure controlled by dielectric barrier" J. Appl. Phys. 83, 2950 (1998)

[3] F. Massines, N. Gherardi, N. Naudé and P. Ségur, "Glow and Townsend dielectric barrier discharge in various atmosphere" Plasma Phys. Control. Fusion 47, B577-B588 (2005)

[4] L. Weber 1998 US Patent 5745086

[5] J. Guikema, N. Miller, J. Niehof, M. Klein, and M. Walhout, "Spontaneous Pattern Formation in an Effectively One-Dimensional Dielectric-Barrier Discharge System", Phys. Rev. Lett. 85, 3817 (2000)

[6] B. Bernecker, PhD dissertation, University of Toulouse, 2010

[7] U. Kogelschatz, « Collective phenomena in volume and surface barrier discharges », 25th Summer School and International Symposium on the Physics of Ionized Gases (SPIG 2010) Donji Milanovac, Serbia, August 30 - September 3, 2010, to be published in J. Phys. Conf. Series (JPCS)

[8] I. Brauer, C. Punset, H-G Purwins, J-P Boeuf, "Simulations of self-organized filaments in a dielectric barrier glow discharge plasma" J. Appl. Phys. 85, 7569 (1999)

[9] B. Bernecker , T. Callegari, S. Blanco, R. Fournier and J.P. Boeuf , "Hexagonal and honeycomb structures in Dielectric Barrier Discharges », Eur. Phys. J. Appl. Phys. 47 22808 (2009)

[10] A. J. Koch and H. Meinhardt, "Biological pattern formation: from basic mechanisms to complex structures", Rev. Mod. Phys. 66, 1481-1507 (1994)

[11] C. P. Schenk, M. Or-Guil, M. Bode, and H.-G. Purwins, "Interacting Pulses in Three Component Reaction-Diffusion Systems on Two-Dimensional Domains", Phys. Rev. Lett. 78 3781 (1997); C. P. Schenk, P. Schutz, M. Bode, and H.-G. Purwins, "Interaction of self-organized quasiparticles in a two-dimensional reaction-diffusion system: The formation of molecules" Phys. Rev. E 57 6480 (1998) ; E. L. Gurevich, A. W. Liehr, Sh. Amiranashvili, and H.-G. Purwins, "Role of surface charges in dc gas-discharge systems with high-ohmic electrodes", Phys. Rev. E 69, 036211 (2004); Sh. Amiranashvili, S. V. Gurevich, and H.-G. Purwins, "Ionization fronts in planar dc discharge systems with high-ohmic electrode", Phys. Rev. E 71, 066404 (2005)

[12] Yu P. Raizer and M.S. Mokrov, "A simple physical model of hexagonal patterns in a Townsend discharge with a semiconductor cathode », J. Phys. D: Appl. Phys. 43 (2010) 255204

[13] L. Stollenwerk, Sh. Amiranashvili, J.-P. Boeuf and H.-G. Purwins, "Measurement and 3D Simulation of Self-Organized Filaments in a Barrier Discharge ", Phys. Rev. Lett. 96, 255001 (2006).

MEASURING ABSOLUTE ELECTRON-ATOM AND ELECTRON-MOLECULE CROSS SECTIONS RELEVANT TO PLASMAS

Michael Allan, Olivier May, Dušan Kubala

[1]*Department of Chemistry, University of Fribourg, chemin du Musée 9, 1700 Fribourg, Switzerland*

E-mail: Michael.Allan@unifr.ch

The problems associated with, and recent progress in, the measurement of absolute cross sections for plasma simulation are discussed. An infrastructure to measure absolute electron-atom (molecule) cross sections for elastic scattering, vibrational and electronic excitation and dissociative attachment built in Fribourg is presented. Emphasis is on accurate absolute values of the cross sections, low-energy capacity, entire range of scattering angles, low background and good resolution. Examples presented include Ne, Kr, CO, C_2H_2, HCN, HBr and HCl, together with the deuterated isotopomers where applicable. The interaction of experiment with theory is discussed.

1. Introduction

Obtaining cross section sets for plasma simulation is a complex and not yet satisfactorily solved enterprise, requiring the input from a number of experiments and from theory. The requirements to be met are:

(1) The cross sections need to be quantitative, extend to low energies, and cover a wide angular range. Satisfying these requirements is the primary goal of the experimental and apparative research in Fribourg.

(2) All the relevant processes should be included. The experimental work in Fribourg and this paper are concerned with elastic scattering, vibrational and electronic excitation, and dissociative electron attachment. Other important processes, not treated here, are ionization, dissociative ionization, bipolar dissociation, and neutral dissociation. A recent introductory article dealing with all these processes can be found in reference [1]. It has been written with the FEBIP (Focused Electron Beam Induced Processing) application in mind, but the conclusions made there are general and apply to a large degree also for plasma simulations.

(3) The cross sections must be available also for targets for which they are difficult or impossible to measure, in particular for electronically excited atoms, vibrationally and electronically excited molecules, and for transient molecules such as radicals, carbenes, or reactive open shell atoms. These cross sections must be supplied by theory, and an important application of the experimental cross sections such as measured in Fribourg is to provide quantitative data on which theory can be tested.

(4) Finally, the set of cross sections for plasma applications must be 'complete', that is, it must correctly reproduce the measured electron transport properties. Because of the inherent errors in both experiments and in theory, and because of missing cross sections for some processes, this is not automatically the case, and the cross section set needs to be adjusted such as to correctly reproduce the measured electron transport properties.

The research in Fribourg concentrates on the evaluation of the fundamental principles and mechanisms of electron-induced processes on isolated molecules and on measurement of high quality quantitative electron-molecule scattering data. Smaller molecules are preferred, but in some cases even larger molecules which may serve as models for biomolecules, or molecules relevant for plasmas and in astronomy, are used. Measurement of experimental data extending down to low energies (about 0.1 eV), covering a wide angular range (for inelastic processes 0-180°), and in particular measurements of quantitative, absolute cross sections, are emphasized.

This article presents illustrative examples of this effort. They are the elastic and the electronic excitation cross section for Ne and Kr, important in the first place for validifying the *B*-spline *R*-matrix theory which has recently achieved an important progress. These cross sections are relevant for the development of discharge lamps.

A second example are the elastic and the vibrational excitation cross sections for CO. This work was motivated by the need in astronomy. At the same time this measurement represents an important test of the relative flow method and of the elaborate procedures for correcting for the instrumental response functions, used by the experiment. This is because the extensive measured set, covering large ranges of scattering angles and extending to low energies, and including many final vibrational states, could be combined to obtain the grand total cross section, which could then be compared to the grand total cross section measured the transmission method. The transmission experiment does not depend on the relative flow method and does not need the instrumental response function, so that the favorable result of the comparison validates the differential measurements. Finally, three examples of dissociative electron attachment (DEA) are presented. HBr is a case which could be treated by the advanced nonlocal resonance theory. This theory is, however, parametrized and limited to one dimension of internuclear motion. Acetylene and hydrogen cyanide are examples, where local *ab initio* theory was applied, explicitly taking into account three dimensions of the internuclear motion.

2. Instruments

The measurements were performed by three complementary instruments:
(1) Quantitative time-of-flight (TOF) mass spectrometer, combined with a total ion collection tube [2], used to measure absolute dissociative electron attachment (DEA) cross sections. In this instrument either the total ion current is measured or the anions are sent into a TOF tube through a slit in the wall of the target chamber. The TOF tube consists of a three-cylinder electrostatic lens, which images the ion exit slit onto a MCP detector. The pressure in the collision chamber is measured by a capacitance manometer. The absolute calibration of the TOF results was against the 4.4 eV band of O^- production from CO_2, the ion collection tube experiment is inherently absolute.
(2) Quadrupole mass spectrometer with a trochoidal electron monochromator (QMS) [3, 4]. This instrument offers higher resolution (60 meV) and higher sensitivity than the TOF instrument. This instrument measures only relative spectra, which are then normalized to the absolute values obtained by the TOF instrument.
(3) Electron spectrometer with hemispherical analyzers [5] is used to measure elastic and vibrationally and electronically inelastic cross sections. This instrument uses crossed gas and electron beams and absolute values of the cross sections were determined by the relative flow technique using the theoretical helium elastic cross sections as reference. Angular distributions are measured using combined mechanical setting of the analyzer and magnetic deflection with the magnetic angle changer [6].

3. Electronic excitation of rare gases

Elastic and electronic excitation cross sections were measured for neon, argon, and xenon in the near threshold region [7–9]. The experimental data has been very useful to validate the recent significant progress in theory, made by means of a *B*-spline *R*-matrix method [10–12].
A representative Ne spectrum is shown in figure 1, based on the data of reference [7,9]. The theoretical and experimental data agree remarkably well above about 17.3 eV, but the experimental cross section is slightly higher within the first about 0.4 eV above threshold. This difference could be due to an overestimation of the instrumental response in this low energy range. This error could be a consequence of using the elastic cross section (in helium) to derive the response function, which was used to correct deeply inelastic data. To by-pass this problem, it would be useful to have very reliable theoretical inelastic cross section for helium, which could be used as a secondary standard in determining the instrumental response function for inelastic scattering near threshold.
Recent calculations in Kr [13] were compared to the early experimental results of Phillips [14], with a generally favorable result except that the theoretical results were about 50% smaller. We therefore embarked on new measurements in Kr, and an example of the result is given in Fig. 2.

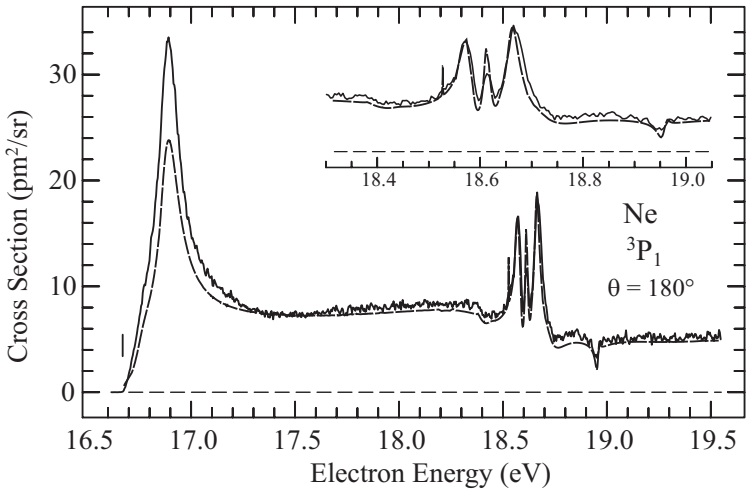


Fig. 1. Experimental (line with statistical noise) and theoretical (smooth dashed line) cross section for exciting the $^3P_1$ state of neon (based on reference [7]).

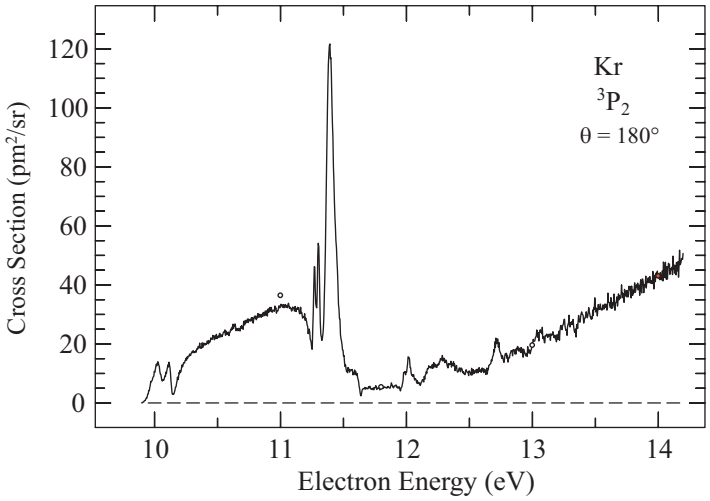


Fig. 2. Experimental cross section for exciting the $^3P_2$ lowest excited state of Kr.

4. Carbon monoxide

This work [19] was motivated by the need of data for simulations of the upper atmospheres of Venus and Mars and cometary comae [20]. Absolute differential elastic and vibrational excitation cross sections up to v = 11 were measured. Integral cross sections were derived by integrating under the angular distributions and an example for the excitation of v = 1 is shown in Fig. 3. Below the resonance region there is a discrepancy between the cross section determined by the present beam experiment and from drift velocity measurements, the latter being smaller.

The sum of the integral cross sections agrees very well with the available transmission measurements of the grand total cross section, thus validating the present measurements [19]. The present elastic differential and integral cross sections are in excellent agreement with the best available measurement [15], but the v = 1 inelastic cross section is about 25% higher. This could have consequences for simulations of cometary and planetary atmospheres.

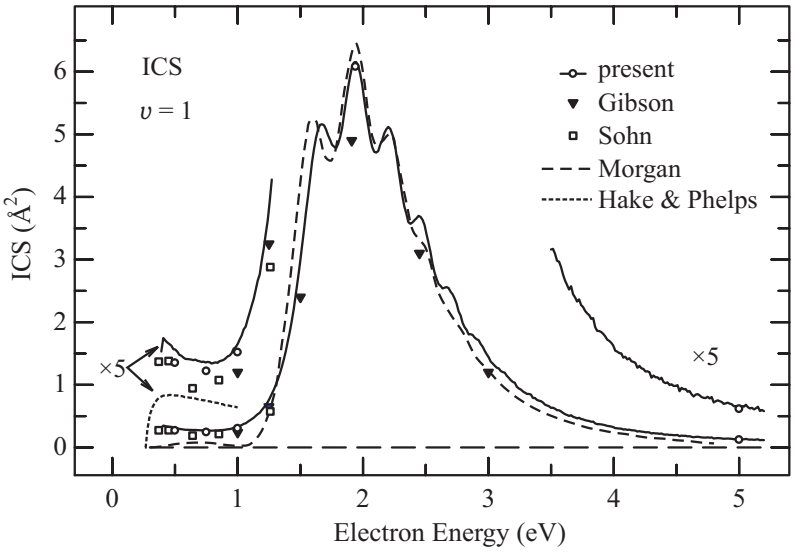


Fig. 3. Integral cross section (ICS) for exciting $v = 1$ in CO. Empty circles show the absolute values obtained by integration under the angular distributions. The solid curve shows the shape of the ICS, obtained as a weighted sum of the shapes of the differential cross sections recorded at various scattering angles. The data of Gibson *et al*. [15] are shown as downward triangles. Also shown is the data of Sohn *et al*. [16], Hake and Phelps [17] (from drift velocity measurements, shown 5× vertically expanded), and Morgan [18] (theory). Adopted from Ref. [19].

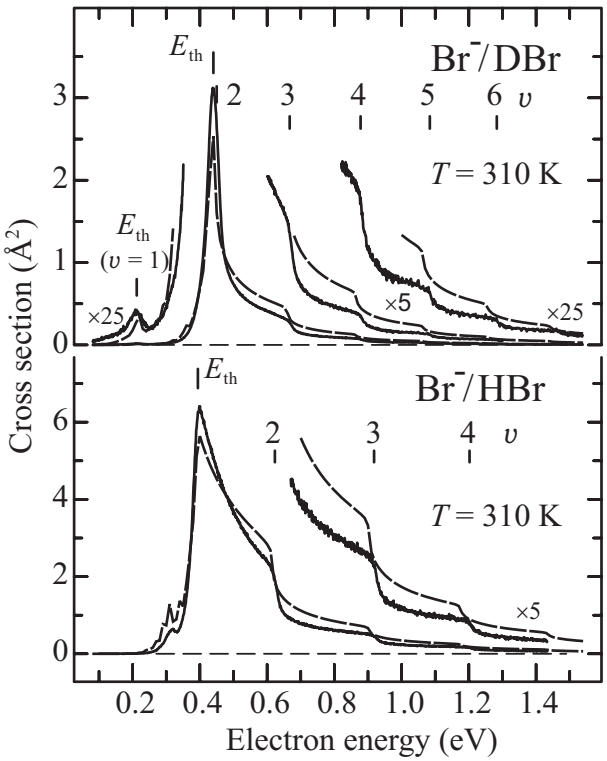


Fig. 4: Solid lines: high resolution (10 meV) absolute cross sections for Br^-/HBr and Br^-/DBr, obtained by normalizing earlier relative spectra [21] to the absolute values measured later [22]. Dashed lines: predictions of the nonlocal resonance theory [21, 23], with the final temperature taken into account, but without convolution with an apparatus function. Note that the experimental and theoretical data sets are independently on absolute scales, without any mutual normalization or scaling! The vibrational thresholds (v) and the DEA thresholds E_{th} are indicated. Reproduced from Ref. [22].

5. HCl and HBr

Absolute DEA cross sections were measured using the TOF instrument [22] in the total ion current mode. The cross sections for HCl were found to be about 3× smaller than the existing theoretical prediction, but an improved theoretical model removed the discrepancy [24]. A high resolution DEA spectrum was obtained for HBr by combining the results from the ELS and TOF instruments, and is shown in Fig. 4. The agreement with theory, both in terms of magnitude and in terms of the detailed shapes, particularly of the downward steps at vibrational thresholds, is very good.

6. C_2H_2 and HCN

The instrument in the total ion collection mode was used to measure acetylene and diacetylene [25], which are of current interest for two reasons: (i) They are in relation with the first observation of negative ions in outer space [26] which were of the type $C_{2n}H^-$ (n = 1, 2, ...). (ii) Acetylene is a good testing ground for the development of the theoretical description of dissociative electron attachment. Chourou and Orel [27] determined the cross sections by calculating both the real and the imaginary parts of the potential hypersurface using the Complex-Kohn scattering theory and then propagating a wave packet of the nuclei on this complex potential. Three internal coordinates were taken into account, representing a great progress in the description of polyatomic molecules.

More recently, Orel and Chourou calculated also HCN and HNC and we embarked on the corresponding absolute measurements of HCN and DCN to provide suitable comparison data [29]. The study was also motivated by the possible role of HCN as an initiator of abiotic synthesis of complex organic molecules in interstellar media and atmospheres of extraterrestrial bodies [30, 31]. Relative yields of the CN^- anions were recorded under higher resolution (60 meV) with the QMS instrument and normalized to the absolute values measured with the TOF instrument. The results are shown in Fig. 5. We interpret the broad structure on both the HCN and the DCN spectra as due to opening of dissociation channels leading to vibrationally excited CN^-. These structures are interesting because they permit determination of the branching ratios into the different final states and thus open an additional dimension for potential comparison with theory. Our peak values are 940 pm^2 for CN^-/HCN and 340 pm^2 for CN^-/DCN (with about 20% error bar), that is, the isotope effect is about 2.8. These numbers can be compared to the recent theoretical results of Chourou and Orel, who predict the values of 2800 pm^2 and 215 pm^2 for the two cross sections [32].

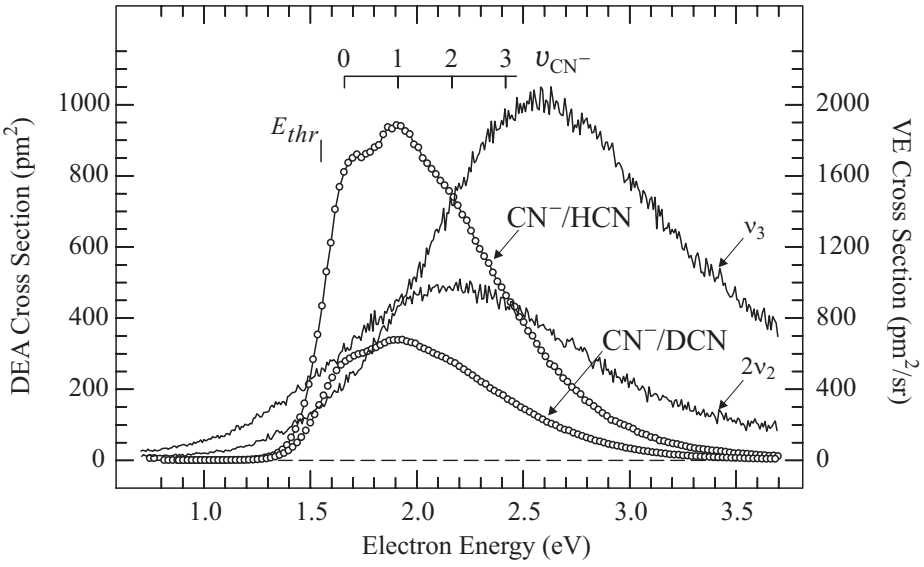


Fig. 5. Circles and vertical scale on the left: Cross sections for the yields of CN^- from HCN and DCN. The grid above the DEA spectra indicates vibrational spacing of the CN^- ion. The intrinsic position and shape of the $^2\Pi$ resonance is indicated by the differential cross sections for the excitation of the ν_3 (CN stretch) and $2\nu_2$ (bend) vibrations of HCN (continuous lines and the vertical scale on the right).

There is a qualitative agreement between theory and experiment in that the HCN cross sections are substantially larger than those for the similar process in acetylene [27], but there is only a modest agreement on the quantitative level. The disagreement in the isotope effect is unexpected in view of the success of the same theory in the case of acetylene. Similar measurement were performed also for acetylene.

7. Conclusions

questioned because of the possible dependence of the gas beam profile on the collisional cross section of the target gas, and of the elaborate procedures for correcting the raw data for the instrumental response function, both in respect to electron energies, and in respect to scattering angle.

The largest challenge for theory is almost certainly the calculation of 'chemical change', in this case the dissociative electron attachment. The HBr example shows that this problem is essentially solved by the nonlocal theory for diatomic hydrides. But this example also shows how complex the problem is for processes near threshold and for molecules having dipole and polarizability bound vibrational Feshbach resonances. The local complex potential approximation is dramatically insufficient in this case.

Unfortunately, the theory successful for HBr cannot be extended to polyatomic molecules, at least not at present. Since the majority of relevant plasmas contains polyatomic molecules, we are left with the general quest for developing the theory of electron-driven chemistry of polyatomic molecules. This quest if far more complex than the (already very difficult) strive to develop theory of photochemical change, because of the additional complications brought by the autodetachment, a process not intervening in photochemistry. The present collaboration between theory at the University of California in Davies and experiment in Fribourg represents an important progress in this strive. The chemistry in the molecules treated here does not occur at very low energies, and they have no (acetylene) or only small (hydrogen cyanide) dipole moment, so that the complex potential approximation is applicable.

The agreement of theory and experiment is not quantitative so far, but encouraging in view of how many orders of magnitude are spanned by DEA cross sections. The trends between acetylene and hydrogen cyanide are correctly reproduced by the theory: Theory correctly predicts that the cross section in HCN should be much larger than that in acetylene. The theory revealed very interesting aspects, namely that the process may be enabled either primarily (in acetylene) by by-passing an activation barrier, that is, vibronic coupling and the ensuing symmetry-lowering dominate the reaction, or (in hydrogen cyanide) by tunneling through the barrier.

The agreement of experiment and theory for acetylene was excellent, but our subsequent measurement of deuterated acetylene with the time-of-flight scheme [2] revealed a discrepancy between experiment and theory in terms of the isotope affect, which was measured to be about 15, and calculated about 30. A subsequent calculation, with the same model but taking into account that a significant fraction of the target acetylene molecules are thermally vibrationally excited at the temperature of the experiment (60°C) and that the cross section rises rapidly with initial quantum of the bending vibrations, could resolve the discrepancy in the isotope effect [28], albeit at the price of a somewhat reduced agreement of the absolute values.

Acknowledgements. This research is part of contract No. 200020-113599/1 of the Swiss National Science Foundation and of COST Action CM0601.

8. References

[1] Moore J H, Swiderek P, Matejcik S and Allan M 2010 *Fundamentals of interactions of electrons with molecules*. A chapter in: *Nanofabrication Using Focused Ion and Electron Beams: Principles and Applications*, Oxford University Press, *in press*.
[2] May O, Fedor J and Allan M 2009 *Phys. Rev. A* **80** 012706.
[3] Stepanovic M, Pariat Y and Allan M 1999 *J. Chem. Phys*. **110** 11376.
[4] Dressler R and Allan M 1985 *Chem. Phys*. **92** 449.

[5] Allan M 2007 *J. Phys. B: At. Mol. Opt. Phys*. **40** 3531.
[6] Read F H and Channing J M 1996 *Rev. Sci. Instrum.* **67** 2373.
[7] Allan M, Franz K, Hotop H, Zatsarinny O and Bartschat K 2006 *J. Phys. B* **39** L139.
[8] Allan M, Zatsarinny O and Bartschat K 2006 *Phys. Rev. A* **74** R030701.
[9] Allan M, Franz K, Hotop H, Zatsarinny O and Bartschat K 2009 *J. Phys. B: At. Mol. Opt. Phys.* **42** 044009.
[10] Zatsarinny O and Bartschat K 2004 *J. Phys. B* **37** 2173.
[11] Zatsarinny O and Bartschat K 2004 *J. Phys. B* **37** 4693.
[12] Zatsarinny O and Bartschat K 2005 *Phys. Rev. A* **71** 022716.
[13] Hoffmann T H, Ruf M W, Hotop H, Zatsarinny O, Bartschat K and Allan M 2010 *J. Phys. B: At. Mol. Opt. Phys*. **43** 085206.
[14] Phillips J M 1982 *J. Phys. B* **15** 4259.
[15] Gibson J C, Morgan L A, Gulley R J, Brunger M J, Bundschu C T and Buckman S J 1996 *J. Phys. B: At. Mol. Opt. Phys.* **29** 3197.
[16] Sohn W, Kochem K-H, Jung K, Ehrhardt H and Chang E S 1985 *J. Phys. B: At. Mol. Opt. Phys.* **18** 2049.
[17] Hake R D Jr and Phelps A V 1967 *Phys. Rev.* **158** 70.
[18] Morgan L A 1991 *J. Phys. B: At. Mol. Opt. Phys*. **24** 4649.
[19] Allan M 2010 *Phys. Rev. A* **81** 042706.
[20] Campbell L and Brunger M 2009 *J. Geophys. Res. Lett.* **36** LO3101.
[21] Čížek M, Horáček J, Sergenton A-C, Popović D B, Allan M, Domcke W, Leininger T and Gadea F X 2001 *Phys. Rev. A* **63** 062710.
[22] Fedor J, May O and Allan M 2008 *Phys. Rev. A* **78** 032701.
[23] Horáček J, Čížek M, Kolorenč P and Domcke W 2005 *Eur. Phys. J. D* **35** 255.
[24] Fedor J, Winstead C, McKoy V, Čížek M, Houfek K, Kolorenč P and Horáček J 2010 *Phys. Rev. A* **81** 042702
[25] May O, Fedor J, Ibnescu B C and Allan M 2008 *Phys. Rev. A* **77** 040701(R).
[26] McCarthy M C, Gottlieb C A, Gupta H and Thaddeus P 2006 *ApJ* **652** L141.
[27] Chourou S T and Orel A E 2008 *Phys. Rev. A* **77** 042709.
[28] Chourou S T and Orel A E 2009 *Phys. Rev. A* **80** 034701.
[29] May O, Kubala D and Allan M 2010 *Phys. Rev. A* **82** 010701.
[30] Gupta S, Ochiai E and Ponnamperuma C 1981 *Nature* **293** 725.
[31] Yelle R V 1991 *Astrophys. J*. **383** 380.
[32] Chourou S T and Orel A E 2009 *Phys. Rev. A* **80** 032709.

INTERPLAY OF VOLUME AND SURFACE PROCESSES IN THE SUSTAINING OF MICRODISCHARGES IN STEADY-STATE DBD

Yuri Akishev, Gregory Aponin, Anton Balakirev, Mikhail Grushin, Vladimir Karalnik, Alexander Petryakov, Nikolay Trushkin

SRC RF TRINITI, Pushkovykh St-12, Troitsk, Moscow region, 142190, Russia
E-mail: akishev@triniti.ru

The results of experimental study on a spatial-time behavior of microdischarges (MDs) in steady-state plane-to-plane DBD are presented. It was revealed MDs have a spatial "memory", i.e. the every subsequent MD does not jump in an arbitrary point of the barrier surface but appears exactly at the same place that was occupied by the preceding MD. This memory is derived from slow recombination of plasma in the MDs channels for a period between two neighbor half-periods (HPs). In such a case, there is no necessity in newly local avalanche volume breakdowns at every HP. In the majority of cases (more than 95%) each MD appears at its fixed place by every HP but only once during the HP. MDs in steady-state DBD have a great scattering with time in their appearance over the every HP. This scattering is attributed to the local surface breakdowns around the every MD. Numerical calculations show that namely surface breakdown is responsible for MD current splash but not an avalanche breakdown of the gap.

1. Introduction

Steady-state plane-to-plane DBD fed with sinusoidal voltage can exist in different current modes. One of them is non-patterned regime [1] with non-regular microdischarges. There is a wide-spread opinion that MDs in such DBD are randomly distributed in time and space, i.e. the MDs have no spatial "memory", and they appear by each half-period always at new points which have no any relation to the former places occupied by the MDs in previous HP. According to such view, every MD is newly formed once an electric field in the gap gets up to the critical value. The formation of alone MD was studied numerically in many publications [2-3]. However numerical calculations of a steady-state DBD with the repeating transient MDs are absent in literature.

Use the models based on the idea of newly gap breakdown by every HP meets with a difficulty to explain the peculiarities of real steady-state DBD. For instance, according to these models, the MDs have to arise by the every HP at well-defined moments correlated with an appearance of the critical electric field in the gap. In reality, the MDs exhibit chaotic behavior in time.

Another difficulty for the models assuming the gap breakdown at fixed voltage is a conclusion that DBD can be sustained only by applying an alternating voltage the amplitude U of which exceeds so-called inception voltage U_1 (the inception voltage corresponds to an appearance of the MD due to the avalanche gap breakdown). However, it is well known that steady-state DBD can exist not only under higher voltages $U \geq U_1$ but under lower voltage $U_1 > U > U_2$ as well. Here U_2 is the extinction voltage which correlates with a full disappearance of a discharge in the gap ($U_2 < U_1$ at that U_2 can be as low as $0.6U_1$ [4]). Note, a sustaining the DBD under lower voltage $U_1 > U > U_2$ has no relation to the thermal effects increasing the reduced electric field strength. This phenomenon takes place even in the case of a negligible gas heating by DBD.

This work was motivated by the aspiration to answer two main questions: 1) Is there a spatial "memory" for MDs in steady-state DBD? 2) What are the reasons for the MD chaotic behavior in time and space? For this purpose we have done a detailed search on spatial-time behavior of MDs in a steady-state DBD. Gas discharge was activated between transparent plane electrodes connected to a power supply with a sinusoidal voltage of variable frequency and amplitude.

2. Experimental setup

The sketch of experimental set up is shown in Fig.1. We have designed four different electrode geometries destined for study of steady-state DBD with abundance of MDs (No1) and with a single MD (No 2-4). Geometry No 1 is typical plane-to-plane geometry of 2-dimensional DBD. A spatial-

time behavior of great number of MDs was observed through transparent plane electrodes (36x36 mm^2) fabricated of very thin metallic mesh with a high degree of geometrical transparence of 92% or vacuum-evaporated Au layer with the optical transparence of 35%. Geometry No 2 enables to realize DBD with a single MD the parameters of which are practically the same as those of MDs in geometry No 1. Geometry No 3 allows us to simulate the surface breakdown in DBD without volume breakdown. Geometry No 4 enables to simulate the volume breakdown in DBD without a surface breakdown. In all cases, DBD was activated with a sinusoidal voltage of variable frequency (from 50 Hz to 100 kHz) and amplitude (up to 20 kV). Inter-electrode gap was varied from 1.2 to 2 mm. Plasma forming gas was ambient air and nitrogen of high purity (99.999%) at atmospheric pressure. To prevent the gas heating in the gap, experiments with steady-state DBD were performed either in gas flow or in gas at the rest but under DBD excitation limited with time of 1-2 s that is much longer compared to HP.

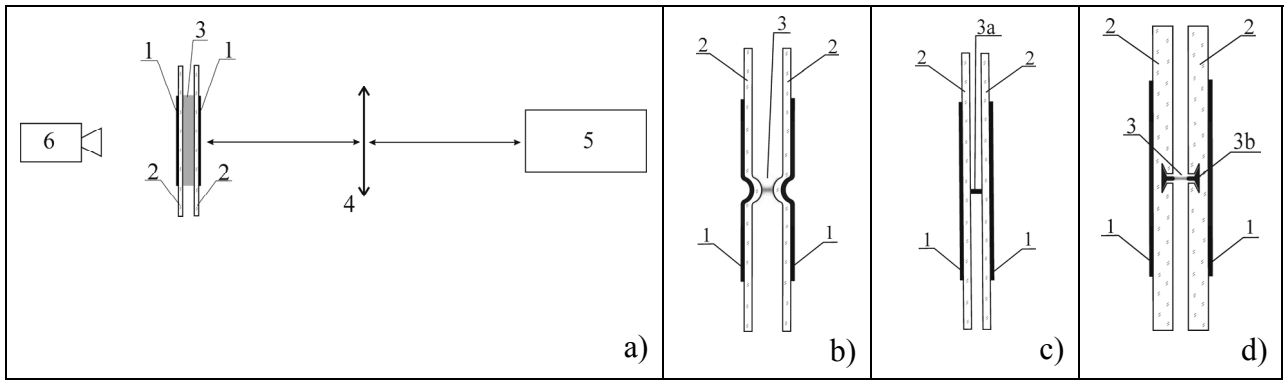


Fig.1 The sketch of experimental set up and the electrode geometries used.
a) electrode geometry No1 for excitation of plane-to-plane DBD: 1 – transparent metallic plate; 2 – glass barriers (ε≈7); 3 – discharge gap varied from 1.2 to 2 mm; 4 – quartz lens (F=112mm); 5 – photomultipliers equipped with optical fibers or high-speed electronic camera with high image intensifying; 6 – video-camera Panasonic NV-GS 500 or digital camera Canon EOS 40D;
b) electrode geometry No 2 for excitation of a single DBD microdischarge: figures 1-3 denote the same as it in a); the length of inter-electrode gap is 2 mm;
c) electrode geometry No 3 for simulation of the surface breakdown of a single DBD microdischarge: figures 1-2 denote the same as it in a); 3a – metallic cylinder of 1 mm in a diameter and 2 mm in the length (this cylinder simulates the MD plasma column);
d) electrode geometry No 4 for simulation of the volume breakdown of a single DBD microdischarge: figures 1-3 denote the same as it in a), 3b – metallic "thumb tacks" tightly fused in the barriers (the tack base of 2.5 mm in a diameter simulates a plasma sheet on the barrier arising due to surface breakdown around MD).

3. Experimental results

We have recorded the optical signals of the light collected by two thin fibers from two different but fixed and very small regions of DBD. The size of the every area was 80 μm in a diameter that is smaller compared to typical diameter of the MD (about 100-200 μm). It means the acquisition system of the every photomultiplier will collect only the light emitted from a single MD. Optical signals of two photomultipliers recorded by the oscilloscope Tektronix TDS 520 are presented in Fig.2.
One can see indeed that MDs appear not always (i.e. randomly) at the fixed place. However if such event happens, the MDs "stay" at this place over many periods – up to 300 HPs at the frequency of 100 kHz (more precisely MDs slowly move through the fixed area). It means that displacement of MD during the one HP of an alternating voltage is smaller than 0.25 μm – this value is negligible compared to the MD diameter.
So this experiment proves unambiguously that MDs in a steady-state DBD have a spatial "memory", i.e. the every subsequent MD does not jump in arbitrary point of the barrier surface but appears exactly at the same place that was occupied by the preceding MD. Further, alone bright point formed with the repeating MDs will be called a spot.

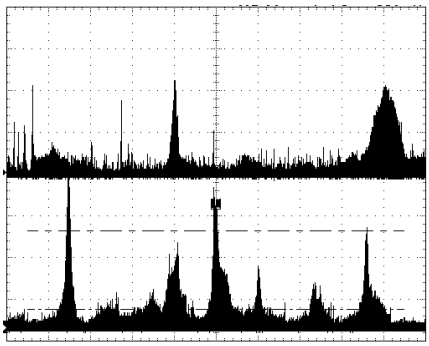


Fig.2. Optical signals recorded by two photomultipliers from different small areas of DBD.
Diameter of the every small area is 80 μm. A distance between two points of observation is 10 mm. Time scale is 5ms/div. The gap is 1.2 mm; ambient air at the rest; average current per HP is 10mA.

If so that MDs have a spatial "memory", another important question appears – how many breakdowns can occur at the same local place over a single HP? To answer this question we recorded the light signal with a high time resolution that allowed us to find out the time behavior of MDs at the fixed small place (80 μm) during the single HP. The results are shown in Fig.3.

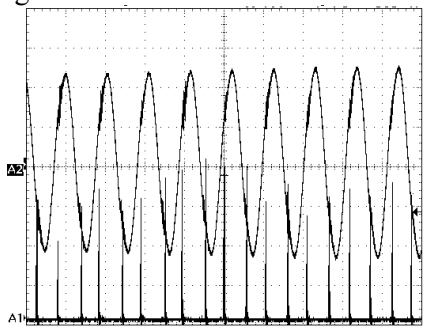


Fig.3. A correlation of the photomultiplier signal from a single MD with the applied voltage.
A1 – photomultiplier signal; A2 – applied voltage waveform. Time scale is 10 ms/div; voltage scale 2.6 kV/div. The gap is 1.2 mm, gas is ambient air at the rest; average current per HP is 10mA.

On closer examination it proved that MD appears at the fixed place every half-period but in the majority of cases (more than 95%) only once during the single HP. This conclusion is fairly for the whole frequency and voltage region investigated. Frequency and voltage amplitude were varied from 50 Hz to 100 kHz and up to 17 kV respectively (i.e. maximum voltage amplitude was much in excess of the inception voltage $U_1 \approx 10.4$ kV). It may well be true that more essential increase in the amplitude of an applied voltage can lead to an appearance of the repeated MD breakdown at the same MDS over a single HP but we did not do such experiments.
A dependence of number of spots (or MDs in HP) on the average current per HP is shown in Fig.4. The average charge per single MD determined from these data. As it turned out, this charge depends on the average current: the charge is equal to (0.6 ± 0.05) nC at small current and drops down to (0.3 ± 0.05) nC at higher current. Current dependency apart, the average charge for DBD in the gap of 1.2 mm is equal to (0.5 ± 0.15) nC. This amount is close to that published in [8, 11].

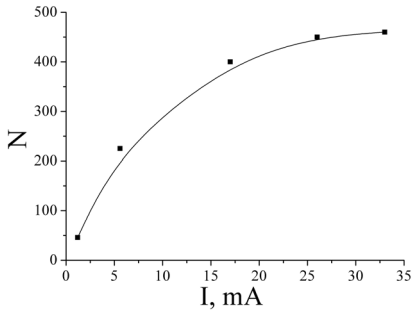


Fig.4. The number of current spots (or MDs in every HP) in steady-state DBD vs average current per HP. The voltage frequency is 100 kHz; discharge gap is 1.2 mm; ambient air at the rest.

Both the time spent by alone spot to cross the fixed area and the time between two visits in this area by different spots vary chaotically. Characteristic time of these variations ranges over 2-20 ms (see Fig.2) that is much in excess of the applied voltage period. It means that DBD spots travel slowly and chaotically in the gap. In such a case, it is possible to catch slow movement of the spots by a normal digital video-camera and trace the trajectories (or paths) of many spots over long time. Such experiments were performed with DBD sustained in gas at the rest and in gas flow.
Remind: 1) DBD is a steady-state discharge if the amplitude U is equal to or exceeds some critical value $U^*<U_1$, and 2) DBD decays very slowly (characteristic time about 1 s) if the amplitude ranges in the limits $U^*>U>U_2$ (see Introduction about U_1 and U_2). The results related to the long-time behavior of MDs in the slowly decaying DBD under voltage amplitude $U^*>U>U_2$ are presented in Fig.5.

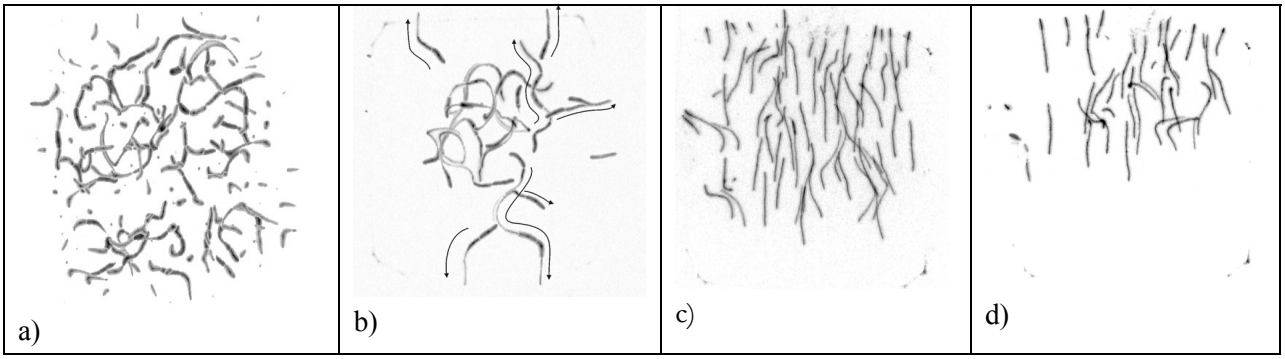


Fig. 5. Images of the decaying DBD (100 kHz) in ambient air at the rest (a, b) and under airflow (c, d). The shots are taken with the camera Panasonic NV-GS 500. The gap is 1.2 mm; voltage frequency is; the averaged current per HP is equal to 6mA. Each line shows trajectory of alone discharge spot. The arrowed lines in Fig 5b show the motion direction of some points. Airflow direction in Figs 5c,d is upward; gas flow velocity is 0.2 m/s. a) – superposition of 3 shots; exposure time of the every shot is 40 ms; the first shot was taken with a delay of 40 ms after DBD breakdown; b) - superposition of 7 shots; exposure time of the every shot is 40 ms; the first shot was taken with a delay of 200 ms after DBD breakdown; c) – a single shot; exposure time of the shot is 40 ms; this shot was taken with a delay of 40 ms after DBD breakdown; d) - a single shot; exposure time of the shot is 40 ms; this shot was taken with a delay of 80 ms after DBD breakdown.

An existence of steady-state DBD under lower voltage $U_1>U>U^*$ is directly related to spatial "memory" of MDs. This memory is derived from slow recombination of plasma in the MDs channels for a period between two neighbor HPs. It means in steady-state DBD always there are many plasma channels shunting the gap. Due to that there is no necessity in newly local avalanche volume breakdowns at every HP - it is sufficiently to create the plasma only one time in the very first (initial) breakdown of the gap under $U\geq U_1$. After that the decaying plasma of the MD channels can be supported periodically by the lower applied voltage due to partial surface breakdowns around the ends of the every plasma channel. This breakdown leads to a quick and short-term increasing of local barrier capacity providing the transfer of MD current through the barrier. The increase in local capacity is accompanied with a sharp current pulse and magnification the plasma density in transient MD to former level. In such an event, the avalanche volume breakdown in a steady-state DBD is of no importance. Because of that, the first current pulse by HP appears at maximum voltage (if $U=U_1$) but the pulses by the second and other HPs appear at lower voltage. This statement is illustrated by Fig. 6.

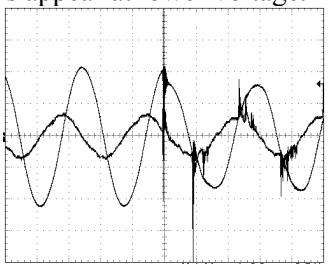


Fig. 6. I-U waveforms showing the first breakdown current pulse and others pulses appearing under lower gap voltage. DBD (50 Hz) in ambient air at the rest. Gas gap is 1.2 mm.

Due to both an existence of a “spatial” memory and the MDs confinement within the discharge area, the number of MDs in steady-state DBD is the same at every HP. However there is strong scattering in time over HP for an appearance of the every MD at the spot corresponding to this MD. Namely this scattering results in well-known chaotic behavior of the DBD current pulses the order and amplitude of which are not reproducible from HP to HP. This scattering is illustrated by Fig.7.

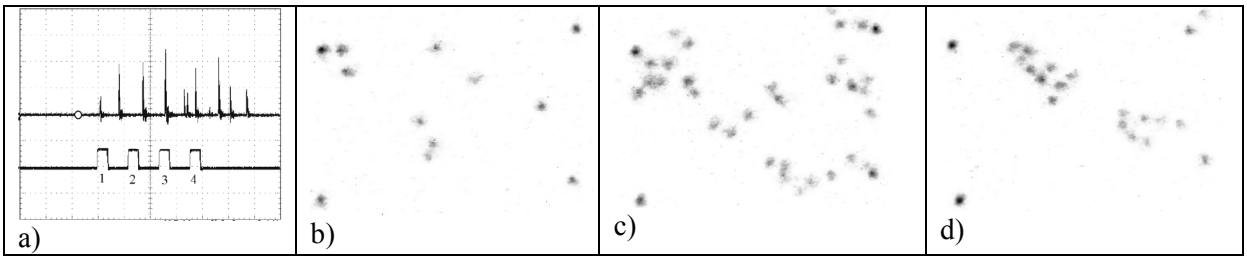


Fig. 7. An illustration of the scattering in time over a single HP for appearance of MDs at their places formed by previous MDs. DBD in ambient air at the rest; F=8 kHz; gas gap is 1.2 mm.
a) the train of current pulses of steady-state DBD over a single HP (upper line); open circle correlates with the moment U(t)=0. The lower line shows the moments when the shots 1,3,4 were taken. Time scale is 2.5 μs/div; current scale is 100 mA/div; b)-d) present the DBD surface shots taken at the moments 1,3,4 with exposure time 1 μs. Four bright points at the corners of the each shot are the bench marks.

4. Conclusions

1. MDs in steady-state DBD have a spatial “memory”, i.e. the every subsequent MD does not jump in arbitrary point of the barrier surface but appears exactly at the same place that was occupied by the preceding MD. This memory is derived from slow recombination of plasma in the MDs channels for a period between two neighbor HPs. It means in steady-state DBD always there are many plasma channels shunting the gap. In such a case, there is no necessity in newly local avalanche volume breakdowns at every HP - it is sufficiently to create the plasma only one time in the very first (initial) breakdown of the gap under $U \geq U1$. After that the decaying plasma of the MD channels is supported periodically by the lower applied voltage due to partial surface breakdowns around the ends of the every plasma channels. The every current pulse correlated with the surface breakdown raises the plasma density in the transient MD to the former level.
2. In the majority of cases (more than 95%), each MD appears at the fixed place by every half-period only once during the HP. It may well be true that more essential increase in the amplitude of an applied voltage can lead to an appearance of the repeated MD breakdown at the same MDS over a single HP but we did not do such experiments.
3. Although the number of MDs at each HP is kept constant, there is a great scattering with time in their appearance over the every HP. This scattering is attributed not to avalanche breakdowns but to the surface breakdowns around the ends of each plasma channel which occur in the every HP.

Acknowledgements. This work was supported in part by the RFBR (grant No. 08-02-00601-a).

5. References

[1] Eliasson B and Kogelshatz U 1991 IEEE Trans. Plasma Sci. 19, 309
[2] Braun D, Gibalov V and Pietsch G 1992 Plasma Sources Sci. Technol. 1, 166
[3] Egli W, Favre J M and Eliasson B 1998 Proc. 4th Int. Conf. on Greenhouse Gas Control Technologies, Interlaken
[4] Samoilovich V G, Gibalov V I and Kozlov K V in Physical Chemistry of the Barrier Discharge, ed. by J.P. F. Conrads and F. Leipold, (DVS-Verlag, Dusseldorf, 1997)

NONTHERMAL PLASMA ACTIVATES CATALYST: FROM CURRENT UNDERSTANDING AND FUTURE PROSPECTS

Hyun-Ha Kim, Atsushi Ogata

National Institute of Advanced Industrial Science and Technology (AIST)
E-mail: hyun-ha.kim@aist.go.jp

Combination of two old-yet-new technologies (plasma and catalyst) is getting attentions for the advanced processes in 21 century. This paper reports the complementary combination of atmospheric pressure nonthermal plasma with catalyst for the air pollution control application. The most important feature of this complementary combination is that plasma enables catalyst to work even at room temperature. Up-to-date data on catalyst screening for the cycled system will be given in terms of enhancement factor and adsorption capacity. Visual observation using ICCD camera was applied to study how discharge plasma interacts with catalyst at atmospheric-pressure and ambient temperature.

1. Introduction

Plasma and catalyst processes have a centuries-old history both in academic study and practical use. Catalytic reaction has long been used as one of key processes in many chemical processes. Haber-Bosch process for NH_3 synthesis is an early example of industrial scale application (the beginning of 1900s) of catalytic reaction. In 1920s FT (Fisher-Tropsch) process was developed to convert gas mixture into liquid fuel, which is also referred to as gas-to-liquid (GTL) process. The FT process is still in use in the fuel process using biomass. Catalyst is also indispensible for car industry; three-way catalyst, NOx-storage catalytic reduction and DPF (diesel particulate filter). The importance of catalyst is still gathering attentions in next-generation industry such as nano-material synthesis, renewable energy (biomass) and fuel-cell. It has many mature markets, while still exploring new applications. On the other hand, plasma-involved commercial market is much less, but its growing rate is much larger than that of catalytic process. Environmental application of plasma also has a long history, but its area was limited mostly to ozone synthesis and its application. In recent years, the application areas of plasma are also expanding rapidly; for example, pollution, semiconductor manufacturing, chemical and material synthesis, surface treatment, drinking- and waste water treatment, sterilization, and medical application. In this regards, these two processes can be referred to as “Old-Yet-New Technology”. At the same time, these two processes are still expected to play a key role in many cutting edge technologies such as nanotechnology, next generation energy (biomass, hydrogen and fuel cell), optical use including plasma display panel, environment, biomedical science.

When it comes to air pollution control, catalytic process has a long history of practical use in car exhaust gas cleaning, catalytic reduction process (SCR) of NOx and VOC oxidation in chemical industries. The bottleneck of catalytic process is the high operation temperature usually up to several hundreds oC, where the catalysts exhibit proper activity. On the other hand, one important merit of nonthermal plasma is low operation temperature. The key feature of the combination lies on the activation of catalyst by the plasma at low temperature. In spite of the limited information on the working mechanism, many synergestic effects have been reported by many research groups. **Figure 1** summarize three key factors required for plasma processing of VOCs. Decomposition of VOCs has been started in 1990s in many countries. Except for alkanes (saturated hydrocarbon) plasma was found to destroy a variety of VOCs. Despite many noticeable achievements in terms of decomposition efficiency, some critical problems have been raised for the commercial use of plasma technology. One is the reduction of energy consumption. The other one is the suppression of unwanted byproducts. Especially, these requirements must be satisfied together with the removal efficiency before the industrial applications. If one of these requirements is not satisfied, the NTP process may lose its potential for the commercial use. As a smart way to solve those problems is the combination of plasma and catalyst. The combination is divided into single-stage and two-stage depending of the position of catalyst. Plasma-driven catalyst combines palsma and catalyst in a single-stage configuration. Two important features of the combination are high selectivity of catalyst and high reactivity of plasma at low temperature. Catalysts are directly placed within plasma zone. This complementary combination

provides some breakthrough of NTP alone process in various aspects. The understading of the interaction between plasma and catalyst is still in early stage due mostly to the lack in fundamental information.
This work reports the current progress on the interaction of nonthermal plasma with catalyst and its application in air pollution control. The basic characteristics, the expected merits and current R&D status will be overviewed. An interesting effect of catalyst-packing on the generation of dishcarge plasma was studied by using microscope-ICCD camera.

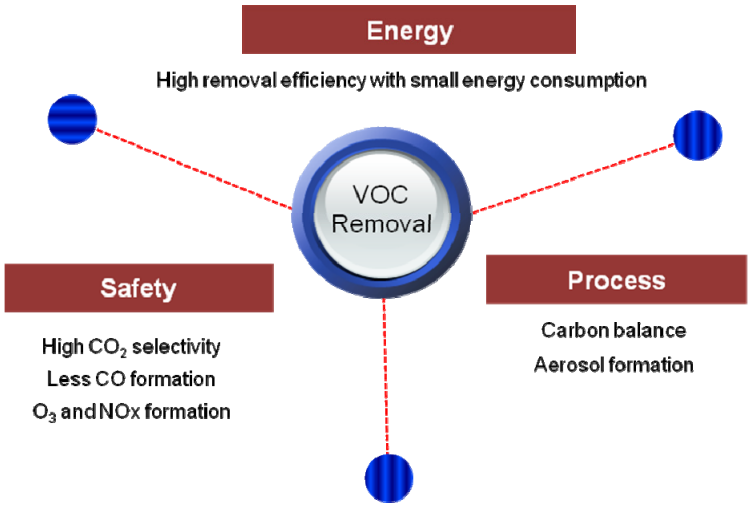


Fig. 1. Three key factors in plasma decomposition of volatile organic compounds (VOCs).

2. Early Development

Langmuir, Nobel laureate in chemistry (1932), is well-known that he first coined plasma as technical term describing the ionized gas mixture. The other important work done by Langmuir is the fumulation of gas adsorption on surface, which is now known as Langmuir isothermal adsorption equation. This approach opened a way for the kinetic calcuation of catalytic reaction. It may be no exaggeration to say that he stand on the contact point of plasma and catalyst.
One of early studies in the surface chemical reactions under the influence of discharge plasma may date back to the ozone generation using electrical discharge coronas. Although being quantitative, Anderegg reported the influence of reactor materials on the corona discharge and ozone formation as well [1]. For given reactor configuration and applied voltage, resulting ozone concentration from corona discharge changed drastically according to the type of metal wires used as corona electrode. Newsome reported that the degree in ozone suppression was in the order of Al > Ag > Au > Cu [2], but the effect varied considerably with time. Similar catalytic effect of corona electrode was also reported by Davidson *et al*. for silver and cuppor in positive corona discharge [3]. In recent years Yehia and Mizuno studied six electrode materials (silver, tungsten, gold, copper, nickel aluinum) and found that ozone suppression by silver was most prominant [4]. Furthermore the effect of silver was more promiment in positive corona in dry than negative polartiy or in oxygen. More recently, Petrov *et al*. reported nanocrystal formation on the surface of copper that has been exposured to a negative corona (Trichel pulse) discharge [5]. It is not clear how does it form and how these nanocrystal interacts with corona plasma, but it remains challenging area. The main drawbacks in using bulk material as catalyst are the small surface area and the amount used. The smaller the size of metals the larger the effective reaction sites and resulting in the enhancement of catalytic reaction. In most cases, the active metals are coated on the surface of substrates (such as γ-Al_2O_3, zeolite, activated carbon) having large surface area.
Combination of plasma with catalyst has been studied sporadically in time and space. One of important landmark in the single-stage plasma-catalyst system may the US patent by Henis in 1976. He proposed a single-stage plasma-catalyst reactor for NOx removal. The system was tested at 100^{o}C and the reactor was filled with various catalyst such as Al_2O_3, zirconium, silicate, cobalt oxide, thoria

(ThO_2), activated carbon, molecular sieve, silica gel. Although the removal efficiency was not high due probably to the absence of reducing chemicals, this patent obiously went ahead of the times.
The combination of plasma with catalyst became popular in the late 1990s. The limitation of the plasma alone process has prompted combination of nonthermal plasma with other techniques including catalyst. Most of recent studies including some commercialized facilities adopt the combined process of NTP and catalyst.

3. Experimental

3.1 Plasma Reactor

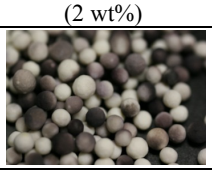
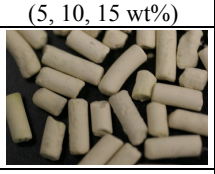
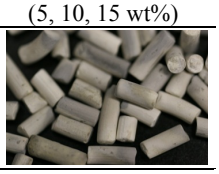
Plasma-driven catalyst reactor packed with various catalysts was made of quartz tube and stainless steel wire for dielectric barrier and high voltage electrode, respectively. The details on the reactor are given in the previous paper [6], so only a brief description will be given here. Chemical activities of the catalysts were tested using a cylindrical barrier discharge reactor. A stainless steel coil (ϕ 0.45 mm) was set in a quartz tube and silver paste was painted on the outer wall of the tube as a ground electrode. Gas flow rates were measured using mass flow controllers (Kofloc Co., FCC-3000). Benzene and tolene were used as model and their concentrations were adjusted by changing the bubbling flow rate or the temperature water bath. A Fourier transform infra red (FTIR, Perkin Elmer Spectrum One) was used for the determination of both benzene and products. One important advantage of FTIR gas analysis over the well-established gas chromatography method (GC) is that it does not interfere with ozone. In the case of GC analysis, coexisting ozone in the sample gas may cause additional decomposition of VOCs in a column, resulting in the overestimation of decomposition efficiency. A time-base software (Perkin Elmer Ver 2.0) was used for the continuous measurement of gas concentration at 2 min intervals by averaging five scans with resolution of 1 cm^{-1}. Power measurement is important in evaluating the performance of plasma reactor. In this work, Lissajous figure software (Insight Co., Lissajous Ver 1.72) was used to measure discharge power (P_{dis} in watt) and to calculate specific input energy (SIE in J/L). SIE, the ratio of input energy to unit gas flow rate, is calculated by the following equation

$$\text{SIE} = \frac{P_{dis}}{Q_f} = \frac{\text{discharge power (W)}}{\text{gas flow rate (L/min)}} \times 60 \qquad (1)$$

3.2 Catalyst

Table 1 summarizes the properties of catalysts used in this study. Zeolites pellets used in this study had a diameter of about 1.6 mm and length of about 2.0 -3.5 mm. Silver nanoparticles were coated on the surface of zeolites by an impregnation method using $AgNO_3$ as precursor substance.

Tab. 1. Catalysts used in this study.

Catalyst	TiO_2	MOR	MS-13X	NaY	HY
Metal loading	Ag (2 wt%)	Ag, Cu, Zr (5, 10, 15 wt%)	Ag, Cu, Zr (5, 10, 15 wt%)	Ag (10 wt%)	Ag, Cu, Zr (5, 10, 15 wt%)
Shape					
Size	1.8 mm	ϕ 1.6 mm × ~ 4 mm	ϕ 1.6 mm × ~ 4 mm	ϕ 1.6 mm × ~ 4 mm	ϕ 1.6 mm × ~ 4 mm
BET area (m^2/g)	59	380	540	750	520
Binder	Alumina 20 wt%	Alumina 20 wt%	Alumina 20 wt%	Alumina 20 wt%	Alumina 20 wt%

3.3 Observation of Discharge Plasma on the Catalyst Surface

Figure 2 shows the schematic diagram of observation system setup. A plate-type DBD reactor was set on a XY stage. The DBD reactor was made of two glass plates with 4 mm separation. Aluminium tapes were attached to the outer sides of the dielectrics, which serve as electrodes. ICCD camera (Hamamatsu Photonics) was used for the observation of surface plasma. Four optical lenses (Mitutoyo,MPlan Apo series) with different magnification were attached to the revolver. The observation area can easily be changed according to the condition. In the case of 5X lense (2.0 mm × 2.6 mm), it is possible to observe the discharge plasma over single catalyst pellet. A digital camera (Cannon EOS-20D) with a macro lense was also used to image the discharge.

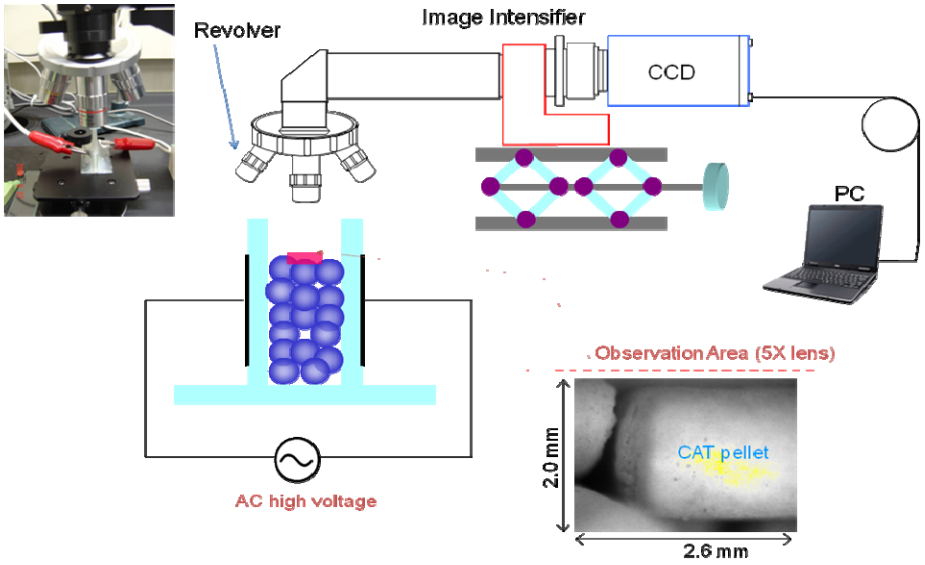


Fig. 2. Microscope-ICCD camera for the observation of discharge plasma on the catalyst surface.

4. Results and Discussion

4.1 Energy-dependent process: PDC

Specific input energy is an important parameter in plasma chemical reaction. There are many different operating parameters in plasma reactor such as applied voltage, type of power supply, reactor type, frequency and so on. For a given reactor, the overall chemical changes are proportional to the specific input energy. In the case of ozone generation, increasing voltage or frequency produces higher ozone concentration. On the other hand, these trends fall onto a single line when they are plotted in terms of SIE [7-8]. This energy-dependent behavior of plasma chemical reaction has been reported for many gas-phase reaction s such as NO reduction in N_2 [9], NO oxidation in dry air [10-11], removal of propane/propene [12]. Figure 3 shows the influence of gas flow rate on the toluene removal. Under this condition, no chemical reactions occurred in the absence of plasma. In the case of 2wt% Ag/TiO_2 catalyst, the numbers of PDC reactor were 1 and 8 for 5 LPM and 100 LPM, respectively. Despite the difference in space velocity the similar decomposition efficiency of toluene was obtained for 5 LPM and 100 LPM. The similar results were also reported for the decomposition of benzene by varying space velocity by a factor of 5 [13]. These results supported that plasma provides a driving force in activating the catalysts.

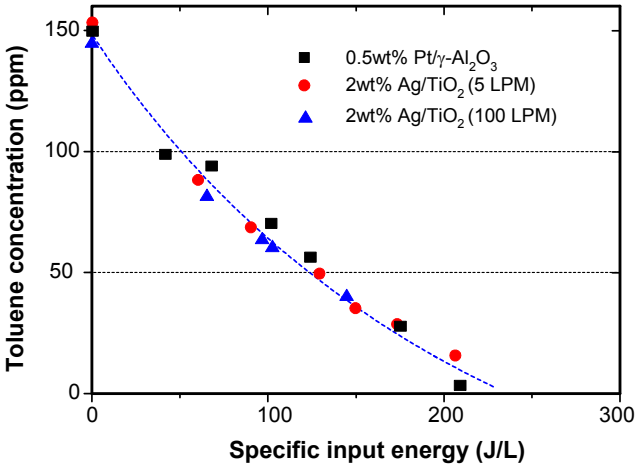


Fig. 3. Energy-dependent properties of plasma-driven catalysis. Decomposition of 150 ppm toluene at 100 °C. In the test of 100 L/min, 8 reactors were connected in parallel. The space velocities were 26000 h^{-1} for Pt/γ-Al_2O_3 or Ag/TiO_2, and 65000 h^{-1} for Ag/TiO_2 (100 LPM).

As mentioned in Section 2, the basic way to enhance catalytic performance is to find proper combination of active metal and substrate. There have been extensive studies on the heterogeneous catalytic oxidation of VOC for several decades. Especially nobel metals such as Pt and Pd have been found to be very effective in the total oxidation of VOC even at relatively lower temperature compared to the other metals [14]. One of the key factors in catalytic reaction is the area of active sites on surface. The surface area of metal catalyst, usually defined by BET area, can be easily enhanced by decreasing its size or increasing the loadding amount. As illustrated in Figure 4 the smaller the size the larger the surface area of active metals for a given amount of use. Considering the cost problem, it is desirable to make smaller the size of active metals supported on the surface of substrates (TiO_2, γ-Al_2O_3 and zeolite). For given amount of active metals, for example, reducing the size from 30 nm to 3 nm results in 30 times larger total surface area of metals. In other words, much less amount of metal will be necessary to get a certain surface area of active metals. Another important advantage in using metal nanoparticles is to lower the total usuage of metals, which is normaly expensive precious metals.

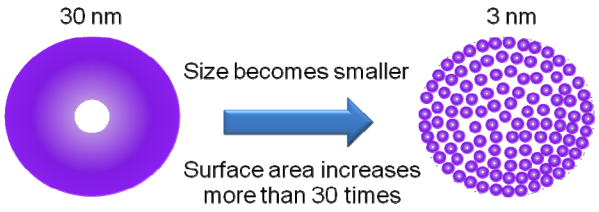


Fig. 4. The important size effect of metal nanoparticles.

4.2 NOx dilemma in nonthermal plasma decomposition of VOC

Figure 5 shows the NOx dilema in the plasma process and diesel engine. In diesel engine, the formation of NOx is primarily a function of temperature, which is called as thermal NOx. Engine operation at low temperature reduces thermal NOx, but it is counterblanced by the enhanced emission of particulate matter (PM). On the other hand, input energy determines the NOx emission in plasma process. Since the plasma decomposition of VOC is basically energy-dependent process, higher energy input leads to a higher decomposition of VOC and a large formation of NOx as well. It is unadvoidable to produce nitrogen oxide during the plasma processing in air-like gas mixtures [15]. The observed N_xO_y in plasma process includes NO, NO_2, N_2O_5, HNO_2, HNO_3, peroxyacetyl nitrate (PAN, $CH_3COOONO_2$), methyl nitrate and methyl ritrite [16]. Except for in-situ measurement, NO is easily oxidized to NO_2 by ozone so it is not detected in the presence of O_3. In this regard, cross check of different measurement techniques is important. Formation and the type of N_xO_y depends strongly on the operation conditions such as oxygen content [6], polarity, humidity, SIE, presence of catalyst [17] or VOC [18-19], dielectric constant [20], temperature and so on. This trade-off between VOC removal and NOx formation restricts the possible energy input to the plasma reactor. Although the presence of

catalyst changes the NOx formation, it is still difficult to suppress it completely. NOx decomposition by plasma is known to possible only if the oxygen content is less than about 4% [21-22], which is unreal for the exhaust gas containing VOC. In the case of gliding arc discharge, the concentration of NO_2 reaches up to several thousands ppm [19]. Kuroki *et al*. reported NOx formation problem from the decomposition of adsorbed xylene on zeolite using AC barrier discharge plasma in air [23].Microwave plasma is also known to produce high concentration of NO and NO_2 when it is operated at air-like mixuture [24]. The common factor for these two methods is high specific input energy up to several tens kJ/L. In this regards, suitable application of MW, RF or gliding arc plasmas will be the decomposition of persistent chemicals with relatively high concentration [25].

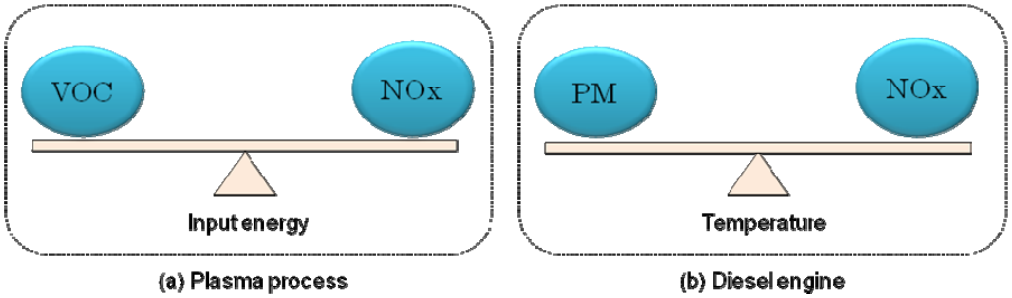


Figure 5. NOx Dilemma in nonthermal plasma processing of VOC and diesel engine.

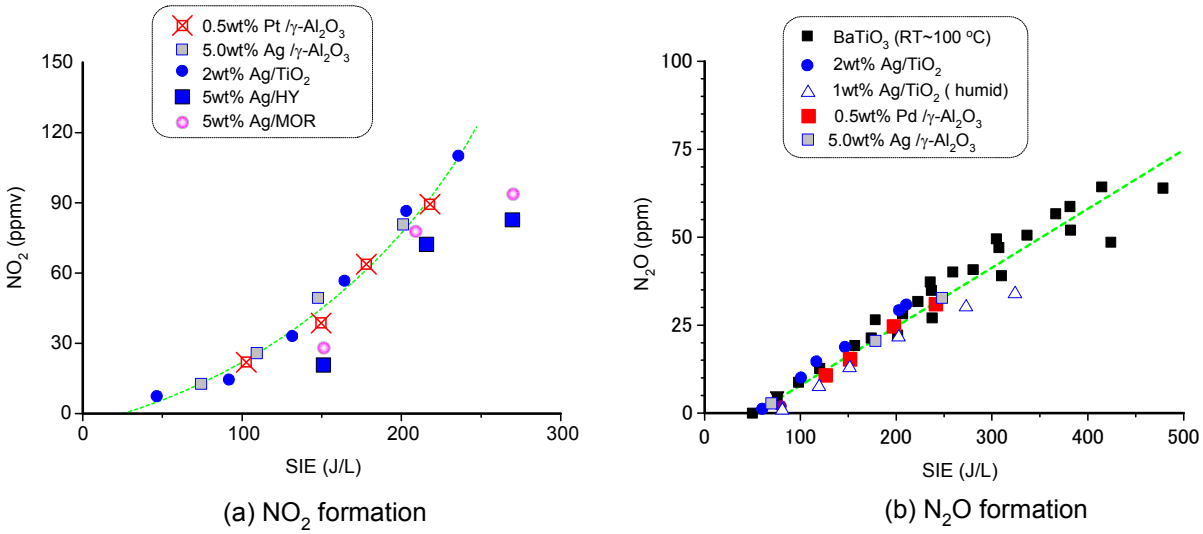


Fig. 6. Formation of nitrogen oxides (N_xO_y) in plasma processing in air.

Figure 6 shows the formation of oxides of nitrogen (N_xO_y) in plasma-driven catalyst reactors packed with different catalysts. Most abundant species of nitrogen oxides was NO_2 and NO was negligible. The formation of NO_2 showed a quadratic function of the SIE. Ag loaded zeolites (HY and MOR) exhibited slightly lower NO_2 formation compared to those with γ-Al_2O_3 or TiO_2. Nitrous oxide (N_2O) is most stable molecules among nitrogen oxides. Humidity slightly reduced N_2O formation, which has been also reported by other studies [26]. It is possible to decompose N_2O to N_2 in reducing gas mixtures, but hard to decompose or oxidize N_2O in air-like mixture. Regardless of the type of packing material, the formation of N_2O in dry air is a linear function of SIE.

$$[N_2O]_{ppm} = 0.17 \cdot SIE - 7.9 \qquad (2)$$

This equation may also be used for the rough estimation of the specific input energy to a plasma reactor.

4.3 Cycled System

The basic idea of the cycled system originates to the unique behavior of PDC system according to the oxygen content in gas mixture. [27]. Figure 7 shows an example how oxygen content influence the

decomposition of benzene in the PDC reactor with 5 wt%Cu/MOR catalyst. When plasma was turned on after the adsorption saturation, a sharp peak of benzene appeared due to plasma-induced desorption and leveled off to certain level. Despite of the constant SIE, the concentration of benzene decreased as the O_2 content increased. The resulting reaction products of CO and CO_2 aoso increased with O_2 content. The reaction immediately stopped as the plasma power was turned off. This highly O_2-content dependent behavior does not appear in the conventinal catalytic reaction or nonthermal plasma alone process [6]. The authors demonstrated complete oxidation of benzene using the Ag/TiO_2 catalyst and O_2 plasma. Recently, Fan *et al*. reported the complete oxidation of benzene using cycled system [28]. They used Ag/HZSM-5 catalyst with SiO_2/Al_2O_3 ratio of 360. For the optimization of the cycled system, it is necessary to sort our which materials are beneficial in terms of adsorption capacity of VOC and catalytic activity under oxygen plasma. We focused on the zeoolites, which have large surface area and characteristic pore sizes.

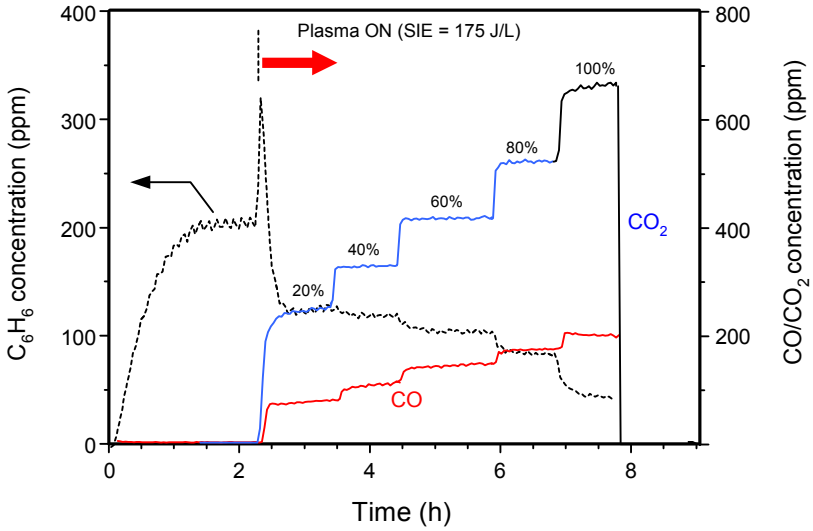


Fig. 7. Effect of oxygen content on the VOC decomposition using the plasma-catalyst reactor (5wt% Cu/ MOR). Applied voltage and frequency were 16 kV and 300 Hz, repectively. Temperature was 100 ^oC. Space velocity was 33000 h^{-1}.

Figure 8 shows the schematic diagram of the cycled system. Cycled system is consisited of two different cycles of adsorption and oxygen plasma. In the adsorption mode, VOCs are removed by adosrption onto the surface of catalyst in the absence of plasma application. When the catalyst bed reached adsorption equilibrium, then the gas flow was switched to the other catalyst bed to sustain the VOC removal. The saturated catalyst bed is purged with oxygen, and then plasma is turned on to decompose the adsorbed VOCs. To assist the catalytic activity, some nanoparticles of active metals (Ag, Cu, Zr) other than nobel metals (Pt, Pd) are loaded on the surface of zeolite. A small additional PDC reactor was set downstream of the main PDC reactor to decompose the desorbed VOC just after the O_2 plasma was turned on. In practical case, it will be beneficial to operate the regeneration mode in closed system after purging the catalyst bed with oxygen. For medium to small scale application, adsorption mode in daytime and regeneration mode in nightime will be possible.
The operation of cycled system is quite similar to that in the conventional adsorption process. The main difference lies in the regeneration process. In conventional adsorption, electrical heating or water vapor is supplied for the desorption of VOC. The resulting VOC with high concentration needs to be treated by catalytic oxidation or thermal oxidation. In the cycled system, the O_2 plasma decomposition of adsorbed VOC and theregeneration of adsorbent occur simultaneously. The highly oxygen content dependent behavior of PDC can enhance energy efficiency. The formation of nitrogen oxides can be also avoided sicnee the plasma is only turned on under oxygen environment. T he major advantages of the cycled system can be summarized as follows.
1) O_2 plasma exhibits higher energy efficiency than that of air plasma.
2) Free from nitrogen oxides formation
3) High CO_2 selectivity (100% for benzene decomposition using Ag/TiO_2)

4) Compact system due to the concentration of dilute VOC with a large volume to a limited space (on the surface of catalyst)
5) Rapid start-up and shutoff
6) High power operation is possible (same reason in 2)
7) Adaptability to the change of concentration and flow rate

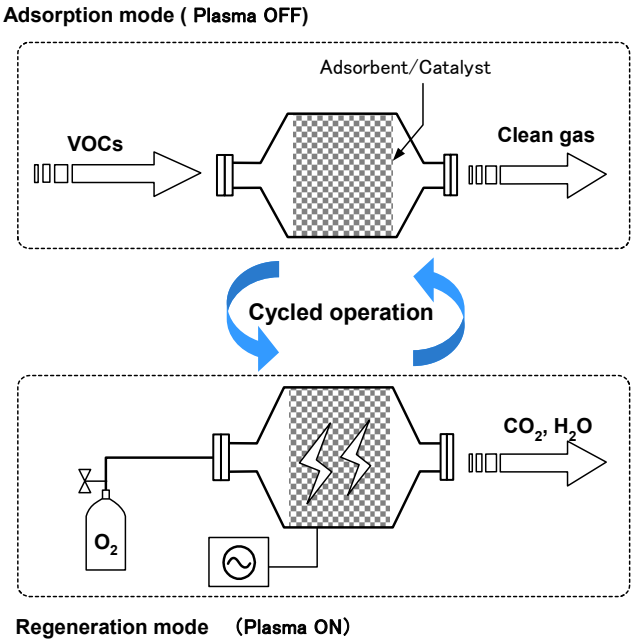


Fig. 8. Schematic diagram of cycled system.

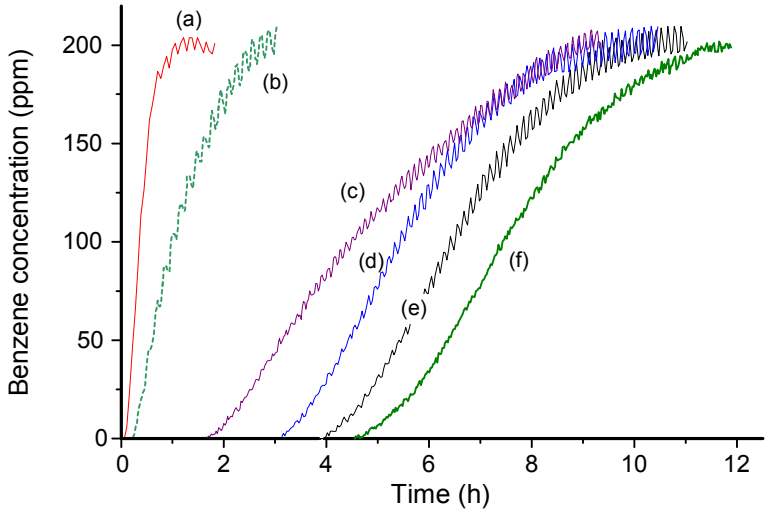


Figure 9. Adsorption capacity of different catalyst at 100°C; (a) 2wt% Ag/TiO_2, (b) 5wt% Ag/MOR, (c) 10wt% Ag/high-S-Y, (d) 5wt% Ag/MS-13X, (e) 5wt% Ag/HY, (f) 10wt% Ag/NaY. Space velocity was 33000 h^{-1} except for (a) 2wt% Ag/TiO_2 (SV = 22000 h^{-1}).

Optimizing the cycled system requires two different properties of adsorption capacity and catalytic activity at high oxygen content. We focused on zeolites dut to their large BET area, characteristic pore size. Some metal nanoparticles were loadded on the zeolites to enhance the catalytic activity. **Figure 9** shows the adsorption breakthrough curves for the different catalysts. Adsorption capacity was roughly

proportional to the surface area and pore size; MS-13X (10Å) ≈ HY (7.4 Å) > MOR (6.7-7.0Å) > ferrierite (4.3-5.5Å). . Since the tested zeolites had larger pore size than the molecular size of benzene (5.9Å), benzene is expected to be adsorbed dominately inside the micro-channels. As expect, TiO_2 exhibited small adsorption capacity compared to those with the zeolites.

Figure 10 shows the catalysts mapping based on adsorption capacity and enhancement factor, which are essential parameters for the cycled system. The enhancement factor is determined from the ratio of DRE at different O_2 partial pressure.

$$\text{Enhancement factor} = \frac{\text{DRE}_{\text{Oxygen}} - \text{DRE}_{\text{Air}}}{[\text{O}_2]_{\text{Oxygen}} - [\text{O}_2]_{\text{Air}}} \times 100$$

where $\text{DRE}_{\text{Oxygen}}$ and DRE_{Air} indicate the decomposition-removal efficiency in oxygen and air, respectively. Catalysts with high EF values indicate proper catalyst in the cycled system. In contrast to the large enhancement factor, the Ag/TiO_2 catalyst has small adsorption capacity of about 2 mg-C_6H_6/CAT-cm^3, which make less attractive to be used in the cycled system. On the other hand, most of zeolites have relatively large specific surface area so that they can be served as good adsorbents. It is interesting to note that the loading of Ag or Cu nanoparticles on zeolites enhanced the EF values by a factor of about 3. This performance enhancement can partly be explained by the increased in the surface area by the small sizes of the metal nanoparticles. For the tested zeolites, silver exhibited slightly larger EF values than those with Cu. The large adsorption capacity together with the high catalytic activity provides high potential of the cycled system to be applied in the real emission sites.

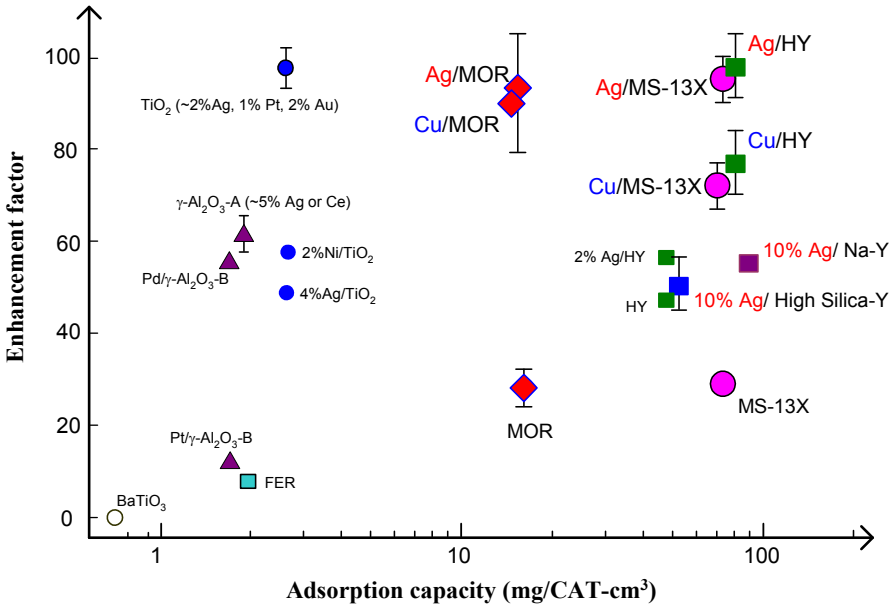


Fig. 10. Catalyst mapping in terms of enhancement factor (EF) and adsorption capacity of benzene (100°C, 200 ppm benzene) [6].

4.4 Surface Plasma Observation Using Microscope-ICCD Camera

To study the fundamental mechanism, metal nanoparticles supported zeolites were also evaluated in terms of physical- and electrical aspects. A microscope-ICCD camera was applied to observe the plasma generation on the surface of zeolite. Figure 11 shows the ICCD camera photographs of the discharge plasma in the MS-13X zeolite packed barrier discharge reactor. Zeolite pellets were packed in a barrier discharge reactor, and the discharge plasma was observed from the top of the reactor. Discharge plasma was influenced not only by the applied voltage but also by the supported amount of Ag. The metal nanoparticles greatly changed the plasma generation on the surface of catalysts and the plasma onset voltage as well. When there was no metal loading, plasma generation was mostly confined to the vicinity of the zeolite pellets.The discharge is stronger when 10wt% of Ag nanoparticles were loaded on the surface. Figure 12 shows enlarged photos showing how discharge plasma propagate on the surface of single catalyst pellet. The Ag nanoparticle helped the surface streamer to be expanded over a wide area. This change was also supported by the voltage-current

waforms [29]. The number of microdischarges (i.e. surface streamers) increased with proportional to the loading amount of Ag nanoparticles, whereas the peak current values were decreased. It is interesting to note that the streamer-like discharge (surface streamer herein after) propate in different shape compared to those in gas-phase. Streamer propagate in gas-phase in a straight manner according to the electric field. As indicated by arrows in Figure 12 (b), however, the propagation of surface streamers is not straight to the electric field, and divaricate randomly.

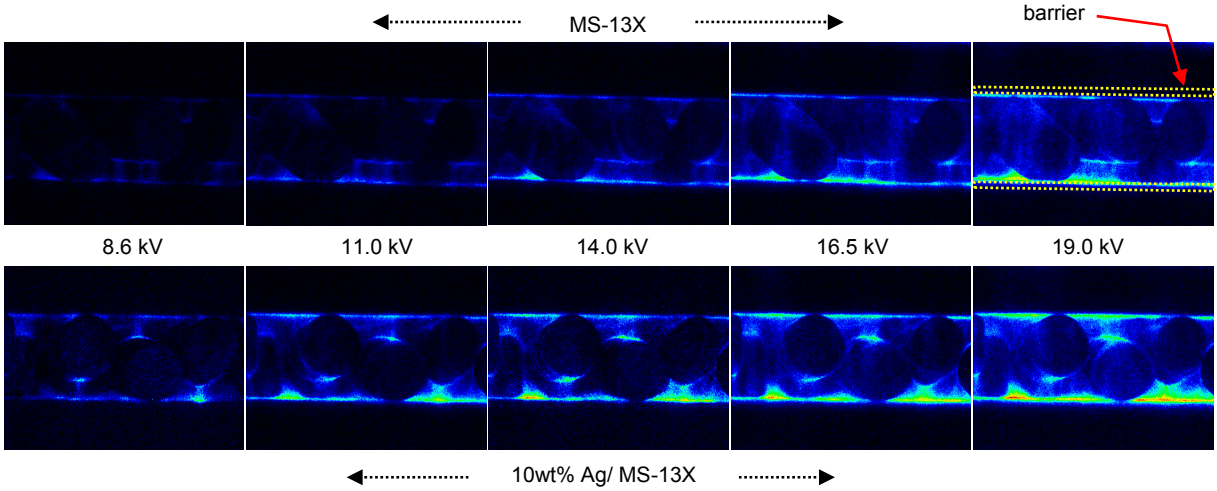
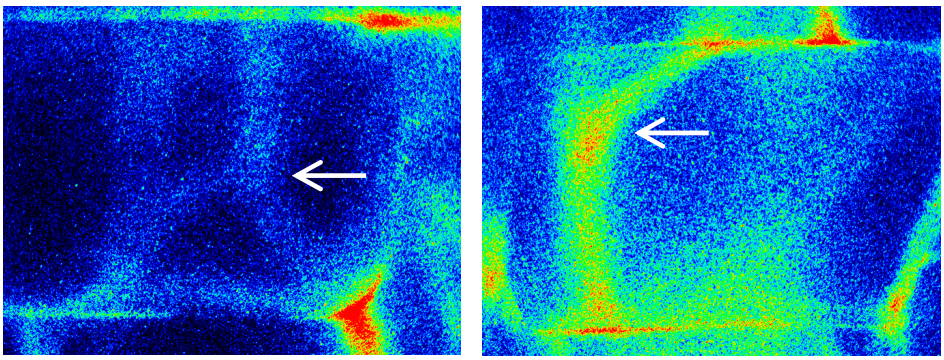


Fig. 11. ICCD camera snapshots of the discharge plasma over molecular sieve 13X zeolite (MS-13X) with or without Ag loading; (Frequency = 50 Hz, 2X lens, 2 mm gap).



(a) MS-13X (b) 10wt% Ag/ MS-13X

Figure 12. ICCD camera images of discharge propatation on the surface of MS-13X zeolites (19 kV, 50 Hz, DBD reactor with 4 mm gap, 5X lense). Exposure time was 40 msec.

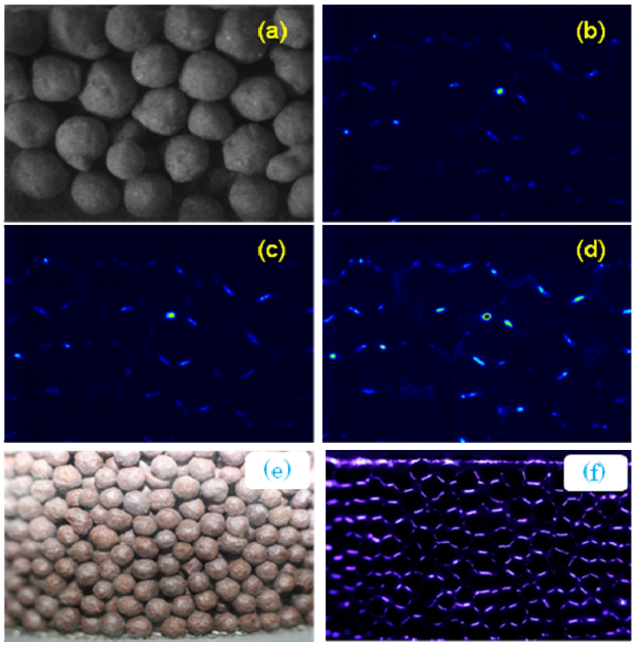


Fig. 13. Discharge snapshots of $BaTiO_3$ (s=10000) packed bed reactor; (a)~(d) ICCD camera ((b) ~(d) 40 msec)) and (e)-(f) digital camera ((f)= 15 sec) .

Figure 13 shows the discharge images by the ICCD and digital cameras for the $BaTiO_3$-packed plasma reactor. Unlike the zeolites packed cases, surface streamers were not observed in the $BaTiO_3$-packed reactor. Discharge plasma was first appeared with several plasma spots at the contact points of $BaTiO_3$ beads. The number and size of plasma spots became large as the applied voltage increased. However, plasma did not propagate on the surface of $BaTiO_3$ beads. Photos with long exposure time ,(f), was consistent with the ICCD camera data.

4.5 Plausible Mechanism

Plasma chemistry consists of complex physical and chemical process, so the clear understanding of overall processes are often difficunt. The chemical reaction in plasma-catalyst process is even more difficult to understand, since it contains interactions between them together with those in each processes. Nevertheless, there have been many papers reporting the synergestic effects in the single-stage plasma-driven catalyst system. Figure 15 summarize the synergy in the complementary combination of plasma with catalyst.

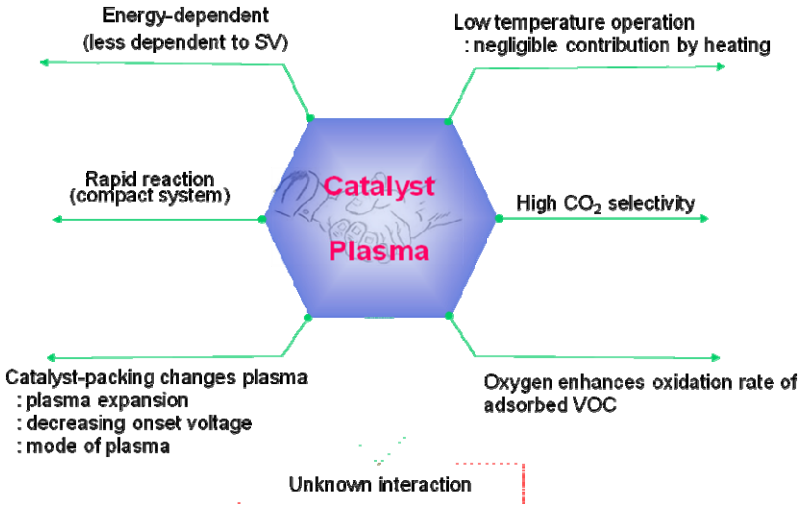


Fig. 15. Synergistic effect in the complementary combination of nonthermal plasma with catalyst.

The combination of nonthermal plasma with Titanium dioxide (TiO_2) was first applied for NOx removal [30-31], then later for the indoor air [32] and VOC [33]. According to the influence of precedent UV-photocatalyst studies at that time, UV was expected to play an important role in the plasma-driven catalytic process as well as the high energy electrons, excited molecules and radicals. Recent studies, however, provided seveal experimental evidence that the role of UV is minor in the PDC process. For example, UV photon flux was too low activate the TiO_2 catalyst [34].
The position of catalyst is also important facotr determining the overall efficiency. Some catalysts exhibits better performance in a two-stage configuration than in a single-stage configuration. There is in fair agreement with several independent works that ozone decomposition catalysts favors two-stage stage configuration [35-37]. Beside the plasma expansion by the metal nanoparticle loading, in interesting way to generate plasma inside honeycomb configuration. External DC field extracted plasma area to the outer zone of the AC plasma region [38-39].
From engineering pointview, rapid start-up and shut-down is important for medium- or small-scale application. Since plasma can activate the catalyst even at room temperature, flick of a switch is enough to start-up the system and vice versa.

5. Summary

Complementary combination of nonthermal plasma with catalyst is gathering attentions for its merits over separate process. Current research trends and the state-of-the-art knowledge have been outlined. For the optimization of cycled system, various metal nanoparticles supported zeolites were prepared and evaluated in terms of catalytic activity and the physic-chemical interaction. The loading of metal nanoparticles provided several interesting merits in the plasma-driven catalyst system. As chemical effects, the active metal nanoparticles enhanced the carbon balance and CO_2 selectivity. The microscope-ICCD camera observation provided some interesting insight into how metal nanoparticle interacts with plasma. In addition to the chemical aspect, the supported metal nanoparticles expanded discharge plasma over wide areas on zeolites. A positive correlation was found between the plasma generation pattern and the catalytic activity in the combined process. The area of discharge plasma was also increased with the loading amount of silver. The influence of metal nanoparticles on the plasma generation was also supported by the voltage-current characteristics. It is straightforward to increase the interaction between the plasma and zeolites as the area of plasma increases. Among tested active metals, silver showed the most prominent influence on the plasma generation. The expansion of plasma area was also influenced by the loading amount. This physical property was also found to be highly correlated with the catalytic activity under plasma activation.
One difficult problem in the study of plasma-catalyst hybrid system is that the well-proven analysis instruments in the field of catalysis cannot be unless significant modification is made. The main reason for this is due to the high voltage and the electromagnetic noise from the plasma. The developed observation system using microscope-ICCD camera can also be used as a rough-but-rapid evaluation tools for catalyst prior to the chemical performance test in a plasma-driven catalyst reactor. Further collection of the fundamental information and the understanding the mechanism will accelerate the technical progress of the plasma-driven catalyst process working at atmospheric pressure and ambient temperature.

6. References

[1] Anderegg F. O. 1923 *Trans. Am. Electrochemical Soc.* **44** 203.
[2] Newsome P. T. 1926 *J. Am. Chem. Soc.* **48** 2035.
[3] Boelter K J and Davidson J H 1997 *Aerosol Sci. Technol.* **27** 689.
[4] Yehia A. and Mizuno A. 2008 *Int. J. Plasma Environ. Sci. Technol.* **2** 44.
[5] Petrov A. A., Amirov R. H. and Samoylov I. S. 2009 *IEEE Trans. Plasma Sci.* **37** 1146.
[6] Kim H. H., Ogata A. and Futamura S. 2008 *Appl. Catal. B: Environ.* **79** 356.
[7] Simek Milan and Clupek Martin 2002 *J. Phys. D: Appl. Phys.* **35** 1171.
[8] Yagi S and Tanaka M 1979 *J. Phys. D: Appl. Phys.* **12** 1509.
[9] Penetrante B M, Hsiao M C, Merritt B T, Vogtlin G E and Wallman P H 1995 *IEEE Trans. Plasma Sci.* **23** 679.

[10] Yan K., Kanazawa S., Ohkubo T. and Nomoto Y. 1999 *T. IEE Japan* **119-A** 731.
[11] Jani Muaffaq A., Takaki K. and Fujiwara T. 1999 *J. Phys. D: Appl. Phys.* **32** 2560.
[12] Jarrige J. and Vervisch P. 2006 *J. Appl. Phys.* **99** 113303.
[13] Kim H H, Ogata A. and Futamura S. 2005 *J. Phys. D: Appl. Phys.* **38** 1292.
[14] Spivey J. J. 1987 *Ind. Eng. Chem. Res.* **26** 2165.
[15] Yamamoto T. 1999 *J. Hazard. Materials* **B67** 165.
[16] Wallington T. J., Hoard J. W., Sulbaekandersen M. P., Hurley M. D., Nakano Y. and Kawasaki M. 2003 *Environ. Sci. Technol.* **37** 4242.
[17] Song Y. H., Kim S. J., Choi K. I. and Yamamoto T. 2002 *J. Electrostat.* **55** 189.
[18] Futamura S, Zhang Z and Yamamoto T 1999 *IEEE Trans. Ind. Applicat.* **35** 760.
[19] Bo Zheng, Yan Jianhua, Li Xiaodong, Chi Yong and Cen Kefa 2009 *J. Hazard. Materials* **166** 1210.
[20] Ogata A, Shintani N, Mizuno K, Kushiyama S and Yamamoto T 1999 *IEEE Trans. Ind. Applicat.* **35** 753.
[21] Masuda S, Hosokawa S, Tu X, Sakakibara K, Kitoh S and Sakai S 1993 *IEEE Trans. Ind. Applicat.* **29** 781.
[22] Yan K., Kanazawa S., Ohkubo T. and Nomoto Y. 1999 *Plasma Chem. Plasma Proc.* **19** 421.
[23] Kuroki T., Hirai K., Kawabata R., Okubo M. and Yamamoto T. 2010 *IEEE Trans. Ind. Applicat.* **46** 672.
[24] Rousseau A., Dantier A., Gatilova L., Ionikh Y., Ropcke J. and Tolmachev Y. 2005 *Plasma Sources Sci. Technol.* **14** 70.
[25] I Y .P., Liu Y. C., Han K. Y. and She T. C. 2004 *Environ. Sci. Technol* **38** 3785.
[26] Futamura S, Zhang Z, Prieto G and Yamamoto T 1998 *IEEE Trans. Ind. Applicat.* **34** 967.
[27] Kim H. H., Oh S. M., Ogata A. and Futamura S. 2005 *J. Adv. Oxid. Technol.* **8** 226.
[28] Fan H. Y., Shi C. S., Li X. S., Zhao D. X., Xu Y. and Zhu A. M. 2009 *J. Phys. D: Appl. Phys.* **42** 225105.
[29] Kim H. H., Kim J. H. and Ogata A. 2009 *J. Phys. D: Appl. Phys.* **42** 135210.
[30] Kim H. H., Katsura S. and Mizuno A.: 1997 *2nd International Symposium on Non-Thermal Plasma Technology (ISNTPT-2)*, Salvador, Brazil,
[31] Kim H. H., Tsunoda K., Katsura S. and Mizuno A. 1999 *IEEE Trans. Ind. Applicat.* **35** 1306.
[32] Mizuno A., Kisanuki Y., Noguchi M., Katsura S., Lee S. H., Hong Y. K., Shin S. Y. and Kang J. H. 1999 *IEEE Trans. Ind. Appl.* **35** 1284.
[33] Li Duan, Yakushiji Daisuke, Kanazawa Seiji, Ohkubo Toshikazu and Nomoto Yukiharu 2002 *J. Electrostat.* **55** 311.
[34] Sano T., Negishi N., Sakai E. and Matsuzawa S. 2006 *J. Mole. Catal. A: Chemical* 235.
[35] Durme J. Van, Dewulf J., Sysmans W., Leys C. and Langenhove H. Van 2007 *Appl. Catal. B: Environ.* **74** 161.
[36] Huang H., Ye D. and Guan X. 2008 *Catal. Today* **139** 43.
[37] Ogata Atsushi, Saito Keiichi, Kim Hyun-Ha, • Masami Sugasawa, Aritani Hirofumi and Einaga Hisahiro 2010 *Plasma Chem. Plasma Proc.* **30** 33.
[38] Sato S., Hensel K., Hayashi H., Takashima K. and Mizuno A. 2009 *J. Electrostat.* **67** 77.
[39] Hensel K, Sato S and Mizuno A 2008 *IEEE Trans. Plasma Sci.* **36** 1282.

BASIC REQUIREMENTS FOR PLASMA SOURCES IN MEDICINE

Klaus-Dieter Weltmann, Thomas von Woedtke

Leibniz Institute for Plasma Science and Technology (INP Greifswald),
Felix-Hausdrorff-Str.2, D-17489 Greifswald, Germany
E-mail: weltmann@inp-greifswald.de

Plasma medicine is emerging worldwide as a new independent medical field. First practical studies have been interpreted to be very promising. For example the plasma treatment of chronic wounds can enable a selective antimicrobial (antiseptic) activity without damaging the surrounding tissue, combined with a controlled stimulation of tissue regeneration. Other promising fields are tissue engineering, treatment of skin diseases, tumor treatment based on specific induction of apoptotic processes, or dental applications. However, a lot of basic research needs to be done to minimize risk and provide a scientific fundament for medical therapies. Of course, therapeutic application of plasmas at or in the human body is not only a task for medicine; it is a challenge for plasma physics as well. Today, concepts of tailor-made plasma sources which meet the technical requirements of medical instrumentation are still less developed. To achieve selected effects and to avoid potential risks, the plasmas must contain certain components in well defined densities and it is necessary to know how to control them by external operation parameters. Therefore, a profound knowledge on their physics, chemistry and parameters must be contributed by physical research. Therapeutic applications required cold, non-thermal plasmas operating at atmospheric pressure. But these plasmas are a huge challenge for plasma diagnostics, because usually they are small scale, constricted or filamentary, and transient. Regarding the manageability in everyday medical life, atmospheric pressure plasma jets (APPJ) and dielectric barrier discharges (DBD) are of special interest for medical applications. Working on open air atmospheres, an input of nitrogen, oxygen and water implying complex plasma chemistry must be expected. Considering that, a great deal of effort combining experimental investigation and modeling will be necessary to provide the required knowledge on plasma sources for therapeutic applications.

1. Introduction

Progress in life sciences is increasingly caused by utilization of unrelated technologies and knowledge. In this spirit, microelectronics, optics, material sciences or nanotechnology became key technologies in modern medicine. A similar trend is expected now concerning plasma technology. Actually, plasma medicine is emerging worldwide as an independent medical field - comparable to the launch of laser technology into medicine years ago. Plasma medicine can be subdivided into three main fields: plasma-assisted modification of bio-relevant surfaces and plasma-based bio-decontamination/sterilization which can be considered as “indirect” medical plasma applications, because in these fields plasma is used to treat materials and products to allow or improve their subsequent medical application. However, the central field of plasma medicine is the direct therapeutic plasma application. Especially for this field, a fundamental knowledge of the mechanisms of plasma interaction with living cells and tissue is essential as a scientific basis.

2. Plasma sources for medical applications

Therapeutic application of plasmas is not only a task for medicine; it is a challenge for plasma physics as well. Even if from plasma physical point of view a large “tool-box” of plasma sources is available (Fig. 1), the intended use in plasma medicine limits the spectrum of useable tools.

Therapeutic applications of plasmas dictate the working in open air atmospheres and thus at atmospheric pressures. Adjusted plasma sources for different applications are required, and the proposed selectivity of plasma action implies a thoughtful control of the performance parameters of the plasma sources. This regards the treatment efficiency but also the potential risks connected with the direct plasma application at or in the human body. In particular, there are three tasks to fulfil:

1. the assessment of risk factors such as gas temperature, power transfer from the plasma, UV radiation, radicals, electromagnetic fields as well as the generation of toxic gases and its release into the adjacencies which could be dangerous for patients or therapists;

2. the characterization of special biologic effects, e.g., antimicrobial efficiency, cell manipulation, or blood coagulation, including the estimation of specific adverse or toxic side effects in the close cell and tissue environment; and
3. the profound understanding and knowledge of processes and physical plasma parameters in order to provide optimal tools for the achievement of specific effects [1].

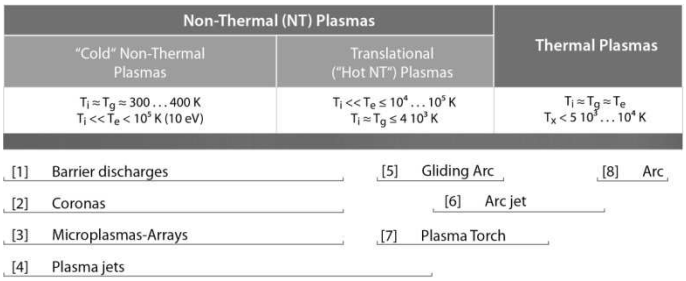


Fig. 1. Atmospheric pressure plasmas – "tool-box"

Nevertheless, during recent years a broad spectrum of plasma sources dedicated for biomedical applications has been reported, for example plasma needle [2], atmospheric pressure plasma plume [3], floating-electrode dielectric barrier discharge (FE-DBD) [4], atmospheric pressure glow discharge torch (APGD-t) [5], microhollow cathode discharge air plasma jet [6], microwave plasma torch [7], helium plasma jets [8-10], dielectric barrier discharge [11], and nanosecond plasma gun [12]. However, this list is far from being comprehensive.

For our own experimental work, up to now we have used mainly three different plasma sources:

- atmospheric pressure plasma jet (APPJ; kINPen 09, neoplas tools GmbH, Greifswald, Germany) with argon as preferred working gas [13]
- surface dielectric barrier discharge (surface DBD) working in atmospheric air [14-16]
- intermittent negative dc-corona discharge with argon as working gas (hairline plasma) [17]

The APPJ kINPen 09 (Fig. 2) is the most developed plasma tool which has been used for numerous biomedical investigations so far [1,13]. The device has got the CE marking (electromagnetic compatibility), thus fulfilling the EU consumer safety, health or environmental requirements.



Fig. 2. Atmospheric-pressure plasma jet (kINPen 09, neoplas tools GmbH,) for experimental biomedical applications (left: CE approved device; right: schematic set-up) [1,13]

It consists of a hand-held unit for the generation of a plasma jet at atmospheric pressure, a DC power supply, and a gas supply unit. The whole system works with all rare gases (especially argon) but also with nitrogen and air and admixtures of molecular gases to the feed gas. The contracted and comparably cold plasmas allow focused small-spot treatments, even of small size objects, also with high aspect ratios as well as large-scale treatments by moving the jet over a selected area by applying blower nozzles [13]. These features make them interesting for the treatment of bodily parts with complex geometries and cavities, e.g. in operative dentistry or dermatology. Furthermore, plasma jets can be arranged in arrays to adapt on special geometries [18].

A surface DBD is a useful device for indirect treatment of surfaces or liquids since the complete electrode design can be incorporated in a single component [1]. The electrode array consisted of epoxy-glass fiber bulk material for circuit boards serving as dielectric with a high-voltage structured copper electrode arrangement on the one side and a non-structured flat copper surface served as

counter electrode at ground potential on the other side (Fig. 3). DBD is performed at ambient air conditions using a pulsed sinusoidal voltage of 10 kV_{peak} (20 kHz)[15,16].

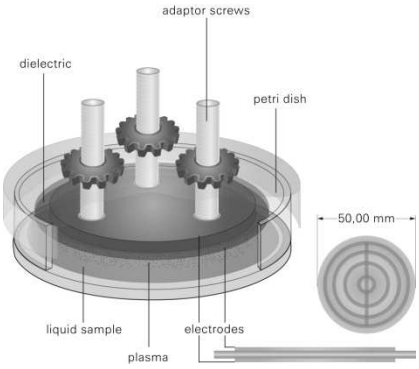


Fig. 3. Surface dielectric barrier discharge arrangement [15,16]

This electrode array was mounted by a special construction into the upper shell of a petri dish in that way that the distance between the high-voltage electrode surface and the surface of the sample in the lower shell of the petri dish can be adjusted variable. This experimental setup makes it ideal for biomedical investigations using microorganism cultures on agar surfaces or cell cultures as well as cells suspended in liquids. Because the plasma is ignited on the surface of the electrode arrangement which can be brought close to the target, there is neither direct plasma contact to the target nor a gas flow. Consequently, all plasma effects are assumed to be indirect effects induced by radiation or diffusion of reactive chemical. Dependent of intended applications other geometries and electrode arrangements are possible [14].

The hairline plasma schematically shown in Fig. 4 is a specially designed plasma source for the generation of a nanosecond-pulsed cold plasma using a simple dc-power supply and is able to penetrate into small and long gaps like tooth root canals [17]. Furthermore, a broad spectrum of other plasma sources is available which can be adapted for the investigation of special biological effects or therapeutic needs [1].

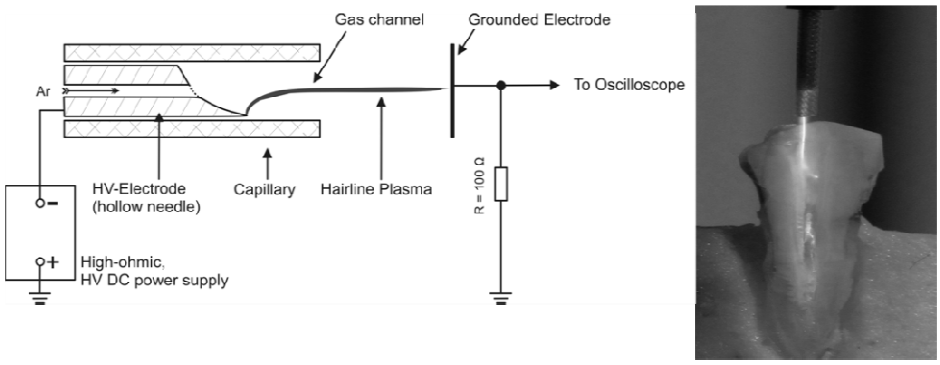


Fig. 4. Left: schematic of the hairline plasma setup; right: hairline plasma filament in a prepared root canal of a human tooth [17].

A decision if an atmospheric pressure plasma source may be useful for biomedical application should be made using the following 10 questions:

Is the clinical efficacy proved? Is the absence of undesirable local or systemic side effects (mutagenic, carcinogenic, toxic effects; pains, scars, pigmentation disorders…) proved? Is the medical effect reliable? Is the medical effect well controllable? Can a quick medical effect be realized? Is it possible to exclude the development of resistances when treating infectious diseases as well as co-treating resident flora? Is it possible to exclude inhibitory effects on normal microbiological flora? Is it cost-effective? Is it sure that there are no alternative solutions with what it could be done easier? Will the plasma treatment be accepted both by patients and physicians?

Only if all or at least most of these questions can be affirmed a further development up to clinical proofs is acceptable. Naturally, the main precondition to deal with these questions is to define an exact field of intended therapeutic application. The first two questions are playing a key role because plasma medical research has to guarantee the application of a Tissue Tolerable Plasma (TTP) with proved

clinical efficacy but without or at most with minimal side effects whose acceptability has to be decided dependent on the intended therapeutic use [19]. For this purpose, both a comprehensive and careful physical characterisation and optimization of the plasma sources and a comprehensive characterization of biological effects is indispensable.

3. Characterization of plasma sources – plasma physics

With regard to medical plasma applications, the estimation of general risk factors is at least that much important to clarify minimum standards for plasma sources to allow it for direct medical applications and for comparison of different sources. From the present point of view the minimum set of global risk factors to be characterized are plasma temperature, UV radiation, and generation of toxic gases and its release into the adjacencies which could be dangerous for patients or therapists.

Especially from the point of practical manageability as well as with regard to the actual state of technical development, atmospheric pressure plasma jet (APPJ) is of special interest for medical applications. Therefore, using the kINPen 09, systematic characterization of global risk factors which could arise but have to be avoided during application of this tool will be demonstrated. The general aim being true for all plasma sources intended for therapeutic applications is the setting up of minimum standards which have to be matched if a plasma source is.

Temperature is one of the most critical factors in connection with plasma treatment of living systems. Tissue temperature should not exceed a threshold of 40°C in general. Axial temperature profiles of the plasma jet can be measured by fibre optic temperature measurement (Fig. 5).

First of all, data presented in Fig. 5 indicate plasma jet temperatures between 63°C and 46°C, dependent on power input and axial distance from the capillary nozzle of the plasma source. But, secondly, it shows also the variable length of the visible plasma jet dependent on power input indicated by circular marks. At this tip of the visible plasma jet, temperatures have been measured more or less constant around 48°C. On principle, these plasma jet temperatures are very close to biological intolerance. However, plasma-caused surface or tissue heating, respectively, is not only dependent on gas or plasma temperature but also a function of contact time. So it could be demonstrated that fast moving atmospheric microwave plasma with a temperature of about 3000°C can be used for decontamination of heat sensitive hollow packaging materials which are melting above 70◦C [20]. If the APPJ will be used for wound antiseptics or skin treatment, respectively, it will not be done as a local spot treatment but by moving the plasma jet over the surface to be treated [21]. Therefore, following adequate application techniques, adverse effects of local tissue heating can be excluded as far as possible. On the other hand, these data demonstrate the necessity of measuring axial temperature profiles of the jet to decide if during practical applications the distance between jet nozzle and target surface will be critical. Because of the relatively constant temperature at the tip of the visible plasma jet independent on its complete length, the visible tip of the plasma jet can be used to adjust a general treatment distance. Using such adjustment, effective antimicrobial effects can be realized as it was demonstrated repeatedly [13, 21, 22].

For further minimization of the temperature problem, alternative working modes can be used like alternating plasma-on/plasma-off phases, net energy input and, subsequently, heating of the plasma can be further reduced to realize plasma temperatures < 40°C over the whole length of the jet [13].

Because the influence of UV radiation on the skin is another potential risk of atmospheric pressure plasma treatment, a careful characterization of optical emission spectra of plasma sources which are intended to use for plasma medical applications is necessary. Especially UV-C around 254 nm is well known for its direct impact in DNA which is one possible component of antimicrobial plasma efficiency but also a safety hazard in the case of plasma treatment of mammalian cells and living tissue. For plasma jets under atmospheric conditions with argon as working gas, the presence of UV-C radiation and its intensity depends strongly on the working conditions. Whereas with a rf-driven plasma jet with 7 mm nozzle diameter and argon gas flow of up to 20 slm distinct UV-C radiation can be measured [23], for the kINPen 09 designated for biomedical applications emission in the UV-A (320-400 nm) and UV-B range (280-320 nm) was found, only [13].

Besides a permanent exposition of parts of human skin to solar UV-A and UV-B radiation, it is used in phototherapy and photochemotherapy to treat skin diseases as psoriasis and atopic dermatitis. Therefore, UV impact on skin is well investigated particularly in dermatology because excess UV exposure causes detrimental effects on skin. To exclude this, according to guidelines of the

International Commission on Non-Ionizing Radiation Protection (ICNIRP), non-therapeutic and non-elective ultraviolet radiant exposure of the skin in the spectral region 180-400 nm should not exceed 30 J/m^2 or 3mJ/cm^2, respectively. This value should be applied for the most sensitive, non-pathologic, skin phototype (known as “melano-compromised”) [24].

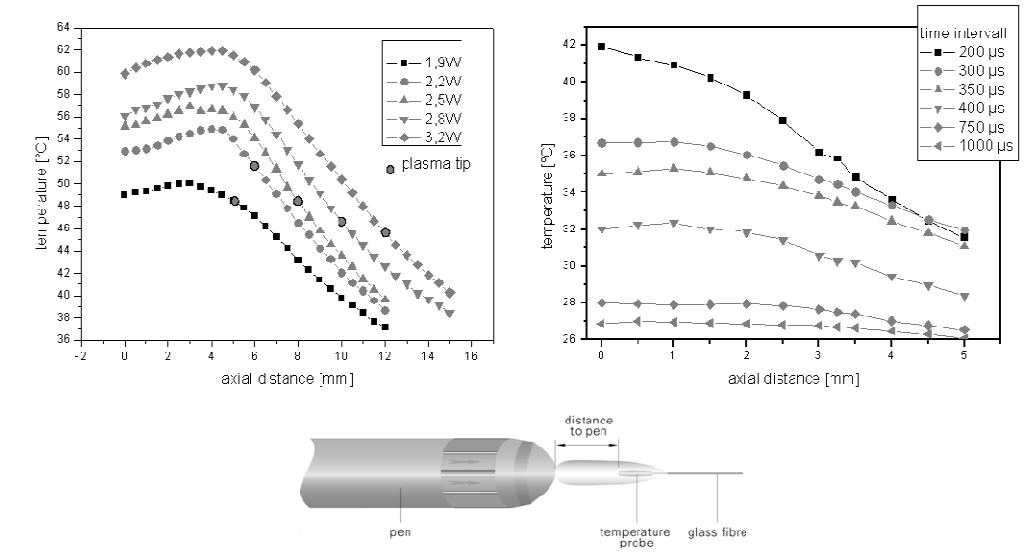


Fig. 5. Gas temperature of the kINPen 09 in the continuous (left) and the burst working mode (right) at an argon gas flow rate of 5 slm dependent on input power and axial distance [13]

To estimate the UV risk of the kINPen, irradiance in the 260-360nm UV range of the plasma jet was measured along the plasma jet at different axial distances and with different input power (Fig. 6).
At minimal distance of 5 mm and maximum power of 6W, maximum irradiance of about 5mW/cm^2 was measured. With increasing distance from the capillary outlet, drastic reduction of irradiance was detected reaching values between 1 and 2 mW/cm^2. Under these conditions, a local spot treatment over several seconds will be possible without exceeding the ICNIRP exposure limit of 3 mJ/cm^2. As mentioned already, practical application of the APPJ will be realized by moving the plasma jet over the wound area, e.g. there are very short contact times at one and the same point. Therefore, with the APPJ demonstrated here and considering the substantially higher UV irradiance used for phototherapeutic purposes, UV caused problematic side effects of the plasma jet can be avoided in principle. However, it has to be noted that all exposure limits and threshold values discussed above are related to a more or less intact and uninjured skin. For open wounds the situation may be very different because in this case the UV protective skin barrier is impaired and the tissue is directly exposed to the UV irradiation. Therefore, UV threshold doses for plasma application for wound healing have to be estimated separately using biological test models.

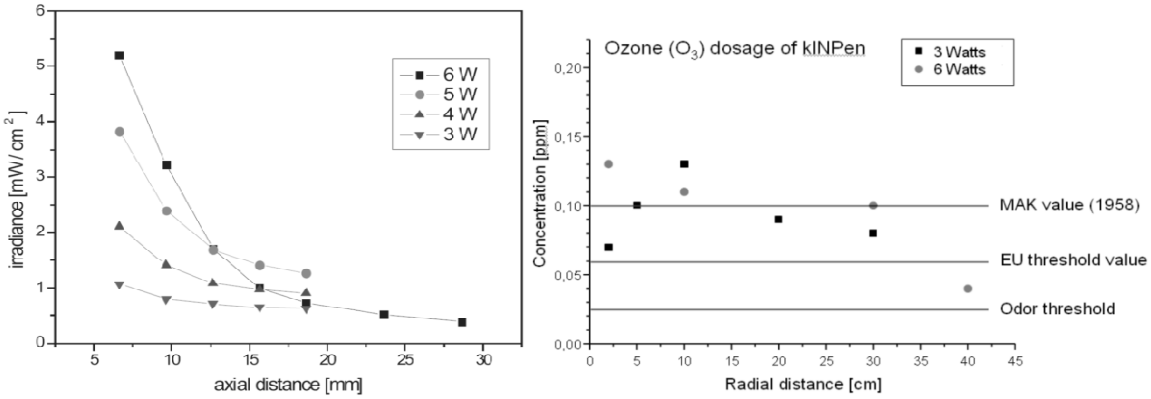


Fig. 6. (left): Irradiance (260-360 nm) of the kINPen 09 dependent on input power and axial distance from the plasma jet nozzle [13].(right): Ozone concentration measured by Dräger tubes at different radial distances around the kINPen 09

Besides UV and heat radiation, plasma sources provide a mixture of charged and non-charged reactive species, above all reactive oxygen species (ROS) and reactive nitrogen species (RNS). Besides its key role in several biological effects, reactions of these species with each other or with surrounding air, respectively, can also induce the production of toxic gases which are emitted into the environment and could harm patients as well as doctors during therapeutic plasma applications. Most important toxic gases potentially generated by atmospheric pressure plasmas are ozone and nitrous gases as nitrogen dioxide. Ozone is an air pollutant with harmful effects on the human and animal respiratory systems. Odour threshold of ozone is at 0.02 ppm or 40 $\mu g/m^3$ air. In the past, of 0.1 ppm or 200 $\mu g/m^3$ was defined as maximum allowable concentration (MAK value). Due to classification as a potential carcinogen (EG category 3: substances which, because of possible carcinogenic effects, are cause for concern), such a MAK value is no longer specified. According to EU directives (2002/3/EG) for long-term expositions, usually as daily eight hour time averages, there is no health risk at concentrations up to 0.055 ppm or 110 $\mu g/m^3$. To test the ozone emission, measurements using Dräger tubes have been done at different radial distances around a plasma jet driven with different power input (Fig. 6). Maximum concentrations between 0.10 and 0.13 ppm have been measured in the close proximity of the plasma jet, only. More afar, ozone gas concentration did not exceed a concentration of 0.10 ppm. Consequently, the permissible exposure limit will be exceeded, but because of short term therapeutic plasma applications not for extended time periods. Nevertheless, designing clinical practicable plasma based medical device, a surrounding gas exhaustion technique should be planned [13].

Nitrogen dioxide is a prominent air pollutant, too, which has a characteristic sharp, biting odor which is also toxic by inhalation. Its odour threshold is at 0.4–5 ppm, MAK value was set at 5 ppm or 9 mg/m^3, but like ozone it is classified as a possible carcinogen and, therefore, a current MAK value is not specified. However, using Dräger tubes for nitrogen dioxide detection, no measurable concentrations of this gas were found around the operating plasma jet [13].

Additional potential risk factors are electromagnetic fields of special frequency generated by the plasma source, which could induce electrolysis in the tissue or stimulate nerve or muscle cells. This problem is solved with the kINPen 09 which have passed a technical certification as CE-certification (electromagnetic compatibility), thus fulfilling the standards for electrical safety in humans. Such kind of certification should be the preferred way to use plasma sources for biomedical applications.

Summarizing all, these four technical characterizations – plasma temperature, UV radiation, generation/emission of toxic gases and electromagnetic compatibility – should be realized with all plasma sources which are designed for biomedical applications independent on their intended use because these parameters could give a basic overview about the quality of the plasma source.

Additional parameters like power transfer or transfer of different reactive species from the plasma to the target have to be investigated in close correlation with biological effects of the respective plasma source with the aim of much more detailed characterization of special safety hazards on the one side and potential therapeutic issues on the other.

4. Characterization of plasma sources – cell-based test models

Characterization of biologic plasma effects has to be a multi-step program starting with investigations of plasma-liquid interactions and has to include a broad spectrum of *in vitro* tests with cells as well as cell and tissue cultures up to isolated tissues or organs to be proved finally with animal experiments and clinical trials

Under *in vivo* conditions, living cells and tissue as well as microorganisms e.g. on wounds are surrounded by a liquid environment necessary for living tissue and supporting survival and proliferation of bacteria. Consequently, plasma effects under these conditions should be at least partially mediated by this vital environment. Recent studies have demonstrated that biological plasma effects like inactivation of bacteria suspended in aqueous liquids are accompanied as well as supported by changes of the liquid environment [15,16]. Decrease of pH and generation of species like nitrite, nitrate or hydrogen peroxide could be measured as a result of atmospheric pressure plasma treatment. Generation of such species cannot only support bacteria inactivation in liquids, but could also play important roles in other biological processes e.g. associated with wound healing. Therefore, plasma-treatment of water and subsequent measurement of pH as well as nitrite, nitrate and hydrogen peroxide can give some basic information about potential biological plasma effects.

To get further basic assessment of biological plasma effects, estimation of antimicrobial activity is a widely used practice. In contrast to the characterization of plasma sources for sterilization or bio-decontamination of materials or devices where highly resistant bacteria spores mostly dried on surfaces are used as test microorganisms, characterization of plasma sources for plasma medical applications needs preferably vegetative microorganisms under *in vivo* like, i.e. above all under humid or liquid conditions. For this purpose, both microorganisms suspended in aqueous liquids or grown on half rigid media (agar) are used [15,21]. *E. coli* is a test microorganisms often used for basic plasma source characterization [13,17]. However, with special microorganisms like wound pathogens or dermatophytes, characterization of the antibacterial plasma effectivity can also give information about possibilities of special plasma applications e.g. for wound antiseptics or treatment of skin infections (Fig. 7) [21,22].The main characteristic of plasma sources for use in medical therapy is its direct application on or in the human body. Therefore, plasma effects on mammalian cells are of basic interest. *In vitro* tests to characterize plasma-cell interactions should include characterization of basic cellular parameters like morphology, viability or proliferation, characterization of special cellular responses like influence on DNA or cellular proteins, and estimation of complex cellular responses like tissue regeneration or selective microorganism inactivation without influence on the surrounding tissue. In recent years several studies about influences of atmospheric pressure plasmas on different cell types *in vitro* have been published [8, 25-39].

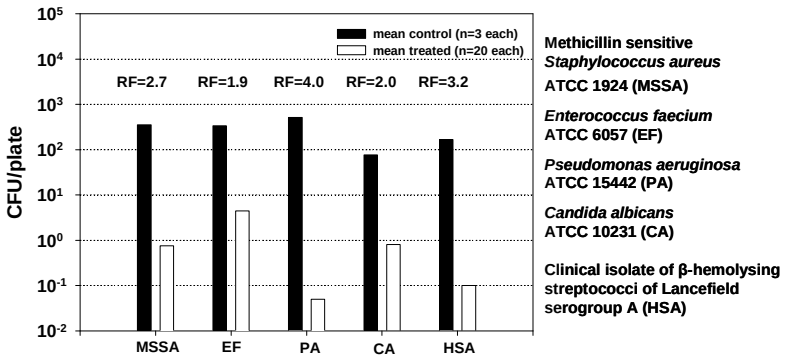


Fig. 7. Results of APPJ treatment of wound-relevant pathogens on agar plates (n=20 each), treatment area 55 cm^2, treatment time 6 min [21]

For our own experiments, so far we are using mainly human spontaneously transformed keratinocytes (HaCaT) [40]. If these cells suspended in nutrient medium are seeded in cell culture dishes they proliferate and grow as a two-dimensional (2D) culture forming an adherent cell monolayer. To investigate plasma effects on cells to characterize basic as well as special cellular responses, two basic experimental setups are used:

- plasma treatment of cells suspended in cell culture media and subsequent cell cultivation in cell-culture dishes
- cultivation of cells in cell-culture dishes and plasma treatment of adherent two-dimensional monolayer cell cultures

Both setups have special advantages dependent on cell responses that are wanted to investigate as well as on the plasma source that should be characterized. One of the basic parameters of plasma-cell interaction is the cell viability after plasma treatment. Using two-dimensional adherent cell cultures, cell viability can be estimated in the simplest case by microscopy or by cell-staining techniques as it is demonstrated in Fig. 8.

In the first case, live and death cells are differentiated by morphologic characteristics. In the second case, mostly fluorescent dyes are used which interact in a specific manner with cellular components of vital or death cells. Such two-dimensional adherent cell cultures are especially useful to investigate effects on already grown cell cultures mostly being in the stationary phase. If extended plasmas e.g. generated by a surface barrier discharge are used, homogeneity of plasma treatment as well as localized plasma effects can be visualized using such cell cultures.

However, because these cell cultures are covered with a thin layer of cell culture medium it is not so easy to characterize plasma sources working with a gas flow like atmospheric pressure plasma jets

(APPJ), because it leads to displacement of medium and subsequent cell death because of drying [41]. In such a case, treatment of cells in suspension is advantageous. Because of the gas flow, stirring of cell suspensions is given resulting in a complete treatment of the bulk liquid and thus of all cells contained. Moreover, investigation using cell suspended in aqueous liquids can be very easy correlated with results of plasma-liquid interactions as described above.

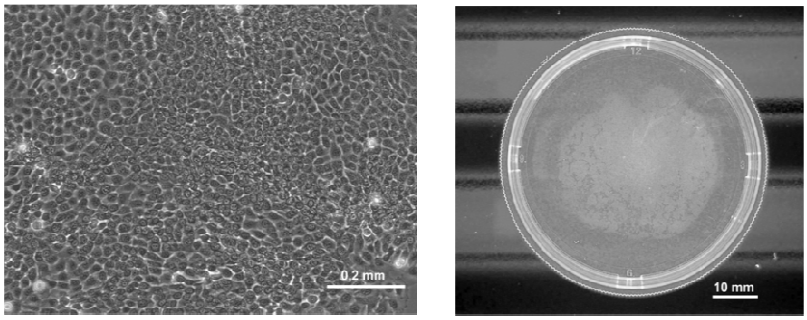


Fig. 8. Adherent human keratinocyte (HaCaT) culture after 20 min treatment by a surface DBD in atmospheric air. Left: By phase contrast microscopy live (center of the picture) and dead cells (along the edge of the picture) are distinguishable by its different morphology. Right: Using the propidium iodide staining technique, brighter colored region in the centre of the cell culture dish indicates death cells.

As it is demonstrated in Fig. 9, with this experimental setup the extent of cell growth and proliferation, respectively, dependent on plasma treatment parameters is estimated. Suspended cells are seeded in cell culture dishes following plasma treatment. After a reasonable time (at least 2 d), the number of cells grown is estimated in relation to an untreated control. The fewer cells survived the plasma treatment in suspension, the fewer cells can proliferate. In the experiment demonstrated in Fig. 9, the number of cells decreased dramatically dependent on argon APPJ treatment time. This becomes particularly clear with the results 4 d after plasma treatment. However, even after 20 min APPJ treatment, surviving cells can proliferate which is indicated by an increasing cell number from day 2 to day 4. Such basic tests of cell viability after plasma treatment have to be the starting point for further detailed characterizations of biological plasma effects. Both cells in suspension and adherent two-dimensional cell cultures can be used to detect the intracellular occurrence of reactive oxygen species (ROS) as an indicator for oxidative stress. For this purpose, special chemical probes are used which can diffuse membranes of vital cells and are oxidized by ROS to fluorescent chemical compounds. It was demonstrated that APPJ treated keratinocytes (HaCaT) showed high levels of intracellular ROS [41]. Because it is generally assumed that ROS are playing a key role in biological plasma effects, these investigations will need much more attention in further research and the characterization of intracellular ROS should be one basic parameter of characterization of biological plasma effects.

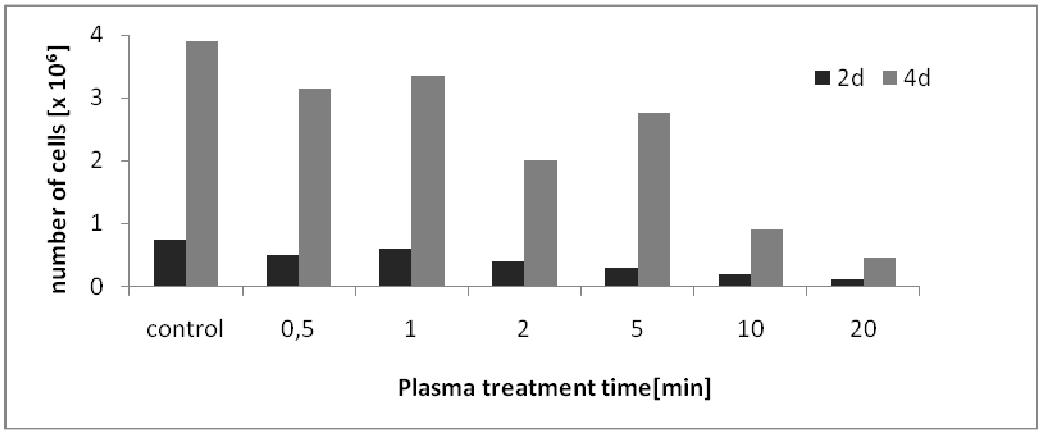


Fig. 9. Number of human keratinocytes (HaCaT) 2 and 4 d following argon atmospheric pressure plasma jet treatment of cell suspensions and subsequent cultivation in cell culture dishes

A further important field of plasma effects on cells is the examination of interactions with biological macromolecules. First of all, interactions with DNA are of key interest especially in terms of safety and estimation of potential risks. To obtain basic information on DNA defects resulting from plasma treatments single cell electrophoresis (Comet assay) is used [42]. First preliminary results show significant influences on DNA (mostly single strand breaks) after APPJ treatment of suspended human keratinocytes (HaCaT), but there was also found a tendency of repair within 4 to 24 h after plasma treatment (unpublished data). Because of its importance, these investigations have to be forced using additional techniques as micronucleus assay, flow cytometry, and fluorescence microscopy to get more detailed information about basic plasma influences on genetic code of cells.
Summarizing this, together with basic technical parameters (see chapter 3), basic biological characteristics of plasma activity like change of water composition, cell growth and viability using suspended cells and/or adherent two-dimensional cell cultures, intracellular ROS generation as well as interactions with DNA are necessary to estimate the potential of plasma sources for therapeutic applications in relation to the risk-benefit balance. Which special cell-based *in vitro* models as well as biochemical and cell biological techniques should be used has to be decided in further experiments. Finally, a spectrum of basic techniques should be available which make possible reproducible as well comparable plasma source characterizations.

5. Applied plasma medicine – standardized medical devices for animal tests, clinical trials and medical applications

The general aim of plasma medicine is to introduce physical plasma into clinical practice. However, plasma physics is a new and unknown field for biologists and physicians even if biology and medicine is more or less strange for plasma physicists. This situation needs reciprocal understanding to be able to realize the full potential of medical plasma applications.
On the other hand, despite the field is very new and mainly in an experimental state of development yet, there are first signs of its huge economical potential. Internationally, the development and application-oriented optimization and adjustment of atmospheric-pressure plasma sources to medical applications are experiencing an enormous upswing. This can be seen at the increasing number of scientific publications, in which plasma sources are declared as adequate “for biomedical applications” but also at first companies which are offering plasma sources for medical applications.
To take account of this ambivalent situation, a responsible use of plasma sources which are designated for biomedical applications is needed. Life scientists as well as physicians have to put in a position to decide if a given plasma source is really useful for medical applications or biological experiments. Consequently, a meaningful and mandatory spectrum of indicators has to be compiled to enable a basic estimation of the potential of a plasma source:
So far, there are no standardized criteria, according to which atmospheric-pressure plasma sources can be assessed as to their suitability for medical applications. Therefore, definitions of physical-technical criteria need to be established, which help to evaluate plasma sources for biomedical applications according to risk analysis. The minimum set of criteria has to include temperature, UV radiation, emission of gaseous products and electromagnetic compatibility in relation to geometry and operative parameters
In addition, definitions of basic criteria for the characterization of biological plasma effects (specific effects on human cells and microorganisms *in vitro*) need to be set up both in consideration of risk analysis and estimation of potential applications. The minimum set of biologic criteria should include influence on aqueous media (pH, generation of stable species), antimicrobial efficacy under *in vivo*-like conditions (wet or humid environment), intracellular occurrence of ROS and influence on intracellular DNA. Other criteria can be added optionally to characterize special biologic effects related to special applications or risks, respectively.
Through the transformation of the latest insights in plasma medical research into rules and standards, the essential prerequisite for the practical application and economic exploitation of research results shall be created.

Acknowledgements. This work was partly supported by the Federal Ministry of Education and Research (BMBF), FKZ 13N 9779 (Campus PlasmaMed). The authors would like to thank all team members and cooperation partners for their motivation and commitment

6. References

[1] Weltmann K-D, Kindel E, von Woedtke et al. 2010 *Pure Appl. Chem.* **82** 1223.
[2] Stoffels E, Flikweert AJ, Stoffels WW et al. *Plasma Sources Sci. Technol.* **11** 383
[3] Laroussi M and Lu X 2005 *Appl. Phys. Lett.* **87** 113902
[4] Fridman G, Peddinghaus M, Ayan Het al. 2006 *Plasma Chem. Plasma Process* **26** 425
[5] Coulombe S, Léveilleé V, Yonson S, Leask RL 2006 *Pure Appl. Chem.* **78** 1147
[6] Kolb JF, Mohamed A-A H, Price Roet al. 2008 *Appl. Phys. Lett.* **92** 241501
[7] Shimizu T, Steffes B, Pompl Ret al. 2008 *Plasma Pprocess. Polym.* **5** 577
[8] Shashurin A, Keidar M, Bronnikov S et al. 2008 *Appl. Phys. Lett.* **93** 181501
[9] Rupf S, Lehmann A, Hannig Met al. 2010 *J. Med. Microbiol.* **59** 206
[10] Lee HJ, Shon CH, Kim YS, Kim S, Kim GC, Kong MG 2009 *New J. Phys.* **11** 115026
[11] Kuchenbecker M, Bibinov N, Kaemling A et al. 2009 *J. Phys. D: Appl. Phys.* **42** 045212
[12] Robert E, Barbosa E, Dozias Set al. 2009 *Plasma Process. Polym.* **6** 795
[13] Weltmann K-D, Kindel E, Brandenburg R et al. 2009 *Contrib. Plasma Phys.* **49** 631
[14] Hähnel M, von Woedtke Th, Weltmann K-D 2010 *Plasma Process. Polym.* 7 244
[15] Oehmigen K, Hähnel M, Brandenburg R et al. 2010 *Plasma Process. Polym.* **7** 250
[16] Oehmigen K, Brandenburg R, Winter J et al. 2010 *HAKONE XII Book of Contributed Papers*
[17] Bussiahn R, Brandenburg R, Gerling T et al. 2010 *Appl. Phys. Lett.* **96** 143701
[18] Weltmann K-D, Brandenburg R, von Woedtke Th et al. 2008 *J. Phys. D: Appl. Phys.* **41** 194008
[19] Kramer A, Hübner NO, Assadian O et al. 2009 *GMS Krankenhaushyg. Interdiszip.* **4** Doc10
[20] Ehlbeck J, Brandenburg R et al. 2008 *GMS Krankenhaushyg. Interdiszip.* **3** Doc14
[21] Daeschlein G, von Woedtke Th, Kindel E et al. 2010 *Plasma Process. Polym.* **7** 227
[22] Daeschlein G, Scholz S, von Woedtke Th et al. 2010 *IEEE Trans. Plasma Sci.* accepted
[23] Brandenburg R, Ehlbeck J, Stieber M et al. 2007 *Contrib. Plasma Phys.* **47** 72
[24] Int. Commission on Non-Ionizing Radiation Protection (ICNIRP) 2004 *Health Physics* **87** 171
[25] Stoffels E, Kieft IE, Sladek REJ. 2003 *J. Phys. D: Appl. Phys.* **36** 2908
[26] Stoffels E, Kieft IE, Sladek REJ et al. 2006 *Plasma Sources Sci. Technol.* **15** S169
[27] Stoffels E, Sakiyama Y, Graves DB. 2008 *IEEE Trans. Plasma Sci.* **36** 1441
[28] Stoffels E, Roks AJM, Deelman LE 2008 *Plasma Process. Polym.* **5** 599
[29] Kieft IE, Broers JLV, Caubet-Hilloutou V et al. 2004 *Bioelectromagnetics* **25** 362
[30] Kieft IE, Darios D, Roks AJM, Stofffels E 2005 *IEEE Trans. Plasma Sci.* **33** 771
[31] Kieft IE, Kurdi M, Stoffels E 2006 *IEEE Trans. Plasma Sci.* **34** 1331
[32] Yonson Y, Coulombe S, Léveillé V, Leask RL 2006 *J. Phys. D: Appl. Phys.* **39** 3508
[33] Fridman G, Shereshevsky A, Jost MM et al. 2007 *Plasma Chem. Plasma Process.* **27** 163
[34] Shi X-M, Zhang G-J, Yuan Y-K, Ma Y, Xu G.M, Yang Y 2008 *Plasma Process. Polym.* **5** 482
[35] Leduc M, Guay D, Leask RL, Coulombe S 2009 *New J. Phys.* **11** 115021
[36] Dobrynin D, Fridman G, Friedman G, Fridman A 2009 *New J. Phys.* **11** 115020
[37] Lee HJ, Shon CH, Kim YS, Kim S, Kim GC, Kong MG 2009 *New J. Phys.* **11** 115026
[38] Shashurin A, Stepp MA, Hawley TS et al. 2010 *Plasma Process. Polym.* **7** 294
[39] Kalghatgi S, Friedman G, Fridman A, Morss Clyne A 2010 *Ann. Biomed. Eng.* **38** 748
[40] Boukamp P, Petrussevska RT, Breitkreutz Det al. 1988 *J. Cell Biol.* **106** 761
[41] Wende K, Landsberg K et al. 2010 *IEEE Trans. Plasma Sci.* **38** 10.1109/TPS.2010.2052835
[42] Rojas E, Lopez MC, Valverde M 1999 *J. Chromatography B* **722** 225

Topic 1
Fundamental problems of high pressure discharges

TRANSIENT SPARK – DC DRIVEN NANOSECOND PULSED DISCHARGE IN ATMOSPHERIC AIR

Mário Janda[1], Adriana Niklová[1], Viktor Martišovitš[1], Zdenko Machala[1]

[1]*Division of Environmental Physics, Faculty of Mathematics, Physics and Informatics, Comenius University, Mlynska dolina F2, 84248 Bratislava, Slovakia*
E-mail: janda@fmph.uniba.sk

We introduce a DC-driven pulsed discharge named transient spark (TS): a repetitive streamer-to-spark transition discharge with short spark duration (~10-100 ns), based on charging and discharging of internal capacity C of the reactor with repetition frequency $f \approx$ 1-10 kHz. TS generates very reactive non-equilibrium air plasma and is applicable for flue gas cleaning, bio-decontamination or other applications, since it can be maintained at relatively low energy conditions (0.1-1 mJ/pulse). Streamer-to-spark transition is governed by the increase of the gas temperature T_g in the plasma channel. Initial T_g at the beginning of the streamer is ~300 K, though it increases with frequency up to ~450 K at 10 kHz. The transition to spark occurs at ~1000 K. This heating accelerates with increasing f, leading to a decrease of the average streamer-to-spark transition time from a few μs to less than 100 ns.

1. Introduction

Atmospheric pressure plasmas in air generated by electrical discharges present considerable interest for a wide range of environmental, bio-medical and industrial applications, such as air pollution control, waste water cleaning, bio-decontamination and sterilization, or material and surface treatment [1-5]. New types of discharges are therefore still being developed and studied, with a focus on efficiency, power requirements, stability, reliability and simplicity [6].

A novel type of transition discharge in air at atmospheric pressure named transient spark (TS) is presented here. TS is a filamentary streamer-to-spark transition discharge initiated by a streamer, which transforms to a short (~10-100 ns) high current (~1-10 A) spark pulse due to the discharging of the internal capacity C of the reactor. TS is based on charging and discharging of C and a repetition frequency of this process from 1 to 20 kHz can be achieved [7].

We observed significant differences between two modes of TS with small and high repetition frequencies [8], studied by time-integrated optical emission spectroscopy. In order to understand the fundamental phenomena related to the evolution of TS and its changes due to increasing repetition frequency, we employed in this study a photomultiplier tube with fast 2.2 ns rise time and appropriate narrow band optical filters, as well as a 2-m monochromator coupled with ICCD camera with 2 ns gate, in order to monitor time evolution of the emission of excited species and of the temperature.

2. Experimental set-up

Experiments were carried out at room temperature in atmospheric pressure air with a radial flow of about 20 cm/s. The distance between stainless steel needle electrode and planar copper electrode (point-to-plane configuration) was 4 mm. A DC High Voltage (HV) power supply connected via a series resistor (R = 6.56-9.84 MΩ) limiting the total current was used to generate a positive TS discharge. The discharge voltage was measured by a high voltage probe Tektronix P6015A and the discharge current was measured on a 50 Ω or 1 Ω resistor shunt. The 1 Ω resistor shunt was used when we focused on TS current pulse itself, whereas the 50 Ω resistor shunt was used to measure current from the streamer. Both voltage and current signals where recorded by a 200 MHz digitizing oscilloscope Tektronix TDS2024.

The emission spectra were obtained using a 2-m monochromator Carl Zeiss Jena PGS2 covering UV and VIS (200-800 nm) and providing spectral resolution of 0.05 nm, cuopled with an intensified CCD camera (Andor Istar). The iCCD camera was triggered by a home-made generator of 5 V rectangular pulses with rise time less than 5 ns. This generator was triggered directly by the current signal, causing an additional delay of less than 10 ns. This delay, plus the delay caused by the transmission of the

signal by BNC cables, was compensated by using 10 m long optical cable (Ocean Optics P400-10-UV-VIS), so that we could see the whole emission profile.
For time-resolved optical emission measurements, a photomultiplier tube (PMT) module with a 2.2-ns rise time (Hamamatsu H955) was also used in place of the monochromator. Its signal was recorded using the oscilloscope. The PMT was triggered by the emission signal itself. Whenever it was necessary to isolate a specific spectral transition for PMT measurements, a band pass interference filter, e.g. Melles Griot 03 FIU127 for the N_2(C-B 0-0) transition, was inserted into the optical path. The experimental set-up is depicted in Fig. 1.

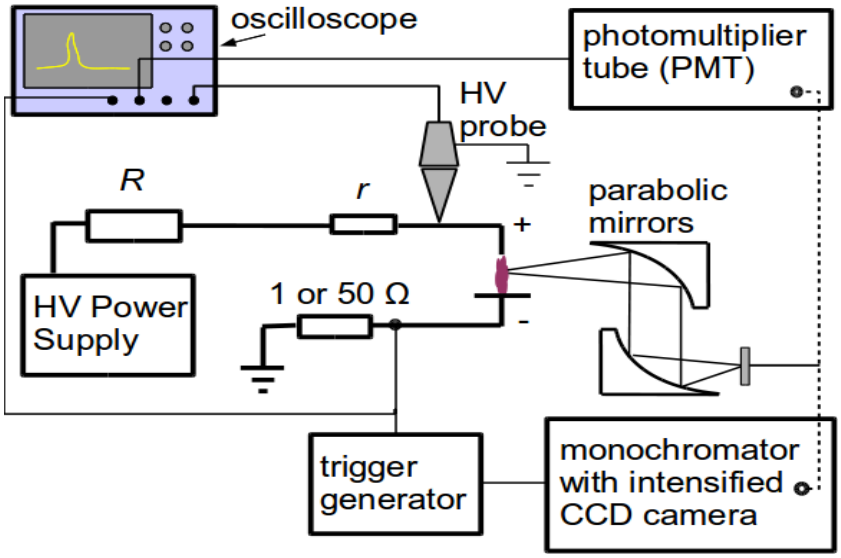


Fig. 1. Schematic of the experimental set-up, HV - high voltage, *R*, *r* - resistors.

3. Results and Discussion

When the high voltage U_{00} applied to the stressed electrode is progressively increased, we first observe a streamer corona. When the breakdown voltage is reached, a transition to TS occurs at the discharge voltage U_{TS}. The typical current and voltage waveforms are shown in Fig. 2a. During the high current phase the voltage drops to zero due to the resistive fall on the ballast resistance *R*. Then, during the quenched phase, the system capacity *C* (composed of the internal capacity of the electrodes, the capacity of the HV cable and of the HV probe) is recharged by a growing potential on the stressed electrode. For typical *R* and *C*, the repetition frequency *f* of this process is in the order of several kHz and grows with increasing U_{00} (Fig. 2b). This is accompanied by changes of TS properties. With increasing *f*, current pulses get smaller and broader (Fig. 3a).

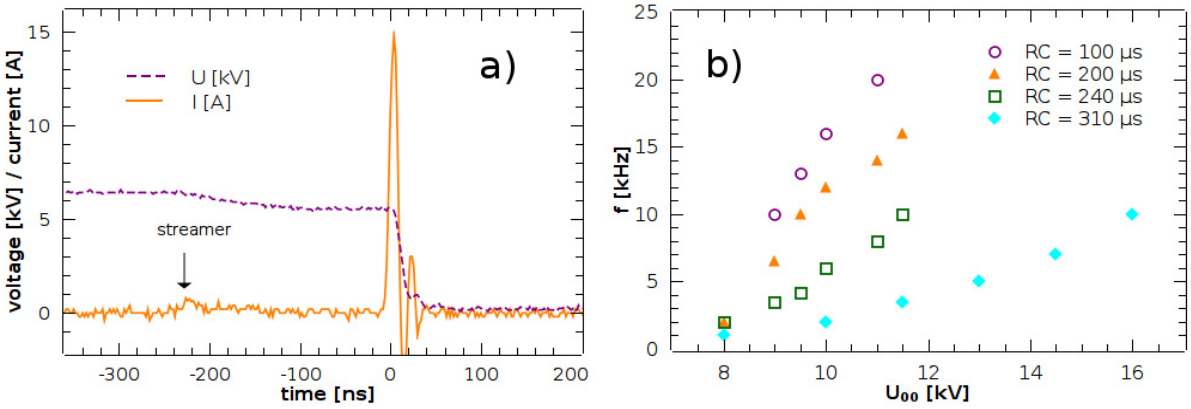


Fig. 2a. Typical TS current and voltage waveform, $f \sim 1$ kHz, $R = 6.6$ MΩ , $C \approx 26$ pF.
Fig. 2b. The dependence of TS repetition frequency on the onset voltage U_{00}.

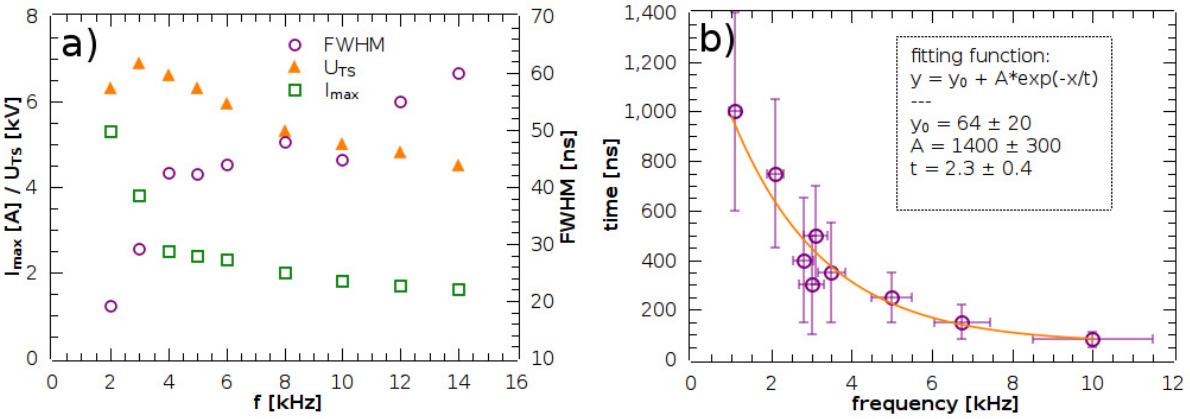


Fig. 3. Dependence of TS properties on f: a) peak current I_{max}, full width at half maximum FWHM of current pulses and breakdown voltage U_{TS}, b) streamer-to-spark transition time, $R = 6.6\,\mathrm{M\Omega}$, $C \approx 26\,\mathrm{pF}$.

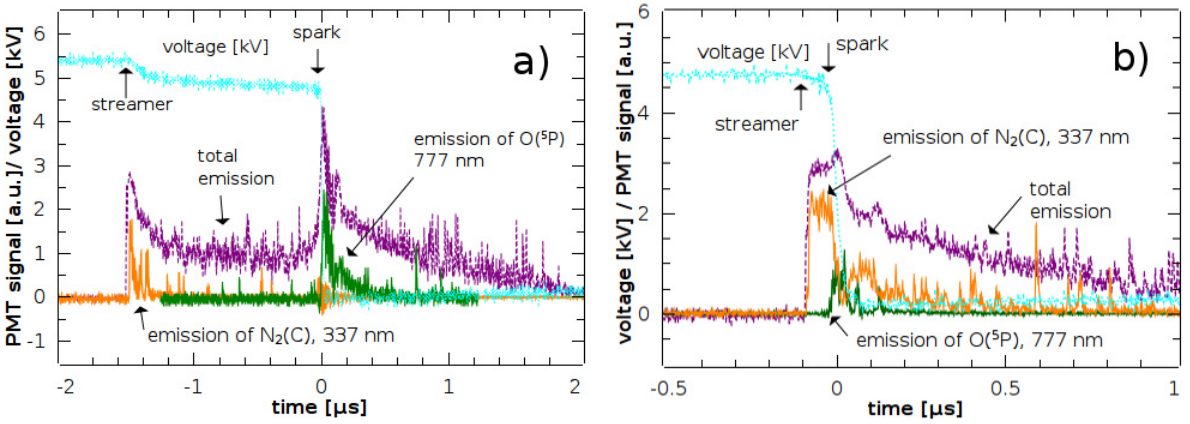


Fig. 4. Typical PMT emission profiles of TS at 2.5kHz (a) and 6 kHz (b), $R = 6.6\,\mathrm{M\Omega}$, $C \approx 26\,\mathrm{pF}$.

It is interesting, that U_{TS} also depends on f (Fig. 3a). The decrease of U_{TS} with f was preliminary explained by the increasing gas temperature T_g, resulting in a decreasing gas density N. Since a certain threshold, the reduced electric field E/N is sufficient to initiate the TS pulse, E and thus also U_{TS} may be lowered [5]. Another reason may be memory effects – the gap remains pre-ionized by previous TS pulses as f increases [7]. Changes of streamer to spark transition time were also observed (Fig. 3b). At lower frequencies (< 2 kHz), the delay between streamer and spark formation is very random and it can vary from several μs to a few hundred ns. As f increases, the average delay time shortens and it becomes more regular.

Significant differences between lower and higher frequency regimes of TS were also observed in time-integrated emission spectra in VIS region. At low frequencies (<3 kHz), the emission of O, N and N^+ atomic lines dominated in the spectra, whereas at higher frequencies these atomic lines almost disappeared and N_2 1st positive system was much stronger. In UV region, N_2 2nd positive system dominated at all frequencies, but its relative intensity compared to atomic lines in VIS region also increased significantly with f. In order to understand this problem, we measured the time evolution of the emission from the strongest atomic line, O(^{5}P) at 777 nm, and from 0-0 band of N_2 2nd positive system at 337 nm by PMT with appropriate interference filters. Figures 4 a) and b) show typical emission profiles at these frequencies, plus the total emission profile at 2.5 and 6 kHz, respectively.

At lower frequencies, we can clearly see two peaks of total emission. The first one is produced by the streamer, whereas the second one corresponds to the short spark. It is obvious, that N_2(C) species are produced mainly during the streamer phase and O(^{5}P) species during the spark phase. The emission profiles also reflect the shortening of the streamer-to-spark delay time with increasing f. The two emission peaks therefore approach to each other and it is difficult to distinguish them at higher f.

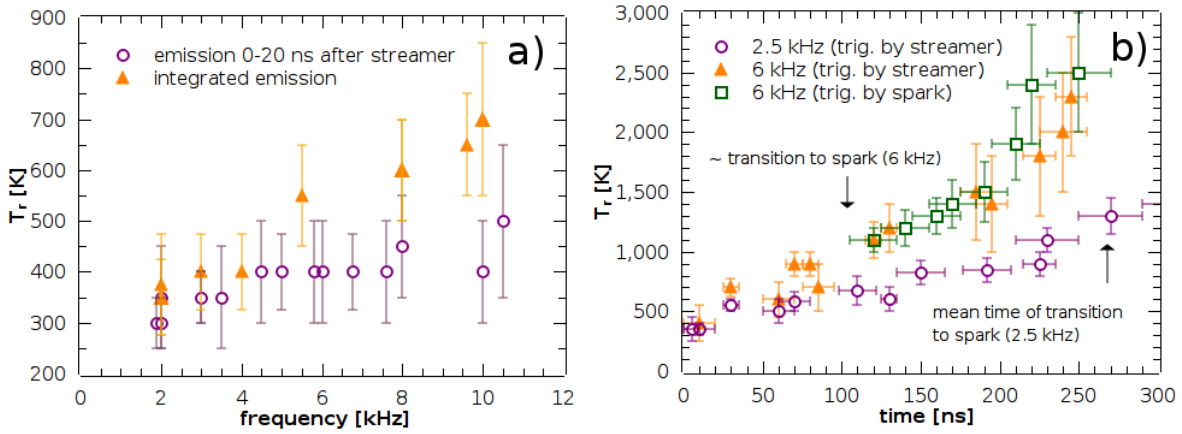


Fig. 5. The rotational temperature T_r of $N_2(C)$ as function of f (a) and time evolution of T_r (b).

The total emission from $N_2(C)$, obtained as an integral of PMT profiles, does not change significantly with f. The reason may be that $N_2(C)$ are mostly produced by collisions of energetic electrons with $N_2(X)$ during the streamer phase of TS and the properties of streamers (E/N, density of electrons n_e) do not change significantly with increasing f. On the other side, the total emission of $O(^5P)$ decreases with f quite significantly. This can be explained by changes of the spark pulse phase of TS with f (Fig. 3a), since $O(^5P)$ are mostly produced during this period. Another possible explanation might be a more complicated mechanism of $O(^5P)$ generation. We suggest the following three step mechanism:

$e + N_2(X) \rightarrow e + N_2(B, C)$ *streamer phase* (1)

$N_2(B, C) + O_2 \rightarrow N_2(X) + 2\,O(^3P)$ *streamer-to-spark transition phase* (2)

$e + O(^3P) \rightarrow e + O(^5P)$ *spark phase* (3)

As the streamer-to-spark transition phase shortens with the growing f, less and less $O(^3P)$ atoms accumulate for the production of $O(^5P)$ during the high current phase by the reaction (3). This does not necessarily mean that the production of $O(^3P)$ decreases significantly with f, it could be just shifted to later phase of TS, after the high current phase. Here, E/N is not strong enough for electrons to gain energy needed to excite $O(^3P)$ to $O(^5P)$. However, we cannot exclude other reactions that could be responsible for the production of $O(^5P)$, e. g. reactions including some metastable species such as $N_2(A)$, $NO(A)$, $O_2(a)$, $O_2(b)$ or $O(^1D)$.

As can be seen in Fig. 4, PMT profiles are quite noisy. The reason is that these emission profiles are from single TS pulses. It was not useful to acquire emission profiles by accumulation of many pulses due to a random character of streamer-to-spark transition. Data from iCCD camera, where the accumulation was necessary, were therefore used mainly for the calculation of rotational temperature T_r of $N_2(C)$ species, obtained by fitting the experimental spectra of N_2 2nd positive system with the simulated ones (using Specair program [9]). We further assumed that in our plasma $T_r \approx T_g$.

Let us explain the reason of the U_{TS} decrease with increasing f from the measured T_r. At the first moment it seems that T_r^{init} calculated from the initial 0-20 ns from the beginning of the emission induced by streamer increases only slightly with f, from about 300 to 450 K, compared to T_r^{total} calculated from time integrated emission of TS (typical integration time 300 μs – 3 ms), which increased to around 700 K (Fig. 5a). However, even this small T_r increase to 450 K is enough to keep an average E/N in the gap about 70 Td when the gap potential at the breakdown voltage U_{TS} decreases from about 7 kV to 4.5 kV (Fig. 3a). The value of T_r^{total} we previously used to describe the increase of T_g with increasing f has actually no physical meaning. To explain it, let us first look at the dependence of T_r on the time from the beginning of the streamer (Fig. 5b).

At both f=2.5 kHz and 6 kHz we observed approximately linear increase of T_r with time, from initial ~300 and ~400 K, respectively. This heating is faster at 6 kHz, but in both cases a streamer-to-spark transition occurs when T_r ~1000 K. We thus suppose that the increase of T_g is a dominant mechanism responsible for the streamer-to-spark transition, leading to the increase of E/N in the streamer plasma column from about 60-70 Td to about ~150-170 Td due to the decreasing N, under an assumption of the constant pressure.

The reason why the delay between the streamer and spark phase shortens with *f* can be explained by a faster growth of T_g with increasing *f*. However, this will require further research and deeper analysis, including kinetic modeling to explain why the growth of T_r accelerates with *f*.
During the spark phase, T_r increases even faster and can reach at least ~2500 K (Fig. 5b), but we were not able to measure it longer than ~250 ns from the beginning of the streamer, because the 2nd N_2 positive signal became too week.
Finally, relatively significant increase of T_r^{total} with *f* can be also explained by a faster growth of T_r with time at higher discharge frequencies. Despite the fact that the whole $N_2(C)$ emission profile contributes to T_r^{total}, we suppose that initial ~100 ns with the strongest intensity dominate. Thus, T_r^{total} represents only something like average T_r during these ~100 ns after the beginning of the streamer emission. At 2.5 kHz, T_r increases to about 600 K during these period, whereas at 6 kHz it is already ~1000 K, which gives T_r^{total} around 400 K and 600 K, respectively. In fact, significant changes of T_r during these ~100 ns also explains large errors of T_r^{total}, despite the signal was strong enough during the measurement of time-integrated spectra. In time-resolved measurements with iCCD gate open for up to 20 ns, the major sources of uncertainties were a weak signal and a random character of TS.

4. Conclusions

We investigated electrical characteristics and time-resolved emission profiles of a DC-supplied periodic streamer-to spark transition discharge in atmospheric air, called transient spark (TS). Thanks to the small internal capacity of the discharge chamber and a limiting series resistor, TS is characterized by the very short spark pulse duration (~10-100 ns) with peak current 1-10 A. TS can be maintained at low energy conditions (0.1-1 mJ/pulse) and generated plasma cannot therefore reach LTE conditions, though the current pulse can lead to temporary increase of temperature to ~2500 K. The global temperature however remains relatively low, since even at repetition frequencies above 10 kHz, each streamer-to-spark process starts at ~450 K.
Subsequent increase of temperature to ~1000 K, accompanied by the increase of the reduced electric field strength inside the plasma channel, governs the streamer-to-spark transition. Shortening of an average streamer-to-spark transition time with increasing TS frequency can be explained by an acceleration of temperature growth. The reason for this acceleration will require further research.
More research is also needed to explain chemical effects of TS. Emission profiles show that streamer is responsible for significant part of the total emission and for almost all emission of N_2 2nd positive system. This proves the importance of streamer in plasma chemistry, but it does not explain why TS was demonstrated more efficient for bio-decontamination than streamer corona. [5] We suppose that during the initial phase of the spark pulse, the strong chemical effect can be maintained thanks to the combination of a relatively strong reduced electric field (>100 Td) and a high electron density.

Acknowledgements. Effort sponsored by the AFOSR, Air Force Material Command, USAF, under grant FA8655-09-1-3110, Slovak grant agency VEGA 1/0293/08 and Slovak Research and Development Agency APVV SK-FR-0038-09.

5. References

[1] Civitano L 1993 Non-Thermal Plasma Techniques for Pollution Control, eds. Penetrante B and Schultheis S E (Springer, New York) NATO Series, Vol. 1, p. 103.
[2] Joshi A A, Locke B R, Arce P, Finney W C 1995 *Journal of Hazardous Materials* **41** 3.
[3] Cernak M et al. 2004 *Contrib. Plasma Phys.* **44** 492.
[4] Pawlat J et al. 2005 *Acta Phys. Slovaca* **55** 479.
[5] Machala Z et al. 2007 *J. Mol. Spectrosc.* **243** 194.
[6] Pai D et al. 2008 *IEEE Trans. Plasma Sci.* **36** 974.
[7] Janda M et al. 2010 *Acta Physica Universitatis Comenianae* **L-LI** 85-93.
[8] Machala Z et al. 2009 *Eur. Phys. J. D* **54** 195.
[9] Laux C O 2002 Radiation and Nonequilibrium Collisional-Radiative Models, von Karman Institute for Fluid Dynamics, Lecture Series 2002-07, Rhode Saint-Genese, Belgium

ELONGATED DBD WITH FLOATING ELECTRODES FOR ACTUATORS

Janusz Podliński[1], Artur Berendt[1], Jerzy Mizeraczyk[1,2]

[1]*Centre for Plasma and Laser Engineering, The Szewalski Institute of Fluid Flow Machinery, Polish Academy of Sciences, Fiszera 14, 80-952 Gdańsk, Poland*
tel.:+48(58)6995122, fax: +48(58)3416144,
[2]*Department of Marine Electronics, Gdynia Maritime University, Morska 81-87, 81-225 Gdynia, Poland*
E-mail: janusz@imp.gda.pl

In this paper a floating interelectrode for DBD plasma actuators is described. The velocity profiles of the airflow produced by the DBD actuator with floating interelectrode are presented. Also doubled DBD and multi DBD plasma actuators with floating interelectrodes are presented in this paper. Each, individual airflow induced in the multi DBD actuator has the same direction which is unique in multi DBD actuators. The obtained results suggest that DBD actuators with floating interelectrodes can be useful for many aerodynamic purposes.

1. Introduction

In the last decade interest in dielectric barrier discharge (DBD) [1] plasma actuators significantly increased. Plasma actuators which use DBD are capable to enhance properties of aerodynamic elements and allow to control laminar–turbulent flow transition, flow separation, reduce drag and improve lift of airfoils [2 – 5].
Usually DBD for actuators were composed of two plane electrodes placed asymmetrically on opposite sides of a dielectric. Typically glass or ceramics of a thickness of a few millimetres were used as the dielectric. The electrodes were made of copper or aluminium foil covering the dielectric surface. One of the electrode was a HV electrode connected to an AC power supply and the second was grounded. Applied high voltage established DBD between electrodes and the plasma appeared on both sides of the dielectric material. Generated plasma produces ionic wind which induces airflow of several m/s [6 – 9], which was tangential to the surface of the dielectric plate.
In most cases, using a single DBD the plasma region (on the actuator surface) expands to about 15 - 20 mm. However, sometimes a longer plasma region is needed, for example, to cover a long surface by a DBD plasma and produce an aerodynamic effect (e.g. airflow) along it. A possible solution is to use a set of single DBD actuators (Fig. 1), parallel one to each other. Unfortunately, such an arrangement requires a distance of a few centimetres between each single DBD to avoid an electric breakdown between the single sets. The region between consecutive DBDs would not be covered by plasma (Fig. 1). It is obviously a drawback for a real scale applications because only a small percent of the surface of an aerodynamic element could be covered by plasma. To get a longer DBD on a surface innovative DBD actuator configurations, like, for example, three electrodes or multiple DBD actuators were investigated [10, 11].
In this paper a new DBD with a floating interelectrode is presented. A set of several single DBD with floating interelectrodes for elongation of airflow on the surface is also described. Such a set may form a useful actuator for many aerodynamic purposes.

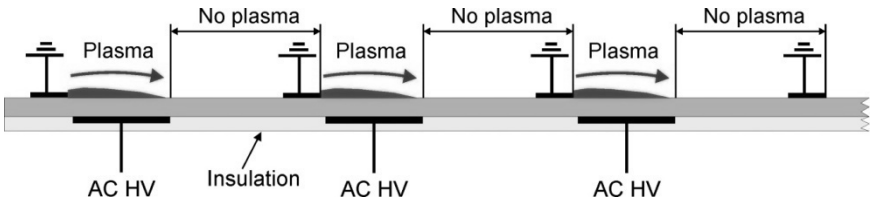


Fig. 1. Schematic view of the classic DBDs sequence used to cover a longer surface with plasma.

2. Experimental set-up

The experimental set-up for measurements of the airflow generated by DBD plasma actuators is presented in Fig. 2. It consists of an AC power supply, an oscilloscope and a standard PIV equipment for measurements of velocity fields. The AC power supply consists of a power amplifier (TREK, model 40/15) which amplified sinusoidal signal (frequency 1.5 kHz) generated by a function voltage generator (METEX MS9150). The discharge current was measured by a Pearson current monitor (Rogowski coil). Voltage and current signals were monitored by the oscilloscope Tektronix TDS 3052B.

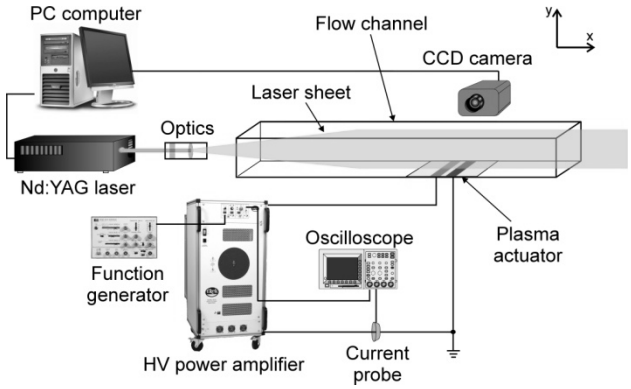


Fig. 2. Experimental set-up.

Single DBD with floating interelectrode

Investigated DBD arrangement was made of copper electrodes mounted on opposite sides of a 2 mm thick glass plate. The single DBD actuator consisted of a HV electrode and a grounded electrode mounted on one side of the glass plate, and an interelectrode at floating potential placed on the opposite side of the glass plate (Fig. 3). All electrodes were made from a 50 μm thick copper tape. The floating electrode was exposed to ambient air, when HV and grounded electrodes were insulated by a kapton tape. Smooth or saw-like electrode (Fig. 4) was used as the floating interelectrode. The floating interelectrode and the HV electrode were 6 mm wide while the grounded electrode was 10 mm wide. The gap between the HV electrode and the floating interelectrode was 1 mm, and between the floating interelectrode and the grounded electrode was 15 mm.

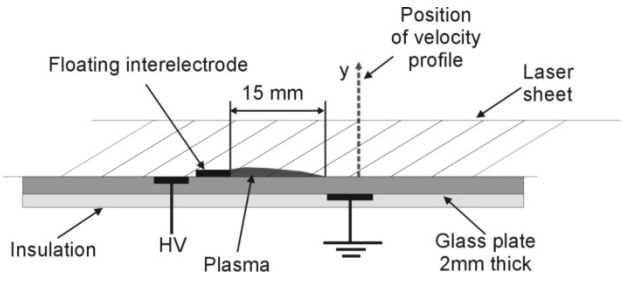


Fig. 3. Schematic view of a single DBD plasma actuator with floating interelectrode.

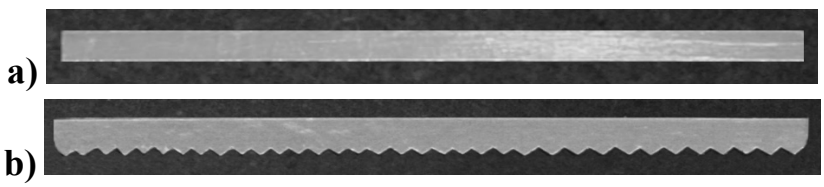


Fig. 4. Images of a smooth (a) and saw-like (b) floating interelectrode made of copper tape.

PIV measurements of the airflow produced by the single DBD plasma actuator were carried out in a plane defined by the laser sheet, which was placed perpendicularly to electrodes at their half-length. 100 PIV instantaneous measurements were carried out and then averaged, which means that the time-averaged flow velocity fields were obtained. Using the averaged flow velocity fields, the flow velocity profiles were determined. The flow velocity profiles were determined in the cross-section placed 20 mm from the floating interelectrode, i.e. from the active blade of the smooth interelectrode or from saw-tooth tips of the saw-like interelectrode. The position at which the flow velocity profiles were determined is marked by a broken line in Fig. 3.

Doubled DBD with floating interelectrode and two grounded electrodes

The doubled DBD was used to produce the elongated discharge on a dielectric surface. The cross-section schematic view of a doubled DBD with a floating interelectrode and two grounded electrodes is shown in Fig. 5. In this configuration the saw-like floating interelectrode was again exposed to ambient air when two smooth grounded electrodes and smooth HV electrode were insulated. The widths of electrodes were as follow: the grounded electrodes - 3 mm; floating interelectrode - 4 mm; HV electrode - 10 mm. The electrode gap between the first grounded (on the left side in Fig. 5) and the floating interelectrode was 10 mm while between the floating interelectrode and the second grounded electrode was 4 mm. There was no electrode gap between the first grounded electrode and the HV electrode, and between the HV electrode and the floating interelectrode.

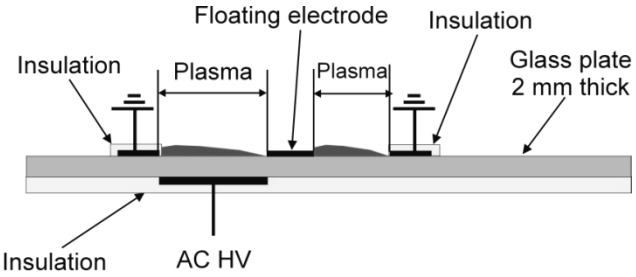


Fig. 5. Schematic view of the doubled DBD for producing the elongated discharge on a dielectric surface.

Multi DBD with floating interelectrodes

The presented above doubled DBD with a floating interelectrode and two grounded electrodes is very easy to multiply on the surface of the dielectric material. To make second doubled DBD three new electrodes were used: a HV electrode, a floating interelectrode and a grounded electrode. The new set of electrodes was mounted directly after the second grounded electrode of initial doubled DBD, i.e. the second grounded electrode of initial doubled DBD was the first grounded electrode of the second doubled DBD. Geometry and placement of new electrodes were the same like for initial doubled DBD. The third doubled DBD was also made on the surface of the dielectric material. In this way a multi DBD was obtained. The cross-section schematic view of multi DBD is presented in Fig. 6.

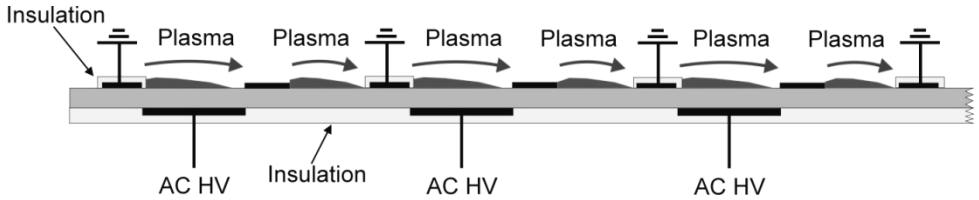


Fig. 6. Schematic view of the multi DBD with floating interelectrodes.

3. Results

The flow velocity profiles obtained from PIV measurements for the single DBD with floating interelectrode are presented in Fig. 7. The obtained results showed that the DBD with floating

interelectrode can produce airflow similarly like a conventional DBD. Moreover, the results showed that velocities of the airflow generated by the DBD with saw-like floating interelectrode are higher than for the DBD with smooth floating interelectrode. The highest velocities obtained are 2.9 m/s and 3.4 m/s for the DBD with smooth and saw-like floating interelectrode, respectively.

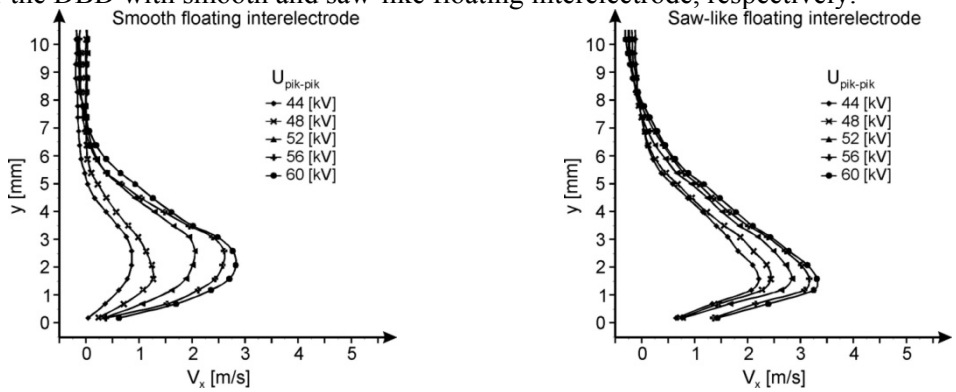


Fig. 7. Flow velocity profiles measured for the single DBD plasma actuator with smooth (a) and saw-like (b) floating interelectrode.

The image of the discharge obtained for the doubled DBD with floating interelectrode is shown in Fig. 8. The plasma generation was observed between the first grounded electrode and the HV electrode and between the floating interelectrode and the second grounded electrode. The plasma observed between first grounded electrode and the HV electrode (both electrodes insulated) was similar like for classic DBD with the discharge electrode exposed to ambient air.

The image of the operating multi DBD with floating interelectrodes is shown in Fig. 9. The plasma observed for consecutive electrode sets of the multi DBD was similar as for the doubled DBD described before. Presented multi DBD allow to cover much higher percent of a dielectric surface when compared to sequence of classic DBDs (as presented in Fig. 1).

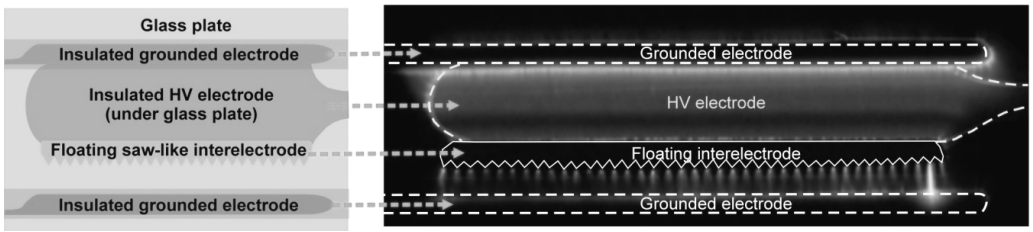


Fig. 8. Image of the discharge obtained for the doubled DBD with floating interelectrode. The applied voltage was 34 kV_{p-p}. The camera exposure time was 0.5 sec.

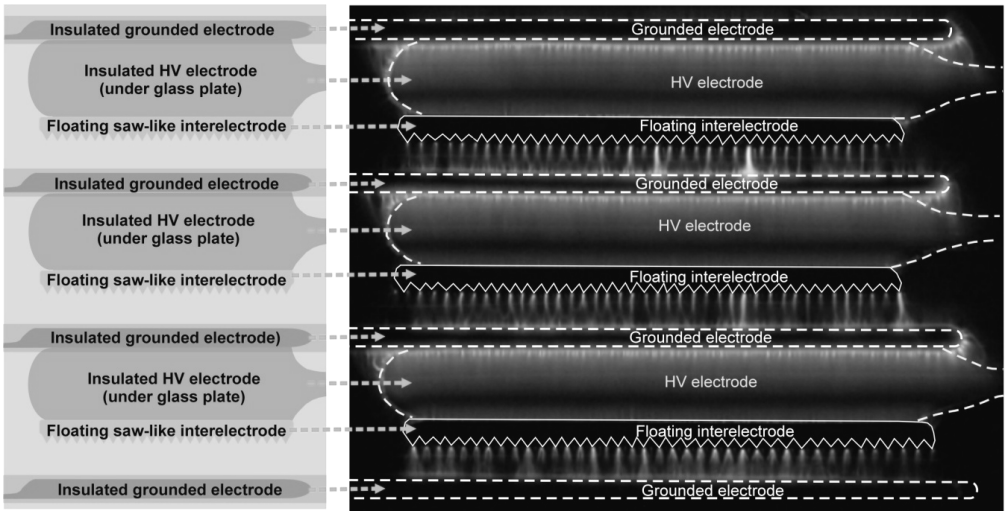


Fig. 9. Image of the discharge obtained for the set of 3 doubled DBDs with floating interelectrodes. The applied voltage was 32 kV_{p-p}. The camera exposure time was 0.5 sec.

4. Summary and conclusions

A new type of the DBD with the floating interelectrode for plasma actuators was presented. The influence of the shape of the floating interelectrode (smooth or saw-like) on the airflow generated by the DBD plasma actuator was investigated using PIV method.
The obtained results clearly show that the DBD with the floating interelectrode can generate airflow above a dielectric surface. The DBD with the saw-like floating interelectrode has lower onset voltage and induces higher airflow velocities then the DBD with a smooth floating interelectrode. It is especially noticeable at relatively low applied voltages.
Also the doubled DBD and the multi DBD were presented in this paper. Using DBD with floating interelectrodes generation of the plasma on a large surface of the dielectric material was allowed. Each, individual airflow induced by the plasma in the multi DBD with floating interelectrodes has the same direction which is unique in multi DBD actuators.
More investigations are needed to understand the physics of the DBD with the floating interelectrode. Usefulness of the DBD with the floating interelectrode as an actuator in aeronautic applications should be a subject of further investigations.

Acknowledgement. The research leading to these results has received funding from the European Community, Seventh Framework Programme FP7/2007-2013 under grant agreement no.: 234201 (PLASMAERO – Useful PLASMas for AEROdynamic control www.plasmaero.eu).

5. References

[1] U. Kogelschatz, Dielectric-barrier Discharges: Their History, Discharge Physics, and Industrial Applications, Plasma Chemistry and Plasma Processing, 23, 1, 1 – 46, 2003.
[2] E. Moreau, Airflow Control by Non-thermal Plasma Actuators, Journal of Physics D: Applied Physics, 40**,** 605-636, 2007.
[3] S. Grundmann, Transition Control using Dielectric Barrier Discharge Plasma Actuators, Shaker Verlag, Aachen, ISBN 978-3-8322-7587-7, 2008.
[4] S. Grundmann, C. Tropea, Delay of Boundary-Layer Transition Using Plasma Actuators, 46th AIAA Aerospace Sciences Meeting and Exhibit, Reno, #1369, Nevada 7 - 10 January, 2008.
[5] T. C. Corke, M. L. Post, D. M. Orlov, Single Dielectric Barrier Discharge Plasma Enhanced Aerodynamics: Physics, Modelling and Applications, Exp Fluids 46: 1–26, 2009.
[6] N. Takeuchi, K. Yasuoka, S. Ishii, Inducing Mechanism of Electrohydrodynamic Flow by Surface Barrier Discharge, IEEE Trans. Plasma Sci., 35, 6, 1704-1709, 2007.
[7] N. Balcon, N. Benard, E. Moreau, Formation Process of the Electric Wind Produced by a Plasma Actuator, IEEE Transactions on Dielectric and Electrical Insulation, 16, 2, 463-469, 2009.
[8] N. Benard, N. Balcon and E. Moreau, Electric Wind Produced by a Surface Dielectric Barrier Discharge Operating in Air at Different Pressures – Aeronautical control insights, Journal of Physics D: Applied Physics, 41, 4, #042002, 2008.
[9] J.P. Boeuf, Y. Lagmich, Th. Unfer, Th. Callegari, L. C. Pitchford, Electrohydrodynamic Force in Dielectric Barrier Discharge Plasma Actuators, Journal of Physics D: Applied Physics, 40, 652, 2007.
[10] E. Moreau, R. Sosa, G. Artana, Electric Wind Produced by Surface Plasma Actuators: a New Dielectric Barrier Discharge Based on a Three-electrode Geometry, Journal of Physics D: Applied Physics, 41, #115204, 2008.
[11] N. Benard, J. Jolibois, A. Mizuno, E. Moreau, Innovative Three-Electrode Design for Definition of Multiple Dielectric Barrier Discharge Actuators, CD proc. de ESA/IEEE-IAS/IEJ/SFE Joint Conference on Electrostatic 2009,#P.1.17, Boston, USA, 16-18 June, 2009.

USING IMS EQUIPED WITH CORONA DISCHARGE TO DETECT TRACE AMOUNTS OF IMPURITIES IN HIGH PURITY NITROGEN

Martin Sabo[1], Štefan Matejčík[1]

[1]*Department of Experimental Physics, Comenius University, Mlynska dolina F2, 84248 Bratislava Slovak Republic*

E-mail: matejcik@fmph.uniba.sk

We have applied the Ion Mobility Spectrometry/Mass spectrometry (IMS/MS) and the Atmospheric Pressure Corona Discharge Ionisation/Mass spectrometry (APCDI/MS) techniques to study the formation of the ions in the positive corona discharge (CD) in highly purified nitrogen with impurities at 100ppt level. The main products observed were $H_3O^+(H_2O)_n$ ions (reduced ion mobility of 2.15 $cm^2V^{-1}s^{-1}$). Additionally, we have observed ions with reduced mobilities 2.42 $cm^2V^{-1}s^{-1}$ and 2.3 $cm^2V^{-1}s^{-1}$. These ions were increasing with the increasing discharge current. These peaks were associated with NH_4^+ and $NO^+(H_2O)_n$. These ions were formed due to presence of O_2 and NH_3 impurities in the nitrogen. On other hand this indicates the ability of the IMS technique and CD ions source to detect impurities below 100ppt level. Using the APCDI/MS technique we have monitored the time evolution of the ions in the CD.

1. Introduction

Almost 50 years ago Shahin [1] performed first Atmospheric Pressure Ionisation Mass spectrometry (APIMS) studies of positive corona discharge (CD) in atmospheric gases. He observed $H_3O^+(H_2O)_n$ as dominant ions. Decreasing the humidity and pressure of the gas he was able to observe the primary ions [2]. Pavlík and Skalný [3] described in details the formation of the ions under different discharge conditions (high and low values of CD currents) and the formation of NO^+ in air.

The ions $NH_4^+(H_2O)_n$, $NO^+(H_2O)_n$ and $H_3O^+(H_2O)_n$ were observed in the positive Ion Mobility Spectrum (IMS) in pure N_2 using radioactive ion source [4]. The ions and their water clusters were not resolved in IMS due to thermodynamic equilibrium between formation and dissociation of the cluster ions in the drift gas [5]. Tabrizchi and co-workers [6] optimized the CD as a ion source for IMS. The problems associated with strong production of new molecular species and radicals in CD were solved by Ross and Bell [7] who suggested the reverse flow corona design. Different solution to this problem was the implementation of the curtain gas by Tabrizchi et al. [8].

The NO^+ production as function of CD current and reverse flow rate in IMS in air was documented in [9] in the attempt to optimize positive corona ion source for explosives detection. Ketkar and Dheandhanoo [10, 11] demonstrated IMS as a lower cost alternative to APIMS technique [12] for monitoring the gas impurities at ppb level.

In this study we present the ability of IMS/MS and APCDI/MS systems to study positive CD. We demonstrate the ability of IMS and IMS/MS systems to detect trace amounts of H_2O, O_2 and NH_3 down to 100 ppt respectively 10ppt level in high purity nitrogen. Additionally, we have measured IMS spectra of the positive ions formed in CD as a function of discharge current and identified the ion peaks in the IMS spectra using the MS. The time evolution of the ions formed in the CD was studied using the APCDI/MS technique.

2. Experiment

The IMS/MS (Figure 1a) and APCDI/MS (Figure 1b) instruments equipped with point to plane CD ion source were described in our previous work [13]. In attempt to reduce the penetration of the neutrals and radicals formed in the CD into the drift region we used single flow IMS system with gas outlet behind the corona discharge. Two positive power supplies (Heinzinger) were used one for CD and one for the drift field. The drift field in IMS was 351,8 V/cm while in APCDI/MS was in range 6000-250V/cm with corresponding drift time of ions from 0.1 to 2ms approximately. The corona current in IMS was varied from 3 to 10μA (limited by HV power supply) while in APCDI/MS was at

the constant value 10μA. The 5.0 nitrogen (Linde) was purified (MICROTORR, MC190-903FV) to reduce the concentration of O_2, H_2O, CO, CO_2, H_2 impurities under 100ppt and NH_3 and amines under 10ppt. The drift tubes of IMS/MS and APCDI/MS instruments were fed by high purity nitrogen with flow rate 900ml/min.

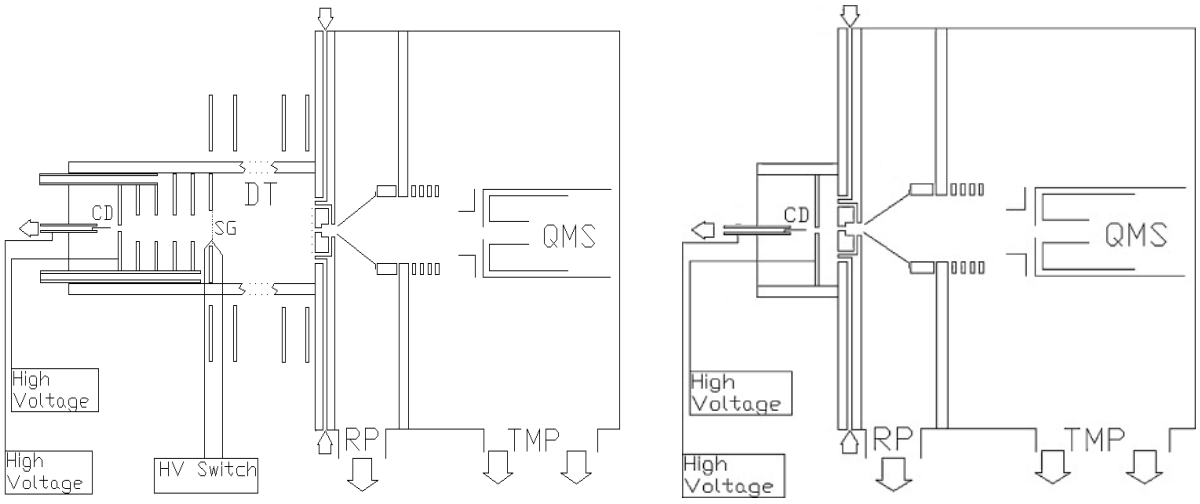


Fig. 1. IMS/MS (a) and APCDI/MS (b) instruments

3. Results and discussion

IMS/MS study

Three peaks with drift times 11.95 ms, 12.6 ms and 13.4 ms were observed in IMS spectrum using positive CD in pure N_2 at low discharge current of 3μA (Figure 2a). The corresponding reduced ion mobilities of these peaks are 2.42±0.05 $cm^2V^{-1}s^{-1}$, 2.3±0.05 $cm^2V^{-1}s^{-1}$ and 2.15±0.05 $cm^2V^{-1}s^{-1}$. The increase of the corona current resulted in increase of the peaks with reduced mobilities 2.42 $cm^2V^{-1}s^{-1}$ and 2.3 $cm^2V^{-1}s^{-1}$ and decrease of the peak with reduced mobility 2.15 $cm^2V^{-1}s^{-1}$ as can be seen from Figure 2a. In the Figure 2b we show the mass spectrum measured at corona current 8μA. The mass spectrum is dominated by $H_3O^+(H_2O)_n$ clusters.

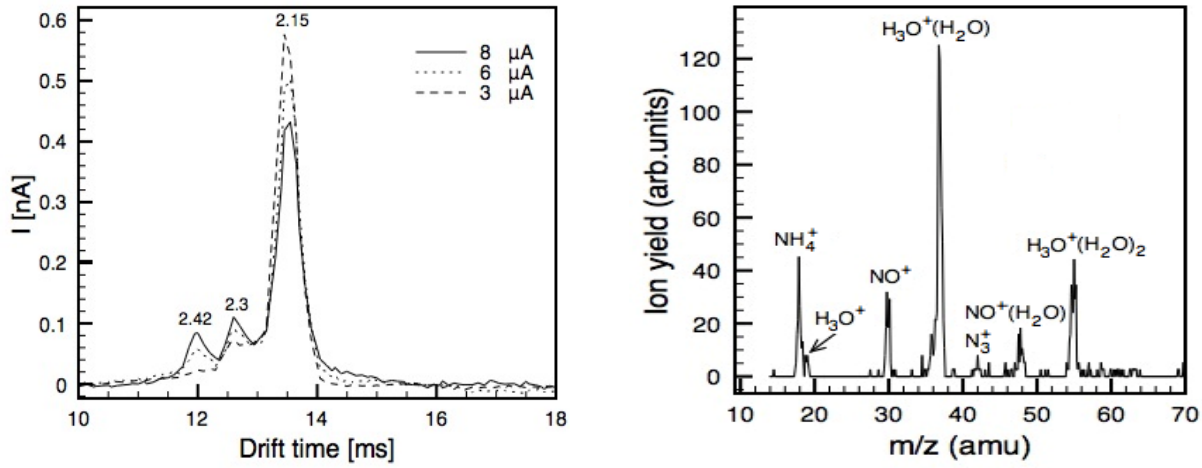


Fig.2. Ion mobility (a) and related mass (b) spectrum observed by IMS/MS technique. The numbers in the IMS spectra indicate the values of the reduced ion mobilities in $cm^2V^{-1}s^{-1}$.

We have also measured mass resolved IMS spectra (Figure 3a), which revealed that the dominant peak with reduced mobility 2.15 $cm^2V^{-1}s^{-1}$ is composed of the ions H_3O^+(m/z=19), $H_3O^+(H_2O)$ (m/z=37) and $H_3O^+(H_2O)_2$ (m/z=55). The H_3O^+ was not detected in this spectrum due to low intensity. The $H_3O^+(H_2O)_n$ are formed from primary ions N_2^+ through well know reactions [14]:

$$N_2^+ + H_2O \rightarrow H_2O^+ + N_2 \quad (1)$$
$$H_2O^+ + H_2O \rightarrow H_3O^+ + OH \quad (2)$$
$$H_3O^+(H_2O)_n + H_2O + M \rightarrow H_3O^+(H_2O)_{n+1} + M \quad (3)$$

As the equilibrium constants for the reactions (3) are known, we are able to measure the water density from the intensity ratio of the $H_3O^+(H_2O)_n$ ions [5]. The ratio $H_3O^+(H_2O)_2/H_3O^+(H_2O)$=0.35 (Figure 2b) at temperature 295K gives water concentration of 94ppt. This result is in very good agreement with the values stated by the manufacturer of the purifier, which guarantee the removal of water from gas at <100ppt level.

The peak with the reduced ion mobility of 2.3cm^{2}V^{-1}s^{-1} is composed of the ions NO^+ (m/z=30) and $NO^+(H_2O)$ (m/z=48). Position of the ion NO^+ in IMS spectrum is shown in the Figure 3a. Due to low intensity of the $NO^+(H_2O)$ we were not able to detect it in mass resolved IMS spectrum. We assume that the formation and decay of $NO^+(H_2O)_n$ ions is in thermodynamic equilibrium [5] and the cluster ion $NO^+(H_2O)$ should be detected at the same position as NO^+ [4]. The presence of $NO^+(H_2O)_n$ ions in positive IMS was in the case of radioactive ion source was well documented by Karasek and Denney [15]. The mechanism of the NO^+ formation was proposed by Dunkin [16]:

$$N_2^+ + N_2 \rightarrow N_3^+ + N \quad (4)$$
$$N_3^+ + O_2 \rightarrow NO^+ + O + N_2 \quad (5a)$$
$$\rightarrow O_2^+ + N + O_2 \quad (5b)$$
$$\rightarrow NO_2^+ + N_2 \quad (5c)$$

where the ions NO_2^+ are not stable under IMS conditions [15].

The N_3^+ (m/z=42 figure 2b) was observed in MS only at high discharge currents. In the IMS we were not able to detect a peak which could be assigned to N_3^+.

The sensitivity of IMS depends generally on the magnitude of the ion current generated in the ion source. In the case of IMS, the CD ion source is much more intense than the radioactive source, which results in high detection limit for O_2 at 100 ppt level. The intensity of the NO^+ peak at high corona currents was relatively strong so the expected limit for O_2 detection could be one order of magnitude lower. The drawback of the CD ion source is the generation of neutrals and radicals which may penetrate into the reaction region or drift tube and initiate there chemical reactions.

The first peak in the IMS with the reduced mobility of 2.42cm^{2}V^{-1}s^{-1} is composed of the ions with m/z=18 (Figure 3a). Since the H_2O^+ ions are not able to survive in IMS conditions [4] we assign this peak to the NH_4^+ ions. These ions are effectively formed via reaction [17]:

$$H_3O^+(H_2O) + NH_3 \rightarrow NH_4^+ + 2H_2O \quad (6)$$

Despite the low concentration of ammonia (10ppt) in our nitrogen we are able to detect this ion in the IMS system. The ratios of the relative intensities of IMS peaks as a function of the corona current are presented in the Figure 3b.

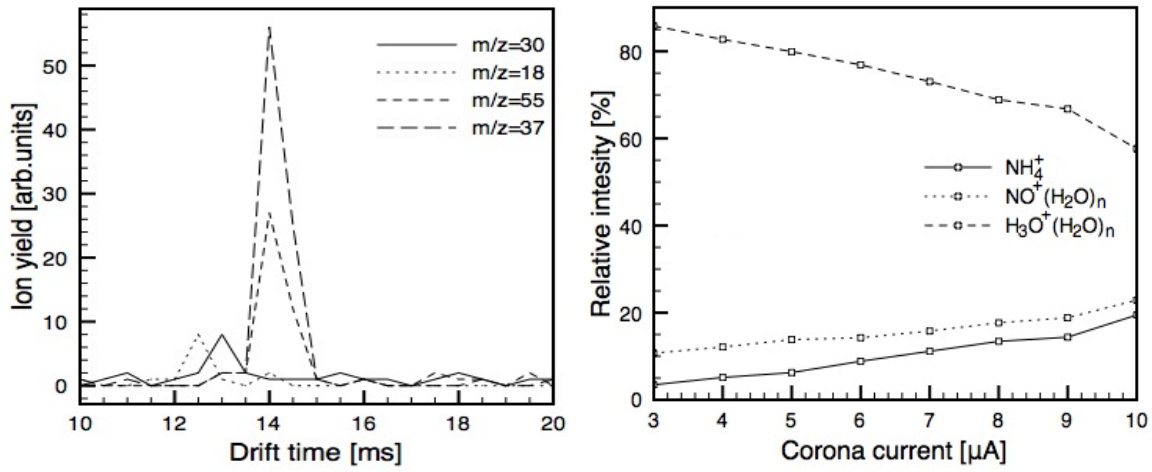


Fig. 3. Mass resolved IMS spectrum (a) and ratio of relative intensities of the peaks in dependence of corona current (b)

APCDI/MS study

The APCDI/MS technique was used to measure the time evolution of the ions formed in CD. At high potential of the plate electrode we were able to detect ions in time scale of around 100 μs after the formation of the primary ions in discharge. At low potential the time window was around 1 ms. At short time the ions with m/z = 19, 30, 32, 36, 37, 42, 46, 48, 50, 55, 60 were detected (Figure 4a). The ions with m/z= 19, 37 and 55 belongs to group $H_3O^+(H_2O)_n$. The masses 30 and 48 can be associated to ions NO^+ and $NO^+(H_2O)$. The ions with m/z=32 and 50 are formed through reaction 5b and belongs to ions O_2^+ and $O_2^+(H_2O)$. The fact that NO^+ ions are formed via reaction of N_3^+ with O_2 was confirmed by the appearance of both ions in APCDI/MS spectrum. In the Figure 4b we see the relative intensities of the ions as functions of the plate electrode potential. This potential is related through the drift velocity to drift time of the ions. Even at high potential (6000 V) the kinetic energy of the ions is below the dissociation limit of the ions.

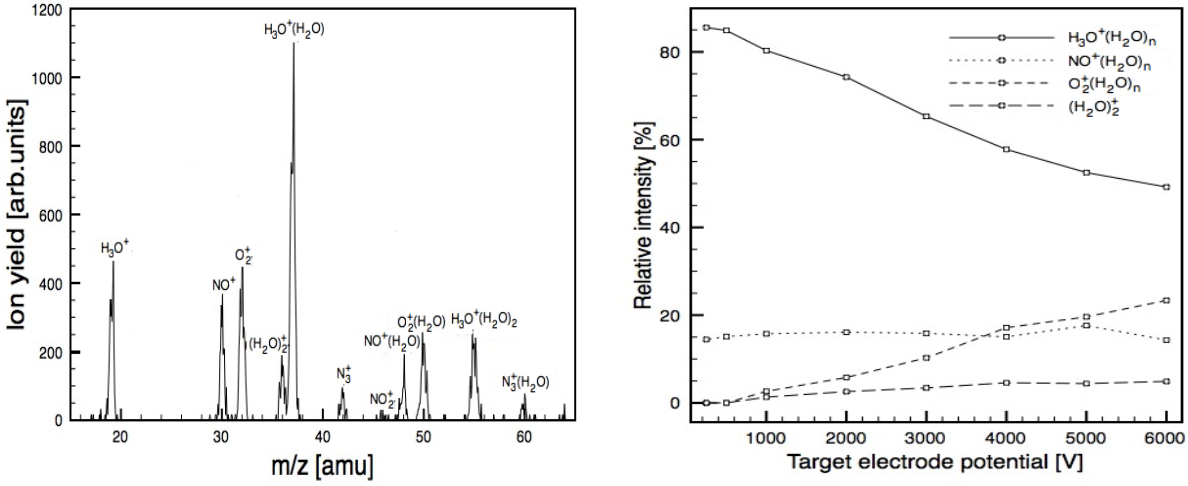


Fig. 4. Mass spectrum at high potential of the plate electrode (a) and the relative intensity of the ions as a function of the plate electrode potential (b)

We see in the Figure 4b that the intensities of the intermediate ions $O_2^+(H_2O)_n$ were decreasing with the increasing drift time. On the other hand the relative intensities of $H_3O^+(H_2O)_n$ were increasing. It is due to effective conversion of the $O_2^+(H_2O)_n$ ions into $H_3O^+(H_2O)_n$ [3]. The $O_2^+(H_2O)_n$ ions are therefore not be observed in IMS due to long time scale (~10 ms). On the basis of the disappearance of

the ions with m/z=36 with increasing drift time (Figure 4b) we assign these ions to $(H_2O)_2^+$. These ions are formed through exothermic reaction [2]:

$$O_2^+(H_2O)+H_2O \rightarrow (H_2O)_2^+ + O_2 \quad (7)$$

The $(H_2O)_2^+$ ions are in next collision with water molecule converted into $H_3O^+(H_2O)$ [2]. This explains the absence of these ions in IMS. $(H_2O)_2^+$ like the ions $O_2^+(H_2O)_n$ contribute to the growth of the relative intensity of the $H_3O^+(H_2O)_n$ with increasing drift time. The ions with m/z=42, 60 and 46 are N_3^+, $N_3^+(H_2O)$ and NO_2^+ (reaction 4 and 5c). Evolution of these ions due to their relatively low concentration is not depicted in the Figure 4b. The fact that ions NH_4^+ were not observed in this study suggests these ions are formed later in the drift.

4. Conclusions

IMS are small portable and relatively inexpensive devices with fast response and low detection limits. Due to relatively low resolution of these instruments and also lack of data on the ion mobilities, the coupling of IMS with MS is of high importance, increases analytical capabilities of IMS and gives possibility to measure the mobilities of the ions. Moreover IMS/MS systems could deliver more insight on the ion-molecule reactions at atmospheric pressure. In this work we have presented the ability of IMS/MS system to study the CD and to detect O_2, H_2O and NH_3 impurities in N_2 at <100ppt level.

Acknowledgements. This work was supported by the Slovak research and development agency projects LPP-06-0146, SK-CN-0015-09 and the VEGA grant No. 1/0051/08.

5. References

[1] Shahin M.M. 1965 *J.Chem.Phys*. **45** 2600
[2] Shahin M.M. 1969 *Chemical Reactions in Electrical Discharges* **Chapter 4** 48
[3] Pavlík J. and Skalný J.D. 1997 *Rapid Communications in Mass Spectrometry* **11** 1757
[4] Carroll D.I., Dzdic I., Stillwell R.N., Horning E.C. 1975 *Anal.Chem*. **47** 1956
[5] Kebarle P., Searles S.K., Zolla A., Scarborough J., Arshadi M. 1967 *J.Am.Chem.Society* **89** 6393
[6] Tabrizchi M., Khayamian T., Taj N. 2000 *Review of Scientific Instruments* **71** 2321
[7] Ross S.K. and Bell A.J. 2002 *IJMS* **218** L1-L6
[8] Tabrizchi M. and Abedy A. 2002, *IJIMS* **218** 75
[9] Tabrizchi M. and Ilbeigi V. 2010 *Journal of Hazardeous Materials* **176** 692
[10] Ketkar S.N. and Dheandhanoo S. 2001 *Anal.Chem*. **73** 2554
[11] Dheandhanoo S. and Ketkar S.N. 2003 *Anal.Chem.* **75** 698
[12] Siefering K., Berger H., Whitlock W.J. 1993 *Vacuum Science and Technology A* **11** 1593
[13] Sabo M., Páleník J., Kučera M., Han H., Wang H., Chu Y., Matejčík Š. 2010 *IJIMS* **293** 23
[14] Howard C. J., Rundle H. W., Kaufman F. 1970 *J.Chem.Phys.* **53** 3745
[15] Karasek F.W. and Denney D.W. 1974 *Anal.Chem.* **46** 633
[16] Dunkin D.B., Fehsenfeld F.C., Schmeltekopf A.L., Ferguson E.E. 1971 *J.Chem.Phys.* **54** 3817.
[17] Fehsenfeld F.C. and Ferguson E.E. 1973 *J.Chem.Phys.* **50** 6272

THE INFLUENCE OF DIELECTRIC FILMS ON THE MACRO- AND MICROSCOPIC PROPERTIES OF THE BARRIER SURFACE DISCHARGES

M.V.Sokolova[1], K.V.Kozlov[2], S.A.Krivov[1], L.A.Maslova[1], A.N.Mitin[1], P.A.Tatarenko[2], V.G.Samoilovich[2]

[1]*Department of Electrophysics and High Voltage Technique, Moscow Power Engineering Institute (Technical University), Krasnokazarmennaya 14, 111250, Moscow, RUSSIA,*
[2]*Department of Chemistry, Moscow State University, Leninskie Gory1, str.9. 119899, Moscow, RUSSIA*
E-mail: mvsokolova@mail.ru

Results of experimental investigation of electric and optical characteristics of surface microdischarges over barriers with surface layers of different dielectric materials are presented. The barriers are piroceramics (polycrystalline aluminium oxide) plates of 1 mm thickness with different surface layers of SiO_2, TiO_2, Barium-Strontium Titanate (BST) and Al_2O_3. The thickness of the films is in the range 100-1000 nm. The photo of microdischarges made by means of a Panasonic DMC-FS3 camera, the spatio-temporal distributions of light emission and the most probable value of the charge formed by individual microdischarges show distinct dependence of the discharge structure and its characteristics on the surface layer material.

1. Introduction

Surface discharge (SD) appears generally in gas at the edge of an electrode placed on the surface of a solid dielectric (barrier) while the other electrode is placed at the reverse side of the barrier. Experimental investigations of SD in such electrode system [1, 2] have shown that the discharge has a form of discrete microdischarges. An analysis of the surface part of the barrier discharge [3] indicates that the γ secondary emission coefficient must depend on the "memory" effect connected with the surface charges. These last appear on the barrier surface during the discharge and practically define the SD conditions. In its turn the surface charge formation depends on the surface properties of the barrier. It was shown in [4] that rough surface of the barrier leads to more powerful microdischarges compared with ones over a smooth surface for the same material and the same thickness of the barrier and the same other conditions of the discharge. The aim of the present work was to obtain new data about the influence of the barrier surface properties on the discharge characteristics. Three types of data are presented for barriers with different films placed on their surface: the photo of the discharge, the oscillograms of current impulses of microdischarges and pictures of spatially-temporal distribution of light emission of the discharge. The results of such investigation permit to analyze the degree of the barrier surface influence on the discharge structure.

2. Experimental conditions and procedure

The electrode system used in the experiments consists of a small aluminium electrode (the grounded discharge electrode) deposited on one side of a ceramic plate (the barrier, 1.1 mm of thickness) by means of an ion-plasma sputtering method, while the other electrode made of a piece of metallic aluminum foil is placed on the back side of the dielectric plate and is a high voltage electrode. The electrode thickness is about 100-200 μm. This electrode system is placed into a discharge cell made of Plexiglas with quartz windows. Barriers are piroceramic (polycrystal aluminium oxide) plates 1 mm of thickness covered by different films of SiO2, TiO2, Barium-Strontium Titanate (BST) and Al2O3. The films are deposited on the barrier surface by a radio-frequency ion-plasma sputtering method and cover the whole surface of the barrier together with the discharge electrode. The film thickness δ is given in table 1. The surface structure of the barrier can be characterised by roughness Δ which is the

difference between the highest and the lowest value on the profile of the surface (fig.1) and by a value ς – the distance between peaks. In table 1 there are given the above characteristics for all barrier surfaces that were analyzed.



Fig. 1. The surface structure of the barrier without a film

For all films the surface structure of the barrier is practically the same as the one without a film. For an Al2O3 film the roughness of the surface is higher than for the original surface of piroceramics. All edges of the electrode with SD, excluding a small part 1.5–2.5 mm long, are coated with an epoxy compound. So only 1–3 microdischarge channels develop from the open edge of the electrode. Pictures of microdischarges over different surface layers were made by means of a Panasonic DMC-FS3 camera.

Tab. 1. Characteristics of films on the surface of the barrier.

Film material	ε of the film material	δ, nm	Δ, μm	ς, μm
Piroceramics without film	8	–	6	20
BST	500	100–200	4	20
SiO_2	4	100–200	–	–
TiO_2	80	100–200	6	20
Al_2O_3	9	1200	12	50

All measurements were done for a weak flow of dry air (the humidity not more than 0.7%). The gas flow rate was about 70 l/min, the gas temperature 23–25oC and the gas pressure 730–750 mm Hg. The optical characteristics of the SD were measured for 2.6 kHz high a.c. voltage, while 14 kHz a.c. voltage was used for measuring the microdischarge current impulses. The system to register the spectrally resolved light emission by means of the cross-correlation spectroscopy method [5] includes two (vertical and horizontal) entrance slits of a MDR-2 monochromator having a high light transform, an exit vertical slit, a quartz lens and two photomultipliers (PM-106). PM1 serves to start the work of the system, PM2 counts single photons. The emission intensity I is defined by the quantity of photons with energy corresponding to 337.1 or 391.5 nm that enters the photomultiplier during 1 second.
To achieve a more detailed picture of the light emission distribution, the integral emission flow corresponding to whole length of the microdischarge channel, is scanned additionally along the channel axis with a step length ΔX equal to 0.2 mm. It must be noted that the presented results of spatially resolved light emission measurements correspond to an integral emission flow of many microdischarge channels that develop during different half cycles of a certain polarity of the applied voltage. The possibility to use such method is based on the series of photos of the discharge channels made with an exposure time 0.125 s. These photos show that the channels do not move along the electrode edge but stay in the places of their origin. It means that microdischarges that appear at different time and during different half-cycles, develop along the same path and the places of their origin are “tied” to certain places at the electrode edge. Such a behaviour of the discharge permits to

use integral emission image of many discharges, the channels of which coincide, for analysis of an individual microdischarge.
The current pulses of microdischarges were measured as a signal over a specially constructed 11.5 Ohm shunt consisting of six low inductance resistors in parallel. The charge formed by an individual microdischarge, is evaluated as an integral of the most probable mean current pulse of at least 40 current pulses measured by means of a Tectronix oscilloscope TDS 2012.

3. Experimental results and discussion

In fig.2 there are presented the most typical photos of microdischarges over barrier without a film and covered with different films. All photos are done for about 20% overvoltage U≈1.2U0, where U0 is the voltage value corresponding to the appearance of the discharge. For different films U0=2.0-2.7 kV. A visible difference in the structure of individual microdischarges for barriers with different layers is seen. The length of the channels and the brightness of the channels vary as well. There is distinct branching of microdischarges channels for SiO2 and Al2O3, while the TiO2 film produce the same length of the channels compared with the case of the barrier without a layer. For BST film the pattern of the channels is near to one without a film, but the channels on BST are more powerful. An increase of the applied voltage leads to an elongation of the channels in all cases. It must be noted that the photos of the discharge give an integral picture of all microdischarges that are formed in both half-periods of the applied voltage during a number of periods.
The oscillograms of current impulses of individual microdischarges show an increase of the most probable amplitude value imax of the current for all cases of a barrier with a surface layer compared to one without a layer. The highest are the amplitudes for TiO2 and Al2O3 and it correlates with the photos of the discharge. The corresponding charges Q formed in individual microdischarges are calculated as an integral of the current curve (table 2).

Tab. 2. The most probable Q, maximum values Qmax and parameters of the integral curves I=f(t) and I=f(S) for different layers.

Film material	Q, pCl	Q_{max}, pCl	τ, ns	S, mm
Piroceramics without film	90	175	5.5	0.8
BST	250	430	2.5	1.2
SiO_2	650	1160	2.5	2
TiO_2	125	500	2	–
Al_2O_3	280	450	2.5	3

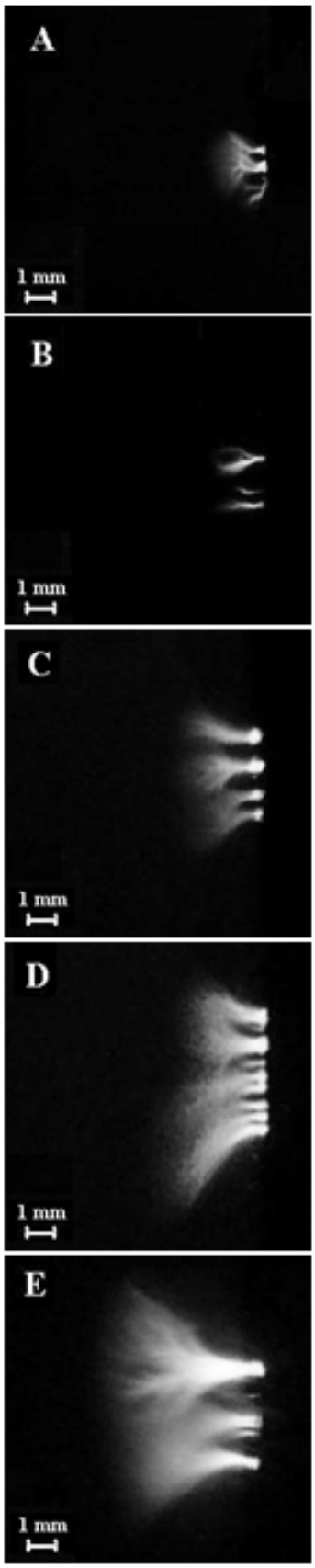


Fig.2. Photos of the SD for different surface films. A– without a film, B–TiO2, C–BST, D–Al2O3, E–SiO2

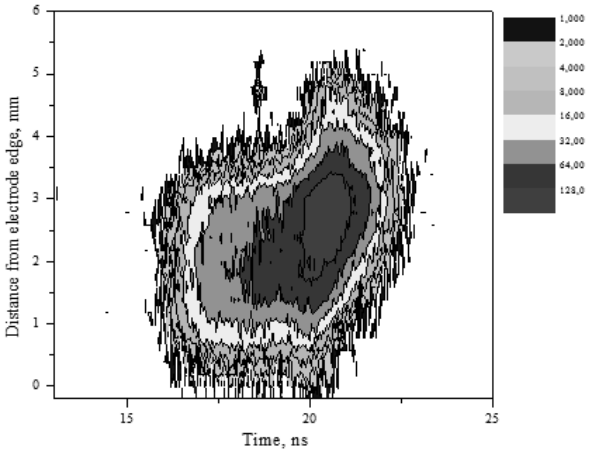
The same pronounced influence of the surface layer of the barrier on the discharge is seen in the images of spatio-temporal distributions (SPD) of the light emission of microdischarges (fig. 3a) for positive and negative polarity of the electrode and for two wave lengths λ = 337.1 nm and λ = 391.5 nm. Curves of normalized values of the integral light emission intensity I as a function of time I=f(t) or of the distance S from the electrode edge I=f(S) for such SPDs over some films are presented in fig. 3b and fig. 3c. The half-value τ of I=f(t) curve (fig.3b) permits to characterise duration of a microdischarge and the S value (fig.3c) for λ = 391.5 nm evaluates the channel length [5]. It is interesting to point out that for all layers for both polarities and both wave lengths the half-width τ of I=f(t) curves is practically the same equal to 2.5 ns and twice less than for the case of the barrier without a layer (table.2). The smallest value has been measured for TiO2 and it correlates with fig. 2 B.

As the surface structure of the barrier for all films but Al2O3, is practically the same as one without a film, it seems reasonable to state that plasma-chemical processes of interaction between the surface and the discharge are defined by chemical composition of the film material and this interaction is concentrated in a thin layer of the barrier surface. An increase of the surface roughness caused by the film (as in the case of Al2O3) leads additionally to an increase of the SD intensity.

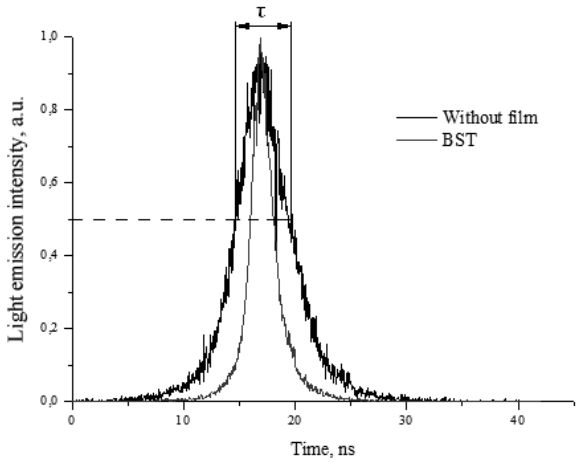
It can be supposed that the film material increase the secondary emission from the surface of the barrier. Such materials as TiO2 or Al2O3 must be analysed additionally as having the most intense influence on the discharge. There are still a range of moments that are not clear. The influence of the film thickness, the distribution of the surface charge over surface of different films during the discharge, the dimensions of the plasma layer formed near the barrier surface - must be additionally investigated to achieve a full picture of plasma-chemical processes that go on in a SD.

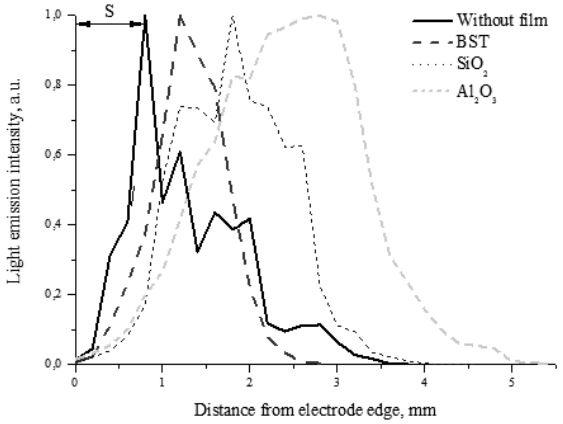
4. Conclusion

The appearence of a thin film on the surface of the barrier leads to a change in the SD structure and in its electric and optical characteristics. The most important properties to change the discharge structure and intensity are the chemical composition of the surface layer and its structure. Higher roughness of the surface leads to more powerful microdischarges, longer channels and their branching. It means that properties of the barrier surface must be included into the parameters if modelling of the SD is done.



a)





b) c)

Fig.3. Examples of a spatio-temporal distribution of light emission for Al2O3 film (a) (λ=391,5 nm) and integral curves I=f(t), positive polarity and λ=337,1 nm (b) and I=f(S) for a set of films, positive polarity and λ=391,5 nm (c).

5. References

[1] Sokolova M.V., Kozlov K.V., Krivov S.A., Tatarenko P.A., Samoilovich V.G. 2006 Contr.Papers of Int.Symp.of HP LT Plasma Chemistry – HAKONE 10, Japan, Saga.
[2] Sokolova M.V., Kozlov K.V., Krivov S.A., Tatarenko P.A., Samoilovich V.G. 2008 Contr.Papers of Int.Symp.of HP LT Plasma Chemistry – HAKONE 11 France, Oleron Island 1 55-59.
[3] M. Sokolova, L. Hulka, G. Pietsch. 2005 Plasma Processes and Polymers 2 162-169.
[4] Massines F., Gherardi N., Naudé N., Ségur P. 2008 Contr.Papers of Int.Symp.of HP LT Plasma Chemistry – HAKONE 11 France, Oleron Island 1 21-30.
[5] K.V. Kozlov, H-E. Wagner, R.Brandenburg, P.Michel. 2001 J. Phys. D: Appl. Phys. 34 3164

Acknowledgement. The work was done in a frame of Grant No 08-09-00274a, supported by Russian Fund of Basic Researches.

STUDY OF DIELECTRIC BARRIER DISCHARGE IN NITROGEN AT ATMOSPHERIC PRESSURE

Haiyun Luo, Xinxin Wang, Zhuo Liang, Zhicheng Guan and Liming Wang

Department of Electrical Engineering, Tsinghua University, Beijing 100084, China
E-mail: wangxx@tsinghua.edu.cn

Dielectric barrier discharge in nitrogen at atmospheric pressure was investigated by means of the electrical measurement, the fast photography and the time-resolved spectroscopy. It was found that the homogenous discharge in a 2-mm nitrogen gap is not readily produced, but produced in a limited range in dependence on the amplitude and the frequency of the applied voltage as well as the gas flow. The homogenous discharge was identified with a Townsend discharge. The Townsend mode DBD is extinguished while the gas voltage continues rising up. This extraordinary way of the discharge extinction suggests that the secondary electron emission from the trapped electrons on the surface of the dielectric plays an important role in maintaining the discharge. It was found that when a stable Townsend discharge is maintained the lowest breakdown voltage of the nitrogen gap is only 4.9 kV, much lower than 8.2 kV that is the steamer breakdown voltage of the gap. The laminar flow effect that had been used to explain the influence of the gas flow on the homogenous dielectric barrier discharge in nitrogen was proved to be not correct according to the discharge photos showing a luminous layer close to the anode. The mechanism for the gas flow influencing the discharge is simpler than the laminar flow effect. With a pure nitrogen flow directly through the discharge gap, the quenchers of the metastable nitrogen molecule $N_2(A)$, especially the density of oxygen from the impurity, are significantly reduced, which was evidenced by the emission spectra of the discharge.

1. Introduction

Dielectric barrier discharges (DBDs) can produce non-thermal plasmas at atmospheric pressure and have found many applications. For some applications it is required to use homogenous DBDs rather than the usually obtained filamentary DBDs. The homogenous DBD in nitrogen at atmospheric pressure is not readily produced but produced in a short gap with a gas flow [1-3]. The mechanisms leading to this homogenous DBD are still not fully understood. In this paper DBD in nitrogen at atmospheric pressure was investigated by means of the electrical measurement, the fast photography and the time-resolved spectroscopy.

2. Experimental setup

The experimental setup is sketched in figure 1. The plane-parallel electrodes, 50 mm in diameter, were covered with a 1-mm thick quartz plate that is of size $100mm \times 100mm$. A gas gap of 2 mm was usually used in the experiment. By pumping, a primary vacuum down to 10^{-2} Pa could be achieved in the working chamber housing the electrode assembly. After pumping, the chamber was filled with nitrogen of grade 5.0 (99.999%) up to 1 atmosphere. Then, a nitrogen flow was added and controlled by a mass flow controller, maintaining the atmospheric pressure by a slightly pumping.

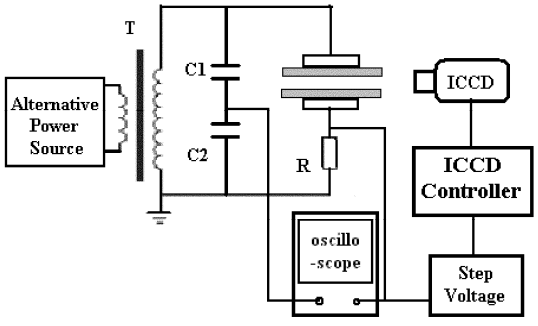


Fig. 1. Schematic diagram for the experimental system

The voltage from the power source was raised up through a transformer and then applied to the electrodes. The frequency of the voltage could be continuously changed from 1 kHz to 35 kHz. The total current was measured with a 50-ohm resistor that connects the bottom electrode and the ground. The applied voltage was measured with a capacitive divider. Both current and voltage signals were fed into a digital storage oscilloscope. An intensified charge coupled device (ICCD) camera was used to take the discharge photographs with short exposure down to 10 ns. The discharge was synchronized with the ICCD gating by using a step voltage generator. A spectrometer was used to record the discharge spectrum. The spectrometer is 50 cm in focal length and equipped with a grating that is 1200 grooves per millimeter and blazed at 300 nm. For taking time-resolved emission spectrum, the ICCD camera was directly installed on the exit of the spectrometer.

3. Results and discussions

Figure 2 shows the typical waveforms and 1-μs exposure photograph of the homogenous discharge in nitrogen. The measured waveform of the total current, figure 2(a), consists of two parts, a hump followed by a peak. The hump is the displacement current and the peak the discharge current. Based on the waveforms of figure 2(a) and by the calculations detailed elsewhere [4], the voltage really applied to the nitrogen gap as well as the displacement current can be deduced. The discharge current, figure 2(b), was obtained by subtracting the displacement current from the total current. Since the homogenous discharge was very weak and with a weakly luminous layer close to the anode, it was identified with a Townsend discharge.

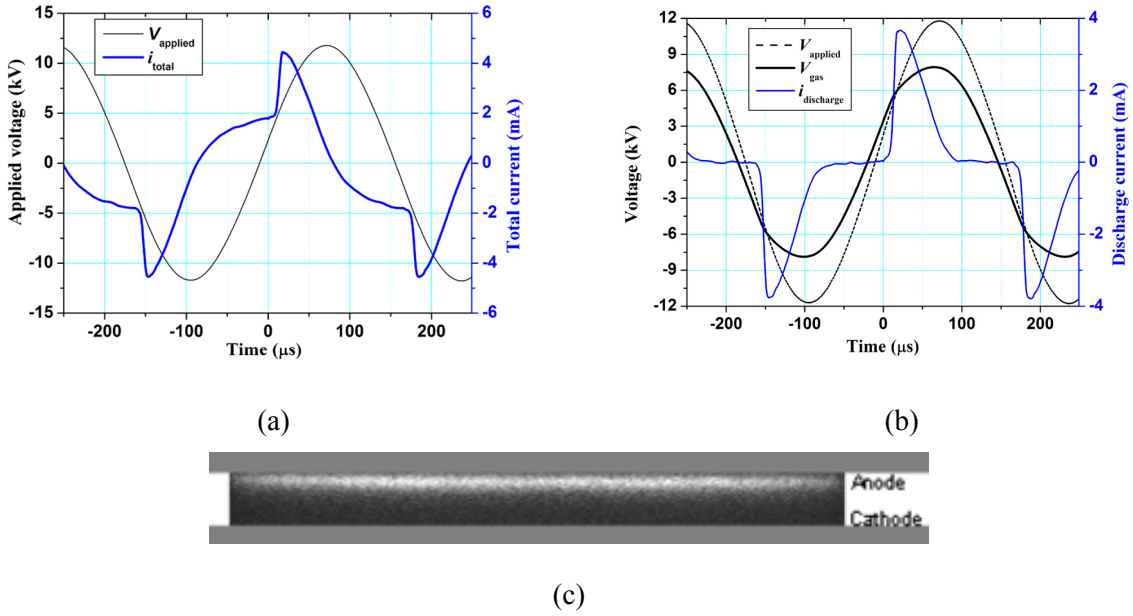


Fig. 2. Typical waveforms and photograph of homogenous DBD in nitrogen

As we know, DBD is usually extinguished with a rapidly reduced gas voltage as the dielectric charges up during the gas discharge. However, the discharge shown in figure 2(b) is extinguished while V_{gas} continues rising up. This extraordinary way of the discharge extinction suggests that the secondary electron emission from the trapped electrons on the surface of the dielectric plays an important role in maintaining the Townsend discharge in nitrogen.

The reason for V_{gas} rising up rather than falling down during the discharge is that the Townsend discharge in nitrogen is so weak that the dielectric is charged up slowly as compared to the rising of the applied voltage. As for why the discharge is extinguished during the rise of V_{gas}, it may be explained based on the condition of self-sustaining Townsend discharge [5]:

$$\gamma\left[\exp(\alpha \cdot d)-1\right]=1 \tag{1}$$

where γ is the coefficient of the secondary electron emission from the cathode, d is the gap length, α is the coefficient of the ionization by electron impact and increases with the electric field or with V_{gas} when the electric field is uniform in the gap.

For DBD in nitrogen, the secondary electron emission mainly comes from the electrons that are in the shallow traps on the surface of the dielectric covering the cathode and had been trapped during the previous discharge when the electrode worked as the anode [6]. Since the total number of the trapped electrons is limited [7] and the discharge lasts for quite a long time, γ will decrease as the discharge goes on. According to formula (1), the discharge will not be sustained if the increase of α due to the rise of V_{gas} failed to compete against the decrease of γ.

The Townsend discharge in nitrogen at atmospheric pressure was not readily produced but produced in a limited range in dependence on the amplitude and the frequency of the applied voltage as well as the gas flow. The working domain of the Townsend discharge in 2-mm gap with a flow velocity of 21 cm/s is shown in figure 3. Two specific voltages were found, V_{min}, the minimum amplitude of the applied voltage below which the discharge can not be initiated and V_{max}, the maximum amplitude of the applied voltage above which the Townsend discharge transits to a filamentary discharge. The breakdown voltage of the gap V_b can be determined from the waveforms of the gap voltage. It was found that when a stable Townsend discharge is maintained the lowest V_b is only 4.9 kV, much lower than 8.2 kV that is the steamer breakdown voltage of the gap.

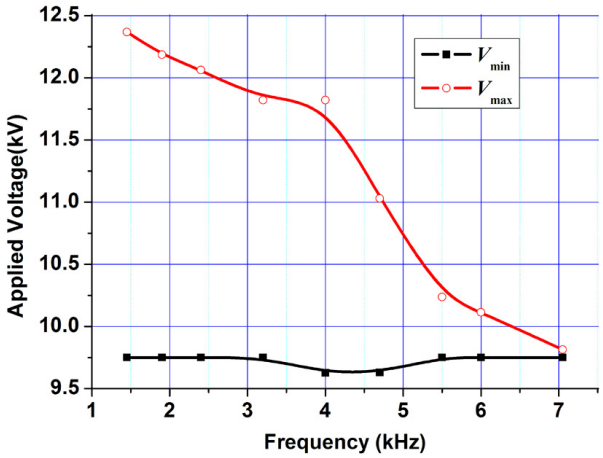


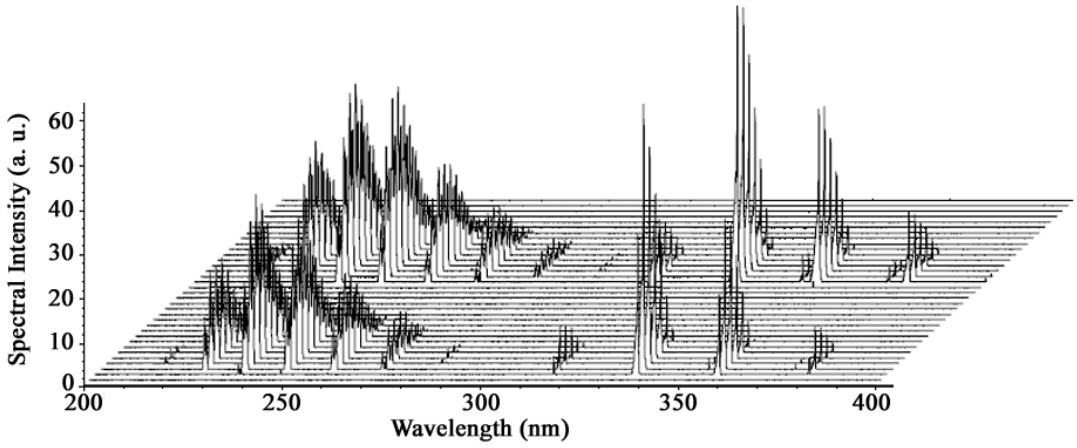
Fig. 3. Working domain of Townsend discharge in a 2-mm gap with a flow velocity of 21 cm/s

The effect of the gas flow on the homogenous discharge in nitrogen had been explained based on the laminar flow effect [1]. It was believed that the N_2 metastables are created within the whole discharge volume whereas the quenchers, the etched products from the dielectric surface, are mainly produced near the surface. When a laminar flow is added, the probability that a N_2 metastable and a quencher meet each other is much decreased. In this case, the creation rate of the N_2 metastable prevails over their destruction rate. If N_2 molecules are involved in a large number of discharges before they leave the discharge volume with the gas flow, a high concentration of N_2 metastables as well as the seed electrons can be achieved to form a homogenous discharge.

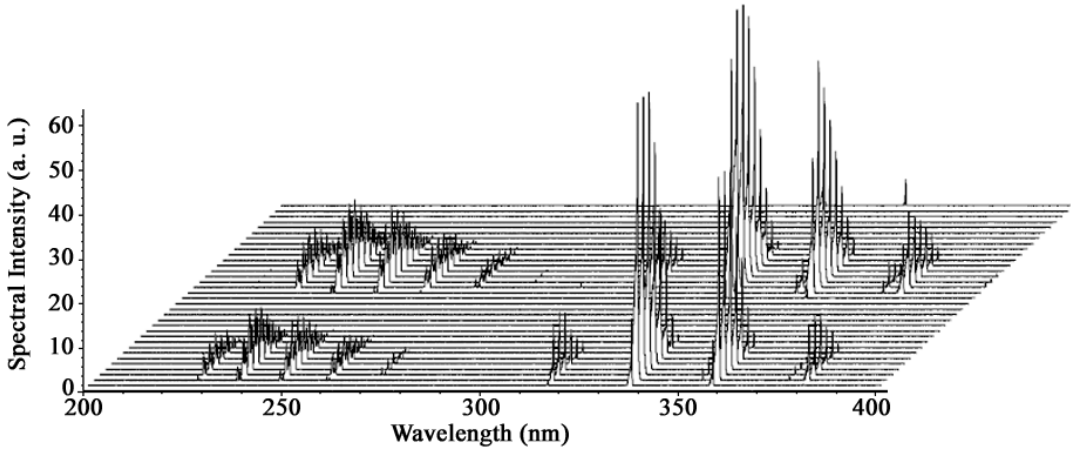
We disagree with the above explanation. For a Townsend discharge as shown in the discharge photo of figure 2, the most of the excited particles including the N_2 metastables are mainly produced close to the surface of the dielectric covering the anode rather than being created within the whole discharge volume. Even with a laminar flow, the probability that a N_2 metastable and a quencher meet each other will not be decreased since both particles are mainly produced near the dielectric surface. In this case, the metastable density is not limited by their creation rate, but by their destruction rate. If N_2 molecules are involved in too many times of discharges, the quencher density will be too high to allow a high concentration of N_2 metastables as well as the seed electrons to form a homogenous discharge. Therefore, the homogenous discharges in our experiment were formed at the applied voltage frequency lower than 7 kHz, as shown in figure 3, and the discharge evolves in a filamentary character above this frequency.

The influences of the gas flow on the discharge are more pronounced in the emission spectrum of the discharge. Figure 4 shows the typical time-resolved emission spectra from the nitrogen discharge during about one period of the applied voltage. Figure 4(a) is for the discharge without nitrogen flow

and figure 4(b) for that with a flow velocity of 25 cm/s. Both figures are composed of 35 emission spectra, each being taken with 1 μs exposure and spaced by 10 μs delay.



(a)



(b)

Figure 4. Time-resolved emission spectra during one period of applied voltage, (a) without nitrogen flow; (b) with a flow velocity of 25 cm/s.

In the wavelength range from 200 nm to 400 nm, the emissions are those of the $NO\gamma$ systems with wavelength of 200 nm ~ 300 nm and the N_2 second positive system (SPS) with wavelength of 300 nm ~ 400 nm. It was found that the influences of the nitrogen flow on the intensities of these two spectral systems are quite different. While the intensities of the N_2 SPS were almost unchanged, the intensities of the $NO\gamma$ systems were much reduced with the gas flow. For quantitative comparison, we focused on two spectral bands. The first spectral band is the N_2 SPS at 337.1 nm that is the result of the following excitation of nitrogen molecule (in the ground state) by direct electron impact:

$$e + N_2\left(X^1\Sigma_g^+\right)_{v=0} \rightarrow N_2\left(C^3\Pi_u\right)_{v'=0} + e, \quad (\Delta E = 11.0eV) \tag{2}$$

and then the transition: $N_2\left(C^3\Pi_u\right)_{v'=0} \rightarrow N_2\left(B^3\Pi_g\right)_{v''=0} + h\nu \quad (\lambda = 337.1nm)$ (3)

The second spectral band is the $NO\gamma$ systems at 236.1nm that is mainly the result of the following reaction of the ground state $NO\left(X^2\Pi\right)$ molecule with the $N_2\left(A^3\Sigma_u^+\right)$ metastable:

$$NO\left(X^2\Pi\right) + N_2\left(A^3\Sigma_u^+\right) \rightarrow NO\left(A^2\Sigma^+\right) + N_2\left(X^2\Sigma_g\right) \tag{4}$$

and then the transition: $NO\left(A^2\Sigma^+\right)_{v'=0} \rightarrow NO\left(X^2\Pi\right)_{v''=1} + h\nu \quad (\lambda = 236.1nm)$ (5)

It was found that the intensity of N_2 SPS spectral band at 337.1nm keeps almost unchanged after the addition of a gas flow at a velocity of 25 cm/s, which indicates that the density of $N_2\left(C^3\Pi_u\right)_{v'=0}$ in the

transition (3) and the electron density as well as its energy distribution in the excitation (2) are more or less the same as those without gas flow. We may conclude that the density of $N_2\left(A^3\Sigma_u^+\right)$ metastable with the gas flow is also more or less the same as that without nitrogen flow since the $N_2\left(A^3\Sigma_u^+\right)$ metastables are produced by the similar excitation as that described in (2):

$$e + N_2\left(X^1\Sigma_g^+\right)_{v=0} \rightarrow N_2\left(A^3\Sigma_u^+\right)_{v'=0} + e \qquad (\Delta E = 6.2eV) \qquad (6)$$

The intensity of the $NO\gamma$ spectral band at 236.1nm was drastically reduced from 30 to 10 by the addition of a gas flow, it could be derived that the densities of the excited state of $NO\left(A^2\Sigma^+\right)_{v'=0}$ in the transition (5) and the density of $NO\left(X^2\Pi\right)$ in the reaction (4) greatly decrease with the gas flow. As we know, NO comes from the reaction of nitrogen with the impurity oxygen mainly from the etched quartz plates by the discharge. With the gas flow, less oxygen will stay in the discharge gap, leading to the density of NO being reduced.

4. Conclusions

Homogenous DBD in a 2-mm gap of nitrogen at atmospheric pressure could be produced under specific conditions and was identified with Townsend discharge. It was usually believed that DBD is extinguished with a rapidly reduced gas voltage as the dielectric charges up during the discharge. However, the Townsend mode DBD in nitrogen is extinguished while V_{gas} continues rising up. The extraordinary extinction of the discharge may be explained with the limited number of the trapped electrons that could not provide the long-time lasting Townsend discharge with sufficient secondary electrons. Therefore, the release of the trapped electrons plays an important role not only in initiating Townsend discharge but also in maintaining the discharge.

The influence of the gas flow on DBD in nitrogen had been explained based on a laminar flow that keeps the $N_2(A)$ quenchers mainly produced close to the dielectric surface separate from $N_2(A)$ created within the whole discharge volume. However, according to the theory of Townsend discharge and the discharge photos we took, the most of the excited particles are mainly produced also close to the surface of the dielectric covering the anode. Thus, the $N_2(A)$ quenchers can not be separated from $N_2(A)$ by a laminar flow. In fact, the mechanism for the gas flow influencing the discharge is much simpler. With a pure nitrogen flow directly through the discharge gap, the $N_2(A)$ quenchers, especially the density of oxygen from the impurity, are much reduced, which was evidenced by the emission spectra of the discharge.

5. References

[1] Gherardi N and Massines F 2001 *IEEE Trans. Plasma Science* **29** 536-544.

[2] Golubovskii Yu B, Maiorov V A, Behnke J F, Tepper J and Lindmayer M 2004 *J. Phys. D: Appl. Phys.* **37**, 1346-1356.

[3] Panousis E, Papageorghiou L, Spyrou N, Loiseau J-F, Held B and Clement F 2007 *J. Phys. D: Appl. Phys.* **40**, 4168-4180.

[4] Luo H, Liang Z, Wang X, Guan Z, and Wang L 2008 *J. Phys. D: Appl. Phys.* **41**, 205205.

[5] Raizer Yu P 1991 *Gas Discharge Physics* (Berlin: Springer).

[6] Golubovskii Y B, Maiorov V, and Behnke J F 2002 *J. Phys. D: Appl. Phys.* **35**, 751-761

[7] Li M, Li C, Zhan H, Xu J, and Wang X 2008 *Appl. Phys. Lett.* **92** 031503.

CONDITIONS OF GENERATING THE ATMOSPHERIC PRESSURE TOWNSEND DISCHARGE IN AIR BY THE BARRIER DISCHARGE DEVICE USING ALUMINA AS A BARRIER MATERIAL

Yoshio Yoshioka[1] and Naoki Osawa[1]

[1]*Kanazawa Institute of Technology, 7-1 Ohgigaoka, Nonoichi, Ishikawa, 921-8501, Japan*
E-mail: yoshioka@neptune.kanazawa-it.ac.jp

There are homogeneous discharge modes in dielectric barrier discharge (DBD). So far, we reported that we can generate an atmospheric pressure Townsend discharge (APTD) at power frequency range using alumina barrier. In this study, we investigated the discharge at two frequency ranges of 60Hz and 18kHz. As the result, it was found that the APTD observed at 60Hz could not be generated at 18kHz. The reasons are discussed in this paper, together with the difference of discharges by a different alumina barrier.

1. Introduction

There are three modes of dielectric barrier discharge (DBD). They are filamentary discharge mode (FD)[1], atmospheric pressure glow discharge mode (APGD)[2] and atmospheric pressure Townsend discharge mode (APTD)[3]. The APGD and the APTD are characterized by a uniform discharge. In our laboratory, we found that we can generate such a uniform discharge in air at the power frequency range by a DBD device using white alumina barrier[4]. The discharge was considered as the APTD because the discharge current waveform has no pulse and the gap voltage during discharge is almost constant. So far, it was known that the APTD mode can be generated in nitrogen, but not be generated in gases containing oxygen. However, the APTD using white alumina barrier could be generated even in pure oxygen. Besides, it was also found that the APTD could not be generated with a black alumina barrier containing different material components. In this study, we investigated discharges using the same DBD device at a higher frequency of 18 kHz. As the results, we found that the white alumina DBD device can not generate APTD. We also found that although the discharge using white alumina at high frequency was not the APTD, but the discharge was different from the FD observed in a black alumina barrier. Since the APTD and the APGD are reported to be generated at higher frequency than 1 kHz, the result we obtained was apparently different from those results. In this paper, we describe the detail of the experimental results, and also discuss the reason why the APTD could not be generated at high frequency range.

2. Experimental setup and experimental conditions

Fig.1 shows an experimental setup. The high voltage source of 60Hz is a neon transformer, and that of 18kHz is an inverter neon transformer. Applied voltage was changed by a slide transformer, which was connected to the primary windings of the neon transformers. Fig.2 shows a DBD device. The DBD device is a parallel plate type, and the barrier materials used are two kinds of alumina with

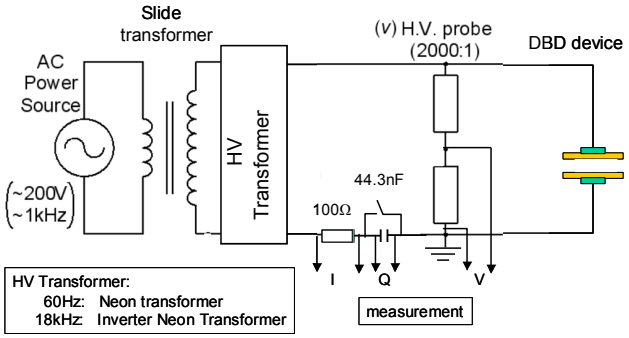


Fig.1. Experimental setup

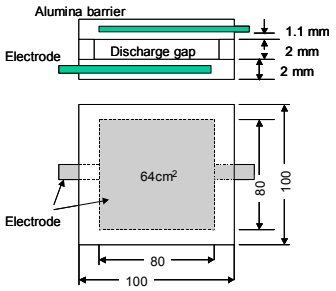


Fig.2. Barrier discharge device (DBD device)

Tab.1. Detail of DBD device

NO.	Items	DBD device 1	DBD device 2
1	Barrier material	White Alumina (Kyocera A473)	Black Alumina (Kyocera A440)
2	Relative permittivity	9.0	9.8
3	Barrier thickness (mm)	1.1	1.1
4	Barrier size (mm×mm)	100×100	100×100
5	Gap length (mm)	2	2

different material component. Table 1 shows the detail of the DBD devices. The thickness of the barrier is 2mm. Thin plane electrode is implanted in the barrier (0.9mm from the surface). The distance between the electrode and the surface of barrier facing to the discharge gap is 1.1mm. The size of the electrodes is 80×80mm^2. The gap length is 2mm. The DBD device was set in a box (180×240×320 mm^3), and air flow was supplied in the discharge gap by a cross flow fan. The applied voltage V and the current were measured by an oscilloscope using a H.V. probe and a shunt resistor of 100 Ω. An integral of the current (charge q) was measured by measuring the voltage of a series (integral) capacitor of 44.3 nF.

3. Experimental results

3.1 Experimental results at 60Hz

Fig.3 (a)(b) show the typical oscillogram of the discharges by the two DBD devices. It is clearly seen that the current of the DBD deice 1 using white alumina barrier is almost continuous and the magnitude is around 1.5mA. However, it is seen that there are some pulse current. On the other hand, the current of DBD device 2 using black alumina is pulsatile and the pulse height is around 300mA.By comparing the two oscillograms, it is understood that the discharge of the two DBD devices are apparently different.

Fig.4(a) and (b) show the applied voltage and the gap voltage of the two DBD devices. The gap voltages were calculated by subtracting the barrier voltage from the applied voltage. The barrier

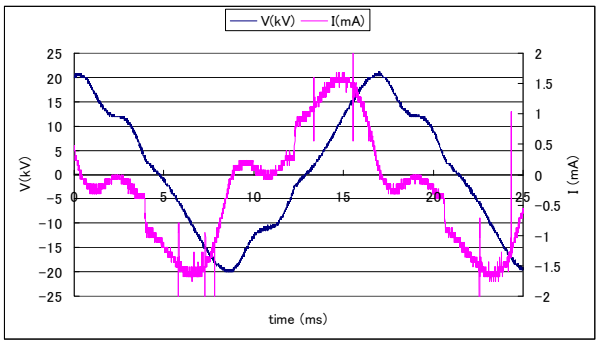


Fig.3.(a) Typical oscillogram of DBD device 1 (60Hz)

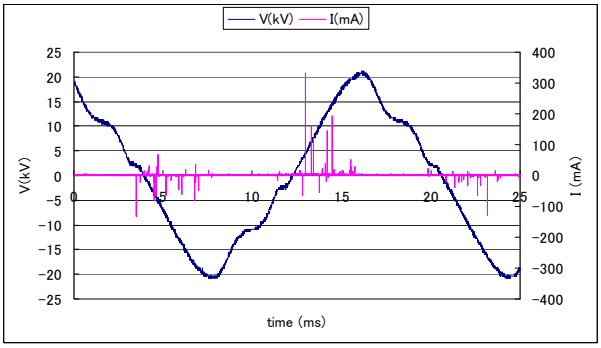


Fig.3.(b) Typical oscillogram of DBD device 2 (60Hz)

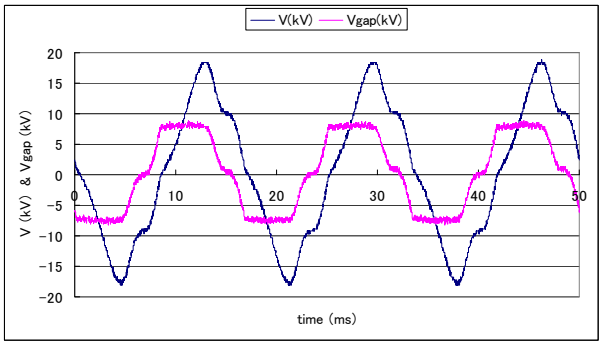


Fig.4.(a) gap voltage of DBD device 1 (60Hz)

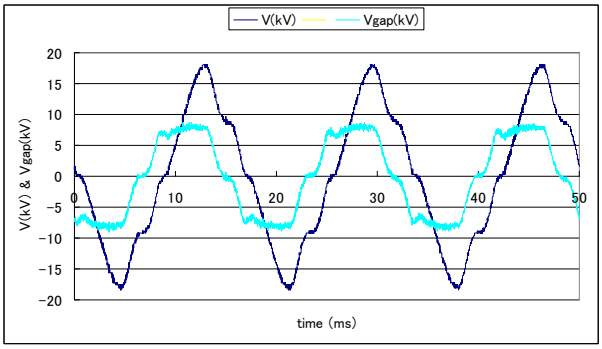
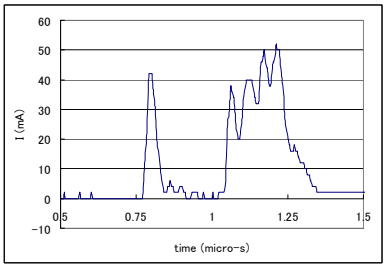


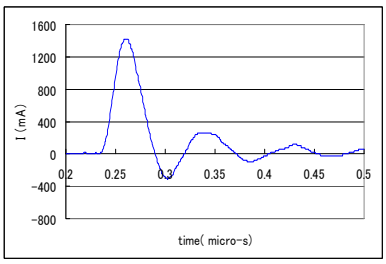
Fig.4.(b) gap voltage of DBD device 2 (60Hz)

voltage was calculated from the voltage of the capacitor inserted in the circuit. As it is seen in Fig.4(a), the gap voltage of the DBD device 1 is almost constant during discharge period and its voltage is

about 7.5kV. In the case of DBD device 2, the gap voltage is also almost flat, but there are small drops soon after the start of discharge. The gap voltage is around 7.5kV, which is almost the same as that of DBD device 1.

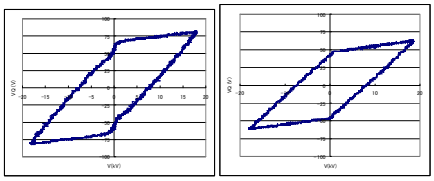
Fig.5 (a) and (b) show the wave forms of the pulse current. As the pulse shapes are not always the same, these are typical wave forms, which represent the difference between the two DBD devices. In the case of DBD device 1, the pulse width is wider like 300ns, and the height is 50mA. It is seen that several pulses are superimposed. As it is seen in Fig.3(a), the pulse current started from the continuous discharge current. It means that the pulse current is a discharge current and not a displacement current. Fig.5(b) shows a detail of the pulse current of DBD device 2. The pulse width is around 50ns, which is shorter than that of DBD device 1 and the height of 1,400mA is higher than that of DBD device 1. It is also noticed that the pulse current is oscillating. In this way, the pulse current measured in the two DBD devices are apparently different. We reported a simulation study of discharge current by an electrical circuit model [5]. The simulation study showed that the oscillating pulse current is not a discharge current, but a displacement current caused by a sudden drop of gap voltage. We also reported that the continuous current is a real discharge current and it is an evidence of a homogeneous discharge. Therefore, the discharge of the DBD device 1 is a homogeneous discharge known as APTD. Fig.6(a) and (b) show the lissajous figure of the two discharges. The lissajous figure of the DBD device 1 is an ideal parallelogram, while that of the DBD device 2 is a bit deforming. The discharge power is 4.59W in the DBD device 1, and that of the DBD device 2 is 5.83W a bit larger than the DBD device1.





(a) DBD device 1 (b)DBD device 2

Fig.5.Pulse shape (60Hz)



(a) DBD device 1 (b)DBD device 2

Fig.6. Lissajous figure (60Hz)

3.2 Experimental results at 18.2kHz

Fig.7(a) and (b) show the oscillograms of the discharge of DBD device 1 and 2 at 18kHz. As you can see, the both cases show pulse currents, although the wave forms are apparently different. The big difference is in their peak current values. In the case of DBD device 1, the pulse height is around 200mA, but that in the DBD device 2 attained to a 400mA level. It is also seen that the pulse current in DBD device 2 is oscillating, which is similar to the case of 60Hz experiment.

Next, Fig.8(a) and (b) show the gap voltages in both DBD devices. It is interesting to notice that the gap voltages are flat at the beginning of discharge and in the later period of discharge, they increase a bit. The gap voltages at the beginning are about 2.5kV in the DBD device 1 and 3kV in the DBD device 2. However, the gap voltages at the end of discharge increased to 3.3kV and 3.5kV respectively. As you may notice, these gap voltages are almost the half of those at 60Hz.

Fig 9(a) and (b) show the detail of the pulse current of the two DBD devices. The pulse current in the DBD device 2 is oscillating with small pulse width and the pulse height is more than 1000mA, but that in the DBD device 1 is not an oscillating wave and the pulse height is around 200mA. The pulse duration is around 100ns or more. The pulse current does not show oscillation. Therefore, it is considered that in the DBD device 1, the discharges in the gap sustained for more than 100ns. On the other hand, the discharge in the DBD device 2 is the typical micro-discharge characterized by a very short discharge time of less than 10ns. Because the discharge stops in such a short time, the displacement current flows in the circuit by a sudden drop of gap voltage.

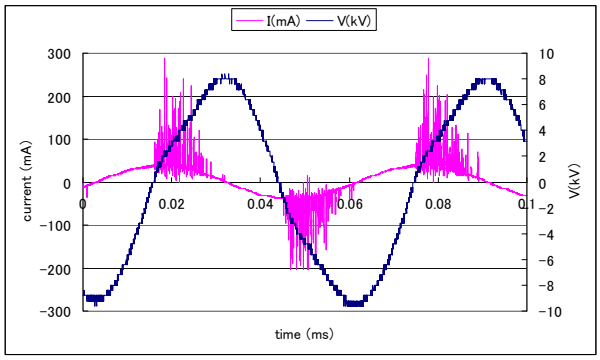


Fig. 7.(a) Typical oscillogram of DBD device 1 (18kHz)

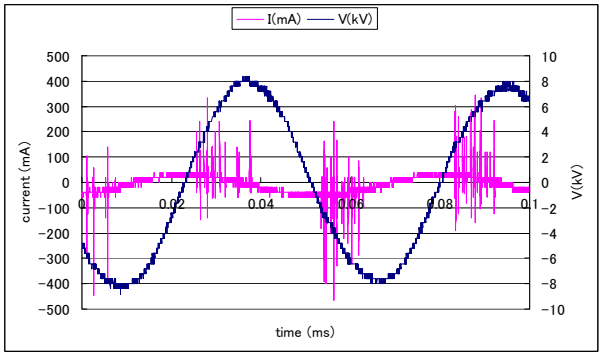


Fig 7.(b) Typical oscillogram of DBD device 2 (18kHz)

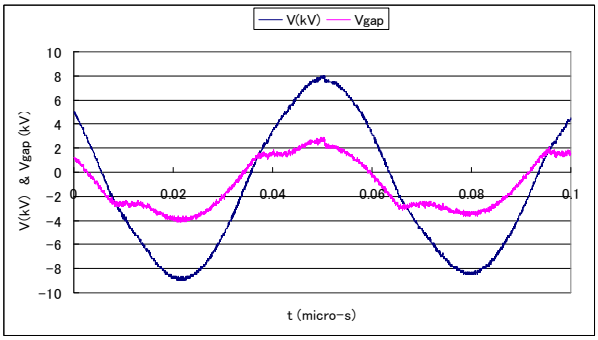


Fig. 8. (a) gap voltage of DBD device 1 (18kHz)

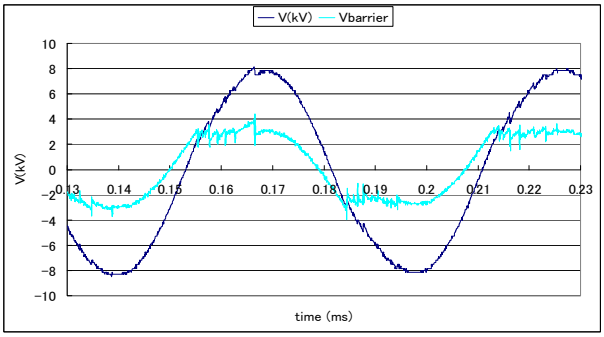
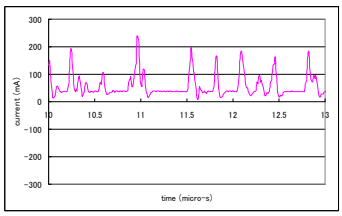
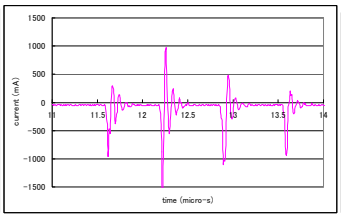


Fig.8.(b) gap voltage of DBD device 2 (18kHz)

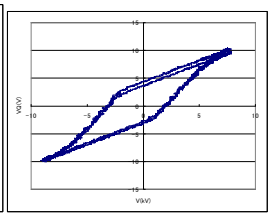


(a) DBD device 1

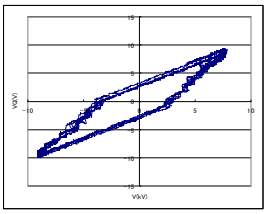


(b)DBD device 2

Fig. 9. Pulse shape (18kHz)



(a) DBD device 1



(b)DBD device 2

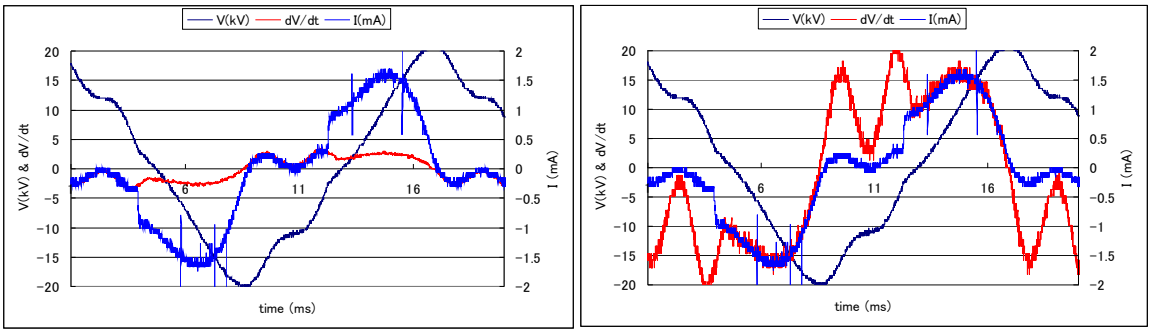
Fig. 10. Lissajous figure (18kHz)

Fig10(a) and (b) show the lissajous figures of the two DBD devices. Here, the lissajous figure of the DBD device 1 is a bit deformed one, but that of the DBD device 2 is a parallelogram. The discharge powers of the two devices are 43.3 and 44 W, and there were no big difference. What is important in these experiments are that even we used the white alumina in the DBD device 1, the APTD could not be generated.

4. Discussion

4.1 Discussion of the discharge current of DBD device 1 at 60Hz

In order to understand the APTD at 60Hz the current was compared with the displacement current. Fig.11(a) shows a comparison of the discharge current and the displacement current (indicated as dV/dt) through the DBD device. During the discharge period, the discharge current is about 7 times larger than the displacement current. Fig.11(b) shows a comparison of the discharge current and the displacement current through only the capacitance of the barrier. The displacement current coincides with the discharge current during the discharge period. These results mean that the current flows continuously through the gap.



(a) Displacement current without discharge (b)Displacement current during discharge

Fig.11. Comparison between discharge current and displacement current (60Hz)

4.2 Conditions of generating APTD

So far, it was known that APTD is generated in gases without containing oxygen and at higher frequency. As we described in the previous section, the DBD device 1 using white alumina generated APTD in air and at a frequency of 60Hz. However, different from the previous researches, the APTD did not generate at a high frequency of 18kHz. Here, we will discuss the reason. As it is seen in Fig.3(a), the maximum continuous current of DBD device 1 at 60Hz was about 1.5mA. We made a simulation of a discharge current on an assumption that the APTD generated at 18kHz. Fig.12 shows the result. It is seen that the DBD device has to carry at least more than 10mA. The reason that the APTD could not be generated at 18kHz seems to be this current value, because this current has to be sustain by the gamma effect. The gamma effect of alumina is larger than the other materials, but the material cannot supply such a high current. The DBD device has an electrode area of 64cm^2. Therefore, the maximum current density of APTD at 60Hz is 23.4 (=1.3mA/64cm^2)μA/cm^2.

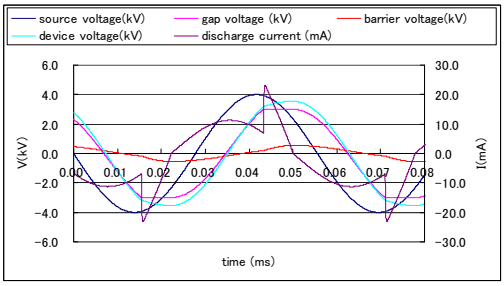


Fig.12. Simulation of APTD at 18kHz.

However, in order to generate APTD at 18kHz, the gamma effect has to sustain 156(=10/64) μA/cm^2. When the current density becomes around this level, the gamma effect in the white alumina can no more sustain the discharge, which leads to the filamentary mode. Since the pulse current had wider width and the pulse height was smaller than that of the FD mode, the discharge of the DBD device 1 with white alumina is the intermediate discharge between the filamentary and the homogeneous discharge. On the other hand, the black alumina may have a poor gamma effect than the white alumina. Therefore, the black alumina can not sustain even the current density of the order of 23μA/cm^2, and the discharge becomes filamentary mode. The black and the white alumina contain some different components, although the base material is alumina. It seems that the small difference in material component influenced the discharge mode.

5. Conclusion

Barrier discharge experiments were carried out using two kinds of barrier materials under different frequency ranges. The DBD device using white alumina generated homogeneous Townsend discharge at 60Hz, but not at 18kHz. The similar DBD device with different black alumina could not generate APTD at 60Hz and also at 18kHz. The reason that the APTD could not be generated at 18kHz with the white alumina seems to be a limit of the current value sustained by gamma effect of the material.

6. References

[1] Eliasson B. and Kogelschatz U., 1991 *IEEE Trans. on Plasma Sci.*, Vol. 19, No. 6, 1063-1077.
[2] Kanazawa S, Kogoma M, Moriwaki T and Okazaki S, J. Phys. D: Appl. Phys. 21, pp838-840, 1988
[3] Kambrome N. J,Gerardi N and Massines F, J. Phys. D: Appl. Phys. 38, pp530-538, 2005
[4] Osawa N., Yoshioka Y., Hanaoka R., Mochizuki Y., Kobayashi Y. and Yamada Y., 2010 *IEEJ Trans. FM*, Vol. 130, 306-312.
[5] Yoshioka Y, Osawa N, 2010 *IEEJ Trans. FM*, Vol. 130, NO.7, in press, 306-312.

PRACTICAL IMPLICATIONS OF THE STREAMER THEORY FOR NEGATIVE CORONA TRICHEL PULSES

Mirko Černák[1, 2], Anna Zahoranová[1], Juraj Halanda[1], Jozef Kúdelčík[3]

[1]*Department of Experimental Physics, Faculty of Mathematics, Physics and Informatics, Comenius University, Mlynská dolina, 842 48 Bratislava, Slovak Republic*
[2]*Department of Physical Electronics, Faculty of Science, Masaryk University, Kotlářská 2, 611 37 Brno, Czech Republic*
[3]*Department of Physics, Faculty of Electrical Engineering, University of Žilina, Univerzitná 1, 010 26 Žilina, Slovak Republic*
E-mail: cernak@fmph.uniba.sk

Negative corona discharge in the Trichel pulse regime, where the corona current consists of regular pulses of frequency ranging from some 1 kHz to 1 MHz is widely used in applied electrostatics and high-pressure plasmachemistry. For more than half of century, the scientific and engineering community has largely accepted a theoretical model of Trichel pulses based on the Townsend ionization mechanism. In the last two decades, however, experimental evidence is mounting that the Trichel pulse phenomenon is associated with a positive streamer ionization mechanism. The experimental evidence for the streamer Trichel pulse mechanism based on the pulse waveform measurements in O_2 + H_2 gas mixtures and implications for practical design of negative corona devices will be discussed.

1. Introduction

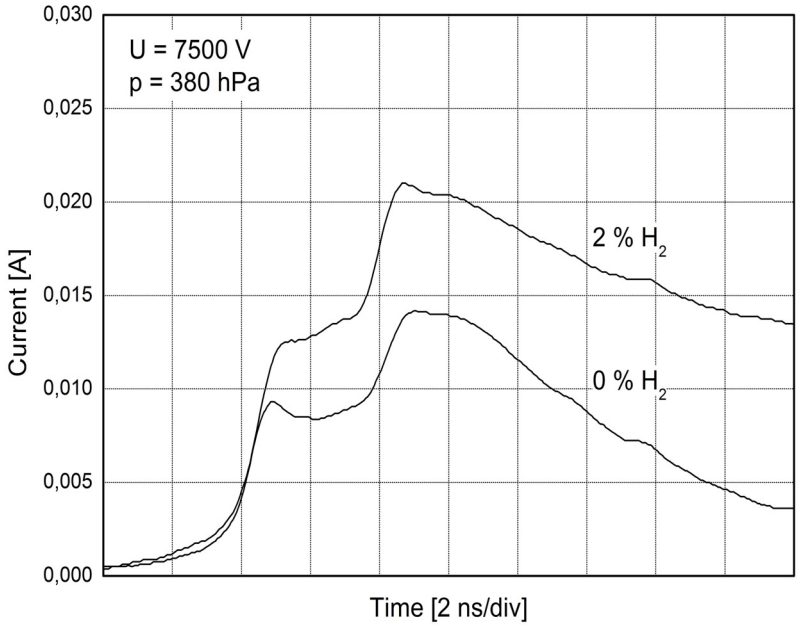
When a sufficiently high negative voltage is applied to the point of a point-plane electrode system in an electronegative gas such as O_2 at pressures above of some 25 kPa, after a statistical time lag a pulsating corona current, the so-called negative corona Trichel pulses (TP), of frequency ranging from 10^3 to 10^6 Hz is observed in the external circuit [1]. The pulses are discerned by a peaked current signal where in several nanoseconds the discharge rises to a current maximum on the order of 1-100 mA. An interesting feature of TP (see Fig. 1) observed for cathode curvature radii above say 0.1 mm is a step on the pulse leading edge.

The TP corona discharge finds widespread applications as negative ion source in applied electrostatics [2-4]. Other practical issues are, for example, elimination of the TP corona discharge formation in high voltage insulating systems [5] and plasmachemical applications as ozone generation [6, 7] and thin layer deposition [8]. Since practical significance of the TP corona discharge, it is important that the phenomenon be well understand theoretically.

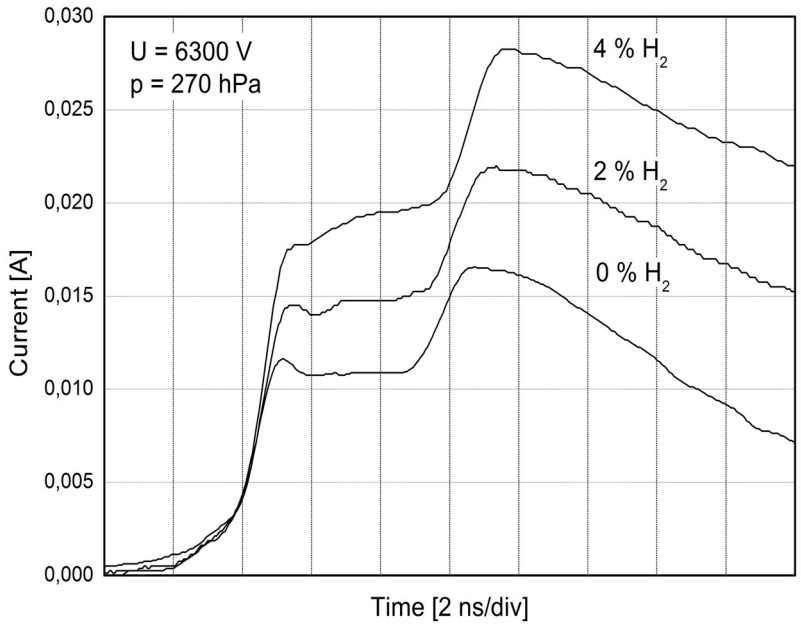
The first quantitative model of TP, which is up to the present time sometimes employed in engineering was develop by Loeb [1] and extended by Alexandrov [9]. According to Loeb the pulse is initiated by an electron released from the cathode surface by some mechanism such as field emission or positive ion bombardment, and proceeds by the Townsend ionization in an initial electron avalanche. The avalanche is produced between the cathode and some position, where the ionization coefficient α is zero. From the initial electron avalanche further avalanches will result by electron liberation at the cathode due to photoemission. The TP pulse current rise cannot continue to value higher than some 10^{-1} A because the electrons rapidly create a negative ion space charge through attachment of the ionizing zone.

In the past two and half decades the TP mechanism has been under active research and several computer models have been proposed [10-16]. Nevertheless, despite the abundance of theoretical models, there is no consensus regarding the discharge mechanism: A quantitative theory of TP, which is accepted by many workers in the field of corona discharges, was published by Morrow [10, 11]. Recently, however, several mutually inconsistent computer simulation models TP have been published [12-16], which differ markedly from the Morrow theory. Besides these computer simulations models, in a series of papers by Černák et al. [17-20] a hypothesis of a positive-streamer like mechanism for TP was advanced. The hypothesis, when applied to the stepped TP, combines some features of

Morrow's model with an assumption that a positive-streamer-like ionizing wave plays a decisive role in the TP formation mechanism.



a)



b)

Fig. 1 a, b). Leading edges of the first TPs in various O_2 + H_2 gas mixtures using a large cathode curvature radius of 1.5 mm at a distance of 12 mm from the anode. Other parameters are shown in the figure.

As already mentioned, apparently because there is no consensus in the scientific literature on a detailed TP mechanism and the interpretation of existing computer simulation models appears too complex for engineers to solve industrial problems from the field of plasma-chemistry and applied electrostatics. As a result, the present paper is aimed to explain how the application of the positive-streamer like mechanism for TP may lead to better designs of the practical devices. Since the majority of the recent computer simulation studies were made in oxygen, some results of the effect of electron detachment on the TP waveforms in O_2 will be used to illustrate basic properties of TPs important for understanding of their mechanism.

2. Experimental and discussion

The first TP waveforms were measured in various $O_2 + H_2$ gas mixtures for a wide range of gas pressures and cathode curvature radii. The experimental apparatus and procedure were the same as described in [19]. Based on the results by Price et al. [21] it was expected that the relatively small admixtures of H_2 gas used do not change the value of the Townsend coefficient α, however, will result in a significant reduction of the electron attachment coefficient by the process:

$$O^- + H_2 \rightarrow H_2O + e$$

Thus, if sufficient hydrogen is added into the oxygen, the associative detachment reaction will remove the O^- ions before they can be converted into nondetaching species by other reactions.
The results obtained for sharp cathodes with the diameter less than some 0.25 mm no step on the leading edge was observed, and the H_2 gas admixtures for the content of H_2 less than 5% have no effect on the pulse leading edge shape and the pulse magnitude. These results are not reported here for brevity.
Using the blunt cathodes the characteristic step on the pulse leading edge was observed, as exemplified by Fig.1. An interesting observation apparent from Fig. 1 is that in striking agreement with the theory by Černák et al. [17-20] the reduction in the attachment coefficient has significant effect on the current rise to the step on the pulse leading edge corresponding to the Townsend ionization, while no effect on the subsequent current rise to the pulse magnitude, which corresponds to the streamer ionization mechanism was observed.
We believe that this conclusion and the results obtained can serve as a necessary guide for further study by experiment or computer simulation.

3. Practical implications

As already mentioned in the Introduction, in applications of negative corona discharges as an ion source or ozone generator the designers have normally employed the model given by Loeb. As already discussed, the basic assumption of the Loeb model is that the majority of electrons is attached in the time scales of the pulse rise just outside the ionization region, inside the zone that extends only a few mm from the cathode. As a consequence, according to the Loeb theory, no free electrons can penetrate outside this narrow region. This is why it is believed that the rest of the interelectrode space is filled solely with negative ions.
Electrostatic precipitators and devices for electrostatic deposition of powders are the most prevalent applications of negative corona as an ion source for charging of dust and powder particles. In these applications the ozone generation is an undesired phenomenon. Traditionally, and in line with the Loeb theory, the charging in the interelectrode space is assumed to be solely due to negative ions, and the dissociation of oxygen molecules is assumed to occur only in the immediate vicinity of the cathode. However, such assumptions can be misleading since in air at atmospheric pressure it has been found [22] that a significant fraction of current can be carried by electrons and that the electrons can play a significant role in the particle charging and oxygen molecules dissociation several cm away from the cathode.
A method for electrets preparation is the charging of nonpolar polymer foils by negative corona discharges. It has been found in ambient air at atmospheric pressure and a cathode to polymer surface spacing of 10 – 13 mm that vibrationally excited molecules act as energy carriers to the polymer

surface and are effective injectors of negative charges [23]. Considering the short lifetimes of vibrationally excited molecules in atmospheric air [23], we hypothesize that these must be generated in collisions with free electrons present near the polymer surface. This is again in apparent contrast to the Loeb theory.

Acknowledgements. This research has been supported by the Slovak Research and Development Agency, Project No. APVV-0491-07, by the research intent: MSM0021622411 funding by the Ministry of Education of the Czech Republic and by the contract KAN 101630651 by Grant Agency of Academy of Science of Czech Republic.

4. References

[1] Loeb L B *Electrical Coronas: Their Basic Physical Mechanism* (University of California, Berkeley, 1965)
[2] Boni Dramane, Noureddine Zouzou, Eric Moreau and Gerard Touchard 2009, *Journal of Electrostatics* **67** 117–122.
[3] Cross J A, *Electrostatics: Principles, Problems and Applications* (Adam Hilger, Bristol, England, 1987).
[4] Cottrell F G, "*The Electrical Precipitation of Suspended Particles,*" 1911 *J. Ind. And Eng. Chem.* **3** 542 (1911).
[5] Mitsui H, Koyanagi, Kenjo S, Yamauchi T and Tari M 1983 IEEE *Trans. Electr. Insulation EI* **18** 536.
[6] Goodman N and Hughes JF 2002 *Clin Exp Allergy.* Apr;**32(4)** 515-9.
[7] Pekárek S 2010 *Eur. Phys. J. D* **56** 91-98 .
[8] Abolmasov S N, Kroely L and Roca i Cabarrocas P 2008 *J. Phys. D: Appl. Phys.* **41** 165203.
[9] Aleksandrov G N 1963 *Sov. Phys. Tech. Phys.* **8**, no. 2, 161-166
[10] Morrow R 1985 *Phys. Rev A* **32** 3821.
[11] Morrow R 1985 *Phys. Rev A* **32** 1799.
[12] Reess T and Paillol J 1997 *J. Phys D* **30** 3115.
[13] Espel P, Paillol J, Reess T, Gilbert A and Domens P 2002 *J. Phys D* **35** 318.
[14] Napartovich A P, Akishev Y S Deryugin A A, Kochetov I V, Pankin M V and Trushkin N I 1997 *J. Phys. D: Appl. Phys.* **30** 2726-2736.
[15] Deepak K. Gupta, Sangeeta Mahajan and John P I 2000 *J. Phys. D: Appl. Phys.***33** 681.
[16] Sattari P, Castle G S P and Adamiak K 2010 *Proc. ESA Annual Meeting on Electrostatics ,* **Paper K4**
[17] Černák M, Hosokawa T and Odrobina I 1993 *J. Phys. D* **26** 607.
[18] Černák M, Hosokawa T, Kobayashi S and Kaneda T 1998 *J. Appl. Phys.* **83** 5678.
[19] Zahoranová A, Kúdelčík J, Paillol J and Černák M 2002 *J. Phys D* **35** 762.
[20] Černák M and Hosokawa T 1991 *Phys. Rev*. A **43** 1107
[21] Price D A, Lucas J and Moruzzi J L 1972 *J. Phys. D: Appl. Phys*. **5** 1249-59
[22] Leal Ferreira C F et. al. 1986 *J. Appl.Phys.* **59** 3045
[23] Haridos S, Perlman M M and Carlone C 1982 *J. Appl. Phys.* **53** 6106

ELECTRON IMPACT EXCITATION OF THE SECOND POSITIVE SYSTEM OF N_2

Marián Danko, Juraj Országh, Anita Ribar, Jaroslav Kočíšek and Štefan Matejčík

Department of Experimental Physics, Comenius University, Mlynská dolina F2, 84245 Bratislava, Slovak Republic
E-mail: matejcik@fmph.uniba.sk

The electron impact excitation of the second positive system of N_2 (2nd PS N_2) have been studied in a new crossed electron/molecular beams apparatus. The excited states C $^3\Pi_u(v')$ (v'=0..4) were excited using electron beam with high energy resolution. The electron induced optical spectra in UV/VIS range (290 – 440 nm), the excitation thresholds of particular vibrational states C $^3\Pi_u(v')$, the emission cross sections of the 2nd PS and the excitation cross sections of the C $^3\Pi_u(v')$ states were measured with high resolution and sensitivity.

1. Introduction

Optical emission spectroscopy (OES) is an important toll to study the properties of the atmospheric pressure plasmas, or discharges. In the case of air the nitrogen molecule plays an important role in OES. The OES yields important information about the plasma and electric discharges, e.g., energy of the electrons, vibrational and rotational temperatures of the gas etc. The second positive system $C\,^3\Pi_u(v') \rightarrow B^3\Pi_g(v'')$ belongs to the most intensive bands in the emission spectrum of the nitrogen, or air. Due to this property the electron impact excitation of the N_2 state $C\,^3\Pi_u(v')$ draws much attention. The upper excited state $C\,^3\Pi_u$ is mainly populated directly by the inelastic scattering of the electrons and in a less extent by the cascading transitions from higher excited states [1].

The process of excitation of the molecules by electron impact and subsequent detection of the photons is often called "electron induced fluorescence" (EIF). The quantity, which describes the efficiency of the EIF process, is called emission cross section. The emission cross sections describes a complex process which consists of the excitation of the molecule into a particular excited state $C\,^3\Pi_u$ and subsequent deexcitation of this state by the photon emission:

$$e(\varepsilon_1) + N_2(X^1\Sigma_g^+) \rightarrow C\,^3\Pi_u(v') + e(\varepsilon_2)$$
$$C\,^3\Pi_u(v') \rightarrow B^3\Pi_g(v'') + h\nu \qquad (1)$$

The emission cross section $\sigma_{v''}^{em}$ is directly measured in the present experiment. On other hand, the excitation cross sections σ_v describes only the first part of the process described by the the emission cross section, the excitation of particular vibrational states of the $C\,^3\Pi_u$. The excitation cross section can be obtained from the measured emission cross sections σ_v^{em} using following relation:

$$\sigma_{v'} = \sigma_{v''}^{em} A_{v',v''} \tau_{v'} \qquad (2)$$

where $A_{v',v''}$ is the transition probability and $\tau_{v'}$ is the mean lifetime of level v'. Excitation cross sections can be measure also by inelastic electron scattering techniques.

The emission cross sections, for the various vibrational bands of the second positive system have been already measured by researchers in several laboratories [1,2,3,4].Up to now there exists only one work, where this excitation has been studied using well defined, high resolution electron beam [2]. In spite of these studies there still exists interest in new data, achieved with high resolution in the electron energy. High resolution experiments may yield more precise values of the threshold energies and also show new phenomena in the excitation cross sections such as resonances. Therefore an accurate knowledge of the excitation cross sections of the $C\,^3\Pi_u(v')$ state is the primary interest for the understanding of several important phenomena in nitrogen.

The emission cross sections for 2nd PS in N_2 have been measured by the detection of the photons from the second positive system in the 290-440 nm spectral range. Excitation functions of several optical lines have been measured and normalized to obtain absolute values of the emission cross sections. The present measurements have been carried out with high electron energy resolution and more accurate electron energy calibration than any previous studies. This has allowed to detect two thresholds in several emission cross sections. Using calibration method (2) we have transformed the emission cross

sections into excitation cross sections. Excitations cross sections for the vibrational states (v'=0,1, 2,3 and 4) of $C\,^3\Pi_u(v')$ have been determined in present experiment.

2. Experimental setup

We have used a new crossed electron – molecular beams apparatus - EIFA to study the EIF in N_2 . The apparatus is shown schematically in the Figure 1. It consists of i) electron monochromator producing a collimated beam of electrons, ii) the collision chamber is filled with a target gas, iii) the detection system detecting spectrally analysed photons.

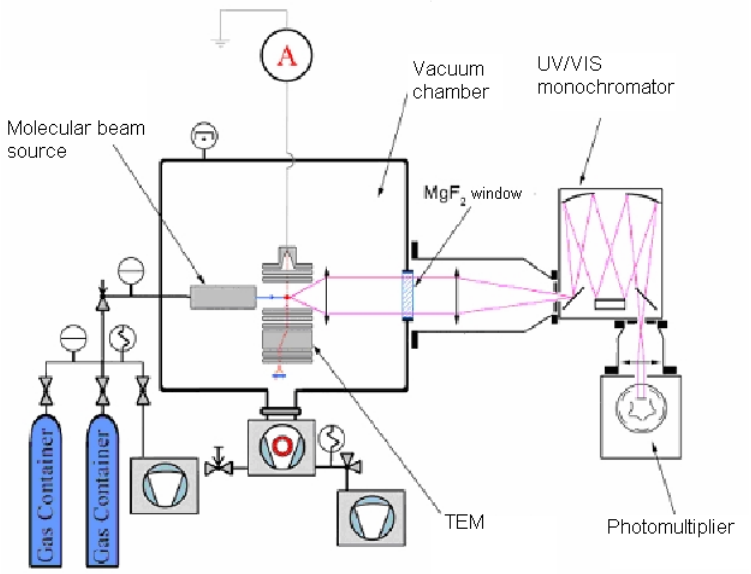


Fig. 1. Experimental setup.

The incident beam with an energy spread of approximately 150 meV and a typical electron current of 90 nA is produced by the trochoidal electron monochromator (TEM). The photons emitted from the collision region are collected by a MgF_2 lens and transmitted via quartz vacuum window outside of the vacuum chamber and refocused by second MgF_2 lens onto the entrance slit of an 0.25 m optical monochromator. The photons are detected at its exit slit by the Hamamatsu H8259 photomultiplier. The photomultiplier works in the photon counting regime and is cooled to -20°C in order to reduce the noise. The magnetic field ($5x10^{-3}$ T) is produced by a pair of coils which allow for accurate alignment of the direction of the field with respect to the electron spectrometer symmetry axis. The measurements were carried out for pressure range of 1.10^{-4} mbar in the collision region which gave linear dependence between detected photons intensity and target pressure. It was also ensured that the detected photon intensity increased linearly with the electron beam current.

3. Results and discussion

The fluorescence spectrum of the 2nd PS N_2 induced by the electrons with kinetic energy of 14.2 eV is shown in the Figure 2. The (v′,v″) transitions of the second positive system have been identified and are indicated in the spectrum. The intensities of the observed transitions enable to estimate the emission cross sections for (v′,v″) transitions of 2nd PS as function of the kinetic energy of the electrons. The emission cross sections for selected $C\,^3\Pi_u(v')$ to $B\,^3\Pi_g(v'')$ transitions are presented in the figures 3a and 3b.

The high energy resolution of the electron beam has been used to estimate the thresholds of the excitation cross sections for particular emission bands of 2nd PS of N_2. The excitation by electron impact is an endothermic process, thus there exist thresholds for these reactions. We have analysed the thresholds (Table 1.) in the electron energy range up to 14 eV. In this energy range we have seen two thresholds in each emission cross sections. We have used fitting procedures described in [5] to obtain the values of the threshold. The nature of the first threshold is not satisfactory explained. The second

threshold, where more intense emission starts, is assigned to the direct excitation of the $C^3\Pi_u$ state by the electron [4]. Shemansky et al. [4] suggested that the emission below the second threshold has origin in the core excited and Feshbach resonances of N_2^- ($E\ ^1\Sigma_g^+$). These resonances have been measured by Maeau et al [6] and Kurzweg et al [7].

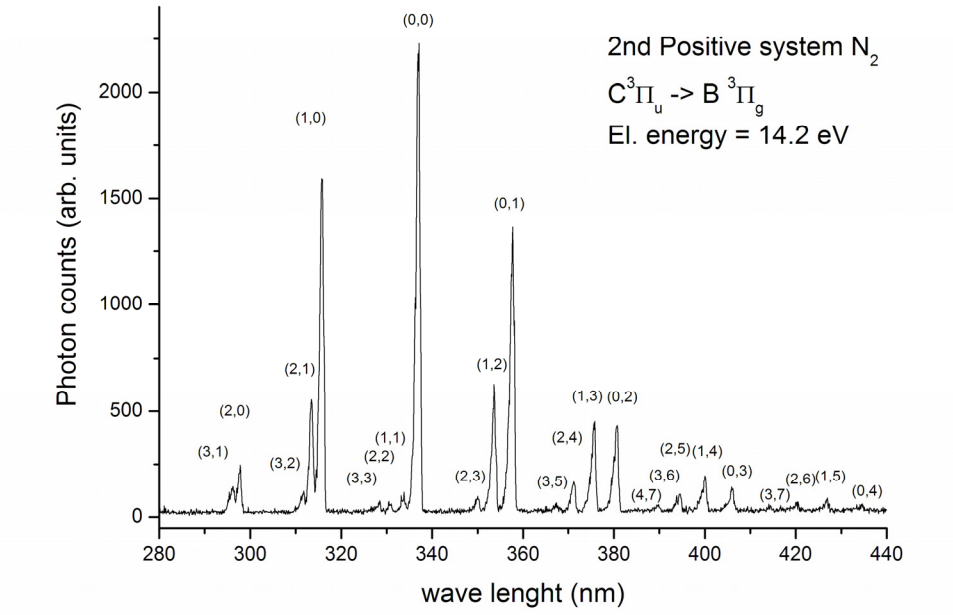


Fig. 2. The fluorescence spectrum of nitrogen 2nd positive system induced by electrons with kinetic energy of 14.2 eV.

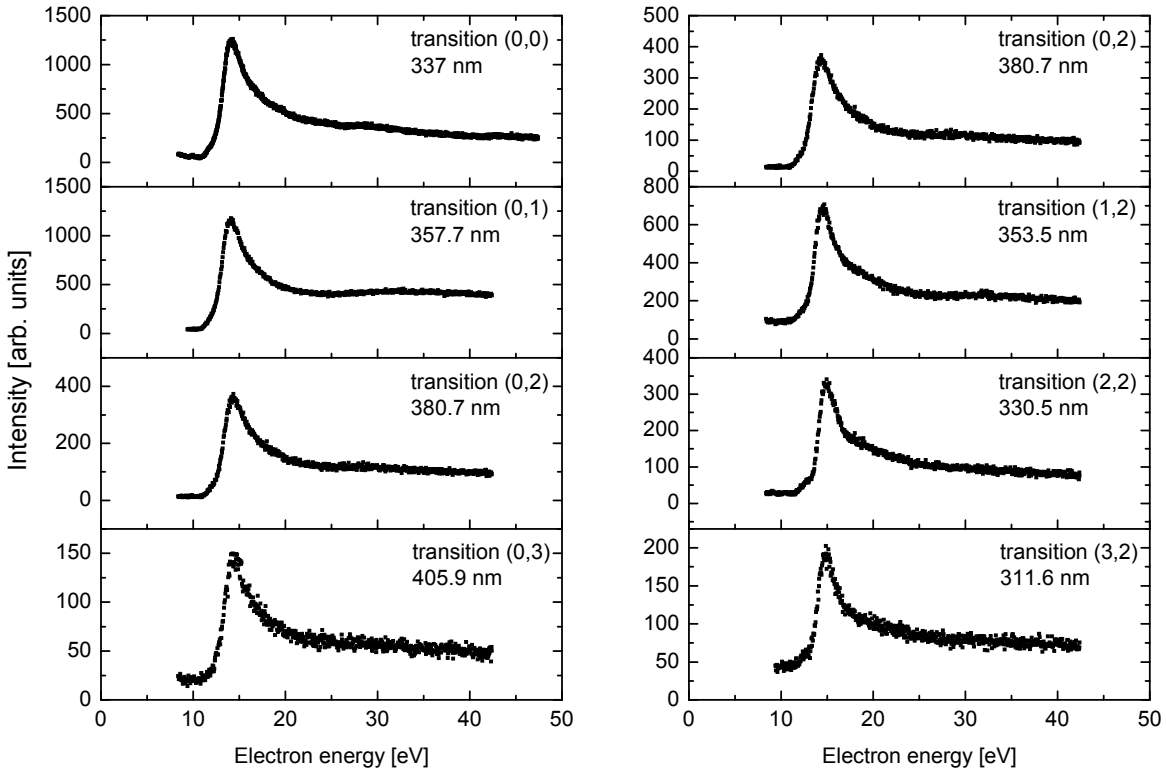


Fig. 3a and 3b. The emission cross sections for selected transitions of the 2nd PS of N_2.

Tab. 1. The threshold energies of emission cross sections for (v', v'') transitions in 2nd PS N_2

v', v''	1st threshold (eV)	2nd threshold (eV)
0.0	10.60±0.12	11.74±0.1
0,1	10.60±0.1	12,20±0.1
0,2	10.66±0.1	12.20±0.1
0,3	10.72±0.1	11.98±0.1
1,1	11.28±0.1	13.10±0.1
1,2	10.90±0.1	12.49±0.1
2,2	11.27±0.1	13.11±0.1
3,2	11.03±0.1	12.99±0.2
3,3	11.18±0.1	13.10±0.2

The data in the Table 1 indicate that there exist differences in the threshold energies of particular vibrational states of $C\,^3\Pi_u$. This is in contrast to former work by Fons [3], who stated that there is no difference in threshold for these states. However, his experiment suffered of weak resolution in the electron energy.

The excitation cross section of the strongest emission band of the 2nd PS $C\,^3\Pi_u(v'=0)$ to $B\,^3\Pi_g(v''=0)$ (337 nm) is presented in the Figure 4. The excitation cross section has been measured in the energy region from threshold to 80 eV and it has been normalised to the absolute emission cross section at its maximum at 14.1 eV. The electron energy range and the absolute value of the cross section have been calibrated to cross section measured by Zubek [2]. Excitation cross sections of additional transition lines of the 2nd PS of the N_2 have been measured.

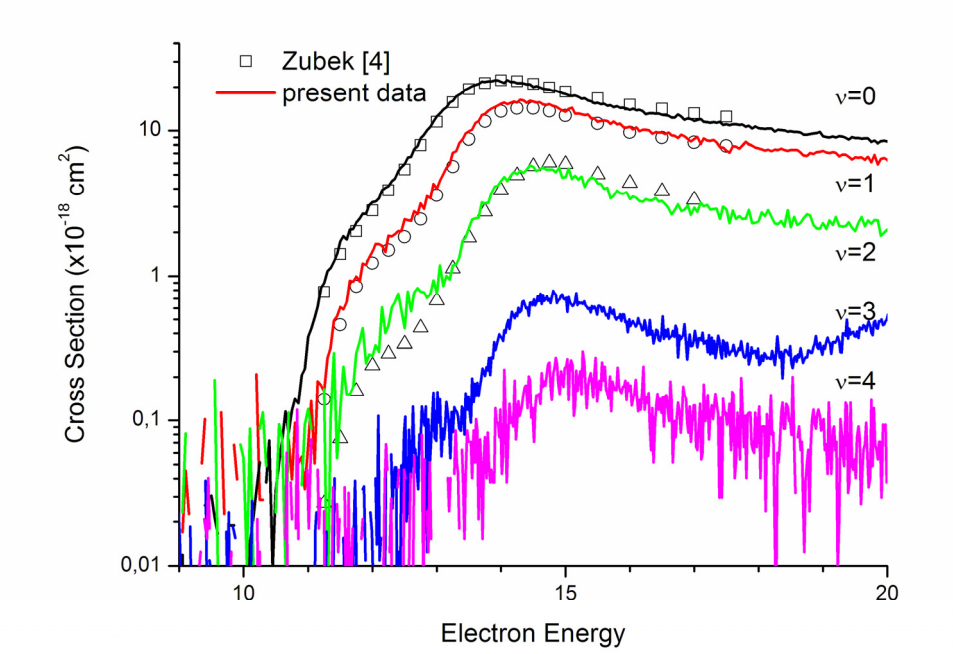


Fig. 4. Excitation cross section of the $C\,^3\Pi_u(v'=0,1,2,3,4)$ N_2 and its comparison with the data of Zubek [2].

4. Conclusions

We have studied the process of EIF in N_2 for 2nd PS. We have measured high resolution emission spectra, emission cross sections and determined excitation cross sections for the excited states $C\,^3\Pi_u$ (v'=0..4) of N_2. We have determined the threshold energies in emission cross sections for particular bands of the 2nd PS of N_2.

Acknowledgments. This work was supported the Slovak Research and Development Agency, project Nr. APVV-0365-07 and LPP-0143-06. In addition this work was supported by Association EURATOM-CU. The content of the publication is the sole responsibility of its publishers and it does not necessarily represent the views of the EU Commission or its services.

5. References

[1] M. Shaw and J. Campos, J. Quont. Speetrosc. Radiat. Transfer 30 (1983) 73
[2] M. Zubek, J. Phys. B: At, Mol. Opt. Phys., 27 (1994) 573
[3] J.T. Fons, Phys. Rev. A, 53 (1996) 2239
[4] D.E. Shemansky, J.M. Ajello, I. Kanik, Astrophys. J., 452(1995) 472
[5] M. Stano, S. Matejcik, J.D. Skalny and T. D. Märk, J. Phys. B: At. Mol. Opt. Phys. , 36 (2003) 261

DISCHARGE PROPERTY OF POROUS CERAMIC ELECTRODE

Yusuke Kano[1], Yoshiyasu Ehara[1]

[1]*Tokyo City University*
1-28-1, Tamazutsumi, Setagaya-ku, Tokyo, 158-8557, Japan
E-mail: ekidenotoko3324koushien1984@yahoo.co.jp

Dielectric-barrier discharge [DBD] is used for generation of ozone. On the other hand, it can apply for decomposition of volatile organic compound [VOCs]. However, when the discharge atmospheric area is kept humid, generating discharge is difficult. However, it is known that when porous ceramic is used for dielectric, discharge is generated higher under humid condition than dry one. In this experiment, TiO2 is chosen as porous ceramic dielectrode. It is formed to plate and discharge property is measured. Discharge occurred between TiO2 plates. Discharge current increased proportional to applied voltage and relative humidity.

1. Introduction

Discharge on atmospheric pressure has been applied for decomposition of VOCs. Recently, DBD is one of famous example. Reactor has one electrode or both of electrodes attached on dielectrics. A lot of discharge pulses are generated between the dielectrics by applied AC high voltage. However it has difficulty in generating stable discharge under humid atmosphere. When porous ceramics is used as dielectrics, similar discharge can be sustained under DC and AC power supply. In this case, discharge is similar to corona discharge. In general, porous ceramic [for example, zeolite honeycomb] is applied for exhaust gas treatment expected effect of additive metallic catalyst. However, it can also apply for discharge decomposition of VOCs. In this discharge, pulse frequency and current increase in proportion to humidity of discharge atmosphere. The phenomenon is thought that water molecule is absorbed on the surface of ceramics, therefore dielectric constant is increased. In this research, ceramic material was focused, the effect of material on the discharge condition has been experimentally investigated.

2. The experimental set-up

2.1 Dielectric sample

Dielectric sample is made from powdered TiO_2 (15 g). Water is added 20 ml. Glass-wool is added as anchor materials. After appropriate mixture, TiO_2 is poured into metallic mold (50 ×50×5 m^3) and pressed. Mold is put into vacuum desiccator; water vapours from internal TiO_2 material, and the vacuum condition is applied one day with rotary pump. After one day's vacuum, TiO_2 material is sintered at 600℃, 30 minutes in the electric furnace.

2.2 Discharge measurement and system

Configuration of discharge generator is shown in Fig.1. Form of discharge generator is similar to VOCs decomposition reactor which uses porous ceramic honeycomb [1]. Stainless mesh is used for metallic electrode. TiO_2 sample plates are set in parallel attached to each stainless mesh and reduplicated three plates. Air gap which can change length arbitrarily is set up between TiO_2 plates. Experimental system is shown in fig.2. Discharge generator is set in the thermostat and humidistat bath which can control temperature and humidity. DC high voltage is applied to discharge generator. Applied voltage and discharge current is measured by oscilloscope. Measurement time length is 20 msec which correspond to period of Japanese industrial frequency. One data under one condition is determined by average of 10 times' measurement. Numbers of pulse, average pulse current, maximum

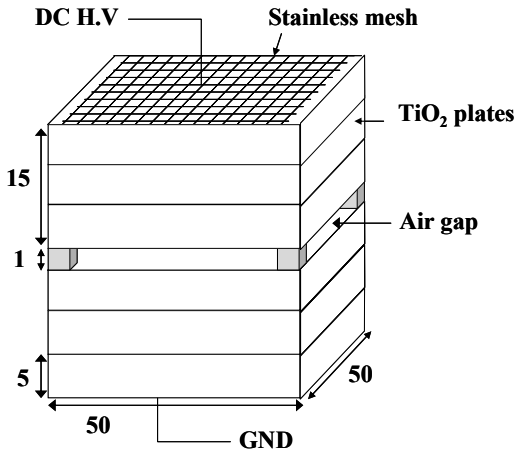


Fig.1. Configuration of discharge generator

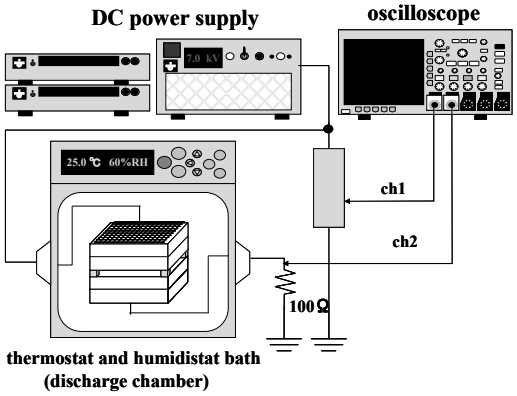


Fig.2. Discharge experimental System

pulse current, total pulse current (in 20msec) and DC current are analyzed from the detected current waveform. By these result mentioned above, discharge property is determined. Experimental condition is as follows. Temperature is set at 25℃ and air gap is set to 1.0 mm. Applied voltage is every 1 kV from DC 2 kV to 6 kV. Humidity condition is changed every RH10% from 30% to 60%.

3. The experimental results and discussion

3.1 Discharge generation

When DC high voltage was applied, discharge was generated between plates under every condition of relative humidity. Fig.3-(a) is normal waveform at RH 60%, 4kV and Fig.3-(b) is normal waveform at RH 60%, 7kV. The numbers of pulses increase with increasing the applied voltage and the humidity. Fig.4 shows photographs of discharge luminescence.

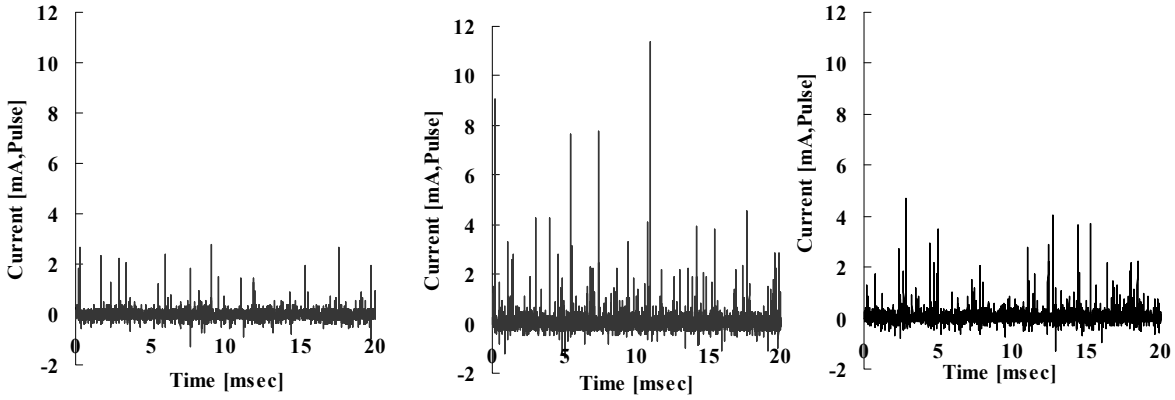
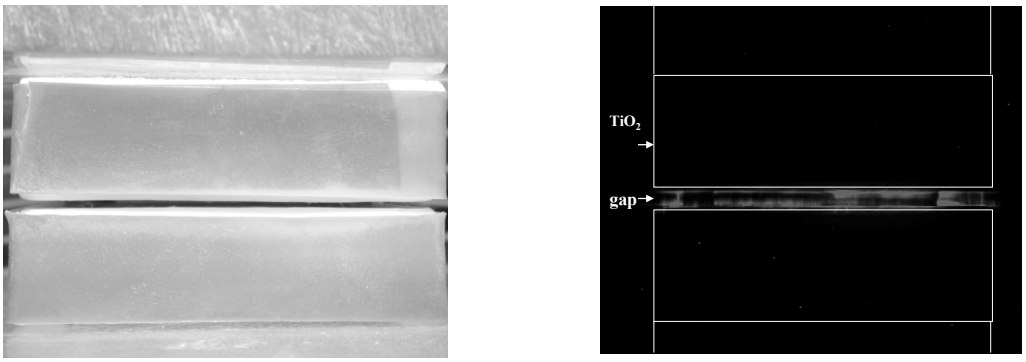


Fig.3 Waveforms of discharge current



(a) Configuration of generator (b) Generated discharge picture (RH60%, 7kV)

Fig.4. Discharge luminescence picture

3.2 Applied voltage property

Discharge current as a function of applied voltage is shown in Fig.5. From 4 to 5 kV, discharge started more or less. Pulse frequency in 20 msec is proportional to applied voltage (a). Since humidity increased, frequency became higher dominantly. Maximum current show similar property with frequency (b). Total pulse current and base current indicate same property (c),(d).

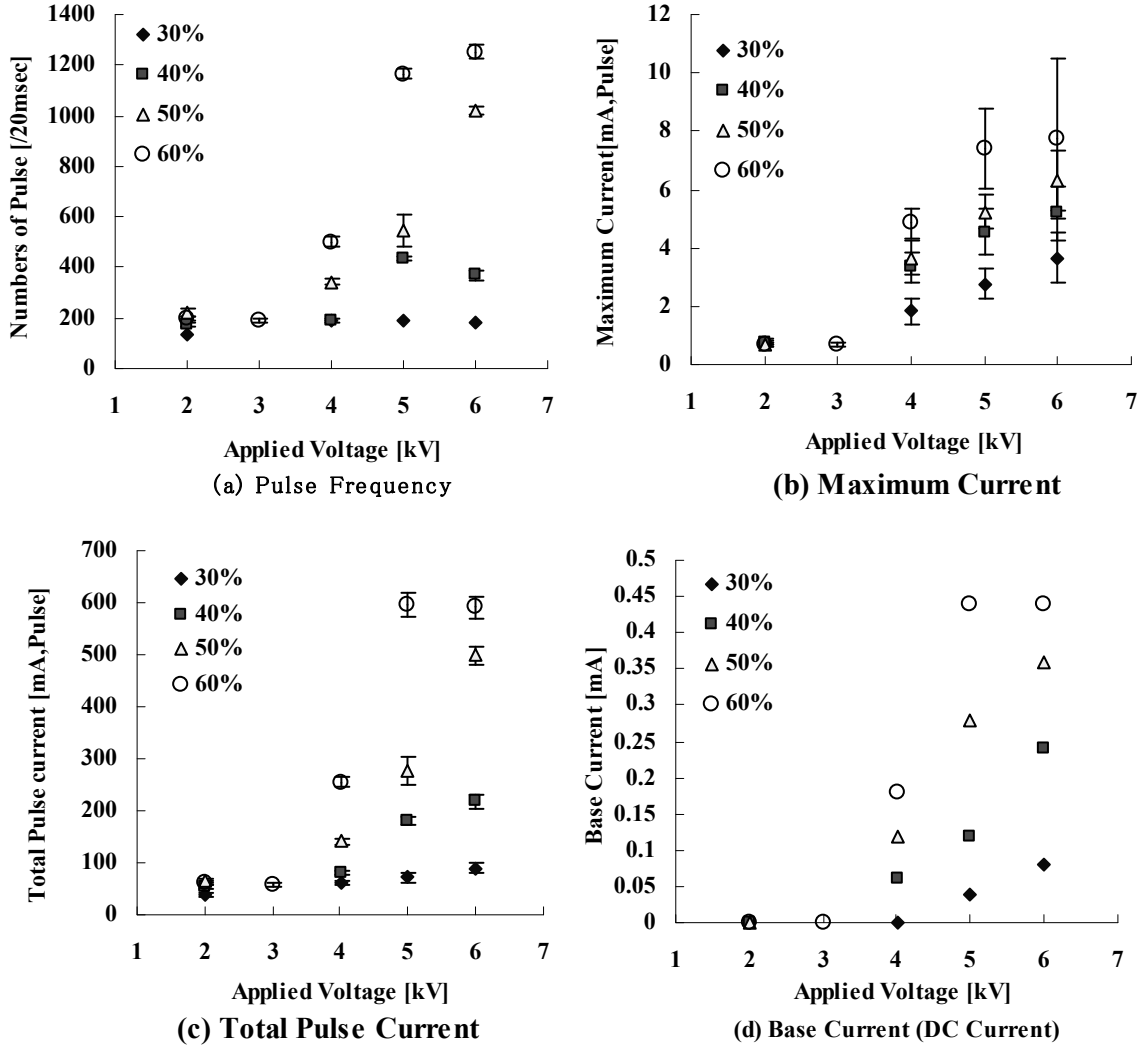


Fig.5. Discharge current property as a function of applied voltage

It is thought that when the humidity of discharge atmosphere becomes high, dielectric constant of discharge generated area and TiO_2 surface increases because of absorbing water molecule. Relative permittivity of TiO_2 itself ε is 83～183, it is higher than that of water(≒80). When the water molecule attaches to wall (plates), dielectric constant of material became high totally. Therefore, electric field between plates gets strong and value of 'applied voltage' when discharge starts comes down.

3.3 Humidity property

Discharge current as a function of humidity is shown in Fig.6. All discharge properties are proportional to humidity. When this discharge generator is applied for decomposition reactor of VOCs, it can accommodate to humid condition which traditional DBD reactor had difficulty in generating stable discharge. In addition, it has possibility of taking advantage of decomposing molecules which have structure of strong binding energy (for example, benzene ring, double bond). Because discharge generates a lot of water-derived OH radical [2]. Most of VOCs have structure of benzene ring. Therefore, the property which is proportional to humidity is useful for VOCs' decomposition reactor.

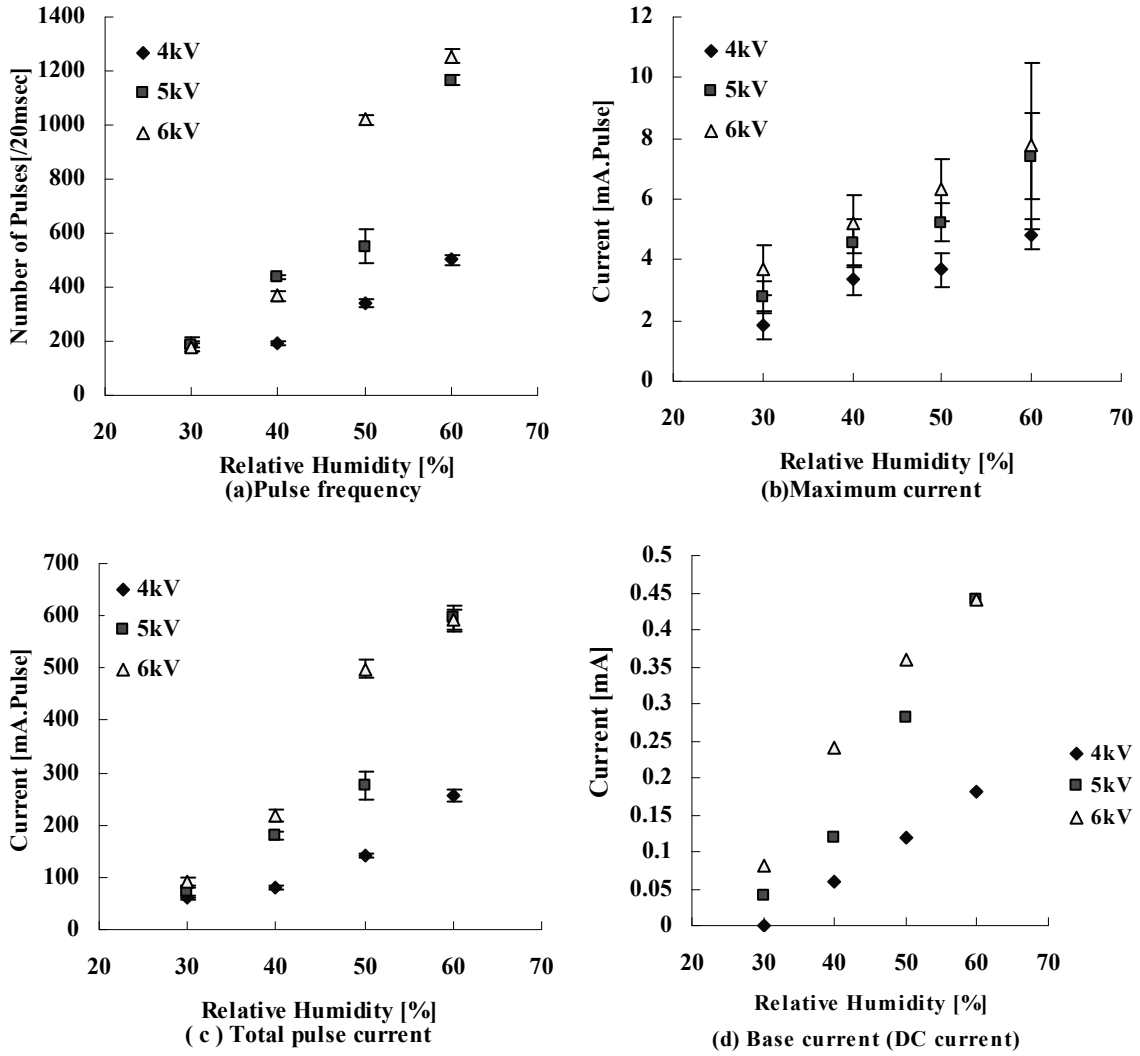


Fig.6. Discharge current property as a function of humidity

4. Conclusion

(1) When sintered TiO_2 is applied for dielectric material, discharge is generated in air gap between TiO_2 plates.

(2) Discharge properties are proportional to applied voltage and humidity of atmosphere of discharge area. It indicates possibility of TiO_2 plate of application for decomposing VOCs.

5. Reference

[1] Y.Ehara, et "Fundamental Characteristics of Discharge Using Honeycomb Type Discharge Reactor and its Decomposition of Toluene" Journal of the Institute of Electrostatics Japan, Vol34, No1, pp19-24(2010).

[2] Y.Nosaka, Behavior of Chemical Species in Photocatalytic Reaction at the Surface of Titanium Oxides, Photochemistry Vol.34, No.1, pp.14-21.

DC BREAKDOWN IN AIR, OXYGEN AND NITROGEN AT MICROMETER SEPARATIONS

Matej Klas[1], Štefan Matejčík[1]

[1]*Department of Experimental Physics, Comenius University, Mlynska dolina F2, 84245 Bratislava, Slovak Republic*
E-mail: matejcik@fmph.uniba.sk

The DC breakdown in Air, O_2 and N_2 has been studied in discharge system consisting of two parallel planar Cu electrodes at separations from 20 to 200 μm and in the pressure range between 6 mbar – 920 mbar. The results are presented in the form of breakdown voltage curves – Paschen curves. The analysis of the experimental data has been carried out in terms of semi empirical Paschen law. The effective secondary emission coefficient γ as a function of the reduced electric field has been estimated from the experimental data.

1. Introduction

In the last decade the microdischarges have attracted much attention as sources of stable and reliable non-equilibrium high pressure plasma [1-5]. One of the most common methods for generation of microdischarges represents the discharge tube with planar electrodes scaled down to the electrode gaps in the micrometer range [6]. Paschen law, which describes the dependence of the breakdown voltage as function of *p.d*, where *p* is the pressure and *d* is the electrode distance, represents an important scaling law. The validity of the Paschen Law was confirmed for variety of DC discharge conditions (pressures, distances, electrode materials) [7, 8]. However, already in fifties of the 20 century, the departures from the Paschen law have been observed at small electrode gaps [9, 10].

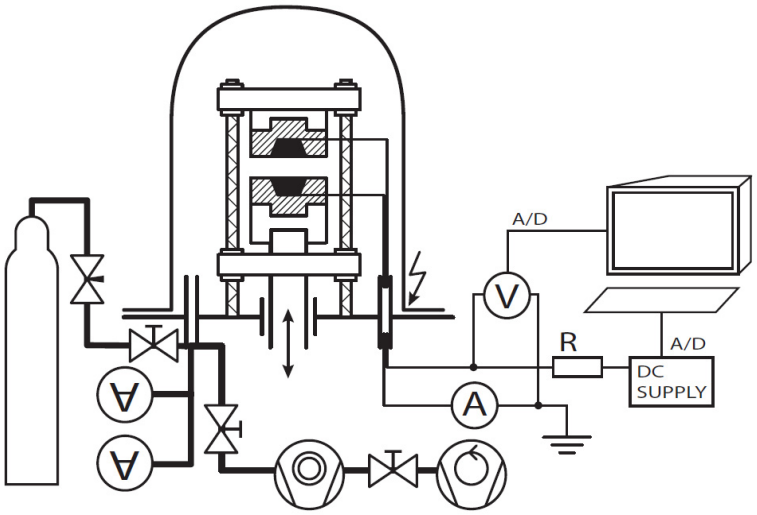


Fig. 1. Experimental setup.

2. Experiment

We have built a system to measure the DC breakdown at micrometer separations between planar metallic electrodes. The separation of the electrodes can be modified under vacuum conditions. The schematic view of the apparatus is shown in the Figure 1. The discharge system is located in the high vacuum chamber. The vacuum is generated by the turbo-molecular pump (Pfeiffer Vacuum TMU 071P) and the background pressure of $2x10^{-5}$ mbar has been achieved. The low pressures were measured by the ionisation gauge (Pfeiffer Vacuum, PKR 261) and the high pressures were measured by the capacitance gauge (Pfeiffer Vacuum, PCR 260 and MKS 626A 100Torr Barratron). The gases used in the experiment were O_2, N_2 (Linde, 5.0 purity) dry ambient air (X13 zeolites) and ambient air (50% humidity at 20°C).

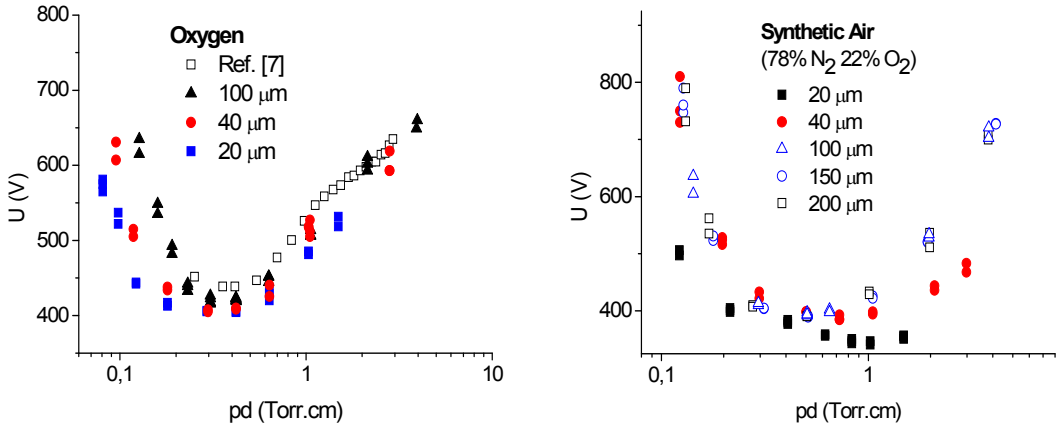


Fig. 2. The experimental Paschen curve for DC breakdown for several electrode gasp a) in O_2, b) in synthetic air.

The discharge system for generation of the microdischarges consists of two planar copper electrodes with diameter of 5 mm. The electrodes were mechanically polished and chemically cleaned in ultrasonic bath. One of the electrodes was fixed and the other was movable continuously with micrometer scale linear feed-through. Both electrodes were equipped with dielectric cap (immune to vacuum, dielectric breakdown strength =13,8 kV/mm) to prevent the ignition of the discharge at longer path at low pressures. One of the electrodes was earthed; to the second electrode we have applied DC voltage (ISEG HPp 20 407). The 0 μm separation of the electrodes was established by checking the electrical contact between the electrodes and then the movable electrode was pulled away by the means of the micrometer screw. The gap between the electrodes was set to the required distance. Maximum current was set to 1,6 mA.
The DC breakdown voltage was determined from the time dependence of the potential difference across the discharge tube, which has been measured using a digital oscilloscope. We have applied very slowly increasing potential to one of the electrodes (ramp speed 0,05 V/s). The potential across the discharge tube was increasing until the point of breakdown was reached. Due to discharge breakdown the potential across the discharge tube decreased rapidly. The breakdown voltage was determined from the maximum potential achieved across the discharge gap. Using this method we were able to measure the breakdown voltage with high reproducibility.

3. Results and discussion

The DC breakdown voltage was measured for several discharge gaps from 20, to 200 μm as a function of *p.d* (Paschen curves). The pressure was varied in the range from 6 mbar up to 920 mbar. The Paschen curves have been measured for pure Oxygen (5.0) synthetic Air (78% N_2 and 22% O_2 both gases in 5.0 purity), dry ambient air, ambient air and N_2 (5.0).
In the Figure 2a we see the Paschen curves for pure oxygen measured at several discharge gaps. The left site of the Paschen curve is identical for all discharge gaps, however, the left site depends strongly on the electrode separation. For given value of *p.d* the DC breakdown voltage is decreasing with decreasing electrode separation. We attribute this behaviour to field emission and ion enhanced field emission of the electrons from the cathode and to the low pressure. Under these conditions the electrons from cathode are able efficiently ionise the gas and develop discharge. On the right site of the Paschen curve in O_2 is characteristic bump is present which was also observed earlier by Meek [7]. This structure in the Paschen curve could be associated with non-dissociative (three body) electron attachment to O_2 which is more efficient at high pressure and low reduced electric fields. With increasing reduced electric field the probability of the non-dissociative electron attachment is less efficient the mean free path of the electrons and the kinetic energy of the electrons is increasing which results in the decrease of the breakdown voltage.

The Paschen curves for synthetic air are presented in the Figure 2b. For large electrode gaps of 100, 150 and 200 μm the experimental Paschen curves are very similar in the shape and values. This indicates that at these electrode separations the Paschen law is valid and the breakdown voltage depends only on the *p.d*. The Paschen curves for electrode separations 20 and 40 μm show different behaviour.

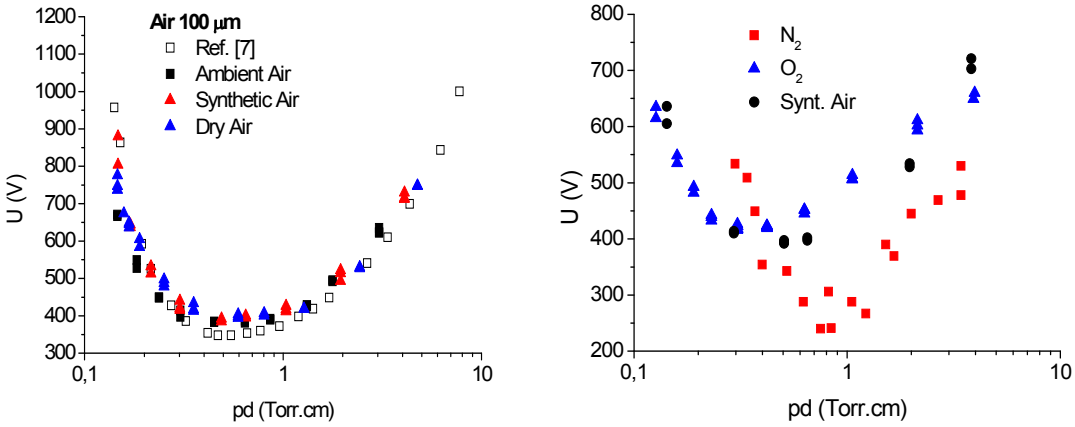


Fig. 3. Comparison of the experimental Paschen curves for DC breakdown at one electrode separation a) in air, the data in [7] where measured at different electrode gap and different electrode material b) in N_2, O_2 and synthetic air

Usually the departures from Paschen law appear on the left site of the Paschen curve and are related to the field emission and to ion assisted field emission of the electrons from the cathode surface. However, in this case we observe deviation also on the right site. This effect could be explained by new surface processes appearing at the cathode in this case initiated by photons. In the Figure 4 a) we see that the effective secondary electron emission coefficient at low values of the reduced electric field shows higher values for short electrode gasps. This could support the hypothesis on the role of photons. In the Figure 3 a) we see the comparison of the Paschen curves measured at electrode separation of 100 μm in ambient air, dry air and synthetic air. The Paschen curves for synthetic and dry air are practically identical in whole range of the *p.d* values. The Paschen curve for ambient air shows some difference to the previous two on the left site of the curve. This difference is resulting from the humidity of the ambient air (approximately 50% at 20° C).
We have tried to analyse the experimental data in the terms of the semiempirical Paschen law (1):

$$U(A,B,\gamma,pd)=\frac{B(pd)}{\ln\frac{A}{\ln(1/\gamma+1)}+\ln(pd)} \qquad (1)$$

where k represents the semi empirical factor equal to k = 1 for molecular gases and k =2 for rare gases [11, 12]. The A and B are the coefficients which are associated with ionization coefficient α, which has for the molecular ´gases form [8]:

$$\alpha = A.p_0\, exp\left(-B(p/E)\right) \qquad (2)$$

The Townsend's coefficients α and γ are related each to other via formula [13]:

$$1+1/\gamma=\exp(\alpha d), \qquad (3a)$$

which can be rewritten in the form:

$$\gamma=1/(\exp(\alpha d)-1) \qquad (3b)$$

We have used the experimental Paschen curves to obtain the effective secondary electron emission coefficient γ [13,14]. Using the formulae (2) and (3) we are able to derive the dependence of the coefficient γ on the breakdown voltage U and hence on reduced electric field E/p.

$$\gamma=\frac{1}{exp\left(A.pd.exp\left(-B\frac{pd}{U}\right)\right)-1} \qquad (4)$$

For the calculations of γ we have applied the values of A and B coefficients given by Reiser [8]. From these calculations we were able to obtain the values of the γ as a function of the reduced electric field E/p. The results of the calculations for particular gas and electrode separations are displayed in the Figure 4.

The results show that the γ depends on the reduced electric field E/p and also depends on the electrode separation. For large electrode separations 100 and 500 μm the γ show similar dependence on E/p in whole range of the E/p (from 40 up to ~2000 $V.cm^{-1}.Torr^{-1}$). At narrow electrode gaps (20 and 40 μm) γ is in very good agreement with those obtained at large separation in the E/p range up to ~300$Vcm^{-1}Torr^{-1}$. For small electrode separations the γ increases strongly with E/p and the increase is

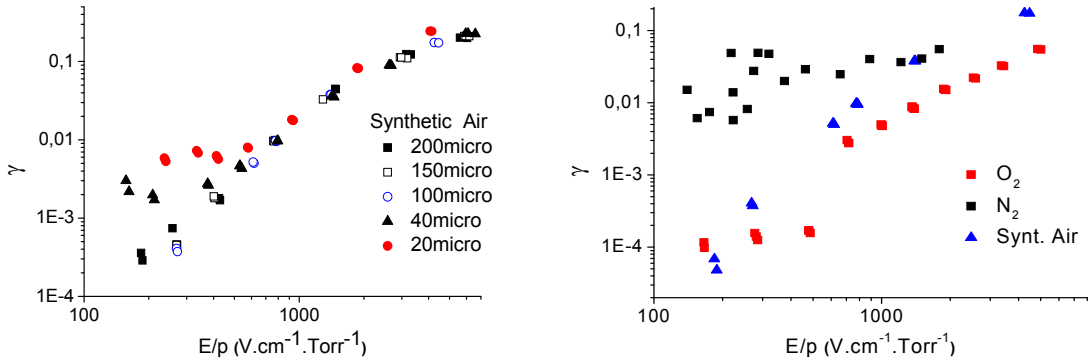


Fig. 4. The second Townsend coefficient γ as determined from the experimental Paschen curves for a) synthetic air at different electrode separations b) in O_2, N_2 and synthetic air at electrode separation of 100μm.

more pronounce at 20μm than at 40 μm. We associate this behaviour with increasing role of the field emission, or ion enhanced field emission from the cathode under these conditions.

4. Conclusions

We have measured DC breakdown curves for ambient, dry and synthetic air, oxygen and nitrogen at micrometer separation of Cu electrodes. The experiment confirmed the validity of the Paschen law for electrode separation greater than 100 μm. For smaller electrode separation departure from Paschen law were observed in the left site of the Paschen curve mainly due to field emission and ion enhanced field emission from the cathode. In the case of air for electrode separations below 100 μm departure from the Paschen law occurs also on the right site of the Paschen curve.

Acknowledgments. This work have been supported by the Slovak Research and Development Agency, project Nr. APVV – 0365-07, VEGA project Nr.: 1/0051/08 and Comenius University Project Nr. UK 456/2010 FMFI.

5. References

[1] Becker K H Schoenbach K H and Eden J G, 2006 *J. Phys. D: Appl. Phys.* **39** R55
[2] Becker K H Kogelschatz U Schoenbach K H 2004 *Non-equilibrium air plasmas at atmospheric pressure CRC Press*
[3] Iza F Kim G J Lee S M Lee J K Walsh J L Zhang Y T and M G Kong 2008 Microplasmas: Sources, Particle Kinetics, and Biomedical Applications *Plasma Process. Polym.* **5** 322
[4] Penache C Gessner C Bräuning-Demian A Scheffler Spielberger P L Hohn O Schössler S Jahnke T Gericke K H and Schmidt-Böcking H 2002 *Proceedings of SPIE Vol*. **4460**, p. 17-25
[5] Foest R Schmidt M Becker K Int. 2006 *J. Mass Spect*.**248** 87
[6] Petrovic Z. Lj., Škoro N., Maric D Mahony C M O Maguire P D Radmilovic-Radenovic M and Malovic G 2008 *J. Phys. D: Appl. Phys.* **41** 194002
[7] Meek J M and Craggs J D 1953 Electrical breakdown of gases *Oxford University Press*
[8] Reizer Y. 1991 Gas discharge physics Springer-*Verlag,. Berlin Heidelberg*

[9] Boyle W S and Kisliuk 1955 P *Phys. Review* **97**(2) 255
[10]Boyle W S and Germer L H 1955 *J. Appl. Phys.* **26**, 571
[11]Sato M Interpretation of argon breakdown in dc and microwave fields *Bull. Yamagata Univ.(Eng.*, Vol**. 25**, No. 2, 119-125
[12] Ward A L 1962 *J. Appl. Phys.,* **33** *2789*
[13] Auday G Guillot Ph Galy J and Brunet H 1998 Experimental study of the effective secondary emission coefficient for rare gases and copper electrodes *J. Appl. Phys.* **83** 5917–21
[14] Mariotti D McLaughlin J A and Maguire 2004 P *Plasma Sources Sci. Technol*. **13** 207–212

MEASUREMENT OF ELECTRON ATTACHMENT RATE TO O_2 AT AMBIENT PRESSURE USING IMS

Marek Kučera [1], Michal Stano[1], Štefan Matejčík[1]

[1]*Department of Experimental Physics, Comenius University, Mlynska dolina, Bratislava, Slovak republic*

E-mail: stano@fmph.uniba.sk

Electron attachment rate constant to oxygen was measured in nitrogen buffer gas at ambient pressure using Ion Mobility Spectrometry (IMS) technique. The range of the values of the reduced electric field *E/n* varied from 0.5 to 2 Td and the content of O_2 in N_2/O_2 mixture was 0.1% to 1.6%. The rate constants for electron attachment were obtained using three different methods.

1. Introduction

The electron and ion processes in air attract attention of the scientist not only due to their importance for the environment, but also due to increasing importance of the atmospheric pressure discharges in various fields of application [1]. In the case of the electron attachment reactions in air an important role has molecular oxygen as the electronegative component of the air. At low pressure and intermediate electron energies, the dissociative electron attachment to O_2 is the dominant reaction.

$$e + O_2 \rightarrow O_2^{-\#} \rightarrow O^- + O \qquad (1)$$

This reaction has been studied in crossed beams experiment [2, 3, 4]. At elevates pressures and low electron energies, different attachment reaction is operative, the non-dissociative (three body) electron attachment.

$$e + O_2 \rightarrow O_2^{-\#} + M \rightarrow O_2^- + M \qquad (2)$$

where $O_2^{-\#}$ is the transient negative ion and M is the third particle (O_2, N_2,...). The third body stabilises the transient negative ion by the quenching of the excess energy. Most experiments devoted to the estimation of the kinetic data for reaction (2) have been carried out in drift tubes at lower pressures (~10 mbar) and the values of the rate constant were extrapolated toward high pressure [5, 6, 7, 8]. One exception is the experiment of McCorkle [9] which has been carried out in large range of pressures starting at 300 Torr up to 10^4 Torr. The three body electron attachment depends not only on the energy of the electrons, the density of the gas, the temperature of the gas, but also on the nature of the buffer gas (third body), which determines the electron energy distribution function and also has the stabilising effect on the molecular ion. Chanin et al. [5] refers that three body electron attachment to O_2 is the most efficient in O_2 and that the efficiency is decreasing in N_2 and even more in He. This paper presents three different methods based on the IMS technique, to measure the kinetics of the three body electron attachment reactions at atmospheric pressure.

2. Experiment

The work was performed using a home made ion mobility spectrometer. Detailed description of the instrument is given in [10]. The electrons are generated in discharge in a point-to-plate geometry (negative potential applied to point electrode) fed by pure nitrogen. In non-electronegative gases as N_2 the discharge current is conducted by electrons. The discharge current is measured on the tip electrode and it was found to be independent on oxygen concentration inside the drift tube. Most of electrons from discharge are collected on a mesh forming the plane electrode and only a fraction of them drift through the instrument. After passing an aperture with 6 mm diameter the electrons are released to drift tube in short pulses controlled by a shutter grid. The current of charged particles (electrons and negative ions) is measured on a collector with placed on the end of drift tube. it is amplified and recorded by an oscilloscope. The length of the drift tube is L=11.1 cm and it is fed by nitrogen buffer gas with small admixtures of O_2. Purity of both nitrogen and oxygen gas was 99.999%. The gas mixture is prepared using MKS‡ mass flow controllers.

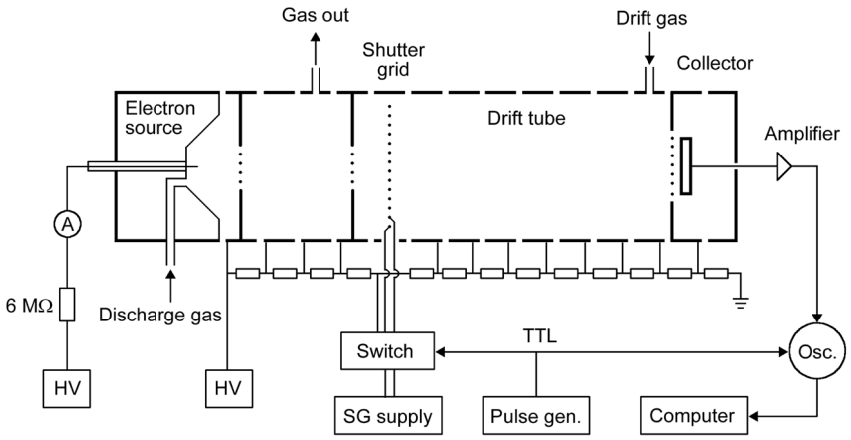


Fig. 1. The experimental setup.

The speed of a three body electron attachment reaction can be expressed as:

$$\frac{d[M^-]}{dt} = -\frac{d[e]}{dt} = k[M][e][X] \tag{3}$$

where [e], [M] and [X] are number densities of electrons, electron attaching gas (O_2) and neutral molecules (N_2 and O_2). [M^-] is the number density of negative ions formed in the reaction and k is the reaction rate constant. Due to the electron attachment reaction the amount of the electrons in the drift tube is decreasing with increasing distance from the shutter grid d according to following formula:

$$[e]_d = [e]_0 \exp\left(-\frac{k[M][X]d}{w_e}\right) \tag{4}$$

where w_e is electron drift velocity and $[e]_0$ is number density of the electrons just at shutter grid.

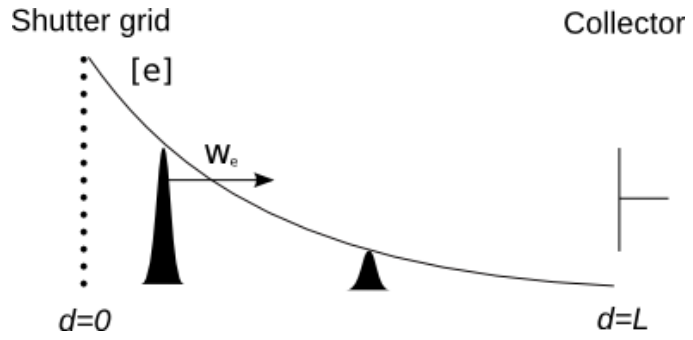


Fig. 2: Concentration of electrons in the drift tube.

The amount of produced negative ions is proportional to the amount of the electrons passing the given location

$$[M^-]_d = k\tau[M][X][e]_d \tag{5}$$

where τ is the shutter opening time. Electron and ion current measured on collector is given by

$$I_e = q_e[e]w_e S \quad \text{and} \quad I_i = q_e[M^-]v_i S \tag{6}$$

where q_e is the elementary charge, v_i ion drift velocity and S cross section of electron and ion beam. Given equations do not account spreading of the electron and ion beam due to diffusion and space

charge effects. Typical oscillographic record of the electron and ion current on collector is shown in the figure 3.

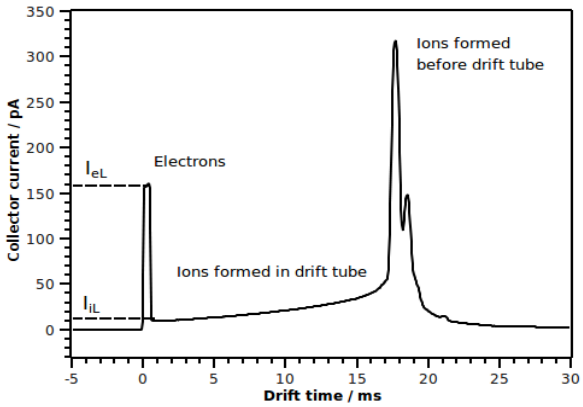


Fig. 3. Oscillographic record of electron and ion current on collector. At $t = 0$ shutter grid is open for 500 μs.

The first peak at very short drift time originates from the electrons. The next part with increasing exponential shape represents the ions formed inside the drift tube due to the electron attachment reaction. The ions formed close to collector arrive first and the ions formed just behind the shutter grid arrive as last. Finally, we see the ion peaks, which consists of ions formed before the shutter grid and which have passed the whole drift tube with fixed drift velocity v_i. In the figure shown we see several peaks which we associate with different types of the ions. This oscillographic record gives us possibility to determine the electron attachment rate constant k using several methods.

3. Evaluation methods

a)

Electron attachment rate constant is calculated from the electron current measured at collector I_{eL} and the current of ions formed just before the collector I_{iL}. Combinig equations (5) and (6) we can calculate k as :

$$k = \frac{I_{iL}}{I_{eL}} \frac{w_e}{v_i} \frac{1}{[M][X]\tau} \tag{7}$$

Ion drift velocity v_i was determined from ion drift time t_d over drift tube $v_i = L/t_d$ and the values of w_e were taken from [11].

b)

The second method for determination of k was previously published by Tabrizchi et al. [12]. The ions formed along the drift tube drift to the collector with velocity v_i. At time t measured from opening of the shutter grid the collector registers ions initially formed at distance:

$$d = L - v_i t \tag{8}$$

from the shutter grid. The concentration profile of negative ions formed along the drift tube is therefore mirrored in the oscilloscopic record of the ion current on collector. Using the equations (4), (5) and (8) the shape of ion current waveform is obtained:

$$I_i \propto \exp\left(k[M][X]\frac{v_i}{w_e}t\right) \tag{9}$$

The attachment reaction rate constant is calculated from the fit of an exponential function to the relevant part of recorded ion current waveform.

c)
The electron attachment rate constant is calculated using the Lambert-Beer law for electron transmittance through the drift tube containing electron attaching gas at various concentrations. If I_0 is electron current transmitted when drift tube is filled with pure N_2 and $I_{[M]}$ when number density of electron attaching gas is [M] the rate constant of electron attachment reaction can be expressed as

$$k = \frac{w_e}{L[M][X]} \ln \frac{I_0}{I_{[M]}} \tag{10}$$

The electrons were released into drift tube in pulses so that electron and ion current on collector could be distinguished. Unlike in previous two methods where k could be determined from a single measurement, at least two measurements at different concentration of electronegative gas are necessary.

4. Results

The rate constants for electron attachment to oxygen obtained using the three methods described above are shown in the figures 4 and 5. The rate constant can be evaluated only if some electrons survive the drift and reach the collector. This limits the maximal O_2 concentration to 0.2% at 0.5 Td, 1.4% at 1 Td and 1.6% at 2 Td. The results obtained using different methods at the same conditions differ by up to factor of 4. The highest differences are at very low concentration of O_2 while agreement becomes better with increasing concentration of O_2. Most of present values are higher than previously reported values [5, 9] at given *E/n* or at corresponding mean electron energy, see the Table 1. In agreement with previous studies the average rate constant is decreasing with increasing *E/n* in the studied range.

Differences in values obtained by different methods indicate their relatively low accuracy. The results of all three methods can therefore be considered as approximate values only. The inaccuracies may result from several effects depending on the method used. If electron current is higher than ion current by several orders of magnitude, the ion current waveform may be deformed by the tail of electron peak. The use of methods a) and b) is limited in such situation. The problem can be suppressed by choosing a lower amplification and a higher bandwidth of the amplifier. However, the amplification must be still sufficient to measure the ion current. The inaccuracies may also arise from diffusion and coulomb repulsion of the electron and ion beam. Although these effects don't influence the results of the method a) their role in the method c) based on the Lambert-Beer law needs further investigation.

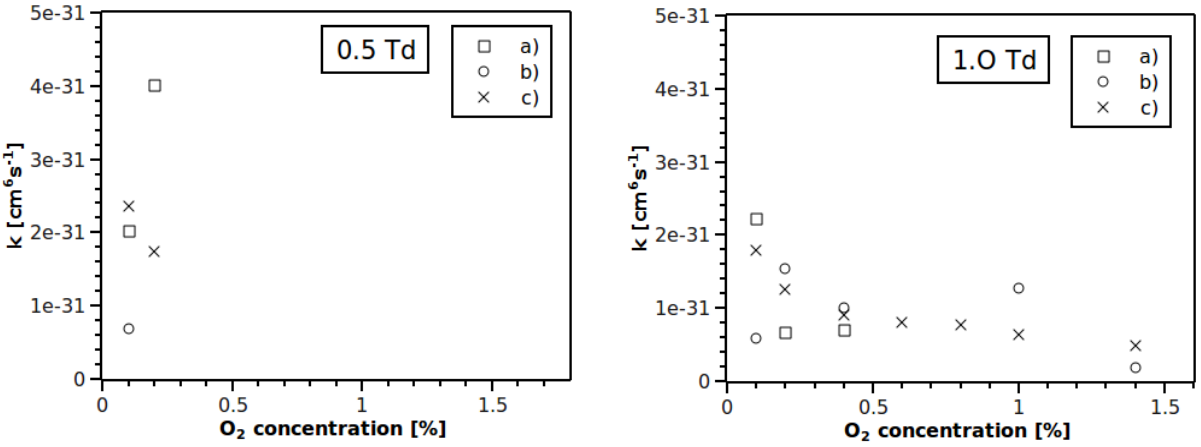


Fig. 4. Rate constants for electron attachment to O_2 at 0.5 Td (left) and 1 Td (right) obtained using methods a) b) and c).

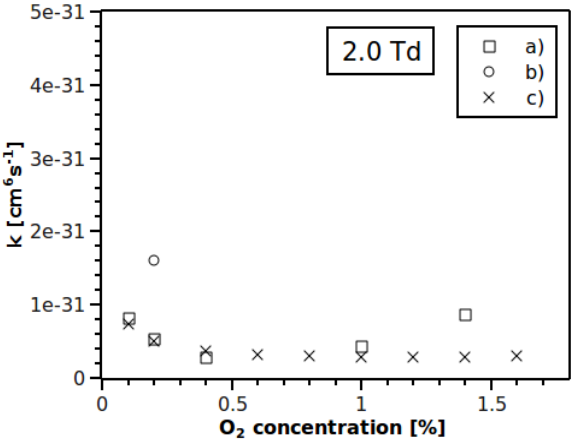


Fig. 5. Rate constants for electron attachment to O_2 at 2 Td obtained using different methods.

Tab. 1. Rate constants of electron attachment for O_2 in N_2 buffer gas.

E/n, Td	k, cm^6s^{-1} Method a)	k, cm^6s^{-1} Method b)	k, cm^6s^{-1} Method c)	<e>, eV [11, 13]	k, cm^6s^{-1} [5]	k, cm^6s^{-1} [9]
0,5	3.010^{-31}	$6.3x10^{-32}$	$2.0xE^{-31}$	0,19	$9,7x10^{-32}$	$\sim5x10^{-32}$
1	$1.2x10^{-31}$	$1.3x10^{-31}$	$9.5xE^{-32}$	0,36	$4,6x10^{-32}$	$3,2x10^{-32}$
2	$5.8x10^{-32}$	$2.1x10^{-31}$	$3.8xE^{-32}$	0,6	$2,0x10^{-32}$	- - -

Acknowledgement. This work was partially supported by the slovak grant VEGA 1/0051/08 and by the Slovak Research and Development Agency, project Nr. APVV-0365-07.

5. References

[1] K. H. Becker, U. Kogelschatz, K.H. Schoenbach, 2004 Non-equilibrium air plasmas at atmospheric pressure CRC Press

[2] G.J. Schulz, *Phys. Rev.* **128** (1962) 178

[3] D. Rapp, D.D: Briglia, *J. Chem Phys.* **42** (1965) 1480

[4] D. Spence, G.J. Schulz, *Phys. Rev.* **188** (1969) 280

[5] L.M.Chanin, A.V.Phelps and M. A. Biondi, *Phys. Rev* **128** (1962) 219

[6] N.E. Bradbury, *Phys. Rev.* **44** (1933) 883

[7] H. Shimamori, Y. Hatano, *Chem. Phys.* **21**(1977) 187

[8] G.S. Hurst, T.E. Bortner, *Phys. Rev.* **112** (1959) 116

[9] D. L. McCorkle, L. G. Christophorou, V. E. Anderson, *J. Phys. B: Atom. Molec. Phys.* **5** (1972) 1211

[10] M. Stano, E. Safonov, M. Kučera, Š. Matejčík, *Chem. Listy* **102** (2008) 1414-1417

[11] G. G. Raju, Gaseous Electronics, Taylor and Francis, 2006

[12] M. Tabrizchi, A. Abedi, *J. Phys. Chem. A* **108** (2004) 6319-6324

[13] S. R. Hunter, J. G. Carter, *J. Chem. Phys.* **90** (1989) 4879

THEORETICAL DETERMINATION OF THE MOBILITYOF NO_3^- ION IN NITROGEN DRIFT GAS

J. Matúška[1], M. Krajči[2], J. Urban[2], Š. Matejčík[1]

[1]*Department of Experimental Physics*
[2]*Department of Nuclear Physics and Biophysics,*
Faculty of Mathematics, Physics and Informatics, Comenius University Bratislava, 842 48, Bratislava, Slovak Republic
E-mail: matuska@fmph.uniba.sk

We have applied the methods of Molecular Dynamics (MD) to calculate the reduced ion mobility of the NO_3^- ion in N_2 gas. The NO_3^- is an important atmospheric negative ion and thus there exist a deep interest in the transport properties of this ion. The calculations have been performed using the MD computational code DL_POLY 3.09. The molecular bonds and the intermolecular interactions were described by the forcefield with the parametrization developed in our group.

1. Introduction

The Ion Mobility Spectrometry (IMS) is an ion separation method based on the fact that different ions have different drift velocities as they drift in a drift gas in a weak homogeneous electric field. IMS has many advantages, e.g., small size, fast response, high sensitivity and that IMS can operate at atmospheric pressure. One of the difficulties in the IMS is the identification of the ions, as there exists only small and very limited number of data linking ion mobilities to the mass of the ion.
One of the possibilities to link ion mobilities to the mass of the ions is to calculate the ion mobilities using the Molecular Dynamics methods. The molecular dynamic methods are based on the classical newton mechanics of the studied system. The differential equations of the motion are solved by numerical integration. The number of particles (atoms, molecules, ions) in the model system are limited only by performance of the computer. The known trajectories of the ions can be used to calculate the diffusion coefficient for selected ion. The mobility of the ion in the buffer gas is obtained using the Einstein equation for diffusion coefficient.
The Ion mobility spectrometer at Department of Experimental Physics, Comenius University is used to analyse the ions produced in the corona discharge at atmospheric pressure. One of the last studied systems was the formation of the ions in the negative corona discharge in the O_2/N_2 mixtures in the nitrogen drift gas. In this experiment the NO_3^- is the most stable negative ion [1].

2. Numerical Model

The present numerical model consisted from 70 of the studied ion and 7000 molecules of the buffer gas. The edge of the simulated cell was 6.61×10^{-8} m long. We have used the cubic periodic boundaries. The size of the simulated cell was chosen to obtain atmospheric pressure at the temperature 300 K with respect to ideal gas law. We were not able to establish exactly the normal conditions because we have used NVE ensemble to preserve system energy and volume. NVE ensemble can't set up exact temperature and pressure, only maintain total system energy. The exact temperature and pressure depend on initial velocities and positions of the molecules, which were defined randomly. Calculations were performed in program DL POLY 3.09 [2]. The evolution of the system was lasted for time period 20 ns.
Previous calculation has shown, that the general forcefield parametrization (e.g. UFF [3]) is yields not accurate results. We have decided therefore to create our own forcefield parametrization for NO_3^- - N_2 potential based on the quantum chemical calculations. We have performed B3LYP density functional method with basis 6-311+G(3d). We have calculated the energy dependence on the distance from 42 different directions equally spread. We have acquired these directions from tessellation of the sphere. One point of the shell was calculated by the minimization of the contributions to the energy caused by the rotational freedom of the N_2 molecule. The values of the one shell were averaged by equation:

$$E(r) = \frac{\sum_i E_i e^{\left(\frac{E_0 - E_i}{kT}\right)}}{\sum_i e^{\left(\frac{E_0 - E_i}{kT}\right)}} \quad (1)$$

Where E_0 is the minimal energy of the shell, E_i is the energy from the i-th direction, T is the thermodynamic temperature 300K and k is the Boltzmann constant.
The calculated dependence of the interaction energy on the distance of the molecules has served as a input data for parameters fitting. To describe the interaction we have chosen Morse potential in form (2)[4,5].

$$E(r) = E_0\left\{\left[1 - e^{-k(r-r_0)}\right]^2 - 1\right\} \quad (2)$$

where E_0 is the energy of the minimum, r_0 is the equilibrium distance and k is parameter describing the "slope" of the potential. This potential has been the most accurate representation of the calculated data. The fitted parameters are in Table 1

Tab. 1. Fitted parameters of the Morse potential

	Value	Std error
E_0 [eV]	5.2936 10^{-2}	1.0768 10^{-3}
R_0 [Å]	3,87	1.8474 10^{-2}
K [$Å^{-1}$]	8.0476 10^{-1}	2.1848 10^{-2}

The result of the MD calculation of the above described system using the DL_POLY 3.09 package was the time dependence of the mean square displacement of the NO_3^-. In Fig. 1 is showed this dependence of the mean square displacement (MSD) on the time for NO_3^-.
The dependence has quadratic and linear part. The slope of the linear part of the dependence defines the diffusion coefficient as:

$$D = \frac{1}{6}\frac{\Delta MSD}{\Delta t} \quad (3)$$

where ΔMSD means change of the mean square displacement during the time interval Δt.
As we can see in Fig. 1, the curve is superposition of a linear part with some noise. The noise results from the chaotic movement of the ions and molecules. It can be reduced by increasing of the particle quantity, but this also increases the computational cost. In order to reduce this noise, the slope was obtained by least-square fitting of the linear part of the curve.
Using the Einstein equation (4) we obtain the mobility of the ion from the diffusion coefficient D:

$$\mu = \frac{Dq}{kT} \quad (4)$$

where q is charge of the ion, k Boltzmann constant and T temperature.

3. Results and Discussion

The results are shown in the Fig. 1. We have used the linear part of the curve from 2ns to 20ns to obtain the slope and to calculate the diffusion coefficient. According to (4) we need the temperature of the gas to calculate the ion mobility. We have used the average temperature of the system on interval from 2ns to 20ns. The average temperature of the system was 300.22 K. The value of the ion mobility was 2.758 ± 0.004 cm2 s-1 V-1. This is the ion mobility at temperature 300.22 K and gas pressure of 1.001 atm. As the mobility depends on the collisions of the ion with the drift gas it depends also on the density of the drift gas. Therefore a correction to the standard conditions (T_0=273 K, p_0=101.3 kPa) is made and resulting value is reported as reduced mobility K_0 given by the formula:

$$K_0 = K\frac{T_0}{T}\frac{p}{p_0} \quad (5)$$

The calculated value of the reduced mobility of the NO_3^- in nitrogen is 2.512 ± 0.004 $cm^2\ s^{-1}\ V^{-1}$.

The most relevant work concerning the ion mobility of NO_3^- in nitrogen drift gas was performed by Viehland et al. [6]. They determined the experimental value of the reduced mobility of 2.33 $cm^2\ s^{-1}\ V^{-1}$. The experiment has been carried out at relatively low pressures (0.12 and 0.2 Torr) and lowest value of the reduced electric field E/N of 5 Td. The reduced ion mobility of NO_3^- has been estimated by extrapolation of the ion mobilities measured under these conditions to the standard conditions. In different experiment Eisele et al. [7] measured the ion mobility of the NO_3^- in nitrogen in the temperature range from 217 to 625 K and and in the gas pressure range from 25 to 40 Torr. The value of the reduced ion mobility was ~2.3 $cm^2\ s^{-1}\ V^{-1}$, which is similar to previous one. Recently Stano et al. [8] measured drift of the negative ions generated in negative corona discharge in nitrogen and detected in the IMS spectrum dominant ion with the ion mobility of 2.21 $cm^2\ s^{-1}\ V^{-1}$, which they assigned to NO_3^-.

The experimental values of the reduced ion mobilities of NO_3^- are considerably lover than our calculated one. The differences may arise from several factors. One of the is the limitation of the present model e.g., short calculation time and/or unbalanced interaction potential between ion and gas. In future we plan to continue our work on the MD modelling in order to get better agreement with experiment. We will focus on improvement of the interaction potential for the system NO_3^- - N_2.

The differences between calculated value and experimental values, but also between the experimental values may arise from the fact that in the experiment, the drift gas always contains trace amounts of H_2O (typically 5 ppm for 5.0 N_2). In such case the clustering reactions:

$$NO_3^-(H_2O)_n + H_2O + N_2 \leftrightarrow NO_3^-(H_2O)_{n+1} + N_2 \quad (6)$$

may play an important role. The peak observed in the IMS spectrum can not be assigned to one ion, but rather to equilibrium mixture of two or more cluster ions, probably NO_3^-, $NO_3^-.(H_2O)$. In our future studies we plan to figure out the exact reason for the differences in the experimental value and present theoretical value.

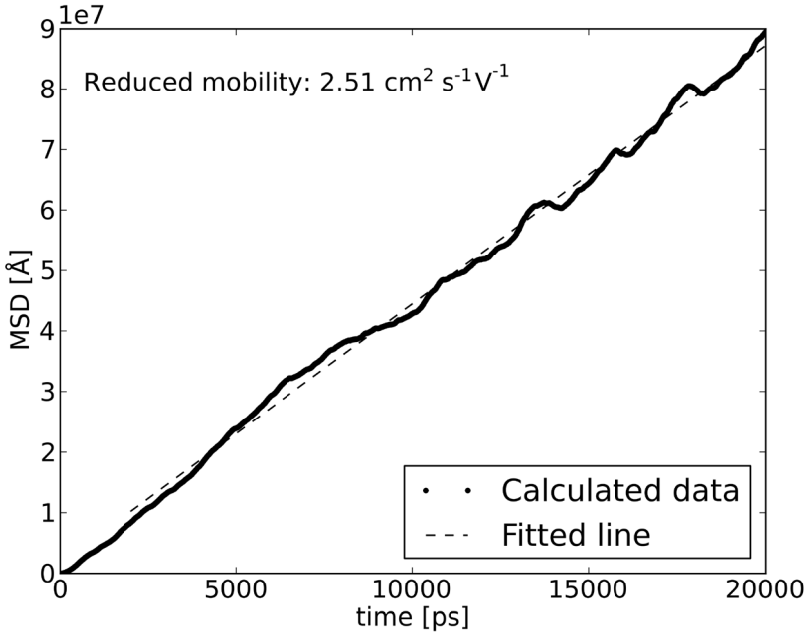


Fig.1: Mean square displacement (MSD) of the NO_3^- anion in N_2 on the time. The calculated mobility was 2.758 ± 0.004 $cm^2\ s^{-1}\ V^{-1}$ at pressure 1.001 atm and temperature 300.22 K. The reduced mobility is 2.512 ± 0.004 $cm^2\ s^{-1}\ V^{-1}$

Acknowledgement. This work has been supported by the Slovak Grant Agency VEGA, project Nr. V-1/0051/08 and by the by the Slovak Research and Development Agency, project Nr. APVV – 0365 – 07.

4. References

[1] K. Nagato, Y. Matsui, T. Miyata, *T. Yamauchi, Int. J. Mass Spectrom.* **248** (2006) 142
[2] www.ccp5.ac.uk/DL_POLY/
[3] A.K. Rappe et al., *J. Am. Chem. Soc.*, **114** (1992) 10024-10035
[4] I.T. Todorov and W. Smith: The DL_ Poly 3 User Manual, STFC Daresbury Laboratory, 2008
[5] P. M. Morse, *Phys. Rev.*, **34** (1929) 57-64
[6] L.A. Viehland, D. E. Fahey, *J. Chem. Phys.* **78** (1983) 435
[7] F.L Eisele, M.D. Perkins, E.W. McDaniel, *J. Chem. Phys.*, **75** (1981) 2473
[8] M. Stano, M. Sabo, M. Kučera Š. Matejčík, H. Y. Han, H. M. Wang, Y. N. Chu , *Acta Phys. Univ. Comeniana*, L-LI (2009-2010) 77

NEGATIVE ION MOBILITY IN O_2/O_3 MIXTURES MEASURED BY VARYING O_3 CONCENTRATION AT ATMOSPHERIC PRESSURE

Yui Okuyama[1], Susumu Suzuki[1], Haruo Itoh[1]

[1]*Chiba Institute of Technology*
E-mail: s0522071ZV@it-chiba.ac.jp

In this paper, we describe the experimental results of negative ion mobility in O_2 containing O_3 at atmospheric pressure. The negative ion mobility was measured using a high-pressure ion drift tube with a Geiger counter that acts as a negative ion detector. It was observed that the mobility decreases from 2.31 $cm^2/V \cdot s$ in pure O_2 to 2.0 $cm^2/V \cdot s$ with an increase in O_3 concentration in O_2/O_3 mixtures under a constant reduced electric field E/p_0 = 0.1 V/cm·Torr. Moreover, a lower mobility of approximately 0.7 $cm^2/V \cdot s$ was observed in an ozone concentration region of more than 1401 ppm (3 g/Nm^3). These results suggest that there are at least two species of negative ions in the O_2/O_3 mixtures.

1. Introduction

Negative ions are particles that constitute a discharge plasma, and many studies on their fundamental properties and wide range of applications have been performed. For example, it has been reported that air pollutants, such as HNO_3 and H_2SO_4, are formed from O_2^-, which acts as nuclei in the atmosphere. Another property of negative ions in air is that they preserve perishable foods. Furthermore, it has been reported that negative ions have some physiological effects on humans and are used in home electric appliances. However, their behaviours are never understood sufficiently in the atmosphere. Mobility is one of the fundamental properties of negative ions under an electric field. The behaviour of negative ions in an ozonization gas including an ozonizer can be understood by investigating their mobility in O_2/O_3 mixtures. Therefore, the negative ion mobility is measured in O_2/O_3 mixtures using a negative ion detector that operates at atmospheric pressure. This negative ion detector is a Geiger counter that consists of a point-plane gap. A stabilized DC voltage V_p is applied to the point electrode P. The region of V_p is considered in the use of the negative ion detector of G_2 for the mobility measurement. Thus, the optimum V_p for the measurement is investigated in O_2/O_3 mixtures, and then the negative ion mobility is measured in the same mixtures by varying the O_3 concentration. As the results, the observed negative ion mobility is 2.31 $cm^2/V \cdot s$ in O_2. In contrast, the observed negative ion mobilities at an O_3 concentration of more than 1401 ppm (3 g/Nm^3) are 2.0 $cm^2/V \cdot s$ and 0.7 $cm^2/V \cdot s$.

2. Experimental method

2.1 Principle of experiment

Figure 1 shows the (a) schematic diagram for the explanation of the principle used in the measurement of negative ion mobility and (b) observed pulse waveform. G_1 is an ion drift space consisting of parallel plane electrodes A and C. Electrode A is an anode and also acts as a cathode of G_2. G_2 is a negative ion detector consisting of a point-plane gap (P - A). A positive voltage V_p is applied to P, and V_p is adjusted to match the voltage range called the Geiger counter region [1]. The center of A is mesh electrode M; thus, pulsed UV light or negative ions can pass through from G_2 to G_1 or from G_1 to G_2, respectively. A constant voltage V is applied to cathode C to form a uniform electric field in G_1. The chamber is filled with high-purity oxygen (99.9999%) to measure the mobility in O_2. Under such a condition, electrodes C and M are irradiated with the pulsed UV light from the outside of the chamber. The pulsed UV light is radiated from a spark gap contracted by a pair of spherical electrodes with a diameter of 10 mm and a gap distance of 1 mm. Then, photoelectrons are released from the surfaces of electrodes C and M. This time is defined as t = 0. The photoelectrons immediately collide with O_2

molecules and form two groups of negative ions of O_2^-. The negative ions belonging to the first group are formed in front of M and begin to drift toward P in G_2. When these negative ions arrive at a certain point near P, electrons detach from them and electron avalanches develop with the collisional ionization of the electrons. Then, the first burst pulse BP_1 is formed and observed as a current pulse on the oscilloscope at time t_1. On the other hand, the negative ions belonging to the second group formed in front of C begin to drift in G_1 and G_2 after passing through M. Then, an electron avalanche develops in G_2 and the second burst pulse BP_2 is formed. It builds up at time t_2. These burst pulses BP_1 and BP_2 (hereafter, denoted as BPs) are observed successively on the oscilloscope with a current detecting resistor r (300 kΩ), as shown in figure 1 (b). Therefore, from the difference in arrival time between the BPs, which is equal to the flight time τ in G_1, the negative ion velocity v and mobility μ^- in G_1 are obtained using Eqs. (1) - (3).

$$\tau = t_2 - t_1 (\mathrm{s}) \quad \cdots\cdots (1)$$

$$v = \frac{d}{\tau} (\mathrm{cm/s}) \quad \cdots\cdots (2)$$

$$\mu^- = \frac{v}{E} = \frac{d^2}{\tau \cdot V} (\mathrm{cm^2/V \cdot s}) \quad \cdots\cdots (3)$$

The reduced ion mobility is defined as the value under the standard conditions of 273 K and 760 Torr, and is given by

$$\mu_0^- = \mu^- \cdot \left(\frac{p}{760} \right) \cdot \frac{273.16}{(273.16 + T)} (\mathrm{cm^2/V \cdot s}) \cdots\cdots (4)$$

d: length of ion drift space (cm),
E: electric field intensity of G_1 (V / cm),
V: voltage across the ion drift space (V),
T: temperature (℃),
p: gas pressure (Torr)

In this manner, the negative ion mobility is determined in pure O_2. The results of this experiment are reported in previous papers [2][3].

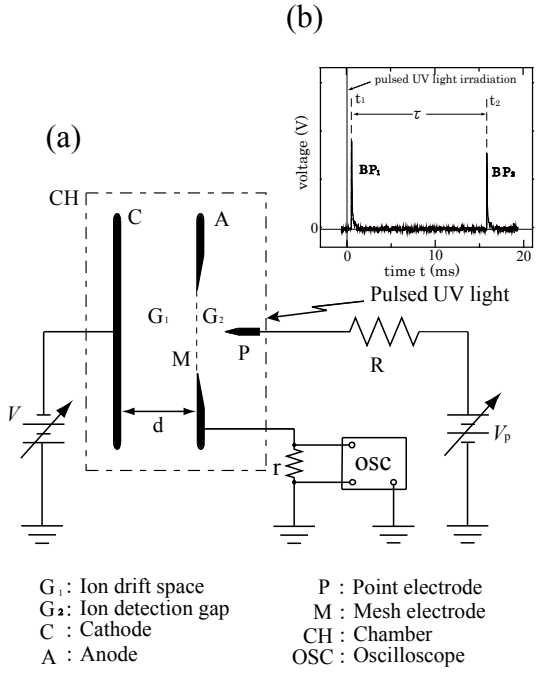


Fig. 1. Schematic diagram of apparatus (a) and observed burst pulse for measurement of negative ion mobility (b).

2.2 Modified method of measuring negative ion mobility in O_2/O_3 mixtures

Figure 2 shows an example of the observed pulse waveforms of BPs at V_p = 4000 V at an O_3 concentration of 4670 ppm (10 g/Nm^3) in pure O_2. In O_2/O_3 mixtures, only a single BP was formed by pulsed UV light irradiation, as shown in figure 2. Therefore, a pair of BPs scarcely appeared, as shown in figure 1 (b). During the experiment, it was observed that the appearance time t_1 of BP_1 formed by negative ions started from M with pulsed UV light irradiation and typically remained the same despite the low appearance probability of BP_1 compared with the case of pure O_2. In contrast, the second group of BPs formed by negative ions

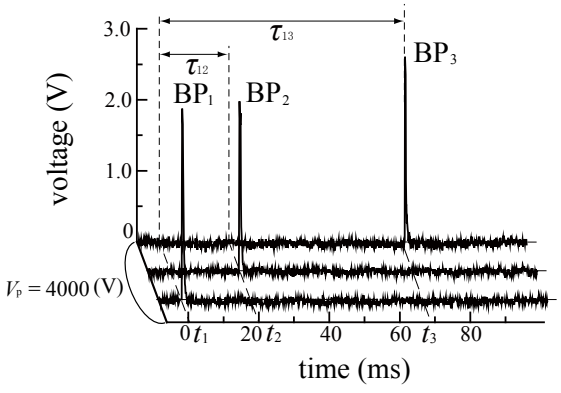


Fig. 2. The pulse wave form of BPs in O_3 concentration of 4670 ppm (10 g/Nm^3) at V_p = 4000 V.

started to appear from C with pulsed UV light irradiation. The appearance times of this group of BPs varied widely. Moreover, these BPs could be separated into the following two groups according to their appearance time: one group appeared at t_2 of approximately 20 ms and the other group appeared at t_3 from 30 ms to 80 ms. Therefore, three groups of BPs appeared in the oscilloscope. Then, we denote the first group of BP and its appearance time as BP_1 and t_1, respectively. Similarly, we denote the second and third groups of BPs, and their appearance times as BP_2 and t_2, and BP_3 and t_3, respectively. Thus, we can estimate the mobility using Eqs. (1) – (4) from the flight time $\tau_{12} = t_2 - t_1$ or $\tau_{13} = t_3 - t_1$. Therefore, we determine the flight times τ_{12} and τ_{13} of the negative ions in G_1 from the observed waveform. Ozone is produced by an ozone generator and is fed to the chamber. The concentration of ozone is observed using a monitor, which is based on the HgI (254 nm) photoabsorption method.

3. Experimental results and discussion

3.1. Pulse waveform

Firstly, the pulse wave form is described because that is an important factor for mobility measurement. Figures 3 and 4 show the variations in the observed pulse waveforms plotted against V_p under a constant reduced electric field of E/p_0 = 0.1 V/cm·Torr at O_3 concentrations of 4670 ppm (10 g/Nm^3) and 14010 ppm (30 g/Nm^3), respectively. In O_2/O_3 mixtures, a new BP appeared at time t_3, which is later than t_2, with low probability.

Each BP is observed at 3750 ≦ V_p ≦ 4000 V in figure 3 and at 4000 ≦ V_p ≦ 4500 V in figure 4. The pulse heights of the burst pulses BP_1, BP_2 and BP_3 increase with V_p. In the same figures, simple pulses without successive pulses are observed and the flight time τ takes a constant value in the same V_p region. The appearance probabilities of the BPs increase against V_p. However, if V_p > 4000 V in figure 3 and V_p > 4500 V in figure 4, successive pulses of BP_2 and BP_3 are observed, and the appearance times t_2 and t_3 of BP_2 and BP_3 become shorter with V_p, as shown in the same figures. Therefore, only the regions of V_p ≦ 4000 V in figure 3 and V_p ≦ 4500 V in figure 4 are acceptable for the mobility measurement at the above-mentioned O_3 concentrations. Therefore, it is thought that these variations in waveforms and appearance times are caused by the distortion of the electric field in front of mesh electrode M [2].

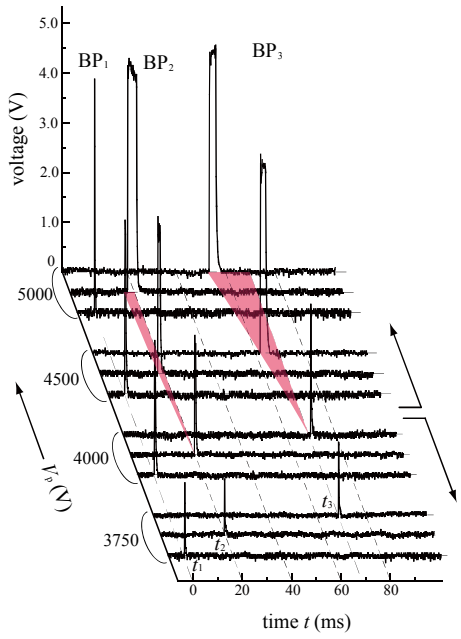


Fig. 3 Observed pulse waveform at E/p_0 = 0.1 V/cm•Torr at O_3 concentration of 4670 ppm (10 g/Nm^3).

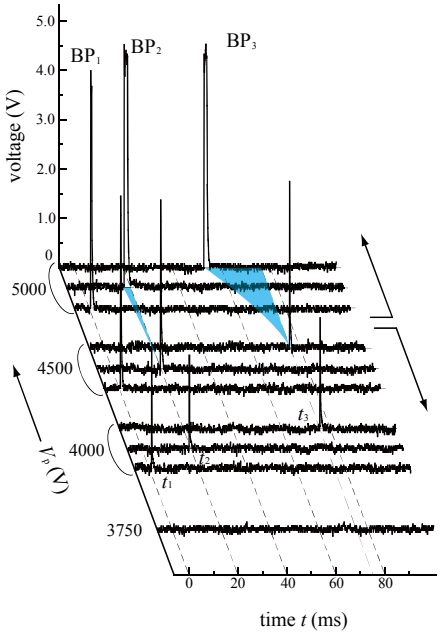


Fig. 4 Observed pulse waveform at E/p_0 = 0.1 V/cm•Torr at O_3 concentration of 14010 ppm (30 g/Nm^3).

3.2 Variations in flight times τ_{12} and τ_{13} with V_p

Figure 5 shows the flight times τ_{12} and τ_{13} of negative ions plotted against V_p at O_3 concentration of 4670 ppm (10 g/Nm^3) and 14010 ppm (30 g/Nm^3). Each plot is shown using the mean value of 30 measurements. The flight times τ are plotted on the vertical axis on a logarithmic scale. The measurement of mobility is carried out under a constant reduced electric field of E/p_0 = 0.1 V/cm·Torr. During this measurement, O_3 concentration gradually decreases with time. Therefore, this measurement is carried out within the period in which O_3 concentration decreases to 90% of the initial O_3 concentration. The period is about 10 min. Thus, it is necessary to end the measurement within 10 min from the start of the experiment. It was found that two mean values of the flight times τ_{12} of around 20 ms and τ_{13} of around 70 ms are observed. The flight time τ_{13} of BP_3 is not observed in pure O_2. In the same figure, two values of the flight times τ_{12} and τ_{13} remain constant in the same V_p region, as observed in figures 3 and 4. In other word, these V_p conditions do not affect the flight times τ for the mobility measurement. Only the regions of $V_p \leqq 4000$ V at an O_3 concentration of 4670 ppm (10 g/Nm^3) and $V_p \leqq 4500$ V at an O_3 concentration of 14010 ppm (30g/Nm^3) are acceptable for the ion mobility measurement. The upper value of V_p is limited by the distortion effect of the electric field caused by the mesh. A more detailed investigation might be conducted.

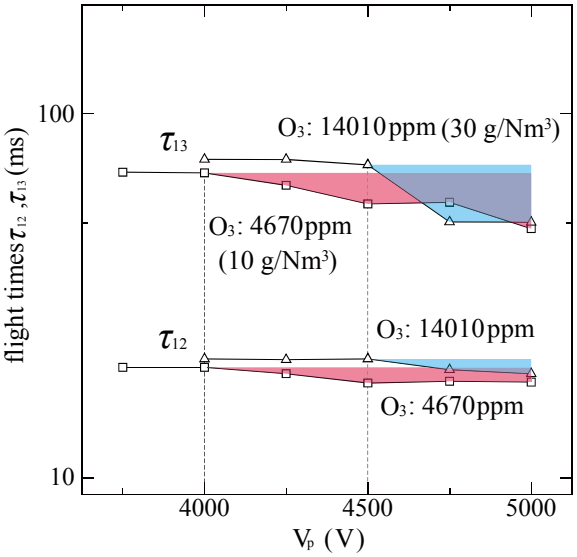


Fig. 5 Variations in flight times τ of negative ions with V_p and upper limit of V_p.

3.3 Determination of flight times τ_{12} and τ_{13} of negative ions

Figure 6 shows an example of the observed appearance times of BPs during the mobility measurement by 1000 pulsed UV light irradiations at an O_3 concentration of 4670 ppm (10 g/Nm^3) at V_p = 4000 V. Plots of open rectangles, triangles and circles show the appearance times t_1, t_2 and t_3, respectively. In the same figure, three couples of BP_1 and BP_2 appear at the times labelled as (b), (d) and (g) in the periods. Another couple of BP_1 and BP_3 appear at times labelled as (a), (c), (e) and (f) in the same period. These appearance probabilities are low compared with the case of pure O_2. The appearance time t_1 of BP_1 takes a constant value of 0.6 ms. Therefore, it is reasonable to use the t_1 of BP_1 as the starting time for all drifting ions from C in G_1. This time can be used to determine the flight times τ_{12} and τ_{13} of negative ions in G_2 at an O_3 concentration of 4670 ppm (10 g/Nm^3).

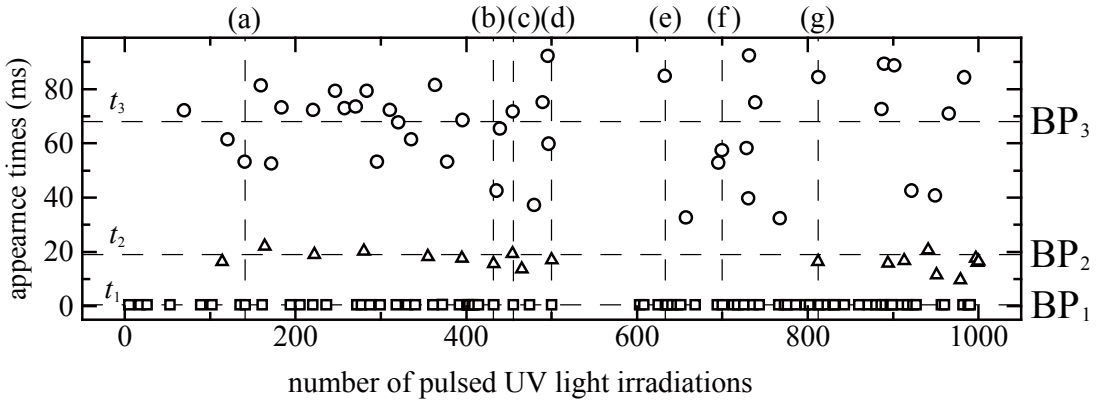


Fig.6. An example of appearance times of BPs at O_3 concentration of 4670 ppm (10 g/Nm^3) at V_p = 4000 V.

3.4 Results of negative ion mobility

Figure 7 shows the observed negative ion mobility in O_2/O_3 mixtures introduced in figure 6. Each plot indicates the mean value of 100 measurements. Figure 8 shows the observed frequency distribution of negative ion mobility obtained using the results shown in Fig. 7. In pure O_2, the observed negative ion mobility is 2.31 $cm^2/V \cdot s$. This value agrees well with that indicated in the previous paper [3]. The two curves varied with O_3 concentration; however, their mean mobilities are measured to be 0.7 and 2.0 $cm^2/V \cdot s$. The mobility decreases from 2.31 $cm^2/V \cdot s$ as a value of O_2^- to 2.0 $cm^2/V \cdot s$ with an increase in ozone concentration. Although the mobility is almost equal to that in pure O_2, we consider the mobility of a particular cluster ion whose nucleus is O_2^- [2] [3]. The decrease in mobility suggests that some cluster ions are formed with an increase in ozone concentration in pure O_2. In contrast, the mobility of 0.7 $cm^2/V \cdot s$ appeared suddenly at an ozone concentration of 1401 ppm (3 g/Nm^3). The appearance of this mobility suggests that the formation of some cluster ions starts when the ozone concentration increases. Matejcik et. al. [4] reported the presence of cluster ions in O_2/O_3 mixtures, such as $O_2^-/(O_2)(O_3)$, $O_4^-/(O_2)(O_3)$, $O_5^-/(O_2)(O_3)$ and $(O_3)^-_m/(O_2)(O_3)$, (where m=1, 2, 3, and 4, respectively). A more precise investigation is now under way to understand the ion transport phenomenon.

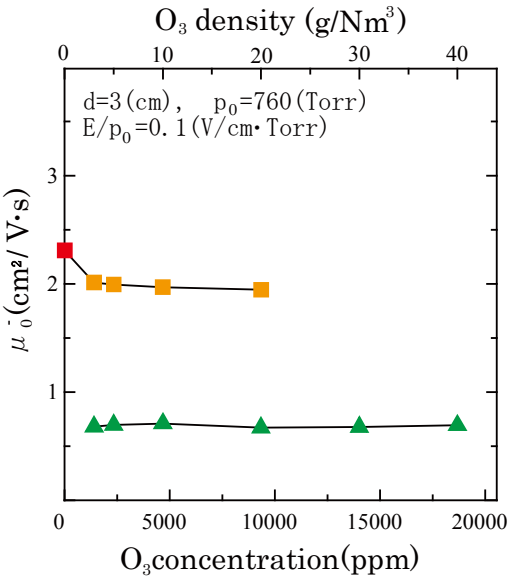


Fig. 7 Measured negative ion mobilities in O_2/O_3 mixtures.

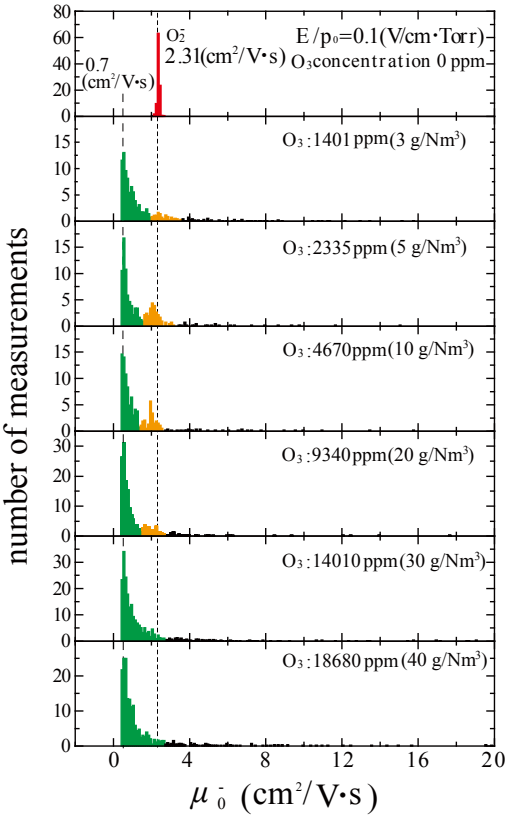


Fig. 8 Observed frequency distribution of negative ion mobility in O_2/O_3 mixtures at E/p_0 = 0.1 V/cm•Torr.

4. Conclusion

Investigations of the optimum values of V_p in an ion detector that determine the sensitivity for the mobility measurement in O_2/O_3 mixtures are carried out as the first step of the study. Subsequently, the measurement of negative ion mobility is carried out by varying the ozone concentration from 0 to 18680 ppm (40 g/Nm^3)in pure O_2 at atmospheric pressure. As the results, the observed mobilities are 0.7 and 2.0 $cm^2/V \cdot s$.

5. References

[1] Y. Gosho and A. Harada, 1983 *J.Phys.D: Appl.Phys*,Vol.16, pp.1159-1166.

[2] Y. Okuyama, S. Suzuki, H. Itoh, 2009 *Proc. K-J Symposium*, Bussan, pp.166-169.

[3] T. Kimura, T. Hayashi, S. Suzuki, and H. Itoh, 2005 *Proc-27th ICPIG*, 02-348.

[4] S.Matejcik, P.Cicman, A.Kiendler, J.D.Skalny, E.Illenberger, A.Stamatovic and T.D.Mark, 1996 *Chem. Phys. Lett.* 261, pp.437-442.

SAW-LIKE ELECTRODES FOR DBD PLASMA ACTUATORS

Artur Berendt[1], Janusz Podliński[1], Jerzy Mizeraczyk[1,2]

[1] *Centre for Plasma and Laser Engineering, The Szewalski Institute of Fluid Flow Machinery, Polish Academy of Sciences, Fiszera 14, 80-952 Gdańsk, Poland*
tel.:+48(58)6995122, fax: +48(58)3416144,
[2] *Department of Marine Electronics, Gdynia Maritime University, Morska 81-87, 81-225 Gdynia, Poland*
E-mail: aberendt@imp.gda.pl

In this paper results of investigations on the saw-like electrode for DBD and comparison of plasma actuators with smooth and saw-like discharge electrodes are presented. Obtained results showed that for the plasma actuator with saw-like electrode the discharge starts at lower voltage, produces more homogenous DBD plasma and generated airflow velocities are higher than for the actuator with smooth electrode.

1. Introduction

Since the middle of the 1990s when 'One Atmosphere Uniform Glow Discharge Plasma' (OAUGDP) was patented by Roth et al [1], interest in plasma-based devices using dielectric barrier discharge (DBD) is growing. OAUGDP is a surface DBD established between electrodes set asymmetrically on top and bottom side of a dielectric material. One of devices using OAUGDP are plasma actuators which are capable to enhance properties of aerodynamic elements modifying airflow around them. Plasma actuators are useful to control laminar–turbulent flow transition, flow separation, reduce drag and improve lift of airfoils [2–5]. Also aeroacustic applications are known [6–8].

In the past ten years lots of plasma actuator configurations were investigated. The greatest research effort was to develop actuators composed of two plane electrodes placed asymmetrically on opposite sides of a dielectric plate. As a dielectric ordinarily glass or ceramics were used and their thickness was around a few millimetres. Electrodes were usually made of copper or aluminium tape mounted on the surface of a dielectric material. One of the electrode was a HV electrode connected to an AC power supply when the second was grounded. When a high voltage was applied DBD established between electrodes and plasma appeared on both sides of the dielectric. In most cases the plasma region expanded to about 15 – 20 mm.

Plasma generated by DBD can produce ionic wind which induces airflow with velocities up to several m/s [9–12] tangential to the surface of the dielectric plate. Often to avoid plasma on one side of the dielectric plate the grounded electrode is insulated.

Actuator properties like size of the plasma region or generated airflow velocity strongly depend on e.g. distance between electrodes, dielectric material properties or applied voltage. Thus many actuator configurations and voltage characteristics were investigated to optimise DBD actuators operation. Usually sine waveform voltage of a magnitude between several kV to tens of kV and frequency ranged from hundreds of Hz to tens of kHz is used. Smooth electrodes with typical distance from 0 to 30 mm are used.

In this paper we propose to modify the shape of electrodes to enhance the DBD. We propose to test the usefulness of a saw-like electrode for generating DBD that is to be used for flow control. To our knowledge, saw-like electrode has not been used for DBD generation, although various kinds of saw- or spike-like electrodes have been used to produce corona discharges. We present results of the investigations on the saw-like electrode and comparison of plasma actuator operation with smooth and saw-like discharge electrodes.

2. Experimental set-up

The apparatus used in this experiment for measurements of the airflow generated by DBD plasma actuators consists of a function voltage generator and a high voltage power amplifier, forming an AC

power supply, an oscilloscope and a standard PIV equipment for the measurement of velocity fields (Fig. 1).
DBD plasma actuators used in our investigations consisted of two electrodes mounted on both sides of a 2 mm thick glass plate. The electrodes were made from a 50 μm thick copper tape. Electrodes were connected to the AC power supply. The HV electrode, on the upper side of the actuator was exposed to ambient air when the grounded electrode was insulated to eliminate discharge on the bottom side of the actuator. Two types of DBD plasma actuators were studied: first, in which the electrode gap was 20 mm and the grounded electrode was 10 mm wide; and second, in which the electrode gap was 0 mm and the grounded electrode was 25 mm wide. Both types of actuators were made in two variants, with a smooth HV electrode and with a saw-like HV electrode (Fig. 2). The width of the HV electrodes was always 6 mm.

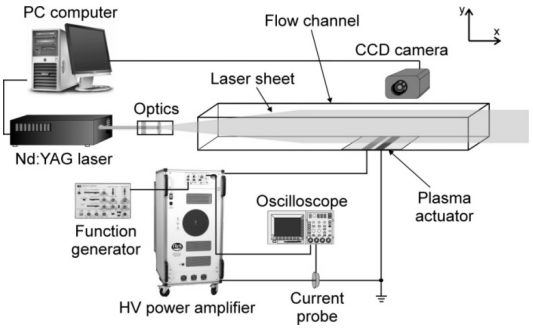


Fig. 1. Experimental set-up.

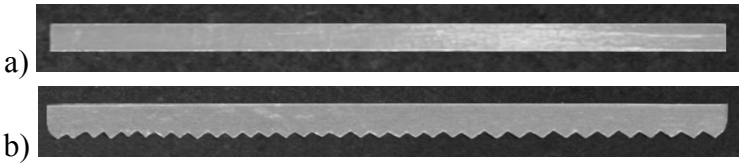


Fig. 2. Images of a smooth (a) and saw-like (b) HV electrode made of copper tape.

The experiments were carried out in ambient air at atmospheric pressure in an end-opened flow channel. Air humidity was 36% and temperature was 20°C. There was no external flow forced in the flow channel. Sinusoidal high voltage (frequency 1.5 kHz) applied to the actuators was generated by the power amplifier (TREK, model 40/15) which amplified signal from the function generator METEX MS9150. Discharge current was measured by a Pearson current monitor (Rogowski coil). Voltage and current signals were controlled by the oscilloscope Tektronix TDS 3052B. The example waveform of the applied voltage and the discharge current are presented in Fig. 3.
PIV measurements were carried out in a plane defined by the laser sheet which was placed perpendicularly to the actuator electrodes at their half-length (Fig. 1). 100 PIV instantaneous measurements were carried out and then averaged, which means that the time-averaged flow velocity fields were obtained. Using the averaged flow velocity fields, the flow velocity profiles were determined.

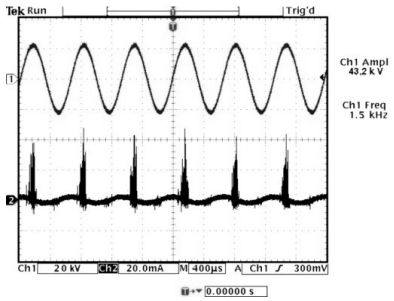


Fig. 3. Example of voltage (1) and current (2) waveforms.

3. Results

The cross-section schematic view of the first type plasma actuator with electrode gap 20 mm is shown in Fig. 4. Both AC HV electrodes, smooth or saw-like, were used. For this type of plasma actuator the flow velocity profiles were determined in the cross-section placed 25 mm from the HV electrode, i.e. from the active blade of the smooth electrode, or from the saw-tooth tips of the saw-like electrode. The position at which the flow velocity profiles were determined is marked by a broken line in Fig. 4.

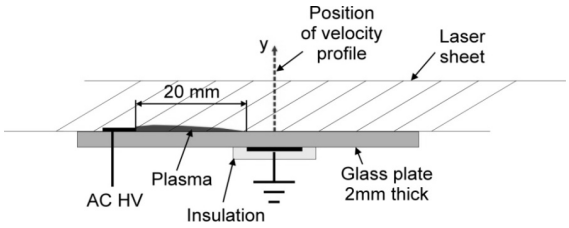


Fig. 4. Schematic view of the plasma actuator with electrode gap 20 mm.

Fig. 5 shows flow velocity profiles obtained for the first type plasma actuator with smooth and saw-like discharge electrodes for five different applied voltages. As can be seen, the velocities of the flow generated by the actuator with saw-like electrode are higher than for the actuator with smooth electrode. The most distinct difference in flow velocities is for the lower voltages. For voltages of 40 kV_{p-p} and 44 kV_{p-p} (pik-to-pik voltage) the maximum flow velocities obtained for the actuator with smooth electrode were 1.3 m/s and 1.8 m/s, while for the actuator with saw-like electrode were 2.2 m/s and 2.7 m/s, respectively.

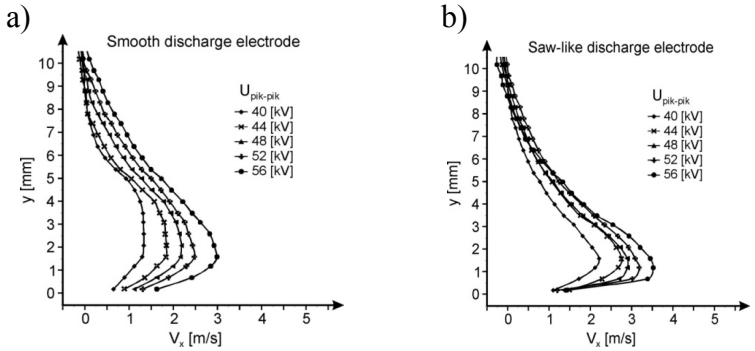


Fig. 5. Flow velocity profiles measured for the plasma actuators with electrode gap 20 mm and with smooth (a) and saw-like (b) discharge electrode.

We observed that for the plasma actuator with saw-like electrode the discharge started at lower voltage than for the plasma actuator with smooth electrode. At the same applied voltage, the discharge current was higher for saw-like electrode case. The lighting of the plasma along the smooth electrode was clearly non-uniform. The discharge spots occurred irregularly. For the plasma actuator with saw-like electrode the discharge spots occurred on every saw-tooth, i.e. much more regularly than for the smooth discharge electrode. This phenomenon can be clearly observed in Fig. 6 which shows images of the discharge obtained for the plasma actuators with 300 mm long smooth (Fig. 6a) and saw-like (Fig. 6b) discharge electrode.

The cross-section schematic view of the second type plasma actuator without electrode gap is shown in Fig. 7. As before, smooth and saw-like AC HV electrode was studied. For this type of plasma actuator the flow velocity profiles were determined in the cross-section placed 12 mm from the HV electrode (Fig. 7).

a)

b)

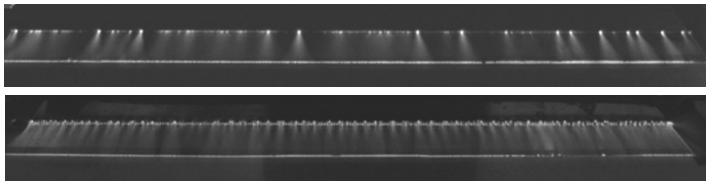


Fig. 6. Images of the discharge obtained for the plasma actuator with smooth (a) and saw-like (b) discharge electrode. The electrode gap 20 mm, the applied voltage was 52 kV_{p-p}, and the discharge current was 90 mA for smooth (a) and 150 mA for saw-like (b) discharge electrode. The camera exposure time was 2.5 sec.

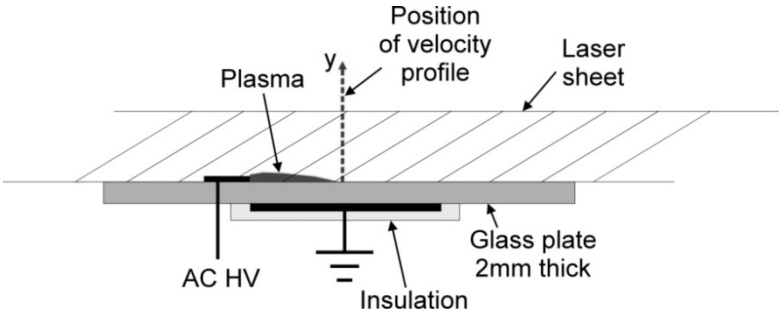


Fig. 7. Schematic view of the plasma actuator without electrode gap.

Fig. 8 shows flow velocity profiles obtained for the second type plasma actuator with smooth and saw-like discharge electrode for five different voltages applied. Similarly to the first type actuator, the flow velocities generated by the actuator with saw-like electrode are higher than for the actuator with smooth electrode. The most noticeable difference in the flow velocities is again for lower voltages, i.e. for 16 kV_{p-p} and 20 kV_{p-p}. At these voltages, the maximum flow velocities obtained for the actuator with smooth electrode were 1.5 m/s and 2.25 m/s, while for the actuator with saw-like electrode were 2.4 m/s and 3.25 m/s, respectively.

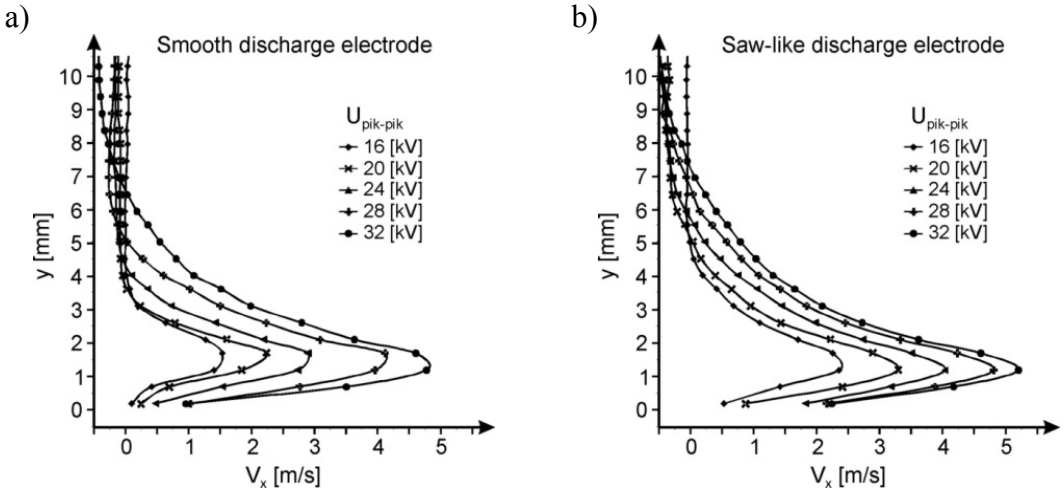


Fig. 8. Flow velocity profiles measured for the plasma actuators without electrode gap and with smooth (a) and saw-like (b) discharge electrode.

4. Summary and conclusions

The two types of the DBD plasma actuators were presented. The first type with electrode gap 20 mm and the second type without electrode gap. The influence of the HV electrode shape on the airflow generated by the DBD plasma actuator was investigated for several applied voltages using PIV method.

The obtained results clearly show that for all applied voltages the airflow velocities were higher for the actuator with saw-like HV electrode, especially when relatively low voltages were applied.
It was observed that for the plasma actuator with saw-like electrode the discharge starts at lower voltage and produces more homogenous DBD plasma than the actuator with smooth electrode. At the same voltages, the discharge current is higher in the saw-like electrode case. These could be reasons of higher flow velocities generated by the actuators with saw-like electrode.
More investigations are still required for better understanding the influence of the saw-like electrode on the generated DBD and induced airflow. Also the saw-like electrode optimisation should be done.

Acknowledgment. The research leading to these results has received funding from the European Community, Seventh Framework Programme FP7/2007-2013 under grant agreement no.: 234201 (PLASMAERO – Useful PLASMas for AERODynamic control www.plasmaero.eu).

5. References

[1] J. R. Roth, P. P. Tsai, C. Liu, M. Laroussi, P. D. Spence, One Atmosphere Uniform Glow Discharge Plasma, United States Patent 5414324, 1995.
[2] E. Moreau, Airflow Control by Non-thermal Plasma Actuators, Journal of Physics D: Applied Physics, 40, 605-636, 2007.
[3] S. Grundmann, Transition Control using Dielectric Barrier Discharge Plasma Actuators, Shaker Verlag, Aachen, ISBN 978-3-8322-7587-7, 2008.
[4] S. Grundmann, C. Tropea, Delay of Boundary-Layer Transition Using Plasma Actuators, 46th AIAA Aerospace Sciences Meeting and Exhibit, Reno, Nevada 7 - 10 January, 1369, 2008.
[5] T. C. Corke, M. L. Post, D. M. Orlov, Single Dielectric Barrier Discharge Plasma Enhanced Aerodynamics: Physics, Modeling and Applications, Exp Fluids 46:1–26, 2009.
[6] X. Huang, S. Chan and X. Zhang, Atmospheric Plasma Actuators for Aeroacoustic Applications, IEEE Transaction of Plasma Science, 35, 3, 693-695, 2007.
[7] X. Huang, S. Chan and X. Zhang, Variable Structure Model for Flow-induced Tonal Noise Control with Plasma Actuators, AIAA Journal, 46, 1, 241-250, 2008.
[8] X. Huang and X. Zhang, Streamwise and Spanwise Plasma Actuators for Flow-Induced Cavity Noise Control, Physics of Fluids, published online 12 March 2008.
[9] N. Takeuchi, K. Yasuoka, S. Ishii, Inducing Mechanism of Electrohydrodynamic Flow by Surface Barrier Discharge, IEEE Trans. Plasma Sci., 35, 6, 1704-1709, 2007.
[10] N. Balcon, N. Benard, E. Moreau, Formation Process of the Electric Wind Produced by a Plasma Actuator, IEEE Transactions on Dielectric and Electrical Insulation, Vol. 16, No 2, pp. 463-469, 2009.
[11] N. Benard, N. Balcon and E. Moreau, Electric Wind Produced by a Surface Dielectric Barrier Discharge Operating in Air at Different Pressures – Aeronautical control insights, Journal of Physics D: Applied Physics, 41, 4, #042002, 2008.
[12] J. P. Boeuf, Y. Lagmich, Th. Unfer, Th. Callegari, L. C. Pitchford, Electrohydrodynamic Force in Dielectric Barrier Discharge Plasma Actuators, Journal of Physics D: Applied Physics, 40, 652, 2007.

IMS/MS AND APCDIMS STUDY OF NEGATIVE CORONA DISCHARGE IN HIGH PURITY O_2

Martin Sabo[1], Ján Paleník[1], Štefan Matejčík[1]
[1]*Department of Experimental Physics, Comenius University, Mlynska dolina F2, 84248 Bratislava Slovak Republic*
E-mail: matejcik@fmph.uniba.sk

Negative ions formed in negative corona discharge in high purity O2 have been studied using the Drift Atmospheric Pressure Corona Discharge Ionisation Mass spectrometry (APCDI/MS) and Ion Mobility Spectrometry/Mass Spectrometry techniques (IMS/MS). The negative ions formed in the negative corona discharge in high purity O2 have been detected and identified using APCDI/MS technique. The ion mobilities of the negative ions were determined from mass selected IMS spectra. In negative corona discharge in pure O2 the spectra have been dominated by negative ion with reduced ion mobility of 2.52±0.05 cm2V−1s−1 and m/z=60 assigned N2O2-. The presence of this ion in IMS and MS spectra is attributed to N2O which is efficiently formed in the negative corona discharge in the reaction of O2 with N2 present in trace amounts (~0.5ppm).

1. Introduction

Formation of negative ions in the negative corona discharge (CD) in air has been studied using mass spectrometry by several authors [1, 2, 3]. The pioneering work of Shahin conducted over a wide-pressure range (up to 100 kPa) found NO_2^- and NO_3^- ions were dominant in negative corona discharge fed by dry air at low pressures [1]. These results were subsequently contradicted by of Gardiner and Craggs [2] who at 1 kPa observed predominately CO_3^- ions, whose abundance was more than double that of O_3^-, O^- and CO_4^-. Only traces of O_2^- ions were detected. Skalny et al. [3] studied the negative ion formation in a negative CD using both dry and 'wet' air at pressures between 5 and 27 kPa. In dry air the dominant ion observed was CO_3^-. In the presence of water this ion was converted to cluster ions containing one or more water molecules. Nagato at al. [4] studied ions formed in negative corona in air at ambient pressure at different reaction times (1 ms and 10 ms). They observed that after 10 ms the number of the ions was significantly reduced and the only ions significant intensity appears at masses 62, 124 and 125 amu. They attributed these masses to NO_3^-, HCO_3^- .HNO_3 and NO_3^-.HNO_3 ions. When the humidity of air was limited to 25 ppm of H_2O the only ion observed was the NO_3^-.

Gravendeel and Hogg [5] studied mass spectrometrically negative corona in N_2/O_2 mixture with ratio 5 to 1. Although they used high purity gases with less than 5 ppm H_2O and 0.1 ppm CO_2 they observed numerous negative ions with O_3^-, OH^-, NO_3^- and CO_3^- being the most intense ones. In this case, however, the time between formation of ions and their entrance to vacuum was short (in order of 10 μs) and thus the primary ions formed directly in discharge were detected.

Hill et al. [6] measured IMS/MS spectra of pulsed corona discharge in positive and negative polarities in air containing water. In negative polarity they detected large variety of negative ions dominated by mass 60 (N_2O_2-, or CO_3^-) and its water cluster, HCO_3^-, NO_2^-, NO_3^- and large amount mixed cluster ions.

Recently Ewing et al. [7] performed IMS/MS study of mechanism of negative reactant ion formation in atmospheric pressure corona discharge in air. They used conventional radioactive ^{63}Ni source of ions. The ^{63}Ni ion source in air generated O_2^- as major negative ion in air. After introduction of the admixture of gas generated in the corona discharge in air into IMS they detected NO_3^- as a major negative ion, followed by CO_3^- and NO_2^- and O_2^- ion disappeared. They attributed this behaviour to the presence of NO_2 in the gas generated by corona discharge.

2. Experiment

The IMS/MS (Figure 1a) and APCDI/MS (Figure 1b) instruments equipped with point to plane CD ion source were described in our previous work [8]. In attempt to reduce the penetration of the neutrals and radicals formed in the CD into the drift region we used single flow IMS system with gas outlet behind the corona discharge. Two positive power supplies (Heinzinger) were used one for CD and one for the drift field. The drift field in IMS was 351,8 V/cm while in APCDI/MS was in range 6000-250V/cm with corresponding drift time of ions from 0.1 to 2ms approximately. The corona current in IMS was varied from 3 to 10μA (limited by HV power supply) while in APCDI/MS was at the constant value 10μA. The 6.0 oxygen (Linde) was purified (MICROTORR, MC190-203FV) to reduce the concentration of H_2O, CO, CO_2, H_2 impurities under 100ppt and NH_3 and amines under 10ppt. The drift tubes of IMS/MS and APCDI/MS instruments were fed by high purity O_2 with flow rate 900ml/min.

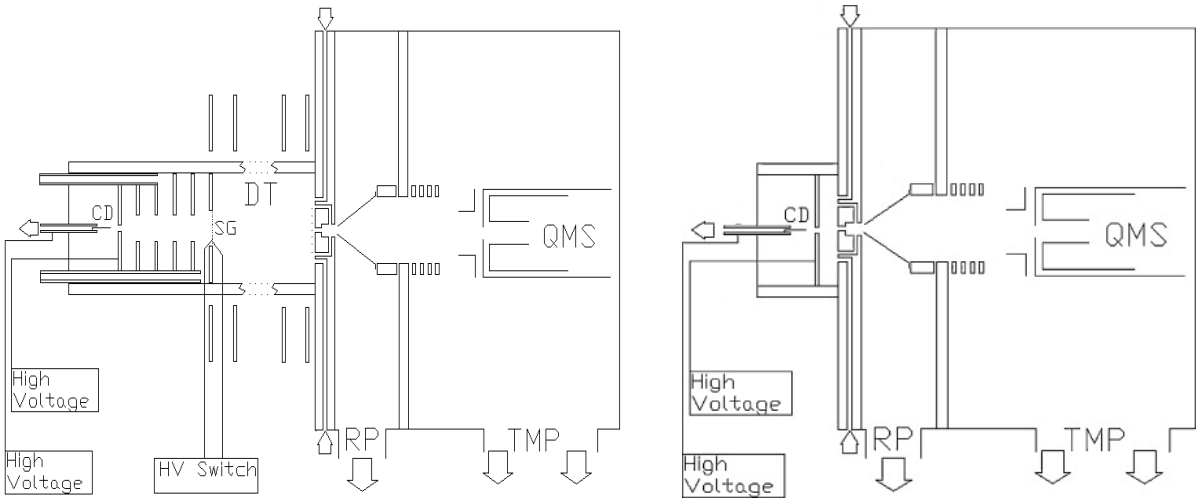


Fig. 1. IMS/MS (a) and APCDI/MS (b) instruments

3. Results and discussion

The IMS spectrum of negative ions formed in the negative corona discharge in pure O_2 is presented in the Figure 2. The spectrum shows main peak at 11.95 ms drift time, which corresponds to the reduced mobility of 2.52(±0.05) $cm^2V^{-1}s^{-1}$. The present experiment shows, that the corresponding IMS/MS mass spectrum (Figure 4, the total drift times of the ions were ~20 ms) is dominated by an ion with m/z=60 and that the O_3^- (m/z=48) has only very weak intensity close to the detection limit. We assign the ion with m/z=60 to $N_2O_2^-$. The m/z=60 has also important atmospheric ion CO_3^- which has also very similar value of reduced ion mobility (2.5 ±0.07 [9] and 2.51±0.07 [10]). So it is difficult to distinguish between these two ions by MS and also IMS. he argument against CO_3^- is the low initial CO_2 concentration in the O_2 in present experiment (according to the data of the getter trap manufacturer, the CO_2 density should be below 100 ppt). We have performed kinetic simulations that show, that at this low value of CO_2 concentration, the CO_3^- can not dominate the mass spectrum.

In previous mass spectrometric studies [5] it was reported that dominant ion in negative corona in O_2 is the O_3^-. The O_3^- ions are effectively formed by several reaction channels. The negative corona discharge in O_2 is source of neutral molecules and radicals one of the most important is the O_3 [11]. Additionally, to the neutral products, primary negative ions O^- and O_2^- are formed in the corona discharge via electron attachment reactions to the O_2 [12]:

$$e + O_2 \rightarrow O^- + O \; k = f(E/N) \qquad (1)$$

$$e + O_2 + M \rightarrow O_2^- + M \; k = 3.4 \times 10^{-30} \; cm^6 s^{-1} \qquad (2)$$

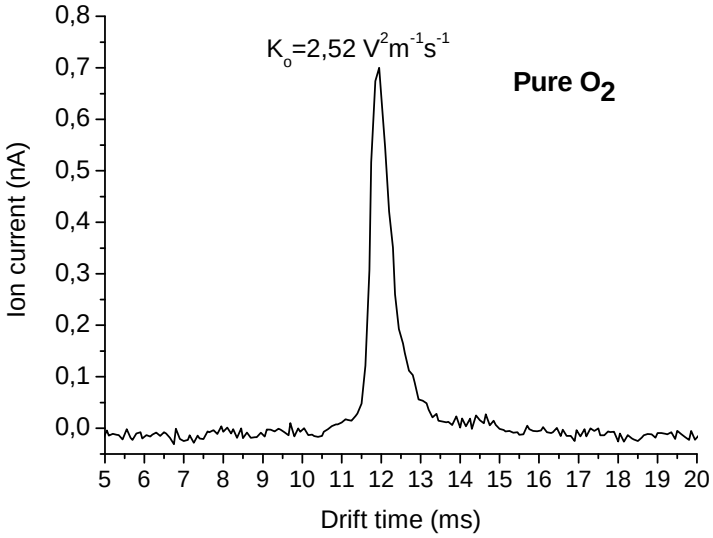


Fig. 3. IMS spectrum of negative CD in pure O_2 in O_2drift gas, the reduced ion mobility of the ions is indicated.

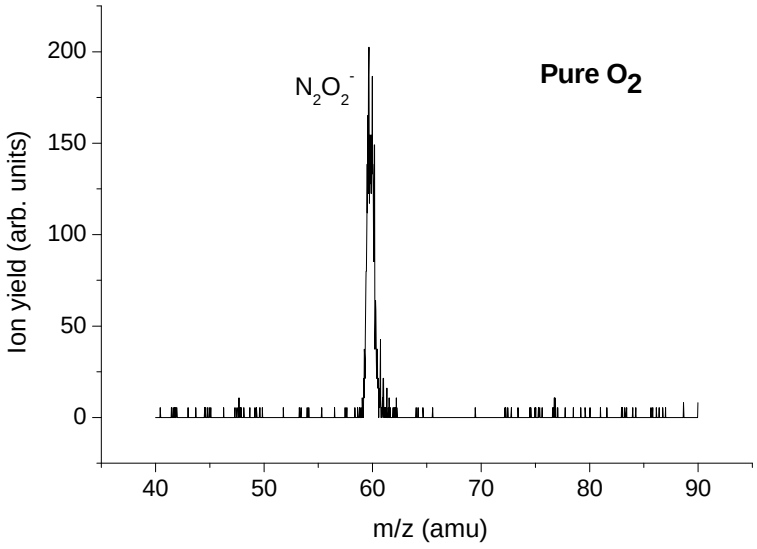


Fig. 4. Mass spectrum of the negative CD in O_2 after drift of the ions in the drift tube filled with O_2.

These primary ions may further undergo binary reactions with O_3 forming O_3^- ions [12]:

$O^- + O_3 \rightarrow O_3^- + O \quad k = 5.3 \times 10^{-10}\ cm^3 s^{-1}$ (3)

$O_2^- + O_3 \rightarrow O_3^- + O_2 \quad k = 4 \times 10^{-10}\ cm^3 s^{-1}$ (4)

As the electron affinity of O_3 (2.10 eV) exceeds those of O (1.46 eV) and O2 (0.45 eV) both reactions are exothermic. Formation of the O_3^- is possible also via three body reactions [12]:

$e + O_3 + M \rightarrow O_3^- + M \quad k = 4.6 \times 10^{-28}\ cm^6 s^{-1}$ (5)

which represent the electron attachment reaction. O_3^- may be formed also via ion-molecule reactions [12]:

$$O^- + O_2 + M \rightarrow O_3^- + M \quad k = 3.3 \times 10^{-31}\ cm^6 s^{-1} \qquad (6)$$

The simulation of the negative corona discharge in pure oxygen in wire to cylinder geometry shows that at large distances from the wire, O_3^- is the dominant ion [13]. Analogical situation should exist also in point to plane geometry as it is in present experiment.
This model is confirmed also by present APCD/MS results. In the Figure 5 we see the APCDI/MS mass spectra for two different drift potentials U_d, between the plane electrode of the corona discharge and the ions collector with pinhole. High value of U_d=4kV (reduced electric field of 28 Tausend) correspond to short drift time (100μs) of the ions in the drift region. In this case we see that the mass spectrum is dominated by O_3^- (m/z=48) and also relatively strong signals for O^- (m/z=16) and $O_3^-.(H_2O)$ (m/z=66) were detected. The O_2^- is also present, however, very weak and the m/z=60 is the second strongest peak in the mass spectrum. In the case of U_d=200V and thus much longer drift time (1 ms), we see that the mass spectrum is already dominated by ion m/z=60.
The nature of the ion with m/z=60 we associate with the most abundant admixture in oxygen, N_2. In the case of N_2 presence in oxygen, the N_2O is efficiently formed [14]. The m/z=60 amu could correspond to stable negative ion $N_2O_2^-$ [15]. The electron affinity of this ion has high value of 3.351±0.010 eV [16]. This ion could be formed by ion molecule reaction of O^- with N_2O:

$$O^- + N_2O \rightarrow (N_2O_2^-)\# \rightarrow NO^- + NO \qquad (7)$$

However, we believe that at high pressure the molecular ion complex could be stabilised by collision with a molecules:

$$O^- + N_2O \rightarrow (N_2O_2^-)\# + M \rightarrow N_2O_2^- + M \qquad (8)$$

Additionally we suggest that following reaction could play an important role:

$$O_3^- + N_2O + M \rightarrow N_2O_2^- + O_2 + M \qquad (9)$$

The reaction *(9)* is confirmed by the APIMS data, where the fast disappearance of the O_3^- from the mass spectra supports introduction of this reaction into the kinetic scheme.

4. Conclusions

Present experiments showed that negative CD in point to plane geometry in high purity O_2 the primary ions are efficiently converted into negative ions with m/z=60 and reduced ion mobility of 2.52(±0.05) $cm^2V^{-1}s^{-1}$. This ion has been assigned to $N_2O_2^-$, formed in reaction of O_3^- ions with N_2O. N_2O is efficiently formed in negative CD in O_2 from the main impurity N_2.

Acknowledgements. This work was supported by the Slovak research and development agency projects LPP-06-0146, SK-CN-0015-09 and the VEGA grant No. 1/0051/08.

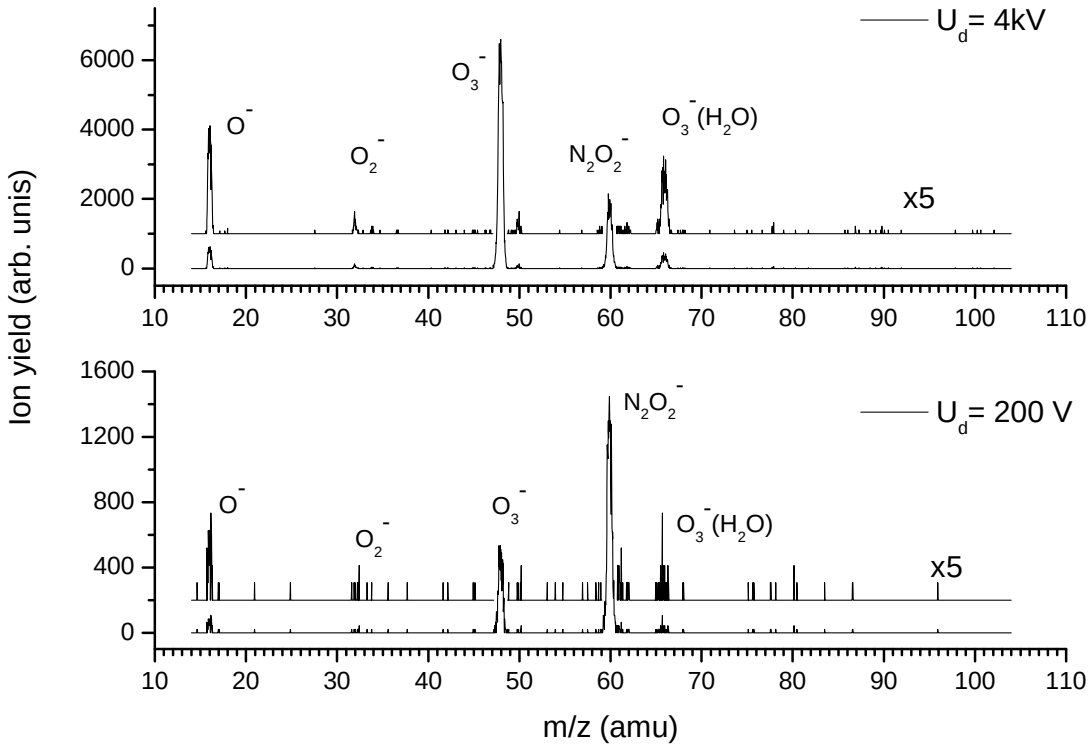


Fig.2. APCDI/MS mass spectra of negative CD in pure O_2 at two different drift fields, corresponding to different potentials U_d.

5. References

[1] Shahin M.M. 1966 *Appl. Opt., Supplement on Electrophotography* **3** 106
[2] Gardiner P.S.,Cragss J. D. 1977 *J. Phys. D: Appl. Phys.* **10** 1003
[3] Skalny J.D:, Mikoviny T., Matejcik S., Mason N.J. 2004 *Int. J. Mass Spectrom.* **233** 317
[4] Nagato K., Matsui Y., Miyata T., Yamauchi T. 2006 *Int. J. Mass Spectrom.* **248** 142
[5] Gravendeel B., Hoog F.J. 1987 *J. Phys. B: At. Mol. Phys.* **20** 6337
[6] Hill C.A. and Thomas C.L.P. 2003 *Analyst* **128** 55
[7] Ewing R.G., Waltman M. J. 2009 *Int. J. Ion Mobil. Spec.* **12** 65
[8] Sabo M., Páleník J., Kučera M., Han H., Wang H., Chu Y., Matejčík Š. 2010 *Int. J. Mass Spectrom.* **293** 23
[9] Snuggs R. M. ,Volz D. J., Schummers J.H., Martin D. W., McDaniel E.W., 1971 *Phys. Rev. A* **3** 477.
[10] Perkins M. D., Eisele F.L., McDaniel E.W. 1981 *J. Chem. Phys.* **74** 4206
[11] Skalny J.D., Mikoviny T., Mason N.J. and Sobek V. 2001 *Ozone Sci. Eng.* **23** 29
[12] Elliason B. 1985 *Electrical Discharge in Oxygen. Part 1. Basic Data*, Rate Coefficients and Cross Sections, Report KLR 83/40 C, Brown Boveri Forschungszentrum, Baden-Dättwil
[13] Soria C., Pontiga F. and Castellanos A. 2004 *Plasma Sources Sci. Technol.* **13** 95
[14] Pontiga F., Fernández-Rueda A., Moreno H., Castellanos A. 2008 *Proceeding of the 18 th ESCAMPIG conference*, Grenada, Spain, Topic Number: 6,10
[15] Arnold D. W., Neumark D. M. 1995 *J. Chem. Phys.* **102** 7035
[16] NIST Chemistry WebBook, NIST Standard Reference Database Number **69**

SPATIO-TEMPORAL AND GLOBAL SURFACE CHARGE MEASUREMENT IN A PATTERNED DBD

L. Stollenwerk[1], U. Stroth[2]

[1]*EMAU, Institut für Physik, Felix-Hausdorff-Str. 6, 17489 Greifswald, Germany*
[2]*IPF, Pfaffenwaldring 31, 70569 Stuttgart, Germany*
E-mail: Stollenwerk@physik.uni-greifswald.de

In this work a planar dielectric barrier discharge system is investigated. The discharge cell is characterised by a very short discharge gap of less than 1 mm in length and a wide lateral extension with a diameter of 40 mm. At a gas pressure of about 100 hPa helium a sinusoidal driving voltage in the range of a few hundred volts is used. A special feature of this set-up is the use of an electro-optic crystal as the single dielectric barrier. This crystal allows for an optical in-situ measurement of the surface charges in the running discharge. Both global and spatio-temporal surface-charge measurements are presented. In the global measurement it is found that the amount of surface charge after the positive and the negative half-cycle is not equal, i.e. a bias charge emerges. In the spatio-temporal surface-charge measurement an inner structure of the current filaments can be revealed. Beside a pure image of the breakdown as it is seen in the emitted luminescence distribution, the surface charge measurement shows different radial shapes for the filaments in the positive and the negative charge distribution.

1. Experimental set-up and type of discharge

The assembly of the discharge cell is sketched in figure 1. On the very right there is the grounded metal electrode. It is covered with a BSO-crystal acting as the dielectric layer. A spacer consisting of an insulating material encloses the BSO-crystal. As the spacer is thicker than the crystal, a discharge volume emerges. The counter electrode is formed by glass plate coated with ITO (Indium Tin Oxide) that is electrically conductive and at the same time transparent. Thus, the discharge can be observed through the electrode in current direction. The discharge cell is driven with a sinusoidal driving voltage.

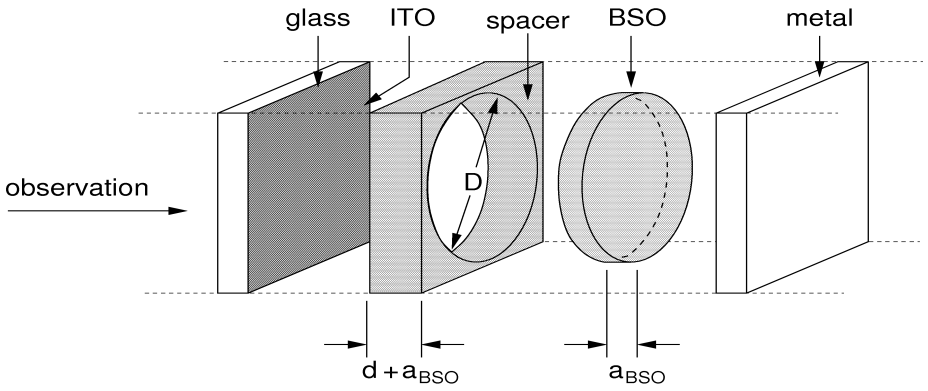


Fig. 1. Discharge cell. Typical parameters: a_{BSO} = 0.7 mm, d = 0.8 mm, D = 40 mm, p = 100 – 300 hPa helium, U = 300 – 1000 V sin, f = 70 – 300 kHz.

The typical current-voltage behaviour of the discharge is shown in figure 2(a). The graph shows both the sinusoidal supply voltage (solid) and the real current (dashed) through the discharge that is separated from the capacitive displacement current by a Wheatstone bridge. There is exactly one current peak per half-cycle of the driving voltage; hence, the discharge is a glow like discharge. However, in contrast to common glow-like dielectric barrier discharges, the discharge is not laterally homogeneous but filamentary. Typical patterns are exemplary shown in figures 2(b) and (c) and comprise hexagonal, dense filament arrangements as well as loose filament arrangements. All these

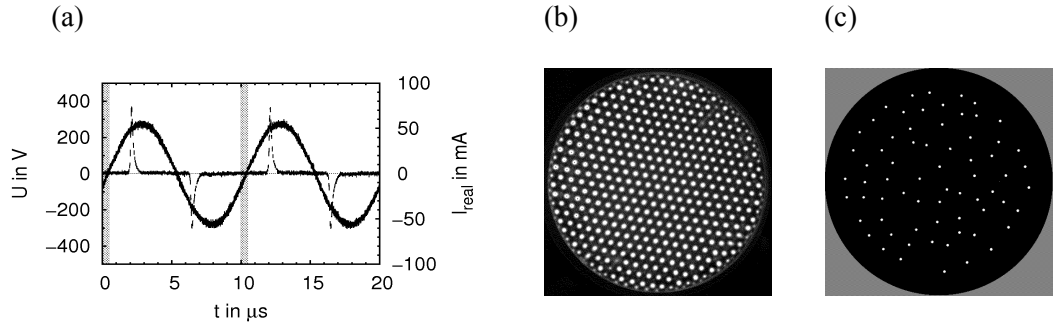


Fig. 2. (a) Supply voltage (solid) and typical real current (dashed) through the discharge. The grey bars depict the time for the surface charge measurement after the negative half-cycle. (b) Hexagonal arrangement of filaments. (c) Typical irregular arrangement of filaments.

patterns are subject to a certain degree of motion. For certain cases the mechanism of motion has been investigated in [1,2].

The principle of charge measurement is sketched in figure 3. On the right hand side the discharge cell is shown. The metal electrode acts as an optical mirror. The discharge cell is illuminated with effectively circular polarised light from an LED (light emitting diode). The incident light passes the transparent electrode and the BSO-crystal. It becomes reflected at the mirror (i. e. the metal electrode) and passes the BSO-crystal and the transparent electrode again. As the BSO-crystal becomes birefringent in presence of an electric field, the reflected light from the discharge cell is elliptically polarised, locally depending on the voltage over the BSO-crystal. The reflected light is coupled out via a beam splitter and is observed through a linear polariser. In this way the lateral voltage drop distribution over the BSO-crystal becomes transferred to the brightness of the camera image.
To assure that the voltage drop across the BSO-crystal originates from the deposited surface charges alone, the measurement has to take place at times where the applied voltage vanishes, i. e., in the zeros of the driving voltage. This condition is realised by illuminating the BSO-crystal only during the zero of the driving voltage after the breakdown of interest. An example of the LED timing for charge measurement after the negative half-cycle is given in figure 2(a).

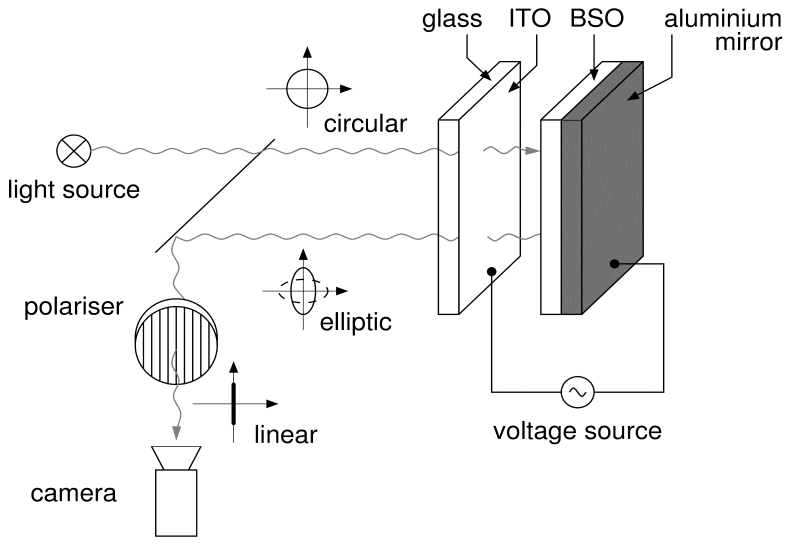


Fig. 3. Sketch of the optical surface charge measurement system.

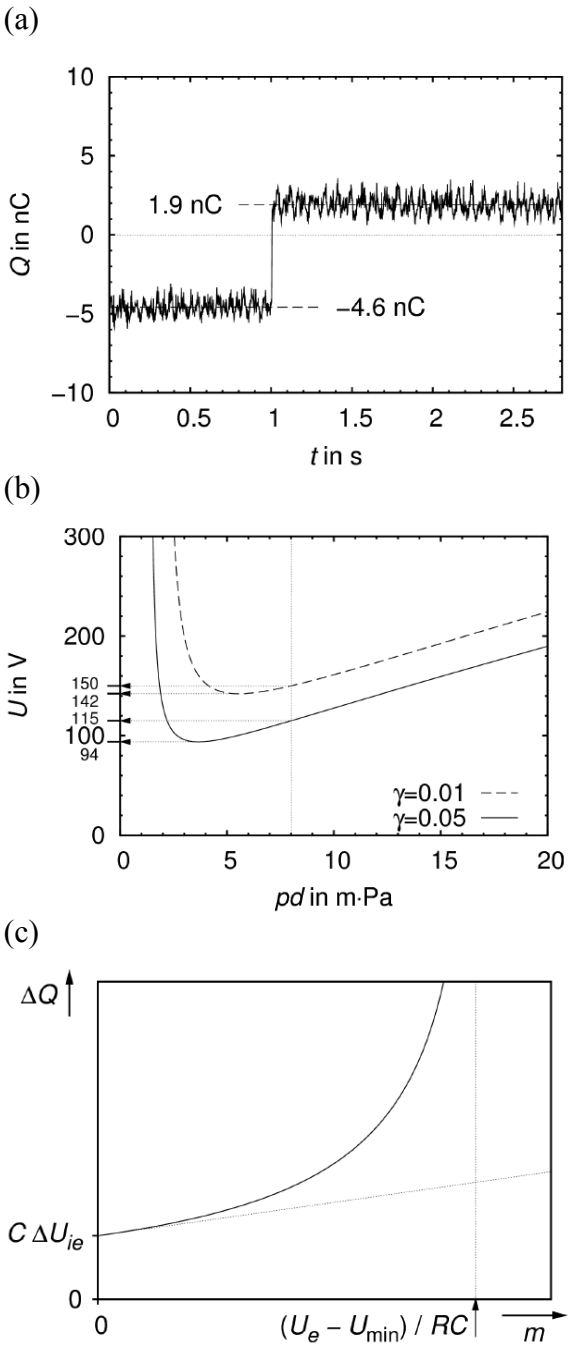


Fig. 4. (a) Evolution of the overall surface charge during 2.8 s. At t = 1 s the measurement is switched from the negative to the positive half-cycle. The average surface charge for both half-cycles is depicted. (b) Paschen curves for helium and different g-values. Both the minimum voltages and the ignition voltages for pd = 8 m×Pa are depicted. The parameters for the Paschen curves are taken from ref. [5]. (c) Sketch of DQ in dependence of m.

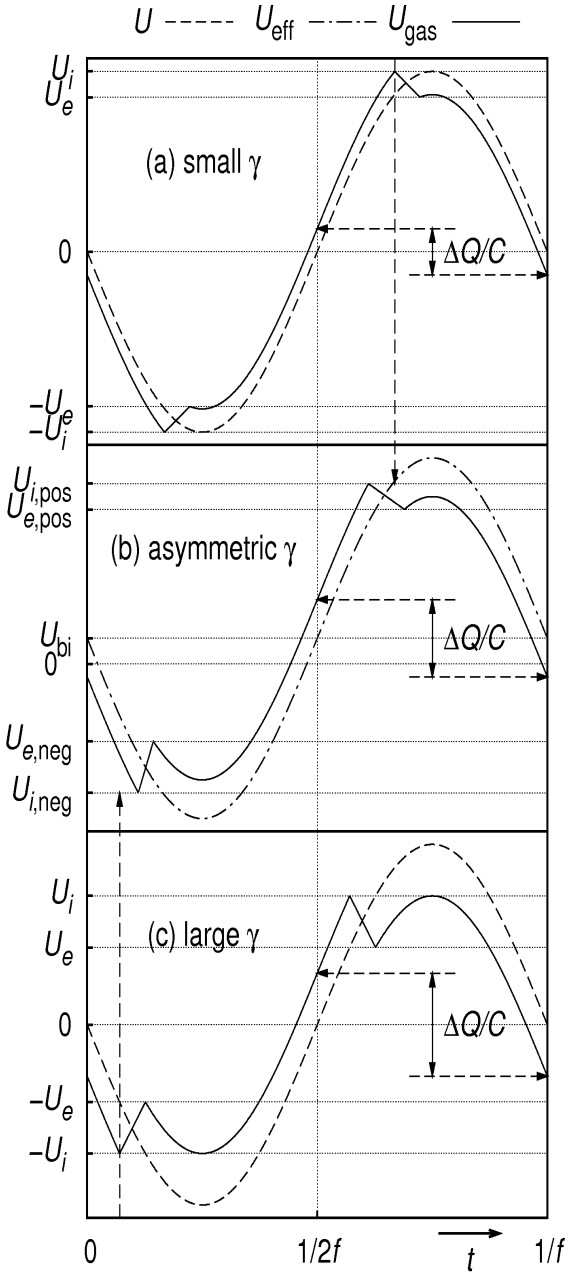


Fig. 5. Sketch of the voltage U_{gas} at the gas gap for a cell with (a) small, (c) large, and (b) asymmetric g. Additionally, the supply voltage U (a, c) and the biased supply voltage U_{eff} = U + U_{bi} (b) is displayed. The transfered charge DQ increases from (a) to (c). The vertical arrows indicate the time shift of the ignition in the asymmetric discharge.

2. Global charge measurement – asymmetry

In figure 4(a) the temporal evolution of the overall surface charge is shown. At t = 1 s the optical measurement pulse according to figure 2(a) is shifted from the negative to the positive half-cycle. Apart from some noise, the surface charge deposited after one breakdown stays stable over time. However, the amount of surface charge differs significantly between the negative and the positive half-cycle. The essential difference in the experimental set-up for both half-cycles is the different electrode material. To understand the arising charge bias, the charge transfer ΔQ per half-cycle has to be estimated, especially its dependence on the electrode material (described by the γ-value) and the ignition phase relative to the driving voltage (described by the voltage slope m). Remember that during a breakdown in a DBD surface charges accumulate on the dielectric surfaces which decrease the voltage drop across the discharge gap until the breakdown extinguishes.

To estimate the dependence of ΔQ on the γ-value, the DBD is regarded as a periodically ignited discharge with an ignition voltage and an extinguishing voltage related to the Paschen-curve as shown in figure 4(b). The ignition voltage is read form the Paschen curve in the usual way at the corresponding pd-value, 8 m·Pa in this case. As in the burning discharge the positive column is a nearly ohmic conductor, the extinguishing voltage is closely related to the Paschen minimum. As can be seen form figure 4(b), with an increasing γ-value both the ignition and the minimum voltage decrease. However, the difference between ignition and minimum voltage increases. Hence, the transferred charge ΔQ necessary to extinguish the discharge increases with increasing γ-value.

To estimate the dependence of ΔQ on the slope m of the driving voltage, think of a newly ignited breakdown in the DBD. The discharge current accumulates charges on the dielectric surface and hence the gap voltage decreases. However, at the same time the applied driving voltage increases with the slope m and hence compensates the voltage drop due to the emerging surface charges partly. Consequently, the breakdown lasts a little longer and more charge has to be transferred to extinguish the discharge. The dependence of the charge transfer ΔQ on the voltage slope m is shown in figure 4(c). C is the capacitance of the discharge cell and R is the resistivity of the discharge system. For m = 0 the transferred charge ΔQ solely has to compensate the voltage difference of the ignition and the extinguishing voltage. $\Delta Q(m)$ has a pole when the supply voltage rises as fast as the discharge current can charge the dielectric surfaces. In this case the discharge never would extinguish. A more detailed calculation describing the dependence of ΔQ on γ and m can be found in [3].

In figure 5 the voltages in a DBD are shown for different γ-values. In figure 5(a) the voltage at the gas gap (solid) and the supply voltage (dashed) are plotted. The situation is sketched for a rather small γ-value leading to a small charge transfer ΔQ. In figure 5(c) the same situation is shown for a large γ-value and hence a large charge transfer ΔQ. For an asymmetric γ–configuration as it is used in the experiment, the charge transfer in both half cycles has to be the same. This is achieved by varying the voltage slope m via a bias voltage U_{bi} resulting in the charge bias known from the experiment. According to figure 5(c) the bias voltage shifts the ignition in the positive half-cycle to an earlier point in time, thus the small charge transfer due to the small γ-value is increased. At the same time, the ignition in the negative half-cycle occurs later than in the symmetric case and thus the voltage slope becomes smaller. Consequently, the large charge transfer due to the large γ-value is decreased. In this way a bias voltage arises that levels the charge transfer difference due to the asymmetric γ–configuration.

3. Spatio-temporal charge measurement – filament interaction

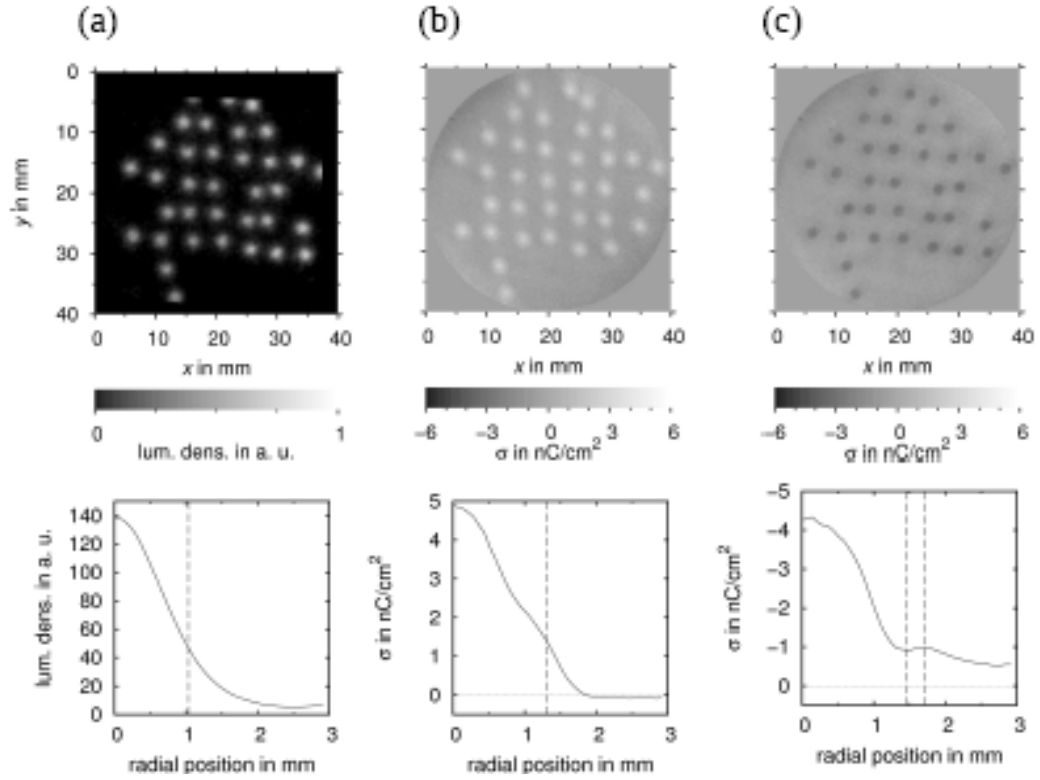


Fig. 6. Column (a) shows in the upper row the luminescence density of a typical patterned discharge as seen with the bare eye. Columns (b) and (c) show the positive and negative surface charge density σ after the corresponding breakdown. The image (c) is taken at the same time as image (a). The graphs in the second row show the radial profile of a filament in the corresponding quantity averaged over all filaments in the image above. For each quantity characteristic filament diameters are depicted.

In figure 6 a patterned discharge (a) along with the corresponding surface charge distributions for positive (b) and negative (c) surface charges is shown. The images (a) and (c) are taken at the same time and it can be seen that the surface charge distribution is basically an image of the preceding breakdown. However, the apparent filament size seems to be larger in the charge images (b, c) than in the visual appearance in (a). For a more precise investigation the radial profile of a filament was calculated for all three quantities. The second row of figure 6 shows the radial filament profile averaged over all filaments in the corresponding image above. For the luminescence density (a) and the positive surface charge (b) the width at 1/3 of the maximum hight was taken as the filament width, denoted with w_{ld} and w_{pos} respectively. In the negative surface charge density (c) the radial profile shows a smaller second maximum, i. e., the filament is surrounded by a ring of negative charge. This ring defines two characteristic filament diameters, one at the charge minimum between filament core and ring (w_{min}) and one at the maximum of the charge ring (w_{max}). The negative charge ring is a remarkable discovery as it reveals the inner structure of a filament. In [4] it has been shown, that this inner filament structure coincides well with characteristic distances during a filament collision.

4. References

[1] Stollenwerk L, Amiranashvili Sh, Purwins H-G 2006 *New Journal of Physics* **8** 217.
[2] Stollenwerk L, Purwins H-G 2005 *Europhysics Letters* **70** 22 – 28.
[3] Stollenwerk L, Stroth U 2010 *Contributions to Plasma Physics*, accepted.
[4] Stollenwerk L, 2009, *New Journal of Physics* **11** 103034.
[5] Raizer, Yu P 1991 Gas Discharge Physics (Springer, Berlin).

COLLISIONAL QUENCHING OF $N_2(A^3\Sigma_u^+)$ BY XYLENE AND THIN FILM DEPOSITION ON ELECTRODE

Susumu Suzuki[1], Haruo Itoh[1]

[1]*Chiba Institute of Technology*
E-mail: susumu.suzuki@it-chiba.ac.jp

Experimental investigation is carried out on the destruction processes of metastable nitrogen molecules $N_2(A^3\Sigma_u^+)$ by xylene using a theoretical procedure that is possible to take into account the reflection of metastables at the boundary. The collisional quenching rate coefficient of $N_2(A^3\Sigma_u^+)$ by *m*-xylene (C_8H_{10}) is determined in the Townsend discharge region.

During the repeated experiment, it is observed regular shift of the current-voltage curves to the higher-E/p_0 region. These changes caused by thin film deposition on the cathode surface with hydro-carbon that is one of the by-products of decomposed xylene.

1. Introduction

The metastable nitrogen molecule $N_2(A^3\Sigma_u^+)$ plays an important role in Air plasma [1]. We have previously determined the collisional quenching rate coefficient of $N_2(A^3\Sigma_u^+)$ by the air pollutant gas, such as CO, CH_4, and NO, CCl_2F_2 and CH_2FCF_3 [2]-[4]. Recently, the collisional quenching rate coefficients of $N_2(A^3\Sigma_u^+)$ by the gas that causes the sick building syndrome such as benzene (C_6H_6), acetone ($(CH_3)_2CO$), toluene ($C_6H_5CH_3$), and formaldehyde (CH_2O) have been determined [5][6].

This paper deals with the determination of the collisional quenching rate coefficient of $N_2(A^3\Sigma_u^+)$ by *m*-xylene (C_8H_{10}). Xylene is used as a solvent and a diluent in adhesives and paints. Among the three isomers of xylene, *m*-xylene, which has the weakest binding strength with methyl groups, is examined in our first attempt. The collisional quenching rate coefficients of $N_2(A^3\Sigma_u^+)$ by xylene (*o*-xylene, *m*-xylene, and *p*-xylene) have not yet been reported to the best of the authors' knowledge. Therefore, this is the first report in which the quenching effect of $N_2(A^3\Sigma_u^+)$ by xylene is described.

Furthermore, when measurements of the current-voltage curves in N_2/*m*-C_8H_{10} mixture are repeated, we observe that the curves gradually move to the high-E/p_0 side with time. This is described because of the decomposition product of the xylene attached on the cathode surface by discharge.

2. Experimental apparatus and method

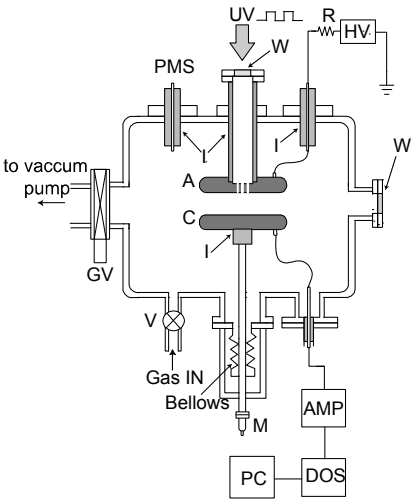
A schematic of apparatus used the study is shown in Fig. 1. A discharge chamber was evacuated down to pressures around 10^{-8} Torr by a turbo molecular pump. A pair of gold plated plane parallel electrodes was mounted on the central part of chamber and a stabilized DC high voltage was applied to the anode. The UV light driven by the pulse lighting of period about 0.4 Hz was irradiated on the cathode through a quartz window and holes on the central part of anode. It was observed the transient ionization current by a fast current amplifier after turning off the UV light. A typical transient current waveform is shown in Fig. 2. This is drawn in the semilogarithmic graph as averaging of 64 times measurement. At the turning off the UV light, a stepwise decrease in the current I_p is found first from the total current I. This component is multiplification current by collisional ionization of electron for photoemission current by UV light and the secondary electron emission current caused by the positive ions and photon so called fast γ action. Then, it was followed by a gradually decreasing current $i_m(t)$ with initial amplitude I_m and a time constant τ_m due to the decay of the electrons released by metastables striking the surface, so-called γ_m process [7]-[10]. By using the observed I, I_m and τ_m, the effective lifetime τ_1 of $N_2(A^3\Sigma_u^+)$ was given [2] by

$$\tau_1 = \tau_m\left(1-\frac{I_m}{I}\right). \qquad (1)$$

In contrast, the effective lifetime τ_1 is introduced from the analysis [2,4,11] which can take account of the reflection of $N_2(A^3\Sigma_u^+)$ on the surface of electrodes. It consists of the diffusion term and the collisional quenching term by $N_2(X^1\Sigma_g^+)$ and C_8H_{10} as follows:

$$\frac{1}{\tau_1} = D_{m1}\frac{\mu_1^2}{d^2}\frac{1}{p_0} + (ak + bk')N_1 p_0 . \qquad (2)$$

Here, D_{m1} ($=D_m \cdot p_0/p_1$) cm^2s^{-1} is the diffusion coefficient of $N_2(A^3\Sigma_u^+)$ at 0℃ under p_1 Torr, k = 1.79×10^{-18} cm^3s^{-1} [4] is the collisional quenching rate coefficient of $N_2(A^3\Sigma_u^+)$ by $N_2(X^1\Sigma_g^+)$, k' cm^3s^{-1} is the collisional quenching rate coefficient of $N_2(A^3\Sigma_u^+)$ by C_8H_{10}, N_1 cm^{-3} is the density of gas molecules at 0℃ under p_1 Torr, d cm is the gap length, a and b (=1 - a) are the number of gas molecule of the fraction of N_2 and C_8H_{10} against the total number of gas molecules in the chamber. p_0 is the reduced gas pressure at 0℃. p_1 is taken to be 1 Torr. μ_1 is the first order constant that describes the density function of the metastables, that is to say, the first root of Fourier Radiation series given by the reflection coefficient R of metastable nitrogen molecules at the surface of electrode.



AMP: High-speed current amplifier, DOS: Digital oscilloscope, PC: Personal computer, GV: Gate valve, HV: High voltage, PMS: Gas pressure measurement system, UV: UV light, M: Micrometer, V: Valve, W: Qurtz window, A: Anode, C: Cathode, I: Insulator

Fig. 1. A schematic of the experimental apparatus.

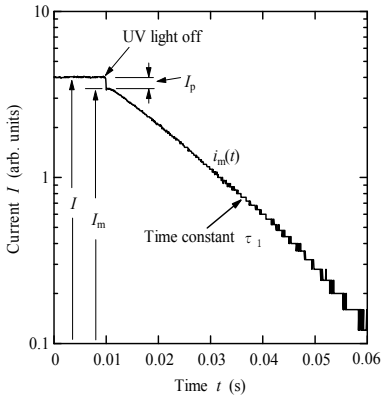


Fig. 2. A typical transient current waveform.

3. Experimental results

3.1 The fundamental constants of $N_2(A^3\Sigma_u^+)$

The transient current waveforms are observed by copper disc and gold plated cathode. Figure 3 shows the gas pressure dependence of the observed effective lifetime τ_1 of $N_2(A^3\Sigma_u^+)$ using the copper disc cathode. The effective lifetime τ_1 is given from the inverse of the slope of the decreasing transient current waveforms as shown in Fig. 2 and according to the equation (1). The obtained effective lifetime is plotted with the error bar of the standard deviation in log-log scale. The solid lines are given by the curve fitting procedure using the equation (2) based on our theory [6]. The curves are proportional to the gas pressure up to 3 Torr after that they takes peak and are inverse proportional to the gas pressure. From these curves, the diffusion coefficient D_{m1}, the collisional quenching rate coefficient k' of $N_2(A^3\Sigma_u^+)$ by m-xylene and the reflection coefficient R are determined as 151 cm^2/s, 4.8×10^{-9} cm^3/s and 0.01, respectively.

Figure 4 shows also the effective lifetime of $N_2(A^3\Sigma_u^+)$ measured by using the gold plated cathode. As well as Fig. 3, from the curve fitting procedure, we determine the diffusion coefficient D_{m1}, the collisional quenching rate coefficient k' of $N_2(A^3\Sigma_u^+)$ by m-xylene and the reflection coefficient R. The values are 152 cm^2/s, 4.0×10^{-9} cm^3/s and 0.1, respectively. Consistent values are obtained in the both

results in Figs. 3 and 4, except for the reflection coefficient of $N_2(A^3\Sigma_u^+)$ at the cathode surface. The result suggest that the diffusion coefficient and the collisional quenching rate coefficient are good agreement to the theoretical curves which are represented by the equation (2). This means the obtained effective lifetimes are well depended to the two process, diffusion of $N_2(A^3\Sigma_u^+)$ in N_2/(1 ppm) *m*-C_8H_{10} and collisional quenching of $N_2(A^3\Sigma_u^+)$ by *m*-C_8H_{10} correctly. We have never found the fact which a latter process appears clearly in Figs. 3 and 4. This is considered that the *m*-C_8H_{10} is decomposed easily by receiving the potential energy from $N_2(A^3\Sigma_u^+)$ by the two body collision. Moreover, the decomposition products which is produced as a by-product through the collisional quenching of $N_2(A^3\Sigma_u^+)$ by *m*-C_8H_{10} have never discomposed again by $N_2(A^3\Sigma_u^+)$. These investigations would be continued to expand the both cause of *o*- and *p*- xylene by the same procedure.

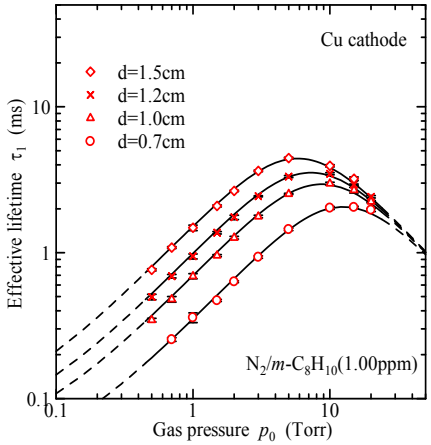


Fig. 3. Effective lifetime of $N_2(A^3\Sigma_u^+)$.

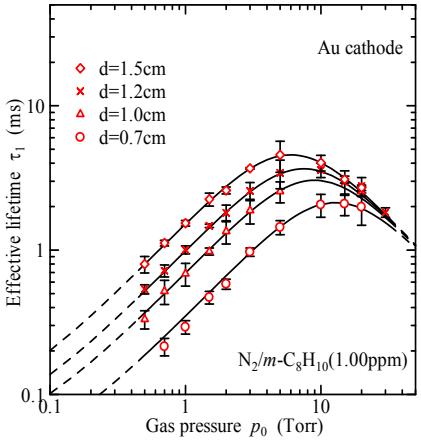


Fig. 4. Effective lifetime of $N_2(A^3\Sigma_u^+)$.

3.2 Variation of current voltage curve after repeated measurements

3.2.1 Experiments using on Au plated cathode

Certain fluctuations are found in the repeated transient current waveform in N_2/(1.00ppm)C_8H_{10} mixture. Therefore, the values of τ_1 are deviated as shown in Fig. 5 and it is impossible to estimate the values in the high gas pressure region which is indicated by dotted lines in the same figure. In this case, the current-voltage curve is observed as shown by (×) in Fig. 6. The curve is jumped up from 1×10^{-9} A to 2×10^{-6} A discontinuously. In contrast, the current-voltage curve shown by (○) in the same figure is carried out at the same time when the results are obtained using Au plated cathode as shown in Fig. 4. The current-voltage curve is varied continuosly with smooth line as a typical curve in the Townsend discharge region. These results suggest that certain obstructions in the electron multiplication process are caused in the gas phase or the surface of the electrode.

3.2.2 Repeated measurements of current-voltage characteristic using copper disc cathode

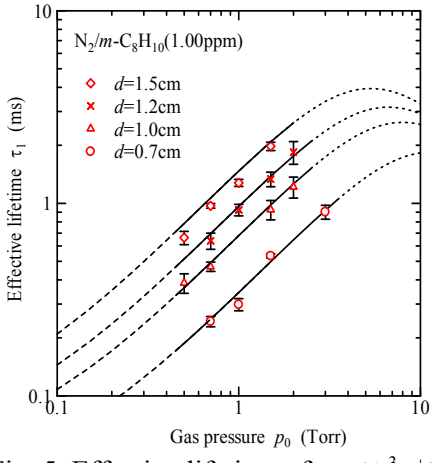


Fig. 5. Effective lifetime of $N_2(A^3\Sigma_u^+)$.

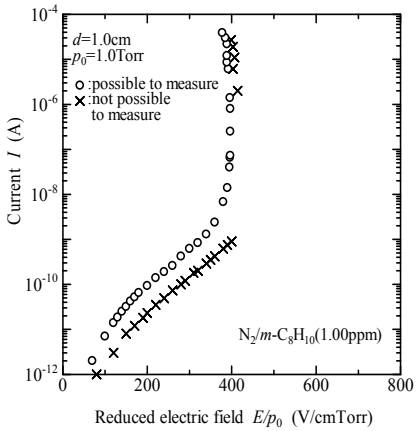


Fig. 6. Current voltage characteristic at 1 Torr, 1 cm in N_2/(1.00ppm) *m*-C_8H_{10}.

The current-voltage curves and the observation of the transient current waveforms in N_2/(1.00 ppm) m-C_8H_{10} mixtures are adapted again using a new copper disc cathode. To observe the difference between the new one and the old one, the comparison of the current-voltage curves is examined using a new copper disc cathode and the old Au plated cathode. Here, the purpose of this experiment is to check the surface condition of the cathode that influence the current-voltage curves. The Au plated electrode is the same as the electrode used for the effective lifetime measurement as shown in Fig. 3. Remarkable changes are found in Fig. 7. Firstly, the initial photo-electron current by UV irradiation is recovered to 2×10^{-12} A at E/p_0 = 10 V/cm·Torr. In contrast, the same current value of 2×10^{-12} A are obtained at last at E/p_0 = 100 V/cm·Torr under the use of the Au plated cathode which are indicated by (△). Secondary, each of the current-voltage curves shifts to low E/p_0 compare with the curves obtained under the use of Au plated cathode. These facts give us the assumption that it would be caused some surface change of the cathode to prevent a current flow between the electrodes. Therefore, we observe the temporal variation of the current-voltage curve by the repetition measurement in the same condition. The experiments are carried out by using the copper disc cathode with 1cm in the gap length and 1 Torr in gas pressure.

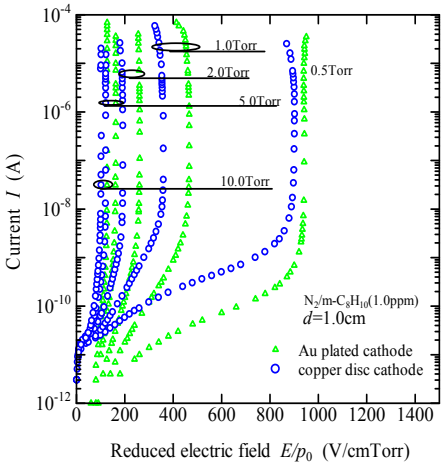


Fig. 7. Current voltage characteristic at 1 cm in N_2/(1.00ppm) m-C_8H_{10}.

Figure 8 shows the temporal variation of current-voltage curves that we experiment every 10 min. During the interval of the current-voltage curve measurement, the constant ionization current of about 40 μA is flowing with the change in the applied voltage for the activation in the gas phase. The current-voltage curves move to right side gradually with the time. It is also found that the no variation of the current-voltage curves is found from 220 to 420 minutes. Therefore, it is thought that the xylene would be decomposed perfectly under the action of the ionization current 40 μA, and certain decomposition product seems as some hydro-carbon attached on the cathode surface [12].

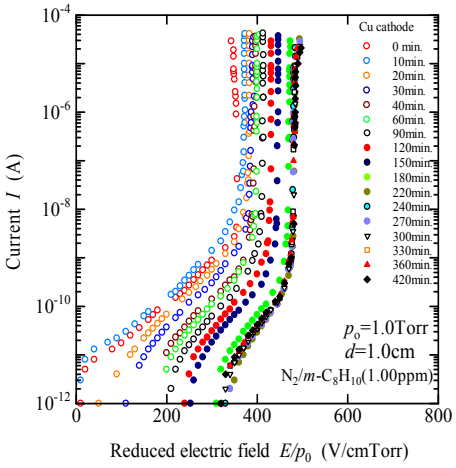


Fig. 8. Current voltage characteristic at 1 Torr, 1 cm in N_2/(1.00ppm) m-C_8H_{10}.

4. Discussions

4.1 The Fundamental coefficients of $N_2(A^3\Sigma_u^+)$

It is confirmed that the difference of the fundamental constants on $N_2(A^3\Sigma_u^+)$ are not found except for the reflection coefficient of $N_2(A^3\Sigma_u^+)$ under the two kinds of cathode materials. The diffusion coefficient D_{m1} is 151.5±0.7 cm^2/s on the average of two each material. The collisional quenching rate coefficients k' of $N_2(A^3\Sigma_u^+)$ by m-C_8H_{10} is $(4.4\pm0.6)\times10^{-9}$ cm^3/s on the average of two kind of cathode material as shown in Table 1. It is also proved that $N_2(A^3\Sigma_u^+)$ surely disappears by quenching through two body collision with m-xylene and $N_2(A^3\Sigma_u^+)$ never again decompose the by-products which is produced from m-xylene. These investigations are now continued to the case of o- and p- xylene.

4.2 Variations of the reflection coefficient of $N_2(A^3\Sigma_u^+)$ and current-voltage curves with the cathode condition

The reflection coefficients on the electrode surface is 0.01 in the Au plated cathode, and 0.1 in copper disc cathode. We will confirm whether the difference of the reflection coefficient is depends on the difference of the film thickness or it is the difference of the different material.

The gradually variation of current-voltage curves disappear after several hours from the starting time of the experiments. It is necessary to make clear this cause by the experiment.

4.3 Variation of current-voltage curves by repeated measurements

In N_2/(1.00 ppm)*m*-C_8H_{10} mixtures, when the measurements of the current-voltage curves are repeated, the curves move to right side gradually with the time. It is thought that the decomposition product of the xylene attached on the cathode surface by discharge of the ionization current 40 μA. The investigation of the decomposition product will also be necessary.

Tab. 1. Collisional quenching rate coefficients *k*' of $N_2(A^3\Sigma_u^+)$ by air pollutions.

Gases	*k*' (cm^3s^{-1})
m-C_8H_{10}	$(4.4\pm0.6)\times10^{-9}$
CF_4	$(6.9\pm0.9)\times10^{-16}$
CH_4	$(1.6\pm0.1)\times10^{-15}$
CH_2FCF_3	$(2.9\pm0.6)\times10^{-15}$
C_2F_6	$(2.9\pm1.0)\times10^{-15}$
CO_2	$(3.8\pm0.4)\times10^{-13}$
CO	$(5.9\pm1.7)\times10^{-13}$
CCl_2F_2	$(8.3\pm0.2)\times10^{-13}$
CH_2O	$(4.7\pm0.4)\times10^{-12}$
NO	$(4.8\pm0.2)\times10^{-11}$
$(CH_3)_2CO$	$(2.2\pm1.3)\times10^{-10}$
C_6H_6	$(3.0\pm0.3)\times10^{-10}$
$C_6H_5CH_3$	$(6\pm3)\times10^{-10}$

5. Conclusions

The diffusion coefficient D_{m1} of $N_2(A^3\Sigma_u^+)$ in N_2/(1ppm)*m*-C_8H_{10} mixtures and the collisional quenching rate coefficient *k*' of $N_2(A^3\Sigma_u^+)$ by *m*-C_8H_{10} is determined as 151.5±0.7 cm^2/s and $(4.4\pm0.6)\times10^{-9}$ cm^3/s, respectively. The collisional quenching rate coefficient *k*' of $N_2(A^3\Sigma_u^+)$ by *m*-C_8H_{10} was the largest value in those values of $N_2(A^3\Sigma_u^+)$ by air pollution gases that have been measured so far. The experimental result of the effective lifetime is consistent to the theoretical curve very well within the new surface electrode. However, the current voltage curve moved to high E/p_0 region because of certain decomposition product of the xylene attached on the electrode surface. More detailed studies including the surface analysis of the cathode are being carried out.

6. References

[1] U. Kogelschatz, in Non-Equilibrium Air Plasma at Atmospheric Pressure, K. H. Becker, U. Kogelschatz, K. H. Schoenbach and R. J. Barker, Eds., IOP Publishing Ltd, Bristol, UK., pp.551-565 (2005)

[2] S. Suzuki, H. Itoh, H. Sekizawa and N. Ikuta, J.Phys.Soc.Jpn.,Vol.62, No.8, 2692-2697 (1993)

[3] S. Suzuki, T. Suzuki and H. Itoh, Cont. of HAKONE X Saga, Japan, 132-135 (2006)

[4] S.Suzuki, H.Itoh, H.Sekizawa and N.Ikuta, Jpn. J. Appl. Phys., 36, 4744-4746 (1997)

[5] T.Suzuki, S.Suzuki and H.Itoh: Proc. 13th Asian Con. on Electrical Discharge, P-2-40 (2006)

[6] S.Suzuki, D. Shibuya, M. Aoyagi and H.Itoh: 29th ICPIG, July 12-17, Cancún, México, PA1-8(2009)

[7] J.P Molnar, Phys. Rev., 83, 933-940 (1951)

[8] J.P Molnar, Phys. Rev., 83, 940-952 (1951)

[9] S.C.Haydon and O.M.Williams, J. Phys. B: Atom. Mol. Phys., 6, 227-231 (1973)

[10] H.Itoh and N.Ikuta, Trans.IEE of Japan, Vol.105-A, No.4, 189-196 (1985) [in Japanese]

[11] S. Suzuki, H. Itoh, N. Ikuta and H. Sekizawa, J.Phys.D: Appl. Phys., 25, 1568-1573 (1992)

[12] M.Shimozuma, G.Tochitani, H.Ohno, H.Tagashira, and J.Nakahara: J.Appl. Phys., 66, pp.447-449 (1989)

DETERMINATION OF SECONDARY IONIZATION COEFFICIENT OF MgO

Takashi Sekizawa[1], Yasuhide Kashiwagi[2], Susumu Suzuki[1], Haruo Itoh[1]

[1]*Chiba Institute of Technology*
[2]*Kisarazu National College of Technology*
E-mail: susumu.suzuki@it-chiba.ac.jp

An investigation of Townsend's secondary ionization coefficient γ of MgO is carried out experimentally, considering the effect of the accumulated charge on the MgO film electrode. Sinusoidal voltage is applied between the MgO film electrode and the stainless steel electrode in the frequency range of 0.1 Hz - 2 kHz. Breakdown voltage is determined from the waveforms of applied voltage, discharge current and accumulated charge on the MgO film electrode. The Lissajou figure is observed simultaneously. The obtained γ of MgO is compared with other results and it is discussed.

1. Introduction

It seems that Auday et al. [1][2] were the first to experimentally determine the secondary ionization coefficient γ of MgO. MgO is utilized as a protective layer on the metallic electrode for the plasma display panels and cold cathode fluorescence discharge lamps. However, MgO is an insulator and not a conductor; thus, it is important to clarify the role that MgO plays as the cathode in this discharge cell.

Auday et al. [1][2] experimentally determined the breakdown voltage Vs and then estimated γ by investigating Townsend's criterion. They applied DC voltage between the aluminum electrode and the MgO film electrode, but presented no detailed description of the discharge phenomenon in their paper.

Firstly, we investigated the procedure for determining γ from breakdown voltage. For this purpose, the breakdown voltages observed by Shiokawa et al. [3] were used in our investigations [4][5]. We then experimentally determined γ under a 0.5 Hz sinusoidal voltage, and compared with the experimental results of Auday et al. [6]. In our experiment, the effect of the induced voltage on MgO films by the accumulated charge was not considered as the same as Auday et al. The obtained γ showed a similar tendency to that in Auday et al. at a reduced electric field intensity $E/p_0 < 60$ V/cm·Torr (E: electric field, p_0: 0℃ reduced gas pressure). Thus, it was considered that the effect of the voltage induced by the accumulated charge on the dielectric electrode at 0.5 Hz could be disregarded.

In the present study, an investigation by the V-Q Lissajous figure method [7] [8] is used to determine the breakdown voltage V_s of a MgO film electrode at frequencies up to 2 kHz. From the results, it is evident that no accumulated charge effect appeared at frequencies lower than 50 Hz of the applied sinusoidal voltage, because the accumulated charge on the MgO film electrode vanished with a time constant of about 40 ms in this case.

2. Experimental apparatus and method

Figure 1 shows the schematic diagram of the experimental apparatus. The sinusoidal voltage generated by a high-speed bipolar power supply is applied to the stainless steel electrode. The stainless steel electrode with a diameter of 20 mm is installed in the glass cylinder with an inner diameter of 20.3 mm mounted on the MgO film electrode to maintain the discharge in the central part of this cylinder space. The applied voltage waveform is monitored using the oscilloscope through a potential divider with the probe. At the same time, the accumulated charge on the MgO film is detected by the capacitor C connected between the MgO film electrode and the ground. The capacitor C is switched to the resistor R when current is measured. In preparation for the experiment, the MgO film electrode is heated using a ceramic heater for at least two hours at 400℃, in accordance with the experiment of Shiokawa et al. [5], and the discharge chamber is evacuated to vacuum by a turbomolecular pumping system. The purity of the Ar used is 99.9995%.

3. Experimental results

3.1 Voltage and current, voltage and charge waveforms

Figure 2(a) shows waveforms of the applied voltage $V(t)$ whose frequency is 500 Hz and the discharge current $i(t)$. In this case, the capacitor C in Fig. 1 is changed to a current-detecting resistor (500 kΩ). The MgO film electrode acts as a cathode when the applied voltage $V(t)$ has a positive polarity, then, the breakdown voltage in this polarity is measured carefully. Current begins to flow at the time A indicated in Fig. 2(a), and this point is considered as the breakdown voltage of discharge between electrodes. Figure 2(b) shows the waveform of the accumulated charge $q(t)$ in the capacitor C.

Figure 2(c) shows the waveforms of applied voltage between the gap $V(t)$, voltage induced by the accumulated charge on the MgO film electrode $V_w(t)$, and the gap voltage between the MgO film electrode and the stainless steel electrode $V_g(t)$. Here,

$$V_g(t) = V(t) - V_W(t)$$
$$= V(t) - q(t)/C_{MgO}.$$

C_{MgO} is the electrostatic capacity of the MgO film, which is estimated from the slop of the straight line in the discharge period of the Lissajou figure. Thus, we can determine the breakdown voltage between the discharge gap, which consisted of MgO film electrodes as to be about 300 V.

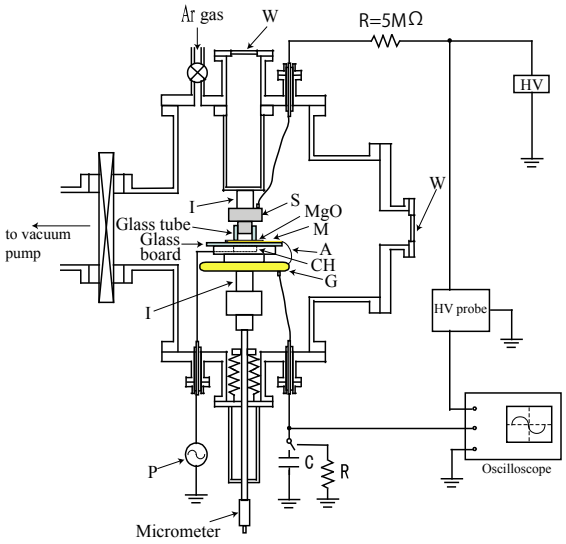


Fig. 1. Schematic diagram of experimental setup. HV: high voltage, S: stainless steel electrode, G: gold film electrode, I: insulator, W: quartz window, M: meshed copper wire, A: aluminum foil, CH: ceramic heator, P: power supply for ceramic heator.

3.2 Breakdown voltage

Figure 3 shows the relationship between the breakdown voltage V_s and the frequency f of applied sinusoidal voltage. The parameter is a product of gas pressure and the gap length p_0d. It is evident that the observed breakdown voltage is independent of the freqency of applied voltage, as shown by the broken lines (d = 0.3 cm) and solid lines (d = 0.2 cm) in the figure. Therefore, breakdown voltage is regarded as dependent on only p_0d. Thus, the relationship between the breakdown voltage V_s and p_0d, so called the Paschen curves, are obtained, as shown in Fig. 4. The breakdown voltage curves obtained at gap lengths d = 0.2 cm and 0.3 cm are indicated by the solid and broken lines in Fig. 4, respectively. The breakdown voltages V_s in the range of $3 < p_0d < 20$ Torr·cm at d = 0.2 cm are slightly lower than that at d = 0.3 cm.

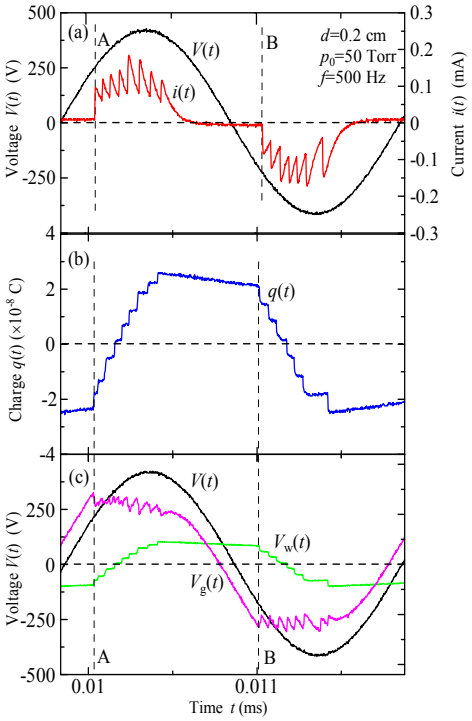


Fig. 2. Voltage - current, voltage and charge waveforms in 500 Hz.

Then, the results of the comparison of the Paschen curves in Fig. 4 and other values including those obtained in our previous investigations are shown in the same figure. The dotted line indicates the obtained values of V_s under the AC 0.5 Hz voltage applied in our previous measurement [6]. V_s is slightly higher than the present value at a p_0d lower than 3 Torr·cm; it is slightly lower at a p_0d higher than 7 Torr·cm, compared with our present values. V_s is also determined as the voltage when the discharge current begins to flow on the order of 10^{-7}A. In addition,

the accumulated charge effect is not considered in this case, and the $V-q$ curve never forms a closed loop. In contrast, as shown in Figs. 2(a) and 3, the discharge current at the breakdown occuring in the present data is on the order of 10^{-4}A. Then, the region of current is markedly different.

Furthermore, the breakdown voltages V_s observed by Shiokawa et al. are also shown in the same figure. The values of V_s observed by Shiokawa et al. are higher than our values in the range of $1.5 \leqq E/p_0 \leqq 60$ V/cm・Torr. They described that breakdown voltage is determined by the voltage immediately before the beginning of the collapse of the applied voltage waveform observed using the oscilloscope. Thus, it could be concluded that Shiokawa et al. did not consider the accumulated charge effect in determining breakdown voltage.

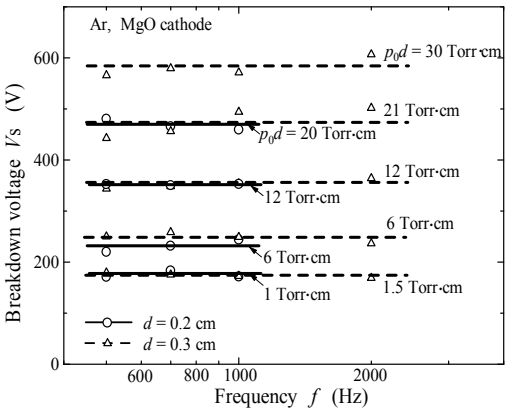


Fig. 3. Relationship between frequency f and breakdown voltage V_s.

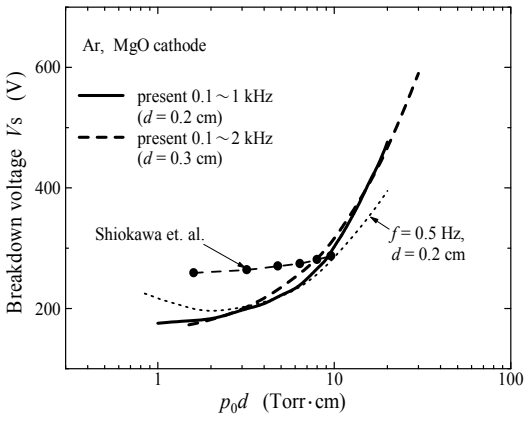


Fig. 4. Paschen curves of MgO cathode in Ar.

3.3 Determination of γ of MgO

Figure 5 shows the average number of ionization collisions between the gap per an electron, $\int_0^d \alpha(x)\mathrm{d}x$, obtained by MCS against a reduced electric field. The electron collision cross section set of the Ar used is reported by Kurachi and Nakamura [10]. The MCS code used in this calculation is one of the flight time integral methods [3][4][11]. The value of the integration of $\alpha(x)\mathrm{d}x$ from 0 to d is sometimes called the ionization index and currently is in the range of 2.2 - 3.6.

Generally, the boundary between Townsend discharge and streamer discharge is given by the ionization index of about 18～20 [12]. Therefore, we consider that the discharges observed in our experiment are Townsend discharges. Then, it is possible to estimate the secondary ionization coefficient γ from Townsend's criterion using breakdown voltage and the gap condition [3][4][6].

$$\gamma = \frac{1}{\exp\left(\int_0^d \alpha(x)\mathrm{d}x\right) - 1}. \qquad (1)$$

Thus, γ is determined according to equation (1) and the results are shown in Fig. 6. At $E/p_0 < 35$ V/cm・Torr, the present γ at d = 0.2 cm increases rapidly with an increase in E/p_0. After that, γ reaches its maximum and decreases gradually against E/p_0. The present γ at d = 0.3 cm shows almost the same variation at d = 0.2 cm. However, the curve is shifted to an E/p_0 region lower than that at d = 0.2 cm.

The γ obtained by Auday et al [2] is shown by a dot-and-dash line for comparison. Their value is obtained in DC voltage. At $E/p_0 < 60$ V/cm・Torr, Auday et al.'s γ almost agrees with the γ that we which is determined [4] using V_s of Shiokawa et al. [5]. However, Auday et al.'s value increases at about $E/p_0 = 60$ V/cm・Torr and decreases from $E/p_0 = 160$ V/cm・Torr. At $E/p_0 > 160$ V/cm・Torr, Auday et al.'s value agrees with the value that we determined under a 0.5 Hz sinusoidal voltage [6].

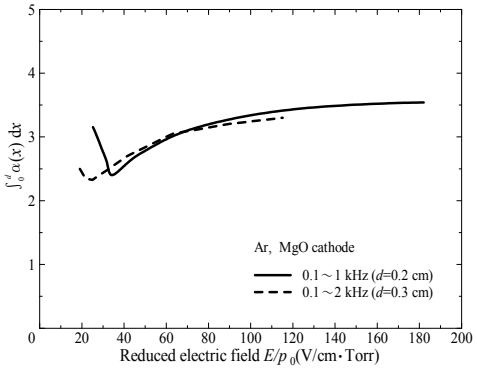


Fig. 5. Ionization index.

In contrast, our previous value obtained using V_s of Shiokawa et al. decreases monotonically up to E/p_0 = 160 V/cm・Torr. This breakdown voltage is obtained using a practical plasma display panel (PDP), which is driven by a 23 kHz square wave voltage between gaps of 160 μm in Ar from 5 to 400 Torr. In addition, before the experiment, they performed the out gas treatment from the MgO surface at 400 ℃ for at least two hours continuously. This rigorous preparation before the experiments and the procedures suggest the validity of utilizing the breakdown voltage obtained using the procedure for our determination of γ. Breakdown voltage was determined by the collapse of the waveform, which is monitored using the oscilloscope. Using the breakdown voltage, we have estimated the values of E/p_0 and p_0d for the calculation to obtain the average number of electron collisional ionizations per an electron, which starts from the cathode in the gap, by a Monte Carlo simulation. The obtained γ - E/p_0 curve was almost similar to those determined by Auday et al., however, our γ was larger than that of Auday et al. in a reduced electric field less than 80 V/cm・Torr. Furthermore, we discussed the effects of the spatial nonequilibrium of electron energy distribution and electron backscattering in front of the cathode on γ.

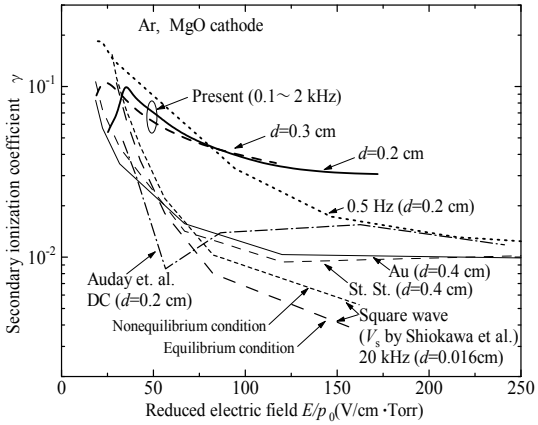


Fig. 6. Secondary ionization coefficients of MgO film cathode in Ar.

Auday et al.'s γ is considered to be divided into two regions; an E/p_0 lower than E/p_0 = 60 V/cm・Torr and an E/p_0 higher than 160 V/cm・Torr. At E/p_0 < 60 V/cm・Torr, a good agreement between Auday et al.'s γ and Shiokawa et al.'s γ is observed. The difference between both is in the frequency of applied voltage with DC and a 23 kHz square wave; also, is both, the accumulated charge effect is not considered. At E/p_0 > 160 V/cm・Torr, a good agreement between Auday's γ and our γ under a 0.5 Hz sinusoidal voltage is found. The gap lengths of both are the same here. We do not consider the accumulated charge effect. The result obtained at 0.5 Hz and d = 0.2 cm in our case that no accumulated charge is considered. Note that, in Auday et al.'s experiment, the accumulated charge was not considered. Therefore, it seems that it is not necessary to consider the effect of the accumulated charge under applied sinusoidal voltages of low frequency, including DC voltage. This is consistent with the result of other experiments showing that the accumulated charge on MgO film electrode vanished with a time constant of 40 ms.

In addition, the γ values of the metallic electrode (gold (Au) and stainless steel (St.St.)) shown in a previous paper [6] and the γ of the MgO film electrode are compared. The γ values of Au and St.St. are shown by the thin solid line and thin broken line, respectively. The γ of the metallic electrode is near the γ obtained by Auday et al. at E/p_0 < 75 V/cm・Torr, and the curve that approaches the γ of MgO is drawn at a higher-E/p_0. It is clear that the γ of the MgO film at all E/p_0 values is larger than the γ of the metal electrode. It is considered that this is due to the difference in material between the film and the electrode.

3.4 Effect of accumulated charge on measurement of breakdown voltage

The ranges of the frequencies f of applied voltage and the gas pressures p_0 in which the accumulated charge on the MgO film should be considered in the measurement are shown in Fig. 7. The gas pressure range in which the accumulated charge on the MgO film is considered is comparatively high at about 40 Torr at a frequency of about 50 Hz. Furthermore, when the frequency exceeds 50 Hz, the effect of the accumulated charge on the MgO film approaches the low gas pressure range.

The frequency dependence of γ was not observed in the parameter range in the present experiment. Moreover, the effect of the accumulated charge appears in the frequency range higher than about 50 Hz, and in the gas pressure range higher than 5～40 Torr.

4. Discussion

From the results of V_s shown in Fig. 4, it is interesting remarkable to see that V_s dose not depend on the change in the frequency of applied voltage. The discharge phenomenon is investigated using a Lissajous figure to understand the change in the frequency of the high-voltage power supply. The ranges of f and p_0 in which the accumulated charge of a MgO film should be considered are confirmed, as shown in Fig. 7. From the result, a difference is seen between Auday et al.' s γ measured using DC voltage and the present data, although the effect of the accumulated charge can be ignored in DC voltage. It is necessary to investigate the difference between the γ values determined under a high-frequency voltage and a low-frequency voltage including DC voltage in the future. Furthermore, we found that the γ of MgO is larger than the γ values of metallic electrodes (Au and St.St.). On the other hand, Auday et al.'s γ almost corresponded to the γ values of our metallic electrodes (Au and St.St.) at a low E/p_0. At present, the reason for the difference in γ depending on the presence of the accumulated charge even if the same MgO film electrode is used canot be sufficiently understood. However, we have taken attention of our interest to Massine's proposal [13] on the shallow trap [14] in the dielectric of the cathode.

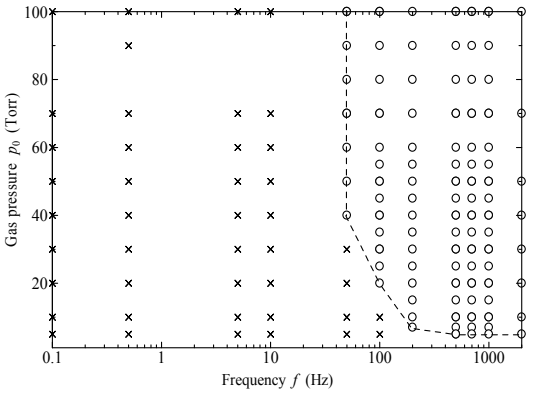


Fig. 7. Range to consider accumulated charge. ○: The accumulated charge affects the applied voltage. ×: The accumulated charge dose not affect the applied voltage.

5. Conclusions

The γ of the MgO film electrode was investigated. The present data determined from V_s at 2 kHz was relatively higher than other previously reported values. It is confirmed that it is not necessary to consider the effect of the accumulated charge under applied voltages of low frequency, including DC voltage.

6. References

[1] G.Auday, Ph.Guillot, J.Galy and H.Brunet, 1999 *Proc. XXIV International Conference on Phenomena in Ionized Gases*, **4**, 69-70.
[2] G.Auday, Ph. Guillot and J.Galy, 2000 *J. Appl. Phys*., **88**, 4871-4874.
[3] A.Shiokawa, Y.Takada, R.Murai and H.Tanaka, 1999 *Proc. of IDW '99*, 519-522.
[4] S.Suzuki and H.Itoh, 2004 *Jpn.J.Appl.Phys.*, **43**, 10, 7234-7239.
[5] S.Suzuki and H.Itoh, 2007 *Jpn.J.Appl.Phys.*, **46**, 1129-1136.
[6] S.Suzuki and H.Itoh, 2009 *IEEJ Trans. FM*, **129**, 909-914 [in Japanease].
[7] M.Tanaka, S.Yagi and N.Tabata, 1982 *T. IEE Japan*, **102**, 10, 533-540 [in Japanease].
[8] K.Teranishi, N.Shimomura, S.Suzuki and H.Itoh, 2009 *Plasma Sources Sci. Technol.*, **18**, 045011.
[9] T.Tamita, A.Iwata and M.Tanaka, 1998 *T.IEE Japan* **118-A**, 4, 353-358 [in Japanease].
[10] Y.Nakamura and M.Kurachi, 1988 J. Phys. D, **21**, 718-723.
[11] K.Yamamoto, 1985 *Bull. Shikoku Women's Univ*., **5**, 83-97.
[12] E.Kuffel, W.S.Zaengl, J. Kuffel, 2000, High Voltage Engineering: Fundamentals, Second Edition (Newnes).
[13] F.Massines, N.Gherardi, N.Naudé and P.Ségur: 2009 *EPJ Appl. Phys.*, **47**, 2, 22805.
[14] Kai Wu and L.A.Dissado: 2005 *IEEE Trans. on Dielectrics and Electrical Insulation*, **12**, 4, 655-668.

INVESTIGATION OF BARRIER DISCHARGE IN He/N_2 MIXTURES BY CROSS-CORRELATION SPECTROSCOPY AND SURFACE CHARGE MEASUREMENTS

Marc Bogaczyk[1], Gleb Fedoseev[2], Robert Wild[1] and Hans-Erich Wagner[1]

[1]*Institute of Physics, Ernst-Moritz-Arndt University, Greifswald, Germany*
[2]*Moscow State University of Design and Technology, 115035 Moscow, Russia*
E-mail: Wagner@physik.uni-greifswald.de

A new set-up was installed which for the first time allows spatio-temporally and spectrally resolved spectroscopic measurements (cross-correlation spectroscopy) in combination with the quantitative detection of residual surface charges. The charge detection succeeded by the application of the optoelectronic Pockels effect in combination with ICCD camera technique. For this a plane BSO crystal operated as one of the dielectric electrodes of the barrier discharge. In the contribution first results on the discharge development and surface charge measurements in pure He and mixtures with N_2 at atmospheric pressure are presented.

1. Introduction

Non-thermal plasmas at atmospheric pressure are effective sources of radicals and excited species. Therefore, they have found many technical applications in the plasma chemistry and lighting. In this group the barrier discharges (BDs) have a key position [1]. It is well-known that BDs can operate in different discharge modes, mainly controlled by the feeding gas, frequency, dielectric electrode material and the reactor geometry (gap spacing). Many investigations in the past have contributed to a deeper understanding of the discharge breakdown and development [2][3]. Finally, the discharge operation mode (filamentary or diffuse) is related to the ratio of the secondary processes at the electrodes (e.g. exoemission of electrons) to the ionization in the gas bulk (Townsend and Penning ionization). Furthermore, the residual surface charge distribution controls the position of the next discharge breakdown. In the last decade the activities of our group have been focused on the spatio-temporally and spectrally resolved investigation of the discharge development in the volume in different gas mixtures, using the method of cross-correlation emission spectroscopy (CCS). Now we started to combine the CCS-technique with the quantification of the residual charges on the dielectric surfaces in a common set-up. The charge detection succeeded by the application of the optoelectronic Pockels effect in combination with CCD camera technique [4][5]. For this a plane BSO crystal was used as one of the dielectric electrodes. In this way we want to contribute to a deeper understanding of one aspect of the interaction of relevant volume and surface processes. In this contribution first (i.e. preliminary) results after the installation of the new set-up are presented.

2. Experimental Setup

The experimental set-up is sketched in fig. 1. Part (A) illustrates the necessary installation for the surface charge measurements, based on the optoelectronic Pockels effect [4][5], and part (B) the well-known scheme for the CCS measurements (details, e.g. in [3]). The discharge cell (located in the center) has two plane dielectric electrodes. A side-view with more details is shown in fig. 2. The upper electrode is made from glass, covered by a conducting ITO layer. The second one is an optoelectronic Bismuth Silicon Oxide crystal (BSO), located on a polished aluminium mirror. The properties and dimensions of the dielectrics are summarized in table 1.

The surface charges are detected on the dielectric BSO crystal. For this it is necessary to illuminate the crystal with a stabilized monochromatic LED light source (λ = 634 nm). The temperature of the LED is controlled by a Peltier element. For the homogeneous illumination of the BSO crystal two lenses and apertures in front of the LED (Koehler illumination) are used. A polarizing beam splitter transmits only one polarized direction of the non-polarized LED light which is reflected to the BSO crystal. Behind the beam splitter a telescopic system enlarges the beam diameter by a factor five up to 30 mm. Between the two lenses of the telescopic system a $\lambda/8$-wave plate is placed. Thereby the linear

polarized light becomes elliptic polarized caused by a phase shift of 45° when the light is passing the wave plate.

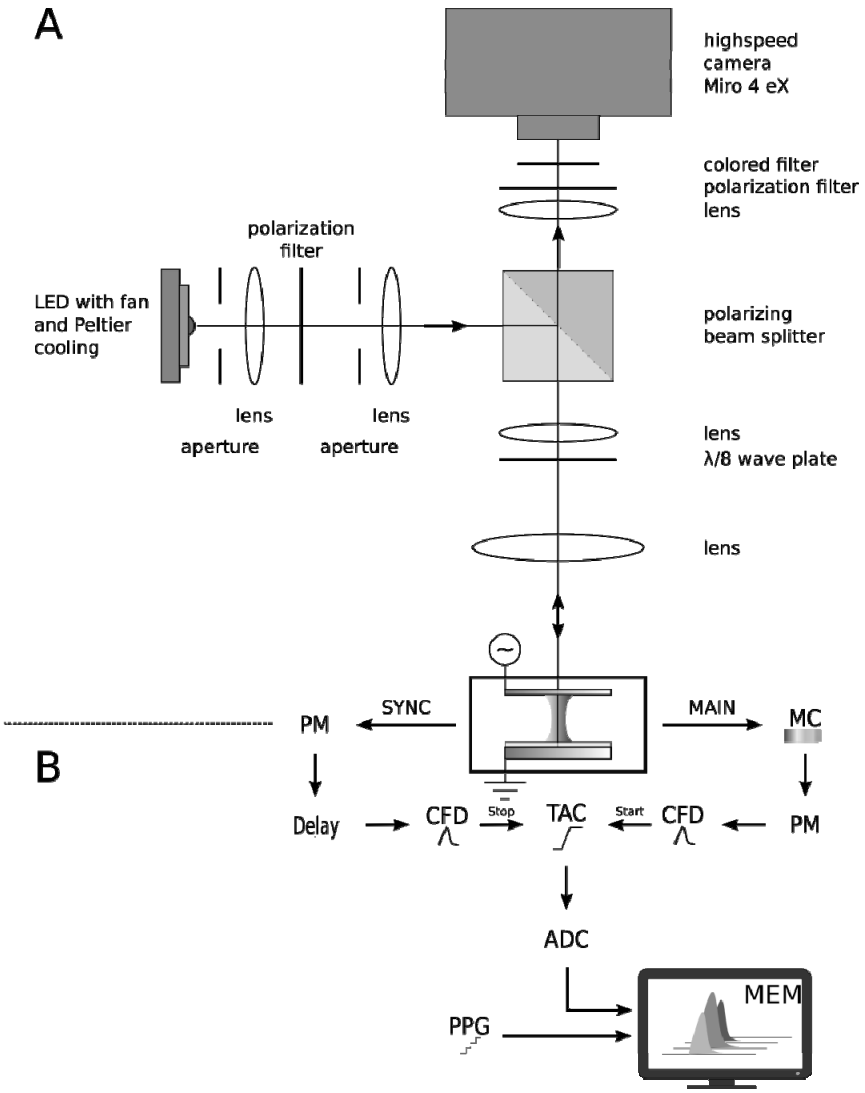


Fig. 1. Scheme of experimental setup with installations for surface charge measurements (A) and spatio-temporally and spectrally resolved spectroscopic measurements in the volume with CCS (B). CCS-setup: PM – photomultiplier, MC – monochromator, Delay – delay generator, CFD – constant fraction discriminator, TAC – time to amplitude converter, ADC – analog-digital converter, PPG – pattern generator, MEM – memory.



Fig. 2. Side-view of the discharge cell.

Tab. 1. Properties of dielectrics.

	BSO $Bi_{12}SiO_{20}$	glass plate
diameter [mm]	22.5	22.5
thickness [mm]	0.7	0.7
dielectric const. ε_r	56	7.6

When the light is passing the BSO crystal twice there is a phase shift and the ellipticity of the light is changing. After that the light passes the λ/8 wave plate and the beam splitter again before the highspeed camera MIRO 4 detects the radiation. In front of the camera a polarizing filter is installed which transmits only linear polarized light. The colored filter (transparent from 620 to 640 nm) is necessary to fade out the light emission of the BD. In this way the camera detects only the intensity

change of the reflected light caused by surface charges. The BSO crystal is isotropic without an electric field and becomes birefringent with surface charges on top of the crystal, causing an electric field. At first, the measurements require a reference photo of the BSO crystal without residual charges. After that, the charges can be calculated from the relative ratio of the intensity with surface charges *I(x,y)* and the intensity without surface charges $I_r(x,y)$. The surface charge density σ(x,y) [C/m^2] depends on the position on electrode. It can be calculated with the following formula [5]

$$\sigma(x,y) = \left[\frac{I(x,y)}{I_r(x,y)}\left(2\frac{2\pi}{\lambda}n_0^3 r_{41} U_{BSO}^r + 1\right) - 1\right]\frac{\lambda}{4\pi n_0^3 r_{41}}\frac{\varepsilon_0\,\varepsilon_{BSO}}{d_{BSO}}, \quad (1)$$

where λ is the wavelength, n_0 is the refraction index, r_{41} is the optoelectronic coefficient, U_{BSO}^r is the voltage drop over the BSO crystal without any surface charges, ε_0 is the vacuum dielectric constant and ε_{BSO} is the dielectric constant of BSO.

3. Results and discussion

In pure helium the barrier discharge operates in the diffuse (glow-like) mode and is characterized by discharge durations in the microsecond scale. With a rising admixtures of nitrogen the mechanism of the electrical breakdown changes. In dependence on the N_2 admixture and/or driving voltage the discharge can operate in the Townsend-like diffuse mode or filamentary mode, respectively [3].

An overview spectrum (range 200-800 nm) for the diffuse discharge operation in He with 0.1 vol.% nitrogen admixture is given in fig. 3. The spectrum is dominated by the first negative system of N_2^+ and second positive system of N_2, the NOγ emission and He lines.

The intensive N_2^+ emission results from an effective Penning process between metastable He* atoms and N_2 in the ground state, producing excited N_2^+(B) molecules via He* + N_2(X) ・・ He + N_2^+(B), followed by the emission of the first negative system by N_2^+(B) ・・ N_2^+(X) + hυ. With increasing N_2 concentrations the N_2^+ emission is drastically reduced because of much less He*. Furthermore, the intensity of the second positive system of nitrogen from lower than from higher vibration levels becomes more intensive.

Fig. 4. shows the temporally resolved light emission profiles for a “pure” helium discharge with small nitrogen impurities. It operates in the glow-like diffuse mode. Despite a long pumping times it is inevitable to have certain impurities inside the discharge cell.

The helium emission (here the 706 nm line) is most intensive at the cathode (glow-like) while the emission of nitrogen second positive system (0-0 transition) is most intensive at the anode (Townsend-like). These investigations are in agreement with former measurements [2,3]. The temporal correlations between the discharge current and the emission of He at 706 nm and N_2 at 337 nm are summarized in fig. 4 (right). The excitation of both lines (gap position 0.6 nm in front of anode) shows a good correlation with the discharge current.

In the diffuse He- BD it was possible to acquire values for the dielectric surface charges in every phase of the applied voltage. Fig. 5 shows some first measurements at different phase positions. The integral positive and negative surface charges follow the discharge breakdown, and change therefore every half period. The charges are nearly constant over one half period. It was found that the total positive charges (integrated over the dielectric area) are greater than the negative ones. Typical values for the positive surface charges are + $6\cdot10^{-10}$ C to $1\cdot10^{-9}$ C the negative charges are about $-2\cdot10^{-10}$ C, a little depending on the applied feeding voltage.

The positive surface charges could originate from the neutralization of positive ions on the surface, hereby collecting electrons. The negative surface charges can be identified with electrons collected on the BSO crystal. After turning off the discharge, the positive and negative charges exist nearly stable for a long time (Fig. 6.). To acquire surface charge decay constants, future investigations have to be extended to several hours. The realization of surface charge measurements in the filamentary mode, required an 10 vol.% N_2 admixture to He. For these conditions in fig. 7 the surface charges (spots) are shown. It can be distinguished clearly between negative (dark) and posive (light) surface charges.

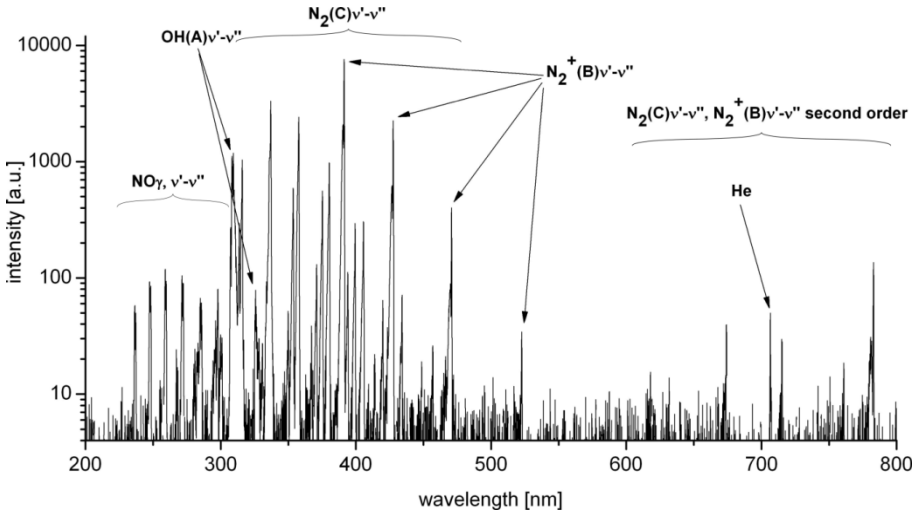


Fig. 3. Overview spectrum from the barrier discharge in helium with 0.1 vol.% nitrogen admixture.

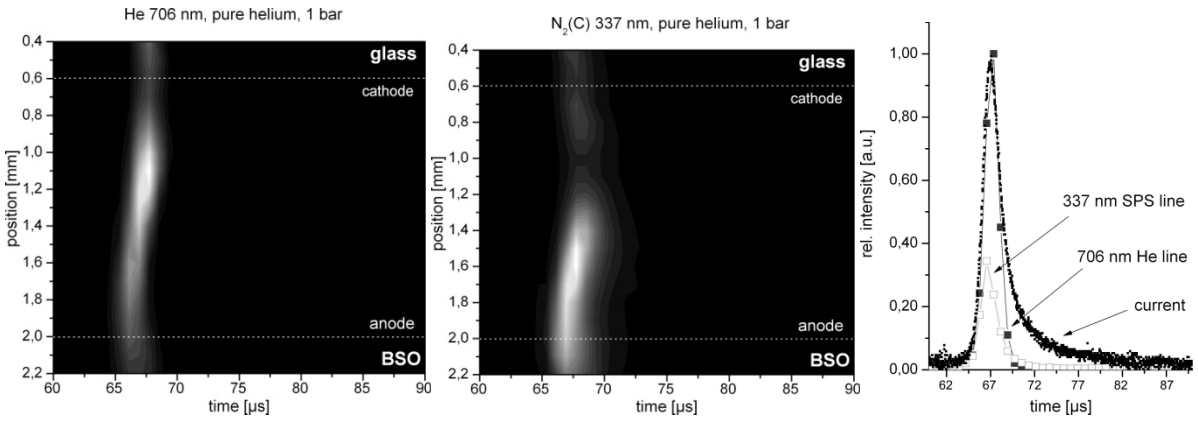


Fig. 4. Spatio-temporal development of the helium diffuse BD. 706 nm line of He (left), 337 nm line of N_2 (middle), discharge current and both lines in 0.6 mm distance to the anode (right).

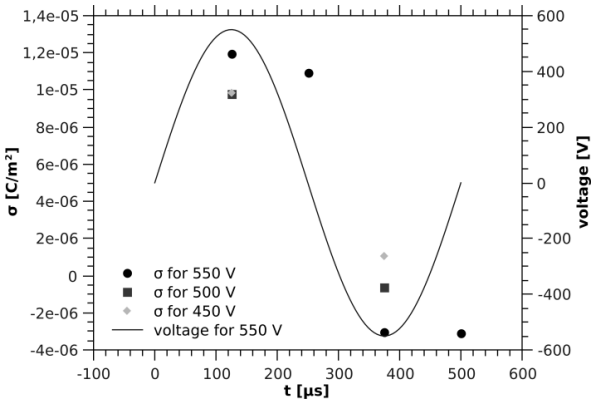


Fig. 5. Surface charge densities in pure He over one period (f = 2 kHz) for different feeding voltages.

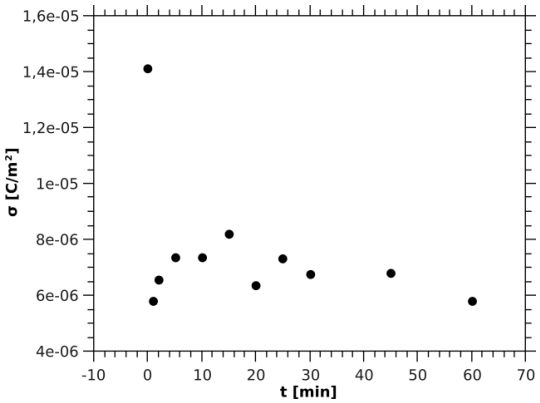


Fig. 6. Time dependence of the positive residual surface charges after turning off the discharge in pure He.

Their distribution functions are significantly different. They mark the momentary footprints of the discharge filaments. The negative surface charge density is about $\sigma \approx -6 \cdot 10^{-5}$ C/m^2. Their profile can be approximated by a gaussian function. The surface charge (integrated over one single distribution) is about $Q \approx -4 \cdot 10^{-11}$ C. The spot has a width of about 1 mm. For the positive surface charges the

situation is similar. Their density amounts approximately $\sigma \approx 7 \cdot 10^{-5}$ C/m^{2,} , the total charge of a single filament is up to $Q \approx 2 \cdot 10^{-10}$ C. Their width is up to 2 mm. Furthermore, it was observed, that some of the negative surface charges exist up to three full periods. These filaments are spatially stationary. Surprisingly, on the dielectric electrode charges of both polarities can exist at the same time (fig. 7, right). This can be explained with the existence of residual charges from former breakdown commonly with charge distributions from filaments of the recent half period.

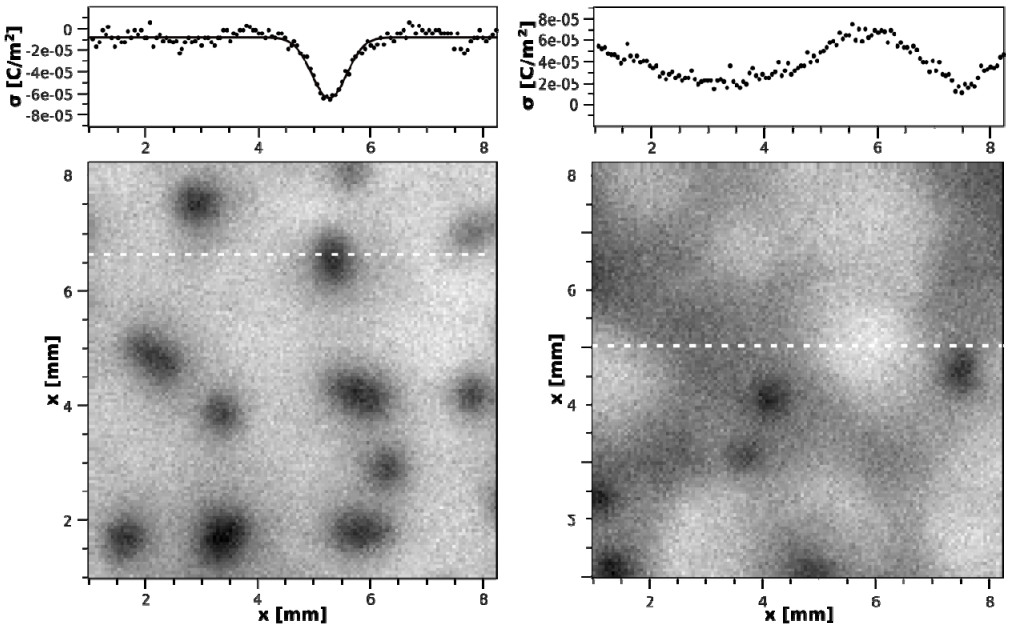


Fig. 7. Surface charge distributions on the BSO dielectric electrode. BD operation in the filamentary mode, He with 10 vol.% N_2 admixture, f = 2 kHz. Left: Negative surface charge density (dark spots) in the minimum of the voltage (-1.5 kV) with a section (white line) through one negative charge distribution. Right: measurement of the positive surface charge density (bright spot) in the maximum of the voltage (1.5 kV). Section through a positive charge distribution. Exposure time: 10 µs.

4. Conclusion

After the successful installation of the new setup which combines the surface charge diagnostics and the cross-correlation spectroscopy, first results have been presented. An important goal for the future will be the measurement of surface charges with a higher temporal and spatial resolution, and thus a direct correlation to the discharge development.

Acknowledgement. The work was supported by "Deutsche Forschungsgemeinschaft, SFB TR 24, 'Complex plasmas' ". The authors express their gratitude to P. Druckrey, U. Meißner and L. Stollenwerk for their technical support and helpful discussions.

5. References

[1] U. Kogelschatz, *Plasma Chemistry Plasma Process.* 23(2003)1
[2] F. Massines, A. Rabehi, Ph. Decomps, Ben Gadri, P.Segur, Ch. Mayox, *J. Appl. Phys.* 28(1998)2950
[3] H.-E. Wagner, K.V. Kozlov, R. Brandenburg, Cross-correlation emission spectroscopy applied to non-equilibrium plasma diagnostics, vol.1, 385, in R. Hippler, H. Kersten, M. Schmidt, K.H. Schönbach (Eds.), *Low Temperature Plasmas: Fundamentals, Technologies and Techniques*. WILEY-VCH Weinheim 2008
[4] A. Yariv, *Quantum electronics*, Viley New York 1989
[5] L. Stollenwerk 2007 *Physicl Review Letters, PRL* **98,** 255001

Topic 2
Modelling and diagnostics

SPECTROSCOPIC INVESTIGATIONS OF CORONA DISCHARGE IN HIGH PRESSURE HELIUM AT 300K

Nelly Bonifaci[1], Zhiling Li[1], Andre Denat[1], Vladimir Atrazhev[2], Vyacheslav Shakhatov[3]

[1] *Laboratoire G2Elab CNRS & Joseph Fourier University. 25 rue des Martyrs, 38042 Grenoble, France*

[2] *Joint Institute for High Temperatures, RAS, Moscow, 125412.*

[3] *Topchiev of Petrochemical Synthesis Institute, RAS, Moscow, 119991.*

E-mail: atrazhev@yandex.ru

Gaseous Helium at 300K and pressure (0.1-3)MPa was excited using a corona discharge both for negative and positive high voltages. The light emitted from the ionization zone of the discharge was analyzed. Asymmetric shape of atomic line 706nm was recorded. Blue wing of the line is more intensive than its red wing. The line shape is described as a convolution of Lorentz profile of the line center and a quasi-statistical profile of a blue wing of the line. Such analysis predicts a weak heating of the gas in the ionization zone for positive corona and considerable heating for negative corona.

1. Introduction

Spectroscopic observations of the light emitted by ionization gases can be used to determine conditions surrounding the emitted atoms or molecules. Corona discharge is characterized by strong spatial inhomogeneity. The corona current is determined by mobility of electrons or positive ions in low-field drift zone but the current density increases strongly with approaching to the region with strong electric field near a tip electrode. This region (ionization zone) is a source of a light emitted by the corona. Excited atoms interact with environment and feature of their spectra gives information about properties of a gas in the ionization zone.

The pressure broadening of spectral lines depends on the gas density. The "impact" interaction of radiator with surrounding atoms determines the Lorentzian profile of spectral lines emitted by a discharge in low pressure gases [1-4]. In this case the width $\Delta\lambda$ (Full Width Half Maximum) of a line and the line shift S relative its non-perturbed location is proportional to gas density. The analysis of the line broadening and shift has been made in [5] for the Lennard-Jones potential of an interaction between excited atom and surrounded atoms in the ground state. The shift sign ("red shift" for the shift toward longer wavelengths and "blue shift" for the shift toward shorter wavelengths) depends on character of radiator-perturbator interaction. The red shift corresponds to significant attraction. Growth of the density of a gas is accompanied by distortion of the "impact" Lorentz profile of a line. It has been shown [6] that the van der Waals attraction between a radiator and perturbators results in increasing of the intensity of a "red wing" of a line as compared with its "blue wing". The asymmetry of a spectral line shape was described using "quasi-static" approach where perturbators are assumed stationary. The quasi-static profile of a line has non-zero intensity for wavelengths which are larger than the wavelength of non-perturbed line. It is due to attractive interaction between radiator and surround atoms.

The corona discharge in helium under pressures up to 5MPa allows us to observe lines of He I in these conditions. It was originally supposed to calculate temperature and density of a gas in ionization zone of corona, using the impact approximation for treatment of the width and the shift of spectral lines. But measurements have detected considerable asymmetry of observable lines. Their "blue" wings have more intensity than "red" wings. It has demanded to include both impact approach and quasi-static one in the analysis of the shape of spectral lines. The impact profile of a line depends on both the gas pressure and the temperature. The quasi-static profile depends on the density only. Ideal gas relation between the density and the temperature at fixed pressure is appended to analysis of the line shape based on impact approximation. The impact approximation describes the central part of the line while the quasi-static approximation describes its wing. The different density and temperature dependences of these mechanisms allow us to treat the experimental data more definitely.

The objective of the report is to predict the gas temperature in the ionization zone using the experimental data on spectral line emitted from the zone. It is shown that the gas is heated in the negative corona but does not in the positive corona

2. Experiments and results

Experiments have been carried out in gaseous He at the fixed temperature 300K of the gas and different pressures in the cell from 0.1MPa up to 3MPa. The corona discharge (ionization of gaseous He) occurred in a vicinity of a tip electrode under high voltage. The discharge domain (ionization zone) had a volume less than an inter-electrode space (drift zone). The corona current has been measured for different temperatures and pressures in a space-charge-limited regime. This regime is characterized by an electric current as a quadratic function of the applied voltage *V*. Electrons with high mobility are the charge carriers in the drift region of the negative corona and it results in large negative corona current. Positive ions with low mobility are the charge carriers in the positive corona. Therefore the current of the positive corona is lower than that of the negative one.

The gaseous sample was produced from helium at the grade N 60 (Air Liquide) with an impurity concentration of about 0.1 ppm of oxygen. The gas was further purified by a series of traps that were filled with a mixture of molecular sieves (3-10 Å) and charcoal, activated under vacuum typically at 350°C for 3 days. The corona discharge cell included a point electrode and had a characteristic impedance of 50 Ohm and it could withstand pressures up to 10 MPa. Before filling the cell was pumped to about 10^{-4} Pa using a turbo-molecular pump. Tungsten tips with a radius of 2.5μm were prepared by electrolytic etching. The electrode spacing was 8 mm. All metallic electrodes were supported by Macor insulators. The high voltage from a stabilized dc power supply (Spellman RHSR/20PN60) was connected to the point electrode. In the cell the temperature of the gas could be adjusted to 300 K at a fixed pressure *P* for each series of measurements.

Light emitted from the region close to the point electrode was analyzed by a spectrograph through a sapphire window. The spectrograph (Acton Research Corporation of 300 mm focal length) was equipped with 3 plane gratings: one with 150 gr./mm and two with 1200 gr./mm that were blazed at 750 nm and 300 nm, respectively. The 2D-CCDTKB-UV/AR detector is located directly in the exit plane of the spectrograph. Its dimensions are 12.3x12.3 mm with 512x512 pixels of 24x24 μm for each pixel. In order to reduce the dark current, the detector was cooled to a temperature of 153 K (dark current <1 e/pixel/hour at 153 K). In our conditions, the instrumental broadening measured by recording profiles of argon lines from a low pressure discharge lamp is $\Delta\lambda_{instr}$=0.1 nm for a 1200 grooves/mm grating.

The light emitted from the corona region was collected and spectra in the range 500 - 1080 nm were recorded. Figure 1 shows a representative spectrum observed. Most of atomic lines and molecular bands were identified. These lines correspond to radiative transitions between excited states of He* atoms and He_2* excimer molecules. At low pressure the lines are sharp and their peak position match the atomic lines and molecular bands of helium from gas phase experiments, Table 1.

Tab. 1. Transitions observed in Helium corona discharge (300K, 0.1MPa).

Atomic lines		Molecular bands	
λ (nm)	Upper-Lower	λ (nm)	Upper-Lower
492,19	4d ^{1}D-2p ^{1}P	464,95	$e^3\Pi_g$- $a^3\Sigma_u^+$
587,56	3d ^{3}D-2p ^{3}P	573,49	$f^3\Delta_u$(v=0)-$b^3\Pi_g$(v=0)
706,52	3s ^{3}S-2p ^{3}P	575	$f^3\Delta_u$ (v=1)- $b^3\Pi_g$ (v=1)
728,13	3s ^{1}S-2p ^{1}P	577	$f^3\Delta_u$ (v=2)- $b^3\Pi_g$ (v=2)
1083,02	2p ^{3}P-2s ^{3}S	639,6	$d^3\Sigma_u^+$- $b^3\Pi_g$
		659,55	$D^1\Sigma_u^+$- $B^1\Pi_g$
		913,61	$C^1\Sigma_g^+$- $A^1\Sigma_u^+$
		918,3	$c^3\Sigma_g^+$- $a^3\Sigma_u^+$

A strong background continuum from 490 to 1100 nm appears in spectra at high pressures above 4.0 MPa. Moreover, the width of the lines increases with pressure and their relative intensity decreases. The noise superimposes on the line shape at high pressures. Though, the qualitative characteristic of the line shape can be recorded for pressures up to 2.5 MPa. Blue shift of line maximum and more

appreciable broadening of lines are observed. Atomic lines manifests asymmetric of their profile which increases with pressure. The skewness of the line shape is exhibited as larger intensity of its blue wing compare with a red wing. This effect is due to interaction of a radiator with surrounding atoms. The treatment of the phenomena is presented below and some properties of the corona ionization zone are predicted based on the treatment. We concentrate our attention on the analysis of shape of the atomic $3s^3S$ -> $2p^3P$ line at 706 nm being broadened and shifted with increasing pressure towards smaller wavelengths (blue shift).

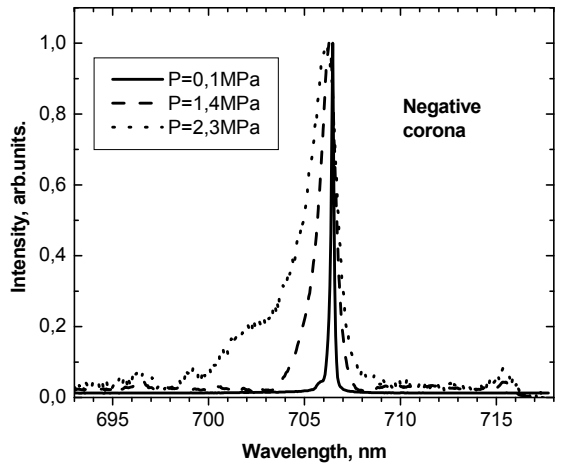


Fig. 1. Experimental spectra obtained for 706nm line in **negative** corona under different pressures.

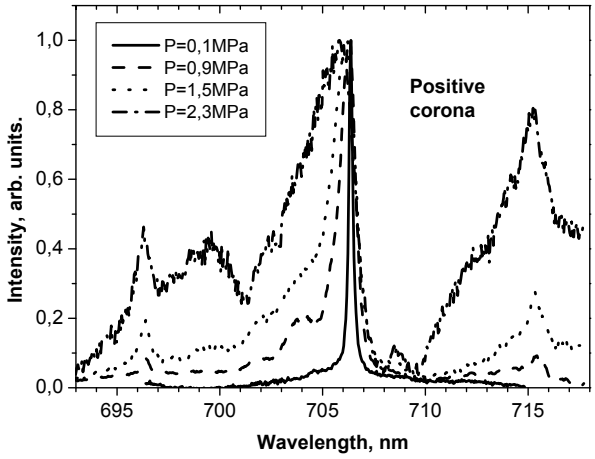


Fig. 2. Experimental spectra obtained for 706nm line in **positive** corona under different pressures.

The shapes of the line observed in negative and positive corona are different, but both spectra exhibit the blue shift and more intensive blue wing. The figures present very interesting phenomenon of "satellites" observed at both 696nm and 715nm. Their intensity increases with pressure and the effect is more appreciable in the positive corona. Here we analyze the shape of the central line and give an explanation in the framework of the classic theory of pressure broadening of spectral lines.

3. Theoretical treatment

The theory of "impact" broadening of spectral lines predicts symmetric Lorentzian profile of the line with shift and width being proportional to a gas density N [1, 2]. The analysis of the line distortion due to model Lennard-Jones potential of the interaction between radiator and perturbators [5] showed that the shift of the line depends on the nature of the interaction. If the van der Waals attraction prevails over the short range repulsion, the shift is toward long-length side. If the repulsion is prevailed, the "blue" shift is predicted. The blue shift has been observed in our experiments and this allows us to assume the repulsive interaction ($U(r) = C_{12}r^{-12}$) between a radiator and perturbators. Within the "impact" approximation for the repulsive interaction, the expressions for the line broadening $\Delta\lambda_L$ and the line shift S_L are given by:

$$\Delta\lambda_L = 6.44\left(\frac{\lambda^2}{2\pi c}\right)w^{9/11}\left|C_{12}\right|^{2/11}N, \qquad S_L = 0.922\left(\frac{\lambda^2}{2\pi c}\right)w^{9/11}\left|C_{12}\right|^{2/11}N \tag{1}$$

Here λ =706nm is the wavelength of the line, $w = 10^4 * T^{0.5}$ is the relative velocity in [cm/s] of the gas atoms with T being the gas temperature in [K], C_{12} is the repulsive Lennard-Jones parameter in [cm^{12} s^{-1}] and N is the gas number density in [cm^{-3}]. The impact approximation predicts the symmetric Lorentz profile of the line with a ratio of the shift and the width of 0.143, which is indeed close to what we find in our experiments with He gas at 300K and low pressures. The theoretical calculations with more realistic description of the interaction than L-J potential [7], gave for the 706nm line shift and broadening at 300K

$$\Delta\lambda_L = 2.9\cdot 10^{-21}\cdot N\cdot (T/300)^{9/22}, \qquad S_L = 0.384\cdot 10^{-21}\cdot N\cdot (T/300)^{9/22} \tag{2}$$

Here T is in K. Using the theoretical value for the broadening (2) and its treatment with the repulsive potential (1) one can estimate the repulsion constant value C_{12}= 1.6*10^{-72} cm^{12}/s.

It has been shown in [6] that the asymmetric line can be obtained in the quasi-static approximation in the frame of the pressure broadening theory. The approximation assumes zero velocity of atoms and it becomes significant for large density of a gas. The profile of a line $I(\Delta\omega)$ as a function of detuning $\Delta\omega$ from the line centre is described by the formula [8]

$$I(\Delta\omega) = \frac{1}{2\pi}\int_{-\infty}^{\infty} \exp\left[i\Delta\omega\rho - 4\pi N V(\rho)\right] d\rho \tag{3}$$

Here a red wing corresponds to $\Delta\omega<0$ and the blue wing is for $\Delta\omega>0$. The interaction between the radiator and perturbators $\Delta U(R)$ as a function of their spacing R is described by the term $V(\rho)$

$$V(\rho) = \int_0^{\infty}\left[1-\exp\left(-i\rho\frac{\Delta U(R)}{\hbar}\right)\right] R^2 dR \tag{4}$$

The property $V(-\rho)=V^*(\rho)$ allows us to rewrite Eq.(4) in the form [6]

$$I(\Delta\omega) = \frac{1}{2\pi}\int_0^{\infty}\left(\exp\left[-i\Delta\omega\rho - 4\pi N V^*(\rho)\right] + \exp\left[i\Delta\omega\rho - 4\pi N V(\rho)\right]\right) d\rho \tag{5}$$

Below we shall use the simple form of the repulsive potential $\Delta U(R) = C_{12}/R^{12}$ with one parameter C_{12}. It allows us to describe the line profile using dimensionless variables

$$I_{wing}(x) = \int_0^{\infty}\exp(-2.41y)\cdot\cos\left(x\cdot y^4 - y\right) y^3 dy \tag{6}$$

Here $x = \Delta\omega/\left(15.02\cdot N^4 C_{12}\right)$. The integral in Eq.(6) differs from zero for $x>0$ (a blue wing of the line) due to positive sign of the repulse interaction. The quasi-static profile Eq.(6) has the blue shift and describes the long frequency wing of the line. The center of the line is described by the Lorentzian profile with the impact broadening

$$I_L(\lambda) = \left(\frac{\Delta\lambda_L}{2}\right)^2\left(\left(\lambda-\lambda_0+S_L\right)^2 + \left(\frac{\Delta\lambda_L}{2}\right)^2\right)^{-1} \tag{7}$$

with the shift S and the width $\Delta\lambda$ are according to Eq.(2). In order to combine the central profile Eq.(7) and the wing-profile Eq.(6), the convolution operation was used in a manner as it been done in [6]

$$I(\lambda) = \int_0^{\lambda_0} I_{wing}(x) I_L(\lambda - x) dx \tag{8}$$

Here the integration variable x is the difference between the wing wavelength and the wavelength of the line center λ_0, $x = (\lambda_0 - \lambda) > 0$. The analytical expression has been used for the total shape of the line, Eq.(8)

$$I(\lambda) = \int_0^{\infty}\frac{z^{0.9}\exp(-0.1\cdot z)}{\left(\left(\Delta\lambda_w + \lambda\cdot z\right)^2 + \left(\frac{\Delta\lambda_L}{2}\right)^2\cdot z^2\right)} dz \tag{9}$$

Here λ is a wavelength from the shifted center of the line, $\lambda_0 - S_L$. The total profile depends on the impact broadening of line center (FWHM is $\Delta\lambda_L$, Eq.(2)) and on the quasi-static parameter $\Delta\lambda_w$

$$\Delta\lambda_w = \frac{15.02\lambda_0^{\,2} N^4 C_{12}}{2\pi c} = 2.48\cdot 10^{-2}[nm/(MPa)^4]\cdot p^4 \tag{10}$$

These parameters have different density dependence. The parameter of impact width of the line center is proportional to gas density, Eq.(2), while $\Delta\lambda_w$ has strong density dependence as

N^4. Figures 3 and 4 show the result of calculation of the 706nm line shape for pressures 1.5 MPa and 2.3 Mpa observed in positive and negative coronas using Eq.(9).
For simulation of the line for the positive corona the gas density was calculated using the pressure values and the temperature 300K in the ionization zone of the discharge. The accordance between experiment and simulation shows that there is no heating of the gas in corona zone in the positive corona, Fig. 3.

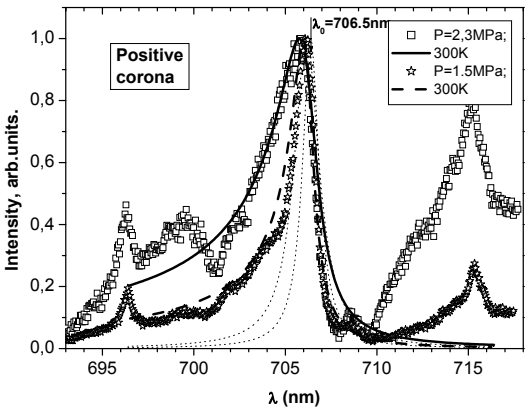


Fig. 3. Simulation of the 706nm line emitted by positive corona at 300K and 1.5 MPa and 2.3MPa – solid and dashed lines; dotted lines – Lorentzian profiles

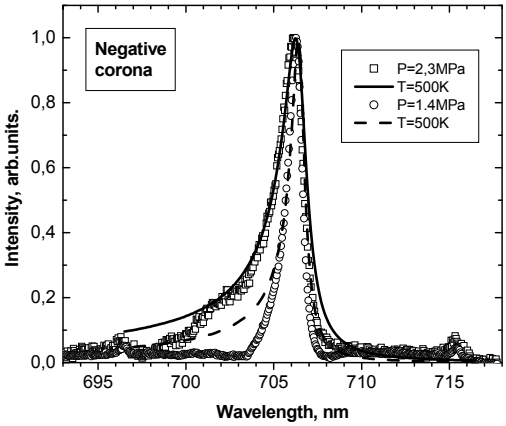


Fig. 4. Simulation of the 706nm line emitted by negative corona at 500K and 1.5 MPa and 2.3MPa – solid and dashed lines.

The line observed in the negative corona has less broadening than predicted by its simulation for the gas density calculated using the pressure values and the temperature 300K in the ionization zone. The heating of a gas in ionization zone was assumed. The heating leads to decreasing of gas density under fixed pressure. The impact broadening of the line centre decreases proportional to the density and increases with the temperature according Eq.(2). The more significant effect is attenuation of the asymmetry of the line shape due to weakening of the quasi-static parameter Eq.(10). The most adequate agreement between the experimental line profiles and their simulation occurs if the temperature 500K is assumed for the ionization zone of the negative corona, Fig.4. Indeed, the negative corona currant in the space-charge-limited conditions is larger than that in the positive corona, because higher electron mobility in the drift zone of the negative corona. The larger current results in possibility of considerable heating of the gas near a tip electrode.

Authors from Russia (V.A. and V.S.) thank Russian Foundation of Basic Researches for support of their work; grant 08-08-00694

4. References

[1] Traving G. 1968 *Interpretation of line broadening and line shift in Plasma Diagnostic* (Chap. 2), edited by W. Lochte-Holtgreven, North-Holland Publishing Company, Amsterdam.
[2] Allard N. and Kielkopf J. 1982 *Rev. Mod. Phys.* **54** 1103.
[3] Lindholm E. 1945 *Ark. Fis. A* **32** 1.
[4] Foley H. M. 1946 *Phys. Rev.* **6**9 616.
[5] Hindmarsh W. R., Petford A. D. and Smith G. 1967 *Proc. of the Royal Society of London. Series A* **297** 296.
[6] Margenau H. 1935 *Phys. Rev.* **48** 755.
[7] Leo P. J., Mullamphy D. F. T., Peach G. and Whittingham I. B. 1992 *J. Phys. B.* **25** 1161.
[8] Anderson P. W. 1952 *Phys. Rev.* **86** 809.

PHASE RESOLVED CROSS-CORRELATION SPECTROSCOPY ON SURFACE BARRIER DISCHARGES IN AIR AT ATMOSPHERIC PRESSURE

Ronny Brandenburg, Helge Grosch, Tomas Hoder, Klaus-Dieter Weltmann

Leibniz Institute for Plasma Science and Technology (INP),
Felix-Hausdorf-Str. 2, 17489 Greifswald, Germany
E-mail: brandenburg@inp-greifswald.de

Recently, spatio-temporally resolved studies of single microdischarges in a surface barrier discharge arrangement were realized. As diagnostic techniques an intensified CCD camera equipped with a far field microscope for two dimensional spatial imaging, as well as Cross-Correlation Spectroscopy for the spatio-temporal development of the discharge within a sub-nanosecond and sub-millimetre scale have been used. In these studies, the surface barrier discharge was driven in order to generate only one microdischarge per half period (single-microdischarge mode). The discharge was driven at conditions resulting in several microdischarges per half period. The CCS setup enables the recording of microdischarge development for different phases of the applied voltage. Distinct differences between the subsequent phase channels in the positive half period are carried out, while the first channel shows similar behaviour as in the single-microdischarge-mode surface discharge.

1. Introduction

Surface barrier discharges (SBDs) in air at atmospheric pressure consist of single constricted microdischarges (MDs) visible as distinct filaments. Due to the erratic appearance, short duration time and small size the investigation of single MDs is a challenging task. Using the method of Cross-Correlation Spectroscopy (CCS), the spectrally resolved luminosity of MDs can be recorded with a high temporal (sub-ns) and spatial (sub-mm) resolution. This has already been demonstrated for different discharge types, e.g. volume barrier discharges (VBDs) and coplanar barrier discharges (CBDs) [1, 2]. Recently SBDs in an asymmetric point-to-point SBD configuration were investigated by means of CCS as well as iCCD-camera enhanced with far field microscope [3]. In these studies the plasma was driven sinusoidal with low voltage amplitudes closed to the burning voltage, resulting in the generation of only one or at most two MDs per half period (single-MD-mode).
However, in many applications barrier discharges will be driven at voltage amplitudes generating a large number of MDs within the same half period. Since CCS offers a phase resolution, too, the development of MDs at different phases within the period of applied voltage can be studied. In case of sinusoidal driven VBDs the MDs development was found to be independent on the phase, i.e. the development is the same for all MDs generated at the same polarity [2]. In CBDs differences due to residual charges on the dielectric surface have been investigated [4]. In this contribution a phase resolved analysis in the positive half period of the applied voltage is made for the SBD arrangement studied in [3]. The aim of the study is (1) to compare the MD development in the single-MD-mode with multiple appearing MDs at higher applied voltage amplitude and (2) to compare MD development for different phases of applied voltage in case of multiple appearing MDs. Such a comparison should give first general facts on the phase dependence of MDs in SBD arrangements.

2. Experimental setup

The discharge was generated in an arrangement consisting of two needle electrodes (syringe hollow needles made of chrome-nickel-steel alloy) placed on the opposite sites of a 0.6 mm thick Al_2O_3 dielectric plate (see Fig. 1). The tips of the electrode faced each other with a gap of d = 1.15 mm. To prevent a parasitic discharge one side was covered in silicone glue (covered electrode). This configuration granted long time stability of well-localised MDs, which is required for CCS studies [5]. The electrode configuration was set in a Plexiglas chamber flushed with dry air. The power supply generated a sinusoidal voltage of several kV_{pp} at frequency of about 60 kHz which was applied to the

covered electrode. The applied voltage and current were measured by probes (see [3] for details) and recorded by a digital storage oscilloscope.

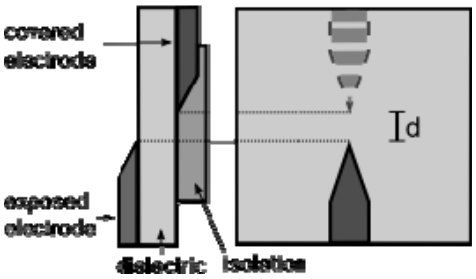


Fig. 1. Scheme of SBD pin-to-pin electrode configuration (left side view; right top view)

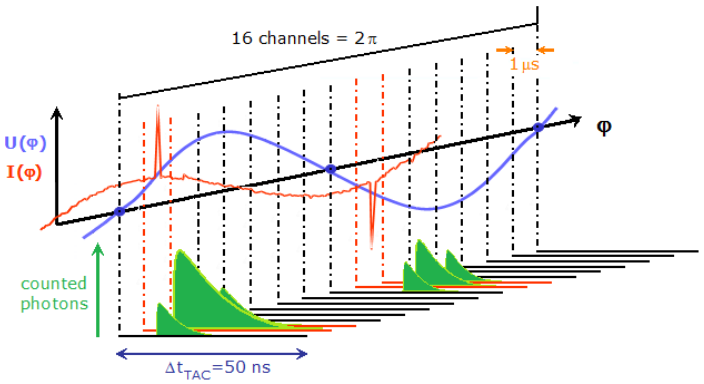


Fig. 2. Scheme of the division of the applied voltage into 16 phase channels for a selected wavelength and spatial position of the CCS measurement

MDs were investigated by means of short exposure time photography (gated iCCD camera) and CCS. The iCCD camera was equipped with a far field microscope to enable spatial resolution of 4 µm. The light of the discharge could be projected by a UV achromatic lens to the entrance slit of a monochromator. On one exit, a CCD camera was located for classical optical emission spectroscopy. On the other exit, a photomultiplier (PMT) behind an exit slit was installed. The combination of the monochromator, two highly sensitive PMTs, a time-correlated single photon counting board and the routing procedure board (DDG - digital delay and pattern generator) made up the CCS, which is described in detail elsewhere [2]. The temporal resolution was 12 ps. The routing procedure of the DDG provided a course time scale, which was synchronized with the phase φ of the applied voltage. This made it possible to differentiate between the positive and negative half period. Nevertheless, the cycle duration of about T = 1/60 kHz ≈ 17 µs was divided into 16 intervals (Δt_{DDG} = T/16 = 1.07 µs), - so called phase channels - to realise phase resolved measurement in one period (see Fig. 2).

3. Experimental results and discussion

Single-microdischarge mode

If voltage with amplitude slightly higher than the burning voltage is applied, only one MD in each half period occurs (so-called single-MD mode). From time to time a second MD appears which could be verified by current measurements. By investigating this with the iCCD camera, different structures for the two individual MDs could be observed. The first MD in each half period propagates on direct path between the electrodes (see Fig. 3 a). The second MD spares the region of the first MD and develops around it (see Fig 3 b). Obviously, the first MD leaves positive charge on the surface decreasing the electric field in this region. Therefore, the next MD is forced on a path outside the low field region [5].

The development of MDs was investigated by the measurement of the spatio-temporal distribution of radiation intensity of the 0-0 vibrational transition of the second positive system of molecular nitrogen (SPS at λ = 337.1 nm; 11 eV excitation energy) with the CCS technique. This molecular band is the most intensive in the optical emission spectrum and represents the convolution of the reduced electric field with the electron density. The pictures in Fig. 4 show the development of the SPS in the subsequent phase channels 1 and 2 (a and b), respectively. The first emission of light appears at the tip of the exposed anode (positioned at 0 mm), followed by a discharge channel propagating in the direction of the covered cathode (position at 1.15 mm) with decreasing velocity. The overall development can be explained similar as in VBDs or CBDs [1]. In the so-called pre-phase, at the tip of the anode a positive charge is generated by means of successive electron avalanches. Reaching a certain threshold of the local electric field, more and more charge carriers are generated in front of the

positive charge and the MD develops as a cathode directed ionization front (positive streamer). In the first phase channel (Fig. 4 a) the velocity of the light emission maximum is about $3.4 \cdot 10^5$ m/s. The decrease of the discharge front velocity might be explained by the configuration of the initial electric field. In the considered geometry, the MD channel propagates into a region of decreasing applied electric field which may lead to a decreasing ionization rate and thus ionization front velocity. However, surface processes and effects caused by residual charges need to be taken into account, too (see [3] for details).

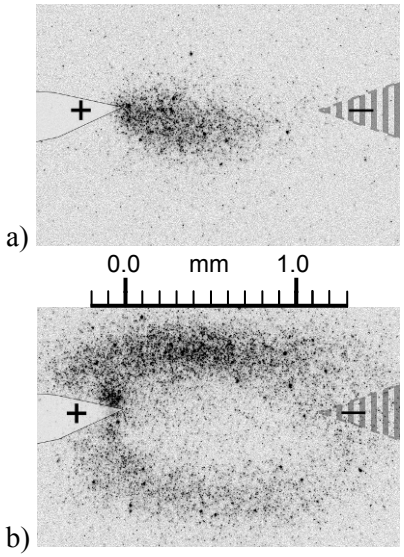


Fig. 3. Negatives of iCCD photos of a) the first and b) the second MD in the positive half period. Exposed anode on the left, covered cathode on the right. (Both photos are accumulated over 20 cycles). [5]

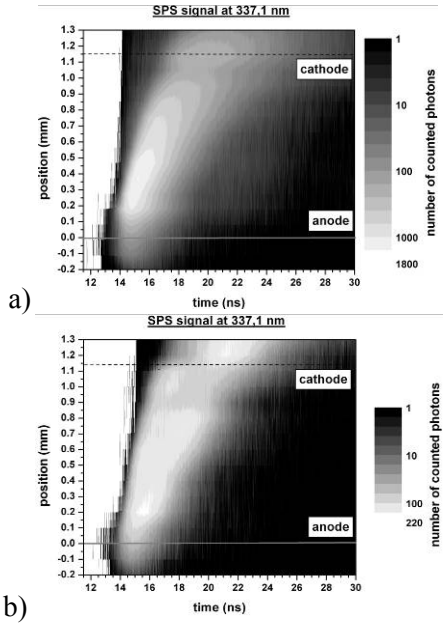


Fig. 4. Spatio-temporal development of the SPS for the a) first and b) second phase channel of the positive half period.

In the second phase channel (Fig. 4 b), the discharge activity is about one order of magnitude lower (1800 vs. 220 counted photons). Obviously, less MDs are generated in the second phase interval, which is in agreement with the current measurements. From the iCCD photo (Fig. 3 b) one can suggest that the second MD within the same half period propagates on a different and longer pathway. Here, the CCS recording is one-dimensional along the electrode axis. I.e. the curved shape of the second MD channel is somewhat projected on the electrode axis and the actual velocities of light propagation can not be determined properly from the plot. Furthermore, the signal in Fig. 4 b may contain photons from first MDs (if they appear later), too. These facts hinder a profound description of the second MD, but at least a similar mechanism as for the first MD can be concluded from these results, namely the pre-phase and cathode-directed ionization front with decreasing velocity.

Multiple-microdischarge mode

At a higher value of voltage amplitude, multiple MDs occurred during the positive half period. At the voltage amplitude of about 10 kV_{pp}, between four and six MDs per half period took place. As already seen in the single-MD mode, the MDs form a structure, in which the path of a previous MD is spared. These patterns emerge very regular, so that they can be observed over multiple cycles of positive half period of the applied voltage via iCCD photography (see Fig. 5). In Fig. 6 the results of the CCS measurement of the SPS for first four subsequent phase channels are shown, covering the first 4 µs of the positive polarity. The CCS measurements were focussed on the anode region and therefore don't show the complete discharge gap.

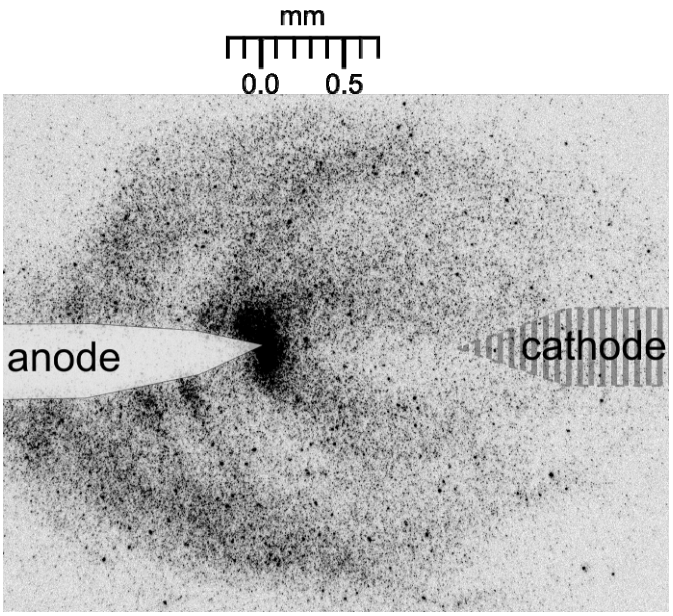


Fig. 5. Negative of iCCD photo showing the emerging pattern of subsequent MDs in the positive half period at higher applied voltages (10.5 kV_{pp}) accumulated over 20 cycles. Exposed anode on the left, covered cathode on the right [5]

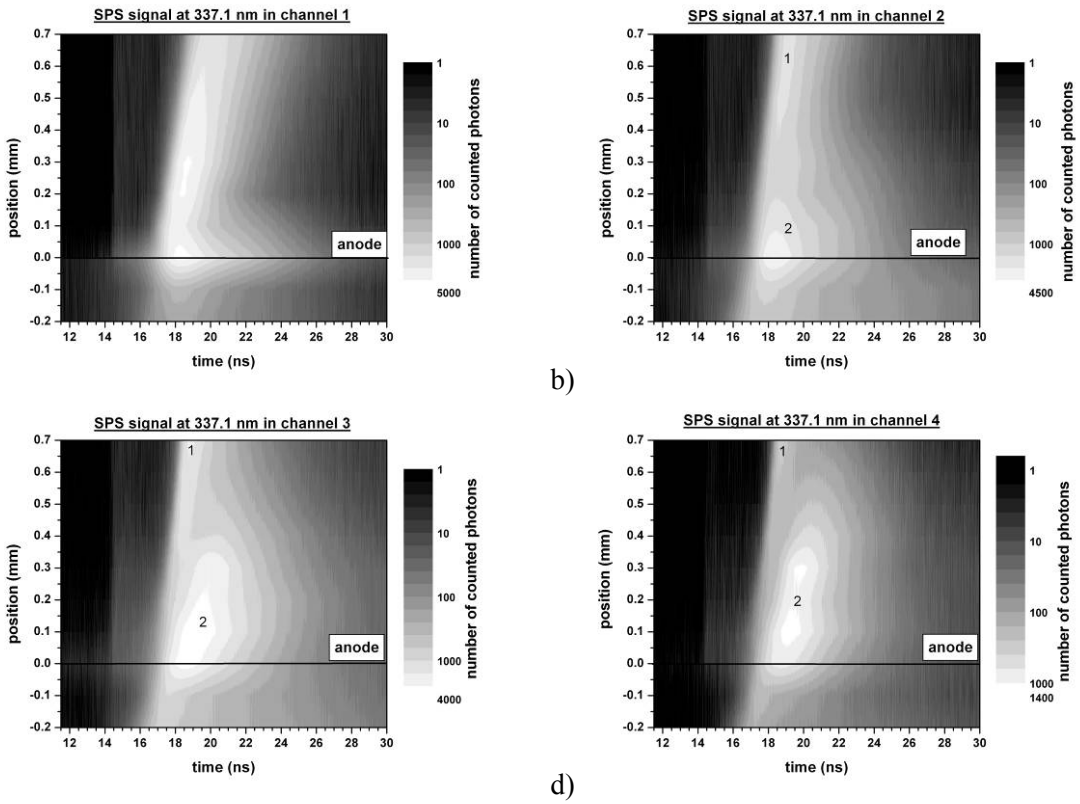


Fig. 6. Spatio-temporal development of the SPS for the first four phase channels (a) to (d) of the positive half period at a voltage significantly larger than the burning voltage (11.4 kV_{pp}).

The overall development in the first time channel (Fig. 6 a) shows the pre-phase and the cathode directed ionization front with a velocity of $3.8 \cdot 10^5$ m/s. In contradiction to the single-MD mode results behind the ionization front a second maximum of light emission is investigated at the anode tip. In the following phase channels the first maximum (correlated with the head of the ionization front) is

shifted towards the cathode. The anode light emission grows up and shows a cathode directed propagation, too (see Fig. 6 c and d). The velocity of the first MD event in a subsequent channel increases from $3.8 \cdot 10^5$ m/s via $5.4 \cdot 10^5$ m/s (channel 2) and $6.5 \cdot 10^5$ m/s (channel 3) to $7.7 \cdot 10^5$ m/s in phase channel 4. The velocity of the anode light emission in channels 2 to 4 also increases at a similar rate (from $1.6 \cdot 10^5$ m/s to $2.4 \cdot 10^5$ m/s to $2.8 \cdot 10^5$ m/s). It has to be mentioned that the actual velocity is higher than determined from the plots in Fig. 6, since the MD channels after the first MD have a curved shape and longer pathway. In fact, the inaccuracy increases with the channel, i.e. that the velocities increase stronger than suggested by the CCS results.

The reason for the second, slower front of luminosity is still to debate. Photons from slower and faster MDs may overlap in one phase channel. In this case the results for all phase channels should be similar, but as mentioned above the velocities are significantly different in the different phase channels. Another explanation is the so-called “backward discharge” as already observed by Gibalov and Pietsch [6] and Starikovskii et al. [7]. In the cited papers, the backward discharge was always observed at the decreasing slope of the applied voltage (discharge mainly generated by pulsed DC) which is a different situation than here (sinusoidal AC, discharge activity investigated only at positive slope of applied voltage). Further investigations supported by numerical simulation are necessary to understand this behaviour. But the results show that the MD development is influenced by the applied voltage amplitude. Furthermore, there is a clear phase dependence, which is already known for CBDs but not for VBDs.

4. Conclusion and Outlook

In this contribution, subsequent MDs in an asymmetric needle-needle SBD arrangement in the positive half period were investigated by iCCD camera, enhanced with a far-field microscope and CCS diagnostic. The results for the multiple-MD mode at overvoltage were compared with the results of the single-MD mode closed to burning voltage.

It was found, that the first MD propagates on the direct way between the pin-electrodes, while the subsequent discharges spared the region of the previous MD, due to positive residual charge on the surface. The CCS results showed, that the first MD event developed in a similar way (pre-phase and cathode directed ionization front) as in other barrier discharge arrangements. If a second MD appears in the same half period a similar mechanism as in the first one was suggested from the results. In case of multiple-MD mode - unlike VBD results - there was a clear dependency on the phase and value of applied voltage. A second maximum of light emission at the anode was observed. Its origin is not clear. Future experiments and simulations are needed to clarify the mechanism. These have to include the influence of the actual electric field and surface processes.

5. References

[1] T. Hoder, R. Brandenburg, R. Basner, K.-D. Weltmann, K. V. Kozlov and H.-E. Wagner, *J. Phys. D: Appl. Phys.*, 43, 124009 (8pp), 2010.

[2] H.-E. Wagner, K. V. Kozlov and R. Brandenburg, *Low temperature plasmas - Fundamentals, Technologies and Techniques*, eds. R. Hippler, H. Kersten, M. Schmidt and K.-H. Schoenbach, Wiley-VCH, 271-306, 2008.

[3] H. Grosch, T. Hoder, K.-D Weltmann, R. Brandenburg, *Eur. Phys. Jour. D* (2010) accepted.

[4] T. Hoder, R. Brandenburg, M. Czernak, *these proceedings.*

[5] R. Brandenburg, H. Grosch, T. Hoder, K.-D. Weltmann, *Proc. of EPS conference on Plasma Physics,* Dublin/IR 2010.

[6] V. I. Gibalov and G J Pietsch, *J. Phys. D: Appl. Phys.* 33, 2000, 2618-2636.

[7] A.Y. Starikovskii, A A Nikipelov, M M Nudnova and D V Roupassov, *Plasma Sources Sci. Technol.*, 18, 2009, 17 pp.

SIMULATION OF THE DISCHARGE PROPAGATION IN A CAPILLARY GLASS TUBE IN AIR AT ATMOSPHERIC PRESSURE

Jaroslav Jánský[1], Fabien Tholin[1], Zdeněk Bonaventura[1,2], Anne Bourdon[1]

[1]*EM2C, UPR CNRS 288, Ecole Centrale Paris, Grande voie des vignes, 92295 Châtenay-Malabry Cedex, France*

[2]*Masaryk University, Faculty of Science, Department of Physical Electronics, Kotlářská 2, 611 37 Brno, Czech Republic*

E-mail: Jaroslav.Jansky@em2c.ecp.fr

The objective of this work is to study the propagation of an air discharge at atmospheric pressure with radial geometrical constraints. These constraints are introduced by placing a capillary glass tube around the discharge area. The problem is studied using a fluid model which allows variation of different physical processes and parameters. Two surface processes are included on the dielectric surface: secondary electron emission by impact of ions and photoemission.The influence of the inner radius of the glass tube, applied voltage shape and the photoemission coefficient on the structure and velocity of the discharge are presented. Two methods are used to calculate the discharge current.

1. Introduction

In recent years, there has been an increasing interest for systems and processes using atmospheric pressure electrical discharges inside random or organized two-phase media such as porous solid, monoliths or foams [1,2,3]. To understand and characterize the discharge dynamics in these complex media, as a first step we propose to study the discharge propagation in a capillary tube.

Recently we have studied the influence of a radial geometrical constraint on the discharge dynamics in air at atmospheric pressure for a constant applied voltage of 9 kV for a dielectric tube of permittivity ε=1 and for different values of the dielectric constant for a constant applied voltage of 6 kV [4]. The objective of this work is to study conditions closer to experiments carried out in LPGP, Orsay [5]. Then we present discharge simulations for a pulsed applied voltage with a maximum of 9 kV in a capillary glass tube with permittivity ε=5.

2. Model description

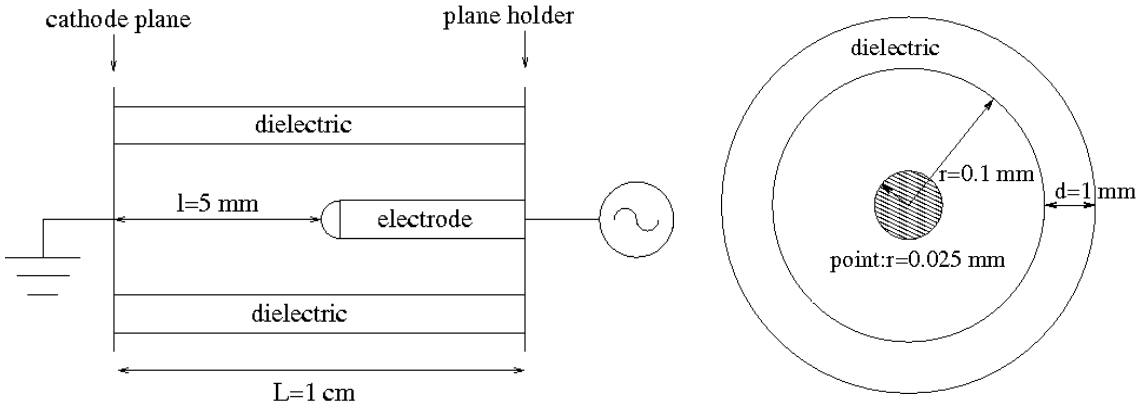


Fig. 1. Sideview and topview schematics of discharge set-up for a capillary tube with an inner radius of 100 μm.

The studied configuration is shown on Fig. 1. A metallic point anode on a plane holder is set at 5 mm of a metallic cathode plane. The tip of the point is a semisphere with a radius of curvature r = 25 mm. The point is immersed in a capillary tube of inner radius varying in range 75-250 mm and 1 mm thick.

A 2D fluid model is used to simulate the discharge propagation in the tube: continuity equations for charged species are coupled to Poisson's equation using cylindrical coordinates. Kulikovsky scheme [6] has been used for drift - diffusion part of continuity equations and a direct solver MUMPS [7] for Poisson's equation. Transport parameters and source terms including photoionization are taken from [8]. On the dielectric interface, we considered secondary emission due to positive ion impact and photoemission [9]. On the metallic cathode, Neumann boundary conditions are used for species fluxes. More detailed description of the numerical procedure is given in [4]. To model the applied voltage shape used in experiments a sigmoid function is chosen (i.e. a smooth function with steep rise and plateau). The rise time of the voltage is 2 ns and the duration of the plateau is 20 ns. To describe the discharge propagation the axial velocity of the discharge is calculated based on movement of the position with the maximum electric field. In this work the velocity is calculated every 0.5 ns.
To compute the discharge current, two different methods are used. First the current is determined from total power:

$$I = \frac{1}{U}\int_V \vec{J}\cdot\vec{E}\,dV\,, \tag{1}$$

where V is the volume of the computational domain, U is the applied voltage, $\vec{J}$ is total current flux and $\vec{E}$ is electric field. This approach of current calculation is presented in [10] but without dielectric interface. The presence of dielectrics requires the calculation of the time derivative of electric field. With small time step and then very small changes in electric field, this part is the most computational demanding one. It is important to note that the use of iterative solver for Poisson's equation does not allow to have an accurate calculation of the capacitive current. In this work we have used a direct solver to solve Poisson's equation. In this case the accuracy of solution is the truncation error of used variables which allows an accurate calculation of the current.
The second method to calculate the current is the integration of the current flux over a surface:

$$I = \int_S \vec{J}\cdot\overrightarrow{dS}, \tag{2}$$

where S is a surface (cut through the whole domain) described by equation {x = Const.}. Taking into account two different surfaces, with conservation of the current, the difference between them is equal to the current flux out of the domain. When the current flux out of the domain is zero, the integrated current is independent on the surface of integration defined by {x = Const.}.

3. Results

In this section, we present simulation results of the discharge propagation in capillary glass tubes with ε=5. First photoemission is not included and its influence is discussed at the end of the section. The discharge starts with very fast expansion phase around the point [4] and then reaches a stable structure with a stable axial propagation. The study of the stable propagation is the main target of this work. One time snapshot representing electric field and electron density spatial distribution in the discharge front at a given time when the discharge is around the middle of the gap for a tube with an inner radius 100 μm is shown on Fig. 2. Maximum of electric field is observed out of axis in the region between the tube interface and the discharge. Its maximum value is over 450 kV/cm. Then electric field is decreasing towards the axis. Electric field on the axis is still higher than usual maximum electric field for an air discharge propagation at atmospheric pressure without capillary tube. Contours of electron density higher than 10^{14} cm^{-3} show a tubular structure of the discharge. First experimental results seem to confirm this tubular structure [5]. Contours of electron density lower than 10^{13} cm^{-3} are more homogeneous.
Then we study the influence of the inner radius of the glass tube on the discharge dynamics. On Fig. 3 (left) is shown the time dependence of the axial velocity for different inner radii of the capillary glass tube in the range of 75 to 250 μm. The axial velocity is calculated when the stable axial propagation of the discharge is obtained, which corresponds to t > 3 ns. We note that the velocity dependence is not monotonic with the inner radius of the tube and a higher limit is reached for radius lower than 150 μm. This is in good agreement with experimental results for the same applied voltage even if the absolute value of velocity is different [5]. Tab. 1 shows that the maximum electric field in the tube is increasing with decreasing inner radius. Smaller inner radius means that the capillary tube is in contact with discharge earlier after initiation and let the discharge propagate with higher maximum electric field. More detailed explanation is presented in [4]. Velocity of the discharge is strongly dependent on the

electron impact ionization. The total ionization is a combination of Townsend ionization coefficient and the area where the ionization takes place. These two parameters have opposite behaviours for a varying inner radius. With decreasing radius the Townsend ionization coefficient is increasing and the area where the ionization took place is decreasing.

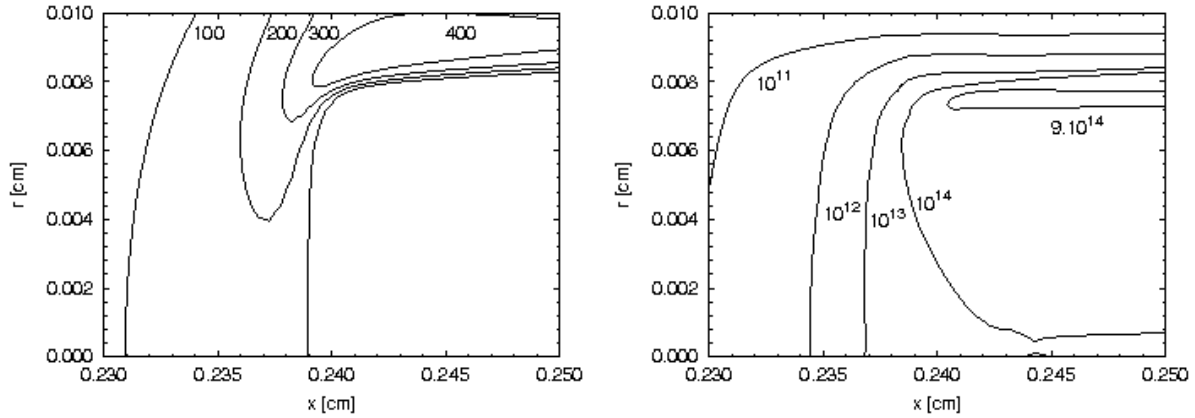


Fig. 2. Electric field and electron density spatial distribution in the discharge front at a given time when the discharge is around the middle of the gap for a capillary glass tube (ε=5) with an inner radius of 100 μm.

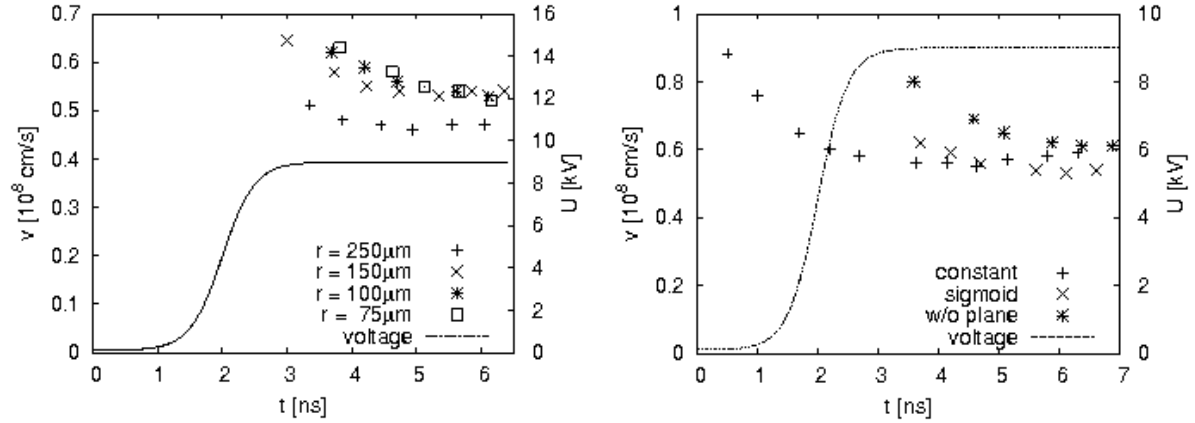


Fig. 3. Axial velocity of the discharge front as a function of time for tubes of inner radii 75 μm, 100 μm, 150 μm and 250 μm (left figure) and for different applied voltage shapes: with constant voltage, sigmoid voltage and sigmoid voltage without plane holder of the metallic point anode are presented (right figure).

The influence of the shape of the voltage pulse is shown on Fig. 3 (right). Constant voltage pulse is compared with the sigmoid voltage pulse with a rise time of 2 ns. With the sigmoid voltage pulse, the discharge is ignited during the voltage rise at a value lower than the maximum voltage. The first nanosecond of the propagation, when the discharge is becoming stable, velocity is decreasing. During this phase the velocity with the sigmoid voltage is slower. When the propagation becomes stable with constant velocity no difference can be observed. Also a comparison with the configuration without plane holder of the metallic point anode (Fig. 1) is shown. It is observed that without plane holder the discharge propagates faster. This corresponds to the increase of the maximum electric field and the maximum electric field on the axis shown in Tab. 1. Without plane holder the electric field enhancement close to the discharge front or point electrode is higher than with plane holder. In the experiment, the geometry of the point anode holder is rather complex with dielectric parts. Therefore

we consider the two configurations with and without plane holder as limit cases to estimate the influence of the holder on the results.
Photoemission is studied separately to clearly demonstrate its influence on the discharge. Due to uncertainity of the photoemission coefficients two values $k=5.10^{-4}$ and $k=5.10^{-3}$ are used [4]. The case with r=100 μm is used for comparison. It is seen from Tab. 1 that the discharge velocity is unchanged with and without photoemission. Based on electron density and electric field values we note that the discharge becomes more nonhomogeneous with increasing photoemission coefficient. With the increase of nonhomogeneity, the discharge propagates slower [4] but the increase of free electrons in front of the head of the discharge compensates it. The discharge is adjusting itself to finally have almost the same axial velocity. This is very interesting for comparison with experiment since axial velocity of the discharge can be used even without exact knowledge of surface emission processes.

Tab. 1. Overview of presented results for 9kV applied voltage and permittivity ε = 5. First 4 lines corresponds to inner radius variation. Next 2 lines are for variation of applied voltage for r=100 μm. For first 6 lines photoemission is not included. Last 2 lines show the photoemission coefficient k variation for r=100 μm. Axial velocity v, maximum electron density n_{max}, ratio of maximum electron density to maximum electron density on the axis, maximum electric field E_{max} and maximum electric field on the axis $E_{max,axis}$ are presented. Time when discharge passes the middle of the gap (2.5 mm from grounded electrode) is chosen for comparison.

conditions	v [10^7cm/s]	n_{max}[cm^{-3}]	$n_{max}/n_{max,axis}$	E_{max}[kV/cm]	$E_{max,axis}$[kV/cm]
r=250 μm	5	$7.0 . 10^{14}$	350	395	76
r=150 μm	5,5	$8.2 . 10^{14}$	35	425	117
r=100 μm	5,5	$9.7 . 10^{14}$	9,5	450	175
r=75 μm	5,5	$1.3 . 10^{15}$	5,6	490	230
const. volt.	5,5	$1.0 . 10^{15}$	9,1	460	177
w/o plane	6,5	$1.15 . 10^{15}$	8,2	495	185
$k = 5 . 10^{-4}$	5,5	$1.25 . 10^{15}$	18	500	155
$k = 5 . 10^{-3}$	5,5	$1.4 . 10^{15}$	120	530	113

Fig. 4 shows the current as a function of time for a discharge with a glass tube of inner radius 100 μm. Only one current is presented because both (from power and integration over surface) are equal with a relative error of order 10^{-2}. We have checked that the integration of current over different surfaces {x=Const.} are also equal with relative error under 10^{-6}. The first current peak at 2 ns corresponds to the capacitive current due to the voltage rise. The current from the expansion phase is much smaller in amplitude and is hidden in this peak (small asymmetry after the maximum of the peak). The current peak corresponding to the impact of the discharge on grounded electrode is shown in zoomed right figure. Maximum value is 0.13 A. These current results have the purpose to verify the calculation procedure. Independent choice of surface to calculate equation (2) shows that conservation of current is valid and equality of two approaches (equations (1) and (2)) shows physical consistency of the procedure. Finally the results show physical behaviour with reasonable values.

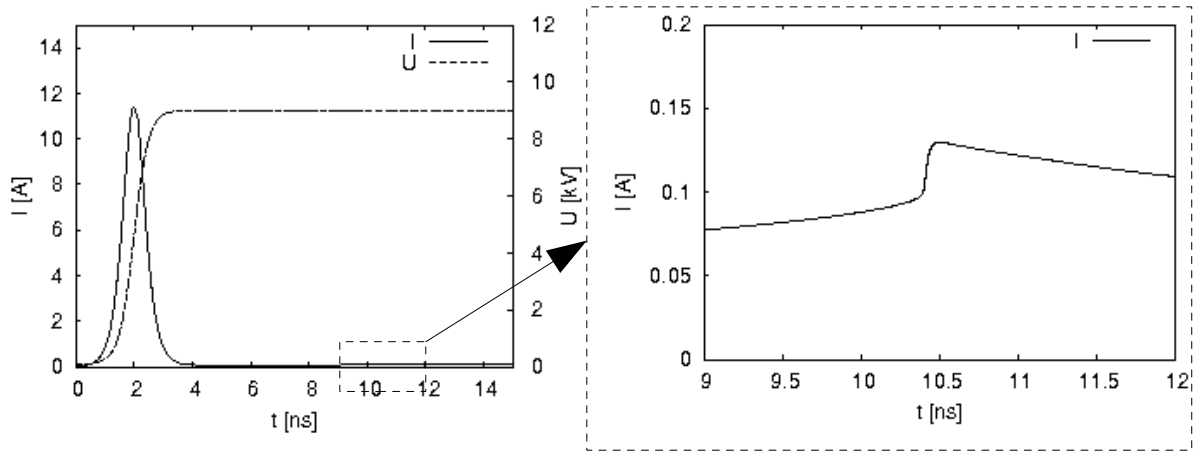


Fig. 4. The current as a function of time for a discharge with a glass tube of inner radius 100 μm. Right figure is a zoom for time corresponding to discharge impact on the grounded electrode.

4. Conclusion

In this work, we have studied the propagation of an air discharge at atmospheric pressure for an applied voltage of 9 kV in a glass tube with permittivity ε=5. These conditions are studied experimentally in LPGP, Orsay. The density and electric field profiles show a tubular structure of the discharge which seems to be in agreement with first experimental results. The axial propagation velocity of the discharge decreases as the inner radius of the glass tube decreases and reaches a higher limit for a radius lower than 150 μm. This is in good agreement with experimental results even if the absolute value of velocity is different. The influence of the shape of applied voltage is shown but has a negligible impact for an applied voltage of 9 kV. The influence of the electrode holder is studied by considering two limit cases with and without plane holder. We note that the discharge propagates faster in the configuration without plane holder. Photoemission has strong effect on the discharge structure but appears to have a negligible influence on the discharge velocity. Current calculation is validated by comparing two different approaches – from total power and integration over surface.

Acknowledgement. The authors thank the Agence Nationale de la Recherche for its support of the ALVEOPLAS project (Grant No. ANR-08-BLAN-0159-01).

5. References

[1] Hammer T 2002 *Plasma Sources Sci. Technol.* **11** A196.
[2] Pasquiers S 2004 *Eur. Phys. J. Appl. Phys.* **28** 319-324.
[3] Kim H H 2004 *Plasma Process. Polym*. **1** 91-110.
[4] Jansky J, Tholin F, Bonaventura Z, Bourdon A 2010 *J.Phys.D:Appl.Phys.* submitted.
[5] Le Delliou L, Tardiveau P, Jeanney P, Bauville G, Jorand F, Pasquiers S 2010 *proceedings of XVIII International Conference on Gas Discharges and Their Applications (GD 2010)*
[6] Kulikovsky A A 1995 *J. Comput. Phys.* **28** 2483-2493.
[7] Amestoy P R, Duff I S ,L'Excellent J Y and Koster J 2001 *SIAM Journal of Matrix Analysis and Applications* **23** 15-41.
[8] Bourdon A, Pasko V P, Liu N Y, Célestin S, Ségur P and Marode E 2007 *Plasma Sources Sci. Technol.* **16** 656-678.
[9] Potin J 2001 *Phd thesis, University Paul Sabatier, Toulouse, France.*
[10] Morrow R and Sato N 1999 *J.Phys.D:Appl.Phys.* **32** L20-L22

SPATIALLY RESOLVED KINETIC SPECTROSCOPY OF THE ATMOSPHERIC PRESSURE BARRIER DISCHARGE PLASMA TORCH

Kirill Kozlov[1], Vadim Korolenko[1], Anton Zagoskin[1], Tatiana Nikitina[2], and Vadim Samoilovich[1]

[1] *Moscow State University, Department of Chemistry, 119991 Moscow, Russia*
[2] *Moscow State University, Department of Physics, 119991 Moscow, Russia*
E-mail: kozlov@kge.msu.ru

Spatially and temporally resolved plasma diagnostics of the barrier discharge plasma torch was carried out by means of the technique of cross-correlation spectroscopy. The discharge was generated in humid argon flowing out from the quartz capillary into the ambient air. The feeding voltage frequency and amplitude were equal to 2.6 kHz and to 4.8 kV, respectively. The emission spectrum of the discharge was found to consist of the argon lines, and of the bands of OH-radical (A-X transition) and of molecular nitrogen (2^{nd} positive system). The spatio-temporal distributions of the radiation intensity for several selected wavelengths (spectral indicators) were recorded with the spatial resolution of 0.2 mm, and temporal resolution in the nanosecond range. Experimental data analysis shows that the torch outside the electrode system appears due to the propagation of the periodical ionization waves moving inside the capillary and coming out of it. The role of the metastable states of argon in the observed radiation kinetics is discussed briefly.

1. Introduction

Non-thermal atmospheric pressure plasma torches (often referred to as plasma jets, and sometimes as plasma plumes or plasma pencils) are playing an increasingly important role in various plasma processing applications. This is because of their practical capability to provide plasmas that are not spatially bound or confined by electrodes [1]. Barrier discharge plasma torches (BDPTs) belong to this particular type of low temperature high pressure plasma sources. As it is known from the literature [1], they can be generated in helium or in argon flowing through a capillary into ambient air. We decided to undertake an experimental investigation of the BDPT in humid argon for the following reasons. Barrier discharges in humid argon can be regarded not only as prospective plasma chemical generators of the OH-radicals [2], but also as useful UV-radiation sources [3]. An improvement of their efficiency is hardly possible without deep understanding of the discharge mechanism and dominant chemical pathways leading to the reaction products of interest. To achieve this, a complete plasma diagnostics including electrical measurements, spatially resolved kinetic spectroscopy, and chemical analysis of stable reaction products has to be carried out. Recently, the authors [4-6] reported the results of successful implementation of the technique of cross-correlation spectroscopy (CCS) for spatially resolved kinetic measurements of the light emission of the localized microdischarges in pure and humid argon. The latter item has become an addition argument in favour of the choice of humid argon as a working gas for the BDPT.

2. Experimental

All the experiments were carried out in an open gas-flow system with argon flow rate of 10-15 l/h at atmospheric pressure. Argon humidity was varied within the range 0.5-10% of relative humidity (RH), corresponding to the range 200-4000 ppm of the water vapor concentration.

General scheme of experimental setup is shown in fig.1. By means of a quartz lens 2, the discharge zone is imaged onto the optical slit. By appropriate adjustment and movement of this slit, the discharge area can be scanned in vertical as well as in horizontal direction with the resolution not worse than 0.1 mm. Thus localized radiation (MAIN signal) is resolved spectrally by a monochromator and detected by the high-gain photo-multiplier (PMT 2) operated in a single photon counting mode. The second detector (PMT 1) provides the synchronizing (SYNC) signal necessary for the CCS measurements (see [4] for the details).

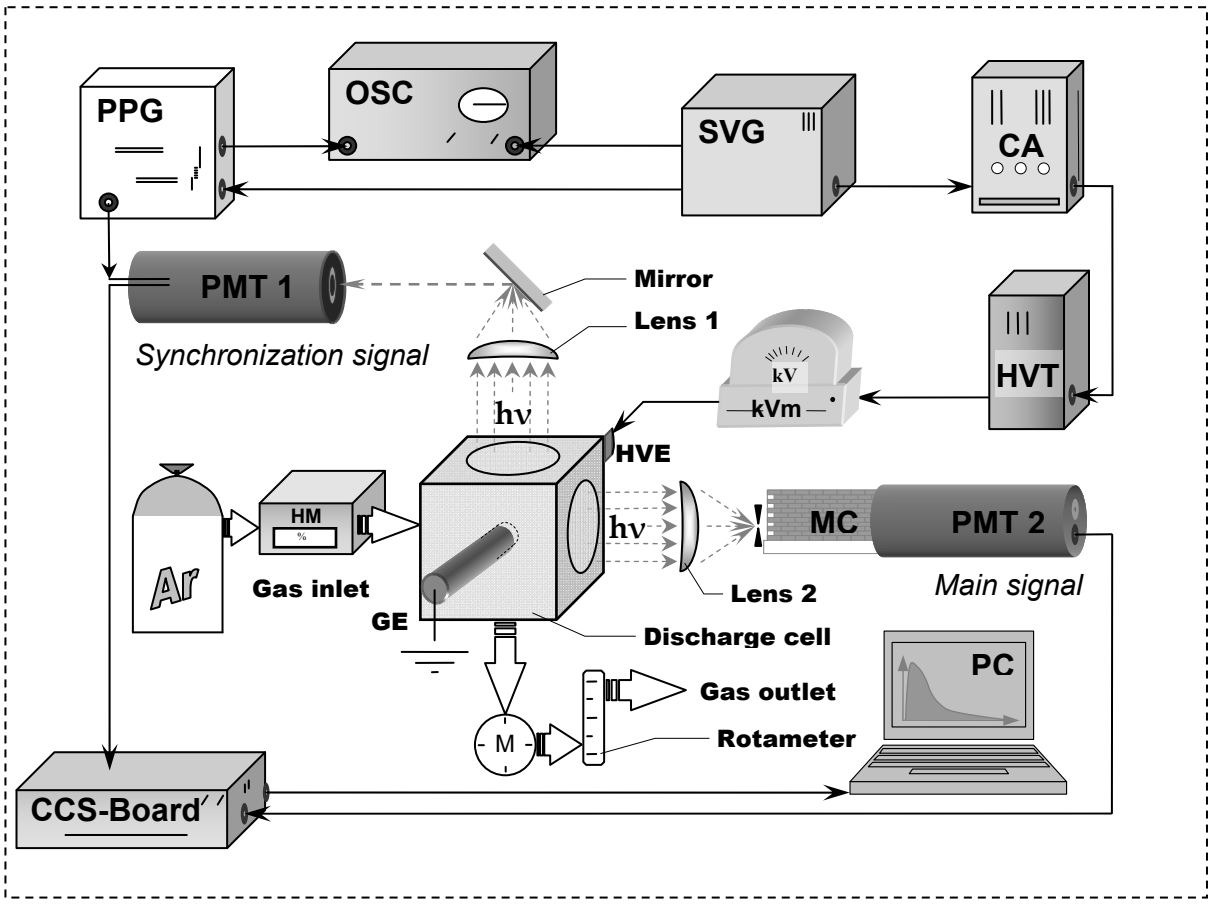


Fig. 1. Schematic drawing of experimental setup. Abbreviations: PPG – pulse pattern generator; OSC – oscilloscope; SVG – sine voltage generator; CA – current amplifier; PMT – photomultiplier tube; kVm – kilovolt-meter; HVT – high voltage transformer; HVE – high voltage electrode; HM – hygrometer; GE – ground electrode; MC – monochromator; PC – personal computer; CCS-Board – data processing system of the CCS-measurements ("Fluor99", see [4] for the details).

Plasma torch was generated in argon flow coming out from the quartz capillary (the inner diameter of about 1 mm) into the ambient air. Two metallic ring electrodes were placed on the outer surfaces of the quartz tube (high voltage) and of the quartz capillary (ground). The feeding voltage frequency and amplitude were equal to 2.6 kHz and to 4.8 kV, respectively. Under these operating conditions, a stable plasma torch a few mm long outside the capillary was clearly seen by a naked eye. The device presented in fig.2 was placed inside the special metallic discharge cell with two quartz windows as it is shown in fig.1. In order to avoid an accumulation of argon inside the discharge cell (but outside the capillary), an additional gas inlet (not shown on the drawing in fig.1) for air was provided, and the volume flow rate of dry air was maintained at the level at least one order of magnitude greater than the flow rate of argon through the capillary.

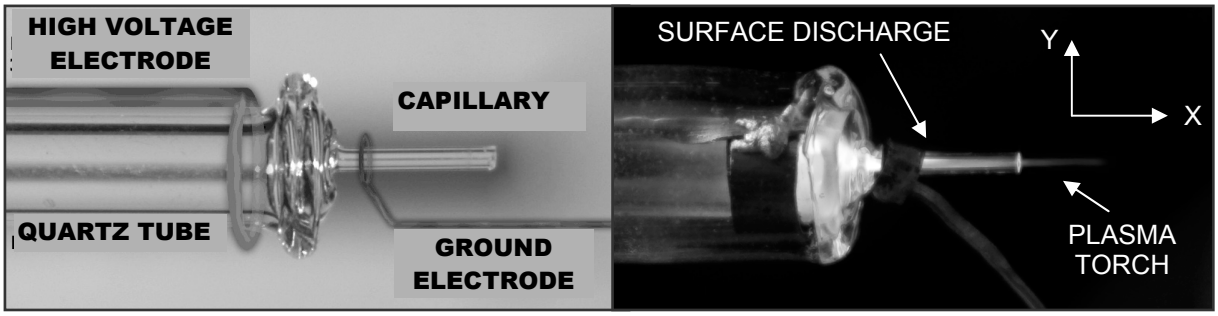


Fig. 2. A scheme of the electrode arrangement (left), and a photo of the discharge with the indication of two different plasma zones and with the definition of the coordinate system used hereafter (right).

3. Results and discussion

The overall emission spectra of the discharge inside the capillary as well as in the torch were found to consist of the peaks of argon, the bands of OH($A^2\Sigma^+$) radical, and the bands of molecular nitrogen (2nd positive system), although the concentration of N_2 in argon was about 10 ppm, only. The most intensive lines corresponding to the mentioned above species were chosen as their spectral indicators (i.e. λ=309 nm for OH(A) radical, and λ=337 nm for N_2(C) molecule). For the radiating states of Ar, we have chosen two lines (696 nm and 772 nm), since the energies of the corresponding excited states differ from each other by a noticeable quantity (about 0.2 eV), therefore they can posess different radiation kinetics.

$$N_2(C^3\Pi_u)_{\upsilon'=0} \rightarrow N_2(B^3\Pi_g)_{\upsilon''=0} + h\nu \qquad (\lambda = 337\ \text{nm}) \qquad (1)$$

$$OH(A^2\Sigma^+)_{\upsilon'=0} \rightarrow OH(X^2\Pi)_{\upsilon''=0} + h\nu \qquad (\lambda = 309\ \text{nm}) \qquad (2)$$

$$Ar^{**} \rightarrow Ar^{*} + h\nu \qquad (\lambda = 696\ \text{nm}) \qquad (3)$$

$$Ar^{***} \rightarrow Ar^{*} + h\nu \qquad (\lambda = 772\ \text{nm}) \qquad (4)$$

Here Ar* are metastable excited states of argon, Ar** and Ar*** denote two corresponding radiating states. These excited species can be produced by direct electron impact as follows:

$$e + N_2(X^1\Sigma_g^+)_{\upsilon=0} \rightarrow N_2(C^3\Pi_u)_{\upsilon'=0} + e \qquad (\Delta E = 11\ \text{eV}) \qquad (5)$$

$$H_2O + e \rightarrow OH(A^2\Sigma^+)_{\upsilon'=0} + H\cdot + e \qquad (\Delta E = 9{,}2\ \text{eV}) \qquad (6)$$

$$Ar + e \rightarrow Ar^{**} + e \qquad (\Delta E = 13{,}33\ \text{eV}) \qquad (7)$$

$$Ar + e \rightarrow Ar^{***} + e \qquad (\Delta E = 13{,}15\ \text{eV}) \qquad (8)$$

Since the radiation lifetimes of the spectral indicators (1-4) are within the range 60-700 ns, while the linear velocity of the working gas in the capillary during all the experiments was less than 20 m/s, the observed spatial distributions of the radiation intensities for the selected wavelengths reflect the corresponding distributions of the radiating species.

A comparison of the temporal distributions of the radiation intensities of the selected spectral indicators recorded in the central part of the plasma torch and in the middle of the capillary (see fig.3) demonstrates a noticeable asymmetry of the discharge with respect to the polarity of the feeding voltage (i.e. the polarity of the high-voltage electrode in fig.2). Namely, in the torch, radiation is detected mostly during the positive semi-wave of the sine voltage, while in the middle of the capillary the radiation intensities for both polarities appear to be comparable, the maximum values during the negative semi-wave being even greater. It means that from the point of view of plasma chemical efficiency of the discharge being considered, the plasma torch itself is much more active during the positive semi-wave of the applied voltage than during the negative one.

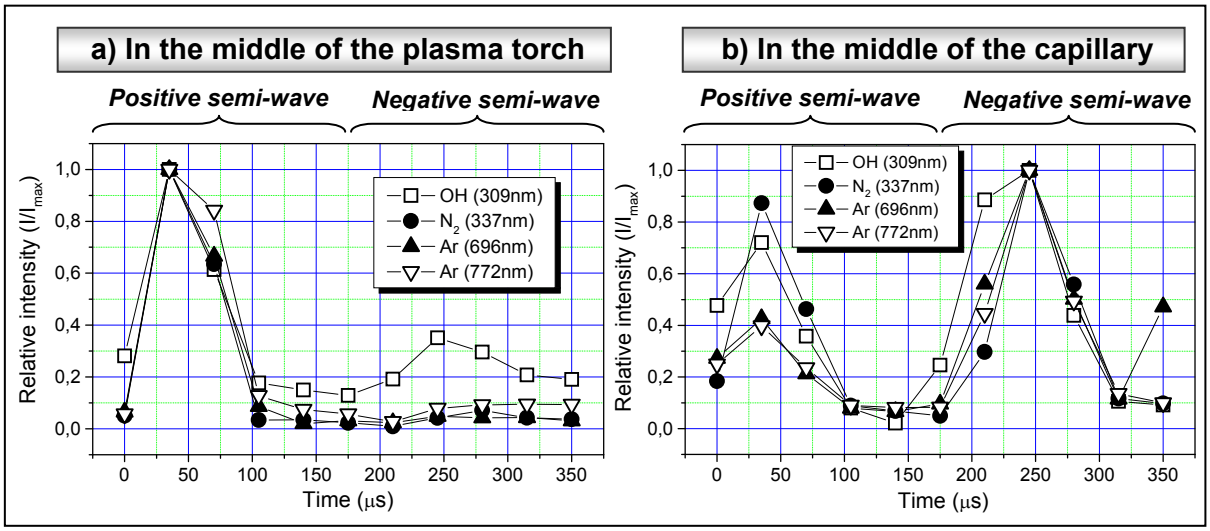


Fig. 3. Temporal distributions of the radiation intensity of the selected spectral indicators recorded in the central part of the plasma torch (a) and in the middle of the capillary (b). RH = 1.2%. The entire time scale (385 μs) corresponds to one cycle of the feeding sine voltage.

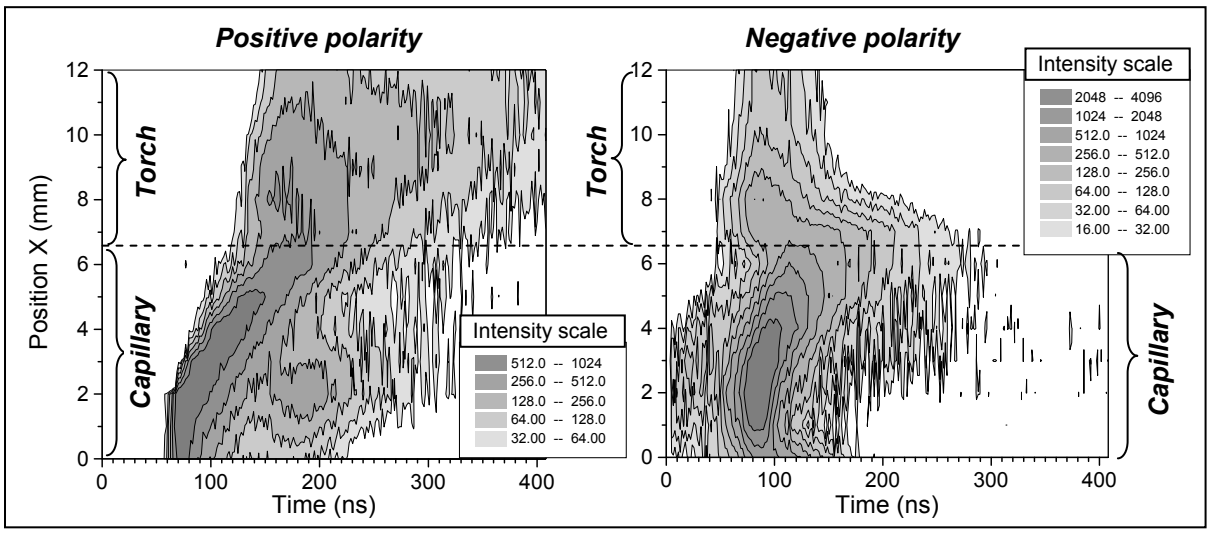


Fig. 4. Spatio-temporal distributions of the radiation intensity of Ar** (λ = 696 nm) recorded for positive (left) and negative (right) polarity of the high-voltage electrode (see fig.2). RH = 1.1%. Position of the capillary end is indicated by the dashed line.

The results presented in fig.3 are partially averaged over time (Δt=35μs). Actually, they describe the discharge development within the frame of a coarse time scale related to the feeding voltage frequency. To investigate the mechanism of electrical breakdown, the CCS-technique providing a fine time scale was used. Such measurement data obtained with a spatial resolution over the axial coordinate X (see fig.4) allow to evaluate the real duration of the breakdown event and to visualize its mechanism. The waves of luminosity are clearly seen in fig.4. They move from the ground electrode through the capillary and come out into the torch. In the case of negative polarity, light emission in the torch starts 40-50 ns before the luminosity wave from the ground electrode reaches the end of the capillary. These luminosity waves can be interpreted as ionizing wave images. Therefore, the velocities of the ionizing waves can be determined from the plots shown in fig.4. Such estimations give the values in the order of magnitude of 10^5 m/s.

The plots in fig.4 characterize an axial structure of the discharge being considered. To study its radial component, we carried out several measurements of the two-dimensional distributions of the emission intensity for selected spectral indicators. In fig.5, such distributions are shown for OH(A)-radicals (309 nm) and for N_2(C) molecules (337 nm). It should be noted that these results are integrated over time and they are not polarity resolved. On both plots in fig.5, the radial axes of symmetry are slightly leaned to the left from vertical direction due to the corresponding deviation of the discharge cell from

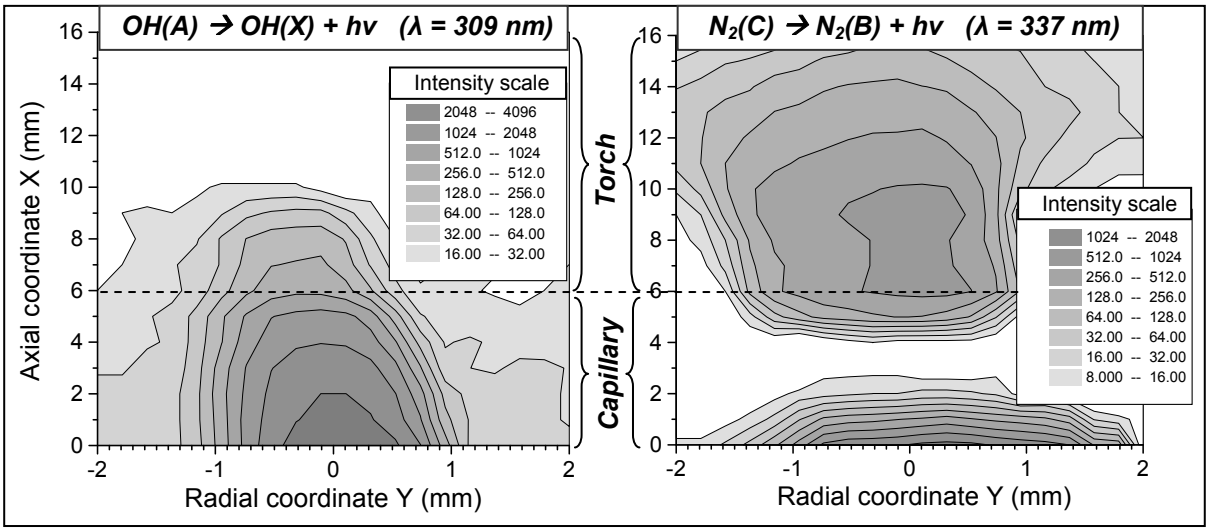


Fig. 5. Two-dimensional distributions of the radiation intensity of OH(A) radicals (left) and N_2(C) molecules (right). RH = 10%. Position of the capillary end is indicated by the dashed line.

the optical coordinate system for spatial scanning. However, this imperfection of experimental arrangement does not disturb the shapes of the real 2D intensity distributions. The axial intensity distribution for OH(A) radicals reaches its maximum near the ground electrode (X=0 on fig.5). From this point the intensity decreases gradually until the end of the capillary and further in the torch. Axial distributions of the radiation intensity for both argon lines (696 nm and 772 nm) exhibit the same characteristic features. In contrast to this, the axial distribution of the radiation intensity for $N_2(C)$ signal (337 nm) appears to be bimodal with the first sharp peak near the ground electrode and the second more diffuse maximum in the torch (see fig.5, the right plot). This peculiar structure of the radiation intensity distribution for $N_2(C)$ can be explained as follow. The first sharp maximum near the ground electrode is caused by a surface discharge burning in air outside the capillary (see fig.2). This weak discharge could be observed by a naked eye. The radiating species in this area are formed by direct electron impact (see reaction (5)). The second diffuse maximum in the torch is caused by the $N_2(C)$ molecules formed by the reaction between argon metastable states and N_2 molecules in their ground states (see reaction (9) below), the latter coming from ambient air outside into the torch.

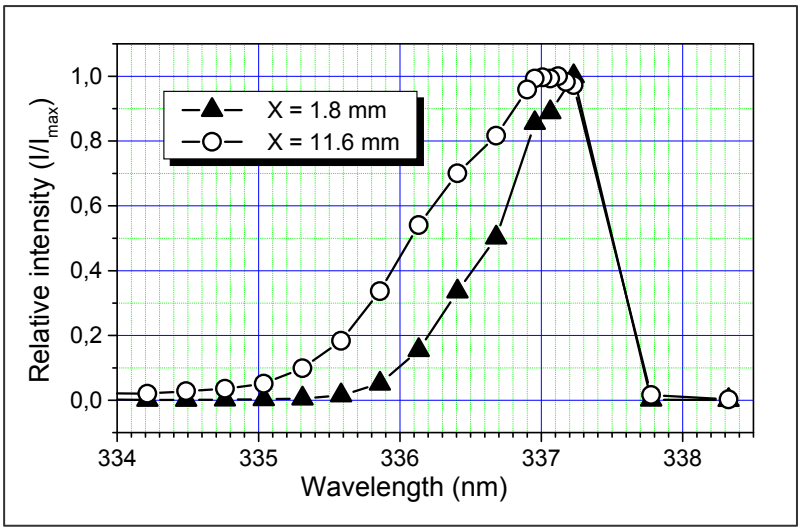


Fig. 6. Comparison of the emission spectra fragments recorded in two different points of the discharge: near the ground electrode (X = 1.8 mm), and in the middle of the torch (X = 11.8 mm).

$$Ar^* + N_2(X^1\Sigma_g^+)_{\upsilon=0} \rightarrow N_2(C^3\Pi_u)_{\upsilon'=0} + Ar \qquad (9)$$

To verify this hypothesis, we compared the fragments of the emission spectra of the 0-0 band of the 2nd positive system of nitrogen. As it is known from the literature (see [9] and [4]), reaction (9) results in the formation of so-called "hot nitrogen" which can be identified by broadening of the spectral bands of the 2nd positive system of nitrogen. Such broadening is clearly seen on the plot in fig.6.

4. Conclusions

The macroscopic spatio-temporal structure of the DBPT in humid argon is similar to the structure of well-known filamentary barrier discharges, i.e. the DBPT consists of a number of the following one another microdischarges of short duration (a few hundred nanoseconds). The torch outside the electrode system appears due to the propagation of the periodical ionization waves moving along the capillary (and coming out of it) at a velocity of about 10^5 m/s.

5. References

[1] Laroussi M. and Akan T., 2007, *Plasma Processes and Polymers* **4,** p.777.

[2] Dodet B., Odic E., Goldman A., Goldman M., Renard D., 2005, *J. Adv. Oxid. Technol.*, **8**, p.91.

[3] Hibert C., Gaurand I., Motret O., Pouvesle J.M., 1999, *J. Appl. Phys.*, **85**, p.7070.

[4] Kozlov K.V., Tatarenko P.A., Samoilovich V.G., 2008, *Proc. 11th Int. Symp. on High Pressure Low Temperature Plasma Chemistry, Oléron Island (France),* p.65.

[5] Kozlov K.V., Tatarenko P.A., Samoilovich V.G., 2006, *Proc. 10th Int. Symp. on High Pressure Low Temperature Plasma Chemistry, Saga (Japan),*p.47.

[6] Kozlov K.V., Odic E., Tatarenko P.A., Dodet B., Fedoseev G.S., Kirkpatrick M.J., Samoilovich V.G., Ganciu M., 2006, *Proc. 10th Int. Symp. on High Pressure Low Temperature Plasma Chemistry, Saga (Japan),* p.124.

[7] Setser D. W., Stedman D. H., and Coxon J. A., 1970, *J. Chem. Phys.* **53,** p.1004.

TIME-SPACE RESOLVED MEASUREMENT OF ELECTRIC FIELD IN DIELECTRIC BARRIER DISCHARGE IN HELIUM

Bratislav M. Obradović[1], Saša Ivković[1], Nikola Cvetanović[2],
Milorad M. Kuraica[1] and Jagoš Purić[1]

[1]*University of Belgrade, Faculty of Physics, P.O. Box 368, 11000 Belgrade, Serbia*
[2]*University of Belgrade, Faculty of Transport and Traffic Engineering, Vojvode Stepe 305, Belgrade, Serbia*
E-mail: obrat@ff.bg.ac.rs

Diffuse DBD in helium was investigated using time-space resolved optical emission spectroscopy. Using emission spectroscopy technique based on the polarization-dependent Stark splitting and shifting of He I 492.19 nm line and its forbidden component, the electric field distribution in the cathode region of DBD in helium is measured during evolution of the discharge. During the whole discharge development period the length of the cathode fall region decreases. Interesting result was that in the period of current decrease, the maximum of the electric field distribution shifts away from the cathode showing the accumulation of negative charge near the cathode surface.

1. Introduction

Experimental and theoretical studies of dielectric barrier discharges (DBDs), which are convenient plasma sources for the generation of non-thermal plasmas at atmospheric pressure, have received much attention on account of numerous industrial applications [1]. At atmospheric pressure DBD often occurs in the form of large number of short-lived tiny micro-discharges (filaments) hence that type of discharge is called filamentary. Under special operation conditions in certain gases, a filament-free and transversely uniform mode of the DBD is formed. This diffuse type of discharge is also called homogeneous DBD or atmospheric pressure glow discharge (APGD). The APGD is advantageous compared to the filamentary DBD for applications that require uniform plasma treatment such as the deposition of uniform thin films or surface treatment. [2-4].

Although uniform APGDs have been demonstrated in different atmospheres like helium [5], neon [6] and nitrogen [7] in this article we focused on helium, in which the APGD was firstly obtained. APGD in helium is characterized by the narrow current pulses (~ 1 μs) of large amplitude (tens of milliamperes) and the spatial structure which resembles that of a dc glow discharge at low pressure. The cathode fall, Faraday dark space, and positive column develop in the time instant of maximal current [5]. The cathode fall is characterized by a strong electric field, which is responsible for the maintenance of the discharge. Therefore, detailed knowledge of electric field time-dependent distribution is necessary for better understanding of the processes in DBD and their practical applications.

Using emission spectroscopy technique based on the polarization-dependent Stark splitting and shifting of visible helium lines and their forbidden components, we proposed the method for measurement of the electric field distribution in the cathode region of DBD in helium [8]. In this article we present time resolved measurements of electric field distribution during evolution of current pulse in the DBD in helium, obtained by this method.

2. Experiment

The experimental set-up is schematically shown in Fig. 1. The discharge is generated in a parallel plane discharge configuration consisting of two metal electrodes (50 x 50 mm) both covered by a 0.65 mm thick alumina dielectric plates (105 x 105 mm; $\varepsilon_r = 9.4$). The electrode edges are rounded in order to reduce electric field at sharp edges. The fixed discharge gap of 2 mm is obtained using glass space holders. The discharge cell is placed in a vacuum chamber which is firstly evacuated down to 10^{-2} mbar, and then filled with helium (purity 99.996 %) at 200 mbar or 800 mbar pressure. The gas, with a flow rate of 2 l/min, is injected into the discharge volume through ten equidistant holes to ensure homogeneous gas flow, see Fig. 1. The discharge is driven by a home made pulse voltage

power supply. One electrode is kept at ground potential, while on the other a pulse potential with amplitude of 1.5 kV and a frequency of 5 kHz is applied. The applied voltage U_a is measured via a 1:1000 P6015A Tektronics voltage probe; the external total discharge current is monitored using current probe. The applied voltage and the discharge current are measured by Tektronics TDS 3032 (300 MHz bandwidth, 2 GSamples/s) oscilloscope.

The gap voltage U_g is calculated according to the procedure described for unipolar-pulsed DBD in Ref. 9:

$$I_g(t) = \left(1 + \frac{C_g}{C_d}\right) I_t(t) - C_g \frac{dU_a(t)}{dt} \tag{1}$$

$$U_g(t) = \frac{C_d}{C_g + C_d} U_a(t) - \frac{1}{C_g + C_d} \int_0^t I_g(\tau) d\tau \tag{2}$$

where $U_a(t)$ is the external voltage applied to the DBD cell; $U_g(t)$ the voltage across the discharge gap; $I_t(t)$ the total external current through the DBD cell; $I_p(t)$ the discharge current in the gap. C_d and C_g are equivalent capacitances of the dielectric barrier and the discharge gap, respectively.

For space resolved emission measurements, projection optics is placed at a distance of double focal length 2*f* from the centre of the electrodes and a discharge gap region, displayed on a bottom picture, is imaged 1:1 onto the entrance slit of a 1-m spectrometer, see Fig. 1. Radiation from the DBD was polarized in the electric field direction (π-polarization) using a plastic polarizer and detected using an ICCD (PI-MAX2, Princeton Instruments) with 256 × 1024 pixels (pixel dimensions: 26 μm × 26 μm). ICCD is triggered with a time delayed pulse, generated initially by the power supply. Each recorded image is made of 50 accumulations, each made of 50 000 gates per exposure. The gate duration of 100 ns limits the time resolution for investigation of discharge development [10,11]. The gate duration was imposed by the low intensity of the forbidden component of He I 492.19 nm line which is crucial for the electric field measurement. Namely, electric field was calculated using peak-to-peak wavelength difference between fitted profiles of forbidden and allowed components of He I 492.19 nm spectral line, consequently the results are very sensitive to the exact position of forbidden line maximum. With entrance slit of 30 μm instrumental Pseudo-Voight profile (sum of Gauss and Lorentz profiles) width was 0.028 nm.

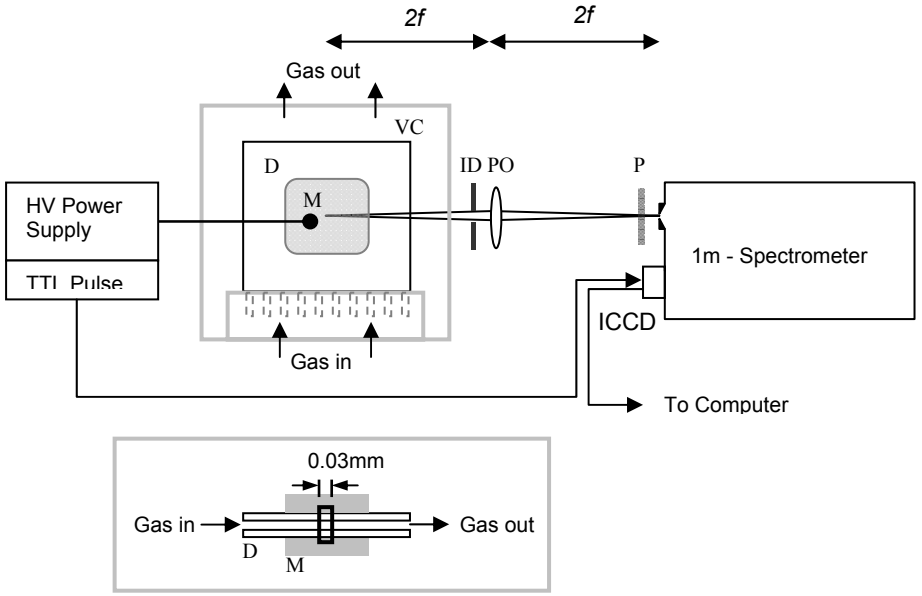


Fig. 1. Schematic picture of experimental set-up with a top view of DBD. M - Metal electrode, D - dielectric layer, VC – vacuum chamber, ID – iris diaphragm, PO – Projection optics, P – polarizer. Bottom picture is a side view of DBD.

3. Results and discussion

One entire period of typical applied voltage signal is presented in Fig. 2(a) while Fig. 2(b) and Fig. 2(c) present external total current density j_t, external applied U_a and internal gap U_g voltages of DBD in 2 mm discharge cell for 200 mbar and 800 mbar pressures. The external applied voltage was pulsed, with voltage drops during the current pulses. These voltage drops originate from the limitations of the power supply. The breakdown voltage was evidently different for different pressures with the same applied voltage. As can be seen from the figure, negative, current pulse is higher and lasts shorter in the discharge at lower pressure.

Using the mentioned spectroscopic method we have measured electric field distributions in several time intervals during the development of the discharge. Results of measurements in the discharges at 200 mbar and 800 mbar are presented in Fig. 3. For those experimental points for which the electric field has evidently linear dependence on the distance from the cathode, we used linear extrapolation as an approximate experimental method for determination of the length of the cathode fall region.

Analyzing the Fig. 3a, the following phases of the breakdown may be distinguished: (i) 100 ns before the maximal current, densities of charged particles are low so the external field is not significantly distorted. The cathode fall region is not yet shorter than the length of the discharge gap. (ii) In the next time interval, the electric field continues to grow nearby the cathode and drops more steeply due to the space charge approaching the cathode therefore decreasing the cathode fall length. This time interval is characterized by the maximal external discharge current and the maximal electric field at the cathode of ~8 kV/cm. (iii) In the following three time intervals that belong to the falling edge of the current pulse, the cathode fall length continues to decrease as well as the electric field at the cathode surface. Furthermore, the electric field distribution in the vicinity of the cathode changes the sign of its slope

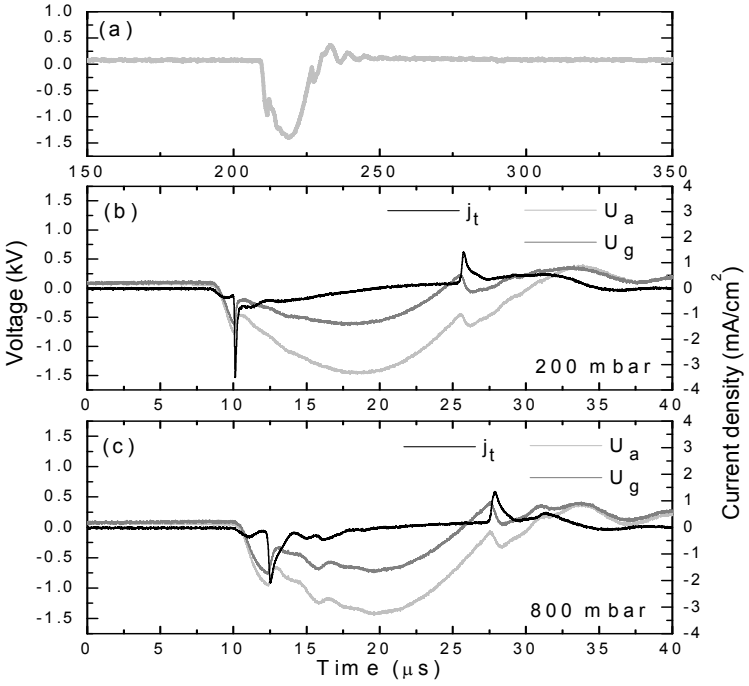


Fig. 2. (a) Example of applied voltage signal of DBD in helium. j_t – external current density, Ua – applied voltage, and Ug – gap voltage oscillograms for (b) 200 mbar and (c) 800 mbar pressures.

and the maximum of the electric field continuously shifts from the cathode. Similar development of the electric field distributions is observed in the discharge at 800 mbar, see Fig. 3b. As expected, the length of the cathode fall region is shorter in the discharge at higher pressure. On the other hand the electric field at the cathode is ~11 kV/cm, which is higher than in 200 mbar discharge.

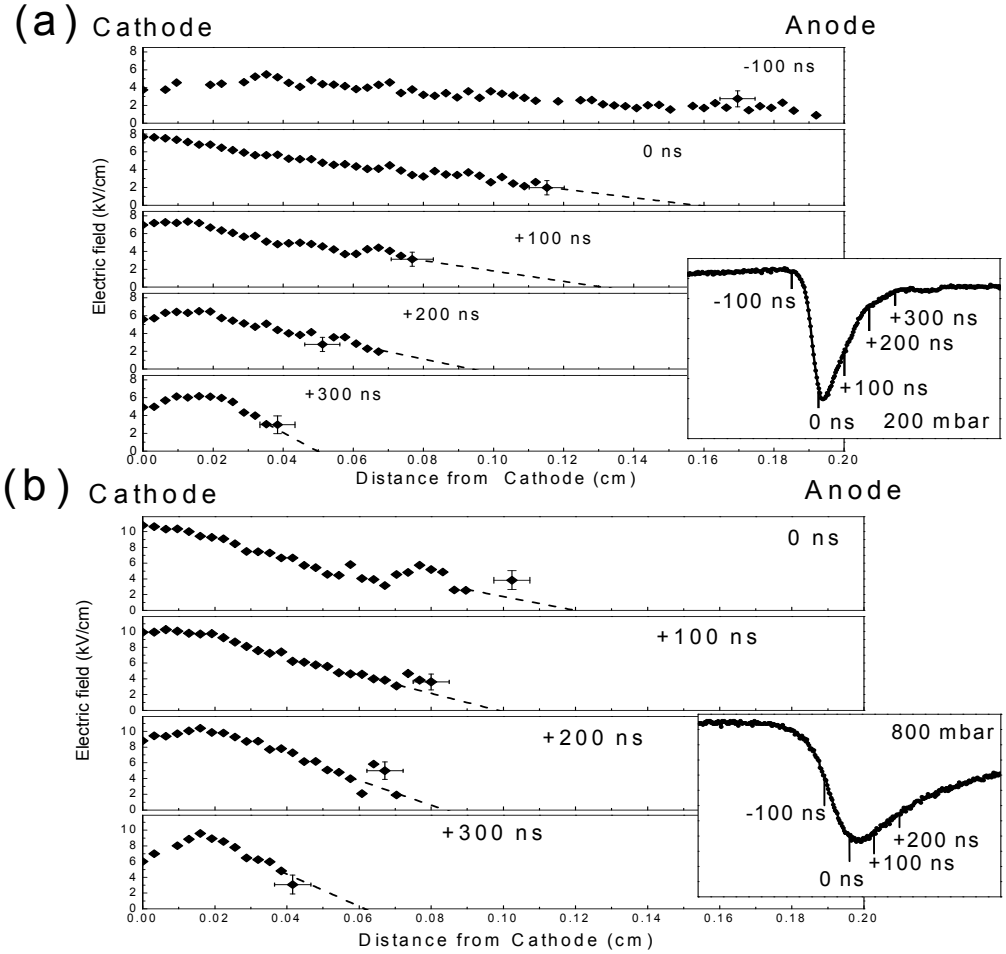


Fig. 3. Development of the electric field spatial distribution in BD in helium at (a) 200 mbar and (b) 800 mbar. Enlarged graphs present current signals.

According to the profiles of the electric field distributions, in the decreasing current phase the overall electric field is reduced and, near the cathode the rising slope of the field is created implying negative charge build up.

Finally in Fig. 4 we present the results of plasma density in two time intervals calculated using corresponding electric filed distribution by using the Poisson equation. It can be clearly seen that at low voltage, when the discharge is in the extinguishing phase, a layer of electrons forms near the cathode. Namely, in this period the voltage is reduced and therefore the extraction of the electrons formed by secondary emission is diminished causing a build up of negative space charge near the cathode. This negative space charge corresponds to the rising slope of the electric field in Fig. 3. Such shapes of electric field and charge density distributions may be found in literature concerning cathode fall of low pressure glow discharge. [12,13]

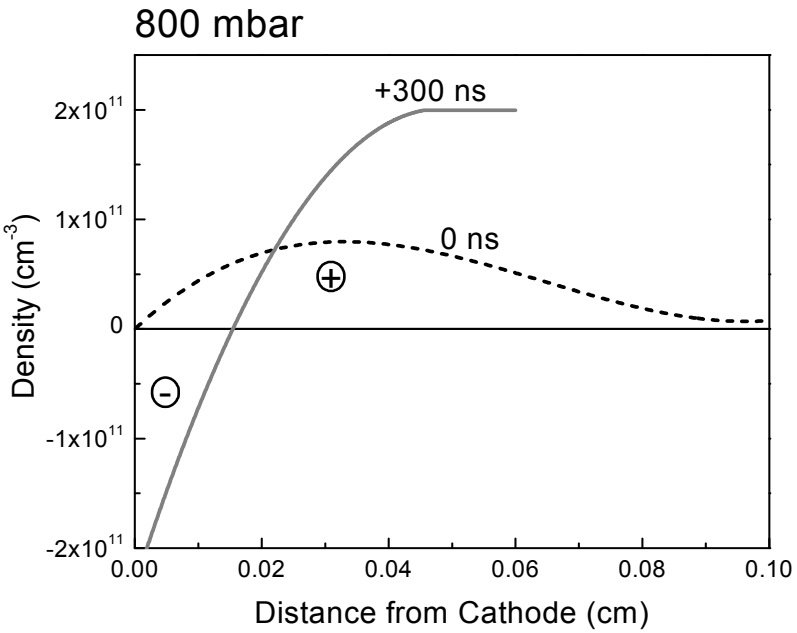


Fig. 4. Net space charge density profiles in the cathode region of DBD at 800 mbar during the maximal current, noted as 0 ns, and 300 ns later.

Acknowledgment. This work within the Project 141043 is supported by the Ministry of Science of the Republic of Serbia.

References

[1] Kogelschatz U 2003 *Plasma Chem. Plasma Proc.* **23** 1.
[2] Trunec D, Navrátil Z, Sťahel P, Zajíčková L, Buršíková V and Čech J 2004 *J. Phys. D: Appl. Phys.* **37** 2112.
[3] Šíra M, Trunec D, Sťahel P, Buršíková V, Navrátil Z and Buršíkov J, 2005 *J. Phys. D: Appl. Phys.* **38** 621.
[4] Šíra M, Trunec D, Sťahel P, Buršíková V, Navrátil Z, 2008 *J. Phys. D: Appl. Phys.***41** 015205.
[5] Massines F, Rabehi A, Décomps P, Ben Gadri R, Séguer P and Mayoux C 1998 *J. Appl. Phys.* **83** 2950.
[6] Trunec D, Brablec A and Buchta J 2001 *J. Phys. D: Appl. Phys.* **34** 1697.
[7] Gherardi N, Gouda G, Gat E, Ricard A and Massines F, 2000 *Plasma Sources Sci. Technol.* **9** 340.
[8] Obradović B M, Ivković S S and Kuraica M M 2008 *Appl. Phys. Lett.* **92**, 191501.
[9] Liu S and Neiger M, 2003 *J. Phys. D: Appl. Phys.* **36** 3144.
[10] Mangolini L, Anderson C, Heberlein J and Kortshagen U 2004 *J. Phys. D: Appl. Phys.* **37** 1021.
[11] Martens T, Brok W J M, van Dijk J and Bogaerts A 2009 *J. Phys. D: Appl. Phys.* **42**, 122002.
[12] Brown S C 1959 *Basic Data of Plasma Physics* (New York : MIT and John Wiley & Sons, Inc.)
[13] Lieberman M A and Lichtenberg A J 2005 *Principles of Plasma discharges and Materials Processing 2nd ed.*, (Hoboken : John Wiley & Sons, Inc.)

ICCD MICROSCOPY AND SPECTROSCOPY OF A SINGLE SURFACE COPLANAR DBD MICRO-DISCHARGE DRIVEN IN N_2, O_2 AND IN SYNTHETIC AIR AT ATMOSPHERIC PRESSURE

Milan Šimek

Institute of Plasma Physics v.v.i., Czech Academy of Sciences,
Za Slovankou 3, 182 00 Prague 8, Czech Republic
E-mail: simek@ipp.cas.cz

Techniques of the ICCD microscopy, ICCD spectrometry and multi-channel photon-counting with nanosecond time resolution were employed to study basic radiative characteristics of a single isolated micro-discharge generated in a surface DBD reactor with nanosecond time resolution. Fast ICCD was utilized to register images and spectrally-resolved emission of individual micro-discharges synchronously either with high voltage waveforms or with micro-discharge current pulses. Build-up and decay time constants of several excited states together with streamer channel diameter were obtained for an isolated micro-discharge which is essentially free of an interference that might be caused by reactive species produced and left by preceding discharges. Such characteristics provide important benchmarks for more complex surface DBD geometries where accumulation of species capable of affecting the physical chemistry of micro-discharges readily occurs.

1. Introduction

Atmospheric-pressure, non-equilibrium plasmas generated by surface dielectric barrier discharges (SDBD) produce highly reactive environment which is suitable for various applications (*e.g.* pollution control, sterilization, ozone generation, surface modification). Major part of reactive species is in the case of SDBD produced in a very thin plasma layer close to the surface of the electrode system. Primary radicals produced by electron impact processes then either induce secondary reactions inside the plasma layer or they can diffuse away from the surface initiating various chemical reactions in the bulk gas. SDBD discharges driven in nitrogen are characterised by substantial quantities of long-living energy carriers (e.g. $N_2(A^3\Sigma_u^+)$, $N(^4S)$, $N_2(X^1\Sigma_g^+,v>5)$ capable of affecting the physical chemistry of the discharge, however the production and relaxation of such species is still not fully explored.

In this work we inspect build-up and decay of UV-vis-NIR emission produced by electronically excited N_2, N_2^+, O_2^+, O^I and NO species generated by a single CSDBD micro-discharge in nitrogen, oxygen and in synthetic air during first 10 microseconds of the micro-discharge evolution. Especially, we focus on basic radiative characteristics of an isolated micro-discharge which is essentially free of potential interferences that might be caused by residual reactive species produced and left by preceding discharges. Such radiative characteristics provide important benchmarks for understanding more complex discharge geometries where accumulation of long-living species (e.g. $N_2(A^3\Sigma_u^+)$, $N(^4S)$, $N_2(X^1\Sigma_g^+,v>5)$ capable of affecting the physical chemistry of micro-discharges readily occurs due to high repetition frequency of the discharge events and/or due to long residence time.

2. Experiment

The single micro-discharge reactor consists of a discharge system placed in a Plexiglass chamber equipped with quartz windows for optical diagnostics, gas feed input/output ports and a high voltage interface. The discharge is produced on the surface of a ∅ 25.4 mm disk (5 mm thick) made from MACOR® machineable glass-ceramic (AC dielectric strength 9.4 kV/mm, dielectric konstant ε_r = 6.03 at 1 kHz and 25°C). The micro-discharges initiate due to electric field formed by high-voltage waveforms imposed on two thin round (∅ 4 mm) silver electrodes embedded ~ 0.4 mm below the disc's surface as shown schematically in figure 1. The surface exposed to micro-discharges was

polished while the opposite side containing high-voltage contacts and leads was filled and covered with Torr Seal Resin Sealant and with insulating RTV silicone.

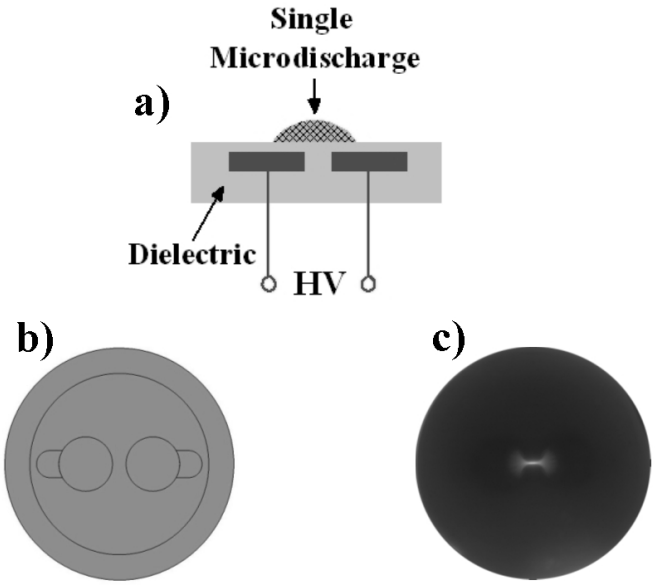


Fig. 1. Single surface coplanar dielectric barrier micro-discharge generator: a) principle of the electrode geometry, b) sketch of the electrode system and c) photograph of the micro-discharge produced in nitrogen.

The discharge is powered by an AC high voltage power supply composed of the TG1010A Function Generator (TTi), Powertron Model 250A RF Amplifier and a high-voltage step-up transformer. Micro-discharges were produced by sine-wave high voltage waveforms (f_{AC}=1-10 kHz) applied with fixed repetition frequency f_M producing high-voltage ON/OFF periods. A fast digitizing oscilloscope was used to record voltage-current discharge characteristics. Current pulses produced by individual micro-discharges were monitored simultaneously through the voltage drop on a non-inductive shunt resistor (R = 1.7 Ω) inserted between grounded electrode and grounding lead (measured by Tektronix P6139A high voltage probe, 10:1@10MΩ, bandwidth 500 MHz) and by the Model 2877 Standard Current Monitor (Person Electronics, Inc.). Typical record of voltage-current characteristics (with one single micro-discharge current pulse produced per one AC half-cycle) is shown in figure 2.
Emission produced by a micro-discharge is collected perpendicularly to the discharge surface by the quartz optical fibre bundle through the pair of iris diaphragms, colour-glass filters and pair of quartz lenses. The output of the fibre bundle is coupled to the iHR-320 (Jobin-Yvon) imaging spectrometer equipped with the DH740i-18U-03 iStar ICCD camera (Andor) to register spectrally-resolved PIE with time-resolution defined by the ICCD gate. Alternately, the output of the fibre bundle is coupled to the HR-320 (Jobin-Yvon) monochromator (1200 G/mm grating, symmetric input/output 100 μm slits) which is used as a narrow-band filter (FWHM ~0.35 nm) at pre-selected wavelengths. The HR-320 output is coupled with a fast Hamamatsu R2949 photomultiplier (PMT) and "monochromatic" PIE waveforms are sampled by the digitizing oscilloscope and by a gated 200 MHz MSA-200 (Becker&Hickl) multi-channel photon counter (MPC) synchronously with the micro-discharge current pulses. To collect magnified micro-discharge images, the reactor can be fixed on the specimen stage of Zeiss Jenavert microscope (equipped with the iStar ICCD) with the discharge surface placed in the focal plane. Andor iStar ICCD camera is therefore utilized to register either images or spectrally-

resolved emission of individual micro-discharges (synchronously either with high voltage waveforms or with micro-discharge current pulses).

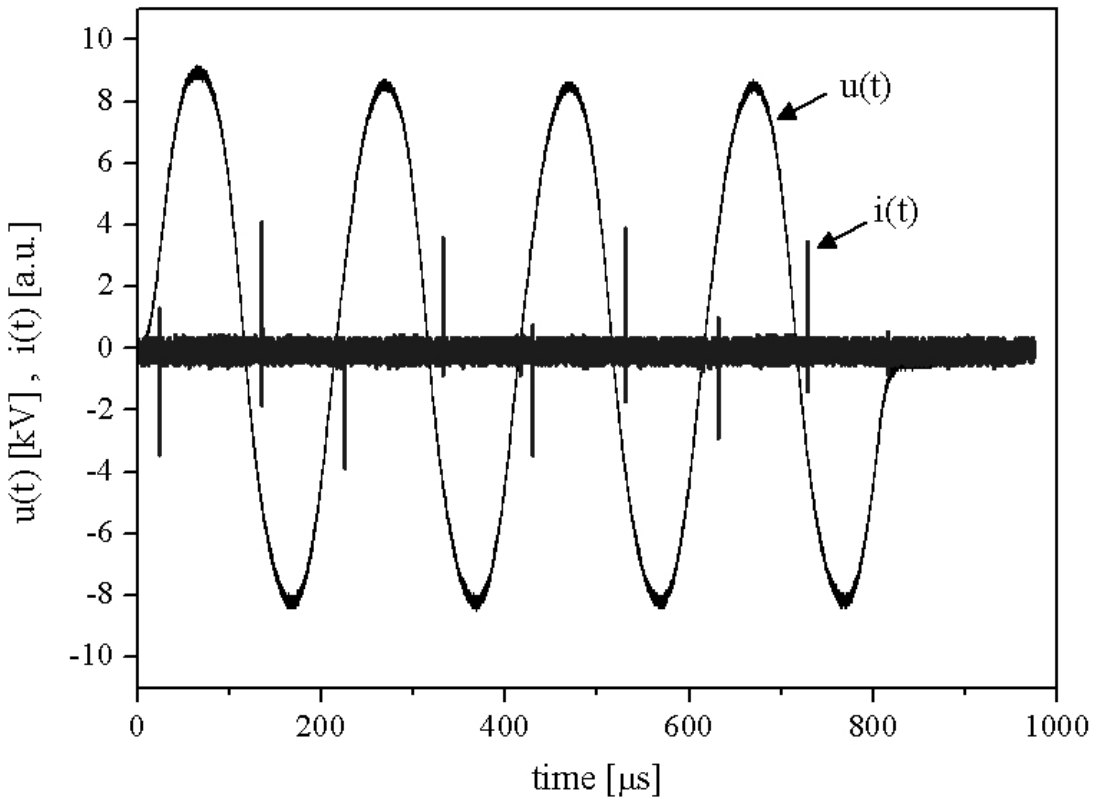


Fig. 2. Typical voltage and current waveforms in the case of four consecutive AC cycles (f_{AC}=5 kHz) applied with repetition frequency f_M = 100 Hz in synthetic air.

3. Results and discussion

Any micro-discharge is a source of intense emission produced in the UV-vis-NIR spectral range. In the case of pure nitrogen or synthetic air, we have registered strong discharge emissions of three electronic systems:

- $N_2^+(B^2\Sigma_u^+ \rightarrow X^2\Sigma_g^+)$ first negative (1.NG),
- $N_2(C^3\Pi_u \rightarrow B^3\Pi_g)$ second positive (2.PG),
- $N_2(B^3\Pi_g \rightarrow A^3\Sigma_u^+)$ first positive (1.PG).

Other weaker emissions can be observed in pure nitrogen during micro-discharge extinction and decay:

- $N_2(C''^5\Pi_u \rightarrow A'^5\Sigma_g^+)$ Herman infrared (HIR),
- $N_2(C'^3\Pi_u \rightarrow B^3\Pi_g)$ Goldstein-Kaplan system (GK),
- NO-γ $(A^2\Sigma^+ \rightarrow X^2\Pi)$ system,
- OH $(A^2\Sigma^+ \rightarrow X^2\Pi)$ system.

In pure oxygen most important emission is produced by neutral atomic oxygen and O_2^+ molecular ion:

- $O^I(3p\ ^5P \rightarrow 3s\ ^5S^0)$ at 777 nm and $O^I(3p\ ^3P \rightarrow 3s\ ^3S^0)$ at 844 nm,
- $O_2^+(b^4\Sigma_g^- \rightarrow a^4\Pi_u)$ first negative system (1.NG).

UV-vis-NIR emission produced by electronically excited species was acquired and analyzed during the first 10 microseconds of the streamer micro-discharge evolution. Figure 3 shows spectral regions used to sample the N_2^+-1.NG (0,0) and N_2-1.PG (2,0) band emission waveforms. Bandpass of detected

emission was determined by the input/output slits (100 μm) and by dispersion grating (1200 G/mm) of the HR-320 monochromator. The build-up and decay of 1.NG and 2.PG emissions produced by the streamer micro-discharge in synthetic air is shown in figure 4.

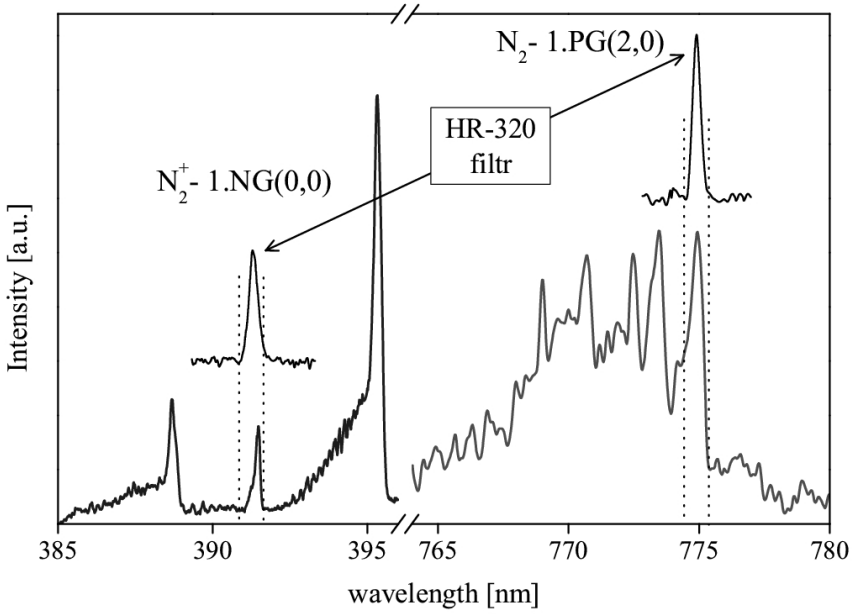


Fig. 3. Typical voltage and current waveforms in the case of four consecutive AC cycles (f_{AC}=5 kHz) applied with repetition frequency f_M = 100 Hz in synthetic air.

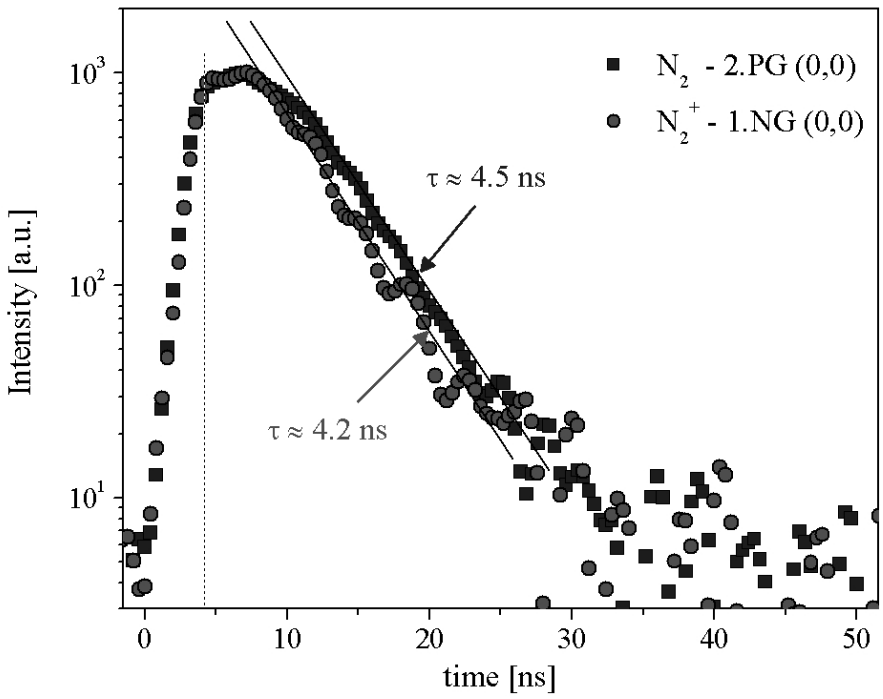


Fig. 4. Build-up and decay of 1.NG and 2.PG emissions produced by the streamer micro-discharge in synthetic air.

Build-up and decay of emissions produced by the streamer micro-discharge in nitrogen is shown in figure 5. Initial decay of N_2^+ 1.NG emission is again comparable with the decay of N_2 2.PG emission intensity. Long tail (0.1-20 μs) of N_2 2.PG, N_2 1.PG and N_2 HIR emissions is caused by $N_2(A^3\Sigma_u^+)+N_2(A^3\Sigma_u^+)$ energy pooling. Concerning the NO-γ bands, the $NO(A^2\Sigma^+)$ electronic state is produced through the well-known resonant energy transfer process $N_2(A^3\Sigma_u^+)+NO(X^2\Pi) \rightarrow N_2+NO(A^2\Sigma^+)$.

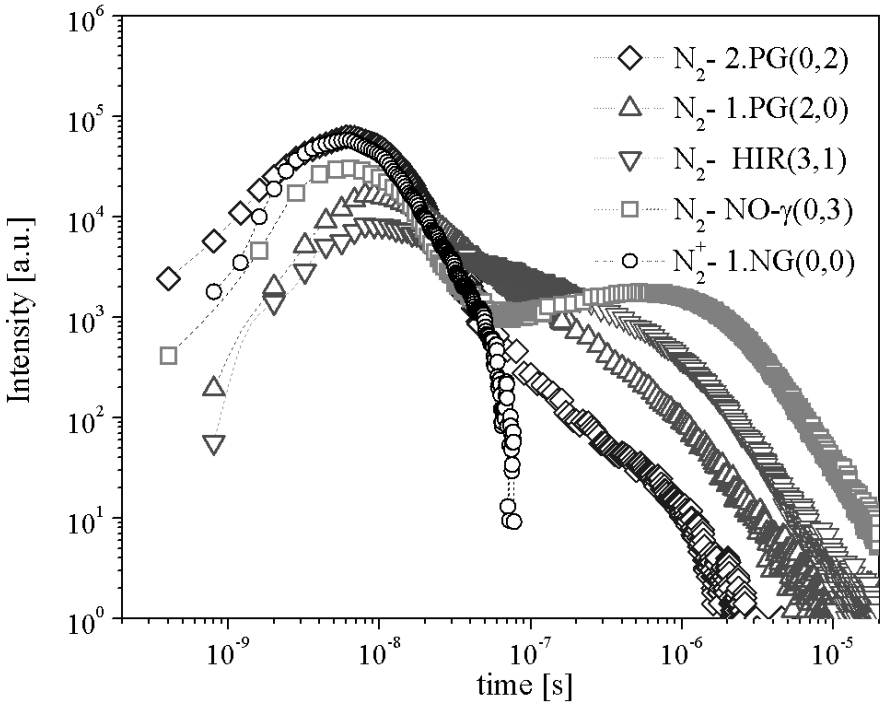


Fig. 5. Build-up and decay of emissions produced by the streamer micro-discharge in nitrogen.

4. Conclusions

Temporal evolutions of observed emission systems induced by a single micro-discharges generated during one AC half-cycle prove that most intense observable emissions are produced by a) energetic electrons through direct electron impact excitation/ionisation/dissociation of N_2/O_2 molecules in the case N_2 2.PG, N_2 1.PG, N_2^+ 1.NG, O_2^+ 1.NG bands and O^I lines, and b) $N_2(A)$ metastable species through $N_2(A)+N_2(A)$ energy pooling and $N_2(A)+NO$ resonant energy transfer processes in the case of N_2 HIR, N_2 GK and NO-γ bands. Microscopic images of individual micro-discharges allow improved evaluation of characteristics streamer dimensions (streamer channel diameter).

Acknowledgments. This work was supported by the Czech Science Foundation (GAČR contract no. 202/08/1106).

AN EXPERIMENTAL AND MODELLING STUDY OF ACETALDEHYDE OXIDATION BY AN ATMOSPHERIC NON-THERMAL PLASMA DISCHARGE

C. Klett, S. Touchard, A. Vega, M. Redolfi, X. Duten, K. Hassouni

Laboratoire d'Ingénierie des Matériaux et des Hautes Pressions,
CNRS-Université Paris 13, 93430 Villetaneuse, France
E-mail: duten@limhp.univ-paris13.fr

Acetaldehyde (CH_3CHO) is a well known indoor pollutant, but recent development of agrofuels, oxygen rich carburant, has led to a new interest in aldehyde abatement researches. This paper reports our results obtained for the degradation of acetaldehyde by an atmospheric plasma corona discharge in a wire to cylinder (WTC) configuration. The process efficiency has been characterized in term of acetaldehyde removal efficiency as a function of the input energy. Main degradation products CO, CO2, CH3OH have been identified and quantified. A homogenous 0D chemical model has allowed us to simulate the studied experimental conditions. Simulation results are in a quite good accuracy with experiments.

1. General

Acetaldehyde (CH_3CHO) is a well known atmospheric and indoor pollutant, coming from natural emissions or human activities. But recent development of agrofuels, for which incomplete combustion produces great amounts of aldehydes, has strengthened the necessity of new abatement researches on this type of molecules [1-7].

Among the air and industrial exhaust gas possible treatments, atmospheric plasma processes have raised a particular interest and demonstrated a quite good efficiency [6-7] particularly for acetaldehyde removal with [8-10] or without a catalyst [11-13].

This work is an experimental and modelling study of acetaldehyde degradation by an atmospheric pulsed plasma reactor device in a wire to cylinder (WTC) configuration.

2. Experimental part

The reactor used in the present work consists in a 100 µm diameter tungsten wire anode placed in a 20 mm diameter cylindrical steel cell (Figure 1).

The atmospheric pressure pulsed corona discharge investigated is generated with the help of a one-stage Marx generator. It produces voltage pulses with durations in the range 50-350 ns. The rate of the voltage increase is of the order of 1-2 kV per ns, while the peak values achieved may be as high as 25 kV. The discharge repetition rate can be varied between 1 and 100 pulses per second.

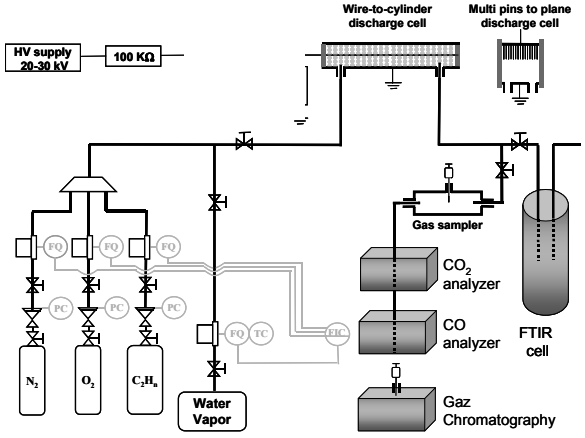


Fig. 1. Experimental setup for investigation of oxidation acetaldehyde in WTC corona discharge

The specific input energy parameter (SIE) corresponds to the energy deposited per unit volume of inlet gas mixture in the discharge cell. It is obtained from the discharge pulse frequency, the energy deposited per pulse and the inlet gas flow rate using the following expression :

$$\mathrm{SIE\ (J.L^{-1})} = \frac{\mathrm{Pulse\ energy\ (J) \times Frequency\ (Hz) \times 60}}{\mathrm{Flow\ rate\ (mL.min^{-1})}}$$

The energy deposited during one discharge pulse is estimated from the measured current and voltage. Figure 2 shows typical voltage and current waveforms associated to the pulsed corona discharge. In the example shown here, the discharge current reaches a maximum of 60 A and is equal to 0 A after 200 ns. The energy absorbed by the discharge during a single pulse was evaluated by integrating the product of voltage and current over the discharge duration. The typical value for the energy deposited in the discharge ranges between 20 and 60 mJ per pulse, which corresponds to an average power of 1 W for a frequency of 1 kHz.

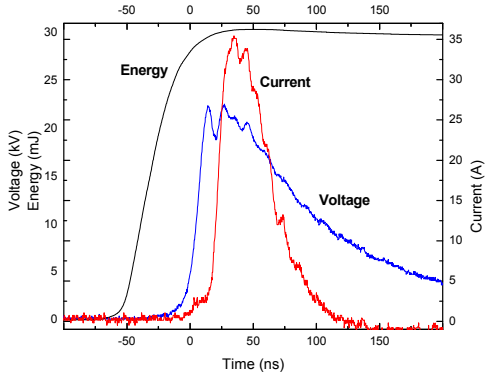


Fig. 2. Typical tension and current temporal profile during one pulse

The feed gas consists of N_2/O_2 mixtures with a small amount of CH_3CHO. The base values of oxygen and acetaldehyde concentrations in the feed gas are 5% and 500 ppm, respectively. The oxygen contents in the feed gas is varied in the range 0-20%.
Acetaldehyde removal efficiency has been evaluated by measuring the pollutant residual concentration as well as the CO and CO_2 one in the cell outlet. Residual acetaldehyde measurements and oxidation by-products identification and quantification are achieved via a Shimadzu GC-2110 Gas chromatography device. The continuous monitoring of CO, CO_2 and H_2O concentrations is realised with a multi gas-analyser (Environnement S.A.) and ozone amounts are monitored by a UV analyser (IN USA).

When the residual fraction of acetaldehyde varies exponentially with the specific input energy SIE, the discharge efficiency for VOC's conversion may be evaluated through the energy cost β as follows:

$$\ln\frac{[CH_3CHO]_{in}}{[CH_3CHO]_{out}} = -\frac{\mathrm{SIE\ (J.L^{-1})}}{\beta\mathrm{(J.L^{-1})}}$$

$[CH_3CHO]_{in}$ and $[CH_3CHO]_{out}$ are the concentrations of acetaldehyde in the feed gas and in the gas flow leaving the discharge cell, respectively.

3. Experimental results

Experimentally, the acetaldehyde removal efficiency has been evaluated by studying the following parameters :

- Residual acetaldehyde as a function of the SIE
- Detection and quantification of by-products.
- Carbon balance and CO_2/CO yields ratio

3.1 Pollutant removal efficiency

Concerning the acetaldehyde removal efficiency, the results reported on figure 3 lead to two main observations. The first one is a change of energetic cost between low and high SIE values. Indeed for SIE values under 100 J/L, the energetic cost β is around 103 J/L, whereas for SIE values over 100 J/L, β decreases to 50 J/L. Considering that, in our conditions, higher SIE values are correlated to higher values of pulse frequency, one explanation could be the higher influence of pulse chemistry in

acetaldehyde conversion at high SIE values comparing to post-discharge chemistry which is predominant at low SIE values. The second observation is that our process is more efficient for an initial gas mixture containing O_2 than for a pure N_2 plasma.

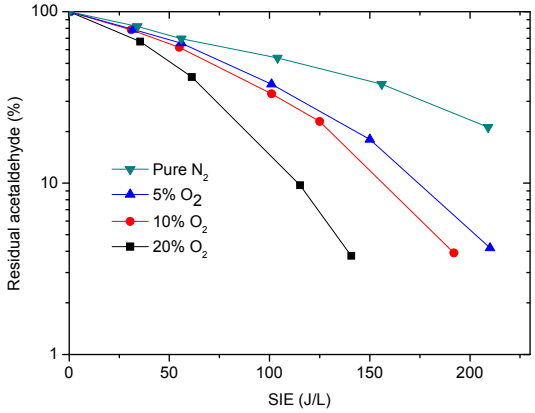


Fig. 3. Residual acetaldehyde as a function of SIE for different O_2 concentration in the inlet gas mixture

Indeed small addition of O_2 in the inlet gas flow increases drastically the efficiency of the discharge, since less than 200 J/L is necessary to obtain 90% of acetaldehyde conversion for a the inlet gas mixture containing 5% of O_2, whereas more than 250 J/L is needed in pure N_2 to reach the same conversion. Adding more oxygen has a real benefit on the acetaldehyde conversion, but mainly for the highest value of SIE. Indeed, on the one hand, for a specific input energy equal to 35 $J.L^{-1}$ the conversion of acetaldehyde increases only by 10% when the percentage of O_2 increases from 5 to 20%, whereas, on the other hand, at 150 J/L, acetaldehyde is almost totally converted with 20% of O_2, 20% of the initial acetaldehyde staying in the gas outlet for 5% of O_2.

3.2 Main detected by-products

The second part of this experimental work deals with the identification and quantification of the acetaldehyde decomposition by-products. In addition to CO and CO_2, methanol, methane, formaldehyde and acetic acid have been identified by gas chromatography, but only methanol and acetaldehyde have been precisely quantified.

Concerning the CO and CO_2 production ratio after conversion of acetaldehyde, it has been estimated by following their yields in initial carbon percentage as a function of SIE. This yield is computed by the following expression:

$$Yield\ of\ CO\ (\%C) = \frac{[CO]}{2 \times [CH_3CHO]_{initial}} \times 100$$

Figure 4 illustrates the evolution of CO and CO_2 yields as a function of the specific input energy for two experimental conditions, without or with 5% of O_2 in the N_2/acetaldehyde inlet mixture.

CO and CO_2 production results show clearly a difference between plasma with O_2 and plasma without O_2 for the CO/CO_2 ratio. In a first analysis, it is not surprising that addition of O_2 leads to an inversion in the CO/CO_2 ratio, CO_2 concentration being predominant on CO one in oxygenated plasma, whereas in pure N_2 plasma, CO amounts are greater than CO_2 ones with a 2,5 factor. The interesting point is in the relative great amount of CO_2 formed in pure N_2 conditions, whereas the only source of O atom is in the C=O bond and the C=O bond energy is around 10 eV. As the electron energy in our plasma doesn't exceed 3-4 eV, the O source can't come from C=O bond breaking. An analysis on possible other pathways of formation of O or OH active species is still in progress.

Influence of the specific input energy, gas temperature and oxygen content in the initial mixture will be presented and discussed during the oral presentation.

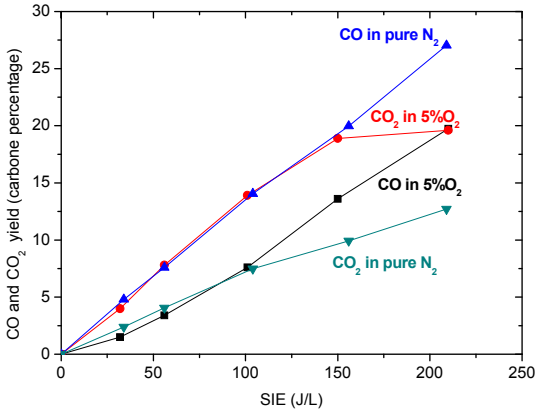


Fig. 4. CO and CO_2 yields in percentage of initial C as a function of SIE

4. Modelling part

4.1 Description of the model

To understand the chemistry and to confirm suspected pathways of decomposition of acetaldehyde as well as to identify other minor by-products , a 0D model of the discharge cell has been developed for this work. It consists in a quasi homogeneous model which is a adaptation of a former model developed for the study of acetylene discharge in a pin to plane configuration [14].

Concerning the chemical scheme, our model includes 90 species reacting in 450 elementary processes. In this chemical scheme some essential reactions often reported in the literature for acetaldehyde decomposition at atmospheric pressure [8-11] have been introduced:

- Electronic impacts for CH_3CHO decomposition, even if the 200 ns discharge time is quite small comparing the post discharge time (100 to 1000 ms).
- Collision of acetaldehyde with N_2 molecules at the first electronic excited state, (mainly $N_2(A^3\Sigma^+_U)$and $N_2(a'^1\Sigma^-_u)$); even if these species have a short life-time in the post-discharge, they seem to play a great role in the pollutant removal when the pulse frequency is high enough.
- Metathesis CH_3CHO decomposition reactions by main active species (O, OH, H, CH_3O), which play the major role in the pollutant removal due to their long lifetime in the post-discharge.

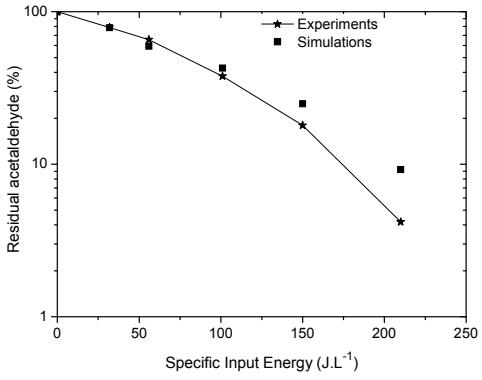


Figure 5. Residual acetaldehyde as a function of SIE for 500ppm of acetaldehyde and 5% of O_2.

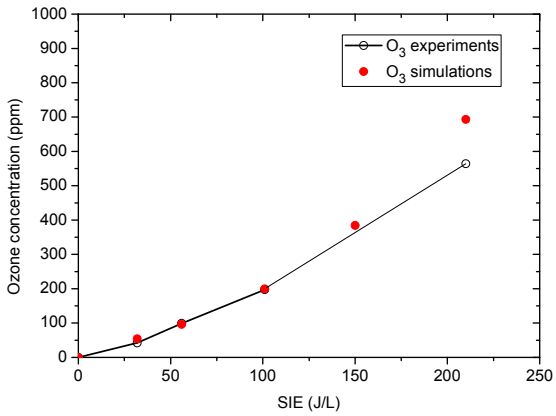


Figure 6. Evolution of ozone concentration as a function of SIE for a 5%O_2 inlet mixture.

4.2 Comparison between model and experiments

Simulated results for conversion of acetaldehyde are shown in figure 8. A quite good accordance between results and simulation for acetaldehyde conversion can be noticed. The selected model has allowed us to reproduce the change of energetic cost β observed experimentally for an SIE exceeding $100J.L^{-1}$.

Concerning the simulation results obtained for main by-product concentrations, comparison between experiments and simulations has shown a very good accordance for O_3 (see figure 5) and CH_3OH (see figure 6). This globally means that chemistry of active species like O and O_2 is well described by the model.
Comparisons between experimental measurements and calculated values of main by-products will be presented and discussed, as well as main pathways of production and consumption of those species.

5. Conclusion

The combined experimental and modelling studies presented in this paper has allowed us to have a first picture of the performance of a pulsed corona discharge working in the nanosecond regime in a wire to cylinder configuration for acetaldehyde removal.
It has been demonstrated that our WTC configuration allows a quantitative oxidation of acetaldehyde (more than 90% conversion) for a specific input energy around 200 $J.L^{-1}$ at ambient temperature and at low oxygen concentration (5%) in the inlet gas mixture. This efficiency can reach a total removal of the 1000 ppmc of acetaldehyde introduced initially, if they are mixed with 20% of O_2. and with only a 150 $J.L^{-1}$ specific input energy .
The quasi-homogeneous model proposed in this study has permitted to have a first approach of the reactivity of acetaldehyde and has allowed us to reproduce with a quite good accordance the main by-products concentration for CO, CO_2, O_3 and CH_3OH.
Acknowledgement. This work has been financially supported by "Agence Nationale de la Recherche" (JCJC BIOPAC).

6. References

[1] Hugo Destaillats, Randy L. Maddalena, Brett C. Singer, Alfred T. Hodgson, Thomas E. McKone, Atmospheric Environment, 42, p. 1371-1388 (2008)
[2] Lisa A. Graham, Sheri L. Belisle, Cara-Lynn Baas, Atmospheric Environment, 42, p. 4498-4516 (2009)
[3] Yage Di, C.S. Cheung, Zuohua Huang, Atmospheric Environment, 43, Issue 17, p. 2721-2730, (2009)
[4] Bang-Quan He, Shi-Jin Shuai, Jian-Xin Wang, Hong He, Atmospheric Environment, 37, p. 4965–4971, (2003)
[5] G. Karavalakis, S. Stournas, E. Bakeas, Science of The Total Environment, 407, p. 3338-3346 (2009)
[6] Hsin Liang Chen, How Ming Lee, Shiaw Huei Chen, Moo Been Chang, Sheng Jen Yu, and Shou Nan Li Environ. Sci. Technol., 43, p. 2216-2227, (2009)
[7] Hyun-Ha Kim Plasma Process. Polym., 1 , p.91-110, (2004)
[8] N. Sano, T. Nagamoto, H. Tamon, T. Suzuki, M. Okazaki, Ind. Eng. Chem. Res., 36, p. 3783-3791 (1997).
[9] A. S. Chiper, N. Blin-Simiand, F. Jorand, S. Pasquiers, G. Popa, C. Postel, J. of Optoelectronics and advanced materials, 8, p. 208 – 211 (2006)
[10] L. Magne, S. Pasquier, V. Edon, F. Jorand, C. Postel, J. Amorim, J. Phys. D : Appl. Phys., 38, p. 3446-3450 (2005)
[11] How Ming Lee, Moo Been Chang, Plasma Chem. and Plasma Process., 21, P. 329-343 (2001)
[12] Jintawat Chaichanawonga, Wiwut Tanthapanichakoon, Tawatchai Charinpanitkul, Apiluck Eiad-ua, Noriaki Sano, Hajime Tamon, Sci. and Techn. of Adv. Mat. 6 319–324 (2005)
[13] J. Van Durme, J. Dewulf, C. Leys, H. Van Langenhove, Appl. Cat. B: Environ., 78, p 324–333 (2008)
[14] M. Redolfi, N. Aggadi, X. Duten, S. Touchard, S. Pasquiers, K. Hassouni, Plasma Chemistry and Plasma Processing, 29, p.173-195(2009)

INVESTIGATION OF THE TRICHEL DISCHARGE IN AIR AT ATMOSPHERIC PRESSURE BY INTENSIFIED CCD CAMERA AND CROSS-CORRELATION SPECTROSCOPY

Sylvain Gaychet[1], Helge Grosch[2], Tomáš Hoder[2], Delphine Bessières[3], Anne Bourdon[4], Florent Lemont[1], Ronny Brandenburg[2*], Nicolas Soulem[3], and Jean-Hugues Paillol[3]

[1]*CEA Marcoule, France*
[2]*Leibniz Institute for Plasma Science and Technology (INP), Greifswald, Germany*
[3]*LGE "Dielectrics and modelling group" University of Pau, Pau, France*
[4]*EM2C group Ecole Centrale Paris, Paris, France*
*E-mail: brandenburg@inp-greifswald.de

Corona Trichel pulses in ambient air are investigated by ICCD recording and cross-correlation spectroscopy. Preliminary results of cross-correlation spectroscopy measurements show that the discharge starts in the volume, approximately 100 μm away from the negative point under given conditions. Results further suggest that a cathode directed as well as an anode directed ionization front appear during Trichel pulse development.

1. Introduction

Negative corona discharges are of considerable importance as a source of active and charged particles in many applications for surface treatment or in plasma chemistry. They present an infinite variety of forms depending on gap length, on gas pressure, or the value of the applied dc voltage [1]. At atmospheric pressure, in the pulsed regime, the luminous emission of these discharges is faint and their duration is very short. In spite of the extensive number of experimental studies, there is still no agreement about the physical mechanisms responsible for the current pulse rise. Negative coronas remain a real challenge for experimental investigations and computational models. The common way to study negative coronas is to use a point to plane electrode system. The point electrode is connected to a DC power supply generating a sufficient high voltage for discharge ignition. The generated discharge typically passes through different stages, by slowly increasing the applied voltage [1]: (1) Field intensified dark current; (2) Trichel pulse corona, mainly in electronegative gases, (3) Negative streamer corona, or directly; (4) Spark breakdown. Trichel pulse corona usually consists of single current pulses at a very regular frequency, up to several MHz. If the voltage is increased, the pulses get larger, and finally a regular current pulse is superimposed to a continuous current. When increasing the voltage, the pulse amplitude decreases whereas the continuous current value increases, finally leading to a pulse less glow regime. If the voltage gets higher, spark occurs.
Because of its application, negative coronas have been widely studied, however some open questions still remain. One of the most important is: What kind of physical mechanism can be responsible for the ignition and development of the pulse in the early stage of the current growth [2, 3]. An answer can be given by recording the luminous emission of discharge generated excited states of nitrogen during the complete current pulse. In this context, cross-correlation spectroscopy technique (CCS) can give a sufficient resolution in time, to measure the emissions during the pulse rise of 1.5 ns, and in space, the discharge develops in a zone close to the cathode of roughly 100 μm long.

2. Experimental setup

The corona discharge in a point to plane electrode system (the radius of curvature of the point was 320 μm or 270 μm, the gap length is 0.7 cm or 1 cm, see Fig.1a) was investigated. The DC positive voltage was applied to the plane electrode. Thus the point served as cathode. The current measurement were done by the voltage probe on a 50 Ω resistor connected to the negative point. For short exposure time images iCCD DiCam Pro SVGA (PCO Imaging) was used combined with the Questar QM 100 far-field microscope with resulting spectral sensitivity in range of 300 to 1300 nm and spatial

resolution down to 4 µm. The iCCD camera was operated in single shot mode, i.e. iCCD photos show individual discharge events. The set-up of the CCS apparatus is given in Fig.1b.

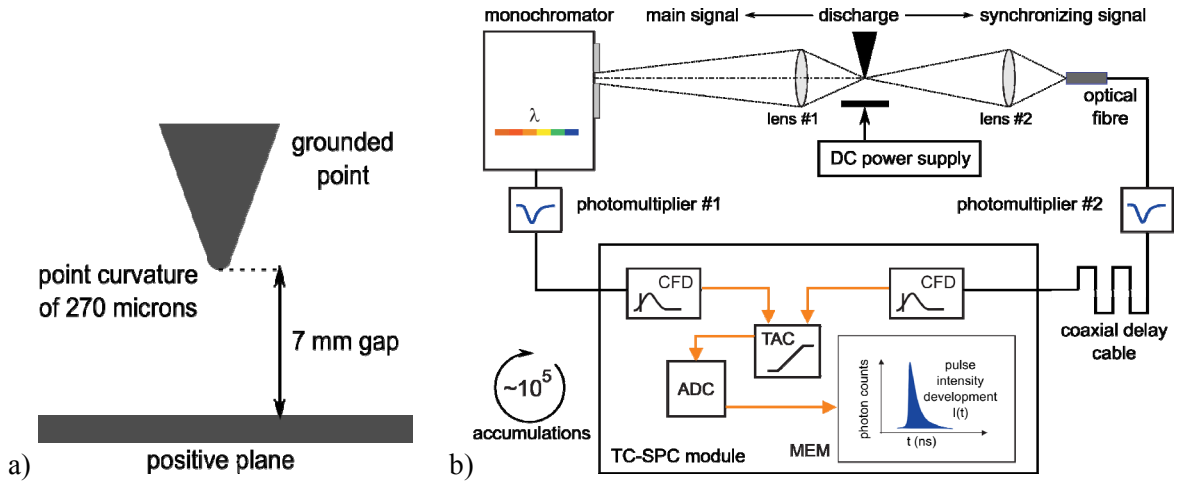


Fig. 1. A scheme of the investigated corona setup a) and the CCS arrangement b).

A detailed description of the method is given elsewhere [4], here only the main features should be given. The CCS is based on single photon counting procedure and the real-time measurement of the discharge event is substituted by the statistically averaged determination of the cross-correlation function between two optical signals, both originating from the same source (microdischarges). The first signal is the spatially and spectrally resolved main signal. For spectral resolution a monochromator (Acton Spectra Pro -500i) is used. In the set-up used here the discharge area is optically magnified by an achromatic lens and directly imaged onto the entrance slit of the monochromator. Spatial resolution is realized by moving of the whole electrode arrangement. The monochromatic light of the main signal is detected by highly sensitive photomultiplier PMT#1 (Hamamatsu, type H5773-04) operating in the single photon counting mode. The second signal is the so-called synchronizing signal. It is received from the entire discharge (taken from the side) and detected by the second photomultiplier PMT#2 (Hamamatsu, type H5773-04) which is set at a lower gain and consequently not operating in the single photon counting mode. The electric pulses of the PMTs are analyzed by means of time-correlated single photon counting module (TC-SPC 150, Becker & Hickl). In order to select pulses with correct amplitude and to determine the exact time of detection, constant fraction discriminators (CFD) are used for both signals. The pulses from the main signal start a linear rise of the voltage of the time-to-amplitude converter (TAC), which is stopped by the synchronizing pulse from the second CFD. The measured voltage amplitude is a measure for the time delay between both pulses and therefore gives the time-information of the detected photon regarding the complete light pulse of the discharge event. This value is converted to the memory address by an analogue-to-digital converter (ADC) and a unit is added to a channel within the memory block (MEM). Consequently, from more than 10^4 counted photons a time histogram representing the spectrally resolved light pulse for a distinct spatial coordinate in the electrode arrangement is accumulated. Indeed a good reproducibility of the light source must be fulfilled and to achieve complete spatio-temporally resolved discharge development the accumulation must be done for all spatial coordinates. The CCS set-up used here enables the achievement of a high temporal resolution of almost 0.01 ns and spatial resolution of 10 µm.

3. Results and discussion

In the described set-up, depending on the value of the applied voltage, the negative corona discharge operates in two different regimes. At lower values of the voltage amplitude the Trichel regime with regular current pulses of 300 ns duration and amplitudes of about 7 mA are investigated. If the voltage exceeds a value of U = 17.8 kV, a continuous current of 0.2 mA is investigated. The iCCD photos are taken with one single exposure gate in order to distinguish between the two different regimes. The

light emitted by the discharge in the visible spectral range for point radius of 320 µm and gap distance of 1 cm is presented in Fig. 2. The exposure time of the CCD sensor covers the whole pulse period (window shown by the dashed line).

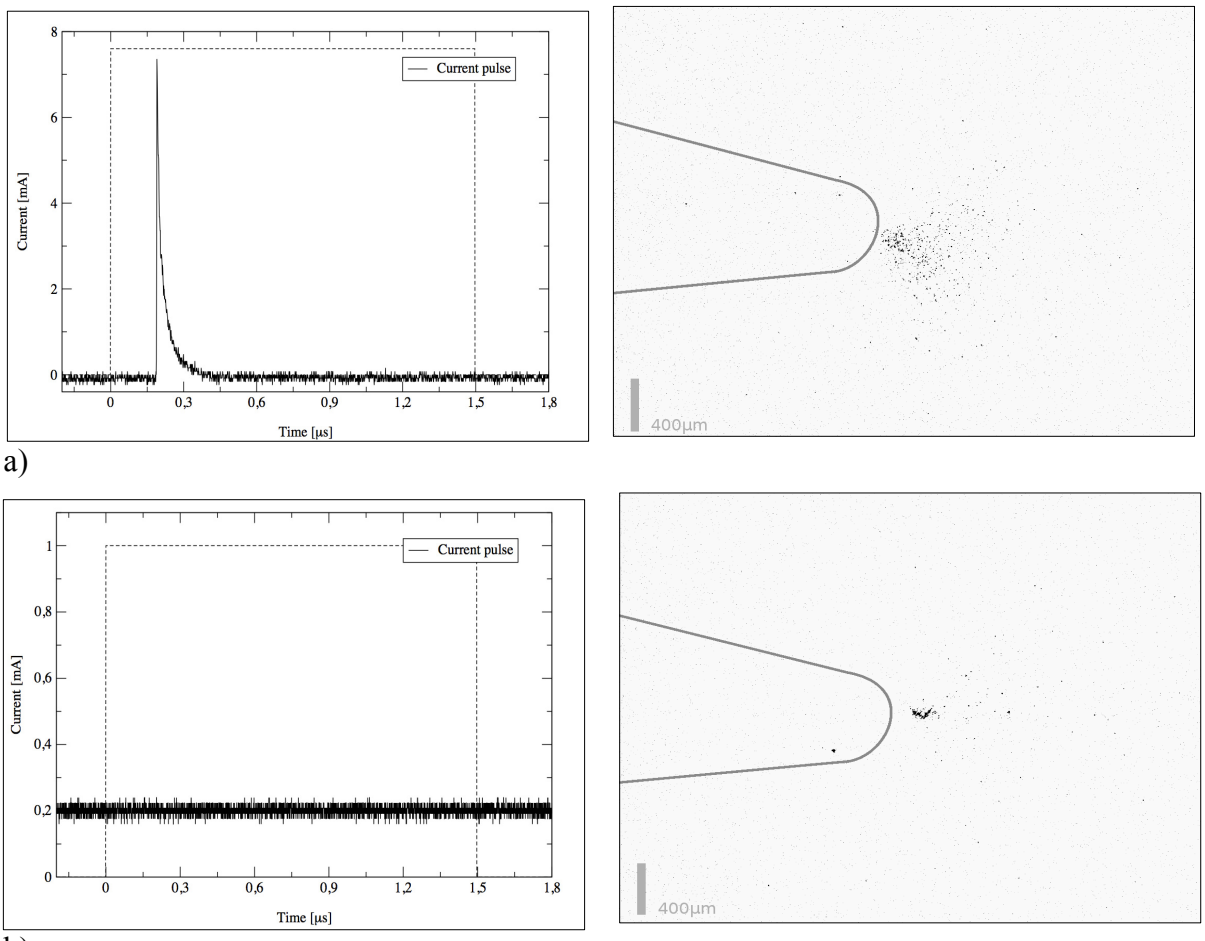


Fig. 2. Current measurement as a function of time with the exposure time of 1.5 µs (left) of the picture of the discharge (on the right) at 12.4 kV a) and 17.8 kV b).

At voltage of U= 12.4 kV (Fig. 2a) there is no continuous current and regular current pulses are investigated. In spite of the weak luminous emission, one can consider that the discharge develops in a zone of a plume shape. In the continuous current regime (Fig. 2b) a thin luminous canal forms in the vicinity of the point followed by a weaker plume shape zone. The canal is separated from the cathode surface by a non-luminous zone of about 20 µm which is in the same order of magnitude than a cathode sheath length at this conditions. The more intense light is emitted by this canal, rather than by the plume.

Because of the regularity of the Trichel pulses, one can attempt to make spatio-temporally resolved CCS measurement for this regime. The optical triggering of the single photon counting on the same discharge event in CCS method is beneficial since the frequency of light pulses fluctuates as a whole although the time delays between direct subsequent pulses are negligible [5]. The CCS measurements are done with a smaller point radius of 270 µm since in this geometry the spatial stability was better than for 320 µm. Considering these experimental conditions, one can observe the light emitted by the discharge as a function of the distance from the cathode and the time. The head of the spectral band of 0-0 vibrational transition of the second positive system of molecular nitrogen (at the wavelength of 337.1 nm) was chosen since it is the most intense emission and reveals a high ionization rate activity in the gas. The result is presented in Fig. 3.

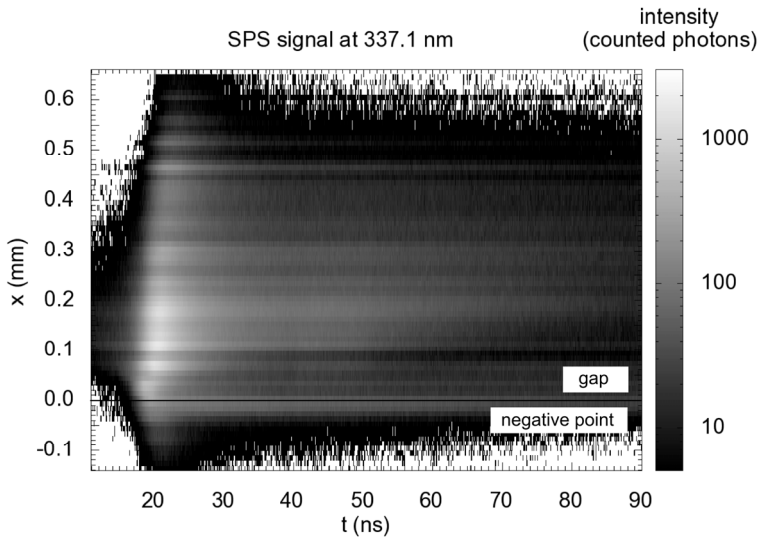


Fig. 3. Spatio-temporally resolved emission of the second positive system of molecular nitrogen at 337.1 nm of regular Trichel pulses at 7 kV. For the iCCD picture see the Fig. 2a).

It can be clearly seen that under given conditions the discharge starts to develop in the gas, approximately 100 μm far from the point position (located at 0 mm). This light emission can be attributed to the electron multiplication phase predicted by Alexandrov [6], observed by Sigmond [1], and numerically simulated by Morrow [7]. Morrow showed that the subsequent phases are associated with a movement towards the cathode of the peak of electron density, positive ion density and light emission. The electron multiplication phase develops in the time window below 15 ns, which is not completely shown in Fig. 3. After the electron multiplication phase (from 17 ns on) one can see an ionizing wave propagating towards the anode forming a 500 μm long zone of intense light emission. The development of a cathode directed ionization wave can be suggested, too but not exactly resolved by this preliminary CCS data. The results are consistent with the suggestion that the ionization mechanism controlling the pulse formation is a positive ionizing wave–like mechanism, as already been proposed in electronegative gases, and gas mixtures, mainly at lower pressure [8].

4. Conclusions

Two different modes of DC negative corona discharges were investigated by iCCD camera photos and current measurements, depending on the applied voltage: Trichel pulse regime and continuous current regime. The first CCS results for Trichel pulses give first impressions on the discharge development at these conditions. An electron multiplication phase as well as cathode and anode directed ionizing waves can be suggested. However, the preliminary CCS data do not allow to exactly resolve the propagation and to clarify the development completely. Therefore additional efforts on discharge stabilization for further CCS studies will be made.

References

[1] Sigmond R.S. 1978 *Electrical Breakdown of gases* edited by Meek and Craggs Wiley 319-384.
[2] Bessieres D., Paillol J., Soulem N. 2004 *J. Appl. Phys.* **95** 3943.
[3] Akishev Yu.S., Kochetov I.V., Loboiko A.I., Napartovich A.P. 2002 *Plasma Physics Reports* **28** 1049.
[4] Wagner H.-E., Kozlov K.V., Brandenburg R. 2008 In : *Low Temperature Plasmas*, 2nd edition, vol 1 editet by Hippler et al. Wiley VCH 271-306
[5] Kozlov K.V., Boksha N.S., Morozov A.M.and Samoilovich V.G. 2002 Proc. Hakone VIII, Estonia
[6] Alexandrov G.N.1968 *Soviet Phys. - Tech Phys 8 - 161*
[7] Morrow R. 1985 *Physical Review A*. **32** N.3 1800.
[8] Cernak M., Hosokawa T., Kobayashi S., Kaneda T. 1998 *J. Appl. Phys*. **83** 5678.

TIME RESOLVED BROADBAND SPECTROSCOPY OF DBD OPERATING FROM HOMOGENOUS TO FILAMENTARY REGIME IN PURE N_2 WITH O_2 TRACES

A. Annušová[1], P. Čermák[1,3], J. Rakovský[1,4], V. Martišovitš[2] and P. Veis[1]

[1] *Department of Experimental Physics, FMPH, Comenius University, Mlynská Dolina, 842 48, Slovakia*
[2] *Department of Astronomy, Physics of the Earth and Metrology, FMPH, Comenius University, Mlynská Dolina, 842 48, Slovakia*
[3] *Laboratoire de Spectrométrie Physique, CNRS UMR 5588, Université Joseph Fourier, Av. de la physique, 38400 Saint Martin d'Heres, France*
[4] *Institut Carnot de Bourgogne, CNRS UMR 5209, Université de Bourgogne, Av. A. Savary 9, BP 47 870, F-21078 Dijon Cedex, France*
E-mail: ann.adriana@gmail.com, cermak@fmph.uniba.sk, veis@fmph.uniba.sk

The spectroscopic study of the dielectric barrier discharge operating from homogenous to filamentary regime is presented. The investigation was focused on the correlation of the temporal behavior of the emission spectra with the different character of the discharge. We used the planar configuration of the reactor with electrodes covered by the Al_2O_3 dielectrics and the gap of 1 mm length. The discharge was generated in pure nitrogen flow with controlled amount of oxygen traces at near atmospheric pressures (80-120 kPa) using the sinusoidal high voltage generator (7-10 kV voltage and 4.85 kHz frequency). We realized time resolved spectroscopic measurements in a broad spectral range (from UV to near infrared 200-1000 nm) with 5 μs time resolution. The emission spectra contained systems from molecular nitrogen (2^{nd} positive, Herman Infrared) and oxy-nitrogen compounds (NO gamma, O-N_2 green) systems.

1. Introduction

Dielectric barrier discharges (DBD) represent an example of high pressure discharges with unique combination of non equilibrium and quasi-continuous behavior. Plasma created by this manner became utilized in numerous applications [1].

It's commonly known, that DBD can be generated in two regimes: filamentary and homogenous (also known as diffuse or glow regime). Under normal conditions (e.g. in air) we generate the filamentary mode, which is characterized by streamer mechanism of ignition, presence of multiple microdischarges with nanosecond durations and low degree of ionization. In comparison, the homogeneous operation mode is significant with one current pulse under each half cycle. This uniform discharge works at relatively low supply voltages. Recently, because of its advantages from an industrial point of view the interest toward it started to grow [2, 3]. The glow regime is formed under specific conditions only. It depends on the properties of the feeding gas and the feeding voltage frequency as was showed previously [3, 4]. Besides it is difficult to prevent the conversion to the unfavorable but much more stable filamentary mode. Therefore there are a lot of works, in which the transition between these two regimes, the generation of the homogenous mode [5-9] and the origins of its destabilization are discussed [10]. Such a diagnostic and modeling is very helpful to determine the parameters of stable glow regime in industrial conditions (often lower gas purity). As it is described for example in [4] a glow DBD in N_2 is characterized with a Townsend breakdown. In order to generate only one current pulse instead of streamers the existence of Penning ionization (thus the presence of metastables), high gas purity and suitable excitation frequency is needed [4]. In our previous work [11] we studied the microdischarge mode of DBD in N_2. Now within the same discharge reactor, but with planar electrodes we succeed to generate the glow mode, then with admixture of O_2 traces we achieved a transient (appearance of current spikes, coexistence of the two regimes) and after that a filamentary regime. This is due to the fact, that oxygen is highly electronegative gas and very effective quencher of $N_2(A^3\Sigma_u^+)$ metastable state. We follow the path of Brandenburg et al. and Kozlov et al. [12, 13] and other authors [14, 15] who studied DBD in mixtures N_2/O_2.

2. Experimental set-up

The experimental arrangement is presented in Fig. 1. The discharge reactor (Fig. 2), made of a rigid steel construction, is suitable to work at both low and high pressures (up to 3 atm.). We used parallel configuration of electrodes covered with Al_2O_3 plane dielectrics of 1 mm thickness (Fig. 2 (a)). The length of a discharge gap during the measurements was set to 1 mm, but it is variable up to several mm. The gas was injected directly into the discharge zone.

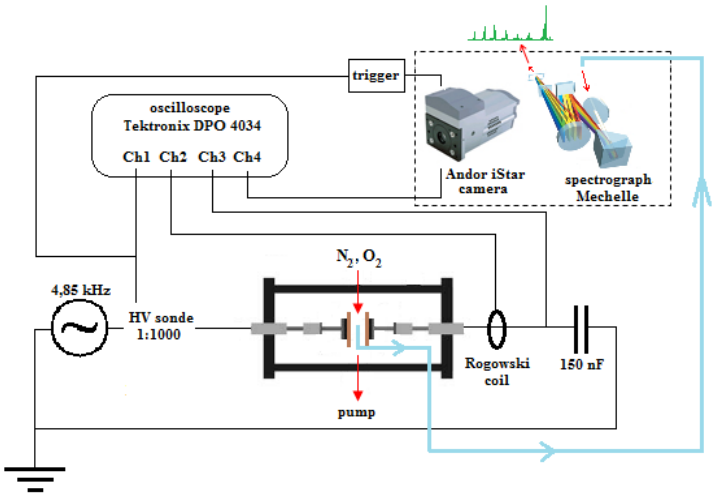


Fig. 1. Experimental set-up

For powering the discharge a sinusoidal high voltage generator operating at 4.85 kHz with configuration of one grounded electrode was used. To measuring the power consumed by the discharge a capacitor (150 nF) in serial connection was used. It was managed by measuring the phase shift of the voltage drop over the discharge and the capacitor. The gating period of the intensified CCD camera was monitored on the oscilloscope together with discharge voltage and current (Fig. 3).

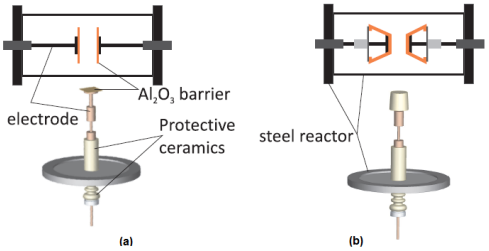


Fig. 2. DBD reactor with two types of dielectric barrier used

For optical diagnostic we utilized spectrometer Andor Mechelle ME5000 equipped with an iCCD detector (Andor iStar camera). It provides the construction of highly resolute spectra ($\lambda/\Delta\lambda$=4000) in range from 200 to 1000 nm. The emitted light was focalized by an MgF_2 lens into the optic fiber and after that to the entrance slit of the spectrometer.

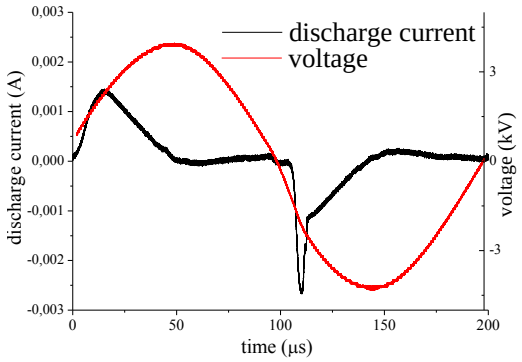


Fig. 3. Discharge current and applied voltage

In this paper we present the study of the effect of oxygen traces (0.01–0.04 %) on the character of the discharge in nitrogen glow DBD. Time-resolved spectra were observed with 5μs windows for a whole period (~200 μs). We report a comparison with our previous work [11], where we used Al_2O_3 barriers (Fig. 2 (b)) in a form of a round cup (with 2 cm bottom diameter and 2 mm dielectric thickness).

3. Results and discussion

3.1 Emission in glow DBD

It is well known, that with presence of oxygen even a few ppm beside the systems from molecular nitrogen - *second positive (R1) and Herman Infrared (R2)* - a high excitation of oxy-nitrogen species occur - *NO_γ system (R3) and ON_2^* green transition (R4)*. Even in pure nitrogen we can observe these species, also in our discharge reactor. They may come from impurities; namely for example from water vapor. Although these impurities are undesirable in the experimental setup, we can get of them valuable results.

$$N_2(C^3\Pi_u)_{v'} \rightarrow N_2\left(B^3\Pi_g\right)_{v''} + h\nu(2^+) \quad \text{(R1)}$$

$$N_2\left(C''^5\Pi_u\right)_{v'} \rightarrow N_2\left(A'^5\Sigma_g^+\right)_{v''} + h\nu(HIR) \quad \text{(R2)}$$

$$NO(A^2\Sigma^+)_{v'} \rightarrow NO(X^2\Pi)_{v''} + h\nu(NO_\gamma) \quad (R3)$$

$$O(^1S)N_2 \rightarrow O(^1D) + N_2 + h\nu(ON_2{}^*) \quad (R4)$$

The upper states of mentioned transitions are strongly excited by metastables states (R5 – R9):

$$NO(X^2\Pi_r) + N_2(A^3\Sigma_u^+) \rightarrow NO(A^2\Sigma^+) + N_2 \quad (R5)$$

$$N_2(A^3\Sigma_u^+) + N_2(A^3\Sigma_u^+) \rightarrow N_2(C'^5\Pi_u) + N_2 \quad (R6)$$

$$O(^3P) + N_2(A^3\Sigma_u^+) \rightarrow O(^1S) + N_2(X^1\Sigma_g^+) \quad (R7)$$

$$O(^1S) + 2N_2 \rightarrow O(^1S)N_2 + N_2 \quad (R8)$$

$$N_2(A^3\Sigma_u^+) + N_2(A^3\Sigma_u^+) \rightarrow N_2(C^3\Pi_u) + N_2 \quad (R9)$$

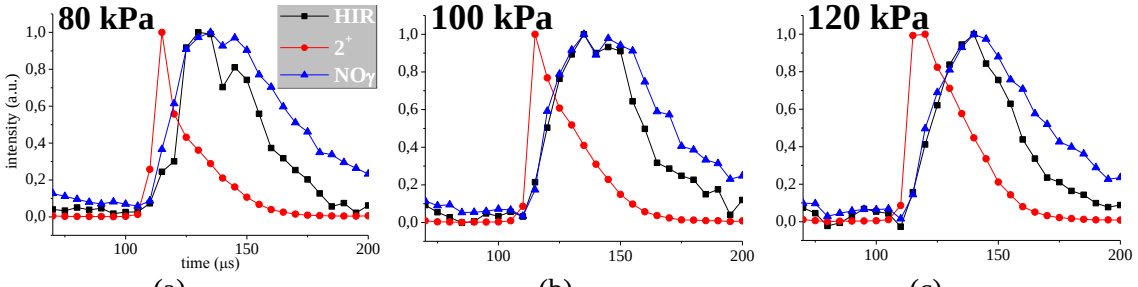
In our case, the assumption of the most probable kinetic scheme (R5 – R11) is based upon [6, 13] (experiments with parallel plate electrode arrangement and two semi-spherical electrodes, respectively). In [6] there was observed a complete match between the emission curve of 2^+ and the discharge current. In [13] there was find a slight deviation between them, which is thought to be due to the two dimensional geometry [13]. In fact, according to the authors, 2^+ system is formed exclusively through reaction (R10) while pooling reaction (R9) is not considered as a probable way of excitation, contrary several types of nitrogen discharges at low pressure. As we will see below, we also noticed a difference between the current and the 2^+ system emission shapes (Fig. 3 and Fig. 5 (a)). Both are similar in pure nitrogen at 80 kPa pressure, start to differ with increasing gas pressure and with oxygen addition become completely different. The latter has a form of a parabola, while the current is characterized by a broke shape in the afterglow region. Meanwhile, we don't exclude reaction (R9). A more supported model will be developed later.

$$N_2 + e \rightarrow N_2(C^3\Pi_u) + e \quad (R10)$$

$$O_2 + N_2(A^3\Sigma_u^+) \rightarrow N_2(X^1\Sigma_g^+) + O + O \quad (R11)$$

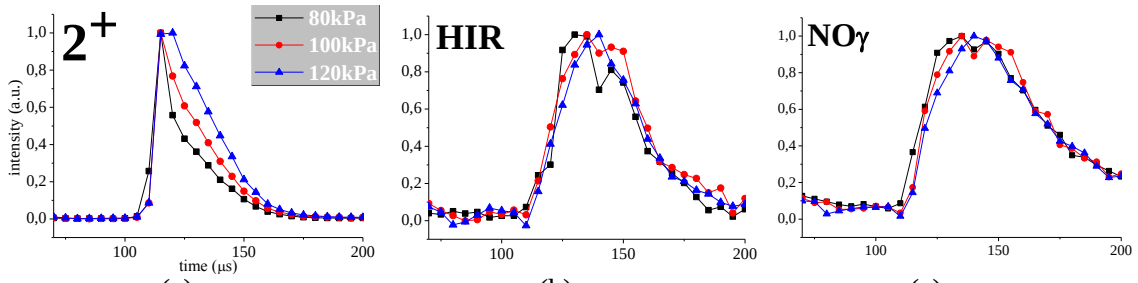
The pictures Fig. 4, 5 and 6 represent the emission intensity of the studied systems normalized to its maximums. Emissions were calculated by integrating the area under the following peaks: transition 0-2 (247,4 nm) for NO_γ, transition 1-0 (752 nm) for HIR, transition 0-0 (337,1 nm) for 2^+ and ON_2* transition at 557 nm. During the measurements we kept the power constant.

When comparing the emission profiles with the discharge current (Fig. 3) we can distinguish the difference between radiative states and long-living states or states repopulate by other metastable states. 2^+ system roughly copies the current and achieves the greatest value at its maximum. The other states reach their maximum and decay later ($N_2(C'^5\Pi_u)$ and $NO(A^2\Sigma^+)$ states). However, $ON_2{}^*$ is the longest radiant system in the plasma, but its signal was far worse in the glow regime comparing to the results of our previous work in the case of filamentary DBD in pure nitrogen [11]. This is in contrast with the results in [6], where it vanished just in the filamentary mode. In fact, the signal to noise ratio is low enough to see a clear behavior. Fig. 7 (a) presents the cases of 0.03 and 0.04 % O_2 traces, where gas mixture with 0.04% is in the transient regime. The excitation of $ON_2{}^*$ is entirely controlled by metastables unlike NO_γ [6] (creation of $NO(A^2\Sigma^+)$ is possible by a small contribution of direct electron excitation from $NO(X^2\Pi_r)$ state too). So in the case of O_2 presence only as impurity another mechanism has to be present, by which the $ON_2{}^*$ state is effectively quenched before that it can be radiated. According to a model published by Brandenburg et al. [12] the destruction of the metastable oxygen is caused by quenching by NO and O_3. So if these processes are very effective, this can explain the low intensity of $ON_2{}^*$ emission in the case of nitrogen with O_2 only as impurities.



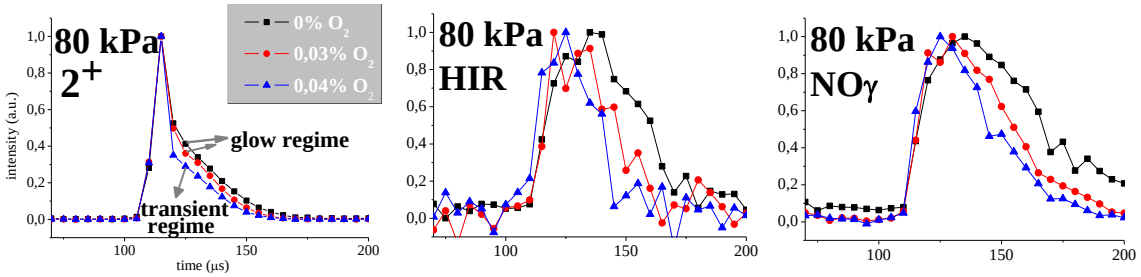
(a) (b) (c)

Fig. 4. Comparison of emission systems at different pressures in pure nitrogen (glow DBD)



(a) (b) (c)

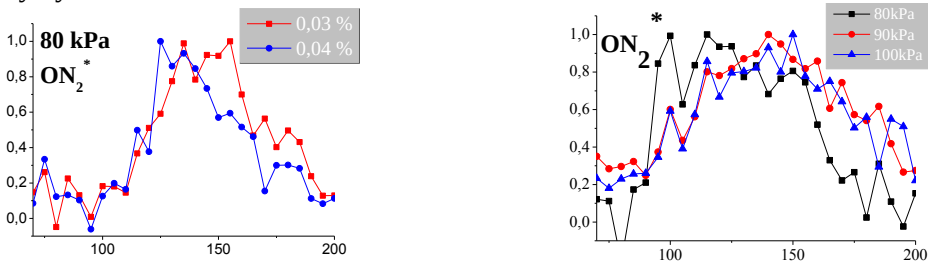
Fig. 5. Evolution of emission systems with pressure in pure nitrogen (glow DBD)



(a) (b) (c)

Fig. 6. Evolution of emission systems, depending on the concentration of O_2 at 80 kPa

With increasing pressure the 2^+ system is more intense (Fig. 5 (a)) but on the contrary its less intense with increasing concentration of O_2 (Fig. 6 (a)). Unlike the 2^+ system (Fig. 5 (a)), there is no change in the emission of HIR and NO_γ with pressure (Figure 5 (b) a (c)). However, with the addition of oxygen we can see decreasing character as in the case of the 2^+ system (Fig. 6). This is due to more important quenching of these states by the increasing amount of O_2 (R11). As we can see, reaction (R9) can be important, because the intensity of the 2^+ system is decreasing in the same way as the other systems affected mainly by metastables.



(a) (b)

Fig. 7. Evolution of ON_2^* emission with pressure in mixture N_2/O_2 (glow discharge)(a) and in pure nitrogen (filamentary DBD)(b)

3.2 Comparison of emissions in glow and filamentary DBD

It's interesting to compare the emission of the studied systems under different discharge mechanism (filamentary regime - our previous publication [11] and transient and glow regime – present results). In the next figures we present the integrated areas of the same transitions as were used in chapter 3.1. These emissions in the filamentary DBD were obtained under the positive half cycle of the period of the supply voltage unlike the glow regime (Fig. 3). The measured power was kept constant and reaches higher values than in the glow regime. The most obvious result is that we observed the same radiation delay in the afterglow region in the case of NO_γ and HIR as in the glow mode, which indicates the effect of metastables (R5, R6).

In the emission of HIR and NO_γ, there is a small peak around 100 μs, which correspond to the position of microdischarge initialization (Fig. 8 (b), (c)). At the same place we can see a maximum for 2^+ system (Fig. 8 (a)). We assume that this point refers to the excitation by direct electron impact, which is considered as a main process in the creation of $N_2(C^3\Pi_u)$ state. The maximum of the other systems is shifted, what is an indicator of the presence of metastables. In the case of ON_2^* there is a relatively

high signal to noise ratio (Fig. 7 (b)). As Fig. 4 – 6 show, in the glow regime the emission curves are more continuous around 100 μs, which indicate a reduced effect of electron excitation. This is in a good agreement with the theory, that $N_2(A^3\Sigma^+_u)$ concentration is higher in the glow mode, same as its contribution to excitation. At lower pressure (80 kPa) there are some variations (Fig. 8). The contribution of electrons is higher, because a sharper peak appears at the start of the radiation. Simultaneously the intensity of 2^+ system decreases more monotonously.

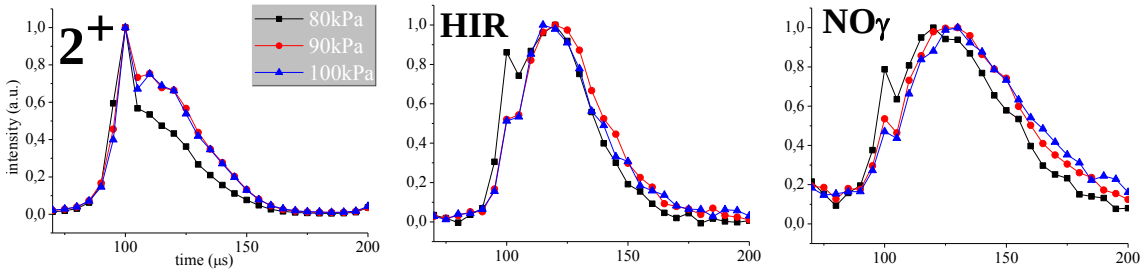


Fig. 8. Evolution of emission systems with pressure in pure nitrogen (filamentary DBD)

4. Conclusion

As we recently made the study of a filamentary DBD we decided to repeat it for the glow regime. We used the same discharge chamber for both. In N_2 plasma with admixture of O_2 traces we observed a simultaneous transition between them. The aim of this paper was to observe the differences between the radiation curves in a glow and a filamentary DBD. The emissions of nitrogen and oxy-nitrogen compounds are presented (2^+, HIR, NO_γ, ON_2^*). In glow regime we noticed a very low radiation of ON_2^* excimer molecule in contrast to the filamentary working mode. We proposed a simple kinetic model, which we want to extend and confirm in the frame of future works.

Acknowledgements. This research was sponsored by the Science and Technology Assistance Agency under the contracts No. APVV-0544-07 and by the Scientific Grant Agency of Slovak Republic No. VEGA 1/0609/08, 1/0851/09 and 1/0512/10.

5. References

[1] U. Kogelschatz 2003 *Plasma Chem. Plasma Process.*, **23**, 1, 1–46
[2] A. S. Chiper, B. G. Rusu, A. V. Nastuta, G. Popa 2009 *IEEE Transactions on Plasma Sci.*, **37**, 10
[3] F. Massines, N. Gherardi, N. Naudé, P. Ségur 2009 *Eur. Phys. J. Appl. Phys.*, **47**, 2
[4] F. Massines, P. Ségur, N. Gherardi, C. Khamphan, A. Ricard 2003 *Surface and Coatings Tech.*, **174-175**, 8–14
[5] N. Gherardi, F. Massines 2001 *IEEE Transactions on Plasma Sci.*, **29**, 3
[6] N. Gherardi, G. Gouda, E. Gat, A. Ricard, F. Massines 2000 *Plasma Sources Sci. Tech.*, **9** 340–346
[7] N. Naudé, J.-P. Cambronne, N. Gherardi, F. Massines 2005 *J. Phys. D: Appl. Phys.*, **38**, 530–538
[8] F. Massines, A. Rabehi, P. Decomps, R. B. Gadri, P. Ségur, Ch. Mayoux 1998 *Journal of Applied Physics*, **83**, 6, 2950-2957
[9] J. H. Choi, T. I. Lee, I. Han, H. K. Baik, K. M. Song, Y. S. Lim, E. S. Lee 2006 *Plasma Sources Sci. Tech.* **15**, 416–420
[10] N. Gherardi, E. Croquesel, N. Naudé, P. Veis, F. Massines 2002 *HAKONE VIII: Contributed Papers, Vol. 1. - Pühajäre : University*, 23-27
[11] P. Čermák, J. Rakovský, A. Annušová, V. Martišovitš, P. Veis 2008 *HAKONE XI: Contributed Papers, Vol. 1. - Toulouse : Université Paul Sabatier*, 163-167
[12] R. Brandenburg, V. A. Maiorov, Y. B. Golubovskii, H.-E. Wagner, J. Behnke, J. F. Behnke 2005 *J. Phys. D: Appl. Phys.* **38**, 2187–2197
[13] K. V. Kozlov, R. Brandenburg, H.-E. Wagner, A. M. Morozov, P Michel 2005 *J. Phys. D: Appl. Phys.*, **38** 518–529
[14] Y. H. Choi, J. H. Kim, Y. S. Hwang 2006 *Thin Solid Films*, 506– 507, 389 – 395
[15] F. Massines, Et. Es-sebbar, N. Gherardi, N. Naudé, D. Tsyganov, P. Ségur, S. Pancheshnyi 2008 *35th EPS Conference on Plasma Phys. Hersonissos, 9 - 13 June 2008 ECA Vol.32D*, P-2.169

SURFACE DISCHARGE DEVELOPMENT IN COPLANAR BARRIER DISCHARGE AT OVERVOLTAGE AND REDUCED PRESSURE IN AIR

Tomáš Hoder[1,2], Mirko Černák[2,3], Hans-Erich Wagner[4]

[1]*Leibniz Institute for Plasma Science and Technology (INP), Greifswald, Germany*
[2]*Department of Physical Electronics, Masaryk University, Brno, Czech Republic*
[3]*Department of Experimental Physics, Comenius University, Bratislava, Slovakia*
[4]*Institute of Physics, Ernst-Moritz-Arndt University, Greifswald, Germany*
E-mail: hoder@inp-greifswald.de, hoder@physics.muni.cz

The coplanar barrier discharge in synthetic air at reduced pressure was studied by cross-correlation spectroscopy and intensified CCD camera technique. At certain experimental conditions the discharge operated in a regime with two temporally and macroscopic spatially localized microdischarges occurring within one half of applied voltage period. In comparison to the previous experiments at atmospheric pressure and burning voltage, distinct differences in the microdischarge development were observed. In particular, an additional cathode directed streamer was detected on dielectric surface far from the electrode gap during the second microdischarge formation. This streamer prolongs significantly the discharge area above cathode. The expansion of the second microdischarge area over the anode was observed, too. This effect is supposed to be caused by the presence of the residual surface charge deposited onto the dielectric surface by the first microdischarge.

1. Introduction

Barrier discharges (BDs) are used in various industrial applications such as ozone generation, plasma display panels, exhaust or surface treatment [1]. There are several geometrical modifications of BDs, namely the volume barrier discharge (VBD), surface barrier discharge (SBD) or coplanar barrier discharge (CBD). The great advantage of the one-sided geometry of the CBD is, that it is suitable for the one-side surface treatment of textiles, paper and other materials [2, 3]. In these industrial applications a high overvoltage is applied to macroscopically homogenize the plasma and increase the active area of the discharge with positive influence on the treatment effectivity. Thus, several subsequent microdischarges (MDs) occur on the pre-charged surface in the same half-period. Further macroscopic homogenization of the discharge can also effectively be achieved by a pressure reduction down to several tens of kPa, too. The evolution of the single MD in CBD configuration, where only one MD appeared during the half-period (i.e. burning voltage treshold), was investigated in [4]. Three phases of the discharge development were described which are similar to the VBD development. These are namely, the pre-breakdown phase, phase of the streamer propagation and the decay phase. It has been also found, that the CBD propagates between the electrodes in a bow-like form in volume at the distance of 0.1 mm above the dielectrics [5] and that the streamers after the impact onto the dielectrics create surface discharges with Lichtenberg figure structures, both facts are similar to VBD (see Fig. 1).

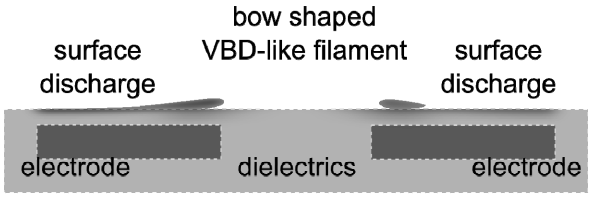


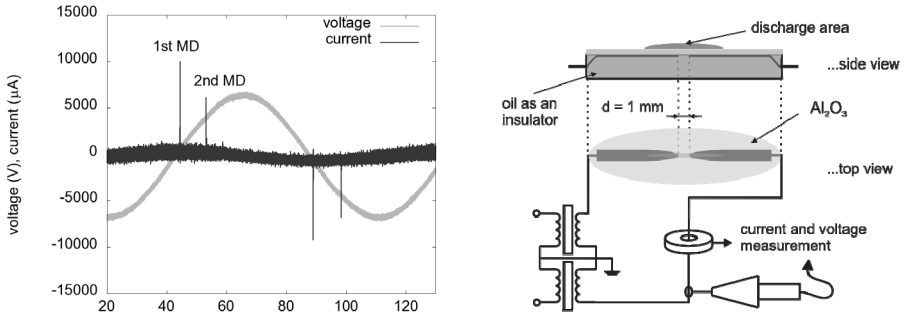
Fig. 1. A scheme of the spatial plasma distribution above the dielectric surface in CBD.

This contribution (comparing the results in [4]) is focused on the study of the CBD operating at overvoltage and reduced pressure where exactly two MDs occurs within one half-period of applied voltage (Fig. 2a). The experimental conditions were found, where these two MDs appear subsequently during one half-period with almost constant time lag in between and they are localized on almost the

same spatial coordinates (by means of pin-to-pin electrode configuration). The role of the residual surface charge is expected to be crucial, if one takes into account that the indispensable part of the MD in CBD develops on the surface [4,5]. The influence of the residual surface charges on the discharge ignition and behaviour in VBD has been shown experimentally as well as theoretically in [5,6]. Here, the CCS technique is applied in order to temporally resolve the propagation of the streamers during the MD development on pre-charged surface. Furthermore, iCCD measurements with high spatial resolution are presented.

2. Experimental setup

The experimental setup is the same as in [4]. The same pin-to-pin coplanar electrode discharge configuration and cell was used (Fig. 1b). The tips curvature was r = 0.25 mm for both electrodes and their mutual distance was 1 mm. Circulating transformer oil was applied to electrically insulate and cool both electrodes. The copper electrodes were deposited by vacuum evaporation on one side of a 0.7 mm thick alumina ceramic (96% pure Al_2O_3). The coplanar discharge cell was situated inside the stainless steel chamber. Before each experiment the flow of 500 sccm of synthetic air (20% O_2 and 80% N_2) was applied for 20 minutes to ensure the composition of working atmosphere. The same flow rate of 500 sccm was used also during experiments. Furthermore, before each experiment the steel chamber was evacuated down to the pressure of 10 kPa. Measurements were carried out at the reduced pressure of 30 kPa. The corresponding voltage for one MD per half-period at this pressure was 7.6 kV_{p-p}. The applied voltage in these experiments was 14.4 kV_{p-p} (90 % overvoltage), which corresponds to the discharge regime of two MDs per half-period. The sinusoidal voltage signal at a frequency of 11 kHz from a function generator was amplified by a 400 W power amplifier and transformed to a high voltage signal by means of two automotive ignition coils connected in parallel (see Fig. 2b). The overview measurement of the current pulses were provided by the Pearson current monitor and measured by the oscilloscope. Two iCCD cameras were used. The first iCCD camera setup was used for overview measurements and comprised the gated nanosecond multi channel plate intensifier unit with controller and a digital CCD (Deltatekh ltd., Moscow & Bastler). For short shots without accumulation the iCCD DiCam Pro (PCO Imaging) was used combined with far-field microscope (Questar).



a) b)

Fig. 2. The voltage and current characteristics for this experiment a) and the experimental setup of the discharge cell with the coplanar electrode arrangements (views from the side and from the top) b).

The principle and setup of used CCS apparatus is given in more detail in [4,7]. The CCS is based on single photon counting procedure. This method allows the substitution of the real-time measurement of the discharge event by a statistically averaged determination of cross-correlation function between two optical signals, both originating from the same source. These two signals are the so called main (spatially and spectrally resolved single photon from the MD) and the synchronizing signal (integral light pulse of the same MD). The time between these signals detections is measured. Consequently, a time histogram of about 10^5 counted photons for all positions is accumulated. A complete measurement is supposed to correspond to the actual light emission of the single MD filament. Of course a condition which has to be fulfilled is the reproducibility of the light source. In this case, this procedure enables to achieve a high temporal resolution of 0.05 ns.

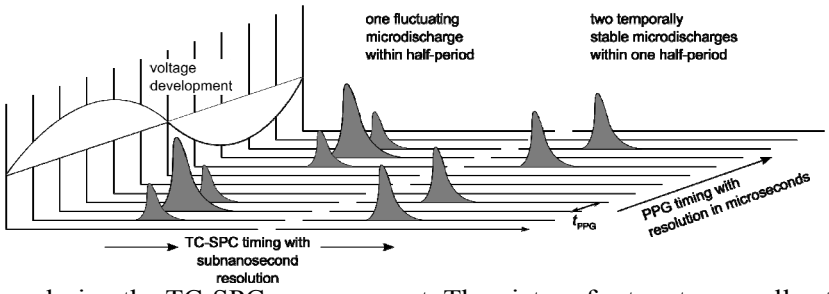


Fig. 3. PPG timing during the TC-SPC measurement. The picture for two temporally stable MDs (right) corresponds to this experiment.

An additional unit of CCS device used in these experiments is the PC Pattern Generator (PPG) unit. The PPG provides segmenting of the applied voltage period in microsecond time scale. This process is triggered by the TTL pulse from the power supply and managed by the computer software. This software generates (based on the TTL pulse detection) TAC channels (12 horizontal lines in Fig. 3), in which the TC-SPC accumulating procedure is initiated. In the experiments presented 32 channels were used resulting in the PPG temporal resolution of $t_{PPG} = 2.8$ µs.

3. Results

It was shown in [6,8], that with increased applied voltage amplitude the size of the VBD or SBD increases stepwise with increasing number of MDs per half-period. Similar behaviour was found here, for the CBD. For the CCS measurements, the studied MD events have to be reproducible and stable. This was established by varying both pressure and applied voltage. The goal was to find two temporally and sufficiently spatially stable MDs appearing within one half-period. The sufficient spatial stability was provided by the pin-shape of both electrodes. Finally, a stable regime was found for 30 kPa and 90 % overvoltage. The time interval between two subsequent MDs was approx. 11 µs. Thus, it was expected that the deposited surface charge from the first MD would have a strong influence on the second one (within the same half-period).

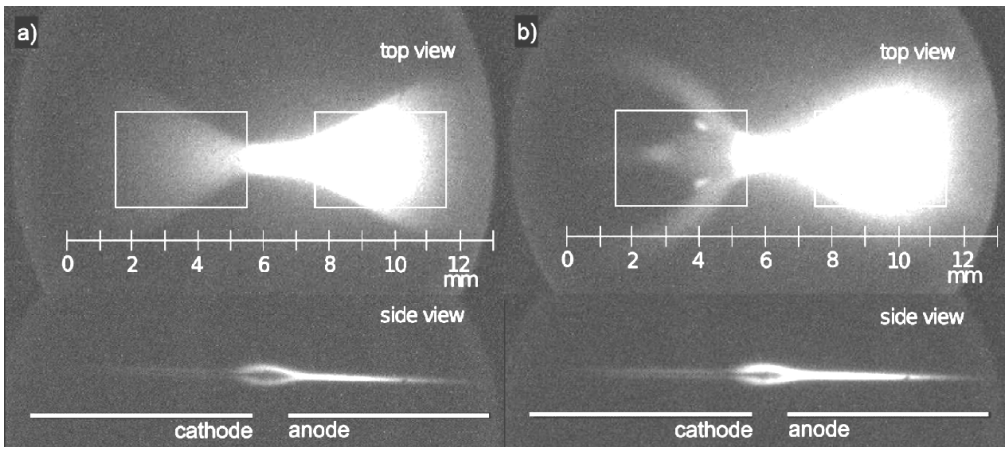


Fig. 4. Accumulated iCCD photos (4500 loops, 500 ns exposure time) of CBD operating at reduced pressure of 30 kPa and burning voltage of 7.6 kV_{p-p} a) and 90 % overvoltage of 14.4 kV_{p-p} b). The white selection rectangles show the area of interest for more precise iCCD measurements in Fig. 5.

From the Fig. 4. one can see the enlargement of the active emitting plasma area at overvoltage, when, instead of one a), two MDs b) are burning during the applied voltage half-period. The emission at overvoltage is significantly higher. In order to understand the enlargement more precisely, the pictures of the first and second individual MD burning at overvoltage were taken separately (Fig. 5). Here, the gate width of 20 µs was used in order to temporally distinguish subsequent MDs within the applied voltage half-period. From presented images one can realize, that the spatial structure of the second MD is more extended. The signal emitted from the anode side shows more intensive and diffuse structure and covers larger area during the second MD, contributing significantly to the homogenization of the

discharge. Moreover, an additional luminous spots appear on the cathode side of the surface. The spot is situated on discharge axial axis (approx. 1 mm from the left edge in the mean high of the picture in Fig. 5 b)) which is also visible in Fig. 4 b) at the corresponding coordinate of 2.5 mm.

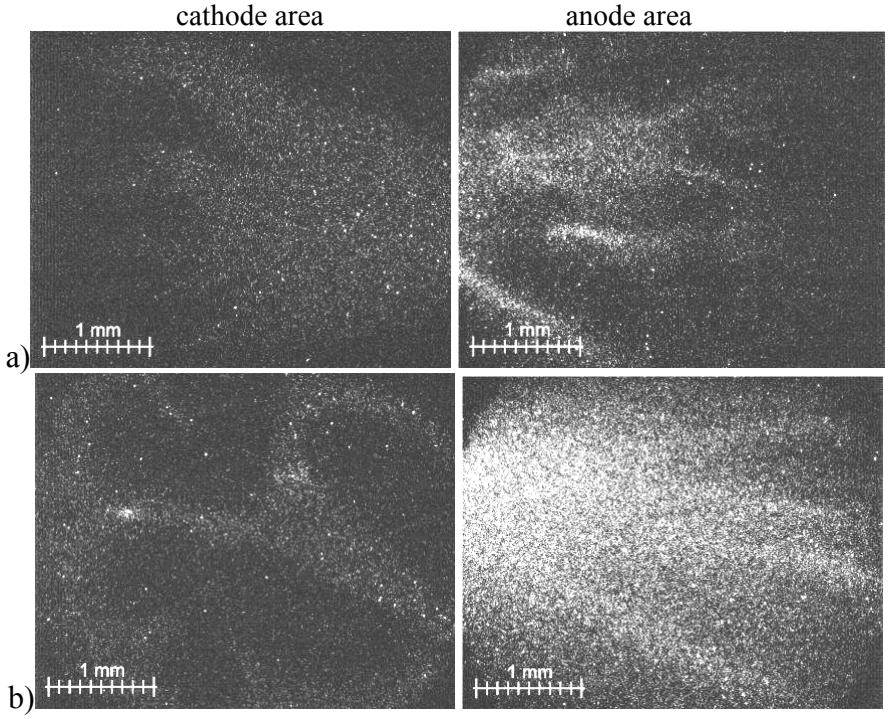


Fig. 5. A typical single shot (1 loop) iCCD pictures of CBD operating at overvoltage from areas of interest, see the white rectangles in Fig. 4. The cathode area of the first MD a) left and its anode area a) right. It is shown similar for the second MD b): cathode left, anode right.

The CCS measurements for both MDs were done for the spectral wavelength of 337.1 nm which corresponds to the emission of the 0-0 vibrational transition of the second positive system (SPS signal) of molecular nitrogen. The results for the first and second MD are shown in Fig. 6. The luminosity of SPS represents the spatio-temporally resolved distribution of the convolution of electric field and electron density [7]. It is evident that the structure of the first MD development remains the same as in atmospheric pressure CBD [4]: The discharge starts by the Townsend phase of long duration. During this phase, a sufficient charge is accumulated allowing the streamer ignition and start of the phase of ionizing waves or streamer propagation, likewise in the VBD [7]. The cathode directed streamer (CDS) propagates from the area above the anode edge towards the cathode. Also a propagation of the second wave (SW or second streamer) of the enhanced luminosity is visible. SW starts later above the anode dielectric surface and propagates above the anode away from the electrode gap. The streamers spread over the dielectric surface and create surface discharges. During the first MD (see Fig. 6 a) on the anode side, the luminosity ends at the area at about x = 8.5 mm and on the cathode side at the coordinate of 3.5 mm approximately. This is an important fact for the development of the second MD luminosity distributions. At these coordinates the typical shape of the luminosity distributions is changed. Firstly, the CDS starts to propagate from the anode edge (see Fig. 6 b)). Several tenths of millimetre behind the cathode edge it reaches its maximum velocity, impacts the surface and starts to slow down. The first CDS is disrupted at about x = 3.5 mm. The propagation follows through the area from 3.5 to 2.4 mm, where two luminous traces are observed simultaneously and decay at the position of about 2.5 mm. At this coordinate a luminous tail of longer duration of about 50 ns is created. This luminous tail corresponds to the elevated light intensity spot above the cathode at the same coordinates on iCCD pictures in Fig. 4 b) and Fig. 5 b). At the same time, the second CDS originates at the coordinate of about x = 2 mm. It propagates away from the gap and decays at x = 0.5 mm. On the anode side the change is not so well pronounced. Generally, the length of the emission traces above

the anode as well as above the cathode is significantly increased in comparison with the first MD luminosity.

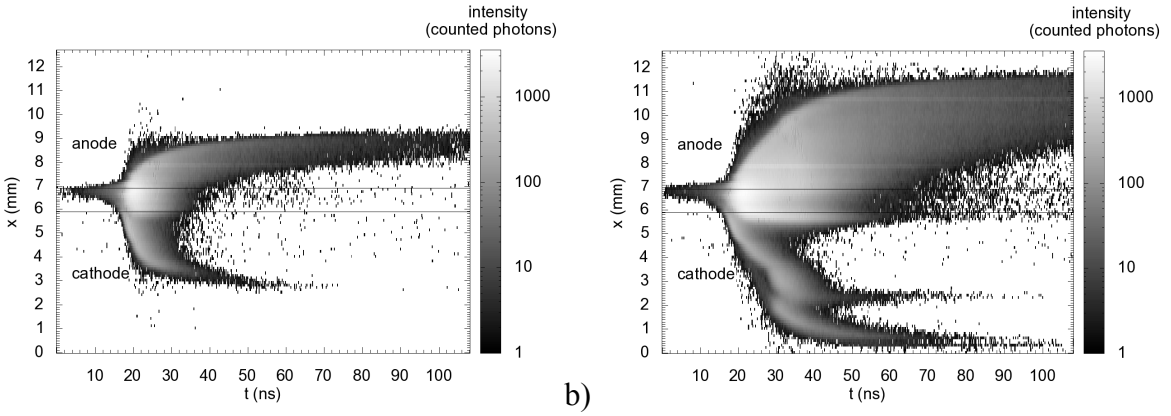


Fig. 6. SPS spatio-temporal resolved luminosities for the first MD a) of the CBD operating in synthetic air at reduced pressure and at overvoltage and for the second MD b). The electrode edges are presented by the vertical black lines at x coordinate of 5.9 and 6.9 mm.

4. Conclusion

According to above mentioned measurements it is concluded that the residual surface charge deposited by the CDS onto the dielectric surface above the cathode (during the first MD) disturbs the propagation of the CDS during the second MD and triggers the ignition of the second CDS which propagates further away from the electrode gap. This additional streamer than causes the increase of the active plasma area and contributes to the macroscopic homogenization of the plasma.

5. References

[1] Becker K H, Kogelschatz U, Schoenbach K H and Barker R J (editors) 2005 *Non-equilibrium air plasmas at atmospheric pressure*, Bristol: Institute of Physics Publishing.

[2] Simor M, Rahel J, Vojtek P, Brablec A and Cernak M 2002 *Applied Physics Letters* **81** 2716-18.

[3] Cernak M, Cernakova L, Hudec I, Kovacik D and Zahoranova A 2009 *Eur. Phys. J. Appl. Phys.* **47** 22806.

[4] Hoder T, Sira M, Kozlov K V and Wagner H-E 2008 *J. Phys. D: Appl. Phys.* **41** 035212 (9pp).

[5] Hoder T, Sira M, Kozlov K V and Wagner H-E 2009 *Contrib. Plasma Phys.* **49** 381-387.

[6] Celestin S, Canes-Boussard G, Guaitella O, Bourdon A and Rousseau A 2008 *J. Phys. D: Appl. Phys.* **41** 205214 (10pp).

[7] Hippler R, Kersten H, Schmidt M and Schoenbach K H (editors) 2008 *Low temperature plasmas*, Weinheim: Wiley-VCH, Vol. 1 271-306.

[8] Gibalov V I and Pietsch G J 2000 *J. Phys. D: Appl. Phys.* **33** 2618-2636.

INFLUENCE OF AMBIENT GAS TEMPERATURE ON THE GLOW REGIME OF NANOSECOND REPETITIVELY PULSED DISCHARGES BETWEEN TWO POINT ELECTRODES IN AIR AT ATMOSPHERIC PRESSURE

Fabien Tholin[1], Zdenek Bonaventura[1,2], Sebastien Celestin[3], Jaroslav Jansky[1] and Anne Bourdon[1]

[1]*EM2C laboratory, UPR CNRS 288, Ecole Centrale Paris, Châtenay Malabry, France*
[2]*Masaryk University, Faculty of Science, Dept. of Physical Electronics, Kotlářská 2, Brno, Czech Republic*
[3]*CSSL, The Pennsylvania State University, University Park, Pennsylvania, USA*
E-mail: fabien.tholin@em2c.ecp.fr, zdenek.bonaventura@em2c.ecp.fr

In this work, we present numerical simulations of discharges in air at atmospheric pressure at 1000K and 300K between point electrodes to better understand and optimize the conditions to obtain a glow-like regime. An important step in the glow to spark transition of the discharge is the time of connection of discharges propagating in the gas gap. In this work we have shown that the voltage rise time and the maximal value of the applied voltage have a significant impact on the connection time. Conversely, the radius of point electrodes appears to have only a small influence on the connection time and the discharge dynamics.

1. Introduction

Low temperature plasma discharges are studied for an increasing list of applications such as ozone generation, pollution control, biological decontamination, plasma assisted stabilization of lean flames, flow control and thin film coatings. Among the different types of discharges at atmospheric pressure, nanosecond repetitively pulsed (NRP) discharges are particularly promising. For ambient air temperature of 1000K a glow-like regime is observed in a thin voltage range of 6-7 kV [1,2]. This regime has an emission which fills the gap in a diffuse manner. For voltages higher than 7 kV, the spark-like regime with significant gas heating and an intense emission is observed [1]. The glow-like regime is particularly interesting for applications as it produces efficiently active chemical species without heating the neutral gas. However, experimentally, the glow-like regime appeared to be very sensitive to several parameters [1,2]: applied voltage, electrode geometry and interelectrode gap distance, pulse repetition frequency, and neutral gas temperature. Then to better understand and optimize the conditions to obtain a glow regime at room temperature (300K), in this work we carry out simulations of the discharge dynamics and structure as a function of the applied voltage, gas temperature and electrode radius of curvature.

2. Model formulation

The studied configuration is a point-to-point geometry with two hyperboloid electrodes (radius of curvature is R=300μm) separated by 5 mm. In this work we carry out 2D axisymmetric simulations of the discharge dynamics of one of the nanosecond pulsed discharges. As many discharges have occurred before the simulated one, we have estimated that the density of the seed charges in the interelectrode gap is on the order of 10^9 cm^{-3} for the 10-30 kHz frequency range studied experimentally. A fluid model is used to simulate the discharge propagation: continuity equations for charged species (electrons, positive and negative ions) coupled to Poisson's equation. Further details on the discharge model can be found in [3,4]. To take into account the fact that the discharge occurs at atmospheric pressure in preheated air at T=1000 K, we have simply changed the value of the total density $N=N_0T_0/T$ where N_0 is the air neutral density at ground pressure and ambient temperature (T_0=300 K). This decrease of the total density by a factor 3, increases by the same factor the local reduced electric field E/N and then has a direct impact on transport parameters and reaction rates in air which are assumed to be functions of E/N.

3. Influence of applied voltage

In [4] a constant voltage was applied to the anode at the beginning of the simulation. Experimentally, the applied voltage has a 5ns rise time before reaching a plateau of 10ns followed by a decrease of about 5ns. Then in this work, we have considered a sigmoid function to model the experimental applied voltage. This function ensures the continuity of the voltage and its derivative (Figure 1).

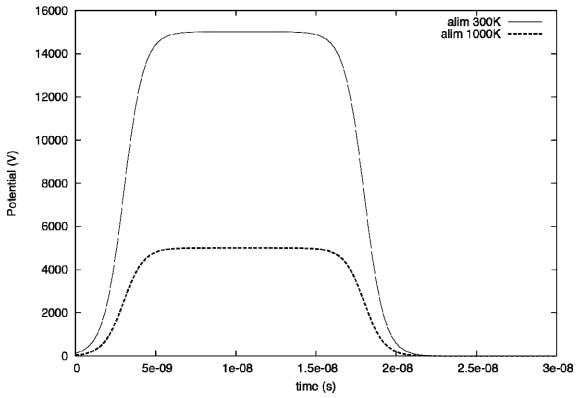


Fig. 1. Evolution of applied voltage with time for 300K (15kV) and 1000K (5kV).

Figure 2 shows the evolution of electric field and electron density on the axis of propagation for T=1000K, and an applied voltage of 7kV with sigmoid shape. In comparison to the results obtained in [4] for a constant voltage of 7kV, we note that with a sigmoid voltage the propagation of the discharges in the inter-electrode gap is slower. It is important to note that after the connection of both discharges a conducting channel is formed between the electrodes. If this channel is formed before the power supply switches off, fast heating processes may take place which may lead to the transition from a glow-like discharge towards a spark. To have a glow-like regime, we assume that the connection time has to be close to 15ns, that is the end of the voltage plateau. On Fig. 2, with a sigmoid voltage, the connection between positive and negative discharges occurs between 7ns and 8ns, while it is at 4ns for a constant applied voltage [4]. In experiments, a glow-like regime is observed at 1000K almost up to 7kV. Then, with the use of a sigmoid voltage, our simulations results are in better agreement with experiments. With a constant applied voltage, propagation starts almost immediately after applying the 7kV potential at the anode. With the sigmoid voltage, the applied voltage has to reach a critical value (around 4.5kV) to allow the discharge propagation to start. This critical value is reached at about 3.5ns with the sigmoid voltage, which corresponds to the delay between the connection times of the discharges for a constant and sigmoid voltage. It is interesting to note that the time evolution of the peak electric field in the positive streamer head is different for a sigmoid voltage and for a constant applied voltage. With a constant applied voltage of 7kV, the peak electric field on the axis is maximum at t=0ns. Then, the peak electric field in the positive streamer head decreases as the discharge propagates, to finally reach some constant value close to 50kV/cm. This decrease of the peak electric field in the discharge head at the beginning is certainly due to the decrease of the Laplacian electric field as the discharge propagates and then leaves the region of high electric field close to the electrode tip. Conversely, with a sigmoid voltage the peak electric field in the positive streamer head is increasing during the first 5ns, that is the voltage rise time. In fact, even if the distance between the positive streamer head and the point electrode increases, the fast rise of the applied voltage produces a higher Laplacian field in front of the discharge. Once the applied voltage has reached the plateau, the peak electric field in the positive streamer head starts to decrease significantly and converges towards the value of 50kV/cm, obtained for a constant applied voltage.

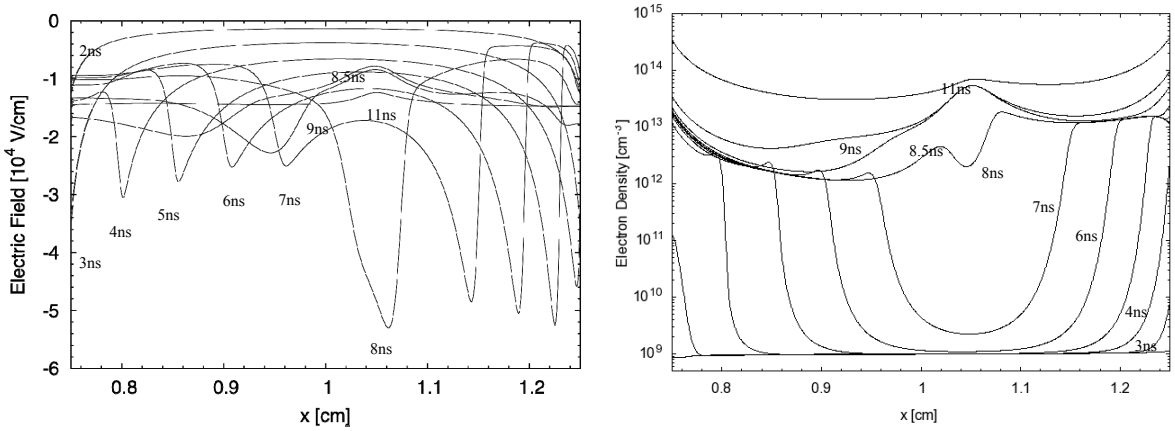


Fig. 2. Electric field (left) and electron density (right) on the axis of symmetry at different times for T=1000K, sigmoidal voltage with a plateau value of 7kV, and R=300μm.

Figure 3 shows the evolution of the electric field and the electron density on the axis of symmetry for a sigmoid voltage with a plateau value of 5kV. We note that the propagation velocity is significantly reduced in comparison to the one obtained for a higher voltage. Then, the decrease of voltage has a significant impact on the connection of positive and negative discharges which occurs at 14ns (to be compared to 8ns for 7kV case on Figure 2). Then for 5kV, in agreement with experiments, we observe a glow-like discharge. It is interesting to note that the peak electric field in the positive streamer head is increasing during all the propagation, even after the time for the applied voltage to reach its plateau value. This behavior could be explained considering the evolution of electron density with time on figure 3. It appears that during the first 4ns when there is no positive discharge propagation, the electron density is increasing close to the anode point. Then, when the propagation of the positive streamer starts, the peak electric field in the head is less than the one required for stable propagation in the gap (50kV/cm). As the positive streamer moves from the point anode, the peak electric field in the positive streamer head increases due to the rise of the applied voltage up to 5ns and then increases to reach the value of 50kV/cm just before the connection of positive and negative discharges.

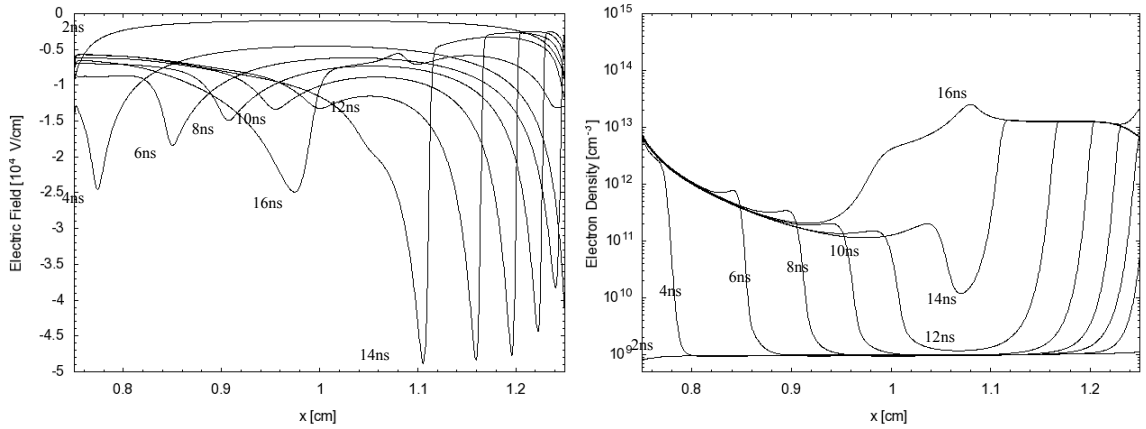


Fig. 3. Electric field (left) and electron density (right) along the axis of symmetry at different times for T=1000K, sigmoidal voltage with a plateau value of 5kV, and R=300μm.

4. Influence of gas temperature

In this section, we study the influence of the gas temperature on the discharge structure and dynamics. At 1000K, we have checked that the lowest applied voltage (with a sigmoid shape of 5ns rise-time) to have the propagation of positive and negative discharges in the gap was 5kV. At 300 K, we have checked that this minimal voltage is 15kV. It is interesting to note that these minimal voltage values follow the scaling of gas density with temperature (the total density at 1000K is about 3 times less than the one at 300K). This result is in good agreement with the fact that the reduced breakdown field in air

is almost constant from room temperature to almost 2000K as explained in [5]. Figure 4 shows the evolution of electric field and electron density on axis for a discharge propagating in air at T_0=300 K for 15kV. As expected, the peak electric field in the positive streamer head during the stable propagation phase is around 150kV/cm at 300K (50kV/cm at 1000K as shown in figs. 2 and 3).

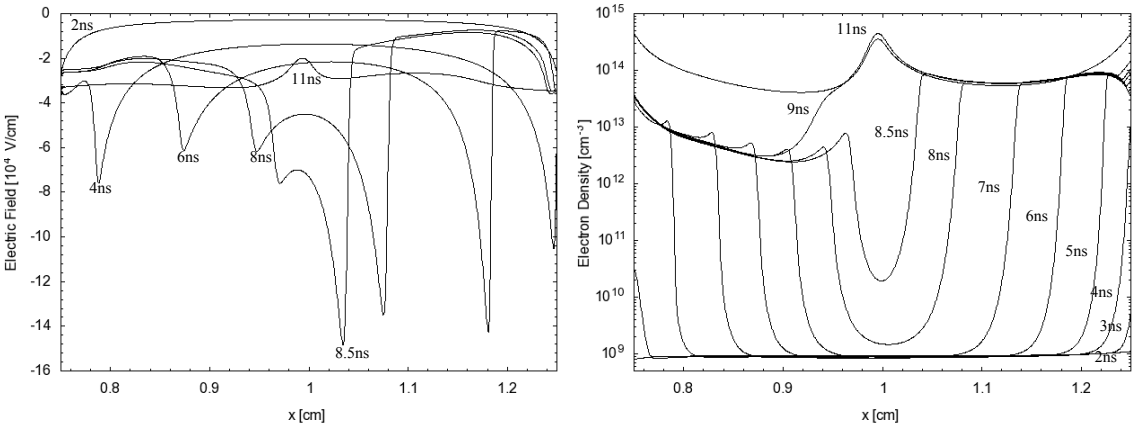


Fig. 4. Electric field (left) and electron density (right) along the axis of symmetry at different times for T=300K, sigmoidal voltage with a plateau value of 15kV and R=300µm.

Figure 5 shows the electric field and electron density evolution at 300K with a higher voltage of 21kV. This value has been chosen because its ratio with 15kV is the same as the ratio between the 5 and 7kV cases studied at 1000K (Figs 2 and 3). Comparing Figs. 4 and 5 (and as already observed on Figs 2 and 3 at 1000K) it appears that the discharge propagates faster with a higher applied voltage and the ratio between the two propagation times is about 0.7 and is the same as the one observed at 1000K between 7 and 5kV cases. For 300 K and 15kV, the peak electric field in the positive streamer head is increasing up to 6ns, that is to say after the end of the rise of the applied voltage. Conversely, for 300 K and 21kV, the peak electric field in the positive streamer head decreases after 4ns while the voltage is still increasing. So there seems to be a strong competition between the increasing rate of the voltage, which tends to increase the peak electric field in the positive discharge head, and its propagation velocity that increases with the applied voltage and tends to decrease the peak electric field in the positive streamer head as the discharge moves farther from the point electrode.

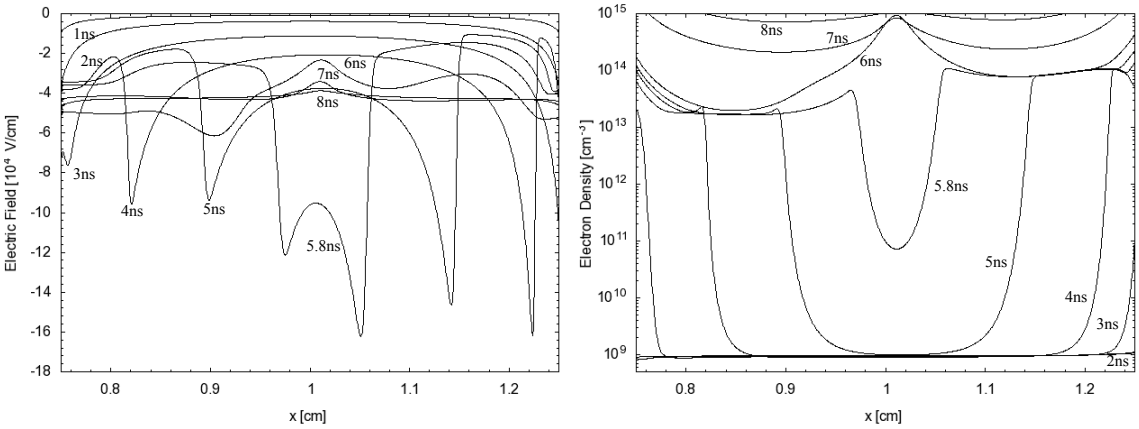


Fig. 5. Electric field (left) and electron density (right) along the axis of symmetry at different times for T=300K, sigmoidal voltage with a plateau value of 21kV and R=300µm.

5. Influence of the radius of curvature of point electrodes

In this section, we study the influence of the radius of curvature of point electrodes on the discharge structure and dynamics. Figure 6 shows the evolution of electric field and electron density on axis for T=300K, a 15kV sigmoid voltage with 5ns rise-time and a radius of curvature of electrodes of 100µm. A smaller radius of curvature for the points increases the peak electric field at the points but reduces

the spatial expansion of the high Laplacian field region close to the electrodes. Then the positive discharge may escape faster from this area which may result in a stronger decrease of the peak electric field in the positive streamer head. This is clearly observed on Fig. 6. We note that the peak electric field in the positive streamer head is decreasing sharply between 4 and 5ns while it was increasing for the case of electrodes with a 300µm radius of curvature in the same conditions (fig. 4). It is interesting to note that the decrease of the radius of curvature influences the ignition phase of the discharge and slightly decreases the peak electric field in the positive streamer head during the stable propagation phase. However it appears that the change of the radius of curvature of electrodes has a small influence on the average velocity of the positive discharge and on the connection time of positive and negative discharges in the gap.

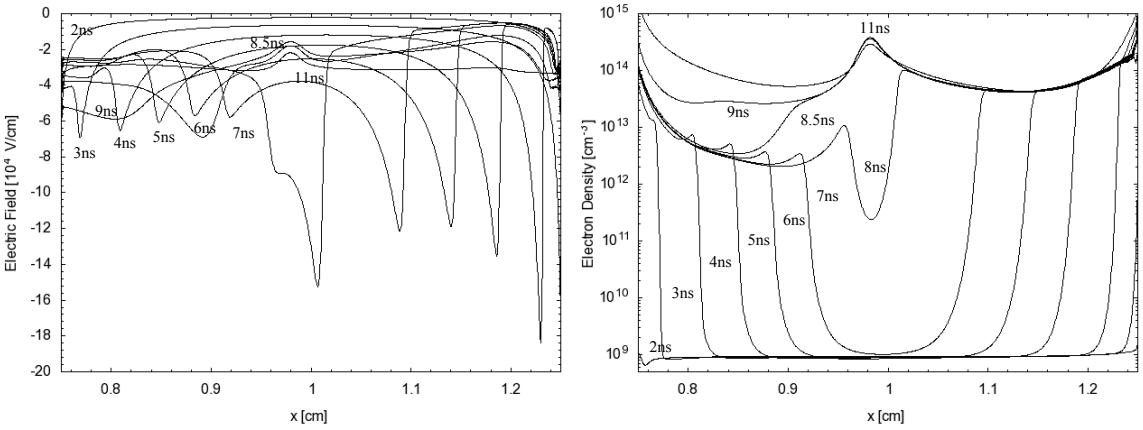


Fig. 6. Electric field (left) and electron density (right) along the axis of symmetry at different times for T=300K, sigmoidal voltage with a plateau value of 15kV and R=100µm.

6. Conclusions

In this work, we have carried numerical simulations of discharges in air at atmospheric pressure between point electrodes to better understand and optimize the conditions to obtain a glow-like regime with no gas heating. An important step in the glow to spark transition of the discharge is the time of connection of positive and negative discharges propagating in the gas gap. In this work we have shown at 1000K that the voltage rise time has a significant influence on the connection time. At 1000K and 300K, we have noted that the maximal value of the applied voltage has a significant impact on the discharge dynamics. We have observed that a small increase of the applied voltage significantly decreases the connection time. However, it is interesting to note that the change of radius of point electrodes has only a small influence of the connection time.

Acknowledgments. The authors thank the Agence Nationale de la Recherche for its support of the IPER (Grant No. ANR-05-BLAN-0090) and PREPA (Grant No. ANR-09-BLAN-0043) projects.

7. References

[1] D. Pai, PhD Report, Ecole Centrale Paris, France (2008)
[2] D. Pai, G. Stancu, D. Lacoste, C. Laux Plasma Sources Sci. Technol. **18** 045030 (2009)
[3] S Celestin, Z. Bonaventura, B. Zeghondy, A. Bourdon, P. Ségur Plasma Sources Sci. Technol. **42**, 065203 (2009)
[4] A. Bourdon, Z. Bonaventura and S Celestin Plasma Sources Sci. Technol. **19**, 034012 (2010)
[5] Y. Tanaka, Z. J. Phys. D: Appl. Phys. **37** 851-859 (2004)

RECONSTRUCTION OF 3D STRUCTURE OF POSITIVE CORONA STREAMER BY LOCAL METHODS

M. Kocik[1], M. Tański[1], J. Mizeraczyk[1,2], R. Ichiki[3], S. Kanazawa[3], J. Dembski[4]

[1] *Centre for Plasma and Laser Engineering, The Szewalski Institute of Fluid Flow Machinery, Polish Academy of Sciences, Fiszera 14, 80-952 Gdańsk, Poland, kocik@imp.gda.pl*
[2] *Department of Marine Electronics, Gdynia Maritime University, Gdynia, Poland*
[3] *Department of Electrical and Electronic Engineering, Oita University, Oita, Japan*
[4] *Faculty of Electronics, Telecommunications and Informatics, Gdańsk University of Technology, Gdańsk, Poland*
E-mail: kocik@imp.gda.pl

The computer algorithms were used for reconstruction of streamer 3D structure. We propose the 3D tree structure model of corona discharge streamer composed with nodes and edges between chosen couples of nodes, which enables easy computation of some important parameters of streamers. The 3D model can be derived directly from two projection images by global methods like evolutionary searching or particle simulations. In this paper however, we focused on another type of methods named local methods. Here, the morphological image operations are used for creation of two 2D models and later 3D model determination after simple computation. As a result, the 3D image of streamer is reconstructed and can be used for measuring of the streamer features such as branching angle and branching length..

1. Introduction

Positive streamers are widely used in the field of air pollution control such as NOx or SOx removal and VOCs decomposition based on plasma chemical reactions. Although the streamers have been studied for many years, they are still not fully understood due to their complex nature. One of such unexplored issue in streamer research is the breakup of single channels, called streamer branching. Streamer branching is commonly seen in experiments [1,2]. Multiple streamer branching actually determines the gas volume that is crossed by streamers and consecutively chemically activated for plasma processing purposes. However, up to now, only the conditions of the first branching event have been resolved in microscopic models. On the other hand, the distribution of branching lengths and angles is an ingredient of models for the complete branching tree on larger scales [3]. Therefore, there is a need for experimental data of streamer branching lengths and angles. For imaging of streamer discharges digital cameras (CCD cameras) or intensified cameras (ICCD) are used. The result of the imaging is two dimensional (2D) representations of what is actually a three-dimensional (3D) phenomenon. These 2D representations can be difficult in the interpretation and measurements of i.e. branching angles can lead to false conclusions. For this purpose, we have implemented a stereophotography method which makes it possible to image streamer discharges in 3D. The stereographical method we used is commonly used for imaging sparks [4], flames [5], dusty plasmas [6] and pulsed streamers [7]. However, in previous experiments (including our own research [8]) reconstruction of 3D structure was done manually what is difficult and time consuming. The limited number of images which are possible to obtain in that way reduce significantly the value of experimental data. To increase the statistics we decided to develop computer algorithms for automatic reconstruction of 3D structure of streamers.

2. Computer algorithms

To reconstruct the 3D streamer structure several numerical methods were applied and compared.

3D streamer reconstruction methods

We can divide 3D reconstruction methods into 2 groups: global and local approaches which is related to global and local error minimization. In the first approach the 3D discharge model is created and subsequently modified to stereophotography matching using particle simulations or evolutionary searching methods [9]. The comprehensive description of global methods used for 3D streamer

reconstruction problem can be found in [10]. In the local approach broadly described in this article in the first step two 2D models are created separately for each of projection photography. In the second step 3D model is built based on 2D projection models. The first step can be divided into image preprocessing stage and lines (curves) + nodes detection which can be named as vectorization stage. The modular structure showed in Fig. 1 provides the possibilities of different methods compositions.

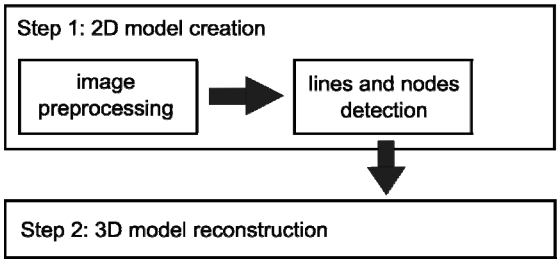


Fig. 1. Modular structure of 3D stream reconstruction

The first step can be accomplished as full manual, semi automatic (interactive) or full automatic process. In the first case the user can draw lines and nodes by hand based on original images. In the second case the user can accept or correct the algorithmical suggestions. In the third case the process is the quickest but demands knowledge incorporation which is the most difficult challenge. The knowledge about physical phenomenon in the most simple approach can be represented by curve continuity and curvature limitation. In more advanced approach the learning based on manually obtained examples can be used to acquire human knowledge from manual and semi automatic methods to full automatic one. The decisions whether any point belongs to node or to a line can be treated as learning objectives. The problem arises from the fact that such tasks are always difficult for computer programs although easy for human, like face detection task.
In this work we have concentrated on full automatic morphological and histogram based 2D model creation methods without learning as a first step of 3D model reconstruction.

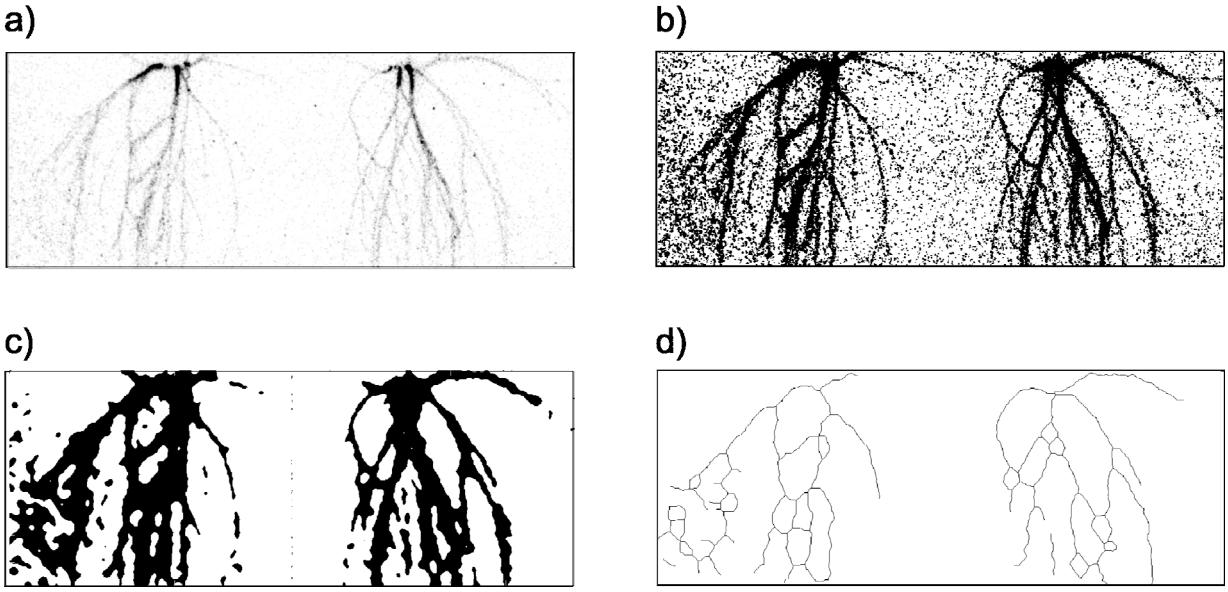


Fig. 2. Morphological operations: a) original images, b) after binarization, c) after closing, d) after skeletonization with short curves reduction.

Morphological method
The main advantages of morphology usage for image preprocessing stage is their generality, speed, and easy nodes detection. It seems that the simplest approach to image preprocessing is to use the well known image processing methods like morphological operations to obtain a skeleton of an image. The

example sequence of operations with example parameter values and on example couple of images were showed in Fig. 2.
The binarization operation (Fig. 2b) changes each image into monochromatic one using chosen threshold value. The morphological closing operation (Fig. 2c) at next step is used for empty areas closing and to cancel the noise spots which are placed rather out of streamer channels. The operation is composed with dilation and erosion and was repeated several times. In this example the dilation determined each pixel value as „1" if more than 3 pixel values from 3x3 adjacent pixels were equal to 1. The erosion worked in the same way but the threshold was equal 7. The skeletonization process (Fig. 2d) is used to obtain the net composed of thin curves which helps to find single curves and nodes. In presented example the thinning algorithm with two structural elements showed at Fig. 3 was chosen from several other methods. Each pixel value on an image was fixed to zero if its 3x3 adjacent pixels matches first structural element (Fig. 3a) (empty squares can be matched to any value) and next after whole image transformation, the second structural element (Fig. 3b) is treated in the same way. Then, this two transformations was repeated for rotated structural elements by 90, 180, and 270 degrees. Simultaneously, during nodes and curves detection stage, the reduction of short curves takes place. The reduction decision is based on the observation if the short curve to be eventually removed belongs to streamer channel or to noise spot.

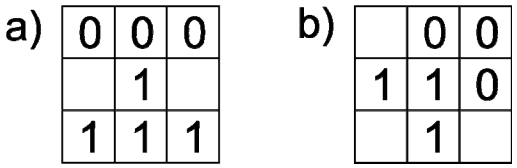


Fig. 3. Structural elements for thinning operation

As can be seen in Fig. 2d the number of nodes and its vertical position are quite different in each projection which makes the 3D stream model reconstruction a difficult task. Other drawbacks of standard morphological operations in discharge 3D streamer reconstruction can be listed as following:

- limited number of node branches ,
- information loss related to binarization operation,
- branch leaving related to discontinuity of stream channel image,
- difficulties with distinguishing branching nodes from line crosses.

Therefore, all operations should be chosen in proper order and with proper parameter values to make 2D models most reliable to human expert e.g. each model should be consistent with human expert knowledge. We can reach high level of consistency using learning system in which several morphological operations with different threshold values are tested using human expert subjective estimation or any consistency criterion between two images.
Another approach to increase object detection quality is connected with direct expert knowledge incorporation by using dedicated image preprocessing methods prepared specially for streamer channel modelling. Histogram based object detection method is considered as an example of such approach..

Histogram based method
For each analysed pixel, histogram based on circular area is calculated. In a simple version each pixel which belongs to area was classified to one histogram bar related to particular angle. The weighted average pixel intensity value for each considered angle was calculated. The weight value is invertly proportional to distance between analysed pixel and considered pixel circular area e.g. when distance is higher the weight is lower. Fig. 4 presents example diagram after normalization and smoothing. Each branch can be detected as peak in the diagram, each straight line can be detected as two peaks shifted by the distance of about 180 degrees. Appearing of more than two peaks (see Fig. 4) suggests the node existence. The learning decision system can be used to classify histogram features using human expert decision. The peaks can be observed in different scales in many area diameters or by distance weights manipulation, providing much information for learning system purposes.

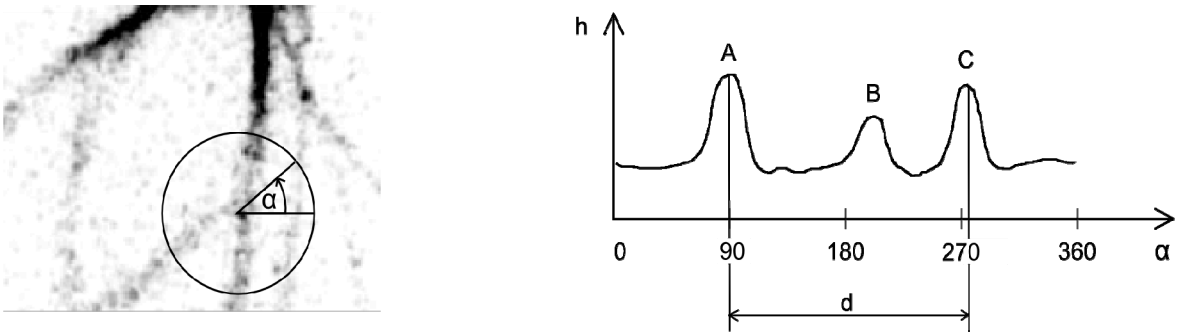


Fig. 4 Histogram-based nodes and lines detection : weighted pixel intensity related to direction angle diagram and diagram calculation area

3. Conclusions

Two methods of image preprocessing and object detection were presented as a local method component. Local methods help to overcome high computational complexity related to global ones by direct application of real streamer features during 2D models creation and simple nodes matching algorithm.

The morphological operations help to detect nodes and curves quickly but not so precisely. Histogram based method is specially prepared for 3D streamer model reconstruction. The main difference between considered methods is due to knowledge incorporation method. In morphological method the parameter optimization techniques can be used based on human expert subjective estimation or any consistency criterion between two images. In histogram based method the knowledge is directly included with optional histogram features interpretation learned from human expert decision examples. During initial experiments the histogram based method seemed to be more accurate but the way of knowledge incorporation makes this method less general than morphological. Moreover, the knowledge used for preparing algorithms may be uncertain or incomplete because physical phenomenon is under investigation.

4. References

[1] R. Morrow, J.J. Lowke, "Streamer propagation in air", J. Phys. D: Appl. Phys., vol. 30, pp. 614–627, 1997.

[2] T. Ohkubo, S. Kanazawa, Y. Nomoto, M. Kocik, J. Mizeraczyk „Characteristics of DC Corona Streamers Induced by UV Laser Irradiation in Non-Thermal Plasma", J. Adv. Oxid. Tech., 8, 2, pp. 218-225, 2005.

[3] M. Akyuz, A. Larsson, V. Cooray, G. Strandberg, "3D simulations of streamer branching in air", J. Electrost. vol. 59, pp. 115-141, 2003.

[4] J. M. K. MacAlpine, D. H. Qiu, and Z. Y. Li, "An analysis of spark paths in air using 3-dimensional image processing", IEEE Trans. Dielectr. Electr. Insul., vol. 6, 331, 1999.

[5] W. B. Ng and Y. Zhang, "Stereoscopic Imaging and Reconstruction of the 3D Geometry of Flame Surface", Exp. Fluids, vol. 34, 484, 2003.

[6] E. Thomas, Jr, J. D. Williams, and J. Silver, "Application of stereoscopic particle image velocimetry to studies of transport in a dusty (complex) plasmas", Phys. Plasmas, vol. 11, L37, 2004.

[7] S. Nijdam, J. S. Moerman, T. M. P. Briels, E. M. van Veldhuizen, U. Ebert, "Stereo-photography of streamers in air", Appl. Phys. Lett., vol. 92, 101502, 2008.

[8] R. Ichiki, S. Kanazawa , S. Akamine, T. Ohkubo, M. Kocik, J. Mizeraczyk, „Reconstruction of 3-dimensional structure of streamer discharges", Annual Meeting of of the Institute of Electrostatics Japan, Tokyo City University, Tokyo, Japan, Sept.10, 2009

[9] D. Goldberg, Genetic Algorithms in Search, Optimization and Machine Learning, Addison-Wesley Inc., 1989.

[10] M. Kocik, M. Tański, J. Mizeraczyk, R. Ichiki, S. Kanazawa, J. Dembski, "Reconstruction of the 3D image of corona discharge streamer", 7th Conference of the French Society of Electrostatics SFE 2010, Montpellier, France, 30.08.-01.09.2010

THEORETICAL STUDY OF INTERACTIONS OF NO_3^- WITH NEUTRAL MOLECULES

P. Mach, M. Krajčí, J. Matúška, J. Urban

Department of Nuclear Physics and Biophysics, Comenius University, Mlynská dolina, Bratislava 842 45, Slovakia
E-mail: mach@fns.uniba.sk

Energetics and structure of clusters of NO_3^- ion with HNO_3, N_2O, NO_2 and N_2 molecules are studied by means of different quantum-chemical methods. Calculated results in the case of NO_3^- - $nHNO_3$ hydrogen bonded clusters are in good agreement with available experimental data. For the NO_3^- … N_2 system the parameters of More-type and Lennard-Jones 6-12 potentials were obtained for further use in molecular dynamics (MD) simulations.

1. Introduction

The nitrate ion has a significant importance in the chemistry of negative ions. Because of its stability it is a terminal negative ion in N_2/O_2 mixtures and can be further stabilized via formation of associates with neutral molecules. For a long time there are known clusters of NO_3- with HNO_3 and H_2O [1]. Besides of primary interest for atmospheric chemistry, these association reactions are also important for detailed understanding of processes in drift tube of Ion Mobility Spectrometer (IMS). For the modeling of ion mobility by means of the MD simulations it is necessary to have reliable potential functions. In the case of ion-molecule interactions, parameters for these functions are not generally available, so we tried to obtain these parameters for NO_3- … N_2 system from *ab initio* calculations.

2. Results and discussion

The enthalpies of association reactions

$$+ \ HNO3 \ \rightarrow NO3\text{-}.nHNO3 \qquad (1).$$

for n=1 to 6 were calculated and compared with available experimental data [1-4] (Figure.1). Calculated enthalpies are in reasonable agreement with available experimental data, but generally they predict smoother trend than actual experimental data. For n >3 the two shell structures of the type NO_3-.3HNO_3.(n-3)HNO_3 are calculated to be more stable. Nevertheless, experimental data are more consistently fitted with one-shell model.

Another important quantity, showing stability of anionic cluster formed – vertical detachment energy (VDE) – was calculated for whole series (Table 1). It is clear that stability increases with clustering – as the number of electronegative atoms in the system increases.

Clusters of NO_3- with NO_2 and N_2O are significantly weaker. From these (non-hydrogen bonded aggregates) the clusters with N_2O are weaker, relative stable are clusters of the structure NO_3-.nNO_2 with n even. These clusters can be described approximately as NO_3-(n/2)N_2O_4 .

On the basis of B3LYP/6-311+G(3d2f) calculations for totally 2700 discrete points the Lennard-Jones potential of the form:

$$V(r) = \varepsilon\left[\left(\frac{r_{\min}}{r}\right)^{12} - 2\left(\frac{r_{\min}}{r}\right)^{6}\right] \qquad (2)$$

for interaction NO_3-...N_2 was fitted with following parameters: ε=0.05 eV and r_{min}=3.97 A

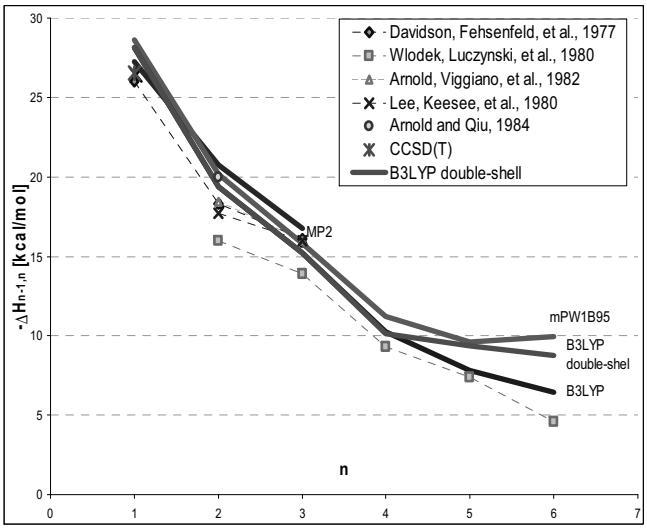


Fig. 1. Experimental (points) and calculated (solid lines) enthalpies for reaction NO_3^-.(n-1)HNO_3 + HNO_3 → NO_3^- .nHNO_3. Corresponding experimental points are connected with dashed line.

Tab. 1. Calculated (using 6-311+G** basis set) VDE [eV] for NO_3- and its clusters with HNO_3. Entries labelled "extrap." are values extrapolated to complete basis at CCSD(T) level.

	NO_3^-	+HNO_3	+2HNO_3	+3HNO_3	+4HNO_3	+5HNO_3	+6HNO_3
B3LYP	4.11	5.61	6.45	7.10	7.45	7.74	7.97
mPW1B95	4.09	5.68	6.60	7.24	7.70	8.01	8.20
MP2	3.48	4.99	5.95	6.57			
extrap.	4.19	5.34					

Acknowledgement. Part of the presented calculations was done using computation resources of the SAS Centre of excelence COMCHEM. Ihis project was financially supported by the APVV grant no. 0310-07

3. References

[1] Davidson, J.A.; Fehsenfeld, F.C.; Howard, C.J., T, Int. J. Chem. Kinet., 9 (1977) 17
[2] Wlodek, S.; Luczynski, Z.; Wincel, H., Int. J. Mass Spectrom. Ion Phys., 35 (1980) 39
[3] Arnold, F.; Viggiano, A.A.; Schlager, H., Nature, 297 (1982) 371.
[3] Lee, N.; Keesee, R.G.; Castleman, A.W., Jr., J. Chem. Phys., 72 (1980) 1089.
[4] Arnold, F.; Qiu, S., Planet. Space Sci., 32 (1984) 169

CORONA AS A TEMPERATURE PROBE FOR ATMOSPHERIC AIR MICROWAVE PLASMA

Lenka Leštinská[1], Viktor Martišovitš[1] and Zdenko Machala[1]

[1]*Division of Environmental Physics, Faculty of Mathematics, Physics and Informatics*
Comenius University, Mlynská dolina, Bratislava 842 48, Slovakia
E-mail: machala@fmph.uniba.sk

A new method for temperature measurements of near-LTE plasmas generated in air at atmospheric pressure was developed and tested. It is based on the combination of microwave and corona discharge. The gas temperature of the MW discharge is determined as the rotational temperature of N_2^* produced in the corona discharge. The temperature was measured by the corona probe method and the thermocouple simultaneously. We found a fairly good agreement between the two methods, with a slightly higher temperatures measured by the corona method. The difference (~100 K) is small relative to the measured plasma temperatures (close to or above 1000 K). This verifies that the corona probe method can be applied to determine the temperature of the near-LTE air plasma and contrary to the thermocouple it can be used also for the high plasma temperatures.

1. Introduction

Atmospheric pressure microwave (MW) plasmas present considerable interest for various industrial or environmental applications such as surface treatment [1], carbon nanotube synthesis [2,3], trace element analysis [4], air pollution control, various biomedical applications [5] etc. The main advantage of MW plasma is electrodeless operation, availability of cheap microwave sources at 2.45 GHz, good microwave to plasma energy coupling and no need of vacuum devices if the discharges are generated at atmospheric pressure. In addition, the operation of such plasmas is cheap, when operated in air.
In general it is very important to know the characteristics of the generated discharge in order to ensure its suitability for a desired application. Optical emission spectroscopy (OES) is a good, reliable and non-intrusive method of plasma diagnostics. It enables identification of active species and radicals in the plasma, as well as temperature measurements (vibrational and rotational temperatures). We introduce a novel temperature-diagnostic method of near equilibrium (near-LTE) air plasmas.

2. Corona probe method

The gas temperature T_g in the plasma, one of the key plasma parameters, can be determined by OES by comparing measured and simulated atomic and molecular emission spectra of the generated plasma. This method is very convenient but sometimes overestimates the temperature if emission spectra of radicals are considered. The radicals can gain energy in the chemical processes of their production, which can contribute to the elevated temperature. This phenomenon was observed by several authors [6,7, 8]. This implies that the best way to determine the plasma temperature by OES is to use the spectra of the particles that are a direct part of the feeding gas. In air plasma, the most convenient is to determine the gas temperature from N_2 spectra, since N_2 molecules are present in the feeding gas and are not produced by chemical processes in the plasma.
In discharges generated in air at atmospheric pressure, the emission of the first and second positive system of N_2 is usually observed. In near-LTE MW plasma generated in air, however, the excitation of N_2 takes place only at the temperatures above 6000 K [9]. Such high temperature is not reached in our plasma; therefore there is no N_2 emission. Furthermore there is even no (or too weak to detect) emission of NO, OH or O_2 that are usually present in LTE air plasmas. With no appropriate radiation it is not possible to perform OES temperature diagnostics of the generated air plasma.
However, it is known that N_2^* is produced in non-equilibrium air plasmas, e.g. in the corona discharge. In this strongly non-equilibrium discharge, T_g is low (close to room temperature) but the high temperature of electrons is sufficient for the excitation of N_2. In the discharges at atmospheric pressure, the rotational temperature balances with the temperature of the surrounding gas T_g. So we put corona discharge directly into the MW plasma. N_2^* is then produced by electron-impact excitation but its rotational temperature equilibrates with the surrounding gas temperature – in our case, the

temperature of the MW plasma. The cold corona discharge (when operated in ambient air, T_g = 300±50 K) does not significantly contribute to the increase of T_g. By using the corona probe, i.e. by combining the MW plasma with corona discharge, we can determine the temperature of MW plasma (as the rotational temperature of N_2^*).
To test the reliability of this new corona probe method, we also measure the temperature by the thermocouple and the probe simultaneously and compare the two measurements. Use of thermocouples to measure the temperature of the plasma generated at low pressures and high temperatures is affected by the heat transfer processes and the method is considered not very reliable in this case. At atmospheric pressure in general, thermocouples can be used for temperature measurements if the gas temperature and the gas flow rate are not too high. It is also suitable to use the thermocouple with the smallest probe diameter possible so that it does not affect the gas flows and the discharge itself. In some cases, the thermocouple is placed in a ceramic tube to prevent the heat losses along the thermocouple wires and also to support the thermocouple in a desired position. Plasma temperature was measured by a thermocouple for example in [10-12].

3. Experimental setup

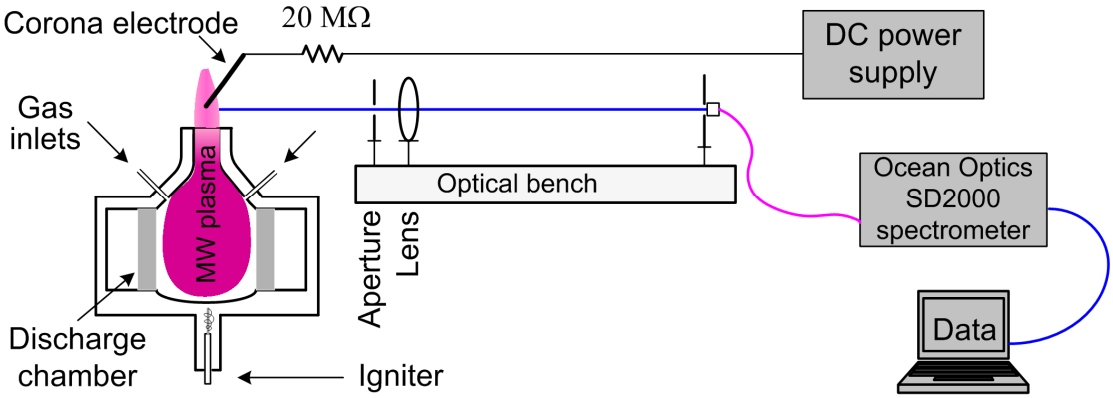


Fig. 1. Experimental set-up. Corona discharge combined with the MW plasma and OES diagnostics.

Litmas Red MW plasma torch powered by a 900 W magnetron, supplied from Richardson Electronics switching power generator SM1050, was used to generate atmospheric pressure air plasma with properties close to LTE. Microwaves generated by a magnetron are focused to the cylindrical plasma chamber made of a hardened teflon or Al_2O_3. A thin teflon tape is placed in the waveguide between the plasma chamber and magnetron to prevent the contamination of the magnetron or the resonant circulator by dust or gases which could cause its malfunction.
The MW discharge is ignited by pneumatic insertion of a metal igniter into the plasma chamber. The brush-shaped igniter (synchronized with microwaves from the magnetron through the electronic unit) causes a local enhancement of the electric field resulting in a discharge ignition. The whole system is externally cooled with water and air. Contrary to the typical MW torch systems, in our case the gas is inserted downstream and tangentially through the two holes of the nozzle into the cylindrical plasma chamber. This is causing the swirl flow in the cylinder and the generated swirling plasma is consequently blown out upstream through the central orifice of the nozzle. Blown-out plasma is then analyzed by optical emission spectroscopy. Emitted light is guided through the optical bench containing an aperture, a fused silica lens and optical fibre holder. Ocean Optics SD2000 spectrometer covering the spectral range of 200-1100 nm is used. The optical bench is movable horizontally and vertically. Experimental set-up and the basic torch characteristics are described in more detail in [13].
For the combination of MW plasma with the corona discharge (figures 1,2), the electrode and power supply for the corona were added.
We use a special 75 mm long hollow syringe needle with a diameter 0.9 mm as a corona electrode. It is very important to be able to get the spectra from the very exact point (the tip of the needle) where

the corona discharge is applied. For this reason, the corona needle is placed in the micrometric movable holder which enables the vertical and horizontal movement.

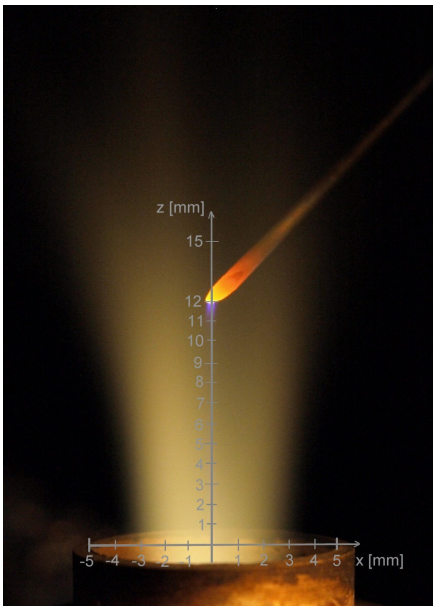


Fig. 2. Corona probe in the MW air plasma.

4. Results

We applied the corona discharge probe into the air MW plasma to measure its temperature. We determined Tg of the MW plasma as a rotational temperature of N_2 generated in the corona discharge. We used SPECAIR [14] for the spectral simulations that were then fitted to the measured spectra. The typical measured N_2 ($C^3\Pi_u$–$B^3\Pi_g$) spectrum is shown in figure 3.

By this method, we measured the temperature profiles (temperatures at various lateral positions x, i.e. distances from the vertical plasma axis) of the MW plasma at various conditions – power P and gas flow rate Q in various heights z. The maximum temperature was not found directly in the centre of the plasma (at the vertical z-axis) as expected but it was shifted to the side. This is a result of the plasma shape which depends on the gas flow conditions. At lower gas flow rates, the generated plasma has a symmetric conical shape and the maximum temperature is usually at (or very close to) the z-axis, which is the case of Q=5 l/min (figure 4).

With the higher gas flow rates, the shape of the plasma was not symmetric, because plasma was being strongly blown out. We would need to increase the power if the conical shape should be maintained but the magnetron power is quite low so in the case of Q=8 or 11 l/min (figure 5) it was not possible to maintain a stable conical-shaped plasma. We also measured the vertical temperature profiles (dependence on the height z above the nozzle). The results show that the temperature is mostly decreasing with z (figure 6).

To test the reliability of the corona probe method we measured the MW plasma T_g by the corona probe and the thermocouple simultaneously. This means that the thermocouple and the corona electrode were placed at the same movable holder and the holder was shifted during the measurement in such a way that either the corona electrode or the thermocouple was in the desired measuring position. The time delay between the corona probe and the thermocouple measurement was only a few seconds (untill the holder was moved from one position to another). During this time, the parameters of the plasma did not change significantly. These experiments were done at two various gas flow rates Q=5 and 8 l/min and constant power P=367 W. We measured the temperature profiles of the MW plasma in the height z=16 mm above the nozzle because it enabled us to measure the whole temperature profile. In the positions z<16 mm, the temperature (in the middle of the plasma, at x=0 mm) was above the thermocouple measuring range (max ~1300 K). In the positions z>16 mm, the N_2 emission was quite weak, especially at the sides of the plasma. The maximum temperature for Q=5 l/min measured by the corona probe was 1450±50 K and by the thermocouple 1350±20 K (figure 7). For the Q=8 l/min, the

maximum temperature measured by the corona probe was 1180±50 K and by the thermocouple 1090±10 K (figure 8).

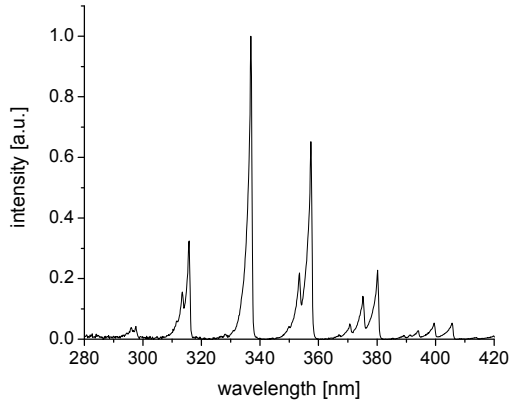


Fig. 3. Typical N_2 2nd positive spectrum measured by the corona probe in the MW air plasma with Q=5 l/min and P=368 W, DC corona 5 kV.

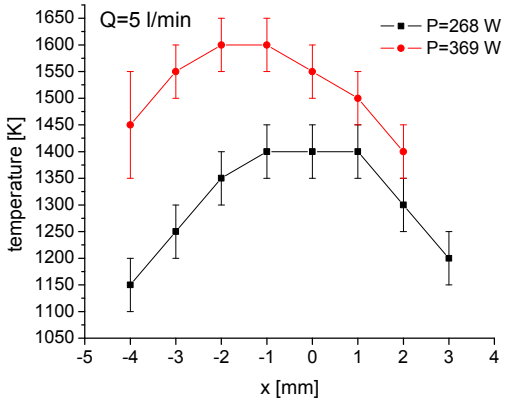


Fig. 4. The dependence of plasma temperature on the lateral position x in z=0 mm for Q=5 l/min.

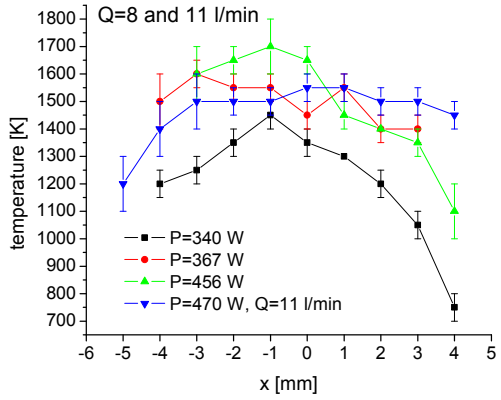


Fig. 5. The dependence of plasma temperature on the lateral position x in z=0 mm for Q=8 and 11 l/min.

368 W. Corona1 and 2 were two sets of measurements.

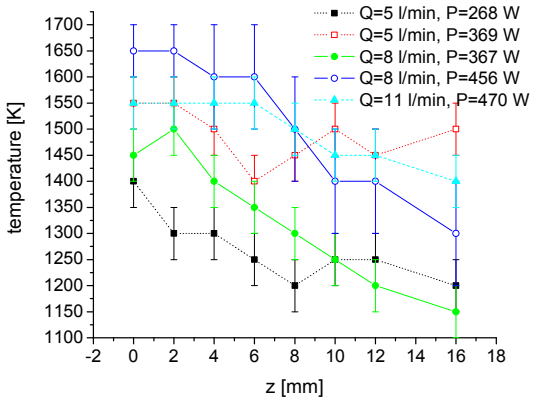


Fig. 6. The dependence of plasma temperature on the height z in x=0 mm at various operating conditions (P, Q).

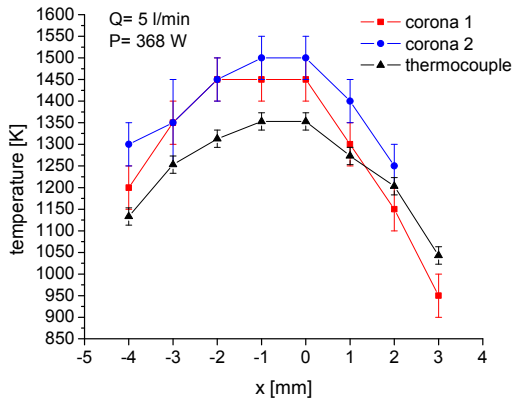


Fig. 7. The comparison of gas temperatures measured by the corona probe and the thermocouple at air flow 5 l/min and MW power

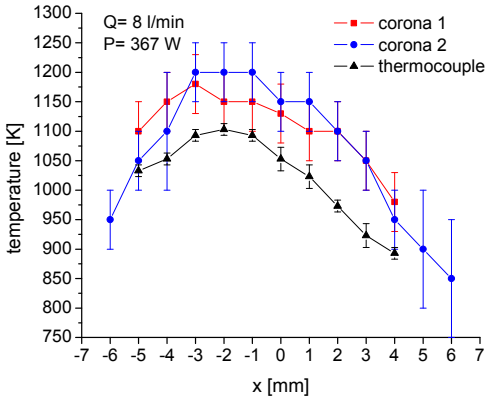


Fig. 8. The comparison of gas temperatures measured by the corona probe and the

thermocouple at air flow 8 l/min and MW power 367 W. Corona1 and 2 were two sets of measurements.

The results show that the temperatures measured by the corona method were slightly higher (up to 150 K) than the thermocouple temperature, but the difference is small relative to the measured plasma temperatures (T_g close to or above 1000 K). This verifies that the corona probe method can be applied to determine the temperature of the plasma and contrary to the thermocouple it can be used also for high plasma temperatures.

5. Summary

We developed and tested a novel diagnostics method of temperature measurements of near-LTE MW air plasma. A strongly non-equilibrium corona discharge applied inside the atmospheric pressure MW air plasma is used as an excitation source for N_2^* suitable for OES diagnostics. The gas temperature lateral and axial profiles of the MW plasma were measured. The comparison of the temperatures measured by the new method and the thermocouple showed a good agreement, with the temperatures measured by the corona probe slightly higher. Nevertheless, the corona probe can be applied even to higher temperature plasmas, out of the typical range of thermocouple use.

Acknowledgements. Effort sponsored by the AFOSR, Air Force Material Command, USAF, under grant FA8655-09-1-3110, and Slovak Research and Development Agency APVV SK-FR-0038-09. We gratefully acknowledge Sencera, Ltd. for providing the MW torch.

6. References

[1] Al-Shamma'a A I, Wylie S R, Lucas J, Pau C F 2001 *J. Phys. D: Appl. Phys.* **34** 2734-2741
[2] Uhm H S, Hong Y C , Shin D H 2006 *Plasma Sources Sci. Technol.* **15** S26–S34
[3] Zajickova L, Elias M, Jasek O, Kudrle V, Frgala Z, Matejkova J, Bursik J, Kadlecikova M 2005 *Plasma Phys. Control. Fusion* **47** B655-B666
[4] Green K M, Borras M C, Woskov P P 2001 *IEEE Trans. Plasma Sci.***29** 399
[5] Lee M H *et al. 2009 New J. Phys.* **11** 115022
[6] Fantz U 2006 *Plasma Sources Sci. Technol.* **15** S137–S147
[7] Machala Z, Janda M, Hensel K, Jedlovský I, Leštinská L, Foltin V, Martišovitš V, Morvová M 2007 *J. Molec. Spectrosc.* **243** 194-201
[8] Staack D, Farouk B, Gutsol A, Fridman A 2005 *Plasma Sources Sci. Technol.* **14** 700-711
[9] Laux C O, Spence T G, Kruger C H, Zare R N 2003 *Plasma Sources Sci. Technol.* **12** 125–138
[10] Moon S Y, Choe W, Uhm H S, Hwang Y S, Choi J J 2002 *Phys. Plasmas* **9** 4045
[11] Anghel S D, Simon A 2007 *Plasma Sources Sci. Technol.* **16** B1–B4
[12] Meng X, Pan W X, Chen X, Wu C K Measured temperature of a laminar plasma jet by using thermocouple at reduced pressure, 19th International Symposium on Plasma Chemistry, Bochum, July 26-31, 2009
[13] Foltin V, Leštinská L, Machala Z 2006 *Czech. J. Phys.* **56** B712-720
[14] Laux C O *Radiation and Nonequilibrium Collisional-Radiative models* von Karman Institute for Fluid Dynamics, Lecture Series 2002-07, eds. D. Fletcher, T. Magin, J.-M. Charbonnier, G.S.R. Sarma, Rhode Saint-Genese, Belgium, June 4-7, 2002

PLASMA-LIQUID SYSTEM WITH REVERSE VORTEX FLOW OF "TORNADO" TYPE

O.A. Nedybaliuk, S.V. Olszewski, V.Ya.Chernyak

Taras Shevchenko National University of Kyiv, Faculty of Radio Physics, Dept. of Physical Electronics, Prospect Acad. Glushkova 2Г, Kyiv 03022, Ukraine
E-mail: oanedybaliuk@gmail.com

This paper presents the results of experimental and theoretical investigations of the process plasma-assisted reforming of aqueous ethanol solutions in the dynamic plasma liquid systems using the DC electric discharges in a reverse vortex gas flow of "tornado" type with a "liquid" electrode (TORNADO-LE). Volt-ampere characteristic of discharge in the current range from 200 to 400 mA and gas flow range from 0 to 110 cm^3 per second for distilled water were measured. The experiments show possibilities and efficiency of low-temperature plasma-chemical conversion of liquid ethanol into hydrogen-rich synthesis gas in different regimes. Plasma emission spectra were registered by the CCD-based spectrometer "Plasma Spec" in the range of 200-1100 nm with spectral resolution 0,6 nm. Excitation temperatures (electronic T_e^*, vibrational T_v^* and rotational T_r^*) were measured.

1. Introduction

Today, hydrogen is considered as one of the most perspective energy sources for the future that can be renewable, ecologically clean and environmentally safe [2]. Among possible technologies for hydrogen (H_2) production, including steam reforming and partial oxidation of hydrocarbons [3], a low-temperature plasma-assisted reforming of biomass-derived ethanol (ethyl alcohol C_2H_5OH) is believed to be a good alternative approach [4].

There are various electric-discharge techniques of plasma conversion of ethanol into H_2 using thermal (equilibrium) and nonthermal (nonequilibrium) plasmas: arc, corona, spark, MW, RF, DBD, etc. Among them, one of the most efficient is the plasma processing in the dynamic plasma-liquid systems (PLS) using the DC discharge in a reverse vortex gas flow of „tornado" type [1] with a "liquid" electrode (TORNADO-LE) [5]. Advantages of this technology are high chemical activity of used plasma and selectivity of plasma-chemical transformations, providing high enough productivity and efficiency of conversion at relatively low power consumption on the high-voltage discharging in the flow at atmospheric pressure. The highly developed plasma-liquid interface with the large surface-to-volume ratio and the deep injection of plasma particles into the liquid also favor to the intensification of the ethanol conversion in the system.

In this paper we report new results of our experimental studies of the plasma parameters and plasma-assisted reforming process of ethanol in the PLS with the DC TORNADO-LE using available methods of diagnostics.

2. Experimental Setup

PLS reactor was prepared with the DC discharge in a reverse vortex gas flow of tornado type with a "liquid" electrode (TORNADO-LE) as is shown in Fig. 1.

It consists of a cylindrical quartz vessel (1) by diameter of 9 cm and height of 5 cm, sealed by the flanges at the top (2) and at the bottom (3). The vessel was filled by the work liquid (4) through the inlet pipe (5) and the level of liquid was controlled by the spray pump. The basic cylindrical T-shaped stainless steel water-cooled electrode (6) on the lower flange (3) made from stainless steel is fully immersed in the liquid. The electrode on the upper flange (2) made from duralumin had a special copper hub (11) with the axial nozzle (7) by diameter 2 mm and length of 6 mm. The gas was injected into the vessel through the orifice (8) in the upper flange (2) tangentially to the cylinder wall (l) and created a reverse vortex flow of tornado type, so the rotating gas (9) went down to the liquid surface and moved to the central axis where flowed out through the nozzle (7) in the form of jet (10) into the quartz chamber (12). Since the area of minimal static pressure above the liquid surface during the vortex gas flow is located near the central axis, it creates the column of liquid at the gas-liquid

interface in the form of the cone with the height of ~1 cm above the liquid surface (without electric discharge).

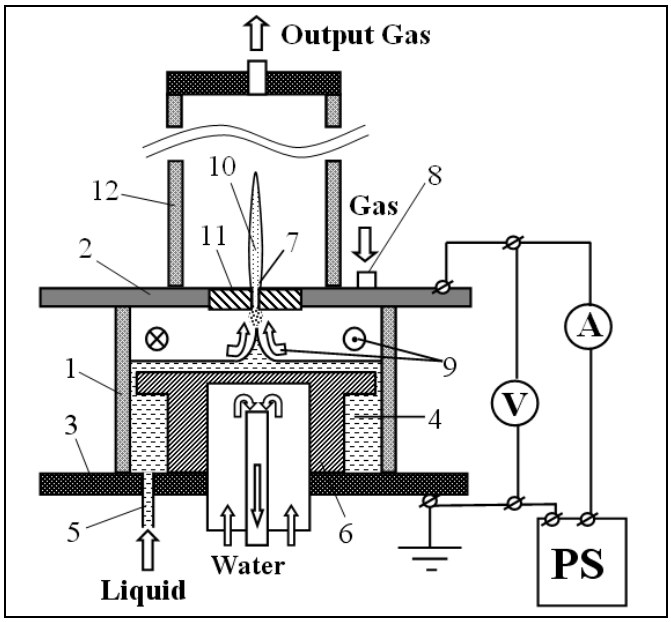


Fig. 1. Schematic of the PLS reactor with the DC discharge in a reverse vortex gas flow of tornado type with a "liquid" electrode.

The voltage was supplied between the upper electrode (2) and the lower electrode (6) in the liquid with the help of the DC power source powered up to 10 kV. Two modes of the discharge operation were studied: the mode with “liquid” cathode (LC) and the mode with “solid” cathode (SC): “+” is on the flange (2) in the LC mode, and “-” is on the flange (2) in the SC mode. The conditions of breakdown in the discharge chamber were regulated by three parameters: by the level of the work liquid; by the gas flow rate G; and by the value of voltage U. The ignition of discharge usually began from the appearance of the axial streamer; the time of establishment of the self-sustained mode of operation was ~1-2 s. The range of discharge currents varied within 100-400 mA. The pressure in the discharge chamber during the discharge operation was ~1.2 atm, the static pressure outside the reactor was ~1 atm. The elongated ~5 cm plasma torch (10) was formed during the discharge burning in the camera.

3. Diagnostic methods

Diagnostics of the PLS TORNADO-LE plasma was conducted by means of optical emission and absorption spectroscopy. A high-speed CCD-based spectrometer “Plasma-spec” with a spectral resolution ~0.6 nm was used for the spectra registration in the range of wavelengths 200-1100 nm.
The characteristic temperatures corresponding to excited states of atoms (electronic temperature T_e^*), and molecules (vibrational T_v^* and rotational T_r^* temperatures) in discharge plasma were determined by different methods. The electronic temperature T_e^* was determined by relative intensities of emission of oxygen multiplet lines (777.2; 844.6; 926.6 nm). To determine vibrational T_v^* and rotational T_r^* temperatures, an original technique with using the SPECAIR [6] was used [7].
Diagnostics by mass-spectrometry using a monopole mass-spectrometer MX 7301 and by gas-phase chromatography using a gas chromatograph 6890 N Agilent with the calibrated thermal conductivity detectors were utilized for the analysis of the component content of output gas products after the processing in the plasma-chemical reactor.

4. Results and discussion

The typical current-voltage characteristics of the TORNADO-LE in the mode with "solid" cathode working in water at different airflow rates are shown in Fig. 2. In our system it was glowing discharge type.

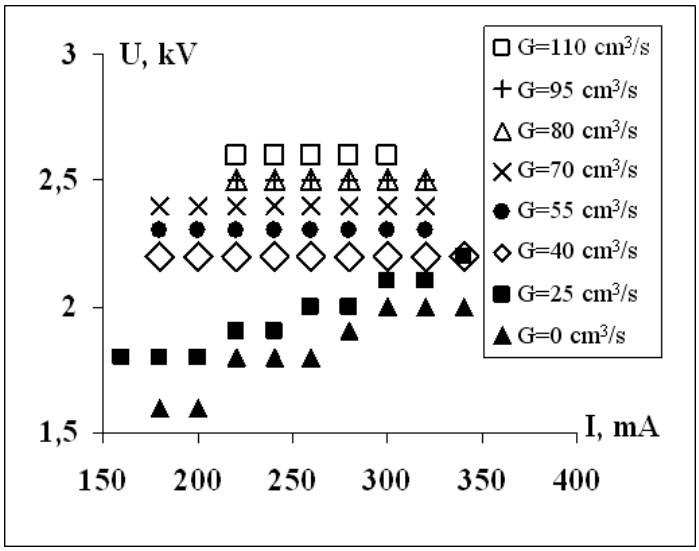


Fig. 2. Current-voltage characteristics of the TONADO-LE with solid cathode working in water at different airflow rates.

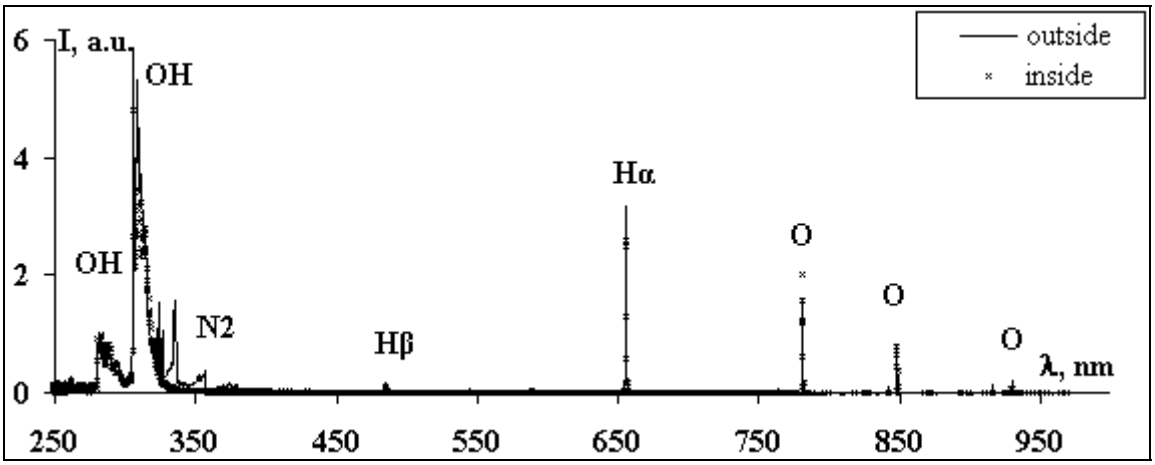


Fig. 3. Typical emission spectrum of discharge plasma inside and outside of system in the TORNADO-LE: I=300 mA; G=110 cm^3/s; U=2,6 kV; working liquid – distilled water; gas flow – air; polarity – „liquid".

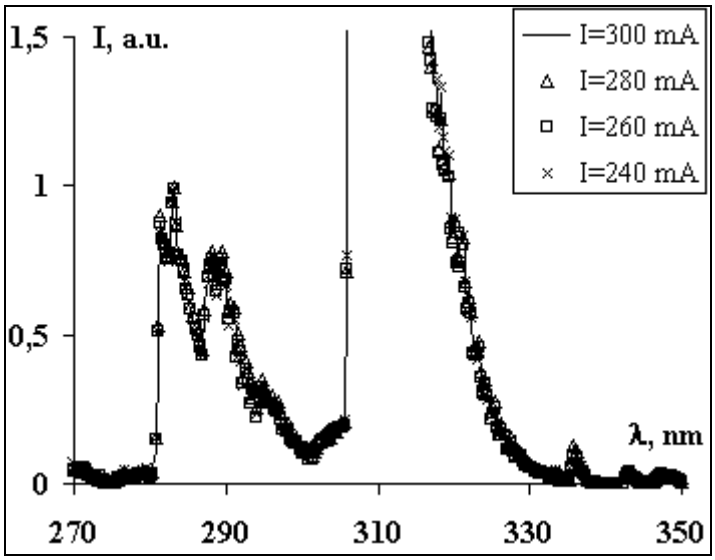


Fig. 4. Experimental plasma emission spectra of TORNADO-LE working on distilled water at different discharge currents I, G=110 cm^3/s, U=2,6 kV.

Typical emission specra of plasma in TORNADO-LE inside and oustide of system are shown in Fig. 3. Nitrogen band N_2(C-B) only outside of system was presented. Also, outside of system copper lines was present. Inside copper lines and nitrogen was absent.
Experimental emission spectra of discharge plasma at different currents and air flows are shown in Fig. 4. And Fig. 5 respectively. Their temperatures are close.

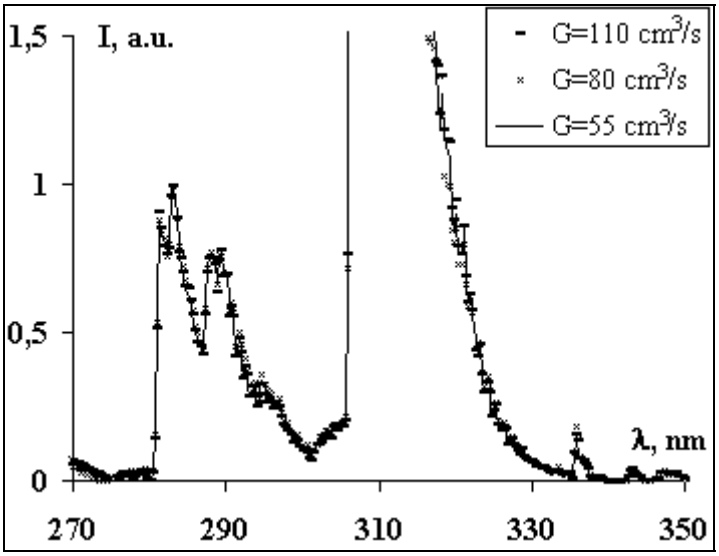


Fig. 5. Experimental plasma emission spectra of TORNADO-LE working on distilled water at different air flows G.

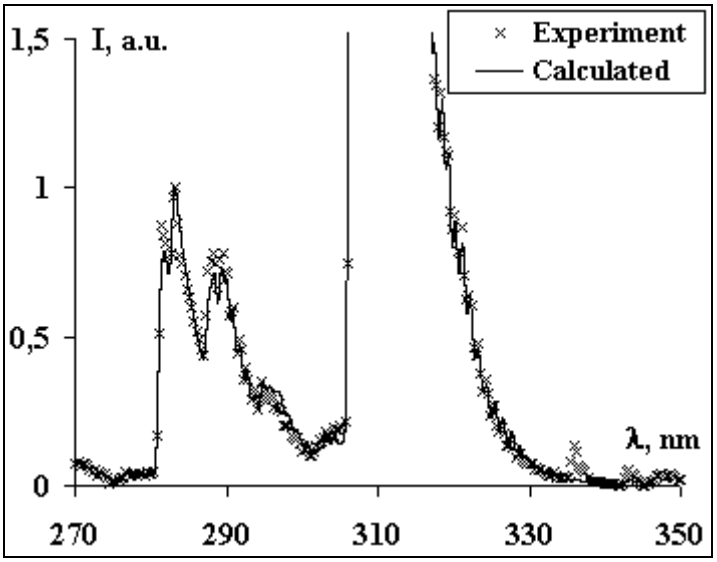


Fig. 6. SPECAIR simulation of OH (A-X) emission bands in the range of wavelengths 270-350 nm at temperatures T_r^*=4000 K, T_v^*=4000K and T_e^*=5000 K and experimental emission spectrum at I=300 mA, G=110 cm^3/s, U=2,6 kV (distilled water).

Experimental and calculated by SPECAIR emission spectra are shown in Fig. 6. Temperatures T_r^*=4000 K, T_v^*=4000K and T_e^*=5000 K for calculating was used. T_e^* was obtained by lines og oxygen. Plasma inside of system was isotermic.
Coefficient of energy transformation for the ethanol reforming in the PLS with the TORNADO-LE of the ethanol concentration 25% in the ethanol-water solution is α=0,86. Speed generation of synthesis gas is 0,2 m^3 per hour.
The results of mass-spectroscopic measurements of the hydrogen concentrations in output gas products after the ethanol processing in the TORNADO-LE are shown in Fig. 7.

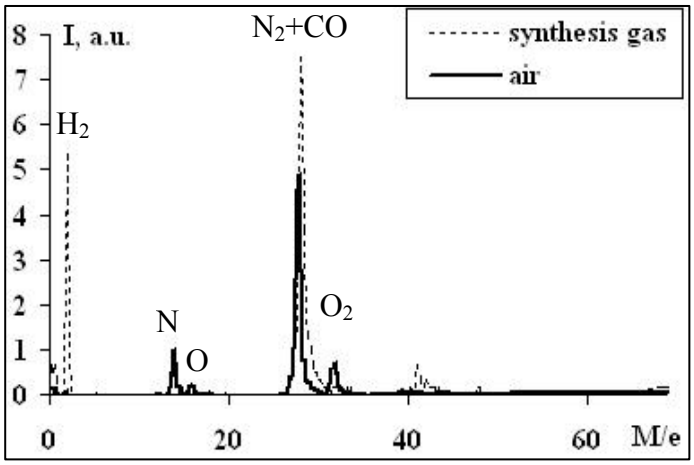


Fig. 7. Mass-spectrometry of gas products after the reforming in the TORNADO-LE with liquid cathode. Voltage 2 kV, current 320 mA, air flow rate 55 cm^3/s, mixture C_2H_5OH/H_2O = 1/7.

Thus, our results of preliminary studies demonstrate that the glow discharge in the reverse vortex flow of Tornado type with the liquid electrode is very perspective for the plasma-assisted reforming of liquid hydrocarbon fuels.

5. Conclusions

The dynamic plasma-liquid systems with the dc discharge TORNADO-LE is quite efficient in plasma-chemical reforming of liquid ethanol into hydrogen-rich synthesis gas.
Two type of plasma attended in PLS TORNADO-LE were isothermic – inside and nonisothermic (decay plasma) – outside.
Molecular nitrogen band N_2(C-B) and copper line Cu were presented only outside of system.

6. References

[1] AlyssaWilson, David Staack, Tanvir Farouk, Alexander Gutsol, Alexander Fridman and Bakhtier Farouk „Self-rotating dc atmospheric-pressure discharge over a water-surface electrode: regimes of operation", Plasma Sources Sci. Technol. 17, 2008, 045001, 12pp.
[2] 18th World Hydrogen Energy Conf., 17-19 May 2010, Essen, Germany. http://www.whec2010.com
[3] M. Ni, D. Y. C. Leung, and M. K. H. Leung, "A review on reforming bio-ethanol for hydrogen production," Int. J. Hydrogen Energy, vol. 32, no. 15, pp. 3238-3247, 2007.
[4] M. Deminsky, V. Jivotov, B. Potapkin, and V. Rusanov, "Plasma-assisted production of hydrogen from hydrocarbons," Pure Appl. Chem., vol.74, no. 3, pp. 413-418, 2002.
[5] O. A. Nedybaliuk, S. V. Olzewski,. V. Ya. Chernyak, and O. I. Lomonos, "Discharge in reverse vortex flow of TORNADO type," Proc. IV Int. Conf. "Electronics and Applied Physics", 23-25 Oct. 2009, Kyiv, Ukraine. Taras Shevchenko Kyiv Nat. Univ., 2009, pp. 142-143.
[6] http://www.specair-radiation.net
[7] Prysiazhnevych I., Lomonos L., Chernyak V. Tecniquesof determining vibrational and rotational excitation temperatures by OH (A-X) AND N2 (C-B) bands for plasma diagnostics // Proc. IV Int. Conf. "Electronics and Applied Physics", 23-25 Oct. 2009, Kyiv, Ukraine.-P.111-112.

ELECTRON DENSITY OF PLASMA PENCIL DISCHARGE ESTIMATED BY BROADENING OF THE SPECTRAL ATOMIC LINES

Dana Skacelova, Pavel Slavicek

Department of Physical Electronics, Faculty of Science, Masaryk University, Kotlarska 2,61137 Brno, Czech Republic
E-mail: ps94@sci.muni.cz

Plasma pencil is a special type of plasma nozzle working at atmospheric pressure, which is interesting for possible applications such as local treatment of surface, deposition of thin films, change surface energy, cutting in surgery, sterilization, etc. Through this nozzle, which is made from quartz tube with typical inner diameter 2 mm, flows working gas (typically argon). The powered electrode is connected through the matching unit to the rf generator.
In this contribution, we present diagnostics of unipolar and bipolar discharge channel generated by the Plasma pencil. For different conditions the parameters of the plasma channel were estimated from optical emission spectra in the spectral range 200 - 900 nm, rotational temperature from OH rotational lines and concentration of electrons from Stark broadening of hydrogen and argon lines were estimated.

1. Introduction

Low-temperature plasmas are extensively used for the plasma processing [1], light sources, various plasma technologies [2] etc. Therefore, the interest for plasma diagnostics is growing. The optical emission spectroscopy (OES) technique is of particular interest, especially if standard spectroscopic instrumentation is available in laboratory. Barrier discharges at atmospheric pressure are intensively studied for possible industrial applications [1,6,8]. In this paper diagnostics of radio frequency discharge by optical emission spectroscopy will be presented.

2. Experimental set-up

The schematic diagram of the experimental arrangement is shown in Fig.1 and photograph is shown in Fig.2. The powered electrode is separated by the dielectric tube (nozzle with the inner diameter of about 2 mm) from plasma. In this experimental device a quartz tube with length 5 cm and 10 cm were used. Through the nozzle flows working gas. Working gas was argon with purity 99.996 %. Note, that the working gas flowing from the nozzle stabilizes the discharge. The detail description and discussion of the several variants of the nozzle were also presented in [6,7]. The electrode is connected through the matching unit to the rf generator Cesar - 1310 by Dressler driven at frequency 13.56 MHz. This type of discharge has a lot of applications [5,6].
Unipolar configuration means that not affect the plasma channel to the ground electrode. Bipolar configuration means that the plasma channel is directly connect to the ground electrode. Both configurations could be used for different applications.

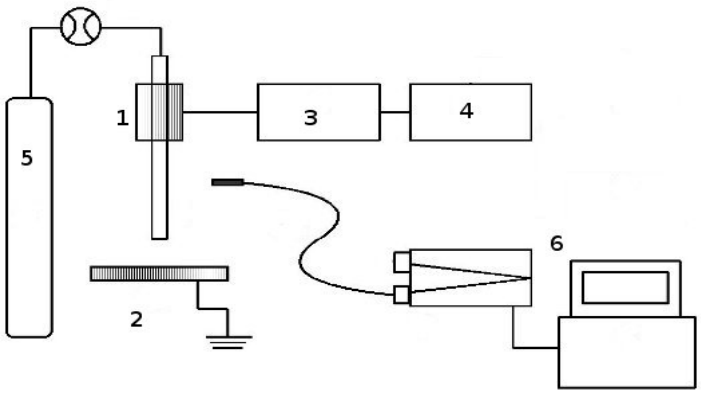


Fig.1. Experimental setup: 1 - nozzle, 2 - ground electrode, 3 - matching unit, 4 - rf generator, 5 - working gas (argon), 6 - spectrometer



Fig.2. Photo of plasma pencil.

Optical emission spectroscopy of the plasma channel was realized by means of the monochromator FHR1000 by Jobin -- Yvon -- Horiba (grid were 2400 gr/mm and 3600 gr/mm, CCD detector Symphony cooled by four stages Peltier cooler). The spectra were recorded perpendicularly to the plasma channel for different discharge parameters and different positions.
Rotational temperature were calculated from rotational lines of OH. Rotational temperature were calculated from Boltzmann plot [3,4].
The most frequently used technique for determination of electron concentration N_e is based on the half-width and shape of the hydrogen Balmer beta (H_β = 486.13 nm) spectral line. Electron concentration also was estimated from broadening of Ar line at 549 nm. Electron concentration was estimated by approximate formula by Wiese et al. [9,10,11,12].

3. Result and discussion

Rotational temperature was calculated from rotational lines of branch Q1. The dependence of the rotational temperature on the distance from end of the nozzle for 5 cm length of nozzle and for rf power 100 W and working gas flow rate 1 slpm is shown in Fig.3. Negative distance was in nozzle, positive distance was out of nozzle.

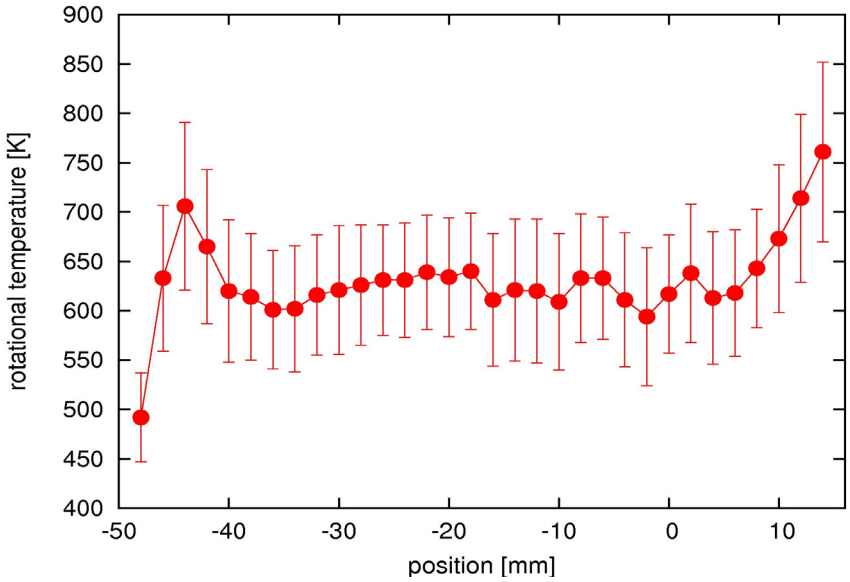


Fig.3 Rotational temperature for unipolar configuration from OH, rf power 100 W, working gas (Ar) flow 1 slpm. Negative distance was in nozzle, positive distance was out of nozzle.

The dependence of the concentration of electron on the distance from end of the nozzle for 5 cm length of nozzle and for rf power 125 W and working gas flow rate 1 slpm, for unipolar configuration is shown in Fig.4. Negative distance was in nozzle, positive distance was out of nozzle.
The dependence of the concentrations of electron on the distance from end of the nozzle for 10 cm length of nozzle and for rf power 125 W and working gas flow rate 1 slpm, for unipolar and bipolar configuration are shown in Fig.5. Negative distance was in nozzle, positive distance was out of nozzle.
Concentrations were estimated from H_β and from Ar line 549 nm.
Error of rotational temperature was about 10%. The rotational temperature was approximately same from power electrode (position -50 mm) to the end of the nozzle (position 0 mm). Working gas (argon) was mixtured with air at atmospheric pressure in range from the end of the nozzle (position 0 mm) to end of plasma channel (position 15-20 mm). Estimated dependence of rotational temperature on rf power show that if rf power is increase than rotational temperature is increase too.
The concentration of electron was in order 1020 m-3 from broadening of hydrogen line and in order 1021 m-3 from Ar line. Estimate error of this value is from this first measurements problematic. New measurement and calculation will be done in near future. Effect of Doppler broadening and instrumental broadening were counted.
The Abel transformation of cylindrical symmetry of discharge was not taken into account for very small diameter of plasma channel(smaller than 1 mm).

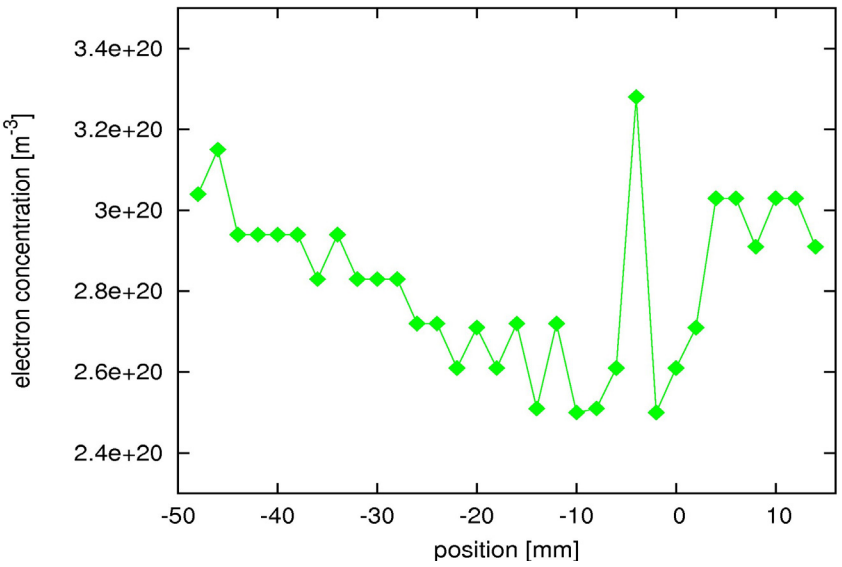


Fig.4 Concentration of electron calculated from broadening of H_b, rf power 125 W. Negative distance was in nozzle, positive distance was out of nozzle.

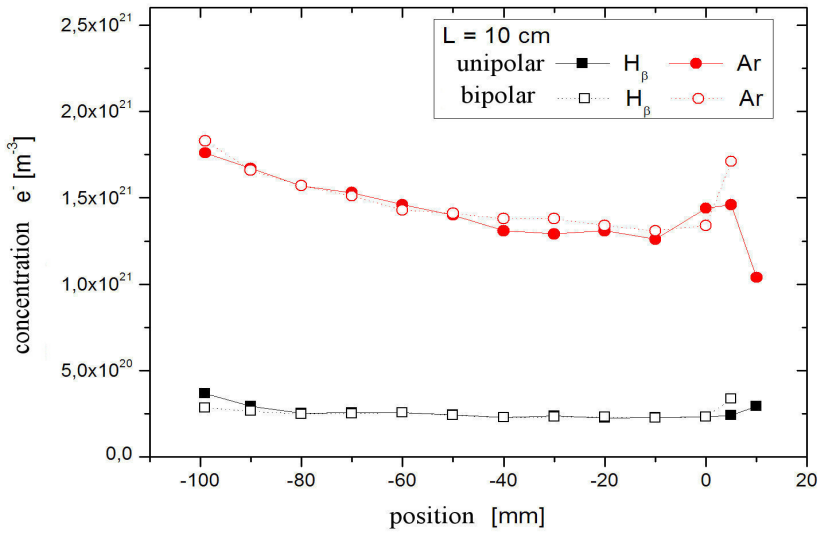


Fig.5 Concentrations of electron calculated from broadening of H_b and Ar line, rf power 125 W. Negative distance was in nozzle, positive distance was out of nozzle.

4. Conclusion

In this article results of electron concentration and rotational temperature in discharge generated by plasma pencil at atmospheric pressure were presented. In calculation of electron concentration other broadening mechanism such as resonance and Van der Waals broadening were ignored, because Stark broadening was dominant.

In this contribution the single nozzle was used, but several nozzles can be applied simultaneously in one device [5], which is more convenient for industrial application.

Acknowledgement. This research has been partially supported by the grant 202/09/2064 , by the Czech Science Foundation and by the research intent MSM:0021622411 funding by the Ministry of Education of the Czech republic and by the contracts KAN101630651, KAN311610701 by Grant Agency of Academy of Science of Czech Republic.

5. References

[1] J. Rahel, M. Simor, M. Cernak, M. Stefecka, Y. Imahori, M. Kando Surf. Coat. Technol, 169-170,(2003) 604
[2] M. Sira, D. Trunec, P. Stahel, V. Bursikova, Z. Navratil *J. , Phys. D*, 2008, 41 015205
[3] H.R.Griem *Principles of Plasma Spectroscopy*, Academic Cambridge Univ.Press, New York,1997
[4] W. Lochte-Holtgreven Ed. *Plasma Diagnostics*, American Institute of Physics, New York,1995
[5] M. Cada, Z. Hubicka, M. Sicha, A. Churpita, L. Jastrabik, L. Soukup, M. Tichy *Surf. Coat. Technol*,174-175 (2003) 530
[6] P. Slavicek, V. Bursikova, A. Brablec, V. Kapicka, M. Klima *Czech. J. Phys*.,54, (2004) C586
[7] P. Slavicek, M. Klima, J. Janca, A. Brablec, J. Kadlecova, P. Smekal *Czech. J. Phys*.B,56, (2006) 56
[8] Z. Hubicka at all Plasma *Sources Sci. Technology*, 11,(2002) 195
[9] W.L. Wiese, D.E.Kelleher,D.R. Paquette *Phys.Rev.A*, 6, (1972) 1132
[10] M. Ivkovic, S. Jovicevic, N. Konjevic *Spectrochimica Acta Part B*, 59, (2004) 591
[11] D.E.Kelleher J. Quant. Spctrosc. *Radiat. Transfer*, 25, (1981) 191
[12] R.Zikic, M.A. Gigisos, M. Ivkovic, M.A.Gonzales, N. Konjevic *Spectrochimica Acta Part B*, 57, (2002) 987

ELECTRICAL AND SPECTROSCOPIC DIAGNOSTICS OF ATMOSPHERIC NITROGEN DIELECTRIC BARRIER DISCHARGE: EFFECT OF PACKING CATALYSTS

Xin Tu[1], Helen J. Gallon[1], J. Christopher Whitehead[1]

[1]*School of Chemistry, The University of Manchester, Oxford road, Manchester M13 9PL, UK*
E-mail: j.c.whitehead@manchester.ac.uk

To get a better understanding of plasma-catalyst interactions, the effects of different packing materials (Zeolite 4A, TiO_2 and quartz wool) on the electrical and spectroscopic characteristics of a cylindrical double-dielectric barrier discharge (DBD) in nitrogen have been investigated. It is found that both the amplitude and number of the current pulses significantly decrease when the catalyst pellets are packed in the gas gap. The N_2DBD with no packing can be characterized as a typical filamentary discharge, while the discharge with the packing materials (Zeolite 4A and TiO_2) is a combination of surface discharge on the surface of the solid pelletsand weak microdischarge generated in the void space between the pellets and the quartz. In addition, optical emission spectroscopy has been employed to determine the rotational and vibrational temperatures of the discharge by using N_2 ($C^3\Pi_u \rightarrow B^3\Pi_g$) molecular bands.

1. Introduction

Atmospheric pressure non-thermal plasmas have been widely used in various applications such as surface treatment, pollution control and biological decontamination [1]-[4]. In the past decade, the application of hybrid plasma-catalysis technology for the abatement of pollutants and hydrocarbon reforming has attracted considerable interest [5]-[8]. Highly reactive species generated in non-thermal plasmas are favourable for both the initiation and propagation of chemical reactions. Meanwhile, the combination of plasma and heterogeneous catalysis could generate a synergistic effect, which may provide a unique way to separate the activation steps from the selective reactions. Recent works have also reported the treatment of supported metal catalysts using non-thermal plasmas [9][10]. A significant enhancement in the dispersion, low-temperature activity and stability of the catalysts has been shown. Up until now, extensive works have been focused on the plasma-catalytic reactions to maximize the process performance, while less attention has been paid on the interaction between plasma and catalyst, especially the influence of catalysts on plasma properties [11][12]. In this paper, the effect of different packing materials (catalysts and quartz wool) on the characteristics of the nitrogen DBD has been investigated by means of electrical and spectroscopic diagnostics.

2. Experimental setup

Fig. 1 shows a schematic diagram of the experimental setup. The experiment is carried out in a cylindrical DBD reactor consisting of two quartz tubes, both of which are covered by a stainless steel mesh electrode. The inner electrode is connected to a high voltage output and the outer electrode is grounded. The discharge length is 50 mm and discharge gap is fixed at 1.5 mm. Nitrogen is used as the working gas. The nitrogen flow rate is controlled by a mass flow controller and varied between 0.1 L/min and 1L/min. The DBD reactor is supplied by an ac power supply with a maximum peak-peak voltage of 22 kV and a variable frequency of 30-40 kHz. Catalyst pellets (zeolite 4A and TiO_2) with diameter between 500 and 850 μm fill the whole discharge gap. The applied voltage is measured by a home-made high voltage probe, while the total current is measured by a Rogowski-type current monitor (Pearson Model 110). An external capacitor (42.4 nF) is used to measure the transferred charge in the discharge. All the electrical signals are sampled by a four-channel digital oscilloscope (Tektronics TDS 2014). A LABVIEW system is used for the measurement of discharge power by the area calculation of Lissajous figures [13]. A thermocouple is fixed on the surface of the outer electrode to measure the surface temperature of the DBD reactor. Emission spectra of the discharge are recorded by an optical fiber connected to a Jarrell-Ash MonoSpec 27 spectrometer with a wide spectral range

from 250 to 900 nm.

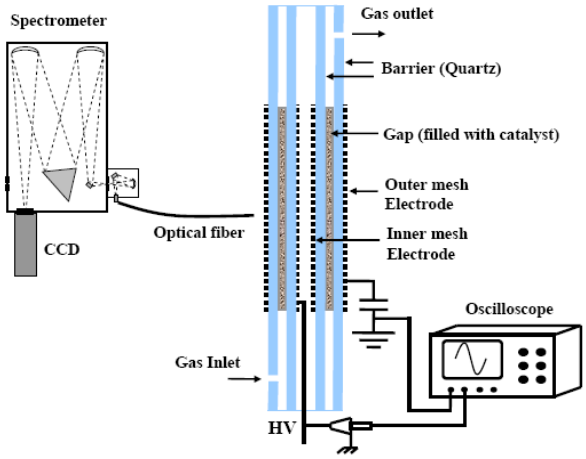


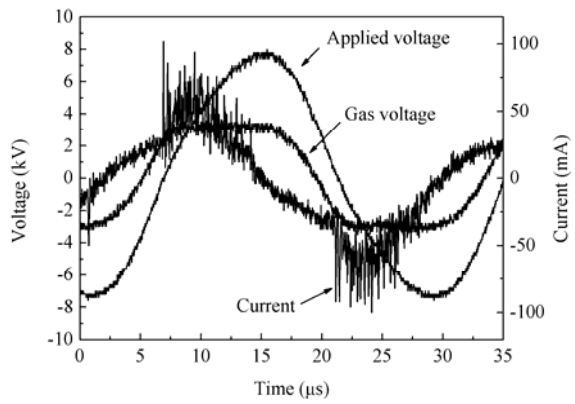
Fig. 1. Schematic diagram of experimental setup

3. Results and discussion

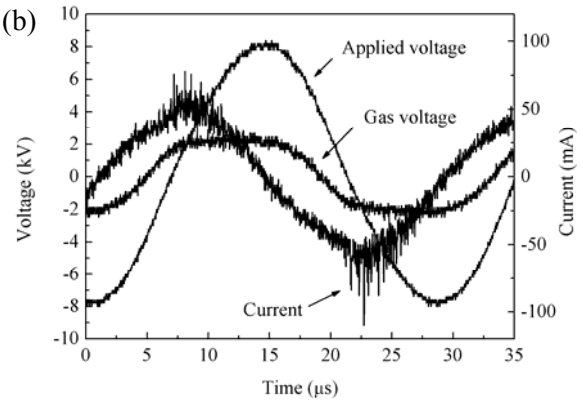
3.1 Electrical characteristics

Fig. 2 presents the electrical signals of the nitrogen discharges with and without packing material at a fixed discharge power of 70 W. We can see that the total current is composed of the quasi-sinusoid displacement current superposed by numerous current pulses per half-cycle. In the experiment, the filaments perpendicular to the electrodes are randomly distributed in the gas gap, while the jumping filaments can be observed with the naked eye. The duration of a single micro-discharge is about 40 ns. The nitrogen DBD without packing material can be characterized as a typical filamentary mode. It is worth noting that both the amplitude and number of the current pulses greatly decrease when the catalysts (zeolite 4A and TiO_2) are packed within the discharge zone. Introducing the catalysts into the discharge leads to a transition of the discharge mode due to a decrease of volume fraction in the gas discharge gap. It is found that the discharge with the catalysts is a combination of surface discharge on the surface of the catalyst pellets and weak microdischarge generated in the void space between pellets and pellets/quartz wall. The behaviour of the discharge mode is dependent on both particle size and volume fraction of the packed materials. In the case of nitrogen DBD filled with the pellets, microdischarges can be observed between the pellets atlow volume fraction of the solid particles. In addition, the current profile of the discharge filled with quartz wool exhibits a similar behaviour as the discharge with no catalyst. Compared with the discharge without packing material, the presence of the metal oxide catalysts (zeolite 4A and TiO_2) in the gas gap requires more input power to sustain the discharge at the same discharge power. In contrast, we found that the presence of a reduced Ni/Al_2O_3
catalyst in the gap leads to the lowing of the input power for plasma due to the presence of conductive Ni metal phase in the gap.

(a)



(b)



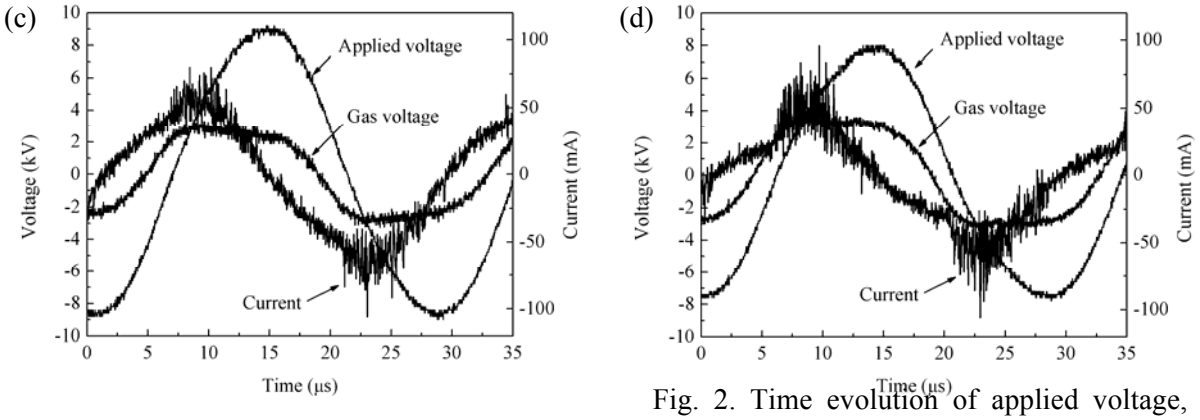


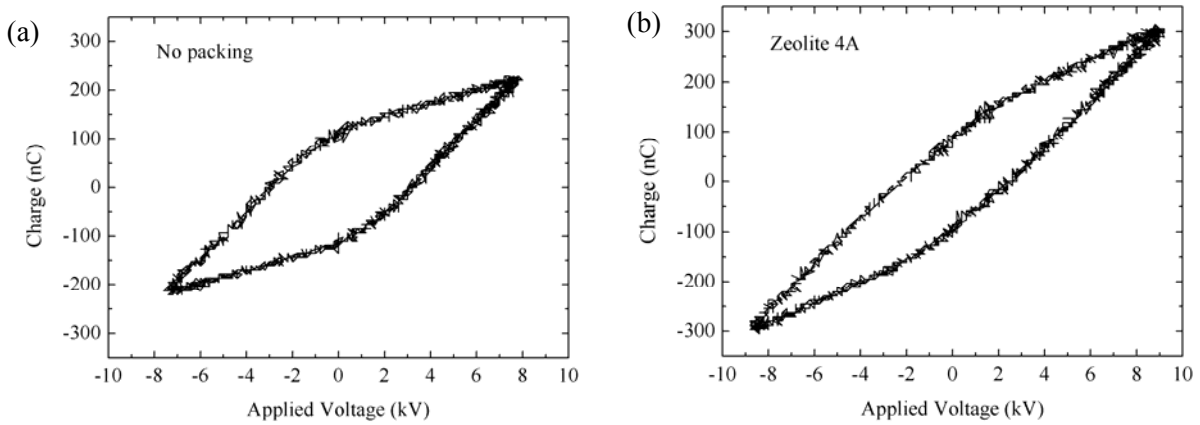
Fig. 2. Time evolution of applied voltage, gas voltage and current in the nitrogen discharges with and without packing material (a) no packing; (b) zeolite 4A; (c) TiO_2; (d) quartz wool (N_2flow rate=0.1 L/min, discharge power=70 W)

Lissajous figures of the nitrogen discharges with and without packing material are shown in Fig. 3. The capacitances of the dielectric material (quartz tube) and gas gap can be derived from the Lissajous figure [1][14]. We can see that the packing materials have a weak effect on the capacitance of the dielectric tube, as shown in Table 1. However, the capacitance of the gas gap greatly increases when the catalysts are introduced into the discharge zone. In the discharge with the catalysts, more charges can be deposited on the catalyst surface, which can be confirmed by the increasing peak-to-peak charge and reduced breakdown voltage.

In the nitrogen discharge with no catalyst, the gas breakdown voltage is about 2.29 kV. When the catalyst pellets (zeolite and TiO_2) are packed in the gap, the breakdown voltage of the nitrogen discharge greatly decreases to about 1.4 kV. The presence of the catalyst pellets in the discharge zone essentially decreases the breakdown voltage due to significant non-uniformities of the electric field and local overvoltage, especially around the contact points between the pellets. We also found that the presence of reduced supported metal catalyst Ni/Al_2O_3further decreases the gas breakdown voltage.

Tab. 1. Parameters of the nitrogen DBDs at a fixed discharge power of 70 W

	C_d (pF)	C_g (pF)	Breakdown Voltage (kV)	Charge discharged (nC)	Total transferred charge (nC)
No packing	47.5	19.02	2.29	318.00	232.00
Zeolite 4A	45.18	41.38	1.36	439.00	226.00
TiO_2	39.1	37.34	1.43	330.00	190.00
Quartz wool	44.88	21.42	2.27	290.00	214.00



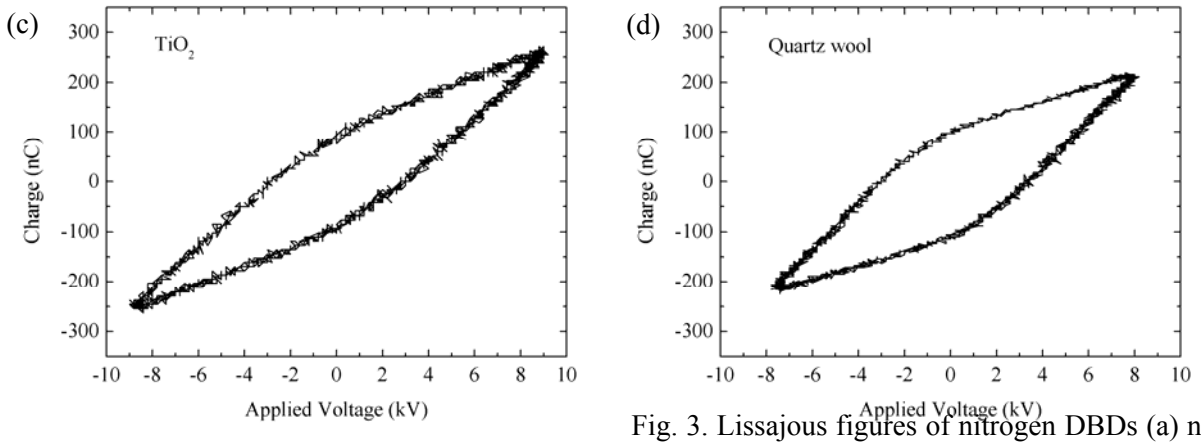


Fig. 3. Lissajous figures of nitrogen DBDs (a) no packing; (b) zeolite 4A; (c) TiO_2; (d) quartz wool (N_2flow rate=0.1 L/min, discharge power=70 W)

3.2 Spectroscopic diagnostics

The spectroscopic technique is performed to measure the emission spectra of the nitrogen discharges under different operating conditions. The spectra are clearly dominated by intensive molecular band N_2 ($C^3\Pi_u \rightarrow B^3\Pi_g$) second positive system ($\Delta v = -3, -2, -1, 0, 1$) within the range of 300 - 450 nm. The (0, 1) molecular band of second positive system at 357.69 nm is chosen to determine the rotational and vibrational temperatures of the discharge by fitting with the simulated spectra. The intensity of the N_2^+ ($B^2\Sigma_u^+ \rightarrow X^2\Sigma_g^+$) first negative system at 391.4 nm is very weak. Compared with the nitrogen discharge without packing material, the intensity of the N_2bands in the discharge is much weaker in the presence of the catalysts, especially for the photocatalyst TiO_2. It suggests that these wavelengths in the UV range are probably absorbed by the catalysts. In addition, weak filamentary discharges resulting from the transition of discharge mode in the presence of the catalysts may also leads to the decrease of the intensity of molecular bands.

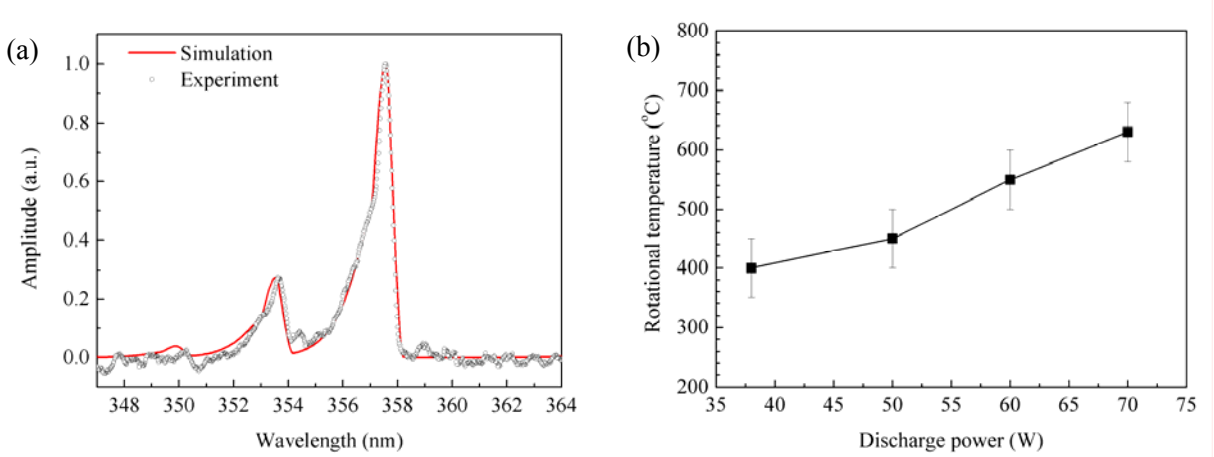


Fig. 4. (a) Comparison between the simulated N_2 molecular band and experimental one (N_2 flow rate=0.1 L/min, discharge power=70 W); (b) Effect of discharge power on the rotational temperature of the nitrogen DBD with no catalyst (N_2 flow rate=0.1 L/min, $U_{pk\text{-}pk}$=15.8 kV)

Fig. 4 (a) shows a comparison between the experimental molecular band N_2 and simulated one. It can be seen that both spectra fit very well with each other. Thus the rotational and vibrational temperatures in the nitrogen DBD with no catalyst are found to be 630 and 3100 ^oC, respectively. The difference between the vibrational and rotational temperatures indicates a significant level of non-equilibrium state in the nitrogen DBD. It can be seen that the rotational temperature of the nitrogen DBD with no catalyst increases with the rising in discharge power from 38 W to 70 W, as presented in Fig. 4 (b). In addition, we found that the presence of the catalysts in the gas gap greatly increases the vibrational temperature of the discharge from 3100 ^oC to 3900 ^oC (for zeolite 4A) and 5000 ^oC (for TiO_2). In

contrast, the catalyst pellets packed in the plasma has weak effect on the rotational temperature of the nitrogen discharge.

4. Conclusion

In this paper, the effect of different packing materials on the characteristics of the nitrogen discharges has been investigated by means of electrical and spectroscopic diagnostics. Introducing the catalysts into the gas gap leads to a transition of the discharge mode, as shown by the lowering of both the amplitude and number of the current pulses. The N_2 DBD with no catalyst can be characterized as a typical filamentary discharge, while the discharge packed with the catalyst pellets is a combination of surface discharge on the surface of the catalyst pellets and weak microdischarge generated in the void space between the pellets and the quartz. The catalysts packed into the nitrogen DBD greatly decrease the gas breakdown voltage due to a significant enhancement of the local electric field and increase charge deposition on the catalyst surface. In addition, the results show that the presence of the catalyst pellets in the N_2 discharge greatly increases the vibrational temperature of N_2 and has only a weak effect on the rotational temperature.

Acknowledgements. Support of this work by SUPERGEN XIV – Delivery of Sustainable Hydrogen and the UK Engineering and Physical Sciences Research Council (EPSRC) is gratefully acknowledged.

5. References

[1] Wagner H E, Brandenburg R, Kozlov K V, Sonnenfeld A, Michel P and Behnke J F 2003 *Vacuum* **71** 417.
[2] Harling A M, Glover D J, Whitehead J C and Zhang K 2008 *Environ. Sci. Technol.* **42** 4546.
[3] Paulussen S, Verheyde B, Tu X, De Bie C, Marten T, Petrovic D, Bogaerts A and Sels B 2010 *Plasma Sources Sci. Technol.* **19** 034015.
[4] Moreau M, Orange N and Feuilloley M G 2008 *Biotechnol. Adv.* **26** 610.
[5] Wallis A E, Whitehead J C and Zhang K 2007 *Appl. Catal. B: Environ.* **74** 111.
[6] Whitehead J C 2010 *Pure & Appl. Chem.* **82** 1329.
[7] Zhang K, Eliasson B and Kogelschatz U 2001 *Energy & Fuels* **15** 395.
[8] Zhang K, Eliasson B and Kogelschatz U 2002 *Ind. Eng. Chem. Res.* **41** 1462.
[9] Zou J J, Zhang Y P and Liu C J 2006 *Langmuir* **22** 11388.
[10] Gallon H J, Tu X, Twigg M V and Whitehead J C 2010 *12th Int. Symp. on High Pressure Low Temperature Plasma Chemistry (Hakone XII)*, *Kupel'na Dvorana, Slovakia*.
[11] Guaitella O, Thevenet F, Guillard C and Rousseau A 2006 *J. Phys. D: Appl. Phys.* **39** 2964.
[12] Kim H H, Kim J H and Ogata A 2009 *J. Phys. D: Appl. Phys.* **42** 135210.
[13] Manley T C 1943 *Trans. Electrochem. Soc.* **84** 83.
[14] Falkenstein Z and Coogan J J 1997 *J. Phys. D: Appl. Phys.* **30** 817.

TIME AND SPACE RESOLVED NH AND NH_2 DENSITIES IN AN RF MICROPLASMA

Martin Visser[1], Andreas Schenk[1], Karl-Heinz Gericke[1]

[1]*Institut für Physikalische und Theoretische Chemie, Technische Universität Braunschweig, Hans-Sommer-Str. 10, D-38106 Braunschweig*

E-mail: k.gericke@tu-bs.de

In order to understand common processes for surface modification, it is crucial to know the concentration and spatial distribution of the most prominent intermediates. In case of the amination of various polymers the most important species are assumed to be the NH and NH_2 radical. In our setup a micro-structured electrode (MSE) is used to generate a RF-driven glow discharge in different mixtures of argon N_2, H_2 and ammonia at pressures between 10 and 100 mbar. Two well-established spectroscopic techniques are employed to obtain the absolute concentration as well as the spatial distribution of the radicals. The spatial distribution can be determined using a PLIF setup where a lasersheet is introduced to the plasma area. An intensified CCD-camera is used as a position sensitive detector. Time resolution is limited by the laser pulse width, which is between 3-5 ns. To minimize the influence of the plasma emission a 5 ns gate is used for the image intensifier and band pass filters are mounted in front of the lens. This approach provides access to relative radical densities. A second method is needed to measure absolute quantities. Absolute concentrations were obtained with a CRDS setup without any means of calibration. The setup consists of two dielectric mirrors forming an optical resonator and a photo multiplier tube for detection. Thorough grounding is necessary to prevent electromagnetic pickup of the plasma frequency. CRDS delivers the average concentration in the line of sight. This data can be used to calibrate the LIF image. A Nd-YAG pumped dye laser system is used for excitation of NH radicals which are detected at 336 nm ($A\ ^3P \leftarrow X\ ^3S^-$, v(0,0)) whereas an excimer pumped dye laser is used to measure the ($\tilde{A}^2A_1 \leftarrow X^2B_1$) transition of NH_2 around 598 nm.

1. Introduction

A field of particular interest in plasma research is the treatment and modification of surfaces [1,2], this, of course, is also the case in the field of microplasmas.

In this work we present some results of the study on a micro structured electrode (MSE) [3] RF powered plasma used for the generation of NH and NH_2 radicals, which are believed to play an important role in forming nitrogen containing functional groups (amino and nitrile) in the surface modification of hydrocarbon polymers. For applications, the spatial density distribution of the species in question may be of great importance. In our approach we use a combination of two spectroscopic techniques. The PLIF technique allows the temporal and spatial mapping of relative number densities. The second method used is CRDS, a sensitive absorption method providing absolute density measurement.

2. Experimental

The details of the LIF or PLIF technique [4,5] and of CRDS [6] can be found elsewhere, so only a brief introduction and a description of the setup will be given here.

Cavity Ring-Down Spectroscopy

Cavity ring-down spectroscopy is an absorption technique using a high finesse optical cavity usually made out of two highly reflective concave mirrors facing each other. Laser light is trapped between the two by irradiating the back of one of the mirrors, the “entrance mirror”, which allows a small fraction of the laser light to enter the cavity. The light then travels back and forth in the cavity after the laser is switched off, gradually losing intensity either by passing through the mirrors or by any other loss mechanisms, one being absorption. The change in intensity in the cavity can be monitored by a detector behind the “exit mirror”, as the intensity leaving the cavity is directly proportional to the

intensity inside. It can be shown [7] that this change in intensity follows an exponential decay, and that its time constant is a direct measure of the losses of the cavity, intrinsic and introduced:

$$I_t = I_0 \cdot e^{-\left(\frac{1}{\tau}+\alpha c\right)t} = I_0 \cdot e^{-\frac{t}{\tau'}} \qquad (1)$$

In which I_t is the intensity of the light leaving the cavity at time t, I_0 is the initial intensity, τ is the time constant of the undisturbed cavity, α is the product of density N and absorption crosssection $\sigma(\lambda)$ of any species that might be present in the cavity, c is the speed of light and finally τ' represents the time constant which is actually measured and which equals the time constant of the undisturbed cavity in the case of zero absorption, neglecting losses other than absorption in this case.
Absorption may then be calculated using the slightly altered equation (1)

$$\frac{1}{\tau} + \sigma(\lambda)Nc = \frac{1}{\tau'} \qquad (2)$$

Furthermore, as the time constant and not the intensity is the value of interest, the method is intrinsically calibration free and partly immune to intensity fluctuations.

Planar Laser Induced Fluorescence
The difference of PLIF compared to common LIF is its added planar resolution which is introduced by using a laser sheet for excitation and detecting the light with 2D resolution rather than gathering all emitted light onto a single detector.

In our experiments, the transition $A^3\Box(v=0)\leftrightarrow X^3\Box^-(v=0)$ [8,9] of the NH-radical around 335 nm is used for both absorption and fluorescence measurements. For NH_2, the Ã2A1 ← X2B1 transition around 598 nm is used for the same purposes.

Experimental Procedure

In Figure 1 a scheme of our experimental setup is shown.
The MSE is mounted on a water-cooled heat sink which can be shifted vertically by a translation stage. This system is placed in a cylindrical vacuum chamber (25x40 cm) with flanges to admit power, cooling water and gas supply to the chamber through mass flow (MKS and Bronkhorst) and pressure controllers (MKS) as well as optical access from the sides and a window insert in the lid to get a close top view with an ICCD camera (LaVision FlameStar II).
The MSE has a comb like structure, as outlined in Figure 1, and a total active area of 1x0.8 cm, details may be found in reference [4], it is driven by a 13.56 MHz radio frequency (RF) generator and associated impedance matchwork (ENI AGC 3b) through which 30 W of RF power are fed to the reactor, the back of the electrode is kept at 20°C by the heat sink and thermal compound.

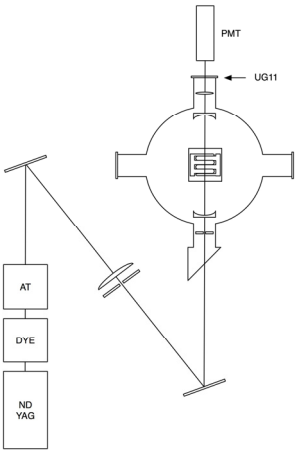


Fig. 1. Top-view scheme of the experimental setup. Only the cylindrical lens outside the chamber together with the aperture inside the chamber are fitted for PLIF; the cavity mirrors, PMT, exit lens and the aperture outside the chamber only for CRDS. Supply lines and the camera (situated directly above the chamber, looking down) are left out for brevity.

For the production of NH, the plasma was ignited in an N_2/H_2 (50%/50%) atmosphere with a constant feed of fresh gas (20 sccm of each component). The total pressure was kept constant at 20 mbar *via* a pressure control valve connected to a rotary vane pump.
First measurements on NH_2 were performed under different conditions, the gas mixture consisting of NH_3/Ar (20%/80%) (20/80 sccm feed) at 60 mbar.

Two different laser systems are used for the two radicals, as two different wavelength ranges are required for NH and NH_2, but the respective lasers can then be used for both PLIF and CRDS measurements. For NH, the components are a pulsed dye laser (Radiant Dyes DL-midi, DCM in dimethylsulfoxide) tunable from 675 to 650 nm pumped by an Nd:YAG laser (Continuum Surelite, 10 Hz) at 532 nm. Frequency doubling is performed by a BBO crystal mounted inside an Inrad autotracker (AT) providing pulse energies around 100 μJ at 333 nm and pulses of 5 ns duration.
For NH_2, a Lamda Physik LPD3000 dye laser with Rhodamine 6G as dye running around 580 nm pumped by a Lambda Physik LPX Excimer laser is used, providing pulses of 10 ns duration and 2 mJ of pulse energy.

For PLIF measurements the laser beam is passed through a cylindrical lens (f=1000 mm) and steered through the measuring chamber with the focused, flattened beam situated just above and parallel to the MSE exciting a broad area (in the x-y plane). Spatial resolution in z direction is made possible by the translation stage as the distance can be adjusted in 10 μm steps. Detection of the fluorescence light is achieved by an ICCD camera equipped with a 50 mm f/1 lens. For measuring NH, a 3 mm Schott type UG11 band pass filter to block visible and deep UV radiation emitted by the plasma itself. For measuring NH_2, an interference bandpass filter (Omega Optical) is used, exhibiting ~90% transmission from 585 to 635 nm. In this configuration the camera has a field of view of approximately 7.5x5 mm (576x384 pixels).
Some straightforward considerations need to be mentioned with respect to the timing of the laser/camera system in relation to the plasma. As the driving frequency of the plasma results in a period of 73.7 ns and the camera is operated at a shutter time of 5 ns, the laser/camera system needs to be synchronized to the RF voltage as the plasma may change its state corresponding to the phase of the voltage. In our setup, the RF voltage is probed by a digital storage oscilloscope (LeCroy WRXi 640). The oscilloscope then issues a trigger pulse at the appropriate repetition rate which is locked to the RF, this pulse in turn triggers the laser/camera through a DG 535 delay generator. Changing the timing of the camera and the laser with respect to the synchronization pulse therefore permits resolving the temporal behavior of the plasma in addition to the spatial resolution.
The images taken during an experiment are then processed by a home made computer program allowing integration of selected areas of each image which may then be plotted versus RF phase, laser wavelength or any spatial position, so full 4D resolution is achieved.

Cavity Ring-Down measurements were performed with the appropriate laser system and mirrors for each species.
NH measurements were made with a linear cavity formed by two plano-concave mirrors (R=200 mm, Layertec) with a centre wavelength of 330 nm. The cavity length is 22 cm and the ring-down time of the empty system has been measured in the range of interest and is around 850 ns. Inside the cavity two 1 mm apertures were placed close to the mirrors to enhance spatial resolution. Behind the exit mirror of the cavity a lens is placed focusing the exiting light through a UG 11 band pass Filter (see above) onto the detector.
To perform measurements of NH_2, the cavity mirrors used had a centre wavelength of 640 nm (R=6 m, Los Gatos Research) and were placed 19 cm apart, resulting in a ring-down time around 700 ns in the range of interest. Apertures and a filter were not used in this case.
For detection, in both cases a photomultiplier tube (PMT) type R1617 (Hamamatsu) was used which was directly connected to the oscilloscope for data acquisition and processing.
The MSE is situated in the middle of the cavity and lifted up as close to the optical path as possible without disturbing the ring-down trace *via* the translation stage.

3. Results and Conclusion

Figure 2 shows spectra of NH and a part of the spectrum of NH_2 recorded using PLIF and CRDS under the conditions mentioned above. In both cases the measurement was conducted

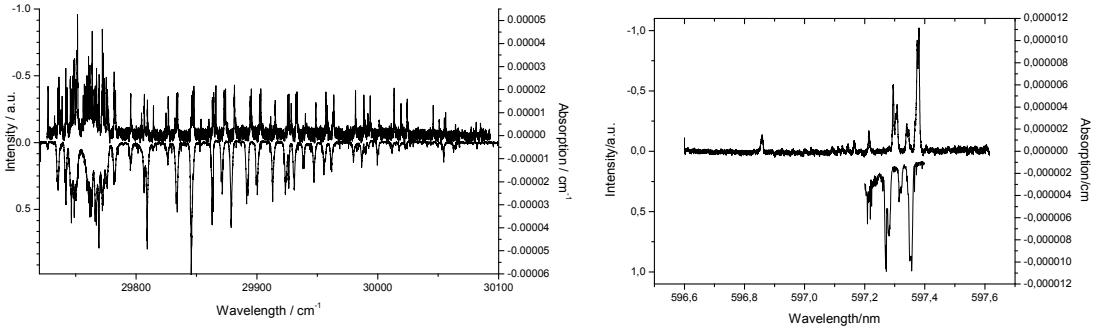


Fig. 2. left: Part of the NH spectrum recorded in the $A^3\Pi(v=0)\leftrightarrow X^3\Pi$-(v=0) band. right: Part of the NH_2 spectrum recorded around 597 nm. Each has top: CRD spectrum, scale on the right. bottom, inverted: PLIF spectrum, scale on left

as close as possible to the MSE surface without disturbing the ring-down, i.e. ~0.6 mm from MSE surface to the beam centre while measuring NH and at most 3 mm while measuring NH_2. The PLIF spectra were recorded in portions and then stitched together, no correction was made for variations in laser intensity which accounts for differences comparing PLIF and CRDS data. The spectra compare well with data by Brazier, Lents [7,8] and Ross et al.[9] confirming the presence of NH and NH_2.
An estimate of the absolute density of NH radicals is difficult due to the complicated determination of the absorption cross section, but was made according to the procedure of van den Oever et al. [11] resulting in a number density of 5.1×10^{12} cm^{-3} at a rotational temperature of around 820 K. For NH_2 these calculations still need to be done.

The dimensions of the NH containing area and height of the plasma including absorption length can be determined from a camera image and measurements at different distances over the MSE such as Figure 3a. Two original camera images are shown. The right image shows

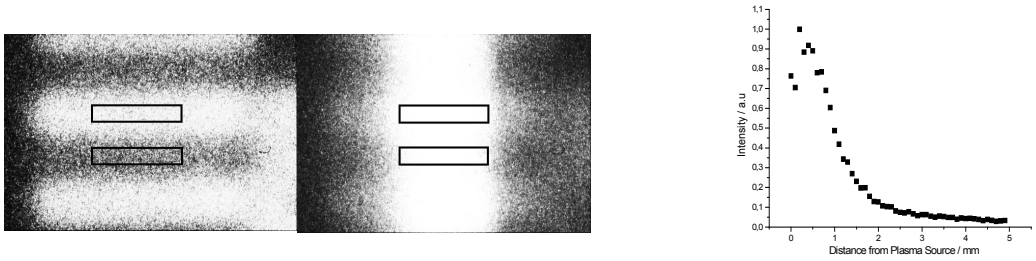


Fig. 3. a) Camera images, left: image of plasma glow, right: plasma glow and NH fluorescence. The rectangles mark the observation areas for each of the two electrode sets. b) Vertical change in fluorescence

the induced fluorescence together with the plasma running, the left one shows the plasma alone. One of the two comb-like sets of electrodes of the MSE can be recognized in this image by its glow. The vertical stripes therefore have a breadth of 1.6 and 0.8 mm and may be used as a measure. As the intensity drops sharply at the edges of the MSE the absorption path length used for the CRDS measurement is estimated to be the same as the width of the MSE, i.e. 8 mm.
In height, the NH containing volume of the plasma can be estimated from Figure 3b. The plot shows the NH fluorescence intensity with the laser passing at different heights above the plasma. The ordinate specifies the traveled distance of the translation stage moving the MSE away from the laser beam. At minimum distance the beam still hits the edge of the MSE, so the fluorescence maximum is observed at a traveled distance of 0.6 mm. It may be assumed, that at this setting the beam is passing

over the MSE at its full vertical diameter of 1 mm. After this, the plot exhibits a fast drop of intensity showing the very small volume of the NH production.

4. Conclusion

It has been shown that using an MSE an NH and an NH_2 producing plasma is obtained at reduced pressures and the distribution of NH in the discharge area can be monitored with spatial resolution applying the PLIF method. Cavity ring-down spectroscopy which is used for calibration of the fluorescence data is applicable under the conditions given and can be used to measure both NH and NH_2 number densities. The rotational temperature of the NH radicals was estimated at 820 K. Using the approach of Luque et al. [5] the absolute values of NH concentration are to be used to calibrate the PLIF data. Estimates of the NH_2 number density are to be done.

5. References

[1] U. Kogelschatz, *Contrib. Plasma Phys*., **47**(**1**-**2**), 2007, 80.
[2] J. Meichsner, *Low Temperature Plasmas (2nd Edition)* **2**, 2008, 739-756, Wiley-VCH Weinheim Germany
[3] L. Baars-Hibbe, P. Sichler, C. Schrader, C. Geßner, K.-H. Gericke, S. Büttgenbach, *Surf. Coat. Technol.,* **174**, 2003, 503.
[4] I. van Cruyningen, A. Lozano, R. K. Hanson, *Exp. Fluids*, **10**, 1990, 41.
[5] J. Luque, J.B. Jeffries, G.P. Smith, D.R. Crosley, *Appl. Phys. B*, **73**, 1990, 731.
[6] A. OKeefe, D.A.G. Deacon, *Rev. Sci. Instrum*., **59**, 1998, 2544.
[7] C. R. Brazier, R.S.Ram, P.F.Bernath, *J. Mol. Spectr*., **120**, 1986, 381.
[8] J. M. Lents, *J. Quant. Spectr. Rad. Trans.,* **13**, 1973, 297.
[9] S.C. Ross, F.W. Birss, *J. Mol. Spectrosc*., **129**, 198, 436
[10] P. J. van den Oever, J. H. van Helden, C. C. H. Lamers, R. Engeln, D. C. Schram, M. C. M. van de Sanden, W. M. M. Kessels, *J. Appl. Phys*., **98**, 2005, 093301.

THE INFLUENCE OF DIFFERENT ELECTRODE CONFIGURATIONS ON BARRIER DISCHARGES IN ARGON AND HELIUM AT ATMOSPHERIC PRESSURE

Robert Wild, Marc Bogaczyk, and Hans-Erich Wagner

Institute of Physics, Ernst-Moritz-Arndt University Greifswald, Germany
E-mail: wild@physik.uni-greifswald.de

The temporal and spatial development of a dielectric barrier discharge depends among other parameters on the geometry and dielectric properties of the electrodes. The capacitance of the set-up is influenced by the dielectric constants of the used materials. For that reason, the development of barrier discharges at atmospheric pressure was comparatively investigated for different electrode configurations.
The presented measurements were done by electrical diagnostics (e.g. Lissajous figures) as well as optical emission spectroscopy and particularly regarding the temporal and spatial development of the discharge with the technique of cross-correlation spectroscopy (CCS).

1. Introduction

Barrier discharges (BD) are generated in an electrode configuration with at least one dielectric covered electrode. This dielectric acts as current limiter and prevents the formation of an arc discharge. That is due to an accumulation of charged particles in close proximity of the dielectric barrier that induce an electric field counteracting the field of the applied voltage. The same charges promote the formation of microdischarges in the following half period of the voltage signal [1].
BDs are greatly influenced by elementary processes in the discharge volume as well as by their interaction with the electrode surfaces [2]. Measuring techniques such as Lissajous figures and cross-correlation spectroscopy allow to describe some aspects of the discharge behavior (i.e. by power measurements and spectrally resolved emission profiles). Using these diagnostics and successively changing the electrode setup by modifying its geometry and dielectric materials will lead to conclusions about the interaction between discharge and dielectric surfaces.

2. Experimental setup

The experimental set-up is composed of two dielectric covered electrodes, which are made up of different geometries and materials (Fig.2). They are situated inside a gas recipient, which is evacuated by a PFEIFFER VAKUUM turbo molecular pump before each experiment. It is possible to run the discharge with a maximum constant gas flow of 1 slm as well as in a system without gas flow. A sinusoidal voltage is generated by a STANFORD function generator and then amplified up to 10 kV_{pp} by a TREK high voltage amplifier. For all presented results the voltage frequency was about 5 kHz. Electrical signals were displayed by a TEKTRONICS oscilloscope. The applied voltage was observed by a TEKTRONICS 1000:1 high voltage probe, the discharge current and transferred charge were measured using a resistor R = 100 Ω and a capacity C = 1 nF, respectively. (Fig.1b) It was therefore possible to measure the discharge power by the encapsulated area of the Lissajous figure Q(U) using formula (1).

$$P = f \cdot \oint Q \, dU \equiv f \cdot \text{AREA OF LISSAJOUS FIGURE} \tag{1}$$

Optical measurements included emission spectroscopy as well as cross-correlation spectroscopy, a single-photon counting technique (Fig. 1a). The main idea here is to convolute two signals, firstly a time-dependent light pulse intensity f(t'), which is emitted from the microdischarge as MAIN-Signal,

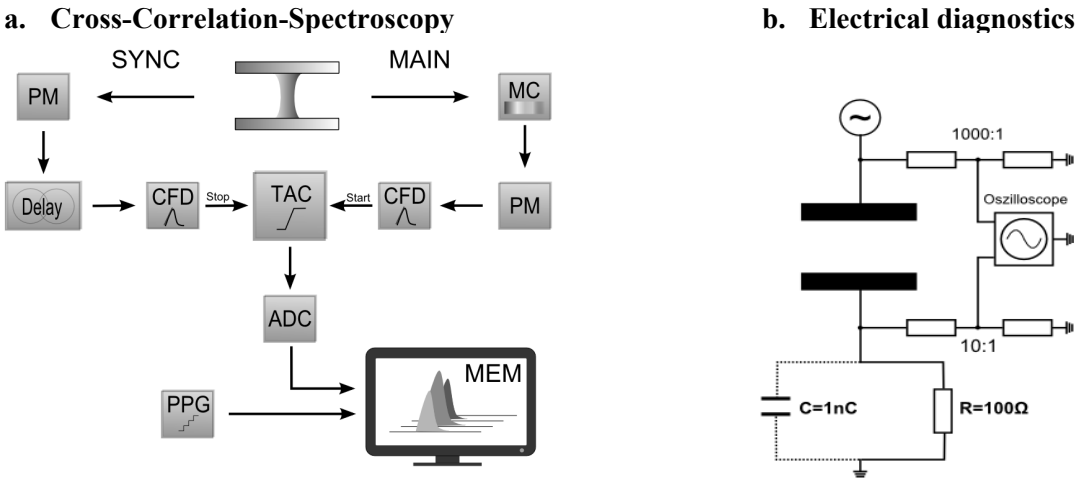


Fig. 1. a. Cross-correlation spectroscopy (CCS) set-up. PM – Photomultiplier, MC – Monochromator, Delay – Delaygenerator, CFD – Constant Fraction Discriminator, TAC – Time-to-Amplitude Converter, ADC – Analog-Digital Converter, PPG – Pattern Generator, MEM – Memory
b. Electrical measurements using a resistor R and a capacity C.

and secondly a delta distribution of the same emission source δ(t'-t). This delta distribution is emitted as SYNC-Signal and defines a relative time scale.

$$f(t) = \int f(t')\delta(t'-t)dt' = I(t) \tag{2}$$

The result would be a temporally resolved intensity distribution that corresponds to the actual emission evolution of the microdischarge. It is issued by an analog-to-digital converter (ADC) as a time-intensity histogram. By means of a square-pulse generator (PPG) it is possible to observe different phase positions of the applied voltage, so that e.g. the intensity distributions in both half-waves of a period can be measured.
In order to resolve the discharge emission intensity spatially, the MAIN-Signal detector can be moved in a way that various axial positions of the cell volume can be observed. A spectral resolution is achieved by a Yobin Ivon TRIAX-320 monochromator (MC).
In order to observe the discharge behavior in certain geometric and electrostatic conditions, three electrode configurations were applied. (Fig. 2) The rod-rod configuration (RR) consists of two steel rods, covered with a semispherical Al_2O_3 ceramic (ε_r = 9). The cylindrical-cylindrical (CC) configuration is composed of the same steel rods, but covered with cylindrical shaped MACOR dielectrics (ε_r = 6). The third configuration (CR) is a hybrid of the previous arrangements, with a cylindrical MACOR electrode on top of a semispherical ceramic rod electrode.

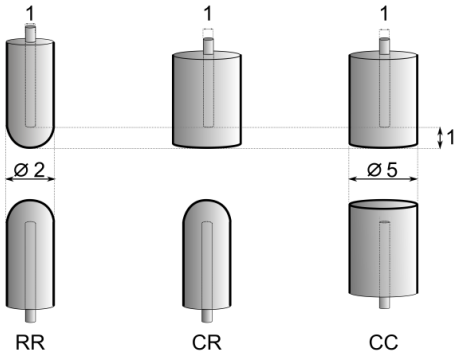


Fig. 2. Schematics of used electrode configurations. Length units in mm and not true to scale.

3. Results and discussion

3.1. Electrical discharge behavior

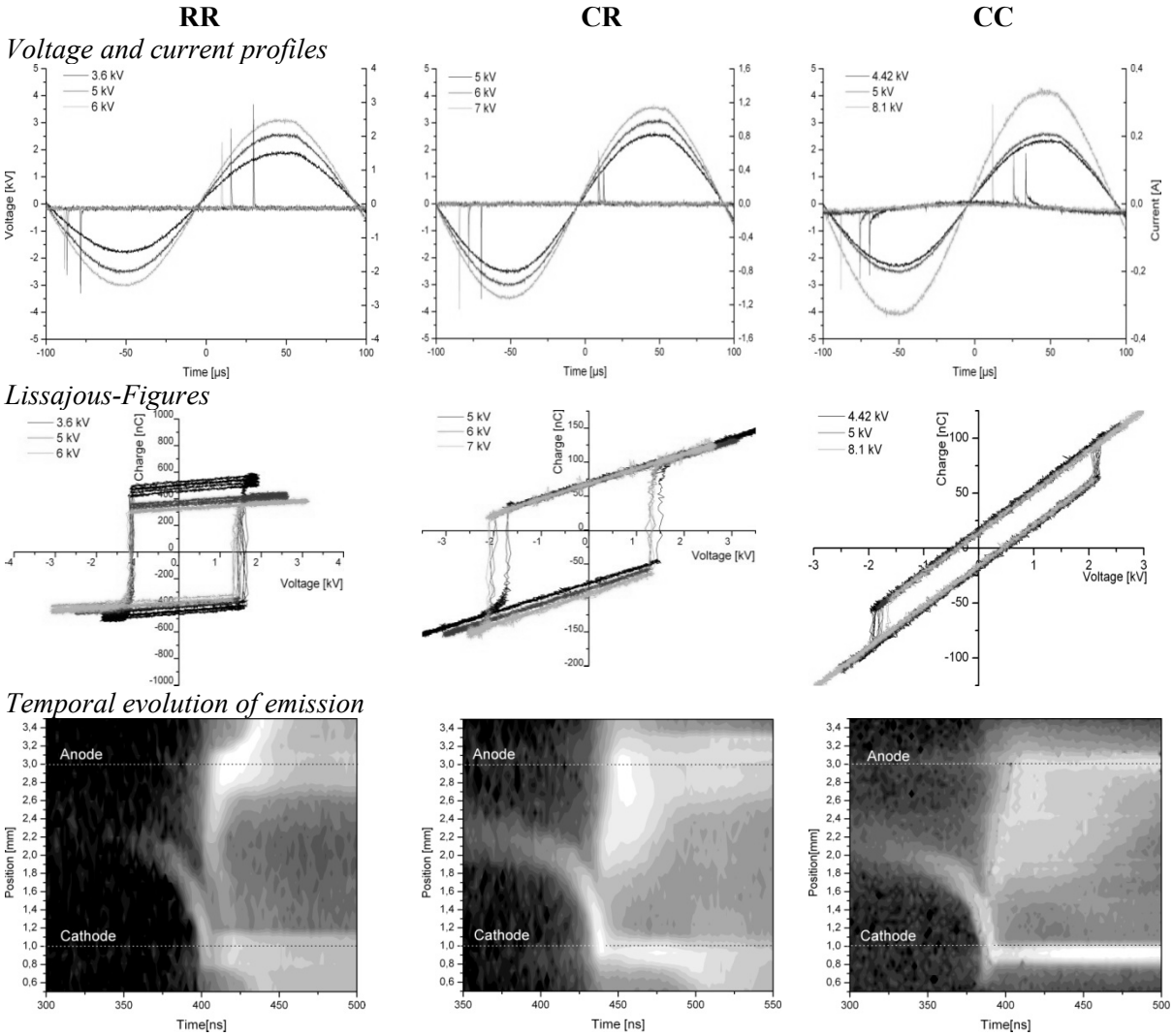


Fig. 3. Discharge comparison of three electrode arrangements with regard to a. Voltage and current profiles, **b.** Power measurements by means of Lissajous-Figures Q(U) and **c.** Temporal emission evolution of Argon 750.4 nm line by CCS. Experimental conditions at gas flow rate F = 100 sccm, electrode distance g = 2 mm, applied voltage U = 5.5 kV.

In Fig. 3 discharge characteristics of an argon mircodischarge are compared with regard to the three electrode configurations. The applied voltage was in a single discharge per half wave domain for all measurements. While the discharge power level rises with increasing voltage in helium, argon discharges show, however, an opposite behavior. The most power to maintain the discharge is required at burning voltage $U_B = U_{min}$ with a decreasing tendency to higher amplitudes (Fig. 4). The corresponding Lissajous figures (Fig. 3b) indicate that the charge transfer is reduced at higher voltages. Comparing them with the voltage und current profiles, one finds that the discharge current peaks last longer at lower amplitudes. That way, the charges, resulting from the time integrated current pulse, exceed at lower voltage amplitudes the charges at higher amplitudes.

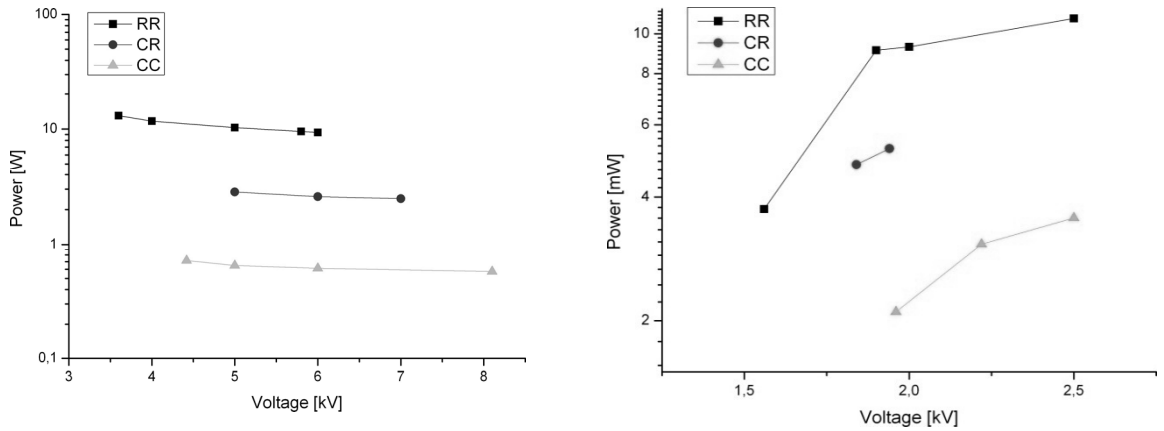


Fig. 4. Power dependence of applied voltage in various electrode configurations. Working gases are argon (left plot) and helium (right plot), electrode distance g = 2 mm.

It is also significant that the discharge power decreases towards a more planar form of the dielectric, such that the RR configuration consumes the most power during one discharge period, while CC consumes the least. This behavior is observed in argon as well as in helium (Fig. 4). One approach to explain this behavior is to establish a connection to the effective capacity C_b of the system. This particular capacity, which depends on material and geometry, can be obtained by a slope measurement in the Lissajous figure. Fig. 5 displays the power dependence of the capacity in a doubly logarithmic scale. The regression line of the argon data has in the given scale a slope of one, thus suggesting a direct proportional link between those quantities. However, the slope of the helium regression features just a value of 0.5. Hence, it is obviously not possible to fully ascribe the observed behavior to the capacity. It is rather likely, that the different forms of the configurations allow a substantial change of the gas flow conditions, by which the discharge is considerably influenced.

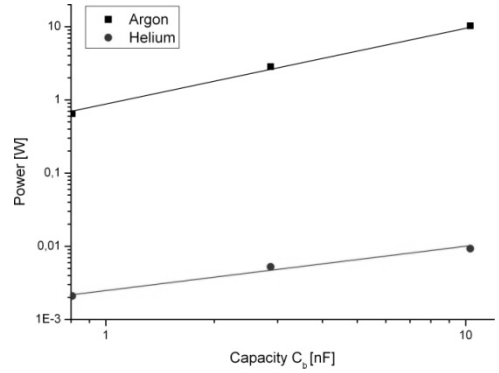


Fig. 5. Relation between power consumption and an allocated effective capacity.

Configuration	Capacity C_b [nF]
RR	10,3
CR	2,9
CC	0,8

Tab.1. Capacities C_b of dielectric barriers, obtained from slope in Lissajous figures of argon, g=2mm

.

3.2. Investigation of discharge emission

Fig. 6 shows an overview spectrum of an argon discharge under the used conditions. It displays a manifold of lines that have their origin in the decay of argon $2p_i$ to argon $1s_j$ states (Paschen notation). $2p_i$ states, that have a total angle momentum of zero J = 0, usually have a small cross section for electron impact transition from metastable $1s_j$ states. It is then convenient to say that those states are mainly populated by electron impact transitions from the argon ground state [3]. Using CCS, we were able to resolve the argon 750.4 nm line temporally and spatially for the three used electrode configurations (Fig. 3c). This particular line is caused by the electronic transition from the $2p_1$ (J = 0) state to the $1s_2$ (J = 1) state.

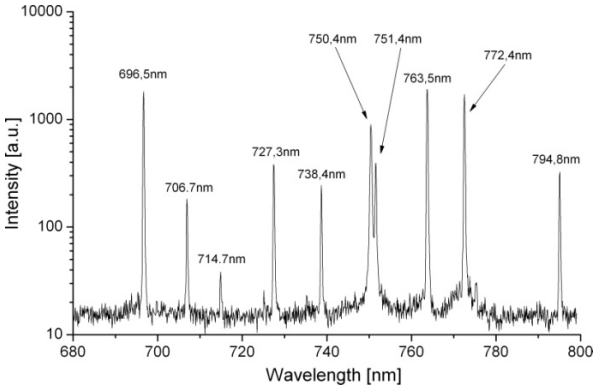


Fig. 6. Selected range of argon overview spectrum at atmospheric pressure.

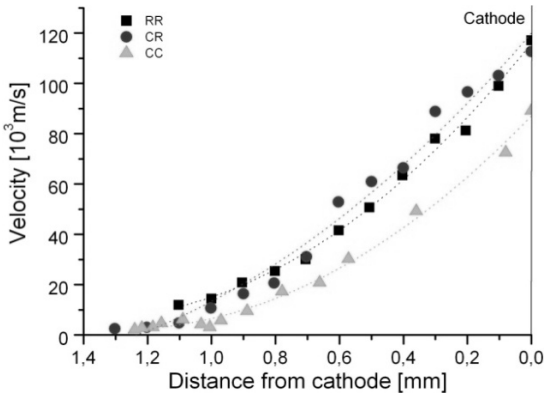


Fig. 7. Streamer velocities with regard to distance from cathode

The results from the CCS show a very distinctive cathode directed streamer in the breakdown phase of the discharges. Retrieving information about the streamer velocity is possible by a geometric approach, namely by measuring the slope $v = dx/dt$.
Apparently, the streamer in the CC configuration is slightly slower than in the other two arrangements (Fig. 7). This may be connected to smaller power consumption in that configuration, as observed earlier. This explanation is, however, inconsistent when comparing the RR and CR configurations.
One also notices that the intensity maximum shifts from the anode to the cathode when comparing the RR with the CC configuration. It is connected with an elevation of the effective lifetime of excited argon species in the anode glow. The mean lifetime of the $2p_1$ argon state is $\tau = 22$ ns [5], from which one can conclude by consulting Fig. 3c that in more planar configurations this particular state is longer excited during the anode glow. That may be due to a reduced electron production because of the already observed reduced power coupling into the plasma. This would result in an elevated reduced field strength E/n_e at the cathode and a reduced electron density n_e at the anode. The current limiting effect of the surface charges would therefore occur delayed.

4. Conclusion

Measurements with different electrode configurations have been made. The dissipated power seems to be reduced in planar forms of electrode configurations. The Lissajous figures also indicate a small gap capacitance C_g for high barrier capacities $C_{b,}$ In such configurations the dielectric loss is the least. [4]
It has also been investigated that the discharge processes such as the cathode directed streamer and the anode glow are slower than in the other configurations. The reason is yet unclear.
Future experiments will involve a planar BSO (bismuth silicon oxide) dielectric, which features a relatively high dielectric constant of 56. Main goal of this project will be a direct correlation between intensity development observed by CCS and deposited surface charges, whose detection is accessible by the optoelectric properties of the BSO crystal.

Acknowledgement. This work was supported by “Deutsche Forschungsgemeinschaft, SFB TR 24, ‘Complex Plasmas’ ”. The authors also wish to thank P. Druckrey and U. Meißner for their technical support.

5. References

[1] F. Massines, N.Gherardi, N. Naudé, P. Ségur, 2008, *Contr.Papers Vol.1* HAKONE XI, France, 25
[2] U. Kogelschatz 2002 *Plasma Chemistry and Plasma Processing.* Vol 23, No 1, 1.
[3] X.-M. Zhu and Y.-K. Pu 2008 *Plasma Sources Sci. Technol.* **17** 024002.
[4] K. Takaki, M. Shimizu, S. Mukaigawa, T. Fujiwara 2004 *IEEE Trans Plasma Sci. 32*.
[5] NIST 2010 Atomic Spectra Database *http://www.nist.gov/physlab/data/asd.cfm*

Topic 3
Molecular synthesis and decomposition

PLASMA REDUCTION OF A NiO/Al_2O_3 CATALYST FOR DRY REFORMING OF CH_4

Helen J. Gallon[1], Xin Tu[1], Martyn V. Twigg[2], J. Christopher Whitehead[1]

[1]*School of Chemistry, The University of Manchester, Oxford Road, Manchester, M13 9PL,UK.*

[2]*Johnson Matthey Plc.Orchard Road, Royston, SG8 5HE, UK.*

E-mail: Christopher.Whitehead@manchester.ac.uk

The activation of a NiO/Al_2O_3 catalyst has been carried out using a CH_4 plasma in an atmospheric pressure dielectric barrier discharge (DBD) reactor. Conversion of CH_4 and the formation of reaction products have been analysed by micro-GC throughout the reduction process. The catalyst was reduced from NiO to the active Ni form, which showed high selectivity for the conversion of CH_4 into H_2 and solid carbon. Characterisation of the reduced catalyst by XRD and SEM analysis revealed the presence of significant amounts of carbon nanofibres on the catalyst surface. Plasma-catalytic dry reforming of CH_4 has been carried out using the reduced Ni/Al_2O_3 catalyst. The major reaction products were H_2 and CO with selectivities of 45.2 % and 23.4 % respectively. The presence of the catalyst improved the selectivity for H_2 production, in comparison to the reaction with no catalyst, resulting in an increase in the H_2/CO ratio from 0.84 to 2.53.

1. Introduction

NiO/Al_2O_3 catalysts are used commercially in steam methane reforming (SMR) at elevated temperatures and pressures for large-scale production of H_2. Prior to SMR, the catalyst must be reduced to Ni/Al_2O_3, the active phase for catalysing methane conversion. In conventional thermal reduction of the catalyst, high temperatures are necessary in order to dissociate the reducing gas adsorbed on the catalyst surface [1], this requires >350 °C in H_2 or >600 °C in CH_4. Non-thermal plasma offers potential for reduction of catalysts at low temperatures by providing an effective means for breakdown of the reducing gas into 'active' species.

Reduction of $NiO/\gamma\text{-}Al_2O_3$ and NiO/SiO_2 has been reported [2, 3] in a H_2/N_2 atmospheric pressure glow discharge plasma jet and has been shown to improve dispersion and reduce particle size of the metallic Ni, compared with samples reduced thermally. Extensive research into the use of Ar plasma for catalyst reduction has been carried out by Cheng et al. [4] in a low pressure glow discharge plasma, which has been successful in reducing a number of supported metal catalysts including H_2IrCl_6/Al_2O_3 [5], $RhCl_3/Al_2O_3$ [6], $PdCl_2/Al_2O_3$ [7], $PdCl_2$/HZSM-5 [8], H_2PtCl_6/TiO_2 [9], H_2PtCl_6/C [10], $AgNO_3/TiO_2$ [11] and $HAuCl_4/TiO_2$ [11], however, not all catalysts could be reduced by this method; in the case of $Ni(NO_3)_2$, [12, 13] and $Fe(NO_3)_2$ [13] only decomposition was observed. Research on the use of DBD for catalyst reduction has been carried out for oxides of Pt and Co catalysts by Kim et al. using a H_2/N_2 mixture as the plasma forming gas [14].

2. Experimental Section

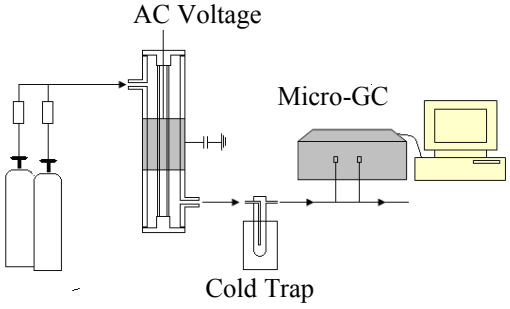


Fig. 1. Experimental Set-Up

Reduction of a 33 % NiO/Al_2O_3 catalyst (Johnson Matthey Plc.) has been carried out in an atmospheric pressure DBD reactor consisting of two coaxial quartz tubes with stainless steel mesh electrodes of 5 cm length and with a discharge gap of 4.5 mm. The catalyst was crushed to give non-uniformly sized particles (18 g) and baked at 350 °C for 3 hours to remove adsorbed H_2O prior to being packed into the discharge region of the reactor, where it was held in place with quartz wool.

CH_4 (99.9 %) was fed into the reactor at a flow rate of 50 ml min^{-1}. A voltage of 21 kV_{pk-pk} was applied at a frequency of 35 kHz. A Picoscope ADC-200 was used to record the waveforms for the high voltage AC sine wave and the voltage across a capacitor. A LabVIEW system was utilised for the measurement of plasma power by the area calculation of Lissajous figures. Gases exiting the reactor were analysed using micro-gas chromatography (Agilent 3000A) with Molsieve 5A and Plot Q columns. A cold trap containing solid CO_2 was placed downstream of the reactor in order to condense liquid products. Calculations for conversions, product selectivities and carbon balances are defined as shown in equations 1 – 4, where the quantities in square brackets are the molar % of the total gas volume.

$$\text{Conversion (reactant)} = \{[\text{reactant}]_{\text{converted}} / [\text{reactant}]_{\text{initial}}\} \times 100\ \% \quad (1)$$

$$\text{Selectivity } (C_n \text{ products}) = \{n[\text{product}] / ([CH_4]_{\text{converted}} + [CO_2]_{\text{converted}})\} \times 100\ \% \quad (2)$$

$$\text{Selectivity } (H_2) = \{[H_2] / (2\,[CH_4]_{\text{converted}})]\} \times 100\ \% \quad (3)$$

$$\text{Carbon Balance} = [CH_4] + [CO_2] + [CO] + 2[C_2] + 3[C_3]\ \% \quad (4)$$

3. Reduction of NiO in CH_4 Plasma

The analyses of gaseous species during the plasma-reduction of NiO are shown in Figures 2 – 4. The conversion of CH_4 increased initially as it was consumed in the reduction of NiO (reactions 5 and 6) and then reached a plateau at ~ 37 % conversion as shown in Figure 2. Reduction products CO_2 and CO peaked at ~ 65 minutes on stream and then decreased after 125 minutes, indicating that the reduction of NiO to Ni had gone to completion (shown by the dashed line). Conversion of CH_4 remained high after complete reduction due to the decomposition of CH_4 catalysed by active Ni sites that were generated during the reduction. Figure 3 shows that the production of H_2 increased during the first 125 minutes as active Ni sites were being generated and then remained steady when reduction was complete. The decrease in carbon balance from 100 % to 64.7 % corresponds to the loss of carbon from the gas stream as a result of solid carbon deposition. The trend for H_2 production and carbon balance clearly mirror each other indicating that CH_4 is being selectively converted into H_2 and carbon and that this reaction (7) is catalysed by active Ni sites.

Reduction of NiO:

$$CH_4 + 4\,NiO \rightarrow CO_2 + 2\,H_2O + 4\,Ni \quad (5)$$

$$CH_4 + NiO \rightarrow 2\,H_2 + CO + Ni \quad (6)$$

CH_4 decomposition catalysed by Ni:

$$CH_4 \rightarrow C + 2\,H_2 \quad (7)$$

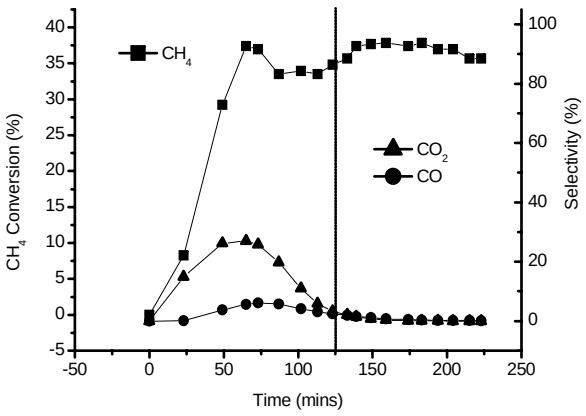


Fig. 2. Conversion of CH_4 and selectivity towards CO_2 and CO during plasma-reduction of NiO/Al_2O_3.

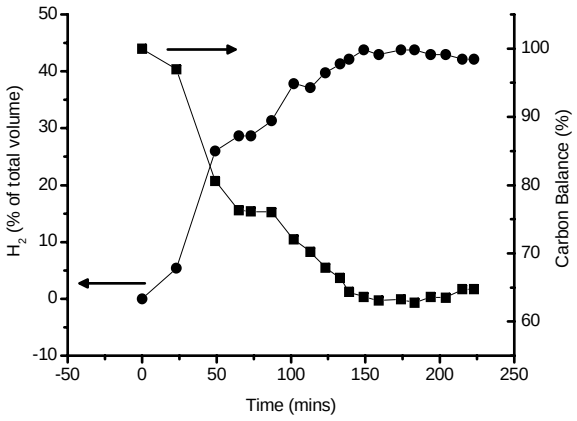


Fig. 3. Formation of H_2 and carbon balance during the plasma-reduction of NiO/Al_2O_3.

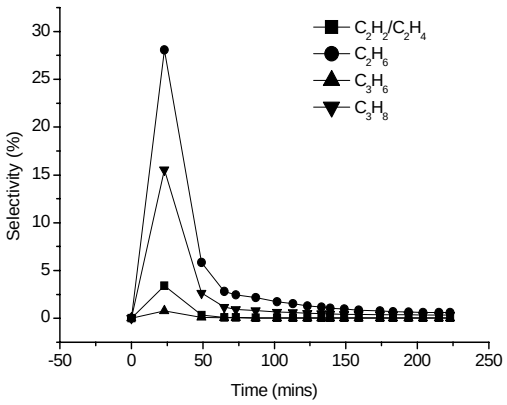


Fig. 4. Higher hydrocarbon selectivities during plasma-reduction of NiO/Al_2O_3.

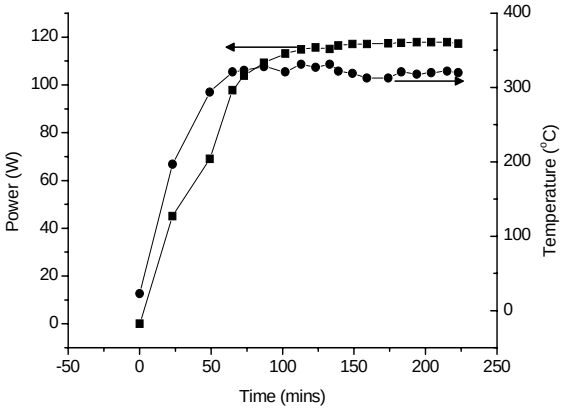


Fig. 5. Power and temperature of outer electrode during plasma-reduction of NiO/Al_2O_3.

The formation of acetylene, ethylene, ethane, propene and propane was observed, as shown in Figure 4. Interestingly, the selectivity of all higher hydrocarbons peaked early in the experiment when the plasma power was low (~ 23 W). Higher hydrocarbons are formed from radical coupling reactions; C_2 hydrocarbons are therefore most likely to be formed, as a second coupling reaction is necessary for C_3 formation. The selectivity of saturated hydrocarbons was higher than that of unsaturated species of the same carbon number. In addition to the observed gaseous products, 0.82 g of liquid was collected in the cold trap, atomic absorption spectroscopy revealed that the sample was almost completely H_2O.

Figure 5 shows the power in the plasma, which increased steadily and then remained constant at ~ 117 W. As the catalyst was reduced to a more conductive form, it is likely that an increased current flow through the catalyst caused the power to increase during the reduction, despite very little variation in the applied voltage (21.0 – 21.9 kV_{pk-pk}). The temperature of the outer electrode was measured using a thermocouple to give an insight into the minimum temperature of the bulk gas. The maximum temperature recorded was 331 °C, which is substantially lower than the temperature required for thermal reduction of the catalyst (>600 °C), suggesting that a mechanism involving non-thermal plasma is responsible for the catalyst reduction and that it is not just a result of dissipated thermal energy allowing a thermal reduction to take place.

The mechanism proposed for catalyst reduction in non-thermal plasma is initiated by the decomposition of adsorbed surface CH_4 (8 – 13) into a highly reactive form of adsorbed carbon, $C_{(ad)}$ that subsequently reduces NiO (14). In addition, reduction of NiO with generated CO (15) and H_2 (16) occur, producing the observed reduction products CO_2 and H_2O respectively. It is possible that a water-gas shift (17) is also established under these conditions.

Decomposition of adsorbed CH_4:	$CH_{4\,(g)} \rightarrow CH_{4\,(ad)}$	(8)
	$CH_{4\,(ad)} \rightarrow CH_{3\,(ad)} + H_{(ad)}$	(9)
	$CH_{3\,(ad)} \rightarrow CH_{2\,(ad)} + H_{(ad)}$	(10)
	$CH_{2\,(ad)} \rightarrow CH_{(ad)} + H_{(ad)}$	(11)
	$CH_{(ad)} \rightarrow C_{(ad)} + H_{(ad)}$	(12)
	$2\,\{H_{(ad)} + H_{(ad)} \rightarrow H_{2\,(g)}\}$	(13)
Reduction of NiO with $C_{(ad)}$:	$C_{(ad)} + NiO_{(s)} \rightarrow CO_{(g)} + Ni_{(s)}$	(14)
Reduction of NiO with CO:	$CO + NiO \rightarrow CO_2 + Ni$	(15)
Reduction of NiO with H_2:	$H_2 + NiO \rightarrow H_2O + Ni$	(16)
Water-gas shift:	$CO + H_2O \leftrightarrow H_2 + CO_2$	(17)

4. Plasma-Catalytic Dry Reforming of CH_4

Plasma-catalytic dry reforming of CH_4 has been carried out with the plasma-reduced Ni/Al_2O_3 catalyst using a mixing ratio of $CH_4/CO_2 = 1$ and a total flow rate of 50 ml min^{-1}. Conversions of both CH_4 and CO_2 increased with increasing plasma power as shown in Figure 6. H_2 and CO were the main reaction products (Figure 7), the selectivities of which increased to 45.2 % and 23.4 % respectively at a plasma power of 97.4 W. Smaller amounts of acetylene, ethylene, ethane and propane were also formed during dry reforming. In contrast, the selectivity of higher hydrocarbon products decreased as plasma power was increased.

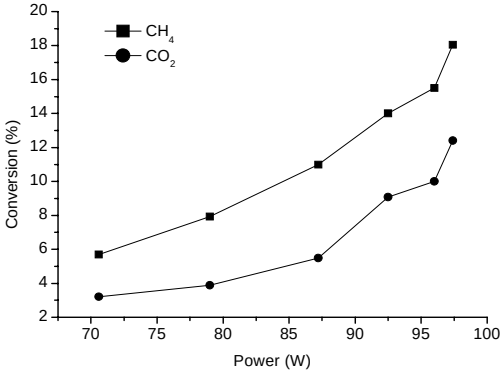


Fig. 6. Conversions of CH_4 and CO_2 during plasma-catalytic dry reforming of CH_4 with Ni/Al_2O_3.

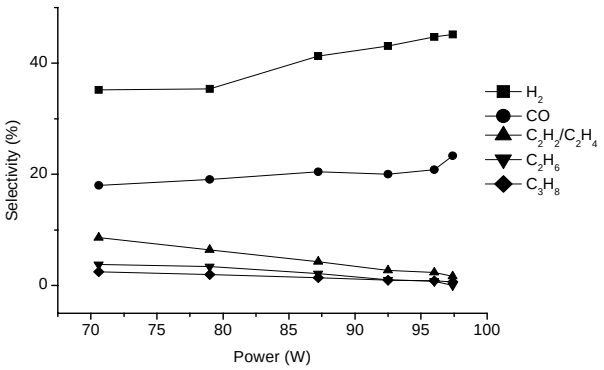


Fig. 7. Product selectivities during plasma-catalytic dry reforming of CH_4 with Ni/Al_2O_3

The presence of the catalyst caused a decrease in conversions of CH_4 and CO_2 in comparison with dry reforming in the absence of a catalyst, however, the H_2/CO ratio was changed significantly by increased H_2 selectivity and decreased CO selectivity. The presence of the catalyst increased the H_2-/CO ratio from 0.84 to 2.53 as shown in Figure 8.

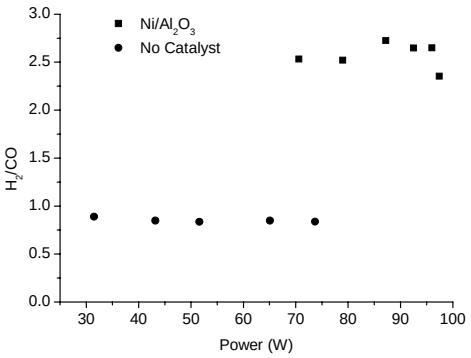


Fig. 8. Comparison of H_2/CO ratio for dry reforming of CH_4 with and without a Ni/Al_2O_3 catalyst.

5. Catalyst Characterisation

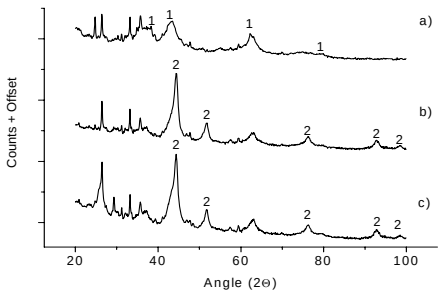


Fig. 9. XRD patterns of a) fresh NiO/Al_2O_3 b) plasma-reduced Ni/Al_2O_3 c) plasma-reduced Ni/Al_2O_3 after plasma-catalytic dry reforming of CH_4.1 = NiO peaks, 2 = Ni peaks.

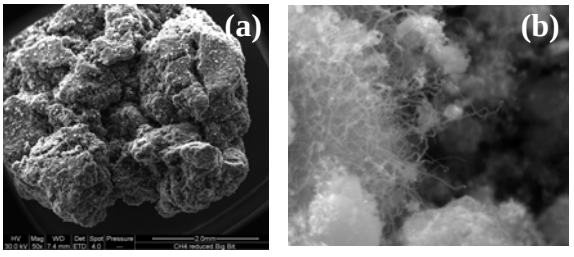


Fig. 10. SEM images of the reduced Ni/Al_2O_3 catalyst (a) 50x mag. (b) 25000x mag. showing carbon nanofibres (~20 – 80 nm in width).

The XRD patterns confirm that the catalyst has been reduced from NiO/Al_2O_3 to Ni/Al_2O_3 after the plasma treatment in CH_4 and that the catalyst is stable to atmospheric conditions. After plasma-catalytic dry reforming of CH_4, the characteristic Ni peaks are still present, showing that the catalyst did not change significantly under CH_4 dry reforming conditions in DBD.
Scanning electron microscopy (SEM) has been used to study the catalyst surface, revealing the presence of carbon nanofibres, shown in Figure 9b. When this catalyst is reduced thermally, a highly exothermic oxidation can occur on exposure to air, however this was not observed for the plasma-reduced catalyst. Carbon nanofibres on the surface of the catalyst provide a physical barrier that prevents reoxidation of the catalyst but did not seem to inhibit the catalytic activity observed for dry reforming of CH_4.

6. Conclusions

It has been shown that a dielectric barrier discharge can be successfully applied for the reduction of supported metal catalyst NiO/Al_2O_3. The reduction takes place at a substantially lower temperature than is required for thermal reduction in CH_4. It is suggested that the reduction in DBD is activated by the decomposition of adsorbed CH_4 on the catalyst surface producing a highly reactive form of carbon which subsequently reacts with NiO to give Ni and the evolution of both CO_2 and CO until the catalyst has completely reduced.
The active Ni sites generated during the reduction catalysed the conversion of CH_4 into H_2 and solid carbon. SEM analysis revealed that the carbon was deposited in the form of nanofibres, which provided a physical barrier which prevented reoxidation of Ni on exposure to air.
The activity of the plasma-reduced Ni/Al_2O_3 catalyst has been tested for dry reforming of CH_4. An increase in H_2 selectivity was observed in comparison to dry CH_4 reforming with no catalyst. The ratio of H_2/CO increased from 0.84 to 2.53 when the catalyst was present.

Acknowledgements. Support of this work by Supergen XIV - Delivery of Sustainable Hydrogen and the UK Engineering and Physical Sciences Research Council is greatly appreciated.

7. References

[1] Alizadeh, R., Jamshidi, E.and Ale-Ebrahim, H., *Kinetic Study of Nickel Oxide Reduction by Methane.* Chemical Engineering & Technology, 2007. **30**(8): p. 1123-1128.
[2] Shang, S.Y., Liu, G.H., Chai, X.Y., Tao, X.M., Li, X., Bai, M.G., Chu, W., Dai, X.Y., Zhao, Y.X.and Yin, Y.X., *Research on Ni/γ-Al_2O_3 Catalyst for CO_2 Reforming of CH_4 Prepared by Atmospheric Pressure Glow Discharge Plasma Jet.* Catalysis Today, 2009. **148**(3-4): p. 268-274.
[3] Liu, G.H., Li, Y.L., Chu, W., Shi, X.Y., Dai, X.Y.and Yin, Y.X., *Plasma-Assisted Preparation of Ni/SiO_2 Catalyst Using Atmospheric High Frequency Cold Plasma Jet.* Catalysis Communications, 2008. **9**(6): p. 1087-1091.
[4] Cheng, D.G., *Plasma Decomposition and Reduction in Supported Metal Catalyst Preparation.* Catalysis Surveys from Asia, 2008. **12**(2): p. 145-151.
[5] Zhao, Y., Pan, Y.X., Xie, Y.B.and Liu, C.J., *Carbon Dioxide Reforming of Methane Over Glow Discharge Plasma-Reduced Ir/Al_2O_3 Catalyst.* Catalysis Communications, 2008. **9**(7): p. 1558-1562.
[6] Wang, Z.J., Zhao, Y., Cui, L., Du, H., Yao, P.and Liu, C.J., *CO_2 Reforming of Methane Over Argon Plasma Reduced Rh/Al_2O_3 Catalyst: A Case Study of Alternative Catalyst Reduction Via Non-Hydrogen Plasmas.* Green Chemistry, 2007. **9**(6): p. 554-559.
[7] Yu, K.L., Liu, C.J., Zhang, Y.P., He, F., Zhu, X.L.and Eliasson, B., *The Preparation and Characterization of Highly Dispersed PdO Over Alumina for Low-Temperature Combustion of Methane.* Plasma Chemistry and Plasma Processing, 2004. **24**(3): p. 393-403.
[8] Liu, C.J., Yu, K.L., Zhang, Y.P., Zhu, X.L., He, F.and Eliasson, B., *Characterization of Plasma Treated Pd/HZSM-5 Catalyst for Methane Combustion.* Applied Catalysis B-Environmental, 2004. **47**(2): p. 95-100.
[9] Zou, J.J., Liu, C.J., Yu, K.L., Cheng, D.G., Zhang, Y.P., He, F., Du, H.Y.and Cui, L., *Highly Efficient Pt/TiO_2 Photocatalyst Prepared by Plasma-Enhanced Impregnation Method.* Chemical Physics Letters, 2004. **400**(4-6): p. 520-523.
[10] Wang, Z., Liu, C.J.and Zhang, G.L., *Size Control of Carbon Black-Supported Platinum Nanoparticles Via Novel Plasma Reduction.* Catalysis Communications, 2009. **10**(6): p. 959-962.
[11] Zou, J.J., Zhang, Y.P.and Liu, C.J., *Reduction of Supported Noble-Metal Ions Using Glow Discharge Plasma.* Langmuir, 2006. **22**(26): p. 11388-11394.
[12] Cheng, D.G., Zhu, X.L., Ben, Y.H., He, F., Cui, L.and Liu, C.J., *Carbon Dioxide Reforming of Methane Over Ni/Al_2O_3 Treated with Glow Discharge Plasma.* Catalysis Today, 2006. **115**(1-4): p. 205-210.
[13] Wang, J.G., Liu, C.J., Zhang, Y.P., Yu, K.L., Zhu, X.L.and He, F., *Partial Oxidation of Methane to Syngas Over Glow Discharge Plasma Treated Ni-Fe/Al_2O_3 Catalyst.* Catalysis Today, 2004. **89**(1-2): p. 183-191.
[14] Kim, S.S., Lee, H., Na, B.K.and Song, H.K., *Plasma-Assisted Reduction of Supported Metal Catalyst Using Atmospheric Dielectric-Barrier Discharge.* Catalysis Today, 2004. **89**(1-2): p. 193-200.

AN OPTICAL EMISSION SPECTROSCOPY OF ATMOSPHERIC GLOW DISCHARGE BETWEEN SHAPED ELECTRODES IN CH_4-N_2 GAS MIXTURE

G Horvath [1, 2], F. Krcma[3], L. Polachova[2,3], K. Klohnova[3], N J Mason [2] , M. Zahoran [1] and S. Matejcik[1]

[1] *Department of Experimental Physics, Comenius University, Mlynska dolina F-2, 842 48 Bratislava, Slovakia, horeszka@gmail.com*

[2] *Department of Physics and Astronomy, The Open University, Walton Hall, MK7 6AA, Milton Keynes, United Kingdom*

[3] *Brno University of Technology, Faculty of Chemistry, Purkynova 118. 612 00 Brno, Czech Republic*

Email: horeszka@gmail.com

An optical emission spectroscopy (OES) of an atmospheric glow discharge induced between shaped electrodes has been studied in N_2-CH_4 gas mixture with CH_4 contents in range from 0.5% to 2%. The measurements were performed in flowing regime at ambient temperature and atmospheric pressure. In the emission spectra the lines of the second positive system of N_2, the CN system and the first negative system of N_2 were found to be the most intensive, the atomic H_α, H_β, and C (247 nm) lines were also observed.

1. Introduction

Since Cassini landed on Saturns largest moon, Titan and sent a wealth of data on the atmospheric and surface composition of Titan, many people are focused on the chemistry if its atmosphere. The dense atmosphere of Titan is mostly composed of N_2 with a few percent of CH_4. The most important minor compounds detected by Cassini-Huygens probe are N-containing organics (HCN, HC_3N, HC_5N, C_2N_2) believed to be formed by as a result of dissociation of nitrogen and methane either by solar induced photolysis or by electron impact [1] and hydrocarbons (C_2H_2, C_2H_4, C_2H_6, C_3H_8, C_3H_4 [1]). In order to understand the physical and chemical processes leading to such observed phenomena a series of laboratory simulations have been made [11-14].

G. Dilecce *et al* [8] reported a spectroscopic study on CH observables including laser induced fluorescence (LIF) on CH and emission spectroscopy on the CH band in N_2-CH_4 atmospheric pressure dielectric discharge. Analysis of CH(A) emission shows that it is due to electron impact in N_2–CH_4 mixture. The analysis of spectra showed that there is a need for more precise knowledge on the collision quenching of electronically excited states and on the electron energy distribution function (EEDF).

In paper [9] authors investigated CN($B^2\Sigma^+ \rightarrow X^2\Sigma^+$) violet system emission and laser induced fluorescence in an atmospheric pressure pulsed dielectric barrier discharge. They found a high degree of vibrational non-equilibrium in both CN(*B, v*) and CN(*X, v'*). Authors observed that vibrational distributions depended strongly on the gas feed composition and on the discharge/post-discharge regime. Analysis of the time resolved laser and emission spectroscopy measurements led to the conclusion that two main chemi-luminescent mechanisms are responsible for the CN(B) excitation. One is the C + N +M → CN(*A,B*) +M recombination, that is dominant in the post-discharge; the other one, active in the discharge, is probably the reaction N +CH → CN(*A,B*) + H. When CH_4 was added to the gas feed, the recombination reaction was strongly inhibited, while CH produced more easily from the methane contained in the gas phase. It is also likely that CN(*X*) was produced by the same reactions after radiative cascade from CN(*A,B*) states.

In this paper we report our results of OES study made in CH_4-N_2 DC glow discharge induced between two shaped electrodes, operated at atmospheric pressure.

2. Experimental set-up

The apparatus used in our experiments is shown schematically in Figure 1. OES using Jobin Yvon TRIAX 550 spectrometer with CCD detector was used for monitoring the optical emission from the N_2/CH_4 plasma. The flow rates through the reactor for both CH_4 and N_2 were regulated using MKS mass flow controllers. The total flow rate used was 200 sccm. The discharge electrode system had the standard configuration of a classical gliding arc, a pair of stainless steel holders positioned in parallel to the iron electrodes but in this case the plasma was not gliding due to the low flow rate and therefore stable abnormal glow plasma occurred between the electrodes at their shortest distance of 2 mm, thus forming plasma channel with diameter of 1mm. Electrical parameters have been measured by Tektronix oscilloscope using high voltage probe and 10 Ω resistor for current monitoring. The reactor chamber had a volume of 0.3L. The discharge was powered by a home-made DC HV source. The present experiments were performed for different N_2:CH_4 ratios in range from 0.5 % to 2% CH_4 in N_2 at atmospheric pressure.

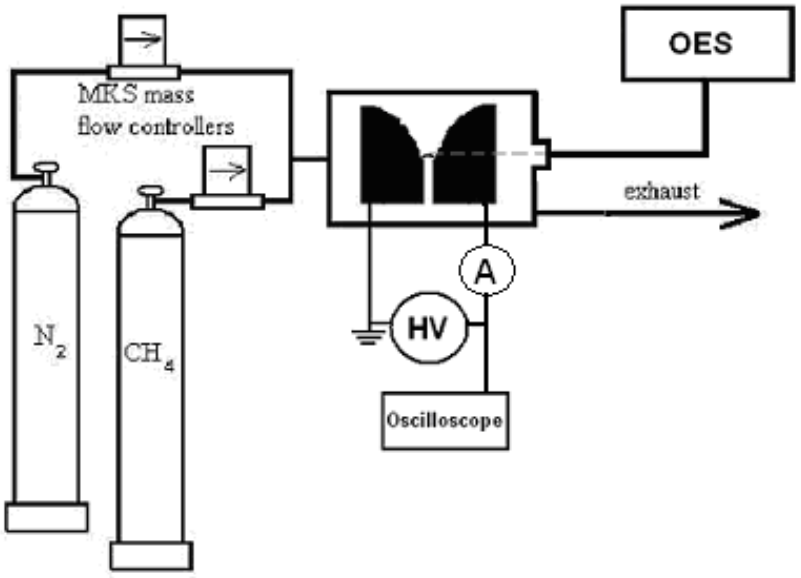


Fig. 1. Schematic diagram of the experimental apparatus used for OES analysis of gaseous products produced in a glow discharge fed by various mixtures of methane in nitrogen.

3. Experimental results and discussion

a. Optical emission spectroscopy of the glow region

Optical emission spectroscopy (OES) is a popular to investigate glow discharges since it produces no perturbation in the plasma. The basic promise of this technique is that the intensity of the light emitted at particular wavelengths from an excited state is proportional to the density of species in that excited state [2]. Therefore measurement of intensities provides a possibility to measure rotational, vibrational, and electron temperatures (T_r, T_v, *and* T_{ve}), the relative concentration of active species, which can be converted into an absolute concentration if we know the Electron Energy Distribution Function (EEDF) and energy dependent cross sections for the electron impact excitation processes [2,3]. Unfortunately, in our case the plasma was not in LTE, thus the molecules do not follow Maxwell-Bolztmann distribution and determination of its absolute concentration from the spectra was not possible. However, the measurements of the intensities of selected emission lines (Fig. 3a, b) provide information about the relative concentration of the active species of the N_2 plasma as a function of discharge current.

A selected part of a typical emission spectrum is shown in Figure 2. As expected N_2 and CN bands were the most dominant. The spectra were composed of the following molecular spectral systems: the second positive system of neutral N_2 ($C^3\Pi_u \rightarrow B^3\Pi_g$), the first negative system of N_2^+ ion ($B^2\Sigma_u^+ \rightarrow X^2\Sigma_g^+$), the CN violet ($B^2\Sigma^+ \rightarrow X^2\Sigma^+$a) and red systems ($A^2\Sigma^+ \rightarrow X^2\Sigma^+$) and the C_2 Swan bands. Besides these the strong atomic H^{α} line, weaker H^{β}line and week lines of C (247 nm were measured in the second order) and N^+(399.5 nm) has been detected.

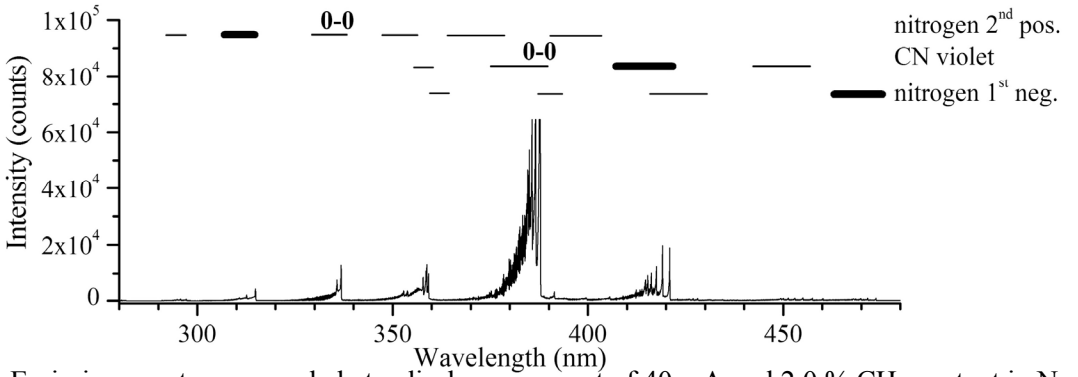


Fig. 2. Emission spectrum recorded at a discharge current of 40 mA and 2.0 % CH_4 content in N_2 with marked bands and sequences used for the further calculations.

The relative emission intensities for the selected emission bands are shown in Figure 3. Figures 3a,b present the variation of the intensity ratio $I(N_2^+)/I(N_2^*)$ with discharge current and suggests a slightly increased occurrence of N_2^+ ions in comparison with N_2^* molecules.

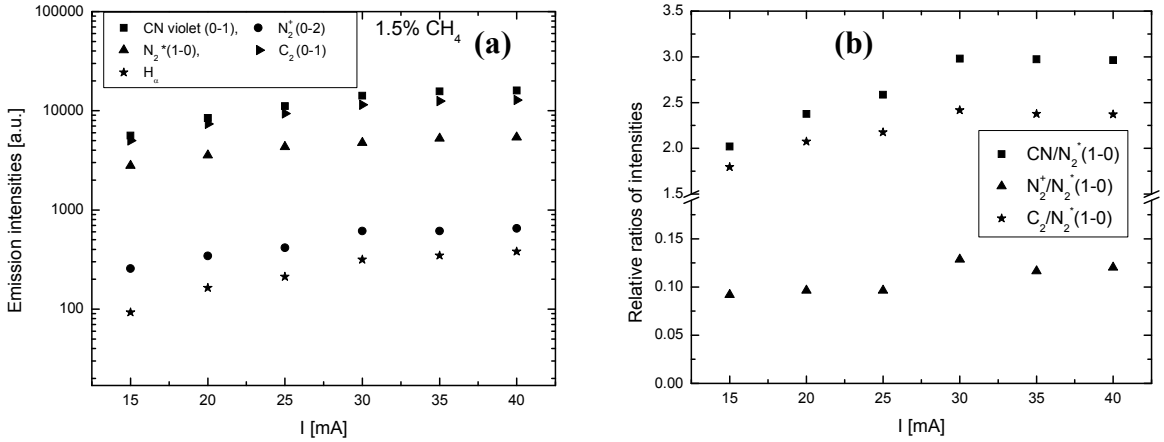


Fig. 3. Emission intensities and ratios for selected emission bands in mixture of 1.5% CH_4 in N_2.

These results may be explained by N_2^+ emission being more sensitive to high-energy electrons than N_2^* due to the higher excitation threshold energy compared with N_2^*. It means that the degree of ionization of the plasma increases with the number of free electrons. On the other hand this small increase in $I(N_2^+)/I(N_{2\,(1\text{-}0)}^*)$ intensity ratio indicates that any increase in the electron energy distribution is also small and the increasing temperature T_g is due to the increasing concentration of electrons. The high emission intensity of C_2 Swan system suggests a high degree of decomposition of CH_4 into C then C_2 radicals which is confirmed by the absence of emission lines of CH_x radicals within the glow region. The dependence of the intensity ratio $I(CN)/I(N_2^*)$ on the current shows an increased content of CN radicals in comparison with N_2^* molecules, which is in good agreement with the increasing HCN concentration measured by FTIR analysis.

Since many emission bands of N_2 and CN overlap we selected some of them for the further detailed analysis and plasma parameters calculation. The CN violet 0-0 band was measured with high resolution (using 3600 gr/mm grating) and it was used for the rotational temperature calculation by classical pyrometric line procedure using rotational lines J = 3, 4, 7-16 and rotational constant given by Prasad. LifBase software was used for the rotational lines assignment. The same procedure was applied also for the neutral nitrogen in C state rotational temperature calculation. In this case, the spectrum of 0-0 nitrogen second positive band (rotational lines with J = 40 – 50) measured using 1200 gr/mm grating was used. The line assignment was done by SpecAir software using rotational constants given in [4].

Vibrational temperature was calculated from nitrogen, CN and C_2 spectra. The bands of -1 sequence of nitrogen second positive and +2 sequence of nitrogen first negative systems were applied with using transition constants (wavelength and transition probability) given in [4]. In the case of CN, spectra of +1 sequence with constants given by [5] were used. Constants given by [6] were used with intensities of -1 sequence for the C_2 molecule vibratonal temperature calculation.
The electron temperature was not calculated because intensity of H□β line was relatively low and was significantly overlapped by C_2 Swan bands.
It can be noted that only bands and lines with signal/noise ratio better than 5 were used for these calculations, the other were omitted. The average uncertainty of calculated values was between 10 and 15%. The N_2 rotational temperature varies over the range 2700 to 3700 K and it's dependence on the discharge current or the CH_4 molar ratio had no obvious functional behaviour, while the CN rotational temperature decreased with increasing current in range from 1200 to 3200 K. The vibrational temperature (4800 – 6200 K) of the N_2^+ ion decreased with increasing CH_4 content and increased with the current, with a rapid fall at 40 mA. The plasma power and CH_4 molar ratio showed a significant effect on the CN vibrational temperature, with values from 4200 to 6500 K and was proportional to the current.

b. Determination of the electron density

Using the simplified relation

$$j = \frac{I}{\frac{1}{4}\pi D^2} \qquad \{1\}$$

it was possible to estimate the current density with an accuracy of an order of magnitude. The typical glow plasma in CH_4/N_2 gas mixture at discharge current I = 15 mA has a diameter D = 1 mm and length 2 mm, j = 1.9 A/cm^2. The electron number density n_e is a very important parameter characterizing the plasma and can be derived from the measured current density and reduced electric field E/N, when N is the gas density for given T. The simplest estimate of n_e can be then obtained using the expression for the current density

$$j = e n_e v_d \qquad \{2\}$$

where e is the elementary charge and v_d is the electron drift velocity. The electron drift velocity is given by the electron mobility μ_e and the electric field strength E:

$$v_d = \mu_e E \qquad \{3\}$$

where E was approximately measured from the applied voltage (400 V) and the plasma column length (2 mm). The reduced electron mobility $\mu_e p$ can be considered constant in our experimental conditions: $\mu_e p = 5.87 \cdot 10^7$ cm^2 Pa V^{-1} s^{-1} [7]. The pressure should be better represented by the gas density N to accommodate for the elevated gas temperatures T_g (to $T_r \sim T_g$ ~2700-3700 K) at p = 101 kPa atm, similar to representing the reduced field as E/N rather than E/p. In N-representation, $\mu_e N$ reached values in range from $1.2 \cdot 10^{22}$ to $7.8 \cdot 10^{22}$ cm^{-1} V^{-1} s^{-1}. This value could be then used in the expression of the electron drift velocity and the electron density can be calculated subsequently:

$$n_e = \frac{j}{e \mu_e N \frac{E}{N}} \qquad \{4\}$$

n_e was estimated to be of the order of ~10^{13} cm^{-3}. With increasing current the electron density was also increased resulting in a more conductive plasma, which was confirmed by the observation of a slight decrease in the applied voltage and an increase in the ion signal.

4. Conclusion

In this paper we present the results of OES study of the gaseous products and radicals formed in a glow discharge fed by four different atmospheric pressure mixtures of N_2:CH_4 (0.5, 1, 1.5 and 2 % CH_4) operated in a flowing regime at different discharge currents (from 15 up to 40 mA) and ambient

temperature. The discharge current has significant effect on the product synthesis and electron density. The continuous glow discharge was the hottest one with T_g reaching 3200 K, since most of electron energy is converted into gas heating. The plasma was close to LTE but not close enough to assume Maxwell distribution. Using our OES study we could estimate temperatures T_r and T_v which -together with the electrical parameters - allowed us to calculate the current and electron number densities in the discharge with typical values of 1.9-5.1 A/cm^2 and $n_e \sim 10^{13}$ cm^{-3}. Such experiments can provide information that can aid our understanding of processes in Titan's atmosphere. Furthermore discharges can provide relevant information on the formation of the anions [2] and have therefore allowed of the anions observed by Cassini to be identified.

Acknowledgments. This research project was supported by: The Slovak Grant Agency, Slovak Research and Development Agency, Grant UK/140/2010, VEGA 1/0051/08, APVV 0365-07, ESF COST Actions CM0601, CM0805 and EIPAM TNA2. Research plan of Czech Ministry of Education No. MSM0021630501.

5. References

1. S. Vinatier and 10 colleagues, Icarus **188**, 120-138 (2007).
2. G. Horvath, Y. Aranda-Gonzalvo, N.J. Mason, M. Zahoran, and S. Matejcik, *Eur. Phys. J. Appl. Phys*. **49**, 13105 (2010).
3. A. Bogaerts, *J. Anal. At. Spectrom.* **14**, 1375 (1999).
4. Yu.P. Raizer, *Gas Discharge Physics*, Springer, New York, 1991.
5. Gilmore FR, Laher RR, Espy PJ, *J Phys Chem Ref Data* **21**, 1005 (1992).
6. Laux CO, "Radiation and Nonequilibrium Collisional-Radiative Models," von Karman Institute Lecture Series 2002-07, Physico-Chemical Modeling of High Enthalpy and Plasma Flows, eds. D. Fletcher, J.-M. Charbonnier, G.S.R. Sarma, and T. Magin, Rhode-Saint-Genèse, Belgium, 2002.
7. King RB, *Astrophys J 108*, 429 (1948).
8. G Dilecce, P F Ambrico, P Tosi and S De Benedictis, *J. Phys. D: Appl. Phys.* **43** (2010) 124004.
9. G Dilecce, P F Ambrico, G Scarduelli, P Tosi and S De Benedictis, *Plasma Sources Sci. Technol.* **18** (2009) 015010.
10. Pintassilgo C D, Jaoul C, Loureiro J, Belmonte T and Czerwiec T 2007 J. Phys. D: Appl. Phys. **40** 3620.
11. Gonzalez R N and Ramirez S I 1997 *Adv. Space Res.* **19** 1121.
12. Gonzalez R N, Ramirez S I, de la Rosa J G, Coll P and Raulin F 2001, *Adv. Space Res* **27** 271.
13. Ramirez S I, Gonzalez R N, Coll P, and Raulin F 2005 *Advances in Space Research* **36** 274.
14. G. Horvath, J. D. Skalny, N. J. Mason and M. Zahoran M., 2009 *Plasma Sources Sci. Technol.* **18** 034016.

GENERATION OF CARBON MONOXIDE IN POSITIVE CORONA DISCHARGE FED BY MIXTURE OF CARBON DIOXIDE WITH ARGON AND HELIUM

Juraj Országh[1], Maria Duffy[2], Zuzana Lichvanová[1], Cristina Sima[3], Štefan Matejčík[1], Nigel J. Mason[2], Peter Papp[1], Rodica Vladoiu[3]

[1]*Dept. of Experimental Physics, Comenius University, Mlynská dolina F-2, Bratislava, Slovakia*

[2]*Dept. of Physics and Astronomy, Open University, Walton Hall, Milton Keynes, United Kingdom*

[3] *Dept. of Plasma Physics, Ovidius University, Mamaia 124, Constanta, Romania*

E-mail: orszagh@fmph.uniba.sk

The effect of argon and helium admixtures in carbon dioxide on carbon monoxide generation was studied. The mixture was flowing through the positive corona discharge. The experiment was done using pure carbon dioxide, carbon dioxide with 5% of argon/helium and carbon dioxide with 10% of argon/helium. The corona reactor was equipped by coaxial cylindrical electrodes. The outer one was made of stainless steel and the inner one was molybdenum wire. The reactor tube itself was used as a cell in the infrared spectrometer as it had germanium windows on each side. The IR spectrometry method was used for carbon monoxide concentration measurement. It was found out that with increasing amount of argon in the mixture the concentration of carbon monoxide was increasing. Such experiment is interesting from the Martian atmosphere point of view. The Martian atmosphere contains a few volume percents of argon.

1. Introduction

Mars has been long regarded as the planet in our solar system most capable of sustaining life, leading to a series of recent space missions to the planet culminating in the NASA Phoenix mission with its in situ search for water in the Martian soil. However in exploring the possibility for life having established itself on the Martian it is necessary to consider the conditions on the Martian surface at the time when life may have developed. All biological molecules on Earth are known to be susceptible to radiation, the effects of which may lead to damage leading either to direct destruction or, in the case of DNA, mutagenesis in which the self replicating molecule is able to replicate itself after damage but with genetic modifications that can lead to cell death or mutation. However, on Earth such biomolecules are protected by the presence of terrestrial ozone layer, which filters the damaging solar UV radiation and prevents it from reaching the surface. Hence the creation of terrestrial ozone layer is believed to have been crucial to life emerging on the terrestrial surface. Accordingly in investigating whether the Martian surface was ever capable of sustaining life it is necessary to investigate whether its atmosphere was ever capable of sustaining ozone concentration sufficient to screen its surface from UV radiation. Small concentration of ozone are found in the present atmosphere of Mars even thought today it is composed of almost pure CO_2. When first detected the presence of ozone was itself a surprise and the mechanisms for its formation questioned. Electrical discharges provide a suitable laboratory analogue of planetary atmospheres with electrical energy mimicking the energy input into the planetary atmospheres by solar radiation. Therefore using a corona discharge we have sought to investigate the chemical processes that lead to ozone formation in the Martian atmosphere.

2. Experimental apparatus

The reactor was composed of cylindrical wire-to-cylinder system of electrodes. The outer electrode with dimensions (diameter 1.6 cm and length 6.5 cm) was made of stainless steel as well as the inner electrode which diameter was 0.125 mm. The scheme of the apparatus is shown in the figure 1.

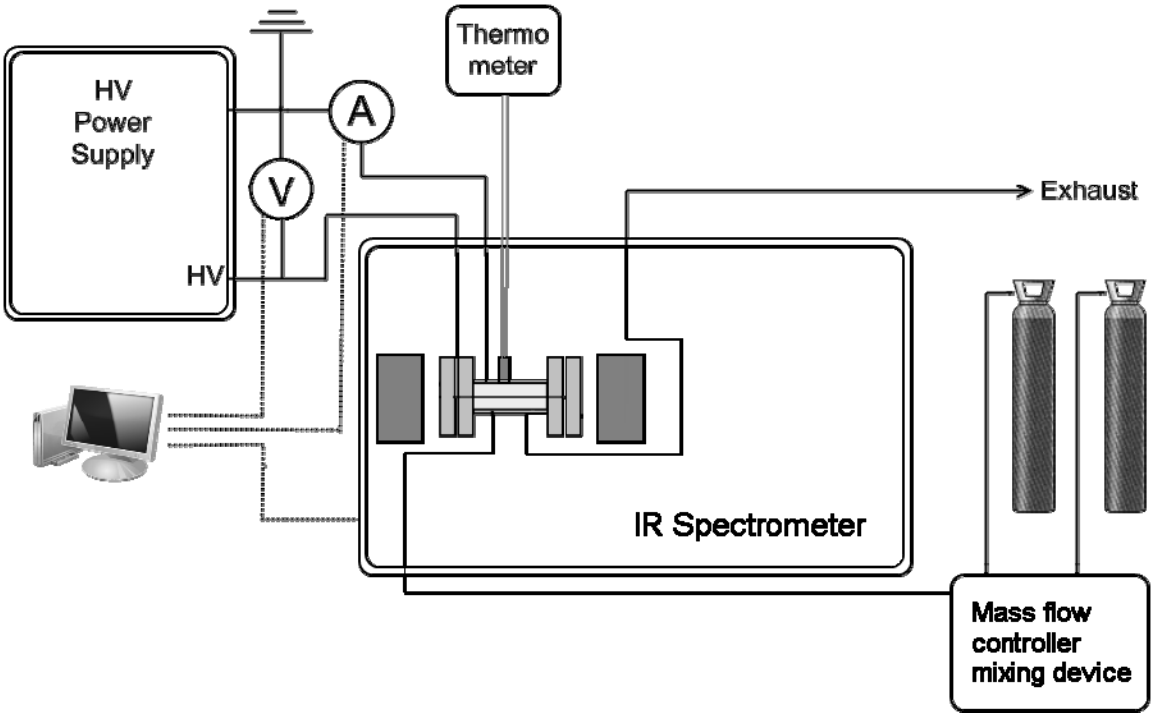


Fig. 1. Simple scheme of experimental apparatus.

First the outer electrode was mechanically cleaned to remove the layer of oxides from its surface. Then the gas mixture was let into the reactor and its flow rate was kept constant (20 cm^3/min) by two mass flow controllers. The background spectrum was taken in this pure gas mixture. Then the corona discharge was generated in the reactor. The voltage on the electrodes was constant and after 30 minutes when the conditions in the reactor were stabilized the IR spectrum was taken. After that the voltage on the electrodes was changed to the higher value and the measurement was repeated. The inner surface of the reactor was cleaned before every set of three measurements. In one set of measurements the gas mixture was the same only the voltage was has been changed to the desired values. The experiments have been carried out at atmospheric pressure and ambient temperature.

3. Results and discussion

In the figure 2 the comparison of measured IR spectra of carbon monoxide is shown. It is evident that the amount of produced carbon monoxide is lowest in pure carbon dioxide, slightly higher in the mixture of carbon dioxide with 5% of helium and significantly higher in the mixture with argon. These measurements were done at the voltage of 7.5kV. In the legend of the figure the discharge current, discharge power and Becker parameter are shown for each curve. The Becker parameter is the amount of energy put by the discharge into the unit volume of the gas. It can be seen that all these values correspond to the amount of generated carbon monoxide. The effect of increasing of the carbon monoxide concentration by adding argon or helium into the carbon dioxide can be explained by the role of metastables of argon and helium. These excited states can conserve energy that is released in collisions with carbon dioxide molecules. In such way it contributes to carbon dioxide decomposition into carbon monoxide. The difference between argon and helium admixtures can be explained by different energies of metastables of these gases. The energy of argon metastable state is approximately 10 eV. On the other hand the energy of helium metastable state is approximately 20 eV. In corona discharge most of the electrons have energies between 1 and 5 eV. Only small amount of them can reach 10 eV and even less 20 eV. That is why the process is more effective in the mixture of carbon dioxide with argon.

In the figure 3 the similar comparison is done for 10% admixtures of argon and helium in the carbon dioxide. In this case there is almost no difference in pure carbon dioxide and carbon dioxide with helium admixture. This phenomenon can be explained by the fact that there is very small amount of

electrons able to excite helium into its metastable state and the amount of carbon dioxide in the mixture is just 90%.

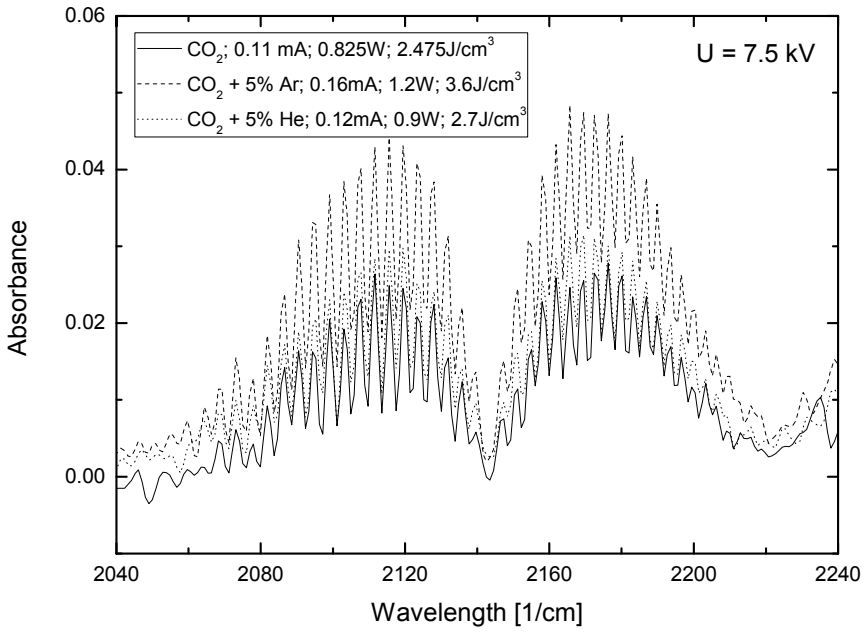


Fig. 2. IR spectrum of carbon monoxide generated by positive corona discharge fed by carbon dioxide or carbon dioxide with 5% admixture of argon or helium.

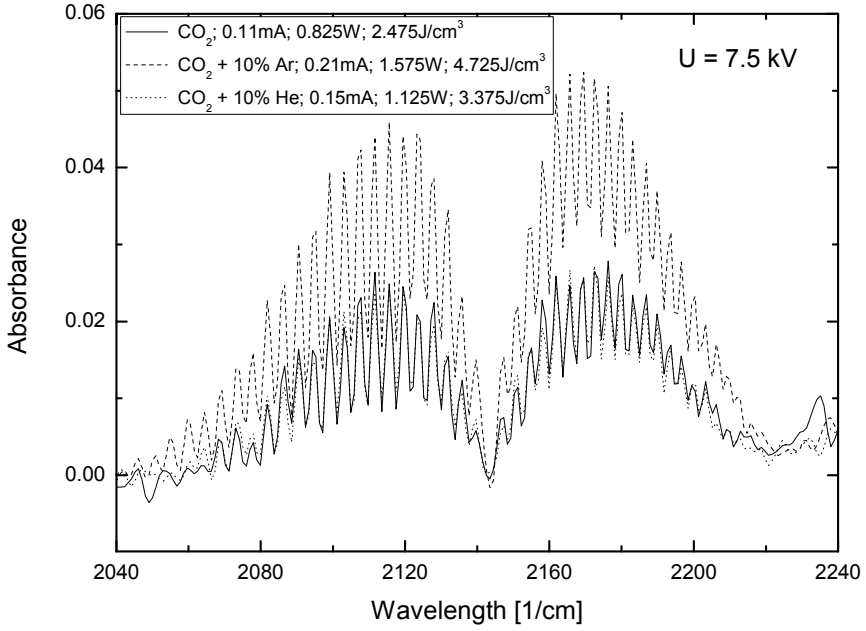


Fig. 3. IR spectrum of carbon monoxide generated by positive corona discharge fed by carbon dioxide or carbon dioxide with 10% admixture of argon or helium.

In the figures 4 and 5 the effect of admixture concentration can be seen for argon and helium mixtures.

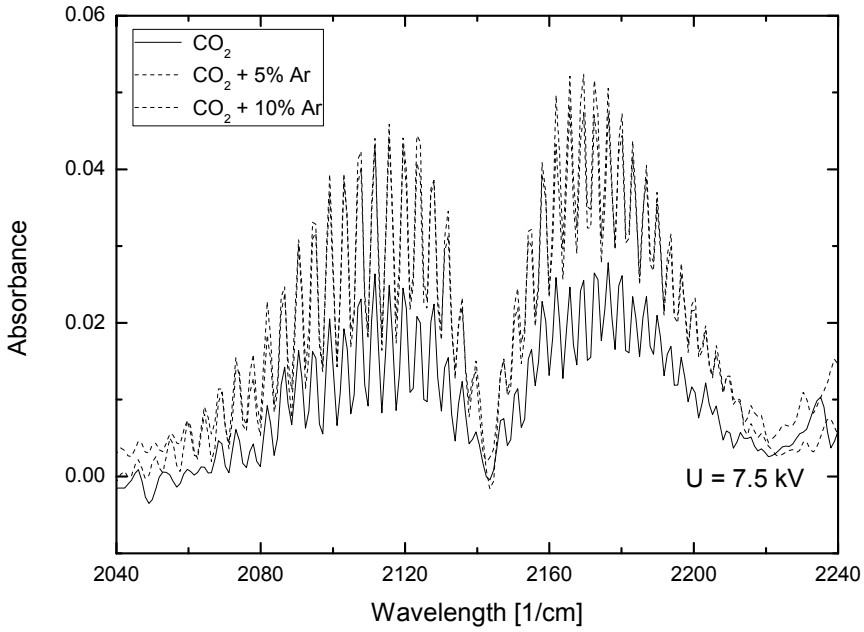


Fig. 4. IR spectrum of carbon monoxide generated by positive corona discharge fed by carbon dioxide or carbon dioxide with 5%/10% admixture of argon.

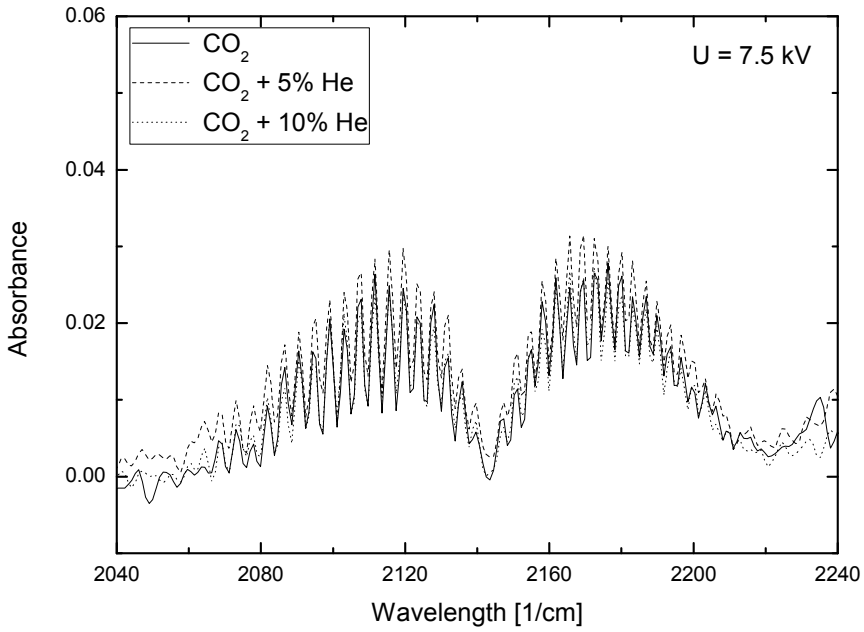


Fig. 5. IR spectrum of carbon monoxide generated by positive corona discharge fed by carbon dioxide or carbon dioxide with 5%/10% admixture of helium.

4. Conclusions

The effect of argon and helium admixtures in the carbon dioxide in positive corona to carbon monoxide generation has been studied. It was found that both argon and helium admixtures cause the increase of carbon monoxide concentration. This effect was explained by the role of metastables of argon and helium.

Acknowledgements. This work was supported the Slovak Research and Development Agency, project Nr. APVV-0365-07 and LPP-0143-06.

TITAN'S ATMOSPHERE CHEMISTRY SIMULATION IN ATMOSPHERIC GLOW DISCHARGE

L. Polachova[1,2], G Horvath [2,3], F. Krcma[1], K. Klohnova[1], N J Mason [2] , M. Zahoran[3] and S. Matejcik[3]

[1] *Brno University of Technology, Faculty of Chemistry, Purkynova 118. 612 00 Brno, Czech Republic*

[2] *Department of Physics and Astronomy, The Open University, Walton Hall, MK7 6AA, Milton Keynes, United Kingdom*

[3] *Department of Experimental Physics, Comenius University, Mlynska dolina F-2, 842 48 Bratislava, Slovakia*

Email: xcpolachova@fch.vutbr.cz

The formation of products produced in an atmospheric glow discharge fed by a N_2-CH_4 gas mixture with CH_4 contents in range from 0.5% to 2% CH_4 has been studied using Fourier Transform Infrared (FTIR). The measurements were carried out in flowing regime at ambient temperature and pressure. Measurements revealed HCN and NH_3 to be the major products of the plasma with traces of C_2H_2. These same molecules were observed by the Cassini-Huygens probe in Titan's atmosphere.

1. Introduction

The Cassini space mission to Saturn and the release of its Huygens probe onto its largest moon, Titan, has led to a wealth of data on the atmospheric and surface composition of Titan. The dense atmosphere of Titan is mostly composed of N_2 with a few percent of CH_4. The most important minor compounds detected by Cassini-Huygens are nitriles (HCN, HC_3N, HC_5N, C_2N_2) believed to be formed by as a result of dissociation of nitrogen and methane either by solar induced photolysis or by electron impact [1] and hydrocarbons (C_2H_2, C_2H_4, C_2H_6, C_3H_8, C_3H_4 [1]). In order to understand the physical and chemical processes leading to such observed phenomena, an additional laboratory simulation are required.

However such models need to be tested against laboratory mimics. Discharges have been shown to be good mimics of planetary atmospheres providing insights into both physical and chemical processes of such atmospheres. DBD, glow, microwave, RF and corona discharges [2-10], have all been used in order to study electron-molecule and ion-molecule reactions in planetary atmospheres.

In this paper we report the results of a new investigation of the organic chemistry prevalent in an atmospheric glow discharge fed by a N_2-CH_4 gas mixture with CH_4 contents in the range of 0.5% to 2%.

2. Experimental apparatus

The apparatus used in our experiments is shown schematically in Figure 1. The flow rates through the reactor for both CH_4 and N_2 were regulated using MKS mass flow controllers. The total flow rate used was 200 sccm. The discharge electrode system had the standard configuration of a classical gliding arc, a pair of stainless steel holders positioned in parallel to the iron electrodes but in this case the plasma was not gliding due to the low flow rate and therefore stable abnormal glow plasma occurred between the electrodes at their shortest distance of 2 mm, thus forming plasma channel with diameter of 1mm. Electrical parameters have been measured by Tektronix oscilloscope using high voltage probe and Rogowsky current probe. The reactor chamber had a volume of 0.3L. The discharge was powered by a home-made DC HV source. The present experiments were performed for different N_2:CH_4 ratios in range from 0.5 % to 2% CH_4 in N_2 at atmospheric pressure and ambient temperature.

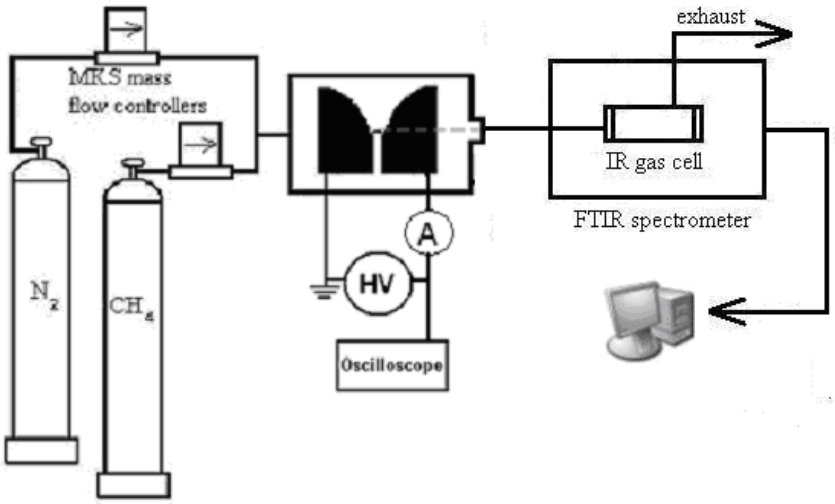


Fig. 1. Schematic diagram of the experimental apparatus used for FTIR analysis of gaseous products produced in a glow discharge fed by various mixtures of methane in nitrogen.

A pure CH_4/N_2 gas mixture without plasma was measured as the background spectra for FTIR measurements. The discharge power was calculated using the formula

$$P = U \cdot I \qquad \{1a\}$$

where U is the voltage drop across the electrodes and I is the discharge current. The specific input energy was calculated using the formula

$$\eta = \frac{P}{Q} \quad [\text{kJ/L}] \qquad \{1b\}$$

where P is the power calculated using {1} and Q is the flow rate. The estimated values were 1.8 kJ/L for the lowest current I = 15 mA and 4.2 kJ/L for the highest current I = 40 mA used in our experiments.

The gaseous product concentrations were calculated using the Beer-Lambert formula {2} using IR absorption cross section data found in the HITRAN* database [11]:

$$A = n.l.\sigma \qquad \{2\}$$

where A is the absorbance measured experimentally, n (cm^{-3}) is the concentration of detected compound, l (cm) is the length of the absorption path in IR cell and σ (cm^2) is the IR absorption cross-section.

All the experiments were carried out at atmospheric pressure and at ambient temperatures. The discharge was typically operated for between 60 and 120 minutes during which time the nascent reactor temperature (as measured by thermocouples on the reactor walls) did not rise above 320 K.

3. Experimental results

3.1 FTIR analysis of products formed in the discharge

A typical FTIR spectrum of products formed in the discharge fed by 2% CH_4 in N_2 is shown in Figure 2. Similar spectra were observed for the other CH_4/N_2 molar ratio conditions. Using HITRAN spectral data individual absorption features can be assigned to specific compounds. Besides the remaining CH_4 (3230–2704 cm^{-1}; 1408–1169 cm^{-1}) obvious infrared spectra absorption bands of C≡C were observed at the wave numbers 3386–3217 cm^{-1} which is the typical C-H stretching band of hydrogen cyanide HCN and acetylene C_2H_2. The strongest feature, at 713 cm^{-1}, is due to HCN, the weak peak at 729 cm^{-1} is due to C_2H_2. However, we found no features corresponding to C_2H_4 (which has a well known band between 800-1100 cm^{-1}, maximum at 956 cm^{-1} and a band between 3000-3200 cm^{-1}, maximum at 3138 cm^{-1}). In contrast to our earlier measurements made in a coaxial corona discharge [12], NH_3 was observed as a new product in the abnormal glow discharge identified by its strong peak at 966 cm^{-1},

surrounded by dense rotational in range 800-1200. Bands at around 3300 cm^{-1} were composed of overlapping bands from HCN, NH_3 and C_2H_2. From the measured absorbance values the concentrations of individual compounds were calculated using the Beer-Lambert formula with molecular IR absorption cross-section data being taken from HITRAN spectral database. The dependence of the concentration NH_3 and HCN on the gas flow rate within the frame of discharge power are shown in Figures 3a-3b. C_2H_2, as the minor product, did not exceed concentrations of 100 ppm during the measurements and found to slightly decrease with increasing power. It should be noted that the diatomic molecules such as H_2 can not be detected using FTIR.
The generation of the energetic electrons has been recognized as the initial step of all the reactions in plasma region. The inelastic collisions of methane molecules with energetic electrons lead to the formation of some active free radicals such as C, CH, CH_2 and CH_3.

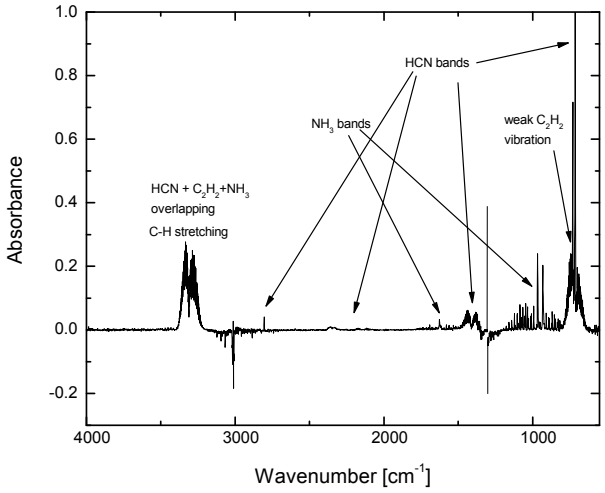


Fig. 2. A typical FTIR spectrum recorded in a gas cell filled with products formed in the discharge reactor fed by a CH_4-N_2 gas mixture with a 2:98 ratio, operated at atmospheric pressure and a total gas flow 200 sccm. The unit energy has a value of 4.8 kJ/L. Note the negative absorbance indicates the loss of CH_4 in the differencial spectra during the operation of the discharge.

It is evident that the product formation is accompanied by a decrease in concentration of CH_4 but because of possible band overlapping of CH_2 and CH_3 stretching in CH_4 region we were not able to estimate the degree of its decomposition from the measured changes of absorbance in the derivative spectra. In exploring the organic chemistry it is to be noted that there is an emphasis on the N-bearing products formed in the CH_4-N_2 discharge. As shown in Figure 3, the discharge current *I* has a significant effect on both HCN and NH_3 synthesis. The larger the value of *I*, the more HCN and NH_3 and the yields of HCN and NH_3 both increase with increasing initial CH_4 content.

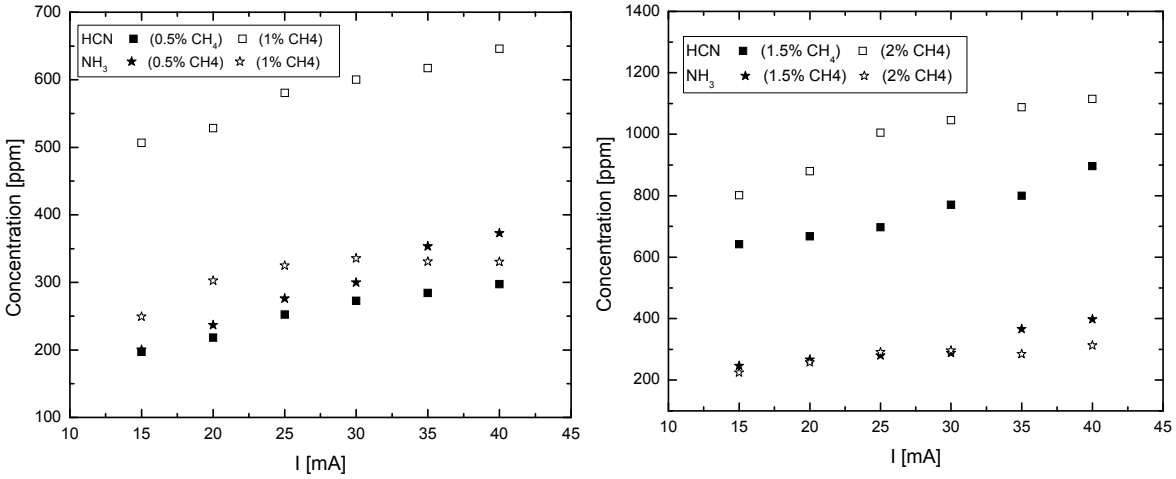


Fig. 3a-3b**.** The dependence of HCN and NH_3 concentrations on a discharge current for different initial CH_4 concentrations (a: 0.5% and 1%; b: 1.5 and 2%) in N_2 plasma.

3.2. Initial reaction channels leading to product formation

Within a CH_4/N_2 plasma discharge, electron-molecule interactions dominate leading to the formation of a large number of chemically reactive species. For example the two lowest excited singlet states $CH_4(S_1)$ (9.6 eV) and $CH_4(S_2)$ (11.7 eV), formed in electron-methane collisions are so unstable that they rapidly dissociate into radicals such as CH_3, CH_2, CH, C [13]

$$e(\varepsilon > 10eV) + CH_4 \rightarrow CH_4(S_1,S_2) + e \quad (1)$$

$$CH_4(S_1,S_2) \rightarrow CH_3 + H \quad (2a)$$

$$CH_2 + H + H \quad (2b)$$

$$CH_2 + H_2 \quad (2c)$$

$$CH + H_2 + H \quad (2d)$$

If the electron energy is higher than 12.75 eV, direct ionization of CH_4 occurs in the discharge:

$$e(12.75eV) + CH_4 \rightarrow CH_4^+ + 2e \quad (3)$$

$$e(14.3eV) + CH_4 \rightarrow CH_3^+ + H + 2e \quad (4)$$

$$e(15.1eV) + CH_4 \rightarrow CH_2^+ + H_2 + 2e \quad (5)$$

$$e + CH_4 \rightarrow H^+ + CH_3 + 2e \quad (6)$$

$$e(22.2eV) + CH_4 \rightarrow CH^+ + H + H_2 + 2e \quad (7)$$

$$e + CH_4 \rightarrow H_2^+ + CH_2 + 2e \quad (8)$$

$$e(25eV) + CH_4 \rightarrow C^+ + 2H_2 + 2e \quad (9)$$

Ionization and dissociation of N_2 molecule produces active molecular and atomic nitrogen species that may also play a significant role in the reaction kinetics:

$$N_2\left(X^1\sum g^+\right) + e(11.1eV) \rightarrow N_2\left(C^3\Pi u^+\right) + 2e \quad (10)$$

$$N_2\left(X^1\sum g^+\right) + e(15.63eV) \rightarrow N_2^+\left(X^2\sum g^+\right) + 2e \quad (11)$$

$$N_2\left(X^1\sum g^+\right) + e(16.84eV) \rightarrow N_2^+\left(A^2\Pi u\right) + 2e \quad (12)$$

$$N_2\left(X^1\sum g^+\right) + e(18.76eV) \rightarrow N_2^+\left(B^2\sum u^+\right) + 2e \quad (13)$$

$$N_2\left(X^1\sum g^+\right) + e(23.53eV) \rightarrow N_2^+\left(C^2\sum g^+\right) + 2e \quad (14)$$

3.3. Influence of the initial CH_4 content and specific input energy on the NH_3 and HCN formation

With increasing initial CH_4 content the concentrations of most of the products was found to increase. Except in case of 0.5% CH_4, NH_3 had the lowest concentration in all CH_4-N_2 mixtures. NH_3 concentration increased with increasing CH_4 content but in all cases it reached values between 200 and

350 ppm while HCN concentrations increased up to 1250 ppm proportionally to additional CH_4. This phenonema can be explained by the high density of active CN radicals within the glow region which consume the missing H atoms to produce HCN faster than the formation of NH_3. The rising density of these products can also be explained by the increasing density of electrons which is caused by the increasing current.

4. Conclusion

In this paper we present the results of FTIR study of stable gaseous products formed in atmospheric glow discharge fed by four different atmospheric pressure mixtures of N_2:CH_4 (0.5, 1, 1.5 and 2 % CH_4) operated in a flowing regime at different discharge currents (from 15 up to 40 mA) and ambient temperature. FTIR analysis of the gaseous products showed that HCN, C_2H_2, NH_3 are the main products of our CH_4/N_2 abnormal glow plasma. The yields of these compounds are such that HCN > NH_3 > C_2H_2. The discharge current has significant effect on the product synthesis. Such experiments can provide information that can aid our understanding of processes in Titan's atmosphere.

Acknowledgments. This research project was supported by: The Slovak Grant Agency, Slovak Research and Development Agency, Grant UK/140/2010, VEGA 1/0051/08, APVV 0365-07, ESF COST Actions CM0601, CM0805 and EIPAM TNA2. Research plan of Czech Ministry of Education No. MSM0021630501.

5. References

[1] S. Vinatier and 10 colleagues, Icarus **188**, 120-138 (2007).
[2] Bernard J M, Quirico E, Brissaud O, Montagnac G, Reynard B, McMillan P, Coll P, Nguyen M J, Raulin F and Schmitt B 2006 *Icarus* **185** 301.
[3] Pintassilgo C D, Loureiro J, Cernogora G and Touzeau M 1999 *Plasma Sources Sci. Technol.* **8** 463.
[4] Szopa C, Cernogora G, Boufendi L, Correia J and Coll P 2006 *Planetary and Space Science* **54** 394.
[5] Imanaka H, Khare B N, Elsila J E, Bakes E L O, McKay C P, Cruikshank D P, Sugita S, Matsui T and Zare R N 2004 *Icarus* **168** 344.
[6] Sekine Y, Imanaka H, Matsui T, Khare B N, Bakes E L O, McKay C P and Sugita S 2008 *Icarus* **194** 186.
[7] Coll P, Coscia D, Gazeau M C, de Vanssay E, Guillemin J C and Raulin F 1995 *Adv. Space Res.* **16** 93.
[8] Ponnamperuma C and Woeller F 1964 *Nature* **203** 272.
[9] Gonzalez R N and Ramirez S I 1997 *Adv. Space Res.* **19** 1121.
[10] Gonzalez R N, Ramirez S I, de la Rosa J G, Coll P and Raulin F 2001, *Adv. Space Res* **27** 271.
[11] http:// www.cfa.harvard.edu/hitran
[12] G Horvath, J D Skalny, N J Mason, M Klas, M Zahoran, R Vladoiu and M Manole 2009 *Plasma Sources Sci. Technol.* **18** 034016.
[13] Bai M, Zhang Z, Bai M, Bai X and Gao H *Plasma Chem Plasma Process* **15**(1):87–107.

DECOMPOSITION OF VOC IN SURFACE AND VOLUME DIELECTRIC BARRIER DISCHARGES COMBINED WITH IN SITU PHOTOCATALYZIS

J. Vyhnalíková, F. Krčma, R. Balaštíkova

Institute of Physical and Applied Chemistry, Faculty of Chemistry, Brno University of Technology, Purkyňova 118, Brno 612 00, Czech Republic

E-mail: xcvyhnalikova@fch.vutbr.cz

The problem of VOC's (volatile organic compounds) is one of the urgent tasks in contemporary research because VOC's vapors escaping into the air contribute significantly to the air pollution. Besides the classical techniques, the plasma assisted combustion methods are widely developed. The contemporary experiment was focused on the VOC decomposition in planar surface and volume dielectric barrier discharges using alumina ceramics. The photocatalytic TiO_2 was prepared by various techniques based on ink-jet printing on inner side of discharge ceramic plates. The exhaust gas analysis was carried out by simple gas analyzer Testo 350-XL that was used for the detection of simple low molecular weight discharge products as CO, NO_2, NO, H_2, etc. The analyses of discharge exhaust gas showed the high concentration of NO_2 and CO in all discharge configurations. The total concentration of non-combusted VOCs was slightly decreasing with the applied power increase. The TiO_2 catalyst induced the reduction down to about 50 %.

1. Introduction

VOCs (volatile organic compounds) are organic chemical compounds that have vapor pressures under normal conditions high enough to significantly evaporate and enter the atmosphere. They are sometimes accidentally released from the industrial processes into the environment, where they can damage soil and groundwater. Vapors of VOCs escaping into the air contribute significantly to the air pollution (e.g. they cause photochemical smog and also contribute to the global warming). In recent years, their influence on the quality of indoor environment has started to be a serious task, too. Common artificial sources of VOCs include paint thinners, wood preservatives or cleaning solvents. Regarding the medical risks, it is known that many VOCs are toxic, several of them are known as human carcinogens [1].

Conventional techniques for the abatement of VOCs, such as thermal and catalytic oxidation, are able to completely decompose the VOCs, but they suffer from the low energy efficiency given by the high operating temperature. The biological degradability of VOCs is also very problematic due to low concentration of VOCs in the gas phase. This degradation way is also impossible for many VOCs based on aromatic ring that could not be biologically destroyed. Technologies based on non-thermal plasmas could offer an alternative and they are capable to remove various pollutants in the gas phase [2]. The plasma decomposition process of VOCs is rather complex and the hydrocarbons are attacked in several ways. In the plasma reactor, the hydrocarbons are partly transformed into oxygenated compounds and into CO and CO_2. Unfortunately, undesirable toxic by-products can be formed.

Various non-thermal atmospheric plasma sources have been studied with respect to VOC destruction [2-4]. This study presents the first results obtained using recently developed surface discharge with in situ TiO_2 catalyst that is nowadays widely used mainly in the surface treatment processes [5].

The new method uses a volume dielectric barrier discharge, which burns throughout the discharge volume between the ceramic plates.

2. Experimental set up

The schematic draw of the experimental device is shown in Fig. 1. The discharge reactor consisted of a surface discharge electrode 10x10 cm^2 connected to the HF power supply. The Al_2O_3 plate covered or non-covered by TiO_2 photocatalyst in the distance of 2 mm above the electrode was installed to close the reactor volume. In case of volume DBD both the Al_2O_3 electrodes were covered on their inner side by TiO_2 photocatalyst, electrodes on their outer side were made of aluminum using PVD technique. The reactor side walls were made of Teflon with one fused silica window oriented in parallel to the gas flow through the reactor. The gas inlet into the reactor was realized by the system of equidistant holes (distance of 5 mm, i.d. 1 mm); the outlet was possible through the open electrode gap on the opposite side. This system guaranteed nearly homogeneous flow of the reacting gas mixture through the discharge.

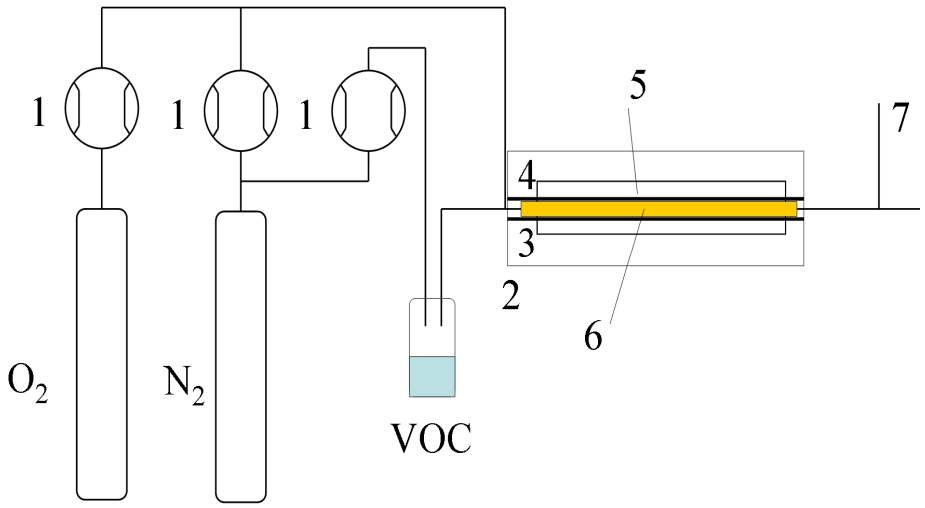


Fig. 1. Scheme of the experimental set up.
1 – mass flow controllers; 2 – Teflon discharge reactor; 3 – surface discharge electrode; 4 – Al_2O_3 plate; 5 – Quartz window; 6 – discharge; 7 – sampling point for the chemical analyzes.

The synthetic dry air was used as the carrier gas and it was enriched by the VOC (toluen) just in front of the reactor. VOC concentration in the reactor was constant at about 1 %. As carrier gas for VOC N_2 was used. Total flow was 4.5 l/s, velocity gas flow was 0.4 m/s and residence time was 0.2 s.
The exhaust gas analyses were caried out by the simple gas analyzer Testo 350 XL. It was used for the detection of low molecular weight discharge products as CO, NO_2, NO, H_2, only. Measurements were carried out by changing the frequency of discharge (= energy supplied to the discharge)[6].

Photocatalyst TiO_2
Layer was prepared according to the procedure by Klusot [7]. It is based on sol-gel process using reverse micelles (Triton TX102 in toluene). The precursor of TiO_2 was titane isobutoxid and his hydrolysis took place inside reverse micelles. The sol was printed using ink jet printer and after it was baked at 450°C.

3. Results and discussion

Surface dielectric barrier discharge

The determined concentrations of low molecular inorganic products as CO, NO_2, NO or H_2 are displayed. The analyses showed in the measurement without VOC a low concentration of CO, NO, H_2 and a high concentration of NO_2. After adding the VOC concentration of NO was decreased. Using a TiO_2 photocatalyst concentration of NO_2 was the lowest. The concentration of NO was a quantitation limit device in all measurements.

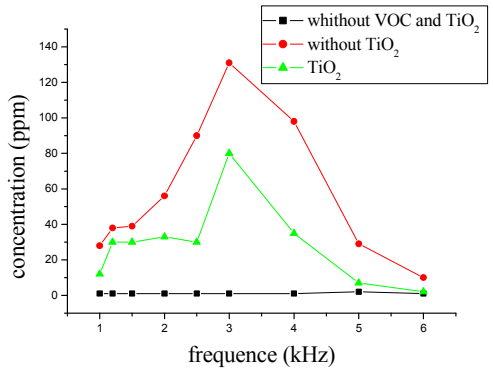


Fig. 2. Concentration of CO products generated by surface discharge in synthetic air with toluene.

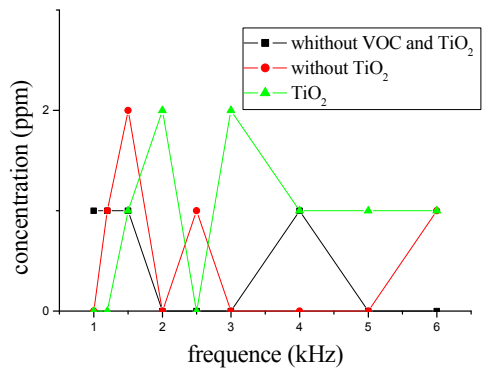


Fig. 3. Concentration of NO products generated by surface discharge in synthetic air with toluene.

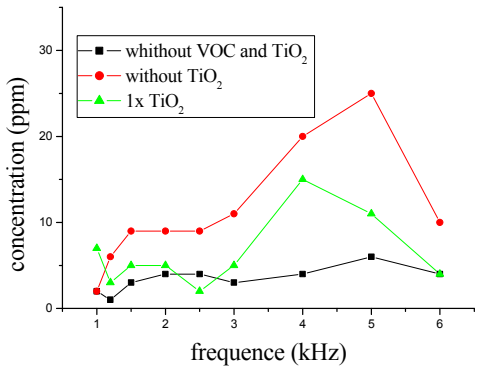


Fig. 4. Concentration of H_2 products generated by surface discharge in synthetic air with toluene.

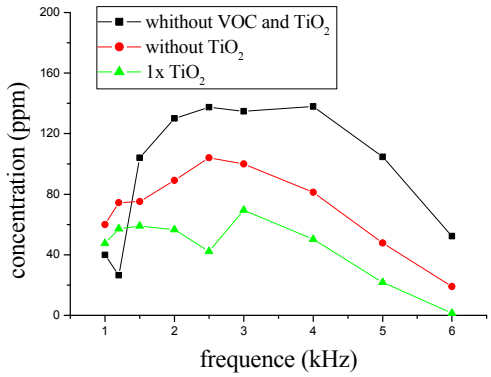


Fig. 5. Concentration of NO_2 products generated by surface discharge in synthetic air with toluene.

The photocatalyst significantly decreases the NO_2 generation in the discharge. If VOC is introduced, the NO_2 presence is smaller due to oxidation of VOC. The similar result was observed for the CO, NO and H_2 generation. The strong effect of TiO2 catalyst was observed. The total concentration of non-combusted VOC's was slightly decreasing with the applied power increase. The TiO2 catalyst induced the reduction down to about 50 %.

Surface versus volume dielectric barrier discharge

Graphs 6-9 show concentrations of low molecular inorganic products as H_2, CO, NO and NO_2 generated by surface and volume discharge in synthetic air with toluene.

The concentration of NO was a quantitation limit device in all measurements. In measurements using a surface discharge, concentrations of low molecular weights were higher, the concentration of CO was 130 ppm and the concentration of NO_2 was 110 ppm. In the volume discharge, concentration weights were significantly lower.

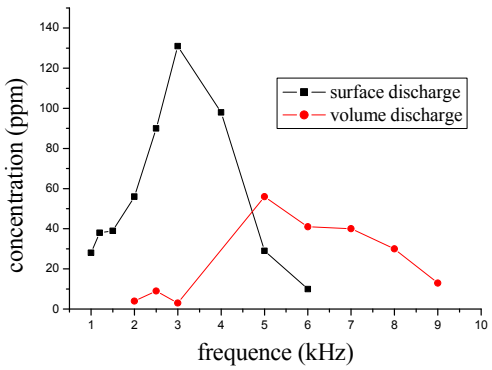


Fig. 6. Concentration of CO products generated by surface and volume discharge in synthetic air with toluene.

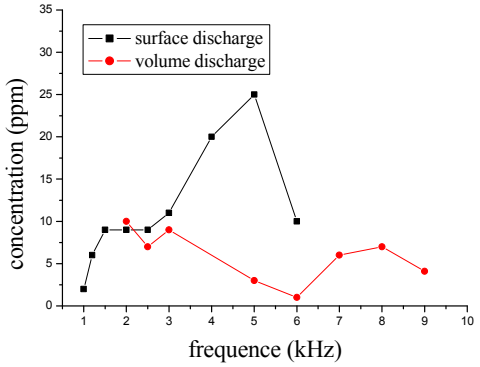


Fig. 8. Concentration of H_2 products generated by surface and volume discharge in synthetic air with toluene.

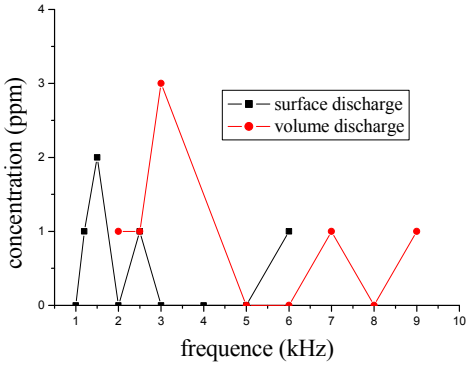


Fig. 7. Concentration of NO products generated by surface and volume discharge in synthetic air with toluene.

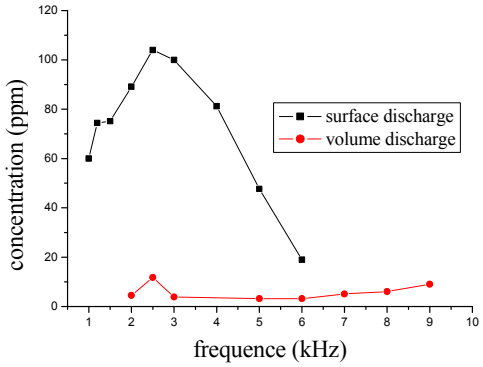


Fig. 9. Concentration of NO_2 products generated by surface and volume discharge in synthetic air with toluene.

The volume dielectric barrier discharge needs to be ignited by higher power than the surface discharge. The volume discharge induces the concentration reduction of low molecular inorganic products to about 50 %.

The first results show that the use of TiO_2 catalyst or volume discharge significantly reduced concentrations of low molecular inorganic products in the exhaust gases. In some cases, the concentrations of the substance were decreased by 50%.

4. References

[1] Jones S. P.: Atm. Envir. 33, 4533 (1999).
[2] Kim H. H.: Plasma Proces. Polymers 2, 91 (2004).
[3] Mutaf-Yardimci Ö., Savaliev A., Fridman A., Kennedy L. A.: J. Appl. Phys. 87, 1632 (2000).
[4] Fridman A., Gutsol A., Cho Y. I.: Adv. Heat Transf. 40, 1 (2007).
[5] Šimor M., Ráheľ J., Černák M., Imahori Y., Štefečka M., Kando M.: *Surf. Coat. Technol*. 172, 1 (2003).
[6] Krcma F., Vyhnalikova J., Polachova L., Grossmanova H., Stara Z.: *VOC decomposition in surface discharge*, Chem. Listy 99, 1234 – 2345 (2008)
[7] Dzik P, Vesely M, Chomoucka J: Thin *layers of TiO2 prepared by ink printing*, Chemicke listy 102, s995-s998, 2008.

Topic 4
Ozone generation and applications

COMPARISON OF THE OZONE GENERATION EFFICIENCY BY TWO DIFFERENT DISCHARGE MODES OF DIELECTRIC BARRIER DISCHARGE

Naoki Osawa[1], Hiroyasu Kaga[1], Yoshihiro Fukuda[1], Shohei Harada[1], Yoshio Yoshioka[2], and Ryoichi Hanaoka[1]

[1]*Department of Electrical and Electronic Engineering, Kanazawa Institute of Technology*
[2]*Office of Industry-University Collaboration, Kanazawa Institute of Technology*
7-1 Ohgigaoka, Nonoichi, Ishikawa, 921-8501, Japan
E-mail: n.osawa@neptune.kanazawa-it.ac.jp

The Dielectric Barrier Discharge (DBD) is composed of many filamentary discharges (FDs), and it can be applied to ozone generation, gaseous pollution control etc. In our laboratory, we investigated efficient cleaning methods of diesel exhaust gas by DBD. From the results of numerical simulation of chemical reactions, a uniform discharge was expected to improve the efficiency of pollution control and also the ozone yield. Recently, we found that a DBD device using alumina as barrier material can generate an Atmospheric Pressure Townsend Discharge (APTD) in air. In this research, we setup two ozonizers with different discharge modes of FD and APTD, and compared the ozone yield. The experimental results showed that the ozone yield was higher by the FD mode than by the APTD mode in lower specific input energy region. However in the region that the specific input energy is larger than 420J/L, the APTD mode showed higher ozone yield than FD mode.

1. Introduction

A Dielectric Barrier Discharge (DBD) is composed of many filamentary discharges (FDs), and it can be applied to ozone generation [1], gaseous pollution control [2], surface treatments [3] etc. Regarding ozone generation and gaseous pollution control, various methods have been studied to improve the efficiency. In our laboratory, we investigated efficient cleaning methods of diesel exhaust gas by the DBD [2]. One of the investigations was a numerical simulation of chemical reactions. In literature [4], the conclusion was that the efficiency was governed by the diffusion process of radicals, which were generated in the very thin micro-discharge column. Therefore, a uniform discharge was expected to improve the efficiency of pollution control and also that of ozone generation. In 2006, we found that glow-like diffuse barrier discharge in air at atmospheric pressure was generated by use of acrylic resin as a battier material [5]. This discharge had interesting features. Namely, in this discharge, many small micro-discharges spread out all over the discharge area and it looks like a uniform discharge, but the current waveform had many pulses. Using this glow-like FD, NO removal experiments from diesel exhaust gas were carried out. As the results, the glow-like FD was found to increase the NO removal efficiency from 19g/kWh to 28g/kWh [5]. Recently, we found that an Atmospheric Pressure Townsend Discharge (APTD) in air or in oxygen was possible by using a simple DBD device consists of alumina barriers and plane electrodes. This discharge is uniform between electrodes and the current waveform has no pulses [6]. As far as we know, it has been a common sense among researchers that the APTD can only be generated in nitrogen gas, and it was very difficult to generate in gases containing oxygen [7]. Therefore, the generation of the APTD in air using a simple DBD device was a new finding. According to the result of the simulation study and the experimental study of pollution control, this uniform discharge is expected to increase the ozone yield.

In this study, we investigated the effect of discharge mode to the formation of ozone and also investigated whether the APTD in air can improve the ozone yield or not.

2. FD, glow-like FD and APTD in air

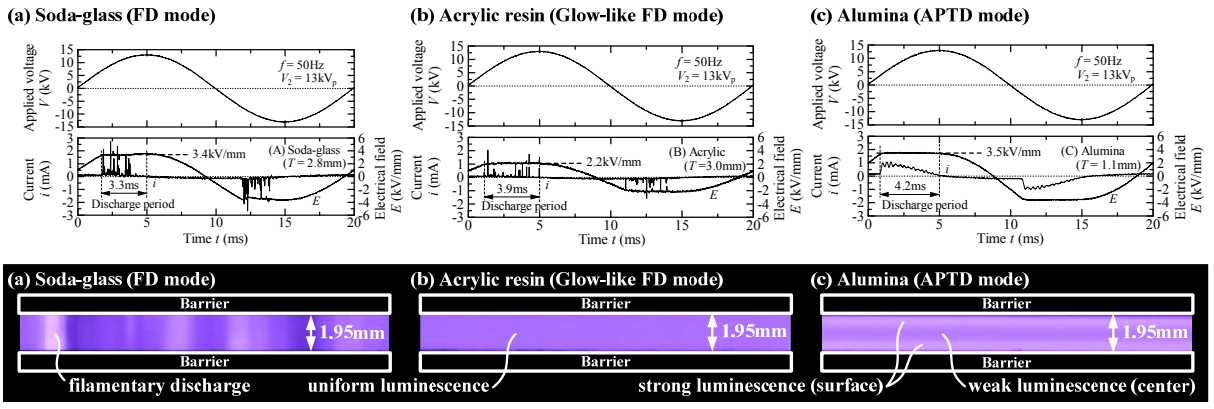
Here, we will introduce the FD, glow-like FD and APTD in air by a simple DBD device [8]. Experiments were carried out in air at atmospheric pressure. During this experiment, air was circulated in the discharge gap by use of a gas circulator. Barrier materials are soda-glass, alumina (Kyocera

A440), acrylic resin (PMMA) and alumina (Kyocera A473). They can generate the FD, glow-like FD or APTD. Thicknesses of barrier are 2.8mm, 1.1mm, 3.0mm and 1.1mm respectively. Their sizes are all 100cm^2. Features of barrier material and discharge are shown in Table 1. The gap length was fixed to 1.95mm. The gap voltage during discharge was calculated from the difference of voltages applied to the discharge device and to the barrier plates. The electrical field strength in the gap was calculated by dividing the gap voltage by the gap length.

Tab. 1. Discharge mode and barrier materials.

Discharge mode	FD (Filamentary Discharge)		(APTD) Atmospheric Pressure Townsend Discharge
Barrier material	Soda-glass / Alumina (Kyocera A440)	Acrylic resin	Alumina (Kyocera A473)
Discharge appearance	Filamentary (Fig. 1 (a))	Uniform (Fig. 1 (b))	Uniform (Fig. 1 (c))
Current waveform	Many pulse and intermittent flow		One pulse and continuous flow
Relative permittivity	7.8 / 9.8	3.8	9.0
Thickness (mm)	2.8 / 1.1	3.0	1.1

Fig. 1(a) (b) (c) shows the photographs of the FD, glow-like FD and APTD in air and waveforms of the voltage, gap voltage and current. In this experiment, the soda-glass, acrylic resin and alumina (Kyocera A473) were used as a barrier material and the voltage of 13kVp at frequency of 50Hz was applied to the DBD device. It is seen in Fig. 1(a) that when the soda-glass was used as barrier material, many FDs are generated in the discharge volume, and that the current waveform has many pulses. This discharge is a typical DBD. However, it is seen in Fig. 1(b) that when we used acrylic resin as barrier material, there were no FDs in the discharge volume and it looks like a uniform discharge. However the current waveform has many pulses like in Fig. 1 (a). Finally, it is seen in Fig. 1 (c) that when the alumina (Kyocera A473) was used as barrier material, the discharge becomes uniform and the luminescence near the barrier surface is brighter than in the central layer between barriers. As it can be seen in the oscillogram, the current has no pulse and flows continuously. In this research, the above stated three modes of barrier discharge were used to generate ozone.



(a) FD mode (b) glow-like FD mode (c) APTD mode

Fig. 1. FD, glow-like FD and APTD mode in air at atmospheric pressure.

3. Experimental setup and experimental conditions

Fig. 2 shows experimental setup for ozone generation. In this system, air was supplied by an air pump to a DBD type ozonizer. This system consists of a H.V. power source, a measurement system of electrical characteristics, air supply equipment, a DBD type ozonizer and an ozone monitor. AC high voltage was applied to the DBD type ozonizer by a step-up transformer. Frequency range of the applied voltage was from 50 to 600Hz, and the maximum applied voltage was 21kVp. The applied

voltage V and the current were measured by an oscilloscope (Tektronix 2024B, 200MHz, 2.0GS/s) using a H.V. probe (Pulse Electronic Engineering, EP-50K, 1/2000) and a differential probe (Yokogawa Electric Corporation, 700924, 100MHz) respectively. An integral of the current (charge q) was measured by measuring the voltage of a series (integral) capacitor. Besides, the discharge power was calculated by multiplying the area of V - q lissajous figure by power frequency. Ozone concentration was measured by an ozone monitor (Ebara jitsugyo, EG 2001-B and PG-320L). The experiments were carried out by changing the applied voltage and the frequency, and also by changing the flow rates. The flow rates were in the range from 2.0L/miin to 5.0L/min.

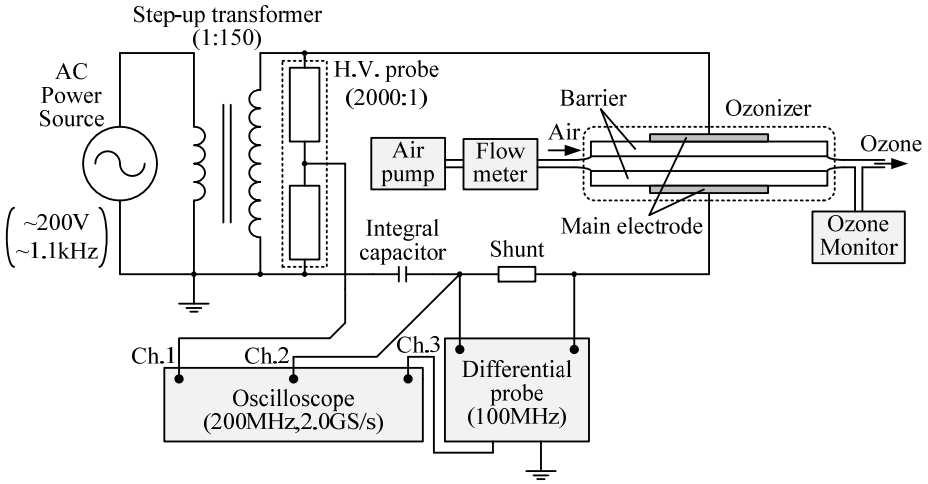


Fig. 2. Experimental setup.

4. Experimental results

The ozone concentration and the ozone yield were plotted against a specific input energy. Here, the specific input energy is the energy input to a unit gas volume, namely it is a ratio of the discharge power to the gas flow rate. Fig. 3 shows the ozone concentration by different discharge modes. In this figure, it is seen that the ozone concentration increased with the increase of the specific input energy. At the specific input energy of 150J/L, ozone concentrations were in the range from 600ppm to 660ppm by both FD mode (soda-glass and A440 alumina) and glow-like FD mode (acrylic resin). On

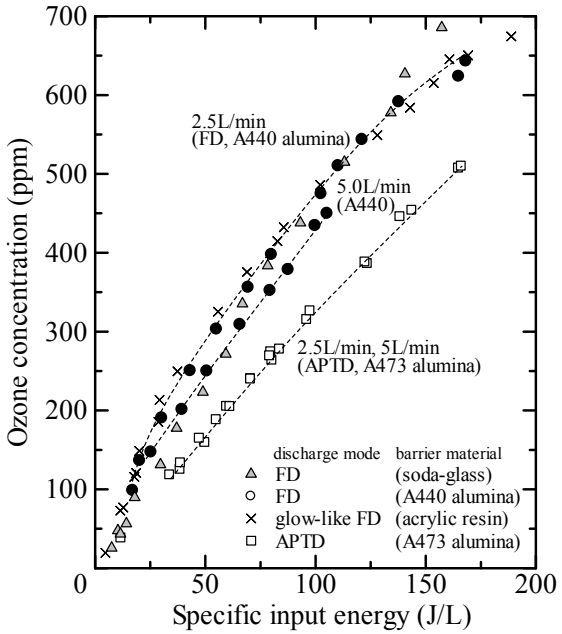


Fig. 3. Ozone concentration versus the specific input energy for different discharge mode.

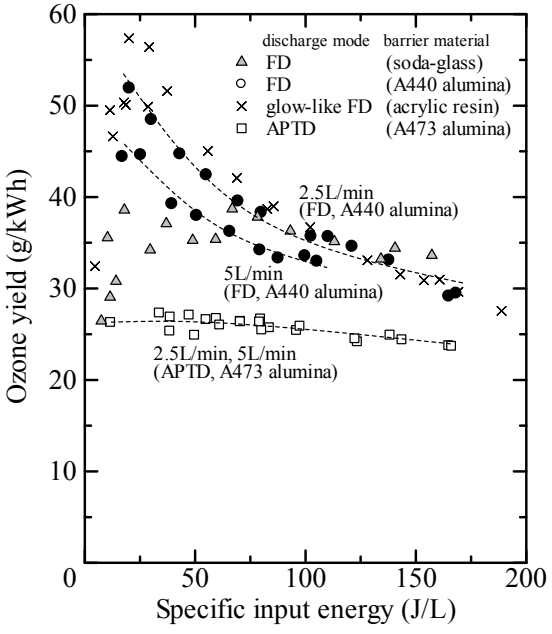


Fig. 4. Ozone yield versus the specific input energy for different discharge mode.

the other hand, the ozone concentration was 467ppm by the APTD mode (A473 alumina). Therefore, it is apparent that the ozone concentration was higher by the FD mode (glow-like FD mode) than by the APTD mode. It is also seen that as for FD mode, the ozone concentration at the flow rate of 2.5L/min was higher than that at the flow rate of 5.0L/min. On the other hand, as for APTD mode, the ozone concentration was not influenced by the air flow rate. Fig. 4 shows the ozone yield by different discharge modes. In this figure, it is seen that the maximum ozone yields obtained by the FD mode at the specific input energy at 20J/L were 39g/kWh (soda-glass) and 52g/kWh (A440 alumina) respectively. As for glow like FD mode, the ozone yield increased with the increase of specific input energy and it attained to 57g/kWh at 20J/L. After the ozone yields of both FD and glow-like FD modes attained to the maximum values, they began to decrease rapidly with the increase of the specific input energy. On the other hand, as for the APTD mode, the maximum yield was 27g/kWh at 40J/L, however the decrease of the ozone yield at higher specific energy was slight. From these experimental results, if the specific input energy becomes very high, the ozone yield by APTD expected to become higher than that of by FD and by glow-like FD. In order to confirm this expectation, the ozone concentration and the ozone yield in the high specific input energy region were investigated.

In this experiment, A440 alumina and A473 alumina were used as barrier material, and the air flow rate was fixed to 2.0L/min. Fig. 5 shows ozone concentration by two discharge modes. As for FD mode, the ozone concentration increased with the increase of the specific input energy, however, the saturation was appeared at the specific input energy of 130J/L. The maximum ozone concentration of 1,100ppm was obtained at 550J/L. As for APTD mode, the ozone concentration increased linearly with the increase of the specific input energy and it attained to 1,500ppm at the specific input energy of 630J/L. The ozone concentration by use of the APTD became higher than that of by use of FD over the specific energy of 410J/L. Fig. 6 shows the ozone yield obtained by the two discharge modes. As for FD mode, the maximum ozone yield of 52g/kWh was obtained at the specific input energy of 25J/L, however it decreases with the increase of specific input energy, and it attained to the minimum value of 17g /kWh at 550J/L. As for APTD mode, the ozone yield increased with the increase of specific input energy and it attained to 23g/kWh at 15J/L. Although it decreased slightly with the further increases of specific input energy, the ozone yield was maintained as 19g/kWh at 630J/L which is larger than that obtained by FD mode.

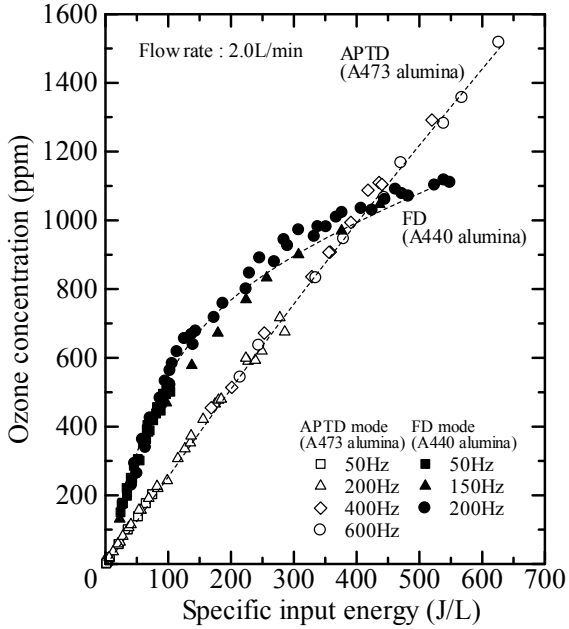


Fig. 5. Ozone concentration versus the specific input energy by APTD and FD.

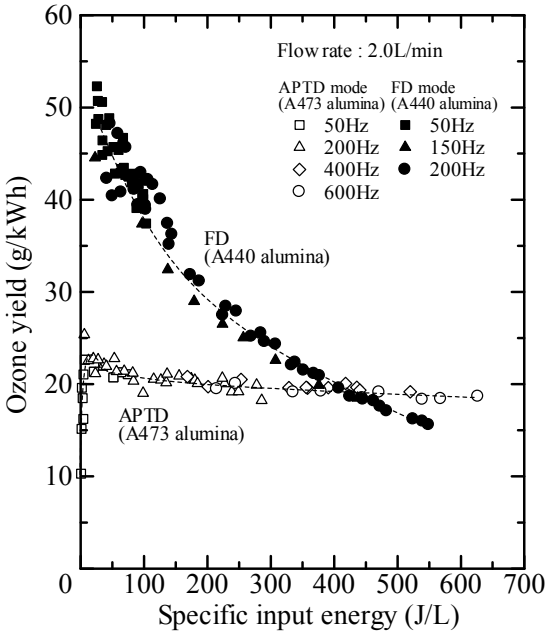


Fig. 6. Ozone yield versus the specific input energy by APTD and FD.

5. Discussions

Here, we discuss why the ozone yield by APTD mode becomes lower than that of by FD mode in a low specific input energy region. The reason seems to be as follows. FD mode was consists of many filamentary micro-discharges (streamer discharges). The electrical field strength at the streamer head

is very high. Therefore the electrons get very high energy and dissociates O_2 molecule into O radicals effectively. However, because the APTD is not a streamer discharge, the electrical field strength in an APTD is quite lower than the local electrical field in a FD. Therefore the electrons cannot get enough energy to dissociate O_2 efficiently. Next, why did the ozone yield by the FD mode decrease with the increase of the specific energy and becomes lower than that of by the APTD mode? We are now thinking that the high specific input energy enhances a destruction of ozone under higher ozone concentration by the collisions between high energy electrons and ozone molecules.

6. Conclusions

We set up DBD type ozonizers with different discharge modes to investigate the effect of discharge mode to ozone generation, and investigated whether the APTD in air can improve the ozone yield or not. The experimental results obtained are as follows;

(1) As for FD mode and glow-like FD mode, the maximum values of ozone yield obtained were 39g/kWh (soda-glass), 52g/kWh (A440 alumina) and 57g/kWh (acrylic resin) respectively at the specific input energy of 20J/L, however they decreased with the increase of the specific input energy and, as for A440 alumina, it attained to 17g /kWh at 550J/L.

(2) As for APTD mode, the ozone yield increased with the increase of specific input energy and it attained to 23g/kWh at 15J/L. It decreased slightly with the further increases of specific input energy, however the decrease was slight and it maintained 19g/kWh at 630J/L.

(3) In summary, the ozone yield was higher by the FD mode and by the glow-like FD mode than by the APTD mode in the low specific input energy region. However in the high specific input energy region, the ozone yield by APTD mode is higher than that by FD modes.

Acknowledgments. Authors would like to thank Ms. Ami Takashi and Mr. Yuuki Nakai for assistance with the experiments.

7. References

[1] Eliasson B. and Kogelschatz U., 1991 *IEEE Trans. on Plasma Sci.*, Vol. 19, No. 6, 1063-1077.
[2] Yoshioka Y., 2007 *Int. J. Plasma Environmental Sci. and Technol.*, Vol. 1, No. 2, 110-122.
[3] Aubrechet L., Pìchal J. and Koshelyev H., 2004 *Int. conf.Gas Discharge and Their Appl. (GD2004)*, Vol. 1, 231-234.
[4] Yoshioka Y. and Shoyama T., 2004 *9th Int. Symp. on High Pressure and Low Temperature Chemistry (HAKONE 9)*.
[5] Yoshioka Y. and Shoyama T., 2006 *10th Int. Symp. on High Pressure and Low Temperature Chemistry (HAKONE 10)*, 217-220.
[6] Osawa N., Yoshioka Y., Mochizuki Y., Kobayashi Y., Yamada Y. and Hanaoka R., 2009 *Proc. of 19th Int. Symp. on Plasma Chemistry (ISPC-19)*, P1.3.02.
[7] Gherardi N., Naudé N., Es-sebbar Et., Enache I., Caquineau H. and Massines F., 2006 *10th Int. Symp. on High Pressure and Low Temperature Chemistry (HAKONE 10)*, 21-24
[8] Osawa N., Yoshioka Y., Hanaoka R., Mochizuki Y., Kobayashi Y. and Yamada Y., 2010 *IEEJ Trans. FM*, Vol. 130, 306-312.

NON TRADITIONAL APPROACHES LEADING TO ENHANCED OZONE GENERATION

Stanislav Pekárek

Czech Technical University in Prague, Faculty of Electrical Engineering, Technická 2
166 27 Prague 6, Czech Republic
E-mail: pekarek@fel.cvut.cz

We have tested new approaches to enhance discharge ozone production. These approaches are based on the 1) application of ultrasound waves on the discharge, 2) application of the magnetic field on the discharge and 3) placement of TiO_2 photocatalyst in the discharge region. For experiments we used hollow needle to plate (mesh, cylinder) negative corona discharge with supply of air into the discharge through the needle. We found that application of ultrasound waves on the discharge about 70 % increases maximum ozone concentration; application of the magnetic field on the discharge about 30 % increases maximum concentration of produced ozone and finally placing TiO_2 photocatalyst on the mesh electrode more than 6 times increases maximum ozone concentration.

1. Introduction

The ozone production by electrical discharge in air is given by a dynamic balance of competitive reactions leading to its production as well as to its destruction [1]. Traditional approaches of ozone production enhancement use namely the effect of temperature or discharge energetization [2]. In contrast to these approaches, we have tested new ideas to enhance discharge ozone generation. These ideas are based on the 1) dependence of reaction rates of ozone formation processes on pressure, 2) application of the magnetic field on the discharge and 3) placement of the TiO_2 photocatalyst in the discharge region. For experiments we used hollow needle to plate (mesh, cylinder) negative corona discharge with supply of air into the discharge through the needle.
All experiments described in this paper were performed with the experimental arrangement, which consisted of a discharge chamber, an electric power supply with electrical parameters diagnostics, air supply system and ozone concentration monitor. Particular experiments differed only by the construction of the discharge chamber and the type of the external field or catalyst used.

2. Ozone production enhancement by ultrasound waves

The first approach which we have tested is based on the application of ultrasound waves on the discharge [3]. In this approach we created a standing waves pattern in the discharge chamber. Associated increase or decrease of pressure in the region of the discharge where the ionisation processes are effective should affect the discharge ozone production.

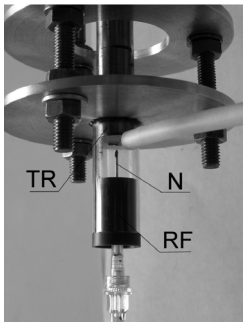


Fig. 1. Discharge chamber in the ultrasonic resonator.

The experiments were performed with the discharge chamber - or in other words with an ultrasonic resonator cell - shown in Fig.1. Stainless steel hollow needle **N** passes through the surface of reflector

RF situated against the plane surface of the ultrasound high power transducer TR. The needle is used as a cathode and grounded transducer surface serves as an anode. The resonant frequency of the transducer is 20.3 kHz. Changing the amplitude of the ultrasound transducer surface vibrations changes the intensity of ultrasound waves. The results presented in Fig. 2 are for the ultrasound transducer surface vibrations amplitude 38 μm, distance between the tip of the needle and the plate 4 mm and for airflowrate 5 slm.

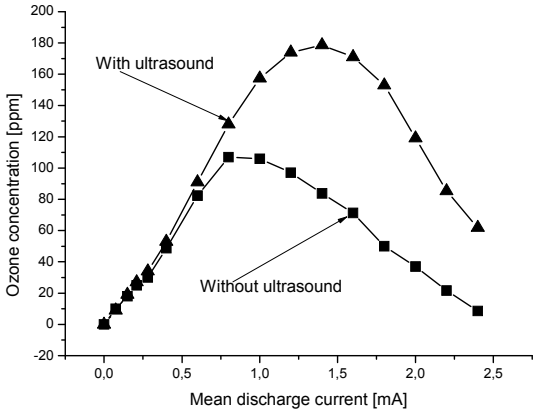


Fig. 2. Concentration of ozone versus mean discharge current, airflowrate 5 slm.

From Fig. 2 can be seen can be seen, that in case when no ultrasound is applied maximum of ozone concentration slightly exceeds 100 ppm and when the ultrasound applied the maximum ozone concentration produced by the discharge increases to about 180 ppm.

3. Ozone production enhancement by magnetic field

Another approach, which we tested for the discharge ozone production enhancement involves applying a magnetic field, produced by permanent magnets, to the discharge [4]. The magnetic field affects motion of electrons, their paths is curved, lengthened, ionisation is enhanced and therefore the discharge performance is affected.

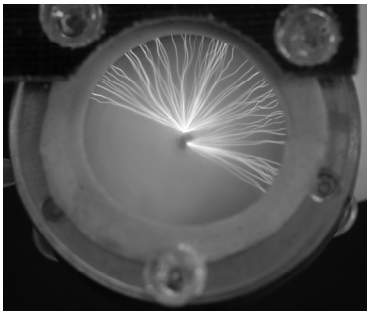


Fig. 3. Discharge in the cylindrical discharge chamber. Discharge voltage 12.3 kV, mean discharge current 0.6 mA, airflowrate 3 slm.

The experiments were performed with a cylindrical discharge chamber, made of non-magnetic materials. As the first electrode – a cathode – we used a stainless steel hollow needle placed at the axis of the cylindrical ring that formed the second electrode – an anode. This brass ring formed the outer wall of the discharge chamber see Fig. 3. The end of the needle was sharpened from two opposite sides so that the end of the needle in the discharge chamber had two tips.
The vector of magnetic induction was perpendicular to the vector of current density. The magnetic induction at the centre of the discharge tube was 0.55 T.

The effect of magnetic field on concentration of ozone produced by the discharge is shown in Fig.4. It is seen that for the low currents magnetic field has no substantial effect on the concentration of ozone that is produced, but application of the magnetic field increases about 30 % maximum ozone concentration. The magnetic field plays important role in ozone production namely for higher currents.

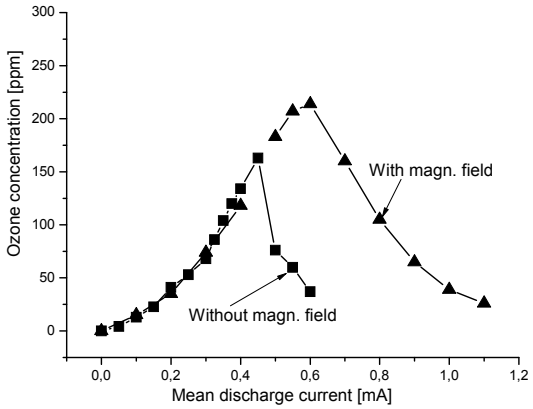


Fig. 4. Concentration of ozone versus mean discharge current, airflowrate 3 slm.

We also found that the magnetic field does not substantially increase the maximum ozone production yield. A major advantage of using a magnetic field for this purpose is that the increase in ozone concentration produced by the discharge can be obtained without additional energy requirements.

4. Ozone production enhancement by TiO_2 photocatalyst

In our third approach we studied enhancement of ozone production of the hollow needle to mesh negative corona discharge with TiO_2 photocatalyst on the mesh [5]. The TiO_2 is a *n*-type semiconductor with the width of the forbidden band of 3.2 eV, which corresponds to the wavelength of 388 nm. When the TiO_2 is illuminated by UV radiation coming from de-excitation processes in the discharge the electron from the valence band is promoted to the conduction band and an electron-hole pair is created. The consecutive processes induced by this TiO_2 photoexcitation lead to the production of active oxygen species, which subsequently enter the chain of reactions leading to the ozone generation.

Photograph of the discharge with a layer of TiO_2 globules on the mesh for the distance between the tip of the needle and the mesh 12 mm, is shown in Fig.5.

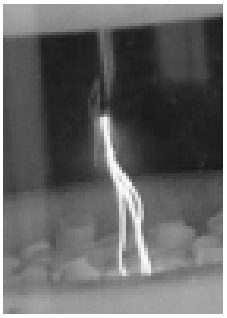


Fig. 5. Discharge with a layer of TiO_2 globules on the mesh. Discharge voltage 13.1 kV, mean discharge current 0.4 mA, airflowrate 1.5 slm, m_{TiO2}=0.7691 g.

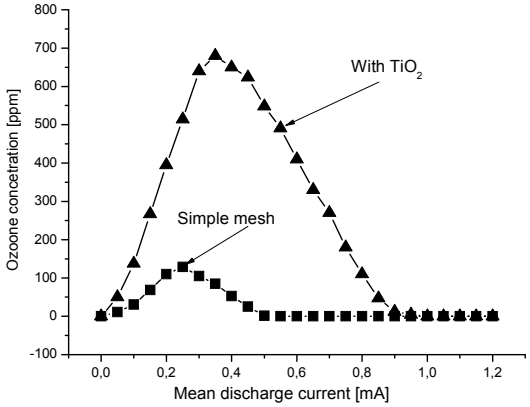


Fig. 6. Concentration of ozone versus mean discharge current, airflowrate 1.5 slm, m_{TiO2}=0.7691 g.

The effect of TiO_2 photocatalyst on the mesh on concentration of ozone produced by the discharge is shown in Fig.6. From this figure can be concluded that for particular current addition of TiO_2 photocatalyst on the mesh electrode drastically increases maximum concentration of ozone produced by the discharge.

5. Conclusions

We performed comparison of ozone production by negative corona discharge in air for the case when we applied on the discharge ultrasound waves, magnetic field and finally we placed TiO_2 photocatalyst in the discharge region.

We found that applying an ultrasound field on the discharge about 70 % increases maximum concentration of produced ozone. However, the use of ultrasound for discharge ozone generation enhancement in real applications is not worthwhile because the energy is required for ultrasound generation. If this energy is included in the calculation of the ozone production yield, the yield is decreased to very low values.

We also found that application of the magnetic field increases about 30 % maximum ozone concentration that is produced by the discharge. From the standpoint of energetic requirements the magnetic field does not substantially increase the maximum ozone production yield.

The best results were however obtained when we placed a TiO_2 photocatalyst in the discharge region. In this way it is possible to obtain not only substantial increase of concentration of produced ozone but also ozone production yield.

Acknowledgement. This research was supported by the Czech Science Foundation grant under contract No. 202/09/0176.

6. References

[1] Kogelschatz U, Eliasson B and Hirth M 1988 *Ozone Sc. & Eng*. **30** 367.
[2] Masuda S, Akutsu K, Kuroda M, Awatsu Y, Shibuya Y 1988 *IEEE Trans. on Ind. Appl.* **24** 223.
[3] Pekárek S and Bálek R 2004 *J. Phys. D: Appl. Phys.* **37** 1.
[4] Pekárek S 2010 *Eur. Phys. J. D* **56** 91.
[5] Pekárek S 2008 *Eur. Phys. J. D* **50** 171.

INVESTIGATION OF OZONE ZERO PHENOMENON USING NEW ELECTRODE AND SURFACE ANALYSIS TECHNIQUE

Masaki Taguchi[1], Yusuke Ochiai[2], Ryuzo Kawagoe[2], Yasuhiro Kato[1], Kenji Teranishi[3], Susumu Suzuki[2] and Haruo Itoh[2]

[1]*R&D Center, Metawater Co. Ltd, Chiba 290-8511 Japan*
[2]*Graduate School, Chiba Institute of Technology, Chiba 275-0016 Japan*
[3]*Institute of Technology and Science, The University of Tokushima, Tokushima 770-8506 Japan*

Results of our experimental investigation on the ozone zero phenomenon (hereafter denote: OZP) suggested us the importance of the electrode surface condition.
This means that the main cause of the OZP, that is, temporal decrease of ozone concentration at the outlet of DBD type ozone generator and the recovery characteristics from the OZP are considered as the surface reaction process, which are influenced strongly by the surface condition. The surface condition is never constant during the ozone generation and varies gradually or remarkably with time depending on the experimental conditions.
Therefore we have been continued to make clear the cause of the OZP, for example, the reproducibility of the OZP, using new electrodes and together with the surface analysis technique etc.
In this paper, we describes on the above results and discussion.

1. Introduction

Studies have been widely conducted on oxygen-fed ozone generators to improve their ozone generation efficiency. Ozone is used in diverse fields, traditional and new, ranging from water and sewage treatment to medical field and semiconductor-manufacturing machinery. Semiconductor manufacturing requires the use of impurity-free ozone gas. Therefore, high purity oxygen is used in this field to generate ozone gas. Inconveniently, however, it has been observed that the ozone concentration in high purity (99.99995 percent-pure) oxygen-fed ozone generators rapidly drops from the initial level to almost zero. This phenomenon is known by the name of *Ozone Zero Phenomenon* (hereafter denote: OZP). Many studies have been conducted to identify possible causes of OZP, and we reported at the latest Hakone XI [1][2] on findings that suggested that one of the possible causes of OZP is influences from the electrode surface.
This time, we continuously operated a 99.99995 percent-pure oxygen-fed ozone generator fitted with new metal electrodes even after the occurrence of OZP to examine the subsequent behavior of the phenomenon. In addition, we analyzed samples taken at the maximum, medium, and minimum ozone concentration points (during OZP) and at a post-OZP ozone concentration recovery point to investigate the condition of the electrode surface over operation time. This paper presents the findings and discussions of our above-described investigation.

2. Experimental setup

The experimental setup is shown in Figure 1, and the experimental condition is shown in Table 1. We used 99.99995 percent-pure oxygen gas for this experiment. Most of the gas lines were made of stainless steel (material), but the pipes installed close to the ozone generator were made of Teflon for insulation. Before the experiment, the pipe between the gas cylinder and the ozone generator was subjected to several cycles of vacuum-pumping and purging with high purity oxygen. A mass flow controller was provided to control the flow rate of high purity oxygen gas to the ozone generator. An ozone monitor was installed to measure the generated ozone, which was reduced into oxygen by an ozone destructor before final release into the atmosphere. A water-cooled chiller was provided to cool the high voltage electrodes and ground electrodes on the ozone generator during operation. Thermocouples (K-type) for the gas temperature monitor were placed in the gas inlet and outlet of the ozone generator.

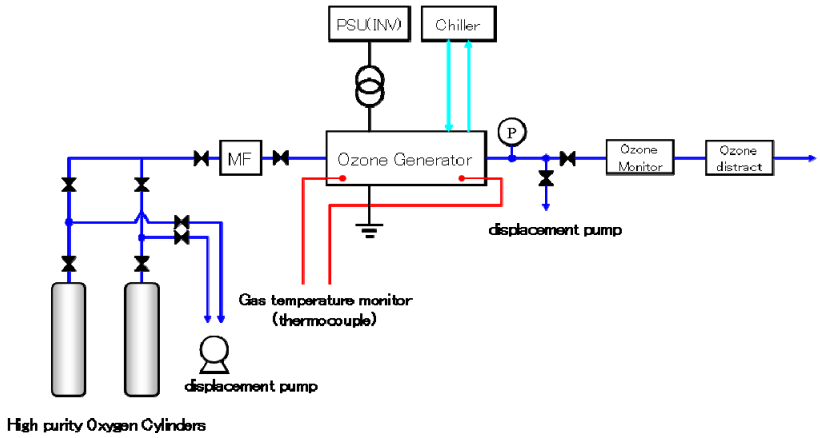


Fig. 1. Experimental Setup

Tab. 1. Experimental Condition

Items	Condition 1	Condition 2	Condition 3
W/S (W/cm^2)	0.1	0.2	0.3
Gas Flow rate (L/min)	1	2.2	3.35
Gas Pressure (MPaG)	0.05		
Gap length (mm)	0.3		
Cooling Water Temperature (ºC)	10		
W/Q (Wmin/L)	200		

3. Results of the experiment and discussion

3-1. Review of the results of the previous studies

In the course of our experiment on OZP, we found that the ozone concentration decreased to varying degrees. Interestingly, the ozone concentration was observed to decrease considerably, but not down to zero. Seeking clues for the cause of the phenomena, we reviewed experimental conditions and results reported in published papers. The rate of decrease in ozone concentration is defined by Equation (1), and results of the investigation are shown Table 2.

$$Cd = (Cimax - Cmin) / Cimax \times 100\ (\%) \ldots (1)$$

Cd (%): rate of decrease in ozone concentration

Cimax (g/Nm^3): initial maximum ozone concentration

Cmin (g/Nm^3): minimum ozone concentration (ozone zero phenomenon)

Tab. 2. Comparison of the Results of the Preceding Experiments

Items	Reference ① [3]	Reference ② [4]	Latest results [5]
Initial max ozone conc	200 g/Nm^3	200 g/Nm^3	262 g/Nm^3
Min ozone conc	1-2 g/Nm^3	50 g/Nm^3	104 g/Nm^3
Rate of decrease in ozone conc	99.5%	75%	60.3%
W/Q	142.6 Wmin/L	145.5 Wmin/L	200 Wmin/L
W/S	0.3 W/cm^2	0.2 W/cm^2	0.1 W/cm^2

The comparison suggested that the two parameters of W/Q and W/S (W: discharge power, Q: flow rate, S: discharge area) were instrumental in the increase in the rate of decrease in ozone concentration. We reported earlier at the Hakone XI [1] conference that the experimental results suggested that one of the possible causes of OZP might be the influence from the electrode surface. Considering that W/S might be an important supporting parameter for our hypothesis, we conducted experiments this time with an investigative focus on W/S.

3-2. Results of the present study

The results of the experiment conducted for the present study are shown in Figure 2 and Table 3. Decreasing ozone concentrations were observed immediately after the start of the ozone generator under all the experimental conditions with the electric discharge power density W/S at 0.1, 0.2, and 0.3 W/cm^2. As shown in Figure 3, the rate of decrease in ozone concentration increased with the increase in the electric discharge power density W/S. The rate of decrease in ozone concentration reached and even exceeded 97% when W/S was at and above 0.2 W/cm^2. The minimum ozone concentration tended to be reached faster when W/S was greater. A theoretical explanation for the fact that OZP occurred differently depending on W/S is probably given by a possibility that the higher levels of W/S accelerated the modification of the metal electrode surface, thereby preventing ozone generation or promoting decomposition of ozone. Additionally, we found that continued operation of the ozone generator during occurrence of OZP led to the recovery of the ozone concentration (from almost zero level). The cause of this seems to have been that the progress of the above-mentioned modification of the surface of the stainless steel electrode resulted in full coverage of the electrode surface with metal oxide generated by the electrical discharge, followed by the effect of reduced ozone generation or accelerated ozone decomposition. After 90-to-100 hour continuous operation the ozone generator, the ozone concentration recovered differently depending on W/S. With W/S at and above 0.2 W/cm^2, the profile of the ozone concentration showed a shift from recovery to stability. Meanwhile, the ozone concentration recovered at slower rates with W/S at 0.1W/cm^2.

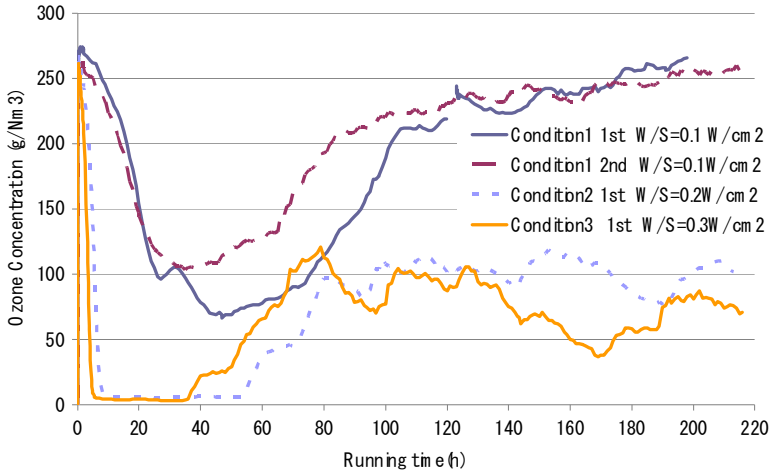


Fig. 2. Influence of W/S on occurrence of OZP

Tab. 3. Comparison of parameters with respect to discharge power density

Discharge power density W/S (W/cm^2)	0.1	0.2	0.3
Max ozone concentration (g/Nm^3)	272/262	268	261
Min ozone concentration (g/Nm^3)	67/104	6	4
Decreasing rate of ozone concentration (%)	75.4/60.3	97.8	98.5
Decreasing time of ozone concentration (h)	47/35	9	8

Based on these results, the surface of the stainless steel electrode was subjected to Auger electron spectroscopy to obtain its historical data for the period from the onset of OZP through the recovery the ozone concentration. Specific sampling points for the analysis of the surface of the stainless steel electrode are as follows and shown in Figure 3 as a profile of the ozone concentration:

(1) Maximum ozone concentration immediately after the start of the ozone generator
(2) Ozone concentration halved during operation of the ozone generator
(3) Minimum ozone concentration (when OZP occurs)
(4) Ozone concentration recovers to half the level of (1)

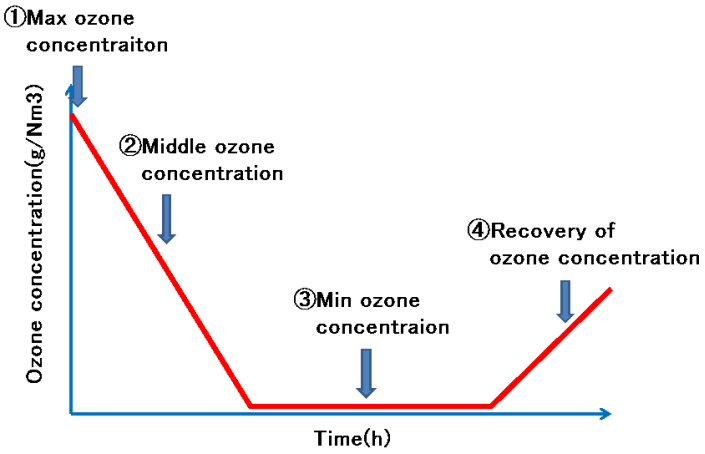
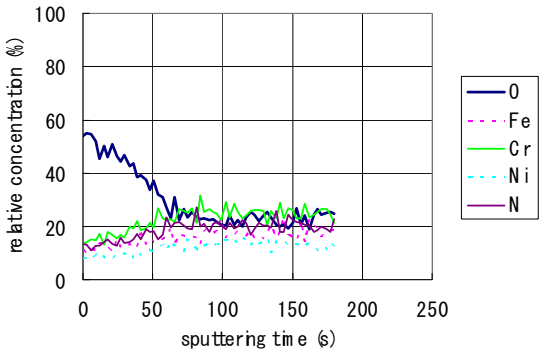
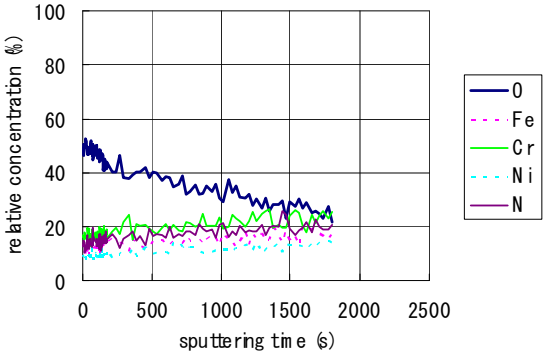
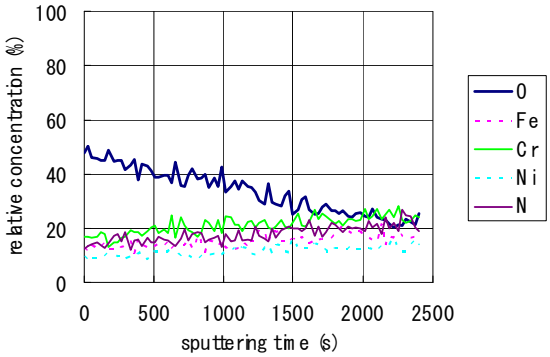


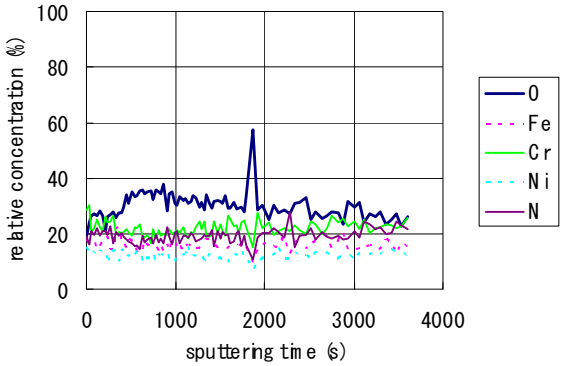
Fig. 3. Sampling points for surface analysis



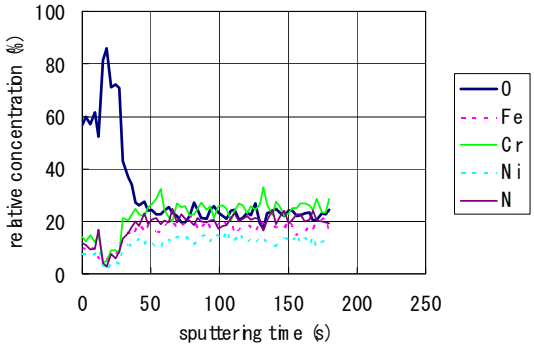


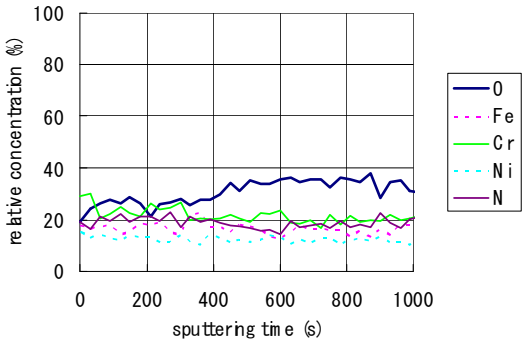
(1) Max Ozone Concentration (6-min point) (2) Middle Ozone Concentration (40-min point)





(3) Min Ozone Concentration (280-min point) (4) Post-Ozone Concentration Recovery





(5) Blank Sample (unexposed to ozone) (6) (4) of extended figure (time scale)

Samples for the surface analysis were made of stainless steel sheets (SUS304) with a thickness of 30 μm. Fitted closely on the stainless steel electrode, each sample was exposed to ozone generated by the ozone generator. When any of the prescribed ozone concentration points was reached under the specified conditions, the samples were taken out for analysis. Each sample was analyzed for three kinds of metals (Fe, Ni, and Cr), oxygen, and nitrogen. The results of the analysis are shown in Figure 4. A comparison of the profiles in Figures 4(1) to (3) revealed that the profiles of iron, chromium, and nickel — the primary materials of the stainless steel electrode — behaved quite similarly. For oxygen, the profile of relative density in the direction of depth in Sample (1) did not significantly differ from the profile of Sample (5) (blank sample). This is because the ozone generator ran only 6 minutes for Sample (1). For Samples (2) and (3) subjected to continuous operation of the ozone generator, however, it was observed that the relative density of oxygen in the direction of depth from the metal surface gradually decreased over the elapsed time of operation of the ozone generator. This occurred probably because during the operation of the high purity oxygen-fed ozone generator, the oxidizing reaction advanced from the surface of the stainless steel in the direction of depth due to both the effect of the electrical discharge and the oxidizing powers of ozone and oxygen. Very interestingly, this tendency was quite similar to that reported last time. The profiles of Sample 4 taken at the post-OZP ozone concentration recovery point differed from those observed with other samples. Unlike in the cases of Samples (1) to (3), the relative density of oxygen near the surface of stainless steel decreased, and the relative density of chromium increased. The results of this analysis suggest that the change in the composition of the surface of the stainless steel was instrumental in the prevention of the persistence of OZP. Further investigations are required to determine whether the prevention of OZP depended on the oxygen density on the surface of the metal electrode, or on the density of chromium, or on some unknown factors other than them.

4. Conclusion

The findings of the present study are as follows:

1) The OZP depends on W/S (W: discharge power, S: discharge area). As W/S increases, the rate of OZP-induced decrease in ozone concentration also increases. This supports that the OZP depends on the condition of the surface of the metal electrode.
2) Continued operation of the ozone generator with W/S at a high level even after the occurrence of OZP causes the ozone concentration to recover from a low level.
3) The results of the surface analysis revealed that oxygen penetrated into the metal electrode from the surface during the presence of the OZP. From the detected relative oxygen concentrations, it was found that the longer the ozone generator ran, the deeper the metal electrode was penetrated with oxygen.
4) The results of the analysis of the metal surface showed that the proportions of chromium and nitrogen relative to oxygen were large after the recovery from OZP. Though oxygen was also observed to penetrate into the metal electrode from the surface, the oxygen concentration at the shallowest point in the metal electrode was significantly lower than when measured under different conditions.

5. References

[1] K. Murayama, N. Matsumura, M. Taguchi, Y. Katoh, K. Teranishi, S. Suzuki, and H. Itoh: HAKONE XI(France) Contrib. Pap., pp. 266-270 (2008)

[2] K. Murayama, N. Matsumura, M. Taguchi, Y. Katoh, K. Teranishi, S. Suzuki, and H. Itoh: Eur. Phys. J. Appl. Phys. 47, 22814 (2009)

[3] K Hashimoto, H Ishioka (2003). Ozone Generation Properties using High Purity Oxygen Gas, The Papers of Technical Meeting on Electrical Discharges IEE Japan ED-00-109 （2000） (in Japanese)

[4] M Taguchi, H Matsushita (2003). Properties of Ozone Generation using High Purity Oxygen Gas, The Papers of Technical Meeting on Electrical Discharges IEE Japan ED-03-153 (in Japanese)

[5] K. Murayama, Y. Ochiai, H. Kuragano, S. Suzuki, H. Itoh, K. Teranishi, M. Taguchi and Y. Katoh: IEE Japan., 1-098 (2010) (in Japanese)

OZONE-ZERO PHENOMENA AND A NITROGEN ADDITION EFFECT ON AN OZONE GENERATION

Chobei Yamabe, Sebastian Gnapowski, Kouji Kayashima and Satoshi Ihara
Department of Electrical and Electronic Engineering,
Graduate School of Science and Engineering, Saga University
E-mail: +81-(0)952-28-8648

A copper-rotating electrode coated by gold was used to eliminate the surface oxidation effect by discharge. The effect of electrode rotation during the ozone generation processes was observed. An ozone generator with a rotating electrode system might be one possible way to increase the efficiency of ozone-synthesis. The ozone concentration increased up to maximum about two times lager compared with the case of no rotation. The input power increased with the rotating speed and discharge area grew up too. Both the obtained ozone concentration and the ozone production efficiency with rotating electrode were improved compared with the case of no rotating electrode. The experimental data for a long time operation with the rotation of electrode and the nitrogen addition effect on ozone generation are presented. During the long time operation, some adsorbed particles such as nitrogen on the electrode surface seem to influence on the ozone production and the discharge onset voltage. Using the rotating electrode we could observe the ozone zero phenomena faster compared with no rotating electrode. Even though the electrical input power was almost same, the measured ozone concentration was big different.

1. Introduction

Recently the applications of ozone have spread widely and some their examples have been found in accordance with the development of the ozone generation technologies. Still the problems or tasks for the ozone generation and utilization technologies are the improvement of ozone generation efficiency (i.e. the reduction of electric cost for the ozone generation), getting the high ozone concentration (i.e. shortening the reaction processing time) under the stability of the ozone supply and making clear the byproducts after treated by ozone (i.e. safety for the human body).

In some field mentioned above applications, the ozone concentration is required to keep constant in the processing with ozone. During the supply of the ozone using pure oxygen, it has been reported that the ozone concentration has rapidly decreased, and some groups have started to find out this reason. It looks that this phenomena has been experienced at the major ozone generator industries and the temporal method to add the small amount of nitrogen to recover this sudden decrease ofozone concentration[1]-[3]. As concerns this strange phenomenon, it has not been widely reported due to the technological know-how. In recent years, P. Uhling, G.J. Pietsch et al. have reported in detail the influence of degree of purify of oxygen (≧99.5% ~ ≧99.99990%), argon content, addition ofnitrogen, water content and nitrogen dioxide admixture etc. on the efficiencyof the ozone generation [1]. According to this report, 1) the efficiency of the ozonegeneration with higher purity of oxygen is not always large compared with that obtained with lower purity of oxygen in the oxygen rich raw gas. 2) So far it has been made light of the behavior of the impurity in the raw gas for the ozone generation. 3) The kind of impurity and itsamount of value are the important condition whether the ozone generator can keep the stable long time operation. The mixture gas of N_2,
$CO_2$and NO_2has the effectiveness on the stability ofthe ozone generation. On the other hand, the rare gas such as argon and helium has no effect so much on the stable operation. 4) The impurity level by which the stable operation isobtained depends on the discharge form. 5) There is a maximum impurity level and above this level the efficiency of ozone generation decreases with the impurity level.

Therefore, it is very difficult to find a clear indication from these explanations about the reason for the suddenly decrease of the ozone generation. For this, a group of Takano and H. ITO et al. has carried out the experiments using two ozone reactors connected in series instead of conventional single reactor to observe the ozone zero-phenomena without discharge. The experimental discussions for the appearance and dissolution of the mechanism of the ozone-zero phenomena have been done and they have reached the following conclusions [4]. 1) It would be determined that the ozone-zero phenomena appeared during the operation of ozone generator is caused in the ozone generator due to the destruction of ozone produced by discharge in high pure oxygen (>99.9995%). 2) It was confirmed that this ozone-zero phenomena was dissolved to add the air or nitrogen etc. into pure oxygen. This method is a conventional way to dissolve it. 3) In the experiments in 2), only nitride oxide (NO_x) could dissolve simultaneously the ozone-zero phenomena with no discharge. 4) In the same way, the ozone-zero phenomena was also dissolved to add the oxygen, air and nitrogen etc into the raw gas including ozone, but both its recovery time and after recovered ozone concentration were long and small respectively. 5) After the ozone concentration recovered, the condition of it continues to keep the sable condition as far as no discharge occurs regardless the degree. 6) According to these results, it would be concluded that the ozone-zero phenomena caused from the change of electrode surface of the ozone generator. Considering the result that the nitride oxide (NO_x) was useful for the dissolution of the ozone-zero phenomena, the ozone-zero phenomena appeared when the nitride oxide (NO_x) didn't exist due to some important factor of the electrode surface. 7) It was also concluded that the ozone-zero phenomena occurred during continuous operation was a completely different phenomena from the decomposition of ozone by the temperature increase of the gas.

Murai A. et al have also reported on their following experimental results obtained in 99.5% oxygen for the improvement of the efficiency of the ozone generation [5][6]. It took for about a few months before the ozone-zero phenomena appeared using a needle-to-plane electrode whose gap distance was 3 mm. The discharge time for the ozone generation was about 200 hours and every time the reactor was filled with the oxygen when it was not operated. Both the applied voltage and discharge current were 2.2-4.0kV and 1-2 μ A. 1) It was shown that no generation of ozone (i.e. the ozone-zero phenomena) occurred by only discharge. 2) It was also confirmed that the ozone was generated whenthe nitrogen as the third particle was mixed with the oxygen which passed through the discharge region. 3) The ozone generation reaction progressed with the nitrogen, argon being absorbed on the electrode surface. Further, G. Sebastian, C. Yamabe et al. have confirmed thatthe ozone has been generated effectively due to some reaction(s) on the electrode surface when the ozone-zero phenomena appeared [7]-[9]. On the other hand, H. Itoh et al have reported the ozone loss rate for different materials such as stainless steel, copper and aluminum of a discharge chamber[10].

2. Experimental set up and procedure

2-1. A needle-to-plate electrode system

The experimental conditions are as follows. A fixed direct discharge current of 1 μ A was used in 99.6 % pure oxygen at the flow rate of 0.50 L/min.The experimental data were accumulated in the personal computer using a logger. At first, the discharge phenomena for the needle-to-plate electrode in pure oxygen were observed changing the gap distance. The ozone generation without spark was confirmed at the gap distance of 2.06 and 1.94 mm. In these cases, the applied voltage and discharge current were about 4kV and 1 μ A. After a long time operation of discharge for the conditioning of the reactor, it was possible to keep very low ozone concentration less than about 0.20ppm during the stable discharge.

Due to the drastic decreasing of ozone concentration during the long time operation it was confirmed to reach to the zero ozone concentration level. After the confirmation of these phenomena, the effect

of nitrogen addition on the change of ozone concentration was measured. In the experiments of nitrogen addition, both flow rate of oxygen and nitrogen were controlled by the mass flow meter keeping the discharge. The addition period of nitrogen gas was 30 minutes feeding the oxygen gas and after stop of the nitrogen addition the discharge continued only in oxygen for one hour. The experiments were repeated changing the nitrogen gas flow rate. In these experiments, the oxygen gas flow rate was fixed at 0.50 L/min and the gas flow rate of the adding nitrogen was changed from 2 to 50 ml/min (2, 5, 10, 15, 20, 25, 30, 35, 40, 45 and 50 ml/min).

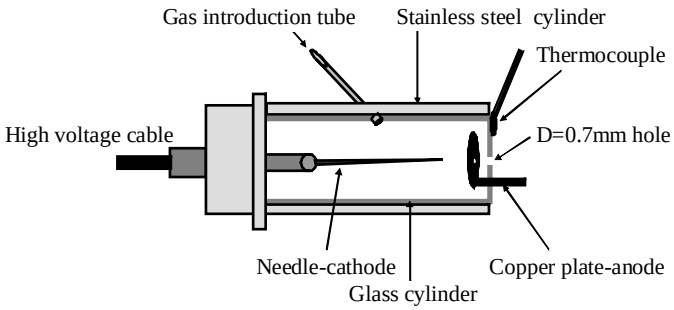


Fig.1 A needle-to-plate electrode system (Gap distance: 1.94mm)

2-2. A coaxial cylindrical type reactor with an inner rotating electrode

A rotating effect on the ozone generation has beenstudied using different material for the inner rotating electrode. The copper, brass and copper based gold electrodes were used for the experiments. Figure 2 shows the schematic diagram of the ozone generator (or ozonizer). The discharge gap distance was 1.1 mm and the discharge length along the reactor was 100 mm. The dielectric barrier covered by a mesh electrode was glass tube whose length, diameter and thickness was 110 mm, 15 mm and 1.25 mm. The outer mesh electrode made from copper wires with diameter of 0.1 mm was grounded. The size of the copper mesh electrode was about 0.2 mm square.

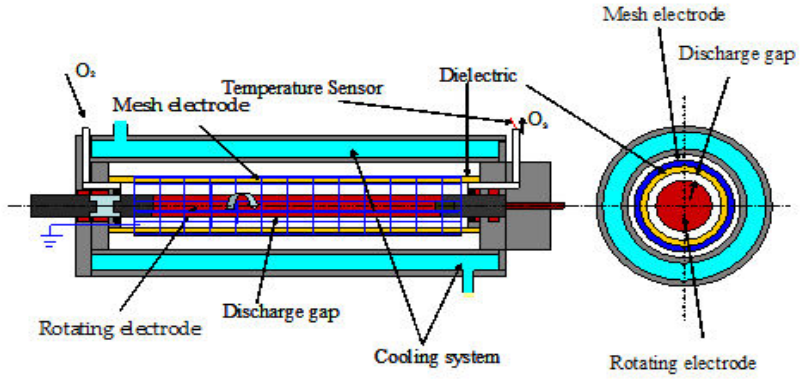


Fig.2 Schematic diagram of ozonizer with an inner rotating electrode.

A 99.5 % oxygen gas regulated by the digital mass flow controller was fed and the gas flow rate was in the range from 0.5 l/min to 2 l/min. Both the applied voltage and its frequency were set to be 9-10 kV and about 12 kHz. The gas temperature at the outlet of the ozone generator was measured during the experiments. These measured data were saved every day in a computer. All experiments were carried out at atmospheric pressure in pure oxygen at around room temperature (15 ~ 30 ºC).

3. Experimental results and discussions

3.1 A ne dle-to-plate electrode system

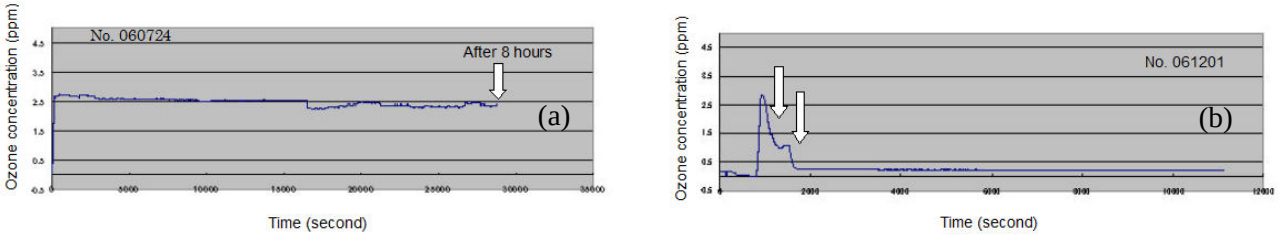


Fig.3 (a) and (b) Ozone concentration with time for 8 hours operation at near the first stage operation (a) and after more than four months from the first stage operation (b) in oxygen.

3-2. A coaxial cylindrical type reactor with an inner rotating electrode

When the rotating speed of the inner electroderose, the ozone concentration increased with the rotating speed as reported before by T. Horinouchi etal.[11]. The discharge input power also increased with the rotating speed and the discharge region became larger. This result was confirmed by the Q (charge) - V (voltage) Lissajous figures. During this experiment the gas flow rate was mainly at 0.5 L/min and the applied voltage was constant to be 10 kV (peak-to-peak). The measured input power was 4.6 W (0 rpm), 5.5 W (200 rpm), 6.6 W (600 rpm) and 6.7 W (800 rpm). Comparing with non-rotation case, the increase of about 20% at the rotating speed of 200 rpm and about 47% increase at 800 rpm were confirmed. We estimated the change of the effective capacitance of discharge region and input power with the rotation speed and these both values increased with the rotating speed. The effective capacitance increased about 51 % with 800 rpm compared with non-rotation case. According to the increase of the capacitance related with the increase of discharge area, it might be estimated that the discharge became more homogeneous with rotating speed. During these experiments, although the ozone concentration without rotation was about 17 g/Nm^{3}at 1 L/min, but more increase of 7 g/Nm^{3}at 200 rpm and 12 g/Nm^3 at 800 rpm were confirmed.

Long time operation is also very importantfor the industrial ozone production. The ozone concentration gradually decreased with time. One ofthe purposes of our experiments is to study what parameters (or reactions) decide this phenomena and how to control it. Previous published papers described that the ozone concentration increased with rotating speed and the discharge was also influenced by it [7][11]. But nobody described the explanation about the mechanisms for these phenomena. In this experiment, discharge was continued for eight hours each day and the operation was repeated about two months. The ozone concentration was keptnear the same level during experiments with a new electrode. The same surface condition of electrode was observed for few days and after that, the ozone concentration decreased dramatically due to some change of metal surface condition. The fluctuation of the ozone concentration between 7-0 g/m^{3}was observed. These situations were observed few days and the ozone production stopped. After the zero ozone concentration was kept for about one hour, 10% nitrogen gas was added for 5 minutes. A few seconds after addition of nitrogen, the ozone concentration recovered again as shown in Fig.4 (a) (b).

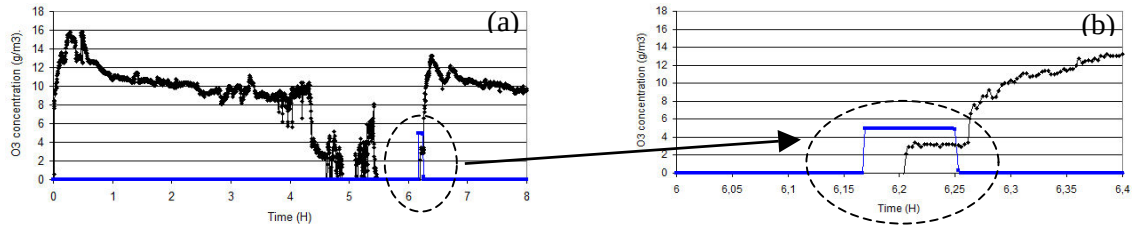


Fig.4 (a) (b) Appearance of ozone zero phenomena and 10 % nitrogen addition for 5 minutes effect in oxygen. (A rotating copper based gold electrode)

The increase of outlet gas temperature was not so much during the experiments (i.e. about 5 degrees C) and every parameter was same except the surface condition (i.e. perhaps the change of adsorbed layer on the metal surface). According to the Lissajous figures, the calculated input power for the zero ozone concentration case and a 15g/m^3 ozone production case was almost same. According to these data, not only the input power but also the surface condition seems to play a very important role for the ozone production. The discharge input power was similar for two cases, but the ozone production was completely different. The nitrogen addition effect at the ozone-zero condition was reported by M. Kuzumoto et al. to improve the ozone production. They pointed out its effect for the stability of discharge due to the generation of initial electrons by a UV emission from the 2nd positive of nitrogen [2].

At the 600rpm operation, after 15 minutes from the start the ozone concentration decreased from 4 g/m^3 to 0 g/m^3 and we kept the parameters to be same for about 30 minutes and added a 10 % nitrogen. The ozone concentration increased to 16g/m^3 and was kept near this level for a while. After stopping addition of nitrogen, the ozone concentration again increased up to about 24 g/m^3 and the ozone concentration was about 6 times higher compared with the initial value. The 10 % (i.e. 50 ml/min) nitrogen seemed to be too much for addition. Nitrogen gas was mixed for 10 minutes. During the experiments, the input power and discharge density was same for the different ozone production.

4. Conclusion

The needle-to-plate electrode system was used for the observation of the ozone-zero phenomena. Under the control of discharge in oxygen with the applied voltage of about 4.5kV and the discharge current of about 1 μ A, it took more than two and half months to prepare the condition for the experiments. At the first stage the ozone generation characteristics were generally the same of the conventional characteristics and gradually the characteristics were unstable before the appearance of the ozone-zero phenomena. After through these processes, relatively stable ozone-zero phenomena established in oxygen gas. The addition effect on the ozone generation was confirmed.

During rotation of electrode, the discharge area became more uniformly. Different ozone production mode was observed with same input power. It seemed due to the change of the adsorbed layer of the metal surface. The ozone concentration seemed to be influenced on the metal surface condition and didn't stabilize during decreasing nitrogen density on the electrodesurface. Nitrogen consumption increased with increasing of rotation speed and it looked about two times more at 600 rpm compared with no rotation.

Acknowledgements. This work was supported by a Grand-in Aid for Scientific Research of the Ministry of Education, Science, Sports and Culture (i.e. KAKENHI 20360128). Authors are also grateful to Dr. Akira Murai (KEPCO in Japan) and Mr. Norihisa Nakahigashi for their useful discussions and experimental support.

5. References

[1] P.Uhlig, M.Haacke and G.J.Pietsch: "On The Impact Of The Feed Gas Quality On The Efficiency Of Ozone Generation",*Proc. Of the 14th Ozone World Congress*, pp.145-159, Dearborn, Michigan, USA (1999).

[2] Masaki Kuzumoto, Yujiro Okihara, Makoto Miyamoto: "Development of New Ozone Generator With Very Narrow Discharge Gap Length", *Technical meeting of the IEEJ*,ED-98-98, pp.29-32 (1998). (in Japanese)

[3] K. Murayama, N. Matsumura, M. Taguchi, Y. Kato, K. Teranishi, S. Suzuki and H. Itoh: "EXPERIMENTAL INVESTIGATION OF OZONE ZERO PHENOMENON", *HAKONE XI*,Oleron Island, France, Sept. 7-12 (2008).

[4] Tetsumi Takano, Keisuke Yamashiro and Haruo Itoh: "Extreme Decreasing of Ozone Product Using High Purity Oxygen", *IEEJ Trans. FM*, 125 (6), pp.508-514 (2005).

[5] Akira Murai, Tsuyoshi Nakajima: "Study of an Ozone Composing Mechanism derived from the Third Element on Surface of Electrode using Oxygen Gas: Part 1", *IEEJ Trans. IA*,127(3), pp.273-278 (2007).

[6] Akira Murai, Tsuyoshi Nakajima: "Study of an Ozone Composing Mechanism derived from the Third Element on Surface of Electrode using Oxygen Gas: Part 2", *IEEJ Trans. IA*,127(3), pp.279-285 (2007).

[7] Sebastian Gnapowski, Chobei Yamabe, Satoshi Ihara: "Ozone Generation Characteristics of Ozonizer with the Rotating Type Electrode", *IEEJ Trans. FM*, 128(10), pp.619-623 (2008).

[8] Chobei Yamabe, Kouji Kayashima, Norihisa Nakahigashi, Sebastian Gnapowski and Satoshi Ihara: "Ozone Production Characteristics including Ozone-zero Phenomena in Pure Oxygen", *The International Conference on Electrical Engineering 2009*,Paper Abstract No.19FP0075, (6 pages on the CD-ROM) , Shenyang, China , July 5-9, 2009.

[9] Sebastian Gnapowski, Chobei Yamabe, Satoshi Ihara: "Long Time Operation of an Ozonizer with a Rotating Type Electrode", Abstracts of Presentations, No. 7-2 (5 pages on the CD-ROM), *19th Ozone World Congress & Exhibition*,Tokyo, Japan, August 31-September 3, 2009.

[10] Haruo Itoh, Tooru Suzuki, Susumu Suzuki, and Ilko M. Rusinov: "Investigation of Ozone Loss Rate Influenced by the Surface Material of a Discharge Chamber", *Ozone Science and Engineering*, 26: 487-497, 2004.

[11] Toshiyuki Horinouchi, Takahisa Hayashi, and Norio Nakajima: "Ozone Generator with Cylindrical Type of Rotating Electrode", Ozone Science and Engineering, 27, 53-57 (2005).

OZONE SYNTHESIS UNDER MIXED CORONA-SURFACE DISCHARGES CONDITION

Sławomir Jodzis[1]

[1]*Warsaw University of Technology, Faculty of Chemistry, Noakowskiego 3, 00-664 Warszawa, Poland*

E-mail: jodzis@ch.pw.edu.pl

Results of investigations on ozone synthesis under electric discharges conditions proceeding in metal mesh-ceramic dielectric system have been presented. The experiments were carried out in the reactor with unique reaction space geometry, through which the gas flowed with the consequently changing linear velocity. The ozonizer high voltage electrode was made of a metal gauze, which caused intensification of mixing of the gas in the reaction space. Using a simple reactor with one-side cooling of the reaction space, high ozone concentrations and energy efficiencies were obtained even at 25ºC.

1. Introduction

Different shapes of electric discharges are continually matter of investigations concerning the obtaining of new solutions in ozone synthesis. Besides the barrier discharge, which is commonly used, also other ones are studied in which the stabilizing effect of the dielectric barrier is exploited [1-3]. The surface discharge, which occurs on the solid dielectric surfaces is sufficiently easy to obtain. In such solutions the electrodes vaporized on the dielectric surface [4,5], laminated [6] or made as a metal element (a bar or a wire) abutted on the dielectric surface [7,8] are used. In the neighbourhood of such elements a strong electric field is induced by the grounded electrode located on the reverse side of the dielectric. Usage a metal mesh as a HV electrode causes generation of numerous, regularly dispersed regions, in which advantageous conditions for oxygen dissociation occurrence exist. As a result, the ozone synthesis is possible. In numerous experimental solutions the turns of thin wire [9,10] for example, are used as an element adjacent to the dielectric. However, experiments described in professional literature concerns ozonizers of tubular type, in which the part of ozone formed is decomposed under process conditions (as an effect of ozone long residence time in the reaction space). The use of such a flowing gas organization, as a result of which the time of ozone residence in the reaction space will be in dependence on the conversion degree obtained, seems more advantageous. Then, as ozone concentration rises, the residence time of the gas in the reaction zone will be shorter and shorter. That is possible to obtain for example in a reactor with a circular symmetry [5,11].

2. Experimental

Fig. 1 depicts the cross-section of an ozonizer with circular symmetry. The ozonizer is equipped with a H.V. mesh electrode adjacent to the ceramic dielectric surface. The gas was introduced through the inlets located outside the ozonizer body, then was flowed out into the ring-shaped channel in the reactor lid. From there gas was directed through the system of openings towards the mesh electrode generating the discharges. The gas flowed towards the middle of the reactor and was removed through the channel in the voltage supplying element. Experiments were carried out using an alumina plate with diameter of 100 mm and the thickness of 1 mm. The thickness of the plate facilitated the heat transfer from the reaction space. The bottom side of dielectric (grounded electrode) was cooled with water (0, 25 and 50^{o}C).

The H.V. electrode was made of metal gauze (brass, mesh 12, wire diameter 0.5 mm) mounted on thin disk of diameter 80 mm. The gauze wire terminals were wrapped around the edge of disk in order to eliminate the local corona effect. The dielectric plate and the mesh were located in the reactor in such a way, to limit the space through which gas could flow, up to approximately 1 mm (the mesh thickness). The gas flowed through the reaction zone with variable linear velocity (from ca. 0.016 up to 0.16 m/s for 10 Ndm^3/h and from ca. 0.06 up to 0.6 m/s for 40 Ndm^3/h), as a result of changing cross-section area of the reaction space. Because of the gauze presence in discharge space the gas in the region of wires changed its direction repeatedly. Besides the main component of gas velocity (in

radial direction) the dynamic components (in orthogonal directions) always occur, which causes the intensification of gas mixing.

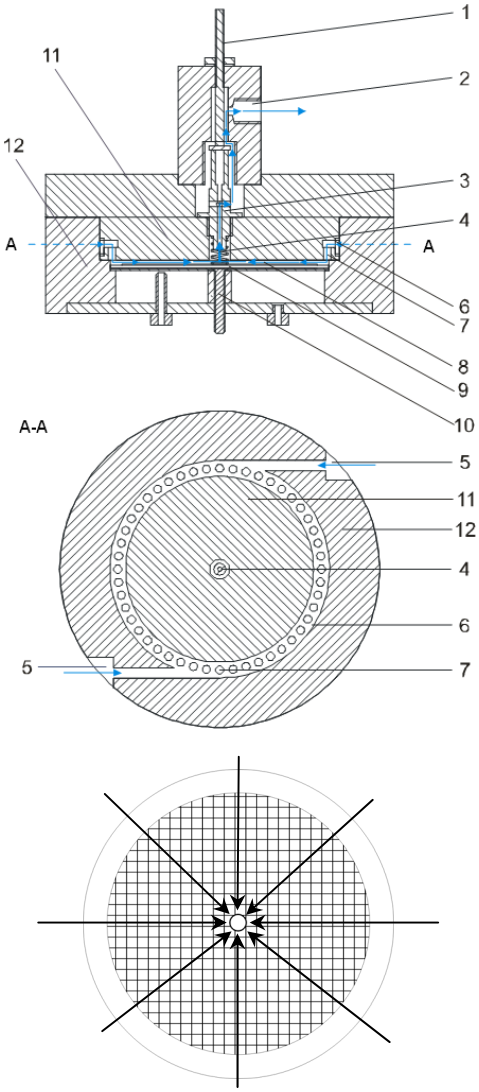


Fig. 1. Schematic structure of the ozonizer; 1 – high voltage clamp, 2 – outlet of the post-reaction gas, 3 – gas ejector and voltage supplying element, 4 – contact spring, 5 – gas inlet channels, 6 – collecting ring, 7 – openings through which the gas enters the reaction space, 8 – reaction space, 9 – metal mesh-ceramic dielectric system, 10 – grounding clamp, 11 – reactor lid, 12 – main body of the reactor.

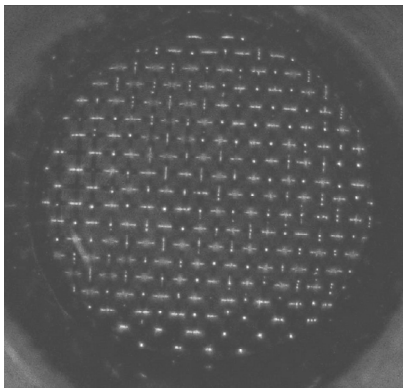


Fig. 2. Organization of the gas flow through the reaction space (a); 1 – ceramic plate, 2 – metal gauze; (b) Picture of the discharges occurring on the mesh electrode in air (photograph taken through the transparent conducting electrode; real diameter ca. 30 mm); exposition time 20 ms. The glow is visible in the places of mesh with dielectric contact.

The studies were carried out in pure oxygen. The gas flow-rates of 10, 20 i 40 Ndm^3/h were used. The concentration of ozone was measured with BMT-963 VENT. The discharge power was evaluated with a TDS3032 oscilloscope equipped with P6015 H.V. probe and a current probe P312 with a TCPA300 amplifier (Tektronix).

3. Results and discussion

Fig. 3 shows the effect of discharge active power on ozone concentration obtained at diversified gas flow-rates (10, 20 and 40 Ndm^3/h) and different temperatures of the liquid cooling the dielectric. All characteristics $c(P_A)$ have a maximum of ozone concentration (c_{max}). That maximum can be treated as an estimator, which determines a critical value of specific energy P_A/V, that means the state of saturation of the reacting system with energy under steady conditions of the process. The location of c_{max} is diversified. It depends on the process main conditions: temperature of the cooling liquid, gas flow rate and energy delivered.

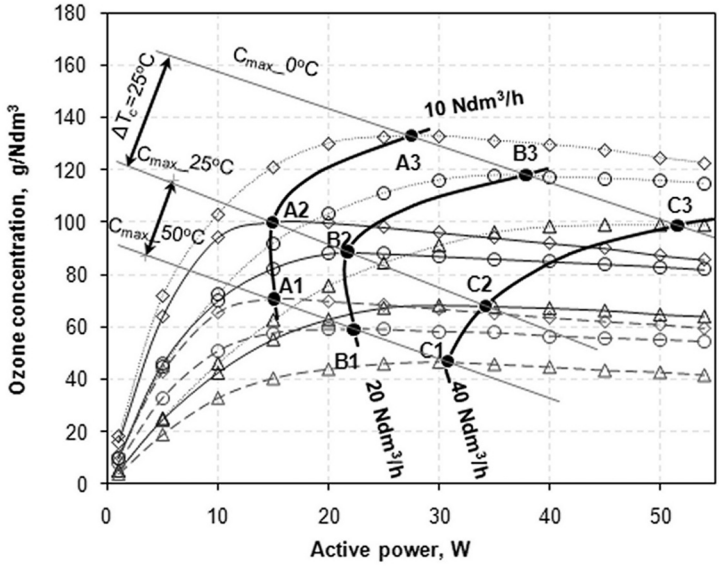


Fig. 3. Effect of active power and temperature of the cooling liquid on ozone concentration; oxygen flow-rates: ◊ - 10, ○ – 20, and Δ - 40 Ndm^3/h; dotted lines - 0°C, solid lines - 25°C, and dashed lines - 50°C; f = 11 kHz.

These parameters are connected together. The increase in active power causes rise of the gas temperature. To a certain degree the temperature in the reaction space could be reduced by increasing of the gas flow rate. The effect of that depends on the gas linear velocity. An increase of the flow-rate at the constant temperature of the cooling liquid causes a decrease in ozone concentration, however, the ozone yield increases (see: Fig. 4). The location of c_{max} drifts towards the higher discharge power (lines A1-B1-C1, A2-B2-C2, and A3-B3-C3). It is worth to take notice of the diminished distance between the lines, observed when the cooling liquid temperature increases.
Fig. 4 depicts the effect of discharge active power, gas flow rate (10, 20 and 40 Ndm^3/h) and temperature of cooling liquid on the ozone yield. It should be noticed that ozone yield is high at easy to provide temperature of 25°C.

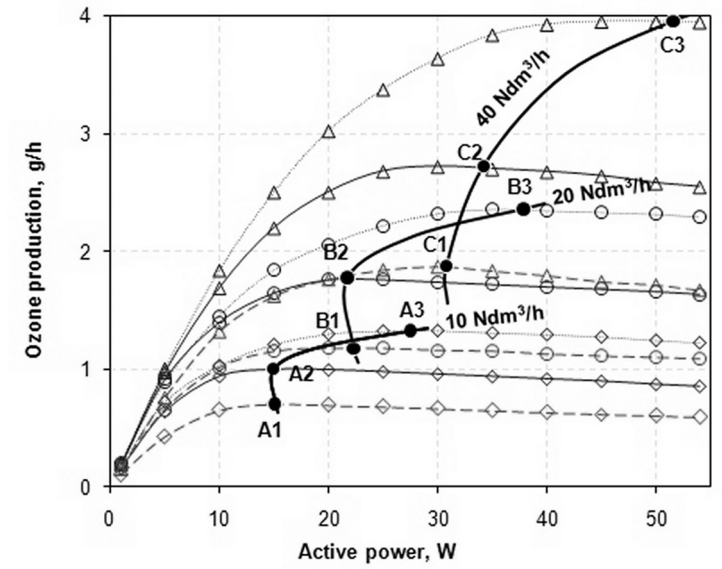


Fig. 4. Effect of active power, temperature of the cooling liquid and gas flow-rate on ozone yield; oxygen flow-rates: ◊ - 10, ○ – 20, and Δ - 40 Ndm^3/h; dotted lines - 0°C, solid lines - 25°C, and dashed lines - 50°C; f = 11 kHz.

Fig. 5 depicts the effect of cooling liquid temperature on ozone concentration obtained under extreme gas flow rates used and selected discharge active power (15, 25, 35 and 45 W). As can be seen, the gas flow rate could have an essential meaning for the process occurrence. This effect is particularly clear at low temperatures, especially at 0ºC. An increase in the energy consumed under the high gas flow rates conditions causes an increasing the ozone concentration.

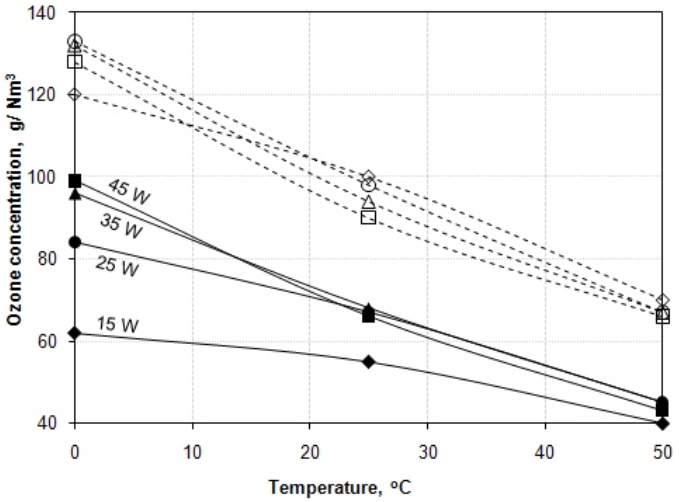


Fig. 5. Effect of temperature of cooling water and discharge active power on ozone concentration; oxygen flow-rates: dashed lines – 10 Ndm^3/h, solid lines - 40 Ndm^3/h.

When the active power is too high (here: 45 W) the inhibition of ozone concentration increase is observed (at 0ºC). At the cooling liquid higher temperatures the effect of supersaturating the reaction system with energy proceeds (overflow of the critical P_A/V value).
At the lower gas flow rate (10 Ndm^3/h) the supersaturating effect occurs at considerably lower powers. At temperatures over ca. 20ºC even a small increase in power (above 15W) causes a consistent decrease in ozone concentration.
The temperature of the cooling liquid T_c is, obviously, only a convenient in usage parameter of the process. However, is does not reflect neither the temperature level in the discharge zone (where the main reactions occur), nor the level of the gas temperature T_g in the reaction space, although a certain correlation between them occurs. Simplifying, it can be written as follows:

$$T_g = T_c + \Delta T_d(T_c, P_A, V) + k \cdot \frac{P_A}{V} \quad (1)$$

where:
T_g – average temperature of a gas in the reaction space,
T_c – temperature of a cooling liquid,
ΔT_d – difference between the temperatures on the opposite sides of a solid dielectric,
k – constant of proportionality,
P_A/V – specific energy, Wh/Ndm^3.

The temperature in the discharge zone is approximately dozens of degrees higher than the average gas temperature in the reaction space [12]. The lowering of the cooling liquid temperature and an increase in the gas flow rate favours the heat transfer conditions in the reaction space. The presence of a gauze is an additional factor improving the heat transfer conditions.

Fig. 6 depicts the energy efficiency of ozone synthesis process vs. ozone concentration obtained at 10, 20 and 40 Ndm^3/h. As can be seen, the energy efficiency at low ozone concentrations attain 200 g/kWh not only at 0ºC. Similar efficiencies were obtained at 25ºC at high flow rates (20 and 40 Ndm^3/h).

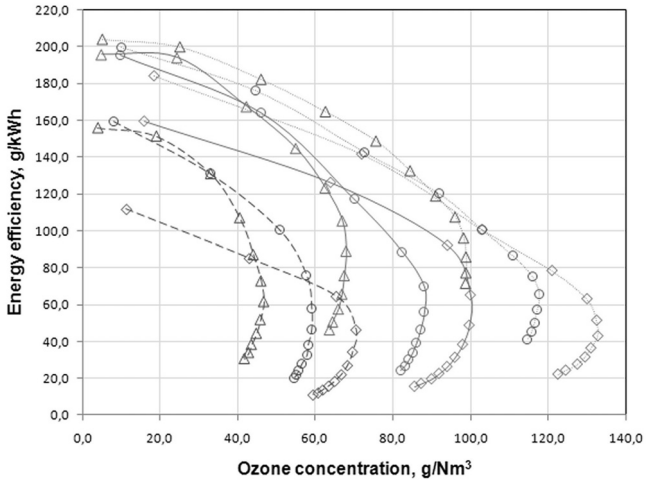


Fig. 6. Energy efficiency of the ozone synthesis process vs. ozone concentration; oxygen flow-rates: ◊ - 10, ○ – 20, and Δ - 40 Ndm^3/h; dotted lines - 0°C, solid lines - 25°C, and dashed lines - 50°C; f = 11 kHz.

4. Summary

In the simple discharge arrangement, in which the metal mesh adjacent to the ceramic plate was used, similar effects as reported in case of more complicated discharge systems were obtained in oxygen. In spite of only one-side cooling of the reaction space the high ozone concentrations and high energy efficiencies of the process, even at 25ºC, were obtained. An essential effect on the results obtained in the presented ozonizer has a manner of the gas flow through the discharge zone. The studies aiming to improve the intensity of heat transfer and ozone concentration obtained are in progress.

Acknowledgements. This study was financially supported by Warsaw University of Technology.

5. References

[1] Haacke M, Humpert C and Pietsch G J 2002 *Ozone Sci. & Eng.* **24** 193.
[2] Samaranayake W J M, Miyahara Y, Namihira T, Katsuki S, Hackman R and Akiyama H 2001 *IEEE Trans. on Dielectrics and Electrical Insulation* **8** (4) 687.
[3] Korzec D, Finantu-Dinu E G, Dinu G L, Engemann J, Stefecka M and Kando M 2003 *Surface and Coatings Technology* **174-175** 503.
[4] Masuda S, Akutsu K, Kuroda M, Awatsu Y and Shibuya Y 1988 *IEEE Trans. on Industry Applications* **24**(2) 223.
[5] Jodzis S, Smoliński T and Sówka P 2010 *12th Int. Conf. on Optimization of Electronic Equipment OPTIM,* Brasov (Romania) 1312.
[6] Williamson J M, Trump D D, Bletzinger P, Biswa N. and Ganguly B N 2006 *J. Phys D: Appl. Phys.* **39** 4400.
[7] Opaits D F, Shneider M N, Miles R B, Likhanskii A V and Macheret S O 2008 *Physics of plasmas* **15** 073505.
[8] Shimosaki M and Yamabe C 2006 *J. Adv. Oxid. Technol.* **9**(2) 188.
[9] Okazaki S, Sugimitsu H, Niwa H, Kogoma M, Moriwaki T and Inomata T 1988 *Ozone Sci. & Eng.* **10** (2) 137.
[10] Ozonek J, Jahołkowski K, Pollo I and Okazaki S 2002 *Int. Symp. on High Pressure Low Temperature Plasma Chemistry* HAKONE VIII Pühajärve (Estonia) Vol. **2** 239.
[11] Jodzis S and Kowalska A 2009 *Prz. Elektrotechniczny (Electrical Review), R.* **85** Nr 5, 118.
[12] Ono R, Oda T 2008 *J. of Phys. D: Appl. Phys.* **41** 035204.

INFLUENCE OF SOLID SURFACE MATERIAL ON OZONE DECOMPOSITION

František Krčma, Zdenka Kozáková, Eliška Krejsková, Ivana Halamová, Věra Sázavská

Institute of Physical and Applied Chemistry, Faculty of Chemistry, Brno University of Technology, Purkyňova 118, 612 00 Brno, Czech Republic
E-mail: krcma@fch.vutbr.cz

Ozone was generated by commercial ozonizer Lifetech with production efficiency up to 0.5 g of ozone per hour. Both technical and synthetic air (mixture of nitrogen and oxygen 80:20) with gas flow varying from 0.3 to 1.8 $L \cdot min^{-1}$ was used for ozone production. Absolute ozone concentration was determined by iodometric titration and by spectrophotometry of oxidized iodine solution. Selected metal materials (iron, stainless steel, copper, brass and aluminium) in the form of hollow tubes were placed in Pyrex glass reactor during the experiment. Changes of ozone concentration produced at different experimental conditions (reaction time, input power, gas flow rate, gas composition) were compared with respect to the used material.

1. Introduction

Nowadays, utilization of ozone in various industrial processes is very wide and thus efficiency of its production and transport is demanded as high as possible. Ozone is an instable gas which is very easily decomposed to atomic oxygen especially when it can react with some compound or solid surface. Storage of ozone is a quite difficult process therefore ozone generators are often used directly at the place of further ozone application. However, in all cases it is important to choose appropriate material for ozone transportation from the generator to the place of ozone consumption. Such material should not catalyse ozone decomposition and thus decrease its production efficiency.

The most inert material with regard to ozone decomposition is glass. However, its disadvantage concerning construction of devices for ozone utilization is its high fragility. Other convenient materials could be found among plastic materials, especially based on fluorinated polymers such as PTFE [1]. On the other hand, using of rubber as a pipeline or packing is almost dangerous because it actively reacts with ozone and it could be even ignited [1, 2]. Also using of polystyrene is impossible for ozone transportation or storage [3]. Nevertheless, these materials still required further investigation. Metals have been the most common materials utilized for pipelines. However, a lot of them are strongly oxidized by ozone and thus these materials easily corrode. Some of them are even used as catalysts for ozone decomposition in silica gel, for example silver [4] or cobalt ions [5]. This work presents results obtained for five common construction metals: iron, stainless steel, copper, brass, and aluminium. Moreover, presence of water vapour in air can enhance corrosive effect of ozone on metal surface because it causes higher ozone decomposition [1]. Therefore influence of air moisture on ozone generation and decomposition is studied, too.

2. Experimental setup

Ozone was generated by commercial ozonizer Lifetech (type Lifepool) with the production efficiency up to 0.5 g of ozone per hour (value 6). Either technical or dry synthetic air (mixture of nitrogen and oxygen 80:20) with gas flow varying from 0.3 to 1.8 $L \cdot min^{-1}$ was used for ozone production. Special Pyrex glass tube reactor (length of 40 cm) was inserted into the apparatus between the ozonizer and ozone determination spot (according to the scheme in Fig. 1). Various solid metal materials (iron, stainless steel, copper, brass, and aluminium) in the form of hollow tubes (total surface of 2.26 dm^2) were selected and subsequently placed in the tube reactor during the experiment. Changes of ozone concentration detected after the tube reactor with particular solid material were determined and compared to the results of ozone pure production. Ozone production itself was investigated in the dependence on several experimental parameters such as input power of ozonizer, gas flow rate, gas purity and reaction time (0.5, 1 or 1.5 min).

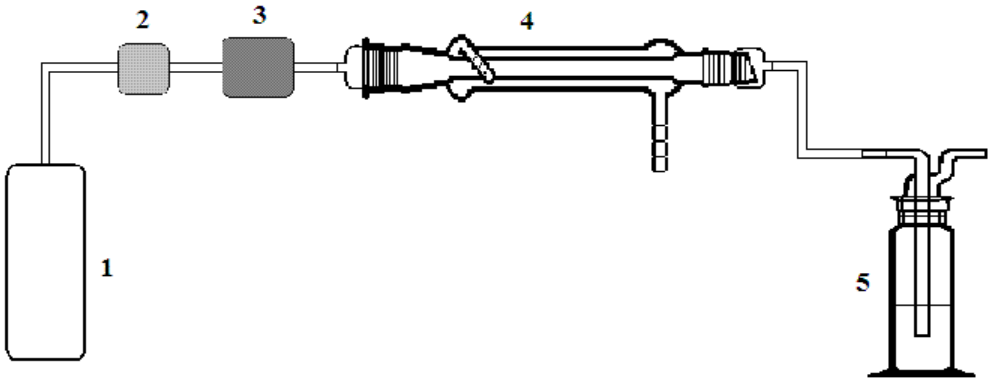


Fig. 1. Scheme of experimental setup: 1 – technical (synthetic) air, 2 – flowmeter, 3 – ozonizer, 4 –Pyrex reactor, 5 – bubbling vessel.

Absolute ozone concentration was determined by iodometric titration. Output gas containing generated ozone was let bubbling through 100 ml of 0.2 M KI solution to produce iodine:

$$2KI + O_3 + H_2O \rightarrow I_2 + 2KOH + O_2 \quad (1)$$

Bubbling (reaction) time was varying from 30 seconds to 1.5 minute according to other experimental conditions. Obtained yellow coloured solution was analysed by absorption spectroscopy at fixed wavelength (maximal absorbance was detected at 352 nm) and subsequently titrated by 0.05 M $Na_2S_2O_3$ with addition of 10 ml 2 M HCl to determine iodine and related ozone concentration:

$$I_2 + 2Na_2S_2O_3 \leftrightarrow 2I^- + Na_2S_4O_6 \quad (2)$$

Final ozone concentration was expressed in mols generated in one dm^3 of used gas ($mol \cdot dm^{-3}$).
For short reaction time and low ozone concentration, iodometric titration was charged by a relatively high measurement uncertainty. Thus data obtained by spectrophotometry were evaluated as more relevant for these experiments. Relation between ozone concentration determined by iodometric titration and absorbance of iodine solution (KI solution after ozone oxidation) is given by following calibration equation (for calibration curve, see Fig. 2):

$$A = 0.026746 * c(O_3) \quad (3)$$

where A is absorbance of oxidized iodine solution at 352 nm (maximum of absorption curve) and $c(O_3)$ is ozone concentration in 10^{-5} $mol \cdot dm^{-3}$.

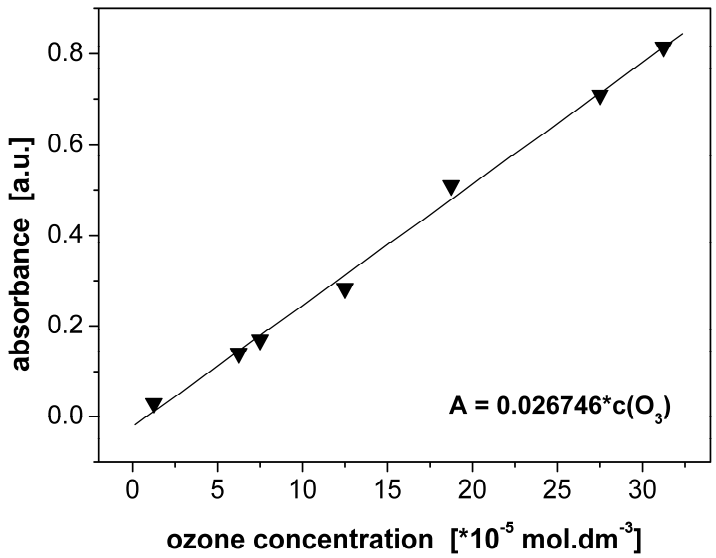


Fig. 2. Calibration curve representing relation between ozone concentration (obtained from iodometric titration) and absorption intensity of iodine solution (produced by ozone oxidation of KI solution), reaction time of 1 min.

3. Results and discussion

Generally, ozone formation was dependent on experimental conditions such as reaction time, input energy, gas flow rate, gas content and purity. Influence of these parameters on ozone production as well as influence of selected metal surfaces on ozone decomposition is presented and discussed in this section.

Generation of ozone by commercial ozonizer Lifepool provided the maximal efficiency of 0.5 g of ozone per hour (from dry air). However, our experiments required lower amounts of produced ozone in order to clearly determine differences in ozone decomposition on various surfaces. Therefore only technical or synthetic air was used for this purpose.

Input power of commercial ozonizer was divided into 6 equivalent steps (values) whereas value 6 meant the highest possible production at particularly given conditions. Results of ozone generation from technical air studied as a function of ozonizer input power are demonstrated in Fig. 3. Experiments were carried out at constant gas flow rate of 0.6 $L \cdot min^{-1}$ and reaction time of 1 minute. Results obtained at these conditions were quite surprising because there was not any significant dependence of determined ozone concentration on input power. The highest production was observed at power value 4. These results were probably caused by lower produced amount of ozone in general.

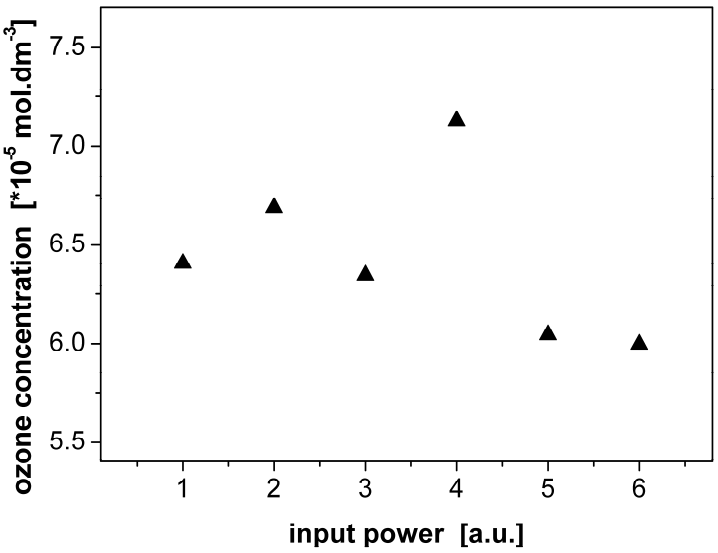


Fig. 3. Ozone concentration as a function of input power of ozonizer (constant flow rate of technical air: 0.6 $L \cdot min^{-1}$, reaction time: 1 min).

Influence of gas flow rate on ozone production is demonstrated in Fig. 4. In this series of measurements, ozonizer was adjusted on constant value 3 for reaction time of 1 minute. Flow rate of technical air was used for ozone generation varied from 0.3 to 1.8 $L \cdot min^{-1}$. Obtained results showed that ozone production was more or less directly proportional to the amount of gas flowing through the ozonizer. The highest ozone production (over $3 \cdot 10^{-4}$ $mol \cdot dm^{-3}$) was achieved at flow rate of 1.8 $L \cdot min^{-1}$ for technical air.

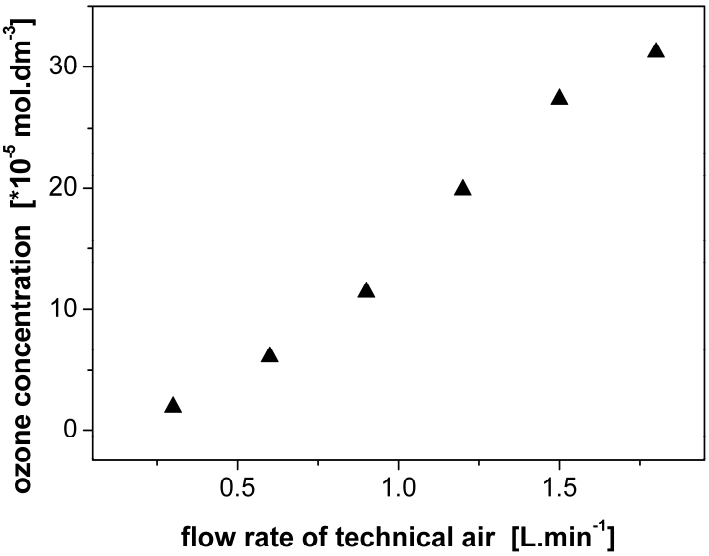


Fig. 4. Ozone concentration as a function of technical air flow rate (constant input power of ozonizer: value 3, reaction time: 1 min).

As moisture presented in technical air can substantially influence ozone concentration in the gas mixture and thus it can cause ozone decomposition [1], a special series of measurements was carried out to evaluate this phenomenon in our apparatus. Dry synthetic air was synthesized by mixing pure nitrogen and oxygen in the ratio of 80:20. Total gas flow rate was adjusted at the same values as in the case of technical air, i.e. 0.6 and 0.9 $L \cdot min^{-1}$. Input power of ozonizer was kept constant at value 3. Production of ozone was determined for two reaction times, 0.5 and 1.0 minute. Results of final ozone concentration obtained by generation from both technical and synthetic air are compared in Table 1. It is evident that ozone production from synthetic air was much higher than from technical air. In the case of lower gas flow rate (0.6 $L \cdot min^{-1}$), ozone concentration generated after both reaction times was almost four times higher when synthetic air was used. In the case of higher gas flow rate (0.9 $L \cdot min^{-1}$), ozone production was enhanced more than twice in synthetic air. Based on these results we can assume that moisture in technical air had a significant effect on ozone production in our experimental system. Next problem could be related to the presence of various oxides of nitrogen in technical air, therefore our further study will be focused on synthetic air containing traces of NO_x, too.

Tab. 1. Comparison of ozone production from technical and dry synthetic air (nitrogen:oxygen 80:20) for two gas flow rates: 0.6 and 0.9 $L \cdot min^{-1}$ and two reaction times: 0.5 and 1 min (constant input power of ozonizer: value 3).

		technical air	**synthetic air**
reaction time [min]	**gas flow rate [$L \cdot min^{-1}$]**	**ozone concentration [$*10^{-5}$ $mol \cdot dm^{-3}$]**	
0.5	0.6	3.8	13.8
1.0	0.6	6.3	24.2
0.5	0.9	6.1	14.6
1.0	0.9	11.4	26.1

Decomposition of ozone on solid surfaces was studied for five metal materials: iron, stainless steel, copper, brass, and aluminium. Ozone was produced by ozonizer adjusted at constant input power (value 3). Technical air (flow rate of 0.6 $L \cdot min^{-1}$) was used for ozone generation and its concentration was determined after three reaction times (0.5, 1.0 and 1.5 minute). Obtained results are graphically evaluated in Fig. 5. Comparison of final ozone concentration revealed that stainless steel and aluminium had the lowest effect on ozone final concentration, i.e. final ozone concentration determined at the output of the reactor with these materials was the highest comparing to the other

materials. Moreover, comparing results obtained in the empty reactor and reactor containing stainless steel or aluminium material we can assume that influence of these materials on ozone decomposition was only negligible. On the other hand, the rest of materials (iron, brass, and copper) significantly decreased ozone concentration and thus they had a substantial effect on ozone decomposition process. These results are in an agreement with facts presented in literature (see Introduction) because iron and copper materials are often used as catalyst in ozone decomposition process. In the case of brass material, it also corresponds to expected results because this alloy contains substantial fraction of copper and thus decomposition effect of ozone could be enhanced.

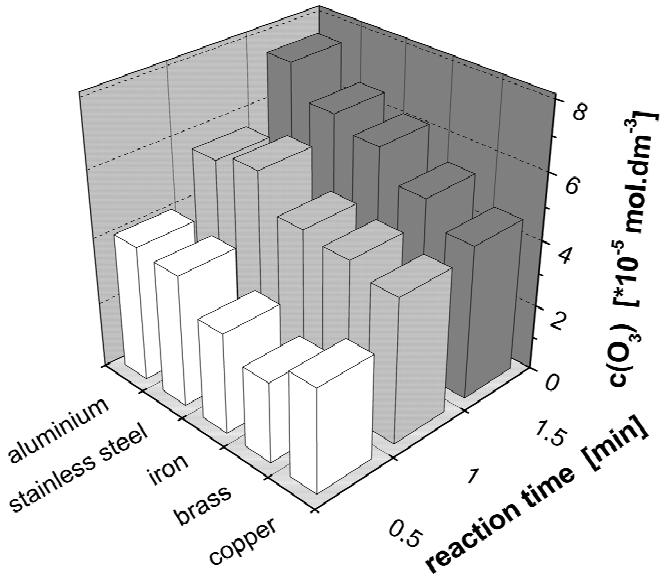


Fig. 5. Comparison of ozone concentration after interaction with five selected metal materials and for three reaction times: 0.5, 1 and 1.5 min (constant input power of ozonizer: value 3, constant flow rate of technical air: 0.6 $L \cdot min^{-1}$).

4. Conclusions

Generation of ozone by commercial ozonizer Lifetech was studied as a function of various experimental conditions and subsequently, influence of five metal materials on ozone decomposition was investigated. Iodometric titration as well as spectrophotometry of oxidized iodine solution was used for determination of absolute ozone concentration. Ozone production was increasing with increasing gas flow rate of technical air. However, input power of ozonizer did not have any significant influence on ozone amount generated after short reaction time up to 1 minute. Based on results of ozone generation obtained in technical and dry synthetic air (mixture of nitrogen and oxygen 80:20) we can assume that moisture presented in technical air substantially influence ozone production in our system. Comparing effects of various metal materials on ozone concentration in the gas mixture it was proved that stainless steel and aluminium had no significant influence on ozone production while iron, copper, and brass significantly decomposed ozone molecule.

Acknowledgements. This work was supported by the Czech Science Foundation, project No. 104/09/H080.

5. References

[1] Horváth M, Bilitzky L and Hüttner J 1985 *Ozone* Budapest: Akadémiai Kiadó 350.
[2] Tausch M and von Wachtendonk M 2001 *CHEMIE 2000+* Bamberg: C.C. Buchner 78.
[3] Obvintseva A D, Klimuk A I et al. 2007 *Russian J Appl Chem* **81** (4) 593.
[4] Konova P, Naydenov A et al. 2008 *Catalysis Today* **137** (2-4) 471.
[5] Ennan A, Rakitskaya T L et al. 1999 *Catalysis Today* **53**.

INFLUENCE OF HUMIDITY ON THE YIELD OF OZONE GENERATORS

Manfred Salvermoser[1], Ulrich Kogelschatz[2]

[1]*Rua Dr. Paschoal Imperatriz 114, Apto. 202A, CEP: 04705-070, Sao Paulo, SP, Brasil*
[2]*Retired from ABB Corporate Research, Baden, Switzerland*
E-mail: msalvermoser@yahoo.com

The presence of trace amounts of water vapour has a detrimental effect on ozone formation. Humidity present in the oxygen feed gas of dielectric barrier discharge (DBD) ozone generators causes the formation of hydroxyl (OH) and hydroperoxy (HO_2) radicals that set up a catalytic reaction cycle resulting in enhanced ozone destruction. Water vapour also increases the energy density inside the DBD microdischarges due to an increase of the surface conductivity of the dielectric barriers induced by the formation of a water layer [1].

Experimental ozone yield (η) vs. ozone density ($n(O_3)$) curves of a DBD ozone generator with well defined trace amounts of humidity (between 1.9 and 376 parts per million (ppm)) in the oxygen feed gas have been analysed and modelled. The model combines the basic kinetic ozone generation scheme for oxygen fed DBD ozone generators published in [2] with the water vapour induced catalytic OH/HO_2 ozone destruction kinetics presented in [3].

This approach allows us to distinguish between water vapour induced surface effects and reaction kinetics effects in the discharge volume. We show that the increase of the microdischarges energy density manifests itself primarily in a decrease of the O_3 yield at zero ozone background concentration. The change of slope $d\eta/dn(O_3)$ of the ozone yield vs. ozone density curves with increasing water content in the oxygen feed gas for small ozone densities can be traced back to catalytic OH/HO_2 ozone destruction kinetics.

1. Introduction

Industrial DBD ozone (O_3) generators depend on very dry feed gas with humidity content below a dew point of - 60°C (11ppm H_2O) in order to work efficiently [1]. It is believed that humidity influences the microdischarges (MD) by a humidity induced surface effect, as well as by inducing catalytical O_3 quenching processes [1]. VUV lamp driven O_3 generators show water induced catalytic O_3 quenching rates proportional to $\sqrt{n(H_2O)}$ [3], [4], [5], [6]. A more recent attempt to describe the influence of water vapour on direct current (DC) corona discharge O_3 generators does not differentiate between the ground-state $O(^3P)$ and excited $O(^1D)$ oxygen (O_2) radical precursors of O_3, suggesting that H_2O attacks the O radical directly with a high rate constant. This approach results in the water induced O_3 destruction rate being directly proportional to $n(H_2O)$ [7], [8]. This paper combines the kinetic O_3 quenching processes as described in [3], [4] with a water induced surface effect on the MD energy density, leading to a decrease in O_3 generation efficiency in DBD based O_3 generators.

2. Experiment

The experiments were performed in a tubular laboratory O_3 generator of 1 m length and 1200 cm^2 electrode area [9]. The d =1 mm wide annular discharge gap was formed by an inner glass tube and a slightly wider double-walled stainless steel cylinder at ground potential. Its temperature T_W= 299K was kept constant by a recirculating fluid connected to a thermostat. The glass tube had an internal aluminum coating serving as the high voltage electrode and was not cooled. A sinusoidal feeding voltage operating at f=625 Hz was used, resulting in a volume averaged discharge power deposition of p_e=2.5W/cm^3 in the O_2 feed gas. O_2 pressure was $p(O_2)$=1.9bar. The water content of the feeding gas was measured using a precise electronic hygrometer.

3. Basic Idea

In DBD O_3 generators MD's generate O-atoms and excited O_2* molecules. Depending on operating parameters a certain fraction of these O radicals form O_3 through 3 body collisions with O_2 (see (R8) in appendix). O_3 destruction happens only in 2. order reactions (binary collisions) with O atoms, excited O_2 molecules, radicals or discharge electrons. As long as O_3 does not alter the MD's electron

energy distribution function (EEDF) significantly, O_3 generation is described by a simple differential equation (1) containing only first order terms in $n(O_3)$.

$$\partial_e n(O_3) = \eta_0 - \varepsilon_0^{-1} \cdot n(O_3) \qquad [1/eV] \tag{1}$$

$e := t \cdot p_e$ is the discharges energy density deposited in the process gas. t is time. p_e is the discharge power density (time and volume averaged). η_0 is the MD's O_3 yield in [1/eV] defined by its intrinsic properties. ε_0 is an energy density determined by the sum of all O_3 destruction processes.

$$\partial_e n(O_3) = \eta_0 - \varepsilon_0^{-1} \cdot n(O_3) \qquad [1/eV] \tag{1}$$

$$\Rightarrow \; n(O_3) = \eta_0 \cdot \varepsilon_0 \left(1 - \exp\left(-e \cdot \varepsilon_0^{-1}\right)\right) \tag{2}$$

$$\text{With } \eta := n(O_3) \cdot e^{-1} \Rightarrow \eta = \frac{n(O_3)}{\varepsilon_0 \cdot \ln\left(\varepsilon_0 \cdot \eta_0 \cdot \left(\eta_0 \cdot \varepsilon_0 - n(O_3)\right)^{-1}\right)} \tag{3}$$

A Taylor series expansion of (3) shows that $\eta\left(n(O_3) = 0\right) = \eta_0$ and $\partial_n \eta\left(n(O_3) = 0\right) = -\left(2 \cdot \varepsilon_0\right)^{-1}$ give direct access to the O_3 source term and O_3 quench term which are closely connected to the MD's EEDF (η_0) and the kinetic equations.

4. Basic data analysis

Since equation (3) should describe the O_3 yield vs. O_3 concentration curves very well for small to moderate $n(O_3)$ densities, experimental data points shown in figure 2 were fitted using 2 fit parameters (η_0 and ε_0) for each humidity level.

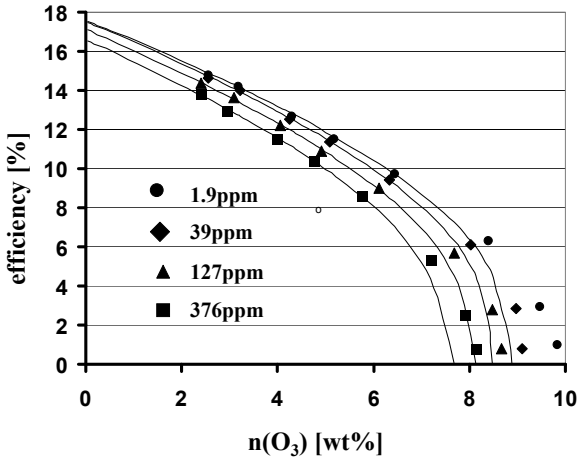


Fig. 1. Experimental O_3 yield vs. $n(O_3)$ curves with well defined amounts of humidity in the O_2 feed gas. Experimental data points were fitted with analytical function (3) with fit parameters η_0 and ε_0 for each humidity level.

1.9ppm: $\eta_0 = 0.1188 eV^{-1}, \varepsilon_0^{-1} = 4.73 \cdot 10^{-20} cm^3 eV^{-1}$; 39ppm: $\eta_0 = 0.1184 eV^{-1}, \varepsilon_0^{-1} = 4.93 \cdot 10^{-20} cm^3 eV^{-1}$;
127ppm: $\eta_0 = 0.1157 eV^{-1}, \varepsilon_0^{-1} = 5.10 \cdot 10^{-20} cm^3 eV^{-1}$; 376ppm: $\eta_0 = 0.1121 eV^{-1}, \varepsilon_0^{-1} = 5.29 \cdot 10^{-20} cm^3 eV^{-1}$

Units: 1 wt% O_3 = $3.12 \cdot 10^{17} cm^{-3}$ for $p(O_2)$=1.9 bar, T_G=331K. 100% efficiency = 1 O_3/ 1.48eV which is equivalent to $1220 g / kWh$ O_3 yield [1].

As one can see (3) describes the experimental data points very well up to $n(O_3) \leq 6$wt%. Above 6 wt% O_3 may alter the MD's EEDF introducing higher order correction terms in $n(O_3)$. The decrease in η_0 with increasing humidity is due to an increase in MD energy density (e_{MD}) induced by increasing surface conductivity of the dielectrics due to formation of a water layer on its surface [1], [9]. The increase in ε_0^{-1} is related to humidity induced kinetic O_3 quenching processes.

5. Model

A model including a 2-D code [10], [11] and all the reaction kinetics is beyond the scope of this paper. Starting with a homogenous O_3 density $n(O_3)$ within the d=1mm high discharge gap, p_e=2.5W/cm^3 causes an average temperature within the gap of $T_G = 331K$ [2], [12]. At $p(O_2)$=1.9bar the initial O_2 density is $n2 = 4.2 \cdot 10^{19}\, cm^{-3}$. In the centre of a volume (Vol) within the discharge gap occurs a MD with fo =2•f =1250Hz. The MD deposits e_{MD} in the process gas creating homogenous $O(^3P)$, $O(^1D)$, $O_2\left(a^1\Delta_g\right)$ and $O_2\left(b^1\Sigma_g^+\right)$ densities within a small cylinder of 1mm height, about 100µm diameter and volume Vol_{MD} [2].

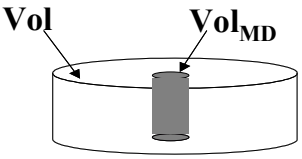


Fig. 2. Illustration of the small thin MD volume Vol_{MD} inside the bigger volume Vol.

Vol and Vol_{MD} are related by the following equation: $f_0 \cdot e_{MD} \cdot \left(Vol_{MD} / Vol\right) = p_e$. The MD is considered instantaneous with respect to the ozone kinetics [2]. The energy density of e_{MD}=100 mJ/cm^3 was determined by dividing a measured n(O) [2] by the MD's O-radical production yield of 4.55eV per O-radical [2]. The O-yield results from the electron energy distribution function EEDF, based on electron collision cross sections by Phelps [13]. The probability $P(O_2^*)$ of the MD's excitation energy going into the respective exited O_2 molecular levels and their excitation energies $\varepsilon(O_2^*)$ was determined from [2] with E/N=110Td [11]. Highly excited O_2 levels $O_2\left(B^3\Sigma_u^-\right)$ ($P(B^3)$=60%, $\varepsilon(B^3)$=8.4eV), $O_2\left(A^3\Sigma_u^+\right)$, $O_2\left(A'^3\Delta_u\right)$, $O_2\left(c^1\Sigma_u^+\right)$ ($P(A^3)$+$P(A'^3)$+$P(c^1)$=20%, $\varepsilon(A^3)$= $\varepsilon(A'^3)$= $\varepsilon(c^1)$=6eV) dissociate into O-Atoms via Reactions (R1a), (R1b), (R1c), (R2). Low lying levels $O_2\left(a^1\Delta_g\right)$ (($P(a^1)$=3.5%, $\varepsilon(a^1)$=0.9eV)) and $O_2\left(b^1\Sigma_g^+\right)$ ($P(b^1)$=1.3%, $\varepsilon(b^1)$=1.6eV) drive O_3 destruction processes (R12) and(R14). The initial densities at t=0 of all the species right after the termination of the MD are:

$$n\left(O_2(X)\right) = n2 - 1.5 \cdot n(O_3),\ n\left(O_3\right) = n(O_3) - \alpha \cdot e_{MD} \cdot n(O_3) / n(O_2(X))$$

$$n\left(O_2\left(a^1\Delta_g\right)\right) = e_{MD} \cdot \left(0.035/0.9eV + \alpha \cdot n(O_3) / n(O_2(X))\right),\ n\left(O_2\left(b^1\Sigma_g^+\right)\right) = e_{MD} \cdot \left(0.013/1.6eV\right),$$

$$n\left(O\left(^3P\right)\right) = e_{MD} \cdot \left(2 \cdot 0.2/6eV + 0.6/8.4eV\right),\ n\left(O\left(^1D\right)\right) = e_{MD} \cdot \left(0.6/8.4eV + \alpha \cdot n(O_3) / n(O_2(X))\right) \quad (4)$$

α describes electron impact dissociation of O_3 ((R3) in appendix). The electron energy dependent dissociation cross section of O_3 is not well known [2], [12]. α can be derived using the experimental data, since α determines the slope of η($n(O_3)$) when no humidity is present. The temperature in the MD region at e_{MD}=100mJ/cm^3 was estimated $T_{MD} = 347K$ according to [2]. T_{MD} is a function of e_{MD} and was used to evaluate the rate constants of reactions (R4) through (R20) shown in the appendix. Only a limited set of reactions is used to keep things simple. Reactions were chosen carefully according to their importance to describe the ongoing physics realistically. The rate constant β describes destruction of vibrationally excited O_3* by oxygen atom collisions after its formation by reaction (R8). Reaction (R11) is according to [14] a complex process. Since the competition between reactions (R9) and (R11) determines the overall O_3 production yield of the MD, β was adapted such that the calculated O_3 yield at $n(O_3)$=0 with dry O_2 describes the experimental data points with 1.9ppm humidity well. We chose that way to describe the discrepancy between the EEDF predicted O_3 yields and the considerably lower experimental yields in light of experiments showing a strong enhancement in the experimental yields when O radical concentrations right after the excitation can be kept low [3], [4], [15], [16]. The residual $n(O_3)$ was calculated numerically for the next 200µs, a time scale much shorter then diffusion processes but long compared to O_3 formation [2]. Diffusion is accounted by: $n(O_3, t = 200\mu s + \delta t) = n(O_3, t = 200\mu s) \cdot \left(Vol_{MD} / Vol\right)$ (5)

The impact of the long living $O_2\left(a^1\Delta_g\right)$states on O_3 formation was included using a volume averaged quasi steady state (QSS) $O_2\left(a^1\Delta_g\right)$ density approximation:

$$n\left(O_2\left(a^1\Delta_g\right)\right)_{QSS} = \left(p_e \cdot 0.035/0.9eV\right)/\left(k_{13}(T_G)\cdot n\left(O_2(X)\right) + k_{12}(T_G)\cdot n(O_3)\right) \quad (6)$$

Reaction (R12) leads to O(^{3}P) production while reactions (R8) and (R10) keep the O density small:

$$n\left(O\left(^3P\right)\right)_{QSS} = \frac{k_{12}(T_G)\cdot n\left(O_2\left(a^1\Delta_g\right)\right)_{QSS}\cdot n(O_3)}{k_8(T_G)\cdot n(O_2(X))^2 + k_{10}(T_G)\cdot n(O_3)} \quad (7)$$

Reaction (R10) is responsible for another O_3 destruction process:

$$\Delta n\left(O_3\right)_a = -\left(f_0^{-1} - 200\mu s\right)\cdot 2\cdot k_{10}(T_G)\cdot n\left(O(^1P)\right)_{QSS}\cdot n\left(O_3, t = 200\mu s + \delta t\right) \quad (8)$$

Humidity induced OH and HO_2 radicals driving a catalytic O_3 destruction cycle, have lifetimes in the ms range. As a result, their impact on O_3 production is also treated using a volume averaged quasi steady state approximation, similarly as described in [3], [4]. OH radicals are predominantly produced in the MDs via reaction (R16) [17]. Already at modest O_3 densities, catalytic O_3 destruction reactions (R17) and (R18) transform OH into HO_2 and HO_2 back into OH so fast, that the OH and HO_2 densities are in a fixed ratio to each other:

$$n(OH)/n(HO_2) = \chi = k_{18}\left(T_G\right)/k_{17}\left(T_G\right) \quad (9)$$

The predominant OH destruction mechanism is reaction (R19), along with (R20), giving rise to a steady state HO and HO_2 densities of:

$$n\left(HO_2\right)_{QSS} = \sqrt{\frac{\left(p_e\cdot 0.6/8.4eV\right)\cdot\left(k_{16}(T_{MD})\cdot n(H_2O)/(k_{16}(T_{MD})\cdot n(H_2O) + k_4(T_{MD})\cdot n(O_2(X))\right)}{k_{19}(T_G)\cdot\chi + k_{20}(T_G)\cdot n\left(O_2(X)\right)}}. \quad (10)$$

This leads to another O_3-loss-term due to humidity induced catalytic O_3 destruction:

$$\Delta n(O_3)_{OH} = \left(\cdot\exp\left(-2\cdot k_{18}(T_G)\cdot n(HO_2)_{QSS}\cdot\left(f_0^{-1} - 200\mu s\right)\right) - 1\right)\cdot n(O_3, t = 200\mu s + \delta t) \quad (11)$$

In the end: $n\left(O_3, t = f_0^{-1}\right) = n(O_3, t = 200\mu s) - \Delta n(O_3)_a - \Delta n(O_3)_{OH}$ (12)

As a result, $\partial_e n(O_3) = \left(n(O_3, t = f_0^{-1}) - n(O_3, t = 0)\right)/\left(e_{MD}\cdot\left(Vol_{MD}/Vol\right)\right)$ (13)

can be computed as a function of n(O_3). $e = \int_0^{n(O_3)} dn\cdot\left(\partial_e n(O_3)\right)^{-1}$ and $\eta\left(n(O_3)\right) = n(O_3)/e$ follow directly after integration.

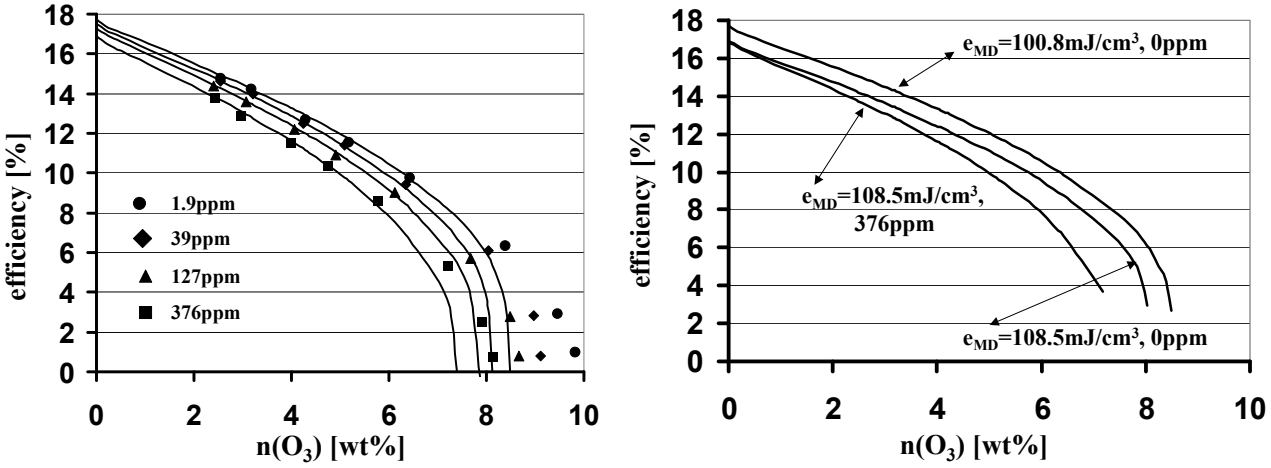


Fig. 3. Left hand side shows the models results for different H_2O content as well as the experimental data points. The graph on the right shows the models result for dry gas, dry gas with enhanced e_{MD}, and enhanced e_{MD} with 376ppm H_2O kinetics effects.

For e_{MD}=100.8mJ/cm^3, $\beta = 4.84\cdot 10^{-14}\,cm^3 s^{-1}$ and $\alpha = 0.848\cdot eV^{-1}$ the model describes the experimental data points for 1.9ppm humidity content very well up to n(O_3) of about 6wt%. Note that

α and β remain fixed for all calculations. β is well within the limits suggested by [14]. α corresponds to a ratio of the O_3 to the O_2 electron impact dissociation coefficient of 6.85 at E/N=110Td [2], [12]. When more water is present, e_{MD} increases resulting in a decrease in yield. For 39ppm humidity content e_{MD}=102.5mJ/cm^3, for 127ppm e_{MD}=104.8mJ/cm^3 and for 376ppm e_{MD}=108.5mJ/cm^3 are used such that the model generates yield curves in good agreement with the experimental data points as shown in fig. 3.

6. Conclusion

The influence of water vapour on O_2 fed DBD generators is well described by the model. The right hand side graph in fig. 3 separates the influence of H_2O induced changes in the reaction kinetics from the influence of the increase in surface conductivity of the dielectric. At 376ppm H_2O content the highest curve is the models prediction for e_{MD}=100.8mJ/cm^3 corresponding to dry process gas. The middle curve uses 0 ppm H_2O in the model, but e_{MD}=104.8mJ/cm^3 characteristic for 376ppm. So the HO-HO_2-catalytic O_3 destruction is omitted, but the surface conduction enhancement effect of water is taken into account. The last curve is the theories regular result for 376ppm H_2O. At low n(O_3), the enhancement of e_{MD} and the so induced loss in the branching ratio from O to O_3 is dominant, while at higher n(O_3) the HO and HO_2 induced kinetic O_3 destruction becomes equally important.

7. Appendix.

(R1a, b, c) $O_2\left(A^3\Sigma_u^+\right), O_2\left(A'^3\Delta_u\right), O_2\left(c^1\Sigma_u^+\right) \rightarrow O\left(^3P\right) + O\left(^3P\right)\Big)$

(R2) $O_2\left(B^3\Sigma_u^-\right) \rightarrow O(^1D) + O(^3P)$ (R3) $e + O_3 \rightarrow e + O(^1D) + O_2(a^1\Delta_g)$

(R4) $O(^1D) + O_2 \rightarrow O(^3P) + O_2$ k_4 [18] (R5) $O(^1D) + O_3 \rightarrow O(^3P) + O_3$ k_5 [18]

(R6) $O(^1D) + O_3 \rightarrow 2O(^3P) + O_2$ k_6 [18] (R7) $O(^1D) + O_3 \rightarrow 2O_2$ k_7 [18]

(R8) $O(^3P) + 2O_2 \rightarrow O_3* + O_2$ k_8 [18] (R9) $O(^3P) + O_3* \rightarrow 2O_2$ k_9=1600*k_{10} [2], [14]

(R10) $O(^3P) + O_3 \rightarrow 2O_2$ k_{10} [18] (R11) $O_3* + O_2 \rightarrow O_3 + O_2$ k_{11}=β [14]

(R12) $O_2\left(a^1\Delta_g\right) + O_3 \rightarrow 2O_2 + O(^3P)$ k_{12} [18] (R13) $O_2\left(a^1\Delta_g\right) + O_2 \rightarrow 2O_2$ k_{13} [18]

(R14) $O_2\left(b^1\Sigma_g^+\right) + O_3 \rightarrow 2O_2 + O(^3P)$ k_{14} [18] (R15) $O_2\left(b^1\Sigma_g^+\right) + O_2 \rightarrow 2O_2$ k_{15} [18]

(R16) $O(^1D) + H_2O \rightarrow 2OH$ k_{16} [18] (R17) $OH + O_3 \rightarrow O_2 + HO_2$ k_{17} [18]

(R18) $HO_2 + O_3 \rightarrow O_2 + OH$ k_{18} [18] (R19) $OH + HO_2 \rightarrow H_2O + O_2$ k_{19} [18]

(R20) $2HO_2 + O_2 \rightarrow H_2O_2 + 2O_2$ k_{20} [18]

8. References

[1] Kogelschatz U 2005 *IOA 17th World Ozone Congress Strasbourg France Paper II.1* (CD ROM)
[2] Eliasson B Hirth M and Kogelschatz U 1987 *J. Phys. D: Appl. Phys*. **20** 1421
[3] Salvermoser M Murnick D E and Kogelschatz U 2008 *Ozone Sci. Eng*. **30** 228
[4] Salvermoser M Kogelschatz U and Murnick D E 2009 *Eur. Phys. J. Appl. Phys*. **47** 22812
[5] Warburg E 1913 *Sitzungsbericht Preuss. Akad. Wiss*. 644
[6] Forbes G S and Heidt L J 1934 *J. Am. Chem. Soc*. **56** 1671
[7] Peyrous R 1990 *Ozone Sci. Eng.* **12** 19
[8] Peyrous R 1990 *Ozone Sci. Eng.* **12** 41
[9] Hirth M 1983 *Brown Boveri Report* 83-178 B (in German)
[10] Yurgelenas Y V and Leeva M A 2009 *IEEE Trans. Pl. Sci*. **37**(6) 809-815
[11] Li J and Dhali S K J 1997 *J. Appl. Phys.* **82** (9) 4205-4210
[12] Kitayama J and Kuzumoto M 1997 *J. Phys. D: Appl. Phys.* **30** 2453-2461
[13] Phelps A V 1985 *JILA Data Center Report* No. 29
[14] Baulch D L 1982 *J. Phys. Chem. Ref. Data* **11**(2) 350
[15] Okazaki K and Nozaki T 2002 *Pure Appl. Chem*. **74**(3) 447-452
[16] Ishimaru K and Okazaki K 1997 *Microscale Thermophysical Engineering* **1** 159-169
[17] Lowke J J and Morrow R 1995 *IEEE Transactions on Plasma Science* **23** (4) 661-671
[18] NIST *Chemical Kinetics Database* (http://kinetics.nist.gov/kinetics/)

PROPERTIES OF OZONE GENERATION USING HIGH PURITY OXYGEN GAS

Masaki Taguchi[1], Yasuhiro Kato[1] and Haruo Itoh[2]

[1]*R&D Center, Metawater Co. Ltd, Chiba 290-8511 Japan*
[2]*Graduate School, Chiba Institute of Technology, Chiba 275-0016 Japan*

It is well-known that ozone concentration decreased during running ozone generator when the ozone generator using high purity oxygen gas ran. Almost experimental units using DBD type ozone generator were set up metal electrode and metal electrode covered with dielectric.
It was thought that Ozone zero phenomenon was generated by metallic oxide on the metal electrode, we studied properties of ozone generation using high purity oxygen gas and an ozone generator with electrodes covered with dielectrics. By using high purity oxygen gas, ozone zero phenomenon was generated. After adding 0.1vol% of nitrogen gas, the ozone concentration increased over the initial ozone concentration. We also studied the effect of liquid oxygen and nitrogen gas ratio on the properties of ozone generation.
In this paper, we reported about results and discussion.

1. Introduction

It is widely known that ozone has strong oxidizing power next to fluorine and disintegrates into harmless oxygen. To make effective use of these properties of ozone, ozone water treatment is being introduced into waterworks for the elimination of foul taste and odor (musty odor) and trihalomethane precursors, all difficult to eliminate via chlorination. Ozone water treatment is also being introduced into sewage treatment facilities for bleaching and sterilization [1] [2]. Moreover, studies on the introduction of ozone-based technology are underway in such fields as the mechanical cleaning of food processing machinery [3], pulp bleaching, and semiconductor manufacturing [4]. Currently, however, high initial and running costs pose a problem to the wider use of ozone water treatment equipment. Further proliferation of ozone water treatment equipment depends critically on size and cost reductions. Among solutions to this problem is high-concentration and high-efficiency ozone generation.
Regarding the behaviors of ozone generators using high-purity oxygen as the raw material (99.99%-pure), it has been reported that the ozone concentration level in an ozone generator decreases over the running time down to approximately 0 g/Nm^3 [5] [6]. We expect that the identification of the causes of this phenomenon will facilitate the enhancement of ozone concentration and generation efficiency.
This time, considering undesirable effect of metal oxide deposition over a metal electrode surface on ozone generation, we examined the phenomenon of the decrease in the ozone concentration in an ozone generator equipped with electrodes not subjected to metal oxide deposition using high purity oxygen. With the same ozone generator supplied with liquid oxygen, we carried out another test on the effects of nitrogen gas addition to determine the optimum amount of nitrogen gas to add. What follows details these experiments and the obtained results.

2. Experimental setup

2.1. Principle of ozone generation

Generally, ozone generation is performed by electric discharge, usually, silent discharge, in a raw material gas containing oxygen. Figure 1 schematically shows the principle of ozone generation by silent electric discharge. The basic configuration comprises a pair of mutually opposing electrodes, at least one of which is covered with a dielectric barrier. Figure 1 gives an example of disc-shaped electrode pair. R&D is underway for alternative configurations comprising concentric tubular or surface discharge electrodes. Typically, a dielectric barrier is made primarily of glass or ceramic.
It is commonly known that, under silent discharge, material ozone undergoes the reactions represented by formulas (1) and (2) to produce ozone. The principle of ozone generation is as follows: When the raw material gas containing ozone flows through a field of silent electric discharge in the air clearance, oxygen molecules collide in the discharge space with electrons accelerated therein and undergo

dissociation into oxygen atoms (formula (1)); then, the dissociated oxygen atoms react (i.e., collide) with oxygen molecules and a third body ("M" in formula (2)) present in the discharge space to produce ozone molecules (formula (2)). Thus, electric discharge is used to generate oxygen atoms and then ozone molecules.

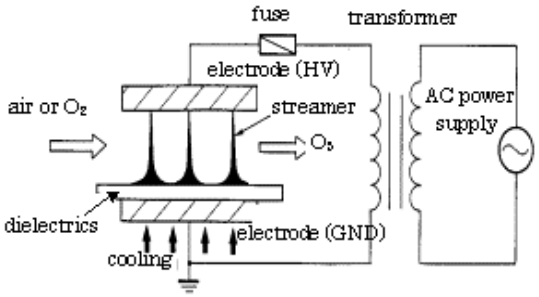


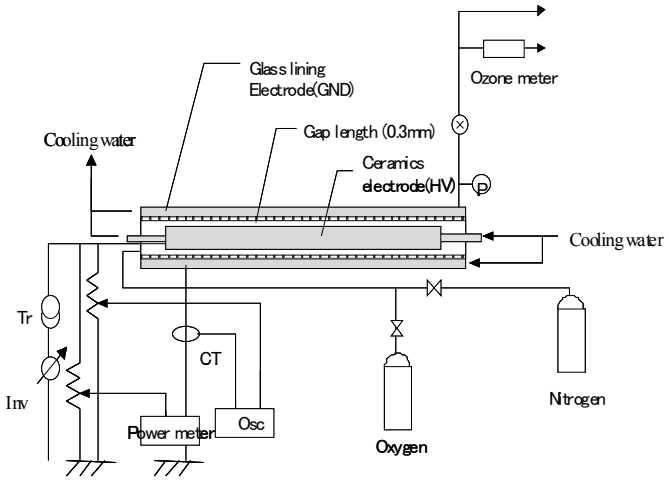
Fig. 1. Principle of ozone generation using silent discharge

$O_2 + e \rightarrow 2O + e$ … (1)
$O + O_2 + M \rightarrow O_3 + M$ … (2)

2.2 Structure of ozone generation

Figure 2 shows the experimental system of ozone generator used this time and the chemical composition of high-purity oxygen supplied to it. The ozone generating electrodes consisted of a glass lined tube provided as the grounding electrode and a ceramic electrode provided as the high-voltage electrode. The high-voltage electrode and the grounding electrode, respectively, consisted of a discharging plate covered with a dielectric barrier to prevent metal oxide deposition on their surfaces during electric discharge. The glass lined tube measured 1,160 mm long and the ceramic electrode 600 mm long. The discharge clearance was 0.4 mm long, and a four-point spacer (points separated by 90°) was fitted circumferentially around the high-voltage electrode surface. The spacer was made of a Teflon sheet and Teflon adhesive tape. A double-side cooling system was adopted for simultaneous cooling of the high-voltage electrode and the grounding electrode. For cooling water, deionized water was used to ensure insulation. A mass flow controller was used to control the flow rate of the raw material oxygen gas and that of the additive nitrogen gas to the ozone generator. The ozone gas generated by the ozone generator was passed through the ozone monitor to measure its concentration and then was reduced into oxygen by an ozone decomposition catalyst (Carulite®) before release into the air.

In the experiments, 99.99%-pure oxygen was used, which is purer than 99.6%-pure liquid oxygen normally used as raw material or than PSA-generated oxygen (with a maximum purity of 95%). To prevent loss of quality of the high-purity gas during the experiments, the ozone generator and the piping were pump-purged of air, followed by several replacements of gas with high-purity oxygen.



Composition	Ratio
O_2 (%)	99.99
N_2 (ppm)	<10
CH_4 (ppm)	<30
Ar (ppm)	<30
CO (ppm)	<1
CO_2 (ppm)	<1
N_2O (ppm)	<1
Dew point (ºC)	<-70

Figure 2: Experiment system of ozone generator and compositions of high purity oxygen

3. Results and Discussion

Figure 3 shows the change in ozone concentration over time during ozone generation using high-purity oxygen. Figures 4 to 6 show the changes in electric current, voltage, and discharge power over time, respectively. The experiment conditions were as follows:

- Discharge power: 400 W
- Gas: High purity oxygen (≥ 99.99%)
- Gas flow rate: 2.75 L/min
- Gas pressure: 0.18 MPa
- Clearance: 0.4 mm
- Cooling water temp: 10ºC (both electrodes)

At the initial stage of the operation of the generator, the ozone concentration was 200 g/Nm3. Then, the ozone concentration gradually decreased with the elapsed time of operation. After approximately 5 hours of operation, the ozone concentration dropped and stabilized at 54 g/Nm3. Thus, it was shown that, after approximately 5 hours from the start of operation, the ozone concentration decreased by as much as 73% from the initial value. The addition of 0.1 volume-percent nitrogen gas (at 2.75 mL/min) at the 6-hour point after the start of operation increased the ozone concentration to 216 g/Nm3, exceeding the initial value. The addition of nitrogen gas fully restored the ozone concentration in approximately 1 minute, which is approximately 10% to 20% shorter than the restoration time required under the conditions of the previously reported experiment(5). The addition of nitrogen gas continued for approximately 1 hour, during which the ozone concentration remained largely stable. Upon the termination of nitrogen addition, the ozone concentration started to decrease again and then stabilized at 53 g/Nm3, almost on a par with the pre-nitrogen addition level. Originally, it took approximately 5 hours for the ozone concentration to decrease. After the termination of nitrogen addition, the time required for the process decreased sharply to approximately 2 hours.

As shown in Figures 4 to 6, the current, voltage, and discharge power measured simultaneously with the ozone concentration were observed to remain almost unchanged, independently of the drop in ozone concentration, until approximately 6 hours elapsed after the start of the oxygen generator. The current, voltage, and discharge power sharply dropped immediately after the addition of nitrogen gas. Then, these electric readings remained stable, respectively, at a lower level than before the addition of nitrogen gas. Following the termination of nitrogen gas addition, the electrical readings rose back to the pre-nitrogen addition levels in an approximately same time as the change in ozone concentration.

The observations above demonstrate that, even in the absence of a discharger consisting of metal electrodes, in other words, under conditions under which metal oxide generation does not occur, the use of high-purity oxygen will reduce the ozone concentration. This suggests that the ozone decomposition catalytic function of metal oxides is only of minor influence or almost not influential at all. While the electrical readings taken this time remained stable, independently of the change in ozone concentration, during the operation using a raw material gas consisting entirely of oxygen, the addition of nitrogen gas caused all these readings to change, clearly indicating that there were changes in electrical discharge.

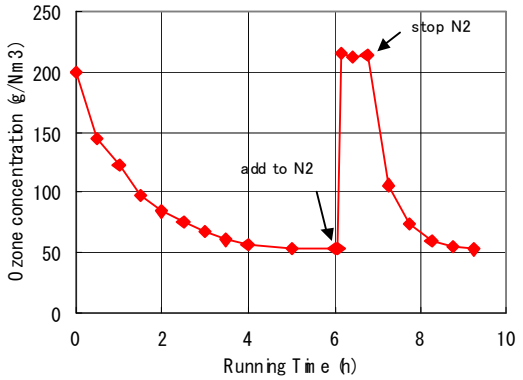


Fig. 3. Temporal change in ozone concentration using high-purity oxygen gas

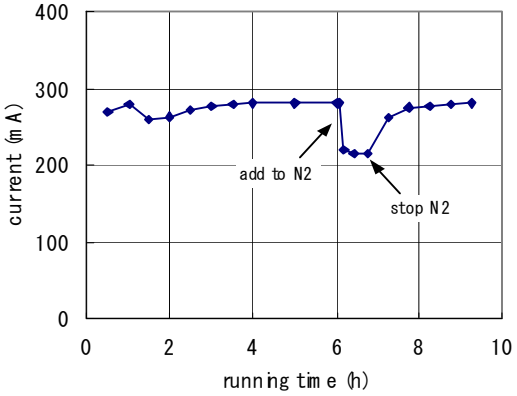


Fig. 4. Temporal change in current

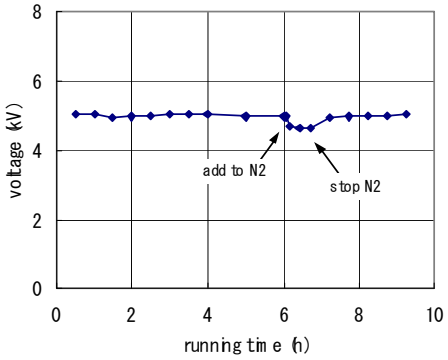


Fig. 5. Temporal change in voltage

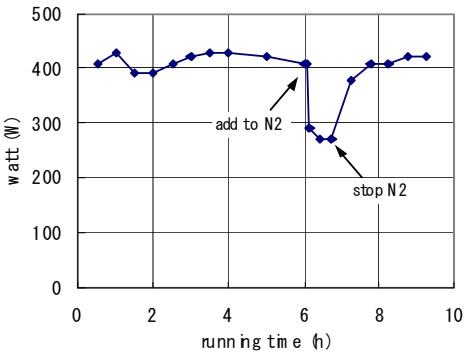


Fig. 6. Temporal change in discharge power

From the experimental results above, the mechanism of ozone concentration decrease during the operation using high-purity oxygen was considered. It is likely that the generation of the third body M in formula (2) depends more heavily on nitrogen atoms or molecules than on oxygen atoms or molecules. In a previously reported experiment[5] using liquid oxygen, too, the ozone concentration decreased albeit to a lesser degree. The initial ozone concentration of 200 g/Nm^3 was observed to drop to180 g/Nm^3 after approximately 13 hours of operation. The raw material liquid oxygen had a nitrogen gas content of 94 ppm, more than 9 times higher than a sub-10 ppm level of high-purity oxygen. The ozone concentration dropped less significantly with the liquid oxygen than with the high-purity oxygen gas. These facts suggest that even a miniscule amount of nitrogen gas is highly effective in preventing the ozone concentration from dropping.

The time required for the ozone concentration to drop and stabilize differed before and after the addition of nitrogen gas. It The originally required time was long due to the influences of impurities, such as organic substances or moisture, on the electrode surfaces.

4. Conclusion

An evaluation was made on an ozone generator equipped with a silent discharger having at least one dielectric-covered metal electrode and supplied with a material gas consisting of high-purity oxygen containing liquid oxygen. The following were revealed:

1) The ozone concentration in an ozone generator dropped when high-purity oxygen alone was used and when the discharge electrodes of the ozone generator had no exposed metal surfaces. The ozone concentration of 200 g/Nm^3 at the initial stage of operation dropped by approximately 73 percent down to 54 g/Nm^3 after 5 hours.

2) When nitrogen gas was added with the ozone concentration at a low level, the ozone concentration rose back and up to 216 g/Nm^3. During the addition of nitrogen gas, the ozone concentration was not observed to drop. Upon the termination of nitrogen gas addition, however, the ozone concentration dropped again down to the pre-nitrogen addition level.

We will follow up with additional investigations and experiments on the mechanism of the so-called ozone zero phenomenon.

5. References

(1)Ozaki: JWWA, Vol.64, No.10, P34-37(1995)
(2)Noguchi at el : 33th JSWA, p690-692(1996)
(3)Satoshi Fukuzaki, Hiromi Urano, Atsuhiko Takehara, Minoru Hiramatsu: Facilitation of cleaning of food-processing equipment,JOA 9th ,p175-178 (2000)
(4)Japan TAPPI, Vol.51, No.5 (1997)
(5)Kohichi Hashimoto, Hisamichi Ishioka: Ozone Generation Properties using High Purity Oxygen Gas, IEEJ Electrical Discharge ED-00-109 (2000)
(6)Yuji Okita, Motoi Noguchi, Takaaki Murata : The Characteristics of Coplanar Discharge Ozonaizer by Changing Feed Gas, IEEJ Electrical Discharge ED-00-108 (2000)

A COMPACT OZONE GENERATION SYSTEM USING PIEZOELECTRIC TRANSFORMER

K. Teranishi[1], Y. Takano[1], T. Anabuki, N. Shimomura[1], S. Suzuki[2] and H. Itoh[2]

[1]*Institute of Technology and Science, The University of Tokushima*
[2] *Graduate School of Engineering, Chiba Institute of Technology*
E-mail: teranishi@ee.tokushima-u.ac.jp

A compact ozone generation system that employs the parallel driving of two piezoelectric transformers (PTs) is developed. The system includes all functions required for the ozone generation in one unit: a dielectric barrier discharge (DBD) reactor that employs the parallel driving of two PTs, its driving and controlling circuits, the gas inlet and outlet ports and gas flowmeter. The ozone generation is performed by feeding 99.9% of the pure oxygen into the ozone generator with the driving voltage of 50-80 V and gas flow rate of 0.2-2.0 L/min. The automatic frequency control for the operation of PTs is also demonstrated for the ozone generation since the resonance frequency of the PTs is fluctuated by the temperature increase inside the reactor and it affects the electrical performance of the PT during the long-term operation.

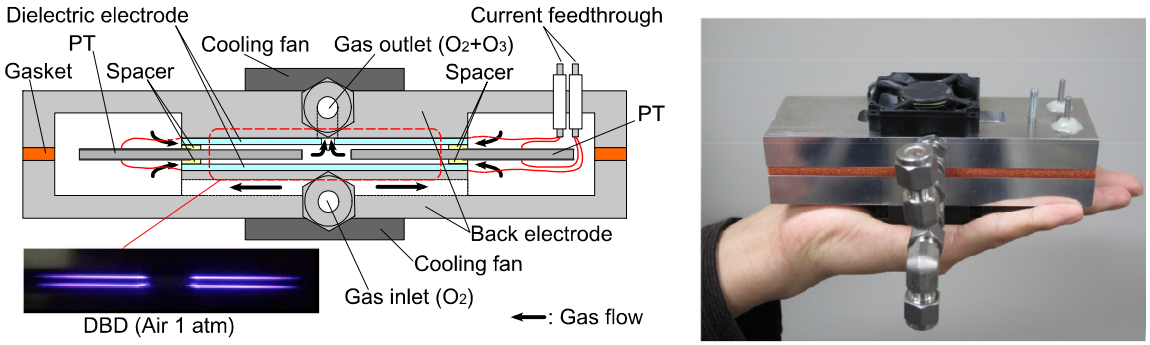
1. Introduction

The authors have developed and studied compact ozone generators using piezoelectric transformers (PTs) which are designed to utilize for a limited scale of the ozone applications to air conditioning, water treatment, sterilization and food processing. The present ozone generators are based on the excitation of dielectric barrier discharge (DBD) [1] generated by the PT surfaces [2] that induce high voltage due to the piezoelectric effect [3]. We previously reported the characteristics of a compact ozone generator constructed of a single PT [2], [4]. The maximum ozone concentration and yield efficiency are obtained to be 20 g/Nm3 and 223 g/kWh, respectively, which are low concentration, however, high efficiency compared to the other type of DBD-ozone generator. In order to improve such low power characteristics of the ozone generator based on the single PT, we have proposed the ozone generator employing the parallel driving [5] of multiple PTs [6].
In this study, we have developed a compact ozone generation system that employs the parallel driving of 2 PTs and contains all functions required for the ozone generation in one unit. This paper presents a general description of the developed ozone generation system and some of the basic results concerning the ozone generation characteristics.

2. Experimental setup

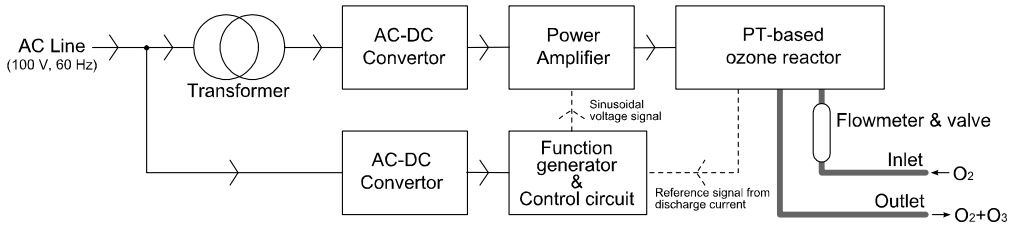
Figure 1(a) shows a configuration of the PT-based ozone reactor. The main frame of the reactor is made of aluminum and the entire dimension is about 150×50×35 mm. The structure of the reactor is basically similar to that reported previously [6]. Two PTs are located between two dielectric electrodes on the contact with spacers, as shown in the figure. The primary terminals of the PTs are connected in parallel so as to be driven by a single power-supply circuit. The discharge gap is formed between the PT surface and dielectric electrode, which is maintained by a 0.3-mm thickness spacer. Two PTs, dielectric electrodes and spacers are fixed by the upper and lower aluminum bodies which act as back electrodes. If a sinusoidal voltage is applied to the primary terminals via the current feedthroughs and the frequency is adjusted to mach a natural vibration of the PTs, a high voltage is induced on both PT surfaces and the DBD appears in the gap space, as shown in the picture. Air cooling fans are attached at both back electrodes to avoid the temperature increase in the reactor. A photograph of the ozone reactor is shown in Fig. 1(b). We succeed in the development of such handheld ozone reactor, which allows us to reduce its size down to approximately 58% in volume ratio compared to that previously reported by the authors [6].
Figure 2 shows a block diagram of the ozone generation system developed in this study. The ozone generation system consists of the ozone reactor indicated in Fig. 1, its driving and controlling circuits, the gas inlet and outlet ports and gas flowmeter with needle valve. Therefore, the ozone generation is possible if preparing additionally gas cylinder, air pump or PSA oxygen generator. An 100 V at 60 Hz from AC line is stepped up by an electromagnetic induction-type transformer and the regulated ±150

V DC output, which is fed to a power amplifier circuit, is obtained by a half-wave voltage doubler circuit. A sinusoidal voltage in the frequency range of 27-28 kHz is synthesized by a function generator IC. It is multiplied by the B-class push-pull power amplifier and then applied to the ozone reactor. Control circuit is based on the microcontroller technology, which enables to precisely control and monitor the driving voltage of the ozone reactor and its frequency. The automatic frequency control is also available so as to follow resonance frequency of the PTs since the resonance frequency is affected by the temperature increase of the PT during the long-term operation. Figure 2(b) shows the picture of the system. The ozone reactor indicated in Fig. 2(b) is mounted inside the chassis of 150×180×280 mm. The front panel has an LCD display, an LED lamp, a push switch, rotary switch, potentiometer, rotary encoder and flowmeter with needle valve. The main power switch, AC plug and the gas inlet and outlet are located at the rear panel. The LCD display indicates the applied voltage to the reactor and the frequency which are adjustable by rotating the potentiometer and rotary encoder dials, respectively. Push switch is to start the ozone generation and the continuous (normal) operation or the automatic frequency control modes are selectable by the rotary switch.



(a) Configuration of ozone reactor (b) Photograph of ozone reactor

Fig. 1. PT-based ozone reactor



(a) Block diagram of ozone generation system



(1) LCD monitoring applied voltage and frequency
(2) LED lamp for resonance frequency detection
(3) Control dial for applied voltage
(4) Control dial for frequency
(5) Rotary switch for function select
(6) Push switch for ozone generation
(7) Gas flowmeter with needle valve

(b) Photograph of the developed ozone generation system

Fig. 2. Ozone generation system

3. Experimental results and discussions

We first estimate the power consumption for the ozone reactor. Figure 3(a) shows the waveforms of the driving voltage $v(t)$ and current $i(t)$ measured using an oscilloscope at the electrical input of the ozone reactor. The driving voltage is adjusted to be 80 V_{rms}. The driving current of 0.12 A_{rms} flows

with 8.2° in leading phase with respect to the voltage waveform. The power consumption P is then estimated by the following equation.

$$P = \frac{1}{T}\int_0^T v(t)\cdot i(t)dt \qquad (1)$$

T is the cycle of the driving voltage and current. Figure 3(b) shows the relationship between the driving voltage and the power consumption for the ozone reactor. By increasing the driving voltage from 50 to 80 V, the power consumption is increased linearly in the range from 5.5 to 11.2 W. The electric energy can be mainly used to excite the mechanical vibration of 2 PTs, then a part of it gets converted to electric energy for inducing a high voltage on the secondary surface of the PTs. Others are dissipated as some losses, such as heating derived from the internal friction in the ceramics due to the elastic oscillation, dielectric losses, vibration leakage at support point and lead wires and so on. In many cases, the ozone generation characteristics are estimated by the discharge power, which does not involve the energy losses due to the power supply. In this paper, the power consumption at the ozone reactor is however used for the estimation of the ozone generation characteristics since the discharge power is not obtainable due to the systems' structure. Therefore, note that the power consumption P in this paper includes the above-mentioned energy losses accompanied by the operation of the PTs.

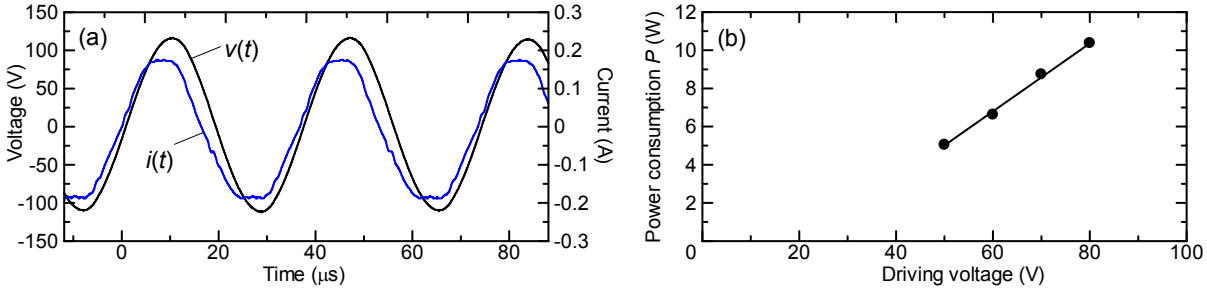


Fig. 3. Driving voltage and current waveforms of ozone reactor (a) and power consumption as a function of driving voltage (b).

Figure 4(a) shows the ozone concentration C as a function of specific energy P/Q. The results are obtained with the driving voltage of 50-80 V and at gas flow rate of 0.2-2.0 L/min. The ozone concentrations in the vertical axis indicate the stable values 5 min after starting the operation of the ozone reactor. In the lower specific energy region, the ozone concentration increases almost linearly by the increasing specific energy P/Q, which is independent of the gas flow rate. However, it tends to be saturated at the higher specific energy region, depending upon the gas flow rate. The higher concentrations are obtained at the lower gas flow rate. The maximum ozone concentration is achieved to be 59.5 g/Nm^3. Also, we can estimate the ozone yield ranging from 0.69 to 1.57 g/h in this study.

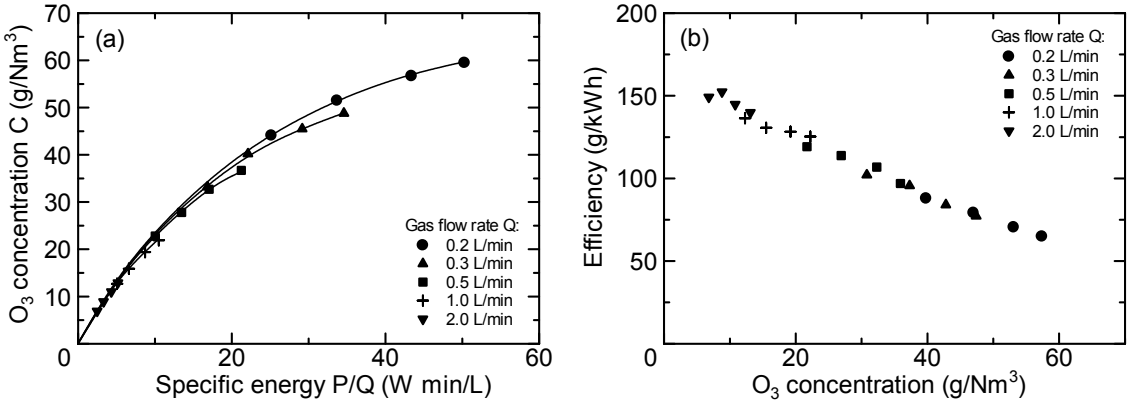


Fig. 4. Ozone concentration as a function of specific energy (a), ozone yield efficiency plotted with respect to ozone concentration (b).

The ozone yield efficiency plotted with respect to the ozone concentrations are indicated in figure 4(b). The ozone yield efficiency is decreased by the increase in the ozone concentration and independent of the gas flow rate. The maximum ozone yield efficiency of 152 g/kWh is obtained at the ozone concentration of 8.8 g/Nm^3 and gas flow rate of 2.0 L/min.

We applied the automatic frequency control for the operation of PTs embedded in the system and demonstrated the ozone generation. Figure 5 shows the temporal variation of the ozone concentrations measured while working the system for 120 minutes. The red and black curves are the results obtained with and without the automatic frequency control, respectively. If the automatic frequency control is enabled, the microcontroller measures periodically the discharge current and repeats the adjustment of the driving frequency until the maximum discharge current is detected. In this experiment, the adjustment width of driving frequency Δf and its repetition cycle Δt is set to be 10 Hz and 100 ms, respectively. In any cases, starting the ozone generation at t=0 min, the ozone concetration increases rapidly upto the maximum concentration and then it decreases gradualy with time, which results in almost constant concentration. The decrease in the concentration between the maximum and constant concentration is due to the dissociation of ozone molecules owing to temperature increase inside the reactor. It is likely to be cased by the gas heating due to the high-current density, dielectric heating and mechanical vibration of the PT. Although the concentrations obtained with and without the automatic frequency control are almost similar in the early stage of the continuous operation, the diffrence in the concentrations is particularly observed for the long-term operation of the ozone generation system. The higher concentrations are obtained by operating the system with the automatic frequency control, which increased up to 10% and 4% at the driving voltage of 60 and 80 V, respectively. By enabling the automatic frequency control, the system follows the resonant frequency of the PT even if it fluctuates slightly with time due to the temperature increase. This is expected to maintain the high-voltage on the PT surface to be always maximum during the long-term operation which results in achieving the higher ozone concentration.

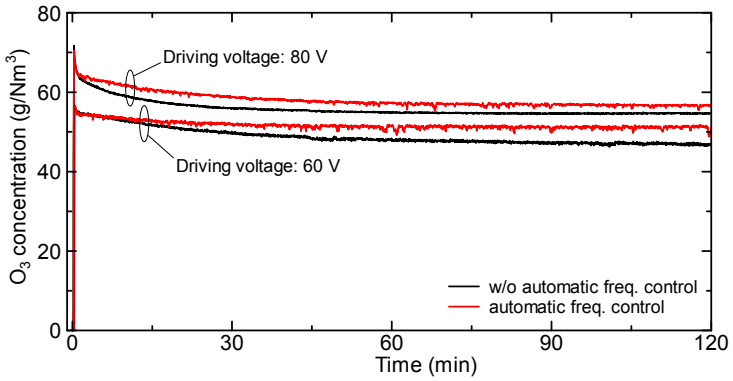


Fig. 5. Temporal variation of ozone concentration obtained with and without the frequency control.

4. Conclusion

The compact ozone generation system using piezoelectric transformers (PT) was developed and the ozone generation characteristics are investigated. The entire dimension of the system is 150×180×280 mm and includes all functions required for the ozone generation in one unit. The maximum ozone concentration and yield efficiency is achieved to be 59.5 g/Nm^3 and 152 g/kWh, respectively. The ozone yield ranges from 0.69 to 1.57 g/h. The automatic frequency control for the operation of PTs is demonstrated for the ozone generation. The effectiveness of the automatic frequency control is particularly observed during the long-term operation of the system. The automatic frequency control leads to increase the ozone concentration up to 10%.

This study was partially supported by Research for Promoting Technological Seeds from JST. The authors would like to also thank Mr. Hisatake for his help in our experiments.

5. References

[1] Becker K H, Kogelschatz U, Schoenbach K H and Barker R J 2005 *Non-Equilibrium Air Plasmas At AtmosphericPressure* (London: Institute of Physics Pub. Inc.).
[2] Itoh H, Teranishi K, and Suzuki S 2006 *Plasma Sources, Sci. Technol.* **15** S51-S61.
[3] Curie J and Curie P 1880 *Bull. Soc. Fr. Mineral.* **3** 90.
[4] Teranishi K, Suzuki S, and Itoh H 2004 *Japan. J. Appl. Phys.* **43** 6733-6739.
[5] Wada T 2006 *IEEJ Trans. FM* **126** 837-843 (Japanese).
[6] Teranishi K, Shimomura N, Suzuki S, and Itoh H 2009 *Plasma Sources, Sci. Technol.* **18** 045011(10pp).

MEASUREMENT OF OZONE CONCENTRATION BASED ON VISIBLE PHOTO-ABSORPTION METHOD

K. Teranishi[1], Y. Shimada[1], N. Shimomura[1] and H. Itoh[2]

[1]*Institute of Technology and Science, The University of Tokushima*
[2] *Graduate School of Engineering, Chiba Institute of Technology*
E-mail: teranishi@ee.tokushima-u.ac.jp

The authors have investigated the measurement of ozone concentration based on the visible photo absorption. An orange LED having emission peak at 604 nm and a phototransistor sensitive at visible light are used for the light source and photo detector, respectively. Simple linear absorption cells having the different light-path length of 10-50 cm are prepared and the absorbance is measured by varying the ozone concentration. The ozone concentration can be measured in the range from 16.9 to 89.2 g/Nm^3.

1. Introduction

Ozone has been widely used for many industrial fields, such as water treatment in sewage treatment plants, sterilizations of virus and bacteria and deodorizations in food factories [1]. In these applications, ozone generation must be performed on site paying attention to its concentration because it is strongly affected on the fluctuations of gas temperature and moisture or some other disturbances. Although there are some techniques to measure the ozone concentration, the ultraviolet (UV) absorption method is commonly used, for which ozone has a nature that strongly absorbs UV light around 200-300 nm [2]. The ozone monitor based on the UV absorption consists of low-pressure mercury lamps, photo-detectors, quartz cell and filters. In most cases, two photo-detectors and a half-mirror are needed to precisely determine the absorbance under the instability of the light source. They could be factors of the instruments to be expensive. In addition, the use of mercury lamp should be avoided from the view point of the recent environment situation. Except for the UV absorption band mentioned above, there is another photo-absorption band, which is distributed broadly in the visible light region between 450 and 850 nm and referred to as Chappuis band [3]-[5]. Although the absorption coefficient in Chappuis band is about 2,000 times lower compared to that of Hartley band, the ozone measurement is possible using the simple devices such as LEDs and photo diodes or transistors. This offers benefits including the low-cost measurements and the mercury-free equipments. Also, the measurement based on the visible photo-absorption method will be available if considering the recent technology trend in ozone applications toward utilizing high-concentration ozone.

Several attempts related to the ozone concentration measurement using visible photo absorption can be found. The measurement of the ozone concentration in the visible photo absorption using an LED source was investigated by Fowles and Wayne [6]. They measured the absorbance in a quartz cell filling with ozone using the yellow-red LED and a photodiode as a light source and photo detector. The relations between the absorbance and ozone concentration are in good agreement with Beer-Lambert behavior. AC amplification was employed for the light-detector circuits in order to heighten the sensitivity of measurement. The ozone concentration was measured in the range from 5 to 56 g/m^3 with 10-cm light path length. Hawe *et al* [7]. proposed the ozone concentration measurement in the visible absorption using an integrating sphere as an absorption cell. Light fluxes emitted from the source repeat the diffuse reflections inside the sphere wall, which allows making the light path to be longer. A 2-inch diameter of the integrating sphere corresponds to nearly 70-cm light path length of linear absorption cell.

In this study, we describe the possibility of the ozone measurement using the visible photo-absorption band [8]. An absorption cells with the length of 10-50 cm are constructed. An LED having a peak wavelength at 604 nm and a photo transistor are used as a light source and a detector, respectively. Absorbance was measured while feeding ozone into the absorption cell through a UV ozone monitor. The effective absorption coefficient was estimated by the fitting procedure based on the Beer-Lambert law. The ozone concentration can be measured by visible photo-absorption method in the concentration range from 16.9 to 89.2 g/Nm^3.

2. Experimental setup

Figure 1(a) shows the configuration of absorption cell used in this experiment. The absorption cells are made of stainless steel tube of inner diameter 0.8 cm. We prepared absorption cells having different light path length of d=50.3, 25.3 and 10.5 cm. An orange LED and phototransistor are equipped at both ends. Light emitted from the LED pass through a soda-glass window and a 2-mm diameter pinhole and enters into the cell filling ozone. Light intensity is then measured by the phototransistor. The LED is driven with DC 12 V through the current regulative diode (20 mA). The emitter current of the photodiode that corresponds to the light intensity is detected by a 47-kΩ shunt resistor as a voltage drop. The voltage is then amplified by an operational amplifier and measured by 5.5-digits digital multi-meter. The experimental system is shown in Fig. 1(b). Ozone is synthesized by a piezoelectric transformer (PT)-based ozone generator [9] with feeding 99.9%-grade oxygen. The ozone concentration is controlled by varying the applied voltage for the PT and the gas flow rate. The generated ozone first flows into an UV ozone monitor for calibrating the given concentration and then toward the test absorption cell. The gas temperature at the inlet of the tested cell is measured by the thermistor. The temperature in the absorption cell for the UV ozone monitor is also obtainable by the system mounted itself. The ozone concentration, the gas temperature and the photo transistor signals are automatically recorded every 0.5 sec using a personal computer via the RS232C interface.

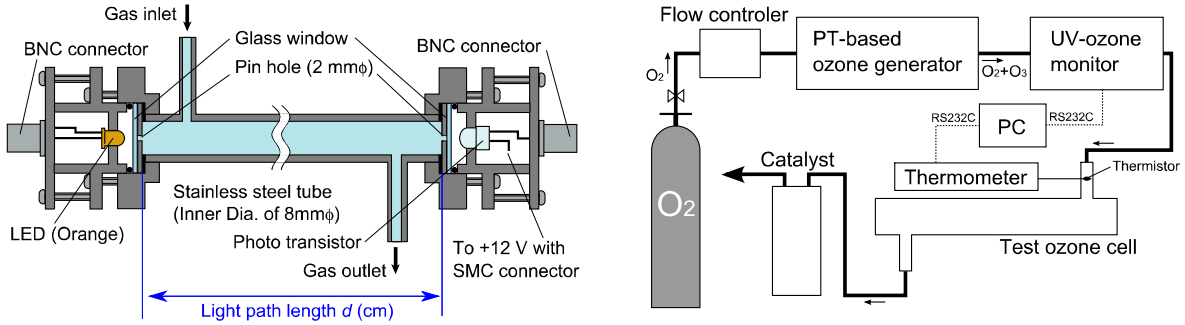


Fig. 1. A schematic diagram of experimental setup

Figure 2 shows photo absorption spectra in the visible region (Chappuis band) reported by Inn and Tanaka [3] and Griggs [4]. In both cases, the absorption band spectra are distributed broadly around 450-850 nm, of which the double peak structure is seen at the wavelengths of 574 and 602 nm. The peak absorption coefficient at 602 nm reported by Griggs is about 9% greater than that of Inn and Tanaka. Also, the measured emission spectrum of the LED source and the spectral sensitivity of the phototransistor are given in the same figure. The peak of the emission spectrum for the LED is found at 604 nm, which agrees almost with the absorption spectrum peak at 602 nm. The spectral response of the phototransistor exhibits the maximum at 800 nm and the relative sensitivity around 600 nm is approximately 40-50%.

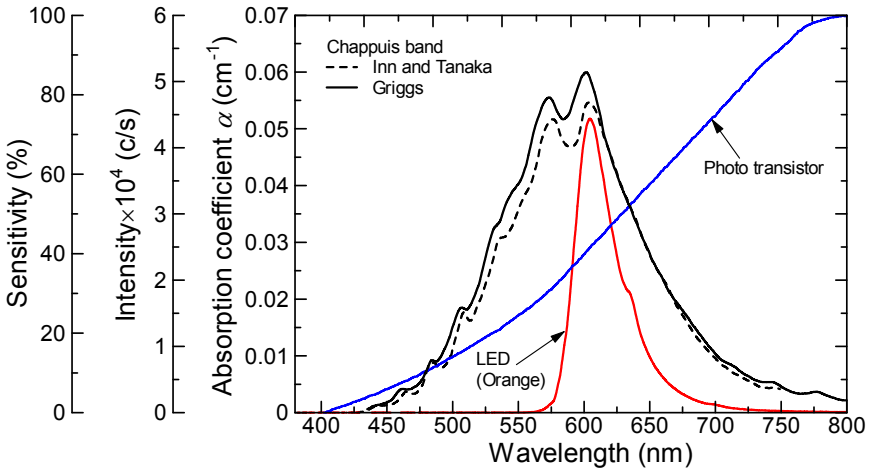


Fig. 2. Photo absorption spectrum in Chappuis band

If a monochromatic light enters into a sample gas at the concentration of C g/m^3 and travels in a length d cm, the absorbance A is defined as

$$A = \log_{10}\frac{I}{I_0} = -\frac{22.413}{48000}\alpha C d\,, \qquad (1)$$

where I_0 and I are the incident and transmitted light intensity, respectively, and α cm^{-1} is the absorption coefficient. Actually, the light intensity I and I_0 is determined from the phototransistor signals which are measured with and without feeding ozone into the cell, respectively. The ozone concentration obtained by the UV ozone monitor and the corresponding transmittance I/I_0 are reduced to those at the standard temperature and pressure (0°C, 1atm) since the temperature in both cells is completely different. Also, the absorption coefficient can be estimated experimentally.

3. Experimental results and discussions

Figure 3(a) shows the temporal variation of the ozone concentration obtained by the UV-ozone monitor and the photo transistor signal for the visible absorption. Ozone is generated by changing the driving voltage of 50-70 V for the ozone generator and the gas flow rate of 0.2-1.0 L/min. The light intensity I_0 is adjusted to be 10.0 V.

Starting up the ozone generator at 70 V with gas flow rate of 0.2 L/min, the ozone concentration rises at t=0 sec and then exhibits the maximum concentration of 91.2 g/Nm^3. After the transient peak concentration, it gradually decreases with time and finally results in the stable concentration C_{st}=84.7 g/Nm^3. On the contrary, the photo transistor signal decreases from 10.0 to 8.0V by increasing the ozone concentration of 84.7 g/Nm^3. Then, as stopping the ozone generation around t=210 sec, the signal returns toward the initial voltage of 10.0 V. The other results measured with the different primary voltages and gas flow rates show the similar tendencies. The greater decrease in the photo transistor signal was observed at the higher ozone concentrations. These results clearly indicate that the photo absorption of the visible light due to the ozone molecules causes inside the cell.

The transmittance I/I_0 is determined with each stable ozone concentration C_{st} and plotted with respect to the product of the ozone concentration C_{st} and the light path length d. The results are shown in figure 3(b). We performed the same experiments for different light path length of 50.3, 25.3 and 10.5 cm. The transmittance I/I_0 is decreased exponentially with respect to $C_{st}\times d$ and is independent of the light path length. The solid line is the fitted curve calculated using equation (1), adjusting the absorption coefficient α so as to best fit the experimental data. The experimental data agrees fairly well with the theoretical curve calculated on the basis of Beer-Lambert law. From the fitting procedure, we can estimate the absorption coefficient $<\alpha>$=0.0522 cm^{-1}. The absorption coefficient obtained in this experiment can be interpreted as an effective absorption coefficient since there exist the spectral dependences of the intensity of the LED source and the sensitivity of the photo transistor.

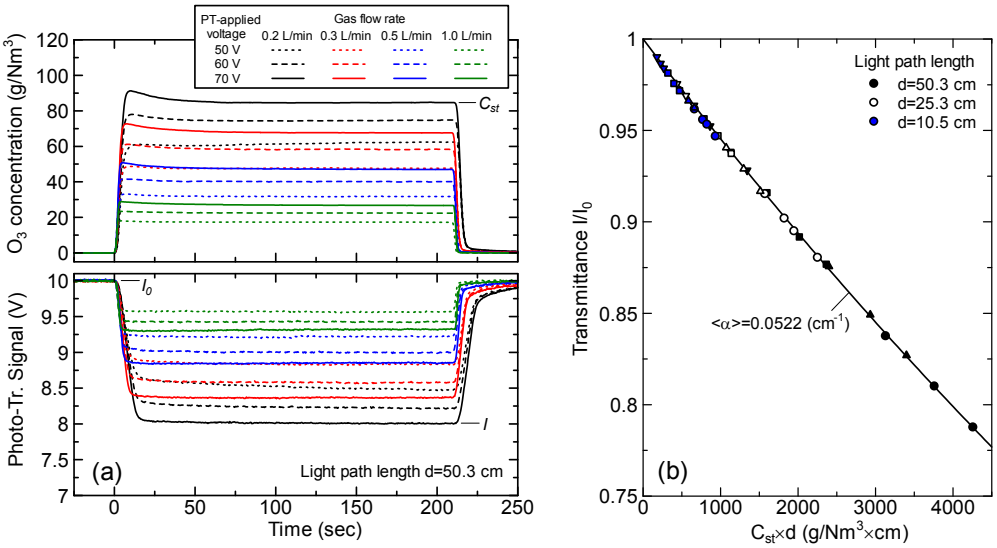


Fig. 3. (a) Temporal variation of ozone concentration measured by UV-ozone monitor and photo transistor signal, (b) Transmittance I/I_0 as a function of the ozone concentration C_{st}

The temporal variation of the ozone concentration determined for the visible photo absorption is shown in Fig. 4(a). The light path length d is 50.3 cm. These results are obtained by substituting the photo transistor signal in figure 2(a) and the effective absorption coefficient $<\alpha>$ into equation (2). In each case, the ozone concentrations obtained by both two methods are almost in good agreement. Although the ozone concentration measured by the UV-monitor shows transient peak, this behavior cannot be seen in the ozone concentration obtained by the visible absorption method. This is derived from the cell configuration used for the visible absorption measurement since the cell length of 50 cm is too long, which results in the slow response time of the signal. For measuring the ozone concentration using the visible photo absorption, the cell length must be elongated in order to get higher sensitivity because of the low absorption coefficient in the visible band. Figure 4(b) shows dependence of the light path length on the ozone concentration data. Shorter light path length leads to enhance the noise signal contained within the detected phototransistor signal. Also, the relatively slow-rate fluctuation is observed with the shorter light path length. This is probably derived from the drift of the LED intensity or detector circuit.

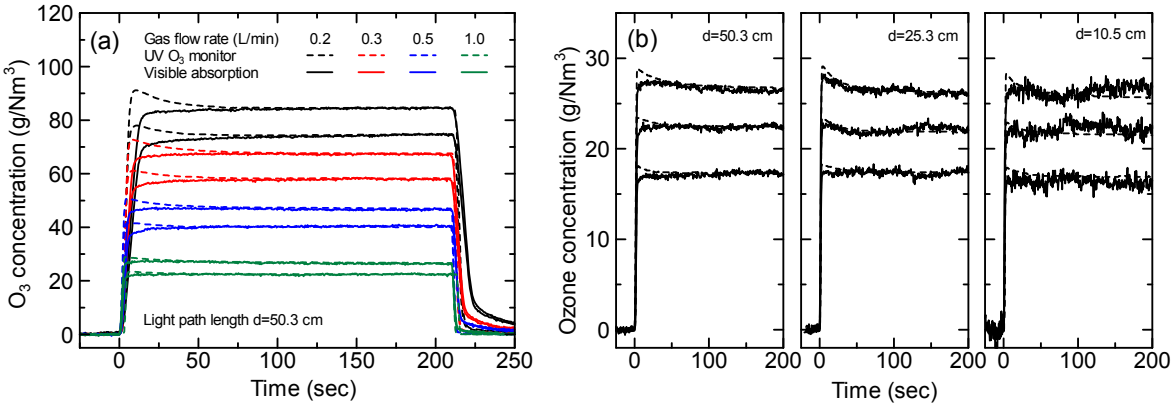


Fig. 4. (a) Comparison of the ozone concentration measured by visible photo absorption and UV-ozone monitor, (b) dependence of light path length on the determined ozone concentration

4. Conclusion

The measurement of ozone concentration based on the visible photo absorption is investigated. An LED having spectral peak at 604 nm and a photo transistor as a light source and photo detector are employed. The decrease of light intensity due to the visible photo absorption is observed by increase in the ozone concentration. The measured absorbance is in reasonable agreement with Beer-Lambert law and is independent of the light path length. The effective absorption coefficient $<\alpha>$ is determined to be 0.0522 cm^{-1}. The ozone concentration determined by the visible photo absorption agrees well with that measured by UV-ozone monitor. In this study, the ozone concentration in the range from 16.9 to 89.2 g/Nm^3 can be measured using the visible photo absorption. We are now considering the absorption cell capable of the simultaneous pursuit of the high sensitivity measurement and compact configuration.

5. References

[1] Loeb B L 2009 *Proc. 19th Ozone World Congress and Exhibition* 3-K-1(20pp).
[2] Hartley W N 1881 *J. Chem. Soc., Trans*. **39** 111-128.
[3] Inn E C Y and Tanaka Y 1953 *J. Opt. Soc. Am.* **43** 871-873.
[4] Griggs M 1968 *J. Chem. Phys.* **49** 857-859.
[5] Voigt S, Orphal J, Bogumil K, and Burrows J P 2001 *J. Photochem. and Photobiol. A: Chem*. **143** 1–9.
[6] Fowles M and Wayne R P 1981 *J. Phys. E: Instrum.* **14** 1143-1145.
[7] Hawe E, Fitzpatrick C, Chambers P and Lewis E 2007 *J. Phys.: Conf. Ser*. **76** 012041.
[8] Shimada Y, Teranishi K, Shimomura N, Suzuki S and Itoh H 2009 *Proc. 19th Ozone World Congress and Exhibition* 11-5(8pp).
[9] Teranishi K, Shimomura N, Suzuki S and Itoh H 2009 *Plasma Sources, Sci. and Technol.* **18** 045011(10pp).

Topic 5
Generation of radiation in high pressure discharges

MULTI-WAVELENGTH MODE OF DIELECTRIC BARRIER DISCHARGE OPERATED WITH THE MERCURY BROMIDE/RARE GASES MIXTURES

Mykola M. Guivan[1], Antonina A. Malinina[1], Hanna M. Guyvan[2]

[1]*Department of Quantum Electronics, Uzhgorod National University, Pidgirna 46, Uzhgorod 88000, Ukraine*

[2]*Department of Optics, Uzhgorod National University, Pidgirna 46, Uzhgorod 88000, Ukraine*

E-mail: m_guivan@rambler.ru

The emission spectra from atmospheric-pressure dielectric barrier discharge (DBD) with HgBr2/He or HgBr2/Xe/Kr mixtures, as well as the electrical characteristics have been investigated at the repetition frequency of sinusoidal voltage pulses up to 125 kHz. In the spectra, the research has revealed radiation from HgBr(B–X, C–X) exciplex molecules, atomic lines of mercury and rare gases, and, in mixtures with xenon, radiation of XeBr(B–X, B–A) exciplex molecules. The high-frequency atmospheric-pressure barrier discharge in mixtures of mercury dibromide with gases can be used in multi-wavelength exciplex lamps, operating in the UV and visible regions.

1. Introduction

Mercury monohalides HgX* (X=Cl, Br, I) are known to be the intense radiation sources in the visible spectral range [1]. Up to now no data are available in the literature on excitation processes of mercury bromide at high repetition rates ($f \sim 100$ kHz) under conditions of high-pressure gas discharge plasma, which is necessary for the creation of efficient and powerful sources of visible light. In this study, the results of our investigation of the spectral and electric characteristics of atmospheric-pressure DBD-driven small-size lamp ($f = 125$ kHz) based on mixtures of mercury dibromide vapour with helium or xenon and krypton have been presented.

2. Experimental

A small-size cylindrical DBD-driven radiator made of a quartz tube with an outer diameter of 6 mm and having one dielectric barrier with the capacitance of $C_d = 6$ pF was used. A molybdenum electrode was placed inside the radiator along its axis. The discharge gap was 1.5 mm. The external electrode, placed on the tube surface, was made of a mesh with the transmission of 90% (Fig. 1). A capillary of 1.5 mm in diameter was made at the end of the quartz tube in order to decrease the outflow of the mercury dibromide vapour from the cell to the evacuation system.

To excite a working mixture a generator of high voltage AC sinusoidal pulses was used; peak-to-peak voltage up to 10 kV, $f = 1 – 125$ kHz. The voltage U applied to the lamp was measured using a high voltage probe (Tektronix P6015A). The waveforms of current I and charge Q were registered by means of a 50 Ω resistor or low-inductance 8 nF capacitor placed in series with the lamp and monitored by digital oscilloscope LeCroy WaveRunner 6100A (1 GHz, 10 GS/s). The radiation emitted by the discharge was registered and analyzed in the spectral range of 200–740 nm. The spectra were recorded by the Jobin Yvon FHR 1000 monochromator (grating 2400 grooves/mm, quartz optical fiber, the spectral resolution of about 8 pm) with the high-speed CCD detector. The system was calibrated in the range of 200–400 nm by a deuterium lamp and, in the range of 400–900 nm, by a reference tungsten lamp.

The working mixtures were prepared directly in the radiation source. A 100 mg of the $HgBr_2$ salt was poured uniformly into the discharge cell. Once the salt was loaded, the source was dehydrated by maintaining a temperature of ~100°C and evacuating for 2 h. In this process, a significant improvement of the discharge glow was observed. The partial pressure of the $HgBr_2$ vapour was determined from the temperature of the coldest point of the radiator. Under these conditions, the range was within 0.1–600 Pa. The partial pressure of the gases was measured accurate to 10 Pa.

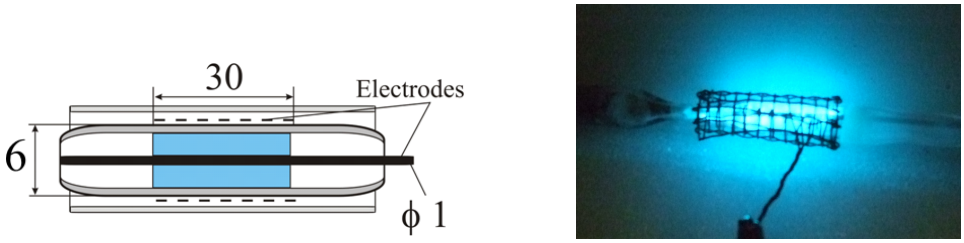


Fig. 1. Schematics (left) and photo in the operation (right) for the DBD-driven HgBr exciplex lamp.

3. Results and discussion

The characteristics of the lamp were studied in the $HgBr_2$/He and $HgBr_2$/Xe/Kr mixtures. At the initial stage (the first 20–30 s), the colour of the discharge was dependent on the component composition of a mixture. As the mixture self-heated, the discharge colour became green-blue.

In each half-cycle of the applied voltage U_0, the current waveform consisted of a displacement current and conductivity current peaks, with characteristics depending on the operating frequency and applied voltage. The peak current did not exceed 52 mA and duration was in the range 0.2–0.5 μs.

The dynamics in the emission spectra of HgBr* exciplex lamp operated with the $HgBr_2$/Xe/Kr mixture (8% Xe + 92% Kr) at total atmospheric pressure and f = 120 kHz with changing of temperature is shown in figure 2. At low temperatures (T ~ 40°C) the emission bands of the exciplex XeBr($B \rightarrow X$) and XeBr($B \rightarrow A$) molecules peaked at 281 and 320 nm together with the atomic mercury lines and OH* bands have been observed (Fig. 2(a)).

In the spectra obtained, a wide band system peaking at λ = 502 nm stands out, which intensity increased with the increasing of temperature (Fig. 2 (b, c)). This system corresponds to the electronic–vibrational $B\,^2\Sigma^+ \rightarrow X\,^2\Sigma^+$ transition of the exciplex HgBr* molecules [2]. The HgBr($B \rightarrow X$) radiation manifests itself starting from λ ~ 340 nm. In addition, the weak HgBr($C \rightarrow X$) bands were observed in the range of 285–295 nm.

Besides the HgBr($B \rightarrow X$) radiation and mercury lines, the emission spectra of DBD in the $HgBr_2$/He mixture included atomic lines of the buffer gas helium at 589 and 706 nm, as well as the $N_2(C^3\Pi_u \rightarrow B^3\Pi_g)$ bands appearing due to a presence of nitrogen as a residual gas (p<10 Pa). The intensity of the helium lines decreased considerably as the working medium warmed up.

It can be assumed that the emission at the observed spectral bands and lines probably occurs through the following reactions:

$$HgBr_2 + e \rightarrow HgBr^* + \begin{cases} Br + e \\ Br^- \end{cases} \quad (1)$$

$$HgBr_2 + Xe^* \rightarrow HgBr^* + Br + Xe, \quad (2)$$

$$HgBr^* \rightarrow HgBr + h\nu, \quad \lambda_{max} = 502\ nm, \quad (3)$$

$$HgBr_2 + e \rightarrow Hg^* + 2Br\ (Br_2^*, Br_2, Br_2^-) + (e), \quad (4)$$

$$HgBr_2 + e \rightarrow Hg^* + Br_2^+ + 2e, \quad (5)$$

$$HgBr_2 + e \rightarrow Hg^* + Br^+ + Br + 2e, \quad (6)$$

$$HgBr_2 + e \rightarrow Hg^* + Br^* + Br + e, \quad (7)$$

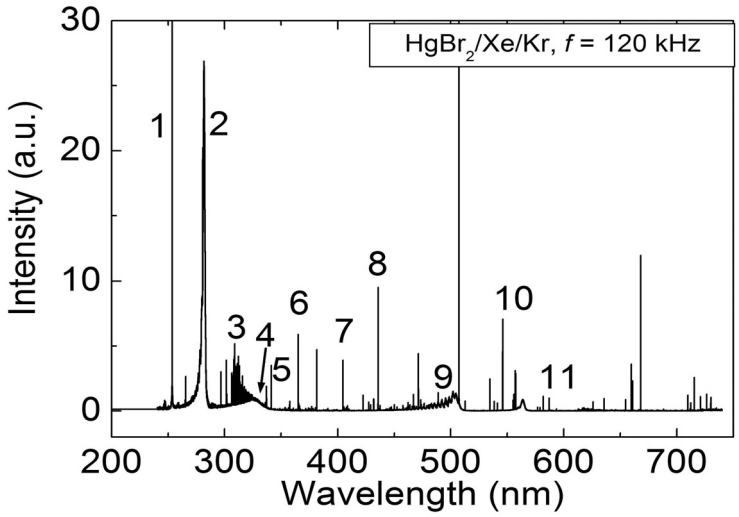
$$Xe^*(Xe_2^*) + Br_2 \rightarrow XeBr^* + (Xe) + Br, \quad (8)$$

$$Xe^+\ (Xe_2^+, Xe_3^+) + Br_2^- + M \rightarrow XeBr^* + Br + (Xe, 2Xe) + M, \quad (9)$$

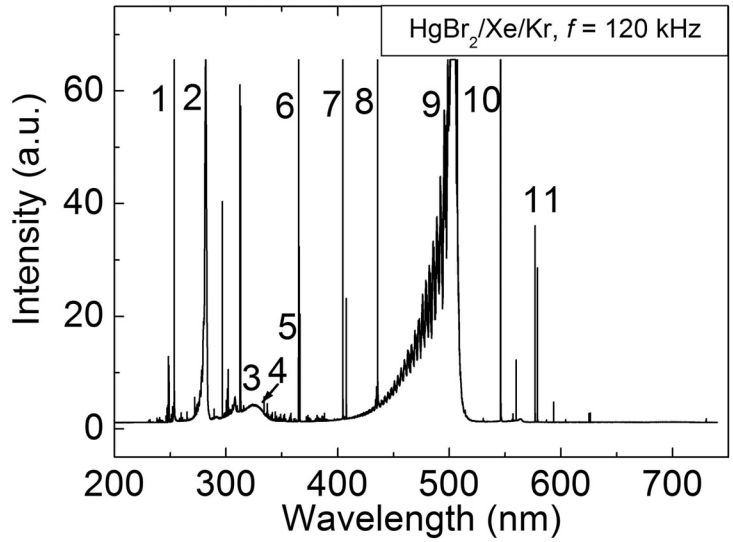
$$Xe^+ + Br^- + M \rightarrow XeBr^* + M, \quad (10)$$

$$XeBr^* \rightarrow XeBr + h\nu, \quad \lambda_{max} = 281\ nm, \quad (11)$$

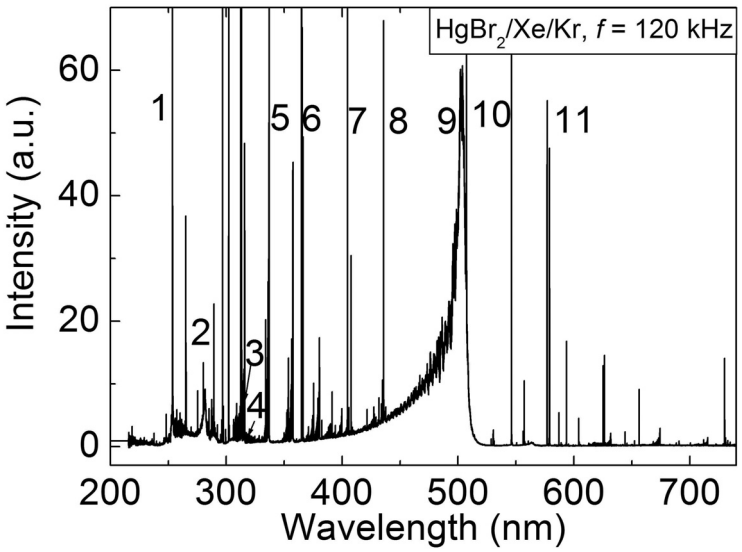
where M is the third particle.



(a)



(b)



(c)

Fig. 2: Emission spectra of a HgBr* lamp with the $HgBr_2$/Xe/Kr mixture: (a) T = 40°C, (b) T = 80°C, (c) T = 160°C. 1 – 254nm Hg*, 2 – 281nm XeBr*, 3 – 306nm OH*, 4 – 320nm XeBr*, 5 – 337nm N_2*, 6 – 365nm Hg*, 7 – 404nm Hg*, 8 – 436nm Hg*, 9 – 502nm HgBr*, 10 – 546nm Hg*, 11 – 578nm Hg*.

4. Summary

The intense broadband radiation of HgBr($B \rightarrow X$) exciplex with a peak at λ = 502 nm has been revealed from the dielectric barrier discharge (f = 120 kHz) in a self-heating mode. The multi-wavelength operation mode of the DBD-driven atmospheric pressure high-frequency HgBr* excilamp has been realized. It has been shown the possibility to regulate the emission spectrum of the excilamp by means of changing the working temperature. An atmospheric-pressure barrier discharge with the $HgBr_2$/Xe/Kr mixture can be used for the creating a self-heated excilamp emitting in the UV and green-blue spectral regions.

Acknowledgment. Authors are grateful to A. Brablec, P. St'ahel and P. Slavicek (Department of Physical Electronics, Masaryk University, Brno, Czech Republic) for the opportunity of using the registration system for our experiments.

5. References

[1] Ch. K. Rhodes, Excimer Lasers (Berlin: Springer) 1979 &1984.
[2] R.W. Pearse, A.G Gaydon, The Identification of Molecular Spectra (New York: Wiley) 1963.

Topic 6
Depollution and environmental applications

NO OXIDATION BY DIELECTRIC BARRIER DISCHARGE AND CATALYST: EFFECT OF TEMPEREATURE AND WATER VAPOR

I. Jõgi, V. Bichevin, V. Sabre, A. Haljaste, M. Laan, H. Käämbre

Institute of Physic, University of Tartu, Tähe 4, 51010 Tartu, Estonia
E-mail: indrek.jogi@ut.ee

The effect of TiO_2 powder on the NO oxidation by DBD was tested at temperatures from room temperature up to 150°C. When only Dielectric Barrier Discharge (DBD) was used at 100°C the NO oxidation decreased, but addition of catalytic TiO_2 powder partially compensated this loss of oxidation ability. The effect of TiO_2 powder decreased in a few minutes but the concentration of NO stabilized at lower level compared to case of DBD. The inclusion of water vapor to the inlet gas mixture resulted to the increased NO removal with and without TiO_2 coating and HNO_3 appeared in the outlet of reactor. Our assumption that oxygen species adsorbed on TiO_2 surface are responsible for the enhanced oxidation of NO to $NO_2$was supported by experiments where TiO_2 surface was initially treated with pure O_2 discharge. When NO was subsequently introduced to the reactor chamber without ignition of DBD, NO_2 appeared in the outlet and NO concentration was initially decreased.

1. Introduction

Fuel burning emits NO_x species to the atmosphere where they pose serious environmental problems. Concentration of NO_x species in exhaust gases could be diminished by dielectric barrier discharges, DBD, [1-4] or using (photo)catalysts, such as TiO_2 [4-6]. When discharge is used for the removal of NO_x in the presence of O_2, the most abundant NO is initially oxidized to NO_2 and N_2O_5 [2-3]. These oxidized NO_x species are then removed by scrubbing, mineralization or selective catalytic reduction to N_2 and O_2 [4].

The efficiency of NO oxidation depends on a number of parameters including O_2 concentration and temperatures of the exhaust gas [2-4]. Several studies have been recently carried out to investigate the possibility to increase NO_x removal efficiency by the inclusion of TiO_2 to the discharge reactor [7-11]. The results were contradicting as in some studies remarkable improvement was achieved with the use of TiO_2 [7-8] while in other studies the effect of TiO_2 was negligible or detrimental [9]. Our own studies carried out at room temperature with various mixtures of NO, N_2 and O_2 demonstrated that the TiO_2 powder coating increased removal of NO only for a short time [10-11]. In addition, the coating of TiO_2 affected the results only at specific input energies (*SIE*) values where the DBD discharge alone was able to oxidize almost all NO [10-11]. The proposed reason for such time dependent removal of NO was initial adsorption of NO_x species on the oxygen activated TiO_2 surface until the active sites were diminished.

At higher temperatures, the efficiency of NO removal by DBD discharge decreases due to O_3 decomposition and backward reaction of $NO_2 + O \rightarrow NO + O_2$ [2]. At the same time, desorption of NO_x species from TiO_2 surface is expected to increase at higher temperatures [12]. Thus, higher amount of active sites should be available on the surface and the removal of NO by the TiO_2 should improve. As a result, at higher temperatures, the effect of TiO_2 should be more pronounced. Presence of water vapor in the exhaust gas can also change the reaction routes for NO oxidation both in the discharge and on the surface [1-2,12].

Present study was carried out to investigate the effect of temperature and water vapor on NO removal by DBD and TiO_2. In addition, the role of plasma-created oxygen species in the improved NO oxidation ability of TiO_2 was further examined.

2. Experimental

All experiments were carried out at atmospheric pressures. The inlet mixture was prepared from 450 ppm NO in N_2 and from dry air by the use of flow controllers. For the addition of water vapor, the mixture was led through a bubbler with H_2O at room temperature (22 °C) resulting in 2 % of water in

the mixture of humid air. The inlet mixture had usually about 200-225 ppm NO and 10 % O_2. The flow rate was 1 l/min unless stated otherwise.
A coaxial DBD reactor with discharge gap of 0.7 mm, similar to the one described in our earlier work [10] was used for the production of discharge. During heating experiments, the DBD reactor was placed in an electrically heated oven. The inlet mixture was also heated before entering the discharge reactor. Commercial Degussa P25 TiO_2 powder mixed in water was pressed on the inner electrode of reactor. The mass of resulting TiO_2 coating was approximately 10 mg/cm^2.
The specific input energy (*SIE*) was determined from the recorded Lissajous figures similarly with our earlier experiments [10].
Concentrations of NO_x, HNO_3 and O_3 were measured at the outlet of DBD reactor by the optical absorption spectroscopy (OAS) method. The measurement setup consisted from a deuterium lamp (DDS-30), an absorption cell with the length of 30 cm and from Ocean Optics USB4000 spectrometer of 0.7 nm resolution. The wavelengths from 200 to 445 nm were used for the determination of various species. To determine the NO concentration, a calibration curve was obtained by mixing 450 ppm NO in N_2 balance gas and pure N_2 with various ratios and measuring the intensity of absorption band at 215 nm. The concentration of other NO_x species and ozone were determined by using the absorption cross section values from literature [13-14].

3. Results

Effect of temperature
In the case of mixture with 10 % of O_2, and 220 ppm of NO in N_2, at room temperature almost all NO was converted to NO_2 and/or N_2O_5 at *SIE* values higher than 100 J/L [10-11]. Figure 1 shows that at reactor temperature of 100 °C, the amount of NO in the outlet was considerably higher (about 150 ppm). In addition, the growth of *SIE* did not result in improved conversion of NO (Fig. 1a) and outlet NO concentration even increased with increasing *SIE* (Fig. 1a).

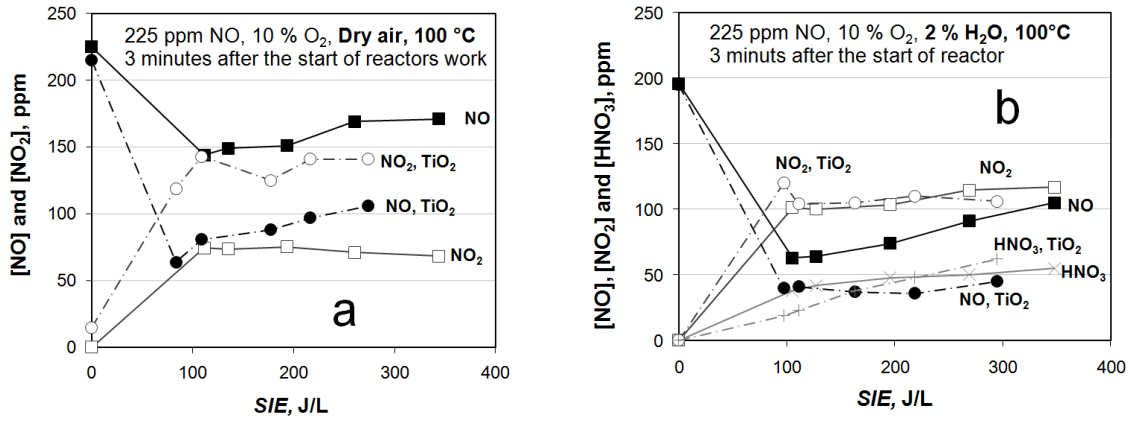


Fig. 1. The outlet concentration of NO and NO_2 as a function of SIE with and without TiO_2 coating at 100°C (a) – in the case of dry air and (b) in the presence of water vapor. In the latter case, the concentration of HNO_3 is also shown.

Similarly to the measurements carried out at room temperature, the presence of TiO_2 coating resulted in decreased NO concentration at the beginning of reactors work (Fig. 2a). At *SIE* values above 150 J/L, all NO was removed from the outlet gas at the beginning of reactors work. The outlet concentration started to increase almost immediately after reaching minimum value and reached a constant value after a few minutes. Higher values of *SIE* resulted in the growth of the final value of NO (Fig. 2a).

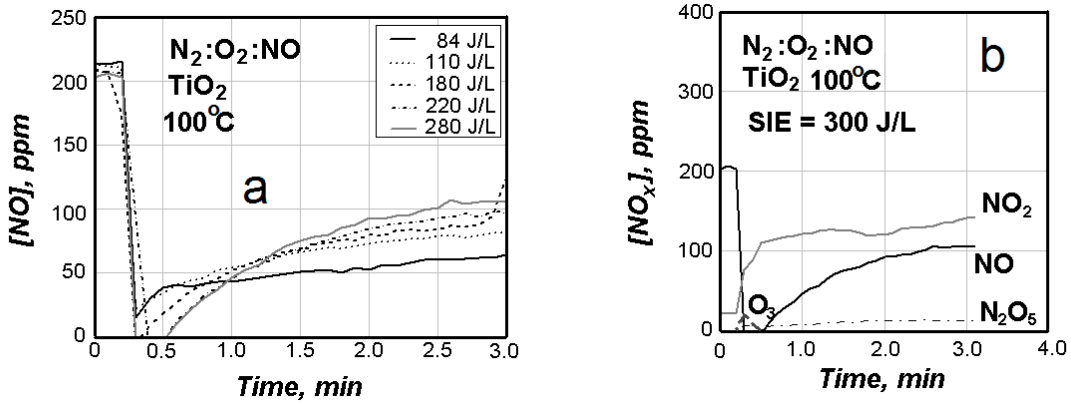


Fig. 2. The time dependent effect of TiO_2 coating on (a) – the outlet NO concentration at various *SIE* values and (b) – various NO_x species and ozone at *SIE* value of 300 J/L(NO – black solid line, NO_2 – grey solid line, N_2O_5 – black dash-dot line, O_3 – dark grey dashed line). The reactor temperature was 100°C.

The time-dependence of the concentration of various NO_x species and O_3 in the outlet gas is shown in the figure 2b. Again, the main features were similar to those at the room temperature [11]. When the NO was absent at the outlet gas, the O_3 appeared. A rapid decay of the outlet O_3 concentration took place with the same rate as the NO_2 concentration grew (Fig. 2b). After the disappearance of O_3, the NO appeared in the outlet and NO_2 concentration increased slowly.
The effect of TiO_2 coating on the NO conversion to NO_2 and N_2O_5 at varying *SIE* values after 3 minutes of reactor work is shown in Figure 1a. Even after 3 minutes, the TiO_2 had remarkable effect on NO oxidation as the outlet NO concentration was more than 50 ppm (25 %) below the value corresponding to reactor without TiO_2. The concentration of NO_2 increased by same value. Thus, at 100°C the oxidation was enhanced in the presence of TiO_2 whereas at lower temperatures, there was no enhancement of NO oxidation after few minutes.

Effect of H_2O

Adding of H_2O to the inlet mixture caused a considerably lowering of outlet NO concentrations even without TiO_2 (Fig. 1a and 1b). Besides, HNO_3 appeared in the outlet (Fig. 1b). When the TiO_2 coating was present, concentrations of NO, NO_2 and NO_3 were again time-dependent (Fig. 3). Compared to the case without water vapor, the increase of the outlet NO concentration was much slower and the NO concentration after 3 minutes was considerably lower. The dependence of final NO concentration on *SIE* remained also smaller.

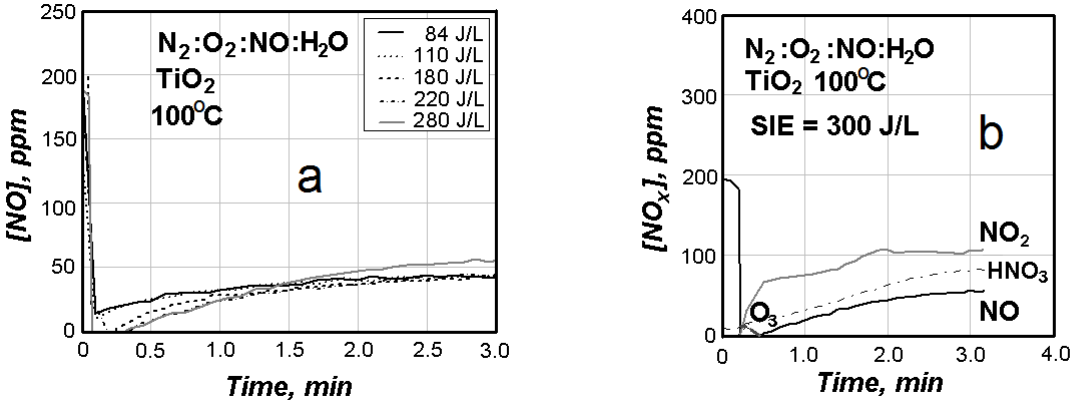


Fig. 3. The time dependent effect of TiO_2 coating on (a) – the outlet NO concentration at various *SIE* values and (b) – various NO_x species and ozone at *SIE* value of 300 J/L (NO – black solid line, NO_2 – grey solid line, N_2O_5 – black dash-dot line, O_3 – dark grey dashed line). The reactor temperature was 100°C.

Effect of O_2 pretreatment

Before introducing NO containing mixtures to the reactor, the TiO_2 surface was influenced by discharge ignited in oxygen. The experiments were carried out either at a fixed *SIE* value (about 200 J/L) but increasing time of the oxygen plasma treatment (1 to 10 minutes) or at a fixed treatment time (5 minutes) and varying *SIE* values (90-300 J/L). After oxygen plasma treatment and without switching on discharge, mixture with 220 ppm of NO in N_2 was directed to the reactor. As a result, a considerable amount of NO_2 appeared in the outlet (Fig. 4a). Besides, NO concentration increased more slowly compared to the case when no oxygen plasma treatment was used. The maximum concentration of NO_2 increased with increasing *SIE* values of oxygen plasma treatment (Fig. 4a) and with increasing treatment time (not shown). In addition, the effect of the oxygen plasma treatment remained same even when the time interval between the end of plasma treatment and introduction of the NO:N_2 mixture to the reactor was 10 minutes. In the case of the oxygen plasma treatment of the reactor without TiO_2 coating, the NO_2 did not appear in outlet when NO:N_2 mixture was directed to the reactor. In addition, without ignition of the discharge, the treatment of reactor by O_2 gas had also no effect even at the presence of TiO_2 coating.

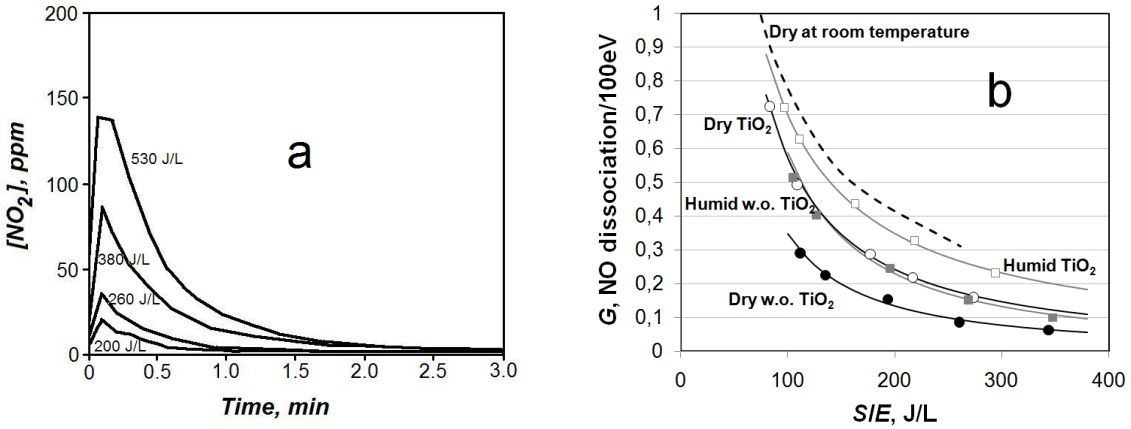


Fig. 4. a – time dependence of outlet NO_2 concentration after NO was directed to the reactor with TiO_2 coating which was previously treated by oxygen plasma at different *SIE* values. b – efficiency of NO removal at different conditions when the temperature was 100°C. Black empty and filled circles correspond to dry mixture in reactor with and without TiO_2 coating whereas grey empty and filled squares correspond to H_2O containing mixture in reactor with and without TiO_2 coating respectively. The efficiency of NO removal from dry mixture without TiO_2 coating at room temperature is marked by dashed black line.

4. Discussion

Expectedly, the oxidation ability of discharge decreased at higher temperature. Increased *SIE* values also decreased the NO oxidation (Fig. 2a). The effect can be caused by the backward reaction of NO from NO_2 and increased production of NO_x species in the plasma at high temperatures: when the reactor temperature was increased to 150°C, the net amount of NO_x species in the outlet was clearly higher than the inlet concentration of NO. The use of TiO_2 coating allowed to decrease the negative effect of temperature.

The efficiency of NO removal, *G,* was calculated by dividing the removed NO with the specific input energy: $G = \Delta NO/(2.5 \cdot SIE)$ (Fig. 4b). The efficiency decreased rapidly with the increase of *SIE* values. At room temperature and at *SIE* values below 100 J/L, the TiO_2 coating had no effect to efficiency [10] while at 100°C, the NO removal efficiency was almost doubled by TiO_2. The effect of TiO_2 coating was especially important at low *SIE* values and below 100 J/L the efficiency of NO removal approached the efficiency obtained at room temperature. Thus, the TiO_2 coating allowed to maintain the oxidation efficiency of plasma at higher temperatures.

The tests with oxygen plasma pretreatment demonstrated that oxygen species are created in the discharge and these species were accumulated on the TiO_2 surface for relatively long time (at least 10 minutes). Directing NO containing mixture to the reactor, the adsorbed oxygen species at the TiO_2

surface oxidized NO and some of the oxidized NO desorbed from the surface in the form of NO_2. At higher *SIE* values of oxygen plasma there were more oxygen species and higher amount of NO was oxidized.
These results obtained from experiments with oxygen plasma treatment are also consistent with trends presented in Fig. 2 where the presence of TiO_2 coating increased the removal of NO by discharge at higher energy densities. After the surface was partially covered with the reaction products, the desorption of these species determined the net effect of TiO_2. This depends apparently mostly on the temperature as the additional effect of TiO_2 was approximately the same at varying *SIE* values (Fig. 2a).
The presence of H_2O also improved the removal of NO. Without TiO_2, the amount of NO_2 created in the discharge was same as in dry mixture, whereas the HNO_3 appeared only at higher *SIE* values (Fig. 3a). Most likely reason for the increased removal of NO was the reaction $NO + OH \rightarrow HNO_2$ whereas HNO_2 was not detectable with the current measurement setup. In the presence of TiO_2, the concentrations of NO_2 and HNO_3 were same as without TiO_2, while the NO concentration was even smaller. Thus, additional HNO_2 was probably created on TiO_2.

5. Conclusions

TiO_2 coating in the DBD reactor was found to be useful for maintaining the oxidation ability of plasma at higher temperatures, where the discharge alone was not able to efficiently oxidize the NO.
The presence of H_2O increased the removal of NO by creating HNO_x species in addition to NO_2 and N_2O_5.
The increased oxidation ability of NO in the presence of TiO_2 coating was shown to be the result of absorbed oxygen species created in the discharge.
The long-term effect of TiO_2 is apparently determined by the desorption kinetics of reaction products.

Acknowledgements. The authors are thankful to the INTERREG BSR program project "PlasTEP" for supporting these studies.

6. References

[1] Gentile A C and Kushner MJ 1995 *J. Appl. Phys.* **78** 2074.
[2] McLarnon C R and Penetrante B M 1998 *SAE Paper No.* 982433.
[3] Vinogradov I P and Wiesemann K 1997 *Plasma Sources Sci. Technol.* **6** 307.
[4] Barman S and Philip L 2006 *Environ. Sci. Technol.* **40** 1035.
[5] Lim T H, Jeong S M Kim S D and Gyenis J 2000 *J. Photochem. Photobiol. A: Chem.* **134** 209.
[6] Devahasdin S, Fan C, Li K and Chen D H 2003 *J. Photochem. Photobiol. A: Chem.* **156** 161.
[7] Kim H H, Tsunoda K, Katsura S and Mizuno A A 1999 *IEEE Trans. Plasma. Sci.* **35** 1306.
[8] Daito S, Tochikubo F and Watanabe T 2001 *Jpn. J. Appl. Phys.* **40** 2475.
[9] Kim H, Jun H, Sakaguchi Y and Minami W 2008 *Plasma Sci. Technol.* **10** 53.
[10]Jõgi I, Bichevin V, Laan M, Haljaste A and Käämbre H 2009 *Plasma Chem. Plasma Technol.* **29** 205.
[11] Jõgi I, Bichevin V, Laan M, Haljaste A, Käämbre H and Sabre V 2009 *Eur. Phys. J. Appl. Phys*. **47** 22817.
[12] Haubrich J, Quiller R G, Benz L, Liu Z and Friend C M 2010 *Langmuir* **26**, 2445.
[13] Orphal J 2003 *J. Photochem. Photobiol. A: Chem.* **157** 185.
[14] Yao F, Wilson I and Johnson H 1982 *J. Phys. Chem.* **86** 3611.

METHANE CONVERSION WITH CARBON DIOXIDE IN PLASMA-CATALYTIC SYSTEM

Pstrągowska S., Młotek M., Sentek J., Ulejczyk B., Krawczyk K., Schmidt-Szałowski K.

Faculty of Chemistry, Warsaw University of Technology, Noakowskiego 3, 00-664 Warszawa, Poland
E mail: kraw@ch.pw.edu.pl

The plasma-catalytic system was tested for the mixture of methane and CO_2 conversion at the pressure of 1.2 bar with a dielectric barrier discharge (DBD) reactor powered at the frequency of about 6 kHz. Molar ratio $[CO_2]:[CH_4]$ in the inlet gas mixtures (CH_4+CO_2+Ar) was 1. Three kinds of packing were selected for this experiment: 1) Fe/Al_2O_3), 2) zeolites NaY and Na-ZSM-5 (Süd Chemie) and 3) Cu-ZSM-5. The effects of temperature (130 – 340 ^{O}C), gas flow rate on the conversion were studied. Hydrogen, carbon oxide, hydrocarbons (ethane, ethylene+acetylene fraction, propane, propylene, n-butane, and i-butane), and alcohols (methanol and ethanol) were identified in the outlet gas. Using the plasma + Fe/Al_2O_3 catalysts system led to obtaining hydrogen, carbon oxide, hydrocarbons and alcohols (methanol and ethanol). The conversion of methane to methanol with Na-ZSM-5 and Cu-ZSM-5 catalysts was not observed. In the plasma – Na-ZSM-5 system aromatic hydrocarbons (methylo- dimethylo- and trimethylo- naphthalene) and a larger amount of *i*-butane was observed in the outlet gas. With the Na-ZSM-5 catalyst, the overall methane conversion was 47% and 66% and the methane conversion to C2-C4 hydrocarbons reached 20% and 16% for gas flow rate 2 and 1Nl/h respectively.

1. Introduction

The conversion of methane with carbon dioxide has become the object of wide studies in the direct synthesis of higher hydrocarbons, liquid fuels, as well as important oxygenates, such as methanol, formaldehyde etc. Nowadays hybrid systems, in which the action of non-equilibrium plasma is combined with a catalyst accelerating the selected reactions between the active gas species at low temperatures is regarded as a new way for a profitable production of valuable chemicals, such as unsaturated hydrocarbons, aromatics, oxygenates. Among a variety of plasma techniques, corona and dielectric barrier discharges (DBD) proved their usefulness in these experiments. When using these kinds of discharges, it is easy to fill the entire discharge space with a bed of catalyst particles. Owing to the proper reaction volume configuration, the time span between active species generation by plasma and their contact with active centers of a solid catalyst may be minimized. The role of catalysts in such hybrid systems is specific. Short living active species produced by plasma (excited molecules, radicals, ions) are involved in the reactions induced by the catalyst. Owing to the high rate of this kind of reactions, they proceed mostly on the active centres placed at the external surface of catalyst particles. The hybrid plasma-catalytic systems basing on gliding, DBD and corona discharges were the object of numerous studies [1-8].

2. Experimental Section

Three groups of packing were selected for this experiment: 1) Fe/Al_2O_3), 2) zeolites NaY and Na-ZSM-5 (Süd Chemie) and 3) Cu-ZSM-5 prepared by Cu^{2+} exchange of a Na-ZSM-5 zeolite. In order to obtain Fe/Al_2O_3 commercial alumina-ceramic carrier (1.0 – 2.0 mm in size) were impregnated with aqueous solutions of ferric nitrate, dried and calcined and reduced with hydrogen at 400°C.
A quartz-glass reactor with an internal diameter of 26 mm was used with the inner high-voltage electrode made of aluminum (Fig. 1). The discharge gap between this electrode and the quartz tube, used as the dielectric barrier, was about 3 mm wide. The grounded electrode was made from silver-paste deposited on the outer surface of the quartz tube. The reactor was powered by the frequency of about 6 kHz and was operated at the pressure of 1.2 bar. The temperature was controlled by the outer electrical heater and was measured with a thermocouple at the surface of the reactor wall. The reactors were powered by a pulsed electric system (Fig. 2). Electric parameters (voltage and current) were

measured using Tektronix TDS 3032. The portion of 80 ml of the catalyst was packed into the reactor discharge gap.

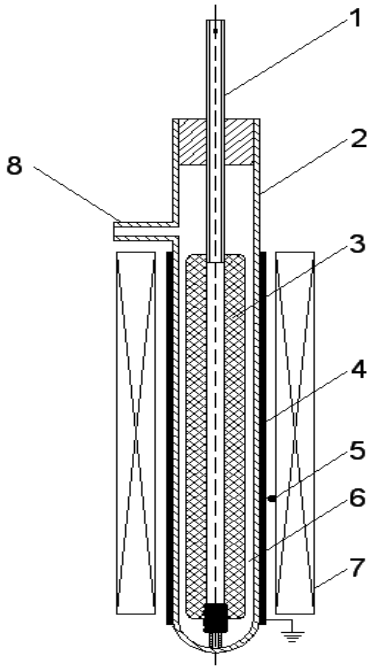


Fig. 1. Reactor for methane conversion in plasma-catalytic system. 1 – gas inlet, 2 – quartz tube, 3 – high voltage electrode, 4 – grounded electrode, 5 – thermocouple, 6 – discharge gap (0.3 mm), 7 – heater, 8 – gas outlet.

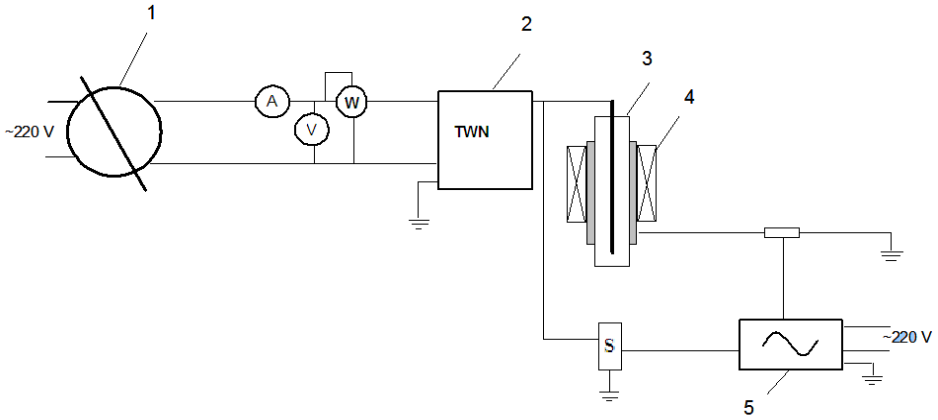


Fig. 2. Electric circuit for the dielectric barrier discharge reactor. 1 – autotransformer, 2 – transformer, 3 – reactor, 4 – oscilloscope Tektronix – TDS3032, S – high voltage electrode. A – ammeter, V – voltmeter, W – wattmeter.

Methane 99.5%, carbon dioxide 99.99%, and argon 99.999% were the components of the feeding gas mixtures. The gas flow rates were controlled by mass controllers. The components of inlet and outlet gases were determined by chromatographic method (GC Agilent 6890N Instrument The share of other products, i.e. higher than C4 and that of non-volatile products, mainly soot, were computed from the carbon balance.

3. Results

Three kinds of packing were selected for this experiment: 1) Fe/Al_2O_3), 2) zeolites NaY and Na-ZSM-5 (Süd Chemie) and 3) Cu-ZSM-5. The effects of temperature (130 – 340 ^{O}C), gas flow rate on the conversion efficiency were studied. The gaseous products (obtained at 240^{0}C) determined by chromatographic analysis are specified in Table 1.

Tab. 1. Conversion of methane and CO_2 in plasma – catalytic conditions. Initial argon concentration was 50%. Molar ratio CH_4:CO_2 = 1

$V_{całkowity}$, Nl/h	packing (240^{O}C)	Overall CH_4	Overall CO_2	Conversion of CH_4,%											
				C_2H_6	C_3H_8	n- C_4H_{10}	CH_3OH	CO	H_2	C_2H_2/C_2H_4	C_3H_6	i- C_4H_{10}	C_2H_5OH	2- C_4H_8	others
2.0	homogeneus	35.3	19.6	7.46	3.71	1.36	2.53	23.74	13.72	1.08	0.19	1.36	0.40	0.00	17.2
	Al_2O_3	37.1	20.2	9.20	4.33	1.59	1.29	10.75	15.21	0.55	0.16	1.47	0.23	0.00	7.5
	Fe/Al_2O_3	33.9	17.5	7.14	4.09	1.75	0.95	1.88	12.6	0.93	0.31	1.17	0.26	0.00	15.4
	NaY zeolit	31.2	13.2	4.97	2.60	0.96	0.00	3.90	13.81	0.92	0.14	0.69	0.45	0.33	17.0
	Na-ZSM-5	47.5	26.8	8.95	4.63	1.76	0.00	4.97	15.16	0.09	0.00	2.65	0.28	1.18	24.2
	Cu-ZSM-5	47.6	27.2	7.88	3.66	1.16	0.10	5.88	13.85	0.20	0.63	1.27	0.14	1.21	27.2
1.5	Fe/Al_2O_3	35.1	16.6	5.34	4.61	1.75	0.26	6.57	15.10	1.31	0.26	1.34	0.26	0.00	12.9
	NaY	36.3	14.0	5.44	2.85	1.24	0.00	6.16	15.41	0.90	0.21	0.95	0.48	0.38	18.1
	Na-ZSM-5	52.0	31.3	8.60	4.34	1.50	0.00	3.91	17.00	0.13	0.00	1.76	0.38	1.30	31.6
1.0	homogeneus	59.4	39.6	9.41	5.14	2.01	3.65	26.56	25.06	0.45	0.25	2.58	0.42	0.00	35.5
	Al_2O_3	54.7	34.6	9.69	5.21	2.14	1.12	23.38	22.51	0.52	0.26	2.00	0.26	0.00	33.5
	Fe/Al_2O_3	45.9	20.4	9.06	5.38	2.18	0.76	13.55	20.83	1.34	0.31	1.79	0.27	0.00	11.2
	NaY	48.7	19.3	5.71	2.72	1.24	0.00	10.26	21.22	0.76	0.20	0.91	0.32	0.36	26.6
	Na-ZSM-5	65.1	40.1	6.68	3.64	1.25	0.00	4.17	21.26	0.08	0.00	1.63	0.32	1.17	47.4
	Cu-ZSM-5	66.9	42.8	6.60	3.82	1.49	0.08	5.48	20.85	0.21	0.08	1.83	0.22	1.69	47.0

These were: hydrogen, carbon oxide, hydrocarbons (ethane, fraction composed of ethylene + acetylene, propane, propylene, n-butane, and i-butane), and alcohols (methanol and ethanol). Among the organic products, ethane was dominant over the entire parameter ranges under examination. During the reaction run, non-volatile products (coke, macromolecular substances) formed a thin but visible film of deposit on the quartz dielectric barrier and metal electrode surfaces**.**

The effects of reactor packing.

Comparing the products generated with the Fe/Al_2O_3, NaY, Na-ZSM-5 and Cu-ZSM-5 packing to these without packing, only few changes could be noticed (Fig. 3 A and B, Table1). Using the plasma + Fe/Al_2O_3 catalysts system led to obtaining hydrogen, carbon oxide, hydrocarbons and alcohols (methanol and ethanol). The conversion of methane to methanol with Na-uZSM-5 and Cu-ZSM-5 catalysts was not observed. With Na-ZSM-5 and Cu-ZSM-5 packing the higher conversion of methane to i-butane and higher overall conversion of methane and CO_2 was observed. With the Na-ZSM-5 catalyst, the overall methane conversion was 47% and 66% and the methane conversion to C2-C4 hydrocarbons reached 20% and 16% for gas flow rate 2 and 1Nl/h respectively.

The hydrocarbons (above 4C) with Cu-ZSM-5 zeolites was higher than that with other catalysts.

The effect of gas flow rate

The conversion of both reagents CH_4 and CO_2 to the main organic products was similar when the gas flow rate was increased from 1 to 2 Nl/h (at $[CO_2]$:$[CH_4]$ = 1), initial argon concentration was 50%.

Amounts of H_2 and CO in the outlet gas decreased when the gas flow rate increased from 1 to 2 Nl/h (Table 1).

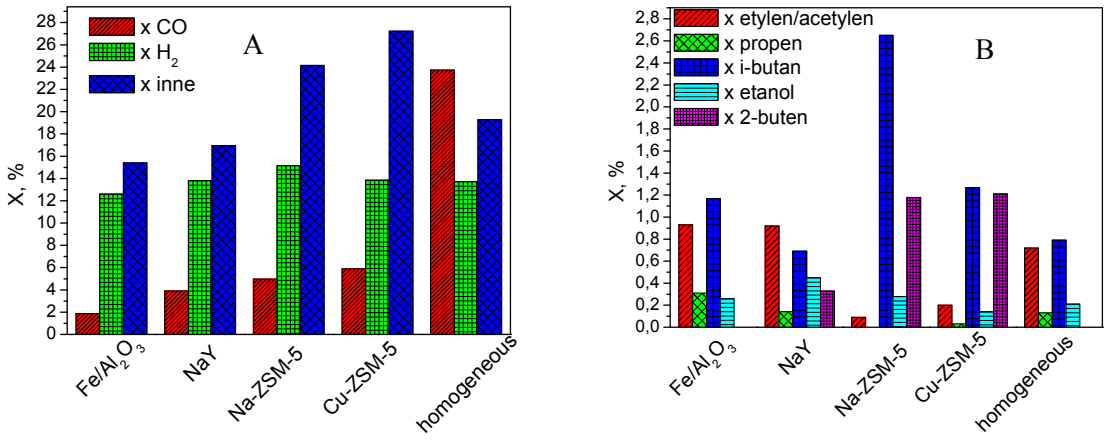


Fig. 3. Effect of catalyst on overall conversion of methane and CO_2 to other unknown substances (A) and conversion of methane to hydrocarbons (B). Gas flow rate – 2 Nl/h, molar ratio $[CO_2]:[CH_4] = 1$, temperature 240^{O}C, initial argon concentration 50%.

The effect of temperature (over the range of 130 – 340 ^{O}C; Fig. 4A, 4B and 4C).

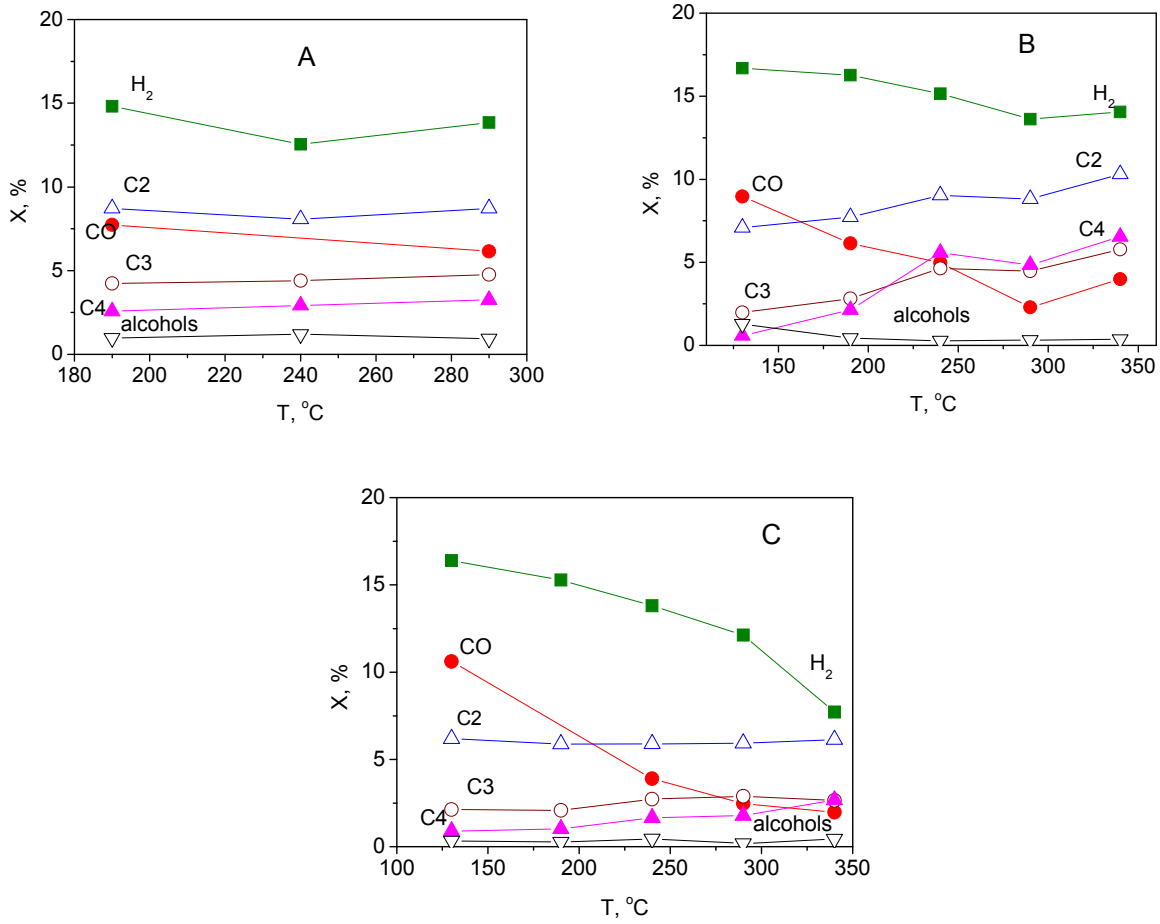


Fig. 4. Effect of temperature on overall conversion of methane and CO_2 A - Fe/Al_2O_3, B – NaY, C – Na – ZSM-5. Gas flow rate – 2 Nl/h, molar ratio $[CO_2]:[CH_4] = 1$.

The temperature did not affect the overall methane conversion with Fe/Al_2O_3, and zeolites NaY, however with Na-ZSM-5 zeolite the increase of methane conversion to C2-4 was observed. At 340^oC in the product of the reaction methylo phenols (mainly dimethylo- phenols) was observed.

4. Summary

The conversion of methane with CO_2 was effectively conducted in a hybrid plasma-catalytic system with the use of a DBD reactor operated at the pressure of 1.2 bar over the temperature range of 130 – 340 ^OC. Hydrogen, carbon oxide, hydrocarbons (ethane, fraction composed of ethylene + acetylene, propane, propylene, n-butane, and i-butane), and alcohols (methanol and ethanol) were found in the outlet stream over the entire rage of process conditions. Ethane was the main component among the organic products. With the Na-ZSM-5 catalyst a liquid of methylo phenols were produced. The most effective among the tested kinds of packing. was Na-ZSM-5 catalyst. With this catalyst, the overall methane conversion and the conversion to C2-4 was higher than with others packing. With Fe/Al_2O_3 and NaY effect of temperature and gas flow rate on conversion of methane and CO_2 was not observed.

Acknowledgements. This work was financially supported by ERA-NET CHEMISTRY (Decision nr 139/ERA-NET/2008)

5. References

[1] Schmidt-Szałowski K., Krawczyk K. and Młotek M. 2007 Plasma Process. Polym. 4 728.
[2] Spiess F.-J., Suib S.L., Irie K., Hayashi Y. and Matsumoto H. 2004 Catal. Today 89 35.
[3] Sentek J., Krawczyk K., Młotek M., Kalczewska M., Kroker T., Kolb T., Schenk A., Gericke [4] K-H. and Schmidt-Szałowski K. 2010 Appl. Cat. B: Environ. 94 19.
[5] Kim S.-S., Lee H., Choi J.-W., Na B.-K. and Song H.K. 2007 Catal. Commun. 8 1438.
[6] Schmidt-Szałowski K., Górska A. and Młotek M. 2006 J. Adv. Oxid. Technol. 9/2 215.
[7] Nozaki T., Fukui W. and Ozaki K., 2008 Energy Fuels 22 3600.
[8] Hammer Th., Kappes Th. and Baldauf M. 2004 Catal. Today 89, 5.
[9] Młotek M., Sentek J., Krawczyk K. and Schmidt-Szałowski K. 2009 Appl. Catal A 366 232.

BIOLOGICAL DECONTAMINATION OF WATER BY HIGH POWER DC DIAPHRAGM UNDERWATER DISCHARGE

P. Lukes[1], M. Clupek[1], V. Babicky[1], P. Sunka[1], E. Spetlikova[2], J. Rihova Ambrozova[2], V. Janda[2], D. Vinklarkova[3], E. Marsalkova[3], B. Marsalek[3]

[1]*Institute of Plasma Physics AS CR, v.v.i., Za Slovankou 3, Prague 8, 182 00, Czech Republic*
[2]*Institute of Chemical Technology, Prague, Technicka 3, Prague 6, 168 28, Czech Republic*
[3]*Institute of Botany AS CR, v.v.i., Kvetna 8, Brno, 603 65, Czech Republic*
E-mail: lukes@ipp.cas.cz

Novel high power DC diaphragm underwater discharge apparatus for decontamination and disinfection of water has been developed. The effects of input power, solution conductivity and method of liquid flowing through the reactor on H_2O_2 production, inactivation of bacteria *E. coli* and *E. faecalis* and algae *Planktothrix* sp. have been determined. It was shown that the apparatus is capable to treat relatively large volume of liquid and efficiently reduce biological contamination in water, especially when the diaphragm discharge reactor is operated in the plug-flow regime.

1. Introduction

Electrical discharges generated directly in water have been demonstrated to initiate a variety of chemical and physical effects, which have been shown to be effective at degrading a variety of organic compounds and also in the inactivation and destruction of microorganisms in water. Since very high-localized electric field of the order of 1 MV/cm is needed for electrical breakdown of water, the pulsed high voltage and electric field enhancing electrode systems are often used to generate electrical discharge in water [1]. However, from technological and application point of view the need of pulsed high voltage brings cost and complexity disadvantages of these systems. In addition, only small volume of discharge is often generated by such types of electrode configurations, which limits the efficiency of these systems.

In this work we present novel apparatus for generation of underwater plasma based on DC diaphragm discharge. The apparatus is operated at the pulse regime although it is charged by DC power supply since pulses are generated by physical processes in the device, and allows deposition relatively high applied power into the discharge (order of kW) [2]. Physical processes induced by the expansion of the discharge from the connecting hole into the surrounding water accelerate transport chemically active species generated by the discharge in the direction of connecting hole axis and their penetration into large volume of treated water. This is significant improvement compared to the previously reported similar systems based on pinhole (diaphragm) or capillary discharge [3-10]. These systems, although charged also mainly by DC (or AC) voltage, however, face problems with their electrical arrangement and wear problems associated with the pinhole in diaphragm layer, which permit deposition only low power into the discharge (order of 10s to 100s of Watts). Thus, only small volume of generated plasma, narrow range of operating conditions and lifetime of the diaphragm is very limiting factor in these systems.

The presented DC diaphragm discharge apparatus seeks to solve these limitations. Details of the discharge reactor are described. Performance of the apparatus is evaluated in dependence on the applied power and the solution conductivity using H_2O_2 as a probe of plasmachemical activity of diaphragm discharge. Biocidal effects of this system are demonstrated on inactivation of bacteria *E. coli* and *E. faecalis*, and on the growth inhibition of freshwater cyanobacterium *Planktothrix* sp.

2. Experimental

Figure 1 shows the scheme of the high power DC diaphragm disharge apparatus used in this work. Two chambers (1,2) provided with inlet (3) and outlet (4) ports are filled with aqueous solution and separated from each other by dielectric diaphragm (7). Electrodes (5,6), one grounded and second connected to the DC high voltage power source (10), are placed in chambers (1,2). High voltage capacitor (11) is connected in parallel to the DC power supply (10) to lower its output impedance. Chambers (1,2) are connected through a connecting hole (9), which is lined with ceramic material (8).

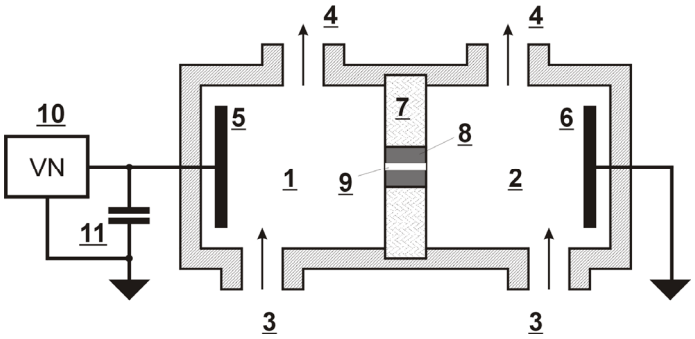


Fig. 1. Experimental setup.

By proper choosing of connecting hole dimensions (its length and diameter) it is possible to establish in the connecting hole (9) an electrical current of sufficient density needed for evaporation of small amount of liquid. Created inhomogeneity allows electrical breakdown of water and an initiation of electrical discharge inside of the connecting hole, which strongly expands into the relatively large volume of surrounding water on both sides of the connecting hole, i.e. discharge of the positive and the negative polarity is generated simultaneously (see Figure 2 showing picture of the underwater plasma generated by the present apparatus). Expansion of the discharge leads to the termination of conditions required for existence of the discharge and to the interruption of the discharge current between electrodes. After the end of this process connecting hole begins to fill back with water and all process is repeated. The power input used in this work was typically 2 kW (with the applied voltage of 6 kV). Capacitance of high voltage capacitor (11) was of 200 nF.

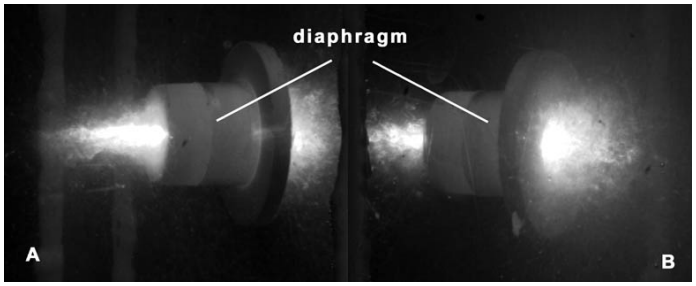


Fig. 2. Photograph of underwater DC diaphragm discharge. Views from positive (A) and negative (B) polarity side of diaphragm.

The biocidal effects of the experimental apparatus were evaluated on bacteria *Escherichia coli* CCM 3954 (ATCC 25922) and *Enterococcus faecalis* CCM 4224 (ATCC 29212). Bacterial suspensions were prepared by preculturing the bacteria cells in the growth medium and then dispersed in NaCl solutions with final solution conductivity of 300 or 500 μS/cm. The discharge chamber was filled with a suspension of bacteria that was circulated through the reactor using a diaphragm liquid pump with the flow rate of 1 L/min. Total volume of bacterial suspension was 6 L. In the case of plug-flow experiments (i.e., without re-circulation of the bacteria suspension back into the discharge reactor) the initial volume of bacterial suspension was 20 L, which was used in aliquot volume parts in three subsequent experiments. The treated liquid was cooled to maintain isothermal conditions of about 23ºC. Number of bacteria cells in the liquid suspension was assayed by counting colony forming units (CFUs) cultivated on agar plates. The initial amount of bacteria was about 10^5 CFU/mL in all experiments performed in this study. The viability of the bacteria was determined as the ratio of the concentration of surviving bacteria to the total concentration. Effects of DC diaphragm discharge on cyanobacterium *Planktothrix* sp. was assayed using algal growth inhibition test. Aqueous solutions of *Planktothrix* sp. were prepared from freshwater and cyanobacteria biomass taken from Plumlov water reservoir, Czech Republic. Total volume of cyanobacteria solution was 20 L. Experiments were performed by the same procedure as with *E. coli* and *E. faecalis*. The initial conductivity of cyanobacterial solutions was 285 μS/cm. The inhibition of cyanobacterium growth by the discharge was evaluated by measuring the cell density of discharge-exposed cyanobacteria cells against the

unexposed control cultures at 24, 72 and 120 hr after treatment by the discharge. The concentration of H_2O_2 was determined colorimetrically using the reaction of H_2O_2 with titanyl ions measuring absorbance of the peroxotitanium (IV) complex at 410 nm.

3. Results and discussion

It is generally accepted that electrical breakdown of water (i.e. discharge formation) proceeds in diaphragm (or capillary) kind of reactor geometries by thermal process when sufficiently high pre-discharge current in the liquid causes strong heating in the small hole or the narrow capillary, inducing formation of vapour bubble inside the diaphragm (capillary) and its subsequent breakdown. Apparently, in such mechanism power input is one of the most important parameters but also solution conductivity (which determines the resistance of water and thus electrical current needed for liquid heating and bubble creation inside the diaphragm) and diameter and length of the diaphragm hole or the capillary (which affects the bubble dynamics and the properties of the discharge). Therefore, performance of the present DC diaphragm discharge apparatus was evaluated in dependence on the applied power and the solution conductivity. Hydrogen peroxide was used as a probe of plasmachemical activity of diaphragm discharge in these experiments since H_2O_2 is one of the major chemical products of the underwater discharges. It should be also noted that the amounts of H_2O_2 presented in this work are in all experiments the sum of H_2O_2 productions obtained by diaphragm discharge in both chambers (i.e., produced by positive and negative polarity discharge simultaneously).

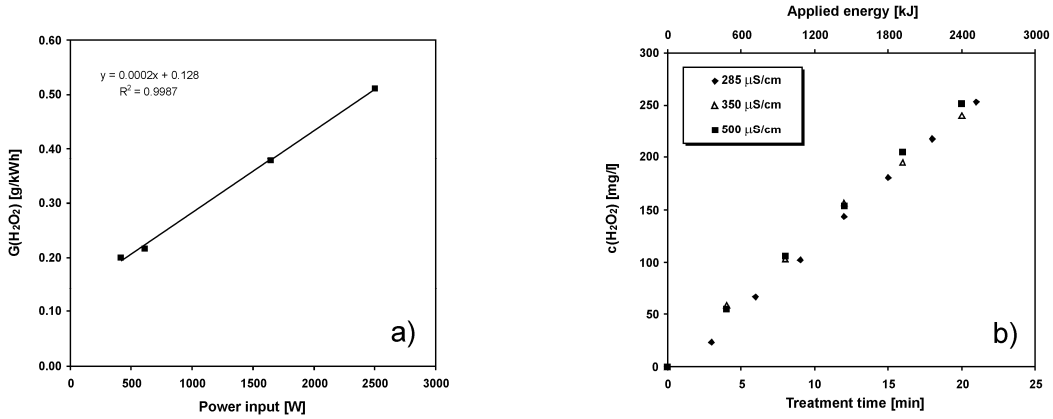


Fig. 3. a) Effect of applied power input on the energy yield of H_2O_2 produced by diaphragm discharge. b) Effect of solution conductivity on the production of H_2O_2 by diaphragm discharge (power 2 kW).

Figure 3a shows the production of H_2O_2 by the diaphragm discharge in water (aqueous solutions of NaCl with the conductivity of 200-500 µS/cm) in dependence on the applied power input in the range of 500-2500 W (expressed in energy yields G_{H2O2}). It is apparent that the yield of H_2O_2 increased linearly with the increasing power input with the maximum yield of 0.51 g H_2O_2/kWh for the highest applied power of 2.5 kW. Similar result was reported also for AC capillary discharge in [6], however, this is quite different result compared to the dependence of H_2O_2 energy yields on applied power, which is typically observed for the production of H_2O_2 by the pulsed corona discharge in water giving the G_{H2O2} independent of the power input [11]. The reason for this difference lies most likely in the different mechanism of electrical breakdown of water between these two types of underwater discharges, i.e. higher power applied into the liquid in the diaphragm reactor advances thermal effects inside the hole (capillary) and, thus, bubble formation and electrical breakdown.

On the other hand, it was found that solution conductivity had very negligible effect on the production of hydrogen peroxide under fixed applied power input. Figure 3b shows the production of H_2O_2 by diaphragm discharge generated in NaCl solutions with the conductivity of 285, 350 and 500 µS/cm and power input of 2 kW. This is also different result compared to the strong decrease of H_2O_2 production with the increasing solution conductivity observed in pulsed corona discharges [12], which might be again related with different breakdown mechanism and propagation of discharge in water.

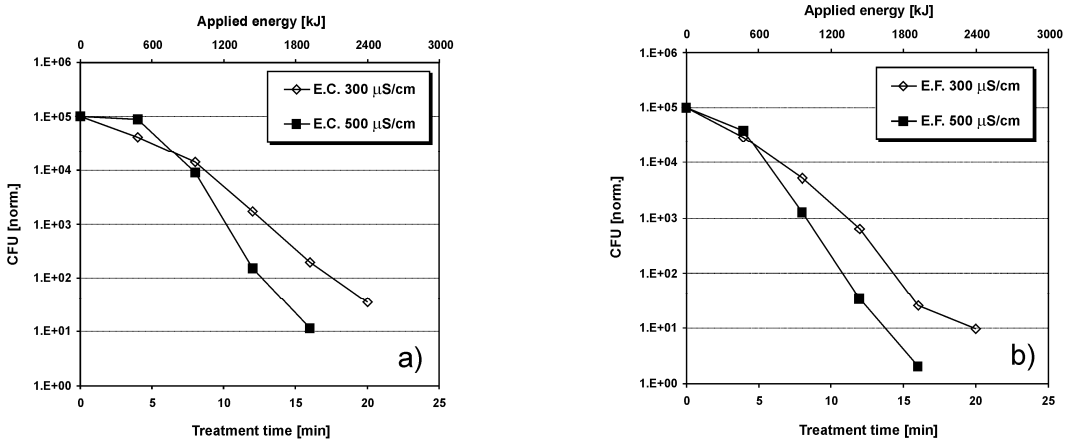


Fig. 4. Bacterial inactivation of *E. coli* (a) and *E. faecalis* (b) in diaphragm discharge reactor operated in continuous regime (NaCl solutions 300 and 500 μS/cm, treated volume 6 L, power input 2 kW).

The biocidal effects of the DC diaphragm discharge apparatus were evaluated on bacteria *Escherichia coli* and *Enterococcus faecalis.* Figure 4 shows inactivation of *E. coli* and *E. faecalis* as a function of discharge treatment time in NaCl solutions with the conductivity of 300 and 500 μS/cm and power input of 2 kW. Gradual decrease in number of survival bacteria was observed with increasing time of discharge treatment for both types of bacteria since amount of bacteria decreased somewhat faster in conductivity of 500 μS/cm compared to 300 μS/cm. 4 to 5-log reduction in number of bacteria was obtained in 6 L volume solution within 15-20 min. The higher efficiency of bacterial inactivation with increasing solution conductivity might be partly related with increasing contribution of UV light radiation emitted from the discharge similarly as it was reported for pulsed corona discharge in [12].

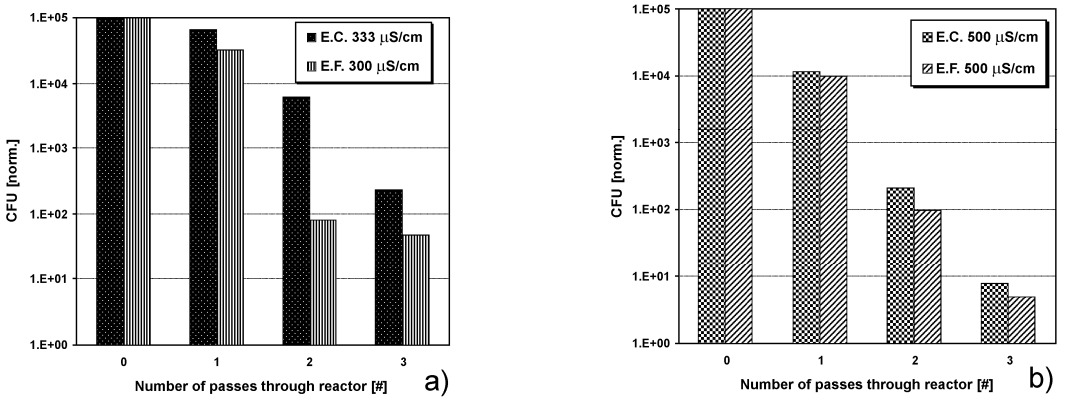


Fig. 5. Bacterial inactivation of *E. coli* and *E. faecalis* in NaCl solutions of 300 μS/cm (a) and 500 μS/cm (b) by diaphragm discharge reactor operated in plug-flow regime (power input 2 kW).

From viewpoint of potential use of underwater plasma technology for biological decontamination of water in the real applications it was interesting to evaluate the inactivation efficiency of the present discharge apparatus when operated in plug-flow regime (i.e., without re-circulation of the bacteria suspension back into the discharge reactor using initial liquid volume of 20 L). Figure 5 shows inactivation of *E. coli* and *E. faecalis* in dependence on number of passes treated bacterial suspension through the discharge reactor. As expected, the bacterial inactivation increased with the number of passes through the reactor. However, 4 to 5-log reduction in number of bacteria was attained already after 3 passes through the reactor compared to 15-20 min in continuous regime (Fig. 4). Thus, using of several discharge setups coupled in series seems to be option to enhance time and energy efficiency and treated liquid volume capacity of the underwater plasma technology in environmental applications.

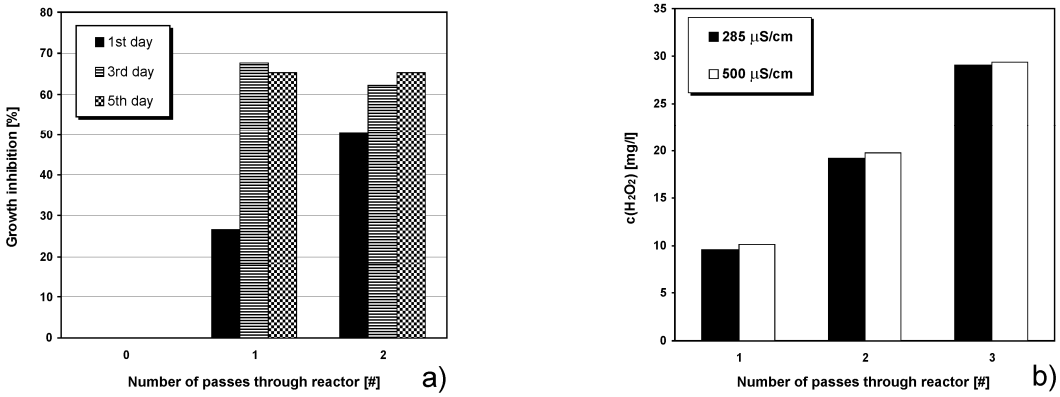


Fig. 6. a) Growth inhibition of *Planktothrix* sp. after exposure to diaphragm discharge; b) H_2O_2 production as function of number of passes through the reactor (freshwater 285 μS/cm, power input 2 kW)

Another advantage to operate diaphragm discharge reactor in plug-flow regime is shown in Figure 6a, which presents an effect of diaphragm discharge on growth inhibition of cyanobacteria *Planktothrix* sp. in dependence on the number of passes through the reactor. Immediate inhibition of cyanobacteria increased with the number of passes through the discharge (similarly to the results obtained for *E. coli* and *E. faecalis* in Fig. 5). However, Fig. 6a shows that growth inhibition of algae further proceeded in next days after the exposure to the discharge and the same degree of inhibition was eventually attained after one pass as after two passes of biomass through the reactor. Various mechanisms might be involved in such prolonged growth inhibition of cyanobacteria (mainly caused by rupture of intracellular gas vacuoles in algae cells by physical effects induced by the discharge and/or by oxidative stress and damage of cells by reactive oxygen chemical species produced by the discharge – either by radicals or by long lived species such as H_2O_2, which production measured under the same experimental conditions is showed at Fig. 6b). Nevertheless, it is seems that for growth inhibition of cyanobacteria one pass of the biomass though the discharge would be sufficient, which is very promising result.

4. Conclusions

Novel high power DC diaphragm underwater discharge apparatus for decontamination and disinfection of water has been developed. It was shown that the apparatus is capable to treat relatively large volume of liquid and efficiently reduce biological contamination in water especially when the diaphragm discharge reactor is operated in the plug-flow regime.

Acknowledgement. Work was supported by the Grant Agency of AS CR (project No. IAAX00430802) and Ministry of Education, Youth and Sports (No. MEB0810116).

5. References

[1] Locke B R, Sato M, Sunka P, Hoffmann M R, Chang J-S 2006 *Ind. Eng. Chem. Res.* **45** 882
[2] Babicky V, Clupek M, Lukes P and Sunka P 2009 *Apparatus for decontamination and disinfection of aqueous solutions*. PCT Application No: WO 2009/033436 A1
[3] Monte M, De Baerdemaeker F, Leys C, Maximov A I 2002 *Czech. J. Phys.* **52** D724
[4] Sunka P, Babicky V, Clupek M, Lukes P 2003 *Digest of Technical Papers IEEE PPC-2003* 229
[5] Stara Z, Krcma F 2004 *Czech. J. Phys*. **54** C1050
[6] De Baerdemaeker F, Simek M, Leys C 2007 *J. Phys. D: Appl. Phys*. **40** 2801
[7] Nikiforov A Yu, Leys C 2007 *Plasma Sources Sci. Technol*. **16** 273
[8] Bruggeman P, Degroote J, Vierendeels J, Leys C 2008 *Plasma Sources Sci. Technol*. **17** 025008
[9] Joshi R, Schulze R-D, Meyer-Plath A, Friedrich J F 2008 *Plasma Process. Polym*. **5** 695
[10] Krcma F, Stara Z, Prochazkova J 2010 *J. Phys.: Conf. Ser*. **207** 012010
[11] Lukes P 2002 *Water treatment by pulsed streamer corona discharge*, IPP AS CR, Prague, CR
[12] Lukes P, Clupek M., Babicky V., Sunka P 2008 *Plasma Sources Sci. Technol*. **17** 024012

CHARACTERIZATION OF PLASMA INDUCED PHENOL ADVANCED OXIDATION PROCESS IN DBD REACTOR

Ester Marotta[1], Milko Schiorlin[1], Elisa Ceriani[1], Volodymyr Shapoval[1], Claudio Ceretta[1], Massimo Rea[2], Cristina Paradisi[1]

[1]*Dipartimento Scienze Chimiche, Università degli Studi di Padova, via Marzolo 1, 35131 Padova - Italy*

[2]*Retired from Dipartimento di Ingegneria Elettrica, Università degli Studi di Padova, via Gradenigo 6, 35131 Padova – Italy*

E-mail: cristina.paradisi@unipd.it

Two prototype reactors were developed and tested for water purification, in which dielectric barrier discharges are applied in air above the solution to be treated. Phenol was used as a model organic pollutant to characterize these non-thermal plasma induced advanced oxidation processes Diagnostics included monitoring of pH and conductivity, analyses by HPLC with UV and MS detectors, ion chromatography, FT-IR, as well as specific mechanistic probes to reveal and quantify highly reactive oxidizing species produced in these systems.

1. Introduction

The application of electrical discharges for water purification into [see for example 1-4] and above aqueous solutions [see for example 5-8] is being proposed and developed as a means to perform advanced oxidation of organic pollutants in waters. Hybrid reactors, which utilize both gas phase non-thermal plasma formed above the water solution and direct liquid phase corona-like discharge in the water, have also been developed [9]. Other types of reactor include systems in which the solution to be treated is supplied into the discharge zone as an aerosol [10] or as a falling-water film [11,12], in order to optimize the transfer of the reactive species.

Many different parameters affect the discharge induced oxidation of the organic compounds depending on the specific experimental configuration employed [3]. In particular, initiation of a discharge in water requires a certain initial conductivity, generally of a few of μS/cm. On the other hand, a high conductivity (> 400 μS/cm) makes streamers shorter and reduces the production of radicals [1]. Thus, a high conductivity affects negatively the efficiency of removal of organic compounds from the solution. For example, Mizeraczyk et al. [4] compared the removal of phenol in distilled water (1 μS/cm), in water containing NaCl (200 μS/cm) and in tap water (600 μS/cm) and found a significant decrease in the efficiency of the process, with phenol in tap water being not decomposed at all. As tap water was used as a model for the application of the process to drinking water and wastewater purification, we undertook a similar investigation by using DBD reactors in which the discharge is applied above the solution. In these systems it is expected that the water conductivity should not affect the discharge voltage and the production rate of radicals in the gas above the solution [13].

2. Experimental Part

Materials

Phenol, substituted phenols, muconic acids and other oxidation intermediates, coumarin 3-carboxylic acid (97%), 7-hydroxycoumarin carboxylic acid (98%) and other chemicals were commercial samples of reagent grade purity. Ultrapure grade water (milliQ water) was obtained by filtration of deionized water with a Millipore system. Gases (pure air, i.e. a synthetic mixture of 80% nitrogen and 20% oxygen, CO_2 and CO standards) were purchased from Air Liquide.

Apparatus

Most of the experiments described in this paper were performed with the first reactor developed, the "2-wires reactor" (Fig. 1a). It consists of a glass vessel (internal dimensions 95x75 mm and 60 mm height) closed by a teflon cover with four passing electrodes of stainless steel which support two parallel wires of 75 mm length and 0.15 mm diameter fixed upon their tips. The wires, made of

stainless steel, are placed at a distance of 38 mm between each other and are kept above the aqueous solution. The outside surface of the reactor base is covered with a film of silver and connected to a grounded plate. The reactor is powered with an AC high voltage transformer with 16.5-18 kV and a frequency of 50 Hz. A flow of air of 30 mL·min^{-1} is swept through the reactor above the solution and the discharge occurs in the gas phase above the liquid surface. To minimize evaporation phenomena from the solution, the air is humidified by passing it through a water bubbler placed ahead of the reactor. During the experiments the electrical power was maintained constant (1.9 W): voltage and current profiles were monitored with a digital oscilloscope (TDS5032B, bandwidth 350 MHz, sample rate 5 Gs/s) to assure the reproducibility of the electrical conditions.

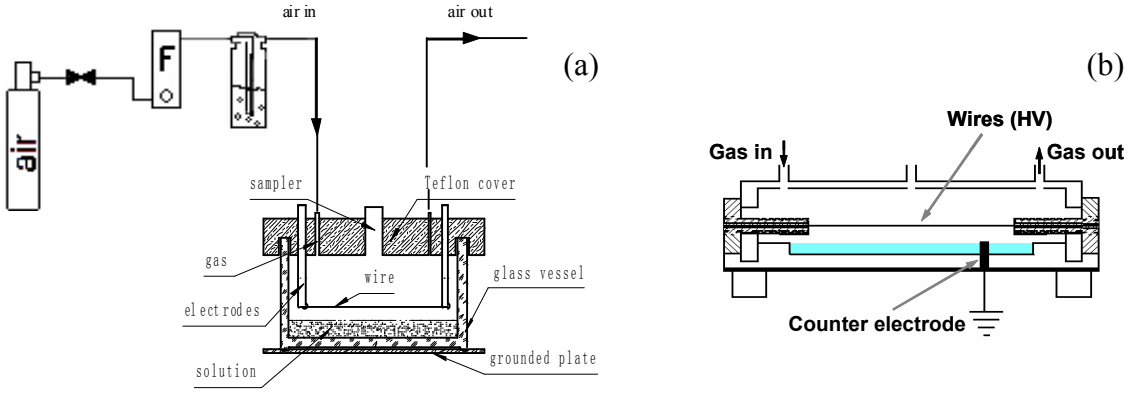


Fig. 1. Schematics of apparatus: (a) 2-wires reactor and (b) 7-wires reactor.

The second reactor developed (Fig. 1b) is made in two pieces, a base and a cover, both of Plexiglas. The outside surface of the base is painted with a film of colloidal silver and connected to a grounded plate. The cover holds in place the active electrodes, seven parallel wires (0.15 mm of diameter and 300 mm length) which are placed at a distance of 18 mm one from the other and fixed to a Teflon frame which can be moved up and down to vary the distance between the wires and the solution. As in the first prototype, the cover of the reactor is equipped with entrance and a exit ports for air circulation and with a sampling port for the withdrawal of samples of the treated solution. The new reactor can be powered not only with AC but also with DC and pulsed high voltage of either polarity.

Procedures

The decomposition process was monitored by measuring the organic pollutant conversion as a function of treatment time. To this end, at desired times the discharge was briefly interrupted and a 0.5 mL aliquot of the treated solution was withdrawn and subjected to HPLC analysis (Shimadzu LC-10AT pump with a UV-Vis Shimadzu SPD-10 detector, monitoring specifically at 210 and 270 nm). The fraction of residual pollutant, C/C_0 (where C_0 and C are the concentrations at time zero and t, respectively), was plotted against the treatment time and the data were fitted to equation 1 to obtain the process pseudo first order rate constant, k.

$$\frac{C}{C_0} = e^{-k \cdot t} \qquad (1)$$

For the identification of the intermediate products selected samples were analyzed by LC/ESI using an Agilent Technologies 1100 series HPLC connected to a diode array and a mass spectrometer detector (MSD SL Trap). The ionization was performed by electrospray (ESI) source alternating positive and negative polarity The assignment of the intermediate products was confirmed by comparison with standards. The sampled solution was also analyzed by ion chromatography (Dionex Series 4000), using a Dionex IonPac AS4A-SC 2 mm (i.d.) x 250 mm column, a mixture of 1.7 mM sodium bicarbonate and 1.8 mM sodium carbonate as eluent and an electrochemical self-regenerating ULTRA II suppressor. pH and conductivity of the initial and final solutions were monitored during the experiments with a pH meter Metrohm 827 and a conductometer Metrohm 660. The gas exiting the reactor was subjected to on line FT-IR analysis (Nicolet 5700) using a 10 cm long flow cell with CaF_2 windows. CO_2 and CO were quantified by means of calibration of the instrument response using commercial standard gas mixtures.

3. Results and Discussion

A first important result obtained with the DBD reactor (Fig. 1a) concerns the greater efficiency of phenol degradation in tap water with respect to pure deionized (milliQ) water (Fig. 2a). This desirable outcome is opposite to that found by Mizeraczyk et al. using discharge in water [4].

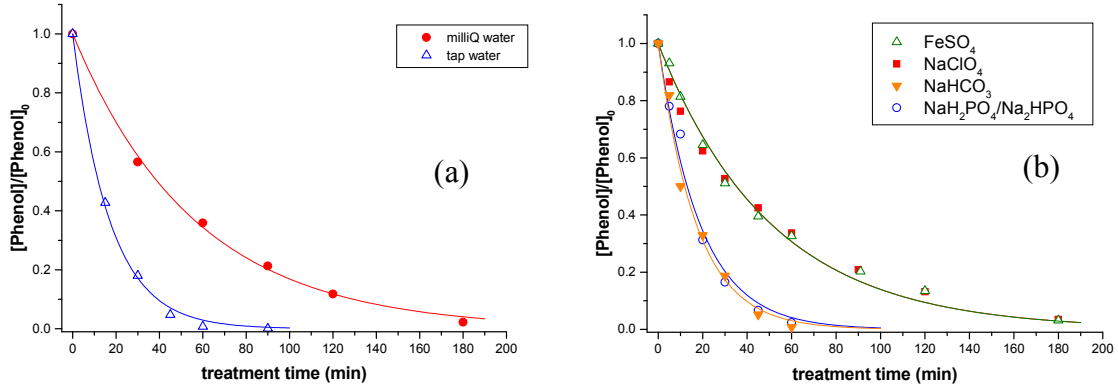


Fig. 2. Decomposition of phenol in solutions prepared in: (a) milliQ and tap water; (b) milliQ water containing $FeSO_4$ (199 $\mu g \cdot L^{-1}$), NaClO (202 $\mu g \cdot L^{-1}$), $NaHCO_3$ (4.4 mM) and NaH_2PO_4/Na_2HPO_4 (4.4 mM, initial pH=6.9).

The reason for the higher process efficiency in tap water could in principle be due to conductivity, to specific catalysis by iron ions in Fenton like processes, to residual active chlorine present after depuration applied to water in Italy to make it drinkable and to buffering of pH by the carbonate system. The results of experiments performed to test these hypotheses, summarized in Fig. 2b, clearly show that neither iron ions or hypochlorite ions produce any significant kinetic effect with respect to milliQ water and that the higher efficiency of phenol oxidation in tap water is to be attributed to the buffered pH of the solution during the treatment: thus, the rate of the process is virtually the same in tap water and in aqueous solutions buffered either with $NaHCO_3$, as in tap water, or with the NaH_2PO_4/Na_2HPO_4 system. In contrast, in milliQ water the pH changes from neutrality to acidic during the discharge treatment due to the production of NOx and consequently of nitric acid.
Preliminary experiments with the new 7-wires reactor confirm the generality of this effect for phenol oxidation induced by DBD discharges. Table 1 reports efficiency data expressed as energy constants, k_E ($L \cdot kJ^{-1}$), for phenol processing in milliQ and in tap water using the two DBD reactors. It is seen that in both cases a greater efficiency is obtained in tap than in milliQ water and also that the 7-wires reactor is more efficient than the 2-wires reactor due an improved design which allows for the development of a more diffuse plasma extending over the entire surface of the liquid. Experiments are underway to compare the efficiency of different types of discharge produced in the 7-wires reactor by DC and pulsed high voltages of either polarity.

Tab. 1. Energy constant, k_E ($L \cdot kJ^{-1}$), for treatment of a $5 \cdot 10^{-4}$ M phenol solution in milliQ and tap water in the two DBD reactors used in this work

Reaction medium	$10^2 \cdot k_E$ ($L \cdot kJ^{-1}$)	
	2-wires reactor	7-wires reactor
milliQ water	1.0	1.9
Tap water	2.9	3.2

The rate of phenol decomposition also depends on the pollutant initial concentration, C_0. Fig. 3a shows that, within the range explored, the rate constant depends linearly, to a reasonable approximation, on the reciprocal of C_0. A similar situation was observed previously for non-therrmal plasma induced

oxidation of volatile organic compounds in air and explained in terms of a mechanism of inhibition by products [14,15].

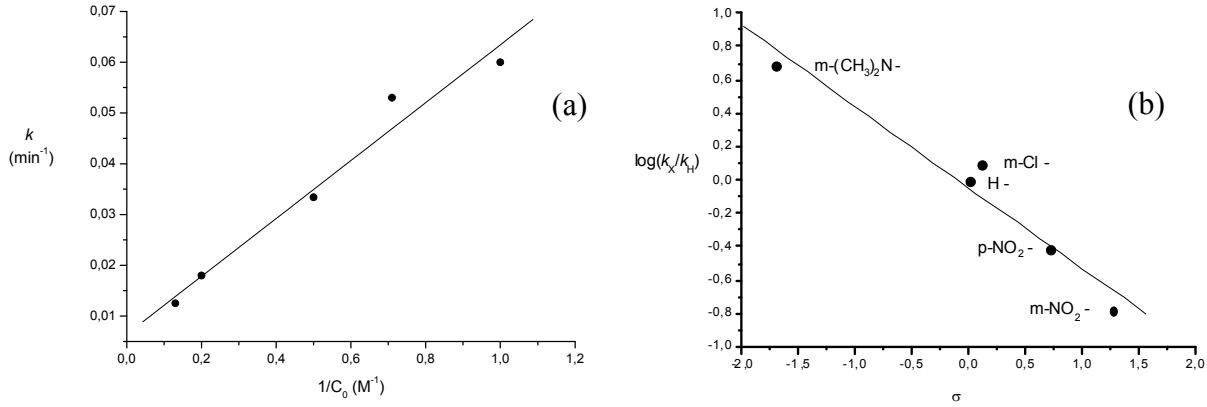


Fig. 3. Effect on decomposition rate due to: (a) phenol initial concentration; (b) substituent on phenol ring.

Besides CO_2, which was monitored and quantified by *on line* FT-IR analysis of the air exiting the reactor (Fig. 4a), several organic products were detected by HPLC analysis and identified by means of LC-ESI spectra (Fig. 4b) and comparison of spectra and retention times with authentic samples. These include dihydroxy benzenes and various organic acids: the time profiles of their concentration in a typical experiment (Fig. 4c) confirm their role as intermediates in the oxidation of phenol to CO_2.

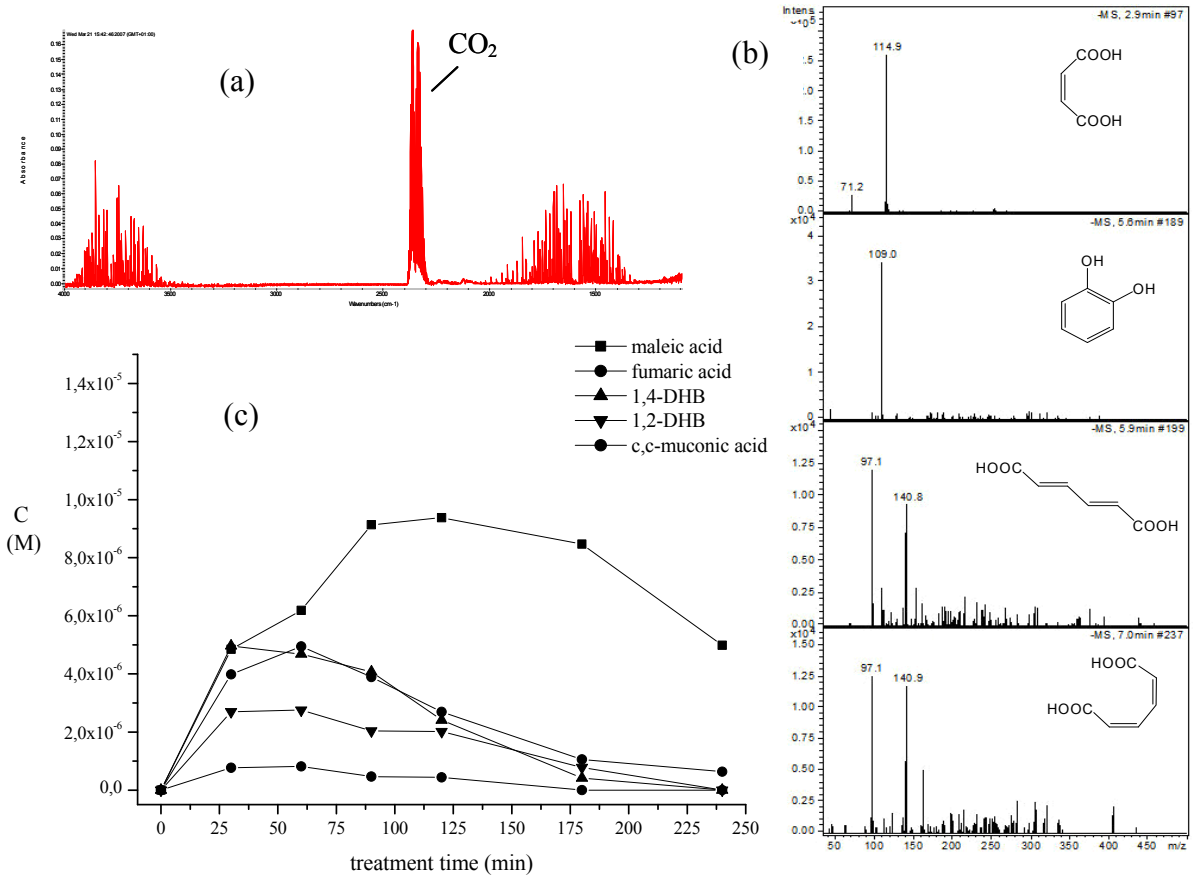


Fig. 4. Products of phenol oxidation: (a) CO_2 determined by *on line* FT-IR analysis; (b) negative ESI-MS spectra and (c) concentration as a function of treatment time of major oxidation intermediates.

Despite their high reactivity these strongly oxidizing environments display remarkable substrate selectivity. Inspection of a series of substituted phenols showed that the rate constant of oxidation

depends markedly on the type substituent (X) and on its site of substitution (Fig. 3b). A reasonably good linear correlation is found between log k_X/k_H and sigma substituent constants, consistent with a mechanism in which the initial stage of oxidation is the electrophilic attack by the hydroxyl radical. The concentration of OH radicals in solution was determined using a well-known chemical probe [16], i.e. its reaction with coumarin 3-carboxylic acid (CCA) to form coumarin 7-hydroxy-3-carboxylic acid, a fluorescent product. Thus, following the decay of CCA by HPLC/UV-Vis and the formation of 7-hydroxy-CCA by fluorescence and using literature data for this reaction, we were able to estimate that, under our standard plasma treatment conditions in the 2-wires DBD reactor, the amount of OH radical produced into milliQ water is $4.4 \bullet 10^{-4}$ $\mu mol \bullet s^{-1}$[17].

4. References

[1] Sunka P, Babicky V, Clupek M, Lukes P, Simek M, Schmidt J and Cernak M 1999 *Plasma Sources Sci. Technol.* **8** 258.
[2] Sun B, Sato M and Clements J S 2000 *Environ. Sci. Technol.* **34** 509.
[3] Locke B R, Sato M, Sunka P, Hoffmann M R and Chang J-S 2006 *Ind. Eng. Chem. Res.* **45** 882.
[4] Dors M, Metel E and Mizeraczyk J 2007 *Int. J. Plasma Environ. Sci. Technol.* **1**76.
[5] Brisset J L 1997 *J. Appl. Electrochem.* **27** 179.
[6] Sano N, Kawashima T, Fujikawa J, FujimotoT, Kitai T, Kanki T and Toyoda A 2002 *Ind. Eng. Chem. Res.* **41** 5906.
[7] Grabowski L R, van Veldhuizen E M, Pemen A J M and Rutgers W R 2006 *Plasma Chem. Plasma Process.* **26** 3.
[8] Sato M, Tokutake T, Ohshima T and Sugiarto A T 2008 *IEEE Trans. Ind. Appl.* **44** 1397.
[9] (a) Lukes P, Appleton A T and Locke B R 2004 *IEEE Trans. Ind. Appl.* **40** 60; (b) Grymonpre D R, Finney W C, Clark R J and Locke B R 2004 *Ind. Eng. Chem. Res.* **43**, 1975.
[10] Burlica R and Locke B R 2008 *IEEE Trans. Ind. Appl.* **44** 482.
[11] Sano N, Yamamoto D, Kanki T and Toyoda A 2003 *Ind. Eng. Chem. Res.* **42** 5423.
[12] Ognier S, Iya-sou D, Fourmond C and Cavadias S 2009 *Plasma Chem. Plasma Process.* **29** 261.
[13] Sano N, Fujimoto T, Kawashima T, Yamamoto D, Kanki T and Toyoda A 2004 *Sep. Purif. Technol.* **37** 169.
[14] Slater C and Douglas-Hamilton D H 1981 *J. Appl. Phys.* **52** 5820
[15] Marotta E, Schiorlin M, Rea M and Paradisi C 2010 *J. Phys. D-Appl. Phys.* **43** 124011.
[16] Newton G L and Milligan J R 2006 *Radiat. Phys. Chem.* **75** 473.
[17] Paradisi C et al. manuscript in preparation.

DECOMPOSITION CHARACTERISTICS OF BENZENE, TOLUENE AND XYLENE IN AN ATMOSPHERIC DC CORONA DISCHARGE

Kohki Satoh[1], Kohji Nagao[2] and Hidenori Itoh[1]

[1] *Muroran Institute of Technology*
[2] *Nippon Paper Industries Co., Ltd.*
E-mail: ksatoh@mmm.muroran-it.ac.jp

Decomposition characteristics of benzene, toluene and xylene in a DC corona discharge in an artificial air at atmospheric pressure are investigated. By-products from benzene, toluene and xylene are identified by infrared absorption spectroscopy, and the decomposition processes in the corona discharge are examined. It is found that CO_2, CO, HCOOH and HCOOCHO are major products, and that C_2H_2, HCN, $C_4H_2O_3$ and $(CHO)_2$ are minor products, from benzene, toluene and xylene. It is also found that $CH_3COOCHO$ is a major product, and that $CH_3COOCHO$, $H_3COOONO_2$, CH_4, HCHO and CH_3COCHO are minor products, measured only in the artificial air containing toluene and xylene. CO_2 is found to be a gaseous end product from benzene, toluene and xylene, and CO, HCOOH, HCOOCHO and $CH_3COOCHO$ are major intermediate products, which tend to be decomposed in the corona discharge; therefore, it is found that benzene, toluene and xylene are chiefly converted to CO_2 via CO, HCOOH, HCOOCHO and $CH_3COOCHO$.

1. Introduction

Since volatile organic compounds (VOCs), such as benzene (C_6H_6), toluene ($C_6H_5CH_3$), xylene ($C_6H_4(CH_3)_2$), etc., are considered to be the cause of suspended particulate matters and photochemical oxidants, and affect human health by a long time exposure even if those concentrations are very low, the VOCs in exhaust fumes must be removed or decomposed before those are released into atmosphere. Conventionally, thermal oxidation, absorption, catalytic oxidation, etc. are used for VOCs removal, and these techniques are suitable to treat exhaust gases with large flow rate (10^3 - 10^5 Nm^3/h) and relatively high concentration (10^2 - 10^4 ppm) [1]. The new gas-clean-up techniques using discharge plasma are applicable for the removal of VOCs with wider range of concentration (1 - 10^4 ppm) though the applicable flow rate of exhaust gases is relatively low (10^{-2} - 10^3 Nm^3/h [1]). Further, active species, which have high oxidation potential, are produced in the discharge plasma [2], and those enable to decompose non-degradable substances; therefore, effective gas clean-up can be achieved by using discharge plasma. In recent works concerning the discharge plasma treatment of VOCs, effects of humidity, gas composition, coupling with catalysis, etc. on decomposition rate and efficiency are investigated [3]-[6]. However, the examination of VOCs decomposition processes based on detailed investigation of by-products from VOCs has reported in few papers.

In this work, we investigate the decomposition process of benzene, toluene and xylene in a DC corona discharge in an artificial air at atmospheric pressure. Gaseous by-products from the VOCs are identified by infrared absorption spectroscopy, and then decomposition processes of the VOCs are examined. Discharge plasma generated at atmospheric pressure, such as barrier discharge, pulsed discharge, corona discharge, etc. have been used for VOCs removal. Especially, streamer corona, which are generated by the application of a DC high voltage, has large discharge volume as compared to the other discharges, and the corona discharge is reportedly a suitable technique for VOCs removal [7]. Therefore, the DC streamer corona discharge is used in this work.

2. Experimental

Fig. 1 shows schematic diagram of experimental apparatus. A multi-needle electrode consisting of thirteen stainless-steel needles and a plane electrode are placed in a cylindrical discharge chamber, made of stainless-steel, with 197 mm in inner diameter and 300 mm in height. Each of the needles has 4 mm in diameter and 55 mm in length, and these are arranged in equal interval on a brass plate with

50 mm in diameter. The plane electrode has 80 mm in diameter and 10 mm in thickness. The distance between the multi-needle electrode and the plane electrode is fixed at 30 mm, and the plane electrode and the discharge chamber are earthed.

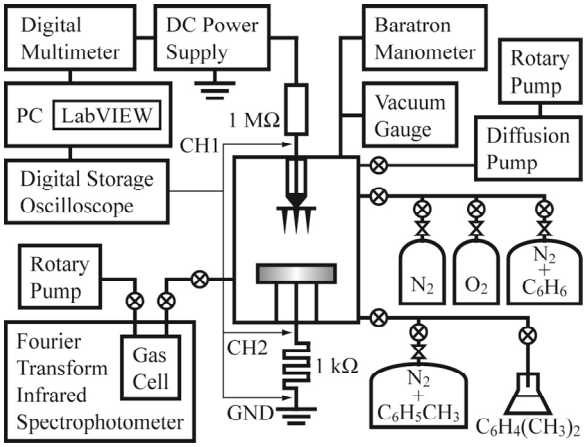


Fig. 1. Schematic diagram of experimental apparatus

A positive DC high voltage (20-28 kV) is applied to the multi-needle electrode by a DC power supply (Max-Electronics Co., Ltd., LS40-10), generating a streamer corona discharge between the electrodes with the discharge current of 0.2 mA. A resistance of 1 MΩ is inserted between the DC power supply and the multi-needle electrode to stabilise the corona discharge; it also protects the multi-needle electrode when the corona discharge changes into a spark discharge. The applied voltage is measured by a high-voltage probe (Tektronix Inc., P6015A) and a discharge current is calculated by a voltage drop across a non-inductive resistance of 1 kΩ, inserted between the plane electrode and the earth. The voltage and current are measured by a digital storage oscilloscope (Yokogawa Electric Corp., DL1620), and the data are acquired through LabVIEW (National Instruments Corop., version 8.0) into a personal computer every two seconds. Electrical energy input to the corona discharge is obtained by the temporal integration of instantaneous electrical power calculated by multiplying the applied voltage by the discharge current.

Initially, an artificial air, the mixture ratio of which are N_2/O_2=80/20(%), with 300 ppm of benzene, toluene or xylene are sealed in the evacuated discharge chamber at 1013 hPa. Gaseous samples are taken from the discharge chamber before and after the corona discharge, and then the concentrations of the gaseous samples are measured by infrared absorption spectroscopy using a Fourier-Transform Infrared Spectrophotometer (Shimadzu Corp., FTIR-8900) equipped with a gas cell (Infrared Analysis Inc., 10PA), which has an optical path length of 10 m.

3. Results and discussion

Figs. 2(a) and (b) show infrared absorbance spectra of gas samples taken from the discharge chamber before and after 30 min streamer corona discharge (corresponding to 10 kJ of electrical energy input), respectively. The absorbance peaks of benzene at 673 and 3068 cm^{-1} decrease after the corona discharge, and at the same time, those of by-products, namely, carbon dioxide (CO_2; 2349 cm^{-1}), carbon monoxide (CO; 2143 cm^{-1}), formic acid (HCOOH; 1105 and 1770 cm^{-1}), acetylene (C_2H_2; 730 cm^{-1}), hydrogen cyanide (HCN; 712 cm^{-1}), ozone (O_3; 1042 cm^{-1}) and nitrous oxide (N_2O; 2224 cm^{-1}), are newly observed. Fig. 2(c) shows the residual absorbance spectra that the absorbance peaks of benzene and the by-products identified above are subtracted from the spectra shown in Fig. 2(b). The absorbance peaks of formic anhydride (HCOOCHO, abbreviated as FAH; 998, 1105, 1767 and 1822 cm^{-1}) and that of glyoxal (HCOCHO, abbreviated as GLY; 2835 cm^{-1}) are also identified. It is, therefore, found that CO_2, CO, HCOOH, C_2H_2, HCN, FAH and GLY are gaseous by-products from benzene in the atmospheric DC corona discharge, and that O_3 and N_2O are produced from the background gas.

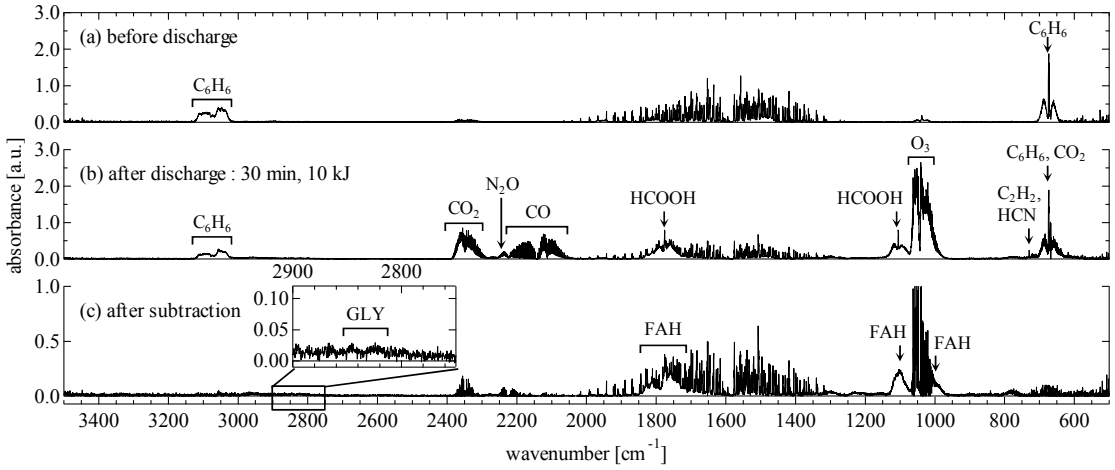


Fig. 2. Infrared absorption spectra before and after discharge in the decomposition of benzene. (a) before discharge, (b) after discharge (30 min, 10 kJ) and (c) after the subtraction of major peaks form (b).

Following the Lambert-Beer's law, the concentrations of gaseous substances can be deduced from the absorbance measured by the FT-IR, so that working curves, which represent relationship between the absorbance and the concentration of gaseous substances, for benzene, CO_2, CO, HCOOH, C_2H_2 and HCN are obtained using standard gases and gas detector tubes. Since the standard gases of FAH and GLY are not supplied, the concentration of GLY is calculated using absorption coefficient reported by Pitts *et al*.,[8] and that of FAH is deduced by the following method.

FAH is known as a by-product when ethylene (C_2H_4) is decomposed by a streamer corona discharge in an artificial air at atmospheric pressure. CO_2, CO, HCOOH, C_2H_2 and HCN are the other by-products, the concentrations of which can be deduced, in the corona discharge; therefore, the concentration of FAH is deduced from mass balance for carbon atoms. Fig. 3 shows the mass balance for carbon atoms as a function of input energy, as shown by stacked graph, when C_2H_4 is decomposed by the atmospheric pressure corona discharge. The number of carbon atoms contained in gaseous substances is evaluated in the unit of ppmC, which is calculated by multiplying the number of carbon atoms in each of the substances by its concentration. Since the initial concentration of C_2H_4 is 300 ppm, and no deposit is observed on the electrodes and the wall of the discharge chamber throughout the experiment, the number of carbon atoms contained in the discharge chamber must be 600 ppmC. In Fig. 3, the sum of the carbon atoms except for FAH is less than 600 ppmC; therefore, the area between the upper line of CO_2 and the line of 600 ppmC can be regarded as number of carbon atoms in FAH. Fig. 4 shows the variations in the number of carbon atoms in FAH and the absorbance of FAH, as functions of input energy in the decomposition of C_2H_4. Those variations agree well with each other, so that the relationship between the absorbance and the concentration of FAH is obtained. From the calibration of FAH concentrations, it is found that CO_2, CO, HCOOH and FAH are major by-products, and that HCN and GLY are minor products, which are the order of ppm.

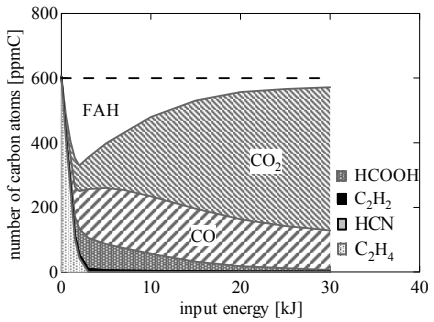


Fig. 3. Variations in number of carbon atoms as function of input energy in the decomposition of C_2H_4

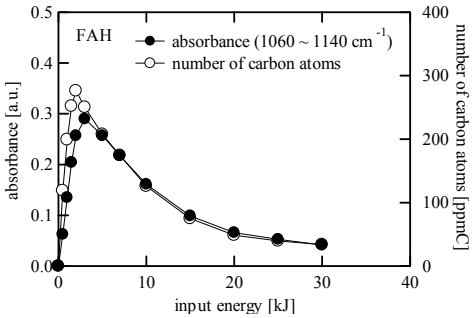


Fig. 4. Absorbance variation of FAH as functions of input energy in the decomposition of C_2H_4.

Figs. 5(a) and (b) show infrared absorption spectra before and after the corona discharge in toluene decomposition. The absorbance peaks of toluene at 729 and 3028 cm^{-1} decrease, and those of CO_2, CO, HCOOH, C_2H_2, HCN, O_3 and N_2O, which are shown in benzene decomposition, are also observed. Fig. 5(c) shows the residual absorbance spectra that the peaks of toluene and the by-products identified above are subtracted from the spectra in Fig. 5(b). The absorbance peaks of FAH, acetic formic anhydride ($CH_3COOCHO$, abbreviated as AFAH; 1178 and 1795 cm^{-1}) and peroxyacetyl nitrate ($CH_3COOONO_2$, abbreviated as PAN; 794, 1163, 1302, 1741 and 1842 cm^{-1}) are identified. Further, the tiny peaks of GLY, methane (CH_4; 3019 cm^{-1}), formaldehyde (HCHO; 2783 cm^{-1}), acetic acid (CH_3COOH; 642 cm^{-1}) and methyl glyoxal (CH_3COCHO, abbreviated as MGLY; 2829 cm^{-1}) are also identified. It is, therefore, found that CO_2, CO, HCOOH, C_2H_2, HCN, FAH, GLY, AFAH, PAN, CH_4, HCHO, CH_3COOH and MGLY are by-products from toluene in the atmospheric DC corona discharge.

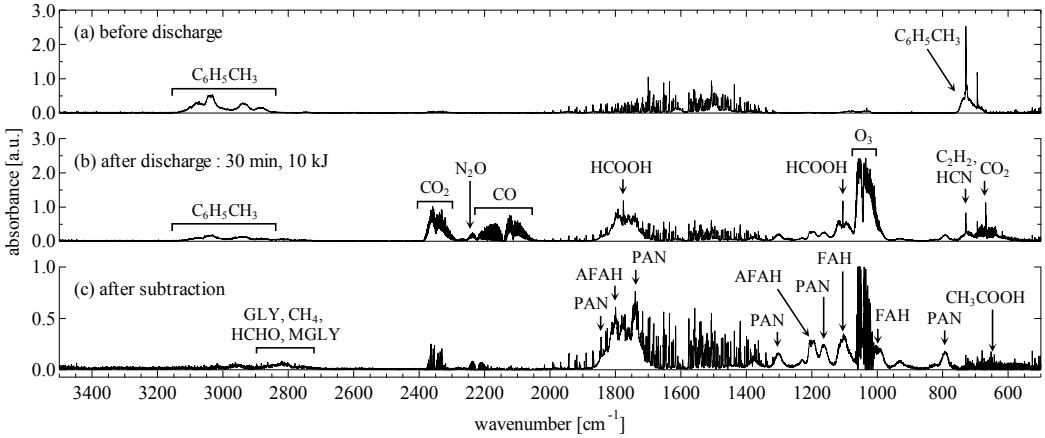


Fig. 5. Infrared absorption spectra before and after discharge in the decomposition of toluene. (a) before discharge, (b) after discharge (30 min, 10 kJ) and (c) after the subtraction of major peaks from (b).

The concentrations of toluene, CH_4, HCHO and CH_3COOH are obtained using standard gases, and those of PAN and MGLY are calculated using absorption coefficients reported by Allen *et al*.[9] and Pitts *et al*.,[8] respectively. AFAH is a by-products when propylene (C_3H_6) is decomposed by a streamer corona discharge in the artificial air at atmospheric pressure, and the kinds and concentrations of the other by-products in the discharge can be deduced. Threrefore, the concentration of AFAH is obtained from the results of C_3H_6 decomposition by the similar method used for obtaining the concentration of FAH. As a result, it is found that CO_2, CO, HCOOH, FAH and AFAH are major by-products from toluene, and that the others are minor products. It is also found that the same by-products identified for toluene are found in the corona discahrge in an artificial air containing xylene.

Fig. 6 shows the concentration variations of benzene, toluene, xylene and major by-products, CO_2, CO, HCOOH, FAH and AFAH, as functions of input energies. It is found that the concentrations of benzene, toluene and xylene decrease monotonously with the increase of the input energy, and that the decomposition efficiencies of benzene, toluene and xylene are respectively 0.8, 1.5 and 2.2 g/kWh. Since the concentration of CO_2 increases with the increase of the input energy, CO_2 is found to be a gaseous end product from the benzene, toluene and xylene. The concentrations of the other products once increase and tend to decrease with the input energies, so that those are found to be intermediate products. This result suggests that benzene, toluene and xylene are chiefly converted to CO_2 via CO, HCOOH, FAH and AFAH in the atmospheric pressure DC corona discharge. Further, since deposits are observed on the plane electrode, etc. after the corona discharge, the decomposition processes of benzene, toluene and xylene in the atmospheric DC corona discharge can be shown as Fig. 7.

4. Conclusions

In this work, we investigated the decomposition characteristics of benzene, toluene and xylene in an atmospheric DC corona discharge. It is found that the concentrations of benzene, toluene and xylene

decrease monotonously with the increase of the input energy, and that the decomposition efficiencies are 0.8, 1.5 and 2.2 g/kWh, respectively. It is also found that the by-products from benzene, toluene and xylene are CO_2, CO, HCOOH, C_2H_2, HCN, FAH and GLY, and that AFAH, PAN, CH_4, HCHO, CH_3COOH and CH_3COCHO are produced only from toluene and xylene. CO_2, CO, HCOOH, FAH and AFAH are major by-products, and that the others are minor products. CO_2 is found to be a gaseous end-product, and the others are intermediate products. It is likely that benzene, toluene and xylene are chiefly converted to CO_2 via CO, HCOOH, FAH and AFAH, and that the some of carbon atoms are deposited on the electrodes and the wall of the discharge chamber.

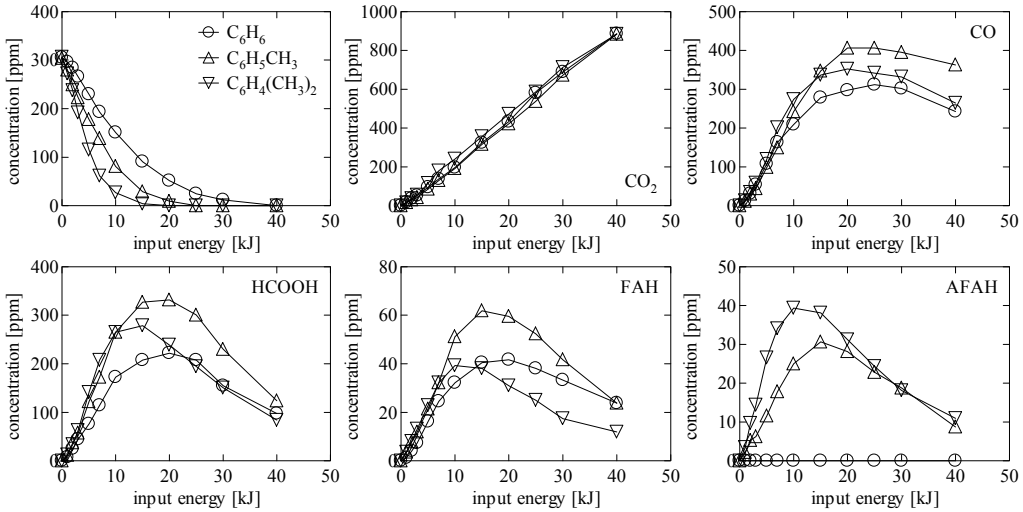


Fig.6. Concentration variations of benzene, toluene, xylene and major by-products as functions of input energies.

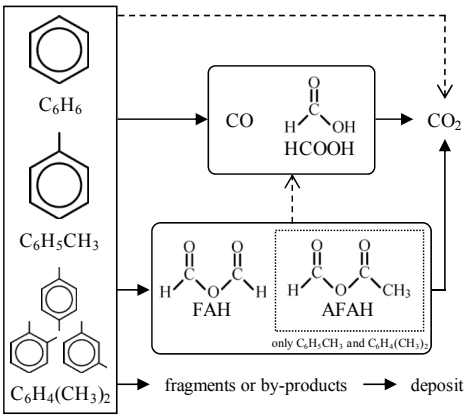


Fig. 7. Decomposition processes of benzene, toluene and xylene in the atmospheric DC corona discharge.

5. References

[1] K. Urashima and J. S. Chang, IEEE Trans. Dielec. Elec. Insula., Vol.7, 602 (2000)
[2] M. Malik, A. Ghaffar and S. A. Malik, Plasma Sources Sci. Technol. Vol.10, 82 (2001)
[3] N. Goto, H. Kurimoto, S. Kudo and Y. Watanabe, IEE Japan, Trans., Vol.123-A, 900 (2003)
[4] H. H. Kim, J. U. Park, et al., J. Inst. Electrostat. Jpn., Vol. 29, 32 (2005)
[5] D. Li, D. Yakushiji, S. Kanazawa, T. Ohkubo, and Y. Nomoto: J. Electrostat., Vol.55, 311 (2002)
[6] H. M. Lee and M. B. Chang, Plasma Chem. and Plasma Proc., Vol.23, 541 (2003)
[7] Y. Yoshioka, IEE Japan. Trans., 122-A, 676 (2002)
[8] J. N. Pitts Jr., et al., Final Report, California Air Resources Board, A2-115-32 (1984)
[9] G. Allen, J. J. Remedios, et al., Atmos. Chem. Phys. Vol.5, 47 (2005)

ACETALDEHYDE OXIDATION USING TWO DIFFERENT ATMOSPHERIC PRESSURE NON THERMAL PLASMA / CATALYST CONFIGURATIONS

Arlette Vega-González, Charles Klett, Khaled Hassouni, Sylvain Touchard, Xavier Duten

Laboratoire d'Ingénierie des Matériaux et des Hautes Pressions,
CNRS-Université Paris 13, 93430 Villetaneuse, France
E-mail: vega@limhp.univ-paris13.fr

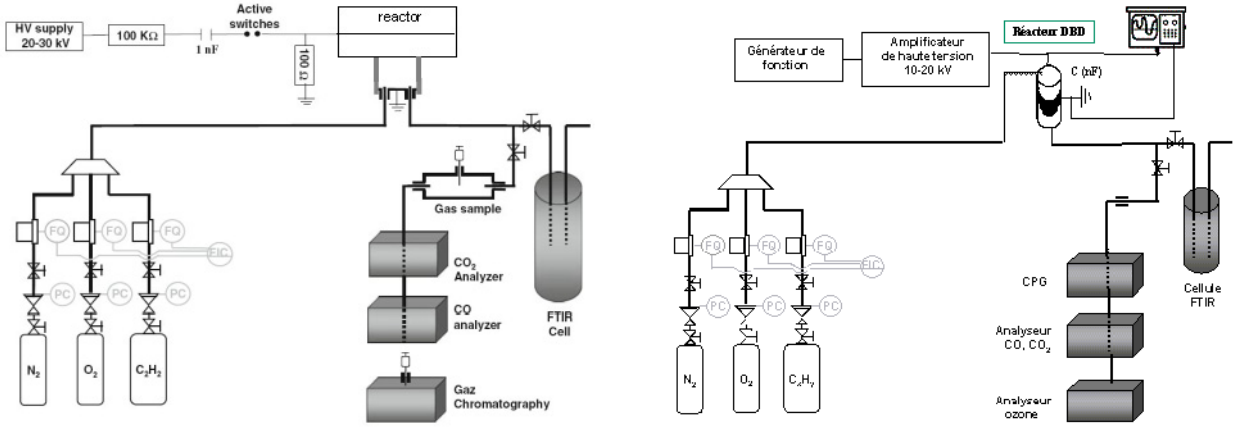
The aim of this work is to study acetaldehyde degradation using an atmospheric pressure non-thermal plasma process (NTP), alone or in combination with a catalyst. Two different set-ups were used, a pulsed corona discharge in a wire to cylinder (WTC) configuration, and a dielectric barrier discharge (DBD). A comparative study of acetaldehyde degradation with these two configurations was carried out.

1. Introduction

Non-thermal plasma (NTP) discharges at atmospheric pressure have gained attention during the last decades as an alternative process for environmental remediation [1]. However, NTP process tend to be less selective than other conventional techniques such as thermal oxidation or adsorption techniques, and undesirable by-products may be formed [2]. In order to increase the mineralization efficiencies of the NTP process, a combination of NTP and heterogeneous catalysis has been proposed for VOC abatement [3]. Most often, results are discussed in terms of decomposition efficiency and COx selectivity.
In this work, acetaldehyde oxidation is discussed in terms of by-products formation, as in addition to COx, methanol, acetic acid and methane had been identified.

2. Experimental set-ups

As shown in Fig. 1, two different experimental set-ups have been used in this study.



(a) (b)

Fig. 1. Experimental set-ups : (a) WTC reactor, (b) DBD reactor.

In the WTC, the corona discharge is generated by a Marx generator allowing obtaining up to 20-30kV voltage on the cathode, a 100mm tungsten wire. The grounded stainless steel cylindrical reactor (20mm diameter) provided a discharge volume of 64 cm^3 for a gap length of 10 mm, and the

corresponding residence time of the gas in the plasma zone was around 38 s. The corona system is used in a pulsed mode, providing a precise control of the energy deposited in the system, and high activation efficiency when processed with very short rise time voltage chocks [4]. The energy deposited during one discharge pulse is estimated from the measured voltage and current.
In the DBD, the plasma is created in a quartz tube (inner diameter 26 mm). A 15mm length metallic grid surrounding the dielectric tube is grounded, while the high voltage is applied on a central metallic rod. Rods with diameters of 20 and 15 mm were used, therefore the discharge gap was 3 and 5.5 mm, respectively. The corresponding residence time of the gas in the plasma zone was around 4s. The total charge was measured with a non-inductive capacitor (C = 44 pF). The voltage, charge and current waveforms were monitored by a digital oscilloscope. The average power dissipated in the discharge was measured by the Lissajous method [5].
In both cases, the gas inlet is mainly composed by a N_2/O_2 mixture containing 5% in oxygen added with 500 ppm of acetaldehyde as the pollutant. Gas flow rate was fixed at 100 mL/min.
The energy deposition of the investigated discharges was evaluated through the specific input energy, SIE. This is the energy deposited per unit volume of gas in the discharge cell. It is obtained from the discharge pulse frequency, the energy deposited per pulse and the gas flow rate. The typical electrical measurements obtained in both configurations are presented in Table 1.

Tab. 1. Electrical parameters.

Parameter	WTC	DBD
Energy/pulse (mJ)	25 - 39	0.4 - 4
Frequency (Hz)	1 - 13	100 - 1000
SIE (J/L)	32 - 210	50 - 2500
Power (mW)	0.5 – 3.5	0.8 - 41

As the packed material, Al_2O_3 pellets and spherical SiO_2 particles have been used. As a catalyst, nano-structured TiO_2 was deposited on SiO_2 particles.
Degradation by-products (CO, CO_2 and $C_xH_yO_z$) and residual pollutant concentrations were measured at the reactor exit. Gas chromatography analysis (SHIMADZU GC 2010) has been used to measure residual pollutant and identify the by-products. A continuous monitoring of CO and CO_2 concentration has been achieved via a non-dispersive infra-red analyzer (Environnement SA MIR 9000). Ozone concentration was followed online by UV absorption spectroscopy (InUSA IN 2000).
The effect of different parameters, O_2 content, presence of a non-porous silica in the discharge zone, nature of the non-porous silica and presence of TiO_2 chemically deposited on the silica particles, on acetaldehyde decomposition was studied.

3. Results and discussion

3.1 Acetaldehyde conversion

3.1.1 Influence of O_2 content on acetaldehyde conversion

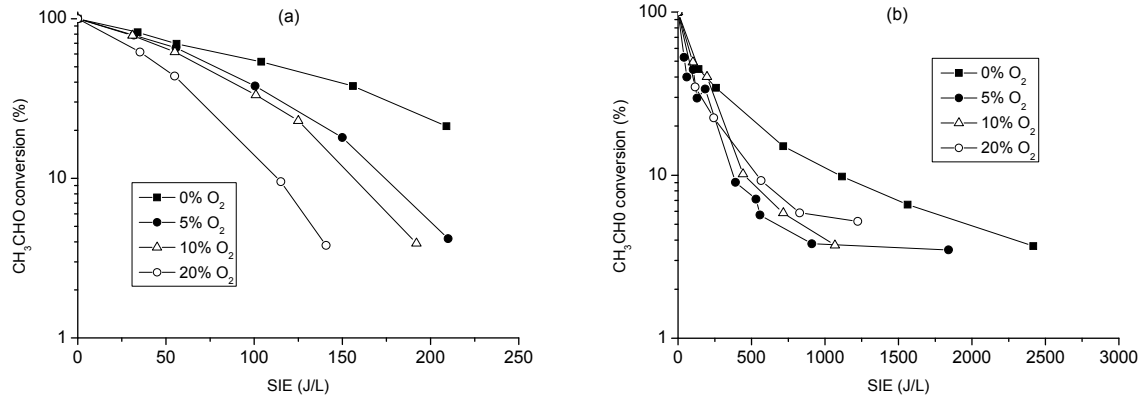


Fig. 2. Evolution of acetaldehyde conversion with SIE, influence of O_2 content: (a) WTC reactor, (b) DBD reactor.

O_2 content was varied between 0 and 20 % v/v. As can be seen from Fig. 2, acetaldehyde degradation increases with O_2 content, particularly for the higher SIE values, and this is true with both configurations. Actually, increasing the O_2 content from 5 to 10% didn't cause a significant improvement in acetaldehyde conversion. With the WTC reactor, an improvement is observed for 20% of O_2, but this behaviour was not observed with the DBD reactor.
Compared to the WTC reactor, for a given O_2 content, higher SIE are needed in the DBD reactor in order to attain a given acetaldehyde conversion. In fact, gas residence time and the energy per pulse introduced in the discharge, are almost ten times lower in the DBD reactor than in the WTC reactor, which could explain the differences observed with these two configurations.

3.1.2 Influence of a packing material

Two different types of non-porous SiO_2 particles (with and without bore) and also TiO_2 deposited on SiO_2 particles were used as the packing material. As can be seen in Fig. 3, with the WTC reactor, no significant difference is observed on acetaldehyde conversion, with or without a packing material. On the other hand, in the DBD reactor, there is an effect of the packing material as higher conversions are obtained in this case.

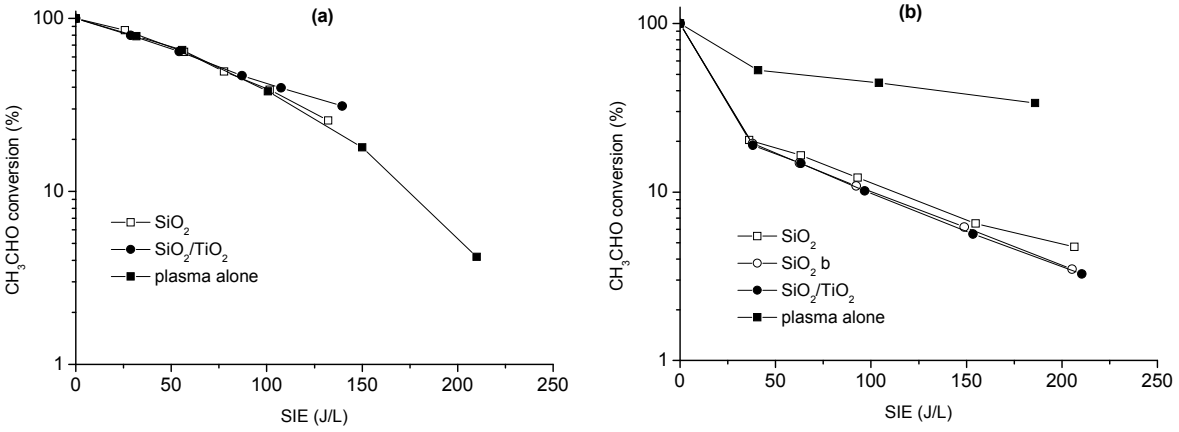


Fig. 3. Evolution of acetaldehyde conversion with SIE, influence of the packing material: (a) WTC reactor, (b) DBD reactor

As a matter of fact, in the DBD reactor, the packing material lead to the discharge electrical characteristics modification (lower energies are injected into the discharge), while no such effect was observed with the WTC reactor. In addition, the residence time is smaller in the DBD reactor, so this cannot explain the experimental results.
Thus, introducing a packing material in the plasma zone could induce the transition between a volume discharge configuration (no packing material) and a surface discharge configuration (with a packing material).

3.2 Oxidation products

3.2.1 CO and CO_2 formation

The effect of the packing material on CO and CO_2 concentration at the exit of the discharge reactor is presented in Fig. 4 and Fig. 5, respectively. For these two compounds, there is an increase in their concentration when a packed bed is used. This increase is more visible for the DBD reactor, but still present in the WTC reactor too.
CO and CO_2 concentration increase with SIE. CO concentration increases continuously for SIE values up to 200 J/L, in both configurations.
CO_2 concentration also increases continuously when using the WTC reactor, whereas there is a slight decrease in its concentration at about 100 J/L when using a packed bed in the DBD reactor.
These results may be due to a surface effect involving acetaldehyde oxidation intermediaries, such as methanol, acetic acid, etc.

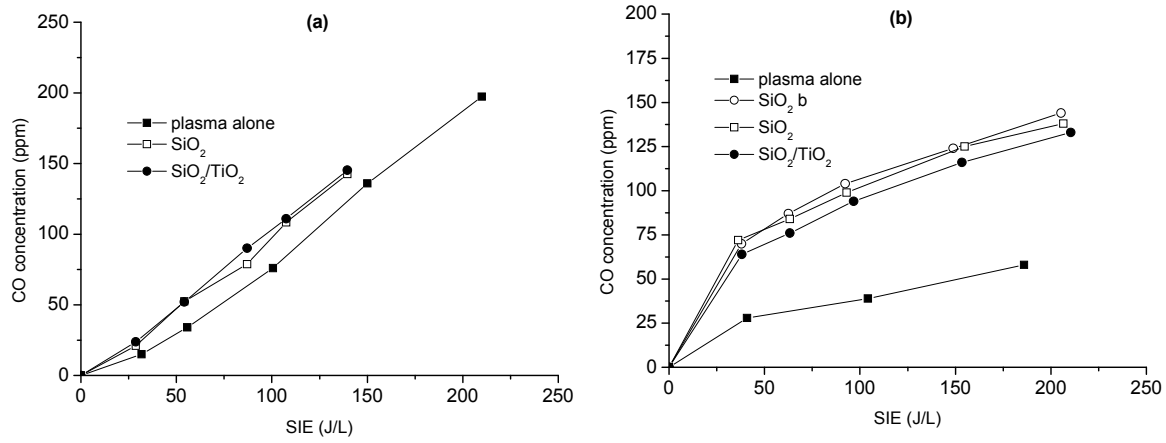


Fig. 4. Evolution of CO concentration with SIE, influence of packing material: (a) WTC reactor, (b) DBD reactor.

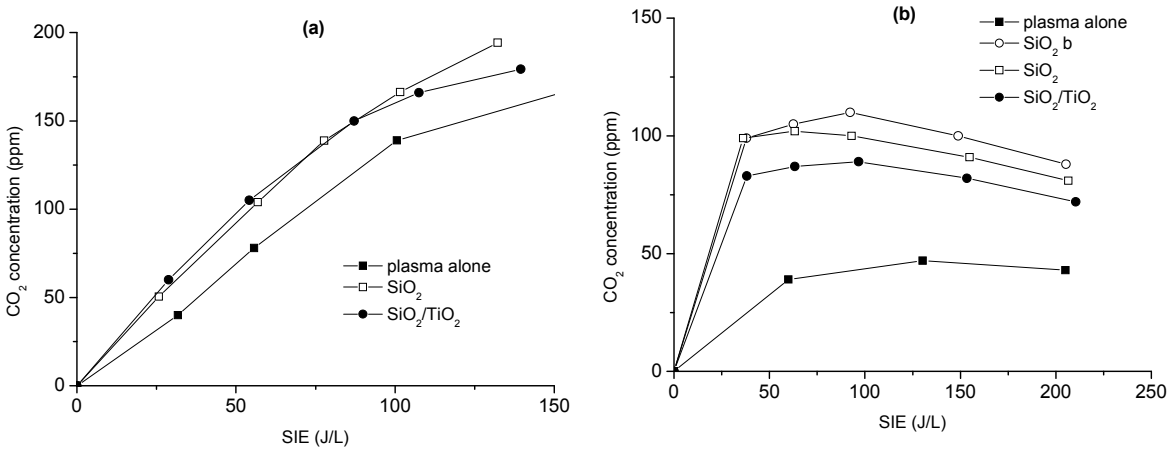


Fig. 5. Evolution of CO_2 concentration with SIE, influence of packing material: (a) WTC reactor, (b) DBD reactor.

3.2.2 Methanol

Methanol concentrations are presented in Fig. 6. We can observe a net decrease in its concentration when using a packed bed.

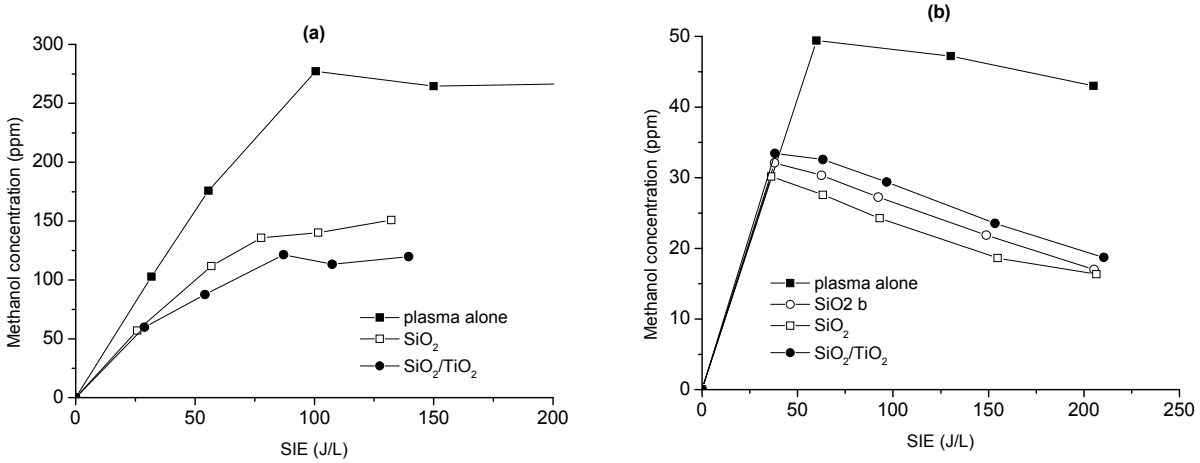


Fig. 6. Evolution of methanol concentration with SIE, influence of packing material: (a) WTC reactor, (b) DBD reactor.

This decrease is certainly due to a surface effect. In fact, adsorption of methanol and/or other acetaldehyde oxidation intermediaries, followed by surface reaction, could lead to a lower methanol concentration at the exit of the reactor, and could also explain the higher CO and CO_2 concentrations when using a packed bed.

4. Conclusions

The purpose of this paper was to study the plasma and plasma/catalyst process at atmospheric pressure, for pollutant degradation. Two different discharge configurations, a WTC and a DBD , were used.
The results allow to draw some conclusions :

- the O_2 content effect is more visible when using the WTC than the DBD configuration;
- when using a DBD reactor, using a packed bed improved acetaldehyde degradation. This behaviour is not observed with the WTC configuration, neither when using a DBD discharge without a packing material. This result may be due to a transition from a volume discharge to a surface discharge in the DBD reactor when a packed bed is present;
- CO and CO_2 concentration at the exit of the plasma discharge zone increases when using a packing material. The same trends are observed with both configurations;
- methanol has been identified as one of the intermediate by-products in acetaldehyde oxidation. In both configurations, methanol concentration at the exit of the discharge zone decreases when a packing material is used;
- for the experimental conditions studied, TiO_2 deposited on silica particles had no particular effect on acetaldehyde degradation.

Introducing a non-porous packing material in the discharge is certainly behind the onset of surface effects, that in turn will modify the oxidation intermediates and by-products, that is to say, the kinetics of the degradation process.

Acknowledgement. This work was financially supported by "Agence Nationale de la Recherche" (JCJC BIOPAC) and Région Ile-de-France (C'Nano, NanoCAT project).

5. References

[1] Mizuno A 2007 *Plasma Phys. Control. Fusion* **49** A1.
[2] Magureanu M., Mandache N. B., Eloy P., Gaigneaux E. M., Parvulescu V. I. 2005 *Applied Catalysis B: Environmental* **61** 12.
[3] Van Durme J, Dewulf J, Leys C, Van Langenhove H. 2008 *Applied Catalysis B: Environmental* **78** 324.
[4] Aggadi N., Redolfi M., Duten X., Touchard S., Michau A., Hassouni K. 2009. *Plasma processes and Polymers*. **6** 347.
[5] Falkenstein Z., Coogan J. J. 1997. *J. Phys. D: Appl. Phys*. **30** 817.

EFFECT ON VOC DECOMPOSITION USING HONEYCOMB TYPE REACTOR

Yoshikazu Ito[1], Yoshiyasu Ehara[1], Toshiaki Yamamoto[1], Yasuhiro Oya[2], Masayuki Iwata[2]

[1]*Tokyo City University*
1-28-1, Tamazutsumi, Setagaya-ku, Tokyo, 158-8557, Japan

[2]*Yamatake Corporation*
1-12-2, Kawana, Fujisawa-cIty, Kanagawa, 251-8522, Japan

There is problem for health and the environment by chronic exposure of volatile organic compounds (VOCs). Non-thermal plasma technology offers a reformative approach to the problem of removing various VOCs. A toluene, which is one of the most commonly used VOCs, was used and the decomposition characteristics by discharge plasma were investigated. In this study, the toluene decomposition using honeycomb type discharge reactor has been experimentally investigated. Discharge plasma was occurred at the gap between zeolite honeycombs. Humidity of the feed gas was considered with discharge parameter on zeolite honeycomb. Discharge pulses were analyzed, the effects of humidity on the toluene decomposition were investigated.

1. Introduction

VOCs in exhaust gas from various industries generated from painting and printing processes is focused attention for serious environmental problems. Toluene, which is one of the most frequently used VOCs, the decomposition of toluene using a discharge plasma was investigated[(1)(2)]. However, it is ineffective and not economical to treat a low concentration and high flow rate VOCs by the conventional technologies, because of the high-pressure power loss. In this study, the toluene decomposition using honeycomb type discharge reactor. Honeycomb configuration, it is low-pressure power loss can be achieved. Discharge plasma was occurred at the gap between honeycombs and humidity promoted gas was considered with discharge parameter. Discharge pulses were analyzed, the effects of humidity on the toluene decomposition were investigated. Toluene removal increases with increasing the discharge pulses. This study was considered a effect of VOCs decomposition using honeycomb type reactor.

2. Experiment

2.1. Experimental system

The schematic diagram of the experimental system is shown in Fig.1. Put in a small bottle for water and toluene diffusion in the separable flask, and coordinated temperature by controlling a heating mantle with a temperature controller. The flow rate of gas through the reactor was held steady at 0.2 L/min using a mass flow controller. The toluene concentration measured it with FTIR（Parkin Elmer: LX20000B）.

The gas, which toluene concentration 400ppm, discharged with a Honeycomb type reactor and treated humidity 0%, 30%, 50%, 80%. The reactor is applied voltage DC 2kV to 12kV.

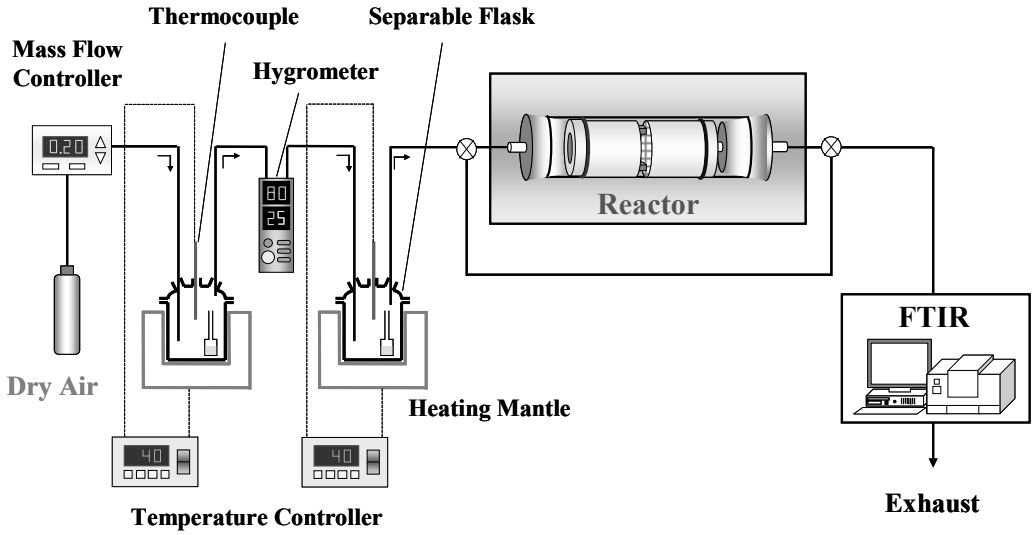


Fig. 1. VOC Decomposition System

2.2. Structure of Honeycomb Type Reactor

The structure of the Honeycomb type reactor detail is shown in Fig.2. Basic material of the honeycomb is zeolite, porous material has the adsorption characteristics. The thickness of the two honeycomb is 8 mm and become the constitution that picked up honeycomb with a mesh electrode (mesh interstice is 0.5 mm). Honeycomb gap space is 1 mm. Electric discharge current waveform is observed by digital oscilloscope and measured electric discharge quantity. The representative electric discharge current waveform show in Fig.3. We integrated value of current Ip [mA] and numbers of discharge N_A [Number/20msec] is assumed to be Discharge Pulse Dp [mA ・pulse].

.

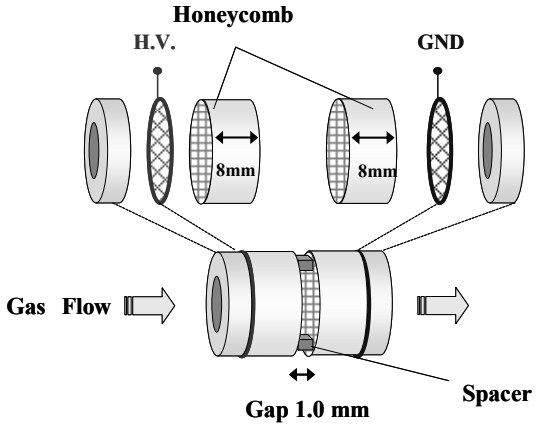


Fig. 2. Honeycomb Type Reactor

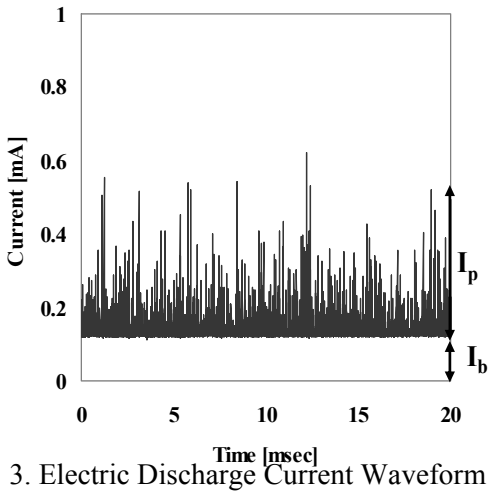


Fig. 3. Electric Discharge Current Waveform

3. RESULT AND DISCUSSION

The toluene decomposition as a function of applied voltage is shown in Fig.4. Toluene decomposition increased with increasing applied voltage and humidity. For this reason, humidity changes the electric property of a honeycomb discharge. Because zeolite, which honeycomb base material, have water absorptivity. When there is water in gaps by low voltage, it is thought that an electric discharge becomes unstable, and the toluene decomposition became low as a cause. In the case of an applied high voltage, the electric discharge is stability occurs regardless of quantity of water.

The discharge pulse as a function of applied voltage is shown in Fig.5. Discharge pulse increased with increasing applied voltage and humidity.

The toluene decomposition as a function of discharge pulse is shown in Fig.6. The toluene decomposition increase with increasing discharge pulse, however a difference appears to the toluene decomposition by quantity of water included in gas when an electric discharge pulse is low.

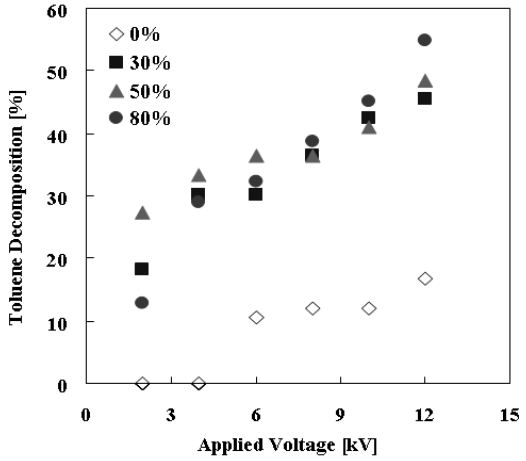


Fig.4. Toluene Decomposition as a function of applied voltage

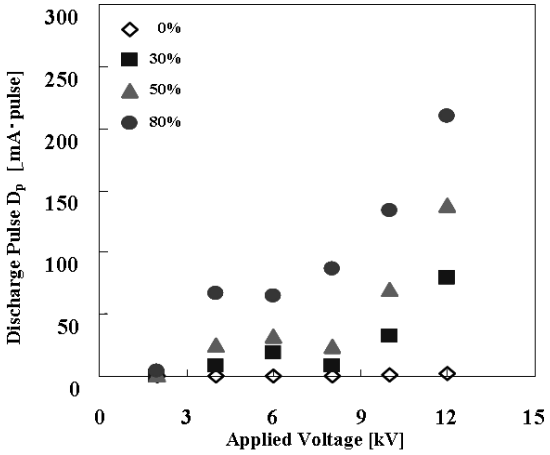


Fig. 5. Discharge pulse as a function of applied voltage

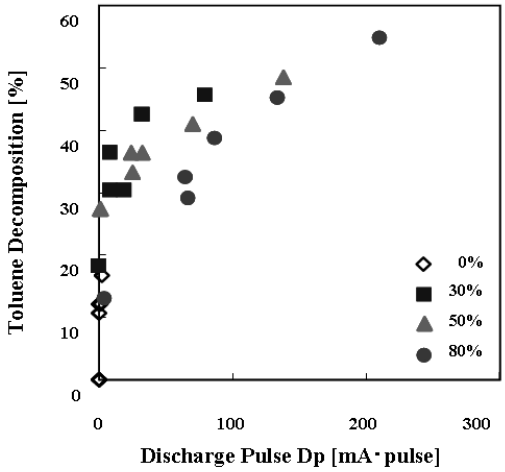


Fig. 6. Toluene Decomposition as a function of discharge pulse

4. CONCLUSIONS

In this study, we generated electric discharge plasma with zeolite honeycomb and considered the electric discharge characteristic and a relationship of the toluene decomposition. The result as follows.
(1) Toluene decomposition increased with increasing applied voltage and humidity.
(2) Humidity changes the electric property of a honeycomb discharge

5. REFERENCES

[1] K. Urashima, J. S. Chang, : “Removal of Volatile Organic Compounds From Air Streams And Industrial Flue Gases By Non-Thermal Plasma Technology”,IEEE Trans. DEI, vol.7,No5pp.602-614 (2000)
[2] Koji Inoue ,Keimei Furuki ,Hiroshi Okano ,Yukihiko Yamagata ,Katsunori Muraoka : “A New Decomposition System for Volatile Organic Compounds Using Combinations of Dielectric Barrier Discharges with Zeolite Honeycomb Sheets”, T.IEEJapan, Vol. 127－B, No.6 pp. 309-316 (2007)

INVESTIGATION OF ELECTRICAL AND SPECTRAL CHARACTERISTICS OF WATER FALLING FILM DBD IN DIFFERENT GASES

Vesna Kovačević, Bratislav M. Obradović, Milorad M. Kuraica and Jagoš Purić

University of Belgrade, Faculty of Physics
Studentski trg 12, 11000 Belgrade, Serbia
E-mail: vesna@ff.bg.ac.rs

Along with widespread use in industrial processing, non-thermal plasma sources proved to be effective for the treatment of polluted water. In order to achieve the best results in water treatment, we designed and constructed the coaxial plasma reactor with water falling film. Efficiency of this reactor is based on the existence of many reactive species and UV radiation in plasma that is formed above the water. An experimental study of coaxial dielectric barrier discharge (DBD) operating in gas and in gas with water is presented. We have investigated electrical and spectroscopic characteristics of DBD in nitrogen, air, helium and argon at atmospheric pressure. The influence of applied frequency on discharge power and emission spectrum is studied in order to achieve the optimum working conditions of DBD reactor. Experimental results demonstrate that in the applied frequency range of 50 to 450 Hz the best operating conditions are reached at a frequency of 300Hz. Emission spectrum of DBD in nitrogen and nitrogen with water show that NO γ bands are not present in the discharge with water.

1. Introduction

One of the major environmental problems is water pollution. Purification and disinfection of polluted water is an open issue and challenge for scientific community and requires emerging technological solutions. Non-thermal plasmas in and in contact with liquids have received a lot of attention in view of their considerable environmental and medical applications. The simultaneous generation of intense UV radiation, shock waves and active radicals makes these discharges particularly suitable for decontamination, sterilization and purification purposes [1]. Toxic compounds like phenols, chlorophenols and azo dyes can be efficiently treated with non-thermal plasma technologies which are excellent alternative for some conventional methods used for water pollution control.

The coaxial dielectric-barrier-discharge (DBD) was originally designed as atmospheric non-thermal plasma reactor for treatment of various water solutions [2]. In this reactor water forms a falling film which is in direct contact with plasma. This reactor configuration was successfully applied for removing of phenols and arsenic from water [3-5]. The non-thermal plasma in water falling film DBD that is formed above the water besides ozone also generates UV radiation and chemically active species like radicals (e.g. OH), excited atoms (e.g. O) and molecules, electrons and ions, which play a very important role in depollution processes. Existence of so many reactive species in plasma and in water is the reason why electrical discharges that have plasma in direct contact with water solutions are very efficient in purification of polluted water. Although the main interest in investigation of this type of discharges is application, because they have good efficiency with relatively low-energy consumption, there is also a wide range of fundamental physical issues about the difference between the discharges in gas and gas with water. This paper presents our results in investigation of electrical and spectral characteristics of water falling film DBD in different gases.

2. Experimental setup

This experimental research was focused on characterization and basic physical properties of the designed reactor. An experimental study of characteristics of the dielectric barrier discharge was carried out with water falling film and without water. The reactor was originally designed and constructed in our laboratory. This configuration was designed in order to examine the interaction of gas discharge with different aqueous solutions. Nitrogen gas, ambient air, argon and helium gases were injected into the discharge volume with a flow rate of ~ 5 L/min. All measurements were done for a discharge reactor operating at an atmospheric pressure and room temperature.

A schematic diagram of experimental setup used in this study is illustrated in Fig. 1. The cylindrical reactor consists of two electrodes and a dielectric barrier. The dielectric is a quartz tube with the inner diameter of 26 mm, length of 500 mm and thickness 1,7 mm. The inner electrode is made of stainless steel with an external diameter of 20 mm and a length of 500 mm. An outer electrode made of stainless steel mesh (length 400 mm, optical transmission 45%) is wrapped around the quartz tube. Quartz tubes, inner and outer electrodes are placed concentrically. Barrier discharge is generated within ~ 3 mm gap between the inner metal electrode and the quartz tube. When the discharge source works as water falling film reactor, water flows up through a vertical hollow cylindrical electrode and flows down making a thin dielectric film over the electrode. Water flows from the reservoir through the discharge by means of peristaltic pump.
DBD is generated in flowing nitrogen, air, argon and helium in the gap between the dielectric and the water layer by applying voltage of up to 20 kV, and the frequency varied from 50 to 450 Hz. The inner electrode is grounded via capacitor of 470 nF and the outer electrode is connected to a high voltage power supply. The frequency and voltage in the primary of HV transformer were regulated by means of AC variable speed drive Emerson Commander SK (SKA 1200075). Electric parameters were measured and recorded using a digital oscilloscope Tektronix TDS 3032 (300MHz bandwidth, 2GSamples/s) and a high voltage probe Tektronix P6015A. Lissajous figures (Q-U graphs) were used for determination of electric power of the discharge.
Emission spectrum from the discharge transmitted through the stainless steel mesh was observed in the UV region. Integral spectrum (without the spatial and temporal resolution) is recorded with spectrometer Ocean Optics QE 65000 (wavelength range 200-400 nm).

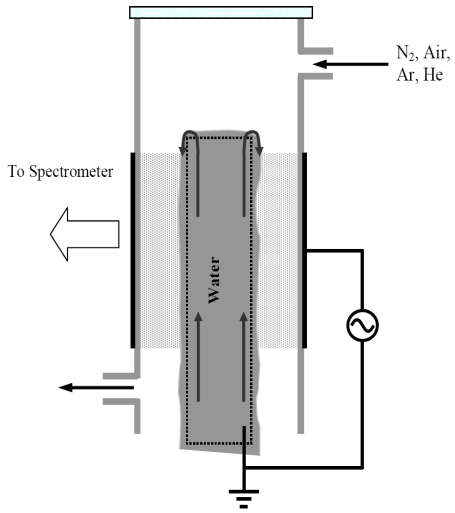


Fig. 1. Experimental setup.

3. Experimental results

Several experimental parameters such as power, frequency, working gas and presence of water in the discharge volume were tested and analyzed. The effect of applied frequency on discharge parameters is investigated. Fig. 2. shows discharge power for different frequencies (50-450 Hz) for air, nitrogen, argon and helium gases and for gases with water. In the range from 50 to 300 Hz the discharge power increases with increase of frequency, then decreases. Dependence of discharge power on frequency is the same for gas and gas with water. Area of Lissajous figure (Q-U graph) represents energy of the electrical discharge. Power is calculated by multiplying area of Lissajous figure with applied frequency. It was noticed during the experiment that optimal operating conditions of DBD reactor are at a frequency of 300 Hz, therefore, the examination of discharge for different applied voltages was carried out at this frequency. Intensity of the light emitted from the discharge is maximal at 300 Hz.

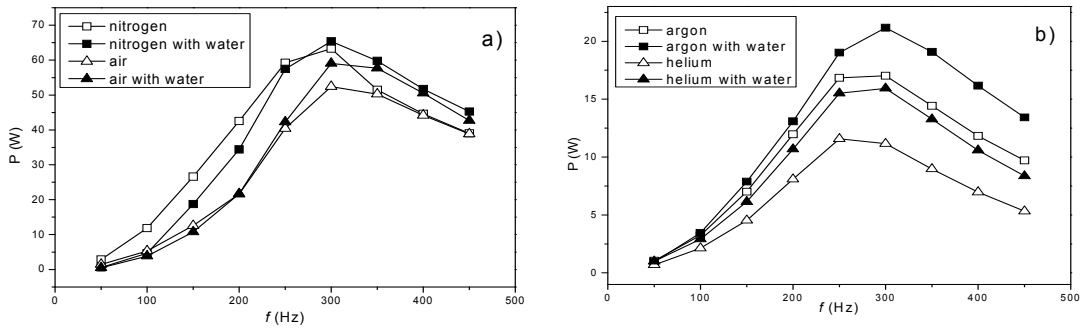


Fig. 2. The effect of applied frequency on discharge power a) in nitrogen and nitrogen with water, and in air and air with water; b) in argon and argon with water, and in helium and helium with water

Lissajous figures obtained for different applied voltages, at 300Hz, in discharge in nitrogen and nitrogen with water are shown in Fig. 3. Lissajous figures in discharge in nitrogen with water are wider compared to those obtained in discharge in pure nitrogen, which means that breakdown voltage increases in discharge with water. This can be explained by decreasing of nitrogen metastable density and will be subject of further investigations. Increasing of supply voltages has no influence on the breakdown voltage in the discharge with nitrogen. In the discharge with water, the increase of supply voltage decreases the breakdown voltage.

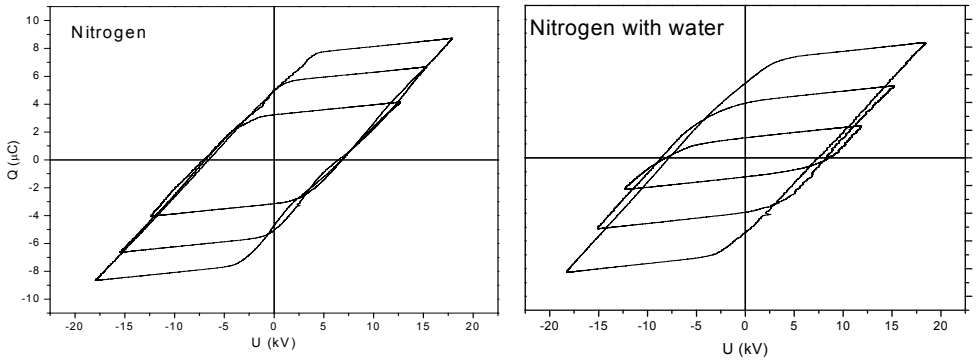


Fig. 3. Lissajous figures obtained for different applied voltages for coaxial DBD in nitrogen and in nitrogen with water

Fig. 4. shows Lissajous figures obtained for different applied voltages at 300 Hz in air without water and with water. In the discharge in air, with and without water, Lissajous figures for lower power supply voltage have the shape of the parallelogram. However, with increasing applied voltage the shape becomes rather asymmetric, which is probably due to asymmetry of the discharge source. Similar to the discharges in nitrogen, breakdown voltage is higher in the discharge with water. In comparison with the discharges in nitrogen, discharges in air have larger breakdown voltages.

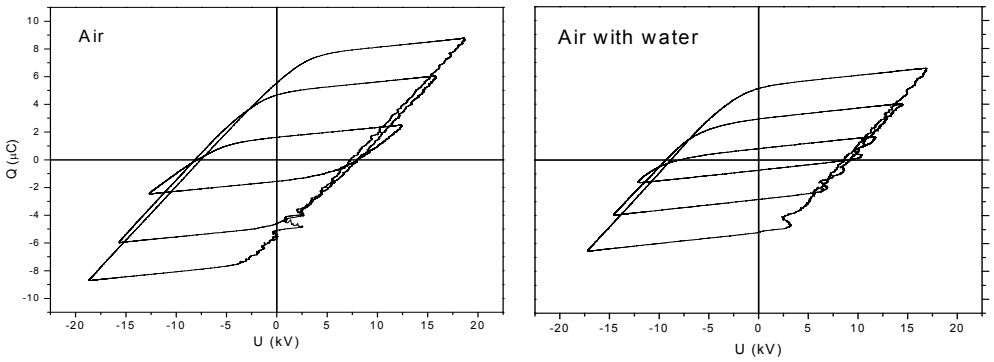


Fig. 4. Lissajous figures obtained for different applied voltages for coaxial DBD in air and in air with water

Figures 5 and 6 show Lissajous figures in argon and helium, respectively, for different energies of discharge. Lissajous figures in Fig. 5 show that breakdown voltage is increased in discharge in argon with water compared to the discharge in pure argon. Change in figure shape is even more pronounced in the case of discharge in helium. In optimal working conditions of coaxial DBD in argon, i.e. for applied frequency of 300 Hz, discharge power in argon and argon with water was 17 W and 21 W, respectively. For the same optimal working conditions as in argon, discharge power of the DBD in helium and in helium with water was 11 W and 16 W, respectively.

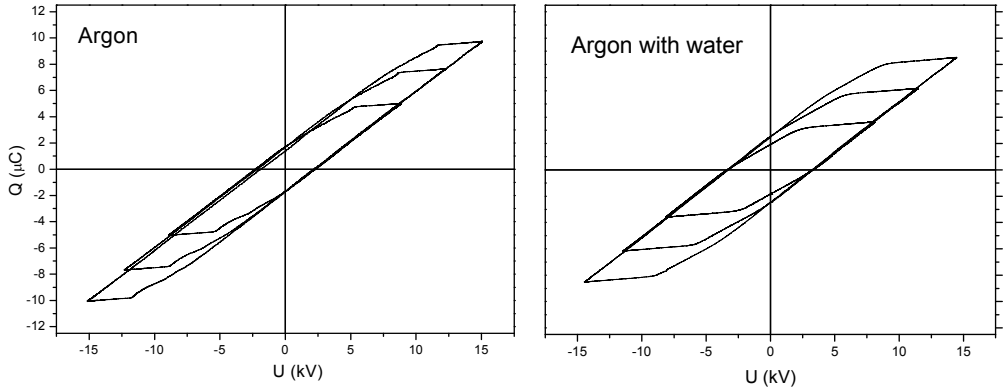


Fig. 5. Lissajous figures obtained for different applied voltages for coaxial DBD in argon and in argon with water

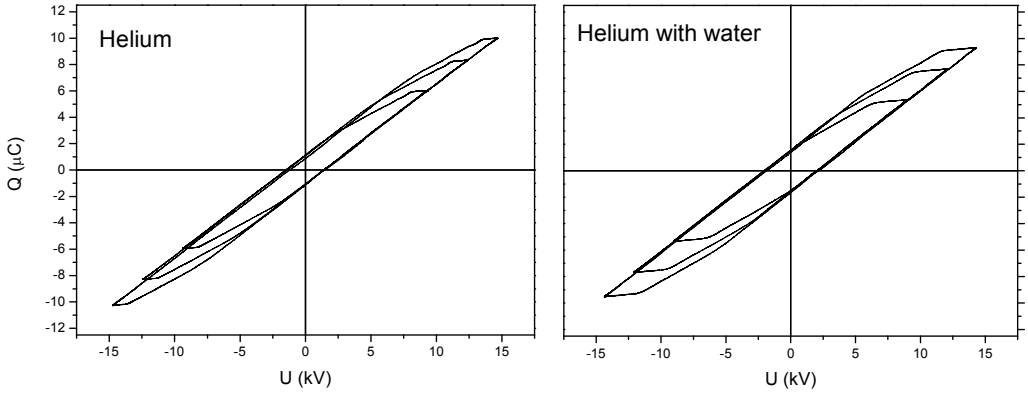


Fig. 6. Lissajous figures obtained for different applied voltages for coaxial DBD in helium and in helium with water

Fig. 7a) and b) represents emission spectra from DBD in nitrogen and nitrogen with water, air and air with water, respectively. Based on the spectra for all gases it can be concluded that the total intensity of all the bands in the range is lower from the discharge with water than from the discharge without water. Emission spectra of nitrogen and air in the UV region consist mostly of the bands of molecular nitrogen (N_2 2nd positive system) and some oxygen bands (Schumann-Runge system). Additionally, in discharge in nitrogen bands of NO γ system were detected. In the discharge with water intensity of NO bands is significantly reduced in comparison with discharge without water. This could be explained by decrease of concentration of NO molecules caused by oxidation of NO to HNO_2 in humid atmosphere in DBD with water film. In such discharge, the H_2O molecule is dissociated and very reactive radicals O and OH are created which react with NO molecule in the following reactions [6]:

$$NO + O + M^* \rightarrow NO_2 + M^* \qquad (1)$$

$$NO + OH + M^* \rightarrow HNO_2 + M^* \qquad (2)$$

Emission spectra from DBD in the observed wavelength range in argon and argon with water is shown in Fig. 8 a) and consists of nitrogen bands (N_2 2nd positive system), oxygen bands and the most intensive are overlapping lines of argon. Argon lines can not be seen as separated because of the characteristics of the spectrometer. Fig. 8b) represents emission spectra of helium and helium with

water, and like argon it mostly consists of nitrogen bands (N_2 2nd positive system) and oxygen bands. Intensity of acquired helium spectra was very low, therefore possible existence of helium lines could not be determined with certainty. The recorded spectra reveal interesting facts and shall be subject of further research.

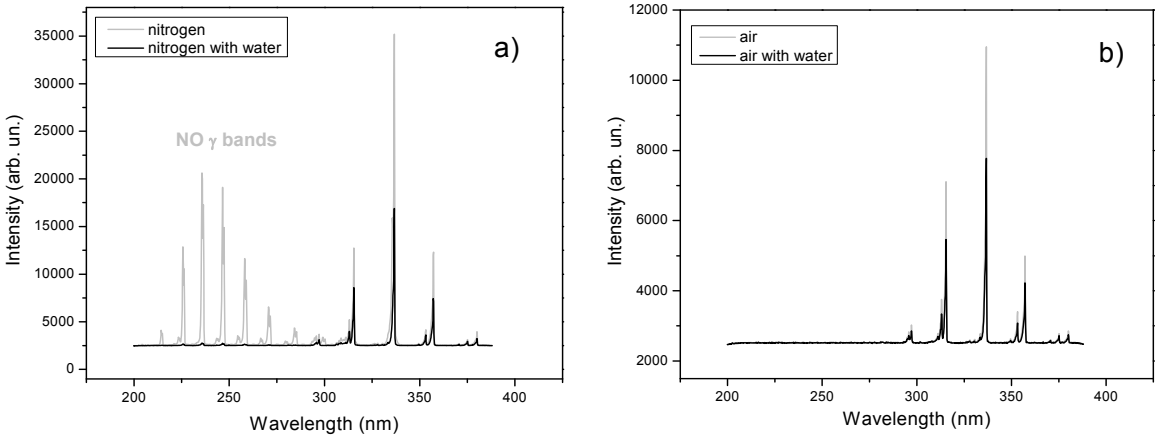


Fig. 7. Emission spectra from coaxial DBD a) in nitrogen and in nitrogen with water; b) in air and in air with water

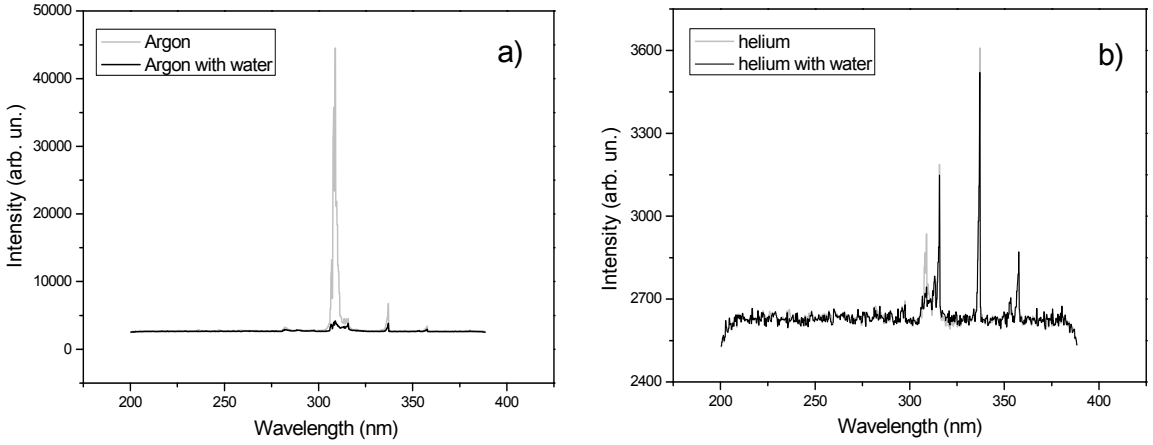


Fig. 8. Emission spectra from coaxial DBD a) in argon and in argon with water; b) in helium and in helium with water

Acknowledgements. This research was supported by the Ministry of Science and Technological Development of the Republic of Serbia through the project No. 141043.

4. References

[1] Bruggeman P and Leys C 2009 *J. Phys. D: Appl. Phys*. **42** 28.
[2] Kuraica M M, Obradović B M, Manojlović D, Ostojić D R and Purić J 2004 *Vacuum* **73** 705.
[3] Manojlović D, Ostojić D R, Obradović B M, Kuraica M M, Krsmanović V D and Purić J 2002 *Desalination* **213** 116.
[4] Dojčinović B P, Manojlović D, Roglić G M, Obradović B M, Kuraica M M and Purić J 2008 *Vacuum* **83** 234.
[5] Manojlović D, Popara A, Dojčinović B P, Nikolić A, Obradović B M, Kuraica M M and Purić J 2009 *Vacuum* **83** 142.
[6] Orlandini I and Riedel U 2000 *J. Phys. D: Appl. Phys*. **33** 2467.

NON-OXIDATIVE METHANE COUPLING IN HYBRID PLASMA-CATALYTIC SYSTEM

Agnieszka Górska, Krzysztof Krawczyk, Krzysztof Schmidt-Szałowski

Faculty of Chemistry, Warsaw University of Technology, Noakowskiego 3, 00-664 Warszawa, Poland

E-mail: agnieszkagorska@wp.pl

Non-oxidative methane coupling into higher hydrocarbons was investigated in dielectric barrier discharge conditions using a stationary catalytic bed (Cu/ZnO/Al2O3). The experiments were carried out at the frequency of about 6 kHz, at 240 oC, at the pressure of 1.2 bar and with the overall gas flow rate 2 Nl/h, the mixture of 50% CH4 + 12.5% H2 + Ar. The effects of packing on the obtained products and stability of the catalyst in time were studied. Hydrocarbons from 2 to 5 atoms of carbon were identified in the outlet gas. It was found that in the presence of catalyst in plasma zone, overall methane conversion decreased, however the conversion towards ethane was higher, as compared to the process without packing.

1. Introduction

Methane is a cheap and promising substrate for the production of some industrially important compounds, such as syngas [1], light hydrocarbons [2,3], aromatic hydrocarbons [4], methanol [5], or formaldehyde [6]. High stability of methane molecule (C-H bond energy ~ 432 kJ/mol), resulting from its symmetry, is a main obstacle for chemical methane conversion. Most of the existing methods of methane conversion are based on thermal or thermocatalytic [7] C-H bond cleavage. It seems that the recent popularity of electroplasmatic methods can have significant effect on the methods of methane conversion.

In our group, DBD reactor has been used for methane conversion with CO_2 (under 1.2 bar pressure) employing a catalyst placed directly in the discharge zone [8]. Two catalysts: Ag/Al_2O_3 and Pd/Al_2O_3, as well as Al_2O_3 support were tested in the 120-290 ^oC temperature range. Hydrogen, ethane, ethene + ethyne, propane, propylene, n-butane, butane, as well as methanol and ethanol were observed as products of this process. The use of Pd/Al_2O_3 catalyst resulted in significant change of products distribution (the increase of C_2 concentration), with simultaneous decrease of methane conversion, as compared to experiments carried out without the catalytic bed.

For direct methane coupling (without oxidants) in barrier discharge, when various materials were applied into the discharge zone, it was observed that at ambient temperature the catalytic bed had some influence on the total methane conversion degree in the CH_4 + Ar mixture of methane concentration 7.5% or 10% [9]. Among tested fillings (quartz glass, barium titanite, silica gel, Fe/SiO_2), only quartz glass and silica gel resulted in the increase of methane conversion in comparison with an empty reactor. $BaTiO_3$ and Fe/SiO_2 induced the decrease in methane conversion. The most promising results, including reaction rate higher by ca. 50% than for an empty reactor, were reported for quartz glass.

Gliding discharge has been also used in our group for methane coupling [10]. In gliding discharge reactor, particles of a catalyst are in constant motion, raised by reagents stream, thus forming so-called fountain bed in the discharge zone. Methane coupling (mixture of 0.4 CH_4 and 0.6 H_2) at medium temperature in GD reactor without a catalyst resulted in acetylene as a mainly product and soot, while the introduction of fountain catalyst bed allowed to change product composition. The presence of Pd/Al_2O_3 and Pt/Al_2O_3 catalysts allowed reducing soot formation with the increase of ethylene and ethane amount and decrease of acetylene selectivity.

High energy demand of the plasma processes was a mayor problem for their wide industrial application, but combined plasma-catalytic systems have an advantage of relatively low operational temperature and a possibility of employing atmospheric (or slightly higher) pressure, as compared to thermal and thermocatalytic methods.

In our earlier work, methane conversion towards higher hydrocarbons in oxidative conditions (i.e. in mixture containing carbon dioxide) was described [11]. Here, we focus on the improvement of the selectivity of methane conversion under non-oxidative coupling conditions in hybrid plasma-catalytic system.

2. Experimental

The scheme of the quartz DBD reactor used in this work is shown in [8]. The discharge zone was formed as a gap of 3 mm width, which gives the gas volume of ~34 cm^3 without packing and ~16 cm^3 with packing. The experiments were carried out under 1.2 atmospheric pressure. Methane (99.5%), hydrogen (purified for flame ionization detector use) and argon (99.999%) were introduced into the reactor by mass flow controllers with the total flow rate of 2 Nl/h. The feed and products were analyzed by gas chromatograph GC (Agilent 6890N) on two kinds of column packing: Carboxen 1000 (Mesh 60/80, 1.5 m x 2 mm) with TCD for analysis of the simple hydrocarbons and Hayesep Q (Mesh 60/100, 3 m x 2 mm) with TCD + FID.

The reactor was supplied by the current at a frequency of about 6 kHz. The reactor was heated by the outer electrical heater and the temperature was measured by the thermocouple place at the outside reactor wall.

The single portion of a catalyst (volume 45 mL) containing Cu (described as $Cu/ZnO/Al_2O_3$) was selected for direct non-oxidative conversion of methane. For comparison, the quartz glass particles of the same size were also used. The catalyst was obtained from commercial catalyst $CuO/ZnO/Al_2O_3$. First, catalyst was frittered to the particles of 1 – 2 mm. Before processing, to reduce copper oxide, the catalyst was dried (1 ^oC /min to 240 ^oC in Ar) then reduced (24 h 3.5 L/h H_2, then 120 h 4-5 L/h) inside the reactor. Crystal structures were identified by powder X-ray diffraction spectroscopy of Seifert GmbH type Bragg-Brentano HZG- 4 (CuK_α, λ = 1.54 Å).

The catalyst composition changed before reduction and after plasmatic processes. Under conditions of the reduction process, only the copper oxide was reduced into metallic copper. The specific surface of the catalyst (portion No. III), measured by the BET adsorption isotherm method, is the same before reduction (32 m^2/g) and after process (31 m^2/g). This fact means that the reduction process does not change the structure of the catalyst.

3. Result

Three kinds of measurements were performed: without packing (plasma process), with catalyst (plasma-catalyst process) and with quartz glass particles of the same size for comparison. The gas pressure was 1.2 atm, and the gas mixture was composed of methane, hydrogen and argon. In the present study, the maximal catalyst working temperature (240 ^oC) has been used. The concentrations of substrates and products (hydrogen, methane, ethane, ethene and ethyne) were determined using Carboxen 1000 column. For chosen experiments, reaction products (other hydrocarbons) were analyzed using on Haysep Q column. Measured products concentrations are shown in Table 1. Besides gaseous products, the formation of a thin layer of solid reaction products, such as soot and polymers, was observed on reactor walls and the electrodes.

Stability of the catalyst

Figure 1 shows the catalyst performance in time. Substantial changes in the catalyst activity were observed during plasma-catalytic process. Fresh catalyst was placed into the reactor discharge zone, where it underwent drying and reduction. Next, a selected gas mixture was passed through the reactor. It is noteworthy that the stream of gas mixture was continuous, except when some additional procedures (as shown by the letter symbols on the diagram) were performed, such as reduction, change of gas mixture composition or turning off reactor heater.

Overall methane conversion diminished in time, though it had a tendency to stabilize. The selectivity towards C_2 hydrocarbons was almost constant, however the amount of produced ethane, which was the only product at the beginning of the process, decreased in time. At the same time, ethene appeared among the products. An additional reduction of the catalyst bed using hydrogen did not led to the recovery of the overall methane conversion. Methane conversion into ethane was not restored neither.

Similar results, in terms of overall methane conversion, C_2 hydrocarbons selectivity and conversion towards ethane, were obtained for two other portions of the catalyst, which were tested for somewhat shorter time.

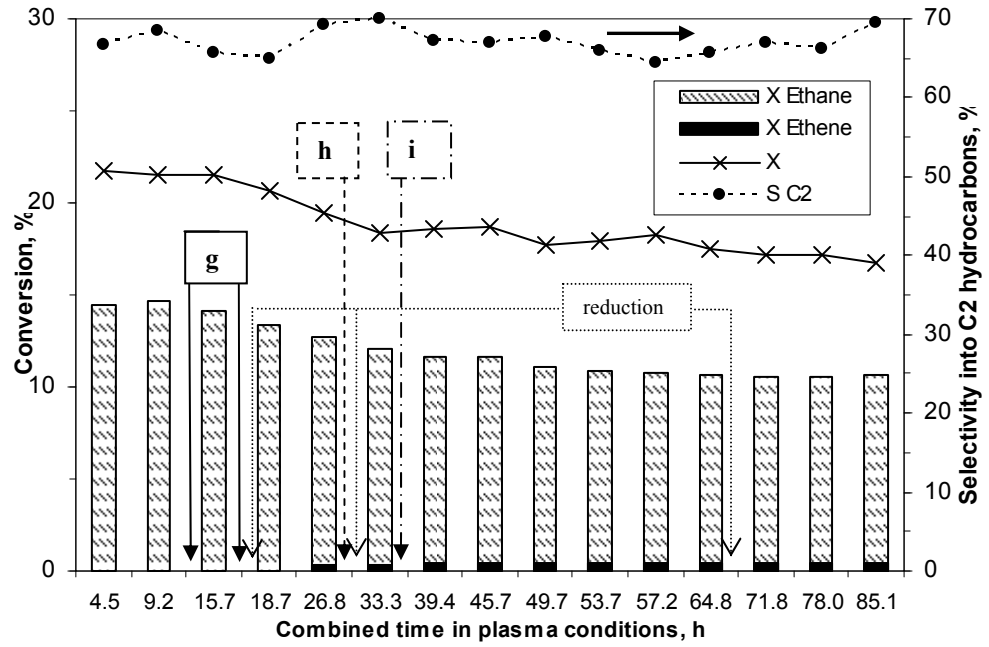


Fig. 1. The behavior of the catalyst (No. III) in time. Temperature 240 ^{o}C, 50% CH_4 + 12.5% H_2 + Ar. The overall methane conversion (X), and selectivity (S C_2) in plasma-catalytic process; g) total flow rate = 1 Nl/h, h) without heating, i) only argon.

The effects of reactor packing

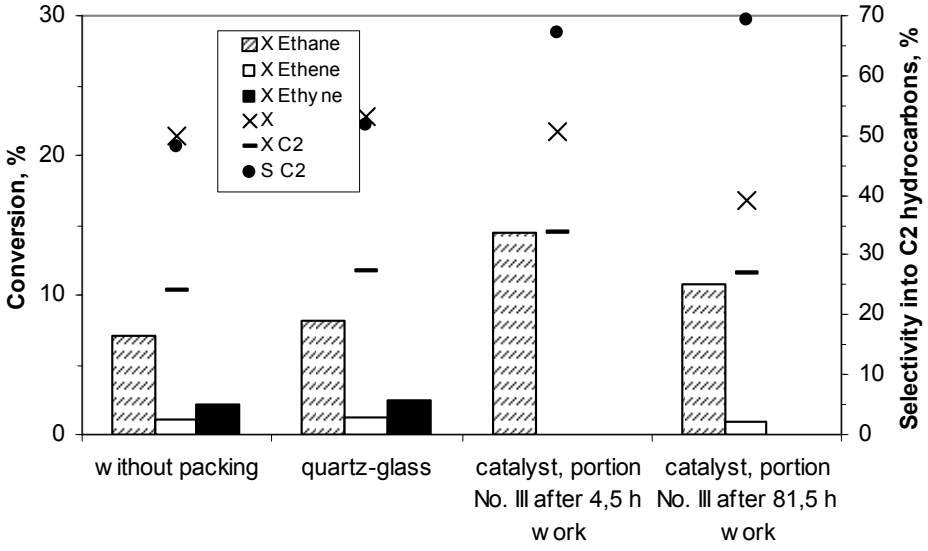


Fig. 2. The effect of reactor packing on the overall methane conversion (X), conversion and selectivity (S C_2) into hydrocarbons. Amount of each C_2 hydrocarbons. Temperature 240 ^{o}C, 50% CH_4 + 12.5% H_2 + Ar. Data from Carboxen 1000 column.

The influence of the presence of the quartz glass or $Cu/ZnO/Al_2O_3$ catalyst on the methane conversion during dielectric barrier discharge has been investigated. With neutral quartz glass packing, the overall products quantity is slightly higher, as compared to the results obtained for an empty reactor. In both cases, all C_2 hydrocarbons (ethane, ethene and ethyne) have been produced (Figure 2). The picture is quite different when catalyst bed is present in the reactor. No acetylene was produced in this configuration.

It should be pointed out that thermo-catalytic methane conversion has also been tested. For that purpose, the mixture of gaseous reagents (50% CH_4 + 12.5% H_2 + Ar) was forced through reactor containing catalyst at 240 ^oC. No products were observed in the outlet gas.
The use of high-sensitivity column (Hayesep Q column) allowed for more precise product analysis. This reveled higher diversity of products, however methane conversion remained unchanged.

Tab. 1. The overall methane conversion and conversion into hydrocarbons in mixture 50% CH_4 + 12.5% H_2 + Ar and temperature 240 ^oC.

	without packing	with quartz	with catalyst (portion No. IV)
Overall conversion of CH_4 (%)			
	22.0	24.5	24.3
Conversion into: (%)			
ethyne	0.38	0.47	0
ethene	0.34	0.17	0.13
ethane	7.14	7.85	13.53
propene	0.22	0.26	0.10
propane	3.32	3.67	2.77
cyclopropane	0.06	0.06	0.06
1-buten /izobutane	0.87	1.02	0.42
1,3-butadien /izobutene	0.10	0.22	0.09
butane	1.04	1.18	0.82
unidentified	0.55	0.49	0.15
unidentified	0.94	1.04	0.37
pentane	0.32	0.39	0.21
unidentified	0.39	0.59	0.15

4. Summary

DBD has been used for examination of non-oxidative methane coupling towards higher hydrocarbons. The use of $Cu/ZnO/Al_2O_3$ catalyst in non-oxidative DBD methane conversion resulted in an increase of ethane selectivity, as compared to plasma process. It should be mentioned that any solid particles in the discharge zone can influence hydrodynamic parameters in the reactor, mainly reaction time. To elucidate this influence, neutral particles of dimensions identical to the catalyst have been used. It has been proved that increased ethane selectivity is caused by the used catalyst.

5. References

[1] Gallon H J and Whitehead J C 2008 *HAKONE XI.*
[2] Kado S, Sekine Y, Nozaki T, Okazaki K 2004 *Catalysis Today*, **89** 47-55.
[3] Rane V H, Chaudnari S T, Chaudhery V R 2010 *J. of Natural Gas Chemistry* **19/1** 25-30.
[4] Vosmerikov A V, Zaikovskii V I, Korobitsyna L L, Echevskii G V, Kozlov V V, Barbashin V E and Zhurevkov S P 2009 *Kinetics and Catalysis* **50/5** 725-733.
[5] Indarto A, Yang D R, Palgunadi J, Choi J W, Lee H and Song H K 2008 *Chemical Engineering and Processing* **47** 780-786.
[6] Lou Y, Tang Q, Wang H, Chio B, Wang Y andYang Y 2008 *Applied Catalysis A: General* **350** 118-125.
[7] de Souza A, Maciel L J L, de Lima Filho N M and de Abreu C A M 2010 *Catalysis Today* **149** 413-417.
[8] Sentek J, Krawczyk K, Młotek M, Kalczewska M, Kroker T, Kolb T, Schenk A, Gericke K H and Schmidt-Szałowski K 2010 *Applied Catalysis B: Environmental* **94** 19-26.
[9] Sentek J, Krawczyk K, Radomyska K and Schmidt-Szałowski K 2004 *Przemysł Chemiczny* **83/7** 40-344.

[10] Młotek M, Sentek J, Krawczyk K and Schmidt-Szałowski K 2009 *Applied Catalysis A: General,* **366** 232-241.
[11] Schmidt-Szałowski K, Jodzis S, Krawczyk K, Młotek M and Górska A 2006 *Current Topics in Catalysis* **5** 39-68.

STUDY OF DIESEL EXHAUST PARTICLE COLLECTION USING ELECTROSTATIC PRECIPITATOR

Masaki Kuboshima[1], Yoshio Kawamoto[1], Yoshiyasu Ehara[1], Toshiaki Yamamoto[1], Akinori Zukeran[2], Hitomi Kawakami[2]

[1] Tokyo City University
1-28-1, Tamazutsumi, Setagaya-ku, Tokyo, 158-8557, Japan
[2] Fuji Electric Systems Co., Ltd.
1-11-2, Osaki, Shinagawa-ku, Tokyo, 141-0032, Japan

An environmental problem is concerned about on a global scale, and air pollution by DEP (diesel disposal fine particles) or the NOx becomes the serious problem now. There are the movement exhaust sources such as a car or the ship as the exhaust source of the main toxic substance. Severe regulation approaches in the post-newly long-term regulation (2009) of the diesel car. In addition, "an MARPOL treaty" was adopted in 1997, and effluent control of the air pollution material from a ship has been begun a full-scale. Effluent gas disposal of various diesel engines is an urgent problem. In this study, I am aimed at removing the discharge particle from a diesel engine with an electrostatic precipitator (ESP) directly.

1. Introduction

DEP(diesel exhaust particle) and the problem of the air pollution by PM(particulate matter) grow big as an environmental problem now. There is a diesel engine used for a car, a ship or a construction machine to one of these main exhaust source. In particular, the density of the effluent gas as for marine application which regards heavy oil with sulfur as fuel is very high with a problem in comparison with the car use. Now an expensive effluent gas treatment of the performance is requested. Therefore, in this study, we paid our attention to electrostatic precipitator (ESP) as a diesel engine direct connection-shaped exhaust gas treatment. When the exhaust gas such as diesel engines is cleaned in ESP, the re-entrainment phenomenon that the captured particle is scattered again becomes the problem [1]. Restraint technology of the re-entrainment to apply AC voltage on the collecting section is put to practical use in ESP for the low particle density and normal temperature in the express highway tunnel [2][3]. Therefore we report it examined the frequency characteristic of the square wave voltage to apply prevention of the re-entrainment on the collecting section under conditions of high temperature effluent gas and high particle density.

2. Experiment

The experiment system was shown in Figure 1. Two stage type ESP was used for this experiment. As for the diesel engine, engine displacement is 0.199 L, and fuel is light oil. The exhaust gas is cleaned in ESP, and it is diluted to 1/100 by dilution device. The particle density was measured with Scaning mobility particle sizer (SMPS) and particle counter (Rion KC01-E). Collection efficiency calculated it from a difference of the particle density of before and after being cleaned in ESP. The experiment condition is engine load 1.0 kW, wind velocity 1.3 m/s, exhaust gas temperature about 180 degrees Celsius, particle density about 15 mg/m^3. Precharge section consists of high voltage electrode of sawtooth form and ground plate electrode. Collecting section is parallel plate type. The applied voltage to Precharge section is DC -7.5kV uniformity. The applied voltage to collecting section is DC -8 kV and 16 kV_{p-p} square wave. The frequency of the square wave changed it with 1-100 Hz. As an example, a voltage wave pattern of 1Hz was shown in Figure 2.

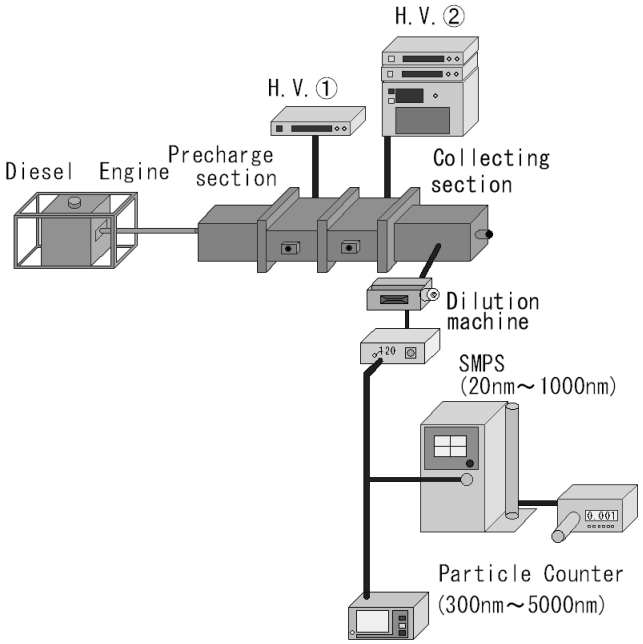


Fig. 1. Experiment system

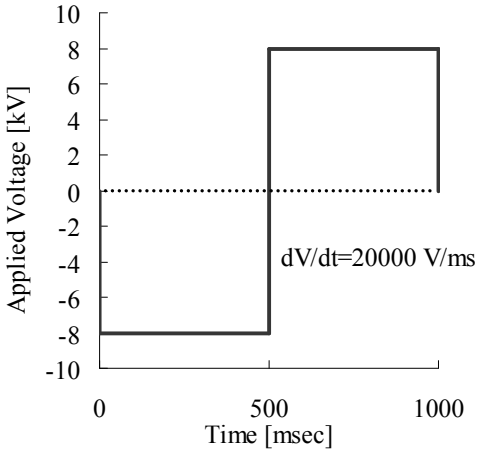


Fig. 2. Square wave (1 Hz)

3. Results and discussion

Particle-size dependent number density is shown in Figure 3. Collection efficiency in the range of 10-1000nm is more than 90% because about double figures particle density decrease as compared with an inlet in any frequency. However, the particle densities rises in more than 1,000nm increase more than the inlet. This reason is because the number of large-size particles increased by a re-entrainment phenomenon.

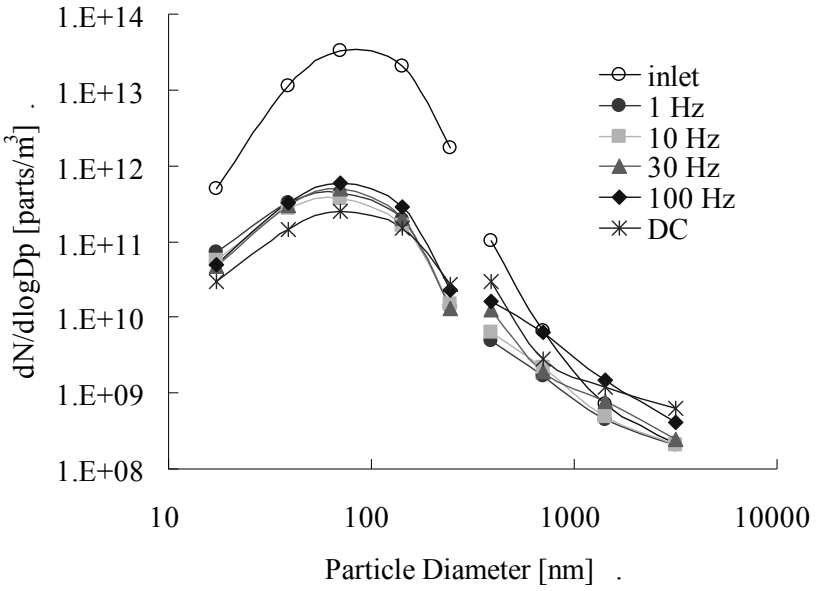


Fig. 3. Particle-size dependent number density

Particle-size dependent collection efficiency is shown in Figure 4. The re-entrainment is alleviated to some degree because collection efficiency is higher square wave (1-30Hz) than the DC. For this

reason, it is considered that collected particles in the shape of pearl chain by applying square wave on the collecting section are changed spherically. In addition, collection efficiency decreases than the DC in the case of frequency 100Hz.

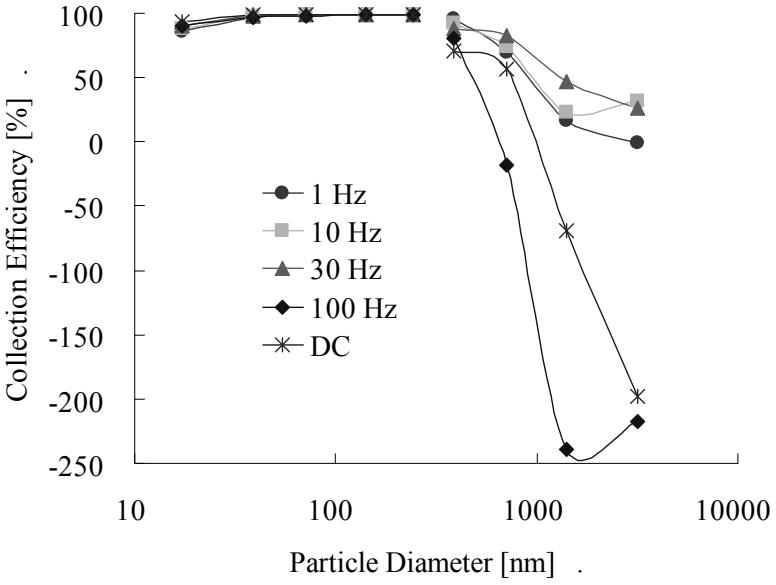


Fig. 4. Particle-size dependent collection efficiency

Frequency dependent collection efficiency is shown in Figure 5. In the comparatively large particle, collection efficiency more than 500nm increase with increasing of frequency untill 30Hz. For this reason, it is considered that it is easy to change particles at the shape of pearl chain spherically because there is much number of times polarity reversal. However, at the frequency more than 100Hz, collection efficiency is decrease. It is considered that a charged particle is trapped in the space between the electrode, and exhausted without collecting in high frequency.

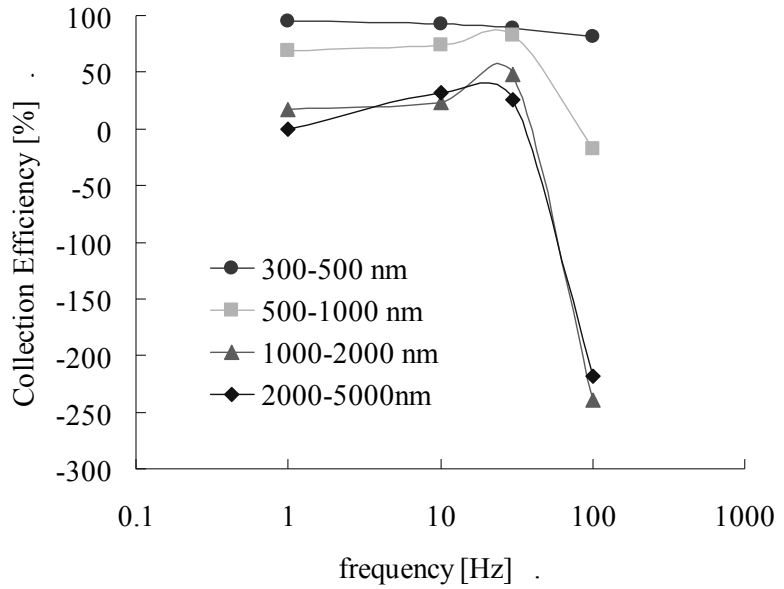


Fig. 5. Frequency dependent collection efficiency

Particle-size dependent weight density for 30Hz is shown in Figure 6. This calculated it by particle size and specific gravity. As for the weight of particles, the ratios of particles more than 500nm increase in comparison with the number of the particles. However, gross weight is 14.6mg/m^3 at ESP OFF and, 0.55mg/m^3 at EPS ON. Thus, collection efficiency by the gross weight is 96.2%.

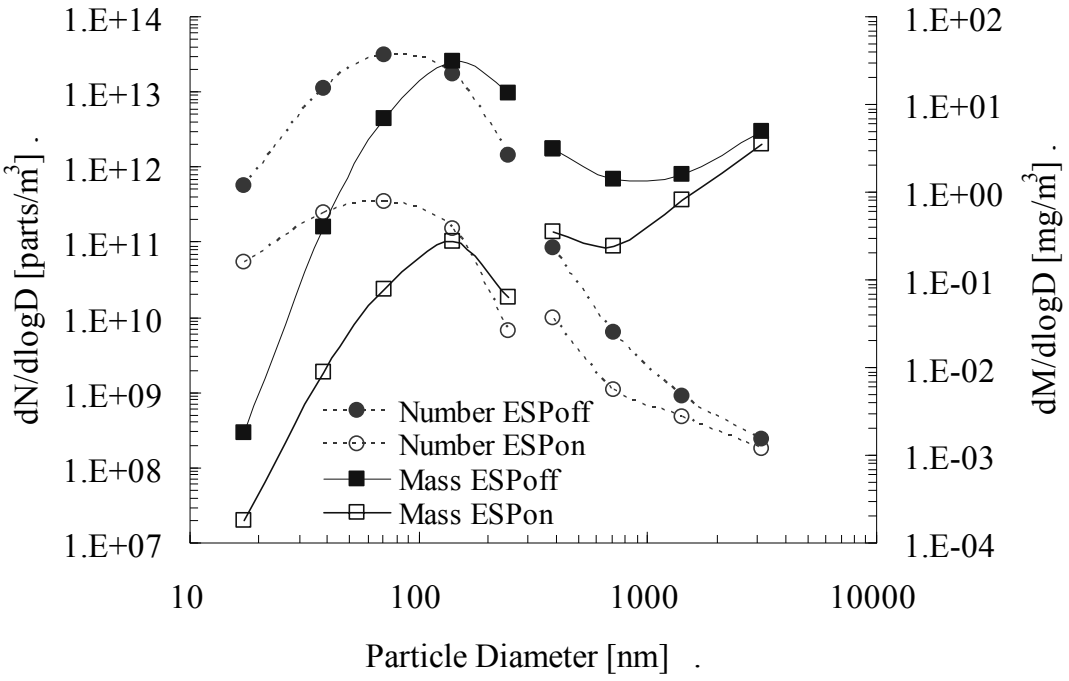


Fig. 6. Particle-size dependent weight density(apply 30Hz)

4. CONCLUSIONS

In this study, we examined the re-entrainment alleviation effect by the square wave for the direct collection.

(1) In the range of particle size 30-500nm, collection efficiency in DC and square wave are more than 90%.
(2) The square wave high voltage is effective in alleviate re-entrainment than the DC high voltage.
(3) Frequency of the square wave high voltage that can alleviate re-entrainment effectively is 30Hz.
(4) Weight collection efficiency is 96.2 %.

5. REFERENCES

[1] A. Zukeran, Y. Ikeda, Y. Ehara, M. Matsuyama, T. Ito, T. Takahashi, H. Kawakami, and T. Takamatsu :“Two-Stage Type Electrostatic Precipitator Re-entrainment Phenomena under Diesel Flue Gases”, IEEE Trans. Ind. Applic., Vol. 35, No. 2, pp. 346-351 (1999)

[2] K. Ysumoto, A. Zukeran, Y. Takagi, and Y. Ehara :“Suppression of particle re-entrainment from electrostatic precipitator with AC electric field and particle deposition onto downstream walls”, J. Soc. Powder Technology, Vol. 43, No. 3, pp. 198-204 (2006) (in Japanese)

[3] Y. Takagi, Y. Ehara. T. Takahashi, M. Yumoto, T. Ito, A. Zukeran, Y. Kawada, Y. Kono, and K. Yasumoto :“Effect of the Applied Voltage Waveform at the Collecting Section on Re-entrainment Phenomena in Two-stage Type Electrostatic Precipitator”, IEEJ Trans. FM, Vol. 125, No. 10, pp. 759-764 (2005-10) (in Japanese)

DECOLORIZATION OF FOUR AZO DYES USING WATER FALLING FILM DBD REACTOR

Biljana P. Dojčinović[1], Bratislav M. Obradović[2], Dragan Manojlović[3], Goran M. Roglić[3], Mirjana Kostić[4] and Milorad M. Kuraica[2]

[1]*Center of Chemistry, Institute of Chem., Technol. and Metallurgy, Belgrade 11000, Serbia*
[2]*University of Belgrade, Faculty of Physics, P.O. Box 368, 11000 Belgrade, Serbia*
[3]*University of Belgrade, Faculty of Chemistry, P.O. Box 158, 11000 Belgrade, Serbia*
[4]*University of Belgrade, Faculty of Technol. and Metallurgy, P.O.Box 3503, 11000 Belgrade, Serbia*
E-mail: kuki@ff.bg.ac.rs

In this paper we present experimental results of the decolorization of four commercial reactive azo dyes using falling film DBD reactor. In this reactor water forms a falling film which is in direct contact with plasma. Water samples containing 40 mg/L of dye were passed from one to seven times through the plasma region of the DBD reactor. Kinetic of the dye decolorization was monitored using spectrophotometer. The dependence of the decolorization on the system parameter solution pH value was investigated. For each dye decolorization has similar kinetics for all three starting solution pH values.

1. Introduction

The largest pollution of natural water resources caused by waste water originates from different industries, especially those in which colour processes are involved as it is the case in textile industry. Among the textile dyes the largest problems are caused by azo dyes, because they represented 90 % of dyes used. At the same time, azo dyes are the most toxic commercial dyes. Reactive dyes are intensively used in the last years due to their superior performance, but they are environmentally hazardous.

In the present paper, the decolorisation of four commercial reactive azo dyes Reactive Black 5, Reactive Blue 52, Reactive Yellow 125 and Reactive Green 15 (Clariant, Germany) was studied using advanced oxidation processes (AOPs) in non-thermal plasma reactor based on coaxial dielectric barrier discharge (DBD).

2. Experiment

The coaxial DBD was designed as atmospheric non-thermal plasma reactor for treatment of various water solutions /1/. In this reactor water forms a falling film which is in direct contact with plasma, see Fig. 1. Such reactor design allowed successful removing of phenols from water /2,3/. This reactor is very efficient because the plasma that is formed above the water besides ozone also produced UV radiation, radicals (e.g. OH), excited atoms (e.g. O) and molecules, electrons and ions.

A schematic diagram of experimental setup is shown in Fig. 1. A cylindrical reactor is made of pyrex glass with the inner diameter of the tube 28.5 mm and length of 600 mm. An outer electrode is made of aluminum foil glued on the outside of the glass tube on a length of 400 mm. The inner electrode was a stainless steel cylinder with a diameter of 21.3 mm. Barrier discharge is generated between the inner metal electrode and the glass tube. When the discharge source works as a falling film reactor, water flows up through a vertical hollow cylindrical electrode and flows down making a thin dielectric film over the electrode. A discharge is generated within ~3.5 mm gap between the glass and the water layer by applying voltage of up to 20 kV at 200 Hz. Discharge power was 60 W.

The capability of the plasma reactor in decolorisation of four azo dyes Reactive Black 5, Reactive Blue 52, Reactive Yellow 125 and Reactive Green 15 was tested with three samples prepared by dissolving of commercial dye without preceding purification in distilled water. In all cases water

samples containing 40 mg/L of dye were passed from one to seven times through the 40 cm long plasma region.

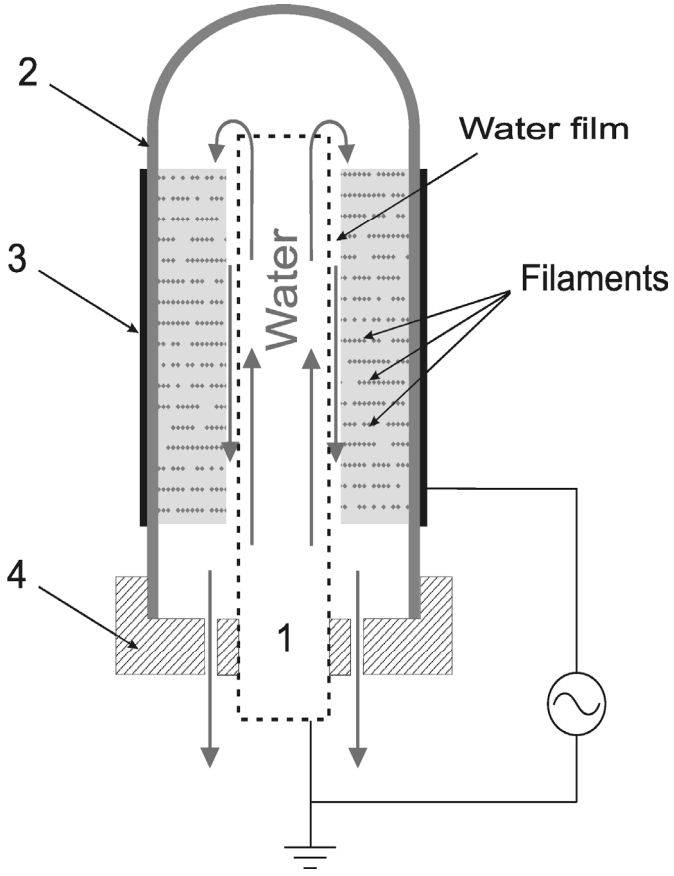


Fig. 1. Schematic picture of coaxial falling film reactor. 1-steel tube, 2-glass, 3-aluminium foil, 4-plastic holder.

Kinetic of the dye decolorisation defined as $(A_0 - A)/A_0$, where A_0 is initial absorption and A - absorption after plasma treatment, was monitored using the spectrophotometer (UV-VIS) at maximum absorption for each dyes. The dependence of the decolorisation on the system parameter solution pH was investigated (pH 9.00, 7.00 and 5.00). Solution pH has been determined after each recirculation.

3. Results

Azo dyes decolorisation has similar kinetics for all three starting solution pH values as shown in Fig. 2. The largest percent of decolorisation has been observed for initial solution of pH 7.00 or 5.00, although similar values have been observed for dye solutions with starting solution pH 9.00. After the period of 24 h from plasma treatment, decolorisation of the solution for the first treatment has been increased for 20-30 %, when compared with decolorisation value obtained 5 min after passing through the DBD reactor. For dye Reactive Black 5 decolorisation value obtained 24 h after the first passing through DBD reactor is equal to decolorisation value obtained after the second passing through DBD reactor measured after 5 min. For dye Reactive Blue 52 decolorisation value obtained 24 h after the first passing is equal to decolorisation value obtained after forth passing through DBD reactor measured after 5 min. For dyes Reactive Yellow 125 and Reactive Green 15, decolorisation value obtained 24 h after the first passing is equal to decolorisation value obtained after the third passing through DBD reactor measured after 5 min.

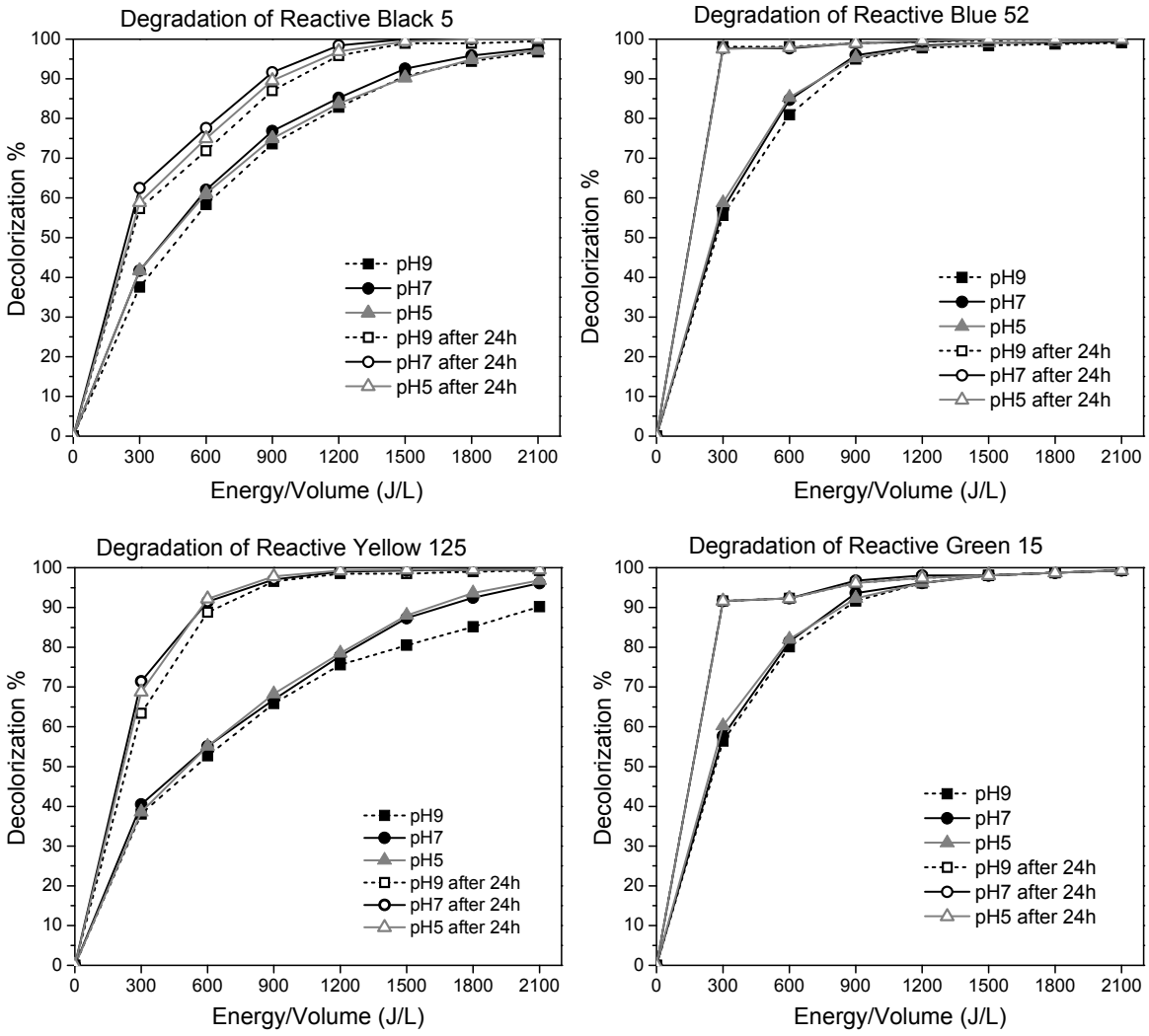


Fig. 2. Effects of pH on the decolorisation efficiency in the DBD plasma reactor. Decolorisation is monitored 5 min and 24 h after the treatment.

The pH value of the solution, 5 minutes after the first passing through DBD reactor for all four dyes and for all three investigated starting solution pH values (pH 9.00, 7.00 and 5.00), has decreased to 3.5 pH. The solution pH values gradually decreased with every passing through DBD reactor, reaching 3.0 after the seventh passing.

4. Conclusion

The waste water containing the investigated dyes, irrespective of acid, base or neutral nature, exhibits very similar, almost same decolonization kinetics. The decolonization percent of solution has significantly increased 24 h after the plasma treatment.

The solution, regardless of the starting pH value, became acidic already after the first passing through the DBD reactor and pH value is slightly changed after subsequent recirculations.

Acknowledgments. This work within the Project 141043 is supported by the Ministry of Science of the Republic of Serbia.

5. References

[1] Kuraica M M, Obradović B M, Manojlović D, Ostojić D R, Purić J 2004 *Vacuum* **73** 705.

[2] Manojlović D, Ostojić D R, Obradović B M, Kuraica M M, Krsmanović V D, Purić J 2007 *Desalination* **213** 116.

[3] Dojčinović B P, Manojlović D, Roglić G M, Obradović B M, Kuraica M M, Purić J 2008 *Vacuum* **83** 234.
[4] Song S, He Z, Qiu J, Xu L and Chen J 2007 *Separation and Purification Technology* **55** 238.

COMPARISON BETWEEN EHD ESP AND CONVENTIONAL ESP FOR COLLECTION OF DIESEL PARTICLES

Takuya Mimura[1], Yoshiyasu Ehara[1], Toshiaki Yamamoto[1]

[1]*Tokyo City University*
1-28-1 Tamatsutsumi, Setagaya-ku, Tokyo 158-8557, Japan

The collection of low resistive particulate matter (PM) generated from marine and automobile diesel engine emission is extremely difficult by the conventional electrostatic precipitators (ESPs). The low resistive PMs are detached from the collection plate by the electrostatic repulsion force caused by induction charge where particle adhesion force was dominated, resulting in particle reentrainment. The new electrohydrodynamically assisted ESP (EHD ESP) was developed to minimize the reentrainment. The EHD ESP utilizes the ionic wind to transport the zero electric field or the pocket attached to the collection plate, where electrostatic repulsion force acting on particles is zero, so that no reentrainment takes place. The collection efficiency was compared between EHD ESP and conventional ESP. The EHD ESP showed a significant reentrainment reduction over the conventional ESP, particularly for the particle size greater than 1,000 nm.

1. Introduction

The particulate matters (PMs) emitted from diesel engine exhaust are low resistive in nature and extremely small in the range of 70~120 nanometers (nm). These particles are penetrated into alveolus and extremely harmful to human health. These particles are generated from various emissions such as diesel automobiles, marine engines, power generation engines, and construction machines. The use of diesel particulate filter (DPF) was widely used for the collection of automobile diesel PM but was not economical and cost effective. The collection of low resistive PM has been known to be extremely difficult by the conventional electrostatic precipitators (ESPs). The low resistive diesel engine particles are detached from the collection plate where the electrostatic repulsion force due to induction charge exceeds particle adhesion force on the collection electrode. This phenomenon has been known as particle reentrainment or resuspension, resulting in poor collection efficiency.

There are few literatures describing the control of particle reentrainment [1-3]. Recently, two-stage ESP using charging zone by DC field, followed by the collection zone by low frequency AC field including the trapezoidal waveforms in the range of 1-20 Hz has been investigated for the collection of diesel particles in tunnel [4-6], while the conventional ESP utilizes DC high voltage. However, these concepts have limited success for minimizing the reentrainment. The wet ESP was another strong candidate for this application but it creates water treatment as opposed to dry process.

Based on fundamentals of reentrainment theory, the new electrohydrodynamically-assisted ESP (EHD ESP) was developed to overcome the reentrainment in the ESP [7, 8]. The EHD ESP, which utilizes the ionic wind to transport the charged particles effectively into the zero electrostatic field zone or pocket zone attached to the collection plate. The captured particles are trapped in the pocket where particle captured in the pocket zone was exposed to zero electric field, so that no electrostatic repulsion force due to induction charge takes place. The effectiveness of the EHD ESP was demonstrated to show the significant suppression of particle reentrainment [7, 8].

In the present study, the EHD ESP and the conventional ESP were compared how significantly the collection efficiency was improved to minimize the reentrainment using both 200 cc diesel engine. The particle size-dependent collection efficiency and the mass-base collection efficiency were determined by Scanning Mobility Particle Sizer (SMPS TSI) with particle size in the range of 20-500 nm and particle counters (PC, RION PC) with particle size in the range of 300-5,000 nm.

2. Experimental setup

2.1 ESP configuration

The EHD ESP and the conventional ESP are shown in Fig. 1 and their dimensions were designated in the figures, while the conventional ESP was the same configuration without pocket. The EHD ESP consists of five teeth shaped electrode and the collection plate with six pockets. The pockets with 10

mm depth are attached to the collection plate with every 60 mm interval. The discharge electrode was the saw type and their teeth were equally spaced with the interval of 10 mm. Negative DC voltage was used for this experiment.

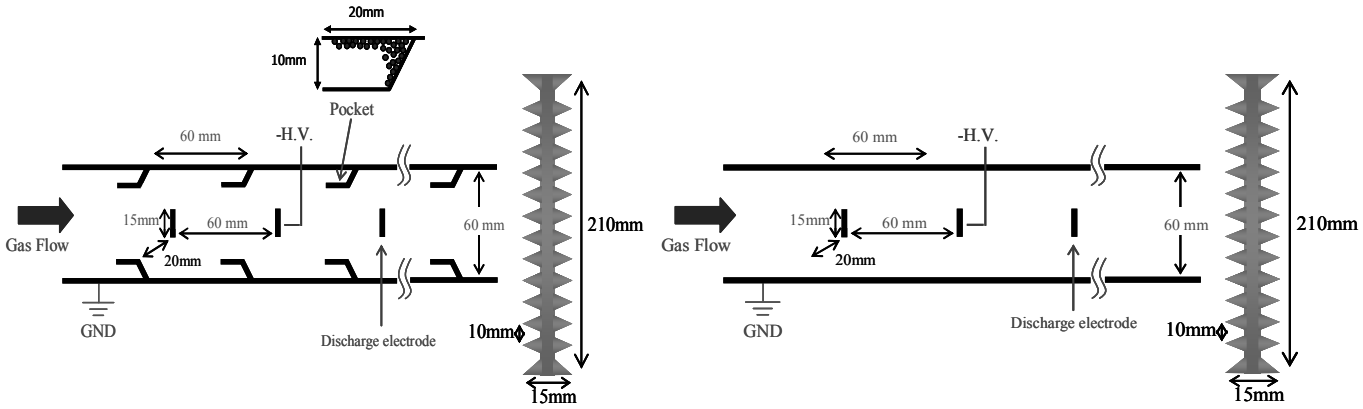


Fig. 1. EHD ESP and Conventional ESP configuration.

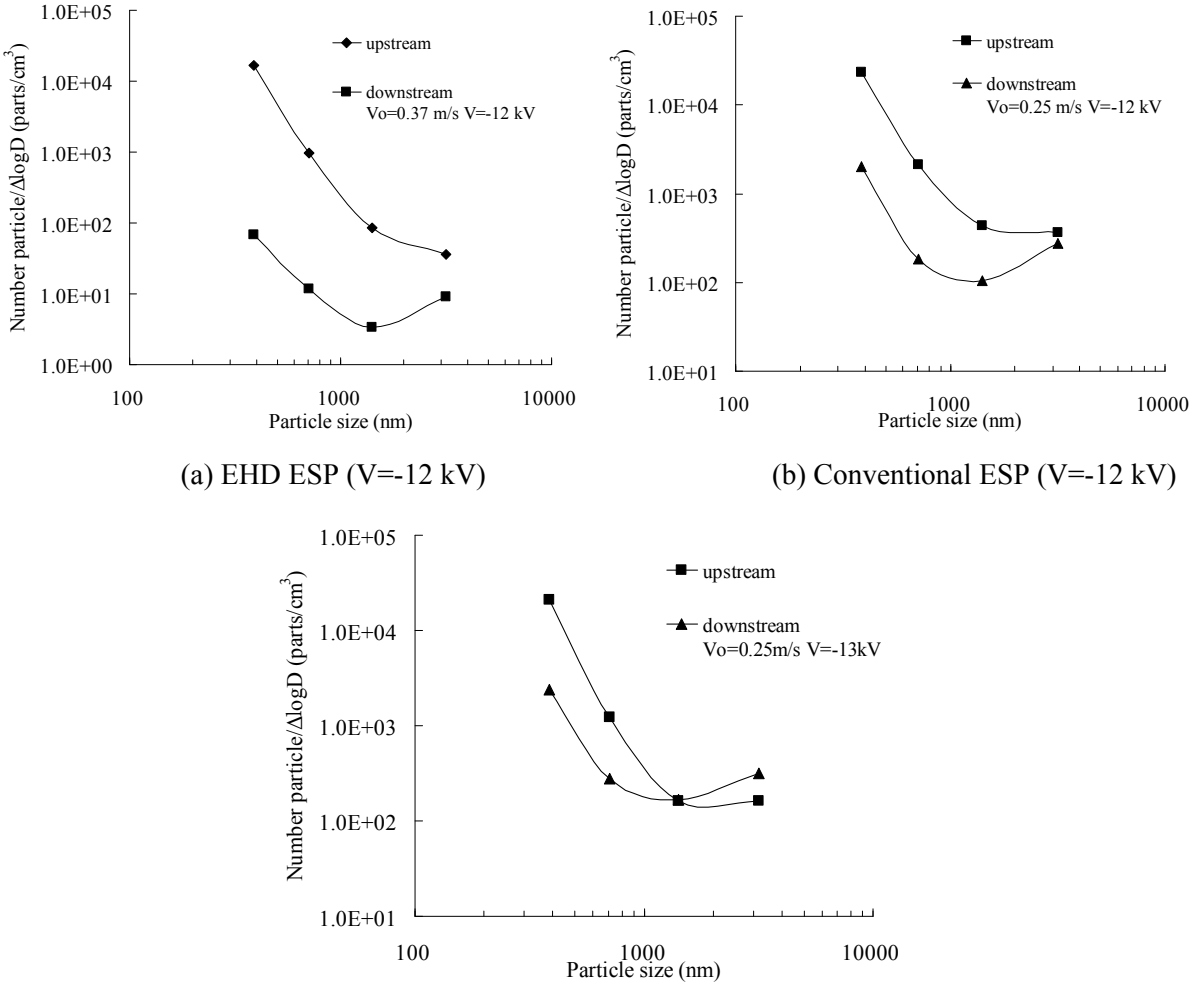
2.2 Experimental system

The exhaust gas of 200cc diesel engine (Yammer YDG200A-5E) using light oil as fuel was flowed into the conventional electrostatic precipitator (ESP) and electrohydrodynamically-assisted ESP (EHD ESP). Particle concentration was diluted with the dilution machine 1,000 times, and was measured upstream and downstream using Scanning Mobility Particle Sizer (SMPS TSI 20-500 nm) and Particle Counter (PC RION 300-5000 nm). The collecting efficiency was computed based on particle concentration of upstream and downstream of the ESPs. The applied voltage was set at -12 kV when the load was 60% (1.0 kW) and the gas velocity was 0.37 m/s for EHD ESP or 0.25 m/s for conventional ESP.

3. RESULTS AND DISCUSSION

Both EHD ESP and conventional ESP showed greater than 90% for the particle size measured by the SMPS (20-300nm). The number density distribution for particle size of 300~5,000 nm were shown in Fig. 2(a) for the EHD ESP, Fig. 2(b) for the conventional ESP with V=-12 kV, and Fig.2(c) for the conventional ESP with V=-13 kV. The collection efficiency is significantly better for the EHD ESP for larger particle size, compared with the conventional ESP. It was clear that the significant reentrainment was suppressed with the EHD ESP. The collection efficiency was further reduced with increased voltage as observed from Fig. 2(c). This was supported by the reentrainment theory which electrostatic particle repulsion was proportional to the square of particle size and electrostatic field [7-8].

Fig. 3(a) shows the time-dependent collection efficiency for the conventional ESP which was measured by PC (300-5000 nm). The collection efficiency was excellent for 300-1000 nm but decreased as particle size increased. The collection efficiency decreased with time elapsed for 2000-5000 nm. Negative collection efficiency indicated that the agglomerated large particles captured at the electrostatic field exposed were detached and reentained by the repulsion force caused by induction charge. Fig. 3 (b) shows the particle size dependent collection efficiency for the EHD ESP measured by PC (300-5000 nm). The excellent collection for 300-2,000 nm was maintained as time elapsed but decreased to 70-90% for particle size of 3,000-5,000 nm but no negative collection efficiency was observed for EHD ESP, which indicated suppression of particle reentrainment for the EHD ESP.

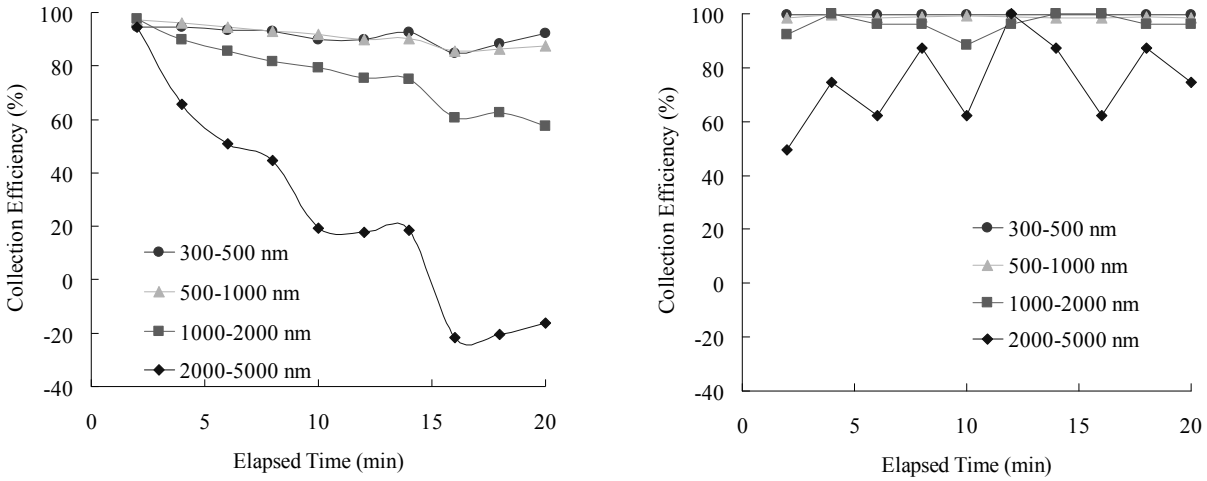


(a) EHD ESP (V=-12 kV)

(b) Conventional ESP (V=-12 kV)

(c) Conventional ESP (V=-13 kV)

Fig. 2. Comparison of number density distribution (a) EHD ESP (V=-12 kV), (b) conventional ESP (V=-12 kV), (c) Conventional ESP (V=-13 kV).

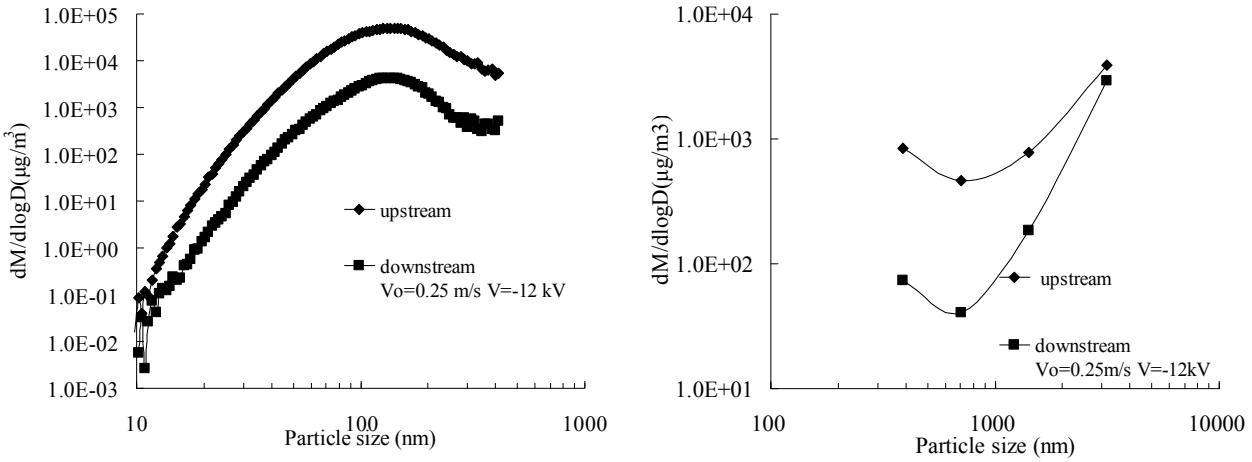


(a) Conventional ESP

(b) EHD ESP

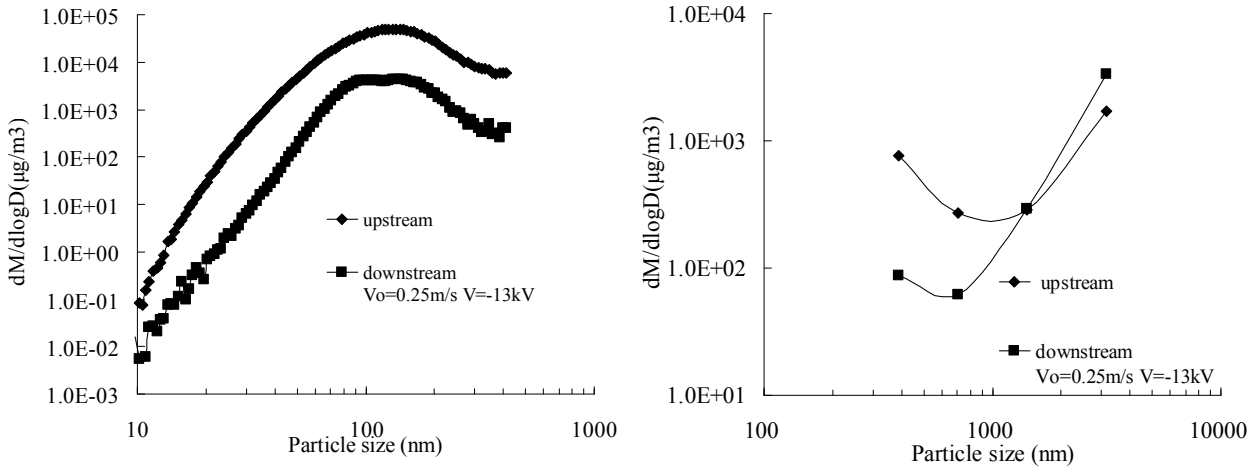
Fig. 3. Particle size-dependent collection efficiency by PC (300-5000 nm).

Figs. 4(a)-(b) show the particle-size dependent mass-density distribution for the conventional ESP with V=-12 kV. The collection efficiency of 92.6% was achieved for particle size less than 500 nm and 41.2% for large particles. The overall collection efficiency was 88.2%.
Figs. 5(a)-(b) show the particle-size dependent mass-density distribution for the conventional ESP with V=-13 kV. The collection efficiency of 91.4% was achieved for particle size less than 500 nm and -43.5% for large particles. The overall collection efficiency was 85.6%.This was attributed to lower number density for large particles. Negative collection efficiency indicated that the agglomerated large particles captured at the electrostatic field directly exposed were detached and reentrained by the electrostatic repulsion force caused by the induction charge. This was attributed due to increased induction charge, which is proportional to square of the electric field for a given particle size [7, 8].



(a) Measured by SMPS (92.6%) (b) Measured by PC (41.2%)

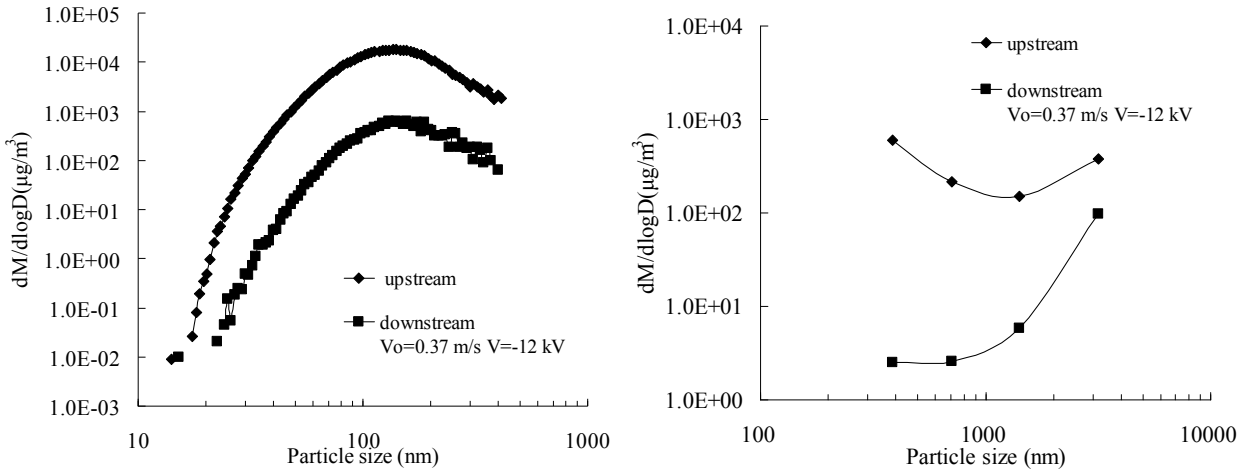
Fig. 4. Mass density distribution for conventional ESP (a) measured by SMPS (92.6%), (b) measured by PC (41.2% and overall collection efficiency of 88.2%).



(a) Measured by SMPS (91.4%) (b) Measured by PC (-43.5%)

Fig. 5. Mass density distribution for the conventional ESP (a) measured by SMPS (91.4%), (b) measured by PC (-43.5% and overall collection efficiency of 85.6%).

On the other hand, Figs. 6(a)-(b) show the particle-size dependent mass-density distribution for the EHD ESP. The collection efficiency was 96.7% for the particle size measured by the SMPS and 89.5% for large particle size measured by the PC. The overall collection efficiency of 96.5% was achieved for the EHD ESP. Based on these results the EHD ESP showed a significant reentrainment reduction over the conventional ESP, particularly for the particle size greater than 1,000 nm.



(a) Measured by SMPS (96.7%) (b) Measured by PC (89.5%)

Fig. 6. Mass density distribution for the EHD ESP (a) measured by SMPS (96.7%), (b) measured by PC (89.5% and overall collection efficiency of 96.5%)

4. CONCLUSIONS

The collection of low resistive particles generated from diesel engines was investigated using the EHD ESP and the conventional ESP. The conventional DC energized ESP showed a good collection efficiency for particle size less than 300 nm where adhesion force was dominated over electrostatic repulsion force but showed severe reentrainment for the particle size greater than 1,000 nm. On the other hand, the EHD ESP demonstrated excellent collection efficiency for particle size less than 1,000 nm and significant suppression of particle reentrainment was achieved for particle size greater than 2,000 nm in comparison with the conventional ESP.

5. REFERENCES

[1] J.D. Bassett, K. Akutsu, S. and Masuda, "A Preliminary Study of Re-entrainment in an Electrostatic Precipitator," *Journal of Electrostatics,* Vol. 3, 1977, pp. 311-257.

[2] R. M. Felder, E. Arce-Medina, "Radiotracer Measurement of Local Despsition Profiles, Friction Reentrainment and Impaction Reentrainment in an Electrostatic Precipitator," *AIChE Journal*, Vol. 31, No. 1, 1985, pp. 82-89.

[3] A. Zukeran, Y. Ikeda, Y. Ehara, M. Matsuyama, T. Ito, T. Takahashi, H. Kawakami, and T. Takamatsu, "Two-Stage Type Electrostatic Precipitator Re-entrainment Phenomena under Diesel Flue gases," *IEEE Trans. Ind. Applications*, Vol. 35, No. 2, 1999, pp. 346-351.

[4] K. Yasumoto, A. Zukeran, Y. Takagi, Y. Ehara, T. Takahashi, and T. Ito, "Suppression of Particle Deposition onto Downsteram Wall in an AC Electrostatic Precipitator with Neutralization," Int. Journal of Environment and Waste Management, Vol. 2 NOs 4/5, 2008, pp.399-411.

[5] A.D. Zimon, Adhesion of Dust and Powder, Plenum Press, New York, London 1969.

[6] T. Yamamoto, T. Abe, T. Mimura, Y. Ito, N. Otsuka, Y. Ehara, and A. Zukeran, "Electrodynamically-Assisted Electrostatic Precipitator for Collection of Low Resisitve Diesel Particulates," Proc. of IEEE-IAS, Edmonton Canada Oct. 5-9, 2008, CDROM 6pagers.

[7] T. Yamamoto. T. Abe, T. Mimura, Y. Ito, N. Otsuka, Y. Ehara, and A. Zukeran, "Electrodynamically-Assisted Electrostatic Precipitator for Collection of Low Resistive Diesel Particulates," IEEE Transactions on Industry Applications, Vol. 45, No. 6, pp.2178-2184, 2009.

[8] T. Yamamoto, T. Mimura, N. Otsuka, Y. Ito, Y. Ehara, and A. Zukeran, "Diesel PM Collection for Marine and Automobile Emissions using EHD Electrostatic Precipitators," Proc. of ESA-IAS-IEJ-SFE-JEA Joint Conference, Boston U.S.A., June 15-19, 2009, 6 pages CD ROM. (In press in IEEE –Transactions on Industry Applications, Vol. 46, No. 4, July/Aug. 2010).

PLASMA ASSISTED CONVERSION OF METHANE AND CARBON DIOXIDE

M. Młotek, K. Krawczyk, B. Ulejczyk, K. Schmidt-Szałowski

Faculty of Chemistry, Warsaw University of Technology, Noakowskiego 3, 00-664 Warszawa, Poland
Email: michalm74pw@gmail.com

Methane coupling in hybrid gliding discharge (GD) plasma-catalytic system was studied. The effects of catalysts on the reaction products were studied. The study was conducted in a homogeneous system (without a catalyst) and in heterogeneous systems (ZSM-5, SAPO11, NaY, natural zeolite, SAPO34, Pd/Al_2O_3). The main products of methane and CO_2 conversion were hydrogen, CO, acetylene and ethylene. The amount of product obtained using a catalyst containing Pd was different than that with zeolite - plasma of gliding discharge conditions. When Pd/Al_2O_3 catalyst was used the methane conversion to ethylene increased to 5.5%. With SAPO 11 catalyst a higher selectivity to C4 was achieved. The overall conversion of methane and CO_2 in homogenous system was slightly higher that that obtained in heterogeneous conditions.

1. Introduction

Methane, the basic component of natural gas, has become one of the most important raw materials for bulk chemical syntheses over the last century. Various kinds of discharges were examined for methane and other simple hydrocarbons conversion: spark, gliding, corona and DBD. The gliding discharge (GD) has been found to be mostly effective for the chemical processes where non-equilibrium plasma is used for the initiation of chemical reactions at atmospheric pressure. The GD applied for destroying the chemically stable pollutants occurring in industrial waste gases, e.g. volatile organic substances, nitrogen oxides, hydrogen sulphide, chlorofluorocarbons [1-10]. Recently, the efficacy of gliding discharge was improved by using new plasma-catalytic systems. In these systems the methane conversion to unsaturated hydrocarbons was studied [11]. Over the last years, efficient processes for methane conversion into synthesis gas were developed with the use of gliding discharge. It was found moreover that unsaturated hydrocarbons (mainly acetylene) and some oxygenates, e.g. methanol, may be obtained in this kind of discharges. Efficiency of plasma-catalytic system depends on the catalyst's activity and selectivity.

The plasma-catalytic system conversion of methane and other light hydrocarbons is regarded as one of the possible way for making the utilization of natural gas resources more efficient from both economical and ecological points of view. The investigation was done on hybrid plasma – catalytic systems for converting methane by oxidative or non-oxidative coupling to obtain olefins, acetylene, aromatics, oxygenates, etc. The main goal of the present study was to examine selected catalysts in plasma-catalytic systems for methane and CO_2 conversion.

2. Experimental

The studies were carried out in a quartz glass gliding discharge reactor of 40 mm inner diameter and 250mm in length (Fig.1). The experiments were carried out in a reactor with a pair of electrodes (90 mm long, made of stainless steel) connected to a high-voltage power supply (50 Hz). The gas mixture was introduced into the interelectrode space by a nozzle 0.8 mm inner diameter. The gas flow rate (methane + carbon dioxide) was 300Nl/h. Catalysts were placed directly below the high voltage electrodes. The height of the packing layer was about 11 mm (volume ~13 cm^3). The temperature of gas was measured by a thermocouple below the catalyst bed.

The gases used are: methane (Messer) 99.5%, CO_2 (Multax). The gases were analyzed using a chromatograph Chrompack 9002 with a Carboxen 1000 column and a TCD detector and Agilent 6890N with Hayesep Q and a TCD and FID detectors connected in series. To determinate the effect of the catalysts on the conversion of CH_4 the gas for analysis was sampled twice: 12 mm above and after used catalysts. The share of non-volatile products, mainly soot, was calculated from the carbon balance. Direct assessment of the soot production was not possible because it was carried out with the gas stream and partly deposited on the surfaces of the vessel, pipes etc.

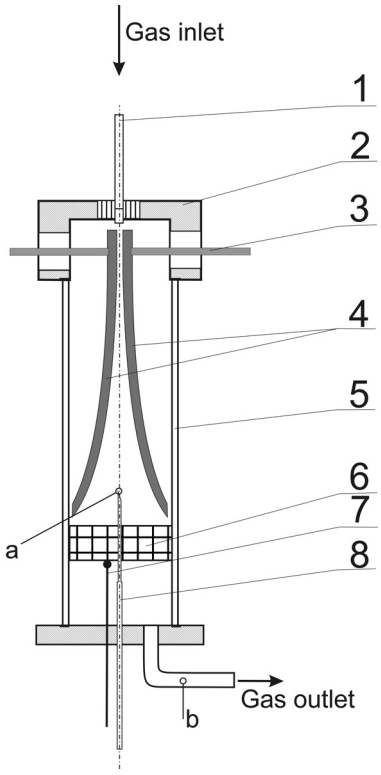


Fig. 1. Gliding discharge reactor. 1 – gas inlet, 2 – metal casing, 3 – inlet wires, 4 – electrodes, 5 – quartz glass tube, 6 – catalysts, 7 – thermocouple, 8 – glass tube for gas sampling, a and b point of gas sampling.

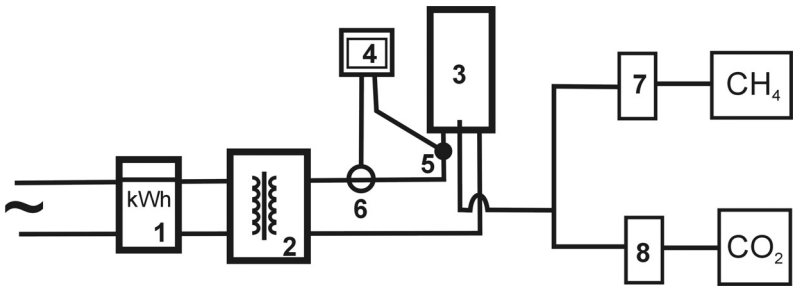


Fig. 2. Experimental set-up. 1 – energy counter, 2 – high voltage transformer, 3 – reactor, 4 – oscilloscope, 5 – voltage probe, 6 - current probe, 7, 8 – mass flow controllers.

3. Results

The effect of catalysts on the reaction products (Table 1) was studied in a homogeneous system (without a catalyst) and in heterogeneous systems with ZSM-5, SAPO11, NaY, natural zeolite (clinoptylolite), SAPO34 and Pd/Al_2O_3. The main products of methane and CO_2 conversion were hydrogen, CO, acetylene. Dependence on packing usage the product composition has changed. Comparing the products generated with ZSM-5, NaY, natural zeolite (clinoptylolite), SAPO34 to those without packing, several changes were observed. The overall conversion of methane and CO_2 in homogeneous system, in both places of gas sampling (a and b) was the same. The overall conversion of CH_4 and CO_2 and conversion of methane to C2 in plasma-catalytic system was slightly lower than that obtained in homogenous system (Table 1). It could be the reason of slightly higher specific energy reached in homogeneous system. Methane and CO_2 conversions were similar when in plasma – catalytic system clinoptylolite, ZSM-5, NaY and SAPO34 were used. However methane conversion to C4 on SAPO34 increased to 0.01. Two catalysts have shown their activity in methane conversion. The

Pd/Al_2O_3 catalyst increased methane conversion to ethylene and reduced to acetylene (Fig. 3). With SAPO11 the higher conversion of methane to C4 hydrocarbon was observed, up to 0.13 (Fig. 4).

Tab. 1. Conversion of methane and CO_2 in plasma – catalytic and in homogenous system

	Average methane conversions						
	homogen.	clinoptylolite	ZSM5	NaY	SAPO11	SAPO34	Pd/Al2O3
Point of gas sampling (a)							
Power [W]	457	405	380	417	384	417	392
SE [kJ/molCH_4]	246	218	204	224	206	224	210
Temp.	365	363	268	349	300	350	259
Overall CO_2	0,21	0,18	0,14	0,17	0,18	0,15	0,16
CO_2 to CO	0,21	0,18	0,15	0,17	0,17	0,16	0,16
Overall CH_4	0,31	0,28	0,24	0,26	0,25	0,28	0,24
CH_4 to CO	0,21	0,18	0,16	0,17	0,15	0,19	0,15
CH_4 to C_2H_2	0,09	0,08	0,07	0,08	0,08	0,08	0,07
CH_4 to C_2H_4	0,005	0,007	0,01	0,006	0,005	0,005	0,012
CH_4 to C_2H_6	0,000	0,000	0,00	0,000	0,000	0,000	0,001
Summ to C_2	0,095	0,090	0,079	0,082	0,083	0,082	0,081
C_3	0,000	0,003	0,000	0,003	0,003	0,003	0,003
C_4	0,000	0,002	0,000	0,003	0,005	0,000	0,002
H_2	0,23	0,21	0,18	0,20	0,19	0,20	0,18
Point of gas sampling (b)							
Power [W]	457	400	382	417	392	417	391
SE [kJ/molCH_4]	246	217	206	224	210	224	210
Temp.	379	370	278	366	300	350	278
Overall CO_2	0,18	0,16	0,13	0,14	0,20	0,14	0,15
CO_2do CO	0,20	0,17	0,14	0,16	0,15	0,16	0,15
CH_4	0,30	0,26	0,23	0,26	0,30	0,27	0,23
CH_4 to CO	0,21	0,17	0,15	0,17	0,09	0,18	0,14
CH_4 to C_2H_2	0,09	0,08	0,07	0,08	0,07	0,07	0,05
CH_4 to C_2H_4	0,003	0,007	0,006	0,006	0,008	0,005	0,024
CH_4 to C_2H_6	0,000	0,000	0,000	0,000	0,000	0,000	0,002
Sum to C_2	0,093	0,085	0,075	0,081	0,075	0,077	0,078
C_3	0,000	0,005	0,000	0,004	0,004	0,004	0,004
C_4	0,000	0,005	0,000	0,003	0,127	0,011	0,005
H_2	0,23	0,19	0,17	0,19	0,17	0,19	0,17

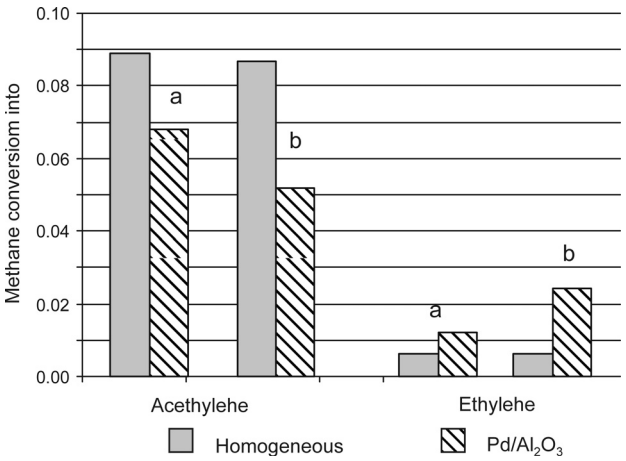


Fig. 3. Effect of catalysts on methane conversion to acetylene and ethylene. a – before catalysts (point a – Fig. 1), b – after catalysts (point b – Fig. 1.).

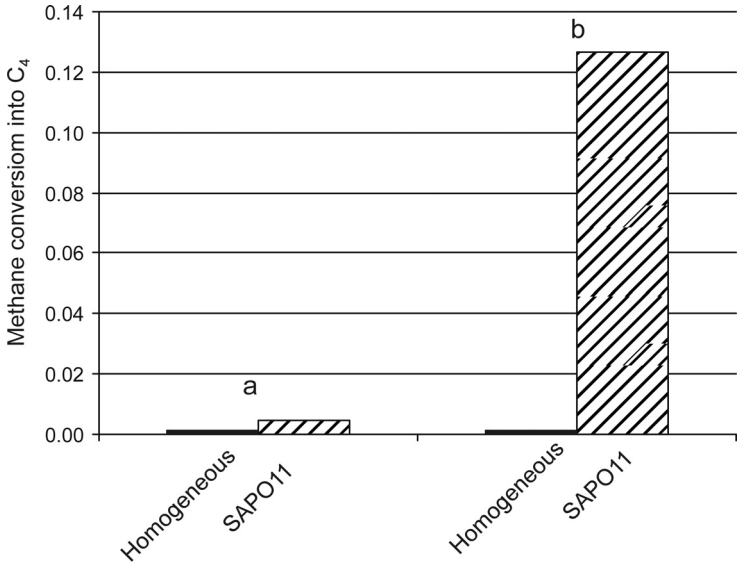


Fig. 4. Effect of catalysts on methane conversion to C4 hydrocarbons a – before catalysts (point a – Fig. 1), b – after catalysts (point b – Fig. 1.).

4. Summary

Our experiments have shown that the hybrid plasma-catalytic system of GD combined with a bed of SAPO 11 can be effectively used for the methane coupling into C4 hydrocarbons. The selectivity of methane conversion to ethane with Pd/Al_2O_3 catalysts was the higher (0.5) than this with other catalysts.

This study has shown that the significant changes in the final products were different due to the activity and selectivity of the Pd/Al_2O_3 and SAPO11 catalysts. Using of appropriate catalysts allows achieve high selectivity of methane and CO_2 conversion to C2 and C4 hydrocarbons.

Acknowledgements. This work was financially supported by ERA-NET CHEMISTRY (Decision nr 139/ERA-NET/2008)

5. References

[1] Czernichowski A, 1994 *Pure & Appl. Chem.,* 66, 1301

[2] Krawczyk K. and Młotek M., 2001 *Appl. Catal. B: Environmental*, 30, 233

[3] Krawczyk K., Młotek M. and Schmidt-Szałowski K., 2001 *High. Temp. Material Processes,* 5, 349

[4] Charamel A., Czernichowski A. and Gorius A., 1998 US Patent 5 711 859,

[5] Opalińska T., Opalska A. and Schmidt-Szałowski K. 2005 *Plasma Processes and Polymers* (ed. R. d'Agostino), (Wiley-VCH Verlag, Weinheim)

[6] Opalińska T., Czernichowski A. and Czernichowski P. 1997 *Plasma Chemistry VI*, Lublin, 149

[7] Krawczyk K. and Ulejczyk B. 2004 *Plasma Chem. Plasma Proc.* 24, 2, 155

[8] Krawczyk K. and Ulejczyk B., 2003 *Plasma Chem. Plasma Proc*., 23, 2, 265

[9] Indarto, D.-R. Yang, J.-W. Choi, H. Lee and H.-K. Song, 2007 *Chem. Engineering Communications* 194/8, 1111

[10] Penetrante B.M., Hsiao M.C., Bardsley J.N., Merrit B.T., Vogtlin G.E., Kuthi A., Burkhart C.P. and Bayless J.R., 1997 *Plasma Sources Sci. Technol*. 6, 251

[11] Młotek M., Setek J., Krawczyk K. and Schmidt-Szałowski K., 2009 *Appl. Cat. A: General* 366 232-241.

INFLUENCE OF CURRENT AND KIND OF GAS ON THE HYDROGEN PEROXIDE GENERATION IN THE WATER SOLUTIONS

L. Nemcova[1], F. Krcma[1], A. Nikiforov[2,3], Ch. Leys[2]

[1]*Brno University of Technology, Faculty of Chemistry, Purkynova 118, 61200, Brno,Czech Republic*
[2]*Ugent, Department of Applied Physics, Jozef Plateaustraat 22B, 9000 Gent, Belgium*
[3]*Laboratory of Non-Linear Plasma Processes, Institute of Solution Chemistry RAS, Academicheskaya 1, 153045 Ivanovo, Russia*
E-mail: krcma@fch.vutbr.cz

This contribution presents results of underwater electric discharge created in the bubbles in NaH_2PO_4. $2H_2O$ solution. This discharge configuration is relatively new one and fully combines both gas and liquid phase discharges. The gas bubbles are introduced into the system by thin stainless steel capillary that plays simultaneously a role of HV pin electrode; water solution of low conductivity up to 0.05 mS is grounded. Thus the HV pin electrode is covered by thin gas layers and the discharge is generated in the gas phase in pin to plane configuration. The discharge streamers (plasma channels) generated in the gas phase are long enough (up to 1 cm) and thus they introduce into the liquid phase and further propagate in it. The streamer length as well as their density is growing with increase of the applied voltage. The DC voltage between 2.0-3.0 kV was used in the contemporary experiment. Discharge current was varied from 20 to 30 mA, lower currents of 10 mA and 15 mA didn't allow stable discharge operation though some streamers were observed. The hydrogen peroxide generation was studied in the time evolution; the applied voltage and discharge current were the other studied parameters. Amount of generated peroxide was more or less directly proportional to the supplied energy. Four different gases (Air, Ar, He and N_2) were used for the bubble generation. Air was the most effective for the hydrogen peroxide generation, the lowest production was observed in nitrogen bubbles. This experimental result should be explained by addition of the molecular oxygen into the system that can recombine with hydrogen atoms generated by the discharge if Air was introduced. On the other hand, in case of nitrogen, a non negligible part of energy can be carried out by various metastable excited states.

Key words: underwater discharge, hydrogen peroxide, gas bubbles

1. Introduction

Underwater electrical discharges have attracted substantial attention as a new and effective alternative method for the treatment and sterilization of solutions as well as surface treatment of various materials. In general, underwater discharges can be divided into two groups based on the method of plasma ignition. Pulsed discharges are generated by high voltage pulses with durations of a few nanoseconds to microseconds with currents up to kA. The second group consists of dc or ac discharges generated in vapour bubbles. During the past two decades, research on electrical discharges in electrically conductive liquids or above these liquids´ surfaces has been focused on getting a better understanding of the pre-breakdown and breakdown phenomena in water and on several applications in water such as degradation of hazardous organic compounds, killing of microorganisms, chemical synthesis, medicine and biomedical engineering. Underwater discharges are effective sources of radicals and active particles: OH, H, O, HO_2, hydrogen peroxide, ozone, UV radiation and shock waves. An essential advantage of such systems is the possibility to combine plasma-induced effects with the highly selective chemical processes occurring in solutions. The destruction of organic compounds is initiated by reactions with hydroxyl radicals, hydrogen peroxide and ozone, if gaseous oxygen is introduced into the system [1, 2].

Hydroxyl radicals

OH radical is characterized by high reactivity with organic compounds and one of the highest redox potential (2.80 V). High value of redox potential guarantees non-selective behaving in oxidative reactions. Hydroxyl radicals are able to react with any organic substance which is presented in solution and therefore OH radicals belong to the most important particles which are generated by electric discharge. Moreover, the OH radical generation by underwater discharges is very effective.

Hydrogen peroxide

Hydrogen peroxide is versatile chemical and strong oxidant with a standard electrode potential of 1.763 V at pH 0 (Eq.1) [1].

$$H_2O_2 + 2H^+ + 2e^- \rightarrow 2H_2O \qquad E^0 = 1.763V \tag{1}$$

While main industrial applications of H_2O_2 are bleaching of textiles and paper, important environmental applications are the removal of inorganic and organic pollutants from wastewater. The use of H_2O_2 as ·OH generating agent in advanced oxidation processes (AOPs) such as ozonation ($O_3/H_2O_2/UV$), hydrogen peroxide photolysis (UV/H_2O_2) and Fenton processes (Fe^{2+}/H_2O_2) improves its effectiveness in industrial technologies [3].

In the present work, the spectrophotometric determination of hydrogen peroxide by the reaction with metavanadate in acidic medium (vanadate method) was used because the H_2O_2 compound gives with metavanadate yellow colored peroxovanadium complex by wavelenght 450nm. (Eq.2) [4].

$$VO_3^- + 4H^+ + H_2O_2 \rightarrow VO_2^{3+} + 3H_2O \tag{2}$$

2. Experimental technique

The principal scheme of the experimental set-up for the generation of the underwater discharge in gas bubbles is presented in Figure 1. The discharge reactor consists of discharge camber (volume 1 L), on the bottom of which the glass capillary (the inner diameter of 1.2 mm, length of 50 mm) is placed. Liquid is connected to ground potential through a shunting resistance of 100 Ohm by stainless steel electrode placed at the upper part of the chamber. The plasma-solution reactor is cooled in order to avoid thermal destruction of hydrogen peroxide at temperatures above 70 °C [5]. The metallic tube with diameter of 0.5 mm is placed inside the glass capillary and it is used as the HV electrode. The gas (Ar, He, Air or N_2) has been applied through this metallic tube in order to produce bubbles. Gas flow in the system was supplied by mass flow control system (MKS 4000). Flow rate of used gases was fixed at 200 sccm in all experiments. The electric discharge was located directly on the surface of the metallic tube inside of bubbles. The DC power supply for the discharge sustaining has been connected to the reactor through a ballast resistor of 30 kΩ. The applied voltage is varied from 1.7 to 2.7 kV.

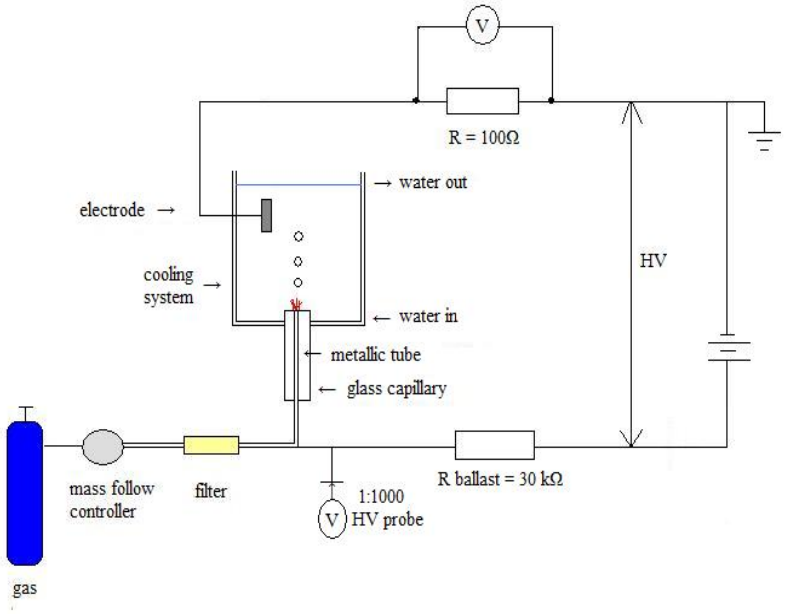


Fig. 1. Experimental set-up.

3. Results and discussion

The hydrogen peroxide was generated in the reactor during 20 minutes. The initial conductivity of NaH_2PO_4 . $2H_2O$ solution was kept in all experiments at 50 µS/cm. The gases He, Ar, Air and N_2 were alternated in the experiments while the other conditions remained constant. The applied voltage in the range 1.7–2.7 kV allowed discharge currents of 10–30 mA. Figure 2 shows hydrogen peroxide generation at the discharge current of 10 mA in all used gases. On Figures 3 and 4 we can see kinetic curves for hydrogen peroxide generation at 20 and 30 mA, respectively. The hydrogen peroxide generation at the lowest current of 10 mA is not effective because plasma is not stable operating and thus the described dependences are not smooth curves. At the higher currents, the discharge operates regularly and the hydrogen peroxide production is nearly directly proportional to the time of discharge operation; the saturation effect can be seen at the latest times (the same see in [6]). The H_2O_2 amount is nearly directly proportional to the applied current (concentration increases from 4.8 mmol/l at current of 20 mA to 8.9 mmol/l at 30 mA in argon). The initial hydrogen peroxide production rates were calculated from the linear (initial) parts of time dependencies and they are shown in table 1. The highest production rate was observed in Air bubbles, probably due to reaction of atomic oxygen (generated by dissociation of oxygen molecules from Air) with atomic hydrogen generated by water dissociation. In the other gases the peroxide production was within the experimental error interval nearly similar.

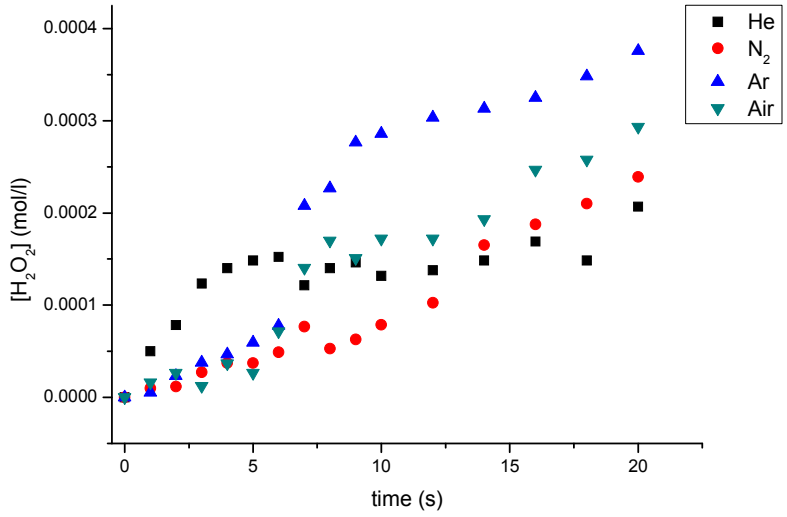


Fig. 2. Hydrogen peroxide generation at the current of 10 mA.

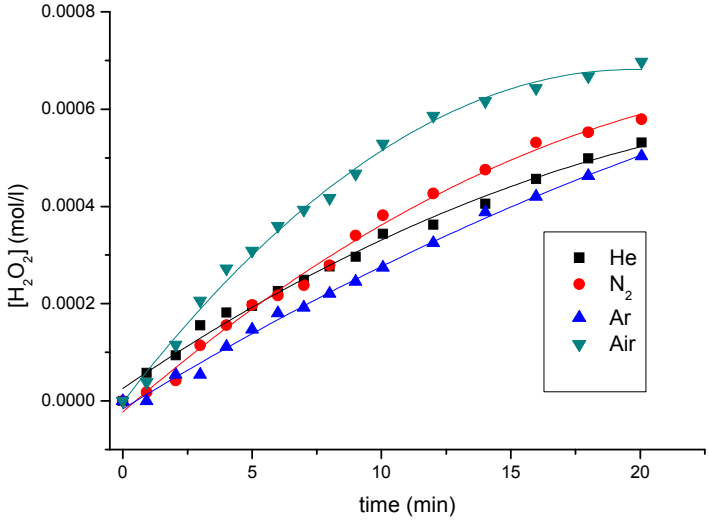


Fig. 3. Hydrogen peroxide generation by using 20 mA.

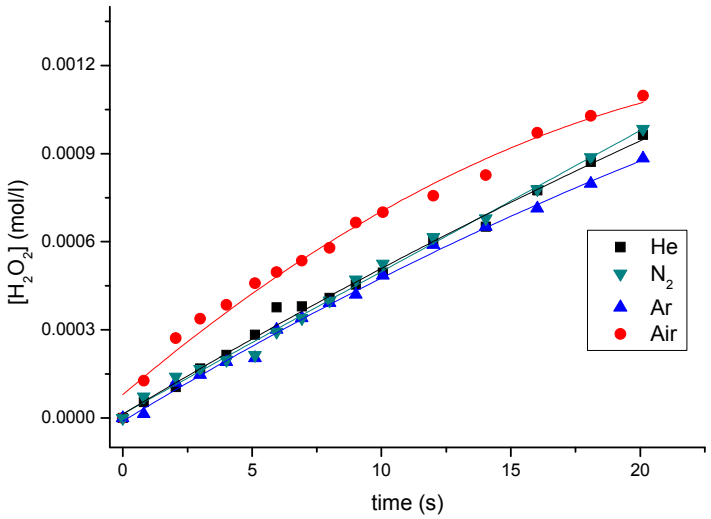


Fig. 4. Hydrogen peroxide generation by using 30 mA.

Tab. 1. Initial rate of hydrogen peroxide formation as a function of discharge current

Current [mA]	**Initial hydrogen peroxide production rate [mmol/l·s]x10^{-4}**			
	He	*Ar*	*N_2*	*Air*
15	3.3	3.6	3.8	4.2
20	4.2	3.7	5.0	5.8
25	5.8	6.1	6.3	6.7
30	8.3	8.3	6.8	8.3

4. Conclusion

This work has been focused on chemical efficiency of the electric discharge generated inside the bubbles in water solution. The influence of the used gas (Air, He, Ar, N_2) and the discharge current on the effectiveness of H_2O_2 production was studied. We observed that concentration of H_2O_2 during discharge operation is linearly proportional to the discharge current. It is also nearly independent on the used gas kind, only in air some hydrogen peroxide production enhancement was determined. The current less than 10 mA is not applicable, because plasma is not stable and thus hydrogen peroxide is generated irregularly.

5. References

[1] Nikiforov A Yu and Leys Ch 2007 *Plasma Sources Sci. Technol.* **16** 273.
[2] De Baerdemaeker F, Šimek M and Leys Ch 2007 *J. Phys. D: Appl. Phys.* **40** 2801.
[3] Pupo Nogueira R F, Oliveira M C and Paterlini W C 2005 *Talanta* **66** 86.
[4] Ryo O and Tetsuji O 2002 *J. Electrostat.* **55** 333.
[5] Schumb W C, Satterfield Ch N and Wentworth R L 1955 *Hydrogen peroxide*, Am. Chem. Soc. Monograph Ser., New York.
[6] Stará Z and Krcma F 2004 *Czech. J. Phys.* **54** C1050.

REMOVAL OF ACETALDEHYDE BY A DIELECTRIC BARRIER DISCHARGE: EFFECT OF TEMPERATURE AND OXYGEN PERCENTAGE

Koeta[1] O., Blin-Simiand[2] N., Pasquiers[2] S., Bary[1] A., Jorand[2] F., Postel[2] C.

[1]*Laboratoire de Chimie Analytique de Radiochimie et d'Electrochimie, Univ. de Ouagadougou, BP 7021, Burkina Faso*
[2]*Laboratoire de Physique des Gaz et des Plasmas, CNRS et Univ. Paris-Sud, 91405 Orsay cedex, France*
E-mail: nicole.simiand@u-psud.fr

The removal of acetaldehyde by a dielectric barrier discharge powered by a HV pulse generator is studied in N_2 and N_2/O_2 mixtures at low O_2 concentration, at 20°C and 300°C. It is shown that the removal efficiency strongly depends on both the temperature and the oxygen content. Analysis of by-products emphasises that dissociation of CH_3CHO by quenchings of N_2 metastable states are important processes, even in mixtures containing oxygen.

1. Introduction

Acetaldehyde (CH_3CHO) is a pollutant coming from building materials in indoor air but also emitted by the combustion of ethanol gasoline or exhausted from incinerators. The use of non thermal plasma for the removal of Volatile Organic Compounds (VOCs) is studied since the 1990s. Few works have been devoted to this aldehyde using filamentary plasmas of dielectric barrier [1-3] or corona [4, 5] as well as homogeneous photo-triggered [6] discharges.

The present study focuses on the effect of temperature (20°C and 300°C) and oxygen percentage (lower than 10 %) on the treatment of acetaldehyde by a dielectric barrier discharge (DBD). Our purpose is to develop knowledge about physical and chemical mechanisms for the conversion of this molecule in filamentary plasma in order to further compare it with the homogeneous one [6]. The identification of by-products is made to better understand the conversion mechanism of this molecule.

2. Experimental set-up

The discharge set-up is identical to the one previously adopted for studies on formaldehyde [7-9]. The transient plasma is produced in a cylindrical DBD (Pyrex tube with a central tungsten HV electrode) energised by a pulsed high voltage generator working at a repetition frequency value up to 200 Hz, in N_2 and N_2/O_2 mixtures (oxygen concentration, P_{O2} : 2 and 5 %) , at atmospheric pressure, with addition of CH_3CHO (up to 1000 ppm), at a constant gas flow of 1 l/mn NTP. The plasma volume is 20 cm^3. The DBD reactor is placed in a thermoregulated oven allowing the control of temperature.

All measurements are performed for a constant applied voltage equal to 40 kV (on a purely capacitive charge, without plasma), and the specific deposited energy is varied by changing the repetition frequency, ν. The specific energy E_S, is simply determined by :

$$E_S = \nu E_{pulse} / F \quad (1)$$

where E_{pulse} is the deposited energy in the plasma volume per current pulse, and F is the flow per volume. E_{pulse} ranges from 50 up to 100 mJ as function of the working conditions, i.e. values of T, P_{O2}, and ν.

FTIR analysis, micro-gas chromatography with a thermal conductivity detector, and gas chromatography coupled to mass spectrometry are used to characterise the gas mixture at the exit of the DBD.

3. Removal of acetaldehyde in the nitrogen plasma

In Figure 1 is plotted the acetaldehyde concentration measured at the exit of the DBD reactor, C_{exit}, as function of the specific energy for an inlet concentration, C_0, equal to 500 ppm in nitrogen, and at a temperature of 300°C. This is a typical example of experimental results. As already shown for CH_2O [7, 8], the removal of CH_3CHO by the HV-pulse energised DBD can be efficient even in absence of

oxygen in the gas mixture. C_{exit} exhibits an exponential decrease for E_S lower then 150 J/l (dashed line in Figure 1), i.e.

$$C_{exit} = C_0 \exp(- E_S / \beta) \quad (2)$$

where β is the characteristic energy (169 J/l in Figure 1). For higher energy values, C_{exit} is lower than the concentration given by (2).

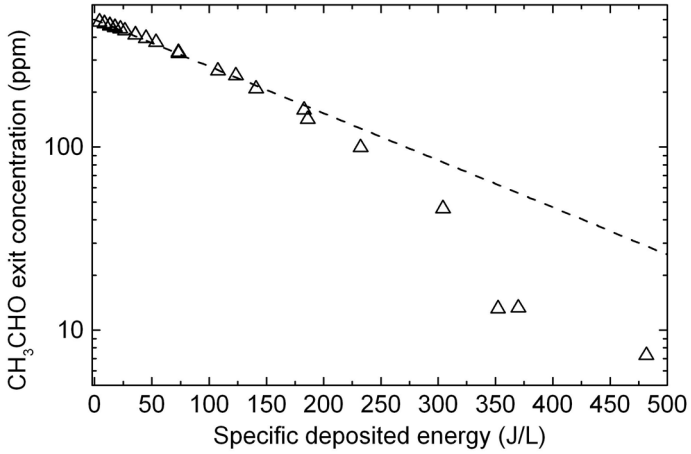


Fig. 1. Example of acetaldehyde concentration measured at the exit of the DBD reactor (T=300°C, C_0=500 ppm). Dashed line : concentration given by equation (2) for β=169 J/l.

Using DBD reactors, we obtained recently the same type of law than (2) (at the lowest deposited energy values studied) in case of formaldehyde or toluene diluted in nitrogen [8, 10]. Moreover, as previously found for CH_2O and $C_6H_5CH_3$, β measured for CH_3CHO at low E_S values decreases when the temperature increases : β=320 J/l and 170 J/l at T=20°C and 300°C respectively.

As for other VOCs, electrons and N_2 metastable states should be involved in the removal of acetaldehyde in nitrogen, i.e.

$$e^- + CH_3CHO \rightarrow \text{products} + e^- \quad (R2)$$

$$N_2(A^3\Sigma^+_u) + CH_3CHO \rightarrow \text{products} + N_2 \quad (R3)$$

and also reactions with other states like $a'^1\Sigma$, $a^1\Pi$ and $w^1\Delta$. Probably nitrogen states are more important than electrons owing to their higher lifetime. It is known that the quenching rate of $N_2(A^3\Sigma^+_u)$ by an hydrocarbon increases when the temperature increases; this was demonstrated for methane and ethane [11]. Because productions of N_2 states by electron collisions do not depend on T in our experiment [10], it should be the same for productions of dissociative electronic excited states of acetaldehyde, reaction (R2). Therefore the decrease of the characteristic energy when T increases should be mainly due to (R3)-type reactions. No data exists on the overall rate constant, k_Q, for such reactions involving acetaldehyde. For ethene, $k_Q = 1.1 \times 10^{-10} cm^3 s^{-1}$ for the $A^3\Sigma^+_u$ state [11] and $k_Q = 4.0 \times 10^{-10} cm^3 s^{-1}$ for the group of singlets ($a'^1\Sigma$, $a^1\Pi$ and $w^1\Delta$) [12] at ambient temperature. Moreover we have found that the characteristic energy measured for CH_3CHO, at a given C_0 value, is about the same than the one for ethene in N_2 [13]. Thus k_Q for CH_3CHO should be comparable to the coefficient for C_2H_4. Additionally, β measured for CH_2O [7, 8] is a factor of two lower that the one found in this work for CH_3CHO, i.e k_Q should be lower for CH_3CHO compared to the coefficient for CH_2O.

In a previous work using a wire-to-cylinder corona discharge powered by a Marx generator, with similar current pulse characteristics than in our experiment, C. Klett et al. [5] have also found that C_{exit} decreases exponentially for E_S lower than 150 J/l, at C_0=500 ppm and ambient temperature. However β=160 J/l in this case, which is a factor of two lower than the characteristic energy we have found for the DBD reactor and same gas mixture and temperature. Thus it is clear that the type of discharge used play a major role in the energy efficiency for the removal of VOCs. Such a difference on the β values established between corona and DBD reactors should be related to different spatial distribution of the deposited energy in the discharge volume. Considering the temperature dependence of the characteristic energy found for different VOCs and discharge types [8, 10, 14], the comparison between β values for different plasma reactors makes sense only if the gas temperature in the discharge volume is known, taking into account heating of the gas by the discharge. In case of a

negligible heating effect, the importance of the energy distribution has been also pointed out for formaldehyde [7] and for isopropyl alcohol [15] diluted in dry air by caparison between homogeneous (pre-ionised) and filamentary (DBD) plasmas.
The decrease law (2) has been found for many VOCs and has been explained by some authors using a simplified global kinetic model [16]. It is obtained when a linear termination reaction is the dominant process for the radical, R, responsible for the conversion of the pollutant molecule,

$$R + BG \rightarrow \text{products} \quad \text{(R1)}$$

where BG is a molecule of the background gases. However, instead of one type of highly reactive specie R (i.e. the oxygen atom for mixtures with O_2), the removal of a particular VOC is more likely due to more than one kinetic process, involving different types of radicals (O, OH, …) or even various molecular excited states (in particular in the N_2 plasma).
Main by-products (concentrations in the range 50-300 ppm) detected in the N_2/CH_3CHO mixture plasma are : CO, HCN, H_2, CH_4, and C_2H_6; a precise quantification of all these compounds is in progress. Detection of CO and CH_4 suggests that CH_3CHO dissociates to produce the methyl radical which later recombines with H, and either CO or the HCO radical, i.e.

$$N_2(A^3\Sigma^+_u) + CH_3CHO \rightarrow CH_3 + HCO + N_2 \quad \text{(R4a)}$$
$$N_2(A^3\Sigma^+_u) + CH_3CHO \rightarrow CH_3 + H + CO + N_2 \quad \text{(R4b)}$$

followed by

$$H + CH_3 + N_2 \rightarrow CH_4 + N_2 \quad \text{(R5)}$$
$$H + HCO \rightarrow CO + H_2 \quad \text{(R6)}$$

The hydrogen atom should also come from two other energetically possible dissociation reactions,

$$N_2(A^3\Sigma^+_u) + CH_3CHO \rightarrow CH_3CO + H + N_2 \quad \text{(R7a)}$$
$$N_2(A^3\Sigma^+_u) + CH_3CHO \rightarrow CH_2CHO + H + N_2 \quad \text{(R7b)}$$

The hydrogen molecule is thus obtained from the recombination of H,

$$H + H + N_2 \rightarrow H_2 + N_2 \quad \text{(R8)}$$

but it should also come from the reaction of the methyl radical with the nitrogen atom,

$$N + CH_3 \rightarrow HCN + H_2 \quad \text{(R9)}$$

which is a possible route for the production of the cyanic acid, amongst others. Detection of ethane emphasises that CH_3 is efficiently produced as the hydrocarbon follows the recombination of this radical,

$$CH_3 + CH_3 + N_2 \rightarrow C_2H_6 + N_2 \quad \text{(R10)}$$

Few ppm of CO_2 were also detected, so that the C=O double bond in CH_3CHO should also be broken following quenching collisions of the singlet states (the energy of the A state is not high enough to induce the bond breaking),

$$N_2(a') + CH_3CHO \rightarrow CH_3CH + O(^3P) + N_2 \quad \text{(R11)}$$

and thereafter CO is oxidised by the oxygen atom,

$$O(^3P) + CO + N_2 \rightarrow CO_2 + N_2 \quad \text{(R12)}$$

4. Effect of the oxygen

Addition of oxygen to the N_2/CH_3CHO mixture does not change the evolution of the acetaldehyde concentration at the exit of the DBD reactor, i.e. the decrease of C_{exit} follows the exponential law (2) when E_S increases up to a value above which the decrease is more rapid. The table 1 gives examples of the characteristic energy values measured at 2 and 5 % of oxygen, together with β for the oxygen free mixture.

Tab. 1. Characteristic energy (J/l) for the gas mixtures and temperatures under investigation, and for C_0=500 ppm.

O_2 percentage (P_{O2})	*T = 20°C*	*T = 300°C*	*ratio*
0	322	169	0.52
2	117	45	0.38
5	99	26	0.26

The characteristic energy decreases (and so the acetaldehyde removal efficiency increases) when the oxygen percentage increases up to 5 %. This decrease is faster for 300°C than for 20°C. At a given value of P_{O2}, β is a decreasing function of the temperature and this effect is the most important at 5 %.

For the wire-to-cylinder corona discharge cited above, C. Klett et al. [5] have found β=125 J/l at ambient temperature and 5 % of oxygen for E_S lower than 75 J/l, i.e. a characteristic energy slightly higher than our measurement for same conditions and energy range. As previously discussed for nitrogen, this difference strengthens the importance of the discharge type (spatial distribution of the deposited energy, …) for VOCs removal by non-thermal plasma.

In oxygen containing mixture, the increase of the acetaldehyde removal efficiency when the temperature increases should be related to the increase of the oxidation reactions efficiencies,

$$O(^3P) + CH_3CHO \rightarrow OH + CH_3CO \quad \text{(R13)}$$

followed by,

$$OH + CH_3CHO \rightarrow H_2O + CH_3CO \quad \text{(R14)}$$

where $O(^3P)$ comes from various oxygen molecule dissociation processes, i.e. electron collisions and quenchings of nitrogen excited states. The coefficient for reactions (R13), k_{13}, is an increasing function of T but remains much lower than the coefficient for (R14), k_{14}, as can be seen on figure 2.

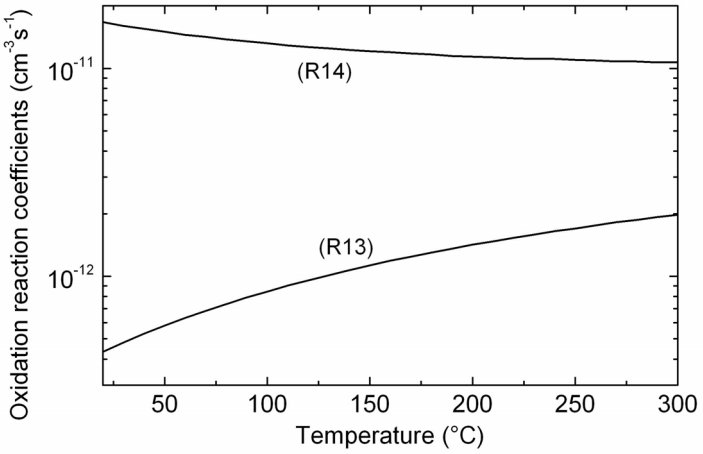


Fig. 2. Coefficients for the oxidation reactions (R13) and (R14) as function of the temperature [17].

The hydroxyl radical is also efficiently created by the addition reaction [18],

$$O + H + N_2 \rightarrow OH + N_2 \quad \text{(R15)}$$

where the hydrogen atom should come from the dissociation of CH_3CHO, (R2) and (R3). Therefore the role of OH in the conversion of acetaldehyde by the DBD reactor is probably important at low temperature even if the inlet mixture does not contain water molecule. Importance of reactions (R4) and (R7) in the removal of acetaldehyde progressively decreases when O_2 is added to N_2/CH_3CHO owing to the quenching of N_2 metastable states by O_2. However (R4) and (R7) should efficiently compete with (R13) and (R14) at low oxygen concentration.

Various by-products are detected in the $N_2/O_2/CH_3CHO$ mixture. Apart carbon oxides, water molecules and ozone, the most abundant compounds are : CH_2O, CH_3OH, HCOOH, CH_3COOH, H_2, CH_4, HCN. Their concentrations depend upon E_S, T and P_{O2} values. At low temperature, methyl nitrate, CH_3ONO_2, and peroxyacetyl nitrate (PAN), $CH_3C(O)OONO_2$, are also detected together with few nitromethane, CH_3NO_2. In figure 3 are plotted CH_3ONO_2 and PAN concentrations as function of the specific energy for C_0=860 ppm, P_{O2}=2 %, and T=20 °C. PAN disappears at 300°C, whereas important concentrations (higher than 100 ppm) of NO and NO_2 are measured. N_2O_5 is present only at 20°C and N_2O is always detected.

Even if O_2 is present in the mixture, the presence of CH_3ONO_2 confirms that CH_3CHO is dissociated to produce CH_3, reactions (R4), and this is also strengthened by the detection of methane (for the formation of methyl nitrate, see also the discussion about the dissociation of toluene in ref.[10]),

$$H + CH_3 + N_2 \rightarrow CH_4 + N_2 \quad \text{(R16)}$$

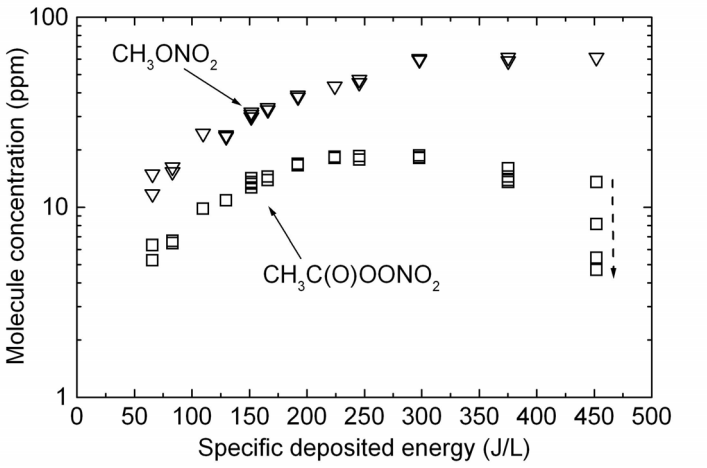


Fig.2 . Concentrations of methyl nitrate and peroxyacetyl nitrate (PAN) at the exit of the DBD reactor for P_{O2}=2 %, C_0=860 ppm, and T=20°C.

On the other hand PAN should follow the production of CH_3CO by (R7a), (R13) and (R14), followed by successive addition of O_2 and NO_2. The PAN concentration saturates and decreases when the specific energy increases above 225 J/l, and, for the highest E_S value studied, it decreases during time (dashed vertical arrow on the figure). This effect is comparable to the decrease of the ozone concentration during time, which has been ascribed to the increase of the temperature in the discharge volume due to the electrical energy deposition until the DBD reactor reaches a thermal equilibrium [10].

5. References

[1] Zlotopol'skii V and Smolenskaya T 1996 *High Energy Chem.* **30** 188.
[2] Kinoshita K, Fujiyama Y, Kim H, Katsura S and Mizuno A 1997 *J. of Electrostatics* **42** 83.
[3] Lee H and Chang M 2001 *Plasma Chem. Plasma Proc.* **21** 329.
[4] Faungnawakij K, Sano N, Yamamoto D, Kanki T, Charinpanitkul T and Tanthapanichakoon W 2004 *Chem. Eng. J.* **103** 115.
[5] Klett C, Touchard S, Vega A, Redolfi M, Duten X and Hassouni K 2009 *Proc. of the ISPC 19* (Ruhr University Bochum, Germany, July 27-31).
[6] Magne L, Pasquiers S, Edon V, Jorand F, Postel C and Amorim J 2005 *J. Phys. D : Appl. Phys.* **38** 3446.
[7] Blin-Simiand N, Jorand F, Magne L, Pasquiers S and Postel C 2008 *Proceedings of HAKONE XI* (Sept. 7-12, Oleron Island, France).
[8] Blin-Simiand N, Pasquiers S, Jorand F, Postel C and Vacher J-R 2009 *J. Phys. D : Appl. Phys.* **42** 122003 (5pp).
[9] Blin-Simiand N, Pasquiers S, Jorand F, Magne L and Postel C, 2010 *Proceedings of ISNTP-7* (June 21-25, St. John's, Newfoudland, Canada).
[10] Blin-Simiand N, Jorand F, Magne L, Pasquiers S, Postel C, and Vacher J-R 2008 *Plasma Chem. Plasma Proc.* **28** 429.
[11] Herron J 1999 *J. Phys. Chem. Ref. Data* **28** 1453.
[12] Magne L, Pasquiers S, Gadonna K, Jeanney P, Blin-Simiand N, Jorand F, and Postel C 2009 *J. Phys. D : Appl. Phys.* **42** 165203 (17pp), and references therein.
[13] unpublished results.
[14] Penetrante B, Hsiao M, Bardsley J, Merritt B, Vogtlin G and Wallman P 1996 *Pure Appl. Chem.* **68** 1083.
[15] Jarrige J, Blin-Simiand N, Jorand F, Magne L, Pasquiers S and Postel C 2005 *Proceedings of 17th ISPC* (August 7-14, Toronto, Canada).
[16] Yan K, van Heesch E, Pemen A, and Huijbrechts A 2000 *Plasma Chem. Plasma Proc.* **21** 107.
[17] IUPAC Subcommittee on gas Kinetic Data Evaluation. http://www.iupac-kinetic.ch.cam.ac.uk/
[18] Magne L, Pasquiers S, Blin-Simaind N and Postel C 2007 *J. Phys. D: Appl. Phys.* **40** 3112

PLASMA STERILIZATION FOR BACTERICIDAL SOIL CONDITIONING

Joanna Pawłat[1], Henryka Danuta Stryczewska[1], Kenji Ebihara[2], Fumiaki Mitsugi[3]

[1] *Faculty of Electrical Engineering and Computer Science Lublin University of Technology Nadbystrzycka Street 38A 20-618 Lublin Poland*
[2] *Environment and Energy Laboratory Ohtemon 1-4-15-404 Chuouku Fukuoka City Fukuoka 810-0074 Japan*
[3] *Graduate School of Science and Technology Department of Electrical and Computer Engineering Kumamoto University Kurokami 2-39-1 Kumamoto 860-8555 Japan*
E-mail: askmik@hotmail.com

This work presents ozone generating system with screw type barrier discharge and surface discharge ozonizers. Set-up was developed exquisitely for the soil conditioning purposes. The gaseous ozone injection system consisted of 10 electrodes and the treatment container for sterilizing of agricultural soil in large volumes. The results of ozone soil treatment for pathogenic *Fusarium oxysporum* are introduced. The destructive influence of ozone on λ-*E.Coli* DNA is presented.

1. Introduction

Anti-microbial properties of plasmas in the case of decontamination of water, ambient air and surfaces were previously widely proven [1-9]. To protect crops and food from the bactericidal, fungal and viral infections usage of ozone was investigated by many research groups.
Pollutants might be distributed in soil in several ways: in soil matrix, vapor phase, non-aqueous phase, or groundwater [10]. Ozone based techniques are good alternative to the traditional techniques like heating, flushing with chemical additives, landfilling, incineration, etc. Benefits of ozone applications in agriculture might be summarized as follows:
-use of ozone in soil treatment will not result in the build-up of any environmentally persistent or toxic compounds but ozone itself and O3 is immediately consumed in the soil treatment process.
-ozone is manufactured on site so it cannot be stored and its sudden release to the atmosphere is not possible like it could occur with compressed methyl bromide or other persistent toxic gases or chemicals used for soil sterilization.
-minimum human toxicity.

2. Experimental Set-up

The soil sterilization system was using high concentration of ozone generated in two types of ozonizers: barrier discharge screw type electrode ozonizer of applied voltage ranging 1.7–5.5 kV [11,12], and TiO_2 based surface discharge commercial OP-20W Iwasaki ozonizer. Ozone generators are presented in Fig. 1A and Fig. 1B, respectively. Ozone generation set-up is depicted in Fig. 1C.
Gaseous ozone injection field-scale system is shown in Fig. 2A. It consisted of 10 electrodes and the treatment container, which was developed for sterilizing and monitoring of agricultural soil in large volume. The pH value, electrical conductivity and temperature of the soil were observed to investigate the effect of ozone treatment on soil properties. Fig. 2B depicts the set-up used for the sterilization of *Fusarium oxysporum* and other microorganisms.
Fusarium fungal species are widely distributed in soils and organic substrates. Deep sowing makes germinating seeds prone to fungal infections, in particular, at the earliest stages of seed germination, when intensive structural and metabolic changes are involved in embryo activation [13, 14].
Fusarium oxysporum colonizes plants through the roots causing vascular wilt, leaf spots, pre-emergent sprout root rot and post-emergent seedling rot in more than 100 species of plants like tomatoes, bananas, melons, asparagus, basil, etc. [15, 16] affecting them worldwide, especially in elevated temperature zones [17]. The fungus can attack both: plants' seedlings in the transplant house and

mature plants in the field. Of the soil-borne diseases *Fusarium* wilt is the most serious in hydroponic cultivation systems.

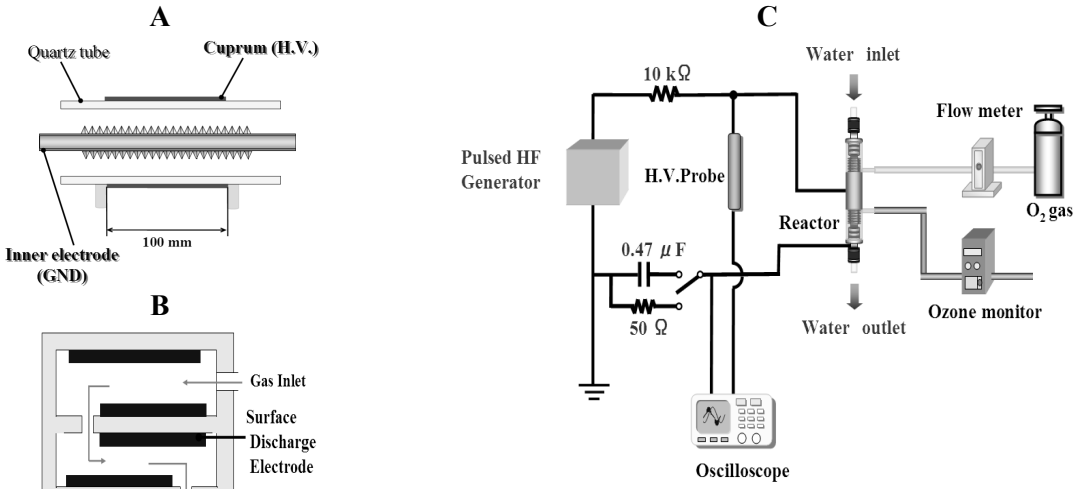


Fig. 1. Ozone generators used in the soil sterilization system: screw type electrode (A), OP-20W surface discharge electrode (B), experimental set-up (C).

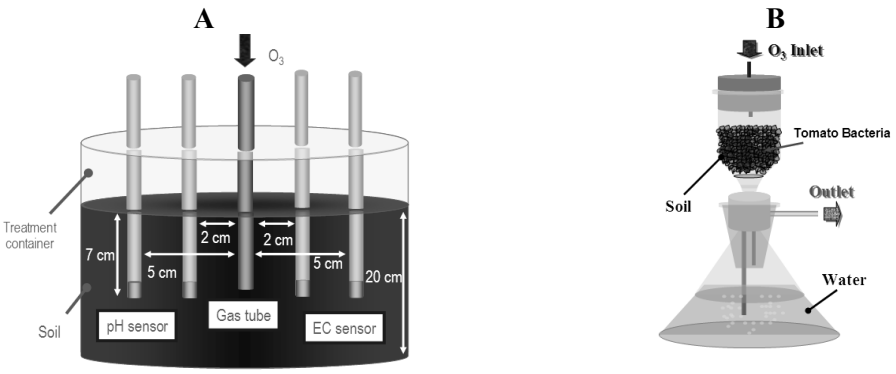


Fig. 2. Experimental set-up for general soil treatment: multi-electrode injection system (A), set-up for sterilization of tomato bacteria (B).

Fusarium species produce secondary metabolites caused mycotoxins. They cause a toxic response termed a mycotoxicosis, when ingested by higher vertebrates and other animals. It can lead to the deterioration of liver or kidney function [18]. Damages caused by main mycotoxins produced by Fusarium are summarized in Tab. 2.

Tab. 2. Fusarium mycotoxines.

Mycotoxins	Risk	References
trichothecenes	Immunotoxic, cytotoxic to mammalian cells, increase the risk of other microbial infections, potent inhibitors of protein synthesis known to cause alimentary toxic aleukia, fusariotoxicoses.	[18-20]
fumonisins	hepatotoxic and hepatocarcinogenic in rats, inhibitors of sphingolipid biosynthesis, carcinogenic (associated with an increased risk of human oesophageal cancer)	[18, 21-25]

There are several traditional methods used in prevention of *Fusarium*-caused infections:
-chemical fumigation (one of the basic fumigants: methyl bromide has been banned worldwide since 2005 due to its environmental risk) [26-28],

-biological suppression (screening and planting resistant cultivars, grafting, intercropping, using antagonists, compost amendment) [29, 30],
- physico-chemical methods: ozone, H_2O_2, UV treatment, soil heating, solarization [31-34].

3. Results and Discussion

The voltage-current characteristics obtained in screw type electrode ozonizer with moderate number of microdischarges to be spotted [35] are depicted in Fig. 3A. Ozone concentrations in dependence on applied voltage and oxygen flow rate are presented in Fig. 3. B. Ozonizer was able to provide high ozone concentration (23 g/m^3) with high efficiency (100 g/kW h).

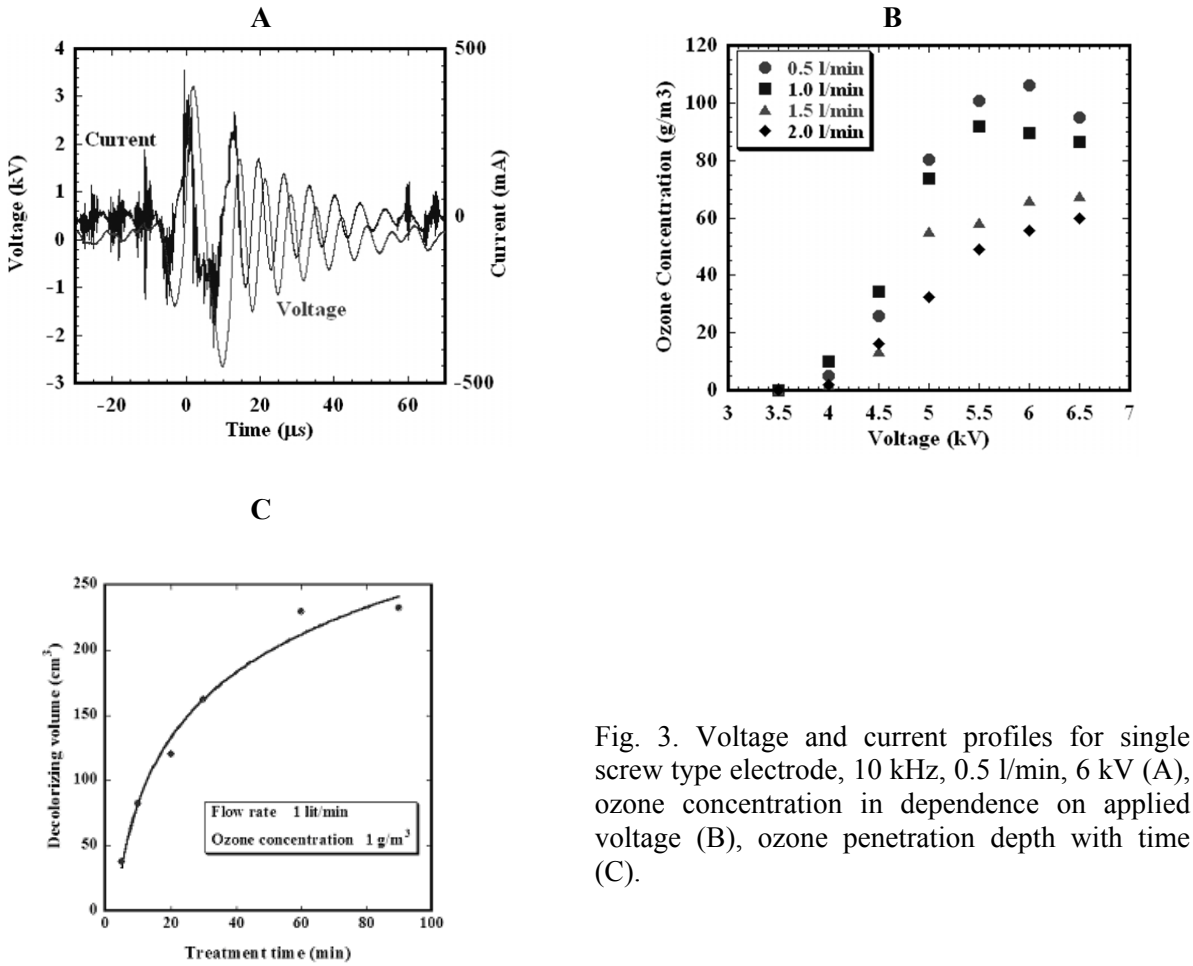


Fig. 3. Voltage and current profiles for single screw type electrode, 10 kHz, 0.5 l/min, 6 kV (A), ozone concentration in dependence on applied voltage (B), ozone penetration depth with time (C).

Experiment with ozone penetration depth, which based on discoloring of indigo with ozone to colorless isatin was performed [35]. It was proven that ozone can spread out to a diameter of 8 cm during 60 min of treatment at 1 l/min of gas flow and ozone concentration of 1 g/m^3. The discolored volume in dependence on treatment time is shown in Fig. 3C.

Tab. 1. Soil sterilization effect on *Fusarium oxysporum* by in-situ ozone treatment.

Ozone concentration (g/m^3)	Flow rate (lit/min)	Treatment time (min)	Dosage (g)	Sterilization rate (%)
0	3	10	0	22.80
10		10	0.3	97.54
20		10	0.6	99.91
40		10	1.2	100.0
38		60	6.84	100.0
38.5		60	6.93	100.0

Ozone sterilization effect on Fusarium oxysporum is summarized in Tab.2.
Conventional biological method of the CFU (colony forming unit) counting showed that bacteria and *Fusarium oxysporum* in the soil were almost eliminated by ozone treatment with the concentration over 20 gO_3/m^3, achieving sterilization rate up to 99.9%. Sterilization requires ozone dosage over 0.6 g for the 50g soil.
0.46 μg/μl of λ-*E.Coli* DNA (Nippon Gene) was diluted with 10 mM Tris-HCL (pH 7.9) and 1.0 M EDTA. The DNA solution was further diluted with 0.5 ml distilled water in a microcentrifuge tube. A stream of oxygen containing 5% wt. ozone was bubbled into the microcentrifuge tube containing the DNA solution. 0.2-1 g of ozone of was supplied to 0.5 ml of DNA solution during 5-20 min of treatment at 0.5 l/min gas flow rate.
Before and post-ozone treatment DNA samples were prepared on the mica substrates. The DNA solution of 10 μl was dropped on the mica substrate and was dried in the chamber at reduced pressure and room temperature.

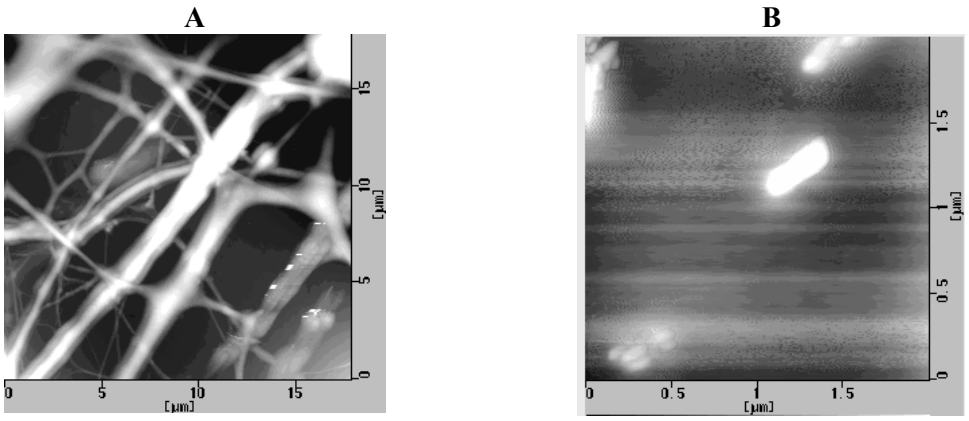


Fig. 4. Sample of DNA *E.coli* (AFM 48 502 base pair 16μm) before ozonation (A), and after 5 min ozonation (B).

Prepared samples were analyzed by Atomic Force Microscopy (AFM) [36] after various treatment times. Fig. 4A depicts the image of DNA sample deposited on the mica substrate. It was found that there were many kinds of structures depending on the location and localized conditions (such as DNA condensation). The molecular structure of DNA collapsed completely when high concentration of ozone was introduced into the DNA solution. The image of the DNA sample which was treated during 5 min is presented in Fig. 4B. It indicated that ozonation process broke the *E. coli* DNA and split it into many fragments (small rectangular pieces distributed on the surface). The typical length and width ranged 380-390 nm and 15 nm, respectively. These peculiar pieces have almost been not observed when the DNA samples were treated for 10 and 20 min that suggests that DNA was decomposed completely.

4. Conclusions

The set up for agricultural microbial ozone sterilization purposes, which based on two types of ozonizers was developed.
It was possible to achieve 99.9% sterilization efficiency in the case of *Fusarium oxysporum* at the ozone dosage over 20 gO_3/m^3.
The fundamental experiments on biological reaction between the λ-*E.Coli* DNA and ozone exposure suggested that the molecular structure of the DNA collapsed completely using 5% wt. ozone concentration.

5. References

[1] Menashi W Treatment of surfaces 1968 *US Patent* 3 383 163.
[2] Pierpoint A Hapeman C Torrents A 2003 *Chemosphere* **50(8)** 1025-1034.

[3] Kamgang-Youbi G Herry J Bellon-Fontaine M Brisset J-L Doubla A Naïtali M 2007 *Appl Environ Microbiol* **73(15)** 4791-4796.

[4] Moisan M Barbeau J Moreau S Pelletier J Tabrizian M Yahia L2001 *Int J. Pharm.* **226** 1-21.

[5] Miller C Valentine R Roehl M Alvarez P 2008 *J. Hazard. Mat.* **158(2-3)** 478-484.

[6] Moreau M Feuilloley M Orange N Brisset J-L 2005 *J. Appl. Microbiol.* **98** 039-1046.

[7] Machala Z Jedlovský I Chládeková L Pongrác B Giertl D Janda M Šikurová L Polčic P 2009 *Eur. Phys. J.* **D 54** 195-204.

[8] Kamgang-Youbi G Herry J Meylheuc T Brisset J-L Bellon-Fontaine M Doubla A Naı¨tali M 2008 *Let. Appl. Microbiology* **48(1)** 13-8.

[9] Deng S Cheng C Ni G Meng Y Chen H 2010 *Current Appl. Phys.* **10(4)** 1164-1168.

[10] Volkering F Breure A Rulkens W 1997 *Bioremediat. Rep.* **86** 401-417.

[11] Ebihara K Sugimoto S Ikegami T Mitsugi F Stryczewska H 2008 *Proc ELMECO-6 Naleczow, Poland* 24-28.

[12] Stryczewska H Ebihara K Takayama M Gyoutoku Y Tachibana M 2005 *Plasma Process. Polym.* **2** 238-245.

[13] Morkunas I Bednarski W Kozłowska M 2004 *Plant Physiology and Biochemistry* **42** 493–499.

[14] Srobarova A Pavlov A 2002 *J. Appl. Genet.* **43A** 193–196.

[15] Agrios G 2005 *Plant Pathology (5th ed)* Academic Press San Diego USA.

[16] Van Hemelrijck W Wouters P Brouwer M Windelinckx A Goderis I De Bolle M Thomm B Cammue B Delauré S 2006 *Plant Science* **171(5)** 585-595.

[17] Windels C 2000 *Phytopathology* **90** 17–21.

[18] Sweeney M Dobson A 1998 *Int. J. Food Microbiology* **43** 141–158.

[19] Prelusky D Rotter B Rotter R 1994 *Toxicology of mycotoxins In: Mycotoxins in Grain Compounds other than Aflatoxins* Egan Press St. Paul Minn 359–403.

[20] Pestka J Bondy G 1994 Immunotoxic effects of mycotoxins *In: Mycotoxins in Grain Compounds other than Aflatoxins* Egan Press St. Paul Minn 339–359.

[21] Gelderblom W Snyman S Abel S Lebepe-Mazur S Smuts C Van der Westhuizen L Marasas W Victor T Knasmuller S Huber W 1996 *Hepatotoxicity and carcinogenicity of the fumonisins In: Fumonisins in Food Advances in Experimental Medicine and Biology* **392** Plenum Press NY 279–296.

[22] Sydenham E Thiel P Marasas W Shephard G Van Schalkwyk D Koch K 1990 J. Agric. Food Chem. **38** 1900–1903.

[23] Merril A van Echten G Wang E Sandhoff K 1993 *J. Biol. Chem.* **268** 27299–27306.

[24] Riley R Wang E Schroeder J Plattner R Abbas H Yoo H Merril A 1996 *Nat. Toxins* **4** 3–15.

[25] Chu F Li G 1994 *Appl. Environ. Microbiol*. **60** 847–852.

[26] Song W Zhou L Yang C Cao X Zhang L Liu X 2004 *Crop Protection* **23** 243–247.

[27] Shi K Wang L Zhou Y Yu Y Yu J 2009 *Chemosphere* **75** 872–877.

[28] Stolarski R Bojkov R Bishop L Zerefos C Staehelin J Zawodny J 1992 *Science* **256** 342–349.

[29] Baysal O Çaliskan M Yesilova O 2008 *Physiological and Molecular Plant Pathology* **73(1-3)** 25-32.

[30] Ren L Su S Yang X Xu Y Huang Q Shen Q 2008 *Soil Biology & Biochemistry* **40** 834–844.

[31] Onishchenko A Kamardin I Radjabov A Avtonomov T Golota V Ibragimov V Taran P 2005 *Химическая и биологическая безопасность* **6** 26-34.

[32] Golota V Dindorogo V Zavada L Kyrychenko V Petrenkova V Pugach S Sukhomlin E Taran G 2004 Proc. *4th International Symposia on Ozone Applications* Cuba.

[33] Morar R Munteanu R Simion E Munteanu I Dascalescu L1999 *IEEE Transactions on Industry Applications* **35(1)** 208-212.

[34] Gullino M Minuto A Garibaldi A 1998 Crop Protection **17(6)** 497

[35] Takayama M Ebihara K Stryczewska H Ikegami T Gyoutoku Y Kubo K Tachibana M 2006 *Thin Solid Films* **506-507** 396 – 399.

[36] Shubo H Ralin D Jun W Xin L Zhou F 2003 *Langmuir* **19** 8943-8950.

OXIDATION OF METHANE IN HE/CH_4/CO_2 MIXTURES: EXPERIMENTAL RESULTS AND ELECTRON KINETICS

N. Pinhão, A. Janeco and J. Branco

ITN – Nuclear and Technological Institute, Estrada Nacional 10, 2686-953, Sacavem, Portugal
E-mail: npinhao@itn.pt

The impact of adding helium to CH_4/CO_2 mixtures used for the production of *Syngas* in a dielectric barrier discharge is discussed. Helium was found to have a major impact on the value of breakdown voltage, conversion values for CH_4 and CO_2, on the rate of increase of conversion with the specific input energy but almost no impact on selectivities. The experimental results are interpreted on the basis of electron kinetics results in these mixtures.

1. Introduction

The use of non-thermal plasmas in the production of hydrogen, *Syngas*, and more complex hydrocarbons from methane mixtures is an interesting alternative to conventional processes [1]. The most common oxidants used with methane are O_2 and CO_2 [2].
We recently reported good conversion and selectivities values using $He/CH_4/O_2$ and $He/CH_4/CO_2$ mixtures in a dielectric barrier discharge – catalyst reactor [3,4]. It was shown that helium has a significant impact on those results, the first evidence of this being a large reduction of breakdown voltage with an increase in helium concentration.
For a fixed input gas composition, the conversion increases linearly with the specific input energy (SIE = Electric Power Supplied / Gas Flux). An increase in helium concentration leads to a significant increase in the rate of increase of conversion with SIE and in the maximum values of conversion attainable for CH_4 and the oxidant used. In spite of the reduction of total CH_4 and CO_2 input with the increase in helium concentration, the increase observed in conversion of these gases was sufficient to compensate for this reduction. The total amount of methane and carbon dioxide converted actually increases with helium concentration.
However it was also found that helium concentration had minimum or no impact on selectivities.
Although a full kinetic model is necessary to understand the details of the discharge in these mixtures, the study of electron kinetics provides useful information on the discharge. In this paper we discuss how the electron kinetics results reported recently [5] contribute to the interpretation of the experimental results observed in $He/CH_4/CO_2$ mixtures.

2. Experimental Set-up

The results were obtained with a cylindrical geometry chamber built from a glass tube covered by a thin aluminium foil, acting as ground electrode, and a central stainless steel AC electrode. The chamber has a porous glass on one end to support a catalyser. In this paper we focus on results obtained without catalyser.
Mixtures of $He/CH_4/CO_2$, where the helium concentration varied between 50-95% were studied. Most of the results were obtained with a $R=[CH_4]/[CO_2]$ ratio of 1.0 and indicated when otherwise. The total gas flow was controlled with standard mass flow controllers ranging from 2 to 6 L/h.
The AC power supply allowed a maximum rms voltage of 10 kV with a frequency range of 4-6 kHz. The Specific Input Energy (SIE) consumed in the discharge systems was measured using both the conventional Lissajous method and a combination of alternative methods [6].
The output gas composition was analyzed online by gas chromatography using a thermal conductivity detector. Furter details of the experimental set-up can be found in [3].

3. Experimental Results

The analysis of the experimental results was based on modified conversion and selectivities ratios defined below as:

The conversion ratio for gas X is defined as the ratio

$$C_X = \frac{\alpha_Q [X]_{\text{in}} - [X]_{\text{out}}}{\alpha_Q [X]_{\text{in}}} \quad (1)$$

where α_Q is the ratio between the fluxes of gas entering and exiting the reaction chamber. This definition generalizes the expression commonly found for the definition of conversion, taking into account that reactions change the number of molecules, thus changing the concentration of the input gases even if they do not react. If pressure is kept constant the change in the number of molecules translates to a change in the flux exiting the chamber. The ratio of fluxes, α_Q, corrects the input concentration for this effect.

We define the selectivity for gas X based on carbon atoms as

$$S_X^{[C]} = \frac{\beta_X [X]_{\text{out}}}{\sum_r \beta_{Y_r} (\alpha_Q [Y_r]_{\text{in}} - [Y_r]_{\text{out}})} \quad (2)$$

where the sum is on all reactants, Y, with carbon atoms and β the number of carbon atoms in the given species. Selectivities based on hydrogen or oxygen atoms are defined in a similar way.

In this paper we focus our attention on the conversion rates for CH_4 and CO_2 and on the selectivities for H_2 and CO production. However in all the mixture studies we have also detected the production of C_2H_4 and C_2H_6 compounds with selectivity between 0.1% and 10%, and of water vapour.

Figure 1 shows the results on conversion (a,b) and selectivity (c,d) for several values of helium concentration.

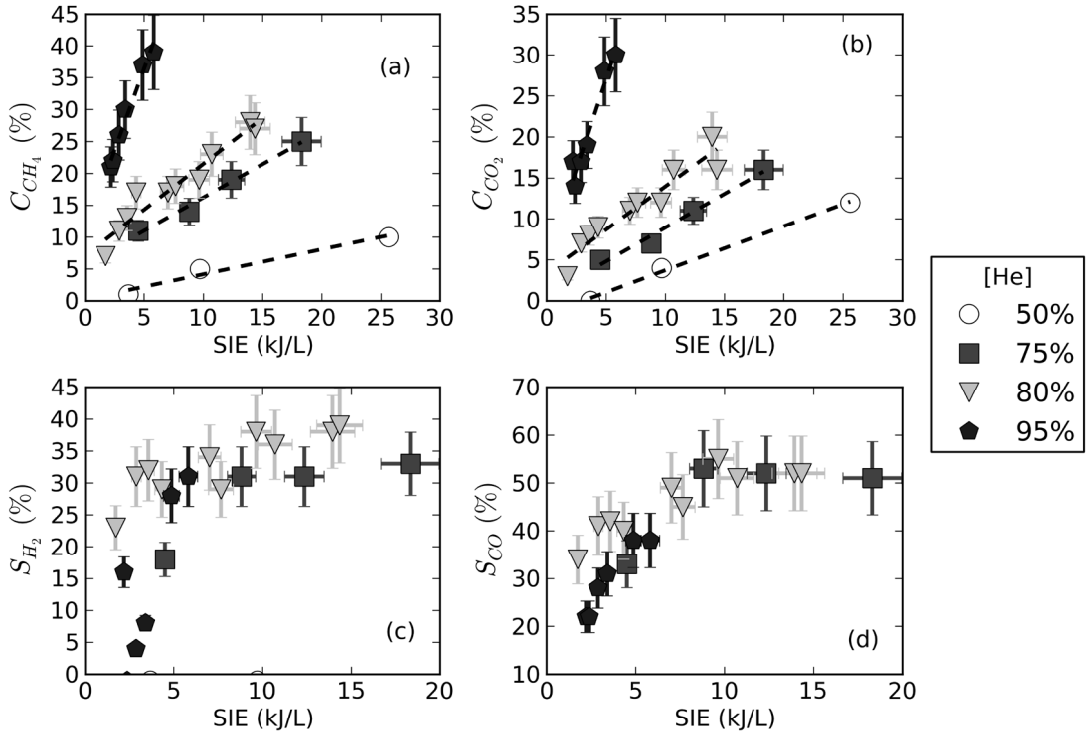


Fig. 1. Variation of conversion or selectivity in $He/CH_4/CO_2$ mixtures with R=1, as a function of the specific input energy supplied to the reactor, for different helium concentrations: (a) conversion of CH_4, (b) conversion of CO_2, (c) H_2 selectivity based on H atoms and, (d) CO selectivity based on C atoms.

The conversion values increase linearly with SIE but mixtures with higher helium concentration show a much faster increase. The values of selectivity start with an increase in SIE but reach a constant value at 10 kJ/L and, in the range of parameters studied these values are practically independent of helium concentration.

For higher values of SIE the development of a thermal instability makes the discharge unstable and leads to the formation of an arc.

4. Electron Kinetics

The electron kinetics in these mixtures was studied solving the Boltzmann equation for an electron swarm in the hydrodynamic regime. The method used is an integral method [7] for the angular dependency of the distribution function equivalent to other multiterm methods. The cross sections for He and CO_2 were taken from [8] while methane cross sections were updated with recent results [9,10] and adjusted to swarm data [5]. The final set includes the momentum transfer cross section, two cross sections for vibrational excitation of modes $\nu_2 + \nu_4$ and $\nu_1 + \nu_3$, the dissociation cross sections for the formation of CH_3 , CH_2 and CH radicals, the formation of H^- and CH_2^- negative ions, and CH_4^+, CH_3^+, CH_2^+, CH^+, C^+, H^+ and H_2^+ ions.
The results were obtained for mixtures $He/CH_4/CO_2$ in the same range of composition of the mixtures used for the experimental measures and a reduced electric field, E/n, ranging from 0.5 Td to 500 Td. However we must be cautious when using these results to interpret the experimental results as the actual composition of the gas mixture in the chamber when the discharge is active is presently unknown.

The presence of helium is responsible for a large shift in the electron energy distribution function (*eedf*) to higher values and a large increase in the rate coefficients for excitation, dissociation and ionisation of CH_4 and CO_2. At the same time the excitation and ionisation rates for helium are much smaller in the mixtures than in pure helium.

5. The effective ionisation coefficient and the breakdown voltage

The increase in helium concentration leads to a shift in the ionisation and attachment coefficients curves to lower E/n values (Fig 2).
The E/n value where the condition $\alpha/n = \eta/n$ is fulfilled decreases from approximately 80 Td to approximately 25 Td when the helium concentration changes from 0% to 80%. The consequence of this decrease is a marked reduction in breakdown voltage with helium concentration.

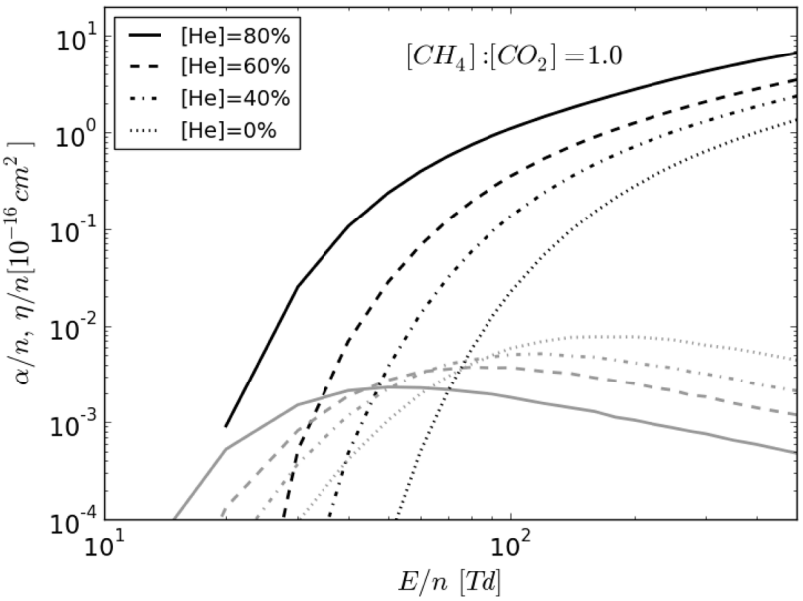


Fig. 2. Ionisation and attachment coefficients in $He/CH_4/CO_2$ mixtures with R=1 as a function of E/n for different helium concentrations. Black lines: ionisation coefficient, α, grey lines: attachment coefficient, η.

Assuming that the discharge starts as a Townsend avalanche, the breakdown voltage can be estimated from the condition for self-sustainment in inhomogeneous fields:

$$\int_{r_0}^{r_M} [\alpha(E(r)) - \eta(E(r))]\, dr = \ln(1 + \frac{1}{\gamma}) \quad (3)$$

where r_0 and r_M are the limits for propagation of the discharge, E(r), the electrical field, α and η, the ionisation and attachment coefficients and γ, the secondary emission coefficient..

Solving (3) for our conditions, mixtures with ratios R = 1 and two values of γ, we can compare (Fig 3) the forecast of this simple model with the experimental values of breakdown voltage obtained from the Lissajous figures for measurement of the power consumption in the discharges.

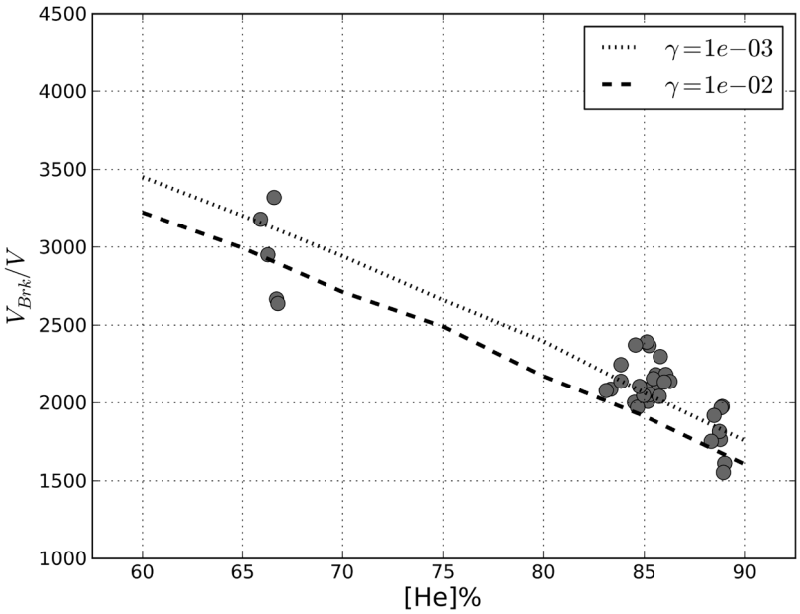


Fig. 3. Variation of the breakdown voltage with helium concentration in mixtures $He/CH_4/CO_2$ for two values of secondary emission coefficient, γ. Lines: values computed using equation (3) for mixtures with R=1. Points: experimental values for mixtures with 0.3 < R < 4.

The figure includes experimental points with different values of R. However it was observed that this ratio has a small influence on the breakdown voltage. We observed that for the same input gas composition, the breakdown voltage depends on SIE. Together with experimental uncertainties this justifies the spread in experimental points.

Taking into account that the experimental values were obtained with a stable discharge where the gas composition is different than the one in the model, the agreement is satisfactory.

6. The collision frequencies and the conversion and selectivity values

To analyse the effect of helium concentration on the discharge we have to consider both the increases in the rate coefficients for excitation and ionisation processes in CH_4 and CO_2 and the decrease of concentration of these gases. The density normalized collision frequencies ($\nu_i^{[X]}/n = [X]k_i$) are the parameters used in this case. Figure 4 shows the normalized collision frequencies for processes in the three gases. Each curve shows results for a class of processes (vibrational excitation, electronic excitation, ionisation or attachment).

As a result of the shift of the *eedf* to higher energies with helium, and in spite of the reduction of CH_4 and CO_2 concentration, the maximum values of the collision frequencies for electronic excitation in these gases are roughly constant while an increase in the ionisation frequencies is observed. The curves shift to lower E/n values and becomes steeper.

These results not only explain the observed increase in CH_4 and CO_2 conversion rates but indicates an increase of the total CH_4 and CO_2 processed for the range of helium concentrations measured.
Vibrational excitation and attachment CH_4 and CO_2 have a negative impact on the discharge efficiency as they are either channels of energy loss or the formation of negative ions. The frequencies for these processes decrease with helium concentration.

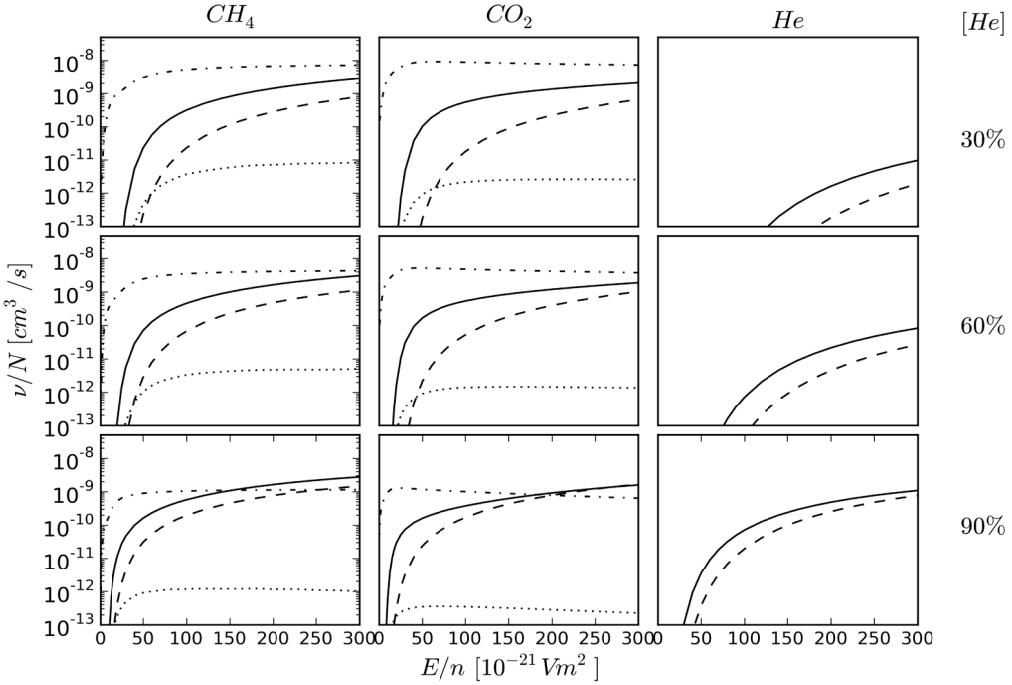


Fig. 4. Density normalized collision frequencies for each gas in $He/CH_4/CO_2$ mixtures with R=1 as function of the reduced field and three helium concentrations. Lines: dash-dot: sum of vibrational processes; solid: sum of electronic excitation processes; dashed: sum of ionisation processes; dotted: sum of attachment processes.

Finally, except for the highest values of helium concentration, the collision frequencies for processes in helium are much smaller than in the other two gases indicating that helium excited states and ions have a minimal or no role in the discharge. This explains why selectivities are not influenced by helium concentration.

Acknowledgment. We acknowledge financial support from FCT under research contract PTDC/EQU-EQU/65126/2006. Thanks are due to D.S. Baracol for revision work.

7. References

[1] A. Indarto, J. Choi, H. Lee, and H. Song, *Journal of Natural Gas Chemistry*, **15** (2006) 87-92
[2] Pietruszka, Barbara and Heintze, Moritz, *Catalysis Today*, **90** (2004) 151-158
[3] N.R. Pinhão, A. Janeco, A.C. Ferreira, and J.B. Branco, *Proc. ISPC 19*, Bochum, (2009), edited by A. von Keudell, J. Winter, M. Böke, V. Schulz-von der Gathen, URL: www.ispc-conference.org
[4] N.R. Pinhão, A. Janeco, A.C. Ferreira, and J.B. Branco, *Proc. XX ESCAMPIG*, Novi Sad, (2010)
[5] N.R. Pinhão, M. Vranic, *Proc. XX ESCAMPIG*, Novi Sad, (2010)
[6] A. Janeco, N. R. Pinhão, J. B. Branco, A. C. Ferreira, *Proc. ISPC 19*, Bochum, (2009), edited by A. von Keudell, J. Winter, M. Böke, V. Schulz-von der Gathen, URL: www.ispc-conference.org.
[7] P. Segur, M. Yousfi and M.C. Bordage, *J. Phys. D: Appl. Phys.* **17** (1984) 2199-2214
[8] A.V. Phelps, http://jilawww.colorado.edu/\texttildelow avp/collision_data
[9] P. Rawat et al. *Int. J. Mass Spectrometry* **277** (2008) 96–102
[10] D.A. Erwin and J.A. Kunc *J. Appl. Phys.* **103** (2008) 064906

REMOVAL OF ORGANIC POLLUTANTS FROM WATER USING NON-THERMAL PLASMA

Daniela Piroi[1], Monica Magureanu[1], Nicolae B. Mandache[1], Vasile Parvulescu[2]

[1] *National Institute for Lasers, Plasma and Radiation Physics, Department for Plasma Physics and Nuclear Fusion, Bucharest-Magurele, Romania*

[2] *University of Bucharest, Faculty of Chemistry, Department for Chemical Technology and Catalysis, Bucharest, Romania*

E-mail: monimag@infim.ro

The decomposition of methylene blue (MB) in aqueous solution was studied using a dielectric barrier discharge operated in pulsed regime. The discharge was generated at the gas-liquid interface. Oxygen was used as working gas. Two discharge geometries were investigated: a coaxial configuration (DBD) and a packed-bed configuration (PB). The comparison showed that faster degradation and higher energy efficiency for the dye degradation were achieved in the DBD configuration. MB degradation obeys a first order kinetics. The best degradation yield at 90% MB conversion was 52 g/kWh. Faster MB decomposition could be obtained by increasing the pulse repetition rate, and implicitly the average power introduced in the discharge, however, this did not improve the decomposition yield. Measurements of the ozone concentration in the effluent gas showed that ozone plays a considerable role in the decomposition of MB, but is less important for the further degradation of reaction products resulting from MB oxidation.

1. Introduction

Removal of organic dyes from waste water has received considerable attention in the last years due to the increasing environmental problems they generate. These problems are related on one hand to the physical and chemical properties (colour, toxicity, etc) of the dyes themselves and on the other hand to the formation of other dangerous by-products by chemical reactions which take place in water [1,2].

Physical techniques can generally be used successfully for dyes removal [3], however they only transfer the organic pollutants from water to solid phase, requiring therefore post-treatment of solid wastes and regeneration of the adsorbent materials [1].

Biological methods are usually ineffective for dyes removal, which is mainly due to the stability of most dyes [1]. In addition, biological degradation requires high reaction volumes as well as long treatment times. Another drawback is that most dyes are not destroyed, but adsorbed by bacteria [1,2].

Advanced oxidation processes (AOPs) have been investigated for the degradation of organic pollutants in water, having as objective either complete mineralization or partial degradation of the compounds in order to make the effluent more amenable to conventional treatment. AOPs are aimed at in situ generation of strong oxygen-based oxidizers, such as hydroxyl radicals, ozone, atomic oxygen, hydrogen peroxide, etc. Especially the formation of OH radicals is desired since they are among the strongest oxidizers and react non-selectively with a broad range of organic compounds.

Among the advanced oxidation processes, electrical discharges in water [4–7] or at the water-gas interface [8–14] have been investigated for the degradation of various organic compounds, including organic dyes [2,6,7,10,12,14]. The formation of OH radicals and atomic oxygen was evidenced by spectroscopic investigations of the light emitted by the plasma [4,8,15]. The generation of ozone and hydrogen peroxide was studied as well [5,16-18].

In the present work the degradation of methylene blue (MB) in aqueous solution was studied using a pulsed dielectric barrier discharge. The discharge was generated at the interface between gas and liquid. Two geometries of the plasma reactor were investigated: a coaxial configuration and a packed-bed configuration. They were compared with respect to the energy efficiency for the dye degradation. The formation of ozone in the discharge as well as its effect on MB decomposition was also addressed.

2. Experimental

The coaxial geometry (DBD) was described in detail in [13,14] and is shown in Fig. 1. Briefly, the plasma reactor was a quartz tube of 19 mm inner diameter, with the outer electrode consisting in a

silver layer of 10 cm length on the outside of the tube and the inner electrode made of metal mesh shaped as a cylinder with a diameter of 16 mm.

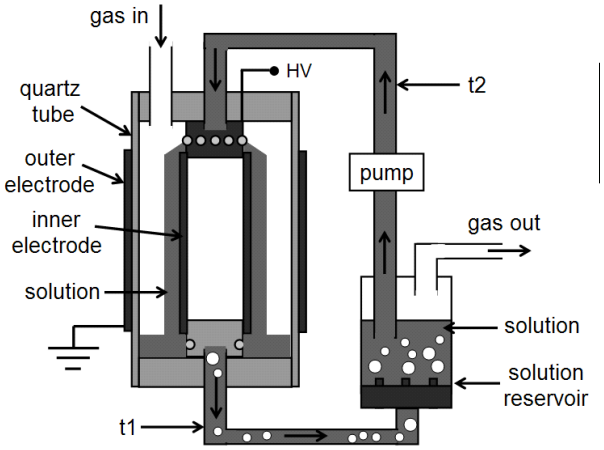


Fig. 1. Experimental set-up: discharge reactor in coaxial geometry.

The dye solution was circulated by a peristaltic pump with a flow rate of 50 mL/min and was made to flow as a film on the surface of the inner electrode, passing through several holes at the top, and out of the reactor through a tube at the bottom (t1), which returns it to the solution reservoir. Oxygen was introduced through a separate entrance in the upper lid of the reactor with a flow rate of 600 sccm. After passing through the plasma reactor the effluent gas containing ozone generated in the discharge exits through the same tube as the liquid and is bubbled through the rest of solution in the reservoir, in order to allow ozone to react with the pollutant molecules in the reservoir.

The packed-bed (PB) reactor was a quartz tube of 30 mm inner diameter with the outer electrode of 15 cm length and the inner electrode of 22 mm diameter. The reactor was packed with quartz spheres of 2 mm diameter. The set-up for gas and solution flow was the same as described above.
In both configurations the discharge was initiated in the gas phase, in fact at the interface between the gas and the liquid.
The discharge was operated in pulsed mode. The inner electrode was connected at high voltage and the outer electrode was grounded. A d.c. high voltage generator (Spellman SL600) of negative polarity charges a capacitor of 2 nF, which is subsequently discharged by means of a rotating spark-gap switch (RSG). The RSG controls the repetition rate of the voltage pulses. The discharge voltage was measured by means of a high voltage probe (Tektronix P6015, 1000x, R_P = 100 MΩ) and the discharge current was determined from the voltage fall on a non-inductive shunt resistor (Rs = 3 Ω) connected in series with the outer electrode.
In each experiment the solution volume was 200 mL. Tap water was used in order to simulate a real situation. The initial solution conductivity was 775 mS/cm, and the pH was 7. The initial concentration of MB in solution was in most experiments 25 mg/L.
UV-visible absorption spectra of the aqueous solutions before and after plasma treatment were measured by a spectrophotometer (Varian Cary 100), in the wavelength range λ = 190–900 nm. According to the Beer–Lambert law, the absorbance is proportional to the concentration of absorbing molecules. The concentration of the dye in solution was determined from the absorption maximum at 660 nm, which was also used for the calibration curves.
The concentration of ozone in the effluent gas was measured by an ozone detector (Anseros Ozomat).

3. Results and discussion

Typical waveforms of the discharge voltage and discharge current are shown in Fig. 2a for the coaxial configuration and in Fig. 2b for the packed-bed configuration, with and without circulating water through the discharge reactor.
Voltage pulses with amplitudes of about 18 kV and short rise time were used. For coaxial geometry the voltage and current pulses have similar shapes when the discharge was operated without circulating water through the reactor (in oxygen) and when water was introduced. The current pulses had amplitudes of 65-70 A and durations of about 33 ns (FWHM). Similar values were obtained also when the MB solution was circulated through the reactor. For the packed-bed geometry the current pulses had about 70 A amplitude and shorter duration (19 ns) in the absence of water. When circulating water through the discharge reactor, the amplitude of the current pulses was also slightly higher and a widening of the pulses to 31 ns FWHM was observed. In the presence of MB solution a further increase in the current amplitude was observed.

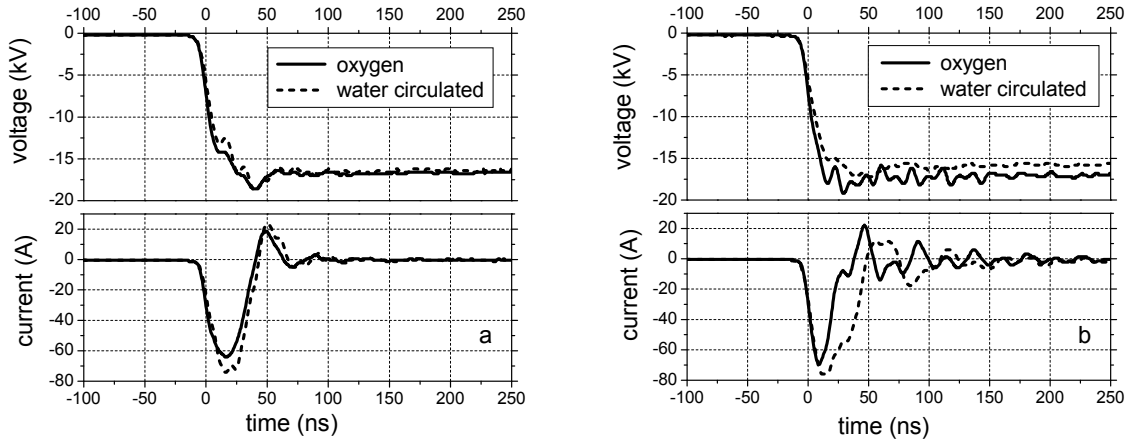


Fig. 2. Typical waveforms of the discharge voltage (upper graphs) and discharge current (lower graphs) for the coaxial geometry – (a), and for the packed bed geometry – (b).

The energy per pulse was calculated by integrating the product of discharge voltage and current over time. For the coaxial configuration the energy per pulse was around 30 mJ. For the packed-bed geometry the energy per pulse was 20 mJ in the absence of solution and almost twice this value (38 mJ) when the MB solution was circulated through the reactor. The pulse repetition rate was varied in the range 30-50 Hz, therefore the average power dissipated in the discharge was below 2 W in all situations and cooling of the reactor was nor necessary.

Since oxygen was used as working gas, one of the major oxidisers generated in the discharge was ozone. Fig. 3 shows the concentration of ozone detected in the effluent gas as a function of the average power dissipated in the discharge for both configurations investigated in the presence and in the absence of water circulation. The power was varied by changing the repetition rate of the pulses.

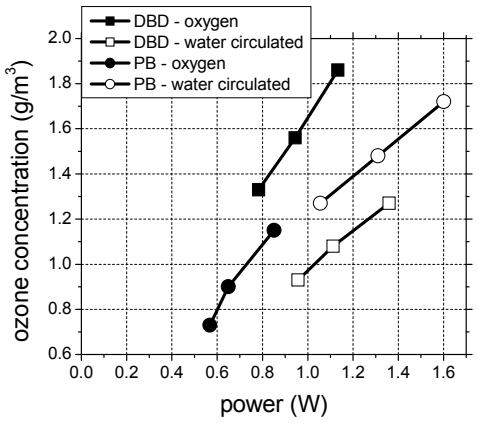


Fig. 3. Ozone concentration in the effluent gas for the coaxial geometry (DBD) and for the packed-bed geometry (PB) in the absence and in the presence of water circulation.

The highest O_3 concentration was detected for the DBD geometry operated in oxygen, without water circulation. When water was introduced a significant decrease in the O_3 amount was observed, from 1.33-1.86 g/m^3 to 0.93-1.27 g/m^3.

In the PB geometry water circulation did not have such an important influence on the concentration of O_3 in the effluent gas. In this case the O_3 concentration was higher than that obtained in DBD configuration, ranging between 1.27 and 1.72 g/m^3.

The degradation of MB was investigated for two values of the pulse frequency (30 Hz and 50 Hz), at constant applied voltage. In this way the average power dissipated in the discharge was varied between 0.9 and 1.45 W for the DBD geometry and in the range 1.2-1.9 W for the PB geometry. MB degradation obeys a first order kinetics. Fig. 4 shows the first order plots of MB degradation as a function of the treatment time in the discharge for both configurations investigated and both pulse frequencies used.

As expected, higher power led to faster decomposition of the dye. For 50 Hz pulse frequency, over 95% conversion was achieved after 8 min treatment, while for 30 Hz the time needed to reach this value was longer. It was also observed that MB was degraded faster in the coaxial configuration as compared to the packed-bed configuration regardless of the average power. For example, at 30 Hz after 8 minutes treatment the MB conversion was 97% in the DBD geometry and only 83.5% in the PB geometry, even if the power was slightly higher in the latter case. Similarly, at 50 Hz after 6

minutes treatment the MB conversion was 96% in the DBD geometry and 86% in the PB geometry.

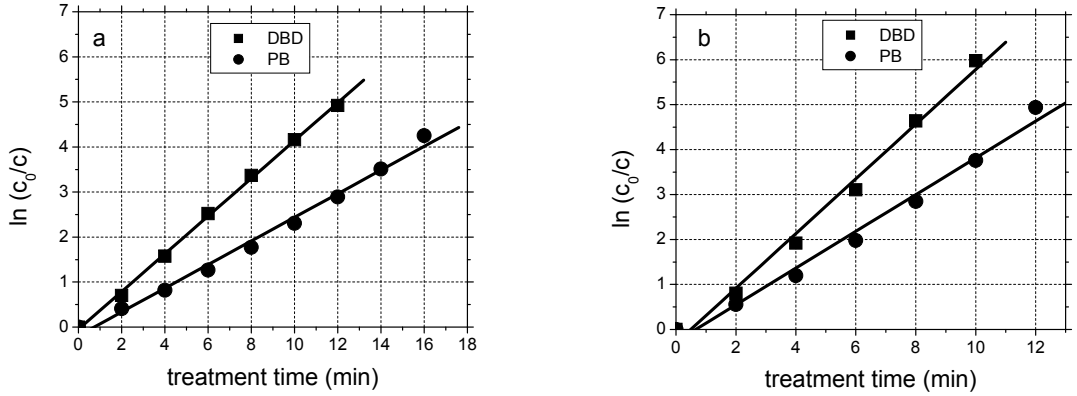


Fig. 4. The degradation of MB as a function of treatment time for the coaxial geometry (DBD) and for the packed-bed geometry (PB), for pulse frequency 30 Hz – (a) and 50 Hz – (b).

The efficiency of pollutant degradation is usually illustrated by the yield, defined as the amount of dye destroyed per unit of energy consumed in the process. Fig. 5 shows the energy yield for both configurations investigated, for the pulse frequencies of 30 Hz (Fig. 5a) and 50 Hz (fig. 5b).

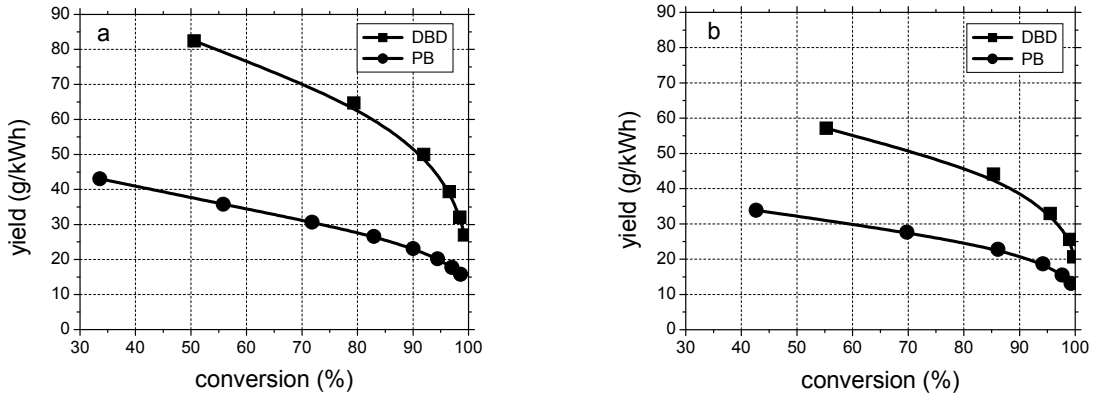


Fig. 5. Energy yield for MB decomposition as a function of conversion for the coaxial geometry (DBD) and for the packed-bed geometry (PB), for pulse frequency 30 Hz – (a) and 50 Hz – (b).

Clearly the yield was higher for the DBD geometry as compared to the PB geometry. The difference was more important at low conversion, but even at 90% conversion the values are about two times higher for the coaxial geometry: 52 g/kWh for DBD versus 23 g/kWh for PB for 30 Hz and 38 g/kWh for DBD versus 21 g/kWh for PB at 50 Hz. Another observation worth mentioning is that higher frequency, and implicitly higher power, does not result in higher energy efficiency, even if it leads to faster MB decomposition.

The difference between the O_3 detected when water was circulated through the reactor and the O_3 detected in the presence of MB solution represents the amount of O_3 consumed in the degradation process and was plotted in Fig. 6 as a function of treatment time.

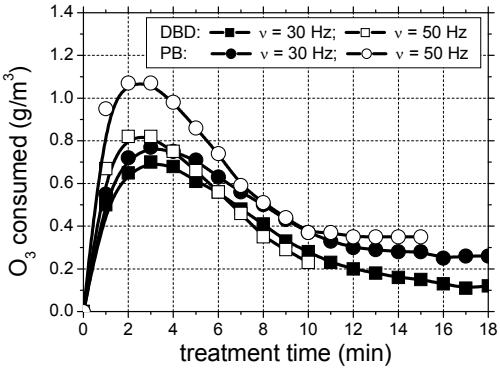


Fig. 6. Ozone consumed in the process of MB degradation.

In the presence of MB solution the ozone concentration detected in the effluent gas was lower due to reactions with the dye molecules as well as with the degradation products resulted from its decomposition.

In the first few minutes of treatment a considerable amount of the O_3 produced in the discharge was consumed in reactions with MB. During this time the MB concentration decreased significantly since,

as mentioned previously, the MB conversion reached more than 80% after 8 min plasma treatment. Ozone reacts as well with intermediates formed from MB degradation, leading to more stable products, which have less affinity to O_3, which is shown by the subsequent decrease in O_3 consumption. After 10 min treatment the amount of O_3 consumed remained approximately constant, showing that a small part of the O_3 slowly reacts with the products of MB degradation.

4. Summary and conclusions

Methylene blue in aqueous solution was successfully decomposed using a dielectric barrier discharge operated in pulsed regime. The solution was completely decolorated after about 8 min of plasma treatment. It was found that MB degradation obeys first order kinetics. The comparison between the coaxial geometry and the packed-bed geometry showed that faster degradation and higher energy efficiency for the dye decomposition were achieved in the DBD configuration. In this case the best degradation yield obtained at 90% MB conversion was 52 g/kWh. By increasing the pulse repetition rate, and implicitly the average power introduced in the discharge, faster MB decomposition could be obtained. However, this did not improve the energy yield, which was higher for the lower power used. Measurements of the ozone concentration in the effluent gas showed that ozone played a considerable role in the decomposition of MB. In the first few minutes of treatment a considerable amount of the O_3 generated in the discharge was consumed in chemical reactions, while the concentration of MB decreased significantly. Ozone reacts as well with intermediates formed from MB decomposition, leading to more stable products. These products have lower affinity to O_3, as shown by the considerable decrease of O_3 consumption for longer treatment time.

Acknowledgement. We acknowledge financial support from UEFISCSU project ID – 223 and from PN 09.39.03.01.

5. References

[1] Konstantinou I K and Albanis T A 2004 *Appl. Catal. B: Environ.* **49** 1.
[2] Grabowski L R, van Veldhuizen E M, Pemen A J M and Rutgers W R 2007 *Plasma Sources Sci. Technol*. **16** 226.
[3] Meshko V, Markovska L, Mincheva M and Rodrigues A E 2001 *Water Research* **35** 3357.
[4] Sun B, Kunitomo S and Igarashi C 2006 *J. Phys. D: Appl. Phys.* **39** 3814.
[5] Joshi A A, Locke B R, Arce P and Finney W C 1995 *J. Hazard. Mater*. **41** 3.
[6] Malik M A, Rehman U, Ghaffar A and Ahmed K 2002 *Plasma Sources Sci. Technol*. **11** 236.
[7] Sugiarto A T, Ito S, Ohshima T, Sato M and Skalny J D 2003 *J. Electrost*. **58** 135.
[8] Sun B, Sato M and Clements J S 1997 *J. Electrost*. **39** 189.
[9] Hoeben W F L M, van Veldhuizen E M, Rutgers W R, Cramers C A M G and Kroesen G M W 2000 *Plasma Sources Sci. Technol*. **9** 361.
[10] Burlica R, Kirkpatrick M J, Finney W C, Clark R J and Locke B R 2004 *J. Electrost*. **62** 309.
[11] Bubnov A G, Burova E Yu, Grinevich V I, Rybkin V V, Kim J-K and Choi H-S 2006 *Plasma Chem. Plasma Process*. **26** 19.
[12] Magureanu M, Piroi D, Gherendi F, Mandache N B and Parvulescu V I 2008 *Plasma Chem. Plasma Process*. **28** 677.
[13] Magureanu M, Piroi D, Mandache N B, David V, Medvedovici A and Parvulescu V I 2010 *Water Research* **44** 3445.
[14] Magureanu M, Piroi D, Mandache N B and Parvulescu V I 2008 *J. Appl. Phys*. **104** art. no. 103306.
[15] Park J Y, Kostyuk P V, Han S B, Kim J S, Vu C N and Lee H W 2006 *J. Phys. D: Appl. Phys*. **39** 3805.
[16] Lukes P, Clupek M, Babicky V, Janda V and Sunka P. 2005 *J. Phys. D: Appl. Phys.* **38** 409.
[17] Lukes P, Appleton A T and Locke B R 2004 *IEEE Trans. Ind. Appl*. **40**, 60.
[18] Holzer F. and Locke B R 2007 *Plasma Chem. Plasma Process*. **28** 1.

PULSED CORONA DRIVEN BY A COMPACT REPETITIVE MARX GENERATOR

Goran B. Sretenović, Bratislav M. Obradović, Vesna V. Kovačević, Milorad M. Kuraica

University of Belgrade, Faculty of Physics, Serbia

E-mail: sretenovic@ff.bg.ac.rs

As a part of a pulsed corona system for pollution control applications, Marx type pulse generator was constructed and tested. It consists of ten capacitor banks which can be connected on different ways to give required voltage and energy and it is able to produce up to 200 kV and 15 J pulses with a respectable repetition rate. For this work we used three and four stages, 40-50 kV generator which gives 4 J per pulse and repetition rate up to 100 pps, according to our laboratory plasma reactor configuration. The generator delivers pulses to the wire-plate reactor with the 40 ns risetime and FWHM of 200 ns. The pulse power system may be used with or without DC bias, with no needs for additional power supply. This arrangement has been tested through the measurement of ozone generation. Finally, the whole system has been used for NO treatment in the laboratory conditions.

1. Introduction

With the rapid increase in electrical power industry, the use of coal is expected to rise by over 70% from 2005 to 2030. Coal share in global electricity generation is set to increase from 40% to 45% by 2030 [1]. In Serbia over 60% of electrical energy is produced by coal-burning power plants. With this increase, coal-fired power plants will emit ever larger amounts of sulphur-dioxide (SO_2) and nitrogen oxides (NO_x), which are the main causes of acid rain and urban air pollution. SO_2 and NO_x coexist in coal flue gas so development of an efficient, simple and environmental friendly technology for simultaneous removal of these two gases is of great interest. The pulsed corona discharge showed encouraging results for the simultaneous removal of NO_x and SO_2 which was demonstrated at industrial level experiments with flow rates from 1000 Nm^3/h to 50,000 Nm^3/h [2]. Advantages of pulsed corona treatment are: simultaneous removal of several pollutants, high destruction efficiency, no demands on temperature and pressure, insensitive to contamination, no damage from high loads, widely applicable, simply installed, compact, little service and small scale [3] .

Reliable, inexpensive pulsed power supplies are vital for the implementation of pulsed corona technology and they are based primarily on the capacitive energy storage and closing switches [4-6]. A good solution for pulsed corona power supply could be a repetitive Marx generator presented in this work. In 1923, Erwin Marx patented the circuit for a high voltage generator with the fundamental principle of charging capacitors in parallel and switching the capacitors in series into a load [7]. We designed a pulsed power supply based on the same principles and used it for pulsed corona generation. Many plasma driven pollution control processes are initiated by ozone, so we measured the plasma production of ozone in the air, to analyze the plasma processing efficiency [8].

2. Experimental setup

For a flue gas treatment by pulsed corona plasma we constructed a compact, repetitive Marx generator with an external trigger. The whole system consists of ten 7 nF, 30 kV capacitors, eighteen 1 mH inductivities and nine spark gap switches. Depending on the capacitors connection the generator can have from two to ten stages, which is determined by plasma reactor configuration. In every mentioned configuration all capacitors are included, so the pulse energy of the generator does not depend of operational voltage which can go up to 200 kV.

For our measurements we used three and four stage generator with operational voltage of 35-50 kV.

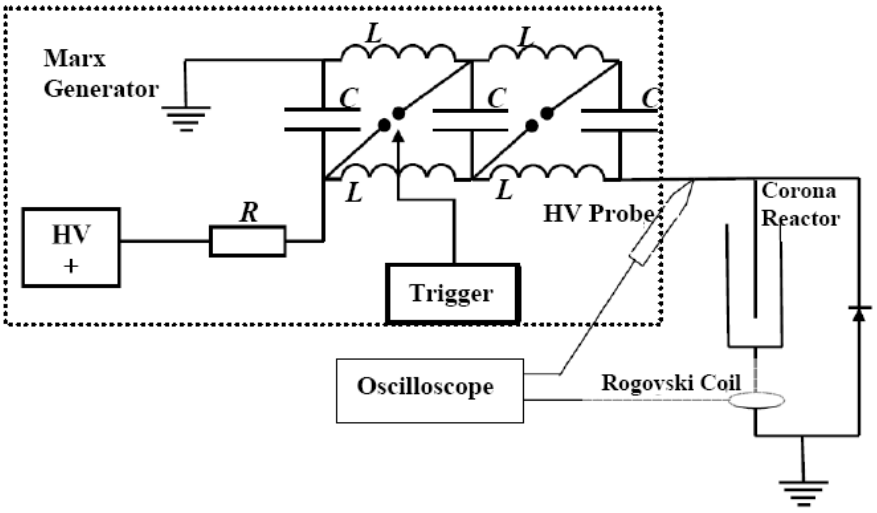


Fig. 1. Schematic overview of three-stage Marx generator with corona reactor.

Three stage Marx generator consists of three 20 nF capacitors in parallel charged via 1 kΩ resistor and four 1 mH inductivities as presented in Fig. 1. The high voltage transformer with rectifier charges the capacitors to the positive charging voltage of 10-12 kV, when trigger pulse fires the first spark gap which then in turn, due to the addition of the voltages, fires the second spark gap. The inductors act as very high reactance due to the speed of the capacitor discharge and thus the spark gaps are fired in series. A positive output pulse is produced with voltage more than three times the charge voltage i.e. ~ 40 kV. Round electrodes of spark gaps were made from brass and placed in a plastic tube at 8 mm distance in between. The tube was connected with an air pump which provided dry air flow through the spark gap switches required for regular work of the power source. In this research we have set the repetition rate of generator at 50 and 100 pps.

Wire-plate corona reactor had seven wires, 0.5 m long and 0.8 mm in diameter, placed at 4 cm distance from parallel positioned stainless steel plates. Dimensions of the reactor are 0.7 x 0.5 x 0.08 m^3. A fan was used to provide 10-60 m^3/h air flow rate through the reactor. Reactor can be coupled via additional spark gap or directly. In the second case, emission electrodes of the reactor are on the high voltage permanently, and practically plasma source works with DC bias without additional high voltage source, which may decrease expenses in cases where DC bias is needed.

For voltage measurement, a high voltage probe Tektronix P6015A (1000:1±3%) was used with a digital oscilloscope Tektronix 3032 (300 MHz, 2.5GS/s). Current measurements were performed with current transformer Pearson Electronics 3025. Probes were positioned as shown in Fig. 1. First testing of the generator has been performed with handmade non-inductive liquid resistor with resistivity of about 300 Ω.

The ozone concentration was determined using the UV absorption (Fig. 2) in the Hartley-band (230-290 nm), where the absorption of ozone is the largest. As UV source a Shimadzu deuterium lamp was used. Ocean Optics QE 65000 spectrometer (200-400 nm, resolution 0.2 nm) was used to acquire the spectra. Measuring cell with quartz windows and optical path length (*d*) of 8 cm was located after the electrode system at distance of approximately 0.5 m.

For the measurements of plasma source denitrification efficiency the NO gas was inserted just after fan. Gas analyses are performed using gas analyzer (MRU VarioPlus Industrial) with electrochemical sensors for NO, NO_2, SO_2, O_2 and CO and an NDIR sensor for CO_2.

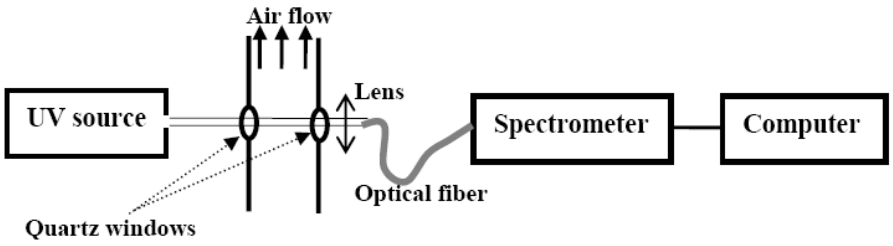


Fig. 2. Shematic owerview of UV absorption technique set-up.

3. Experimental results

First testing of the Marx generator was performed using pure resistive load with resistivity of about 300 Ω. It was important to know the fraction of accumulated energy in the power source that was lost during its operation, i.e. it was important to obtain efficiency of the source. Results are presented in Fig. 3.

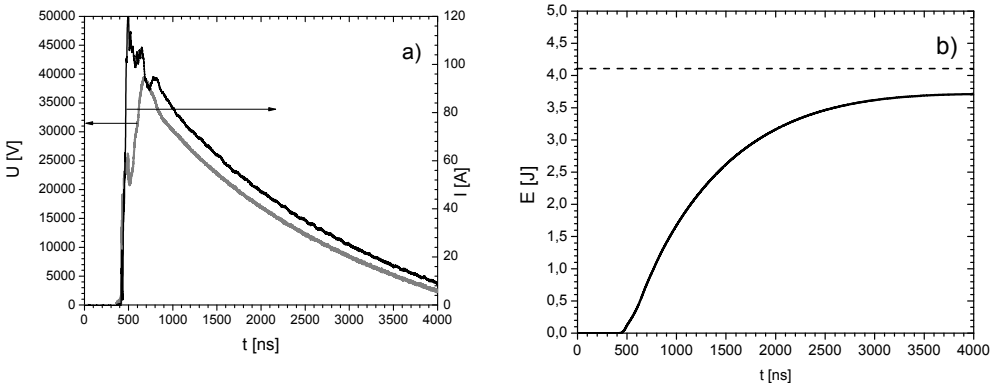


Fig. 3. a) Current and voltage waveforms for 300 Ω resistive load. b) Energy delivered into load (straight line), and energy accumulated in Marx generator (dashed line). Results are obtained for the three stage Marx generator.

Fig. 3. b) shows that energetic efficiency of the Marx generator is about 90% which was important and encouraging for further investigation. This graph shows that even the largest losses in spark gap are acceptable. Further examinations have been performed with the corona reactor. Results of the electrical measurements are presented in Fig. 4. We measured electrical characteristics of pulsed plasma system for two types of power source arrangement, two stage (a) and b)) and three stage Marx generator (c) and d)). First, we obtained voltage and current waveforms for three stage Marx generator. Power is calculated by multiplying voltage and current waveforms. Energy is determined by integrating the power waveform. The risetime of the pulse is about 40 ns. For energy of ~1 J/pulse, the half-width of power signal is about 200 ns. For this arrangement energy delivered from the power source to the plasma reactor was less than 25 %, which is unsatisfactory, so we decided to examine the efficiency of energy delivery depending on wire length, i.e. plasma reactor capacitance and its active resistivity. We measured energy delivered to the reactor for seven wire lengths, from 0,5 to 3,5 m. Results are presented in Fig. 5. It is clear that amount of energy delivered to the reactor depends linearly on wire length, and considering that, one can conclude that the ideal wire length of our reactor should be about 17.5 m. As it was not possible to change the reactor configuration, the applied voltage was changed, but with the same energy accumulated in reactor. Therefore the power source was prearranged to four stage Marx. The voltage was increased for about 20%, which resulted in increase of energy delivered to the reactor almost twice, and the whole energy efficiency to 38% as shown in Fig. 4. d). This is encouraging, but still bellow the requested efficiency, so more work is needed to

reach it. Further increasing of voltage could be problematic, because, due to the reactor arrangement, sparks may appear in large numbers instead of a pulsed corona discharge.

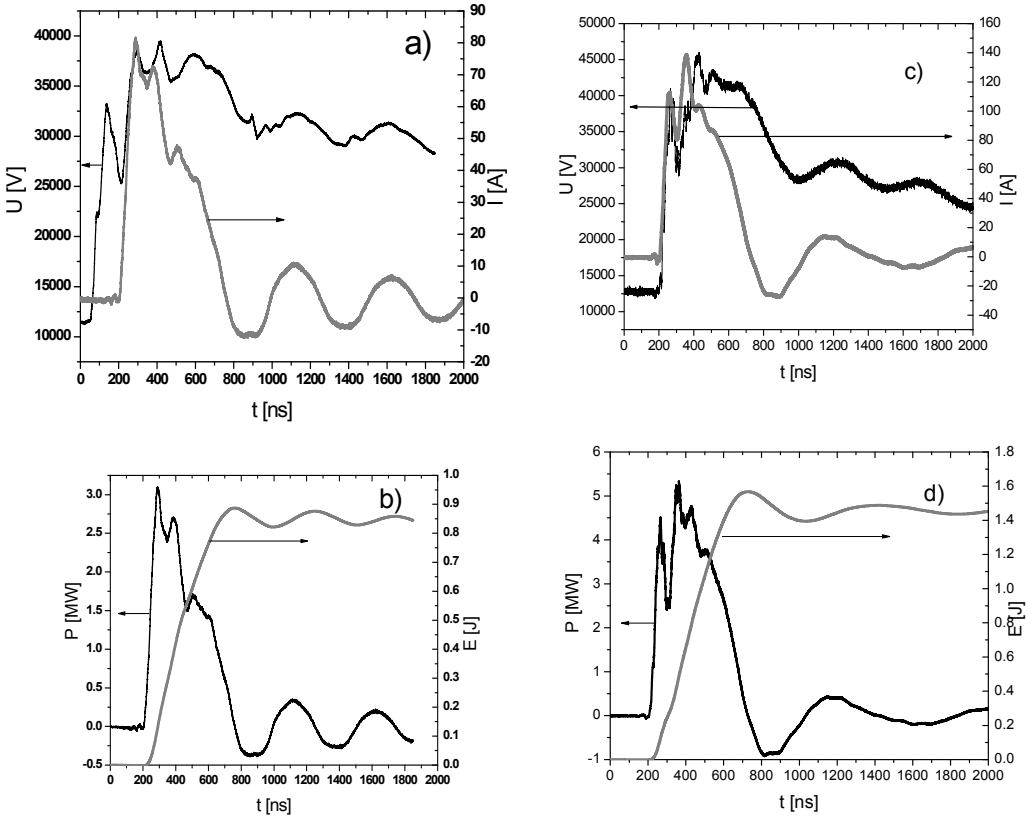


Fig. 4. Voltage and current signal of pulsed corona discharge: a) three stage Marx and c)four stage Marx. Power and energy delivered to the corona reactor: b) three stage Marx and d)four stage Marx.

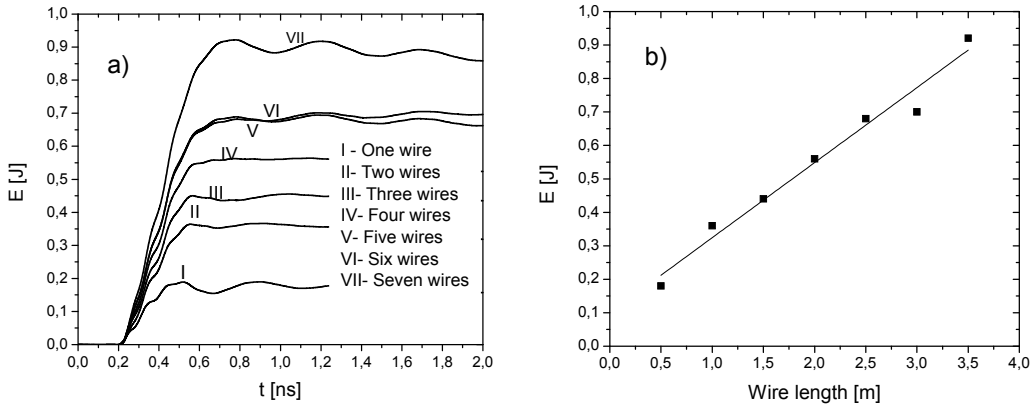


Fig. 5. Energy delivered to the plasma reactor in dependence of wire length.

Ozone production was measured as an indicator for chemical activity of pulsed corona. Analyzing Fig. 6.b) it can be concluded that the ozone concentration increases almost linearly with increase of energy density. Obtained results are in good agreement with results presented in literature [4], so we decided to use our plasma system for NO treatment for different repetition rates (Fig. 7). Preliminary results of NO treatment presented in Fig. 7 show good performance of our plasma system in the denitrification processes. It is interesting to note that with increase of inserted energy, not only the NO concentration decrease (in processes of oxidation to NO_2), but also the total NO_x concentration decreases due to processes of reduction and converting of NO_2 to HNO_3 in a presence of water vapour which is not negligible in laboratory conditions [9].

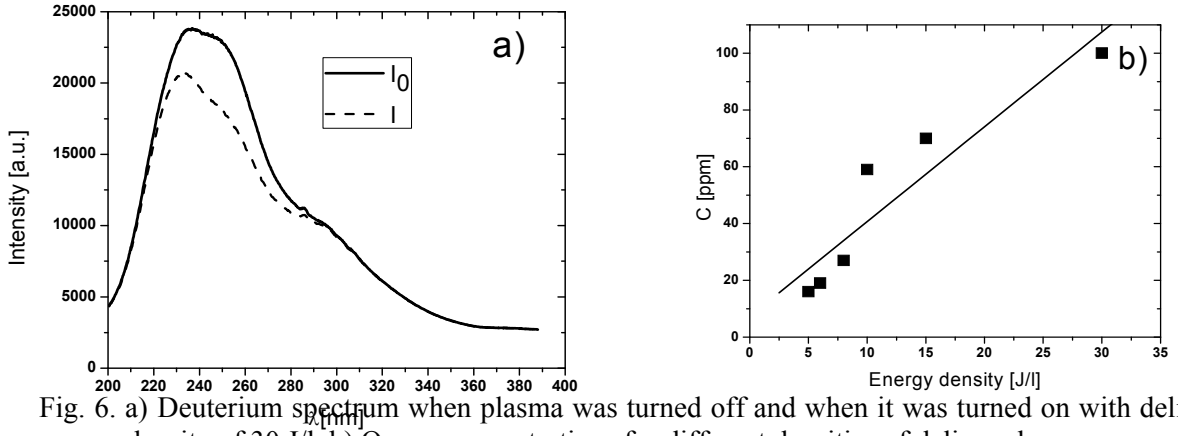


Fig. 6. a) Deuterium spectrum when plasma was turned off and when it was turned on with delivered energy density of 30 J/l. b) Ozone concentrations for different densities of delivered energy.

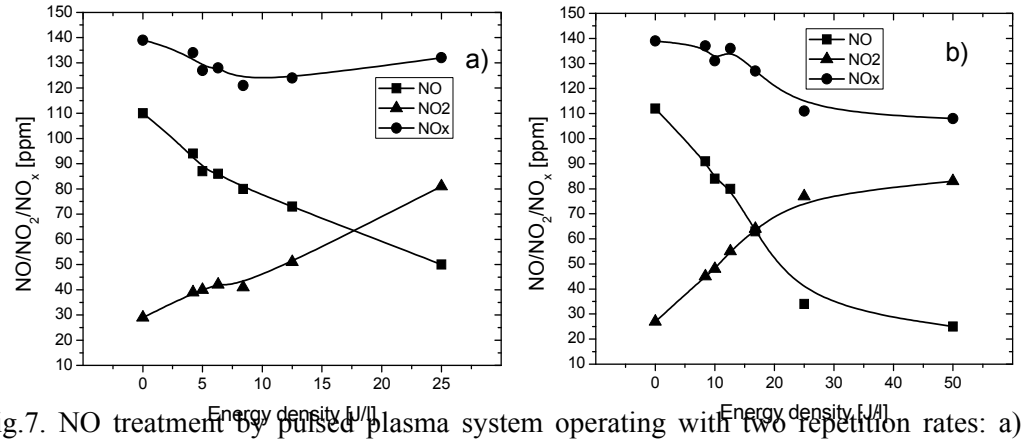


Fig.7. NO treatment by pulsed plasma system operating with two repetition rates: a) 50Hz and b) 100Hz

Acknowledgements. This work is supported by the Ministry of Science and Technological Development of the Republic of Serbia through the project No. 141043.

4. References

[1] International Energy Agency 2007, World Energy Outlook 2007
[2] Kim, H. H. 2004, *Plasma Process. Polym.* **1**, 91
[3] van Veldhuizen E. M. (ed) 2000: Electrical Discharges for Environmental Purposes: Fundamentals and Applications, *Nova Science Publishers*
[4] Winands, H. G. J. J., Yan, K., Nair S.A., Pemen G. A. J. M., van Heesch B. E. J. M. 2005 *Plasma Process. Polym*., **2**, 232
[5] Pokryvailo A., Wolf M.,Yankelevich Y.,Wald S, Grabowski L. R., van Veldhuizen E M, Rutgers W.R.,Reiser M, Glocker B., Eckhardt T., Kempenaers P. Welleman A. 2006 IEEE *Trans. Plasma Scie.* **34**, 1731
[6] Yan K., Hui H., Cui H, Wu X., Baa C., Li R.: 1998 *Journal of Electrostatics* **44**, 17
[7] Marx E. 1923 *Deutsches Reich Reichspatentamt Patentschrift* **455933**
[8] Kuraica M. M., Obradović B. M., Sretenović, G., Kovačević V., Dojčinović B., Manojlović D. 2008 *Hakone XI Conference* 352
[9]Orlandini I., Riedel U. 2000 *J. Phys. D: Appl. Phys.* ***33*** *2467*

CHEMICAL ACTIVITY OF THE PULSED CORONA DISCHARGE IN WATER IN DEPENDENCE ON SOLUTION CONDUCTIVITY – YIELDS OF H_2O_2 AND H_2

Irena Tothova[1], Petr Lukes[2], Martin Clupek[2], Vaclav Babicky[2], Vaclav Janda[1]

[1]*Department of Water Technology and Environmental Engineering, Faculty of Environmental Technology, Institute of Chemical Technology, Technicka 5, Prague 6, 160 00, Czech Republic*

[2]*Department of Pulse Plasma Systems, Institute of Plasma Physics, Academy of Sciences of the Czech Republic, v.v.i. Za Slovankou 3, Praha 8, 180 00, Czech Republic*

E-mail: irena.tothova@vscht.cz

Reactor of point to plate electrode geometry has been used to study production of H2O2 generated by the pulsed corona discharge in water in dependence on added OH radical scavengers (dimethylsulfoxide, potassium bromide and methanol). The production of H2O2 decreased with higher concentration of scavenger. Furthermore, yields of hydrogen were measured, both dissolved and gaseous. The production of hydrogen increased rapidly in water/methanol solution.

1. Introduction

Non-thermal plasma processing in aqueous solution by applying a high voltage power is considered to be an attractive method for the production of highly active chemical species directly in water. It has been demonstrated that the pulsed high voltage discharges generate in water plasma that initiate a variety of physical and chemical effects as high electric field, intense ultraviolet radiation, overpressure shock waves and, especially, formation of various reactive chemical species such as radicals ($OH^{\cdot}$, $H^{\cdot}$, $O^{\cdot}$, $HO_2^{\cdot}$) and molecular species (H_2O_2, H_2, O_2). It is expected that primary chemical activity of electrical discharges in water is associated largely with the initial production of OH and H radicals formed by electron collisions with water molecules in the plasma discharge zone. Electron impact dissociation of water forms H and OH radicals with threshold electron energy of 5.1 eV. These radicals react with each other to form molecules H_2 and H_2O_2, which has been approved by chemical methods [1], or occur in the solution to be able to act as reactive species in solute. Generation of OH and H radicals by the electrical discharge in water has been proved by emission optical spectroscopy [2, 3]. Beside H_2 and H_2O_2, molecular oxygen is formed by the reaction of O radical with OH radical. Overall production ratio H_2O_2:H_2:O_2 is 2:4:1 [4] or 0.61: 1.19: 0.24 [1]. Production of H_2O_2 strongly depends on the solution conductivity, when the increase of solution conductivity results in the decrease in H_2O_2 production by the discharge. It was shown that to some extent this can be attributed to the effect of increasing UV radiation from the discharge leading to the increasing photolytic decomposition of H_2O_2 [5]. Even though many reactions and schemes of the chemical activity of electrical discharge in water have been described in the literature, the exact mechanism is still unknown. Recent paper [7] proposes chemical activity in polar organic solvents after applying electrical discharges. Among others, a particular attention is paid to hydrogen production in water/methanol solution.

In this work, yields of H_2O_2 by the pulsed electrical discharge in water generated in the reactor with point to plane geometry of electrodes were determined as a function of free radical scavenging property of dimethylsulfoxide, potassium bromide and methanol. These substances are highly reactive with OH radicals and, thus, capable to influence both the production of H_2O_2 formed by recombination of OH radicals as well as to eliminate a possible decomposition of H_2O_2 by OH radicals. Consequently, chemical activity of the discharge is evaluated with regard of the effects of solution conductivity on the production of H_2O_2, dissolved and gaseous H_2 in the range of 100-500 μS/cm.

2. Experimental

The reactor used for generating of the pulsed corona discharge with needle-to-plate electrode geometry in water was described in detail in previous work [3]. Briefly, needle electrode, made of tungsten rod, was in the distance of 52 mm from the second electrode and almost totally insulated from surrounding

water by Teflon insulator. Both electrodes were immersed in the liquid. A pulsed high voltage applied to the needle was provided by a pulse power supply. All experiments were conducted with fixed applied voltage of 27 kV or 21 kV, pulse repetition frequency of 35-60 Hz and charging capacitance of 7 nF. The mean electrical power, P, applied to the reactor was calculated from the applied voltage, U, charging capacity, C, and pulse repetition frequency, f, as $P = f E_p$, where the pulse energy, E_p, was evaluated as the storage energy of the charged capacitor $E_p = ½ CU^2$. The experiments were made in solutions with initial conductivity of 100 - 500 μS/cm. The reactor vessel was cooled during the whole experiment by a water circulating system to avoid heating of the solution and maintain isothermal conditions of about 16 ºC. Aqueous solutions were prepared in most case by the addition of dilute sulfuric acid to deionized water to reach the needed solution conductivity. In the experiments with scavengers, methanol or dimethylsulfoxide as non-conductive organic compounds were added to the solution of sulfuric acid. Potassium bromide as an inorganic conductive solute was used on its own.
The actual concentration of hydrogen peroxide was determined spectrophotometrically using the colorimetric reaction of H_2O_2 with titanyl ions. When dissolved and gaseous H_2 was measured solution was purged by argon at flow rate of 1 l/min before starting the experiment and during the experiment from the bottom of the beaker to avoid contact of argon with the plasma discharge. 1 l Tedlar bags (Supelco) were used to sample gaseous hydrogen. Content of hydrogen in collected gas mixture was further analysed using the gas chromatograph CE Instruments GC 8000 with thermal conductivity detector HWD 800. A column 2 m x 3 mm i.d. packed with molecular sieve 5A and argon as a carrier gas was used in chromatographic analysis. Concentration of dissolved hydrogen was determined using H-meter developed at the Institute of Chemical Technology, Prague, Czech Republic.

3. Results and discussion

To investigate the role of OH radicals in the yield of H_2O_2, the free radical scavenging property of dimethylsulfoxide, potassium bromide and methanol was used. On one hand OH radicals recombine to produce H_2O_2, on the other hand OH radicals are involved in H_2O_2 decomposition. Radical scavengers are highly reactive with OH radicals ($k_{DMSO+OH} = 7.1\times10^9$ l mol^{-1} s^{-1}, $k_{KBr+OH} = 1.1\times10^{10}$ l mol^{-1} s^{-1}, $k_{CH3OH+OH} = 9.7\times10^8$ l mol^{-1} s^{-1}) and, thus, capable to influence both the production of H_2O_2 formed by recombination of OH radicals as well as to eliminate a possible decomposition of H_2O_2 by OH radicals. Scavenging capacity is defined as a product between the rate constant k_{OH+S} and scavenger concentration [S].

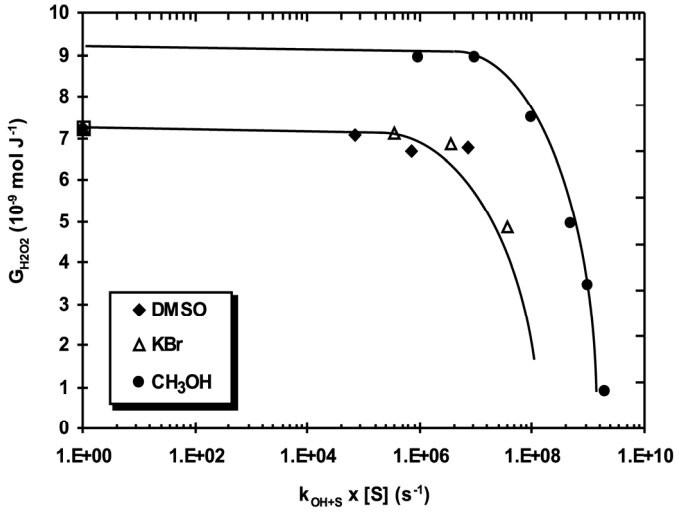


Fig. 1. H_2O_2 yield as a function of scavenging capacity of KBr, DMSO and CH_3OH (500 μS/cm, 27 kV, 90 W).

The yield of H_2O_2 in dependence on the scavenging capacity is shown in Fig. 1. It is obvious that the production of H_2O_2 decreases with increasing concentration of scavenger. The higher the concentration of the scavenger is available in the solution, the more it can participate in the OH

radicals recombination processes. It shoud be noted that the amount of potassium bromide (i.e., its scavenging power) used in these experiments was limited by the conductivity of the KBr solution. Therefore, the maximum concentration of KBr was 3.25 mmol/l, which corresponds to the conductivity of 500 μS/cm. Similarly, the maximum concentration of dimethylsulfoxide used in the experiments was limited up to 10^{-2}mol/l. The reason for this was the fact that although dimethylsulfoxide is non-conductive compound, its degradation by-products (sulfate anion and methanesulfonic acid) are conductive, which changed the conductivity of solutions during the experiments with DMSO above of 10^{-2}mol/l significantly. On the other hand, the effect of methanol on H_2O_2 production was investigated without any concentration limitations since methanol does not change the solution conductivity. As it is shown in Fig. 1 the methanol addition in the concentration of 5 mol/l was sufficient to suppress almost completely the production of H_2O_2, and, thus, to scavenge nearly all OH radicals produced by the discharge. Therefore, it is apparent that the formation of H_2O_2 by the electrical discharge in water can be directly related with the production of OH radicals in the plasma, i.e. with the recombination of OH radicals into H_2O_2.
Consequently, production of molecular hydrogen by the discharge in both gaseous and dissolved form was investigated with regard to the effect of solution condcutivity. It is known that the production of H_2O_2 by pulsed corona discharge in water depends on the solution conductivity when the yield of H_2O_2 decreases with the increasing conductivity [5]. Similar results were determined also for the production of gaseous hydrogen, shown in Fig 2, when 1.5 times higher yields of hydrogen were measured at 100 μS/cm than at 500 μS/cm.

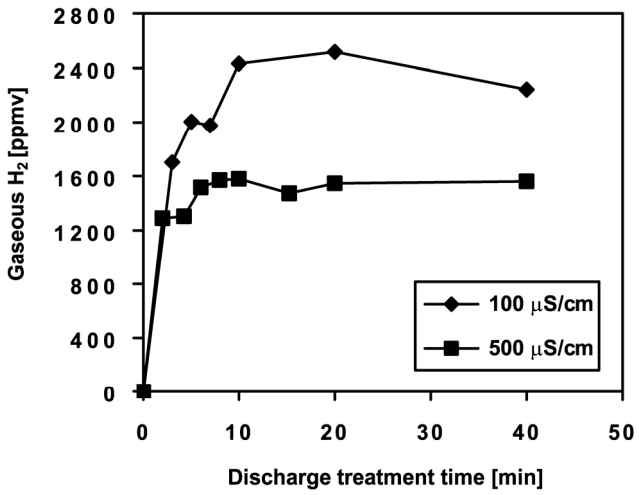


Fig. 2. Production of gaseous H_2 in water in dependence on solution conductivity (27 kV, 35 Hz, 90W).

This observation is in agreement with [6]. However, no observable differences were observed in the production of dissolved hydrogen in solutions of different conductivity (Fig. 3). This discrepancy obtained for production of gaseous and dissolved hydrogen might be related with the limited solubility of hydrogen in water, however, more research is needed to fully explain these results.
In addition, the role of applied power on the production of gaseous and dissolved hydrogen was investigated by varying of applied voltage (21 and 27 kV) and pulse epletion frequency (35 and 60 Hz). Figs. 4 and 5 show that the yield of dissolved and gaseous hydrogen increased with the increasing electrical power applied to the reactor. This is rather expected result. However, it was further found (Fig. 4) that the yield of dissolved hydrogen increased with the addition of 1M methanol into the solution (more than 50%). In the case of gaseous hydrogen, the yield was even four times higher with addition of 1M methanol (Fig. 5). The similar effect of methanol on the yield of molecular hydrogen was observed also by Thagard et al [7]. Nevertheless, increase of H_2 in the presence of methanol is significantly different result compared to the production of H_2O_2, which decreased by 50 % with the addition of 1M methanol (Fig. 1). The reason for this might be caused by the formation of hydrogen radicals due to methanol decomposition in plasma as follows [7]:

$e^- + CH_3OH \rightarrow \cdot CH_2OH + \cdot H$ (1)

$e^- + CH_3OH \rightarrow \cdot CH_3O + \cdot H$ (2)

$e^- + CH_3OH \rightarrow \cdot CH_3 + \cdot OH$ (3)

Hydrogen and hydroxyl radicals may subsequently react with methanol as

$CH_3OH + \cdot OH \rightarrow \cdot CH_2OH + H_2O$ (4)

$CH_3OH + \cdot H \rightarrow \cdot CH_2OH + H_2$ (5)

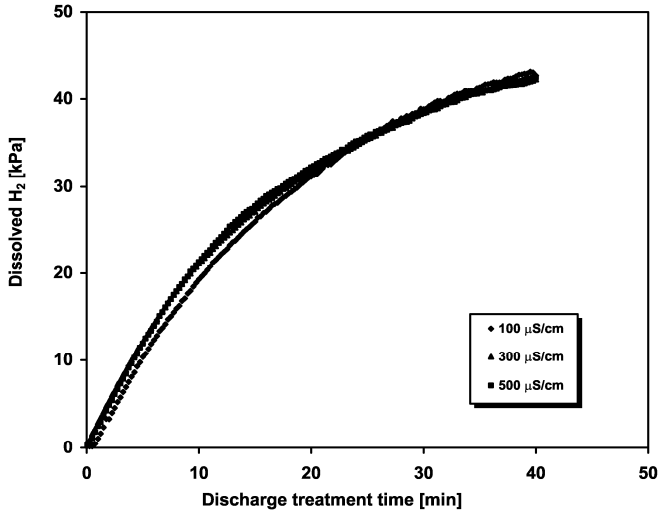


Fig. 3. Effect of the solution conductivity on kinetics of dissolved H_2 production in water at applied voltage 27kV, pulse repetition frequency 35 Hz, applied power input 90 W.

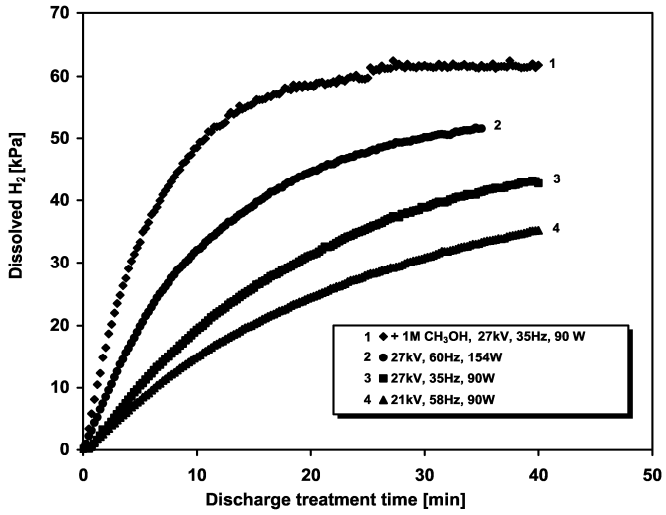


Fig. 4. Production of dissolved H_2 in water in dependence on solution composition (presence of methanol) under various applied parameters in solution of the conductivity of 100 μS/cm.

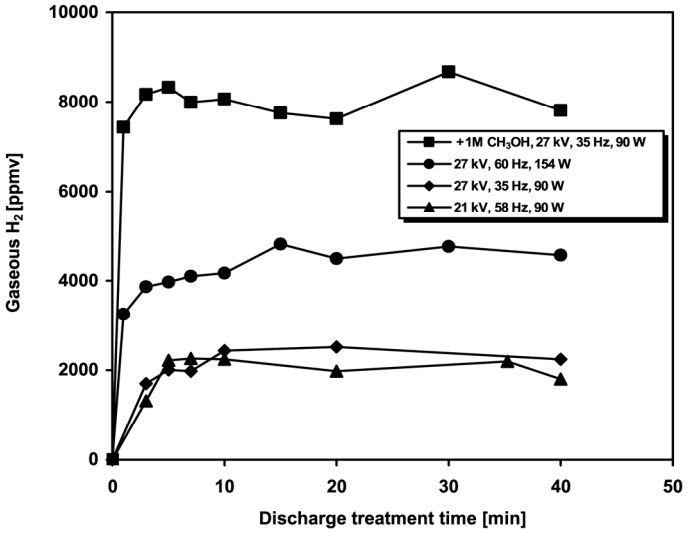


Fig. 5. Production of gaseous H_2 in water in dependence on solution composition (presence of methanol) under various applied parameters in solution of the conductivity of 100 μS/cm.

However, as a matter of fact, the rate constant of the reaction of methanol with hydrogen radical (Eq. 5) is rather low (2.6×10^6 l mol^{-1} s^{-1}) compared to the hydrogen radicals recombination (Eq. 6) with the reaction rate constant of 1.0×10^{10} l mol^{-1} s^{-1}.

$$\cdot H + \cdot H \rightarrow H_2 \quad (6)$$

Thus, it can be expected that hydrogen radicals formed from methanol (via routes described in Eqs. 1 and 2) can further recombine into hydrogen molecules (Eq. 6), which in consequence may lead to the higher yield of hydrogen as it was observed experimentally in the presence of methanol (Figs. 4 and 5).

4. Conclusion

Free radical scavenging property of DMSO, KBr and CH_3OH has been used to investigate mechanism of formation of H_2O_2 by the pulsed electrical discharge in water. The yield of H_2O_2 decreased with increasing scavenging capacity of the entire scavenger. Based on these results it was determined that the formation of H_2O_2 can be directly related with the production of OH radicals in the plasma, i.e. with the recombination of OH radicals into H_2O_2. On the other hand, in the case of dissolved and gaseous H_2 higher yields were determined in the presence of methanol in the solution, which was caused by additionally formed hydrogen radicals due to methanol decomposition in the plasma and their subsequent recombination into H_2.

Acknowledgement. This work has been supported by the Grant Agency of the Academy of Sciences of the Czech Republic (No. IAAX00430802), the Czech Science Foundation (No. 104/09/H080) and Ministry of Education, Youth and Sports (No. MEB0810116).

5. References

[1] Locke B R, Sato M, Sunka P, Hoffmann M R, Chang J-S 2006 *Ind. Eng. Chem. Res.* **45** 882.
[2] Sun B, Sato M, Clements J S 1997 *J. Electrostat.* **39** 189.
[3] Sunka P, Babicky V, Clupek M, Lukes P, Simek M, Schmidt J, Cernak M 1999 *Plasma Sources Sci. Technol.* **8** 258.
[4] Mededovic S, Locke B R 2007 *J. Phys. D: Appl. Phys.* **40** 7734.
[5] Lukes P, Clupek M, Babicky V, Sunka P 2008 *Plasma Sources Sci. Technol.* **17** 024012.
[6] Kirkpatrick M J, Locke B R 2005 *Ind. Eng. Chem. Res.* **44** 4243
[7] Thagard S M, Takashima K, Miyuno A 2009 *Plasma Process. Polym.* **6** 741.

CONVERSION OF TETRACHLOROMETHANE BY PULSED CORONA DISCHARGE

Bogdan Ulejczyk, Sławomir Jodzis, Krzysztof Krawczyk,
Krzysztof Schmidt-Szałowski

Faculty of Chemistry, Warsaw University of Technology,
Noakowskiego 3, 00-664 Warszawa, Poland
E-mail: bulejczyk@ch.pw.edu.pl

Volatile organic compounds are responsible for destruction of the ozone layer and development of respiratory system illnesses. In recent year's attempts to destroy of volatile organic compounds by using of non-equilibrium plasma generated by glow, corona, gliding, barrier, microwave and surface discharges have been made. This study is focused on corona discharge.
The conversion of CCl_4 in argon – oxygen mixtures was investigated at normal pressure in a new type of pulsed corona discharge reactor. The newly designed reactor made of a quartz-glass tube, 17 mm in diameter, contains a ceramic electrode 9 mm in diameter and about 30 cm long. The new construction of the reactor improves the efficiency of the chemical reactions initiated by the corona discharge. In this reactor the gas stream was passed through channels in the porous ceramic tube. On the outer surface of the porous tube platinum coil (high voltage electrode) was placed. Gas permeating through a porous wall of the ceramic tube passes through the active zone of corona discharges, located around the emission electrode. This construction enables a better contact of the gas stream with plasma of corona discharge. The new reactor was compared with other types of reactors, in which other type of high voltage electrode was used.
Chlorine was the main reaction product with small amounts of C_2Cl_6, C_2Cl_4 and $COCl_2$. The highest overall CCl_4 conversion in the new reactor, that is 67%, was observed in the reactor with a ceramic tube and a platinum electrode. In this type of reactor the most favourable conversion of tetrachloromethanu was achieved.

1. Introduction

Volatile organic compounds (VOCs) contribute to the formation of the so-called greenhouse effect and some of them are responsible for destruction of the ozone layer. In recent year's attempts to destroy of VOCs by using of non-equilibrium plasma generated by corona, gliding, barrier, microwave and surface discharges have been made [1-8]. This study is focused on pulsed corona discharge. A significant advantage of the pulsed corona discharge is higher efficiency in decomposition processes of stable chemical compounds than that in the case of decomposition carried out in non-pulsed systems.
In this paper, we presents results of decomposition of CCl_4 using the pulsed corona discharge. The decomposition process was run in a newly constructed reactor to improve the efficiency of the chemical reactions initiated by the corona discharge. In this reactor, the gas stream was passed through channels in the porous ceramic tube. Gas permeating through the porous wall of the ceramic tube passes through the active zone of corona discharge, located around the emission electrode. This construction enables better contact of gas stream with the corona discharge plasma. The new reactor was compared with other type of reactor, in which other type of high voltage electrode was used.

2. Experimental

Tetrachloromethane was decomposited in an argon-oxygen gas mixture in two reactors (Fig. 1) at the same total gas flow (10Nl/h), CCl_4 concentration (0.4%) and O_2 concentration (25%).
One reactor (Reactor I) consisted of a quartz tube, high-voltage and ground electrodes, and a porous ceramics tube. Gas was introduced by the porous tube into the active zone of corona discharge. It's is the main advantage of the reactor. The grounded electrode was made by appling a silver paste onto the quartz tube. An outer diameter of the quartz tube was 19 mm and the wall thickness was 1.2 mm. The high-voltage electrode was composed from platinium coils on the porous ceramics tube with an outer diameter of 9 mm.

The difference betwee Reactor I and Reactor II was the gas inlet and the high-voltage electrode. The high voltage electrode was made from straight platinium wire with diameter of 0.3 mm. Gas was introduced to a whole volume of the reactor.

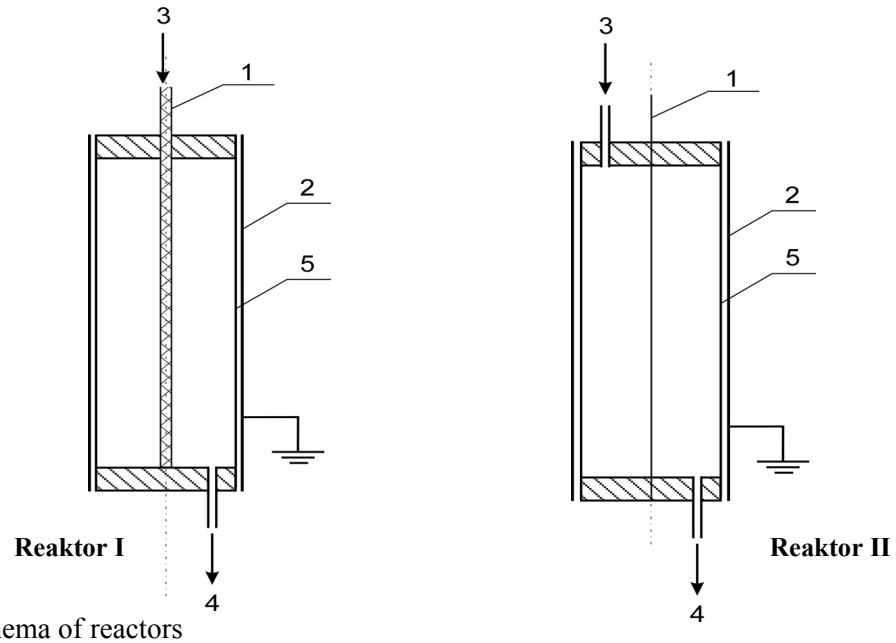


Fig. 1. Schema of reactors
1 – high-voltage electrode, 2 – grounded electrode, 3 and 4 – gas inlet and outlet, 5 – dielectric barrier

The reactor was powered by a pulsed supply system. The frequency, the current and voltage traces of a given pulse were recorded by using oscilloscope Tektronix TDS 3052 with a voltage probe Tektronix P6015A and a current probe Tektronix TCP202. The discharge power was calculated according to the formula:

$$P = f\int I(t)U(t)d(t) \tag{1}$$

P – discharge power, W
f – frequency, Hz
I – current, A
U – voltage, V
t – time of the pulse start and end, s

Products of the plasma decomposition of CCl_4 were analyzed by using gas chromatography and titrate analysis. Hewlett-Packard HP 6890 with an FID detector and packed column with 5% Fluorocol on 60/80 Carbopack B was used to determine the concentrations of CCl_4, C_2Cl_4 and C_2Cl_6. Cl_2 and $COCl_2$ were periodically passed by two bubblers with KI solution. In this solution Cl_2 react with KI to I_2 and KCl. $COCl_2$ react with H_2O to HCl and CO_2. The solution was titrated with a 0.05 M Na_2SO_4 solution to determine the amount of I_2 and 0.1 M NaOH was used to determine that of HCl. Basing on these measuring data a flow rate of products of the CCl_4 decomposition was calculated.
The overall CCl_4 conversion, the specific energy and the energy consumption were calculated according to formulas:

$$X = \frac{W_0[CCl_4] - W[CCl_4]}{W_0[CCl_4]} \bullet 100 \tag{2}$$

X – overall CCl_4 conversion, %
$W_0[CCl_4]$ - CCl_4 flow rate at the inlet, mol/h
$W[CCl_4]$ - CCl_4 flow rate at the outlet, mol/h

$$SE = \frac{P \cdot 3.6}{W_0[Ar] + W_0[O_2] + W_0[CCl_4]} \quad (3)$$

SE – specific energy, kJ/mol of gas

W_0[Ar] - Ar flow rate at the inlet, mol/h

$W_0[O_2]$ – O_2 flow rate at the inlet, mol/h

$$EC = \frac{P \cdot 3.6}{W_0[CCl_4] - W[CCl_4]} \cdot 0.001 \quad (4)$$

EC – the energy consumption, MJ/mol CCl_4

3. Results and discussion

Fig. 2 shows the results for CCl_4 decomposition for two reactors and various specific energies. The magnitude of the specific energy influenced on the overall CCl_4 conversion for both reactors. It is seen in Fig. 2 that the overall CCl_4 conversion increases with the specific energy increase. Similar effect is reported in other papers [1-3].

In Fig. 2 is seen that in the reactor with gas introduce into the active zone (Reactor I) the same overall CCl_4 conversion was achieve for the smallest specific energy than in reactor with gas introduction to the whole volume of reactor (Reactor II). The specific energy for two reactors is not comparable because pulses current was drastically changed with change of reactors (Fig. 3). It's is probably a result of distance change between the high-voltage and the grounded electrodes. However, some impact may come from changing of shape of the high-voltage electrode.

The maximum CCl_4 decomposition ratio, which was obtain in Reactor I, was only 67%. It is much less than was obtain in Reactor II (92%). Increase of the specific energy for Reactor I was impossible because a range of the frequency change was too small for pulsed power supply system, which was used.

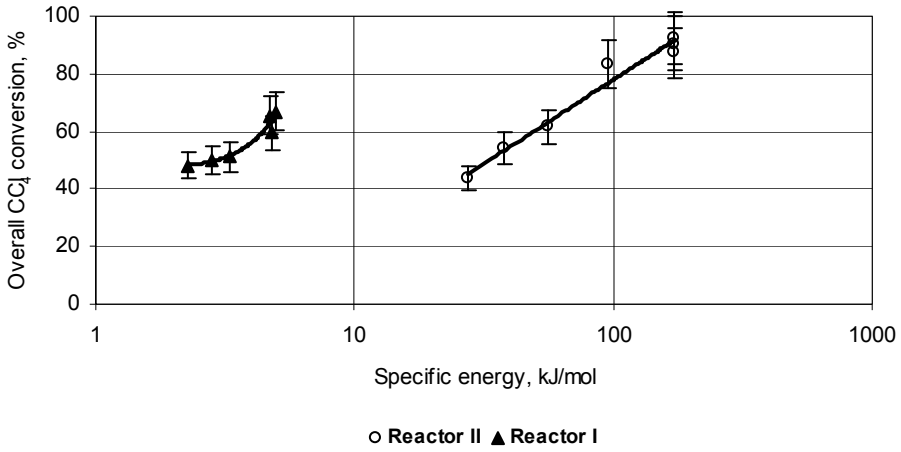


Fig. 2. The specific energy influence on the overall CCl_4 conversion for two types of reactors
Reactor I – gas was introduced into the active zone of corona discharge
Reactor II – gas was introduced into the whole volume of the reactor

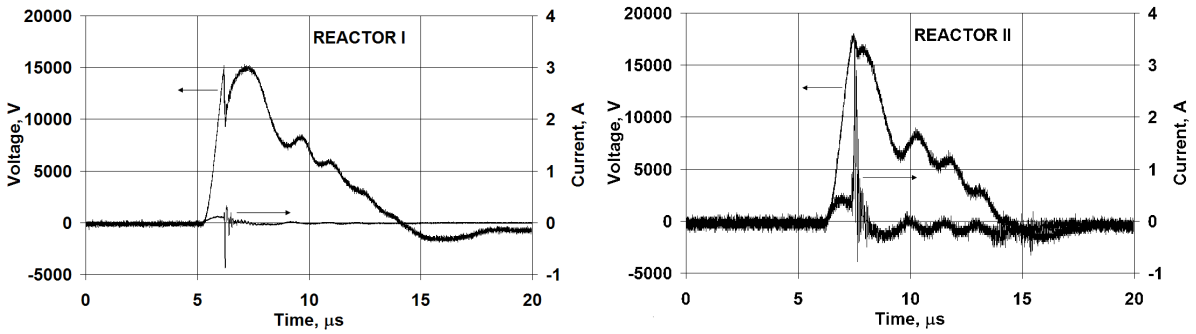


Fig. 3. Typical traces of pulses voltage and current for two types of reactors

Fig. 4 shows dependence between energy consumption and the overall CCl_4 conversion for both reactors. The energy consumption for Reactor I with gas introduce into the active zone was few times smaller than for Reactor II. This result is a consequence of the change of the pulse current. In Fig. 4 shows that increase of the overall CCl_4 conversion caused increase the energy consumption.

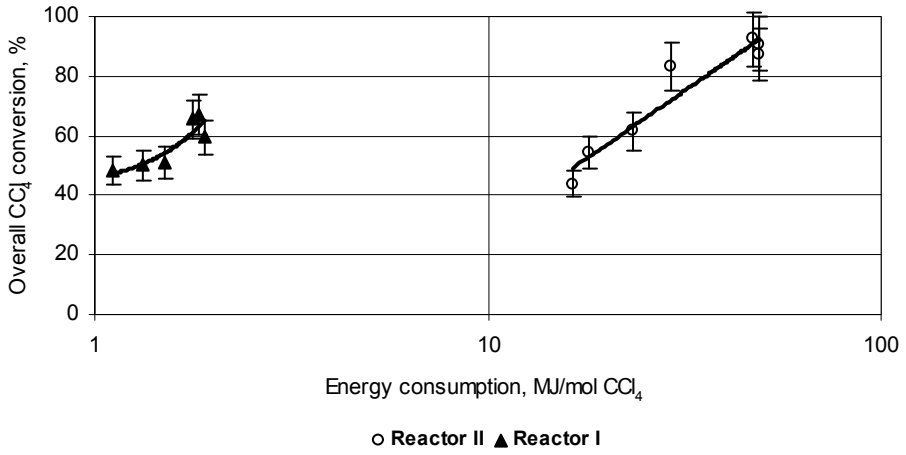


Fig. 4. The dependence between the overall CCl_4 conversion and the energy consumption for two types of reactors
Reactor I – gas was introduced into the active zone of corona discharge
Reactor II – gas was introduced into the whole volume of the reactor

The main product of the CCl_4 decomposition is Cl_2, for both reactors. Besides Cl_2, $COCl_2$, C_2Cl_4 and C_2Cl_6 formed during the CCl_4 decomposition process; however flow rates of $COCl_2$, C_2Cl_4 and C_2Cl_6 were a few times smaller than the Cl_2 flow rate (Fig. 5). C_2Cl_6 flow rate was between 0-0.002 mmol/h. Is worth to mention, that the Cl_2 flow rate increased and flow rates of other products not increased with increase of the specific energy.

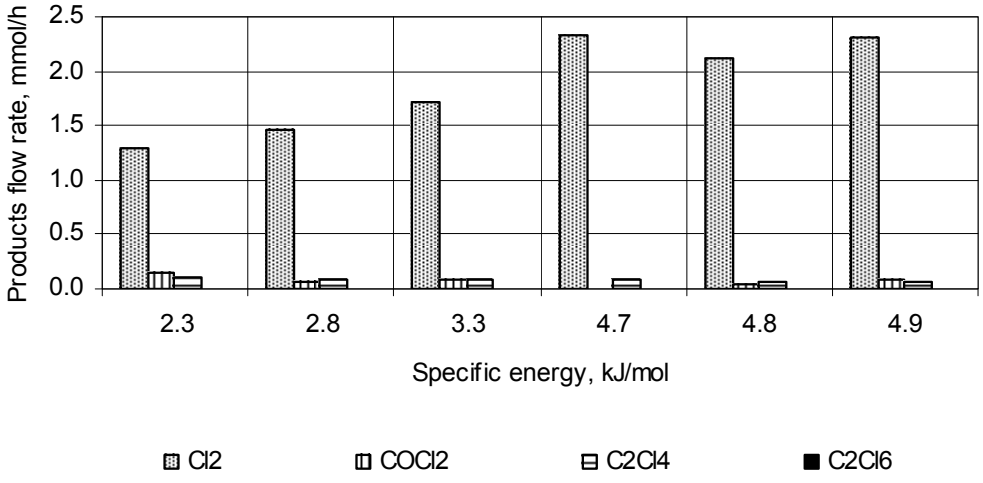


Fig. 5. The dependence between the specific energy and products flow rates for Reactor I
Gas was introduced into the active zone of corona discharge

4. Conclusions

CCl_4 can be effectively decomposed by using the pulsed corona discharge in both reactors. The highest overall CCl_4 conversion (92%) was achieved in Reactor II, when gas was introduced to the whole volume of reactor but the energy consumption was also high (49 MJ/mol CCl_4).
Reactor I, when gas was introduced into the active zone of the corona discharge, was consumed between 1.1 and 1.8 MJ/mol CCl_4 of energy and obtained the overall CCl_4 conversion between 48 and 67%.
Reactor I expend about 15 times less energy to achieve similar overall CCl_4 conversion than Reactor II. Cl_2 is the main product of the CCl_4 decomposition process. Besides Cl_2, a small amount of $COCl_2$, C_2Cl_4 and negligible amount C_2Cl_6 formed during the CCl_4 decomposition process.

Acknowledgment. This work was financially supported by the Polish Ministry of Science and Higher Education from Research Program Nr. PBZ-MEiN-3/2/2006.

5. References

[1] Li D, Yakushiji D, Kanazawa S, Ohkubo T and Nomoto Y 2002 *Journal of Electrostatics* **55** 311.
[2] Satoh K, Matsuzawa T and Itoh H 2008 *Thin Solid Films* **516** 4423.
[3] Kirkpatrick MJ, W.C. Finney WC and Locke BR 2003 *Plasmas and Polymers* **8** 165.
[4] Krawczyk K and Ulejczyk B 2003 *Plasma Chemistry and Plasma Processing* **23** 265.
[5] Magureanu M, Mandache ND and Parvulescu VI 2007 *Plasma Chemistry and Plasma Processing* **27** 679.
[6] Jasiński M, Szczucki P, Dors M, Mizeraczyk J, Lubański M and Zakrzewski Z 2000 *Czechoslovak Journal of Physics* **50/S3** 285.
[7] Lamenta A, Jodzis S, Krawczyk K and Schmidt-Szałowski K 2009 *Polish Journal of Chemistry* **83** 169.
[8] Harada N, Matsuyama T and Yamamoto H 2007 *Journal of Electrostatics* **64** 43.

INFLUENCE OF THE GAS FLOW ON PLASMA REFORMING OF FUELS IN PLASMA-LIQUID SYSTEM

Vitaliy Yukhymenko[1], Valeriy Chernyak[1], Serge Olszewski[1], Serge Sidoruk[1], Dmitry Levko[2], Anatolij Shchedrin[2], Vadim Naumov[1], Valentina Demchina[3]

[1]*Faculty of Radio-Physics, Kyiv National Taras Shevchenko University, Prospect Acad. Glushkova 2/5, Kyiv 03022, Ukraine;*

[2]*Institute of Physics, Ukrainian Academy of Sciences, Prosp. Nauki 46, Kyiv 03028, Ukraine;*

[3]*Institute of Gas, National Academy of Sciences of Ukraine, Degtyarevskaya 39, Kyiv 03113, Ukraine*

E-mail: yvitaliy@ukr.net

This paper presents the results of experimental and theoretical investigations of the process of non-thermal plasma-assisted reforming of aqueous ethanol solutions in the dynamic plasma liquid systems using the DC electric discharges in a gas channel with liquid wall and the additional excitation of ultrasonic field in liquid. Excitation temperatures (electronic T_e^*, vibrational T_v^* and rotational T_r^*) dependences of plasma components on the discharge current were investigated for different regimes (with and without ultrasound presence in the working fluid). The experiments show possibilities and efficiency of low-temperature plasma-chemical conversion of liquid ethanol into hydrogen-rich synthesis gas in different regimes.

1. Introduction

From physics and chemistry of fuel combustion it is known that addition of light inflammable gases (H_2, CO) essentially improves ignition/combustion of heavy oil and bio-fuels [1]. Therefore hydrogen is considered as one of the most prospective energy sources for the future that can be renewable, ecologically clean and environmentally safe [2]. Among possible technologies for free hydrogen production, including steam reforming and partial oxidation of bio-fuels, a low-temperature plasma-assisted fuel reforming is believed to be a good alternative approach. Although the plasma reforming process needs some additional electric power, its potential advantages: fast start-up, easy control, cooking reliability, compact design, etc provide good perspectives in its applications in aerospace technologies. For plasma fuel reforming, various methods using thermal and non-thermal plasma are known. One of the potential sources of non-thermal plasma that can provide simultaneously a high level of non-equilibrium and high density of reacting species in the plasma-liquid system is the electric discharge in a flowing gas channel with liquid wall (DGCLW). The main idea is that DGCLW can be burning directly within the liquid hydrocarbon fuels without preliminary gasification. Another pecularity is that DGCLW can work in the bubbling microporous liquid which has a very large ratio of the plasma-liquid contact surface to the plasma volume. As is known the ultrasonic (US) cavitation is a very effective method for creating micropores in liquid [3]. Therefore, the DGCLW with additional US pumping is also very interesting for research and development.

The objective of this work is to develop and to study new methods of low-temperature plasma-enhanced reforming of liquid hydrocarbon fuels for applications in prospective plasma-assisted aerospace combustion technologies.

2. Experimental set-up

Experimental set-up for conversion of ethanol in synthesis – gas is shown on Fig. 1. It consists of a cylindrical quartz test-vessel (1) sealed at the top and at the bottom by duralumin flanges (2) with a built-in electrode system (3). The cooper rod electrodes (3) were inserted into the quarts tubes (4) and installed coaxially one opposite other. The tubes (4) served also for the gas (air) inlet. A compressed atmospheric air was injected along electrodes (3) through the open nozzle ends (4) and formed a stable counter-flow gas channel surrounding by liquid ethanol (6). The electric discharge (5) was burned in the gas channel between the immersed electrodes where an electric breakdown occurred. The solution was filled into the reactor through the drain pipe (7) at the bottom flange. The outlet connections (8) and (9) at the top flange were connected with a system of communicating vessels allowing control of the liquid level and pressure in the reactor. The outlet pipe (9) served for transportation of the

synthesis gas products from the reactor to the condensing vessel and further to the gas analysis. Because of the electric-discharge heat release and heating of plasma-treated solution in the reactor, an auxiliary cooling was provided by the water-cooled jacket (10).
Another reactor (Fig. 2) was prepared with the discharge in a gas channel with liquid wall (DGCLW)

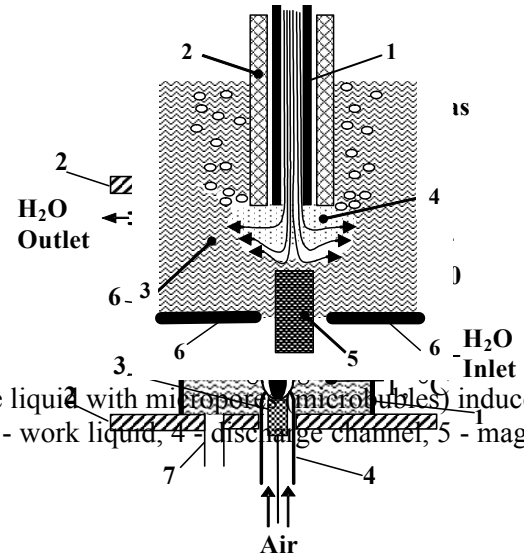


Fig. 2. DC DCGLW in the liquid with microporous (microbubbles) induced by US cavitations. 1- copper tube, 2 - glass insulator, 3 - work liquid, 4 - discharge channel, 5 - magnetostrictive US transmitter, 6-electrode in liquid.

Fig. 1. Experimental set-up for conversion of ethanol in synthesis – gas.

working with the air flow in the liquid under the induced microporous inhomogeneous conditions. The airflow was injected into the work liquid through a tube covered by a glass insulator and it ran over a flat dielectric surface of the magnetostrictive transmitter which produced ultrasonic (US) cavitations, so the discharge channel was formed by the air flow and water vapours (microbubbles). The US transmitter worked at the frequency of 18 kHz with the power ~20 W [10].
Various modes of the operation of the setup were studied: the mode where the voltage was applied to the electrodes mounted into the lower and upper flanges (the discharge was initiated between them); the mode where "+" was applied to the electrode mounted into the lower flange, whereas "–" was applied to the liquid ("liquid" cathode mode); the mode where "–" was applied to the electrode mounted into the lower flange, while "+" was applied to the liquid ("liquid" anode mode).
The mass-spectrometric and gas chromatography techniques for investigation of stable gas-phase conversion products were used.
Diagnostics of plasma parameters in the PLS was carried out by using optical emission spectroscopy (OES). A portable high-speed CCD-based spectrometer "Plasma-spec" with a spectral resolution ~0.6 nm was used for recording spectra in the wavelength range 200-1100 nm. Deuterium lamp was used as light sources for measuring absorption spectra of plasma-treated liquids. Excitation temperatures (electronic temperature T_e^*, vibrational T_v^* and rotational T_r^*) in discharge plasma were determined by OES methods. The electronic temperature T_e^* was determined by relative intensities of emission of atomic hydrogen lines (H_α 656.3 nm, H_β 486.1 nm). To determine vibration T_v^* and rotation T_r^* temperatures SPECAIR simulation of molecular bands: C_2 Swan-system (d-a), OH UV-system ($A^2\Sigma^+$-$X^2\Pi$), CN Violet-system ($B^2\Sigma^+$-$X^2\Sigma^+$) was made.

3. Results and discussions

The impact of the plasma-forming gas on the ethanol reforming in the DGCLW was studied. For that, the composition of gas-phase products of conversion in the reactor and the coefficient of energy transformation were studied at different gas flow rates. Research was conducted for the mode of solid electrodes. The composition and mixture ratio under the ethanol reforming was (5 mole of ethanol : 1 mole of water). The discharge current varied between 100 and 400 mA, the air flow rate varied from 0 to 110 cm^3/s.

The results for discharge current I= 100 mA demonstrates a good matching between gas chromatography and mass-spectrometry data. For other currents the same matching is observed. It should be noted that with increasing air supply in the discharge the concentration of H_2 in syngas products decreases. In fact, the highest yield of H_2 is observed in the discharge mode without air supply. But the time of H_2 production in this case increases considerably, and the power consumption also increases. All this reduces the coefficient of energy transformation (Fig. 3). Moreover, this

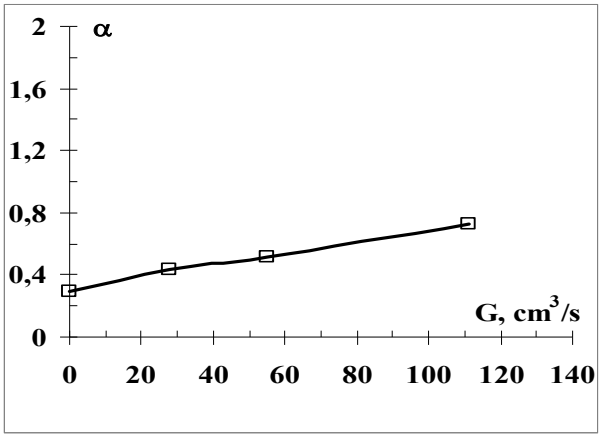


Fig. 3. Coefficient of energy transformation of the ethanol processing in the DGCLW as function of air flow rate. Ethanol-water solution (5/1), Id= 100 mA, solid electrodes.

decreases the lifetime of the system. Therefore, the total system performance without air supply seems to be not very good .processing in the PLS with the DGCLW.

Fig. 4 shows the results of experiments and numerical modeling of concentrations of H_2, CO_2 and other main stable components in output gas products after the ethanol processing in the PLS with the DGCLW. The qualitative and quantitative agreement between calculated and measured data is quite good, at least, for main components. One can see that the output concentration [H_2] grows linearly with the discharge current and it reduces exponentially with the gas flow rate.

In the discharge conditions, the kinetics of the H_2 formation is determined mainly by the reaction $C_2H_5OH + H \rightarrow CH_3CH_2O + H_2$. Since the ethanol concentration [C_2H_5OH] in solution changes slowly, the [H_2] production is determined entirely by the concentration of atomic hydrogen [H].

In the case under consideration, the main process responsible for the generation of H is the dissociation of water molecules H_2O by the direct electron impact. The rate of this process is proportional to the specific electric power deposited to discharge (i.e., discharge current). Therefore, the [H_2] production is also a linear function of the discharge current in accordance with experimental data. Outside the discharge, the only process that influences the H_2 concentration is the water-gas shift reaction $CO + H_2O \rightarrow H_2 + CO_2$. Via this process, the system reaches the complete conversion of CO into CO_2 and H_2.

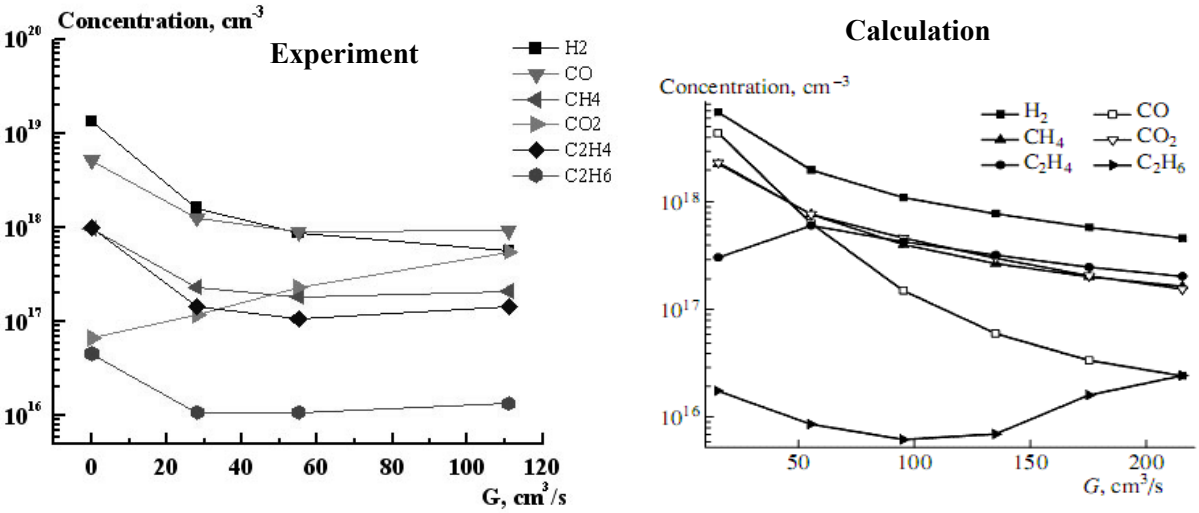


Fig. 4. The results of experiments and numerical modeling of concentrations of H_2, CO_2 and other main stable components in output gas products after the ethanol reforming. Solid electrodes.

The typical emission spectrum of plasma of the DGCLW working in ethanol-water solution is shown on Fig. 5. Observed spectra of investigated plasma are multicomponent and contain emission lines of

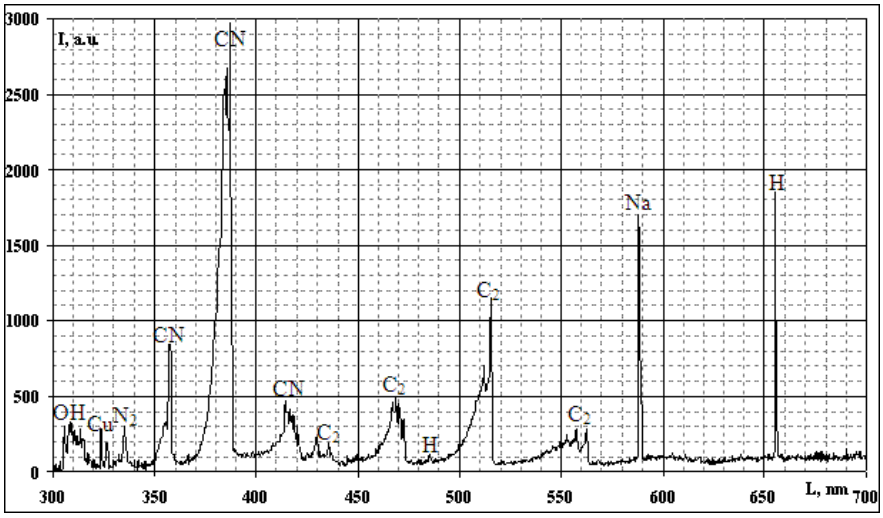


Fig. 5. Typical emission spectrum of DGCLW for regime with "liquid" anode.

H_α, H_β, electrode material lines Cu I (324.75, 327.4 nm), Na (588.58 nm), molecular bands of C_2(Swan system), CN(B-X), OH(A-X), a weak radiation of N_2(C-B).
The results of OES diagnostics of plasma in the DGCLW working in the mode with the liquid anode

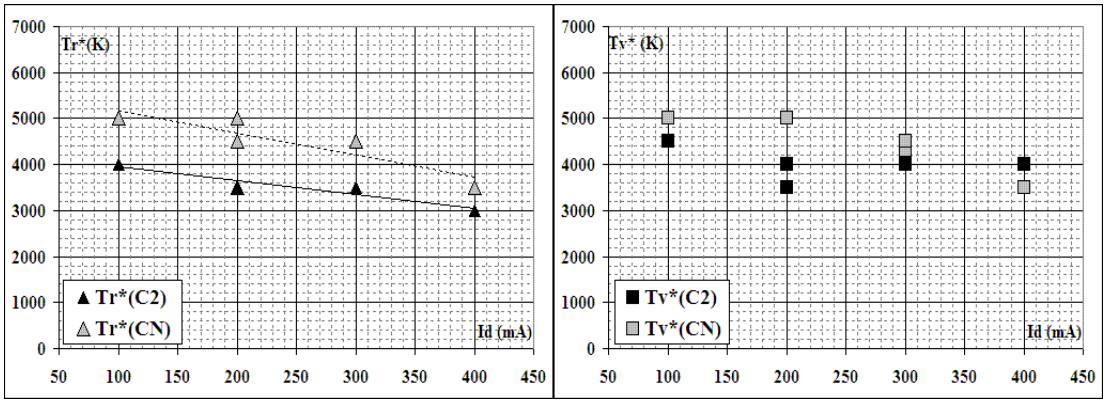


Fig.6. Dependences of rotational T_r^* and vibration T_v^* temperatures of the plasma components (CN, OH and C_2) from the discharge current I_d for regime with "liquid" anode.

in ethanol/water mixture (5/1) at the air flow rate G=55cm^3/s at currents I_d=50-400 A are shown in Fig. 6. From the temperature dependences obtained one can reviled that in the investigated regimes in the DGCLW working with the liquid anode, the characteristic temperatures for radical CN are close T_v(CN) ≈T_r(CN) and for molecule C_2 are differ T_v(C_2) >T_r(C_2). At that, T_v(CN) and T_r(CN) exceed T_v(C_2) a little bit (~20%). With increasing discharge current from 100 mA to 400 mA, all temperatures are decreased from 5000-4000 K to 4000-3000 K.

Fig. 7 shows the fragments of emission spectra related to the C_2 ($d^3\Pi_g$-$a^3\Pi_u$) Swan band emission in the spectral range 516-570 nm as obtained in plasma of the DGCLW with the liquid cathode working

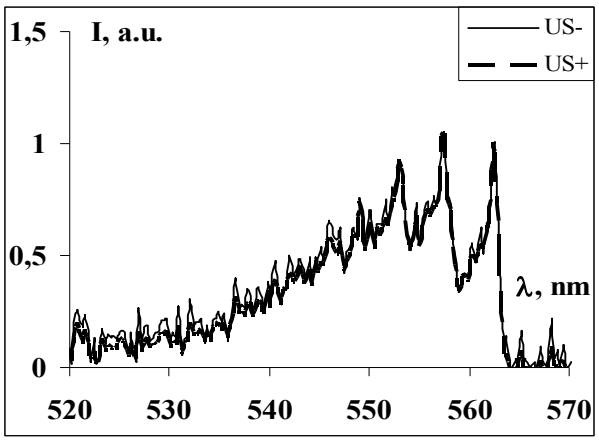


Fig. 7. Spectral distribution of the C_2 ($d^3\Pi_g$-$a^3\Pi_u$) emission in plasma of the DC DGCLW with liquid anode working in ethanol/water mixture (5/1) with and without US field. Discharge current I_d = 100 mA, air flow rate G=55 cm^3/s.

in ethanol/water mixture (5/1) with and without US field. One can see that fragments are almost identical, so the effect is practically absent. It can be explained by the possible depletion of US cavitations in the work liquid caused by additional gas evolution in plasma-liquid system due to reforming.

4. Conclusions

The composition content of syngas and the power inputs on the ethanol conversion in the DGCLW discharge depends on the gas flow rate and on the ethanol-water ratio in the solution.

It was shown that electronic temperature T_e^*(H) almost doesn't depend on the discharge current I_d, while vibration T_v^* and rotational T_r^* temperatures slightly decrease with I_d increasing.

The low-frequency ultrasonic field in liquid phase does not influence on the electronic T_e^* vibration T_v^* and rotational T_r^* temperatures of plasma components for investigated regime of the discharge.

The kinetic plasma-chemical modeling is in a fairly good agreement with experimental data, at least, for the main syngas components, H_2 and CO, predicting a non-thermal plasma-chemical mechanism of the ethanol conversion in the investigated plasma-liquid system.

Acknowledgements. This work was partially supported by the STCU Grant P-354 (EOARD 0880001, National Taras Shevchenko University of Kyiv, National Academy of Sciences of Ukraine,

5. References

[1] Warnatz J., Maas U., Dibble R.W. 2001. Berlin: Springer.

[2] 2010 18th World Hydrogen Energy Conf.. Essen, Germany. http://www.whec2010.com

[3] Velikodnyi V., Berkova M., Vorotinilin V., Grishin V., Kruchenko O., Popov V., Rychagov E., Polotnyuk O., Bykov A., Dobryneths Ya., Tolkunov B. 2007 Abstracts *Intern. Conf. "Energy Efficiency-2007"*. Kyiv, Ukraine. P. 91-93.

INVESTIGATIONS OF WATER VAPOR PHOTOLYSIS BY MEANS OF VUV EXCIMER LAMPS

Galina Zvereva

S.I.Vavilov State Optical Institute, St-Petersburg, 199034, Russia
E-mail: zvereva@soi.spb.ru

Calculations of water vapor decomposition products under the influence of vacuum ultraviolet (VUV) emission (Xe excimer lamp, 172 nm) have been carried out. High reactive radicals OH^* are shown to have been appeared effectively and destroyed pollutants added to vapor.

1. Introduction

It is known, that under influence of emission with λ<190 nm water is effectively decomposed with $^*OH$ radical formation. The main reaction of decomposition is :

$$H_2O + h\nu \rightarrow {}^*OH + H^*$$

Absorption coefficient k= σN (N- concentration of water molecules) of saturated water vapor at room temperature reaches values of 1-10 cm^{-1} at λ<172 nm (Figure 1), this provides emission absorption in several centimeters layer.

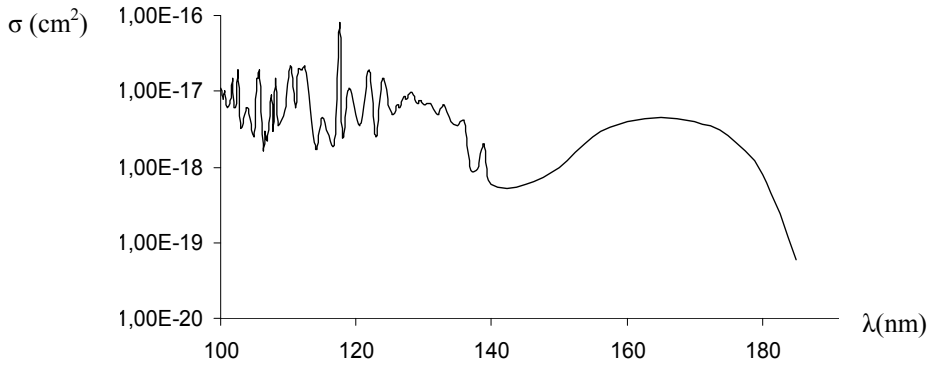


Fig.1. Water vapor absorption cross section σ as a function of wavelength [1].

Investigation of the new methods of $^*OH$ radicals formation is an actual task. Radical $^*OH$ is a powerful oxidant which oxidation potential (2.8 eV) exceeds oxidation potentials of such widely used oxidants as chlorine (1.4 eV), hydrogen peroxide (1.8 eV) and ozone (2.1 eV). Modern oxidation technologies based on advanced oxidation processes (AOPs) use for the toxic organic compounds decomposition mostly hydroxyl radical [2]. In AOPs, the organic compounds can be completely decomposed to CO_2 and H_2O. Depending on AOPs, $^*OH$ radicals are generated by different methods: by chemical oxidation using H_2O_2 , O_3, in Fenton's reactions; by radiation methods including UV radiation, γ-radiation, e-beam; by photocatalysis using TiO_2 etc [3].
At present time technologies based on VUV water decomposition are in the stage of research [4], this in particular is connected with absence of acceptable VUV light sources . However, at last two decades intensive research and development of excimer VUV light sources based on barrier discharges in high pressure rare gases were carried out [5,6]. Emission spectra of such excimer lamps are occupied wavelengths region of 120-180 nm , efficiency of conversion of electric power to emission one can reaches 60%. In this way excilamps give a new methods of radical $^*OH$ formation.

2. Investigations of water vapor photolysis

During decomposition of water vapor following products are generated H_2O_2, H_2,$^*H$,$^*OH$,O_2, $HO_2{}^*$,O, $O(^1D)$, O_2 [7,8]. Unknown concentrations were found by solution of system of differential equations:

$$dN_i/dt = \Sigma_l F_{il}^{+} - \Sigma_m F_{im}^{-} \qquad (i = 1\text{–}9),$$

where N_i – concentration of *i-th* products , F_{il}^{+}, F_{im}^{-} – flows of formation and decomposition of *i-th* product in reactions *l* и *m*. Velocities of reactions and parameters of photo processes were taken from [2,7,8]. As a VUV light source Xe excimer lamp (λ=172 nm , surface intensity I=10 mW/cm^{-2}) was considered.

In Figure 1 concentrations of main components of water vapor VUV-photolysis are presented. Calculations were made for vapor layer thickness x=1cm irradiated during time interval t=10^{-3} s. In Figure 2 concentrations of *OH radicals generated by photolysis of saturated vapor at different temperature are shown. In Figure 3 time behavior of radicals *OH and pollutants concentrations in irradiated water vapor (T=24 ºC) are presented. Initial pollutants concentration was equal to $1\cdot10^{14}$ cm^{-3} , the main reaction of its destruction was proposed to be:

$$^{*}OH + \text{pollutants} \rightarrow \text{products}$$

with velocity equal to typical value k=$1\cdot10^{-11}$ cm^{3}s^{-1} [9].

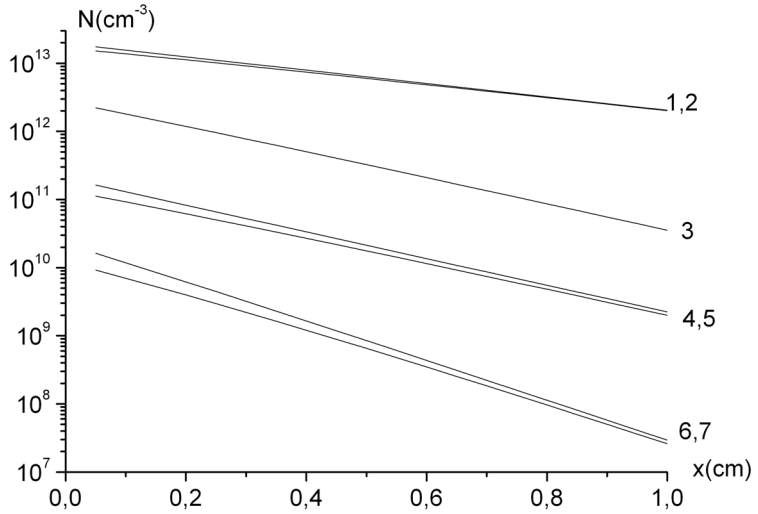


Fig. 1. Concentrations of saturated water vapor (T=24 ºC) VUV –photolysis products:
1 –H*, 2– *OH, 3 – H_2O_2, 4 – H_2, 5 – O, 6 - O_2, 7– HO_2.

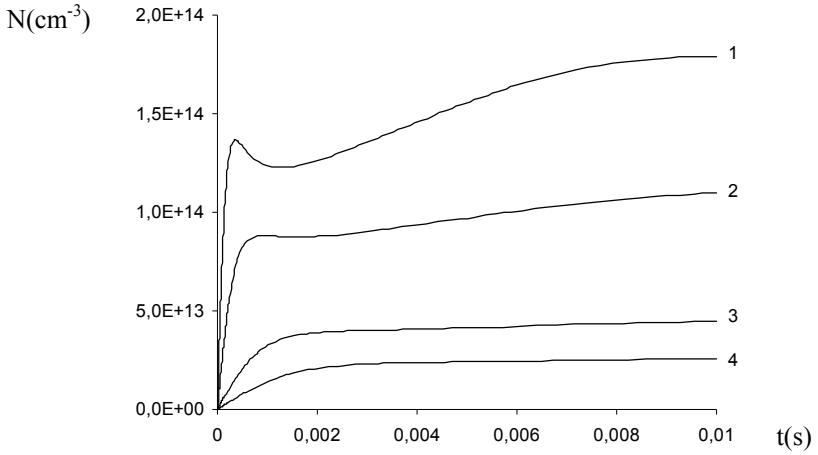


Fig. 2. Time behavior of concentration of *OH radicals generated by VUV photolysis of different temperatures saturated vapor, 1 – 90^{o}C, 2 – 60^{o}C, 3 – 24^{o}C, 4 – 7^{o}C.

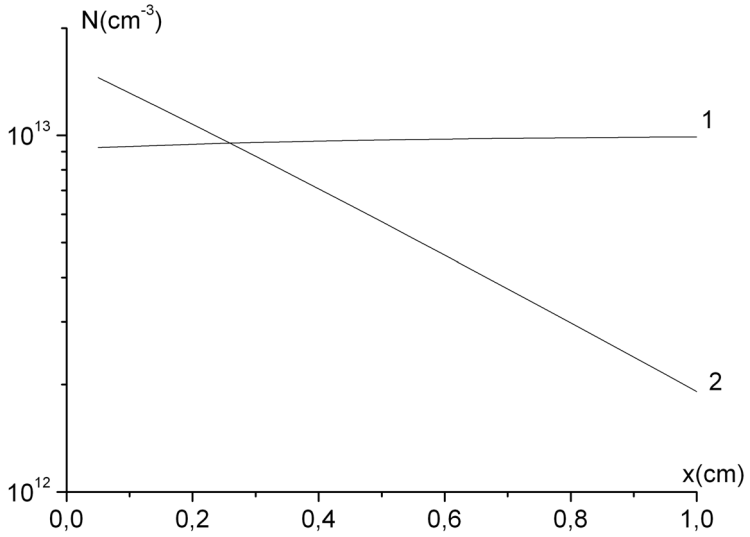


Fig. 3. Space distribution of radicals *OH (1) and pollutants (2) concentrations in water vapor (T=24 ºC) irradiated by VUV emission.

3. Conclusions

Numerical investigations have shown possibility of formation of high reactive radicals *OH during VUV photolysis of water vapor. Calculations of pollutants degradation under influence of water photolysis products have been carried out. These calculations have shown possibility of pollutants destruction in these conditions.

4. References

[1] K.Watanabe and M.Zelikoff 1953 *J. Opt. Soc. Am.* **43** N9 753 .
[2] Th.Oppenlander *"Photochemical Purification of Water and Air"* Wiley-VCH 2003 Weinheim.
[3] *Handbook of Environmental Engineering* **4** ed. By L.K.Wang, Y.-T Hung, and N.K.Shammas, NJ 2006.
[4] *Handbook on advanced photochemical oxidation processes* 1998 EPA/625/R-98/004.
[5] G.A.Volkova, N.N.Kirillova, E.N.Pavlovskaya and I.V.Podmoshenskii 1982 *Bill. Tov. Zn. (rus.)* N41 179.
[6] U.Kogelschatz 2003 *Plasma Chem. and Plasma Process.* **23** N1 1-46.
[7] R.Atkinson, D.L.Baulch, R.A.Cox, J.N. Crowley, R.H. Hampson, R.G. Hynes, M.E.Jenkin, M.J.Rossi and J.Troe 2004 *Atmos. Chem. Phys.* **4** 1461.
[8] I.M. Piskarev 2000 *J.Phys.Chem (rus.)* **74** N3 546 .
[9] M.Mandalakis, H.Berresheim and E.G.Stephanou 2003 *Envir. Sci. Technol.* **37** 542.

Topic 7

Surface processing and technology (cleaning, coating, etching and modification equipment)

A DIRECT COMPARISON BETWEEN GAS STATE AND ATOMISED LIQUID STATE PRECURSOR IN THE DEPOSITION OF FUNCTIONAL COATINGS BY PIN CORONA PLASMA

P.A.F. Herbert[1] and Justyna Jaroszyńska-Wolińska[2]
[1]*Plasma Ireland, 22 Summerhill North, Cork, Ireland*
[2]*Faculty of Civil Engineering and Architecture, Lublin University of Technology, Nadbystrzycka 40, 20-618 Lublin, Poland*
E-mail: therbert@irishprecisionoptics.com

An atmospheric pressure pin corona plasma jet was used to deposit polymeric coatings from monomer precursor in both vapour and liquid aerosol states to allow a direct comparison of the as-deposited coatings with respect to the achievement of soft plasma polymerisation (SPP) where the coating exhibits minimal fragmentation or damage to the monomer molecule while, at the same time, being highly cross-linked. A long chain perfluorocarbon molecule was introduced into the helium plasma and coatings deposited at rates of up to 50 nm/min. XPS, FTIR, contact angle and ellipsometric measurements indicated that a controlled polymerization reaction had taken place in the case of the vapour deposited samples through the vinyl group of the monomer, with only minor fragmentation of the functional perfluoro chain. Furthermore, a high level of cross-linking was achieved and the coatings were stable to a toluene wash. In contrast, while the liquid deposition samples showed good retention of monomer molecular structure, they exhibited negligible cross-linking and were readily removed by immersion in toluene rendering them functionally useless.

1. Introduction

In conventional PECVD, gas precursors are bombarded with aggressive plasma species to produce fragmentation and re-arrangement of the precursor monomers so that coating functionality remains limited to simple materials such as SiO_x, SiN or TiO_2 and complex chemistry cannot be deposited using such systems. In contrast, "soft plasma polymerisation" (SPP) is the ability to plasma deposit a cross-linked solid film with a very high degree of structural retention of the starting precursor so that the deposited coating retains the molecular complexity, functionality and value of the monomer. The prospective benefits of SPP include single-step industrial coating of substrates with, for example, complex and valuable, but sensitive, bio-active macromolecules such as enzymes and nucleic acids for applications such as biosensors, lab-on-a-chip and biomedical devices and many other processes.

Around 2000, Badyal et al combined helium atmospheric pressure glow discharge plasma with liquid aerosol precursor delivery to produce thin films with a high degree of monomer functionality retention [1], [2]. This technology was further developed by Dow Corning Corporation [3], [4]. The introduction of the liquid as aerosol was thought to protect the precursor from aggressive plasma species by encapsulating it in a droplet to minimise fragmentation. The use of aerosol delivery systems, however, produces complexities related to stability of the spray, control of droplet size, generation of an even precursor distribution over wide areas, the requirement to accurately dispense low volumes of liquid at a constant rate and rapid build-up of unwanted deposits on reactor surfaces.

In 2009, Herbert et al [6] introduced precursor as a vapour rather than aerosol into a non-thermal pin corona plasma previously used for so-called liquid deposition. The introduction of vapours rather than liquids allows for standard PECVD equipment (bubblers, mass flow controllers) to be used to generate an easily controlled, even flux of precursor onto a substrate. The coatings were shown to have the same functional chemistry retention and deposition rate as seen in liquid deposition plasma coatings. It could be deduced that control of the reaction mechanism cannot be predominantly dependent upon the presence of the monomer as an aerosol droplet but that that the key control parameter is the low plasma power coupled per unit of monomer, resulting in coatings being deposited in the power deficient regime described by Yasuda in vacuum polymerisation systems [7]. It was concluded that the specific plasma type used, the pin corona, is inherently predisposed to deliver low specific energy into the reaction zone and, hence, to SPP, even using gas precursors.

The result was confirmed by further experiments using this plasma type in which O'Neill, Herbert et al [8] showed that hexamethyldisiloxane (HMDSO) underwent SPP when injected into the plasma in the vapour phase. In the same work the liquid deposition technique failed to polymerise non-volatile polymethylhydrogen siloxane (PMHSO) atomized droplets at all flow rates. This deficiency in the ability of the pin corona liquid deposition technique to cross-link monomer precursor had been previously implied by work done by O'Neill et al [9] where PMHSO delivered as an aerosol into a pin corona system similarly could not be plasma cured except through the addition of 25 – 75% by volume of highly volatile tetraethylorthosilicate.

This work attempted to directly compare the performance of precursor in the conventional gas state and in the so-called liquid deposition state applied to surfaces via a pin corona plasma of low specific energy ~0.1 J/cm^3. The precursor used was 1H, 1H, 2H – Perfluoro – 1 – Decene (HDFD) and the resulting coatings were analysed for the two key performance parameters, namely the degree of polymerisation/cross-linking and retention of molecular structure and functionality. The precursor was chosen as it contains a polymerisable alkene group and fluorocarbon chain that can be readily characterized: CH_2=CH-$(CF_2)_7$-CF_3.

2. Experimental

A plasma jet was constructed based on the aerosol-plasma jet system described by O'Neill and O'Sullivan [10]. It consists of a dielectric head housing two tungsten needle pointed electrodes to which are applied in parallel an alternating current voltage. A space around each needle allows a 5 L/minute flow of helium ballast gas to enter the device. Between the two needle electrodes is a port for insertion of a pneumatic nebuliser through which 2 L/minute of helium was input into the pneumatic gas feed port and a flow of 5 μL/minute of liquid precursor delivered by syringe pump was input to the liquid feed port ensuring aerosol is introduced directly into the plasma region.

Alternatively, if the system is to be run in gas deposition mode, the working nebuliser is replaced in the electrode head by a 'dummy' nebuliser in which the liquid input port is blanked and a precursor plus helium carrier gas flow is fed into the gas input port. This precursor plus helium flow is the flow output by the real, working nebuliser which was configured to discharge into a heated flask the output of which flask fed directly into the dummy nebuliser. The flask was immersed in an oil bath at 200°C in order that the precursor with a boiling point of 146°C should be vaporised on emerging from the working nebuliser nozzle. The ~2 L/minute flow rate of precursor plus helium carrier gas ensured that the time between leaving the working nebulizer and reaching the plasma region was <1 second reducing the time available for cooling and condensation of the precursor. No evidence of such condensation was seen.

Very Low Frequency electrical power was delivered to both electrodes at a frequency of c. 19 kHz and a peak-to-peak voltage of c. 23 kV. The helium-precursor mix exited through a 75 mm x 15 mm diameter fluoropolymer tube in which the corona plasma was generated from the tips of the vertical needles. Coatings were deposited onto substrates placed directly under and 2 – 3 mm from the end of the tube. Samples were generated in both vapour and liquid deposition modes at the following power supply set powers as a percentage of full power: 2%, 5%, 10%, 20% and 40%. All coating runs were 180 seconds duration. The sample was then measured for coating thickness by ellipsometry. In order to determine the degree of cross-linking a toluene wash was carried out on selected samples for 5 minutes. The sample was then again characterized for coating thickness by ellipsometry.

FTIR, contact angle and XPS measurements were taken. The droplet size distribution of atomised liquid and vapour phase precursor was examined using the laser diffraction technique. Electrical characterisation was by high voltage probe and toroidal current transformer.

3. Results

Discharge powers were in the range 1.4 to 4.9 W. The introduction of liquid droplets into the discharge at constant set power resulted in a fall in measured discharge power of from 19% to 63% depending on the setting. The laser particle size data showed that the liquid spray system introduced droplets into the plasma region with a mean particle size of less than 10 microns in all cases. Increases in precursor flow rate produced larger droplets and a wider distribution of particle sizes. Production of

larger droplets with increasing flow seems intuitively reasonable due to the fixed nebulising gas flow rate of the atomizer being distributed over a larger volume per second of liquid. No droplets were observed in the vapour deposition mode confirming effective evaporation of all of the introduced HDFD and no re-condensation of the vapour.
Contact angle data was taken on samples run at all 5 power settings in both vapour and liquid deposition modes. In the case of the liquid deposition samples no reliable contact angle data could be obtained. Contact angles dropped from an initial value of approximately 120° to approximately 30° in 5 minutes for all liquid depositions. Coatings were not well cured being liquid in appearance and were readily removed by wiping. However, for the vapour deposition samples the contact angle dropped by approximately 10° in the first 5 minutes after deposition and then stabilised to give values between 107° and 122°, typical for plasma polymerised perfluoro compounds [11].
Figure 1 shows FTIR spectra of original monomer and as-deposited samples on KBr substrates.

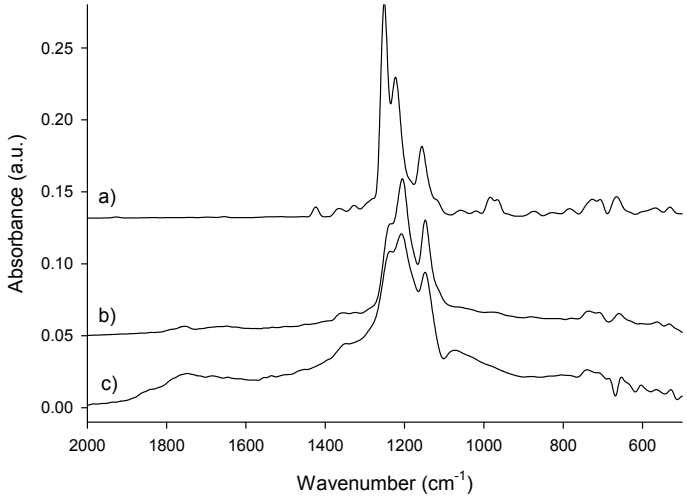


Fig. 1. FTIR spectrum of a) 1H, 1H, 2H-Perfluoro-1-Decene monomer, b) liquid deposition plasma polymerisation 2% set power and c) vapour deposition plasma polymerisation 2% set power

The original monomer shows major peaks at 1253, 1222 and 1155 cm^{-1} attributed to stretching modes of the CF_3 and CF_2 groups of the perfluoro chain. Both the vapour and liquid deposited films also contain peaks around 1240, 1210 and 1145 cm^{-1}, reflecting the shift to lower wavenumbers reported in plasma deposited fluorocarbon films and sometimes ascribed to the reduction of fluorine content in the film or to formation of a disordered and cross-linked coating [12]. As both fluorocarbon peaks are still well resolved in both deposition processes, it can be deduced that the fluorocarbon chain has not undergone significant levels of fragmentation and degradation in either plasma process. The as-deposited spectra show loss of the monomer peaks at 1425, 967 and 990 cm^{-1} corresponding to loss of the C=C bonds of the vinyl group. Both vapour and liquid deposited samples show slight peaks in the region 1700 – 1800 cm^{-1} which may suggest some C=O formation [11], [14] in agreement with the XPS analysis. The vapour deposited samples also showed peaks below 3000 cm^{-1} indicative of saturated alkane chemistry and confirming polymerisation through the vinyl group. These hydrocarbon features were not seen in the liquid deposition mode samples.
XPS analysis determined the following CF_2:CF_3 ratios for comparison with the ratio of 7:1 for the theoretical molecule: 2% set power liquid deposition sample –5.8:1; 2% set power vapour deposition sample –5.6:1. These values are lower than expected from the starting monomer indicating that some degradation of the monomer has occurred, as is typical of all such plasma processes [6], [10], [11], [14]. However, approximately 80% of the perfluoro chain has been retained intact, which compares favourably with previously reported soft plasma polymerisation processes [16].
The C 1s high resolution curve fitting suggests some cross-linking in the vapour samples which is not seen in the liquid sample. A shift in binding energy position of the peak assigned to CF_3 from 292.9 eV in the liquid deposition sample to 293.8 eV in the vapour deposition samples suggests the presence of the CF_3 species in a pendant position in the vapour samples rather than at the end of a linear chain.

This may indicate scission and reformation of the molecule in the vapour phase and confirms that the fluorocarbon chain has undergone a cross-linking reaction.
Figure 2 shows the ellipsometric data from all ten vapour and liquid deposition samples before and after toluene wash. Vapour sample deposition rate at up to 50 nm/minute drops off slightly with increasing plasma power perhaps related to higher cross-linking producing a denser film at high power. Liquid sample deposition rate is erratic and does not correlate well with discharge power and may be related to the unstable contact angle data, confirming that a stable coating was not formed using the aerosol assisted process. Vapour phase coatings produced significantly higher deposition rates for most power settings. Coating stability was determined by immersing the samples in toluene and re-evaluating the coating thickness using ellipsometry. The wash test results appear to be highly significant. The vapour samples all show a minor loss of coating thickness after washing, probably due to removal of any residual poorly polymerised material. However, the cross-linking detected in the high resolution curve fitting of the XPS spectra appears to be sufficient to stabilise the film and provides for significant wash resistance. In contrast, in the liquid samples almost no cross-linking has taken place so that wash resistance is non-existent and the entire coating is removed in all cases.

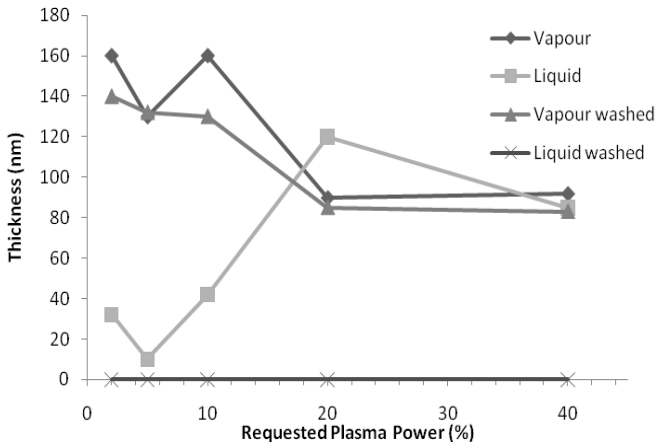


Fig. 2. Ellipsometric coating thickness data from vapour and liquid deposited samples at 5 set powers before and after toluene wash

4. Discussion

A low power, atmospheric pressure pin corona plasma has been used to deposit plasma polymerised coatings from HDFD monomer precursor in both the gas state and in the liquid aerosol state.
The large reduction seen in discharge power on introduction of the aerosol appears due to the nebulised droplets acting as a sink for free electrons. Fast electrons will be preferentially lost due to their increased collision rate and because they are able to better overcome the negative potential of the plasma sheath (the floating potential) set up by the droplet to ensure overall charge neutrality. Essentially, the liquid droplets act as a cold boundary surface to the plasma sinking charged species and imposing an overall cooling effect on the plasma. They are likely to change the Electron Energy Distribution Function by reducing both the mean electron energy and the high energy end or tail of the distribution. This reduction in electron density reduces the number of free electrons available to sink power directly resulting in the decrease in plasma power seen.
The vapour deposited samples showed that it was possible to deposit cured polymeric coatings which substantially retained the chemical structure of the precursor monomer so that the process could be characterised as SPP. Analysis shows that the precursor has undergone a controlled polymerization through the vinyl component of the molecule with low fragmentation of the functional fluorocarbon chemistry of the monomer. Some levels of oxidation of the coatings were evidenced by carbonyl and water peaks detected by FTIR and oxygen by XPS, as might be expected in this open perimeter system with the substrate exposed to ambient air. The absence of complete oxidation is consistent with the low specific power levels generated by this plasma type. The resultant coatings, however, produced XPS and FTIR spectra fully comparable to those produced by pulsed vacuum plasma or by liquid

aerosol plasma processing. Furthermore, wash tests, FTIR and XPS data showed clear evidence of a high level of cross-linking, an essential attribute of a viable functional coating.
In contrast, although the liquid deposition samples showed good chemistry retention, the XPS data suggested that cross-linking within the deposited coatings was negligible and the resultant wash tests rendered the coatings functionally useless, even at plasma power levels equal to those of vapour deposition processes. Difficulty in obtaining adequate levels of polymerisation of liquid state atomised precursors with pin corona has been seen in previous work [8], [9].
Both deposition rate and the extent of cross-linking of the deposited coating should be associated with the degree of monomer interaction with the plasma at the molecular level. It is self-evident that monomer molecules in the vapour phase will be fully exposed to interaction with plasma species from entry into the plasma region, throughout their flight and on the substrate surface. In contrast, most monomer in the liquid state will be shielded from the plasma, certainly during flight and possibly to a significant extent on the substrate surface. Vapour phase monomer molecules will, therefore, have a much higher probability of engaging in plasma induced chemical reactions than liquid phase molecules so that the vapour phase reaction rate is likely to be substantially higher generating more cross-linking and thicker coatings at low plasma power.

5. Conclusions

This paper details what appears to be the first reported direct comparison of coatings targeting SPP from both gas and liquid aerosol state precursors using a cool, atmospheric pressure, highly non-isothermal equilibrium pin corona discharge with a low specific energy ~0.1 J/cm^3.
The work confirmed that, with this type of corona discharge, largely damage-free polymerisation of monomer to deposit a functional coating can be readily achieved with precursor in the conventional gas state operating in standard PECVD mode. The use of precursor in the liquid state as nebulised droplets is, thus, not required to achieve SPP, as has been suggested elsewhere [1], [2], [3], [18], [19], [20], [21]. Vapour deposition showed high retention of monomer molecular structure in the coating combined with excellent cross-linking and durability, the two key SPP parameters of merit.
In contrast, the same process but using precursor as liquid aerosol in the so-called liquid deposition mode was unable to achieve a comparable coating. Good retention of monomer molecular structure was seen in the liquid coatings, but cross-linking within the coating was negligible thereby rendering the deposits functionally useless.

6. References

[1] Ward, L.J. et al, *Chem. Mater*, 2003, *15,* 1466
[2] Ward, L.J. et al, *Langmuir,* 2003, *19*(6), 2110
[3] O'Hare, L.-A.; O'Neill, L.; Goodwin, A. J. *Surf. Interface. Anal*., 2006, *38 (11),* 1519
[6] Herbert, P.A.F., O'Neill, L., Jaroszynska-Wolinska, J., *Chem. Mater.*, 2009, 21, 4401-4407
[7] Yasuda, H. *Journal of Polymer Science: Macromolecule Reviews*, 1981, *16*, 199
[8] O'Neill, L., Herbert, P.A.F., Stallard, C., Dowling, D.P, *Plasma Process. Polym.*, 2010, 7, 43-50
[9] L. O'Neill et al, "Plasma Polymerised Primers – Improved Adhesion through Polymer Coatings", Society of Vacuum Coaters, 50th Annual Technical Conference Proceedings, 2007
[10] O'Neill, L.; O'Sullivan, C. *Chem Vap. Dep*., 2009, *1-3*, 21
[11] Coulson, S. R. et al, *Langmuir*, 2000, 16, 6287 – 6293
[12] Fanelli F., Fracassi, F, d'Agostino R., *Plasma Process Polymer*., 2007, 4, S430-434
[14] Laguardia, L. et al, Macromol. Symp., 2007, 247, 295–302
[16] Coulson, S. R. et al, *Chem. Mater.*, 2000, 12, 2031
[18] Heyse, P. et al, *Plasma Process. Polym.,* 2007, *2*, 145
[19] Tatoulian, M. ; Arefi-Khonsari, F. *Plasma Process. Polym*., 2007, *4,* 360
[20] Beck, A.J.; Short, R.D.; Matthews, A. *Surf. Coat. Technol*., 2008, 203 (5-7), 822-825
[21] Hynes, A. et al, *Hakone IX International Symposium on High Pressure, Low Temperature Plasma Chemistry*, Padova, Italy, 2004, 8O-03

STUDY OF EFFECTS RELATED TO THE CONTINUOUS OPERATING REGIME OF DCSBD

Dušan Kováčik[1], Zlata Tučeková[1], Jana Kubincová[1], Anna Zahoranová[1], Miroslav Zahoran[1], Mirko Černák[1, 2], Miroslav Hnatko[3]

[1]*Department of Experimental Physics, Faculty of Mathematics, Physics and Informatics, Comenius University, Mlynská dolina, 842 48 Bratislava, Slovak republic*
[2]*Department of Physical Electronics, Faculty of Science, Masaryk University, Kotlářská 2, 61137 Brno, Czech Republic*
[3]*Department of Ceramics, Institute of Inorganic Chemistry, Slovak Academy of Sciences, Dúbravská cesta 9, 842 36 Bratislava, Slovak republic*
E-mail: kovacik@fmph.uniba.sk

Many potential plasma applications (surface treatment and activation of nonwoven fabrics and other planar materials) of Diffuse coplanar surface barrier discharge (DCSBD) require it to be operating in continuous regime. Thus the continuous regime of DCSBD with the different geometry of electrodes system and the suppressed triple point was investigated. To compare particular electrodes geometry and lifetime of DCSBD, the electrical properties and efficiency of cooling system was measured. Tripple point (ceramics-silver electrode-transformer oil) was analyzed by SEM method before and after continuous test. The potential changes in electrical properties of transformer oil used as insulation and cooling fluid in DCSBD was investigated after approx. 1 month non-stop operation.

1. Introduction

In recent years, there is a huge interest in non-equilibrium plasma applications for surface modification of low cost materials as polymers [1-3], textiles [4], polymer films [5-7], nonwoven fabrics [8-10] in order to gain surfaces with required properties for further utilization. Since low-pressure plasma technologies are high-priced with long processing time admittedly there is an effort to realize surface modifications at atmospheric pressure and restrict the need of costly vacuum systems [11-15]. On the other hand, plasma at atmospheric pressure is quite different from that at low pressure. Typical diffuse plasma generated easily at low pressures e.g. by glow discharge has with increasing gas pressure tendency to overcome into hot filaments, so called microdischarges of streamer character. Such plasma is hardly used in surface modification processes of thermally sensitive materials. One of possibilities how to prevent plasma thermalization at higher pressures is to separate at least one of electrodes from discharge area by dielectric layer. After supplying by AC high voltage with frequency from 50 Hz to several kHz this electrode system enables to generate in the narrow gap (1-5 mm) between electrodes dielectric barrier discharge (DBD) [16]. Due to the present of dielectric and accumulation of charge on its surface during first half-period of voltage the electric field strength in concrete spots is reduced and filaments become extinct. In the next half-period this charge facilitates the ignition of micro-discharge on the same spot ad whole process continues by contraries [17]. This mechanism of short microdischarge duration (1-10 ns) [18] explains the thermal non-equilibrium of DBD plasma with high temperature of electrons and low temperature of heavier ions and neutral molecules. Although the non-equilibrium plasma of DBD fulfils the requirements for surface treatment of materials from the thermally surface damage point of view the randomly distributed narrow filaments can result in inhomogeneous and insufficient surface treatment. To prevent the plasma filamentation and operate the discharge in glow-like regime [19, 20] many atmospheric pressure plasma devices require helium and occasionally neon containing working gas. However, the cost associated with using large amounts of noble gases makes such atmospheric pressure plasma treatments impractical.

There are several electrode systems configurations using which dielectric barrier discharges (DBDs) can be generated [16, 18]. For surface treatment of planar materials and nonwoven fabrics the surface DBDs [8-10] seem to be the most applicable. This type of discharges is characterized by plasma generated on the surface of dielectric layer consisting of numerous to the surface parallel orientated microdischarges. Surface treatment of material can be achieved by bringing it in the direct contact

with plasma for sufficient time. This plasma exposure results in surface properties changes of treated material. In this way e.g. hydrophobic surface of polymer materials can be inverted to the hydrophilic due to polar groups and radicals formation induced by plasma. Therefore plasma can offer an alternative method to the conventional chemical and environmentally unfriendly methods for surface treatment of nonwoven fabrics whose production continually grows.
Potential non-equilibrium plasma sources for particular surface modification of materials have to fulfil several requirements. The most important one is to realize plasma surface modification in low-cost working atmosphere at atmospheric pressure without any presence of rare gases that can provide diffuse mode of discharge plasma. Such plasma source also should generate plasma with high power density and in case of its implementation into industry lines its lifetime must not be limited what means that plasma source have to enable continuous operation for very long time (several months).
On the basis of about mentioned aspects Diffuse coplanar surface barrier discharge (DCSBD) seems to be the most applicable from surface modification point of view. Special design and geometry of DCSBD electrode system gives possibility to generate non-equilibrium plasma practically in any gas of atmospheric pressure. From another properties of DCSBD the macroscopically homogeneous plasma concentrated in very thin layer (~0.3 mm), as shown in Fig. 1a, high plasma power density and unlimited lifetime of DCSBD should be emphasised [21-23]. DCSBD was successfully tested for surface treatment of polypropylene nonwoven fabrics, foils, paper and wooden, glass and aluminium surfaces [24-30] and its effect on various surfaces is investigated not only at FMFI UK, Bratislava but also at several research institution and traditional industrial sectors in Slovak (VÚTCH, Žilina – Fig. 1b,c; SAV, Bratislava) and Czech republic (INOTEX, Dvůr Králové nad Labem; TONAK, Nový Jičín – Fig. 1d, PEGAS, Znojmo – Fig. 1f), Germany (pmTUC, Chemnitz; INP Greifswald), Poland (IW, Lodz – Fig. 1e), Sweden (YKI, Stockholm) and in near future it will be delivered to Spain (IRIS, Castelldefels).

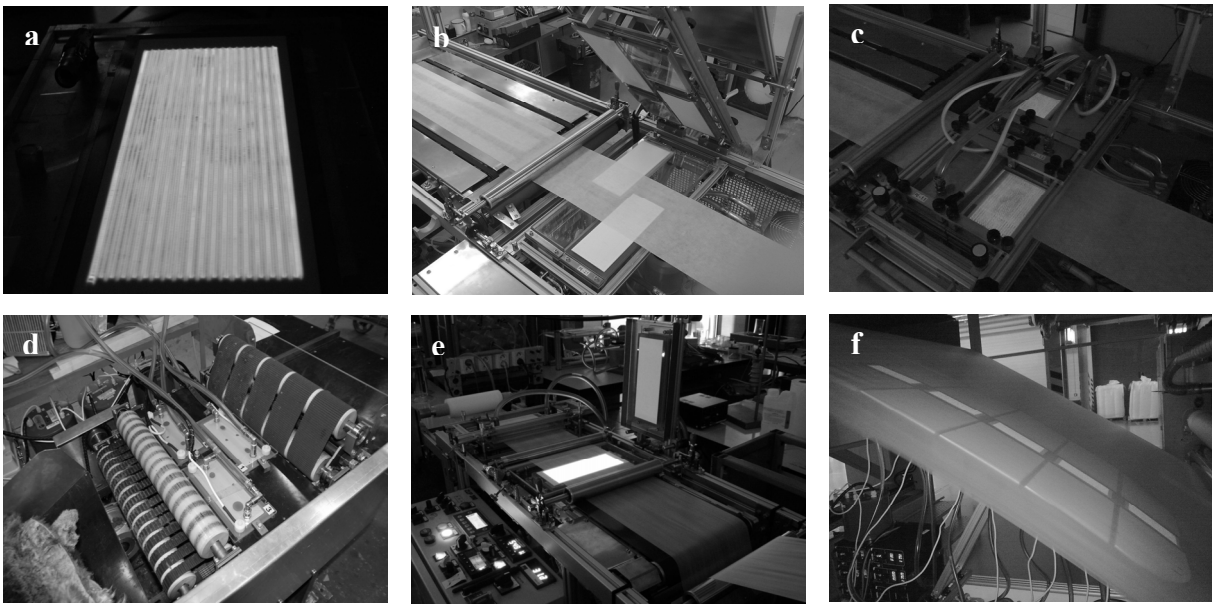


Fig. 1. Illustrative photos of DCSBD utilization in different plasma devices for surface treatment: a) macroscopically homogeneous plasma of DCSBD burning in ambient air at power consumption 400 W, b) ZUP 400 plasma device for continuous surface treatment of textiles (width till 40 cm) with four DCSBD elements - VÚTCH, Žilina, c) ZUP 400 device in operation regime with two visible plasma areas of bottom DCSBD elements, d) plasma device for surface treatment of rabbit hairs on the rabbit pelts – TONAK, Nový Jičín, e) ZUP 200 plasma device for continuous surface treatment of textiles (A4 size) with two DCSBD elements - FMFI UK, Bratislava, IW, Lodz, f) in-line plasma surface activation of polypropylene nonwovens using plasma system of 5 DCSBD elements - PEGAS, Znojmo.

2. Experimental

DCSBD discharge system* consists of several parts (Fig. 2a) of which the most important one is the electrode. Electrode with the active plasma area of 200 x 80 mm consists normally of silver strip electrodes embedded 0.5 mm below the surface of 96 % Al_2O_3 ceramics (Fig. 2b) and is cooled by circulating insulation oil at the side with electrodes. Both the width of silver electrode and the inter-electrode gap is 1.3 mm.

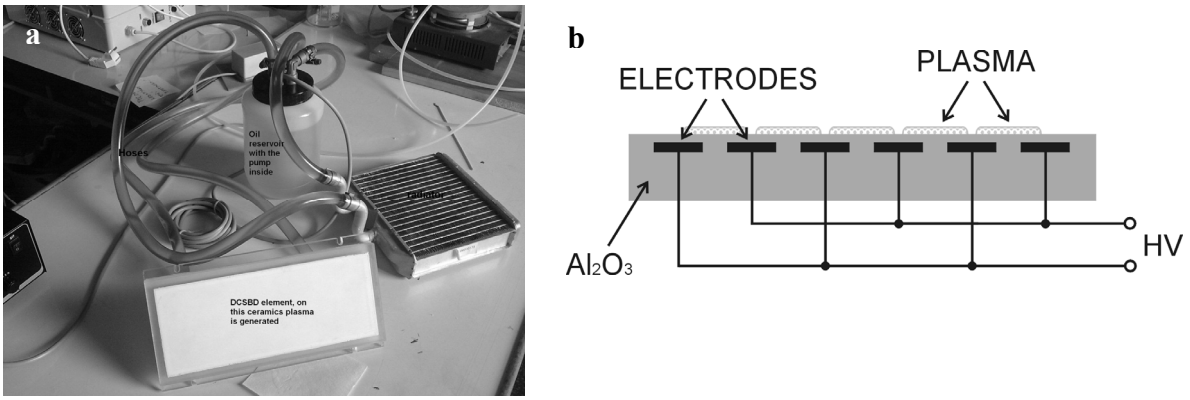


Fig. 2. DCSBD system with its components: DCSBD element – electrode, oil reservoir with pump, radiator (a), DCSBD electrode system in detail (b).

To prevent undesirable sparking between near-by electrodes, these are separated by 0.5 mm high insulating barriers, which were prepared by milling the 1 mm thick ceramics into 0.5 mm depth and plotting on the strip electrodes in these grooves (Fig. 3a). Since technical realization of the grooved ceramics is quite complicated we investigated the DCSBD electrodes that were prepared using 0.5 mm thick planar ceramics with strip electrodes 3 mm wide and separated by 1 mm-inter-electrode gap, as shown in Fig. 3c. Moreover, to suppress the influence of triple point (ceramics-silver electrode-insulating oil) the ceramics with electrodes were covered by thin ESL glass dielectric layer (Fig. 3b). The DCSBD electrodes were energized by 18 kHz sinusoidal high voltage, supplied by HV generator – Plasma Power Supply PPS02, KAMEA Electronics. Pearson current monitor Model 4100 and two high voltage probes Tektronix P6015A (1:1000) monitored the electrical parameters of discharges. The signals from all three electrical probes were recorded by Tektronix TDS 2024 oscilloscope (200 MHz). Obtained electrical waveforms were used to calculate the real electrical power of discharge plasma. DCSBD systems based on the discharge elements of different electrodes geometry was studied from the thermal and electrical properties point of view in continuous operation in duration min. 30 min. For ceramics temperature measurements the Micro-Epsilon CS series infrared thermometer was used. After extreme long continuous regime (weeks) of DCSBD the potential changes in the area of triple point were detected by SEM method and after the tests the insulating oil was analyzed with the purpose to get information concerning the breakdown voltage and water content changes.

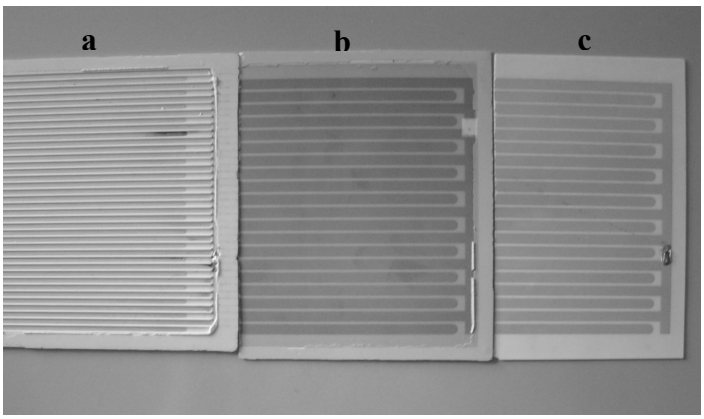
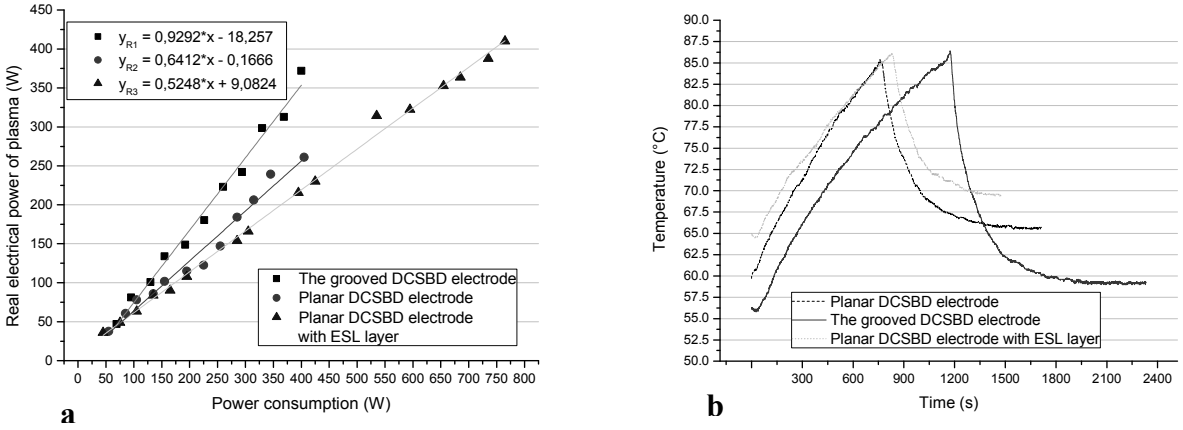


Fig. 3. Photos of investigated DCSBD electrode systems: 1 mm thick ceramics with 1.3 mm-wide strip electrodes in the 0.5 mm deep grooves (a), planar ceramics of thickness 0.5 mm with strip electrodes of width 3 mm and inter-electrode gap 1 mm covered by ESL dielectric layer (b) and without ESL layer (c).

*developed at Department of Experimental Physics, Faculty of Mathematics, Physic and Informatics, Comenius University, Bratislava

3. Results and discussion



After calculating the real electrical power of plasma we plotted the calibration curves (Fig. 4a) whose formulas enable to determine the real plasma power when power consumption of HV power source is known. It is evident that the most efficient energy transmission to plasma was observed in case of the grooved DCSBD electrode.Fig. 4. a) Calibration curves for determining the real plasma power of particular DCSBD electrodes, b) time dependence of ceramics temperature measured in the middle for particular DCSBD electrodes in the regime without and with ventilator.

In consequence of burning DCSBD the ceramics plate is warming end electrode must be cooled. The heat is taking away through insulating oil that is after that cooled in radiator with ventilator. To ascertain the ventilator importance we measured temperature on the ceramics in the middle of plasma area without and with ventilator. As it can be seen in Fig. 4b without ventilator the ceramics temperature was in all cases linear increasing till the moment of ventilator switching on when the temperature reached the value of 85ºC. The slowest warming of ceramics was observed in the case of grooved DCSBD electrode due to the largest surface that is in contact with oil.
For failure-free continuous operation of DCSBD it is very important to use as electrodes insulating and cooling medium synthetic oil with very good dielectric properties. From this reason we studied the breakdown voltage and water content for several samples of oil. The results are listed in Tab. 1. values in column “Oil No.1” represent dielectric properties of quite new unused oil. Due to filling up the cooling circle with oil and manipulation with it in laboratory ambient the dielectric properties are getting worse (column “Oil No. 3”). The influence of more than one month-continuous DCSBD operation of DCSBD on oil properties is illustrated by the values in column “Oil No. 2”. Column “Oil. No. 4” represents the breakdown voltage value for oil that was stored for 45 days in jerrycan inside which also some volume of ambient air was.

Tab. 1. Dielectric properties of insulating oil samples that is used in DCSBD also as cooling medium.

	Oil No. 1	**Oil No. 2**	**Oil No. 3**	**Oil No. 4**
Breakdown voltage [kV/2.5 mm]	87	39	47	77
Water content [mg/kg]	115	631	-	-

Influence of DCSBD operation in continuous regime on the possible electrodes erosion in the area of triple point was analyzed by SEM. Images in Fig. 5 illustrate the cross-section views of the triple point for particular DCSBD ceramic with one silver electrode. Fig. 5a shows the reference planar ceramic (from left: ceramics, silver electrode). In Fig. 5b it can be seen the silver electrode erosion after DCSBD continuous operation in duration approx. 10 days. Fig. 5c shows DCSBD electrode whose electrode system was covered by ESL dielectric layer (from left: ceramics, silver electrode, ESL dielectric layer). Protective effect of ESL layer is visible in Fig. 5d where no erosion of electrode was observed although this electrode was generating DCSBD for more than one month without interruption. Quality of ESL layer is represented by Fig. 5e where the present of air micro-bubbles indicates its low degree.

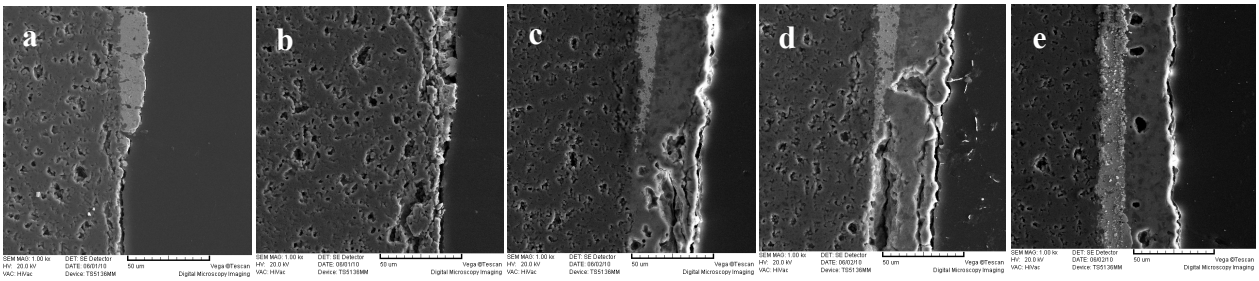


Fig. 5. SEM images of triple point cross-section for particular DCSBD electrodes: reference planar ceramics with silver electrode (a), planar ceramic after 10 days of continuous operation (b), planar ceramics with silver electrode covered by ESL layer (c), planar electrode with ESL layer after one month of continuous operation, air micro-bubbles in ESL layer (e).

Acknowledgement. This research has been supported by the Slovak Research and Development Agency, Project No. APVV-0485-06 and VEGA grant No. 1/0783/10.

4. References

[1] Chan C M, Ko T M, Hiraoka H 1996 *Surf. Sci. Rep.* **24** 1.
[2] Carrino L, Moroni G, Polini W 2002 *J. Mater. Process. Technol.* **121** 373.
[3] Mühlhan C, Weidner S, Friedrich J, Nowack H 1999 *Surf. Coat. Tech.* **116-119** 783.
[4] Xu W, Liu X 2003 *Eur. Polym. J.* **39** 199.
[5] Kröpke St, Akishev Yu.S, Holländer A 2001 *Surf. Coat. Tech.* **142-144** 512.
[6] Sellin N, Campos J S 2003 *Mater. Res.* **6** 163.
[7] Chen J R, Wang X Y, Tomiji W 1999 *J. Appl. Polym. Scie.* **72** 1327.
[8] Gulejova B, Simor M, Rahel J, Kovacik D, Cernak M 2002 *Czech. J. Phys.* **52** 1.
[9] Rahel J, Simor M, Cernak M, Stefecka M, Imahori Y, Kando M 2003 *Surf. Coat. Tech.* **169-170** 604.
[10] Simor M, Rahel J, Cernak M, Imahori Y, Stefecka M, Kando M 2003 *Surf. Coat. Tech.* **172** 1.
[11] Bardos L, Barankova H 2010 *Thin Sol. Film* in press.
[12] Väänänen R, Heikkilä P, Tuominen M, Kuusipalo J., Harlin A 2010 *AUTEX Res. J.* **10** 8.
[13] Kaplan S 2004 *Surf. Coat. Tech.* **186** 214.
[14] Friedrich J F, Rohrer P, Saur W, Gross Th, Lippitz A, Unger W 1993 *Surf. Coat. Tech.* **59** 371.
[15] Kwon O J, Tang S, Myung S W, Lu N, Choi H S 2005 *Surf. Coat. Tech.* **192** 1.
[16] Kogelschatz U 2003 *Plasma Chem. Plasma Process.* **23** 1.
[17] Pochner K, Neff W, Leber R 1995 *Surf. Coat. Tech.* **74-75** 394.
[18] Xu X J 2001 *Thin Sol. Film* **390** 237.
[19] Rombola G, Parisi F, Pavan C and Dapra D 2006 *Czech. J. Phys.* **56** 1021.
[20] Trunec D, Brablec A, Buchta J 2001 *J. Phys. D: Appl. Phys.* **34** 1697.
[21] Simor M, Rahel J, Vojtek P, Cernak M 2002 *Appl. Phys. Lett.* **81** 2716.
[22] Cech J, Stahel P, Navratil Z, Cernak M 2008 *Chem. Listy* **102** 1348.
[23] Cernak M, Cernakova L, Hudec I, Kovacik D, Zahoranova A 2009 *Eur. Phys. J. Appl. Phys.* **47** 22806.
[24] Kovacik D, Zahoranova A, Bucek A, Cernak M 2008 *Hakone XI: Contributed Papers* **2** 493.
[25] Stahel P, Bursikova V, Bursik J, Cech J, Janca J, Cernak M 2008 *J. Optoelectr. Adv. Mat.* **10** 213.
[26] Kovacik D, Zahoranova A, Bucek A, Rahel J, Cernakova, L, Cernak M 2007 *Proc. of the 17th Symposium on Physics of Switching Arc, Contributed Papers* **1** 129.
[27] Odraskova M, Rahel J, Zahoranova A, Tino R, Cernak M 2008 *Plasma Chem. Plasma Process.* **28** 203.
[28] Toth A, Cernakova L, Cernak M, Kunovska K 2007 *Holzforsch*. **61** 528.
[29] Bucek A, Havel J, Homola T, Cernak M 2006 *Proc. of Moderní trendy ve fyzice plazmatu a pevných látek* **2** 59.
[30] Bonova L, Bucek A, Plecenik T, Zahoranova A, Cernak M *Chem. listy* **102** 1452.

POLYMERIZATION OF ALLYL ALCOHOL USING ATMOSPHERIC PRESSURE GLOW DISCHARGE

Masuhiro Kogoma, Kenji Tsuji and Kunihito Tanaka

Department of Materials and Life Sciences, Faculty of Science and Technology, Sophia University
7-1 Kioi-cho, Chiyoda-ku, Tokyo, Japan
E-mail: m-kogoma@sophia.ac.jp

Plasma polymerization of allyl alcohol was done by atmospheric pressure glow discharge(APGD) to attach hydroxyl groups to the glass surfaces. Allyl alcohol vapour was introduced by He bubbling system. LF(300kHz) discharge power from 10 to 30 W was applied to parallel electrode discharge apparatus. The deposition rate on the glass substrate which was inserted between the electrodes reached about 0.4□m min^{-1}; this rate was much higher than that obtained in the low pressure system. Hydroxyl group contents on the deposited surfaces were about 18% and this concentration remained for the higher power values.

1. Introduction

The introduction of hydroxyl chemical groups on the solid surfaces is very useful as the pre-activation step before the surface coating such as the silane coupling reaction to insert functional chains and the grafting of PEG for biocompatible surface.

We previously reported the surface oxidation to improve the wettability on the polyethylene powder using APGD[1]. The plasma oxidation of the polymer will produce a mixture of -COOH, –CO and –OH groups as the hydrophilic groups on the treated surfaces. It is thus difficult to obtain -OH group without production of any other oxidants on the treated surfaces. Gombotz et al. [2] introduced hydroxyl groups by low pressure glow plasma CVD of allyl alcohol on the PET film to activate the surface before immobilizing the PEG on the surface. However, they could not obtain the complete surface coverage of hydroxyl groups by low pressure PCVD. In the low pressure glow discharge, the high velocity ion impact leads the degradation of the deposited surface. The results show that the hydroxyl groups in the monomer molecule cannot easy to remain on the deposited surface. So the low pressure PCVD of allyl alcohol could not have enough concentration of hydroxyl groups on the surfaces. On the other hands, because the low ion energy in high pressure discharge, APGD CVD can eliminate the possibility of any reaction which would be attributed to the ion impact reaction on the surface. We report here the thin layer deposition on the glass surface by the APGD-CVD using allyl alcohol(AA).

2. Experimental

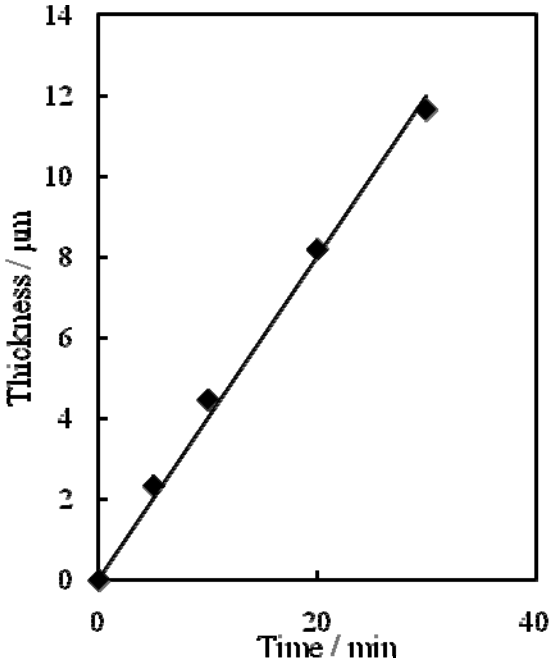
LF(300 kHz) discharge power from 10 to 40 W are applied to a discharge apparatus that is composed of parallel Pylex^{R} glass plates and outer metal electrodes. Allyl alcohol was used as a monomer substance as the simplest alcohol molecule which has a double bond in the structure. The 2 slm of He gas is mixed with 30-50 sccm of allyl alcohol vapour, then introduced to the discharge zone. A glass plate(0.5 mm×10 mm×30 mm) is used as the substrate inserted in the discharge zone. The discharge gap is 2 mm. The deposited films are investigated by surface roughness profiler, wettability measurements using water contact angle method, elemental analysis and XPS for the chemical derivatisation techniques to measure the absolute concentration of hydroxyl groups on the deposited surfaces.

3. Results and discussions

Deposited film surfaces are slightly yellowish brown and are not soluble in water or ethanol.

Figure 1 shows the deposition thickness as a function of the discharge time at 30 W of the discharge power and 7 sccm of the monomer flow rate.

The film thickness is almost linearly dependent on the discharge time. A deposition rate of about 0.4μm min^{-1} is attained. This rate is 30 times faster than that obtained in low pressure discharge[2].



, Fig. 1 Deposited film thickness as a function of the discharge time.
Discharge power: 30 W ; Monomer flow rate: 23.2 sccm; Carrier He gas flow rate: 2.0 slm

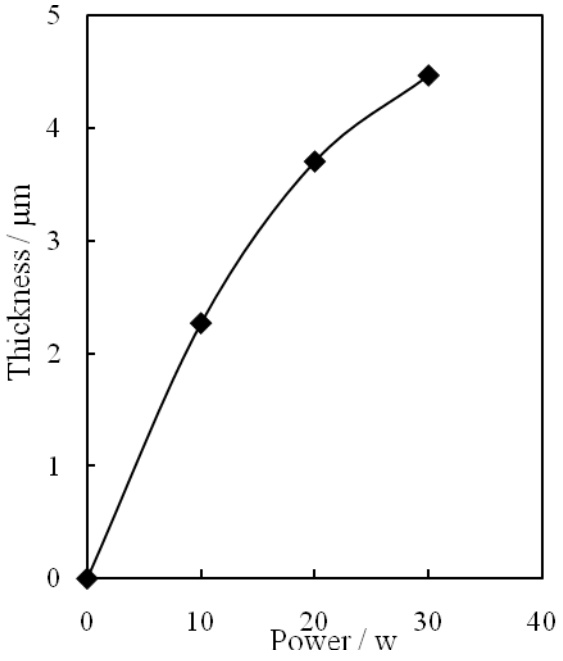


Fig. 2 Film thickness as a function of the discharge power. Monomer flow rate: 23.2 sccm; Carrier He gas flow rate: 2.0 slm; Discharge time: 10min.

This means that the APGD-CVD is a very efficient deposition system for a polymer deposition. In general, the polymer deposition reaction will takes place not only on the substrate but also on the wall of the chamber in the low pressure PCVD. But in the APGD CVD, deposition reaction only takes place in the narrow plasma zone which is restricted between the parallel electrodes. That is the main reason why the APGD CVD has such high rate deposition. Figure 2 shows the deposition thickness as a function of the discharge power. The deposition rate is little bit decreased at the high power region. This means that a monomer flow limitation will be attained at the high power region.

Figure 3 shows the film thickness as a function of the monomer flow rate.

The thickness is almost linearly dependent on the flow rate of the monomer. Even in the highest flow rate, the thickness is still increasing linearly. This means that the flow rate limitation is not reached in the figure. It seems that if we increase the flow rate higher than 23.2 sccm, we will obtain higher than 0.4 μm min^{-1} as shown in Figure 1.

Figure 4a shows the XPS C_{1s} spectra of the deposited film surface. Figure 4b shows the C_{1s} spectra of the surface after being treated by

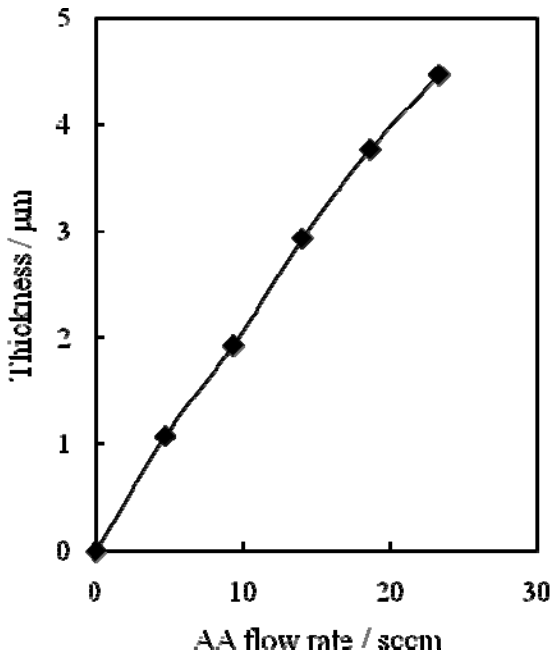


Fig. 3 Film thickness as a function of the monomer flow rate. Discharge time: 10 min; Carrier He gas flow rate: 2.0 slm; Discharge power: 30W.

trifluoroaceticacid anhydride(TFAA). After treatment with TFAA, two new peaks appeared in the high binding energy region they are attributed to $\underline{C}F_3$ and $\underline{C}OO-CF_3$. We can calculate the OH group surface concentration by comparing XPS spectra data of the TFAA-treated standard material such as poly-vinylalcohol(PVA) and using equation (1).

$$R–OH + (CF_3CO)_2O \rightarrow R–OCOCF_3 + CF_3COOH \qquad (1)$$

Figure 5 shows the concentration of hydroxyl groups on the deposited films as a function of the discharge power measured by chemical derivatisation technique. The figure shows that we attained about 18% of OH group on the deposited film surfaces. The OH group concentration is almost constant between 10-30W of the discharge power.

The elemental analysis was done with the deposited films to confirm the results obtained by chemical derivatisation technique. For the measurement of the elemental analysis, the sample materials were collected from the deposited films by scrubbing of the substrates. The collected samples were combusted in the fine tubing with oxygen. Elemental analysis was based on weight changes after oxidation of the samples. Table 1 shows the mean data of the elemental analysis of the deposited material. Differences between XPS data and elemental analysis data will be attributed to the small amount of carbonyl group which are included in the deposited materials and to the structure changes due to the cross linking of the allyl alcohol polymer.

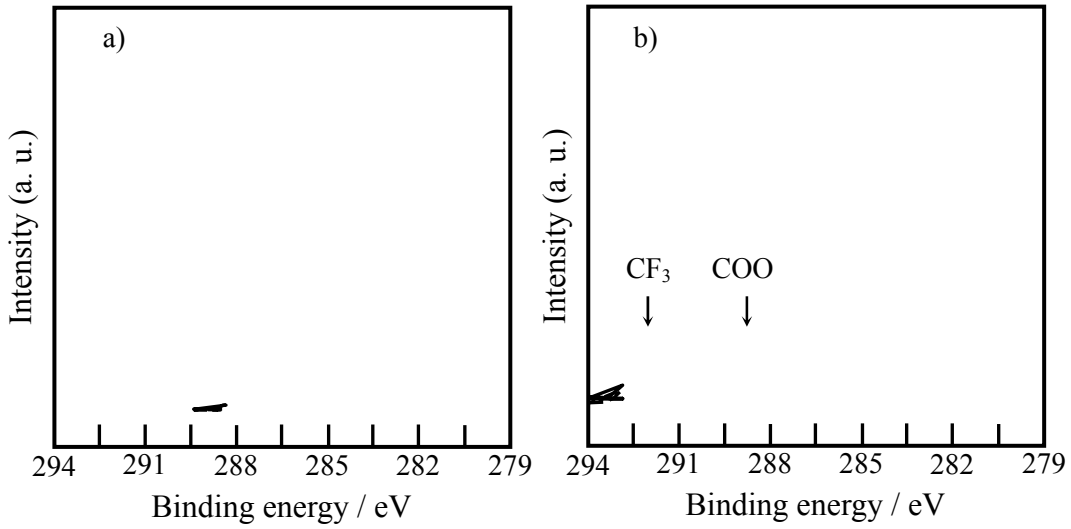


Fig. 4 XPS C1s spectra of a) the deposited film surface and b) the deposited film surface after being treated by TFAA.

Tab. 1. Elemental analysis of the sample of deposited materials collected from the deposited substrates. Residual % is nitrogen.

Elements	Carbon / %	Hydrogen / %	Oxygen / %
Analysis	63.97	8.65	25.47
Calc. value of AA	62.04	10.41	27.55

4. Conclusion

We succeeded in depositing the cross-linked solid polymer film which shows very analogous composition for that of the allyl alcohol. Thirty times higher deposition rate was attained than in low pressure PCVD.

The obtained films contained about 18% of the hydroxyl groups on the deposited surfaces.

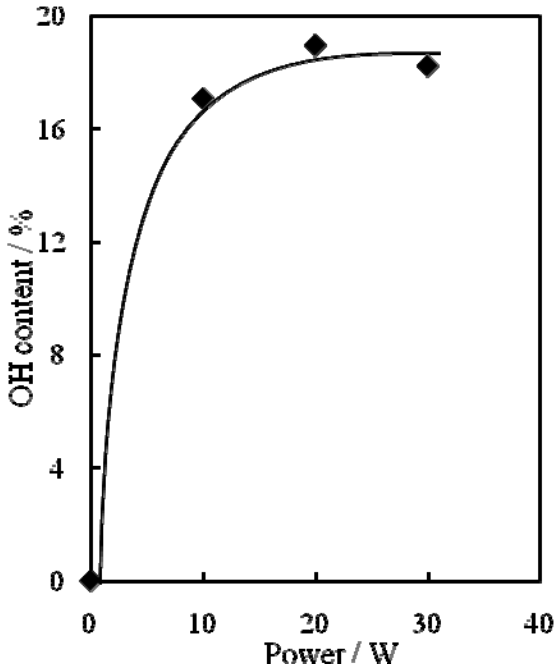


Fig. 5 Concentration of hydroxyl groups on the deposited films as a function of the discharge power.

5. References

[1] M.Kogoma et al., Proceedings of HAKONE XI, pp460-463(2008).

[2] W.R.Gombotz, Guaghui , T.A.Horbett, Hoffman A.S., J. Biomed. Mater, Res., **25**, 1547 (1991).

[3] C. L. Rinsch et al , Langmuir, **12**, 2995-3002 (1996).

MICRO RAMAN SPECTROSCOPY STUDY OF THE PENETRATION OF THE DBD TREATMENT EFFECT INTO THE WOOL FIBRE

I. Kulyk [1], M. Scapinello [2], M. Stefan [1]

[1] *CIVEN (Interuniversity Coordination of Veneto for Nanotechnology), Via delle Industrie 5, 30175, Marghera Venezia (VE), Italy*

[2] *Dipartment of Chemical Sciences,Università di Padova, Via Marzolo 1, 35131 Padova, Italy*

E-mail: kulyk@civen.org

The application of the atmospheric plasma for wool fabric offers a valid alternative to the nowadays wet chemistry processes. Treatment of wool by means of Dielectric Barrier Discharge (DBD) is the ambient friendly alternative solution for existing technological processes for textile finishing.

The oxidative effect on the fiber is penetrative in case of liquid chlorination processes on wool. In the case of plasma treatment, the oxidation is considered to be the superficial effect. The micro Raman analysis permitted us to monitor the propagation of plasma oxidation effect into the fiber, at least for the level of some microns. The penetration depth of the oxidation was found to be proportional to the energy of the applied plasma treatment. It was found that oxidation process occurs not only during DBD treatment but that it continues also in the post treatment period.

1. Introduction

The application of the atmospheric plasma for wool fabric offers a valid alternative to the nowadays wet chemistry processes, widely used in the textile industry. The conventional use of liquid chlorine solutions for the finishing of wool textiles produces hard effluent load on the ambient and doesn't correspond to the new coming ecological legislation. Atmospheric Plasma and Dielectric Barrier Discharge (DBD) in particular offer the elegant solution for the finishing of wool and, in general, of textile materials. The shrinkproofing treatment of wool, the optimization of dyeing and printing processes by means of DBD is the advanced solution for such kind of technological processes [1].

It is believed that the level of the fiber surface oxidation due to the plasma treatment is one of the factors responsible for the hand feel of the fabric, - very important commercial characteristic of the wool fabric. The optimization of the oxidation level of the wool fiber can influence on the acceptance of the garments made from the plasma treated wool by the market. Actual presentation is dealing with the application of micro Raman spectroscopy for the investigation of wool fiber oxidation in the DBD discharge and in the post treatment period.

The penetration of the oxidative effect in the fiber is typical for the liquid chlorination processes on wool. In the case of plasma treatment, especially for low pressure plasma, the oxidation was considered mostly as the superficial effect [1, 2]. The micro Raman analysis permits us to monitor the propagation of the DBD discharge oxidation effect into the wool fiber, at least for the depth of some microns.

2. Experimental

Materials

The experiment was performed with raw wool fibres of 20÷25 μm of diameter. Wool fibres were scoured with dichloromethane for 24 hours using Soxhlet extraction [3]. The scoured fibres were washed twice with ethanol and rinse twice with deionised water. The cleaned fibers were finally dried.

DBD treatment

The fibres were treated with a special CIVEN apparatus that permits to treat fixed fabric sample of lab scale (about 30 x 30 cm^2). The discharge was generated between a moving unit of two ceramic electrodes and the grounded electrode (Fig. 1).

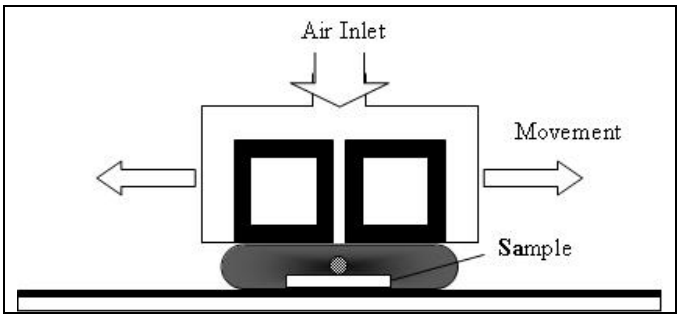


Fig. 1. Schematic drawing of DBD Apparatus.

The samples of single fibres were mounted on a 0,1 mm thick glass slide, fixed at the ends with an adhesive tape, and placed on the plane grounded electrode covered with the insulating silicone sheet. The gap of 0.8 mm was maintained between the surface of glass slide and ceramic electrodes. The treatments were performed using air as working gas (50 slpm, 30 % RH), at DBD discharge frequency 40 kHz, at a specific power 3,9 W/cm^2, with periodic movement of the electrodes with the speed 10 m/min. After the treatments the samples were aged at ambient conditions.

Micro Raman Spectroscopy

Raman spectra were collected with WiTec Alpha 300s. The laser beam was focused to a spot of ca. 1 μm on the surface of the sample and ca. 3 μm on z direction. The spectra were collected in a range between 430 and 1600 cm^{-1} with a resolution of about 1,1 cm^{-1}. For statistical analysis there were considered 3 points for each fibre; each point was measured 4 times.

The position of the laser spot was verified by optical microscope to be focused on the fiber surface and then the sample plate was moved upward, to make the spot enter into the fiber. The spot position corresponding to z = 0 corresponds to complete immersion of the spot into the fiber, when spot still includes the surface layer (Fig. 2). The measurement starts from z < 0 position, by shifting the spot from the inner fiber volume (cortex), crossing the fiber surface (cuticle) until complete exit of the spot from the fiber.

Data treatment

To study the oxidative the spectral signals for disulphide bond -S-S- groups and for R-SO_3H cysteic acid bands were acquired and were normalized on the spectral signal for CH_2 back bone groups (considered to be unchanged with the plasma treatment). Total spectrum was measured in the integration range 430 – 1600 cm^{-1} with the sample plate shifting from z = -4 μm to z = 3 μm. The signal correspondent to CH_2 scissoring band was measured at 1450 cm^{-1}. The signal correspondent to -S-S- band was measured at 520 cm^{-1} and the signal correspondent to R-SO_3H cysteic acid band was measured at 1045 cm^{-1} [4, 5].

3. Results and discussion

Fig. 2 represents typical signal acquired for one fiber treated by plasma at 212 J/cm^2 and one another (not treated) fiber. Fig. 3 represents (in the upper part) the spectra obtained for 3 different fibers, treated at different applied specific energy (71, 212 and 565 J/cm^2). All spectra were obtained in z = 0 spot position and then normalized on the spectral signal for CH_2 back bone group. It can be seen the increasing of the oxidation effect (increasing of the R-SO_3H cysteic acid groups) with the increasing of applied energy of plasma treatment. In the lower part there are two spectra measured on the same untreated fiber, at different spot position, one for the z = o and another for z = -3 μm. It can be seen that the presence of the R-SO_3H cysteic acid groups is almost same for different spot positions inside the fiber.

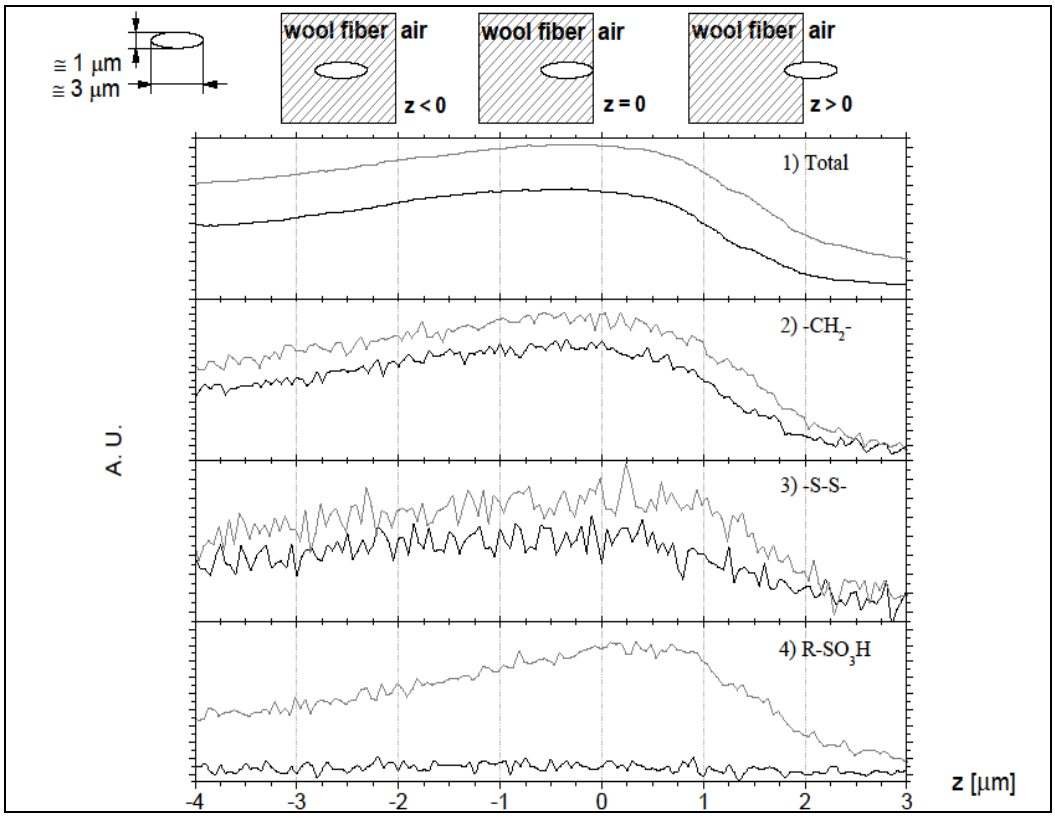


Fig. 2. Example of micro Raman measurements through the single wool fibre: scheme of laser spot penetration into the fibre (in the upper part) and typical measured signals (not normalized). The upper curves in all (1 – 4) pictures correspond to one treated fibre (212 J/cm^2), the lower curve - to another (untreated) one. 1) Total measured spectrum; 2) CH_2 scissoring bands signal; 3) -S-S- bands signal; 4) R-SO_3H bands signal.

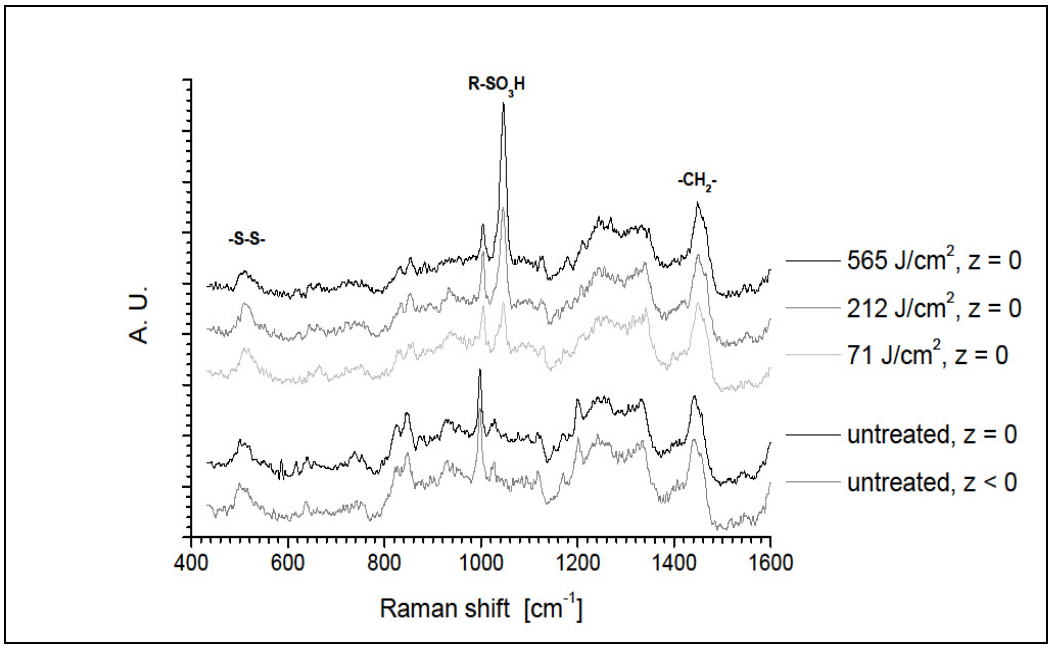


Fig. 3. In the upper part: the spectra measured at z = 0 (position of maximal signal) for different treated fibres. In the lower part: two spectra for the same untreated fibre acquired in spot position z = 0 and z < 0.

For the interpretation of the data presented in Fig. 4 the effective dimension of the laser spot should be considered. As it was described before, z = 0 level corresponds to the position when the spot (as big as

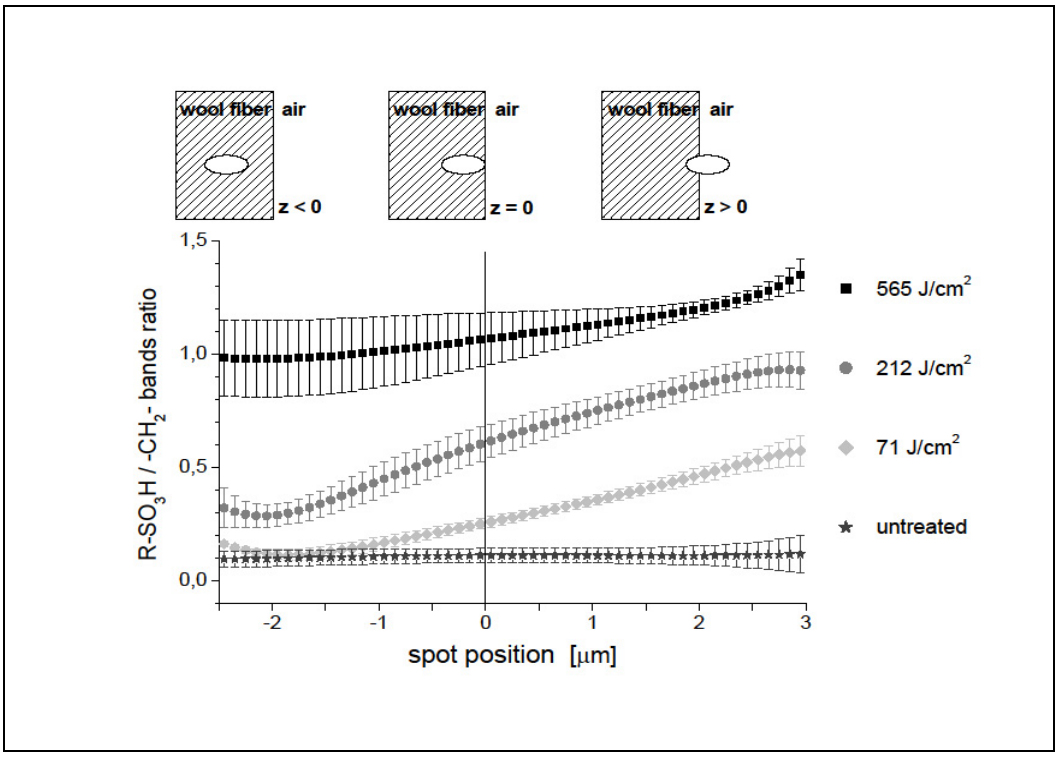


Fig. 4. The dependence of R-SO_3H band signal (normalized on signal for CH_2 groups) from the laser spot penetration into the fiber. Different fibers are treated at powers 0 (untreated); 71; 212 and 565 J/cm^2. Micro Raman analyses were performed 7 days after the treatment in the case of specific energy of treatment 71 J/cm^2, after 5 days in the case of 212 J/cm^2 and after 2 days in the case of 565 J/cm^2.

3 μm in vertical Z direction) is completely immersed into the fiber and still touches the fiber surface. With this consideration one can see that at plasma treatment level of 71 J/cm^2 the oxidation regards not only the surface but also some inner layer. Only with complete immersion of the spot below 1,5 μm under the surface, the oxidation signal drops to zero level. At higher energy (212 J/cm^2) the oxidation level is not become zero even for deep immersion of the spot. Further growth of the signal with depth more than 2 μm can be attributed to the increasing of the experimental errors due to the decreased absolute level of signals. At the highest applied energy (565 J/cm^2) much larger oxidation level is clearly observed inside the fiber. It can be concluded, in qualitative way, that for all reported energies of plasma treatment, the oxidation regards inner layer of the fiber with a characteristic thickness in μm range. The depth and the level of oxidation increase gradually with the applied plasma energy.
With continuing movement of the spot the growth of normalized R-SO_3H/CH_2 signal was observed up to z = 3 μm, that corresponds to complete exit from the fiber. This fact proves the highest concentration of oxide R-SO_3H groups on the surface of the fiber.
After the DBD treatment the fibers were monitored by micro Raman spectroscopy for more than 8 weeks. For all applied treatment energies it was observed gradual increase of the oxidation level during the post treatment period (Fig. 5). The velocity of post treatment oxidation is found to be proportional to the applied energy. As one can see, the oxidation level was almost stable in first 10 days. This fact permits us to consider that data presented on Fig. 4 (obtained after 2 - 7 days after treatments) to be correspondent to the moment of the treatment. On this basis we conclude that DBD has affected the inner layer of the fibers just during the treatment and that the oxidation level was increased further in the post treatment period.
As we know from literature, the energetic plasma treatments of both atmospheric and low pressure plasma [1, 6] not only partially eliminate the lipid layer but produce different defects on the fiber surface. Strong erosion of the fibers at high DBD treatment energy was also observed by us (Fig. 6). In our micro Raman studies the plasma treatments were applied to the single fibers, thus increasing the effect.

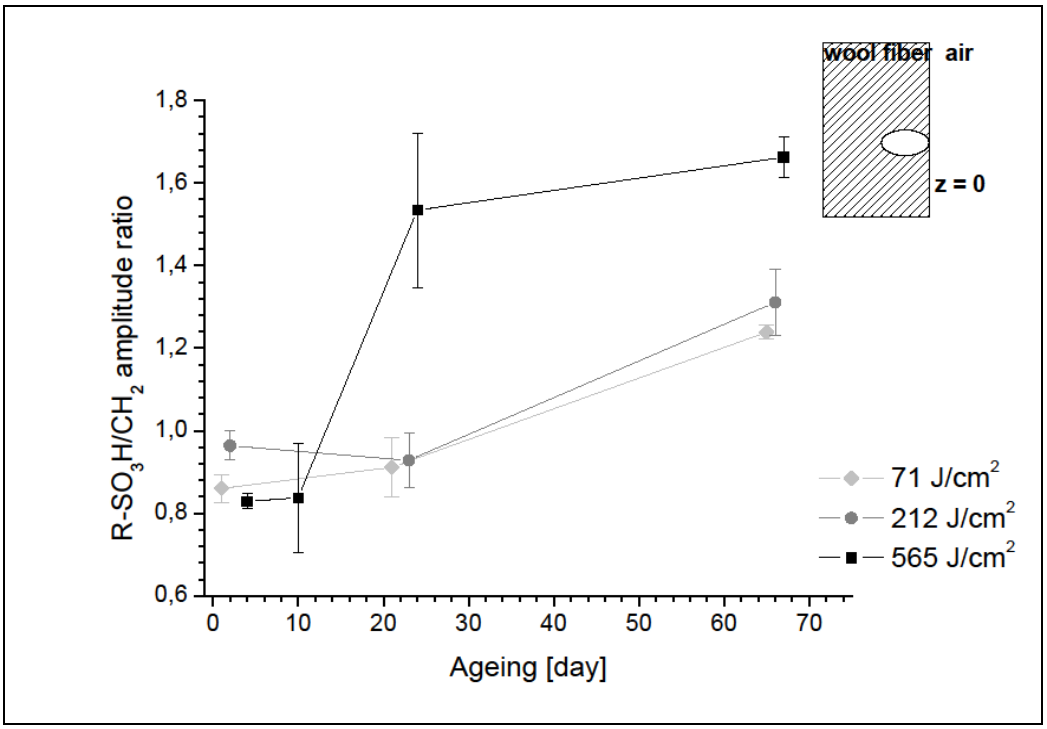


Fig. 5. The post treatment monitoring of wool fibres: normalized signals of R-SO_3H bands for spot position z = 0, in function of the period of time after the treatment.

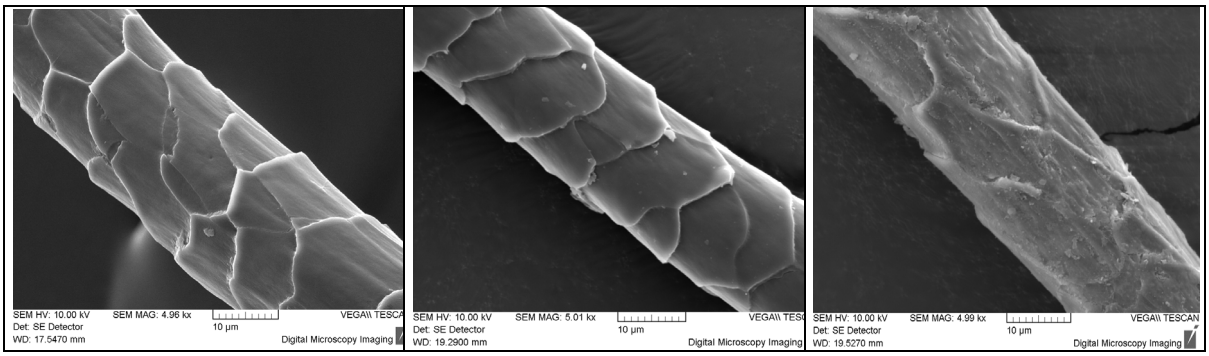


Fig. 6. SEM images (from left to right): untreated, DBD treated at low energy (40 J/cm2) and DBD treated at high energy (400 J/cm2) wool fibers. DBD treatment was performed for a group of fibers extracted from industrially scoured knitted fabric.

4. Conclusions

We suppose that the oxidation of the inner layer of the fibre (at a scale of 1 μm) occurs during plasma treatment due to the diffusion of the generated radicals through the reduced lipid barrier layer (of nanometer scale). The oxidative effect in the inner layer of the fiber continues also in the post treatment period due to the ambient oxygen. The velocity of post treatment oxidation is proportional to the energy of applied atmospheric plasma treatment.

5. References

[1] Thomas H 2007 *Woodhead Publ. Ltd. ISBN 1845690737*
[2] Hesse A, Thomas H and Hocker H 1995 *Text. Res. J. 65, 335-361*
[3] Kan C W, Chan K and Yuen C W M 2004 *Fibers and Polymers, Vol. 5, No. 1, 52 – 58*
[4] Paquin R and Colomban P 2007 *J Raman Spectr. 38, 504-514*
[5] Church J S and Millington K R 1996 *Biospectroscopy. Vol. 2, 249-258*
[6] Kan C W and Yuen C W 2007 *Textile Progress 39:3, 121-187*

ATMOSPHERIC PRESSURE PLASMA JET FOR THE DEPOSITION OF OXIDES THIN FILMS AT HIGH RATES

Jerome Pulpytel[1], Sudhir Bhatt[1], František Krčma[2], Věra Mazánková[2], Farzaneh Arefi-Khonsari[1]

[1]*Laboratoire de Génie des Procédés Plasmas et Traitements de Surfaces (LGPPTS), Université Pierre et Marie Curie (UPMC), Chimie Paristech*
[2]*Institute of Physical and Applied Chemistry, Faculty of Chemistry, Brno University of Technology, Purkyňova 118, 612 00 Brno, Czech Republic*
E-mail: krcma@fch.vutbr.cz

The atmospheric pressure plasma enhanced chemical vapour deposition is one of hot topics in the field of plasma applications during last years especially due to considerably high growth rates and lower costs. This work deals with the deposition of silicon oxide from hexamethyldisiloxane (HMDSO) thin films using an atmospheric pressure plasma jet (APPJ) system in open air conditions. A sinusoidal high voltage with a frequency between 19-23 kHz at power up to 1000 W was applied between two tubular electrodes separated by a dielectric material. The main gas flow consisted of dry air which was introduced through the torch at a flow rate of 108 l/h. The jet, characterized by T_g ~600-800K, was mostly laminar (Re ~1200) at the nozzle exit and became partially turbulent along the torch axis (Re ~3300). The spatially resolved emission spectra showed OH, N_2, N_2^+ and CN molecular bands and O, H, N, and Cr lines as well as the NO_2 chemiluminescence continuum (450-800 nm). Thin films with good uniformity on the substrate were obtained at high deposition rate, between 800-1000 $nm.s^{-1}$, and AFM results revealed that coatings are relatively smooth (Ra ~2 nm).

1. Introduction

Nowadays, the application of various atmospheric pressure discharges becomes one of the most popular directions in plasma technologies. The main advantage of these techniques is moderate price because no expensive vacuum systems are needed [1]. With respect to the deposition processes of various coatings the high deposition rate is the main profit [2]. Unfortunately, the atmospheric pressure deposition systems are mainly based on jets that have very small uniformity and the properties of prepared layers thus strongly depend on the plasma conditions and position of substrate with respect to the plasma jet [3]. At the common applications, the plasma operating in continuous regime is used however some pilot studies have been made with discharges operating in pulsed regime, mainly at lower pressure [4]. The presented contribution brings some first results of thin layer deposition using the atmospheric pressure plasma jet operating in continuous as well as pulsed regime. He work is supported by the plasma jet characterization and some basic properties of deposited layers are demonstrated.

2. Experimental set up

The commercial device Plasmatreater AS400 was used for the presented study. The scheme of this atmospheric operating plasma jet is given ion Fig. 1. Inside the nozzle, the rotating arc operating at the audio frequency (19-23 kHz) is generated. Applied power was kept at 900 W for in the continuous regime, 1000 W were applied in pulsed regime. The plasma before the output of nozzle is enriched by monomer vapors. The plasma flow through the nozzle is nearly laminar (Re ~1200) and becomes partially turbulent along the torch axis (Re ~3300). The plasma jet length was about 1 cm with diameter up to about 2 mm at the maximum (see Fig.1) however the active particles were determined in larger vicinity of the jet (see later). The discharge was created in the air at flow rate of 1800 Sccm, the monomer flow rate was up to 1000 Sccm. The deposition rate was up to 1 micron per second. To obtain uniform coatings, the plasma jet was continuously moved over the substrate by the speed of 0.5 m/s. The optical emission spectra during the treatment were collected using Ocean Optics HR4000 spectrometer covering wavelength range 330-790 nm with relatively good resolution of 0.14 nm that

allowed determination of various atomic and molecular species. The double mask in the front of optical fiber entrance was applied to obtain the space resolution better than 0.5 mm.

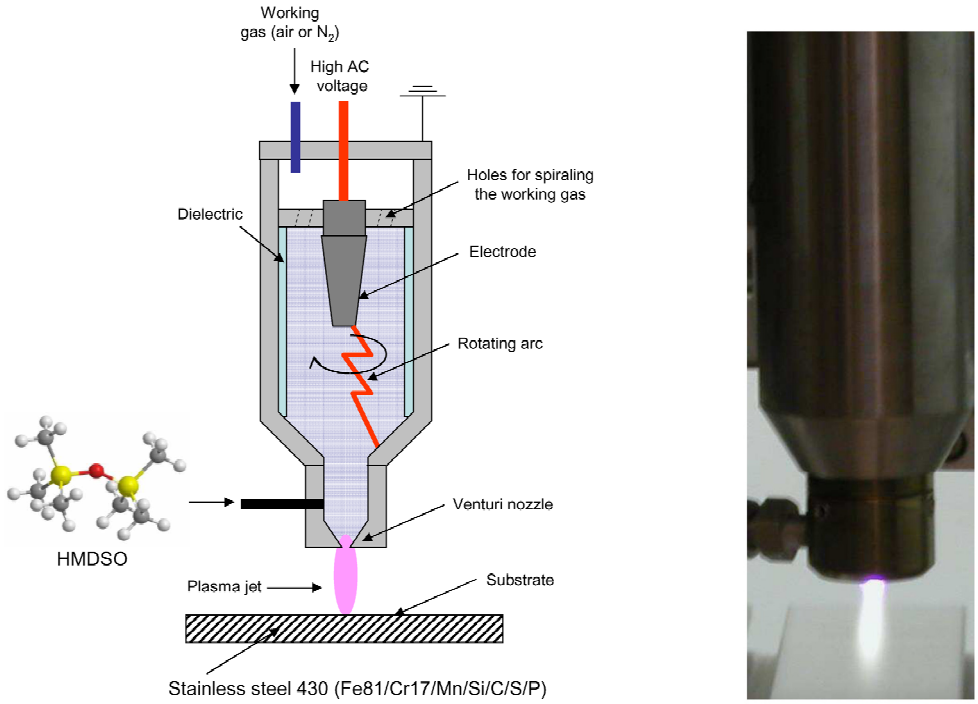


Fig. 1. Scheme of experimental setup (left) and plasma jet in air with HMDSO precursor at operation.

3. Results

The first part of the presented results shows the properties of plasma jet generated in the dry air without any precursor in continuous regime.

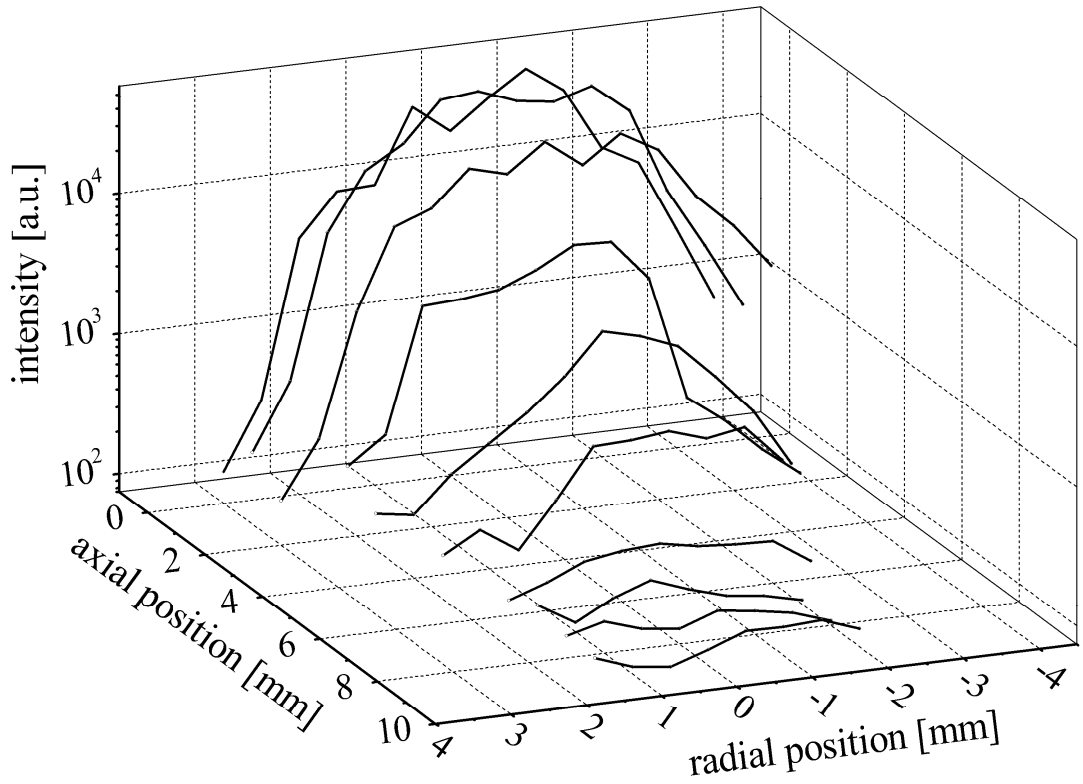


Fig. 2. Spatially resolved intensity of oxygen 777.194 nm line – profile of the plasma jet.

It can be clearly seen that the discharge is nearly symmetric with some turbulences at its edge. The same profiles have been obtained also for the other particles identified in the spectra, i.e. atomic and molecular nitrogen and lines of chromium and copper introduced into the plasma due to the electrode erosion. The intensity of NO_2 continuum produced by recombination processes was presented with remarkable intensity in about two times larger volume and its intensity at the jet central part was relatively lower with respect to the other species. To characterize the plasma it self, the electron temperature has been calculated using the intensities of 15 chromium lines. The vibrational temperature was calculated using nitrogen second positive bands of -2 sequence. Results obtained at the jet axis are presented in Fig. 3. Electron temperature more or less linearly increases along the jet axis and it is determinable within 15% uncertainty up to the distance of 5 mm form the nozzle. The radial profile of the electron temperature is very flat; the temperature at the plasma edge is about 500 K higher than it was determined at the axis. Vibrational temperature of about 3500 K (with uncertainty again of about 15%) is nearly independent on the discharge position.

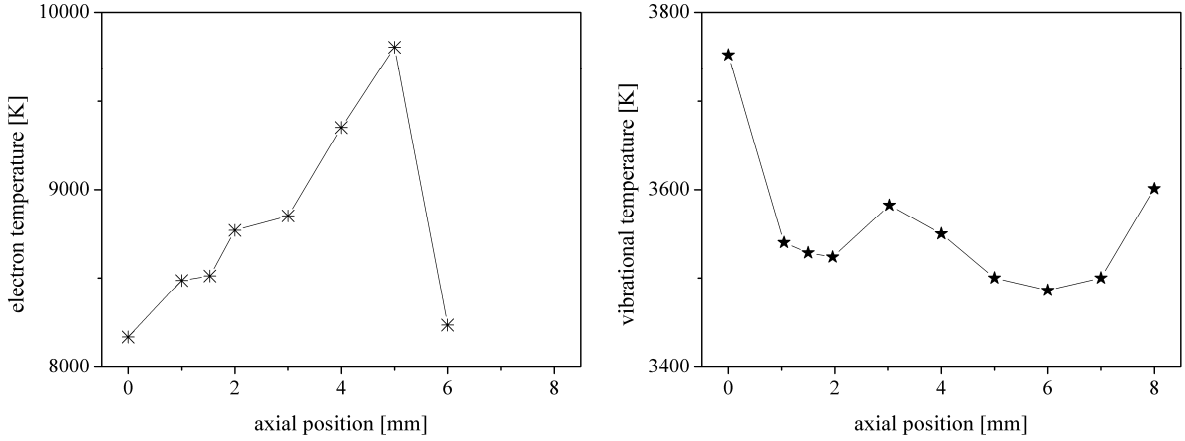


Fig. 3. Electron and vibrational temperatures in plasma jet generated in dry air.

Both temperatures were determined also in the dependence on the monomer flow rate at the same dry air mass flow as above. The results presented in Fig. 4 demonstrate that there is no significant change of the electron temperature value, but no temperature elevation with increase of the axial position was determined and thus the temperature is nearly constant at about 8500 K. Vibrational temperature determined from nitrogen second positive system is about 500 K higher than in the plasma without monomer but is nearly independent on the monomer flow. The temperature increase at larger distances from the nozzle is probably due to some energy transfer reactions in the decaying plasma.

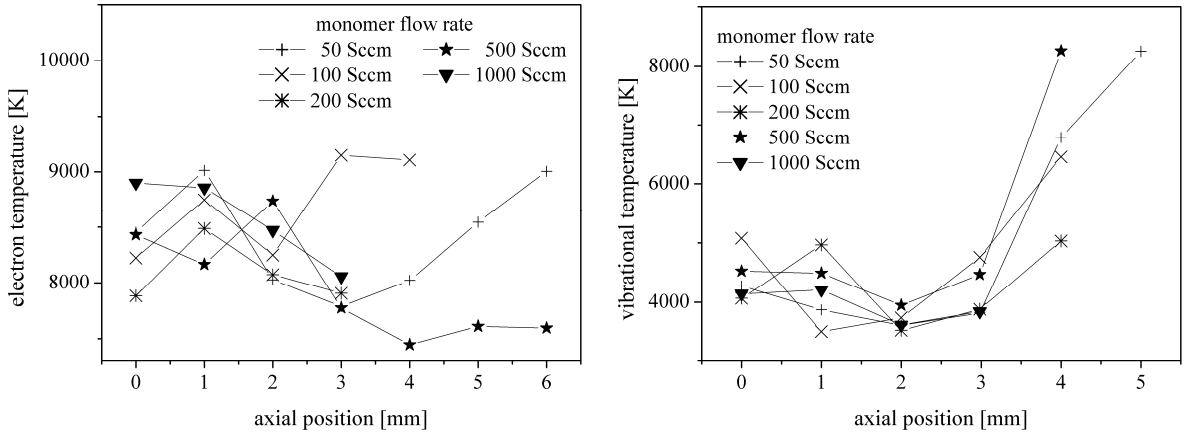


Fig. 4. Electron and vibrational temperatures in plasma jet generated in dry air enriched by HMDSO monomer at different mass flow.

The intensities of all species mentioned above as well as of atomic hydrogen and CN radical show the similar profiles in the plasma jet as it was presented in Fig. 2 for atomic oxygen. The intensity increase

proportional to the monomer flow was observed for the species incoming form monomer (H, CN) but the others were more or less independent on the monomer mass flow rate.
The first results with respect to the pulsed discharge regime are depicted in Fig. 5. The monomer flow was kept at 500 Sccm at the applied power during the pulse of 1000 W. As it can be seen plasma generated at small duty cycle under 50% was nearly non-radiating and thus also the temperature has been not determined. At the higher duty cycles more or less no dependence on the duty cycle parameter was obtained. The discharge shape was nearly independent on the duty cycle however its dimensions (both axial and radial) increased with the increase of the duty cycle.

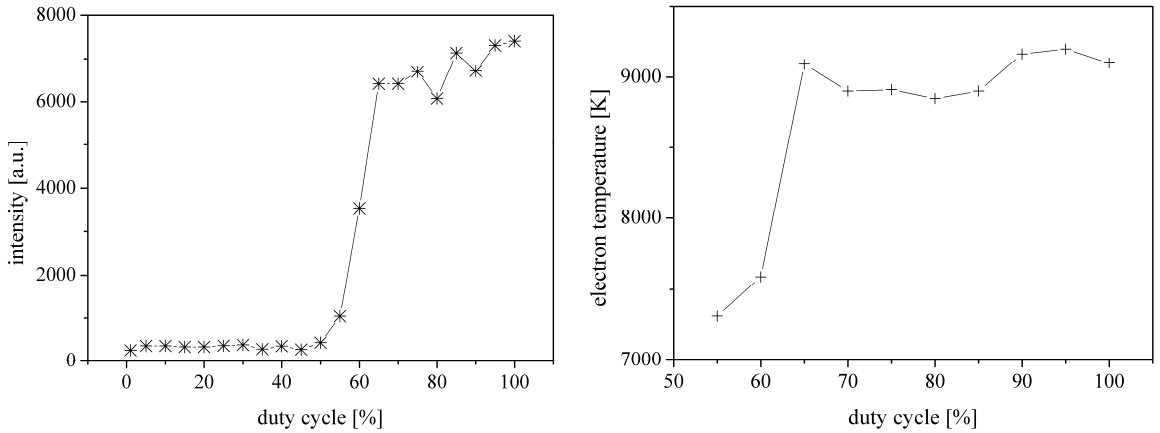


Fig. 5. Intensity of oxygen line at 777.194 nm and electron temperature in plasma jet generated in dry air enriched by 500 Sccm of HMDSO monomer as a function of duty cycle.

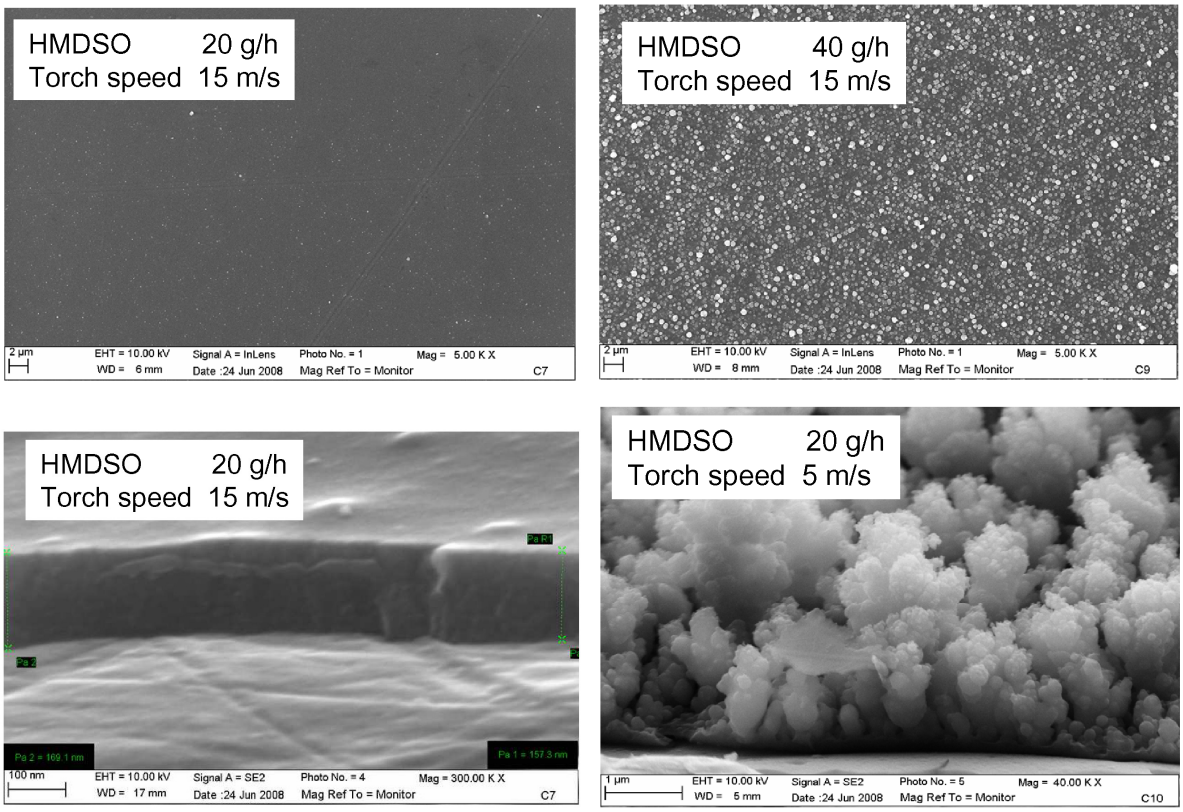


Fig. 6. Structure of thin films deposited at different conditions (scale units of the upper pictures are 2 μm, 100 nm for the left bottom picture and 1 μm for the right bottom picture).

The deposited thin layers analyzes are demonstrated by Figs. 6 and 7. It can be clearly seen that the layer structure significantly depends on the deposition conditions. Very smooth (R_a = 2.04 nm; R_q = 2.74 nm) and compact SiO_x layers can be created using the fast speed of gas through the nozzle

(15 m/s) at moderate concentration of precursor. The nanoparticles of SiO_x are created in the plasma phase if very high amount of HMDSO is used and they are built in into the deposited coating, i.e. the deposited thin film has a nanocomposite structure. On the other hand, if low plasma jet speed is applied, the coating structure is nearly opened dendrite with very high effective surface. This structure should have a great application potential mainly in deposition of photoactive titanium dioxide based thin layers. The deposition rate of these films as it is marked in Fig 6 is very high and it was typically of 800–1000 $nm.s^{-1}$ for the uniform films and over 3000 $nm.s^{-1}$ for nanocomposite layers.

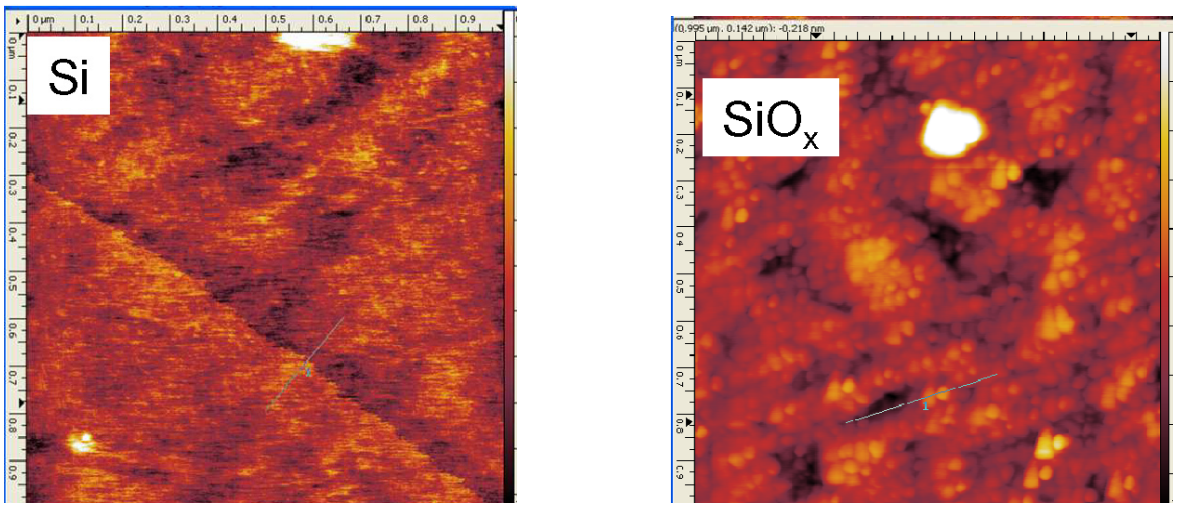


Fig. 7. AFM pictures of silicon wafer surface (left) and the most smooth plasma deposited thin film (right).

4. Conclusion

The atmospheric pressure plasma enhanced chemical vapour deposition of silicon oxide from hexamethyldisiloxane (HMDSO) thin films using an atmospheric pressure plasma jet (APPJ) system in open air conditions was studied. The jet, characterized by T_g ~600-800K, was mostly laminar (Re ~1200) at the nozzle exit and becomes partially turbulent along the torch axis (Re ~3300). The spatially resolved emission spectra show OH, N_2, N_2^+ and CN molecular bands and O, H, N, and Cr lines as well as the NO_2 chemiluminescence continuum (450-800 nm). Electron temperature of about 9000 K was determined from Cr spectral lines and it was nearly spatially independent within the jet. Vibrational temperature determined from nitrogen 2nd positive system was between 3500 – 4000 K. Both temperatures were independent on the monomer flow rate.

Thin films with good uniformity on the substrate were obtained at very high deposition rate between 800–1000 $nm.s^{-1}$, and AFM results revealed that coatings are relatively smooth (Ra ~2 nm). The thin film structures were strongly dependent on the plasma jet speed and precursor flow. Depending on these parameters, the smooth, nanocomposite or opened dendrite structure films were obtained.

5. References

[1] Ráhel' J, Šimor M, Černák M, Štefečka M, Imahori Y, Kando M 2003 *Surf. Coat. Technolf* **169-170** 604

[2] Benedikt J, Woen RV, van Mensfoort SLM, Peřina V, Hong J, van de Sanden MCM 2003 *Diamond Rel. Mater.* **12** 90

[3] Auner N, Weis J 2005 *Organosilicon Chemistry VI: From Molecules to Materials* John Wiley and Sons

[4] Přikryl R, Čech V, Zajíčková L, Vaněk J, Behzadi S, Jones FR 2005 *Surf. Coat. Technol.* **200** 468

EFFECT OF ELECTRODES CONFIGURATION ON POLYIMIDE SURFACE ETCHING PROCESS IN BARRIER DISCHARGE

Małgorzata Kalczewska , Teresa Opalińska , Maciej Więch
Tele & Radio Research Institute, ul. Ratuszowa 11, 03-450 Warsaw
E-mail: malgorzata.kalczewska@itr.org.pl

Surface of polyimide foil was etched in dielectric barrier discharge generated in argon using sinusoidal alternating current of 50 Hz frequency under atmospheric pressure. The thickness of foil was 0,025 and 0,125 mm. Three configurations of electrodes were applied: polyimide foil on metal - gas layer - ferroelectric ceramics on metal (Variant A), gas layer between two polyimide foils on metal (Variant B), metal electrode– gas layer - polyimide foil on metal (Variant C). The highest mass reduction of foil sample was observed in Variant C. The highest etching rate (3,22 $\mu g \cdot cm^{-2} \cdot min^{-1}$) was obtained for thicker foil, when the discharge was generated in Variant A. Optimal discharge gap depends on electrodes configuration. For Variant A electrodes discharge gap should be 0,3 mm, while for Variant B it should be from 0,5 to 0,8 mm. The etching process causes changes in the foil surface chemical composition. XPS spectra showed, that mainly benzene rings were broken and short aliphatic hydrocarbons were formed. SEM and AFM researches showed that treated polyimide surface became rougher than surface of raw polyimide.

1. Introduction

The purpose of this research was to define the most advantageous electrodes configuration in polyimide surface etching process with a use of dielectric barrier discharge. According to references [1–5], a few different reactor constructions were used to modify polymers surface. The most common is a plasma system, where the discharge is generated between a high-voltage electrode and polyimide foil, which is simultaneously a dielectric barrier, mounted on the lower electrode [1, 2, 3, 4]. In another construction, where the lower electrode is a part of a moving system, the foil moves through the discharge zone [5]. A construction, where the discharge is generated between two polyimide surfaces is also used in the etching process [6]. Efficiency of modification is verified frequently with a use of a wettability measurements, based on determination of contact angles of test liquids on the polyimide surface [3, 5-7] and the roughness changes measurements [2, 4, 5, 7]. According to mentioned researches, the purpose of this work was to reveal which type of the constructions in a system, with two stationary electrodes, is the most advantageous in polyimide etching process in argon, considering discharge gap. Efficiency of foil etching modification is showed as a relation between a polymer mass reduction and etching time and a relation between etching rate and etching time. Additionally, changes in polyimide surface morphology (SEM), roughness changes (AFM) and surface chemical composition (XPS) were studied.

2. Experimental

The experimental set-up consisted of working gas vessel, mass flow controller (Brooks Instrument, model 5850S), a plasma reactor and a power supply . Argon, with a flow rate of 0,195 $Ndcm^3/h$, was the working gas . The plasma reactor was supplied with 50 Hz sinusoidal alternating current. The barrier discharge was generated under atmospheric pressure between two electrodes with three different configurations: Variant A – metal/polyimide (grounded electrode) and ferroelectric ceramics/metal (high-voltage electrode); Variant B – polyimide/metal (both electrodes); Variant C – metal/polyimide (grounded electrode) and metal (high-voltage electrode). All experiments were performed on samples of Kapton HN with a thickness of 0,125 mm from DuPont and 0,025 mm thick from Suzhou Kying Industria Materials Co., Ltd. The electric parameters of the discharge were measured with a use of oscilloscope Tektronix 2430A. Maximal voltage on electrodes varied in range 1,47 - 2,87 kV, current in outer circuit varied in a range 0,20 - 0,46 μA, depending on electrodes configuration.

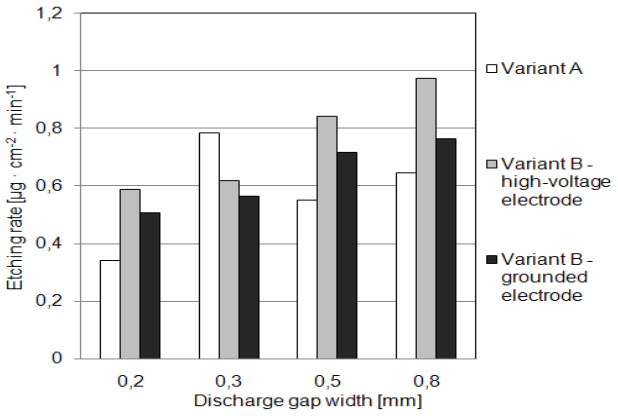
Polyimide samples were treated in plasma for 5, 10, 15, 20, 25 and 30 minutes and weighted before (m_1) and after plasma process (m_2) with accuracy of 0,00005 g. Samples mass reduction (Δm) was calculated from the equation:

$$\Delta m = (m_1 - m_2)/S \qquad [\mu g\ cm^{-2}] \qquad (1)$$

where: (S) is an electrode's metal part area, assuming it as a discharge area.
XPS investigations of treated polymer surface were performed using a VG Scientific photoelectron spectrometer ESCALAB-210 using Al Kα radiation (1486.6 eV) from an X-ray source operating at 15 kV and 20 mA. The surface morphology were examined by scanning electron microscopy SEM, model Zeiss SUPRA, equipped with a Gemini column. Examined samples were coated with thin Au-Pd layer since polyimide foil is a good dielectric. The surface topography was examined with atomic force microscopy AFM, model Nanoscope V Veeco, equipped with standard silicon nitride cantilever NP Veeco.

3. Results and discussion

The theoretical and applied research of the barrier discharge [8] shows that a discharge gap enlargement causes changes in the discharge microscopic and macroscopic conditions. Maximal voltage on electrodes and value of charge transferred in particular microdischarges increase with discharge gap enlargement. In this connection, two sets of experiments, that verify a relation between thin (0,025 mm) polyimide foil etching rate and discharge gap for Variants A and B of electrodes construction were undertaken. Results are shown on Fig. 1. The discharge gap was optimal when the surface etching rate was the highest. For Variant A, the optimal discharge gap was 0,3 mm and for Variant B it was 0,8 mm. That is why all experiments for Variant A were carried out for this discharge gap. All experiments for Variant B were carried out for the discharge gap 0,5 mm. Applying wider discharge gap (>0,5 mm) causes transfer of significant charge in a particular microdischarge. It makes a possibility to micro-holes formation. Results of polyimide etching process in plasma generated between the polymer surface and the ferroelectric ceramics surface are shown on Fig.2. and Fig.3. Unexpectedly, the etched samples mass reduction did not increase linearly with the time of discharge duration. For both samples, regardless of the thickness, a maximum of mass reduction was obtained for process lasting 20 minutes. For this reason the etching rate depends on the time of process. For thinner foil the etching rate decreased with time and for thicker foil it reached the maximum for 10 min. At this moment we could not explain this phenomenon. Probably a form of discharge was changed as a result of the ferroelectric electrodes heating while the process time was lengthened. The mass reduction of the thicker foil was several times higher than the thinner foils, because the electric parameters of discharge changed with dielectric thickness increase. The increase of polyimide foil thickness caused the discharge current increase from 0,20±0,014 to 0,26±0,004 mA.
Relations between foil mass reduction and etching time for Variants A, B and C are showed on Fig. 4.
In Variant B of electrodes configuration, the relation between mass reduction and etching time was linear (Fig.4), in consequence etching rate value was constant and did not depend on etching time. The etching rate of foil placed on high-voltage electrode was 0,82 ± 0,03 $\mu g\ cm^{-2}min^{-1}$ and for foil put on grounded electrode was 0,72 ± 0,02 $\mu g\ cm^{-2}min^{-1}$. The etching rate was calculated from simple equation as a slope coefficient.
For Variant C this relation is linear, thus the etching rate was constant and amounted to 0,49±0,06 $\mu g\ cm^{-2}\ min^{-1}$. The sample mass reduction is the highest when the discharge is generated between the polyimide surface and the surface of metal. The reduction of samples mass is similar for Variant A and B up to 20th minute of discharge duration. For etching time longer than 20 minutes, PI mass reduction is higher for Variant B in comparison with Variant A. Sample mass decrease indicates, that the polyimide surface was decomposed as a result of discharge treatment.
To define changes of chemical composition on polyimide surface, XPS spectra of foil with a thickness of 0,025 mm, treated for 15 minutes and XPS spectra of untreated foil were undertaken. Carbon, oxygen and nitrogen contents in surface layer of polyimide are presented in Table I. Plasma treatment causes, first of all, loss of carbon from the surface, that takes effect in C/N ratio decrease. The content of various forms of C, O, and N in the surface layer of treated and raw foil are presented in Table II.



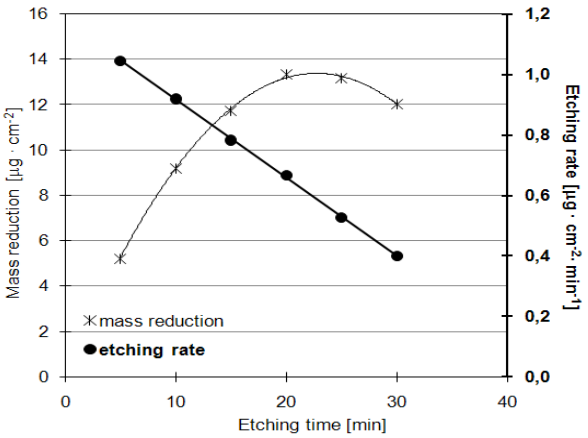
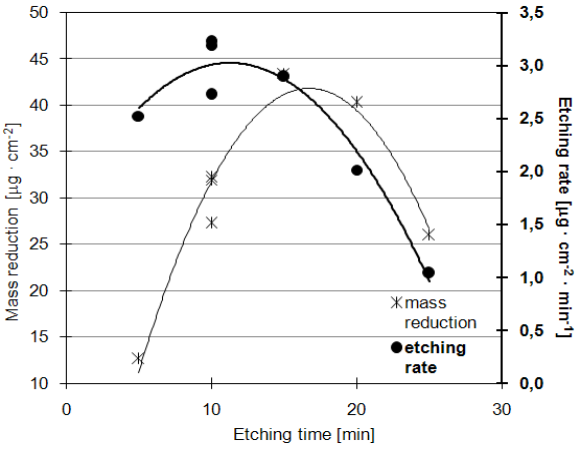


Fig. 1. Effect of discharge gap on PI foil (s = 0,025 mm) etching rate (left).
Fig. 2. Effect of etching time on the PI mass reduction and the etching rate; Variant A of electrodes configuration; d = 0,3 mm; s = 0,025 mm (right).



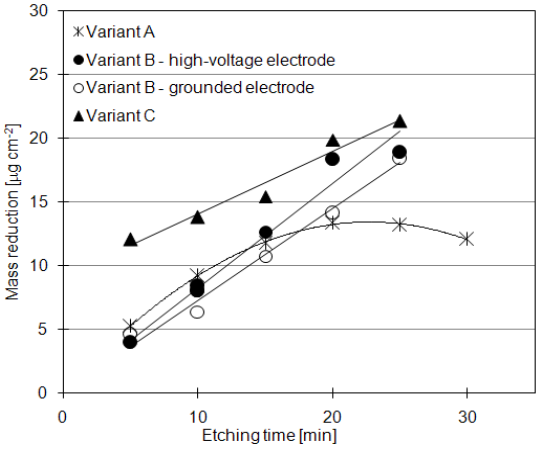
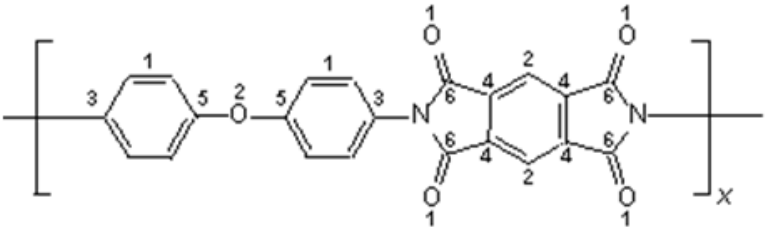


Fig. 3. Effect of etching time on the PI mass reduction and the etching rate; Variant A of electrodes configuration; d = 0,3 mm; s = 0,125 mm (left).
Fig. 4. Effect of etching time on mass reduction of PI foils (s = 0,025 mm) in Variant A, B and C of electrodes configuration (right).

Three N1s peaks, three O1s peaks and five C1s peaks were identified in XPS spectra of the treated foil surface. The XPS spectra untreated polyimide revealed two N1s peaks, two O1s peaks and five C1s peaks. Form of individual elements attributed to determined binding energies were identified on the basis of literature references [9, 10]. The XPS spectrum of Kapton HN [9] was assumed as a standard spectrum of untreated PI:



Polyimide surface plasma etching caused the decrease of C form from benzene ring (placed in position 1 and 2) concentration in comparison with concentration of these atoms on untreated surface. The concentration of C forms placed in position 3, 5 and 6 increased in comparison with these forms on raw PI surface.

The changes in contents of carbon forms on PI surface showed, that while plasma treatment, benzene rings were broken and short aliphatic hydrocarbons were formed in a first place. While hydrocarbons switched from the surface to the gas phase, the specimen weight was reduced.

Table I. Elements content on the PI surface layer treated in plasma in comparison with surface layer of untreated foil (left).

Table II. Oxygen, nitrogen and carbon content on plasma-treated polyimide film compared to untreated polyimide (right).

At. [%]	Untreated foil	Foil treated for 15 minutes
N	6,25	8,10
O	18,04	23,08
C	75,70	68,81
O/N	2,89	2,85
O/C	0,24	0,34
C/N	12,11	8,50

Form of element	Binding energy [eV]	At. [%]	
		Untreated foil	Foil treated for 15 minutes
C=O-N-C=O (ring)	400,70	6,02	7,11
C^{ar}-CO-NH-C^{ar}	402,60	0,23	0,59
C^{ar}-NH_2; C^{ar}-CO-NH_2	399,13	-	0,40
C=O	532,30	12,44	14,61
C^{ar}-O- C^{ar}	533,50	5,60	7,58
O-H	534,40	-	0,89
C^{ar} (1)*	284,70	27,74	19,75
C^{ar} (2)	285,20	14,17	10,23
C^{ar}-N (3); C^{ar} (4)	285,80	13,74	14,05
C^{ar}-O- C^{ar} (5)	286,40	12,89	14,89
C=O (6)	288,70	7,15	9,89

*) position

This conclusion was corroborated by oxygen forms changes, that concentrations increased on the treated surface in comparison with the raw surface.

SEM research showed, that the surface of sample treated in plasma differs from surface of untreated sample. Marks in the form of roughness are noticeable on the modified surface (Fig 5a). Changes on the surface of thin foil appear as hollows and bulges with a size of several dozen nanometers, while surface of untreated sample is smooth (Fig 5b).

AFM research showed, that surface of untreated polyimide foil with a thickness of 0,125 mm is not smooth (Fig 6a). It contains unevenness: hollows and bulges placed randomly.

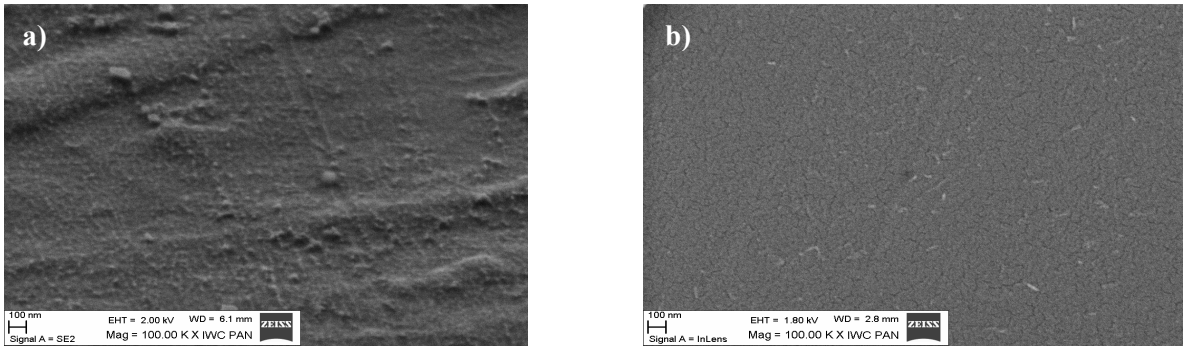


Fig. 5. SEM images of PI samples (s = 0,025 mm) treated in argon for 15 minutes in Variant B (a) and untreated sample (b).

Difference of heights between maximum and minimum level (R_{max}) for this sample is from 0,756 to 5,597 nm, that means samples surface is not smooth. Surface of polyimide with a thickness of 0,125 mm treated for 15 minutes is markedly changed (Fig 6b). Larger hollows and bulges were smoothened; however numerous slight depressions and bulges appeared, as a result, surface seemed

to be rough. R_{max} for this sample is from 5,217 to 10,721 nm. It means that examined sample had strongly changed surface.

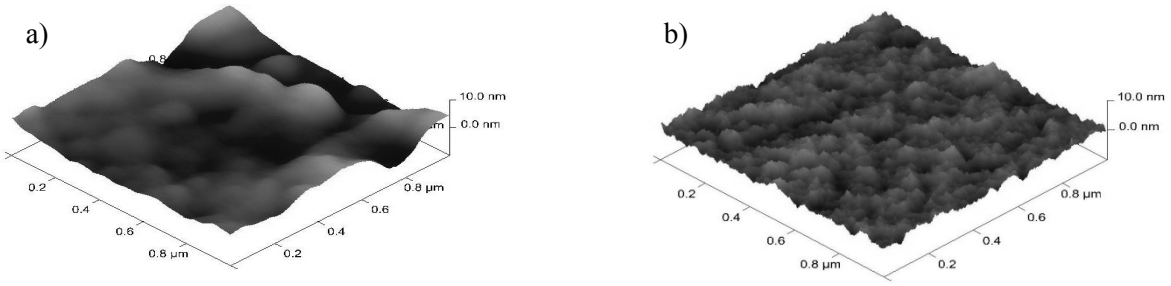


Fig. 6. AFM micrographs of PI films with a thickness of 0,125 mm: untreated (a) and treated in argon for 15 minutes (b).

4. Conclusion

It can be concluded, that it is possible to etch polyimide surface with a usage of dielectric barrier discharge generated under atmospheric pressure in argon using 50 Hz sinusoidal current.

The optimal experimental conditions are when the discharge is generated between metal electrode and polyimide foil surface, being simultaneously dielectric barrier (Variant C) or when the discharge is generated between two polyimide surfaces (Variant B). Then, etching rate is constant. For Variant B, the etching rate amounted to 0,82 ± 0,03 µg $cm^{-2}min^{-1}$ for high voltage electrode and 0,72 ± 0,02 µg $cm^{-2}min^{-1}$ for grounded electrode. For Variant C, the etching rate amounted to 0,49±0.06 µg $cm^{-2}min^{-1}$

Discharge gap, which determines the most advantageous process conditions depends on applied construction of reactor. When the discharge is generated between surfaces of polyimide and ferroelectric ceramics, the discharge gap should be 0,3 mm. When the discharge is generated between two polyimide surfaces or between surfaces of polyimide and metal the discharge gap should be from 0,5 to 0,8 mm.

Etching process causes changes in surface chemical composition. Polymers molecular structure was transformed. Plasma treatment causes forming of unevenness with a depth from several to several dozen nanometers. Distance between depressions depends on etching time and variant of electrodes construction applied.

Acknowledgement. This work was supported by the Polish State Committee for Scientific Research under the framework of Tele & Radio Research Institute Statutory Fund.

5. References

[1] Kim S H, Cho S H, Lee N-E, Kim H M, Nam Y W and Kim Y-H 2005 *Surf. Coat. Technol*. **193** 101.
[2] Seeböck R, Esrom H, Charbonnier M and Kogelschatz U 2001 *Surf. Coat. Technol*. **142-144** 445.
[3] Seeböck R, Esrom H, Charbonnier M and Romand M 2000 *Plasma and Polymers* **5** 103.
[4] Esrom H, Seeböck R, Charbonnier M and Romand M 2000 *Surf. Coat. Technol*. **125** 19.
[5] Park S-J and Lee H-Y 2005 *Journal of Colloid and Interface Science* **285** 267.
[6] Park W J, Yoon S G, Jung W S and Yoon D H 2007 *Surf. Coat. Technol*. **201** 5017.
[7] Eom J S and Kim S H 2008 *Thin solid films* **516** 4530.
[8] Samoilovich V, Gibalov V and Kozlov K 1997 *Physical Chemistry of barrier discharge* DVS-Verlag Düsseldorf.
[9] Beamson G and Briggs D 1992 *High Resolution XPS of Organic Polymers. The Scienta ESCA300 Database* John Wiley & sons Chichester.
[10] Russat J 1988 *Surf. Interface Anal.* **11** 414.

THE EFFECTS OF OXYGEN ON PLASMA-POLYMERIZATION OF HMCTSO USING AN ATMOSPHERIC PRESSURE DIELECTRIC BARRIER DISCHARGE

Yoon-Kee Kim, Gi Taek Kim

Department of Welding and Production Engineering, Hanbat National University
E-mail: ykkim@hanbat.ac.rk

Hexamethylcyclotrisiloxane and oxygen was used to deposit SiO_2-like thin films with a helium dielectric barrier discharge operated at 4kV 30kHz at atmospheric pressure. FTIR, FESEM, and XPS were used to analyse the layers. The film deposited without oxygen has many large pores and particles. The films deposited with low oxygen flow have a cauliflower-like structure with embedded agglomerates. As increase of oxygen content in reaction gas, the films are flat and dense. From the FTIR results, the amount of Si-O-Si bond in the films deposited with large amount of oxygen is significantly increased.

1. Introduction

Plasma polymerized films using organosilanes have attracted great interest due to many applications in electronics, optics, barrier film for food packaging, and corrosion protection of metals.[1-4] Most of plasma-polymerizations were conducted in the low pressure vessels with expansive vacuum system and were not suited for mass production for large surface. Recently several researchers tried to study the plasma-polymerization at atmospheric pressure using non-thermal plasma, especially dielectric barrier discharge (DBD).[5-7] Because DBDs can easily be formed and sustained at atmospheric pressure they are well known to be mass production methods to cleaning and surface modification of many substrates, such as metals, glasses, polymers etc.

Tetraethoxysilane (TEOS) and hexamethyldisiloxane (HMDSO) are the most utilized precursors for the deposition of organosilicon layers because they are non-toxic, non-explosive, and safer to handle than silane gases. The films formed by AP-CVD have large amount of carbon and hydrogen so that they could not directly perform as a barrier to protect oxidation or corrosion.[8] Silicon dioxide films were good barrier for protection of oxygen permeation and for enhancement of corrosion behaviour of metals. There are many reports that SiO_2-like films have been deposited using HMDSO at low pressure and a few papers at atmospheric pressure.[7.9-12] However, most of them tried to form SiO_2-like films using only HMDSO even though there are many siloxane precursors.

In this work, we have tried to deposit SiO_2-like films using hexamethylcyclotrisiloxane (HMCTSO) in atmospheric pressure DBD. HMCTSO is one of the best organosiloxane precursors due to high Si contents in a molecule, non-toxic, non-explosive, and high vapour pressure at room temperature even though it is a solid. The chemical structures of film were controlled by oxygen content in feed gas. The coatings were characterized by Fourier transform infrared spectroscopy (FT-IR), x-ray photoelectron spectroscopy (XPS), scanning electron microscopy (SEM). The effects of oxygen concentration of reaction gas on the surface morphologies and bonding structures of the films were investigated and discussed.

2. Experimental

The configuration of the atmospheric pressure DBD system is shown in Fig. 1. A couple of metal electrodes covered with alumina as the dielectric barrier to sustain stable DBD were connected with 30 kHz a.c. power. The reaction gas was sprayed through the slit made at the alumina tube between the couple of high voltage electrodes to the substrate, silicon (100) wafer ($15x30mm^2$), on the grounded electrode-plate. The gap between high voltage electrode and top of substrate was set at 1.2 mm. The Si wafer on the moving plate was repeatedly passed through discharge at 1mm/sec. A treatment with 10 passes lasted 5min. The monomer vapour in the glass bubbler containing HMCTSO (Sigma-Aldrich, ≥98%) was feed into DBD using helium carrier gas flowed at 50sccm. In order to study the effect of

oxygen on the chemical structure of deposited film, the flow rate of oxygen was varied in the range of 5~500sccm.
The chemical structure of the films was evaluated by FTIR spectroscopy (Nicolet, Magna IR550) in attenuated total reflectance (ATR) modes. The XPS analyses were carried out in a MultiLab ESCA2000 spectrometer. The x-ray source was a MgKα(1235.6eV) radiation. Field emission-SEM analysis was carried out on Hitachi S-4800 in order to estimate the growth rate of films and observe microstructures.

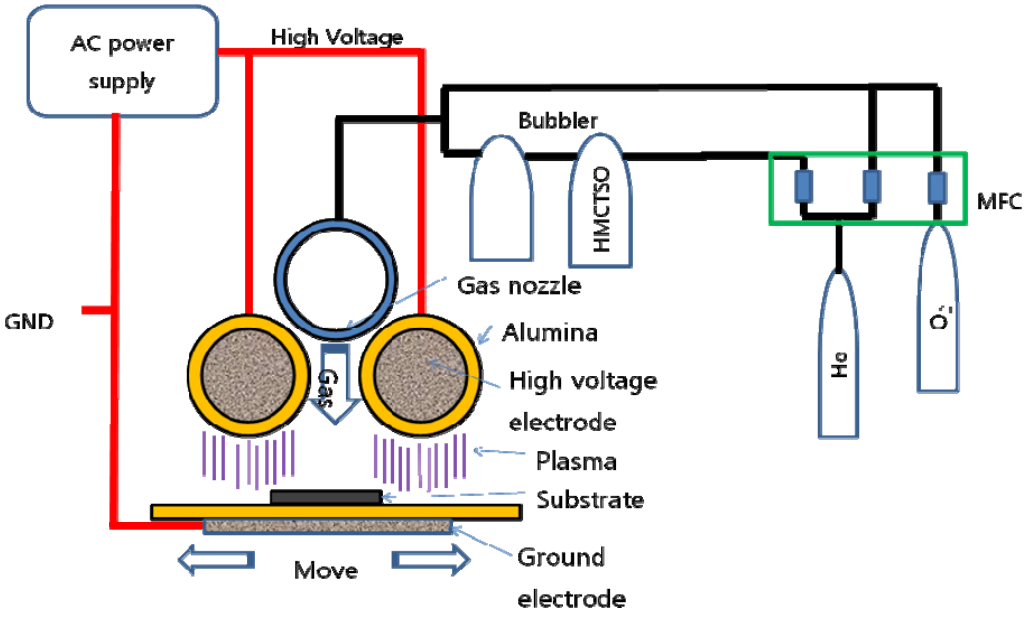


Fig. 1. Schematic diagram of atmospheric pressure DBD systems for deposition of SiO_2-like films

3. Results and Discussion

The cross-sectional SEM morphologies of the films deposited on Si substrate at several flow rate of oxygen are shown in Fig. 2. The film deposited without oxygen has very porous structure with many spherical particles as shown in Fig. 2 (a). It is a typical CVD film structure when film is deposited with high supersaturation of gas phase and low substrate temperature. In this experiment, the substrate temperature covered with He DBD generated at 4kV 30 kHz is near room temperature. The large pores in films were disappeared as adding oxygen but many hemispheres were still existed on the surface of film deposited with 20sccm of oxygen. At 30 sccm of oxygen, the surface of film became very flat and dense as shown in Fig. 2(c). The structure was not significantly changed as increasing oxygen flow rate up to 500 sccm.
The FTIR spectra of the layers deposited at the several flow rates of oxygen are shown in Fig. 3. The spectrum of the layer deposited without oxygen shows a broad absorption feature centred at 1110 cm^{-1} and a weak absorption band centred at 1195cm^{-1} assigned to the Si-O-C and rocking vibrational mode of Si-O-CH_3 group, respectively.[6,13] A broad absorption band centred at 930cm^{-1} was attributed to the Si-OH stretching vibration. As adding small amount of oxygen, weak absorption peaks were appeared at 820 cm^{-1} and 1056 cm^{-1} corresponding to the Si-O-Si bending and asymmetric stretching, respectively.[14,15] A absorption peak was also appeared at 1275 cm^{-1} assigned to Si-CH_3 stretching in $Si(CH_3)_n$ (n=1,2 or 3) and slightly increased the intensity of peak at 1195cm^{-1}. The absorption peak at 840 cm^{-1} corresponding to Si-CH_3 stretching in the $Si(CH_3)_3$ groups was not found all of the spectra. From the FTIR spectra it is believed that oxygen should increase the number of Si-O-Si bonding and Si-CH_3 in $Si(CH_3)_n$ (n=1or 2). The intensity of the absorption peak centred at 820 cm^{-1} and 1056 cm^{-1} was significantly increased due to large amount of oxygen flow as shown in Fig. 3(b). This result shows that the inorganic nature of the layer was increased with flow rate of oxygen. Tab. 1. shows the chemical composition of the layers measured by XPS. Even though the atomic ratio of Si, O, and C in a HMCTSO molecule is 1:1:2, the layer deposited without oxygen showed high content of oxygen and

very low content of carbon. The carbon content was significantly decreased as adding small amount of oxygen in the feed gas. From the XPS results, it is believed that the chemical composition of the layers should be similar to SiO_2.

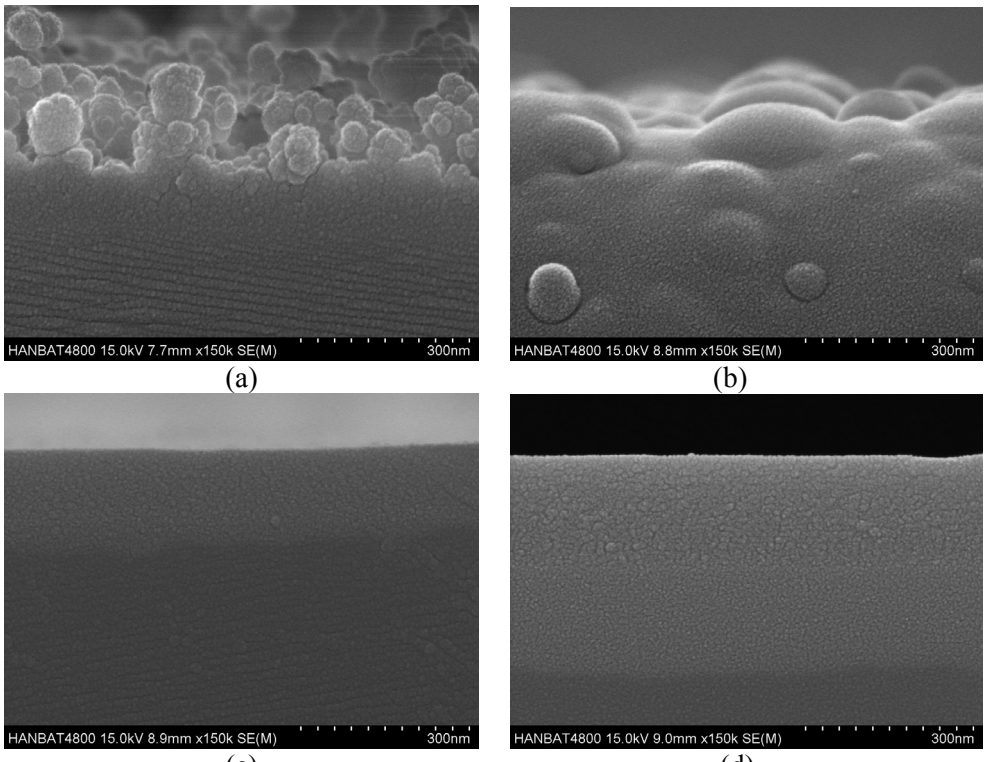


Fig. 2. SEM morphologies of the films deposited on Si substrate at the oxygen flow rate of (a) 0 (b) 20 (c) 30 (d) 350 sccm.

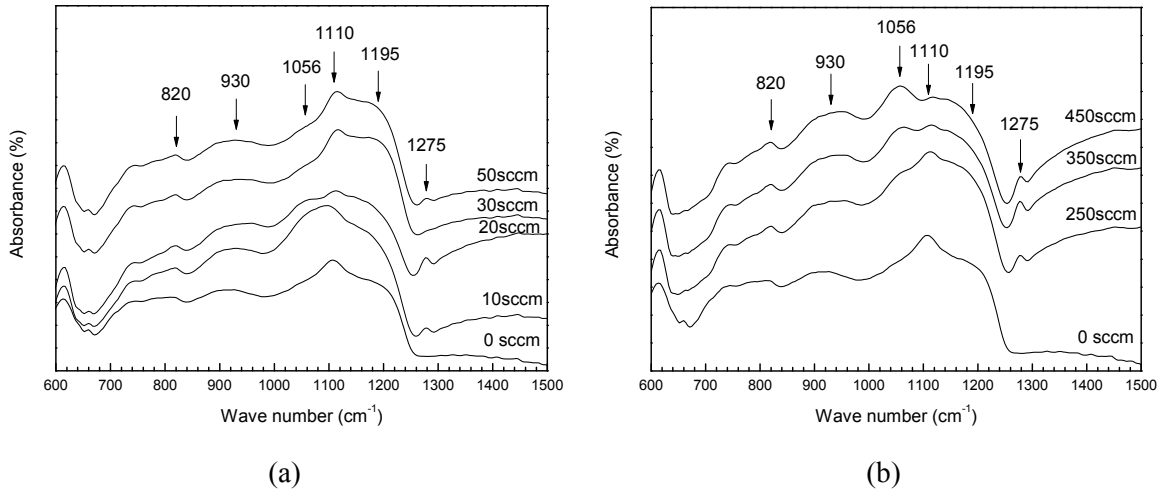


Fig. 3. FTIR-absorption spectra of films deposited in different oxygen flow. (a) small amount of oxygen (b) large amount of oxygen

Tab. 1. Chemical composition of the layers deposited with and without oxygen.

	Chemical composition (%)		
oxygen flow rate (sccm)	silicon	oxygen	carbon
0	27.8	68.0	4.3
5	28.7	68.7	2.6
500	30.0	68.4	1.6

4. Conclusions

The present study reports the deposition of SiO_2-like layer using DBD in He/HMCTSO with oxygen at atmospheric pressure. The layer deposited using only He/HMCTSO has a cauliflower-like structure and many large pores. Adding oxygen to reaction gas, the films have a glass-like structure with embedded particles. Finally, the films become flat and dense as oxygen flow rate is increased. From the FTIR results, the Si-O-C bond is reduced with increase of oxygen flow and Si-O-Si bond is significantly increased. As a result, this work showed that it should be possible to deposit a smooth SiO_2-like film at atmospheric pressure DBD using HMCTSO and control microstructure and chemical bonding of the layer with oxygen content in the reaction gas.

5. References

[1] Templer T, Vallier L, Madar R, Oberlin J C, Devine R A B 1994 *Thin Solid Films* **241** 251
[2] Tien P, Smolinsky G, Maretin R 1972 *J. Appl. Opt.* **11** 637
[3] Inagaki N, Kondo S, Hirata M, Urushibata H, 1989 *J. Appl.Polym.Sci.* **30** 3385
[4] Schreiber H P, Wertheimer M R, Wrobel A M 1980 *Thin Solid Films* **72** 487
[5] Vinogradov I, Lunk A 2009 *Plasma Process. Polym.* **6** S514
[6] Rohani V, Bauville G, Lacour B, Puech V, Duminica F D and Silberberg E 2008 *Surf. Coat. Technol.* **203** 862
[7] Premkumar P A, Starostin S A, de Vries H, Paffen R M J Creatore M, Eijkemans T J, Koenraad P M, van de Sanden M C M 2009 *Plasma Process. Polym.* **6** 693
[8] Bour J, Bardon J, Aubriet H, Frari D D, Verheyde B, Dams R, Vangeneugden D, Ruch D 2008 *Plasma Process. Polym.* **5** 788
[9] Etienne C P, Tatoulian M, Mabille I, Sutter E, Khonsari F A 2007 *Plasma Process. Polym.* **4** S562
[10] Fracassi R, d'Agostino R, Palumbo F, Angeline E, Grassini S, Rosalbino F 2003 *Surf. Coat. Technol.* **174-175** 107
[11] Momose Y, Tomii M, Maruyama T, Shimoda T, Motohashi Y 2003 *Surf. Coat. Technol.* **169-170** 682
[12] Sawada Y, Ogawa S, Kogoma M 1995 *J. Phys. D: Appl. Phys.* **28** 1661
[13] Eufinger S, van Ooij W J and Conners K D 1996 *Surface and Interface analysis* **24** 841
[14] Alexander M R, Jones F R, and Short R D 1997 *Plasmas Polym.* **2** 277
[15] Basner R 1998 *Int. J. Mass Spectrom* **176** 245

PERMANENT HYDROPHILIC SURFACE MODIFICATION OF NONWOVEN FABRICS BY PLASMA INDUCED GRAFTING IN GAS PHASE

Jana Kubincová[1], Dušan Kováčik[1], Ondrej Bogár[1], Anna Zahoranová[1], Mirko Černák[1, 2]

[1]*Department of Experimental Physics, Faculty of Mathematics, Physics and Informatics, Comenius University, Mlynská dolina, 842 48 Bratislava, Slovak Republic*
[2]*Department of Physical Electronics, Faculty of Science, Masaryk University, Kotlářská 2, 611 37 Brno, Czech Republic*
E-mail: jana.kubincova@fmph.uniba.sk

In our contribution we present results on hydrophilic surface modification of polypropylene (PP) nonwoven fabrics that were surface-activated by atmospheric-pressure plasma generated by Diffuse Coplanar Surface Barrier Discharge (DCSBD) in ambient air. Subsequently, the plasma-activated samples were grafted by acrylic acid monomer gas. Surface properties of the plasma activated and polyacrylic acid post-plasma grafted nonwovens were tested by common strike-through time and critical wetting surface tension (CWST) measurements. The layer of polyacrylic acid grafted on the fibres was verified by ATR-FTIR.

1. Introduction

Polypropylene nonwoven fabrics have found great utility in many diverse applications. Most of these applications require making naturally hydrophobic PP nonwoven permanently wettable. One of the conventional methods, how to achieve desired properties, is chemical graft polymerization however the ecological requirements force the industry to search alternative environmental safety methods.
An environmentally attractive alternative is the low-temperature plasma surface activation of PP nonwoven fabrics. The majority of known low-temperature plasma activation of nonwovens for subsequent grafting has been done at low pressures [1−3]. However treatment times at low pressures are relatively long for practical applications and the plasma equipment expensive what makes low-pressure plasma processes costly and continuous operation practically impossible. Plasma processes at atmospheric pressure appear to be more economical than at low pressure, moreover atmospheric plasma has significant commercial potential for in-line textile treatment.
In presented contribution we summarize our results concerning hydrophilic surface modification of PP nonwovens by plasma induced grafting method. Plasma surface activation was realized using *ZUP 200* plasma device (Fig. 1) based on Diffuse Coplanar Surface Barrier Discharge (DCSBD). This type of dielectric barrier discharge is characterized by microdischarges of high density generated on a dielectric planar plate [4-6]. Due to high power density (100 W/cm^3) of DCSBD non-equilibrium plasma concentrated in the thin layer and possibility to keep the good contact between PP fabric and plasma layer the treatment time can be significantly reduced.. It is supposed that as reactive species for subsequent acrylic acid (AAc) grafting in gas phase surface radicals generated by the plasma activation are used [7]. The surface properties of the AAc grafted PP nonwoven fabrics were characterized by ATR-FTIR analyse. Liquid transport capabilities were analysed by common strike-through time measurements and CWST measurements.

2. Experimental

In all experiments as tested material the industrial polypropylene nonwoven (18 g/m^2, surface tension 39 mN/m) supplied by PEGAS Nonwovens Company (Czech Republic) was used. As the plasma gas ambient air was employed and in all of grafting experiments AAc stabilised with hydroquinone monomethyl ether (MERC Ltd.) was used.
DCSBD was fed by sinusoidal high voltage (20 kV peak-to-peak) with frequency of 15 kHz. The power of DCSBD was adjusted to the value of 400 W. Experimental apparatus for study of AAc

plasma induced grafting in gas phase is illustrated by Fig. 1 and 2. Fig. 1a shows the general view of ZUP 200 plasma treater for continuous hydrophilic plasma surface treatment of fabrics. Plasma of DCSBD burning in ambient air during treatment process can be seen in Fig. 1b. Fig. 1c offers the scheme of DCSBD electrode system consisting of silver strip electrodes embedded 0.5 mm below the surface of 1mm thick Al_2O_3 ceramics.

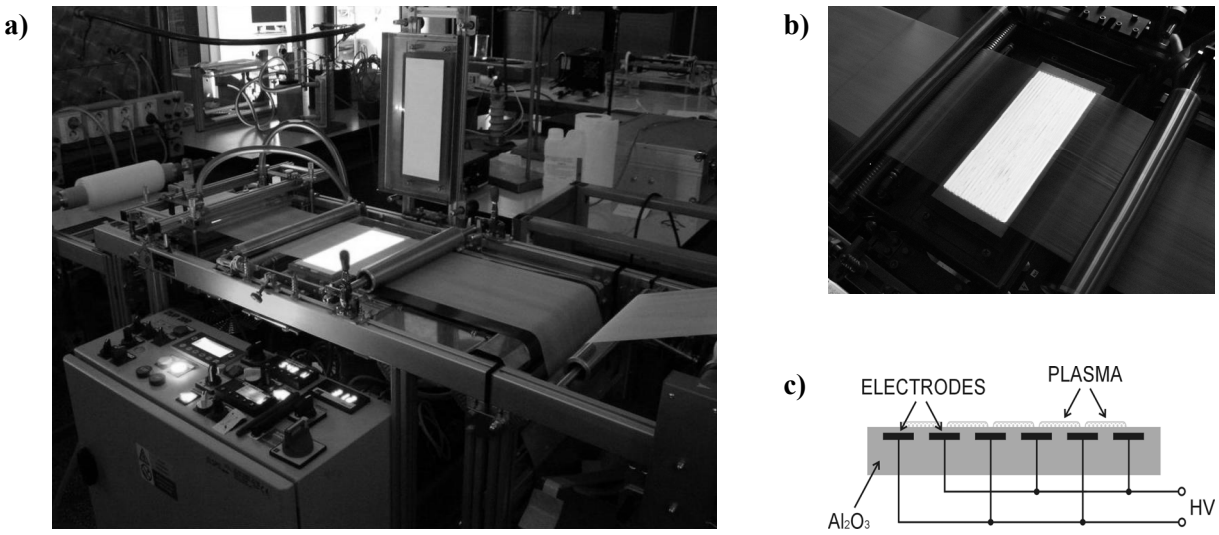


Fig. 1. Photos showing ZUP 200 plasma treater for continuous fabrics treatment, the general view of device with open chamber inside of which two DCSBD electrodes are placed (a), the bottom DCSBD electrode in operation with visible plasma area generated in ambient air (b), and the scheme of DCSBD electrode system (c).

The whole grafting procedure was realized as follows in these steps:

- PP nonwoven fabrics were surface-activated by device ZUP 200 in ambient air
- plasma-activated samples were placed into the glass chamber, which was closed and evacuated to the pressure less than 20 kPa
- technical purity nitrogen was flowing through the bubbler with acrylic acid and introduced to the glass chamber with various concentrations (*AAc/N_2 mixture*) determined by different nitrogen flow rate, see Fig. 2
- after reaching an atmospheric pressure inside the chamber nonwoven fabrics were kept in glass chamber for different grafting times.

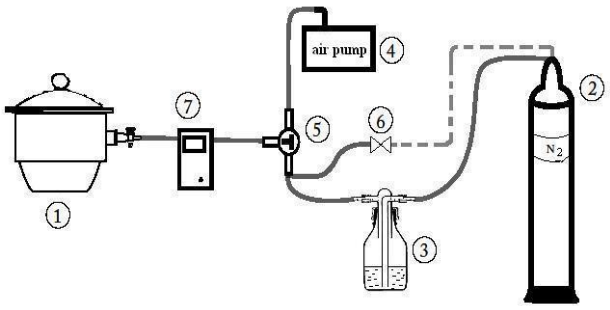


Fig. 2. The sketch of experimental arrangement for grafting: (1) glass chamber, (2) gas cylinder with nitrogen, (3) bubbler, (4) air pump, (5) three way valve, (6) inlet valve, (7) vacuometer.

3. Results and Discussion

As can be seen in Fig. 3 and 4, our tests clearly showed hydrophilic effect of post-plasma grafting in gas phase onto PP nonwoven fabrics. Before plasma activation tested samples were hydrophobic with strike-through time more than 40 sec, moreover due to its inhomogeneous structure some fabric

samples exhibited values more than 100 sec or test liquid did not even penetrate at all through samples. Fig. 3 shows strike-through time values measured immediately after treatment. It is evident, that PP fabric is after plasma induced grafting characterized by hydrophilic surface. The quality of grafted surface markedly depends on grafting time and plasma pretreatment time. The best results were achieved for plasma activation time 2.4 sec and grafting time 30 min, therefore in all other experiments samples were kept in glass chamber with AAc/N_2 mixture for 30 min.

a) **b)**

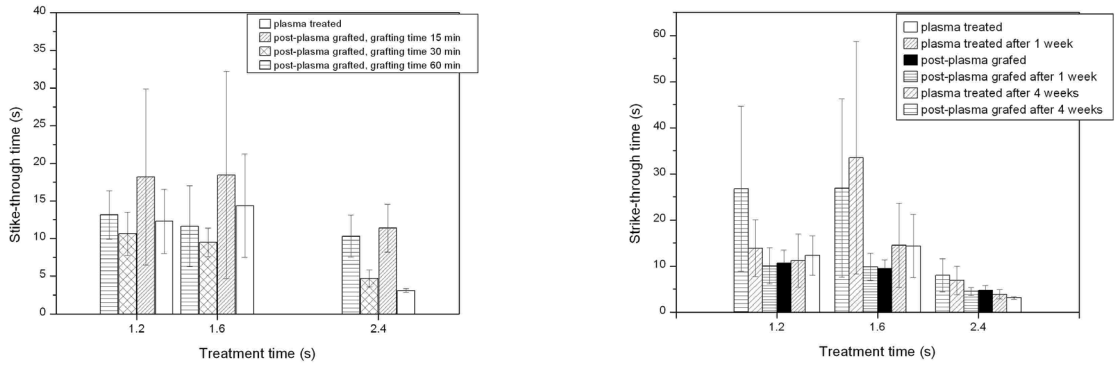


Fig. 3. (a) Strike-through time values of PP nonwoven fabrics as a function of DCSBD plasma pretreatment time and AAc grafting time, measured immediately after treatment. The AAc/N_2 mixture flow was 5 l/min. (b) Dependence of strike-through time on storage time (treatment ageing) for plasma pretreated and AAc grafted PP fabrics, grafting time was 30 min and the N_2 flow through the bubbler was 5 l/min.

In order to markedly assign to influence of AAc grafted amount on PP nonwovens hydrophilicity nitrogen was flowing also through two into series integrated bubblers with AAc. As can be seen in Fig. 4, in this case for shorter exposure times better values of strike-through time were achieved.

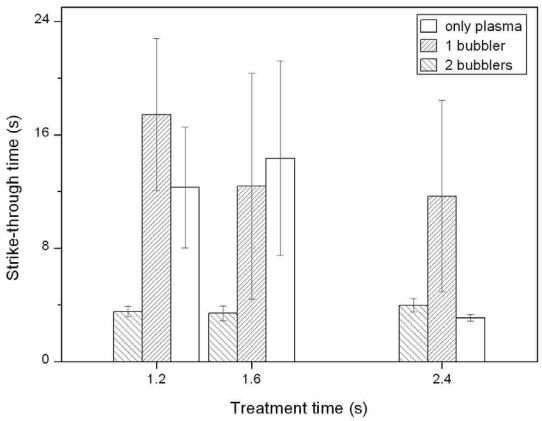


Fig. 4. Comparison of strike-through time values for 1 and 2 bubblers integrated in the experimental apparatus measured immediately after plasma induced grafting. Nonwoven fabrics were plasma pretreated for different time, N_2 flow rate was 1 l/min and grafting time 30 min.

Tab. 1 summarizes the effect of atmospheric pressure plasma pretreatment (30 sec) and plasma induced AAc grafting in gas phase (N_2 flow rate 1 l/min, grafting time 30 min) on PP nonwoven fabric hydrophilization at fixed plasma power. The presented values of surface tension were measured immediately after experiment and then also 4 weeks after experiment date.

Tab. 1. Surface tension values for DCSBD plasma pretreated and AAc grafted nonwoven fabric samples measured immediately after treatment and 4 weeks after plasma induced grafting in gas phase.

SAMPLE OF PP NONWOVENS	SURFACE TENSION
untreated sample	39 mN/m
plasma activated	76.8 mN/m
post-plasma grafted	85.5 mN/m
4 weeks after post-plasma grafted	70 mN/m

The surface of the untreated and the AAc grafted PP nonwovens was analysed by ATR-FTIR spectroscopy (Fig. 5). There is the conformity between untreated and grafted sample. AAc exhibits a sharp band associated with vibration bond C=O between 1680 and 1725 cm-^{1}. Characteristic vibration bond OH appears as a broad peak in the 2500 to 3000 cm^{-1} region. In the case of post-plasma grafted nonwoven fabrics the shape of spectrum at 3000-4000 cm^{-1} is evidently changed however there is no peak at 1715 cm^{-1}. Therefore we changed treatment conditions, specifically plasma treatment time to 30 sec, N_2 flow was 1 l/min and grafting time 30 min. The spectrum for this case is shown in Fig. 6.

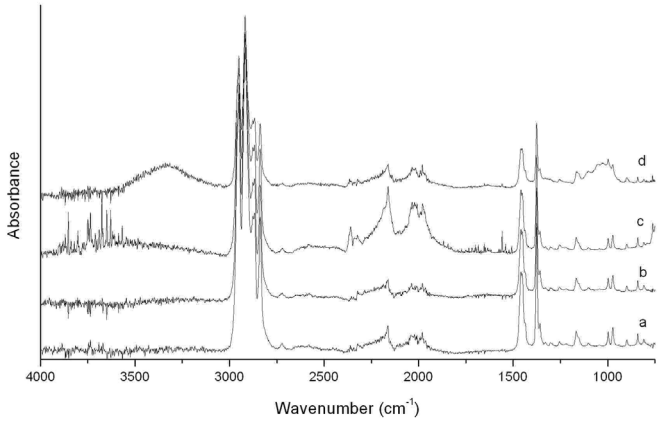


Fig. 5 Comparison of (a) untreated, (b) AAc grafted (without plasma pretreatment), (c) plasma treated and (d) post-plasma AAc grafted samples.

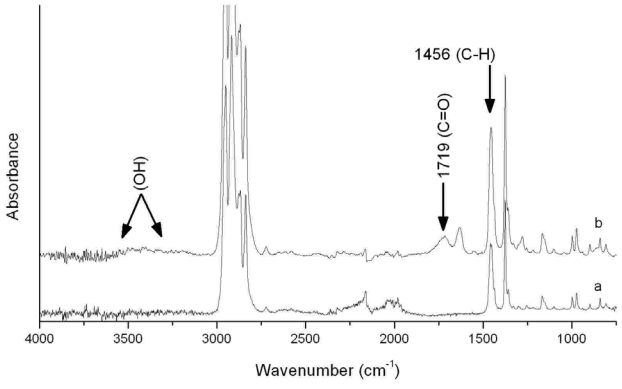


Fig. 6 ATR-FTIR spectra of (a) untreated PP fabric and (b) post-plasma AAc grafted fabric. The grafted layer is characterized by the carbonyl band of C=O group at 1719 cm^{-1}.

4. Conclusion

In presented work possibility of permanent hydrophilic surface modification of PP nonwoven fabrics by the post-plasma AAc grafting method was investigated. As initiator of grafting process plasma of DCSBD installed in ZUP 200 device was used. After this plasma pretreatment nonwoven samples were grafted by AAc in gas phase. Quality and permanency of post-plasma grafted PP fabrics were tested by common strike-through time measurements, CWST and ATR-FTIR analyse.

Results confirmed increase of initially low surface energy of post-plasma AAc grafted PP nonwoven fabrics with strike-through time dependent on plasma pretreatment and grafting time. On the other hand relatively long grafting times, high statistic error values of measured data indicating inhomogeneously grafted layer of AAc on the fibres surface and plumbless wastage of AAc monomer gas make this treatment method impractical. Moreover, AAc grafted surface of PP fabrics was not stable in time what indicates non-permanent modification. Presence of grafted AAc on the PP fabrics surface was confirmed by ATR-FTIR spectroscopy. Spectrum for the post-plasma AAc grafted sample was characterized by typical carbonyl and carboxyl band that is a conclusive evidence of AAc layer.

Acknowledgments. This research has been supported by the Slovak Research and Development Agency, Project No. APVV-0485-06 and VEGA grant No. 1/0783/10.

5. References

[1] M. R. Young, K. S. Chem, J. C. Rsai, C. C. Tseng, and S. F. Lin 2002 *Mater. Sci. Eng., C-bomet. Supramolecular Syst.* **20** 167.

[2] A. M. Sarmadi, T. H. Ying, and F. Denes 1993 *Text. Res. J.* **63** 697.

[3] Y. C. Tyan, J. D. Liao, R. Klauser, I. D. Wu, and C. C. Weng 2002 *Biomaterials* **23** 65.

[4] D. Kováčik, A. Zahoranová, A. Buček, J. Ráheľ, Ľ. Černáková, M. Černák, *Proceedings: Contributed Papers of the 17th Symposium on Physics of Switching Arc,* **Vol. I***,* Nové Město na Moravě, September 10-13, 2007, Czech Republic, pp. 129–132.

[5] D. Kováčik, A. Zahoranová, A. Buček, M. Černák, *Contributed Papers of HAKONE XI*, **Vol. 2**, Oléron Island, September 7-12, 2008, France, pp. 493-497.

[6] M. Černák, Ľ. Černáková, I. Hudec, D. Kováčik, A. Zahoranová 2009 *Eur. Phys. J. Appl. Phys.* **47** Art. No. 22806.

[7] Ľ. Černáková, D. Kováčik, A. Zahoranová, M. Černák, M. Mazúr 2005 *Plasma Chem. Plasma Process.* **25** 427-437.

ATMOSPHERIC PRESSURE DCSBD PLASMA TREATMENT OF AL SURFACE: STUDY OF SURFACE MORPHOLOGY AND CHEMICAL COMPOSITION

V. Prysiazhnyi[1], M. Cernak[1,2], P. Vasina[1]

[1]*Masaryk University, Faculty of Science, Department of Physical Electronic, Brno, Czech Republic*

[2]*Comenius University, Faculty of Mathematics, Physics and Informatics, Bratislava, Slovakia*

E-mail: mr.vodik@gmail.com

In this paper we present the results on ambient air plasma cleaning of aluminium surfaces using the Diffuse Coplanar Surface Barrier Discharge (DCSBD). The plasma cleaning effect was proven by means of Attenuated Total Reflectance FTIR spectroscopy. A ToF LDI MS study has shown that the DCSBD plasma treatment modifying upper surface region. The plasma treatment has resulted also in a significant increase in functional OH groups' number and in aluminium surface oxidation. The results of AFM measurements have indicate that the DCSBD plasma treatment does not increase the surface roughness.

1. Introduction

In-line atmospheric pressure plasma cleaning is a hot subject of applied and industrial plasma research. Two main reasons are the low cost of processing and environmental advantages comparing to low pressure plasma treatment or treatment using chemicals [1]. The simplest in-line plasma treatments are cleaning and activation of aluminium surfaces prior subsequent application of a surface coating [2,3].

For a long time aluminium and especially its alloys are at tremendously high use in different areas of industry and human life. Although there are still questions how to prepare fast, how to do it cheap and control the properties of aluminium surface to get desirable adhesion to functional coatings. That essentially means metal surface cleaning and activation.

Subject of this paper is related to aluminium surface cleaning and activation. To define the surface properties more precise than in case of industrially made aluminium or its alloys, thin model aluminium layers deposited on glass substrates were used. For air plasma treatment an atmospheric pressure plasma source called the Diffuse Coplanar Surface Barrier Discharge (DCSBD) was used. The changes in surface properties as a result of the DCSBD plasma treatment will be presented and discussed.

2. Materials and methods

Thin aluminium films were deposited by DC magnetron sputtering on glass substrates cleaned by Ar ions bombardment. The deposition conditions were: i) working gas in chamber – Ar; ii) deposition pressure in chamber – 3 Pa; iii) plasma driven by power – 6 W/cm^2; iv) distance between target and substrate – 7 cm.

For the surface treatment atmospheric pressure plasma source called the Diffuse Coplanar Surface Barrier Discharge (DCSBD) was used. The DCSBD is a special type of barrier discharge plasma source, in which both electrodes are embedded into Al_2O_3 ceramics in the same plane. Detailed description of the DCSBD plasma electrode could be found elsewhere [4]. In the present work optimized conditions for aluminium surface treatment were used [5]: i) distance between coplanar electrode and the sample surface was set to 0.35 mm; ii) the power density was about 40 W/cm^3 meaning about 300W from network. The DCSBD plasma treatment time changed from 3 s up to 100 s and treatment was done in ambient air at atmospheric pressure with relative humidity at about 40 %.

ThermoMicroscopes Autoprobe was used for the AFM measurements. The measurements were carried in ambient air using standart AFM tips for contact mode measurements.

Attenuated Total Reflectance FTIR (ATR FTIR) measurements were carried on Bruker VERTEX v80 spectrometer. The spectrometer was equipped with MIRacle single reflection diamond ATR plate. All

measurements were done at pressure 25 Pa in spectral range from 600 cm^{-1} to 4000 cm^{-1} with spectral resolution 4 cm^{-1}.
Time-of-Flight Laser Desorption Ionisation Mass Spectroscopy (ToF LDI MS) was measured using an AXIMA CFR (Kratos Analytical, Manchester, UK) instrument equipped with a nitrogen laser emitting at 337 nm. The laser source was operated in a repetition mode at 10 Hz frequency with a pulse time width of 3 ns and has power up to 6 mW. All the measurements were carried in the vacuum with pressure not more than 10^{-5} Pa.

3. Results and discussion

a. AFM measurements

The goal of AFM measurements was to check how the DCSBD plasma influences the morphological surface state. The structure of untreated by plasma magnetron sputtered aluminium surface is grainy. For the untreated surface typical grain size was about 700 nm and the surface had typical RMS at about 6-8 nm. On the surface were presented relatively high islands more than 100 nm height. Evidently, these islands are not the small dust particles because after few scans on the same spot they are remaining on the surface without changing their shape, position and height. Apparently, the grains are due to non-uniform growth of the film and surface oxidation.
After the DCSBD plasma treatment the aluminium surface state was changed significantly. After 3 s treatment the average grain size decreases to about 150 nm and falls to about 100 nm for 100 s plasma treatment. We believe that this is due to plasma cleaning of the aluminium surface, which is proven by the other experiments discussed later.
The second very important observation is concerned with changes in surface roughness. Increasing the treatment time the DCSBD plasma treatment slightly increases the surface roughness. Although after the plasma treatment there was fewer amounts of mentioned high islands on the surface. The images of the typical surface topography are shown in Fig. 2. Some general statistical results about the surface morphology are presented in Table 1. The values in the Table are the typical values measured as an average from at least four successful AFM scans for each sample. As it can be seen, the DCSBD treatment is very „gentle“ to the surface. This fact can be important, for example, in modern microelectronic applications where typical scale of elements is less than 100 nm.

Tab. 1. Statistical data from the AFM measurements of aluminium surface depending on the DCSBD plasma treatment time.

	Peak-to-peak height, nm	RMS, nm	Average grain size, nm
Not treated Al	78.72	8.93	600-900
3 s treatment	63.8	7.92	130-180
10 s	83.18	9.47	110-170
40 s	90.3	9.57	90-160
100 s	51.5	6.18	80-120

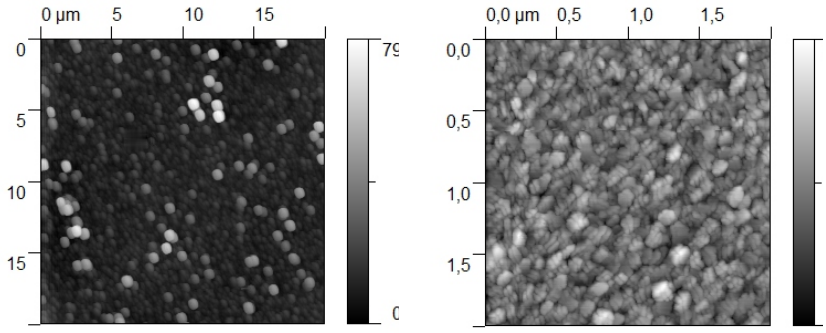


Fig. 2. AFM images of untreated aluminium surface (left) and 100 s DCSBD plasma treated aluminium surface (right)

b. Attenuated Total Reflection FTIR measurements

The ATR FTIR method is widely used for characterisation of organic or polymer coatings and interface aluminium substrate/polymer film [6], [7]. Although the presence of oxide layer on aluminium surface allows to use FTIR in ATR mode even on the non-coated surface, in the case of non-coated aluminium surface we observed that the ATR signal is very weak. For example, the typical values for FTIR peaks in ATR mode usually about 0.2 a. u. and higher and for our case the peak's value were not more than 0.05 a. u. However this limitation still allows us to get some important information.

ATR FTIR spectra of untreated aluminium surface has peaks related to Al-O stretching (with wavenumber about 940 cm^{-1}), water and OH vibrations (wide peak or few peaks in wavenumber range from 3000 cm^{-1} to 3800 cm^{-1}) and number of peaks related to the hydrocarbon contamination of the surface. Peaks characterised hydrocarbon contamination are: i) C-H stretching doublet for sp^3 hybridisation with wavenumbers 2956 cm^{-1} and 2872 cm^{-1}; ii) C-H stretching doublet for sp^2 hybridisation with wavenumbers 2926 cm^{-1} and 2853 cm^{-1}; iii) C=C stretching with wavenumber 1633 cm^{-1}; iv) H-C-H stretching with wavenumber 1455 cm^{-1}; v) and peak of CH_2 wagging vibrations with wavenumber 1280 cm^{-1} [8].

Figure 2 presents evolution of i), ii) and v) FTIR peaks after the DCSBD plasma treatment. The inverse peak's direction is because ATR FTIR measurements involving background measurement and sometimes peaks may behave in this way. This result is corresponding to our earlier conclusions based on AFM measurements regarding the cleaning of aluminium surface by the DCSBD plasma treatment. Table 2 indicates how typical relative intensity changes of mentioned peak's related to the hydrocarbon contamination depend on the DCSBD treatment time. For relatively small DCSBD treatment times (up to 10 s) it was observed that the surface cleaning is not uniform and from point to point the relative changes in peak intensity are not constant. For higher DCSBD plasma treatment times the effect of plasma is constant on the whole surface.

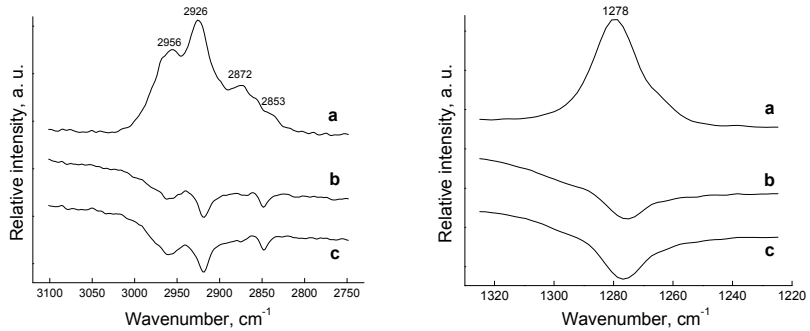


Fig. 3. ATR FTIR spectra of aluminium surface: a) untreated surface; b) 10 s DCSBD air plasma treatment; c) 100 s air plasma treatment.

Tab. 2. Relative values of ATR FTIR peaks of different vibrations depending on the DCSBD plasma surface treatment.

	C-H stretching, 2926 cm^{-1}, a.u.	C=C stretching, 1633 cm^{-1}, a.u.	H-C-H stretching, 1455 cm^{-1}, a.u.	CH_2 wagging, 1278 cm^{-1}, a.u.
Untreated Al surface	0.012..0.015	0.01..0.012	0.009..0.01	0.013..0.014
3 s DCSBD pl. tr.	-0.0015..0.008	-0.0025..0.004	0.001..0.006	-0.0012..0.01
10 s DCSBD pl. tr.	-0.0027..0.002	-0.0038..-0.0012	-0.002..0.002	-0.0015..0.005
40 s DCSBD pl. tr.	-0.0035..-0.0029	-0.0055..-0.0040	-0.0023..-0.0018	-0.0028..-0.0016
100 s DCSBD pl. tr.	-0.0039..-0.0031	-0.0062..-0.0053	-0.0028..-0.002	-0.003..-0.002

c. TOF LDI MS measurements

ToF LDI MS is sensitive tool for surface chemical composition analysis on a nanoscale level. This method allows to get the information analysing positive or negative ions ablated by pulsed laser shot from the surface. For current measurements laser power was set to constant value 6 mW with pulse duration 3 ns. All the samples was analysed in profile scanning mode.

Some general features similar for both positive and negative spectra were reveal during measurements. Sample surface can be divided into two regions: i) region of adsorbed molecules, up to first 30 laser shots at one place; ii) bulk material with characterised by stable peaks positions and intensities, from 30 laser shots up to few hundred shots. Transition of the spectra from one region is shown of fig. 4. Spectra were accumulated as a sum of 10 laser pulse shots. The region of adsorbed molecules characterises by higher than in bulk region number of peaks because of different adsorbed molecules. Characteristics of this region are: i) small aluminium (27 atomic mass), aluminium oxide (43 a. m.) and aluminium hydroxide (44 a. m.) peaks; ii) presence of carbon clusters patterns (24, 36, 48, 60, 72, 84, 96 a. m.), which is due to adsorption of hydrocarbon contamination from air; iii) high mass fragments (from few hundred a. m.) which is strongly believed to be a fragments of organic contamination. The structure of spectra is depended on the number of shots made by laser. After about 30 shots for all samples spectra changed to the bulk region. With respect to the DCSBD plasma treatment compared to non-treated samples there are some changes in the spectra for region of adsorbed molecules, although there are no systematical changes. It can be explained by the fact that samples were exposed by air at least for one hour before they were measured by ToF LDI MS.

The bulk region is characterised by sharp peaks with high intensities. Major peaks in spectra are the hydroxide (17 a. m.), aluminium (27 a. m.) and its oxide (43 a. m.) and hydroxide (44 a. m.) and aluminium dihydroxide (60 a. m.). Comparison of non-treated and plasma treated aluminium surfaces gives very strong and uniform changes in the bulk region (fig. 5). After the DCSBD plasma treatment the in the spectra appears additional peaks of water (18 a. m., 36 a. m. and 38 a. m.), oxygen (32 a. m.), tetrahydroxide (68 a.m) and aluminium oxide (102 a. m.) peaks. Also the intensity of hydroxide (17 a. m.) and aluminium dihytroxide (60 a. m.) peaks are greatly increases. These changes in the spectra allow us to conclude that the DCSBD plasma treatment is modifying the aluminium surface by increasing the number of chemically active hydroxide groups and also leading to the surface oxidation. However, our preliminary trying to estimate the changes in oxide layer thickness by optical ellipsometry was not successful.

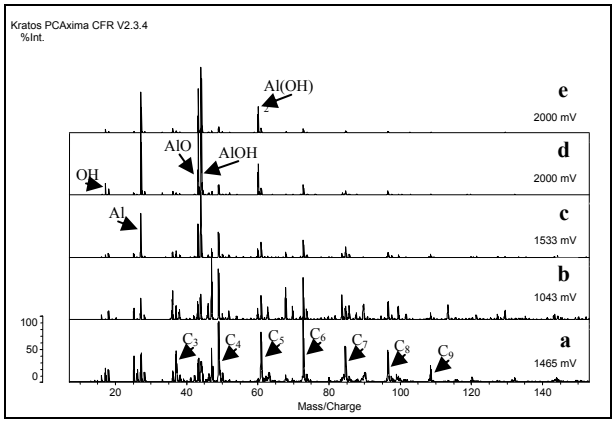


Fig. 4. ToF LDI MS spectra of negative ions for as received Al film: a) 10 laser shots deep; b) 20 laser shots deep; c) 30 laser shots deep; d) 40 laser shots deep; e) 100 laser shots deep.

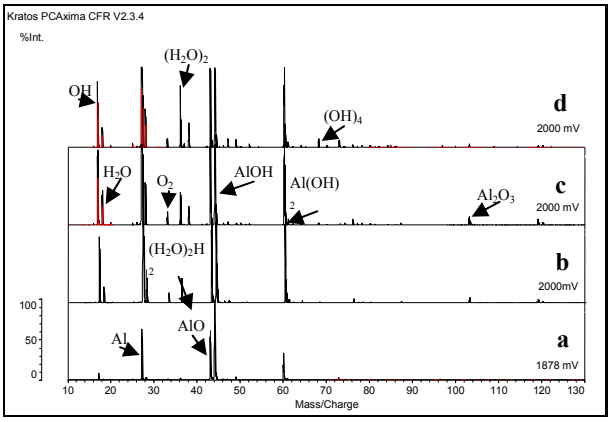


Fig. 5. ToF LDI MS spectra of negative ions for: a) as received Al film; b) 40 sec DCSBD air plasma treated Al surface; c) 75 sec DCSBD pl. tr. Al surface; d) 100 sec DCSBD pl. tr. Al surface.

4. Conclusions

Obtained results provide additional information about the effects of ambient air plasma exposure to the aluminium surface. It was shown that the DCSBD plasma treatment leads to the efficient aluminium surface cleaning and activation. The effect of plasma treatment on the aluminium surface depends on the treatment time and for current experimental setup for uniform surface treatment exposure more than 10 s is needed. Generally, the features of the plasma-surface interaction could be presented as follows: i) a short 3-sec DCSBD plasma treatment leads to cleaning of the aluminium surface from hydrocarbon contamination which is clearly indicated by the AFM measurements; ii) a longer exposure have led to surface activation and surface oxidation. The ATR FTIR measurements for the

non-coated aluminium surface were presented. We are not aware of any previous evidence work which presents results of such measurements.
Open questions for this work are obtaining information about the oxide layer thickness after the DCSBD plasma treatment and detailed measurement of oxide layer properties.

Acknowledgements. The authors thank to prof. RNDr. Josef Havel, DrSc. for providing the ToF LDI MS analysis.
This research has been supported by the KAN 101630651, MSM 0021622411, APVV-0491-07 and 104/09/H080 grants.

5. References

[1] J. R. Roth: *Industrial Plasma Engineering Vol II. Applications to Non-Thermal Plasma Processing.* (Institute of Physics Publishing 2001, Bristol and Philadelphia)
[2] H. Li, A. Belkind, F. Jansen, Z. Orban. An in situ XPS study of oxygen plasma cleaning of aluminium surfaces. *Surface and Coating Technology* 92 (1997) 171-177.
[3] H. Kersten, H. Steffen, J.F. Behnke. Investigations on plasma-assisted surface cleaning of aluminium contaminated with lubricants. *Surface and Coating Technology* 86-87 (1996) 762-768.
[4] M. Černák, L'. Černáková, I. Hudec, D. Kováčik and A. Zahoranová:“ Diffuse Coplanar Surface Barrier Discharge and its applications for in-line processing of low-added-value materials” *Eur. Phys. J. Appl. Phys*. 47, 22806 (2009)
[5] V. Prysiazhnyi, P. Stahel, M. Cernak. Plasma Treatment of Alumina Surface by DCSBD. *17th Symposium on Application of Plasma Processes, Visegrad Workshop on Research of Plasma Physics*, Liptovskij Jan, Slovakia, 2009.
[6] M. Pantoja, B. Diaz-Benito, F. Velasco, J. Abenojar, J.C. del Real. Analysis of hydrolysis process of 3-methacryloxypropyltrimethoxysilane and its influence on the formation of silane coatings on 6063 aluminium alloy. *Applied Surface Science* 255 (2009) 6386-6390.
[7] M. Ohmar, D. Persson, C. Leygraf. In situ ATR-FTIR studies of the aluminium/polymer interface upon exposure to water and electrolyte. *Progress in Organic Coatings* 57 (2006) 78-88.
[8] D.W. Mayo, F.A. Miller, R.W. Hannah. *Course notes on the interpretation of infrared and RAMAN spectra*. ISBN: 0-471-24823-1, Wiley 2004.

EFFECT OF THE PARAMETERS OF COATING DEPOSITION, FROM DECAMETHYLTETRASILOXANE AS PRECURSOR, ON THEIR TRIBOLOGIC PROPERTIES

Rżanek-Boroch Zenobia[1], Zychewicz Agnieszka[1], Lisowski Wojciech[2], Kisielewska Aneta[3], Krawczyk Krzysztof[1]

[1]*Faculty of Chemistry, Warsaw University of Technology, Noakowskiego 3, 00-664 Warszawa, Poland*

[2]*Institute of Physical Chemistry Polish Academy of Science, Kasprzaka 44-52, 01-224 Warsaw Poland*

[3]*Faculty of Physic and Chemistry, University of Lodz, Pomorska 149/153, 90-236 Lodz, Poland*

E-mail: rzanek@ch.pw.edu.pl

The coating deposition process on a surface of mono-crystalline silicon was carried out by the PE-CVD method under atmospheric pressure from 0.1%DMTOS+He, 0.1%DMTOS+He+(0.2-2%)O_2 mixtures, and for additional coating carbonification from a 0.1%DMTOS + He + (0.05-1%)CH_4 mixture.

On the basis of the performed studies it has been shown that it is possible to obtain coatings of better tribologic properties than those of the covered silicon support.

1. Introduction

The studies presented in the paper are a continuation of works on plasma deposited coatings characterized by a small friction coefficient [1-7]. The deposition was performed in the dielectric barrier discharge (DBD) by the plasma enhanced chemical vapour deposition (PE-CVD) method under atmospheric pressure. Decamethyltetrasiloxane (DMTOS) (FLUKA, cat. no. 30537) was the coating precursor. The precursor concentration in the gases was 0.1% at constant gas mixture flow of 9 dm^3/h. The coatings were deposited on plates of mono-crystalline silicon Si (100).

The purpose of the research was to determine the optimal deposition parameters, i.e. surface temperature, time of carrying out the process, and composition of the gas mixture containing oxygen (0-2%) or methane (0.05-1%) to obtain coatings with a friction coefficient smaller than that of the silicon surface. The coatings were deposited during 5 to 30 minutes, changing the surface temperature from 100°C to 400°C in subsequent experiments. The obtained coatings were subjected to spectroscopic (FTIR, XPS), tribologic and microscopic (AFM) studies.

2. Discussion of Results

In the first stage of studies, the coatings were deposited during 5-30 minutes, at temperatures from 100°C to 400 °C, from a 0.1%DMTOS+He mixture. On the basis of spectroscopic studies (FTIR), no relationship between the deposition time and qualitative composition of the coatings was found. On the other hand, it was found that a change in the surface temperature affects only its quantitative composition. The largest intensity of the absorption bands, corresponding to the Si–O–C bonds, was recorded for the wavelength 1030 cm^{-1}. Simultaneously, the presence of bands corresponding to Si–O–Si, Si–O–C and Si–CH_3 linkages of wavelength 799 cm^{-1} was observed. An increase in the surface temperature causes a decrease in the intensity of absorption bands at 844 and 1260 cm^{-1}) characteristic of Si–CH_3 linkages. At higher temperatures (300 and 400 °C) the intensity of bands characteristic of the groups: CH_x group (2966 cm^{-1}), Si–O–Si, Si–O–C, Si–CH_3 (799 cm^{-1}) as well as Si–O–C (1030 cm^{-1}) increases (Fig. 1).

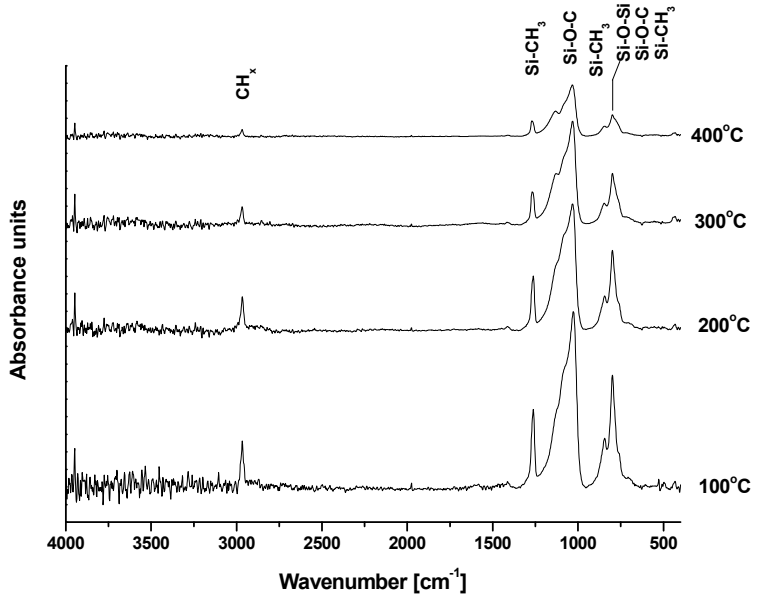


Fig. 1. FTIR spectra of the films deposited from the mixture of 0.1%DMTOS+He, at temperatures 100°C-400°C. Deposition time 15 min.

From tribologic studies it results that coatings deposited from a 0.1%DMTOS+He mixture at surface temperature of 100 °C are characterized by low friction coefficient (Fig. 2). An increase in the surface temperature causes a considerable increase in the friction coefficient, irrespective of the process time. The layers deposited during 30 minutes, irrespective of the surface temperature, were characterized by worse tribologic properties than those of the silicon surface on which they were deposited. For easier comparison of the results, the friction coefficient value of the silicon surface (0.157) has been marked by a horizontal line.

On the basis of composition studies by the XPS method and FTIR studies it has been found that coatings deposited from a 0.1%DMTOS+He mixture contain carbon (45-37%), silicon (34-37%) and oxygen (19-26%)

3. Coatings deposited from an oxygen containing mixture

In subsequent experiments, oxygen (0.2-2%) or methane (0.05-1%) were introduced to the mixture to carbonize the coatings.

FTIR spectra show that an increase in oxygen concentration in the mixture causes an increase in the SiO_2 content in the coating and a decrease in the share of the organic residue (CH_x and $Si–CH_3$). On the basis of the results of XPS studies of coatings deposited during 10 minutes from a 1% DMTOS+He+(0-2%)O_2 mixture at various surface temperatures (100-400 °C), an evaluation of the effect of oxygen addition on their composition has been carried out. It was found that a 0.2% oxygen addition does not cause any change in the coating composition. An increase in the oxygen concentration above 0.2% causes an increase in the silicon and oxygen content in the coating (Tab. 1). The highest carbon content (~46 at. %) was observed for coatings deposited from mixtures without oxygen and at its 0.2% content.

Tab. 1. Percentage content of particular elements in layers deposited for 10 minutes from 0.1%DMTOS+He+(0-2%)O_2 mixtures

Mixture composition	DMTOS+He	DMTOS+He +0.2% O_2	DMTOS+He +1% O_2	DMTOS+He +2% O_2
Temp. [°C]	C [at. %]			
100	45.87	45.87	5.56	21.08
200	43.35	39.40	38.51	4.31
300	38.25	40.04	10.86	19.17
400	36.45	34.84	32.23	11.61

Mixture composition	DMTOS+He	DMTOS+He +0.2% O_2	DMTOS+He +1% O_2	DMTOS+He +2% O_2
Temp. [°C]	Si [at. %]			
100	34.63	34.07	43.09	40.63
200	34.76	36.25	28.14	43.16
300	36.69	34.68	41.20	37.45
400	36.68	37.10	37.70	41.55

Mixture composition	DMTOS+He	DMTOS+He +0.2% O_2	DMTOS+He +1% O_2	DMTOS+He +2% O_2
Temp. [°C]	O [at. %]			
100	19.50	20.06	51.35	38.29
200	21.89	24.35	32.2	52.53
300	25.06	25.28	47.94	42.86
400	26.87	28.06	30.07	46.84

The carried out tribologic studies of the obtained coatings showed that the lowest friction coefficient – 0.019 was achieved for the coating deposited for 10 minutes at the surface temperature of 100 °C from a 0.1%DMTOS+He mixture. The other coatings deposited from the same mixture for a longer time, as well as at higher surface temperature, did not show better tribologic properties.

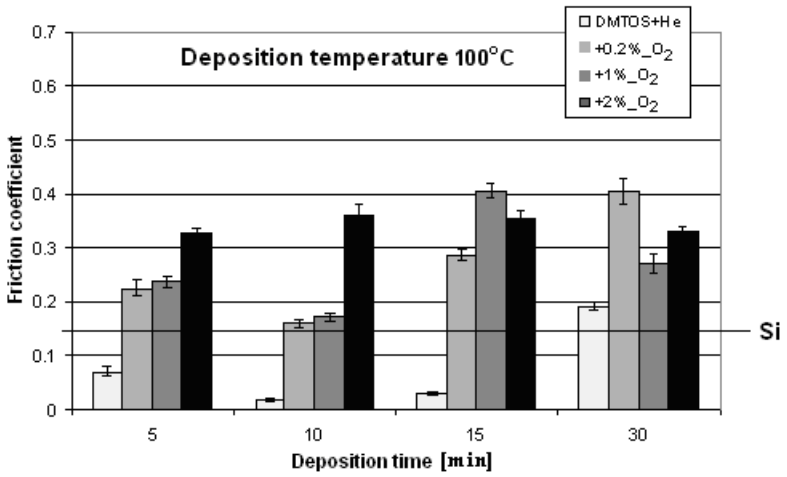


Fig. 2. Dependence of the friction coefficient value on the process time for coatings deposited from a 0.1%DMTOS+He mixture at various surface temperatures.

4. Coatings deposited from mixtures containing methane

FTIR spectra of coatings deposited during 15 minutes at the surface temperature of 100 °C from 0.1%DMTOS+He+(0-1%)CH_4 mixtures are collected in Fig. 3.

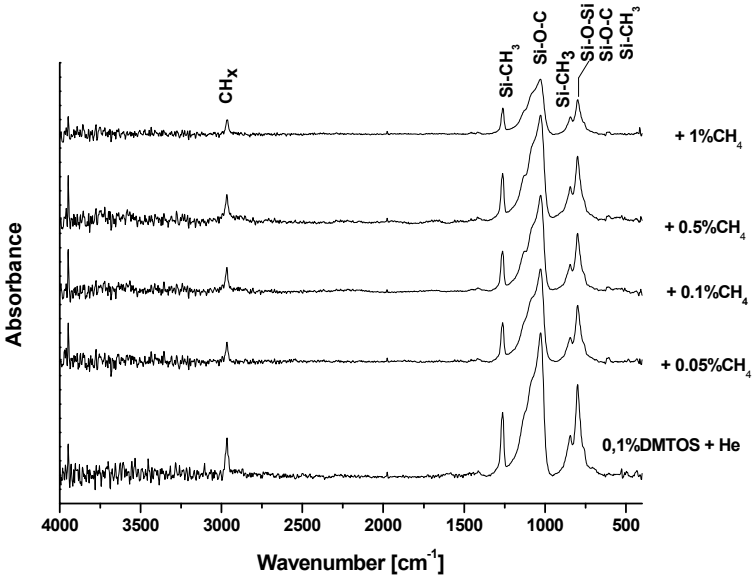


Fig. 3. FTIR spectra of coatings deposited from 0.1%DMTOS+He+(0-1%)CH_4 mixtures at surface temperature of 100°C. Deposition time – 15 minutes.

The most intensive absorption bands of wavelength 1026-1028 cm^{-1} correspond to Si–O–C linkages. Bands characteristic of Si–CH_3 (844 and 1260 cm^{-1}), CH_x (2966 cm^{-1}), Si–O–Si, Si–O–C, and Si–CH_3 (799 cm^{-1}) linkages are also observed. From the spectra presented it results that an increase in the methane content in the mixture causes a decrease in the intensity of all the absorption bands.

An analysis of the FTIR spectra (Figs. 1 and 3) does not show any differences in the qualitative composition of coatings obtained from mixtures with and without methane. The observed wavelength shifts from 1030 cm^{-1}, characteristic of Si–O–C linkages, towards lower wavelengths of 1026-1028 cm^{-1}, which probably results from the addition of methane to the gas mixture.

The friction coefficient values of coatings deposited during 15 minutes from 0.1%DMTOS+He+(0-1%)CH_4 mixtures are presented in Fig. 4. The coating deposited at the surface temperature of 100 °C from a mixture containing 0.05% of methane showed a similar friction coefficient value to that of the coating obtained at the same conditions but without the addition of methane. Moreover, both mentioned coatings were distinguished from among all those studied by very low friction coefficients (0.029±0.003, 0.038±0.006, respectively). The coating obtained at 100 °C from a mixture containing 0.1% of methane exhibited a friction coefficient smaller than that of the silicon surface. The other coatings, obtained from mixtures containing methane, showed tribologic properties similar to that of the surface. An exception were coatings obtained at 300 and 400 °C from 0.1%DMTOS+He+2%CH_4 mixtures, characterized by high friction coefficient.

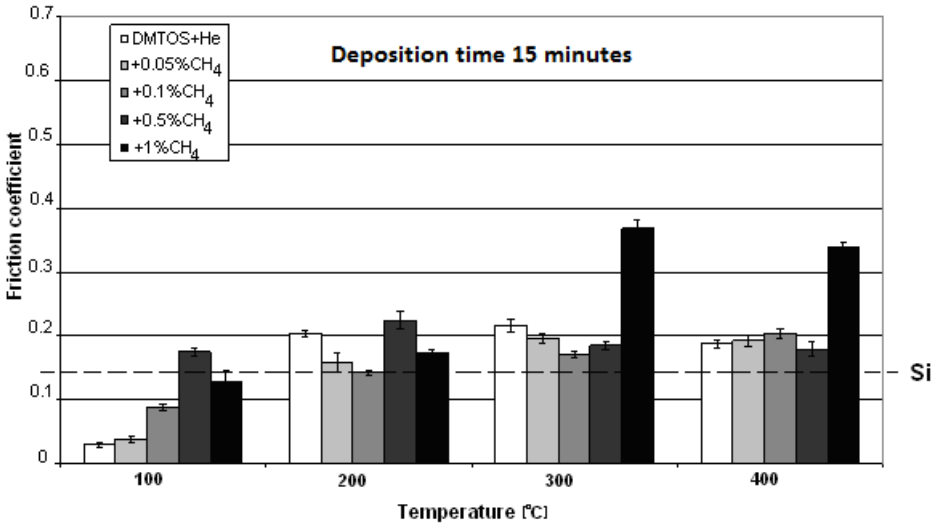


Fig. 4. Dependence of the friction coefficient values of layers deposited for 15 minutes from 0.1%DMTOS+He+(0-1%)CH_4 mixtures on the surface temperature.

For layers deposited from 0.1%DMTOS+He+(0-2%)CH_4 mixtures very differentiated friction coefficient values were obtained. An analysis of the presented diagrams did not show any general relationships between the particular process parameters (concentration of the added oxygen, surface temperature) and the friction coefficient.

For coatings deposited from methane containing mixtures, and showing the lowest friction coefficients, composition studies were performed by the XPS method and it was found that a small (0.05-0.1%) addition of methane to the gas mixture (0.1%DMTOS+He+CH_4) causes a slight increase (46.8-47.4%) in the carbon content in the layer with a simultaneous decrease in the silicon and oxygen content.

5. Conclusions

On the basis of the performed studies it has been shown that it is possible to obtain layers of better tribologic properties than those of the covered silicon surface.
An eight-fold lower friction coefficient (0.019) was exhibited by the coating deposited during 10 minutes at 100 °C from the 0.1%DMTOS+He mixture. From the point of view of its tribologic properties it was better than coatings obtained from mixtures containing a 1% additive of oxygen (friction coefficient 0.101) or 0.05% of methane (friction coefficient 0.038).
Layers obtained from a 0.1%DMTOS+He mixture, due to their excellent tribologic properties, can find numerous applications in MEMS devices.

Acknowledgments. This work was financially supported by Warsaw University of Technology

6. References

[1] Abraham S., Choi E.I., Kang N., Kim K.H., Surface & Coatings Technology 2007, **202**, 915
[2] Rżanek-Boroch Z., Lamenta A., Ilik A., Micro System Technologies 2005, 606
[3] Fanelli F, R. d'Agostino, F. Fracassi, Plasma Process. Polym. 2007, **4**, 797
[4] Rżanek-Boroch Z., Jóźwik K., J.Adv.Oxid.Technol. Vol.9, No.2 (2006) 237
[5] Rżanek-Boroch Z., Gradkowska K.,. Ilik A. and Kosiński A., Chem. Listy 2008, **102,** 1455
[6] Rżanek-Boroch Z., Wojucki M., Ilik A., Kosiński A, Contributed papers Hakone X, Japan 2006, 318
[7] Rymuza Z., Misiak M., Rżanek-Boroch Z., Janowska, Solid Films 466 (2004) 158

INVESTIGATION OF SILICON SURFACE WETTABILITY AFTER PLASMA TREATMENT

Dana Skácelová[1], Pavel Sťahel[1], Martin Haničinec[1], Mirko Černák[1,2]

[1]*Department of Physical Electronics, Faculty of Science, Masaryk University, Kotlářská 2, 611 37, Brno, Czech Republic*

[2]*Department of Experimental Physics, Faculty of Mathematics, Physics and Informatics, Comenius University, Mlynska dolina F2, 842 48, Bratislava, Slovak Republic*

E-mail: danka@physics.muni.cz

The effects of the ambient air plasma generated using the Diffuse Coplanar Surface Barrier Discharge (DCSBD) on crystalline Si (100) surface was studied. The Si surfaces cleaned and activated by the plasma treatment were investigated by AFM and contact angle measurements. It was found that the surface wettability increased by the plasma treatment tends to decay over time. Surprisingly, when the plasma treated sample is stored in water the wettability is increased again.

1. Introduction

Nowadays, plasma technology provides an innovative, economical and environmentally friendly tools, that are able to replace or improve some of the chemical production processes including cleaning, activation or passivation of the surfaces, coating, etching.

In this paper we present the surface plasma modification of crystalline (c-Si) silicon samples. The attention was paid to the c-Si due to its great importance in many fields of modern industry, mainly microelectronics industry [1]. This study could bring interesting results for future use or improvement of already existing production processes.

The changes of the c-Si surface properties after plasma treatment were studied by contact angle measurement and AFM. Because of the difficulties to measure directly the surface free energy (SFE) of solids, contact angle measurement provides an indirect and very simple method to determinate SFE [2]. The knowledge of surface free energy, as well as, the wettability of surfaces is very important in a wide range of applications.

It was found that the plasma treated surfaces do not show a stable behavior with time, the water contact angles tend to increase, an indication that an aging process called hydrophobic recovery occurs. Surprisingly it was found that the wettability increased once again, if the aged treated sample was immersed in water solution and dryed.

2. Experimental setup

Dielectric barrier discharge the so called DCSBD (Diffuse Coplanar Surface Barrier Discharge) was used to plasma treatment (Fig. 1) [3]. Electrode system was made by parallel metallic electrodes embedded in Al_2O_3 ceramic dielectric. This construction provides the large area of thin layer of highly non – isothermal cold plasma. Vacuum sample holder on the rails enables to move with samples in accurately adjustable distance from the dielectric barrier in plasma layer.

The crystalline polished Si (100) n – type wafers doped with antimony were used. Samples were sorted into two groups: the samples cleaned by isopropyl alcohol (IPA) and the samples cleaned by IPA and then immersed in 1% HF solution at room temperature for 45s. The silicon surface cleaned by IPA is terminated by native oxide. In case of the silicon surface cleaned with HF solution the native oxide layer was etched and the surface tends to be hydrogen termination [4].

Contact angle measurements were realized by Surface Energy Evaluation System (SEE System). Surface free energy was calculated by Acid – base model. In the case of this model, SFE is divided into two components, one including the long – range interaction, called the Lifshitz – van der Waals component (LW) and the other including the short – range interaction, called acid – base component (AB) [2]. Water, glycerol and diiodomethane were used as the measuring liquids.

Plasma treatment was realized in air at atmospheric pressure, discharge power was 300 W, treatment time 2.4 s. The distance between the sample surface and the ceramic plate was 0.3 mm.

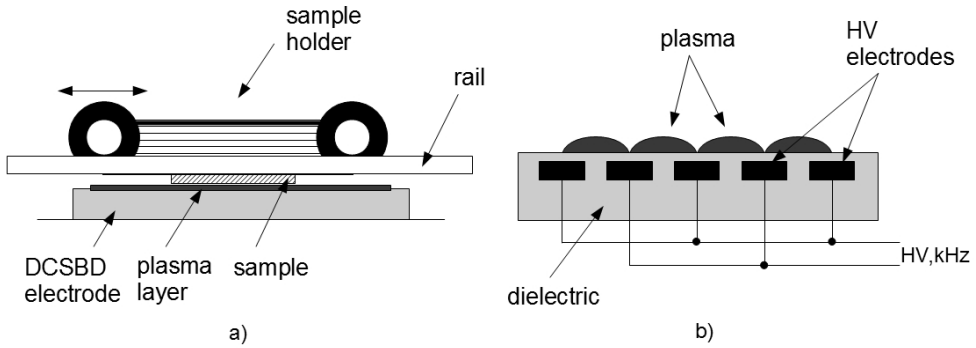


Fig. 1. Experimental device. a) DCSBD reactor with movable sample holder, b) detail of the discharge electrode (cross – section).

3. Results and discussion

The contact angle values of water and surface free energy for the different samples and condition of samples are summarized in Tab. 1. The plasma treatment of silicon surface makes the sample hydrophilic and the degree of hydrophilicity depends on the way, how the surface is cleaned (Fig. 2).

Tab. 1. Water contact angle (WCA), surface free energy (SFE) and its components of untreated and treated silicon surface with and without native oxide.

	Untreated With native oxide	Treated With native oxide	Untreated Without native oxide	Treated Without native oxide
WCA [°]	38.6 ± 2.7	5.0 ± 0.9	84.6 ± 1.8	11.1 ± 0.3
Total SFE [mJ/m^2]	56.7 ± 1.7	62.0 ± 0.6	48.8 ± 0.9	62.9 ± 0.8
LW component [mJ/m^2]	41.2 ± 1.2	43.1 ± 1.6	47.9 ± 0.4	44.1 ± 1.2
AB component [mJ/m^2]	15.4 ± 1.8	19.3 ± 1.1	0.9 ± 0.2	18.2 ± 1.0

The behavior of cleaned silicon surface, without any plasma modification is in principle known [4], [5]. After immersion in HF solution, a clean Si surface becomes hydrophobic due to the absorbtion of hydrogen ions. On the other hand, in non – HF solution, silicon surface remains covered with an oxide film and silicon oxide layer is hydrophilic [4].

After plasma modification, the situation was changed significantly. The surface free energy decreased considerably and the wettability increased. This fact could be explain partly due to removing of contamination from the surface, partly due to increase in hydroxyl OH groups density, which are responsible for hydrophilic properties of silicon surface [4]. This fact is confirmed by increase of AB components of total surface free energy in case of HF treated and IPA cleaned investigated samples.

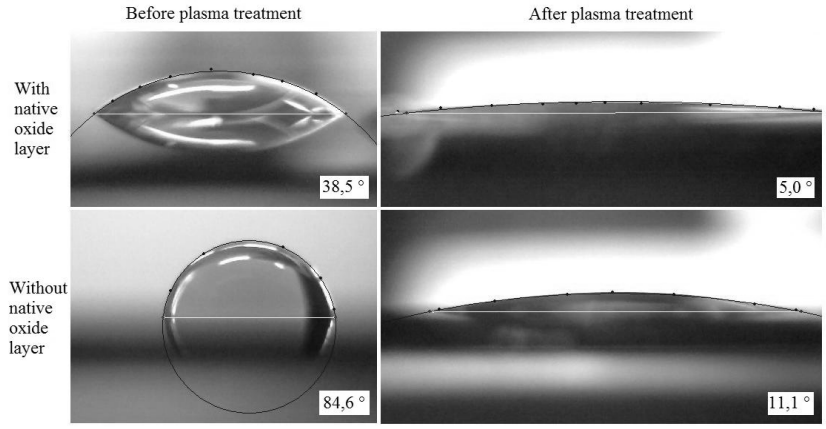
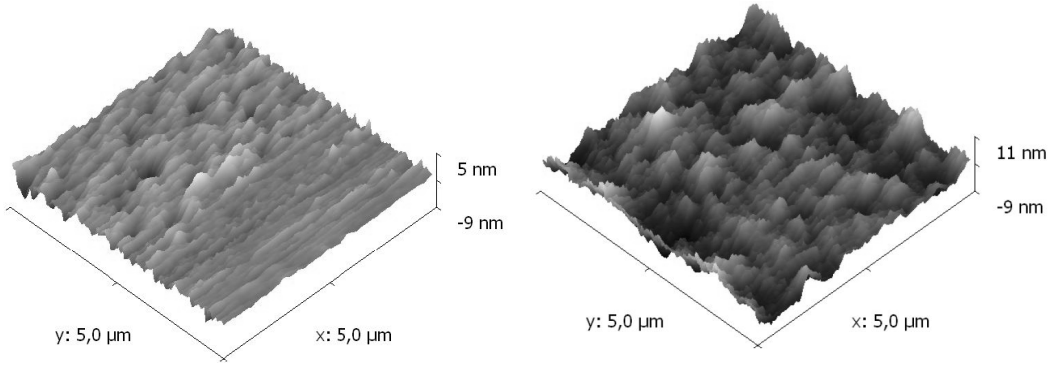


Fig. 2. Contact angle measurement of silicon surface. Water drop on the silicon surface with and without native oxide layer before plasma treatment and after plasma treatment.

AFM images of untreated and 1s treated surface (Fig. 3) show that the plasma has an influence on the surface morphology too. Fig. 3a) shows the typical surface of clean polished silicon wafer and the change of surface morphology after 1s plasma treatment is shown in Fig. 3b). RMS roughness increased from 2.23 nm before plasma treatment to 19.6 nm after 1 s plasma treatment.



a) b)

Fig. 3. AFM images of a) typical surface of polished silicon wafer and b) the change of surface morphology after 1 s plasma treatment.

In Fig. 4 and Fig. 5 the ageing effect of the both types of treated surfaces is shown. It is evident, that values of water contact angle (Fig. 4) increased during the storage time, but the behaviour of ageing process is different for the two investigated samples. In case of the sample without native oxide layer before plasma treatment, etched in HF solution, contact angle of water rapidly increased within a few hours. In principle, within ten hours the water contact angle achieved the value that changes during another hours slightly. On the other hand, the samples with native oxide film aged more slowly. Within the first day, the increase of water contact angle was practically negligible.
The both samples exposed to an ambient air more than 150 hours tended to achieve almost the same values of water contact angle. For completeness, Fig. 5 shows the course of surface free energy during ageing process, which corresponds with the water contact angle.

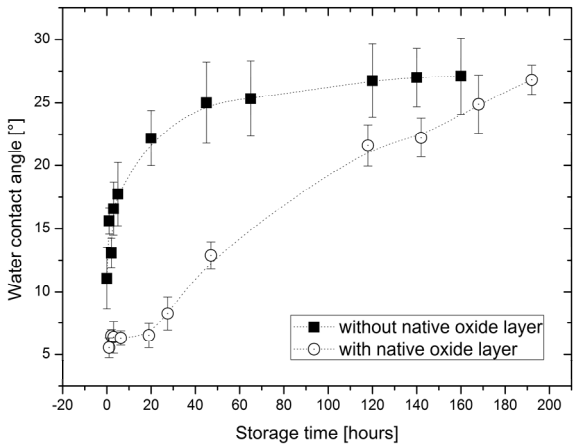


Fig. 4. Ageing effect of treated surface with and without native oxide layer which is exposed to an ambient air. Contact angle of water increased within the time. Moreover, this ageing process depends on the cleaning method before plasma modification.

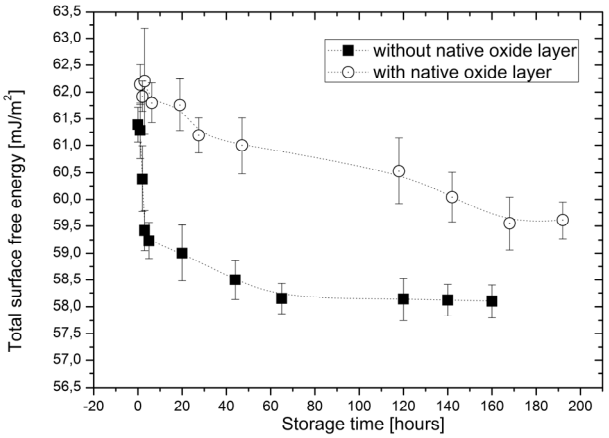


Fig. 5. Ageing effect of treated surface with and without native oxide layer. The values of total surface free energy corresponding with the previous water contact angle.

To prove that hydrophilic OH groups could rotate to bulk material we dipped samples to water. It was found, that the aged sample immersed in water solution made the sample more hydrophilic once again. The results for both samples are summarized in Tab. 2. After plasma treatment samples were exposed to an ambient air for 60 hours, corresponding values of water contact angle are in Tab.2 labeled as Aged sample. After that, the samples were dipped in water solution at room temperature for 1 minute, 60 minutes and 240 minutes. After water immersion, samples were dried and the changes of wettability were investigated. In both cases, the water contact angle decreased, the wettability improved.

Tab. 2. Water contact angle of aged samples (60 hours after plasma treatment) and subsequent change of contact angle after water immersion.

	Aged sample [°]	After 1min immersion [°]	After 60min immersion [°]	After 240 min immersion [°]
With oxide layer	11.5 ± 1.0	3.3 ± 0.1	3.4 ± 0.6	3.9 ± 0.9
Without oxide layer	27.3 ± 3.2	19.4 ± 2.9	17.3 ± 0.9	17.7 ± 1.6

Generally, the well-known hydrophobic recovery of SiO_2-coated surfaces after air plasma treatment is assigned to the recontamination by hydrocarbons due to exposure to the ambient air. This, however, does not provide any explanation for the observed hydrophilic recovery due to immersion. Consequently, we hypothesize that, similarly as in the case of plasma-treated polymer surfaces [4],

likely cause of hydrophobic recovery is surface reorientation of the polar OH groups caused by plasma treatment away from the surface. If the interfacial environment is aqueous due to a strong interaction with water molecules they are drawn out to the surface and make it hydrophilic, if it is air the surface OH groups will reorient to the bulk.

4. Conclusion

In the current work, the properties of silicon surface before and after plasma modification were studied. In addition to, the influence of different cleaning process on the subsequent properties was investigated. It was found, that the cleaning process of silicon surface influence, not only the properties before, but also the properties after plasma treatment. The ageing process of surface with removed native oxide film was much faster than in case of the sample with oxide film. By means of the immersing the aged treated sample in water it was possible to partly restore the wettability. Also, the plasma treatment of silicon roughed its surface.

Acknowledgements. This research has been supported by the research intent MSM:0021622411 funding by the Ministry of Education of the Czech Republic, by the contract KAN101630651 by Grant Agency of Academy of Science of Czech Republic and by contract APVV-0144-07 of Slovak APVV Grant Agency.

5. References

[1] Siffert P and Krimmel E 2004 *Silicon:evolution and future of a technology*. (Springer – Verlag) Berlin, Heidenberg, New York.
[2] Zenkiewicz M 2007 *Journal of Achievments in Material and Manufacturing Engeneering* **24**.
[3] *http:/gimmel.ip.fmph.uniba.sk/treaters/*
[4] Zhang X G 2003 *Electrochemistry of Silicon Surface and Its Oxide*. (Kluwer Academic Publisher) New York.
[5] Cerofoliny G F, Meda L 1995 *Applied Surface Science* **89** 351 – 360.

SELF-CLEANING EFFECT OF AL_2O_3 COPLANAR BARRIER DISCHARGE ELECTRODE WITH TIO_2 FUNCTIONAL COATING

Zs. Szalay[1], Z. Machala[2], K. Hensel[2], J. Ráhel'[1]

[1]*Department of Experimental Physics,*
[2]*Division of Environmental Physics,*
Faculty of Mathematics, Physics and Informatics, Comenius University, Mlynská dolina, 84248 Bratislava, Slovakia
E-mail: szalay@gimmel.ip.fmph.uniba.sk

The chemical effects of coplanar surface DBD at atmospheric pressure in air and air with diluted toluene (500-2000 ppm) were investigated comparing two electrode ceramics – 96% Al_2O_3 and the same ceramics with the TiO_2 functional coating. In air with diluted toluene, the toluene decomposition was observed with the efficiencies increasing with the energy density, reaching 67% (Al_2O_3) and 95% (TiO_2). The gaseous products of toluene decomposition were mostly CO_2, CO, HCOOH, HNO_3 and water. A substantial difference was observed in the formation of solid organic polymer deposit between both ceramics. The simultaneous presence of discharge plasma microfilaments and TiO_2 coating resulted in the complete absence of deposit formation. This self-cleaning effect has some important application in the field of plasma mediated polymer materials treatment.

1. Introduction

The Diffuse Coplanar Surface Barrier Discharge (DCSBD) generates a thin layer of atmospheric pressure non-thermal plasma on the surface of dielectric electrode [1]. Typically DCSBD employs Al_2O_3 as dielectric barrier owing to its excellent dielectric strength and good thermal conductivity. Titanium dioxide (TiO_2) is well known for its UV-photocatalytic properties for generation of atomic oxygen. Having poor dielectric and mechanical properties, TiO_2 is not suitable as material for dielectric electrode elements. However a thin layer of TiO_2 on Al_2O_3 surface can operate as a catalytic functional coating without negatively affecting the dielectric strength of discharge system. Properties of such enhanced Al_2O_3 ceramics were studied on plasma decomposition of toluene, a common VOC. In this paper effectiveness of toluene removal by DCSBD, products of decomposition and the effects related to the presence of TiO_2 on the surface of discharge ceramic are investigated.

2. Experimental

2.1. DCSBD reactor and gas flow system

The DCSBD electrode element is made up of a square shaped plate (101x101x0.635 mm) of alumina ceramic (96% Al_2O_3) with two screen-printed circular silver electrodes in concentric configuration (inner electrode diameter 20 mm; interelectrode gap 1.5 mm) on one side. Some of the discharge ceramics were coated with sol-gel made TiO_2 (1 – 3 layers) fired at various temperatures to alter the rutil/anatase ratio phases of final TiO_2 layer. Each TiO_2 layer (1 ml of TiO_2 sol per layer) was spin-coated on cleansed ceramics at rotational speed of 1100 rpm. After setting the prepared ceramics samples were fired in oven at 350, 700 and 900 °C for duration of 1 hour each. The electrode was mounted to the PMMA made fixture, equipped with the gas feed system to the discharge plasma zone and with the insulation oil cooling system. To avoid unwanted electrical breakdown between screen-printed silver electrodes, circulating synthetic transformer oil insulated the electrodes. The flow of transformer oil enabled thermal stability of investigated dielectric electrode. The electrode reactor was driven by a LIFETECH VF700 power supply (10 kV, 38.5 kHz).

Atmospheric air was used as carrier gas in our experiments. Air was bubbled through liquid toluene to get enriched by toluene vapours. Using two flow controllers with maximum ranges of 1 and 2.5 l/min respectively we have set the total flow rate of gas mixture (0.5-2 l/min) as well the exact concentration of toluene (500-2000 ppm). Temperature was controlled to ensure constant concentration of toluene saturated vapours in the mixture. The air-toluene mixture obtained in the mixing chamber was led to the discharge chamber. The discharge chamber was optimized to the volume of the generated plasma.

The gaseous products of toluene decomposition were continuously transported through the outlet tube into a glass gas cell of 10 cm length equipped with KRS-5 windows, residing inside FTIR spectrometer (BRUKER Vector 22).

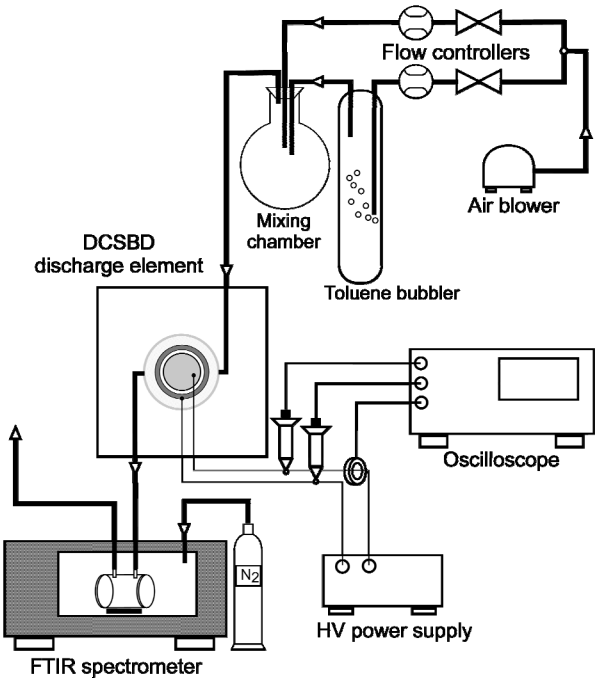


Fig. 1. Schematics of the experimental setup.

2.2. Diagnostics

The V-A characteristic of the discharge was measured with Tektronix P6015A HV probe and Pearson current monitor Model 4100. Signals were processed by Tektronix TDS 2024 (200 MHz, 2.5 GS/s) digital oscilloscope. The discharge power was calculated from the obtained waveforms using Tektronix Wavestar software.

The products of chemical reactions initiated by the DCSBD plasma were analyzed by Fourier Transform infrared (FTIR) spectroscopy using BRUKER Vector 22 spectrometer. Absorption spectra were obtained in continuous flow regime from sets of 10 scans per sample from spectral range of 4000-500 cm^{-1} with 1 cm^{-1} resolution. Nitrogen was let into the sample chamber to minimise ambient CO_2 influence on absorption spectra. The decomposition efficiency of toluene was measured from the decrease of absorbance of the typical toluene absorption band at 3040 cm^{-1}.

Uncoated and TiO_2-coated ceramics were used for evaluation of the self-cleaning effect reported in [2]. The experiments were made for total gas flow of 0.5 l and toluene concentration of 1000 ppm for all types of ceramics. The duration of toluene products deposition to the surface of the electrode elements was set to 2 hours + 2 hours. After 2 hours of operation the inlet and outlet gas feed tubes were swapped. This approach made possible to obtain more homogenously distributed deposit on the ceramic surface. The amount and distribution of the formed deposit on the electrode elements were compared to each other.

3. Results and discussion

The calculated discharge power of the Al_2O_3 ceramic during our experiments was 13±1 W, on the TiO_2 coated ceramics was slightly higher, 14±1 W. The discharge in air produced mostly ozone, N_2O_5 HNO_3 and small amounts of NO_2, N_2O and water. The TiO_2 ceramic boosted the ozone, N_2O_5 and water production.

3.1. Toluene decomposition

The typical spectra of toluene in air before and during discharge are shown on Fig. 2. The gaseous products of plasma initiated toluene decomposition are mainly CO_2 (667 and 2359 cm^{-1}), CO (2172 cm^{-1}), HNO_3 (878, 1325 and 1718 cm^{-1}) and HCOOH (1105 and 1775 cm^{-1}). Besides C-containing products water, ozone (1055 cm^{-1}) and noxious gases like N_2O (2236 cm^{-1}), N_2O_5 (1246 cm^{-1}) and NO_2 (1628 cm^{-1}) are present in the spectra. There was no significant difference in spectra for both Al_2O_3 and TiO_2. The concentration of noxious gases increased linearly with energy density. The TiO_2 ceramic surface produced less NO_2 than Al_2O_3. The N_2O generation rate was independent from ceramic type and toluene concentration. N_2O_5 is a transient product and contributes to HNO_3 production as we examined from the spectra of time evolution of absorbance levels of gaseous products.

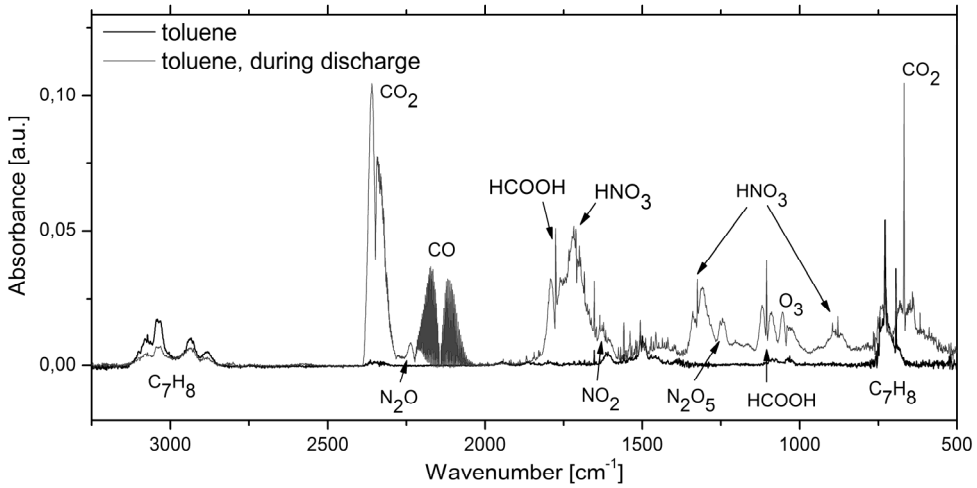


Fig. 2. Typical spectrum of gaseous products of 1000 ppm toluene decomposition. TiO_2 ceramic at 1000 ml/min.

The decomposition efficiency on TiO_2 coated ceramics is higher than on pure Al_2O_3 at the same energy density (Fig. 3.).

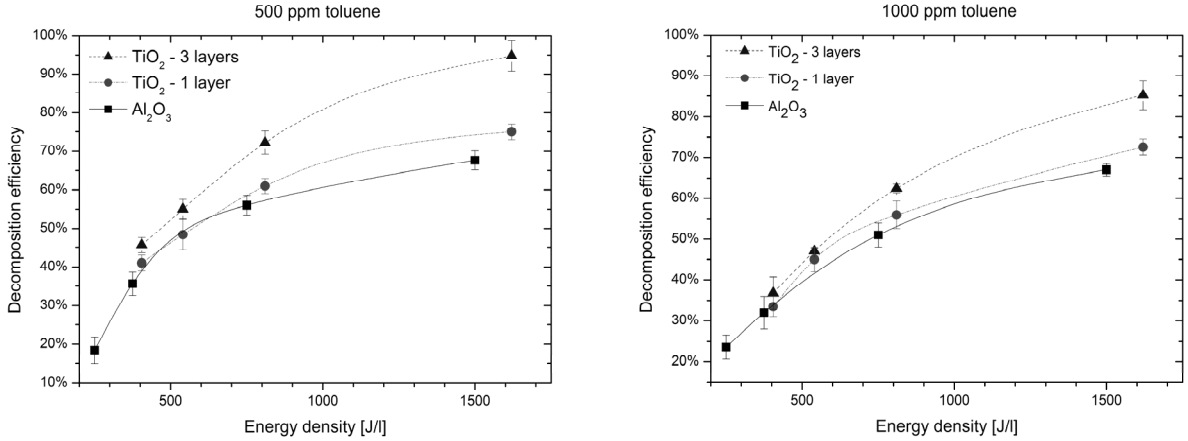


Fig. 3. 500 ppm and 1000 ppm toluene decomposition efficiency as function of energy density, based on 3040 cm^{-1} absorption band.

The toluene removal for 500 ppm (1000 ppm) concentration reaches 75% (72%) for 1 layer and 95% (85%) for 3 layers of TiO_2 coating. One can clearly see that the maximum decomposition efficiency for Al_2O_3 ceramic is peaking around 70%. Further lowering of flow rates would bring marginal increase in performance at unreasonably high energy costs. At lower energy densities both types of ceramics deliver approximately the same performance.

The TiO_2 ceramic surface can cope more effectively with higher toluene concentrations than Al_2O_3 (Fig. 4.). The toluene decomposition efficiency decreases approximately linearly with increasing toluene concentrations in the gas mixture. The production of ozone in air-toluene mixture is peaking

around 600 J/l for Al_2O_3 and 700 J/l for TiO_2 both for 500 and 1000 ppm toluene (Fig. 5.). The only difference between the two measured concentrations was in 2 times higher maximum for 500 ppm. Further increase of energy density results in decrease of O_3 levels, which indicates direct involvement of O radicals in toluene decomposition process.

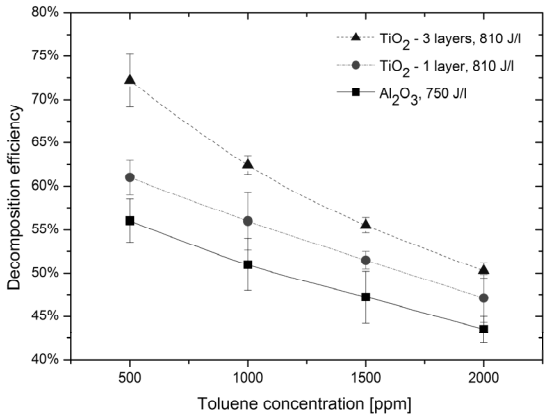


Fig. 4. Toluene removal efficiency as function of toluene concentration.

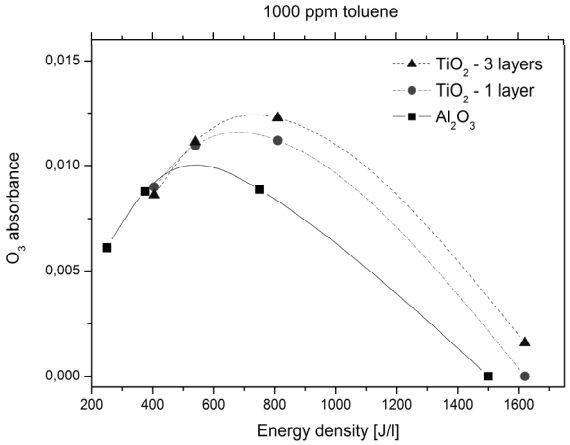


Fig. 5. Ozone absorbance levels in air-toluene mixture during plasma decomposition as function of energy density, based on 1055 cm^{-1} absorbance band.

3.2. Deposit formation

During the experiments formation of a brown-yellowish deposit layer on the discharge ceramics took place. FTIR analysis of deposit identified it as a complex mixture of organic compounds. For Al_2O_3 ceramic surface the characteristic pattern of formed deposit with the traces of filamentary channels is shown on Fig. 6.

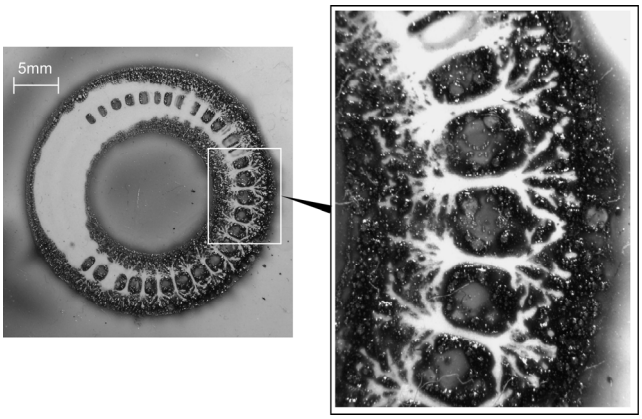
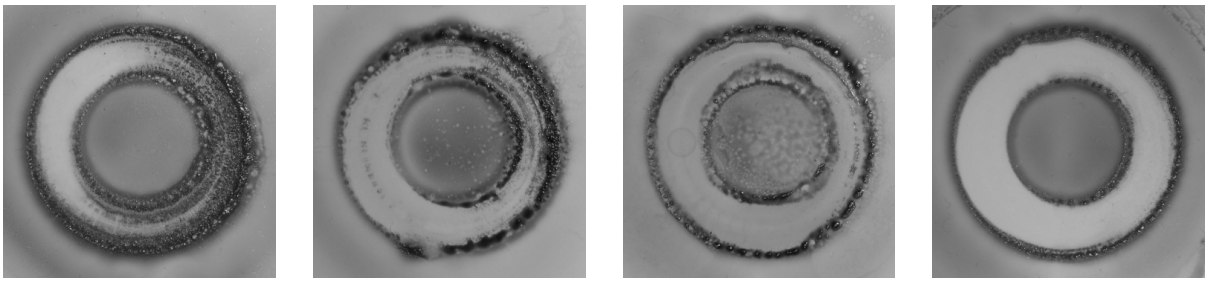


Fig. 6. Toluene deposit pattern on discharge ceramic with high constrast detail on microdischarge traces. Al_2O_3 ceramic, 2000 ppm toluene after 1 hour of continuous operation at 13 W.

We have observed that the rate of deposit formation was substantially reduced for TiO_2 ceramic surfaces in contact with plasma (self-cleaning effect). The microdischarges on Al_2O_3 surface had tendency to get localized on several spots approximately evenly distributed along the electrode gap as is shown on Fig. 6. In contrast, the microdischarges on TiO_2 functional coating had generally lower probability of reappearing on the same spots and thus allowing less deposit to aggregate on the ceramic surface. The greater mobility of microdischarges due to possibly altered surface morphology of TiO_2 coating and more effective chemistry assisted by TiO_2 seems to be accountable for observed self-cleaning effect. The deposit formed on the pure Al_2O_3 ceramic and TiO_2 coated ceramics are shown on Fig. 7. It is clearly visible that with increased number of TiO_2 layers the amount of deposit (aggregates) formed in area of plasma microdischarges significantly decreases. Presence of 3 layers of

TiO_2 results in complete absence of organic deposit in area of plasma. Our study showed that the number of deposited layers has higher influence on discharge performance than the firing temperature of sol-gel layer.



Al_2O_3 | TiO_2 700°C 1 layer | TiO_2 700°C 2 layers | TiO_2 700°C 3 layers

Fig. 7. Deposit formed on Al_2O_3 and TiO_2 ceramics.

4. Conclusion

Properties of pure Al_2O_3 and TiO_2-coated ceramics were tested on a DCSBD plasma reactor for decomposition of toluene in air-toluene mixtures containing 500–2000 ppm toluene. TiO_2 seems to be better choice over Al_2O_3 regarding the decomposition efficiency. The TiO_2-coated ceramics removed up to 95% of toluene and coped generally better with higher toluene concentrations as well. Besides better efficiency we have observed a self-cleaning effect on TiO_2 surface too. We have shown, that presence of 3 layers of TiO_2 on ceramic surface results in complete absence of organic deposit in area of plasma microdischarges. The self-cleaning effect seems to be a result of changed microdischarge behavior due to possibly altered surface morphology of TiO_2 coating together with its photocatalytic effect. These phenomena will be subject of further investigation.

Acknowledgement. This work was supported by Slovak Research and Development Agency APVV-0485-06.

5. References

[1] M. Šimor, J. Ráhel' et al.: *„Atmospheric-pressure diffuse coplanar surface discharge for surface treatments"*, Appl. Phys. Lett. 81 (15), 2002, pp. 2716-2718

[2] Z. Machala, K. Hensel, J. Síč, J. Ráheľ: „*Chemical activity of coplanar DBD with Al_2O_3 and TiO_2 electrodes tested on VOC decomposition*", 29th International Conference on Phenomena in Ionized Gases (ICPIG), Mexico, 2009

FLUORINE REMOVAL TREATMENT OF POLYTETRAFLUOROETHYLENE SURFACE BY ATMOSPHERIC PRESSURE GLOW PLASMA WITH BORON COMPOUNDS

Kunihito Tanaka, Kazuo Takahashi and Masuhiro Kogoma
Department of Materials and Life Sciences, Faculty of Science and Technology, Sophia University
7-1 Kioi-cho, Chiyoda-ku, Tokyo, Japan
E-mail: tanaka@mls.sophia.ac.jp

Polytetrafluoroethylene (PTFE) sheets were treated by the diborane/H_2/He plasma for the deflurination to improve the painting performance and the adhesive strength with an epoxy glue. Diborane was generated by the H_2/He plasma treatment of a boron plate. And then, the defluorination plasma treatment with this diborane/H_2/He mixture gas performed to PTFE sheet. Fluorine atom content of treated PTFE surface was decreased to about one hundredth of that of untreated PTFE. The water contact angle of treated PTFE was also decreased from 120º to 50º. A paint coated on treated PTFE adhered to its surface strongly.

1. Introduction

Fluorinated polymers such as polytetrafluoroethylene (PTFE) have many unique characteristics: for example, high chemical resistance, high dielectric constant, high heat resistance and low coefficient of friction. Thus, they have been used as typical inert materials for many situations, such as packaging materials. They have a big problem, however: the difficulty of the paint and adhesion. Some agents that contain metallic sodium are often used for surface treatment of these polymers to improve the paint and adhesion. However, this treatment needs a large amount of cleaning water and the disposal of much waste fluid. Moreover, their surfaces become blackish through the wet treatment. So a new dry process instead of the wet treatments has been desired.

In our previous studies, the APG plasma treatment was found to be able to improve the adhesion strength between some kinds of fluorinated polymer films and epoxy glue [1-3]. Generally, the low surface energies of the fluorinated polymers lead to the low adhesive strength between such polymers and glue, and the fluorine atoms on the fluorinated polymer surface lead to the low surface energy of the polymers [4]. We considered that the fluorine atoms generated through the dissociation of C-F bonds by the plasma needed to be changed into a gaseous compound by reacting with some reactants, and that the gaseous compound had to be removed from the polymer surface as fully as possible. Boron trifluoride (BF_3) is one of the gaseous fluorine compounds at room temperature and the bond enthalpy of fluorine with boron (757 kJ mol^{-1}) is bigger than that of fluorine with hydrogen or carbon (570 or 552 kJ mol^{-1}) [5]. Thus, trimethoxyborane ($(CH_3O)_3B$, TMB) was selected as a source of boron atoms and the effect of this reactant on the adhesive strength was examined in the previous study [3]. TMB/H_2/He plasma treatment improved the adhesion property greatly. However, the adhesive strength of PTFE was still weaker than that of the wet method, and a small amount of boron oxide was deposited on the sample surface since TMP contains oxygen atom. Thus, this result indicated that diborane (B_2H_6) is best boron source, but we cannot use diborane as a boron source lightly since it is very ignitible and toxic gas. Ohmi et. al. reported that diborane was generated by the H_2/He plasma treatment of boron plate in their recent research paper [6]. Therefore, we tried to examine the defluorination of PTFE by the combination of the diborane generation plasma and the B_2H_6/H_2/He plasma surface treatment in this study.

2. Experimental

Fig. 1 shows the discharge apparatus which had two discharge areas. The discharge areas were bounded for quartz glass plates, and so H_2/He mixture gas flowed in one direction. The upstream and downstream discharge areas were used for diborane generation and PTFE surface treatment, respectively. The boron plate (thickness, about 0.1 mm) was prepared from boron and binder (polyethylene powder) mixture powder by pressing. PTFE sheet, whose sizes were 20 × 20 × 0.2 mm, was washed by ultrasonic cleaner with trichloroethylene and deionized water before treatment.

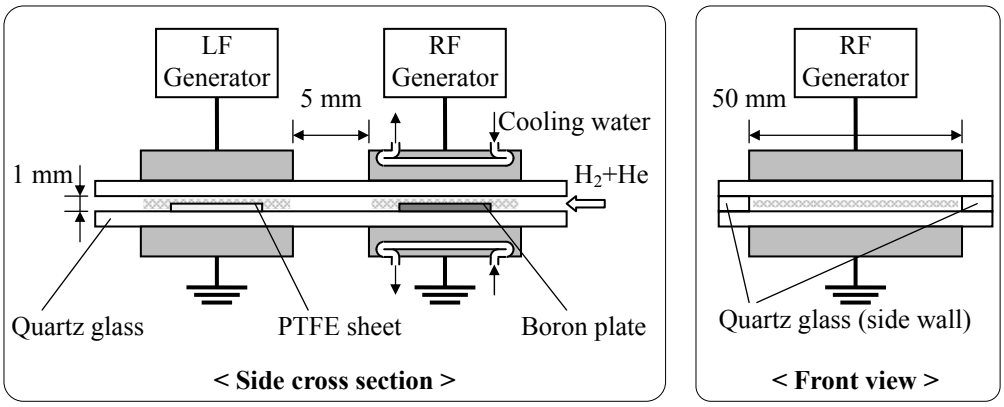


Fig. 1 Schematic diagram of the discharge apparatus.

The discharge apparatus was placed in the atmosphere, and the discharge area was purged with H_2/He mixture gas. The upstream plasma for diborane generation and downstream plasma for PTFE treatment were generated with a 27.12 MHz and 300 kHz power supply, respectively. Table 1 shows the plasma treatment conditions. Treated PTFE sheets were examined using XPS, water contact angle (WCA) measurement, paint abrasion test and peel test.

Tab. 1. The plasma treatment conditions.

Discharge power of diborane generation	500 W
Discharge power of PTFE treatment	50 W
Treatment time	0.5 ~ 5 min
He flow rate	2 slm
H_2 flow rate	10 sccm
Pressure	atmospheric pressure

The chemical state was measured with the XPS (ULVAC-Phi, ESCA-5800ci). The x-ray source provides monochromatized Al Kα radiation at a power of 350 W. The takeoff angle used in these experiments is 45°. The binding energies of XPS spectra were corrected with the C_{1s} peak position (C-C, 284.6 eV) and the F_{1s} peak position (PTFE, 689.0 eV) [7, 8]. The water contact angle measurement was carried out as follows: a treated sample was laid on a level plane and 1μl of diluted water was dropped on its surface. Then the angle was measured with a goniometer. The value of the contact angle was the average of angles measured at 5 points on the sample. The paint abrasion test was carried out as follows: a black dye ink was coated on a sample surface. Then, it was abraded by a tissue (Kimberly-Clark Co., Kimwipe) abraider under 1 kg loading on 100 ~ 300 times. The samples for the peel test were prepared in the following way. First, a treated sample film was glued on an aluminum plate with epoxy glue (Ciba-Geigy Co., Ltd., Araldite standard grade). Then the film was pressed and kept at 50ºC for 12 hours. When the peel strength was measured, the peel speed was fixed at 200 mm min^{-1}. In this study, a film treated with a sodium solution (NILACO Co., Ltd., Tetra Etch) was used as a control sample: each film was soaked in the sodium solution for 10 seconds, and then it was rinsed with ethanol and diluted water.

3. Results and discussions

Fig. 2 shows the variation of the WCA of treated PTFE. The WCAs of H_2/He plasma (without diborane) treated PTFE (sample A) were decreased to about 70º only by 30 seconds treatment. According to the WCA of a general polyethylene film (about 80 º), chemical state of the H_2/He plasma treated PTFE surface came close to that of polyethylene because of the defluorination of PTFE and the additional reaction of hydrogen atoms. The WCAs of diborane/H_2/He plasma treated PTFE (sample B) for 0.5 and 1 minutes showed same values of sample A, but those for more than 1 minute showed lower WCAs. Meanwhile we tried that PTFE treatment was started in two minutes after diborane generation was started (sample C). The WCAs of sample C, shown with filled triangle in Fig. 2,

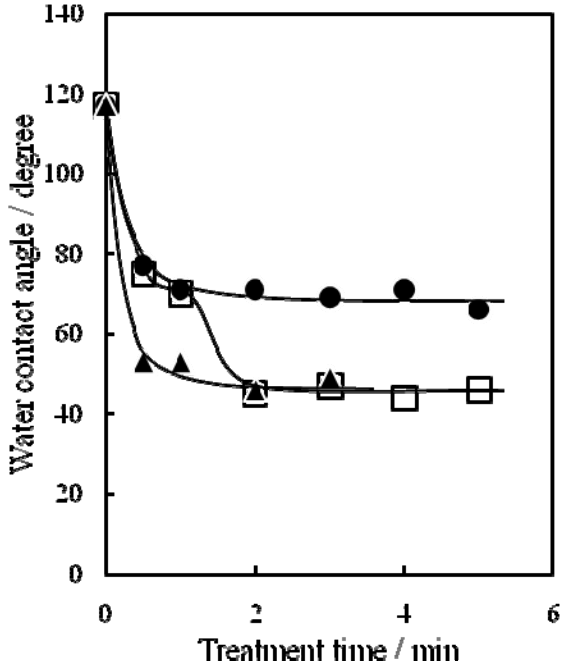


Fig. 2 The variation of the water contact angle as a function of the treatment time. ●, H_2/He plasma treatment; □, diborane/H_2/He plasma treatment; ▲, PTFE treatment was started in two minutes after diborane generation was started.

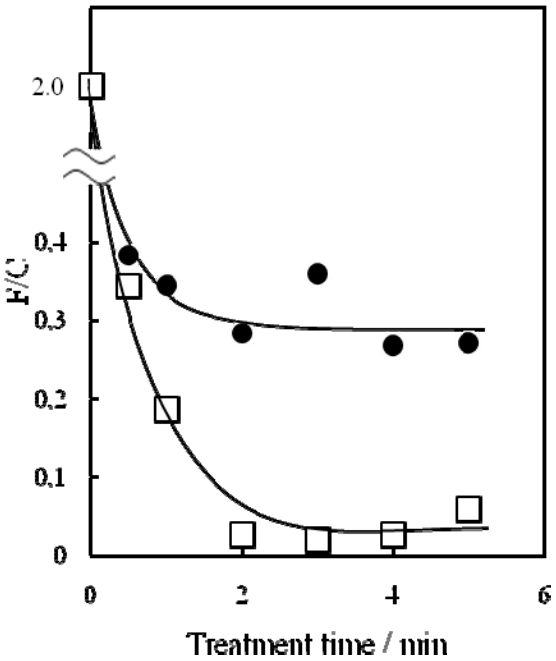


Fig. 3 The variation of atomic content ratio F/C as a function of the treatment time. ●, H_2/He plasma treatment; □, diborane/H_2/He plasma treatment.

indicated same values of the sample B for more than 1 minute. Therefore, this result indicated that diborane generation had not been started until 2 minute. This reason was supposed that the boron plate needed about 2 minutes heating to obtain enough temperature to vaporize diborane [6].

Next, to investigate the chemical states of sample A and B, the sample surfaces were measured by XPS. Fig. 3 and 4 show the variation of atomic content ratio F/C and O/C, respectively. And the C_{1s} and B_{1s}, XPS spectra were shown in Fig. 5 and 6, respectively. The F/C of sample A was severely decreased by the plasma treatment without diborane. However, a peak assigned the CF_2 group was remained in the C_{1s} spectrum of the sample A surface as shown in Fig. 5 b). This result indicated that the defluorination was not completed. And the sample A surface was slightly oxidized as shown in Fig. 4. We supposed that the oxidation was occurred by the plasma treatment with residual air in the discharge area and/or post-oxidation. The F/C of sample B was significantly decreased as shown in Fig. 3. Though quite small amount of fluorine atoms remained on the sample B surface, there was no peak related to the CF_x group in the C_{1s} spectrum of the sample B surface as shown in Fig. 5 C). And the B_{1s} spectrum of the sample B surface as shown in Fig. 6 indicated that some fluorinated and oxidized boron compounds deposited on the sample B surface. Therefore, we considered that slightly-remained fluorine atoms derived from boron compounds on the sample B surface, and that the defluorination of PTFE surface was done completely.

Finally, we examined the adhesive strength between a dye paint and PTFEs via the paint abrasion test. Fig. 7 shows the photographs of PTFE sheets used for the paint abrasion test. While the black dye on the untreated PTFE was removed easily, those on the sample A and B were hardly removed. Moreover the amount of the removed dye of sample B was smaller than that of the sample A. We assumed that the boron compounds deposited on the sample B did not effect on the adhesive strength between the dye and treated PTFE since the amount of the boron compounds was quite small (B/C ≈ 0.03).

4. Conclusion

The defluorination of PTFE was completely succeeded by the combination of the diborane generation plasma and the PTFE treatment. Since the diborane/H_2/He plasma treated PTFE (sample B) surface became the polyethylene like surface, we considered that more low WCA value and much higher adhesive strength will be obtained only by the O_2/He plasma treatment on the sample B.

5. References

1. H. Nakamura, M. Kogoma, H. Jinno and S. Okazaki, Proc. 11th Inter. Symp. Plasma Chem., 1192 (1993).
2. K. Tanaka, T. Inomata and M. Kogoma, Thin Solid Films, 386, 217 (2001).
3. K. Tanaka and M. Kogoma, Inter. J. Adhesion Adhesives, 23, 6, 515-519 (2003).
4. G. Gierenz and W. Karmann, ed., Adhesives and Adhesive Tapes, WILEY-VCH, Weinheim, 97 (2001).

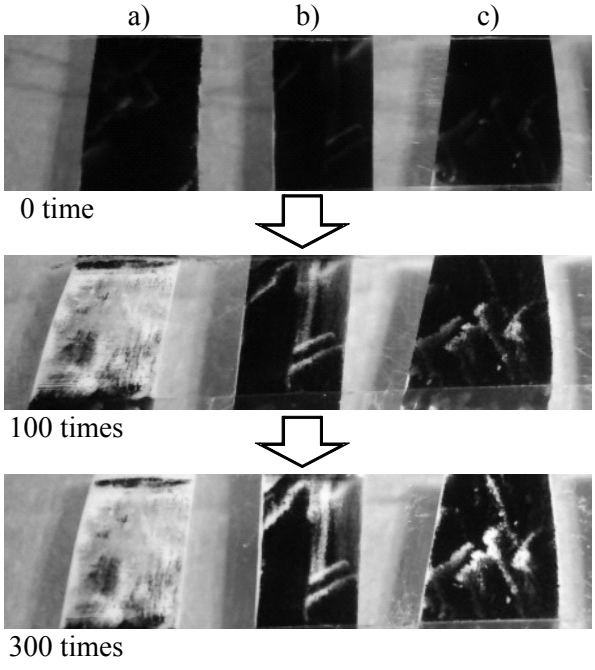


Fig. 7 The photographs of. a) untreated, b) H_2/He plasma treated and c) diborane/H_2/He plasma treated PTFE sheets used for the paint abrasion

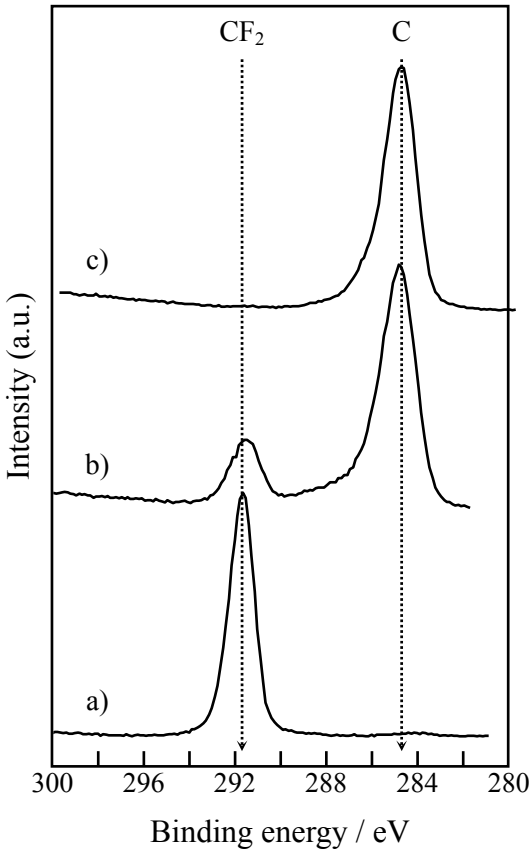


Fig. 5 The C_{1s}, XPS spectra of a) untreated, b) H_2/He plasma treated and c) diborane/H_2/He plasma treated PTFE. The treatment times of b) and c) were 5 minutes.

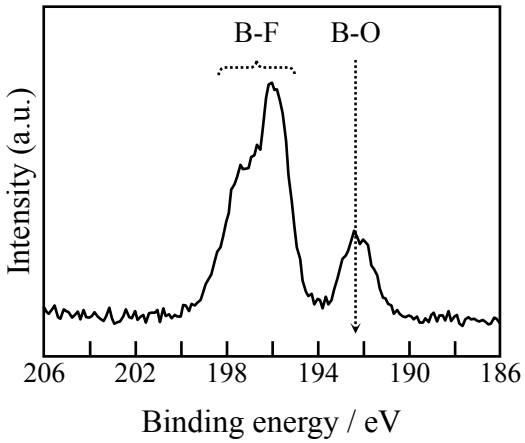


Fig. 6 The B_{1s}, XPS spectra of diborane/H_2/He plasma treated PTFE which was the same sample as Fig. 5 c).

5. D. R. Lide (ed.), Handbook of Chemistry and Physics, 81st edition, CRC Press, USA (2000).
6. H. Ohmi, H. Kakiuchi, Y. Hamaoka and K. Yasutake, J. Appl. Phys. 102, 023302 (2007)
7. U. Gelius, P. F. Heden, J. Hedman. B. J. Lindberg, R. Manne, R. Nordberg, C. Nordling and K. Siegbahn, Phys. Scr., 2, 70 (1970).
8. D. T Llark, W. J. Feast, D. Kilcast, and W. K. R. Musgrave, J. Polym. Sci., 11, 389 (1973).

DEPOSITION OF THIN FILMS IN ATMOSPHERIC PRESSURE HOMOGENEOUS DISCHARGE

David Trunec[1], Pavel Sťahel[1], Vilma Buršíková[1], Lenka Zajíčková[1], Filip Studnička[1] and Vratislav Peřina[2]

[1]*Dep. of Physical Electronics, Masaryk University, Brno, Czech Republic*
[2]*Institute of Nuclear Physics, Academy of Sciences, Řež, Czech Republic*
E-mail: trunec@physics.muni.cz

The atmospheric pressure dielectric barrier discharge burning in nitrogen in homogeneous mode was used for the deposition of thin films. The films were deposited on glass and silicon substrates from hexamethyldisiloxane (HMDSO) vapours and propane-butane. The substrate temperatures during the deposition process were elevated up to values within the range 25 – 200 °C in order to obtain hard thin films. The deposited films were characterised by Rutherford backscattering and elastic recoil detection methods, infrared spectroscopy measurements and depth sensing indentation technique. It was found that the films properties depend significantly on substrate temperature at deposition. An increase of substrate temperature during deposition leads primarily to an increase of film hardness.

1. Introduction

The homogeneous DBD burning in nitrogen at atmospheric pressure (called atmospheric pressure Townsend-like discharge - APTD) is suitable discharge type for thin film deposition [1]. In our previous study [2] we were able to deposit thin films from HMDSO in nitrogen APTD. However, the deposited films were polymer-like, their maximum hardness was 0.6 GPa and contained about 40% of carbon. Because such films cannot be used as hard protective layers, procedures for obtaining harder films were needed. In this contribution we report a possibility to increase the film hardness by the increase of substrate temperature during the deposition process. We deposited two types of thin films: the SiO_x films were deposited from HMDSO vapours, the a-CN_xH_y films were deposited from propane-butane.

2. Experimental

The experiments were carried out in a metallic discharge reactor with the dimensions 500 mm × 500 mm × 500 mm. The discharge burned between two planar metal electrodes, the upper covered with Simax glass, 1.5 mm in thickness. The bottom electrode was rectangular with dimensions 150 mm × 60 mm, the upper electrode was circular with a diameter of 36 mm. The bottom electrode could be heated using a heating spiral and the electrode temperature was measured with a thermocouple. The films were deposited on thin glass substrates with dimensions 160 mm × 65 mm × 1 mm and 500 μm silicon wafers, 76 or 102 mm in diameter. The glass substrates were placed directly on the bottom electrode. In the case of silicon (Si) substrate, a 1 mm thick glass plate was placed between the bottom electrode and Si. The discharge gap between the substrate and the upper electrode was set to 0.5 mm.

The SiO_x films were deposited in homogeneous mode of DBD (APTD) from HMDSO vapours mixed with synthetic air and pure nitrogen. The 6 or 16 sccm of synthetic air bubbled through liquid HMDSO in a glass bottle container. It was then mixed with the main nitrogen flow of 6 slm. The HMDSO flow rate was determined by weighting the liquid before and after the deposition. The concentration of HMDSO in nitrogen was 70 ppm and 173 ppm whereas the concentration of oxygen was 200 ppm and 532 ppm for the air flow rates of 6 sccm and 16 sccm, respectively. The CN_xH_y films were deposited from propane-butane mixture. The 13 sccm of propane-butane was mixed with the main nitrogen flow of 6 slm. Configuration of gas supply was optimized in preliminary deposition experiments. The final set-up, used for the depositions discussed in this paper, was as follows. The working gas mixture was supplied through an inlet in the upper corner of the discharge reactor. The reactor was pumped out from the opposite bottom corner. The deposition uniformity was further improved by gas exhaustion of 50 sccm through an opening in the centre of the upper electrode.

Before starting the experiments the discharge chamber was pumped down to a pressure of 20 Pa and then filled with nitrogen to a pressure of 101 kPa. Atmospheric pressure during the deposition was maintained by slight pumping. High voltage with a frequency of 6 kHz was used for discharge generation. The type of discharge, as concerns filamentary or homogeneous mode, was determined from the current-voltage measurements recorded by the digital oscilloscope HP 54820A Infinium (500 MHz, 2 GS/s). The input power to the 6 kHz high voltage generator was 26 W for the homogeneous mode deposition on glass substrates. Maintenance of the homogeneous discharge mode restricted the input power as well as applied voltage in a small range, especially for Si.
In this case, the input power ensuring the homogeneous mode was only 15 W and the flow of air bubbled through liquid HMDSO was only 6 sccm. The power consumed in the discharge was several watts depending on input power and used substrate [3].
The chemical structure of the films was studied by Fourier Transform Infrared Spectroscopy (FTIR) using a Bruker Vertex 80v spectrometer. The films deposited on Si were measured in transmittance mode taking bare Si substrate as a reference. The films on glass substrates were measured in attenuation total reflection (ATR) mode using diamond crystal (one ATR reflection, angle of incidence 45°). The sample compartment was evacuated down to 2.51 hPa in both measurement modes. The resolution of the spectrometer was set to 4 cm^{-1}.
The complete atomic composition was determined by ion beam methods combining Rutherford backscattering (RBS) and elastic recoil detection analysis (ERDA). The atomic fractions of C, O and Si were measured by RBS using 2.4 MeV protons perpendicularly bombarding the surface. The sensitivity to carbon content was enhanced using proton resonance effect at the energy of 1.74 MeV. ERDA and RBS with an incident beam of 2.75 MeV α-particles at 75° to the surface normal were simultaneously used to determine the percentage of H.
The hardness and elastic modulus values were assessed from depth sensing indentation tests using a Fischerscope H100 tester with Vickers indenter. The load and the corresponding indentation depth were recorded as a function of time for both loading and unloading processes. The desired material parameters were obtained from analysis of loading and unloading curves. The indentation tests were carried out for several different indentation depths (i.e. several different applied loads) in order to map the mechanical properties of the film/substrate system from near surface up to the film--substrate interface. The applied load ranged from 1 to 100 mN with the force resolution of 0.04 mN. The accuracy of the indentation depth measurement was ±1 nm. Each indentation test was repeated at least 16 times.

3. Results

SiO_x films

The elemental composition of thin films deposited on Si substrates (air flow rate of 6 sccm through liquid HMDSO) was studied by RBS/ERDA measurements. The results of RBS/ERDA analyses showed that the carbon content in films decreased with temperature from 23 to 2.5% (see Fig. 1), the oxygen-to-silicon ratio increased with increasing temperature. This ratio reached 2.3 for 150 °C but not all the oxygen atoms were bonded in the Si-O-Si network as revealed by the presence of OH groups in the FTIR spectra. The film density increased from 1.0 to 2.0 g cm^{-3}.
The film elastic modulus and plastic hardness increased with increasing deposition temperature approaching the mechanical properties of SiO_2 in the temperature range 120 – 150 °C. The film microhardness in dependence on temperature is depicted in Fig. 2.
The deposition rate decreased with increasing temperature from 5 nm min^{-1} at 25 °C to 2.8 nm min^{-1} at 150 °C. However, the chemical structure, optical and mechanical properties of the films deposited at 150 °C approached those of SiO_2 films deposited in low pressure discharges. More information on the film properties can be found in [4].

films deposited from propane-butane

Information about chemical structure of the films deposited from propane-butane/N_2 mixture was obtained by ATR-FTIR spectroscopy. Since diamond was used as ATR crystal the detected intensity was very low in the range 1800—2700 cm^{-1} and, therefore, the typical peak of C≡N bond at about 2200 cm^{-1} could not be observed. Two regions, 500--800 and 2650--4000 cm^{-1}, with the peaks related to absorption in the film and glass substrate are shown in Figs. 3 and 4.

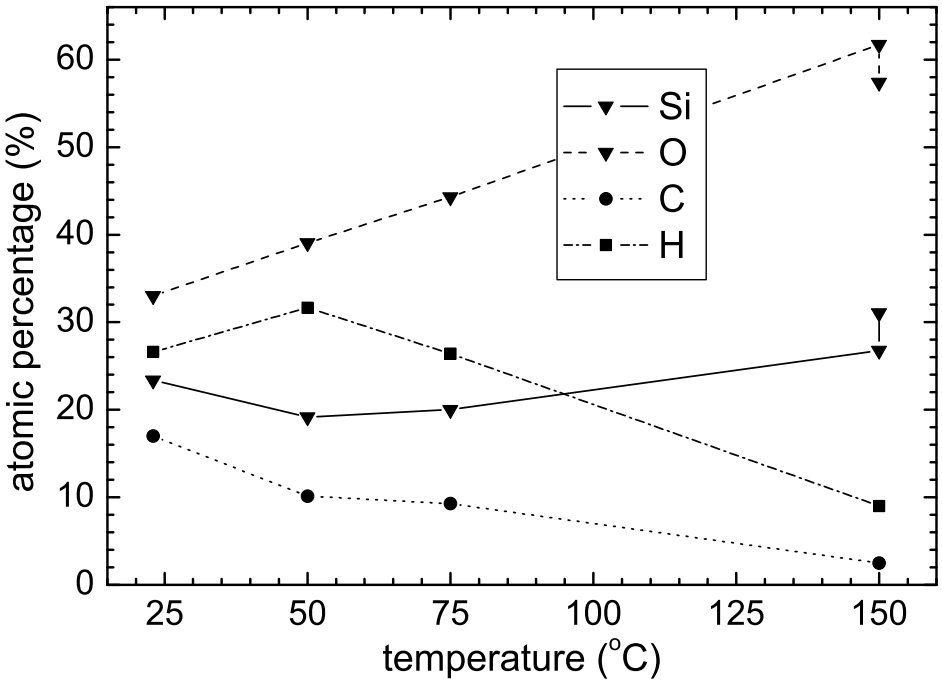


Fig. 1. Elemental composition of thin films deposited on Si substrates (air flow rate of 6 sccm through liquid HMDSO) obtained from RBS/ERDA measurements.

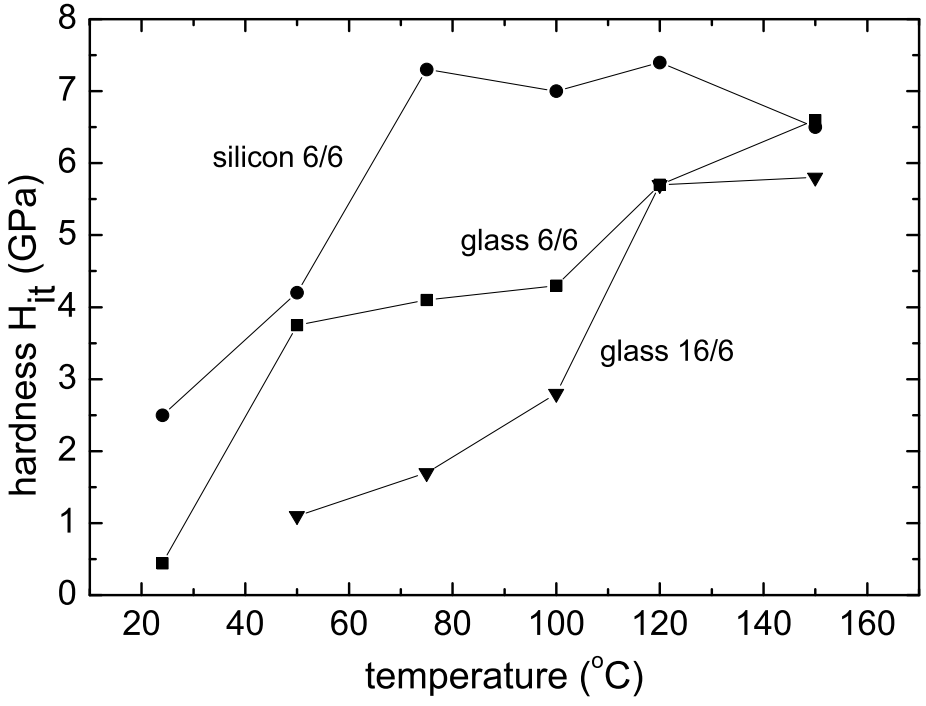


Fig. 2. The film microhardness for different deposition conditions. The numbers at curves indicate air flow in sccm / nitrogen flow in slm during the deposition.

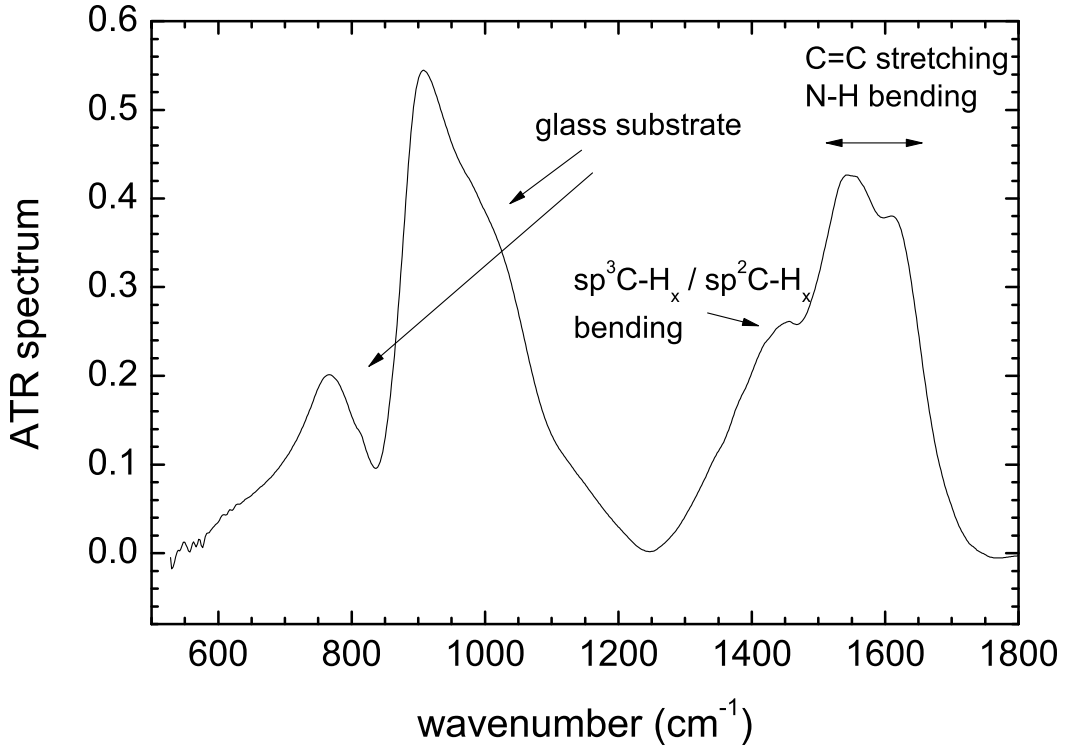


Fig. 3 ATR spectrum of films deposited from propane-butane at substrate temperature of 200 °C.

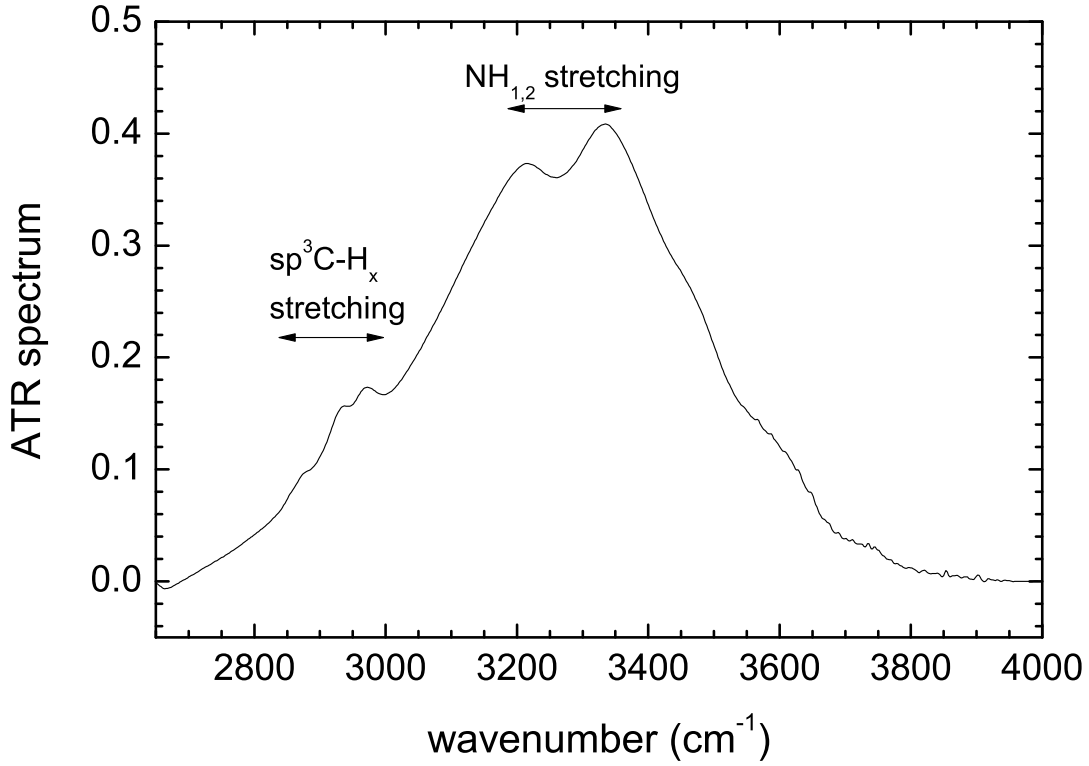


Fig. 4 ATR spectrum of films deposited from propane-butane at substrate temperature of 200 °C.

High frequency region (Fig. 4) shows weak absorption peaks attributed to C-H stretching of hydrocarbon groups that can be generally found overlapping each other in the region 2850--3100 cm^{-1}. Three maxima at 2875, 2932 and 2964 cm^{-1} can be distinguished but peak fitting confirmed five expected peaks corresponding to sp^3 $C\text{-}H_{1,2,3}$ stretching. Two broad peaks at 3213 and 3331 cm^{-1} were attributed to stretching of primary amines $R\text{-}NH_2$. They could also overlap a stretching peak of secondary amine =NH or sp^2 C-H peaks.
Low frequency region (Fig. 3) reveals typical peaks of Si-O-Si stretching and bending absorption peaks in the range below 1100 cm^{-1} (from glass substrate). Peaks between 1250 and 1480 cm^{-1} were assigned to sp^3 $C\text{-}H_x$ or sp^2 $C\text{-}H_x$ deformation modes. Two maxima at 1550 and 1610 cm^{-1} can be an overlap of C=C stretching with N-H bend of primary and secondary amines.
Mechanical properties of the films deposited from propane-butane are similar as for soft a-C:H films according to Robertson's classification of amorphous carbon films [5]. The hardness of the films deposited at 200 °C ranged from 0.5 to 0.8 GPa in case of deposition on glass substrate and from 1.3 to 1.5 GPa for films on silicon substrates. These values are at least one order of magnitude higher than hardness of common polymers, for example polyethylene, which hardness is around 0.01GPa [5]. However, the films exhibited similar indentation response as polymer like carbon materials, they exhibited significant indentation creep and anelastic deformation. The elastic modulus of these films was in the range from 12 to 27 GPa. The films were resistant against delamination and cracking.

Acknowledgement. The present work was supported by the Ministry of Education of the Czech Republic under contract MSM0021622411 and by Institutional Research Plan No. AV0Z10100521.

4. References

[1] Gherardi N, Martin S and Massines F 2000 *J. Phys. D: Appl Phys.* **33** L104.
[2] Trunec D, Navrátil Z, Sťahel P, Zajíčková L, Buršíková V and Čech J 2004 *J. Phys. D: Appl. Phys.* **37** 2112.
[3] Šíra M 2009 *PhD thesis* (Brno: Masaryk University) http://is.muni.cz/th/13705/prif_d/dis-is.muni.cz.pdf p. 78
[4] Trunec D, Zajíčková L, Buršíková V, Studnička F, Sťahel P, Prysiazhnyi V, Peřina V, Houdková J, Navrátil Z and Franta D 2010 *J. Phys. D: Appl. Phys.* **43** 225403.
[5] Robertson J 2002 *Mat. Sci. Eng. R* **37** 129.

APPLICATION OF LOW-TEMPERATURE PLASMA GENERATED AT ATMOSPHERIC PRESSURE FOR MODIFICATION OF GLASS SURFACES

Anna Zahoranová[1], Richard Krumpolec[1], Andrej Buček[1], Dušan Kováčik[1], Mirko Černák[1, 2]

[1] *Department of Experimental Physics, Faculty of Mathematics, Physics and Informatics, Comenius University, Mlynská dolina, 842 48 Bratislava, Slovak Republic*
[2] *Department of Physical Electronics, Faculty of Science, Masaryk University, Kotlářská 2, 611 37 Brno, Czech Republic*
E-mail: zahoranova@fmph.uniba.sk

Glass is widely used material, but for many applications it's surface characteristics are necessary to be modified. One possibility is a preparation of hydrophobic coating on the glass surface. In our work the non-thermal plasma generated at atmospheric pressure was used to investigate the preparation of hydrophobic silane layers on the glass surface. We compared the properties of films prepared on glass non-activated/activated using low temperature plasma generated at atmospheric pressure in the air. As a model silane we used 3-aminopropyltriethoxysilane (APTES). Properties of the silane layer created have been analyzed by the means of the contact angle measurements. Persistence of the silane layers has been tested by the means of the boiling test.

1. Introduction

Surface modification by a silanization reaction is a technique often used in different areas: nanotechnology, microelectronics, biotechnology etc. It is a successful method for the initial treatment of substrates in the production of biomaterials and biosensors, where there are high requirements for biocompatibility and adhesion. Silanes are deposited on the substrate surface which is typically inorganic and to be linked with an organic polymer, where they act as an adhesion promoter.

Among the most studied and promising materials in this area, being already used as substrates, are glass and silicon [1]. Large number of publications devoted to the study of silane layers deposition onto glass and silicon substrates has been published recently [2, 3, 4, 5, 6, 7]

Glass is by chemical composition essentially a silicon oxide (SiO_2), so the knowledge gained by studying the glass surface can also accordingly be used for silicon, surface of which rapidly oxidizes in ambient air and becomes covered with a layer of native oxide with possibly adsorbed impurities. These impurities may be mechanical (dust) and of organic or inorganic origin (grease, oil depletion, chemical residues from the production). The presence of adsorbed substances on the glass surface can lead to deterioration of the glass surface properties and prevents the creation of chemical bonds between the glass surface and functional layer being prepared on it.

Silanes are chemical substances based on silicon, having a general summary formula $R_nSiX_{(4-n),}$ where R and X are functional groups that have different properties. R is an organic functional group attached to the silicate in hydrolytically stable state and X are hydrolysable groups that are converted by hydrolysis to silanol groups (Si-OH). Silanol groups will then react with the hydroxyl groups (OH) on the surface of inorganic substrate, in our case the surface of glass.

Surfacing materials are at present still mostly carried out by the chemical methods, so-called "wet chemical method". The wet chemical methods are based on using various chemical substances, which, however, are often toxic and dangerous not only for humans but also the environment and there is a problem with their subsequent disposal. With the development of plasma technology in recent decades, the use of low-temperature plasma for the surface treatment materials becomes favoured increasingly. Low temperature plasma can change the surface energy of treated material, respectively the type and density of functional groups on it's surface and so can change the surface reactivity towards a wide range of materials. Depending on the working gas, in plasma are generated active particles appropriate for plasma treatment, as electrons, ions and various excited and metastable particles. Excited particles have sufficient energy to break the chemical bonds on the surface of the substrate. Because the resulting breaked chemical bonds are unstable in terms of thermodynamics, functional groups are

trying to minimize their energy state and therefore willingly enter chemical reactions. Another advantage of using low temperature plasma for surface treatment is the fact that heavy particles present in the low-temperature plasma have low temperature, resulting in surface changes of only a few molecular layers without damaging the bulk of material.
Non-equilibrium plasma processes using plasma generated at low pressures are well studied and realised above all in microelectronics. For these processes a vacuum equipment is necessary, causing many problems and limiting their wider application, especially in continuous processing. Recently, a suitable alternative became available, using dielectric barrier discharges (DBD) able to generate non-equilibrium plasma at pressures close to or equal to atmospheric pressure. Barrier discharges achieve high efficiency of formation of radicals and metastables suitable for activation of material's surface [4, 8; 9]. Plasma technology using the DBD provides an effective tool for surface treatment of materials, especially for in-line treatment of flat materials (e.g. non-woven textiles, glass, wood), not only in research but also in industrial applications [10, 11, 12, 13]. In our experiments a novel atmospheric-pressure plasma source, the so-called Diffuse Coplanar Surface Dielectric Barrier Discharge (DCSBD) was used. The DCSBD generates a thin uniform layer of macroscopically homogeneous plasma with high plasma power density (up to ~100 W/cm^3) at atmospheric pressure and without any inert gas admixture [14]. This type of discharge is therefore appropriate to modify the surface of smooth and planar materials such as non-woven textile, glass, silicon and wood. The input energy is directly used for plasma processing, which allows short treatment times and the incorporation of the DCSBD directly in continuously working production lines.

2. Experiment

The objective of the experimental part of our work was to compare silane layers prepared on chemically cleaned glass surfaces and glass surfaces activated by plasma. In our work we used (3-Aminopropyl) triethoxysilane (APTES, molecular formula $C_9H_{23}NO_3Si$ supplied from Merck Company, Germany) for preparing the silane layers. This type of silane has many applications as a component improving layer compatibility, adhesion promoter in the manufacture of glass fibres and in many other finishing processes. In small quantities it is also used in sealants, gaskets and paint coatings.
On the surface of glass under normal conditions there are four different hydroxyl -OH groups [3]. They are responsible for the hydrophilic properties of glass and condensation reactions by which it can bind other chemical compounds to the surface of glass. To create quality silane layer on the glass surface high concentration of surface OH groups is very important [3]. Completely clean glass surface is hydrophilic, contact angle of water drops on a clean glass reaches a value <2º. When the hydrophilic SiO_2 surface is exposed to moisture (e.g. water vapour contained in ambient atmosphere), there is adsorbed water layer, which is bonded to the surface through hydrogen bridges. Contact angle of water on the clean glass exposed to open atmosphere is about 30º. Plasma is able to activate the glass surface and therefore we expect that by the use of plasma we could prepare silane layers with better parameters (more homogeneous and more resistant) than on the glass, which was not activated using the plasma. Under the activation of a surface we understand the removal of contaminants from the surface and the establishment of functional groups that can react chemically. To clean and activate the surface of the glass we used DCSBD plasma source that has been tested as an effective tool to increase hydrophilicity and to activate the surface by removing of organic contamination and possible increase in the concentration of the surface OH groups. No significant changes in surface roughness of glass have been observed at treatment times up to 20 s, which was verified by measuring the surface morphology by AFM [15].
As the glass substrates were used microscope slides with dimensions 26 × 76 × 1 mm^3. To establish well defined initial conditions, before the experiment all the glass samples were chemically pre-cleaned by the following procedure: 3 min sonicating in acetone, 3 min sonicating in isopropanol (IPA) and 3 min sonicating in distilled water. After each sonication the surface was dried by the means of a stream of pure nitrogen.
The plasma cleaning was carried out using the Diffuse Coplanar Surface Barrier Discharge (DCSBD) [14] generated in atmospheric-pressure ambient air, at the discharge power of 400 W and the treatment

time 5 s, using continuous mode of treatment, when the sample was moved over the DCSBD electrode surface (Fig.1, left) at the distance of 0.3 mm.

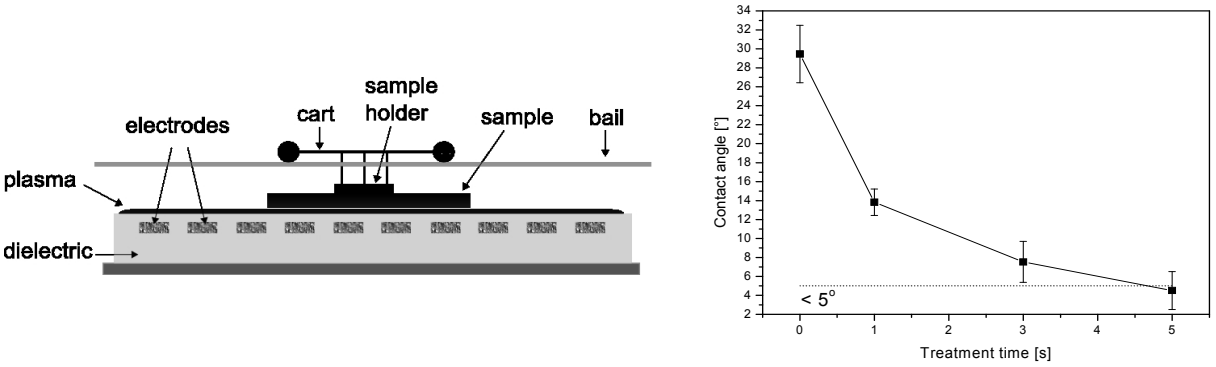


Fig. 1: Schematic diagram of the plasma treatment set-up (left), contact angle measurements on glass samples treated by the plasma generated at the discharge power of 400 W in ambient air (right).

The surface of the glass samples was investigated by contact angle mesurements using the Surface Energy Evaluation System (Advex Instruments s.r.o., Czech Republic)[16]. Analysis of the contact angles is very quick and simple macroscopic analytical method for the determination of hydrophilic, respectively hydrophobic surface properties. The contact angles of droplets of distilled water (2 µl) on plasma untreated and plasma treated glass samples were measured. The reported contact angle value represents a mean of 20 measurements. Results of the contact angle measurements for plasma activated glass are shown in Fig. 1 (right). A significant decrease in the contact angle value is observable already at very short treatment times (1 s).
The silanization was carried out in 1% solution of APTES in toluene. Both untreated/plasma treated samples have been silanized for various time intervals: 10 minutes, 1, 2, 3 and 24 hours. After the silanization the samples have been sonicated for 10 min in toluene. The silane layers have been afterwards cured at 120°C for 1 hour. After the cooling, contact angle measurements and boiling test have been carried out on the silane layers.
The persistence of the layers has been analyzed by the means of the boiling test. Silanized glass samples have been cooked at the boiling point in distilled water. After certain times of boiling, the contact angle measurements have been carried out.

3. Results and discussion

The contact angle analysis showed that after the silanization the surface of the glass samples is more hydrophobic than before the silanization. The values of contact angles measured on plasma treated samples have been in general greater than the ones measured on untreated samples (Fig. 2, left). This can be credited to the plasma-cleaning effect and, possibly, to the increased surface OH groups density on the plasma activated samples, due to which the silane hydrolyses more readily at the surface of the sample, thus creating a denser silane layer.
The boiling test showed that the plasma treated samples retain greater hydrophobic character than the untreated samples (Fig. 2, right). The overall results show better quality of the silane layers created on the plasma activated glass surfaces.

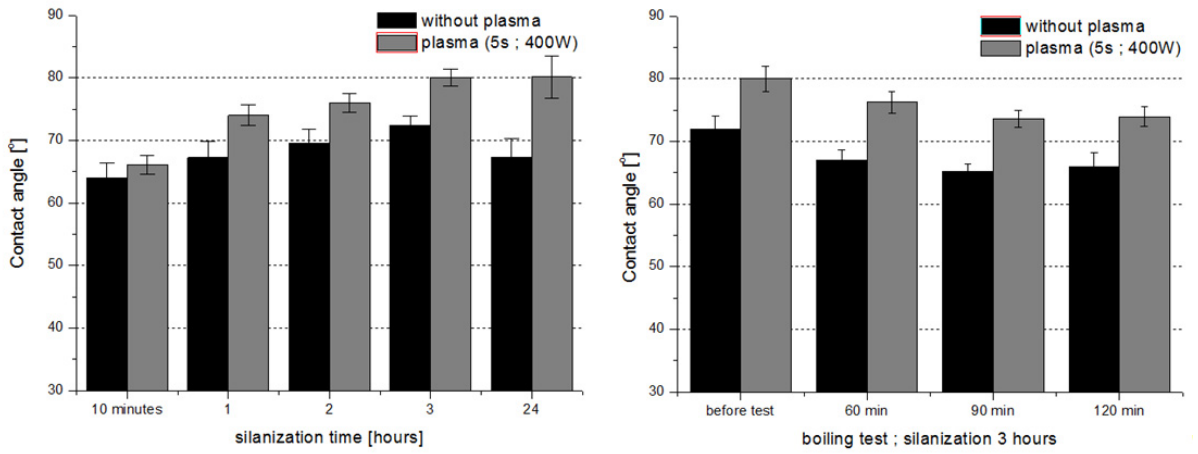


Fig. 2: Contact angle measurements on glass samples silanized for various time intervals (left), contact angle measurements on glass samples boiled for various time intervals; the silanization time was 3 hours (right).

4. Conclusion

In this work we addressed the silanization of the glass surfaces using plasma pretreatment of glass samples. As the model silane the 3-aminopropyltriethoxysilane (APTES) was used.
The values of contact angles have been in general bigger for the plasma treated samples when compared with the untreated samples.
The results of the boiling test showed, that the plasma treated samples retain greater hydrophobic character than the untreated samples.
The above mentioned results have been credited to the cleaning effect of the atmospheric-pressure non-equilibrium DCSBD plasma with a possible increase in the OH groups density on the surface of the plasma activated samples.
Presented results suggest that using the plasma activation it is possible to prepare silane APTES layers with better properties than for the non-activated, chemically cleaned glass surfaces.

Acknowledgements. This research has been supported by the Slovak Research and Development Agency, Project No. APVV-0491-07, by the research intent: MSM0021622411 funding by the Ministry of Education of the Czech Republic and by the contract KAN 101630651 by Grant Agency of Academy of Science of Czech Republic.

5. References

[1] Han, Y. et al. 2006 *Thin Solid Films*, **510**:175-180.
[2] Nai-Yi Cui et al. 2007 *Applied surface Science*, **253**:6932-6938.
[3] Dugas, V., Chevalier, Y. 2003 *Journal of Colloid an Interface Science*, **264**:354-361.
[4] Kaplan, S. L. 2003 *Fourth International Symposium on –silanes and Other Coupling Agents*, Orlando, Florida.
[5] Simon, A. et al. 2002 *Journal of Colloid Interface Sci*. 251:278-283.
[6] Cras, J.J. et al. (1999) *Biosensors & Bioelectronics*, **14**:683-688.
[7] Gonzales-B. J. et al. *Journal of Applied Polymer Science*, **62**:375-384.
[8] Roth, J.R. (2001). Industrial Plasma Engineering Volume 2: *Applications to Nonthermal Plasma Processing*. Institute of Physics Publishing, pages 540-611, ISBN 0 7503 0544 4.
[9] Kogelschatz, U. 2003 *Plasma Chemistry and Plasma Processing*, **23**, No. 1.
[10] Yamamoto, T. et al. 2004. *Plasma Chemistry and Plasma Processing*, **24**, No.1:1-12.
[11] Gibalov V. I., Pietsch, G. J. 2004 *Journal of Physics D: Applied Physics*, **37**, 2082-2092
[12] Goosensa, O., et al. 2001 *Surface and Coatings Technology* **142-144**:474-481.
[13] Xu, X. 2001 *Thin Solids Films*, **390**:237-242.

[14] Černák, M. et al. 2009 *Eur. Phys. J. Appl. Phys*. **47**, 22806.
[15] Buček A. et al. 2008 *Chem.Listy **102**, p.1459-1462*
[16] Buršíková, V., et al. 2004 Brno, ISBN 80-210-3563-3.

ACTIVATION OF THE SILICON SUBSTRATES SURFACE IN LOW TEMPERATURE PLASMA GENERATED AT ATMOSPHERIC PRESSURE

Anna Zahoranová[1], Veronika Medvecká[1], Dušan Kováčik[1], Tomáš Plecenik[1], Ján Greguš[1], Mirko Černák[1, 2]

[1]*Department of Experimental Physics, Faculty of Mathematics, Physics and Informatics, Comenius University, Mlynská dolina, 842 48 Bratislava, Slovak Republic*
[2] *Department of Physical Electronics, Faculty of Science, Masaryk University, Kotlářská 2, 611 37 Brno, Czech Republic*
E-mail: zahoranova@fmph.uniba.sk

Silicon and silicon wafers are an essential element in the semiconductor and microelectronics technology. They serve as a basis for electronic devices and MEMS (Micro-Electro-Mechanical System) or in SOI (silicon-on-insulator) materials. Bonding of silicon wafer with each other and with other materials is an important technological step, and depends on activation and surface treatment, which uses different chemical processes. The work is devoted to the activation of silicon surface using non-thermal plasma generated by novel atmospheric-pressure plasma source, the so-called Diffuse Coplanar Surface Barrier Discharge (DCSBD). Changes of the surface energy were investigated by measuring of contact angle and surface topology by AFM.

1. Introduction

Currently a trend towards miniaturization in the development of integrated circuits requires new technologies to design nano-sizing and increased amount of components. Microelectronics, optoelectronics and photovoltaic applications are using a combination of several materials and their properties in various structures. MEMS technology [1] integrates a variety of mechanical and electromechanical elements on the substrates (usually silicon wafer) in which the crucial role is preparation of thin film structures and wafer bonding with each other or with other materials (wafer direct bonding - WDB) [1-5], which require a specially treated surface. Finishing of the silicon wafer includes repairing damage after cutting from the parent crystal, perfect smoothing, and cleaning and surface activation. For this purpose a different mechanical and chemical processes (CMP- chemo-mechanical polishing) are used. The processes of smoothing the surface, etching and cleaning are complicated and today it is a tendency to replace wet chemical and high-energy processes with plasma based technology, which is environmentally friendly and economicaly advantageous solution [6-8].
The silicon surface in ambient air is quickly covered with a thin layer of native oxide (1-2 nm), which is ended with OH-groups [3]. So the surface of silicon, which is naturally hydrophilic, is covered with the layer of various adsorbed impurities. The larger particles and objects (dust) and organic contaminants (e.g. oil vapour) from materials which have been in contact with the silicon surface have affect the adhesion of silicon wafer [3]. Cleaning and surface activation is essential process for further use of the silicon wafer and it is important to avoid its degradation. The wafer direct bonding requires clean, smooth and hydrophilic surface (it means high density of active OH-groups on the surface) [5].
Non-equilibrium plasma has in comparison with classical methods of surface finishing a number of advantages. High-temperature processes may cause degradation of the material, many structures are sensitive to high temperature (low melting point materials) and different thermal expansion coefficients may damage the connections. In the case of wet chemical processes use of harmful chemicals and subsequent drying is required, which may be problem from ecological and economical point of view. The criterion for suitability of plasma based cleaning and activation processes is the low temperature of ions and neutral particles to prevent damage the surface and high temperature electrons are needed to ensure activation of the surface.
It is known, that non-equilibrium plasma can be relatively easily generated at reduced pressures (10^{-3} - 10^{3} Pa), however, there are vacuum and pumping equipment needed and so investment costs, batch-wise processing and relatively long treatment times may be an restriction for wider implementation. A

suitable alternative is using of the Dielectric Barrier Discharges (DBD). Dielectric barrier prevents the accumulation of large charge in discharge gap and plasma overheating. At present volume DBD - so called industrial corona is mainly used. In this type of plasma source diffuse nature of the discharge is provided by the carrier gas flow or admixture of noble gases. In our work we used the Diffuse Coplanar Surface Barrier Discharge (DCSBD) [9] with unique properties. DCSBD enables to generate a thin uniform plasma layer with the high power density (100 W/cm^3) in any working gas without any admixture of rare gases. Due to temperature non-equilibrium, plasma generated by DCSBD is suitable for surface treatments of materials and was successfully used for such treatment of various materials as non-woven textile, wood, aluminium, glass [10-13].

2. Experiment

The plasma treatment of silicon samples was carried out using the DCSBD [9] plasma source working at atmospheric pressure in ambient air. The DCSBD electrode geometry consists of many parallel strip-line silver electrodes embedded 0.5 mm below the surface of 96 % Al_2O_3 ceramics (Fig. 1a). The discharge was powered by 18 kHz sinusoidal voltage with amplitude of approximately 10 kV, supplied by HV Plasma Power Supply PPS02 (Kamea, Slovak republic). The effective thickness of discharge plasma generated above Al_2O_3 ceramics was approximately 0.3 mm. The design of plasma reactor, allowing treatment of the samples in a continuous mode is seen in Fig. 1b. The sample (4) was placed on the moving cart (3) and a distance between the sample and electrode surface was manually adjusted, in our case this distance was 0.3 mm. By activating programmable stepper motor the cart with the sample was moved above the electrode surface (1) with specific speed, which determinate the treatment time and exposed the whole sample surface to the active plasma area (2).

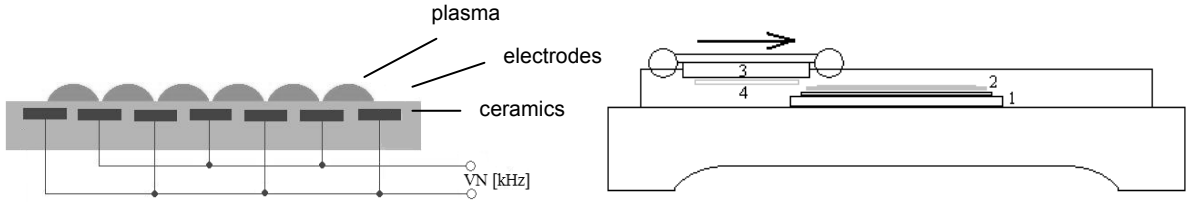


Fig. 1. The scheme of DCSBD electrodes system (a), schematic sketch of the plasma treatment set-up (b), 1 – DCSBD electrodes system, 2 – plasma, 3 - moving cart, 4 – sample.

The electrical parameters of discharge were monitored by Pearson current monitor Model 4100 and two high voltage probes Tektronix P6015A (1000:1). The signals from all three electrical probes were recorded by the digitizing oscilloscope Tektronix TDS 2014B. The total power consumed by plasma was calculated from measured current-voltage waveforms.

The silicon wafers used in this study were N-type, doped with phosphorus, Si(111), having resistivity (33-45).10^{-3} Ω.cm, from ON Semiconductors Czech Republic, s.r.o. Wafer diameter was (100.0±0.5) mm and thickness (381±25) μm.

In our experiments the effect of the atmospheric plasma tretment on three type of precleaned silicon wafer surfaces has been investigated: the wet chemically cleaned surface, silicon oxide surface prepared by thermal oxidation and silicon surface cleaned in solution of hydrofluoric acid. The first type of samples (samples A) were before plasma treatment cleaned in ultrasonic bath in acetone, isopropanol and distilled water for 6 minutes in each liquid. Another way how to create a hydrophobic surface is oxidation of silicon wafer at high temperature (500 °C for 1 h) in an oxygen atmosphere. Thermally oxidized silicon surface (sample B) is dehydrated and so lack of silanol groups on the surface make it hydrophobic. The third type silicon samples (samples C) were after wet chemically cleaning (a savoir samples A) immersed into solution of hydrofluoric acid (HF/H_2O, 1:10 in volume), which removes the top layer of oxide and immediately creates a new thin layer of native partially dehydrated oxide. Using this process silicon samples were turned to hydrophobic, what enabled verification of the plasma treatment effectivity to return the samples surface to hydrophilic [3].

The plasma treatment was carried out using the DCSBD plasma source in atmospheric pressure ambient air, at the discharge power of 300 W, the treatment time was 3, 5 and 10 sec respectively, using continuous mode of treatment.
The surface energy changes of the silicon samples before and after plasma treatment was evaluated by measuring the contact angle. The contact angle measurement is a widely used method to determine the surface wettability or hydrophilicity. As a measurement device we used Surface Energy Evaluation System (See System, from Advex Instr. Co. Ltd., [14]), as a test liquid distilled water (volume drops 1.5 μl) was used. The surface energy of concrete samples was determined by using the acid-base model for three-liquid method (in our case: distilled water, glycerol and diiodomethane) through the imaging the contact angle of liquids and his evaluation using software SeeSoft.
Morphological changes on the surface of silicon samples have been mapped by Atomic Force Microscopy (AFM).

3. Results and discussion

As illustrated in Fig. 2 showing the analysis of the water contact angle measurement (Water Contact Angle - WCA) of samples A, B, C before plasma treatment it is clear that the initial values of surface energy were different depending on the precleaning process of the surface. Most hydrophobic surface has been measured in the case of sample B – precleaned with hydrofluoric acid. After plasma treatment at the exposure time 10 sec, the surface of all samples became hydrophilic and the WCA-value was below the measurable value of 5 degrees. Therefore, we determined the surface energy values of the samples after ageing 24 hours since plasma treatment, when the surface still showed a hydrophilic character.

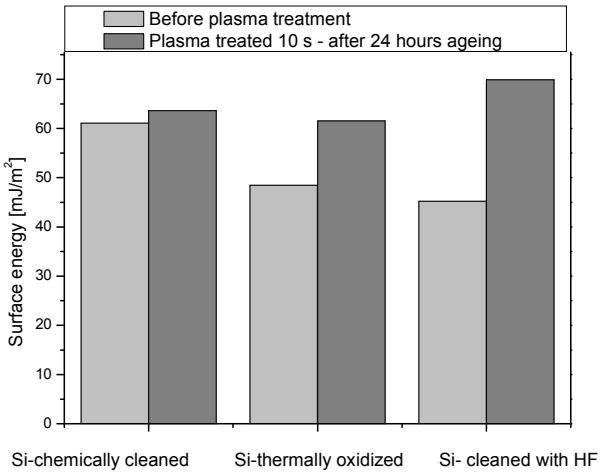


Fig. 2. Effect of the atmospheric plasma treatment on the value of surface energy for three types of silicon samples, plasma treatment time was 10 sec, discharge power 300 W.

Plasma treatment of silicon samples results in the reduction of the WCA after short exposure time in plasma (3 sec) to less than 5°, which indicates hydrophilic character of the surface. Silicon surface ageing of the sample A after plasma treatment is shown in Fig. 3, which illustrates that ageing of the silicon surface is strongly depended on the treatment time. The WCA value has been returned to the value of a reference sample after a few days, however, for most applications it is important to keep the stable hydrophilic character of surface only for several hours.

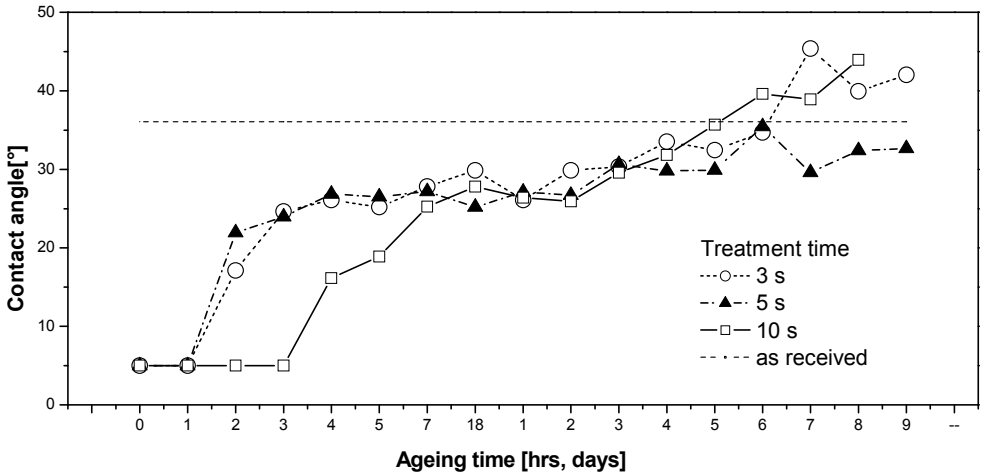


Fig.3. Ageing of plasma treated silicon surfaces (A) for several treatment times: 3, 5, 10 sec, treatment was done in ambient air of atmospheric pressure at discharge power 300 W.

As illustrated in Fig. 3, samples exposed to the plasma for 10 sec remained hydrophilic for the first three hours. Fluctuating nature of the "ageing curve" can be partly explained by the sensitivity of the activated hydrophilic silicon surface to the external conditions (ambient air), and also by the fact that silicon as semiconductor material is very sensitive to certain gases from the air [15]. Therefore it can be assumed that the ageing of treatment was affected by adsorbed impurities and gases from the air and manner of storage.

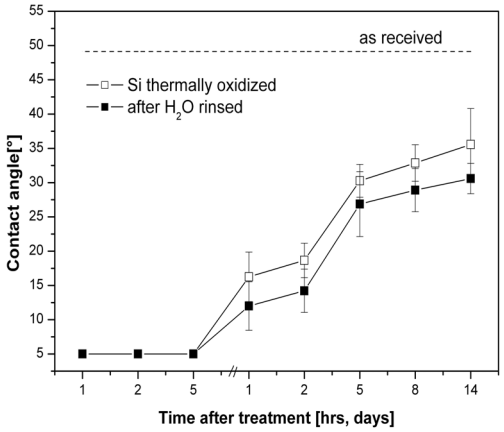


Fig.4. Ageing of plasma treated thermally oxidized silicon surface (B) for treatment time 7 sec, discharge power 300 W, in atmospheric pressure ambient air.

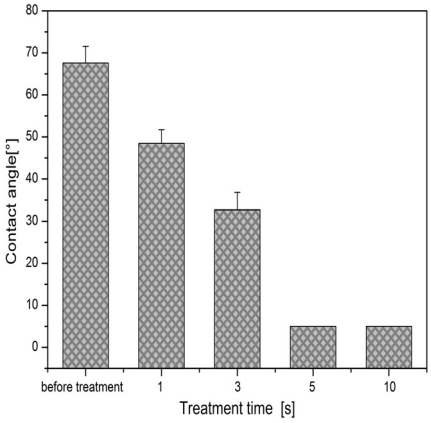


Fig. 5. Contact angle values of plasma treated silicon surfaces precleaned with HF (C) as function of exposure time.

The reference sample of thermal oxidized silicon (B) have a higher WCA value (49.14° ± 4.09°) than chemically cleaned silicon (A) (36.08° ± 1.22°). Plasma treatment of samples B at the treatment time 7 sec (Fig. 4) leads to strongly decreasing of WCA-value stable for 5 hours. This hydrophilic surface shows slower ageing compared with the surface of sample A and after 14 days its WCA value is less than the reference sample´s contact angle. The behavior of ageing plasma treated samples after their contact with water was also investigated. As can be seen in Fig. 4, the aged samples rinsed in distilled water tend to decrease the contact angle, what may be caused by reorientation of polar groups on the surface.

The WCA-value of the sample cleaned by hydrofluoric acid (C) was studied as a function of plasma treatment time (Fig. 5). The measured initial WCA-value was of 67.60° ± 3.97°, what means that these samples had the most hydrophobic surface. As illustrated in Fig. 5, 1 sec exposure time in plasma leads to a decrease of WCA-value and after 5 sec treatment time WCA - value is less then 5°.



a) b)

Fig.6. AFM images of the thermally oxidized silicon surface (sample B) before plasma treatment (a), for 7 s plasma treated in ambient air atmospheric pressure DCSBD, discharge power 300 W (b).

Morphological changes due to plasma treatment were investigated using AFM measurement conducted on the plasma treated silicon surface. Fig. 6 shows the AFM images of the untreated and plasma treated (7 sec) thermal silicon oxide surface, which illustrate negligible changes in surface roughness moreover in some cases the surface is even smoother. For hydrophilic surface treatment of silicon the short treatment times are sufficient thus in this case the changes in surface roughness play no role.

4. Conclusions

The obtained preliminary experimental results show the availability of using DCSBD discharge for surface treatment of silicon wafer in the air at atmospheric pressure. Even short treatment times, on the order of seconds, were sufficient to increase the surface energy of silicon substrates. This type of discharge appears to be promising and suitable for a dry low-temperature processes without damaging the silicon surface.

Acknowledgements. This research has been supported by the Slovak Research and Development Agency, Project No. APVV-0491-07, by the research intent: MSM0021622411 funding by the Ministry of Education of the Czech Republic and by the contract KAN 101630651 by Grant Agency of Academy of Science of Czech Republic.

5. References

[1] Gabriel M et al. 2006 *Microsyst Technology* **12** 397-400
[2] Goustouridis D et al. 2004 *Sensors and Actuators* **A 110** 401-406
[3] Plößl A, Kräuter G 1999 *Material Science and Engineering* **R 25** 1-88
[4] Tong B Q, Gösele U M 1999 *Advanced Materials* **11** 17 1409-1425
[5] Wolffenbuttel R. F., Wise K. D. 1994 *Sensors and Actuators* A **43** 223-229
[6] Ramm J et al. 1993 *Thin Solid Films* **228** 23-26
[7] Pasquariello D et al. 2000 *Sensors and actuators* **82** 239-244
[8] Kowal J et al 2009 *Sensors and Actuators* **A 155** 145-151
[9] Šimor et al 2002 *Applied Physics Letters*, **81**, 15 2716-2718
[10] Bónová L et al 2008 *Chem. Listy* **102** 1452−1454
[11] Gulejová B et al. 2002 *Czech. J. Phys., Suppl. D*, **52** 861-865
[12] Buček A et al. 2008 *Chem.Listy **102**, p.1459-1462*
[13] Odrášková M et al 2008*Plasma Chem Plasma Process* **28** 203–211
[14] Buršíková V et al. 2004 Brno, ISBN 80-210-3563-3.
[15] Noboru Yamazoe Kengo 2008 Shimanoe *Sensors and Actuators,* **B 128** 566-573

Topic 8
Biological applications

INACTIVATION OF MICROORGANISMS IN RIVER WATER USING ELECTRICAL DISCHARGES

Tomasz Izdebski[1], Mirosław Dors[1], Jerzy Mizeraczyk[1,2]

[1]*Centre for Plasma and Laser Engineering, The Szewalski Institute of Fluid Flow Machinery, Polish Academy of Sciences, Fiszera 14, 80-952 Gdańsk, Poland*

[2]*Department of Marine Electronics, Gdynia Maritime University, Gdynia, Poland*
E-mail: mdors@imp.gda.pl

This work was aimed at the investigation of inactivation of all kinds of microorganisms, total *coli* and *E. coli* in river water using corona and spark discharges in water, corona discharge in gas, ozonation and Fenton reaction. Our experiments demonstrated that ozonation and Fenton reaction are the most efficient method of water disinfection comparing to pulsed spark and pulsed corona discharges. The pulsed spark discharge in water is capable of killing all microorganism similarly to ozonation, however, with much lower energetic efficiency. The pulsed corona discharge turned out to be the less effective method of water disinfection.

1. Introduction

In spite of extensive investigations in many laboratories, there is still not enough data on surface water (rivers, lakes) purification by the electrohydraulic discharges. Electrohydraulic discharges in water cause the destruction and inactivation of viruses, yeast, and bacteria. It is generally assumed that the mechanism responsible for killing microorganisms through electrohydraulic discharges involves an electric field, shock wave, UV radiation and radical reactions. The destruction of microorganism depends on the microorganism cell structure. It is different for each bacteria species and depends also on the mode of electrohydraulic discharge [1]. In the case of the corona discharge, *E. coli* bacteria cells are destroyed mainly due to reactions with oxidizing radicals OH and H_2O_2 with compounds forming the bacteria cell wall [12], whereas in the spark and arc discharges they are mainly damaged by shock waves and UV radiation [3, 4].

In this work we investigated the influence of corona and spark discharges in water and gas phase as well as conventional ozonation of water and Fenton reaction on inactivation of all kinds of microorganisms, total *coli* and *E. coli*. Water samples were taken from the Strzyża river, in Gdańsk region. The Strzyża is a type IV sanitary class river, so it has a total coli number of over 3000 colony forming units (cfu) in 100 ml. Due to this fact, it cannot be used to supplying region inhabitants with drinking water. This would be possible only after complete removal of *coli* bacteria, e.g. by plasma processing.

2. Experimental setup

The processing of the river water samples was conducted in a reactor of corona discharge in water and in a reactor of corona discharge in gas with water aerosol. Corona discharge in water was performed in a glass tube reactor (inner diameter of 22.5 mm) equipped with water pumping and cooling systems (Fig. 1). Every sample had a volume of 400 ml. Water samples were being pumped once through the reactor tube at different flow rates and discharge voltages. A pulsed positive discharge was generated between a high voltage stainless steel hollow needle electrode and a grounded brass rod electrode (10 mm in diameter), both immersed in the water. The inner and outer diameter of the hollow needle were 1.4 mm and 1.6 mm, respectively. The discharge was generated at the edge of the hollow needle, whereas the rest part of the needle was covered with an insulator. Corona discharge was generated when the needle-rod spacing was 45 mm, whereas the spark discharge was formed in the spacing of 9 mm. Positive high voltage pulses were applied to the hollow needle electrode from a discharge capacitor C_1 (2 nF) – Fig. 1. The pulse repetition rate of 50 Hz was fixed by the rotation velocity of a rotating spark gap switch. The amplitudes of the voltage and current corona pulses were up to 40kV and 35 A, respectively, with a full width at half maximum (FWHM) of 3,8 μs and an energy of 0,42 J. The amplitudes of the voltage and current spark pulses were up to 27 kV and 30 A, respectively, with FWHM of 1,4 μs and an energy of 0,17 J.

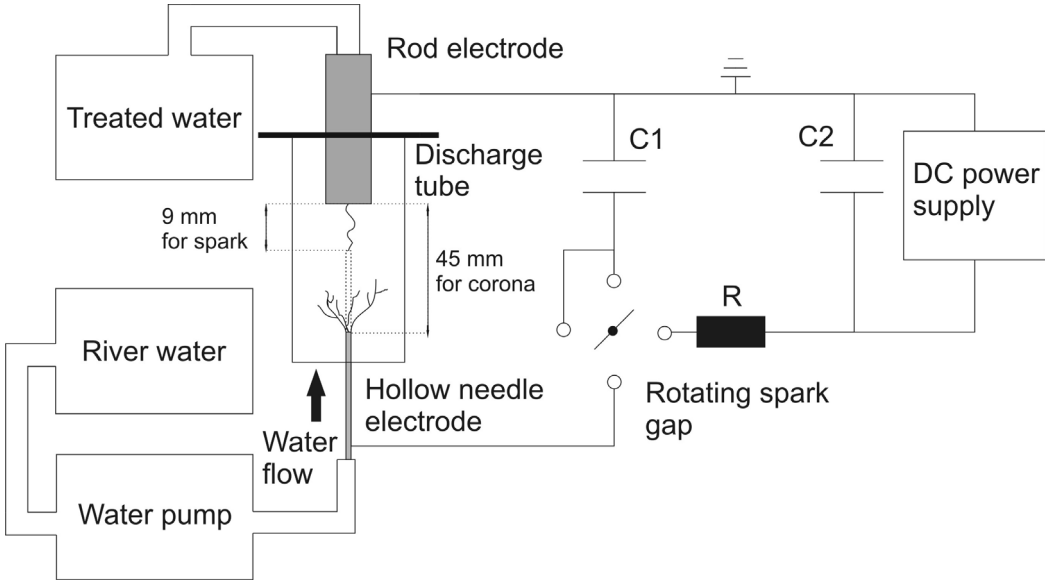


Fig. 1. The corona and spark discharge reactor with water pumping and cooling system and pulsed power system (C1 = 2 nF, C2 = 22 nF, R = 10 kΩ).

One set of polluted water samples was processed by corona discharge at 3 different flow rates: 36, 69 and 175 ml/min. Another set of samples was treated by spark discharge at a flow rate of 38 and 71 ml/min.

The treatment of river water was also performed using gas phase corona discharge in a nozzle-to-mesh reactor (Fig. 2). The gap between the nozzle and mesh was 45 and 60 mm, but discharge length depended on the water spread, and was about half the length of the gap.

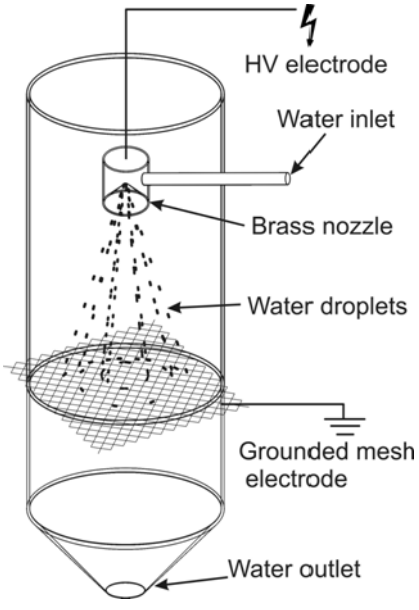


Fig. 2. Gas phase corona reactor.

The oxidisation processes, i.e. ozonation and Fenton reaction, were also held in a 400 ml volume samples. For ozonation, the process employed a bottle washer that washed the sample with ozone for 60 seconds. The O_3 concentration in the inlet gas was 20 g/m^3. The ozone was created in Direct Barrier Discharge (DBD) reactor from pure oxygen, at a flow rate of 1 l/min. The ozonator was operating at 15 W. Samples were treated by ozonation for 45 s, 91 s, 152 s, and 212 s. Fenton reaction was performed by adding 1 ml of Fe_2SO_4 and 0.17 ml of H_2O_2 (3% solution). Initial pH of distilled water, and river water were 6.5 and 8.1 respectively. In some samples the pH value needed to be adjusted through acidic or alkali solution. Some water samples were treated both with hydrogen peroxide and ozone after fixing pH at 7.8. This was to induce peroxone reaction instead of Fenton:

$$2\,O_3 + H_2O_2 \xrightarrow{pH > 5} 2\,OH\cdot + 3\,O_2$$

The processed water was taken from the Strzyża river in February 2010. The water initial characteristics was as follows: temperature 18°C, Total number of *coli* bacteria 11750 cfu/ml, number of *E. coli* 280 cfu/ml, total number of microorganisms at 36 and 22^{0}C were 30500 and 74500 cfu/ml, respectively.

Every water sample was tested for microbiological markers such as: number of microorganisms in 36^{0}C after 72 h of growing, number of microorganisms in 22^{0}C after 24 h of growing, total number of

coli bacteria and number of *E. coli* bacteria.
In all samples, the concentration of the non-purgable organic carbon level (NPOC) was determined using Sievers InovOx Total Organic Carbon (TOC) analyzer.

3. Results and discussion

A comparison of bacteriological results of the total number of microorganisms and coli concentrations in river water samples treated by corona discharge, spark discharge and ozonation are presented in Figs. 3 and 4. The energy efficiencies of various treatments are presented in Fig. 5. It is seen that processing by corona discharge caused significant reduction in the concentrations of microorganisms and bacteria but did not kill them completely. The lower the flow rate, the more energy efficient it was.

The spark discharge was even more effective than the corona, causing a 100% decrease in the number of microorganisms and bacteria after 622 s of processing, except for the total number of microorganisms in 36^0C which survived in the number of 36 cfu/ml. The energy efficiency of spark discharge was three times higher than the corona, but still much below that of ozonation.

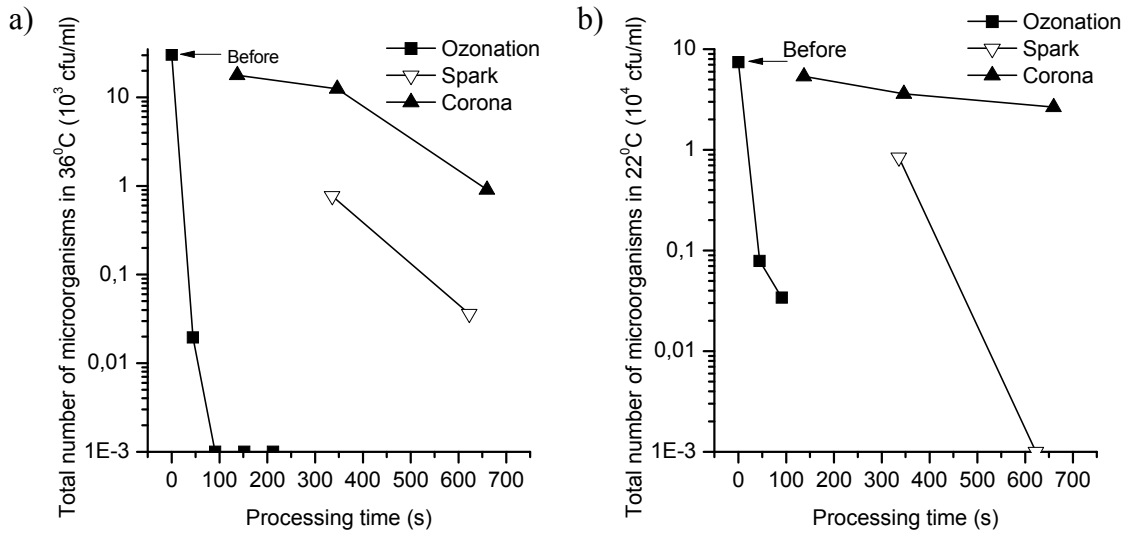


Fig. 3. Concentration of a) microorganisms in 36^0C, b) microorganisms in 22^0C in river water samples as a function of processing time using ozonation, spark discharge and corona discharge.

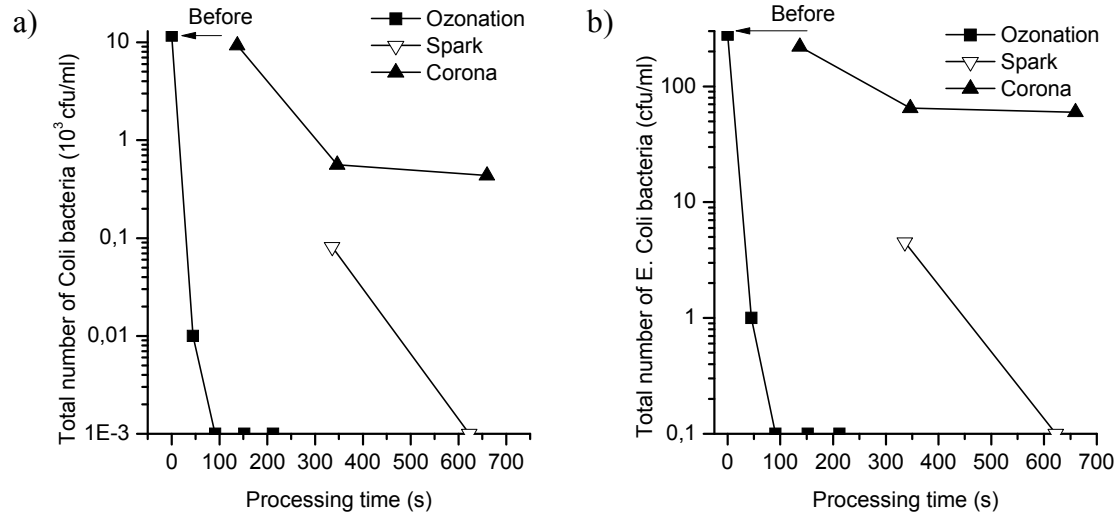


Fig. 4. Concentration of a) total number of *Coli* bacteria, b) total number of *E. Coli* bacteria in river

water samples as a function of processing time using ozonation, spark discharge and corona discharge. The ozonation process caused a fast decrease of total bacteria concentrations when increasing treatment time. After 45 s of processing, the total *coli* number dropped from initial 11750 cfu/ml to 10 cfu/ml and *E. coli* number from 280 cfu/ml to 1 cfu/ml. Processing time of 152 s resulted in killing the *coli* bacteria and microorganisms. The energy efficiency was a magnitude higher than that of the electrohydraulic discharges.

The Non-Purgable Organic Carbon (NPOC) concentrations measured in every water sample are similar, i.e. 5±0,4 ppm. It is seen that NPOC concentrations were not affected by the treatment in this experiment. It shows that neither electrohydraulic discharges, nor ozonation oxidized organic compounds to CO_2. Thus, their action is limited to inactivation of microorganisms, possibly with destruction of their structure, and to oxidation of one organic compound into another.

The process of water treatment using gas phase corona discharge showed no significant change in microbiological pollution levels. It could be due to the small spread of water droplets, or high water pressure. Further study of this system is needed.

The oxidization processes showed, that the sample with reduced pH Fenton reaction treatment was the most effective in reducing the number of microorganisms (Fig. 6). *E. Coli* and *Coli* numbers dropped to 0 cfu/ml and the concentration of microorganisms in 22^0C and 36^0C decreased from 7800 and 565 cfu/ml to 100 and 19 cfu/ml, respectively.

4. Conclusions

Our experiments demonstrated that ozonation and Fenton reaction are the most efficient method of water disinfection comparing to pulsed spark and pulsed corona discharges. However, Fenton reaction to be most efficient, it requires a reduction of the pH level and Fe^{2+} addition. The pulsed spark discharge in water is capable of killing all microorganism similarly to ozonation, however, with much lower energetic efficiency. The pulsed corona discharge turned to be the less effective method of water disinfection.

The nozzle treatment corona discharge proved to be ineffective in its current configuration. However, further studies using other electrode configurations and materials as well as high voltage power supply may improve energy efficiency of spark or/and corona discharge and make them competitive to ozonation.

5. References

[1] Locke B.R., M Sato, Sunka P., Hoffmann M.R., Chang J.S., Electrohydraulic Discharge and Nonthermal Plasma for Water Treatment, *Ind. Eng. Chem. Res*., **45**, 882-905, 2006

[2] Emelko M.B., Arnold A.J., Santillan C.A., Dickson S.E., Chang J.S., Treatment of drinking water with pulsed arc electrohydraulic discharge: promising outcomes and future challenges, Asia-Pacific Int. Symp. on Air and Water Treatments by Green Oxidation/Reduction Technologies - Catalyst, Plasma and Hybrid Systems, Dalian, China People Rep., 2006

[3] Abou-GhazalaA. A, Katsuki S., Schoenbach K.H., Dobbs F.C., Moreira K.R., Bacterial Decontamination of Water by Means of Pulsed-Corona Discharges, *IEEE Trans. Plasma Sci*., **30**, 4, 1449-1453, 2002

[4] Ching W.K., Colussi A.J., Sun H.J., Nealson K.H., Hoffman M.R., Escherichia coli disinfection by electrohydraulic discharges, *Environ. Sci. Technol.*, **35**, 4139-4144, 2001

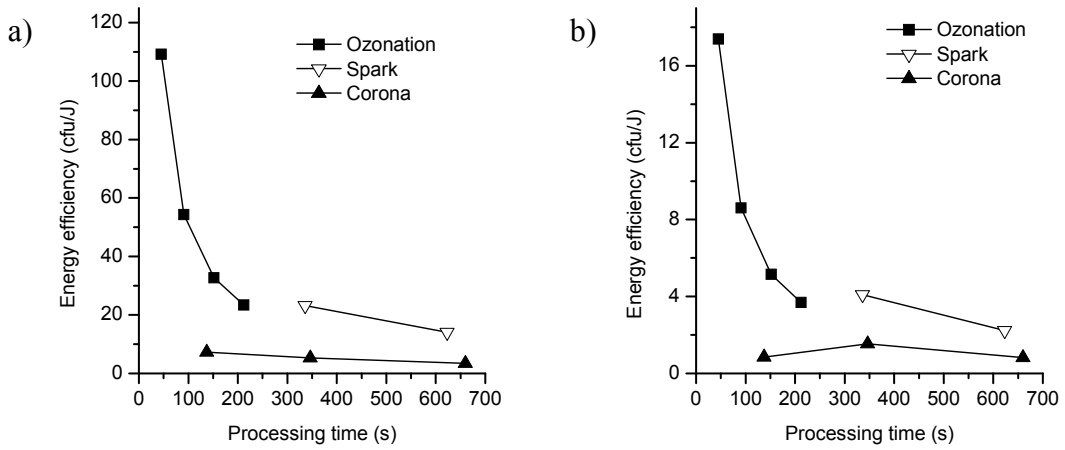


Fig. 5. Energy efficiency of killing a) microorganisms in 22^0C, b) total number of *Coli* bacteria in river water samples as a function of processing time using ozonation, spark discharge and corona discharge.

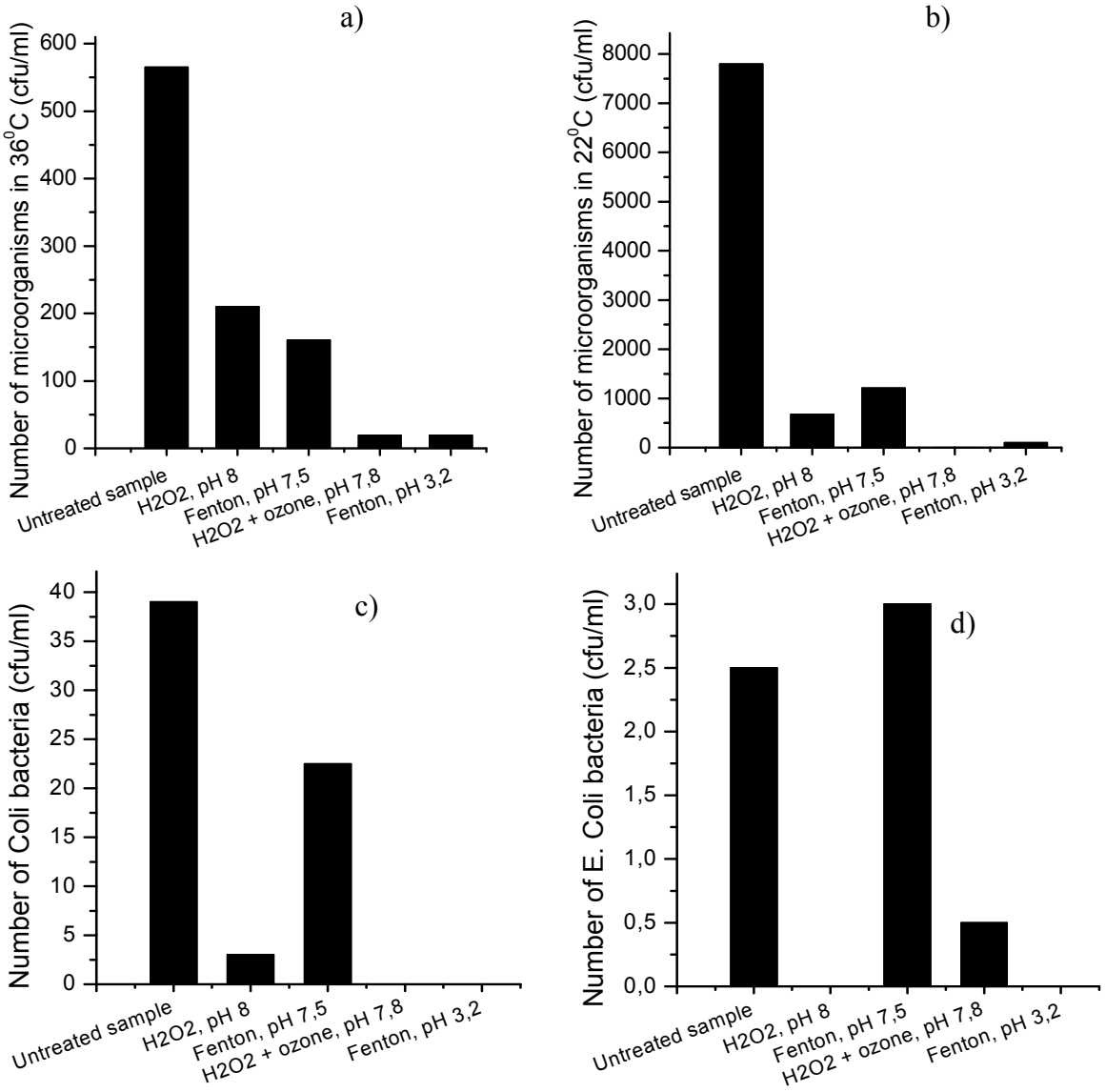


Fig. 6. Concentration of a) microorganisms in 36^0C, b) microorganisms in 22^0C, c) *Coli* bacteria, d) *E. Coli* bacteria in treated samples.

SURFACE MODIFICATION OF CLOSED PLASTIC BAGS FOR ADHERENT CELL CULTIVATION

K. Lachmann[1], A. Dohse[1], M. Thomas[1], S. Pohl[2], W. Meyring[3], K. E. J. Dittmar[2], W. Lindenmeier[2], C.-P. Klages[1]

[1]*Fraunhofer Institute for Surface Engineering and Thin Films IST, Bienroder Weg 54 E, 38108 Braunschweig, Germany*
[2]*Helmholtz Centre for Infection Research HZI, Inhoffenstr. 7, 38124 Braunschweig, Germany*
[3]*Städtisches Klinikum Braunschweig GmbH, Freisestr. 9/10, 38118 Braunschweig, Germany*
E-mail: kristina.lachmann@ist.fraunhofer.de

In modern medicine human mesenchymal stem cells are gaining increasing importance. Using helium-based gas mixtures (He + N_2 + H_2) as well as helium enriched with suitable film-forming agents the inner surface of polymer bags can be modified with a plasma process developed at Fraunhofer IST. The effect of plasma treatment is investigated by FTIR-ATR spectroscopy as well as surface tension determination based on contact angle measurements. Plasma treatment in nominally pure helium increases the surface tension of the polymer foil due to the presence of oxygen traces in the gas and oxygen diffusing through the gas-permeable foil, resp., reacting with surface radical centres formed in the discharge. For the same reason the area density of primary amino groups on the surface obtained by treatment in mixtures with nitrogen is comparably small. With regard to their applicability in cell cultivation three different coatings (bases on APTMS, DACH and TMOS) were tested. It is shown that primary amino groups play an important role in cell cultivation of adherent growing bone marrow mesenchymal stem cells.

1. Introduction

Living cells are being used more and more frequently in modern medicine such as stem cell therapy, blood transfusion and bone marrow transplantation or in the case of deep burns. Since the cultivation of cells in open systems carries a high risk of the cell cultures becoming contaminated, a new procedure has been developed in which closed bag systems are used in order to exclude the possibility of contamination. The internal surfaces of the bags are coated by means of atmospheric-pressure plasmas so as to enable adherent cell growth on these surfaces using automated equipment. Functionalization of polymer surfaces can be easily achieved by plasma treatment using oxygen or nitrogen containing gas-mixtures [1-3]. In order to ignite a discharge exclusively in the inside of a closed volume, which is surrounded by dielectric walls, but not in the immediately adjacent gas (normally air), to create functional groups on the interior walls, it is necessary to use process gases with smaller breakdown field strengths than the gas in the environment. For this purpose a new efficient atmospheric-pressure plasma process has been developed, utilizing reactive gas mixture or an organic film forming agent in combination with helium as process gas in order to create a coating containing functional groups such as primary amines ($–NH_2$) or silanols (Si-OH) on the inner walls of the bag.

2. Experimental

Gas permeable and transparent bags made of polyolefin suitable for suspension cell culture (Miltenyi Biotec) were used for coating and adherent cell cultivation experiments.
The plastic bags were filled automatically with the corresponding gas mixture in an automated filling system developed at Fraunhofer IST. Addition of film-forming agents like 3-aminopropyl-trimethoxysilane (APTMS), 1,2-diaminocyclohexane (DACH) or tetramethoxysilane (TMOS) to the plasma gas was accomplished by passing helium trough a bubbler containing the liquid monomer at room temperature. To ensure a defined gas mixture within the bags, they were emptied and refilled several times. The plasma treatment was also integrated in the automated filling system. It was performed using a DBD arrangement with electrodes located above and underneath the bag, so that the discharge ignited exclusively inside the bag upon application of an alternating voltage of sufficient magnitude [4].

As a high voltage electrode a 150 x 300 mm^2 steel electrode, covered with a 3.4 mm thick glass plate as a dielectric, was used, a thin aluminum plate (150 x 300 mm^2) covered with a 5 mm thick polyethylene sheet served as a ground electrode. Typical parameters used include an electrical power of approx. 50 W and a treatment duration of several seconds (5-20 s).

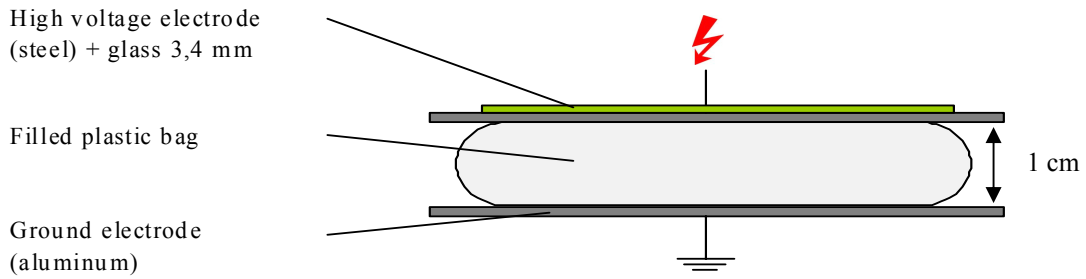


Fig. 1: Schematic illustration of the plasma treatment procedure

Table 1: Gas mixture and film--forming agent and created surface functional groups

Gas mixture / film- forming agent	**Surface functional groups**
Pure Helium	O-containing groups
Helium with additions of N_2 and H_2	$-NH_2$, -NH
3-Aminopropyl-trimethoxysilane (APTMS)	$-NH_2$, Si-OH
1, 2-Diaminocyclohexane (DACH)	$-NH_2$
Tetramethoxysilane (TMOS)	Si-OH

APTMS (> 97 %), DACH (99 %) and TMOS (98%) were supplied by Sigma-Aldrich. The purity of helium was > 99.999 % (Air Liquide).

The modified internal surfaces of the bags were analyzed using FTIR-ATR spectroscopy (FTIR Nicolet 5700, Thermo Fisher Scientific Inc., Waltham, MA, USA) equipped with an MCT detector and a DuraSamplIR single-reflexion 45° diamond ATR crystal using unpolarized light and a spectral resolution of 4 cm^{-1} for qualititative measurements and a spectral resolution of 1 cm^{-1} for the determination of the amino group density on the derivatized samples.
The number of primary amino groups per square nanometer on surface functionalized polymer bags (treatment: He + N_2 + H_2) was determined by chemical derivatization with 4-trifluoromethyl-benzaldehyde (TFBA, > 98 %, Sigma-Aldrich) followed by quantitative FTIR-ATR measurements (CD FTIR-ATR) of the absorption band area generated by the vibrations of the C-CF_3 moieties in the resulting 4-trifluoromethyl-benzaldimines. A detailed description of the method is given in [5].
Surface tensions were calculated from contact angle measurements (OCA 60, dataphysics) using the approach of van Oss and Good where the total surface tension of a material *i* can be expressed as the sum of the Lifshitz-van der Waals component and the Lewis acid-base component [6], [7].
As test liquids served water (Mili-Q-grade), ethylene gylcol (> 99%, Sigma-Aldrich) and diiodomethane (> 99 %).
Cell cultivation of bone marrow mesenchymal stem cells was performed at Helmholtz Centre for Infection Research HZI. The cells were stained with DIOC6 and measured with a fluorescence microscope.

3. Results and Discussion

3.1 Surface analysis

Surface modifications of the plastic bags were carried out using several different procedures. On the one hand surface functionalization was performed by defined gas mixtures (pure helium or He + N_2 + H_2) resulting in the incorporation of functional groups on the polymer surface using atmospheric pressure plasmas with a DBD arrangement. On the other hand surface coatings were achieved using the same arrangement, but using helium enriched with suitable film-forming to generate functional groups (-NH_2, Si-OH) as well as Si-O-Si networks on the inner wall of the bag surface. Three different monomers were chosen for plasma-polymerization. Tetramethoxysilane (TMOS) provides Si-OH groups, 3-aminopropyl-trimethoxysilane (APTMS) was used to equip the surface with both Si-OH and primary amino groups. Silicon-free amino-group containing coatings were deposited using 1,2-diaminocyclohexane (DACH).

The results in **Tab. 2** summarize the increase of surface tension due to the incorporation of functional groups depending on the gas mixture used. The increased surface tension on plasma treatment with pure helium is comparable to that of the modified polymer surfaces after incorporation of primary amino groups by plasma treatment in mixtures of helium, nitrogen and hydrogen or helium enriched which amino containing film-forming agents. The reaction of helium with the polypropylene surface leads to the formation of radicals on the polymer surface. Due to diffusion of oxygen through the polymer walls during or after the treatment, oxygen containing functional groups are incorporated on the polymer surface resulting in an increased surface tension.

Tab. 2. Surface tension components and total surface tensions [mN/m] of the treated polymer depending on the gas mixture and the film-forming agent resp. after 10 s of plasma treatment

Gas mixture / film- forming agent	γ_{total} **[mN/m]**	γ_{LW}	γ_{AB}
Pure Helium	34,9	34,5	0,4
Helium + N_2 and 1 % H_2	36,1	33,0	3,1
APTMS	37,7	34,1	3,6
DACH	41,1	40,8	0,3
TMOS	36,5	35,1	1,1
Polypropylene untreated	26,3	26,3	0

The coating of the internal surfaces of the plastic bags was characterized by FTIR-ATR-spectroscopy. To eliminate substrate interference difference spectra were obtained by subtracting a spectrum of an untreated polymer bag from the spectra obtained after the treatment. The FTIR-ATR spectra in **Fig. 2** show the most prominent absorption bands characteristic of the molecular structure of the plasma-polymerized coating. In the case of TMOS-coated polymer bags the dominant peak at approx. 1050 cm^{-1} is attributed to Si-O-Si and Si-O-C vibrations. The absorption band of Si-O-H is located at wave numbers greater than 3000 cm^{-1}. Silicon-free coatings are obtained by coating the polymer bag with 1,2-diaminocyclohexane (DACH). The characteristic absorption bands are identified at ~ 1650 cm^{-1} originating from the deformation vibration of primary and secondary amino groups. N-H stretching vibrations are located at wave numbers > 3000 cm^{-1}. In the case of APTMS-coated polymer bags the deposited coating contains a Si-O-Si network (~ 1100 cm^{-1}), Si-OH (> 3000 cm^{-1}) as well as primary amino groups (~1650 cm^{-1}, > 3000 cm^{-1}).

Regarding different treatment times, it can be seen that the precursor inside the bag is consumed within the first 5 s as no significant differences in the FTIR-ATR spectra are observed for prolonged treatments. To minimize damages of the polymer surface which is known to lead to the generation of low molecular weight oxidized material (LMWOM) [8] or to an etching of the coating the plasma treatment time should be chosen as short as possible.

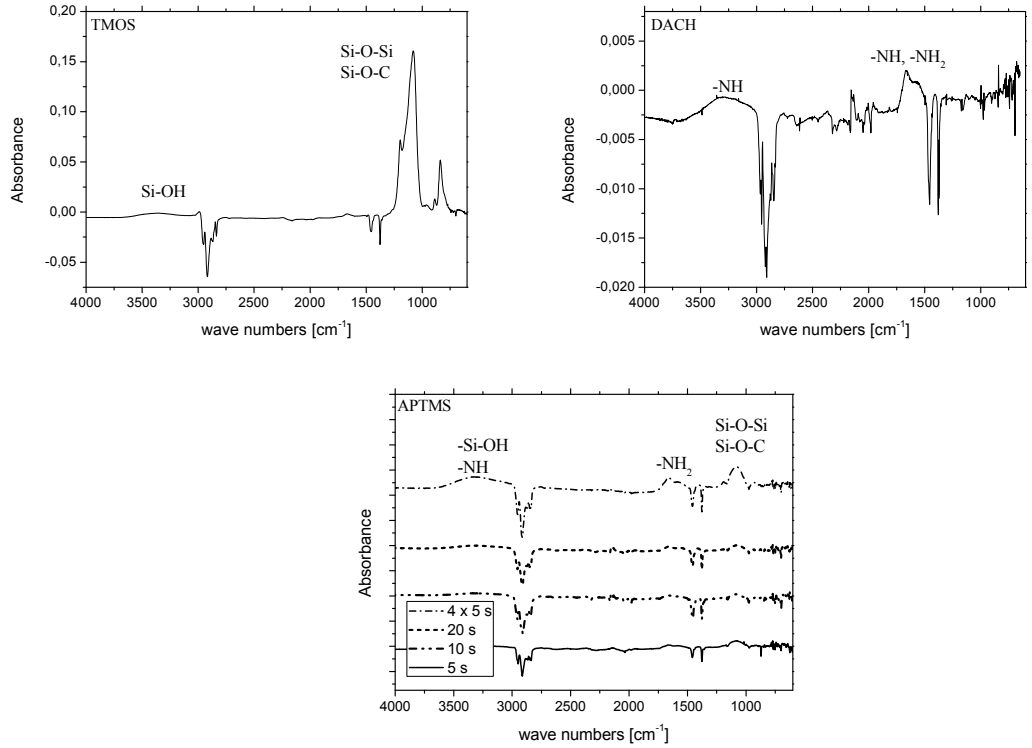


Fig. 2: FTIR-ATR difference spectra of plastic bag coated with tetramethoxysilane (top left), 1,2-diaminocyclohexane (top right) and 3-aminopropyl-trimethoxysilane (bottom)

The number of primary amino groups per square nm was determined by the CD FTIR-ATR measurements as described in [5]. For polymer foils functionalized with gas mixtures containing nitrogen and hydrogen about 0.7 $–NH_2/nm^2$ could achieved after the addition of 9 % nitrogen and 1 % hydrogen and slightly more primary amino groups, about 0.9 $-NH_2/nm^2$ were achieved after the addition of 18 % nitrogen and 2 % hydrogen. By chemical derivatization of APTMS and DACH-coated plastic surfaces only the accessible primary amino groups are detected. In the case of APTMS 1 $-NH_2/nm^2$ was determined after a plasma treatment of 10 s, whereas in the case of DACH up to 4 $-NH_2/nm^2$ were detected under the same process conditions.
The comparatively low amount of primary amino groups can be explained by residues of oxygen in helium as well as by oxygen which diffuses through the polymer foil during plasma treatment as the plastic bags are gas permeable.

3.2. Cell Cultivation

Cell cultivation of bone marrow mesenchymal stem cells was performed at Helmholtz Centre for Infection research. In Fig. 3 the influence of different surface modifications are compared among each other. At day three of cell cultivation there is no significant difference found between the three coatings. The density of growing cells seems to be comparable to cell cultivation on a conventional cell culture plate, whereas on the untreated polymer bag no adherent cell growth is observed. After 14 days of cultivation confluent cell growth is observed on the amino-containing coatings, but on the TMOS-coated plastic surface the cells have detached. The effect of nitrogen-rich plasma polymer films is already described in the literature [9].

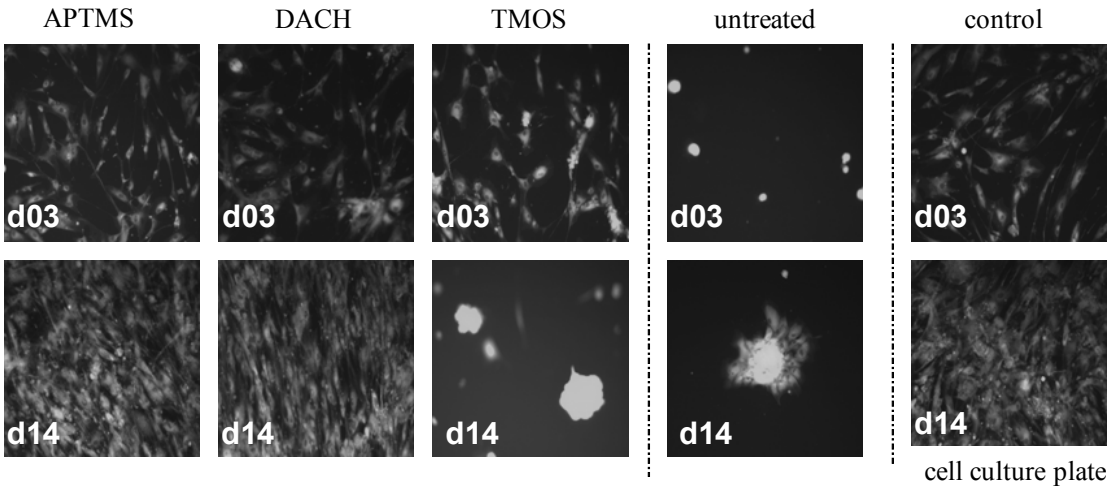


Fig. 3: Cell cultivation of adherent bone marrow mesenchymal stem cells on the modified plastic bags at day 3 of cultivation (above) and at day 14 of cultivation (below). As control serves a commercial availiable cell culture plate, magnification 10x.

4. Conclusions

Using gas mixtures of helium and suitable reactive species or film-forming agents, plastic bags can be modified for the use in adherent cell cultivation. Due to residual oxygen in the gas mixture or the diffusion of oxygen through the gas-permeable polymer wall even the treatment with pure helium leads to a rise in surface tension which is comparable to the surface tension achieved by coating with APTMS or surface functionalization in gas mixtures of helium, hydrogen and nitrogen. Traces of oxygen within the gas mixture also lead to a reduced amount of primary amino groups. Performing cell cultivation of adherent bone marrow mesenchymal stem cells the role of primary amino groups on the surface was highlighted. In the case of TMOS-coated plastic bags only initial adherence was observed, but after 14 days in culture the cells had detached. In contrast, the use of amino-containing monomers leads to confluent cell growth on the modified surfaces. In further experiments the plasma process should be optimized to generate higher concentrations of primary amino groups on the surface, e.g. to perform secondary modifications such as biotinylation or coupling of specific markers.

5. References

[1] R. Dorai and M. J. Kushner, J. Phys. D: Appl. Phys. **36**, 666 (2003).
[2] G. J. Courval, D. G. Gray, and D. A. I. Goring, J. Polym. Sci.: Polym. Lett. Ed. **14,** 231 (1976).
[3] S. Guimond, I. Radu, G. Czeremuszkin, D.J. Carlsson and M.R. Wertheimer, Plasmas Polym. **7**, 71 (2002).
[4] German patent DE102006036536 B3
[5] C.-P. Klages and A. Grishin, Plasma Process. Polym. **5**, 368 (2008).
[6] C. J. van Oss, Interfacial Forces in Aqueous Media, Dekker, New York, (1994).
[7] C. J. van Oss, M. K. Chaudhury, R. J. Good, Chem. Rev. **88** 927 (1988).
[8] L.-A. O'Hare, S. Leadley, B. Parbhoo, Surf. Interface Anal. **33**, 335 (2002).
[9] P.-L. Girard-Laurialt, F. Mwale, M. iordanova, C. Demers, P. desjardins, M. R. Wertheimer, Plasma Process. Polym. **2**, 262(2005).

BIOCIDAL AGENTS IN BIO-DECONTAMINATION BY DC DISCHARGES IN ATMOSPHERIC AIR

Zdenko Machala[1], Lenka Chládeková[1], Michal Pelach[1], Barbora Tarabová[1]

[1]*Division of Environmental Physics, Faculty of Mathematics, Physics and Informatics, Comenius University, Mlynská dolina, 84248 Bratislava, Slovakia*
E-mail: machala@fmph.uniba.sk

Bio-decontamination of water and surfaces contaminated by bacteria (Salmonella typhimurium, Bacillus cereus) was investigated in two types of positive DC discharges in atmospheric pressure air, in needle-to-plane geometry: the streamer corona and its transition to a novel regime transient spark with short high current pulses of limited energy. Both generate cold non-equilibrium plasma. Electro-spraying of the treated water through the needle electrode was applied for the first time and resulted in fast bio-decontamination. Experiments providing separation of various biocidal plasma agents, along with the emission spectra and coupled with oxidation stress measurements in the cell membranes helped better understanding of the mechanisms of microbial inactivation. The indirect exposure of contaminated surfaces to neutral active species was almost as efficient as the direct exposure to the plasma, whereas applying only UV radiation from the plasma had no biocidal effects. Radicals and reactive oxygen species were identified as dominant biocidal agents.

1. Introduction

Nonequilibrium plasmas, thanks to their reactive nature, find numerous biological and bio-medical applications, especially at atmospheric pressure for no need of costly vacuum equipment. Atmospheric pressure plasmas applied for sterilization and bio-decontamination are mostly generated by radio-frequency (RF) [1-2] discharges, and various plasma jets and afterglows [1-5], usually in rare gases (He or Ar) with/without admixtures of O_2 (or H_2O). They have been tested on a large variety of prokaryotic microorganisms (bacteria, spores, viruses) and some eukaryotic yeasts, fungi and microalgae, resulting in partial disinfection up to complete sterilization. Atmospheric air plasmas have additional advantages of no need of special gases and an easy application in ambient environment. Bio-decontamination by air plasmas was tested in DC [3, 6], dielectric barrier (DBD) [4, 7-10], RF [1], and pulsed discharges [4, 7]. The plasmas can be also generated directly in water or on water-air boundary [3, 8-9, 11], which is of great interest for water decontamination.

In bio-decontamination by plasma, it is crucial to understand the role of various mechanisms involved. The significant mechanisms depend on the plasma composition (gas), temperature, treated microorganisms and the environment (air, water, surfaces, etc.). In atmospheric pressure plasmas, the major role is typically attributed to radicals and reactive oxygen species (ROS, e.g. OH, O, O_3) [1, 2, 3-4, 6, 9-11] and to charged particles, especially O_2^- [7] affecting the cell membranes. UV radiation plays a role only if photons in UV C germicide region (220-280 nm) or in vacuum UV are produced [10-11]. In cold air discharges (corona, DBDs, pulsed discharges), NO γ and other sources of UV C or VUV are usually not generated, so radicals and ROS are identified as the dominant bio-inactivation agents [3-5, 8-9].

In this paper, the biocidal effects of two plasma sources in atmospheric air with water are investigated – positive DC *streamer corona* (SC) and a novel regime named *transient spark* (TS). Despite DC applied voltage, these discharges have a pulsed character with nanosecond repetitive pulses. We focus on the identification of the dominant plasma agents in bio-inactivation by coupling the electrical discharge characteristics, their emission spectra, and biocidal effects. Comparing direct with indirect plasma effects enables separation of various biocidal plasma agents. In addition, measurements of the oxidative stress induced in microbial cells applied for the first time in plasma bio-decontamination enable further indicate their respective roles.

2. Experiments

2.1 Experimental set-ups

The experimental setup for fundamental investigations of the DC discharges in point-to-plane geometry, with a high voltage (HV) hollow needle electrode enabling water flowing through the

discharge zone and a plane or mesh electrode is depicted in figure 1. The gap spacing was varied from 5-10 mm. A positive DC high voltage was applied through the ballast resistor *R* (20 MΩ for SC and ~5 MΩ for TS). The discharge voltage was measured by a high voltage probe Tektronix P6015A. The discharge current was measured: on a 50 Ω (SC) or 1 Ω (TS) resistor and by a Rogowski current monitor PEARSON 2877. The current and voltage signals were processed by a digitizing 200 MHz oscilloscope Tektronix TDS 2024. The discharges were photo- and video-documented with digital cameras Olympus E410 or Nikon Coolpix S10.

The emission spectroscopy optical system comprised a dual fibre-optic spectrometer Ocean Optics SD2000 for fast scanning in the UV and VIS-NIR regions (200-500 and 500-1050 nm, resolution 0.6–1.2 nm), fused silica lenses, and fibre optics. The discharge set-up was placed in a Faraday cage together with the optical components mounted on lateral and vertical translation stages.

The bio-decontamination effects of the DC discharges were tested on flowing water of ambient temperature. We also compared direct and indirect plasma effects on contaminated solid agar surfaces (Figure 2). A needle electrode was placed about 1 cm above the agar surface in the centre of the Petri dish and the discharge was applied for 1 or 2 min. In direct treatment, the agar was grounded with a wire. Indirect plasma effects on the contaminated agar were tested by:

1) placing the grounded mesh electrode ~2 mm above the agar, this shielded the electric field and trapped the charged particles, letting but neutral particles and partial UV light to reach the surface;
2) placing the 3 mm thick quartz window onto the agar surface and a grounded ring electrode on its top, this let only the light emitted from the discharge to reach the agar, including UV. We also tested MgF_2 window transmitting vacuum UV.

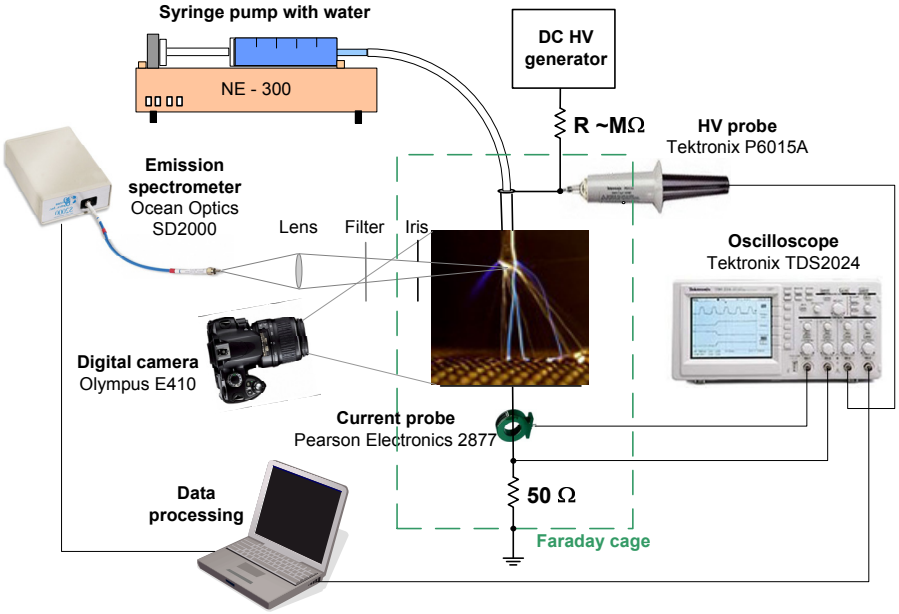


Fig. 1. Experimental set-up for DC discharges, with a high voltage hollow needle electrode enabling water flowing through the discharge zone and a plane or mesh electrode.

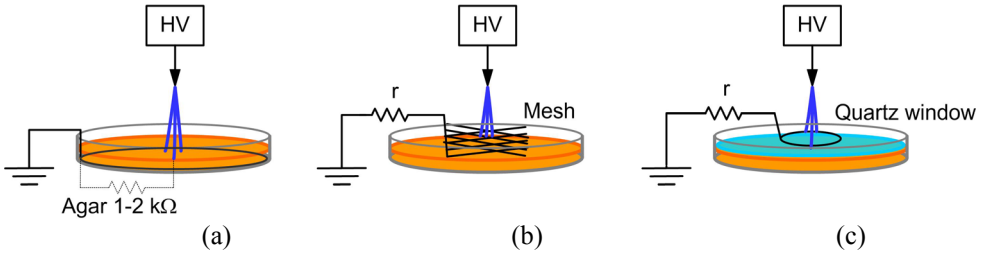


Fig. 2. Electrode arrangements for (a) direct and (b, c) indirect plasma treatment of contaminated agar plates. (b) Mesh electrode ~2 mm above agar surface trapped the charged particles and shielded the electric field. (c) Quartz (MgF_2) window only transmitted light from the discharge (including UV).

The agar in the direct treatment (Figure 2a) represents a certain electrical resistance, typically 1-2 kΩ depending on the water content. In indirect set-ups (Figure 2b,c), a small resistor *r* was inserted between the mesh (or ring) and the ground to simulate the agar's resistance. Its exact value was set empirically from case to case to make the discharge pulses of about the same amplitude and shape as in the direct treatment on agar. This ensured the same discharge properties in all three set-ups.

2.2. Treated microorganisms and microbial cultivation

Bio-decontamination effects of investigated DC discharges were tested on selected Gram-negative bacteria *Salmonella typhimurium* and Gram-positive *Bacillus cereus* in distilled water with initial populations 10^3 - 10^7 colony forming units per mL (CFU/mL), or directly spread on the solid nutrient (agar, Roth Ltd.) on a Petri dish, about 10^6 per dish. The microbial cultivation was carried out in a sterile environment. The plasma experiments were performed with both discharges, at various parameters and treatment times and repeated 5-8 times. 3–4 Petri dishes from each sample were taken for statistical evaluation. These were incubated during 12–24 h in a thermostat at 37 °C. The grown CFUs on the samples were counted and evaluated.

2.3. Measurements of the oxidative stress

Interaction of ROS with the bacterial cell membranes results in the peroxidation of membrane lipids. The final product of lipoperoxidation is malondialdehyde (MDA), quantifiable by spectrophotometry after the reaction with thiobarbituric acid (TBA) at 90–100 ◦C [12]. This method of *thiobarbituric acid reactive substances* (TBARS) was applied for the first time to measure the oxidative stress induced in bacteria in water exposed to SC and TS. We assigned the TBARS concentrations from the absorbance of MDA at 532 nm from Lambert-Beer's law with absorption coefficient 1.57×10^5 mol^{-1} L cm^{-1} [12].

3. Results and discussion

3.1. Applied DC discharges and their emission

Two types of positive DC discharges operating in atmospheric air with water were investigated: a well-known *streamer corona* (SC), and a novel *transient spark* (TS). These discharges generate non-equilibrium plasmas inducing various chemical and biological effects important in bio-decontamination. Their electrical parameters and emission spectra were documented in detail in our previous works [13-14]. SC is typical with small current pulses of streamers (~10 mA) with a repetitive frequency of ~10 kHz and generates cold plasma (~300 K).

With further voltage increase, the streamers establish a conductive channel that gradually leads to the spark pulse. However, when the sparks forms, it is in our set-up only transient since the discharged energy given by the external circuit is small (0.1–1 mJ). This *transient spark* is a repetitive (0.5–10 kHz) streamer-to spark transition discharge, with each spark pulse (~1 A) preceded by one or a sequence of streamer pulses. Thanks to the very short pulse duration (~10–100 ns) given by the small circuit capacity and a limiting series resistor *R*, the plasma cannot reach equilibrium conditions and remains at relatively low gas temperature, depending on frequency (~500–1500 K).

We employed optical emission spectroscopy, a powerful technique of plasma diagnostics to both SC and TS. They both generate cold, nonequilibrium plasmas (300–550 K) in the discharge channel. OES characteristics of the applied discharges described in detail in [13] showed that electrons with the highest energies were present in TS. These electrons initiate dissociations, ionizations and excitations of various species. Atomic O, N and H radicals, and the N_2^+ ions have only been detected in TS, and there were a lot of OH radicals. Part of O radicals reacts with air O_2 and forms ozone O_3. There was no UV C radiation detected from SC and TS.

3.2. Flowing water treatment through the stressed electrode

The contaminated water flew directly through the stressed hollow needle electrode, and so through the plasma active zone in its proximity, which substantially improved the volume efficiency compared to our previous set-ups for water treatment [15]. The effect of electrostatic spraying (electro-hydro-dynamic atomization, EHDA) occurred when the high voltage was applied on the needle electrode [16]. The temperature of the treated water did not change in SC and was increased by maximum 10 K in TS. The lethal heat effect of the discharges to bacteria can be excluded.

3.3. Oxidative stress induced in bacteria

Figure 3 shows the TBARS concentration gain Δc(TBARS) correlated with the bio-decontamination efficiency of SC and TS applied to the electro-sprayed water with *S. typhimurium* and *B. cereus*. The same samples were irradiated by biocidal UV C radiation (Hg lamp, 254 nm, 1 min) for comparison. UV C radiation induced almost no Δc(TBARS) despite its efficiency was very high. Obviously, UV dominant biocidal mechanism is not peroxidation of cell membranes. On the contrary, SC and TS treatments significantly enhanced Δc(TBARS). This indicates that oxidations of cell membranes by ROS are important in microbial inactivation. More ROS is linked with the higher efficiency.

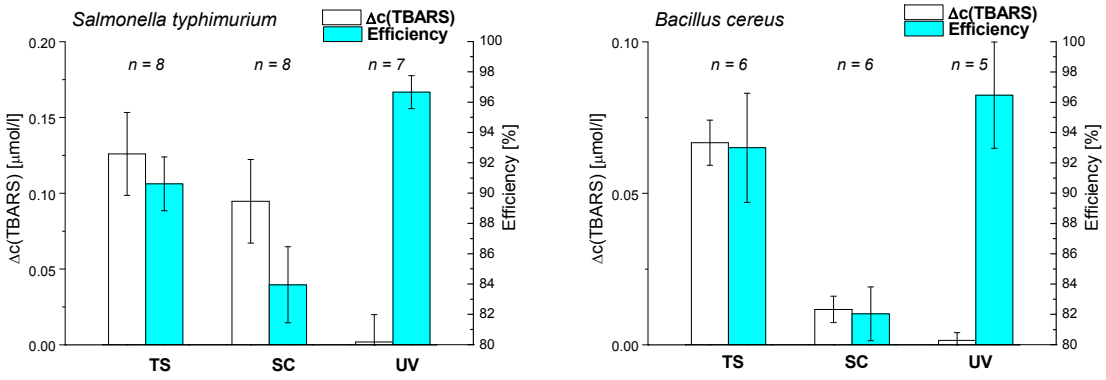


Fig. 3. TBARS concentration gains and decontamination efficiencies of *S. typhimurium* (left) and *B. cereus* (right) in water treated by SC and TS with electro-spray, compared with 1 min exposure to UV C (shown with standard error of the mean, *n* – number of repeated experiments).

3.4. Direct vs. indirect plasma treatment

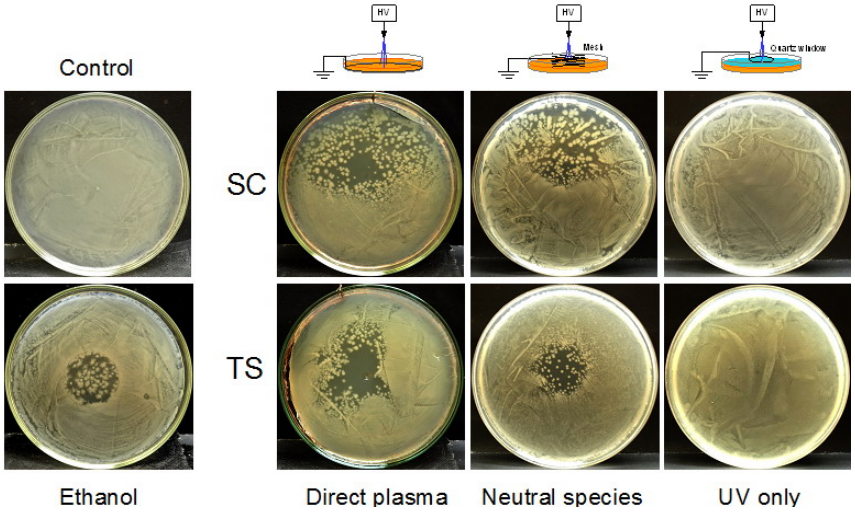


Fig. 4. Photographs of Petri dishes with contaminated agar by *S. typhimurium*; left side: untreated control and treated by ethanol, right side: treated by SC (upper row) and TS (lower row) direct, neutral species only, and UV light only. Results with *B. cereus* were similar.

We compared direct SC and TS plasma treatment with 2 types of indirect exposure described in section 2.1. Figure 6 shows the photographs of the Petri dishes with contaminated agar after direct and both indirect treatments, together with the untreated control sample, and a sample treated with 50 μL drop of liquid ethanol (96%) for comparison. The effects of plasma (and ethanol) on contaminated agar are clearly visible as dark voids, whereas control sample is homogeneously covered by cultivated bacteria (bright). Dark voids with bright spots represent incomplete decontamination, the spots are CFUs grown from single bacteria. With respect to the total number of bacteria spread on one Petri dish

(10^6), a few tens of survived bacteria that cause these bright CFUs in the voids are quite negligible.
Both direct plasma and indirect exposure to neutral reactive species (and partial UV) caused apparent bio-decontamination (voids) with on tested bacteria. SC resulted in a larger treated area on the Petri dish, likely due to the electric wind that drives active species from the point towards and along the agar surface in one preferential direction. TS treatment was localized in the dish centre but more intense.
Interestingly, there was very little difference between the direct and indirect plasma treatments with both discharges. This indicates that neutral reactive species are crucial even in the direct exposure. Exposure to the UV light only, transmitted by quartz or MgF_2 windows demonstrated no visible decontamination. This correlates with the emission spectra of SC and TS lacking any UV C or VUV.
Similar effects of direct and indirect plasma treatment agree with the emission spectra, oxidation stress measurements and our previous findings [15]. Apparently, radicals and ROS (O, N, H, OH, O_3, O_2^-) represent the dominant biocidal agents in atmospheric air SC and TS discharges.

4. Conclusions

Bio-decontamination of water and surfaces contaminated by bacteria (*S. typhimurium* and *B. cereus*) was tested in two types of positive DC discharges in atmospheric pressure air in point-to-plane geometry. The streamer corona with small current pulses generates cold non-equilibrium plasma. With increasing applied voltage, the streamers transit to the novel regime transient spark with short (<100 ns) current pulses (~1-10 A) of 0.5–10 kHz repetitive frequency and very limited energy. Thanks to the very short spark pulse duration, the TS plasma remains relatively cold (~500 K).
Both SC and TS were found very efficient when the contaminated water was sprayed through the high voltage needle electrode and thus through the active discharge zone. EHDA effect occurring with corona discharge in this regime applied for the first time enhanced the efficiency of the process.
The comparisons of direct and two types of indirect exposure of contaminated agar plates to the plasma of SC and TS enabled the separation of the various biocidal agents. We demonstrated that the direct plasma and indirect exposure to separated active neutral species had almost the same effect on bacteria. On the other hand, separated plasma radiation, including UV, had no significant effect. These investigations, together with the emission spectra, indicated the major role of radicals and reactive oxygen species (O, OH, O_3). Their role in the plasma treatment was confirmed by the absorption spectroscopic detection of the products of cell membrane oxidation stress in TBARS method.
In summary, we demonstrated that cold atmospheric air DC discharges can be efficiently used for bio-decontamination of water and surfaces. The dominant biocidal plasma agents are radicals and ROS, which agrees with findings published by many other authors.

Acknowledgements. Effort sponsored by Slovak grant agency VEGA 1/0293/08 and Slovak Research and Development Agency APVV SK-CZ-0179-09.

5. References

[1] Montie T C, Kelly-Wintenberg K and Roth J R 2000 *IEEE Trans. Plasma Sci.* **28** 41
[2] Brandenburg R, Ehlbeck J, Stieber M, Woedtke T v et al. 2007 *Contrib. Plasma Phys.* **47** 72
[3] Akishev Yu, Grushin M, Karalnik V, Trushkin N, et al. 2008 *Pure Appl. Chem.* **80** 1953
[4] Deng X, Shi J, and Kong M G 2006 IEEE *Trans. Plasma Sci.* **34** 1310
[5] Lu X, Ye T, Cao Y, Sun Z, Xiong Q, Tang Z, et al. 2008 *J. Appl. Phys.* **104** 053309
[6] Sigmond R S, Kurdelova B and Kurdel M 1999 *Czech. J. Phys.* **49** 405
[7] Fridman G, Brooks A D, Balasubramanian M, et al. 2007 *Plasma Process. Polym.* **4** 370
[8] Tang Y Z, Lu X P, Laroussi M and Dobbs F C 2008 *Plasma Process. Polym.* **5** 552
[9] Qiong T, Wenju J, Zhang Y, Zhishan Y and Mariana L T 2009 *J. Phys. D: Appl. Phys.* **42** 095203
[10] Laroussi M and Leipold F 2004 *Int. J. Mass Spectrom.* **233** 81
[11] Lukeš P, Člupek M, Babický V and Šunka P 2008 *Plasma Sources Sci. Technol.* **17** 024012
[12] Bachowski G J, Pintar T J and Girotti A W 1991 *Photochem. Photobiol.* **53** 481
[13] Machala Z, Janda M, Hensel K, et al. 2007 *J. Mol. Spectrosc.* **243** 194
[14] Machala Z, Jedlovský I and Martišovitš V 2008 *IEEE Trans. Plasma Sci.* **36** 918
[15] Machala Z, Jedlovský I, Chládeková L, et al. 2009 *Eur. Phys. J. D* **54** 195

[16] Borra J-P, Ehouarn P and Boulaud D 2004 *J. Aerosol Sci.* **35** 1313

SELECTIVE INACTIVATION OF *STAPHYLOCOCCUS EPIDERMIDIS* ON HUMAN KERATINOCYTES BY NON-THERMAL ATMOSPHERIC PRESSURE PLASMA JET (APPJ)

Kati Landsberg[1], Kristian Wende[2], Eckhard Kindel[1], Ronny Brandenburg[1], Ulrike Lindequist[2], Klaus-Dieter Weltmann[1], Thomas von Woedtke[1]

[1] *Leibniz Institute for Plasma Science and Technology (INP Greifswald), Felix-Hausdorff-Str. 2, 17489 Greifswald, Germany*

[2] *Institute of Pharmacy, Ernst Moritz Arndt University Greifswald, F.-L.-Jahn-Str. 15, 17489 Greifswald, Germany*

E-mail: landsberg@inp-greifswald.de

Direct medical application of atmospheric pressure plasma is a growing field of research interest. One focus is on plasma supplemented wound healing. Normally, wound healing starts a few minutes after tissue injury. However, under certain pathological conditions this process can be impeded and chronic wounds may arise. A main problem of chronic wounds is its contamination or infection by microorganisms. It is well known that microorganisms can be inactivated by atmospheric pressure plasma treatment. However, if plasma will be used to treat chronic wounds, any negative effects on healthy cells and tissue have to be excluded. Using a simple *in vitro* wound healing model (scratch assay), the response of human skin cells (keratinocytes) to plasma treatment, with and without co-cultivated microorganisms is investigated. *S. epidermidis* was used as test microorganism because it is an opportunistic pathogen member of the human skin flora, which can be very dangerous to immunocompromised patients. We examined the growth rate of adherent keratinocytes in a modified scratch assay with and without *S. epidermidi*s co-cultivation and the response of this system to argon plasma treatment using a non-thermal atmospheric pressure plasma jet (APPJ). It could be demonstrated that microorganisms are inactivated effectively by plasma treatment. Moreover, the healing rate of plasma treated artificial "wounds" contaminated with microorganisms could be improved compared to the untreated control. With these results a first simple proof of the potential of atmospheric pressure plasma to act selectively in wound antiseptics was given.

1. Introduction

In Germany alone, some 2.5 million people living with poorly healing chronic wounds. Colonization or infection by microorganisms is one of the main reasons for massive impediment and delay of healing and tissue repair processes possibly leading to chronicity of the wound. Therefore, effective wound antisepsis is a prerequisite for an undisturbed and uncomplicated wound healing. In medicine various antiseptic agents are used for antimicrobial treatment of wounds [1]. Ideally, wound antiseptics should act selectively i.e. should inactivate microorganisms without deterioration of the surrounding tissue. In best case, a wound antiseptic has an additional potential to stimulate tissue repair. However, one of the major drawbacks of actually used wound antiseptics, like octenidine, povidone-iodine and polihexanide, is that its antimicrobial effects are mostly accompanied by impediment of tissue regeneration.

A promising alternative to chemical antiseptics may be non-thermal atmospheric pressure plasmas. The possibility to inactivate microorganisms by non-thermal plasmas has been shown several times [2]. Up to now such applications are mainly focused on surface decontamination, e.g. for heat-sensitive medical devices or pharmaceutical packing materials [3]. The direct application of atmospheric pressure plasmas on the human body for wound treatment purposes represents a new quality of plasma application and is one of the main tasks of the new research field called plasma medicine. However, to estimate the healing potential of physical plasmas and to exclude unwanted side effects, research in plasma medicine has to be accompanied by detailed *in vitro* studies using cell-based models. The aim of our work was to adapt the scratch assay, a well-established *in vitro* wound

healing assay [4], as a basic test model to investigate the selective antiseptic effectivity of an atmospheric pressure plasma jet (APPJ).

2. Material and Methods

Cell line: Adherent human keratinocyte cells (HaCaT, provided by Prof. Fusenig, German Cancer Research Center, Heidelberg, Germany) were cultivated in RPMI 1640 cell culture medium (Roswell Park Memorial Institute Lonza, Verviers, Belgium) supplemented with 1 % penicilline / streptomycine (Biochrom, Berlin, D) and 8 % fetal calf serum (Sigma Aldrich, Taufkirchen, Germany) at 37 °C / 5 % CO_2. Cells were seeded at a density of 4 * 10^5 cells per 60 mm plastic dish. The tests were performed after 4 days at 100 % confluency.

Scratch Assay: To simulate the situation of mammalian cells in connective tissue, the original scratch wounding assay [5] was modified. Following mechanical scratching, confluent cells were protected by a 0.6 mm 1,5 % agarose-RPMI overlay. After 10 min gelling time 4 ml fresh RPMI 1640 were added. In case of cell co-cultivation with *S. epidermidis*, an additional scratch was made to penetrate the agarose layer (Fig. 1). The size of the scratch was observed by microscopy and recorded subsequently by measurement of the scratch width using Adobe Photoshop Software. Scratch reduction was calculated by subtraction of scratch width at t=n hours from scratch width at t=0 hours.

Plasma treatment: The APPJ (kINPen 09, INP Greifswald, Germany) used in this paper is shown in Figure 2. The device has got the CE marking which certifies that the product has met EU consumer safety, health or environmental requirements. The device consists of a hand-held unit (Dimensions: length = 170 mm, diameter = 20 mm, weight = 170 g) for the generation of a plasma jet at atmospheric pressure, a DC power supply (system power: 8 W at 220 V, 50/60 Hz), and a gas supply unit. The device consists of a quartz capillary (inner diameter 1.6 mm) containing a centered 1 mm pin-type electrode. In the continuous working mode, a high frequency (HF) voltage (1.1 MHz, 2-6 kVpp) is coupled to the pin-type electrode. The plasma is generated from the top of the centred electrode and expands to the surrounding air outside the nozzle. The plasma jet is about 7 mm long and about 1 mm wide. Plasma temperature did not exceed 50 °C at the tip of the visible plasma jet [5].The scratched region was plasma treated in that way that the visible tip of the plasma jet was just in contact with the scratched cell layer or agarose overlay. The length of the treated scratch line was 40 mm. The speed of the plasma jet over ground was 10 mm/s. Treatment time was 40 s.

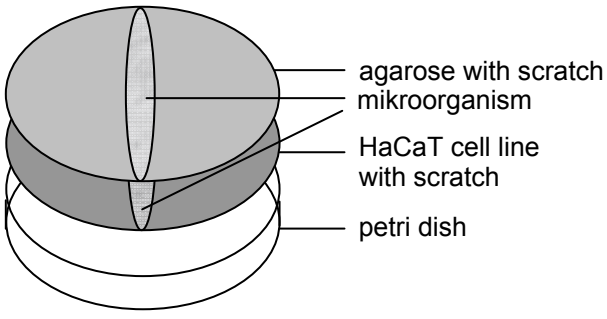


Fig. 1: Schematic assembly of the modified atmospheric scratch assay

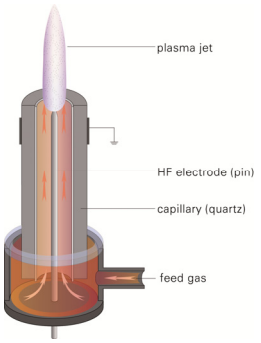


Fig. 2: Schematic setup of the atmospheric pressure plasma jet

3. Results and Discussion

The aim of the present work was to investigate the selective interaction of an atmospheric pressure plasma jet with eukaryotic cells (mammalian cells) in the presence of prokaryotic cells (microorganisms). We used the immortalized, human, non-tumorigenic keratinocyte cell line HaCaT, which is often deployed as a substitute for native human keratinocytes. This spontaneously transformed epithelial cell line, which largely keeps their proliferation potential and their biochemical

performance in culture in contrast to other immortalized cell lines, comes with the same differentiation properties like human keratinocytes [6].

In the well-established scratch assay used in this study, mechanically injured (scratched) keratinocytes showed rapid and directed proliferation in case of damage of the confluent cell layer. Similar to the *in vivo* situation, mechanical injuries (scratches) of two-dimensional keratinocyte layers are closing from the borders to the centre. (Fig. 3). Control HaCaT cells are closing such an artificial wound with a speed of about 1 mm/day.

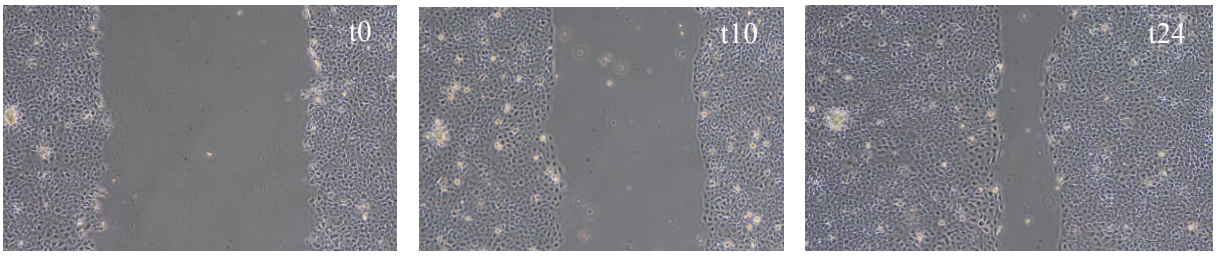


Fig. 3: HaCaT human keratinocytes immediately (t_0), 10 h (t_{10}) and 24 h (t_{24}) after artificial injury by mechanical scratching („wounding“)

To come near to in-situ conditions of mammalian cells in connective tissues, the cell layer was shielded by a carbohydrate gel overlay comparable to the outer layer of wounds caused by secretion (ichor). It was shown that this overlay allows penetration of low-molecular reactive species. Additionally, the layer effectively prevents drying phenomena caused by the APPJ gas flow but leaves cell performance unchanged. Time to “wound” closure in the scratch assay remains unaltered compared to uncovered cells (Fig. 4). Due to the agarose overlay, the cells were additionally protected from the plasma jet temperature. The physiological temperature for the optimal growth of eukaryotic cells is 37 °C and a deviation of 3-4 °C in either direction will be tolerated [7]. HaCaT keratinocytes were even shown to have increased proliferation rates at 38.5 °C [4]. A significant decrease of (mammalian) cell survival might be observed at temperatures above 42 °C and long incubation times (>50min).

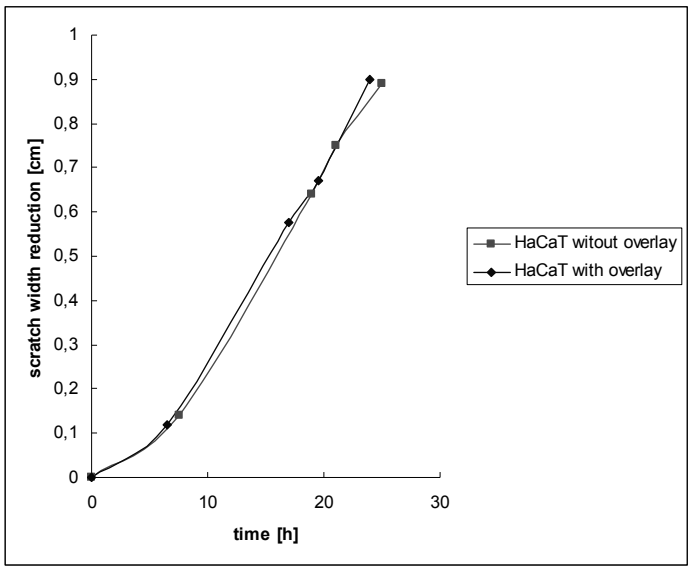


Fig. 4: Scratch assay using HaCaT human keratinocytes; comparison of scratch assay with agarose overlay and without agarose overlay

To simulate the situation in an infected wound, a suspension containing 10^4 microorganisms (*S. epidermidis*) was placed directly into the scratch line. Subsequently, this area was treated by APPJ for 40 s and cell proliferation was monitored. As it is shown in Figure 5, infected and APPJ treated

cells showed a better overall performance compared to infected but not APPJ treated cells. After 24 hours cell growth slowed down probably due to strong growth of remaining microorganisms (Fig. 5, ◆). In infected but not APPJ treated cell cultures, besides a slower "wound healing" in general due to the higher microorganism load, cell detachment was found and scratch width increased again after about 24 hours (Fig. 5, ■).

In general it is not necessary to sterilize colonized or infected wounds, but to reduce the microbial load below a critical colonization rate. Commonly, a contamination rate of 10^5 viable microorganisms per gram of tissue is given as critical value for wound infection but this depends strongly on patients' individual situation. However, a reduction of microbial load will result in an improvement of wound healing at organisms with otherwise intact immune status [8]. A considerable reduction of the microorganisms was shown by plasma treatment. Immediately after addition of *S. epidermidis* in the produced "wound" a plasma treatment followed. The treated suspension with microorganisms was centrifuged. The same was done with an untreated microorganism suspension. The resulting microorganism cell pellets showed significant differences indicating a substantial inactivation of the microbial load by plasma treatment (Fig. 6).

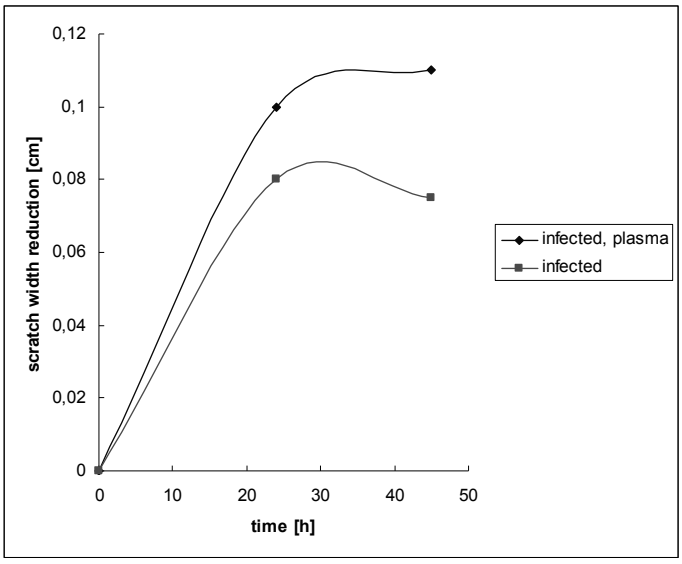


Fig. 5: Scratch assay using HaCaT human keratinocytes: performance of cells after infection. Comparison of scratched cells treated with APPJ (infected, plasma) and cells without APPJ treatment (infected)

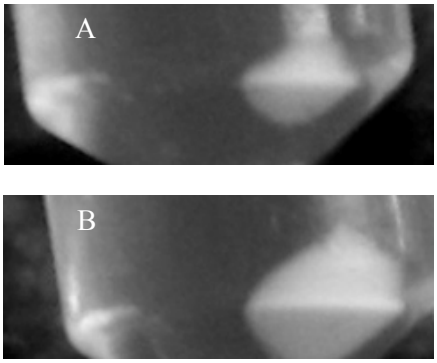


Fig. 6: Microorganism cell pellet after 40 s plasma treatment (A), and without plasma treatment (B)

4. Conclusions

Human keratinocytes did not lose the ability of proliferation after injury by mechanical influences. Moreover, cells covered with an agarose layer showed identical growth characteristics after artificial "wounding" compared to cells without agarose overlay. Consequently, the practicability of the modified scratch assay as in *in vitro* test model to investigate biological effects of an APPJ was proved.

An APPJ treatment of 40 s reduced the cell-growth impeding activity of the co-cultivated microorganisms markedly whereas the ability of human keratinocytes to proliferate was kept. A fast and sustained closure of an artificial "wound" (scratch) occurred in the plasma treated systems, only. Contaminated but not APPJ treated systems were overgrown by *S. epidermidis* right from the start of the experiment resulting in impeded cell growth, cell detachment and death. Using this simple *in vitro* wound healing model, the potential of atmospheric pressure plasma to allow a selective antiseptic treatment was demonstrated in principle.

Acknowledgements. This study was realized within the joint research project “Campus PlasmaMed” supported by the *German Federal Ministry of Education and Research* (grants no. 13N9774 and 13N9779).

5. References

[1] White R J and Cutting K F 2006 *Ostomy Wound Management* **52** 50.
[2] Laroussi M 2005 *Plasma Processes and Polymers* **2** 391.
[3] Weltmann K-D, Brandenburg R, von Woedtke Th, Ehlbeck J, Foest R, Stieber M, Kindel E 2008 *Journal of Physics D: Applied Physics* **41** 631.
[4] Matsuura K, Kuratani T, Gondo T, Kamimura A, Inui M 2007 *European Journal of Pharmacology* **563** 83.
[5] Weltmann K-D, Kindel E, Brandenburg R, Meyer C, Bussiahn R, Wilke C, von Woedtke Th 2009 *Contributions to Plasma Physics* **49** 631
[6] Boukamp P, Petrussevska R T, Breitkreutz D, Hornung J, Markham A, Fusenig N E 1988 *Journal of Cell Biology* **106** 761
[7] Hildebrandt B, Wust P, Ahlers O, Dieing A, Sreenivasa G, Kerner T, Felix R, Riess H 2002 *Oncology/Hematology* **43** 33.
[8] Robson M C and Heggers J P 1970 *Journal of Surgical Oncology* **2** 379.

PLASMA-WATER-INTERACTIONS IN AMBIENT AIR: CHEMICAL AND ANTIMICROBIAL IMPACTS

Katrin Oehmigen, Ronny Brandenburg, Jörn Winter, Marcel Hähnel, Klaus-Dieter Weltmann, Thomas von Woedtke

Leibniz Institute for Plasma Science and Technology e.V. (INP Greifswald)
Felix-Hausdorff-Str. 2, D-17489 Greifswald, Germany
Email: oehmigen@inp-greifswald.de

Indirect plasma treatment of non-stirred distilled water (5 ml) by surface dielectric barrier discharge (DBD) in ambient air results in acidification and generation of nitrate (NO_3^-), nitrite (NO_2^-) and hydrogen peroxide (H_2O_2). After 30 min plasma treatment, pH<2.8 was found as well as concentrations of 113 mg · l^{-1} NO_3^-, 1.5 mg · l^{-1} NO_2^-, and 18 mg · l^{-1} H_2O_2, respectively. Furthermore, high concentrations (10^6 - 10^8 cfu · ml^{-1}) of suspended vegetative microorganisms like *Escherichia coli* were inactivated in non-buffered aqueous media within 5 – 15 min plasma treatment. To clarify possible mechanisms of reactive species generation as well as of microorganism inactivation in plasma-treated water, the interface between plasma and liquid phase was analyzed by Fourier transformed infrared spectroscopy (FT-IR) and optical emission spectroscopy (OES). Neither UV-C radiation nor cytotoxic nitric oxide ($NO^•$) or hydroxyl radicals ($HO^•$), but nitrous oxide (N_2O), ozone (O_3) and nitric acid (HNO_3) were measured. Possible reactions of these gaseous molecules with the aqueous liquid could result in acidification and generation of NO_3^-, NO_2^- and H_2O_2. Furthermore, these species detected in the gas as well as liquid phases, could serve as reaction partners to generate $NO^•$, $HO^•$, nitrogen dioxide ($NO_2^•$), pernitro acid (ONOOH) and hydroperoxy radicals ($HOO^•$) in the liquid which could be responsible for antimicrobial effects.

1. Introduction

Inactivation of microorganisms in liquids by plasma treatment is a well known phenomenon. It was demonstrated both by direct plasma treatment, i. e. plasma generation directly in or in close contact with liquids [1-3], and by indirect plasma treatment where the plasma is generated in close vicinity to but without direct contact with a liquid surface [4]. In several studies, acidification and generation of nitrate, nitrite and hydrogen peroxide was found as a result of plasma treatment [3-7]. The aim of this paper is to analyze the genesis of low-molecular reactive species in non-stirred distilled water after indirect treatment by a surface dielectric barrier discharge (DBD) in ambient air. Interpretation of data from plasma diagnostics and liquid analytics combined with theoretical considerations and microbiological investigations will help to get more insight into the complexity of plasma-water interactions as well as into possible mechanisms of microbial inactivation

2. Experimental Part

Surface dielectric barrier discharge:

Plasma treatment of a 5 ml liquid volume was realized using a surface dielectric barrier discharge (DBD) arrangement based on an electrode array consisting of 1.5-mm-thick epoxy-glass fiber bulk material for circuit boards (50 mm diameter; breakthrough voltage of 40 kV · cm^{-1}) with two 35-µm-thick copper electrodes (Fig. 1). On the one side, the high-voltage part of the DBD array had an etched line-like structure consisting of four concentric 0.75-mm-wide ring-shaped electrodes (diameter of the outer ring: 35 mm; distances between the ring-shaped electrodes: 3 mm). On the other side a 35-mm-diameter round non-structured flat copper surface served as counter electrode at ground potential. This electrode array was mounted by a special construction into the upper shell of a petri dish (60 mm diameter) in that way that the distance between the high-voltage electrode surface and the surface of a liquid in the lower shell of the petri dish was adjusted at 5 mm. All experiments are performed at ambient air conditions using a pulsed sinusoidal voltage of 10 kV_{peak} (20 kHz) with a 0.413/1.223 s plasma-on/plasma-off time. Energy of 2.4 mJ was dissipated into the plasma in each cycle of high voltage [4].

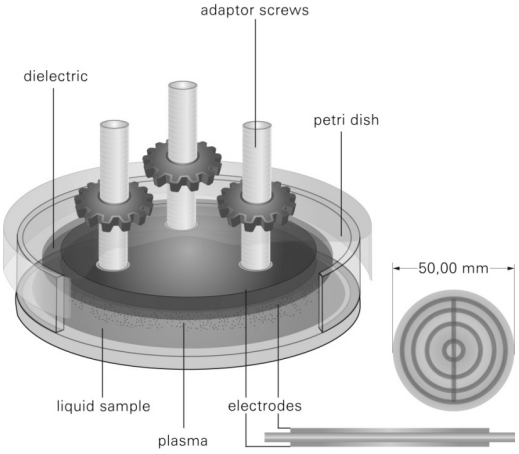


Fig. 1. Schematic drawing of the indirect surface DBD arrangement [4].

Physical methods:
Optical emission spectroscopy (OES) in the UV spectral range was performed using a compact spectrometer (AvaSpec-2048, Avantes) with an entrance slit of 25 µm and a spectral resolution of 0.6 nm. Due to the small plasma intensity a large exposure time of 10 s and a two scan average was necessary to obtain a valuable spectrum.
The Fourier transformed infrared spectroscopy (FT-IR) was performed with the multicomponent FT-IR Gas gas analyser Gasmet CR-2000 (ansyco). For data analyzing the software CALCMET was used.
Chemical methods:
For all photometric measurements a UV/VIS Spectrophotometer SPECORD® S 600 (analytic jena GmbH, Jena, Germany) was used. Nitrate as well as nitrite concentrations in plasma treated distilled water are estimated by photometric analysis using commercially available test kits (Spectroquant®, Merck). Nitrate reaction with 2,6-dimethylphenol gives, after a reaction time of ten minutes 4-nitro-2,6-dimethylphenol, an orange colored product, whose absorption was measured at 340 nm. Nitrite reacts with sulfanilic acid and N-(1-naphthyl)-ethylen diamine hydrochloride via azo sulfanilic acid to a magenta colored azo dye whose absorption at 525 nm was measured. Hydrogen peroxide detection based on the reaction of titanyl sulfate to yellow-colored peroxotitanyl sulfate, which was detected at 405 nm.
For pH measurement, a semi-micro pH-electrode (4.5 mm diameter; SENTEK P13, Sentek Ltd., UK) was used.
Biological methods:
As test microorganism overnight cultures of *Escherichia coli* NTCC 10538 (Institute of Hygiene and Environmental Medicine, University of Greifswald, Germany) were diluted using physiological saline (NaCl 0.85 %; 8.5 g NaCl per 1000 ml water), respectively, to get concentrations of 10^6-10^8 colony forming units per milliliter (cfu · ml^{-1}). The number of viable microorganisms (cfu · ml^{-1}) was estimated by the surface spread plate count method using aliquots of serial dilutions of microorganism suspensions according to the European Pharmacopoeia. Detection limit of this procedure was 10 cfu · ml^{-1}. Inactivation kinetics of microorganisms is depicted in semi-logarithmic plots. If the number of microorganisms fell below the detection limit, i. e. no viable microorganisms have been found, for clearness these values in the graphs are set at 5 cfu · ml^{-1}.

3. Results and discussion

In non-buffered physiological saline solution, *E. coli* was completely inactivated after 7 min treatment by surface DBD (Fig. 2). Similar treatment of 5 ml water resulted in a steep decrease of pH from 7 to less than 4 within the first 5 min of plasma treatment, followed by a slight further decrease reaching more or less stable pH values between 2 and 3 within 30 min (Fig. 3A).

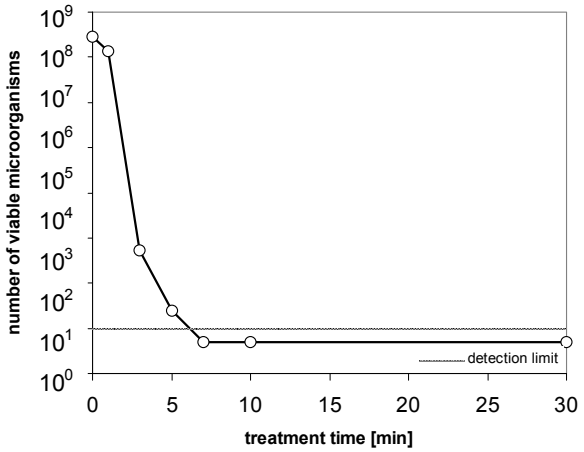


Fig. 2. Inactivation of *E. coli* suspended in non-buffered physiological saline by plasma treatment.

A supporting effect of acidic pH for antimicrobial plasma activity has been found elsewhere, too, but it was also found that acidification alone was not sufficient for bacteria inactivation [1, 4, 8]. Furthermore, nitrate (NO_3^-) as well as nitrite (NO_2^-) concentration in plasma treated 5 ml water was measured using spectrophotometric methods. NO_3^- increased within 30 min indirect DBD treatment from zero to 113 mg · l^{-1} (Fig. 3 B). Similar kinetics has been found by Moussa *et al*. working with gliding electric discharge in wet air [9].

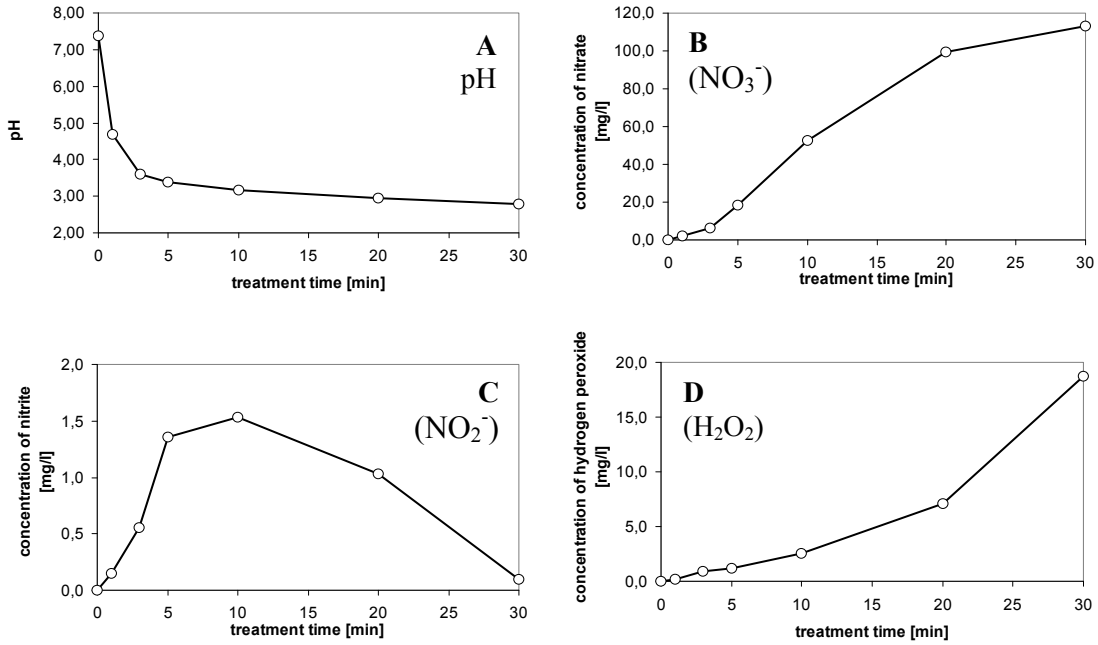


Fig. 3. Liquid analytics of plasma treated water: pH (A), nitrate (B), nitrite (C), hydrogen peroxide(D).

NO_2^- increased from zero to 1.5 mg · l^{-1} within the first 10 min of plasma treatment, but declined back to near zero after 30 min plasma treatment (Fig. 3 C). This short-term increase of NO_2^- as well as its relatively low concentration compared to NO_3^- can be explained by the fact that the transformation of NO_2^- into NO_3^- is accelerated at acidic conditions. Moreover, this transformation is self-catalyzed by NO_3^-. Both the increasing and relatively high NO_3^- concentration in parallel to decreasing pH caused by indirect DBD plasma treatment is evidence to suggest that generation of nitric acid (HNO_3) may play a central role in liquid acidification. Furthermore, HNO_3 is able to diffuse into the liquid. Additionally, a clear H_2O_2 generation occurred in water during indirect DBD plasma treatment. The concentration increased up to 18 mg · l^{-1} within 30 min indirect DBD plasma treatment (Fig. 3 D) [4].

In order to understand the plasma-induced acidification and generation of NO_3^-, NO_2^- and H_2O_2, as well as inactivation of microorganisms in liquid, the gas/plasma phase was analyzed by FT-IR and OES. OES indicates nitrogen-related bands in the UV-A and UV-B range (second positive and first negative system of N_2) but no emission in the bactericidal effective UV-C range (Fig. 4 A). By FT-IR, no cytotoxic nitric oxide ($NO^\bullet$), but nitrous oxide (N_2O), ozone (O_3) and traces of nitric acid (HNO_3) were measured (Fig. 4 B). These findings are in agreement with numerous investigations of the chemistry in non-thermal plasmas, e.g. [20].

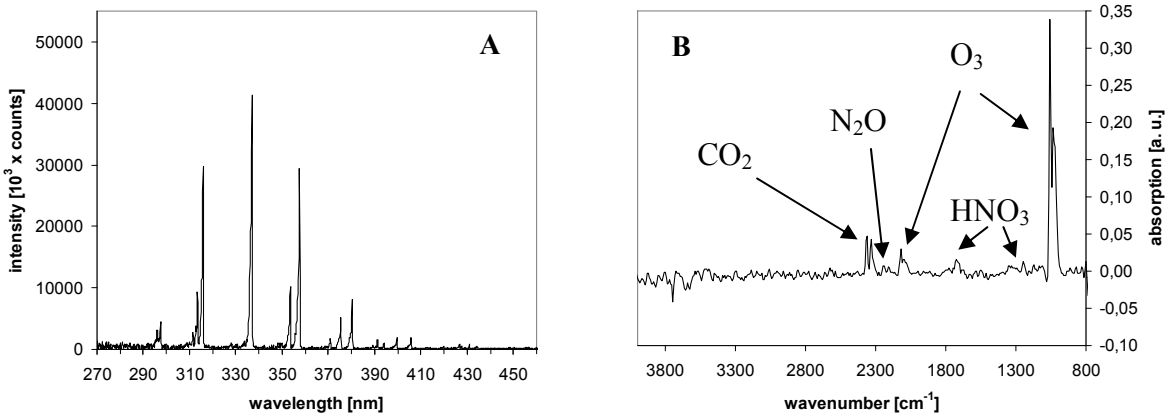


Fig. 4. OES (A) and FT-IR spectra (B) of the gas/plasma phase

These detected gaseous molecules may interact with the aqueous surface or diffuse directly in the liquid. Possible reaction channels resulting in acidic protons (H^+), nitrate, nitrite and hydrogen peroxide are shown in Fig. 5 just as reactions to generate nitrogen oxide ($NO^\bullet$), nitrogen dioxide ($NO_2^\bullet$), hydroxyl radicals ($HO^\bullet$), pernitro acid (ONOOH) and hydroperoxy radicals ($HOO^\bullet$) which may act as antimicrobial effective agents.

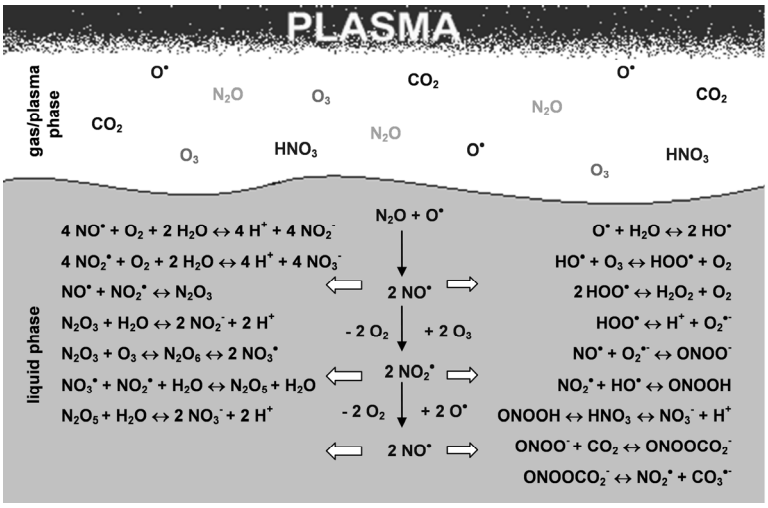


Fig. 5. Possible (air-)plasma/gas-liquid-interaction and reaction channels [3, 8, 10-18].

To explain the complexity of these reactions and the resulting biological effects, some examples should be mentioned in a more detailed manner. Ozone (O_3), which is better soluble in water than oxygen (O_2) is a strong oxidizing agent. Its oxidizing effect is intensified in acidic media. Nitrous oxide ($NO^\bullet$) is well soluble in water, too. O_3 can be decomposed by $NO^\bullet$ to nitrogen oxide ($NO_2^\bullet$) and O_2 [15]. Dinitrogen trioxide (N_2O_3), which can be generated from a reaction of $NO^\bullet$ with $NO_2^\bullet$, can react as nitrosating agent with thiols, primary and secondary amines [18]. Radicals like the superoxide anion radical ($O_2^{\bullet-}$) or the hydroperoxy radical ($HOO^\bullet$) with short life times exist a few seconds or minutes, only. In acidic media $O_2^{\bullet-}$ is converted into $HOO^\bullet$ ($pK_a = 4.8$). This small uncharged molecule can penetrate the cell membrane, converted back to $O_2^{\bullet-}$ in the neutral cytoplasma and can react with intracellular components [3, 11, 19]. Additionally, other reactions resulting in toxic

products can be mentioned. Dinitrogen pentoxide (N_2O_5), which can be formed by a reaction of $NO^{\bullet}$ with $NO_2^{\bullet}$, or 2 $NO^{\bullet}$ with 3 O_3, has strong oxidizing properties, too [10, 20]. Peroxonitrite may oxidize lipids, fatty acids and proteins directly [11]. Furthermore, it is able to react with carbon dioxide (CO_2) to $ONOOCO_2^-$ and dissociate to nitrogen dioxide ($NO_2^{\bullet}$) and carbonate radical ($CO_3^{\bullet-}$). The latter initiates many destroying reactions and is more toxic than $HO^{\bullet}$. [18] Two protons (H^+) and one NO_2^- can react to nitrosooxidanium ($H_2NO_2^+$) which may break down to water and nitrosonium cation (NO^+) [21]. NO^+ reacts with many biomolecules [11, 18].
Consequently, the generation of ozone and nitrous oxide in the plasma/gas phase may be the initial point of a multiplicity of chemical reaction cascades in water resulting in the secondary generation of radicals and other low-molecular products. Some of them or the "cocktail" of all may cause biological effects as the inactivation microorganisms as it was demonstrated by *E. coli*. To approve these theories of chemical reactions and deduced biological effects, a lot of further investigations must follow. However, liquid analytics for specific detection of radicals as well as low-molecular ions will play a key role in this research. Furthermore, the role of ions in the plasma/gas-phase must be considered, too.

4. Conclusion

The indirect surface DBD treatment of 5 ml water in ambient air under atmospheric conditions resulted in decrease of the pH, as well as genesis of nitrate, nitrite and hydrogen peroxide. Furthermore, inactivation of *E. coli* suspended in non-buffered physiological sodium chloride solution was found. The analysis of the plasma/gas phase by FT-IR and OES show the existence of dinitrogen oxide and ozone.
Several reaction channels starting from ozone and dinitrogen oxide can be hypothesized which may lead to decrease of pH as well as the generation of nitrate, nitrite, hydrogen peroxide, and other secondary reaction products which could be responsible for biological effects like bacteria inactivation. In future, more effective and detailed liquid analytics will play a key role to clarify both mechanisms of plasma-liquid interactions and biological plasma effects.

Acknowledgements. This study was realized within the joint research project "Campus PlasmaMed" supported by the *German Federal Ministry of Education and Research* (grant no. 13N9779).

5. References

[1] Chen C W et al. 2008 *IEEE Transactions on Plasma Science. Vol.* **36** *215 - 219.*
[2] Liu F et al. 2010 *Plasma Processes and Polymers. Vol.* **7** *231-236.*
[3] Ikawa S et al. 2010 *Plasma Processes and Polymers. Vol.* **7** *33-42.*
[4] Oehmigen K et al. 2010 *Plasma Processes and Polymers. Vol.* **7** *250-257.*
[5] Lukes P et al. 2008 *Plasma Sources Science and Technology. Vol.* **17**.
[6] Burlica R et al. 2006 *Journal of Electrostatics. Vol.* **64** *35-43.*
[7] Helmke A et al. 2009 *New Journal of Physics. Vol.* **11**.
[8] Satoh K et al. 2007 *Japanese Jounal of Applied Physics. Vol.* **46** *1137-1141.*
[9] Moussa D et al. 2007 *IEEE Transactions on Plasma Science. Vol.* **35**.
[10] Holleman A F et al. 2007 *Lehrbuch der Anorganischen Chemie.* **102nd** *Edition*.
[11] Daiber A and Ullrich V 2002 *Chemie in unserer Zeit. Vol.* **6** *366-375.*
[12] Amatore C et al. 2000 *Faraday discussions. Vol.* **116** *319-333.*
[13] Hornig F S 2007 *Thesis, University Duisburg-Essen.*
[14] Butler A R and Feelisch M 2008 *Circulation. Vol.* **117** *2151-2159.*
[15] Ravishankara A R et al. 2009 *Sciencexpress. Vol.* **326** *123-125.*
[16] Radcliffe C E et al. 2003 *Journal of Dentistry. Vol.* **31** *367-370.*
[17] Lundberg J O et al. 2008 *Nature reviews drug discovery. Vol.* **7** *156-167.*
[18] Pacher P et al. 2007 *Physiological reviews. Vol.* **87** *315-424.*
[19] Gaunt L F et al. 2006 *IEEE Transactions on Plasma Science. Vol.* **34** *1257-1269.*
[20] Eliasson B and Kogelschatz U 1986 *Journal de Chimie Physique et de Physico-Chimie Biologique. Vol*. **83** *279-282.*
[21] Anbar M and Taube H 1954 *Journal of the American Chemical Society. Vol.* **76** *6243-6247.*

Topic 9
Miscellaneous

LOW ENERGY ELECTRON BEAM DRIVEN RADIOLYSIS

Andreas Ulrich[1], T. Heindl[1], T. Dandl[1], R. Krücken[1], and J. Wieser[2]

[1]*Physik Department E12, Technsiche Universität München, James-Franck-Str. 1, 85748 Garching, Germany.*

[2]*Optimare GmbH & Co Kg, Ems-Str. 20,26382 Wilhelmshaven, Germany.*

E-mail: andreas.ulrich@ph.tum.de

A concept to induce chemical reactions in dense gases by ionizing radiation is described. Electron beams of 12 keV particle energy are used as the radiation source. The electrons are sent through thin (300 nm) ceramic membranes into the gas. The table-top setup can be used with pulsed as well as continuous beams. It is shown that dose rates of more than 10^{23} and 10^{28} eV/(gs) can be achieved in continuous and pulsed mode, respectively. Radiolysis of isopropanol which has been performed in a test experiment is described to demonstrate the concept.

1. Introduction

Most chemical reactions require external energy transferred to the reactant species to drive the reaction or at least to overcome the activation energy for starting the reaction. Heat is the most common form of energy to be used for that purpose. Here we discuss the deposition of the kinetic energy of electrons as an alternative. Chemical reactions induced by particle radiation are well known and if molecules are destroyed by the radiation the process is called "radiolysis". In most cases this is an unwanted side effect of radiation fields in the form of bleaching, formation of color centers in optical elements, damaging electronic equipment, and in the worst case radiation sickness of people exposed to ionizing radiation. However several experiments have been performed in which high energy particles were used to deliberately induce chemical reactions. Sterilization is an example for radiation treatment of biological material. Dissociation of carbon dioxide is an example from inorganic chemistry which is of interest in the context of attempts to process flue gases emitted from installations which burn fossil fuels such as coal burning power stations.

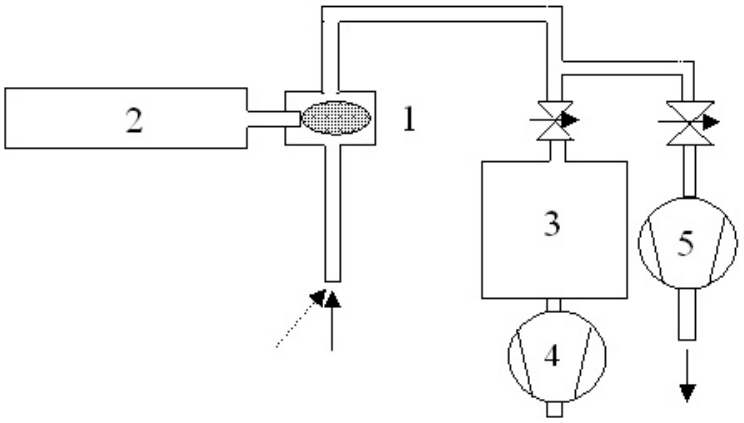


Fig. 1. Schematic drawing of the test setup. The electron beam is formed in the vacuum device (2) and sent into the reaction cell (1). Air is pumped through the system with a membrane pump (5). Gas composition is measured in the mass spectrometer (3) evacuated by a turbo-molecular pump (4). The thick arrows indicate the main flow of air and the dashed arrow the admixture of isopropanol.

Here we discuss a novel technology which can be used for small-scale, table-top laboratory experiments in which both very high doses and dose rates can be applied to matter. Scaling to larger devices may be possible by up-scaling some of the parameters and parallel operation of many of the devices described here. We focus on the treatment of a flow of gas irradiated by low energy electrons. To put the parameters into perspective with earlier experiments we will compare them with an

experiment which has been published by R. A. Lee in which CO_2 was dissociated by applying a 600 keV electron beam [1].

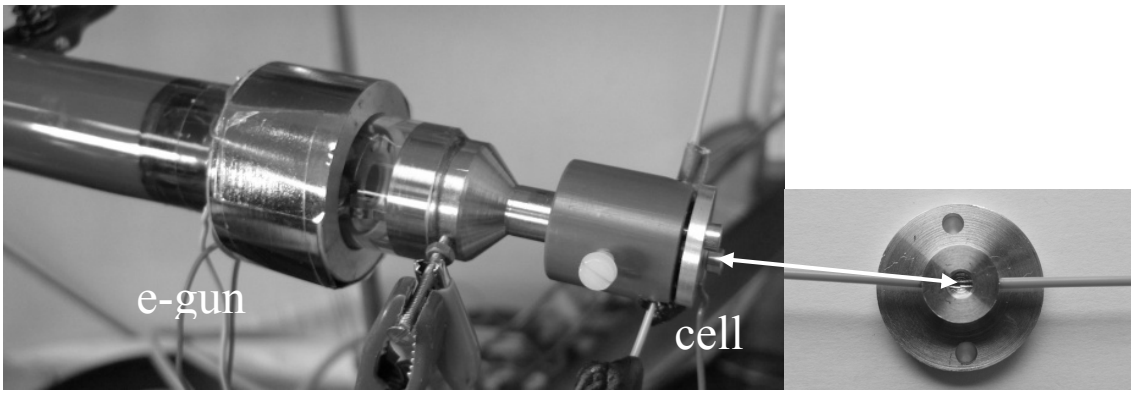


Fig. 2. Photograph of the e-gun (left) and reaction cell (right). The electron beam comes from the left side and is stopped in the small volume in the Al part shown in the insert.

The basic concept of the technique described here is to reduce the particle energy of an electron beam from several hundred keV to the 10 keV region. Since the electronic stopping power increases strongly when the velocity (and thereby the kinetic energy) of the projectiles is decreased [2,3] there is a much higher specific energy transfer from the beam to the target material and high doses and dose rates can be achieved with low or moderate beam currents. The only price which has to be paid is the reduced amount of material which can be treated because the low energy beams have a rather low total power. However, since dose and dose rate are parameters normalized to the amount of material the only requirement for experimental studies is to use a sensitive diagnostics which works for small samples. An advantage of using low energy beams is that no hard x-ray radiation is produced so that the experiments can be performed in any laboratory environment. This is the general concept. It is also used to realize brilliant light sources [4] and several aspects of the technology have been studied in this context [3,5,6]. Aspects of the technology concerning gas chemistry and examples of the parameters in comparison with ref. [7] and ref. [8] are discussed in the next paragraph.

2. Experimental Parameters

Here, low energy electron beams are sent into gases at atmospheric pressure to induce chemical reactions. The typical particle energy is 12 keV. Very thin entrance windows are required for sending electrons of this energy into gases without significant energy loss. Ceramic material in the form of 300 nm thin silicon nitride membranes is used for that purpose. The technique has so far mainly been used to realize vacuum ultraviolet light sources by sending electron beams into rare gases where they induce intense excimer emission in the 80 to 200 nm wavelength region [6]. Free standing silicon nitride membranes are routinely manufactured by the solid state industry for various purposes such as pressure sensors. A silicon nitride layer is deposited on both sides of a silicon wafer. Then the wafer is structured on one side, opening the chemically stable silicon nitride surface layer. Then the bulk silicon material is etched away in these areas. The etching process stops at the silicon nitride layer on the other side of the wafer thereby forming the free standing membrane. The membrane material actually has to be either non-stoichiometric silicon nitride or a double layer of nitride and oxide to limit the internal stress of a free standing membrane.

The energy loss of low energy electrons traversing such a 300 nm membrane has been studied both experimentally and by model calculations [5]. The energy loss depends partly also on the gas filling due to backscattering in the gas and is on the order of 15% for the experimental conditions described here. The power deposited in the gas can therefore be estimated by multiplying the beam current by 10 kV. Various geometries of the membranes can be used. Quadratic membranes of 0.7×0.7 mm^2 are routinely used for our experiments. Slit foils 0.7×40 mm^2 are also available as an alternative. The current which can be sent through the membranes is limited by the thermal stability of the membrane which is heated by the energy loss in the membrane. Heat conduction along the membrane, radiation, and, most effectively, contact with the gas is cooling the membrane. In practice up to about 10 µA

corresponding to 100 mW average beam power can be sent through the 0.7×0.7 mm^2 membranes into the gas.

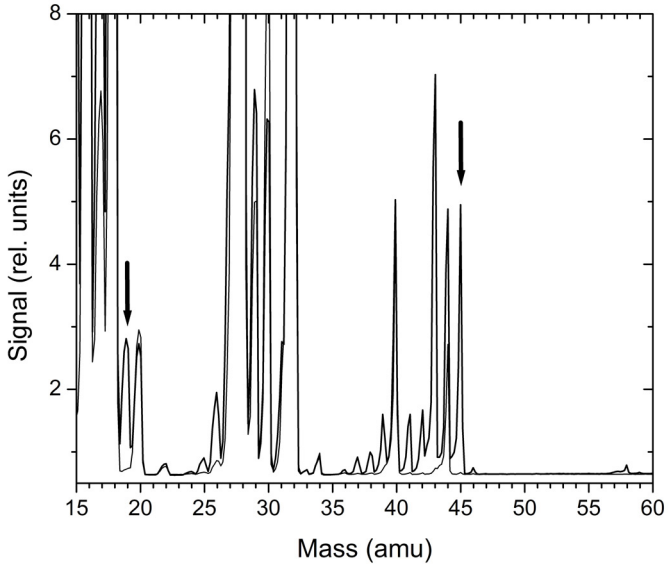


Fig. 3. Mass spectrum of air with isopropanol added. The thin line shows the spectrum of air alone. Isopropanol has mass 60. The heaviest fragment observed here is m = 58. Mass 45 can be interpreted as isopropanol with one CH_3 group removed and mass 19 as OH_3.

Electronic stopping is the dominant mechanism of the interaction of electrons in the membrane and also in the gas. This means transfer of kinetic energy of the projectile electrons to the bound electrons of the target material. This "stopping power", the energy transfer per unit length along the path of the electron can be described by the Bethe-Bloch formula. However, the path of the electrons has a very complex geometry due to multiple scattering of the low energy electrons. This leads to an effective range of the electrons which is much shorter than the path of the electrons. Monte Carlo calculations are therefore required to describe the power deposition in the target material quantitatively. A study on this issue has been published in ref. [3] for the conditions of the experiments described below. Applying this study to air, approximated by nitrogen or CO_2 at atmospheric pressure, it is found that 1 mm is a typical range for the 10 keV electrons exiting the foil and that the beam power is deposited within a volume of about 1 mm^3. Note that there are regions in the center and close to the foil where the dose rates are significantly higher than the average values which will be estimated from the beam power and the 1 mm^3 volume.

There is another aspect of the technology described here which can be important for studying particle beam induced chemical reactions: pulsing of the beam. A strong dependence of the efficiency for inducing reactions via radiolysis from the dose and the flow of material has been described in the literature [7]. This can be understood qualitatively based on the following arguments. A gas kinetics aspect is emphasized in ref. [7]. If the ionization rate is high, the electron density and recombination rates are high and the electrons recombine with the ions before they can form negative molecules. The reaction pathway may for this or similar reasons depend on the dose rate. Also, if the material which has been treated by the beam is not removed from the irradiated volume, back reactions can occur which will reduce the net efficiency of the process which should be induced. A similar situation is found for example in excimer lasers where the laser medium is removed from the laser cavity after each shot to be cooled, cleaned and chemically restored before it flows back into the discharge region of the laser.

The electron beams used here can be pulsed easily with a wide range of pulse lengths. It can therefore be considered to adjust the pulse length and the flow of material for optimum efficiency of the reaction to be induced. The instantaneous beam power can be significantly increased in the pulsed mode of

operation. The heat capacity of the material of the membrane can store energy deposited in the foil which is then removed during the time between pulses. As long as the beam energy deposited in the membrane stays below a certain limit, the instantaneous beam power can be very high. In the case of the 300 nm thick, 0.7×0.7 mm^2 membranes an experimental limit of 2 A * 10 kV = 20 kW over 50 ns corresponding to 1 mJ per pulse has been found. This corresponds to a dose on the order of 1 J/cm^3 or ~1000 J/g = 10^6 J/kg = 1 MGy) in the ~1 mm^3 volume described above if nitrogen at atmospheric pressure (1.25 mg/cm^3) is used as a typical example of molecular weight and target density. Note that essentially all combinations of pulse energy and pulse duration resulting in the same pulse energy can be selected for the experiments. For comparison: the dose delivered to CO_2 in ref. [1] per shot from a Febetron 706 electron accelerator was 0.69 Mrad = 6900 Gy.

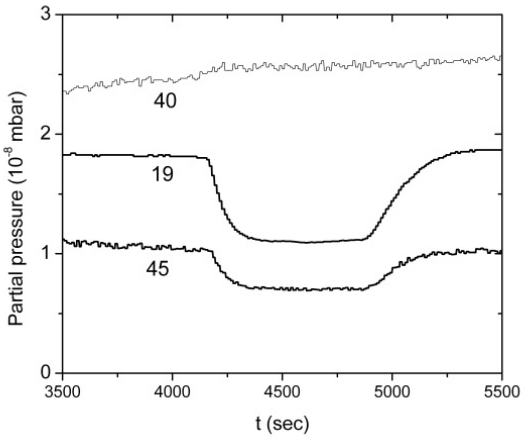


Fig. 4. Time dependence of the partial pressures of m = 19, 40, and 45 is shown. Around t = 4200 s the electron beam was switched on and around t = 5000 s it was switched off again. The modification of gas composition of reactive species is obvious whereas the concentration of argon (m = 40) is unaffected by the electron beam.

The key parameter for radiolysis experiments defined in the literature is the so called G-value. It describes the number of molecules produced per 100 eV radiation energy deposited in the medium. Typical G values for example for dissociating CO_2 into CO and oxygen can be found in the literature. Several earlier experiments are summarized and compared in a paper by R. Kummler et al. [7]. A numerical model based on a large number of reactions with their corresponding rate constants is established in this paper and the model is compared with experimental results. An important finding is that the G-value depends strongly on the dose rate (see Fig. 1 in ref. [7]). Dose rates from 10^{14} to 10^{28} eV/(gs) are discussed and a variation from G=0 up to G=9 is found for this specific reaction. The highest G-values ($G \approx 8$) are found for dose rates above 10^{26} eV/(gs). A practical energy efficiency for the radiolysis process of 25% can be calculated from G=9 taking the dissociation energy of ~3 eV for CO_2 into C+O into account. The energy efficiency of the radiation source would of course have to be taken into account in an actual device for gas chemistry.

The well studied example of CO_2 radiolysis can be used to judge the usefulness of the low energy electron beam technology for basic studies by estimating the dose rates which can be achieved in the experiments. A 10 keV electron beam deposits its energy in about 1 mm^3 CO_2 at atmospheric pressure. This corresponds to 2×10^{-6} g CO_2. With a beam current of 10 μA and 0.1 W = 6.24×10^{17} eV/s results a dose rate of 3×10^{23} eV/(gs) for the dc beam described above. With the current increase up to a factor of 2×10^5 (10μA to 2A) which is possible in the pulsed mode tests with dose rates up to 3×10^{28} eV/(gs) can be performed. The coincidence of the parameters which are possible for the table top device which is described here with the dose rates which are discussed in the literature for efficient gas kinetic reactions is our key argument to suggest the application of the low energy electron beams for radiolysis experiments.

It should be noted that the technology has already been used for gas chemical experiments several years ago in collaboration with the Siemens Company in the context of reformation of methane fuel. Here we describe a renewed and more general approach. For that purpose we have built a small gas cell in combination with some basic diagnostics using a mass spectrometer and performed a test experiment.

3. Test Experiment

The test setup is schematically shown in Fig. 1. A photograph of the setup is shown in Fig. 2. The 12 keV electron beam is produced by a cathode ray tube and sent through the silicon nitride membrane into a small cylindrical aluminum of 3 mm diameter and 2 mm long cell. The gas which should be treated by the beam was slowly sucked through the cell with a membrane pump. The flow was regulated with a needle valve. Gas analysis was performed with a (Ametek, Dycor D200MP) mass spectrometer (MS). The MS was pumped with a small turbo-molecular pump (Pfeiffer DCU). The gas inlet was realized by a needle valve which was regulated for a pressure on the order of 10^{-5} mbar from a background pressure on the order of 10^{-6} mbar. Thin tubes with 1 mm inner diameter were used to connect the cell and the MS-inlet to allow short reaction times of the system.
Unfortunately we could not perform a test experiment which corresponds directly to the radiolysis experiments of CO_2 which we have referred to above because the reaction product CO has the same mass (28) as the nitrogen molecule and could not be distinguished in our makeshift setup. To demonstrate that chemical reactions can be induced with the table-top, low energy electron beam irradiation technique we added some isopropanol vapor to air. It shows up with a set of peaks in the mass spectrometer as shown in Fig. 3. The electron beam ionization in the mass spectrometer obviously leads to signficant fragmentation of the isopropanol molecules. The MS was then set to a mode in which peaks at M = 19, 40, and 45 could be monitored with time and the electron beam was switched on and off to search for an effect on the signal. The result is shown in Fig. 4. It clearly shows that reactions can be induced by the electron beam which leed to a modification of the gas composition.
In summary we have developed a technique which allows experiments for radiation induced chemical reactions with compact and safe laboratory devices. It may be used for fundamental studies and to find reactions which are of practical importance and make use e.g. of existing radiation fields like in nuclear reactors or which justify from their commercial or environmental interest the investment in an up-scaled facility for electron beam induced chemistry.

4. References

[1] R. A. Lee, Radiation Research **77**, 233 (1979).
[2] S. Valkealahti, J. Schou, R. M. Nieminen, J. Appl. Phys. **65**, 2258 (1989).
[3] A. Morozov, R. Krücken, A. Ulrich, J. Wieser, J. Appl. Phys. **100**, 093305 (2006).
[4] A. Ulrich, T. Heindl, R. Krücken, A. Morozov, C. Skrobol, J. Wieser, Eur. J. Appl. Phys. **47**, 22815 (2009).
[5] A. Morozov, T. Heindl, C. Skrobol, J. Wieser, R. Krücken, A. Ulrich, Eur. Phys. J. D **48**, 383 (2008).
[6] A. Morozov, T. Heindl, R. Keücken, A. Ulrich, J. Wieser, J. Appl. Phys. **103**, 103301 (2008).
[7] R. Kummler, C. Leffert, K. Im, R. Piccirelli, L. Kevan, C. Willis, J. Phys. Chem. **81**, 2451 (1977).

EFFECT OF THE MAGNETIC FIELD ON ELECTRICAL CHARACTERISTICS OF THE DC CORONA DISCHARGE

Stanislav Pekárek

Czech Technical University in Prague, Faculty of Electrical Engineering, Technická 2
166 27 Prague 6, Czech Republic
E-mail: pekarek@fel.cvut.cz

The important quantities, which affect performance of corona discharge based devices such as electrostatic precipitators are discharge voltage and power. We studied the effect of a magnetic field on the needle to plate DC corona discharge in stationary air or with flow of air through the discharge chamber with the aim to increase discharge voltage and power. We found that for low currents and for both polarities of the needle the magnetic field has no substantial effect on discharge voltage. On the other hand for the needle negative and for higher currents magnetic field increases discharge voltage and power.

1. Introduction

Corona discharges have wide range of applications such as source of ozone for treatment of water, electrostatic printers, surface treatment and electrostatic precipitators (ESP). The quantities, which affect performance of corona discharge based devices such as ESP are the electrode design, the gas velocity distribution in the discharge chamber and namely the values of operating voltages and power delivered to the discharge [1].

This paper is focused on study of the needle to plate DC corona discharge with the aim to increase discharge power through application of the stationary magnetic field on the discharge. The magnetic field was applied perpendicularly to the vector of the current density.

The papers that have dealt with studies of the effect of magnetic field on different types of electrical discharges at atmospheric pressure are not too numerous [2-5]. These papers use the fact that magnetic field affects motion of electrons. Their paths are curved, lengthened, ionization is enhanced and therefore the discharge performance could be affected.

2. Experimental arrangement

The experimental arrangement, see Figure 1, consisted of a discharge chamber, an electric power supply with electrical parameters diagnostics and an air supply system.

The discharge chamber was made from non-magnetic materials. The chamber had rectangular cross section with inner dimensions 10×25×30 mm. At the axis of the discharge chamber was placed stainless steel needle electrode of the diameter 0.8 mm. As a second flat electrode we used brass parallelepiped. The distance between the tip of the needle and the plate electrode was 10.2 mm. At the side of the discharge chamber there was one opening for the input and the second opening for the output of air. The experiments were performed with air from a cylinder. A mass flow controller MFC adjusted the airflow through the discharge chamber. The experiments were performed either with stationary air (0 slm) or with the flow of air through the discharge chamber 1.5 slm. We also measured the relative humidity RH of input air.

The discharge chamber was placed either away of the magnetic field or between two $Nd_2Fe_{14}B$ permanent magnets (dimensions 35×35×10 mm). The magnetic induction at the center of the discharge chamber at the place of the tip of the needle was 5500 gauss.

The DC regulated high voltage power supply provided voltage up to 30 kV. The needle was ballasted by a resistor R_B = 6.89 MΩ. The mean value of the discharge current was determined from the magneto-electric system miliammeter or as the mean value of the signal obtained from the voltage drop on the earthed resistor R_I = 55 Ω. This signal was recorded on the first channel of the DS 1150C digital storage oscilloscope. The discharge voltage was determined as the mean value of the signal recorded through the high voltage probe HVP on the second channel of this oscilloscope.

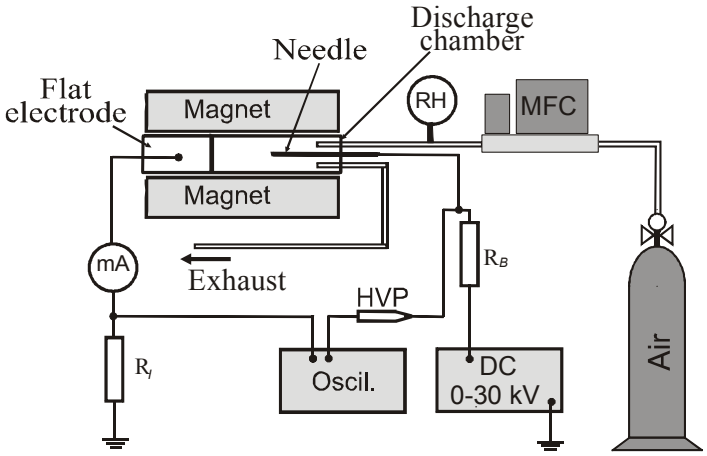


Fig. 1. Experimental arrangement. RH – relative humidity sensor, MFC – mass flow controller, R_B– ballast resistor, R_1 – earthed resistor.

3. Experimental results and discussion

Our experiments were performed for both polarities of the needle and for the discharge in stationary or in a flowing air. The corona discharge for each polarity of the coronating electrode can exist in different regimes. These regimes for the positive corona are burst - pulse corona, streamer corona, glow corona and finally a spark. In case of negative corona these regimes are Trichel pulse regime, pulseless glow regime, filamentary streamer regime and a spark [6]. For the purpose of this paper we will therefore denote the lower currents region (smaller than approximately 0.15 mA) as a region, which corresponds to the discharge glow regime and the higher current region (currents exceeding 0.15 mA), which corresponds to the discharge streamer regime.

The effect of magnetic field on the V-A characteristics of the discharge in the low current region, for both polarities of the needle electrode and for airflow rates 0 and 1.5 slm is shown in Figure 2.

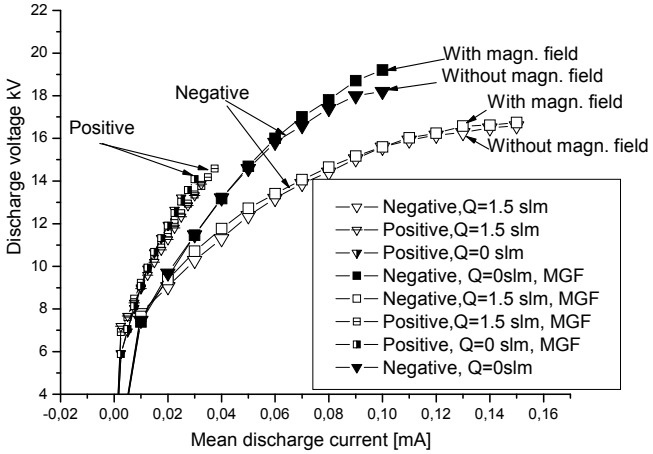


Fig.2. Effect of the magnetic field and flowrate on the V-A characteristics of the discharge in the low current region for both polarities of the needle. Distance d=10.2 mm. MGF–with magnetic field.

In this figure is seen a strong polarity effect as well as the fact that in this current region the more important role is played by the airflow rate through the discharge chamber than the role of the magnetic field. It is also seen that the application of magnetic field for both polarities of the neeedle has no substantial effect on V-A characteristics both for the discharge in stationary air as well as for the discharge with the flow of air through the discharge chamber 1.5 slm.

The effect of the magnetic field on electrical parameters of the discharge for the needle negative, for higher currents that is for the discharge in the glow and streamer regime, and for airflow rates 0 and 1.5 slm is shown in Figure 3.

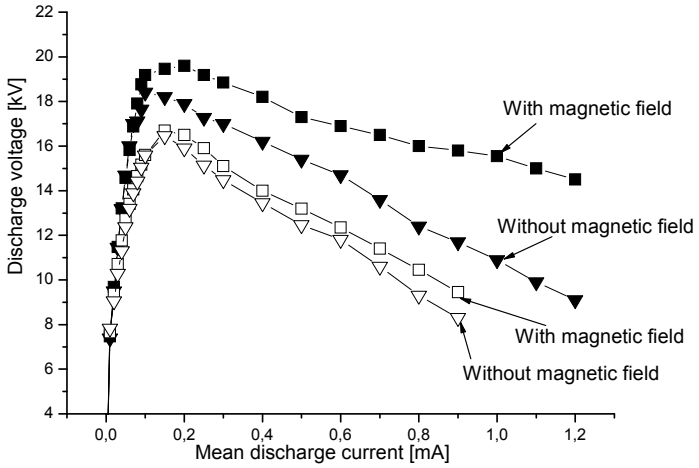


Fig.3. Effect of the magnetic field and flow rate on V-A characterists of the discharge for the needle negative, for the glow and streamer regime. Full symbols – airflow rate 0 slm; empty symbols– airflow rate 1.5 slm. Distance *d*=10.2 mm.

As it is seen from Figure 2 and Figure 3 the effect of the magnetic field on the discharge voltage is different for the discharge in different regimes. For the discharge in the low current region, both polarities of the needle (Figure 2) and for both values of airflow the magnetic field has no substantial effect on the discharge voltage. By contrast for the needle negative and for the discharge in a streamer regime (Figure 3) applying a magnetic field increases for particular current the discharge voltage.
These results results can be explained in the following way. The electrons leaving the needle electrode due to the applied electric field **E** move toward the flat electrode, and because of the Lorentz force they are accelerated. The volume density of this force is $\mathbf{f}_{\mathrm{e}} = \mathbf{F}_{\mathrm{e}} n = \mathrm{q}\, n\, \mathbf{E}$, where n stands for the density of the electrons. When the magnetic field is applied in the expression for the volume density of the Lorentz force, there appears also the magnetic component $\mathbf{f}_m = \mathbf{F}_{\mathrm{m}} n = \mathrm{q}\, n \left(\mathbf{v} \times \mathbf{B}\right) = \mathbf{j} \times \mathbf{B}$, where **j** stands for current density and **B** is magnetic induction. This expression shows that not only the magnetic induction but also the current density determines magnitude of this force. In case of higher currents the corona discharge exists in the filamentary streamer regime. Due to these higher currents, and because streamers are accompanied by a sharp decrease in the area crossed by electrons, the current density is strongly increased. Therefore the Lorentz force volume density $\mathbf{f}_m = \mathbf{j} \times \mathbf{B}$, caused by applying a magnetic field on moving electrons, is substantially increased. Due to the action of this force the paths of the electrons are curved and consequently to maintain a constant current the discharge voltage must be increased. The increase of the discharge voltage when the magnetic field is applied is certainly related to the increase of power delivered to the discharge.
The effect of the magnetic field on the discharge power for the needle negative and for airflow rates 0 and 1.5 slm is shown in Figure 4. From this figure it is seen that for higher currents application of the magnetic field increases discharge power. For the lower currents the increase of power is not substantial.
The corona power is a quantity, which strongly influences performance of corona discharge based devices such as electrostatic precipitators.
In fact the ESP collecting efficiency strongly depends on corona power. In the lower range of collecting efficiencies, relatively small increases in corona power result in substantial increases in

collecting efficiency. On the other hand, in the upper ranges, even large increases in corona power will result in only small efficiency increases.

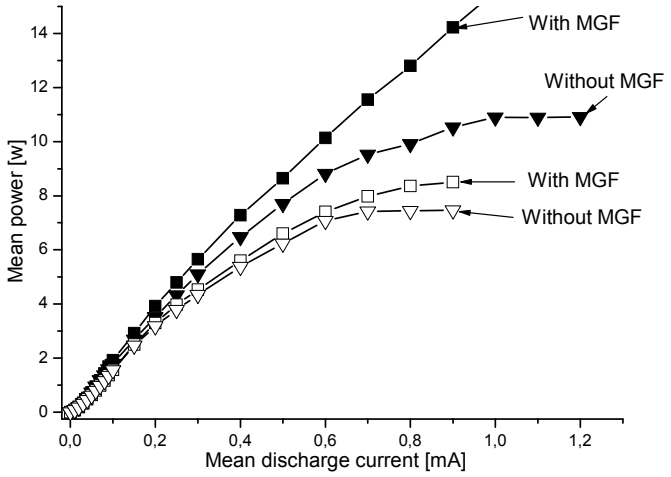


Fig.4. Effect of the magnetic field on the discharge power for the needle negative. Full symbols – airflow rate 0 slm; empty symbols– airflow rate 1.5 slm. Distance d=10.2 mm.

4. Conclusion

We studied the effect of the stationary magnetic field on electrical parameters of the needle to plate DC corona discharge. For magnetic induction at the place of the tip of the needle 5500 gauss we found that:

a). For low discharge currents, both polarities of the needle and for the discharge in stationary air or for the discharge with airflow through the discharge chamber 1.5 slm the magnetic field does not substantially affect electrical parameters of the discharge.

b). For the needle negative and for higher currents (corona in the filamentary streamer regime) the magnetic field for particular current increases discharge voltage. This effect is stronger for the discharge in stationary air than for the discharge in flowing air.

The obtained results can be considered as a certain contribution to the functioning of corona discharge based devices, for example electrostatic precipitators.

Acknowledgement. This research was supported by the Ministry of Education, Youth and Sports of the Czech Republic (Research Plan MSM 6840770017 of the Czech Technical University in Prague).

References

[1] Dascalescu L, Samuila A, Rafiroiu D and Iuga A 1999 *IEEE Trans. on Industry Appl.* **35** 543.
[2] He Z H, Yu F S, Hu F, Yuan Y, Guo L N, Li J 2007 *Plasma Sc. & Tech.* **9** 706.
[3] Xu D X, Sheng L X, Wang H J, Sun Y H, Zhang X Y, Mi J F 2007 *J. of Electrost.* **65** 101.
[4] Rong M Z, Liu D X, Wang X H, Wang J H 2007 *Plasma Sc. & Tech.* **9** 717.
[5] Pekárek S 2010 *Eur. Phys. J. D* **56** 91.
[6] Akishev Yu, Grushin M, Kochetov I, Karalnik V, Napartovich A and Trushkin N 2005 *Plasma Sources Sci. Technol.* **14** S18.

PULSED PLASMA ASSISTED PYROLYSIS OF ETHANOL

S.M. Sidoruk[1], V.Ya. Chernyak[1], S.V. Olszewski[1]

[1]*Dep. of Physical Electronics, Faculty of Radiophysics, Kyiv National Taras Shevchenko University, Prospect Glushkova 4Г, Kiev 03122, Ukraine*

E-mail: chern@univ.kiev.ua

Plasma assist high temperature partial oxidation pyrolysis of ethanol was investigated. The energy efficiency vs. pyrolysis chamber temperature and vs. ethanol-to-oxygen molar rate was obtained. The best regimes for highest energy efficiency were obtained. The outflow syngas components were investigated.

1. Introduction

From physics and chemistry of fuel combustion it is known that addition of light inflammable gases (H_2, CO) essentially improves ignition/combustion of heavy oil and bio-fuels [1]. Therefore hydrogen is considered as one of the most prospective energy sources for the future that can be renewable, ecologically clean and environmentally safe [2]. Among possible technologies for free hydrogen production, including steam reforming and partial oxidation of bio-fuels [3], a low-temperature plasma-assisted fuel reforming is believed to be a good alternative approach [4,5]. Also the use of fuel reforming can be rather perspective for hypersonic ($M > 5$) aircrafts as will allow solving two basic tasks: the presence of quickly combustible fuel on board of aircraft and the maintenance of cooling of aircraft systems. The possible approach to the decision of these tasks can be on-board reforming of fuel (for example, kerosene), i.e. its conversion into H_2 and CO_2: hydrogen can be used for combustion and carbon dioxide - for aircraft cooling purposes.

For plasma fuel reforming, various methods using thermal and non-thermal plasma are known [6]. Thermal plasma, which is thermodynamically equilibrium, has characteristics of high ionization by higher energetic density. This has merits of good rate of fuel decomposition but demerits of poor chemical selectivity and high specific energy consumption. Non-thermal (low-temperature) plasma, which is kinetically non-equilibrium, has characteristics of low ionization but benefits of high reactivity and selectivity of chemical transformations providing high enough productivity at relatively low energy consumption; this can be obtained by high voltage discharge in a flow at low or high atmospheric pressures [7,8].

For reforming with plasma support (pyrolysis, steam reforming, partial oxidization) it is preferable to utilize the high plasma flow rate generators: the pulsed systems and systems on the base of TORNADO discharge type [9] etc.

Thus, in work ethanol reformation at high temperature partial oxidation pyrolysis with pulsed plasma assist was investigated.

2. Experimental setup and analyse methods

The pyrolysis of ethanol after initial plasma-assisted ethanol reforming was studied by using the pulse DGCLW. The unit with pulse DGCLW was shown in Fig. 1. The installation consists of two main parts: 1) electric discharge plasma reactor, which generates a pulsed discharge in gas channel with liquid ethanol, and 2) pyrolytic reactor, which treats ethanol-air vapors mixed with products generated by plasma reactor, where (1) is a Teflon insulator around the steel pins, (2) are steel pins through which voltage is applied, (3) are copper electrodes, conical bottom and top cylinder, (4) is a discharge plasma zone between electrodes, (5) is a bubble between electrodes, (6) is a bubbling zone in the liquid, (7) is a work liquid (solution of 96% pure ethanol and distilled water), (8) are mixing inlet and outlet chamber, (9) is a steel pyrolytic chamber; (10) are electric heaters, (11) is a casing; (12) are thermocouples for temperature control, (13) is a glass vessel (0.5 l) for syngas collection.

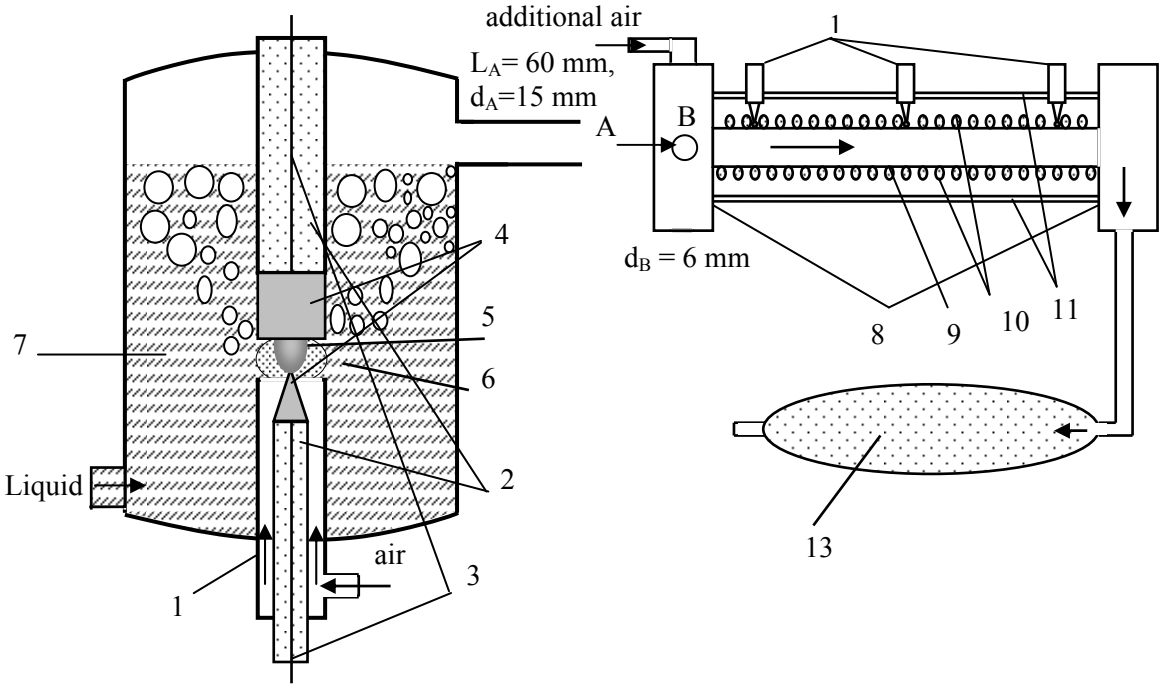


Fig. 1. Schematic of ethanol pyrolysis after plasma-assisted reforming of ethanol in the DGCLW.

For gas analyse gas chromatography (GS) by chromatograph 6890 N Agilent and masspectrography (MS) by monopolistic mass-spectrometer MX 7301 methods were used.

3. Results

Typical voltage and current oscillogrammes presented in Fig. 2:

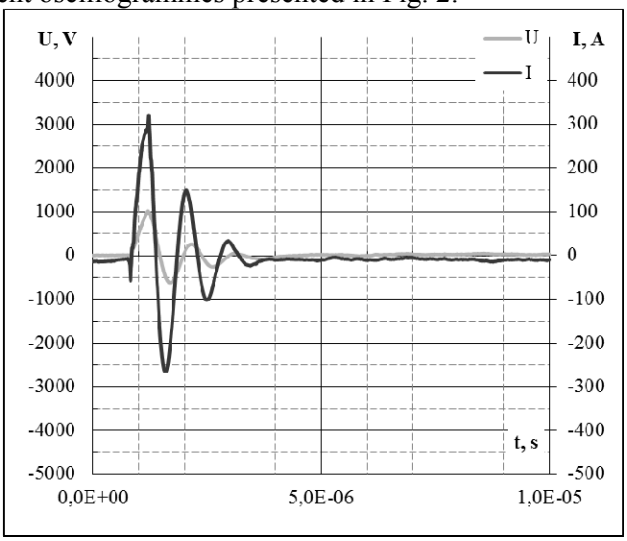


Fig. 2 Discharge current and voltage oscillogrammes

Here you can see that discharge current was about hundreds of Ampere when voltage was about thousand Volts and pulse duration was about few microseconds.

The ethanol postdischarge pyrolysis studies results after initial plasma-assisted ethanol reforming are presented in Figs. 3 — 4. The parameters in the system were following: pulsed discharge frequency of 400 Hz, air flow rate of 17-28 cm^3/s, time of treatment (measurements) up to 10 min (600 s); the temperature in the pyrolytic chamber varied from 0 to 870 K. Fig. 3 shows the H_2 intensity obtained by mass-spectrometry and the partial H_2 content in syngas products measured by

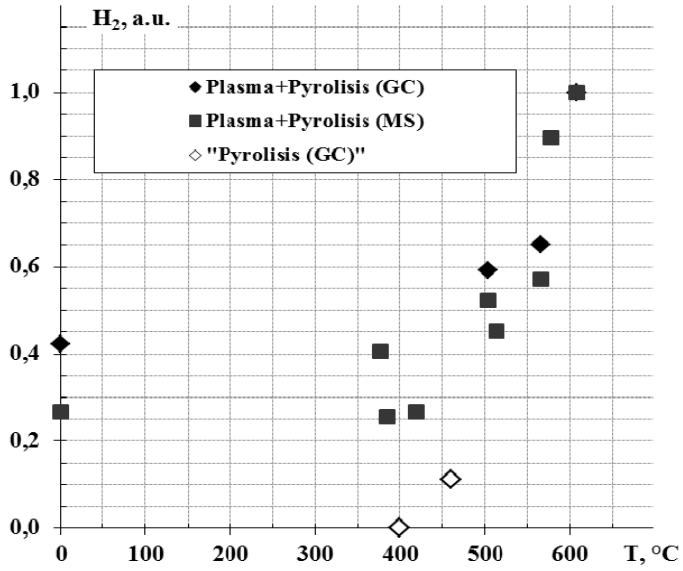


Fig. 3. H_2 intensity (MS) and partial H_2 content in syngas products (GC) after the ethanol reforming versus postdischarge pyrolitic chamber temperature

gas-chromatography after the treatment. One can see a good correlation between gas chromatography and mass-spectrometry data.

Fig. 4 shows the values of energy efficiency α in the system depending on temperature in the postdischarge pyrolytic chamber. It is seen an energy efficiency increase with increasing temperature. Some modes with the change of air flow modes (correspond to additional air supply into the pyrolytic chamber compared with an air supply in the discharge) have lower energy efficiency than the mode with a constant air flow because of varying partial output of isobutene ${}_iC_4H_{10}$.

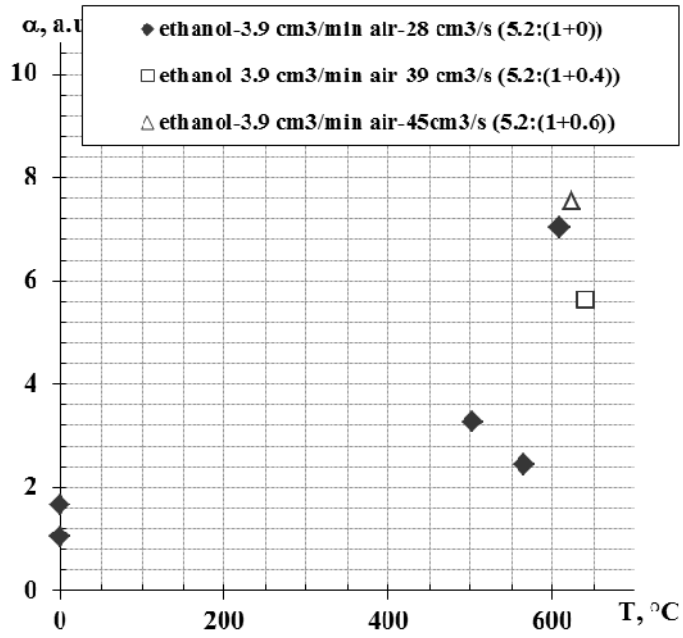


Fig. 4. Energy efficiency of ethanol reforming versus temperature in the postdischarge pyrolytic chamber.

Energy efficiency calculation formula:

$$\alpha = \frac{\sum_i Syngas_i \times LHV(Syngas_i)}{IPE}$$

In this formula LHV means syngas component low heat value when IPE means electrical power for plasma. The next Fig. 5 shows the rates of syngas generation in the system. One can conclude that the investigated combination (electric discharge+postdischarg pyrolysis) reforming of ethanol demonstrates smart efficiency of this approach.

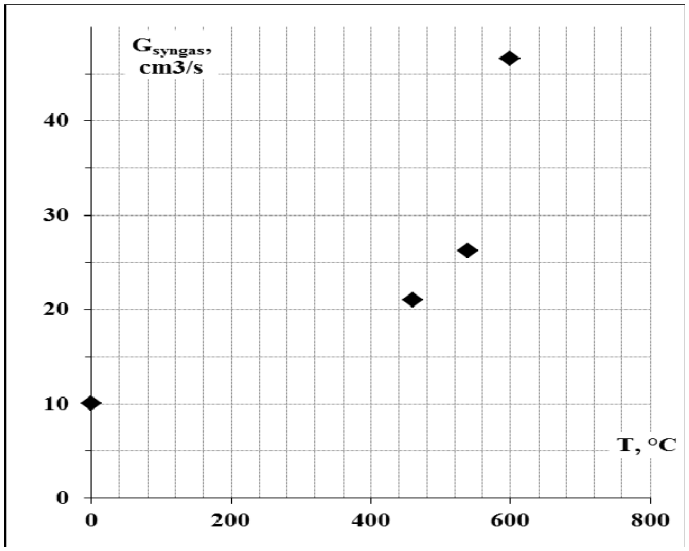


Fig. 5. The rate of syngas generation versus temperature in the pyrolytic chamber.

The next Fig. 6 shows LHV of syngas that depends from ethanol/oxygen-in-air molar rate due to stehiometric ethanol partial oxidation formula:

$$C_2H_5OH + {}^{1}/_{2}O_2 \rightarrow 3H_2\uparrow + 2CO\uparrow$$

So we can see the LHV enhancement when ethanol/oxygen-in-air molar rate moving to 2.

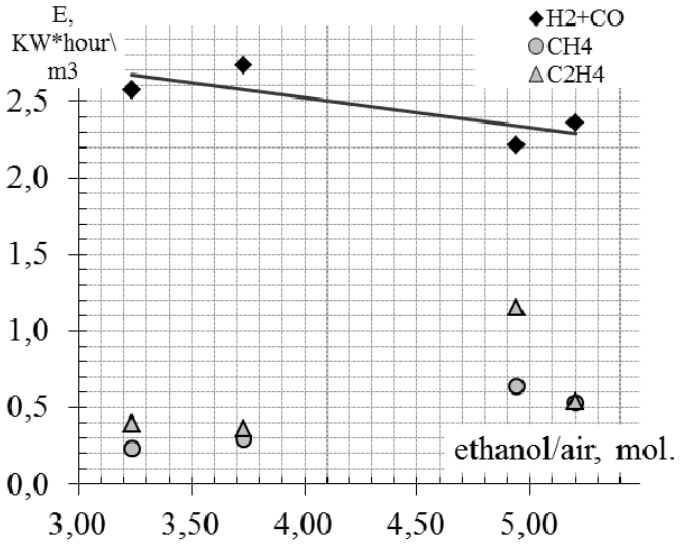


Fig. 6 Syngas components LHV versus ethanol/air molar rate

The next Fig. 7 demonstrated MS data of H_2 intensity for pulsed plasma assisted pyrolysis and only pyrolysis with ethanol/oxygen-in-air molar ratio 5.2:1. From this picture seems no synergism between pulsed plasma ethanol reforming and hightemperature partial oxidation pyrolysis processes. Pulsed plasma assist pyrolysis energy efficiency was sum of pulsed plasma ethanol reforming and only pyrolysis energy efficiencies. "D+P" markers show plasma assist pyrolysis process MS data when "P" shows only pyrolysis process MS data.

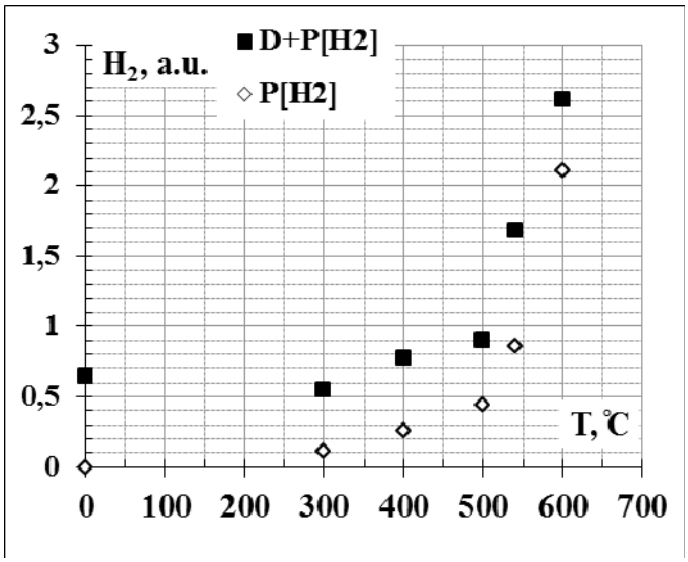


Fig. 7 H_2 intensity (MS) pulse plasma ethanol reforming and hightemperature partial oxidation pyrolysis versus postdischarge pyrolytic chamber temperature

4. Conclusions

1. The use of pyrolytic chamber allowed getting the energy efficiency value more than three time higher that such value for the similar plasma-liquid systems without pyrolytic chamber.
2. Process energy efficiency was the sum of pulsed plasma reforming and hightemperature partial oxidation pyrolysis processes.
3. The best energy efficiency is observed at the maximal pyrolytic chamber (600 °C).
4. The ethanol/oxygen molar ratio increasing decreases H_2+CO LHV and improves CH_4 LHV and C_2H_2 LHV.

5. References

[1] Warnatz J., Maas U., Dibble R.W. *Combustion. Physical and Chemical Fundamentals, Modeling and Simulations, Experiments, Pollutant Formation*. - Berlin: Springer, 2001.
[2] 18th World Hydrogen Energy Conf., 17-19 May 2010, Essen, Germany. http://www.whec2010.com
[3] Ni M., Leung D.Y.C., Leung M.K.H. A review on reforming bio-ethanol for hydrogen production // *Int. J. Hydrogen Energy*. - 2007. - **32**. - P. 3238-3247.
[4] Deminsky M., Jivotov V., Potapkin B., Rusanov V. Plasma-assisted production of hydrogen from hydrocarbons // *Pure Appl. Chem*. - 2002. - **74**, N 3. - P. 413-418.
[5] Bromberg L., Cohn D.R., Rabinovich A., Nadidi K., Alexeev N., Samokhin A. Plasma catalytic reforming of biofuels // MIT Plasma Sci. Fusion Center, Cambridge, MA, Report PSFC/JA-03-28. - 2003. Available http://www.psfc.mit.edu
[6] Petitpas G., Rollier J.-D., Darmon A., Gonzales-Aguilar J., Metkemeijer R., Fulcheri L. A comparative study of non-thermal plasma assisted reforming technologies // *Int. J. Hydrogen Energy*. - 2007. - **32**. - P. 2848-2867.
[7] Fridman A. *Plasma Chemistry*. – N.Y.: Cambridge Univ. Press, 2008.
[8] Fridman A., Kennedy L. *Plasma Physics & Engineering*. – N.Y.: Taylor & Francis, 2004.
[9] V. Chernyak, S. Olszewskii, O. Nedybalyuk, S. Sydoruk, V. Yukhymenko, I. Prysiazhnevych. Plasma reforming of ethanol in dynamic plasma-liquid systems//Proceedings of the ICCEU2010. – 2010.-Mugla University,Turkey-P. 295-300.

INFLUENCE OF ARGON CONCENTRATION ON THE PROCESSING GAS ON GLIDING ARC DISCHARGE'S POWER CONSUMPTION

H.D. Stryczewska, J. Diatczyk, G. Komarzyniec, T. Janowski

Institute of Electrical Engineering and Electrotechnologies,
Faculty of Electrical Engineering and Computer Science, Lublin University of Technology,
Nadbystrzycka 38-A, Lublin 20-618, Poland;
E-mail: h.stryczewska@pollub.pl

Power consumption of the gliding arc discharge plasma rector and its stable operation depends on many factors, among which the most important are: power supply system configuration, processing gas flow rate and its chemical composition. Trace gases admixtures can essentially influence the plasma chemistry process. Argon admixture to the processing gas stabilizes the discharge and makes possible to transfer larger power from the power supply system to the discharge. Correctly selected power supply system decides about plasma chemistry and technological application of this kind of nonthermal plasma.

1. Introduction

Atmospheric pressure low temperature plasmas are applied in many industrial processes. They are: treatment of flue gases emitted by industrial processes of combustion, painting and varnishing, wastes utilization, deodorization, disinfection and sterilization, material processing and new material manufacturing for application in microelectronics and nanotechnologies. Non-thermal and non-equilibrium plasma based methods allow treatment of organic materials, like rubber, fabrics, biomaterials and they are ecologically justified alternative for chemical ones [1].

In Poland the plasma processes, although investigated in research laboratories, are applied in industry at much less scale than in industrialized countries of Europe and all other the World [2]. Polish power industry is based on fossil fuels combustion that emits pollution in the form of sulphur and nitrogen oxides, soot and ashes, necessary to utilize. Plasma technologies can be the reasonable alternative for chemical, gypsum based wet methods, environmentally noxious, but still applied in power industrial practice.

Investigations in the field of industrial application of plasma chemical methods, conducted in many research centres and universities in Poland and abroad, are now concentrated on obtaining controllable plasma parameters and chemical reactions in large volume of treated gases [3, 4, 5, 6, 7]. Repeatability of the plasma-chemical process depends on stability of plasma parameters, which influence the proper chemical reaction path. The main parameters: are the chemical composition of the plasma gas, its pressure, flow rate, geometry of plasma reactor and electrical parameters of power system, i.e. value and form of supply voltage, power, and frequency.

Arc discharge can be the source of non-thermal and non-equilibrium plasma at some conditions of power supply system, reactor electrodes' geometry and gas flow rate [8, 9]. The gliding arc discharge plasma is the example of this kind of low temperature plasma that can be generated in multi-electrode reactors at atmospheric pressure.

Gliding arc reactor considerably differs from other non-thermal plasma sources. The resistance of inter-electrode gap depends on the kind of gas, its flow rate, degree of ionization and it also changes its value in wide range during the single operation cycle. Moreover, the discharge is displacing through electrodes periodically starting from the thermal short arc in the least electrode distance and increases its volume and length with the fast gas flow and electrodes' distance growth. Plasma generated in the gliding arc reactor is in non-equilibrium state: the temperature of "hot electrons" (T_e) is much higher then gas temperature (T_g) [10].

This kind of source of high energy electrons without heating the plasma gas in the whole volume of plasma reactor chamber is essential for typical plasma chemistry applications.

2. Experimental setup

In experiment we use three electrodes gliding arc plasma reactor with ignition electrode. Plasma is generated in the chamber of reactor in one of the processing gases: argon, nitrogen and air, at the atmospheric pressure. We use different gas flow rates – from 0.3 m^3/h to 3.5 m^3/h. The gas flow less then 0.5 m^3/h was used only for argon, in which discharge can be sustained at much lower voltage than in nitrogen and air. Figure 1 presents our laboratory stand. Reactor's geometry, diagnostic conditions and operation parameters of the investigated suppliers are gathered in table 1.

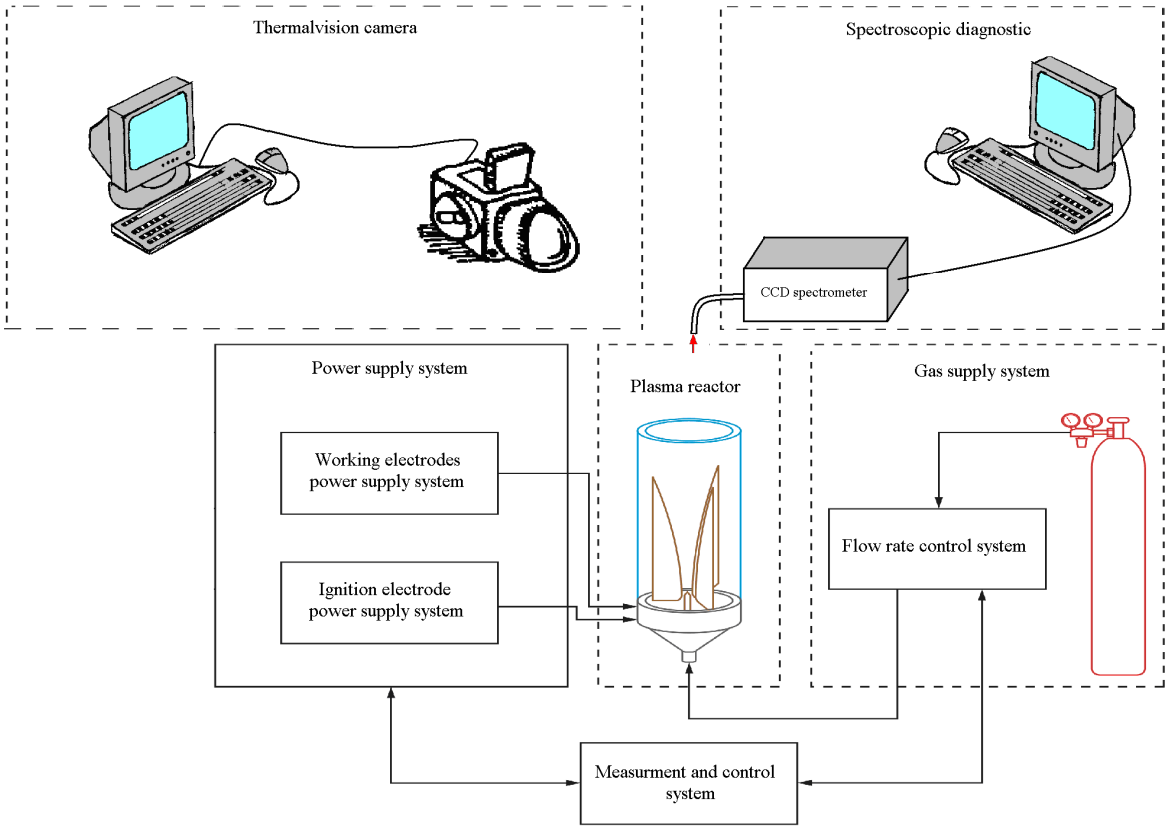


Fig. 1. Laboratory stand: plasma reactor – 3-eletrodes GA with ignition electrode; optical diagnostic – spectrometer: SOLAR TII SL40-2-3648-USB, calibration light sources: OceanOptics AR-1 and CAL-2000; flow rate controller – Bronkhorst High-Tech EL-Flow E-7000; thermovision camera – VIGO System V-20 ER005-10; oscilloscopes – Tektronix TDS-380 and TDS-2024B with Tektronix P2220 1x/10x and P6015A 1000x probes.

We use three power supply systems for gliding arc discharge plasma reactor. Each power supply system is based on three phase transformers with different limbs' material and different ignition systems. The first is the "integrated" power supply system (figure 2a) based on transformers with the soft external characteristic. Using non-linearity of magnetic circuit we can obtain the integration of basic functions of power supply in one device: preliminary ionization, 150 Hz ignition and sustaining the discharge during operation cycle, limitation of current value [11]. The second is the power supply system based on transformers with the amorphous limbs (figure 2b) with external 15 kHz ignition system. And the last is the power supply system based on five-limbs transformer with four winded cores in which the windings of external limbs are used to supply the 50 Hz ignition electrode (figure 3) [12].

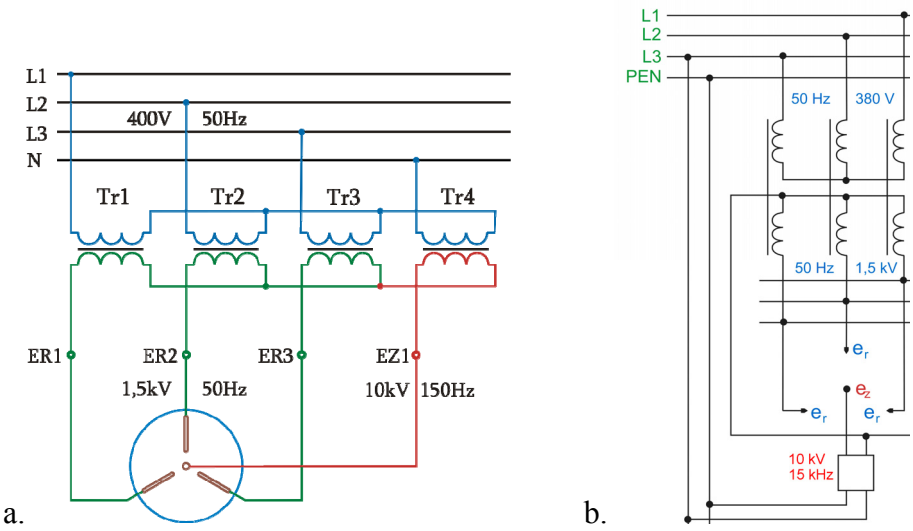


Fig. 2. Integrated power supply system.

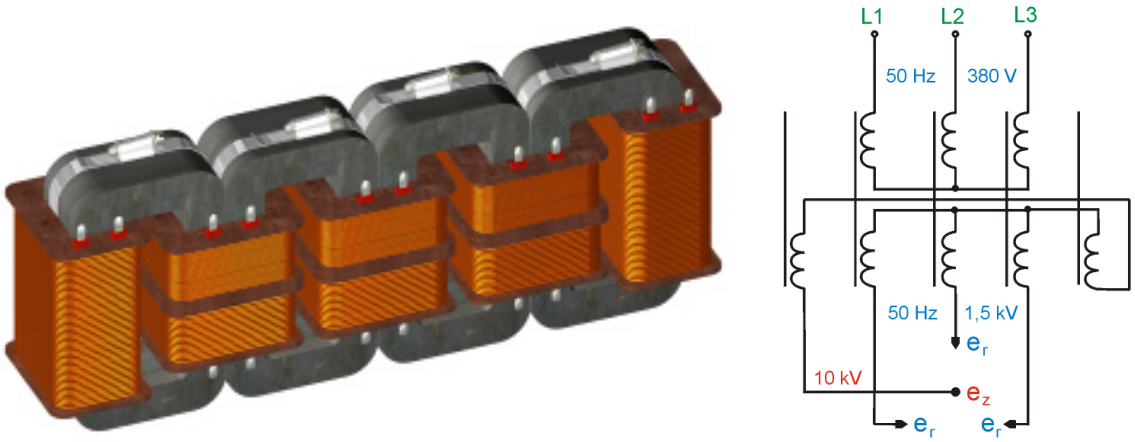


Fig. 3. Power supply system based on five-limbs transformer.

Tab. 1. Working parameters of the gliding arc plasma reactor.

Discharge chamber geometry	
chamber diameter	80 mm
electrode length	141 mm
electrode distance in the ignition area	6 mm
electrode distance in the extinction area	35 mm
Gas parameters	
process gases	argon, air, nitrogen
gas flow rates	0.3 – 3.5 m^3/h
Power supply system parameters	
inter-electrode voltage	400 – 1500 V
electrode current	1.0 – 3.5 A
ignition voltage frequency	50 Hz, 150 Hz, 15 kHz

3. Results and discussion

Chemical composition of the processing gas together with gas flow rate growth causes the changes of power transferred to the gliding arc plasma reactor. Power consumption as a function of gas flow rate is presented on figure 4.

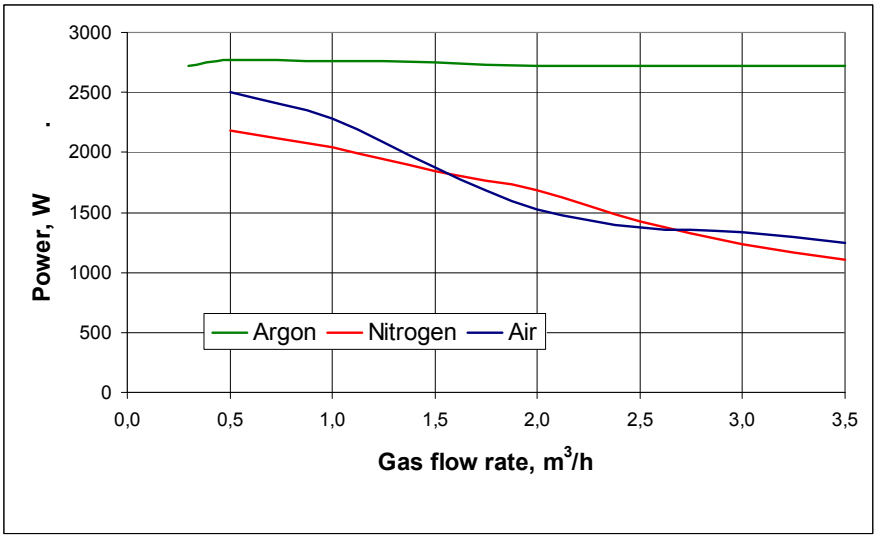


Fig. 4. Power consumption for different gases and flow rates (power supply system based on transformer with amorphous limbs, primary windings voltage: 130 V).

In case of argon as a processing gas, we obtained a linear power consumption characteristic. Otherwise, for nitrogen and air, the power consumption decreases with gas flow rate growth.
For the same power supply system we obtained power consumption for various argon concentration in processing gas (figure 5).

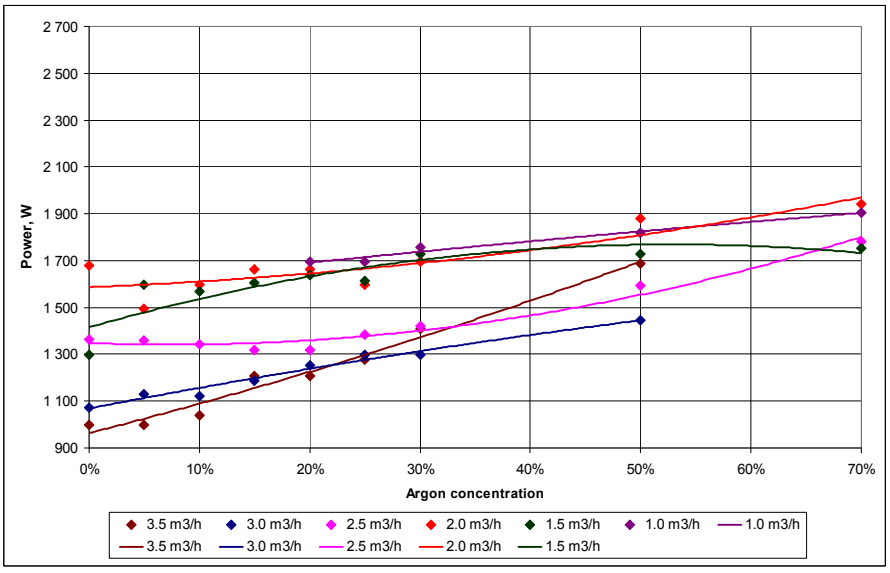


Fig. 5. Power consumption for various argon concentration in working gas (power supply system based on transformer with amorphous limbs, primary windings voltage: 130 V, processing gas: nitrogen).

Increase of argon concentration in processing gas enlarge power consumption and stabilizes discharge, that is critical for low gas flow rates.
For integrated power supply system we obtained ignition at lower voltage, but for argon concentration in processing gas less then 30%, we observed discharge instability (figure 6).

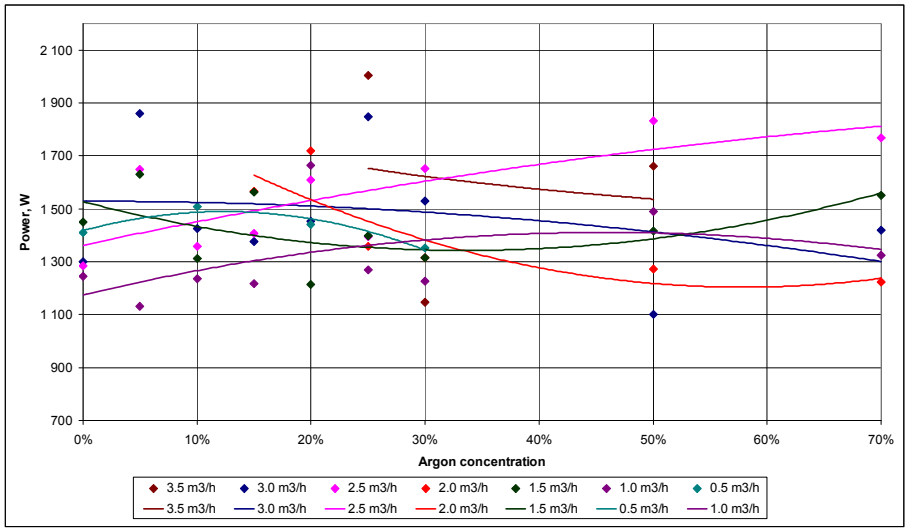


Fig. 6. Power consumption for various argon concentration in working gas (integrated power supply system, primary windings voltage: 230 V, processing gas: nitrogen).

We also observed close to linear characteristics of power consumption for different gas flow rates (in case of argon concentration in processing gas is greater then 30%).
For power supply system based on five-limbs transformer obtained results show, that power transferred to discharge increases with the gas flow rate growth. Higher argon concentration in processing gas didn't affect discharge power and its only stabilize the discharge (figure 7).

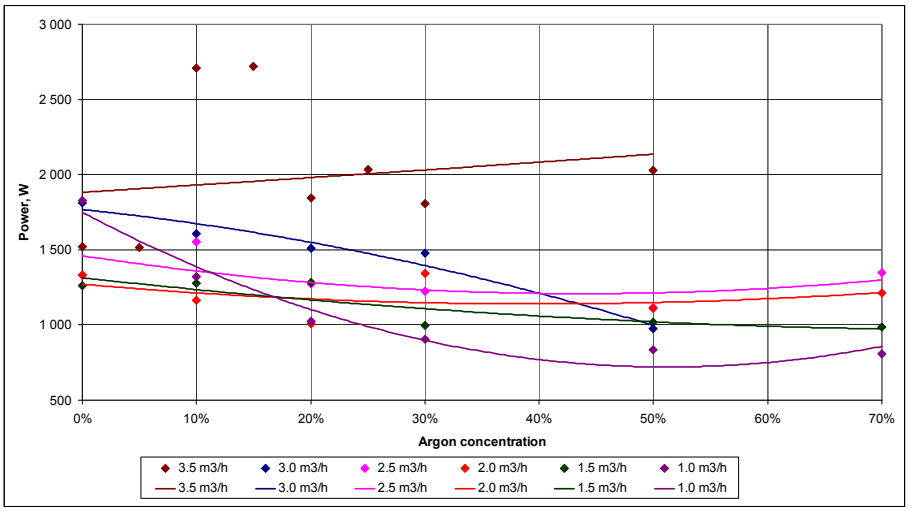


Fig. 7. Power consumption for various argon concentration in working gas (power supply system based on five-limbs transformer, primary windings voltage:110 V, processing gas: nitrogen).

We also measured the changes of discharge current for different power supply systems and various argon concentrations in processing gas (figure 8). For all power supply systems we observed increase the discharge current with the increasing of argon concentration in working gas.

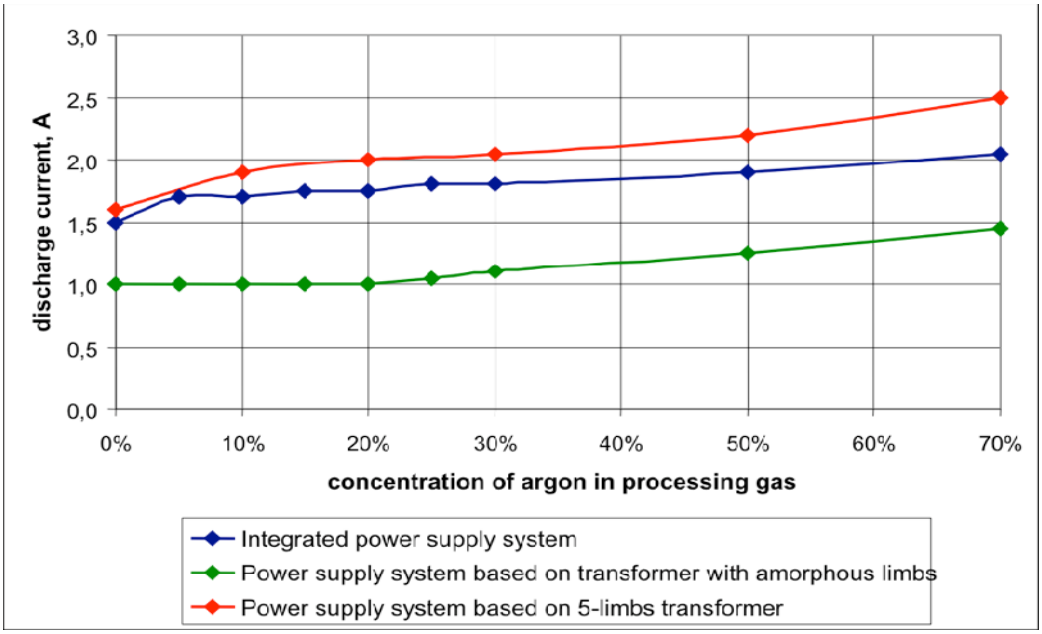


Fig. 8. Discharge current as a function of argon concentration in processing gas for different power supply systems.

Plasma-chemical processes request controllable parameters of plasma generated in the reactors with gliding arc discharge. Repeatability of the process depends on stability of plasma parameters, which influence the proper chemical reaction path. The main parameters: are the chemical composition of the processing gas, its pressure, flow rate, electrons and heavy particles temperature, geometry of plasma reactor and electrical parameters of power system, i.e. value and form of supply voltage, power, and frequency. Properly selected power supply system together with chemical composition and flow rate of the processing gas allows reaching the request plasma parameters.

Power transferred to discharge primarily depends on power supply system configuration, and especially on the internal reactance of transformers supplying the working electrodes of GA. Power transferred to the chemical process can be controlled by using different power supply systems. On the other hand, for all power supply systems maximum voltage value is limited by the minimal voltage required to breakdown which depends on chemical composition of processing gas. So, the controllable composition of the processing gas can be used to change the power transferred to discharge. For the constant maximum voltage value we can control the current value by power supply system internal reactance or by argon concentration in the processing gas. An increase the current value causes increasing the power transferred to discharge, and simultaneously decreasing the energy efficiency because generated plasma becomes more thermal. Higher gas temperature also affects the faster thermal destruction of working electrodes.

4. Conclusions

Power consumption of the gliding arc discharge plasma rector and its stable operation depends on many factors, among which the most important are: power supply system configuration [10, 13, 14], processing gas flow rate and its chemical composition. Trace gases admixtures can essentially influence the plasma chemistry process. Argon admixture to the processing gas stabilizes the discharge and makes possible to transfer larger power from the power supply system to the discharge.

Correctly selected power supply system decides about plasma chemistry and technological application of this kind of nonthermal plasma.

5. References

[1] Addou A, Ghezzar R.M., Abdelmalek F., Brisset J.L., *Proceedings of ISPC-17*, (2005), CD.

[2] Sawicki A., Krouchinin A.M. “Modeling of electrical and thermal processes in stream

plasmatrons", *IEEE Transactions on Plasma Science*, vol. 28, no 1, (2000), pp. 242-247.
[3] Heeren T., Ueno T., Wang D., Namahira T., Katsuki S., Akiyama H. "Novel Dual Marx Generator for Microplasma Applications", *IEEE Transaction on Plasma Science*, vol. 33, no 4, (2005), pp. 1205-1209.
[4] Rutberg Ph.G., Safronov A.A., Popov S.D., Surov A.V., Nakonechny Gh.V. "Investigation of voltage and current variations in a multiphase AC electric arc system", *12th International Congress on Plasma Physics*, 25-29 October, Nice (France), (2004)
[5] Wang F, Kuthi A., Gundersen M.A. "Compact High Repetition Rate Pseudospark Pulse Generator" ,*IEEE Transaction on Plasma Science*, vol. 33, no 4, (2005), pp. 1177-1181.
[6] Xia W., Fulcheri L., Gonzalez-Aguilar J., Hui L., Gruenberger T.M. "Characterization of a 3-Phase a.c. Free Burning Arc Plasma", *Plasma Science & Technology*, vol. 8, no 2, (2006), pp. 156-163.
[7] Lesueur H., Czernichowski A., Chapelle J., French Patent 2639172, (1990).
[8] Czernichowski A. "Gliding arc: Applications to engineering and environment control", *Pure Appl. Chem.*, vol. 66, no 6, (1994), pp. 1301-1310.
[9] Diatczyk J., Komarzyniec G., Stryczewska H.D. "Determination of the Gliding Arc Discharge Critical Length", *1st Central European Symposium on Plasma Chemistry*, Gdańsk, May 28 – 31, (2006), pp. 27-29.
[10] Stryczewska H.D., Komarzyniec G., Diatczyk J. "Technological Features of Gliding Arc Discharge Plasma", *Przegląd Elektrotechniczny* (*Polish Electrical Review*) no 7, (2008), pp. 170-173.
[11] Stryczewska H.D., Technologie plazmowe w energetyce i inżynierii środowiska, *monograph, Komitet Elektrotechniki PAN*, Lublin, (2009), pp. 106-124.
[12] Komarzyniec G. „Analiza pracy transformatora pięciokolumnowego w układzie zasilania łukowego reaktora plazmowego", *PhD Thesis*, Lublin University of Technology, Lublin, (2008).
[13] Stryczewska H.D., Diatczyk J., Komarzyniec G. „The influence of power source parameters on the gliding arc characteristics", *Przegląd Elektrotechniczny* (*Polish Electrical Review*), no 7, (2008), pp. 60-63.
[14] Stryczewska H.D.: Układ zasilania reaktorów plazmy nietermicznej, Patent, P 317110, 2000.